European Joint Programme
on Radioactive Waste Management

Deliverable D6.7:

Gas transport mechanisms: diffusion, retention and advection processes. Task 2. Final technical report

Work Package 6

This project has received funding from the European Union's Horizon 2020
research and innovation programme under grant agreement N° 847593

https://www.ejp-eurad.eu

Document information

Project Acronym	**EURAD**
Project Title	**European Joint Programme on Radioactive Waste Management**
Project Type	**Deliverable**
EC grant agreement No.	**847593**
Project starting / end date	**01/06/2019–30/05/2024**
Work Package No.	**6**
Work Package Title	**Mechanistic understanding of gas transport in clay materials**
Work Package Acronym	**EURAD-GAS**
Deliverable No.	**D6.7**
Deliverable Title	**Gas transport mechanisms: diffusion, retention and advection processes. Task 2. Final technical report**
Lead Beneficiary	**SCK CEN and UKRI-BGS**
Contractual Delivery Date	**29/02/2024**
Actual Delivery Date	**30/05/2024**
Type	**Deliverable**
Dissemination level	**PU**
Authors	**Elke Jacops and Olaf Kolditz (editors)**
Contributors	**Experimental team: Elke Jacops, Aadithya Gowrishankar, Li Yu, Guangjing Chen, Anneleen Vanleeuw, Jon Harrington, Robert Cuss, Caroline Graham, Katherine Daniels, Andrew Wiseall, Elena Tamayo-Mas, Qian Zhang, Cameron Fletcher, Elliot Bird, Philip Neep, Simon Kemp, Lorraine Field, Laurent Truche, Magdalena Dymitrowska, Pedro L. Martín, José M. Barcala, Guillermo García-Herrera, Marketa Kucerova, Jan Smutek, Richard Giot, Rafael Chaves-Deptulski, Kui Liu** **Modelling team: Nathan Amrofel, Victoria Burlaka, Sergey V. Churakov, Frédéric Collin, Gilles Corman, Anne-Catherine Dieudonné, Magdalena Dymitrovska, Richard Giot, Fabrice Golfier, Sylvie Granet, Norbert Grunwald, Alireza Hassanzadegan, Zhaojiang Huang, Olaf Kolditz, Joaquín Liaudat, Christian Müller, Sebastia Olivella, Michael Pitz, Jerry-Peprah Owusu, Eric Simo, Alexandru Tatomir, Anne-Julie Tinet, Erdem Toprak, Philip J. Vardon, Gesa Ziefle**

To be cited as

Elke Jacops and Olaf Kolditz (editors) (2024). Gas transport mechanisms: diffusion, retention and advection processes. Task 2. Final technical report. Final version as of 30/05/2024 of deliverable D6.7 of the HORIZON 2020 project EURAD. EC Grant agreement N˚ 847593.

Disclaimer

authors' view.

Acknowledgement

This document is a deliverable of the European Joint Programme on Radioactive Waste Management (EURAD). EURAD has received funding from the European Union's Horizon 2020 research and innovation programme under grant agreement N° 847593.

Status of deliverable		
	By	Date
Delivered (Lead beneficiary)	SCK CEN	01/03/2024
Verified (WP Leader)	ONDRAF/NIRAS Séverine Levasseur	05/03/2024 22/05/2024
Reviewed (Reviewers)	Paul Marschall (Nagra) Simon Norris (NWS)	28/04/2024 04/04/2024
Approved (PMO)	Bharti Reddy (Nuclear Waste Services	28/05/2024
Submitted to EC (Coordinator)	Coordinator (Andra)	30/05/2024

Executive summary

This report summarises the final results of the task 2 of the WP GAS of EURAD (Mechanical understanding of gas transport in clay materials). Task 2 “Transport mechanisms” focused on the characterisation of the main gas transport mechanisms which will take place in a disposal system in the post-closure phase. Subtask 2.1 was dedicated to gas diffusion and retardation processes at high level of water saturation, while Subtask 2.2 dealed with advection processes (displacement vs. dilation).

Reported experimental and modelling progresses on gas diffusion and sorption (**Subtask 2.1**) comprise:

Quantification of H2 uptake by clays (Boom Clay and Callovo-Oxfordian claystone) by ISTerre. Upon heating of Boom Clay and Callovo-Oxfordian Clay, gases such as CO_2, H_2 and CH_4 are generated. The assessed hydrogen update by dry COx at 25℃ and 100 bar is 0.02 wt%.

Determination of the diffusion coefficient in synthetic and natural clay materials (UKRI-BGS). BGS has successfully measured the permeability and diffusion coefficients for Boom Clay, a sample of the Eigenbilzen Sand under two different stress regimes, and a range of synthetic samples manufactured with different mineralogical compositions, all adding to the knowledge pool for these materials. Diffusion of helium was also shown to occur preferentially along bedding planes with approximately 60% of the diffusional capacity of Boom Clay moving parallel to bedding (which was a key research aim for the project). However, of greater importance was the observed coupling between diffusion and intrinsic permeability which was very clear in the synthetic sample data. Examining the data as a whole suggests a fundamental relationship exists between permeability and diffusivity, and when plotted in logarithmic scale the Boom Clay and Eigenbizen sand fall on a common projection. If correct, such relationships could be used to predict diffusivity across a range of material and permeability scales. However, before this can occur substantially more experimental evidence is required to improve/disprove these correlations.

Diffusion of gases in unsaturated clay (SCK CEN). SCK CEN developed a set-up to measure diffusion of gases (He and Ar) in unsaturated synthetic clay samples. So far, diffusion was measured in two sample types, containing different amounts of clay, silt and sand, at saturation degrees between 73 and 100%. Results showed that diffusivity increased only slightly, about 20% when desaturating the sample towards 73%. As a general conclusion and based on the data collected so far, one can state that the rate of gas transport is marginally increased in partially saturated clay-based materials as opposed to rates of ionic tracers, which decrease with desaturation. It is recommended to study also lower saturation degree and samples with variable clay content to improve process understanding.

In situ diffusion experiments with Neon (SCK CEN). The NEMESIS experiment (Neon diffusion in MEgaS In Situ) was started in September 2023 and will run for at least 5 years in the HADES URL (experiment performed in collaboration with ONDRAF/NIRAS and EURIDICE). During the preparation phase, a validation test (3D in-diffusion experiment with helium) was performed in 2 filters (D8 and A21) which are not involved in the final NEMESIS experiment. Based on the helium pressure loss due to in-diffusion, and by using the newly developed model, the fitted diffusion coefficient of, for instance, filter A21 was estimated at 80% of the value measured in the lab which is considered to be a good result.

Characterization of the pore networks of clay materials (IRSN). The aim was to study water-air distribution during onset of desaturation in argillaceous rock, in order to confirm whether small scale samples can be considered homogeneous in desaturation, an assumption which is often made for further evaluation of unsaturated transport properties (suction, diffusion, ...). For this purpose, X-ray Synchrotron imaging and lab-based CT facilities were used to study the host rock candidates (Toarcian, Sand of Eigenbilzen) at a sub-micron scale. Porosity profile observations indicate that desaturation takes place in the largest pores first, and may be homogeneous within sub-centimeter size samples, even when close to the full water saturation.

Modelling gas diffusion in saturated and unsaturated conditions (PSI). PSI investigated the transport mechanisms of gas in porous clay materials and explored the relationships between the structural properties of the clay minerals and the mobility of small gaseous molecules. Specifically, it focused on smectite-rich clay rocks. Molecular dynamics simulations have been employed to observe fluid behavior at the nanoscale, and a methodology has been developed to upscale the results to a pore scale using pore-scale simulations. Findings revealed that the diffusion of gases is significantly influenced by three key factors: the mineralogy of the confinement (specifically, the type of clay), the size of the clay nanopore, and the hydrodynamic radius of the gas molecule (which indicates the gas type). Simulation results for unsaturated clay suggest that the gas-diffusive behavior in this system exhibits a transition regime characterized by a combination of molecular diffusion and Knudsen diffusion. As a result, Fick's law, which is commonly used to describe diffusion processes, is not suitable in this case. Our findings highlighted that gas diffusion is influenced by multiple factors, including the thickness of the water films, the mean free path of the gas molecules, and the average available pore width.

Modelling gas diffusion in saturated conditions (BGR). Diffusion processes of gas dissolved in a pore liquid are characterized by multicomponent effects. In the framework of EURAD-GAS, diffusion effects are captured, for instance, by using the TH2M model OpenGeoSys 6 (OGS6). The TH2M model was validated against the double through-diffusion experiment performed by SCK CEN, which is characterized by full saturation of the sample (modeling single-phase flow), no deformation, isothermal conditions and no liquid pressure gradient (advection negligible). The diffusion processes of the components were captured by multiple superimposed TH2M runs (validated with a 4-component formulation implemented in Python). Over all, the experimental and numerical results matched very well, thus increasing confidence in the numerical model.

From an advection point of view (**Subtask 2.2**), reported experimental and modelling progresses comprise:

Long term gas injection under controlled loading (SCK CEN). SCK CEN, in collaboration with ONDRAF/NIRAS, performed a long term gas injection experiment with one Boom Clay sample. This was performed under isostatic conditions at gas pressures slightly inferior to the confinement pressure. Together with BGS, the diffusion coefficients of helium and CH_4 were measured and the test enabled to show that (1) only minor differences are observed when different loading conditions (constant volume versus isotropic loading) are considered and (2) tests performed with pure gas or dissolved gas provide same results. No conclusions can be drawn yet, however, regarding the limits of diffusive transport of dissolved gas and a possible transition to free gas flow during a long gas injection time as the results are not clear and experiments need to be repeated, considering some improvements such as (1) the CT scanning of the sample prior to use, (2) the inclusion of all connections inside the isostatic cell, (3) the use of CH_4 instead of He and (4) the use of a detailed standard protocol for this type of test.

Triaxial tests (UKRI-BGS). BGS performed four triaxial gas injection experiments on Boom Clay and Callovo-Oxfordian claystone at two different confining pressures in order to determine whether stress controls the transition from visco-capillary flow to dilatant pathway formation. The apparatus allowed the measurement of radial strains. All tests showed that (1) visco-capillary flow was not observed during gas injection with dilatancy controlled flow the only mechanism observed; (2) the control of the gas entry pressure was the minimum principal stress and (3) the dilatant pathways are not fracture related. Significant differences between tests of different geometry (small injection filters versus full-face filters) were observed and thus, the direct comparison between tests performed in different laboratories might be controversial as a result of the filter geometry selection. No conclusive conclusions can be drawn yet regarding (1) the role of stress as a control of the physics of gas flow and whether (2) there is a transition from visco-capillary flow to dilatant pathway formation.

Lasgit (UKRI-BGS). Lasgit was a full-scale demonstration experiment operated by The Swedish Nuclear Fuel and Waste Management Company (SKB) at the Äspö Hard Rock Laboratory at a depth of 420 m, with the two main objectives of providing quantitative data to improve process understanding and validating modelling approaches used in performance assessment. All observations from Lasgit support the idea that gas is mainly transported through dilatant pathways (and diffusion), which is consistent with observations made within the laboratory. Full-scale observations showed that (1) the movement of gas occurred at a pressure very close to the local total stress; (2) no signs of localised consolidation of the bentonite were observed, (3) the measured peak gas pressures should not lead to any mechanical damage to the buffer or to other barrier components in the repository, (4) peak gas pressure is linked to the hydraulic permeability of the buffer and the ease at which gas can exit a deposition hole, (5) gas is transported through a small number of time-dependent dilatant pathways, (6) no desaturation of the bentonite buffer as a result of gas transport was observed; (7) over the timescale of the project, pathway closure was only partially successful in the absence of injected water; (8) the gas pathways are expected to slowly close at a finite “shut-in” pressure; (9) gas migration through a bentonite is highly unlikely to alter the favourable hydromechanical properties of the barrier and (10) the impact of emplaced and long-lived persistent heterogeneities within the bentonite on gas pressure remains unclear.

Gas flow analysis using a fracture visualisation approach (UKRI-BGS). A series of 25 experiments using the Fracture Visualization Rig has been performed by the Transport Properties Research Laboratory (UKRI-BGS) to answer fundamental questions about gas flow in clay-rich rocks. These experiments have confirmed that (1) multiple pathways form at the same time, and these vary in size and distribution within the sample; (2) the velocity of pathway growth varies between pathways, with some pathways migrating quicker and others at a slow rate; (3) the distribution of pathways is stochastic; (4) the walls of a dilatant pathway elastically compress to accommodate the pathway and (5) self-sealing is observed. The experimental programme has not yet been completed. Thus, further experiments can be conducted to look at other specific problems, such as salinity, stress, layering of rocks or the influence of voids.

Laboratory scale testing of synthetic materials (UKRI-BGS). BGS has carried out six different tests to examine the role of clay content (in relation to other constituents) on the favoured gas advection mechanism and the resulting distribution of transported gas within the flow regimes. A sample compaction procedure has been developed to create synthetic compacted clay samples with a controlled mineralogy. These samples have then been subjected to gas injection experiments in a constant volume cell after an initial rehydration and swelling phase. A heavily instrumented and novel test cell has been designed and constructed and hence, the mechanical response of the clay has been monitored in detail to provide meaningful insight into the mechanisms and distribution of gas flow during these experiments. The analysis of these tests leads to the following key learning points: (1) as expected, swelling pressure is correlated with clay content in engineered clays and anti-correlated with sand+silt fraction in synthetic mixtures; (2) at fully saturated conditions, pathway dilatancy can occur at lower clay contents than previously thought; and (3) clay content appears to play a significant role regarding the stress field behaviour and to directly relate to gas entry pressure. Two different metrics have been defined to provide some information regarding the increase and decrease in clay permeability as pathways open and close. This should allow a substantial improvement in our capacity to simulate this complex process.

Characterisation of advective gas transport in FEBEX bentonite (CIEMAT). An experimental programme aimed at discerning the mechanisms controlling advective gas flow in the Spanish reference barrier material (FEBEX) has been undertaken by CIEMAT. All these tests have been performed on initially fully saturated FEBEX bentonite and in them, two gas transport mechanisms have been identified, depending on the gas pressure level. Below a value referred as gas entry pressure, the predominant transport mechanism is the diffusion in porewater. Once this gas entry pressure is exceeded, gas flows through existing porosity or via self-created and stress-induced pathways. Gas flow is then localised and little water is displaced. At the tested dry densities (1.5, 1.6 and 1.7 g/cm^3), gas flow seems to occur by the formation and propagation of dilatant pathways. Therefore, this knowledge needs to be included into the Thermal Hydrological and Mechanical (THM) modelling and thus, discrete pathways approaches could probably reproduce better the experimentally-observed breakthrough phenomena.

Gas entry and flow through a bentonite barrier (CTU, SÚRAO). An experimental programme has been undertaken by the Czech consortium with the objective of investigating the gas breakthrough behaviour of samples of Czech Ca-Mg BCV bentonite with varying dry densities. Although this material was already known to behave similarly to bentonites tested in other countries (e.g., Mx-80, GMZ) in terms of gas permeability, tests in this experimental design have shown that (1) the formation of dilatant pathways via gas-exerted pressure occurs following the exceeding of the measured axial total stress, which is related to the swelling pressure of the material; and (2) the source of gas injection exerts no influence on the breakthrough pressure value.

Gas breakthrough experiments on different types of bentonites (ÚJV, SÚRAO). The aim of the ÚJV experimental research is to conduct and subsequently evaluate the gas pressure testing of three types of bentonites (BCV, Mx-80 and Kunipia) in order to compare Czech BCV bentonite with the bentonite that is most commonly used abroad (Mx-80). Multiple gas injection tests using a relatively simple apparatus were performed on samples of different dry densities (1400 kg/m^3 and 1600 kg/m^3). The experiments confirmed the existing knowledge of gas flow through dilatant pathways: in general, BCV bentonite does not differ from the reference material (Mx-80) in terms of gas flow processes and gas breakthrough occurs at pressure levels lying within the theoretical swelling pressure range. Further knowledge acquired within the experimental programme concerns (1) the acquisition of data from the direct comparison of the behaviour of hydrogen and air, from which it was determined that the type of gas has no effect on the gas breakthrough pressure values; and (2) the demonstration of the re-sealing capability and integrity of a BCV bentonite barrier.

Visualization of multiphase flow in nanopores network (IC2MP, Univ. Poitiers, CNRS). A gas injection test on a sample of small size inside a miniaturised and optimised triaxial cell is intended to be performed by CNRS-IC2MP in order to provide an insight into the micro-structural changes inside the claystone (COx) due to gas entry and propagation in the porous network. This test is intended to be performed by the end of the year 2023 (assuming different injection pressures but the same mechanical loading) and hence, no experimental results are yet available.

A coupled Pneumo-Hydro-Mechanical (PHM) Finite Element model within LAGAMINE (TU Delft). The TU Delft team has developed a numerical model capable of simulating gas migration in water saturated clay. This model is able to simultaneously reproduce, within a unified framework, the diffusion and advection of dissolved gas and the displacement of the liquid phase filling the clay pores by the invading gas, together with the localised gas flow along macroscopic cracks induced and propagated by the gas pressure. To do so, this model extends a pre-existing two-phase two-species hydro-mechanical model for bulk porous media by means of zero-thickness interface elements. For this purpose, a new PHM triple-node zero-thickness interface element has been developed. Main progresses comprise: (1) the explicit representation of the PHM behaviour of sample–device interfaces; (2) the initiation and propagation of macroscopic gas cracks inside the water saturated bulk material; (3) the modification of the flow patterns inside the bulk material as a consequence of the localised flows along the cracks; (4) the sharp drop of the gas injection pressure when the gas crack reaches the back-pressure filter, followed by some fluctuations before reaching a steady state; and (5) the closure (self-sealing) of the gas cracks when the gas injection ceases. The performance of this approach has been validated with synthetic benchmark examples. However, further developments are still necessary to allow a quantitative validation of the model, such as the implementation of the pathway dilation mechanism, the introduction of variability/heterogeneity of the material properties, and extension to a three-dimensional setting.

Conceptualisation of the gas transport processes taking place in the post-closure phase within LAGAMINE (University of Liège). A multi-scale modelling approach has been adopted by the University of Liège to simulate the gas transport mechanisms in low permeable sound clay rocks as well as their accompanied hydro-mechanical processes. This model takes into account the role played by the rock structure at a micro-level in the initiation and propagation of such a macro-scale gas transport mechanism. Based on experimental data, a suitable Representative Element Volume has been defined to idealise the material microstructure with different families of discontinuities, and an assembly of tubes substituting the flow behaviour of the porous matrix blocks. The transition between the two scales is achieved by means of homogenisation and localisation techniques. The approach has been implemented in the Finite Element code LAGAMINE and first applied to a lab-scale case study. Then, it has been extended to a more general and random configuration, which has been up-scaled in order to evaluate the possibility to extrapolate the lab observations of gas-induced damage processes on a larger scale. Simulations highlight two essential aspects in the development of preferential pathways: (1) the more continuous the connectivity between the disturbed planes is, the faster the gas flow through this discrete zone; and (2) these links between the planes of weakness need to be repeated regularly to ensure a rapid gas propagation at a larger scale. Further developments are, however, still required (1) to allow them to be predictive, as some model parameters are tuned in order to mimic the experimental data; (2) to up-scale the laboratory-scale results to the in situ-scale behaviour, since the microstructural heterogeneity of some clay properties (stiffness and strength) and the connectivity of the macro-pores and micro-fractures cannot be easily defined at a large scale; and (3) to reduce computational costs associated to up-scaled meshes and geometries.

Benchmarking of a new non-isothermal two-phase flow in deformable porous media approach within the open-source simulator OpenGeoSys (BGE, UFZ and BGR). The BGE in collaboration with the UFZ and the BGR has further developed an approach to simulate non-isothermal two-phase–two-component flow in deformable porous media (TH2M). Different gas permeability models have been tested and implemented: (1) a gas pressure dependent permeability model, which assumes that permeability changes increase significantly when a specific gas pressure threshold is exceeded with micro-cracks being formed through the development of a percolation network; (2) a strain dependent permeability model, which assumes that gas permeability depends on both the total volumetric elastic strain and an equivalent plastic strain, and describes an increase of permeability as soon as a plastic failure occurs; (3) a failure index permeability model, which describes intrinsic permeability as a function of a Mohr-Coulomb failure index; and (4) an embedded fracture permeability model, where the clay is supposed to be an idealised setting with fractures, whose parameters are employed to define the intrinsic permeability. This OGS approach has been validated via a benchmark test, originally proposed by the French National Radioactive Waste Management Agency (ANDRA) as part of the MoMaS project and successfully captures the transition from a single-phase to a two-phase gas transport.

Direct Numerical Simulations (DNS) of multiphase fluid transport through deformable nanoporous materials (IRSN and CNRS-Georessources). IRSN and CNRS-Georessources have conducted numerical simulations of multiphase flow through deformable materials using DNS modelling approaches, which require the description of both (1) the physical phenomena at the pore scale and (2) the pore space. On the one hand, a DNS of a dilatancy flow has been performed using an extended Smoothed Particle Hydrodynamics (SPH) code. This method can be successfully employed to simulate (1) the explicit interaction of a pressurised fluid through a deformable elastic media and (2) hydrofracturing if damage is assumed. On the other hand, a DNS of flow and transport phenomena using the mesoscopic lattice Boltzmann method (LBM) has been developed. These two models (SPH and LBM) have been used to assess different processes regarding gas flow, including evaporation (considering Kelvin effect), visco-capillary flow, dilatant flow and fracturing. Both of them have proved to be feasible in terms of numerical stability for adequate physical parameters. It has also been observed that FIB-SEM (Focused Ion Beam Scanning Electron Microscope) images can be used with DNS to compute upscaled properties. However, there are still limitations in computational capacity to describe (1) domain sizes smaller than the REV or (2) multiscale heterogeneities. It has also been proved that the Kelvin effect is a significant phenomenon highly impacting the breakthrough time and breakthrough saturation that needs to be accounted for.

Hydro-mechanical simulations of breakthrough tests on FEBEX material using CODE_BRIGHT (UPC). A standard two-phase flow model has been used to simulate gas breakthrough tests on FEBEX material. This has been enhanced with a complex hydro-mechanical model, based on a rate dependent permeability (assuming a cubic law) and a calibrated Barcelona Basic Model (BBM) for the mechanical part. The model has proved successful to describe gas breakthrough tests (including saturation, gas injection, draining of gas, re-saturation and second gas injection) under a three-dimensional full geometry. The model considers arbitrarily random distributions of permeability zones. Their definition needs to be improved by providing, for instance, a better instrumentation and sensor data, imaging techniques and transparent walls. The localisation of heterogeneous permeability fields has not been possible and thus, the collection of realistic distributions of density or porosity for real samples (both before and after testing) is highly recommended.

Table of content

List of figures

List of tables

General introduction on EURAD-GAS, Task 2 “Gas transport mechanisms”

EURAD-GAS, WP6, focused on the “Mechanistic understanding of gas transport in clay materials”.

The main objectives of this WP were:

- To improve the mechanistic understanding of gas transport processes in natural and engineered clay materials, their couplings with the mechanical behaviour and their impact on the properties of these materials;
- To evaluate the gas transport regimes that can be active at the scale of a geological disposal system and their potential impact on barrier integrity and repository performance.

The programme of work aimed to provide results that are applicable to a wide range of National Programmes. This is possible because the results of previous efforts on the identification and characterisation of the possible gas transport processes suggest that the mechanisms at play in different clays are generally similar, while the conditions (gas pressure, stresses/deformations, saturation, . . .) for the transition from one transport regime (diffusion, two-phase flow, pathway dilation and fracturing) to another strongly depend on the specific properties of a given clay material.

This WP also aimed to transfer knowledge gained from lab and in situ experiments to configurations that are commonly found in current repository designs, to address key questions from the end-users:

- How could gas migrate within the repository and which water soluble and volatile radionuclide transport could be associated with it?
- How and to what extent could the hydro-mechanical perturbations induced by gas impact barrier integrity and long term repository performance?

This report describes the progress made in the Task 2 of EURAD-GAS which specifically examined the characterisation of gas transport mechanisms.

Description of Task 2 “Gas transport mechanisms”

Task 2 “Transport mechanisms” focused on the main gas transport mechanisms which will take place in a disposal system in the post-closure phase. Different mechanisms are generally expected to be of importance in a geological repository:

- Gas produced within the system can dissolve in the pore water and can then be transported by diffusion. The diffusion of dissolved gas may be retarded by physio-sorption on the solid phase. Improving the mechanistic understanding of diffusive transport of dissolved gas and retention mechanisms was the general objective of **Subtask 2.1** “Gas diffusion and retardation processes at high level of water saturation”.
- If the gas production rate exceeds the rate at which gas can be dissolved and evacuated by diffusion, a free gas phase will develop. As gas pressure increases, advective transport will occur. Two primary modes for advective gas transport are proposed; (i) visco-capillary flow and (ii) the formation of discrete gas-filled pathways. Exploring which transport mechanisms prevail under which range of conditions and understanding how the coupling between pressure in the liquid and gas phase are the stresses in the solid phase control gas transport was a general objective of **Subtask 2.2** “Advection (displacement vs. dilation)”.

Specific objectives of Subtask 2.1 “Gas diffusion and retardation processes at high level of water saturation”

In order to compare the rates of gas generation and gas evacuation by dissolution and diffusion, knowledge of the diffusion parameters of dissolved gas through the used materials is essential. Up to now, diffusion parameters are available essentially in water saturated systems. As partial desaturation might occur at some point during the repository evolution, this WP extended the available experimental data for gas diffusion to partially desaturated conditions.

In line with the general objective to improve mechanistic understanding, interpretation of the experimental results was supported by pore network modelling. The experimental and modelling work programme aimed in particular to investigate how petrophysical parameters (e.g. mineralogy and density) and the stress state influenced the diffusion parameters.

While diffusing through the pore water, dissolved gas might also interact with the barrier materials. Up to now, interactions (mainly gas sorption) have only been studied under dry conditions. In particular, hydrogen uptake due to sorption processes has only been studied under dry condition. One objective of this subtask was to determine if gas sorption could be a relevant retardation mechanism for diffusive transport under repository conditions, in clays that are partially or fully saturated with pore water. Again, the impacts of the pore network morphologies and the nature of the mineral assemblages on the gas sorption mechanisms was investigated.

Key objectives of Subtask 2.1 were thus:

1. to determine gas diffusion parameters on different clayey materials at different degrees of water saturation and support experimental data interpretation by pore network modelling, and
2. to understand gas physisorption mechanisms in microporous systems.

The gas of interest in this task is chiefly H_2, but other apolar gases such as CH_4 (by-product of bacterial activity), He, Ar (naturally occurring noble gases) and Ne (H_2 proxy) was also planned to be investigated in order to i) avoid artefacts related to bacterial activity triggered by H_2, ii) overcome safety problem especially in underground laboratories, and iii) probe the effect of polarizability and kinetic diameter on apolar gases mobility in porous networks.

Specific objectives of Subtask 2.2 “Advection (displacement vs. dilation)”

From previous work (including work done in the previous EC project FORGE), two primary modes for advective gas transport through natural mudrocks are proposed:

- visco-capillary flow, where capillary forces must be overridden in order to allow displacement of the wetting phase, by migrating gas,
- the formation of discrete gas-filled pathways, by localised consolidation of the clay matrix.

The potential for one specific mechanism to prevail is dependent on a range of factors, including the saturation state of the clay and the ratio of the clay to sand fraction. Natural heterogeneity within clay-hosted repositories may also play an important role in the migration of gas and the mitigation of peak gas pressure. For fully-saturated, pure clay bentonite materials, such as those used in engineered barriers, experimental evidence indicates that gas flow by pathway dilation is the preferred mode of transport. In such cases, significant hydromechanical coupling is observed, which cannot be satisfactorily explained by visco-capillary flow processes. This hydromechanical coupling between the immiscible phase, the interstitial fluid, and the total stress, remains unclear. Understanding these relationships, how they vary from one formation to another, and what impact, if any, they have on the integrity of the host rock, is now a priority research issue.

Through new experimental studies, this subtask aimed to:

1. Provide reference data for various natural and engineered clay materials under a sufficiently broad range of conditions, which will make it possible to investigate in a more systematic way how petrophysical parameters, like mineralogy or density, and conditions such as the stress state influence free gas transport.
2. Improve understanding of the observed gas transport modes and identifying their main controls, through interpretation of the experimental results by models in which the representation of crack propagation and pathway dilatancy is implemented at a process level.
3. Conceptualisations of the transport mechanisms limited to the macro-scale (continuum representation + discrete conducting features) such as those developed, for instance, in the FORGE EC project were compared to conceptualisations in which the micro-scale is also represented to better improve understanding of how micro-level heterogeneities and deformations affect macro properties.

The experimental and modelling programmes of the Subtask 2.2 aimed at characterising and understanding advective gas transport in fully saturated (or close to saturation) clayey materials.

.

Subtask 2.1:

Diffusion and retention processes

1. Subtask 2.1: Diffusion and retention processes

Experiments

.

ISTERRE

1.1. Gas sorption processes (ISTERRE)

1.1.1. Introduction & Objectives

After the closure of the underground nuclear waste repository, complete resaturation of the clay by the formation water and anaerobic conditions will be reached rapidly (within a few hundred years). Aqueous corrosion of the steel canister and, to a lesser extent, radiolysis of water will produce significant amounts of H_2. The generation and accumulation of H_2 gas in the back-filled emplacement tunnels may significantly affect long-term repository safety (Gallé, 2000; Ortiz et al., 2002; Lassabatère et al., 2004; Truche et al., 2013a). Reactive transport simulations indicate that a maximum hydrogen pressure of 70–100 bar can be reached in the waste canister with a radial extension of 20–50 m after 5000 years (Xu et al., 2008). Until now, most of the experimental studies related to nuclear waste disposal have focused on iron–clay interaction and iron corrosion rate (de Combarieu et al., 2007; Martin et al., 2008; Bourdelle et al., 2017), whereas the hydrogen mobility and reactivity is poorly documented. In the absence of bacteria, the geochemical impact of H_2 as a reducing agent is still not taken into account in the long-term waste storage performance assessment. Hydrogen is poorly reactive, because of the strength of the H-H σ-bond (436 $kJ.mol^{-1}$) and its absence of permanent dipole moment. However, catalytic processes at the fluid-mineral interface may promote abiotic redox reaction induced by hydrogen (Truche et al., 2010, 2013a, b, c). Hydrogen can also be trapped or adsorbed at the surfaces of clay minerals (Didier 2012, Didier et al, 2012, Truche et al., 2018).

While diffusing through the pore water, dissolved gas might interact with the clayey barrier materials (either parts of the EBS and/or the host rock) and gas sorption on the clay minerals might occur. This would result in a retardation of gas transport. On the other hand, sorption processes would remove free and dissolved gas thus playing a role on the pressure build-up in the hostrock.

In dry conditions, the molecular sorption of H_2 onto clay minerals is indeed recognised as a retardation mechanism that could contribute to a reduction in gas pressure build-up (Didier, 2012; Didier *et al.*, 2012; Bardelli *et al.*, 2014; Mondelli *et al.*, 2015). However, the available data are spurious as they indicate very weak temperature effect on adsorption within the 25-90℃ range, and surprisingly high H_2 uptake when comparing isotherms from intermediate specific surface areas of claystones ($30 < S_{BET} < 60$ m^2/g) with, for example, very high specific surface areas of synthetic metal organic frameworks ($S_{BET} > 3000$ m^2/g).

The objectives of this study is to precisely document H_2 uptake by claystones at high hydrogen pressure and ambient temperature using states of the art technique. In particular, we pay attention to the preliminary outgassing stage and to the generation of gas while heating claystones at temperature ranging from 50-200℃.

1.1.2. Materials and Methods

1.1.2.1. Claystone samples

The two samples used in the present study are: 1) Callovo-Oxfordian EST63112, and 2) Boom Clay (BC) CG 78-79W from the Hades horizontal borehole. Theses samples were characterized by X-ray Diffraction (XRD), Thermogravimetric analyses (DSC-TGA), and N_2 physisorption to derive their mineralogical composition, thermal stability and specific surface areas.

1.1.2.2. Gas generation/release upon heating at 50 to 200℃

Stainless steel (316L) Parr® autoclaves were used for the experiments. The internal volume of the autoclaves is 300 mL, the pressure is monitored at ± 0.1 bar, and temperature is controlled at ± 1 ℃. The autoclaves were loaded with 500 g of BC samples, then closed, flushed with Ar at about 2 bar total pressure for 20 minutes, and then heated to the desired temperature in less than 10 minutes thanks to an external oven. Gas samples were taken from time to time thanks to a valve connected to the head of the autoclaves. Experiments were either conducted using a fixed temperature mode (50 and 100℃), or at a step by step heating mode (100, 150 and 200 °C). After the experiments, the autoclaves were cool down to 25 °C, and the dead volume (i.e. the free gas volume from the head space inside the autoclave) was measured by equilibrating pressure in-between a calibrated cylinder filled with helium and the autoclave.

The BC sample was either loaded as is (without any pre-treatment) in the autoclave. In this case the BC core was just crushed in centimetre size blocks to be loaded inside the autoclave. Two experiments were also carried out with BC samples either lyophilized or outgassed at 150 °C under secondary vacuum prior being loaded inside the autoclave.

Gas samples (about 5 mL at 1 bar and 25 °C) from the low temperature (50 - 200 °C) gas generation experiments were taken from time to time thanks to a calibrated transfer syringe connected to the gas sampling valve of the autoclave. This syringe was equipped with a three-way valve. One way was connected to the autoclave, whereas the other one was fitted with a rubber septum. Gas from the transfer syringe was then transfer to the gas chromatograph (GC) via a 250 µL gas-tight syringe by piercing the septum fitted on the three-way valve. The gas samples were analyzed using a Perkin Elmer® CLARUS 500 GC equipped with a thermal conductivity detector (TCD) and a 2-m long column (RESTEK® Shin Carbon ST 80/100) traversed by Ar as carrier gas. The GC was calibrated using several Ar + H_2 + CH_4 + CO_2 + CO gas mixtures of different concentrations injected with a gas-tight syringe of calibrated volume. The estimated analytical error is ±3% at the 95% confidence level. For comparative purpose, the measured H_2, CO_2 and CH_4 concentrations were normalized to the total number of moles of these gases generated per kg of BC.

1.1.2.3. Hydrogen adsorption at low and high pressure

All samples (BC and COx) were initially degassed at 150 °C for 6 h under vacuum. Nitrogen and hydrogen physisorption experiments were first carried out 77 K up to 1 bar pressure, at ISTerre laboratory using a volumetric gas sorption instrument ASAP 2020 PLUS from Micromeritics Instruments®. From N_2 isotherms, the specific surface area of powdered samples (150 - 500 mg) was estimated using the Brunauer–Emmet–Teller (S_{BET}) equation in the $0.05 \leq P/P0 \leq 0.4$ interval of relative pressure and using a cross-sectional area of 16.2 Å² for molecular N_2. Data analyses were performed using ASAP 2020 Plus software from Micromeritics®. The presence of micropores in the sample ($Ø_{pore}$ < 2 nm) was assessed using the t-plot method (de Boer et al., 1966).

Hydrogen isotherms were acquired with an equilibration interval of 60 seconds for routine analysis (~ 5 to 8 hours for a complete isotherm acquisition). An ultra-high purity grade of H_2 (99.999% purity) was used throughout the adsorption experiments.

High pressure hydrogen experiments were also performed at 298 K and up to 120 bar at the Neel Institute using a PCT Hiden® IMI system apparatus (volumetric measurements) and data analyses were performed using Isochema® software. Around 200 to 600 mg of powdered samples were inserted inside a steel sample holder (internal volume ~ 200 mm^3), with a small amount of glass wool to prevent powder removal during vacuuming steps. Adsorption and desorption isotherms were performed with an equilibration time of 15 - 30 minutes for routine analysis. As for low pressure analysis, each sample was heated and outgassed at 150 °C for at least 6 hours prior to each measurement.

1.1.2.4. X-ray diffraction and Thermogravimetric analyses (DSC-TGA)

XRD patterns were recorded using a Bruker D8 diffractometer operated at 40 kV and 40 mA, and equipped with a SolX Si(Li) solid state detector from Baltic Scientific Instruments®. Intensities were recorded at 0.04° 2θ step intervals from 2 to 50° 2θ range (6 s counting time per step – CuKα_1+2 radiation). Oriented mounts were prepared by drying a smectite suspension onto glass slides. Ethylene-glycol (EG) solvation of the slides was achieved by exposing them to EG vapor at 50 °C for a minimum of 12 h.

TG/DSC curves were recorded on a TGA/DSC3+ Mettler Toledo® instrument. Approximately 50 mg of sample (+/- 30 mg) were placed in a 150 µL alumina crucible. The experiments were carried out under N_2 atmosphere with a flow rate of 20 mL/min. Sample mass loss and associated thermal effects were recorded from 25 to 900 ℃ using a constant heating ramp of 5 ℃/min.

1.1.3. Results

1.1.3.1. Mineralogy and surface properties of the samples

Diffraction patterns collected on whole rock and purified clay fraction of BC and COx are displayed on Figure 1.1. The quantitative mineralogical analysis of these patterns is reported on Table 1.1. COx claystone mostly consists of quartz (26%), calcite (26%), smectites (11%) and kaolinite (6%), whereas BC is much more enrich in phylosilicates with ilite-smectite (24 to 27%), mica (21 %) and kaolinite (15%), being the dominant phases -the other major minerals being quartz (24%) and microcline (6%).

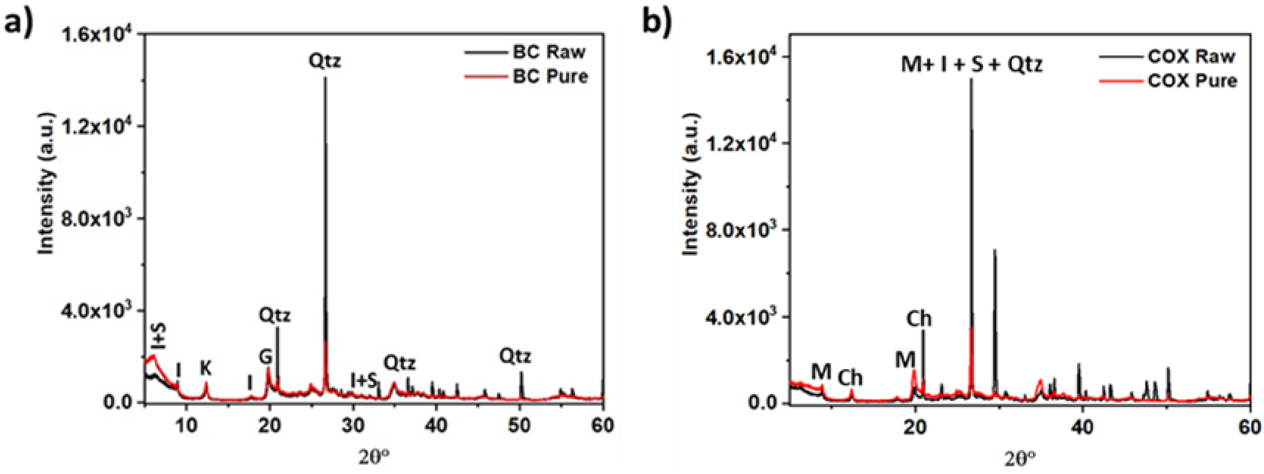

Figure 1.1: The whole rock powder diffraction patterns of samples a) Boom Clay (BC_{raw}, BC_{pure}), b) Callovo-Oxfordian (COX_{raw}, COX_{pure}).

a)

b)

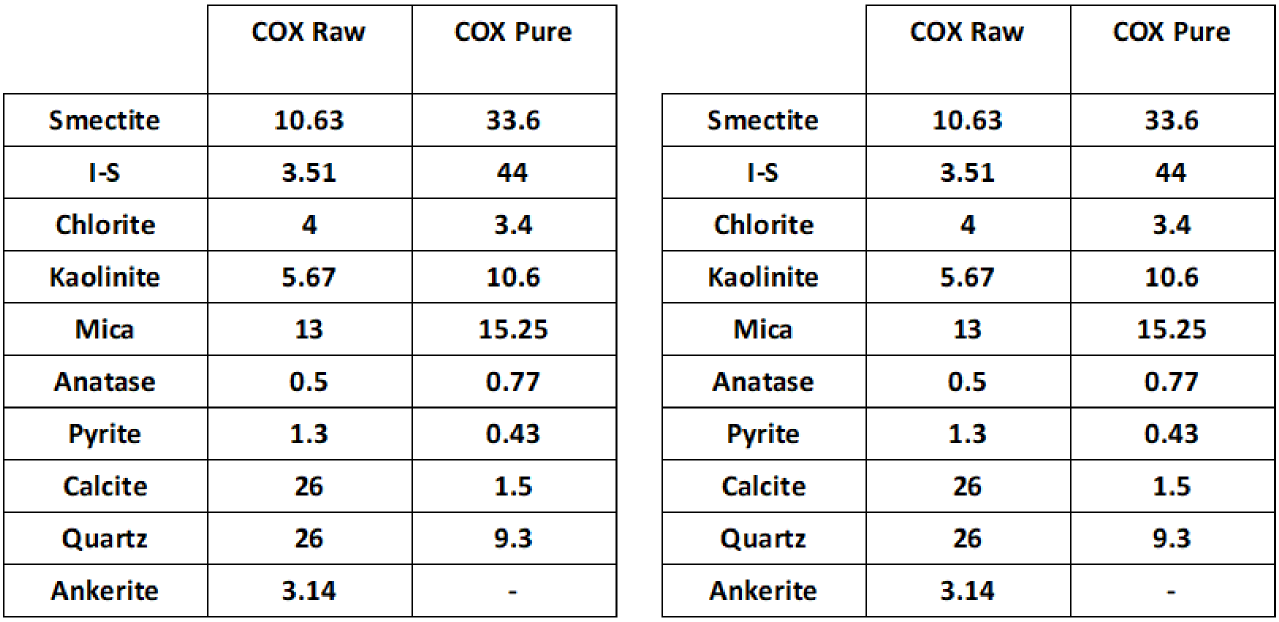

	COX Raw	COX Pure
Smectite	10.63	33.6
I-S	3.51	44
Chlorite	4	3.4
Kaolinite	5.67	10.6
Mica	13	15.25
Anatase	0.5	0.77
Pyrite	1.3	0.43
Calcite	26	1.5
Quartz	26	9.3
Ankerite	3.14	-

	COX Raw	COX Pure
Smectite	10.63	33.6
I-S	3.51	44
Chlorite	4	3.4
Kaolinite	5.67	10.6
Mica	13	15.25
Anatase	0.5	0.77
Pyrite	1.3	0.43
Calcite	26	1.5
Quartz	26	9.3
Ankerite	3.14	-

Table 1.1: Mineralogical composition of a) Callovo Oxfordian Claystone (EST63112), and b) Boom Clay (CG 78-79W) sample and their respective purified clay fraction.

Thermogravimetric analysis of these samples (Figure 1.1) reveals two major weigh loss at 100℃ and 360℃. The first weight loss (1 wt % for COx and 4 wt% for BC) corresponds to the release of physisorbed water, while the second weight loss, reaching 15 wt% for COx and 10 wt% for BC, is due to the deshydroxylation of the clay fraction. The COx raw (whole rock) sample displays a third major weight loss (20 wt%) at 750℃, corresponding to the removal of carbonate phases.

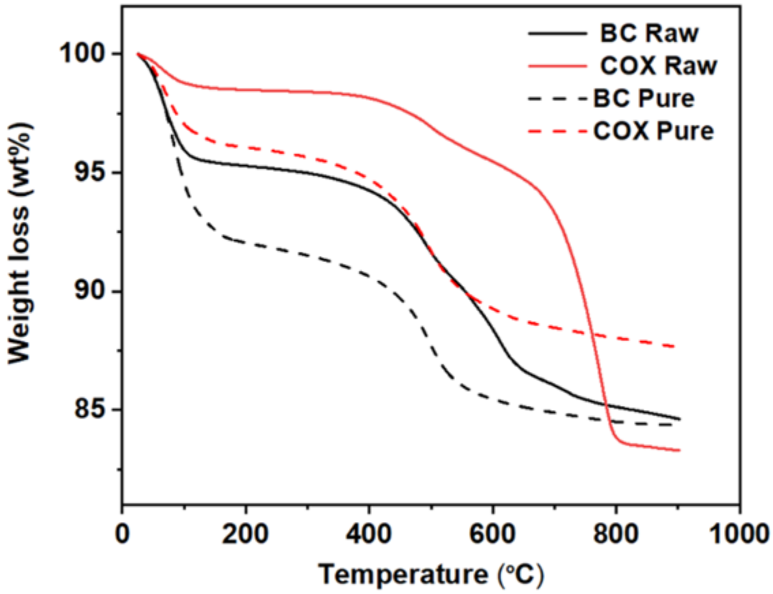

Figure 1.2: Thermal analysis curves of Callovo-Oxfordian (COX_{raw} , COX_{pure}) and Boom Clay samples (BC_{raw}, BC_{pure}).

The specific surface area of the samples, as measured by the BET method is as follow:

- COX raw: 20 m^2/g; and COx purified clay fraction: 59 m^2/g
- BC raw: 52 m^2/g; and BC purified clay fraction: 89 m^2/g

Adsorption isotherms (Figure 1.3) are of type IV according to the IUPAC classification with minor hysteresis indicating capillary condensation effects occurring inside the pore space of the samples. Here, all samples show hysteresis loops of H3/H4 types from the IUPAC classification, typical of platy-shaped particles (H3) such as clay minerals. As it from Figure 1.3, the steep parts of the isotherms at very low pressures (reaching 0.05 P/P0) reflect the relative proportion of micropore. However, the BJH, HK and DFT calculations were not applied on these samples, because their respective isotherms do not belong to a clearly defined type according to the IUPAC classification.

1.1.3.2. Gas generation/release upon heating at 50 to 200℃

Heating BC from 100℃ to 200℃ results in gas generation (Figure 1.4). Over the 100 to 200℃ temperature range, CO_2 is the main gas produced during heating (>90%), followed by H_2 (about 10 %), and minor methane (up to 0.2%). The amount of gas produced increased with temperature, with a marked increase when reaching 200℃. At 200℃, the amount of gas released seems to reach a plateau value after 5 days. The amounts of CO_2, H_2 and CH_4 produced at 200℃, after 10 days at this temperature are as follows: 32, 3.6, and 0.65 mmol/kg of BC, respectively.

Additional experiments have been conducted at a fixed temperature of either 50℃ or 100℃ for about 20 days (Figure 1.5 and Figure 1.6). At such temperatures and heating duration, CH_4 was not detected even after 20 days elapsed time. However, CO_2 and H_2 were continuously produced, without reaching a plateau concentration value. At 100℃, about 0.02 mmol of H_2 and 2.8 mmol of CO_2 were produced per kg of BC

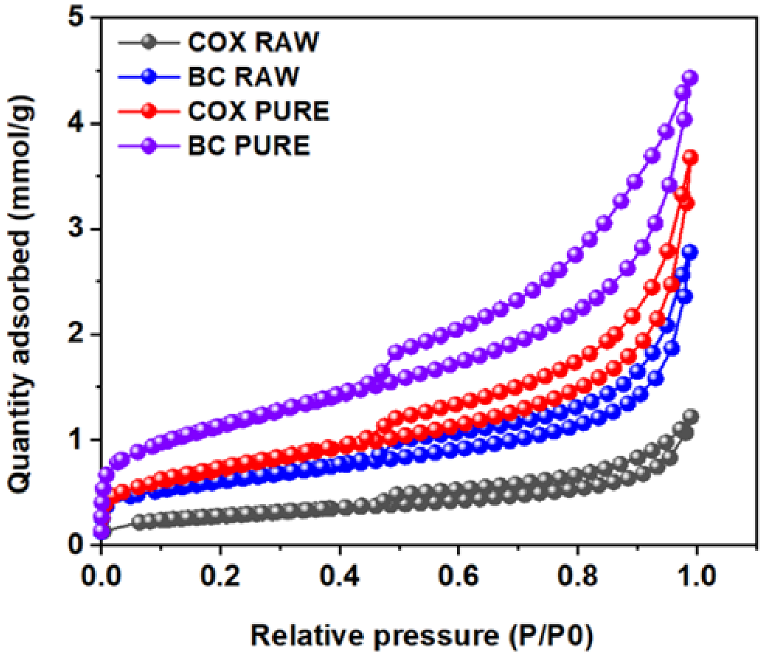

Figure 1.3: N_2 adsorption isotherms for Callovo-Oxfordian (COX_{raw}, COX_{pure}) and Boom clay BC_{raw}, BC_{pure}) samples.

after 16 days. At 50℃, about 5 ×10^{-3} mmol of H_2 and 2.0 mmol of CO_2 were produced per kg of BC after 26 days.

At 50℃, BC samples that have been previously degassed at 120℃ or lyophilized produce less H_2 and CO_2 than the untreated raw sample (Figure 1.5). When BC is lyophilized, H_2 is no more produced, whereas the amount of CO_2 reaches a plateau value at about 0.4 mmol/kg of BC after 10 days. When BC is outgassed, one can observe that H_2 is still continuously produced even if the total amount of H_2 produced after 26 days is about two times less than with the raw BC sample (2.8 ×10^{-3} mmol/kg of BC). After outgassing, CO_2 production at 50℃ is low and does not exceed 0.34 mmol/kg of BC after 26 days.

1.1.3.3. Hydrogen adsorption at low and high pressure

Hydrogen adsorption isotherms were first collected at 77K and up to 1 bar (Figure 1.7a). Hydrogen uptake by BC (0.17 mmol/g @ 1 bar) is much higher than for COx (0.06 mmol/g @ 1 bar). The purified clay fractions of these respective samples displayed an enhanced H_2 uptake, with 0.28 mmol/g for the purified CB and 0.19 mmol/g fore purified COx. It is noteworthy that the adsorption process is fully reversible as the desorption path is strictly identical to the adsorption one. Clearly, under such conditions, the H_2 uptake is linearly correlated to the specific surface area of these samples (Figure 1.7b).

Hydrogen (H_2) adsorption isotherms have been measured under dry condition at elevated H_2 pressure (up to 110 bar) on the COx sample at three different temperatures: 0, 25 and 90℃. The measurements have been collected on a PCT Hidden volumetric apparatus available at Institute Néel (Grenoble, France). The COx sample was outgassed at 150℃ under secondary vacuum prior the measurements. The results are displayed on Figure 1.8.

First, one can observe that the H_2 uptake by COx decreases with temperature as thermodynamically expected. Second, H_2 uptake is very low. It is almost null at 90℃ and the bell shape of the blue curve is due to uncertainty propagation along the acquisition of the isotherms. Under such temperature condition, the measurements are close to the quantification limit of the technique used. At 0 and 25 ℃, the maximum H_2 uptake at 100 bar is 0.02 and 0.04 wt%, respectively. To put these values into perspective, one may compare with saponite (a smectite), laponite (a nano-hectorite) and MOF-177 (a metal organic framework).

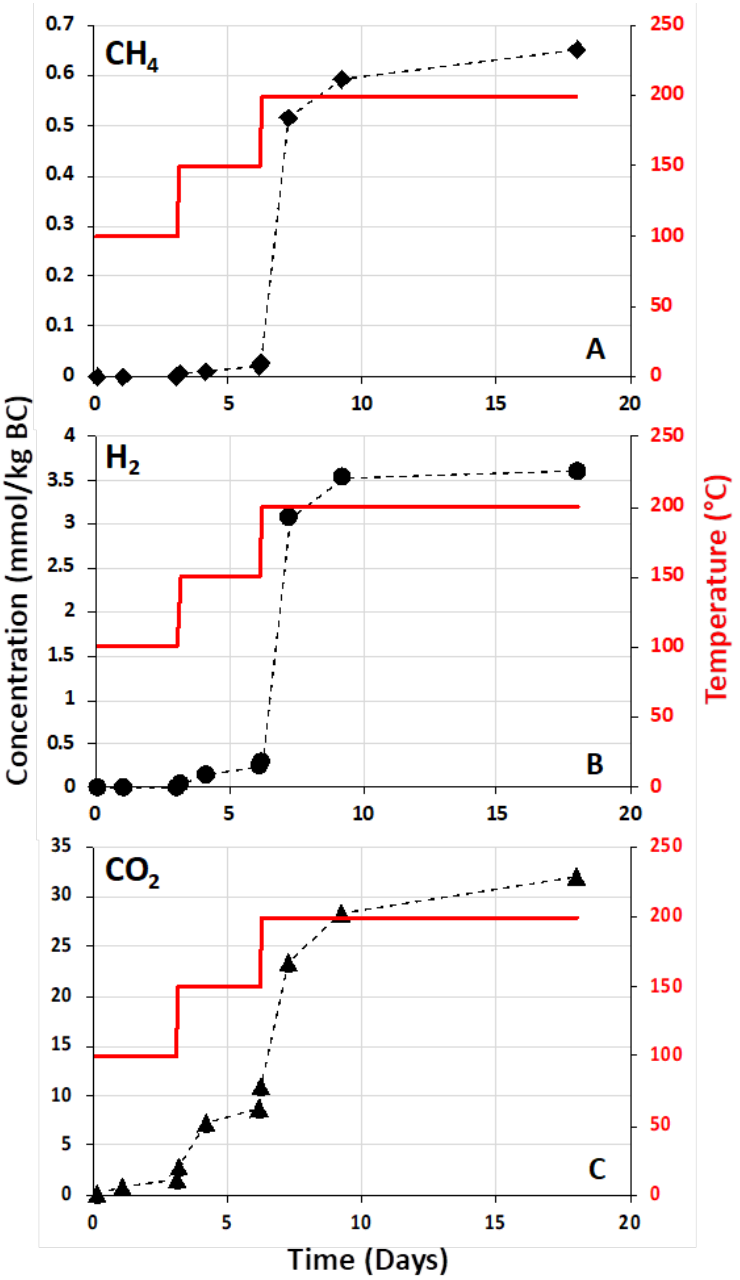

Figure 1.4: Amount of A CH_4, B) H_2; and C) CO_2 released during step heating of Boom Clay (CG 78-79W) at 100, 150 and 200℃.

Here is the H_2 uptake recorded for these 3 materials at 100 bar and 25℃: 0.05, 0.1, 0.5 wt%, respectively. Of course, the specific surface of these materials is the primary driver of their H_2 uptake. The specific surface area as measured by the BET technique using N_2 as sorbent gas is: 22 m^2/g for COx, 45 m^2/g for saponite, 350 m^2/g for laponite, 3800 m^2/g for MOF-177. Third our results on H_2 adsorption on COx disagree with the data previously reported by Bardelli et al. (2014). We consider these later data as spurious for the two following reasons: 1) the authors report slightly higher H_2 uptake at 90℃ than at 25℃ – such a results is physically impossible, 2) the H_2 uptake at 25℃ and 90 bar H_2 pressure is about 0.2 wtH_2 uptake would mean that COx (S_{BET} = 22 m^2/g S_{BET}) has similar H_2 adsorption properties as laponite (S_{BET} = 350 m^2/g) or MOF-177 (S_{BET} = 3800 m^2/g), two materials that have specific surface areas of 2 to 3 orders of magnitude higher. This is just impossible.

Coming back to our results, we have measure a maximum **H_2 uptake of 0.02 wt% at 25℃ and 100 bar**

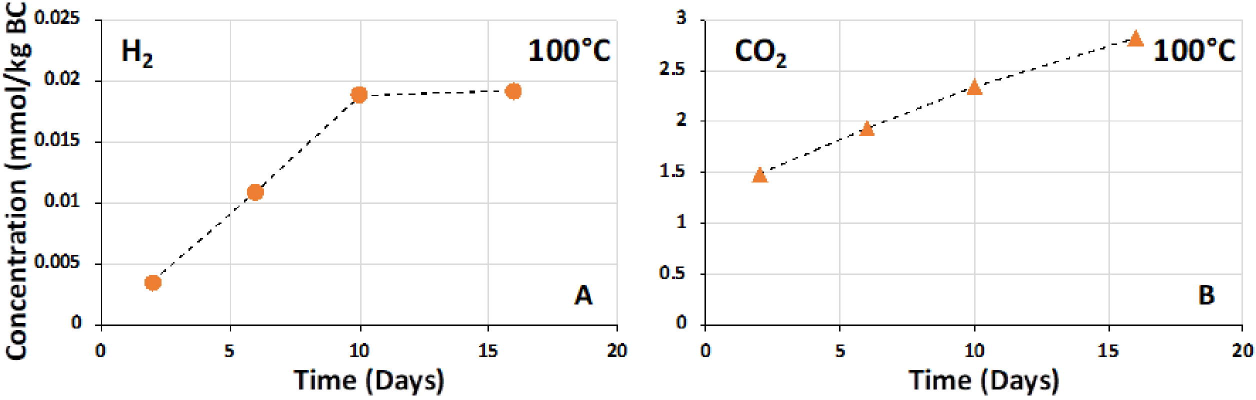

Figure 1.5: Amount of A) H_2 and B) CO_2 produced during heating of Boom Clay at 100 ℃.

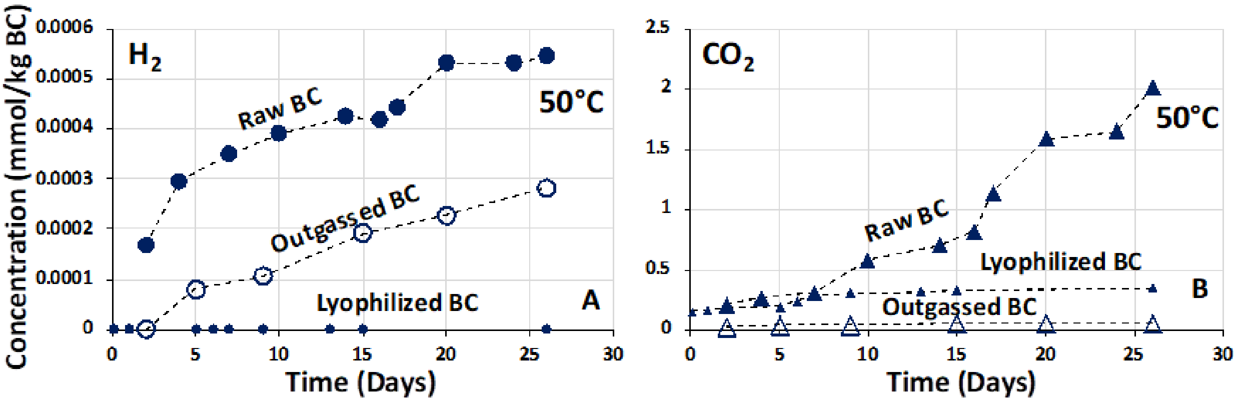

Figure 1.6: Amount of A) H_2 and B) CO_2 produced during heating of Boom Clay (BC) at 50 ℃. Three different type of samples have been tested: i) "Raw BC" corresponds to Boom Clay sample without pre-treatment, ii) "Outgassed BC" corresponds to Boom clay sample exposed to primary vacuum at 120 ℃ for 48 hours before the experiment, and iii) "Lyophilized BC" corresponds to Boom clay sample that has been lyophilized or freeze-dried before the experiments.

under dry condition. This would mean that **0.001 km^3 (a cube with sides of 100 m) of COx (density taken at 2.4) can adsorb 480 tones of H_2 under such temperature and pressure condition. Thus, even if H_2 adsorption on COx is intrinsically low, it must not be neglected once the scale of the geological formation and H_2 plume propagation is accounted for**. We hereby recognize that water humidity or even saturation may drastically decrease this H_2 uptake, but dry condition may also exist if the gas pressure build-up, or the steel canister corrosion desaturate the host-rock locally.

1.1.4. Summary

The main conclusions of this study are as follow:

1) Heating Boom Clay and COx at temperature ranging from 50 to 200 ℃ results in CO_2, H_2 and CH_4 gas generation. CO_2 is the most abundant gas produced, but H_2 is also well quantifiable event at temperature as low as 50 ℃.
2) This observation implies that outgassing the samples at 150 ℃ under secondary vacuum, prior adsorption isotherm acquisition may be inappropriate as gas will be constantly produced during the process.

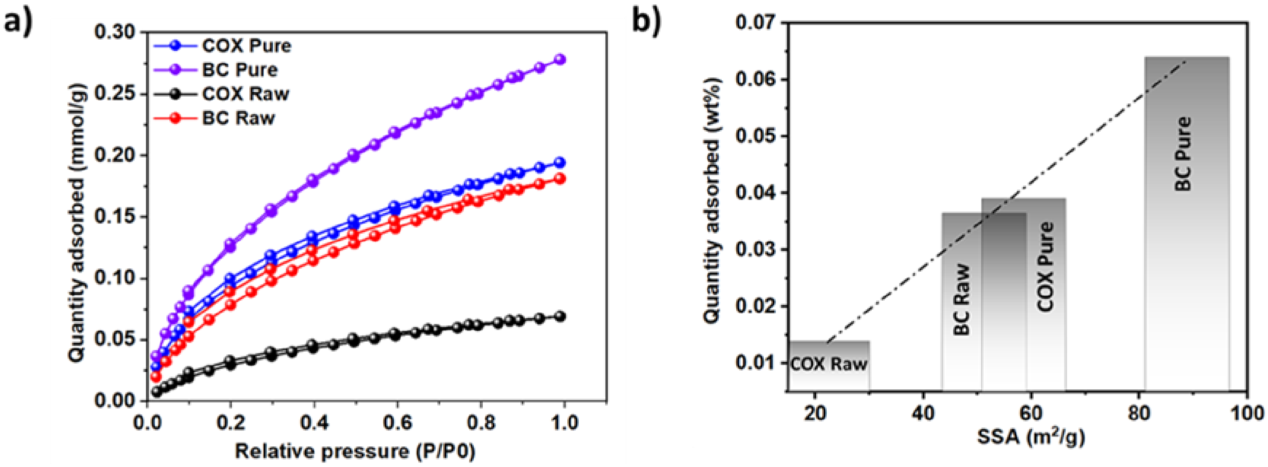

Figure 1.7: a) H_2 adsorption isotherms for Callovo-Oxfordian (COX_{raw} , COX_{pure}), and Boom clay (BC_{raw}, BC_{pure}) samples collected at 77K and up to 1 bar. b) Correlation between H_2 quantity adsorbed and specific surface area.

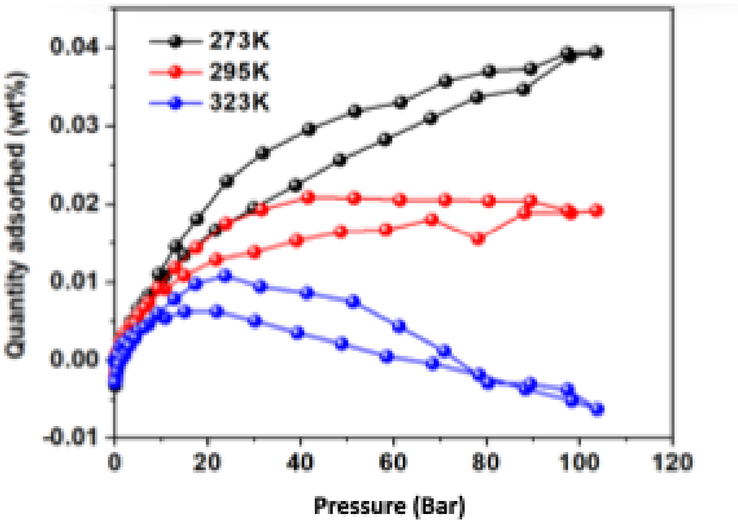

Figure 1.8: H_2 adsorption isotherms recorded at elevated H_2 pressure (up to 110 bar) and at 3 different temperature: 0 ℃ (black dots), 22 ℃ (red dots), and 50 ℃ (blue dots) on COx sample. The adsorption and desorption paths are shown. Adsorption is nearly reversible as both paths and superimposed.

3) Hydrogen uptake by dry COx at 25 ℃ and 100 bar is 0.02 wt%. This value translates into 480 tones of H_2 adsorbed per 1 x10^6 m^3 of dry COx.

1.1.5. Uncertainties and knowledge gaps

The remaining uncertainties regarding the above-mentioned results are as follow

- What is the impact of water humidity or other competing adsorption gases (e.g. CO_2) on H_2 uptake?
- What is the role of organic matter content of H_2 uptake?
- What is the impact of the outgassing condition? The outgassing conditions prior isotherms acquisition have an impact on the subsequent H_2 uptake measurements. Water adsorbed on clays minerals is removed and interlayer may collapse at 150 ℃. It has also been shown that COx and Boom Clay generate gases (CO_2, CH_4 and H_2) upon being heated. This has been observed at temperature

as low as 50℃ over few months. Thus, the outgassing stage may also generate gases, probably through organic matter degradation or cracking. The incomplete desaturation of the sample prior isotherm acquisition, may question the representatively of the measurements.

One may also question the adsorption mechanism in itself. What is the nature of the H_2 sorption sites? Where H_2 is adsorbed? What is the relative contribution of the different mineral phases including organic matter? Neutron spectroscopy may be extremely valuable to exanimate these questions in details.

References

Bardelli F., Mondelli C., Didier M., Vitillo J. G., Cavicchia D. R., Robinet J.-C., Leone L. and Charlet L. (2014). Hydrogen uptake and diffusion in Callovo-Oxfordian clay rock for nuclear waste disposal technology. Applied Geochemistry **49**, 168–177.

Bourdelle, F., Mosser-Ruck, R., Truche, L., Lorgeoux, C., Pignatelli, I., Cathelineau, M., Michau, N. (2017). A new view on iron-claystone interactions under hydrothermal conditions (90 ℃) by monitoring in situ pH evolution and H_2 generation. Chemical Geology, 466, 600-607de Combarieu, G., Barboux, P., Minet, Y. (2007). Iron corrosion in Callovo-Oxfordian argilite: From experiments to thermodynamic/kinetic modelling. Phys. Chem. Earth, 32, 346-358

Didier M. (2012). Etude du transfert réactif de l'hydrogène au sein de l'argilite. PhD thesis, Université de Grenoble 1, Institut des Sciences de la Terre.

Didier M., Leone L., Greneche J.-M., Giffaut E. and Charlet L. (2012). Adsorption of Hydrogen Gas and Redox Processes in Clays. Environmental Science & Technology **46** (6), 3574–3579.

Lassabatère, T., Dridi, W., Servant, G. (2004). Gas transfer and mechanical incidence on storage barriers. Applied Clay Science 26, 511–520. Martin, F.A., Bataillon, C., Schlegel, M.L., (2008). Corrosion of iron in flow alloyed steel within a water satured brick of clay under anaerobic deep geological disposal conditions: an integrated experiment. Journal of Nuclear Materials 379, 80–90.

Mondelli C., Bardelli F., Vitillo J. G., Didier M., Brendle J., Cavicchia D. R., Robinet J.-C. and Charlet L. (2015). Hydrogen adsorption and diffusion in synthetic Na-montmorillonites at high pressures and temperature. International Journal of Hydrogen Energy **40** (6), 2698–2709.

Ortiz, L., Volckaert, G., Mallants, D., (2002). Gas generation and migration in Boom clay, a potential host rock formation for nuclear waste storage. Engineering Geology 64, 287–296.

Truche, L., Berger, G., Destrigneville, C., Pages, A., Guillaume, D., Giffaut, E. et Jacquot, E. (2009). Experimental reduction of aqueous sulphate by hydrogen under hydrothermal condition: implication for the nuclear waste storage. Geochim. Cosmochim. Acta, 73, 4824-4835.

Truche L., Berger G., Destrigneville C., Guillaume D. and Giffaut E. (2010). Kinetics of pyrite to pyrrhotite reduction by hydrogen in calcite buffered solutions between 90 and 180℃: Implication for the nuclear waste disposal. Geochim. Cosmochim. Acta., 74, 2894-2914.

Truche, L., Jodin-Caumon, M.C., Lerouge, C., Berger, G., Mosser-Ruck, R., Giffaut, E., Michau, N. (2013a). Sulphide mineral reactions in clay-rich rock induced by high hydrogen pressure. Application to disturbed or natural settings up to 250 ℃ and 30 bar. Chem. Geol. 351, 217-228.

Truche L., Berger G., Albrecht A., Domergue L. (2013b) Engineered materials as potential geocatalysts in nuclear waste repositories: a case study of the stainless steel catalytic effect on nitrate reduction by hydrogen. Applied Geochem., 35, 279-288.

Truche L., Berger G., Albrecht A., Domergue L. (2013c). Abiotic nitrate reduction induced by carbon steel and hydrogen: Implications for environmental processes in waste repositories. Applied Geochem., 28, 155-163.

Xu, T., Senger, R., Finsterle, S. (2008). Corrosion-induced gas generation in a nuclear waste repository: reactive geochemistry and multiphase flow effects. Applied Geochemistry 23, 3423–3433.

.

British Geological Survey (BGS)

1.2. Gas diffusion (BGS)

1.2.1. Introduction and objectives

The rate at which diffusion can dissipate the accumulation of generated gases is an important consideration in their treatment within a safety case for the geological disposal of radioactive waste. Understanding variations in the diffusive transport of gas through the host rock and overlying strata therefore emerges as a key factor in the treatment of gas in repository settings. To better understand processes impacting gas diffusion, the British Geological Survey (BGS) proposed a series of bespoke experiments, performed on natural and synthetic samples. The natural samples (Boom Clay) have been subjected to an isotropic stress field, generally undertaken at a reference compaction state (circa 400 m) agreed in advance with ONDRAF/NIRAS (Belgian nuclear waste management agency) and COVRA (nuclear waste management agency of the Netherlands). In the tests on natural samples, the role of anisotropy has been examined by performing diffusion measurements, both normal and perpendicular to bedding. The output from these tests will quantify the role of anisotropy due to bedding and its impact on the development of a gas phase within the Boom Clay and is, therefore, relevant to the development of a robust safety case. Alongside the experiments proposed by the BGS on gas diffusion through the Boom Clay, the BGS has proposed a complementary suite of experiments on synthetic samples. In these tests, the diffusion coefficient to gas will be determined as a function of mineralogy and dry density (i.e., compaction state). A matrix of compositions that is representative of the broad range of the compositions of the natural host rocks available to many European nations will be explored, providing diffusion coefficient measurements that are applicable to many different national concepts. In this way, the fundamental controls governing the magnitude of the diffusion coefficient can be defined, ultimately providing in the future reference values for different mineral combinations across a range of conditions and end-users.

To date, the BGS has successfully performed 5 laboratory-scale tests on samples of Boom Clay (BC), one on the Eigenbilzen sand and four on synthetic samples with differing mineralogical compositions, in which all have been subjected to a detailed sequence of intrinsic permeability (k_i) and gas effective diffusion (D) measurements to define the transport behaviour of each sample. The aim of this section is to define (i) the hydraulic properties of the sample prior to gas testing, (ii) the diffusion coefficient across the sample and (iii) the hydraulic behaviour following gas diffusion tests to quantify any changes in behaviour. In addition, the BGS has honed and refined the manufacturing process of the synthetic samples to consistently produce test samples, which have also been sent to SCK CEN and IRSN for their test programmes.

1.2.2. Experimental set-up

1.2.2.1. Description of apparatus

To characterise the hydraulic and gas diffusion behaviour of the test samples under more realistic experimental conditions, the BGS has developed a bespoke apparatus in which samples are subjected to an isotropic confining stress and exposed to either synthetic porewater solution or gas (either neon or helium). All aspects of the test system are designed to minimise the possibility of gas (and water) leakage to define the mass transport characteristics of the material more accurately. As the test program for the natural samples is ahead of the synthetic programme, any early-stage issues with the synthetic apparatus and its set up have been encountered and modifications made to the test rig to ensure performance.

The basic permeameter (Figure 1.9 and Figure 1.10) consists of five main components: (1) a specimen assembly, (2) a 10 MPa rated pressure vessel and associated confining pressure system, (3) a fluid injection system, (4) a backpressure system, and (5) a PC-based data acquisition system. The specimen is subject to an isotropic confining stress and was sandwiched between two stainless steel end-caps, wrapped in aluminium foil[1] and jacketed in heat-shrink Teflon to exclude confining fluid. A unique lock-ring system built into each end-cap compresses the Teflon against a Viton "O"-ring to provide a leak-tight seal.

---

[1] This was implemented after the initial test following detailed characterisation of the Teflon sheath.

The inlet and outlet zones for water or gas flow through the specimen are provided by porous filter discs 50 mm in diameter and nominally 3-5 mm thick. These act as either source or sink for the injection of test permeants. During hydraulic measurements, all the filters are saturated with an aqueous porewater solution.

The injection system is itself comprised of two sub-systems, one dedicated to the measurement of hydraulic properties and the other, configured specifically for gas diffusion testing. The latter circuit is configured around a single pre-charge vessel (with welded tubing connections) with only metal to metal connections linking it to the test sample, thereby minimising the chance of leakage. The development of this system was implemented after the initial test on Boom Clay, FPR-19-006, which experienced excessive gas loss during diffusion testing. The addition of foil wrapping also came into effect after this test as a preventative measure to limit gas loss into the confining fluid.

Volumetric flow rates are controlled or monitored using a pair of ISCO-260, Series D, syringe pumps operated from a single digital control unit. The position of each pump piston is determined by an optically encoded disc graduated in segments equivalent to a change in volume of 16.6 nL. Movement of the pump piston is controlled by a micro-processor which is continuously monitored and the rate of rotation of the encoded disc is adjusted using a DC-motor connected to the piston assembly via a geared worm drive. This allows each pump to operate in either constant pressure or constant flow modes. A programme written in LabVIEW^{TM} elicits data from the pump at pre-set time intervals. Testing is performed in an air-conditioned laboratory at a nominal temperature of 20ºC. A typical test history comprises a sequence of test stages, each designed to examine a particular system response, as described in Section 1.7.

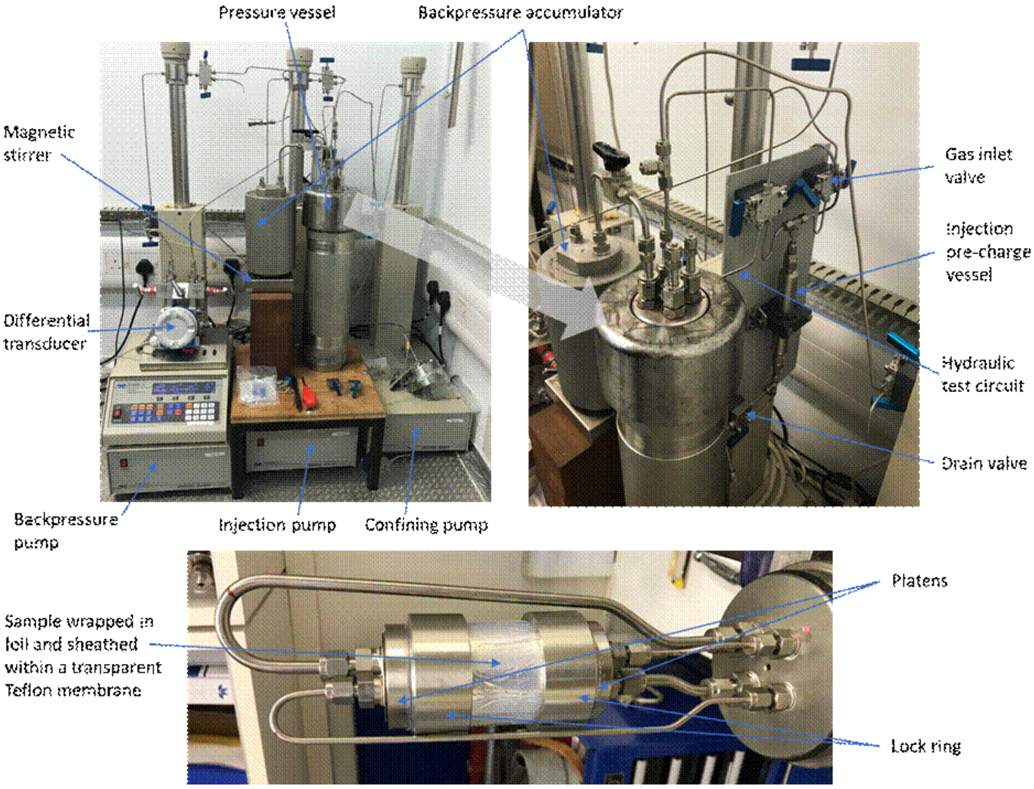

Figure 1.9: The experimental apparatus. Top left image shows the complete apparatus with control pumps, pressure vessel backpressure accumulator, magnetic stirrer, and differential transducer. Top right image is a close-up of the top of the pressure vessel and injection manifold. Bottom image shows the sample assembly and connecting tube-work to the pressure vessel end-closure

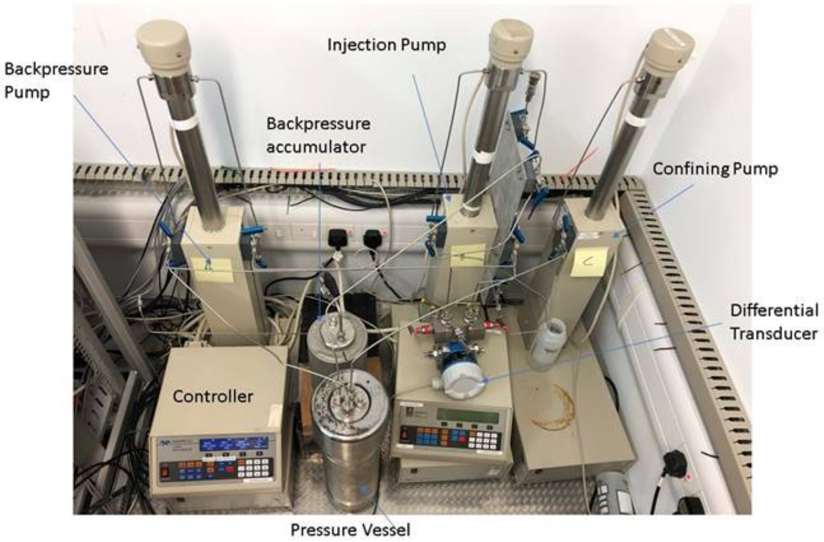

Figure 1.10: The complete experimental apparatus for the synthetic test programme showing control pumps, pressure vessel, backpressure accumulator, magnetic stirrer, and differential transducer.

1.2.2.2. Calibration

Calibration of the injection, backpressure and confining pump pressure responses was done against a known laboratory standard, itself calibrated to a Nationally recognised accreditation. Pressure increments, then decrements were applied to each pump and a least squares regression of the data undertaken. Corrections were then applied to each pump response to minimise the chance of inadvertently creating a pressure differential across the sample. Given the highly sensitive nature of the differential pressure transducer (rated 0-100 kPa) used during diffusion measurements, it was not possible to recalibrate this using standard laboratory techniques.

1.2.2.3. Testing fluids

Rehydration of the Boom Clay samples and subsequent permeability measurements were undertaken using a synthetic porewater solution, matched to that of the ground water at the HADES laboratory in Mol, Table 1.2. Due to its low salinity, manufacture of the synthetic samples was done using a synthetic porewater matched to that of the COx according to a recipe supplied by ANDRA, Table 1.3.

	mg/l	mmol/l
Ca	2	0.05
Fe	0.2	0.003
Mg	1.6	0.06
K	7.2	0.2
Si	3.4	0.1
Na	359	15.6
Al	0.6×10^{-3}	2.4×10^{-5}

	mg/l	mmol/l
Total S	0.77	0.02
Cl -	26	0.7
SO_4^{2-}	2.2	0.02
HCO_3-	878.9	14.4

Property	Unit	Value
pH		8.5
pCO_2	Atm	$10^{-2.62}$
Eh	mV	-274
Ionic strength		0.016

Table 1.2: Chemical composition and properties of the synthetic Boom Clay solution used for the natural samples in this study.

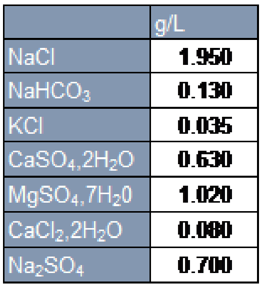

	g/L
NaCl	1.950
$NaHCO_3$	0.130
KCl	0.035
$CaSO_4.2H_2O$	0.630
$MgSO_4.7H_20$	1.020
$CaCl_2.2H_2O$	0.080
Na_2SO_4	0.700

Table 1.3: Chemical composition of the synthetic COx solution used for the manufacture of the synthetic samples in this test programme.

1.2.3. Material Properties

Natural samples were prepared by machine lathing to produce high-quality cylindrical specimens whose dimension and bulk densities are presented in Table 1.4. Synthetic samples were manufactured by the BGS using a bespoke sample press. Figure 1.11 shows the synthetic sample composition matrix. For a number of reasons including the covid-19 pandemic the test matrix was reduced to the testing of sample compositions 2B, 3B, 7 and 8. The clay component of each sample was made from a 80%:20% mixture of MX80 bentonite and kaolinite measured under ambient condition where the start moisture contents of each material was approximately 8% and 2% respectively. The bentonite was been milled to a grain size of no larger than 30 microns. The silt fraction was pure muscovite mica and the sand fraction was derived from high purity quartz sand supplied by Lochaline Quartz Sand Ltd, which was sieved to obtain particles in the range 63-125 microns.

	Sample no.	**Height (mm)**	**Diameter (mm)**	**Bulk density (kg/m^3)**
Pre-test	**FPR-19-006**	20.14	50.28	2028
Post-test	**FPR-19-006**	-	-	-
Pre-test	**FPR-21-011**	35.65	49.92	2069
Post-test	**FPR-21-011**	34.98#	49.97	2032
Pre-test	**FPR-21-028**	20.94	49.90	2058
Post-test	**FPR-21-028**	21.02	50.30	2037
Pre-test	**FPR-21-055**	29.97	49.79	2022
Post-test	**FPR-21-055**	30.30	49.49	1994
Pre-test	**FPR-21-040_S**	38.51	49.92	1832
Post-test	**FPR-21-040_S**	38.59#	48.69	1888#
Pre-test	**FPR-22-013**	36.95	49.60	2020
Post-test	**FPR-22-013**	37.16	49.40	1981
Pre-test	**FPR-22-038**	34.51	49.12	2018
Post-test	**FPR-22-038**	34.02	47.69	2085
Pre-test	**FPR-22-117_S**	34.45	49.97	1884
Post-test	**FPR-22-117_S**	35.02	49.67	1895
Pre-test	**FPR-23-008_S**	34.25	49.75	1872
Post-test	**FPR-23-008_S**	34.59	49.33	1862
Pre-test	**FPR-23-010_S**	31.32	49.16	1966
Post-test	**FPR-23-010_S**	-	-	-
Pre-test	**FPR-23-037_S**	29.97	49.83	1697
Post-test	**FPR-23-037_S**	-	-	-

Sample no.	Height (mm)	Diameter (mm)	Bulk density (kg/m^3)

Table 1.4: Pre- and post-test sample dimensions and bulk densities for the samples tested in this study. $^{\#}$represents an approximate value only, as the sample damaged during dismantling of the apparatus. The suffix S indicates a synthetic sample.

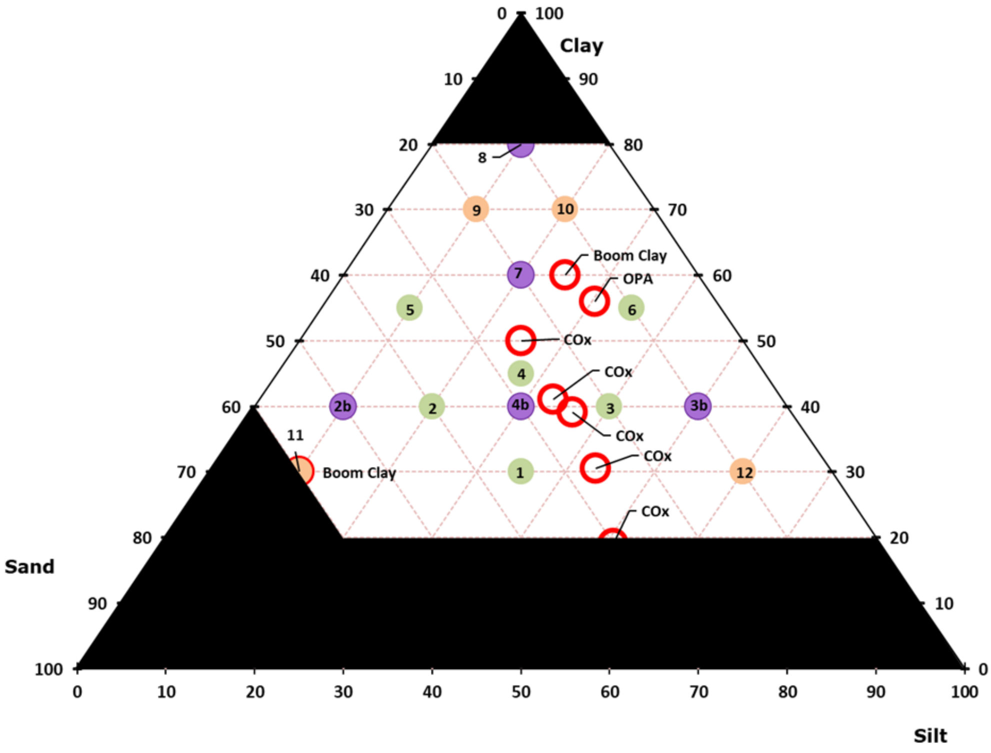

Figure 1.11: Planned test compositions shown by the purple circles (the green and orange circles were those originally planned but were subsequently pared down following the covid pandemic). The black shaded area at the base of the triangle shows the minimum likely clay fraction and the maximum likely sand fraction.

Sample Number	Test material	Composition	Mineralogy Clay %	Silt %	Sand %
FPR-21-040_S	Synthetic	7	60	20	20
FPR-23-008_S	Synthetic	8	80	10	10
FPR-23-010_S	Synthetic	2B	40	10	50
FPR-23-037_S	Synthetic	3B	40	50	10

Table 1.5: Summary table showing the mineralogical composition of synthetic test samples. The percentage values are by weight for each mineral component.

1.2.4. Computed tomography methodology

To gain a detailed understanding of the structures present in the Boom Clay, as well as any potential properties which may lead to deleterious laboratory testing results, a careful imaging process took place.

Cores were initially removed from their aluminised vacuum packing then wrapped in cling film and re-vacuum packed in an X-ray transparent material as quickly as possible to reduce any moisture loss. Where possible, the entire length of core was then imaged in both 2D and sometimes 3D in the BGS Core Scanning Facility CSF). These images were then analysed (see details below) and studied for any factors, such as obvious fracturing or core damage, which could affect the sample making procedure.

Test samples were then manufactured by machine lathing, re-preserved to prevent moisture loss and returned to the CSF for detailed CT imaging. At this size sample, it was possible to achieve resolutions down to approximately 50 microns.

The X-Ray CT scanner in the Core Scanning Facility is a Geotek Rotating X-Ray Computed Tomography scanner (see Figure 1.12) and is capable of scanning core of diameters up to 150 mm and up to 1.5 m in length. The sample sits between an X-ray source and detector which rotate around the sample to ensure the sample does not move during imaging. For this project two-dimensional scans were quickly produced and were taken orthogonally from each other to give further detail of the structure of the sample. For 3D imaging the sample was imaged in XY slices taken as TIFF files. These slices were then stitched together using a pre-processing file to form a 3D image. This pre-processed 3D stack of images is then stitched together, where several noise reducing filters were applied to the images to enhance the imaging process.

Figure 1.12: Geotek Rotating X-Ray CT scanner in the BGS Core Scanning Facility. The scanner is capable of scanning in both 2 and 3D. For the current study both modes were used. For the three-dimensional image, files were taken in an XY orientation down the length of the sample.

To carry out further image processing and analysis, the data was then transferred to the Pergeos software. This is a purpose-built digital rock analysis software provided by Thermo-Fisher Scientific which has been specifically designed for the purpose of both quantitative and qualitative image analysis from both 2D and 3D images.

Initially, different image processing techniques were applied to remove any artefacts left over from the scanning, such as beam hardening or edge effects. A slight cropping of the image was also required to remove the edge of the vacuum packaging which the sample was contained within. Once this was achieved further filtering of the image took place in the means of a Non-Local Means filter. This was chosen to reduce the noise and smooth out any artefacts remaining from the scanning process. This algorithm compares the neighbourhoods of all voxels in a given search window with the neighbours of the current voxel to determine the new value for the current voxel. The similarity between the neighbours determines the weight with which this will affect its neighbours (Thomson et al., 2018). The next step was to perform a Top Hat analysis of the image. That is, to apply a smaller scale analysis to pick out edge features of areas of the image we want to segment. This was done by eye within the software by applying a slight threshold where the user believes the boundaries best lie. Further detail on this type of image processing is provided in Thomson et al. (2018).

An example showing the types of images derived from this type of analysis is illustrated in Figure 1.13. Probable bioturbation features can be seen in the images and their orientation and connectivity can be assessed to provide quantitative information on the characteristics of each core, part of which has been summarised in Table 1.6.

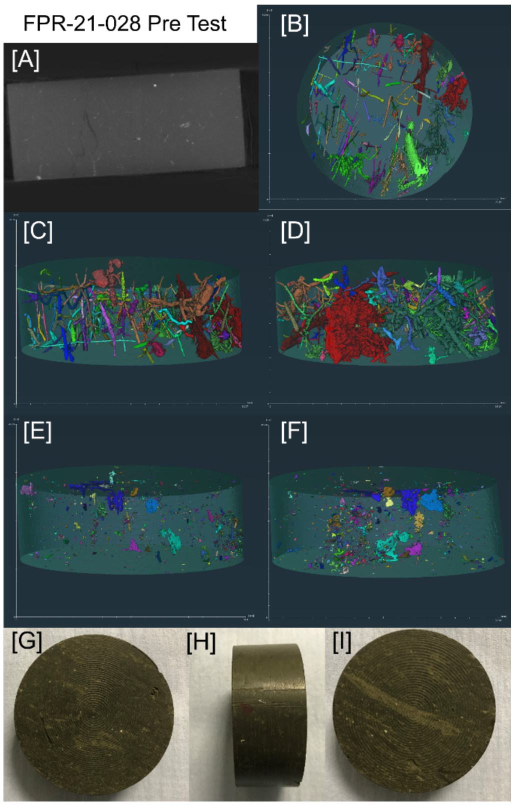

Figure 1.13: Pre-test imaging of sample FPR-21-028. [A] Orthogonal CT; [B] CT image of features XY orientation; [C] CT image of features XZ orientation; [D] CT image of features YZ orientation; [E] CT image of fractures XZ orientation; [F] CT image of fractures YZ orientation; [G] injection face; [H] side view of sample; [I] backpressure face of sample.

Test No.	Total feature volume (mm^3)	'Feature Ratio'	Volume fraction >0.5mm^3	Volume percent of features above 0.5mm^3
FPR-19-006	984.07	2.95%	885.23	2.65%
FPR-19-006	385.83	1.34%	330.17	1.15%
FPR-19-006	2728.24	9.48%	2650.37	9.21%
FPR-21-011	732.09	1.28%	585.19	1.02%
FPR-21-028	853.92	2.81%	574.86	1.89%
FPR-21-028	73.98	0.24%	48.25	0.16%
FPR-21-055	811.20	1.50%	687.19	1.27%
FPR-21-040	44.80	0.05%	1.95	0.00%
FPR-22-013	461.65	0.93%	377.70	0.76%
FPR-22-038	19.30	0.04%	0.00	0.00%

Test No.	Total feature volume (mm^3)	'Feature Ratio'	Volume fraction >0.5mm^3	Volume percent of features above 0.5mm^3

Table 1.6: Observed feature volumes derived from CT analysis of each sample. Total feature volume equates to the volume of features identified in the CT images. Feature ratio represents the features as a percentage of the sample volume. Volume fraction greater than 0.5mm^3 equates to combined volume of the features whose individual volume is greater than 0.5mm^3

1.2.5. Testing protocol

Figure 1.14 shows the testing protocol developed at BGS during the course of this project. This has been undertaken, in consultation with SCK CEN and the Catholic University of Leuven, in an attempt to fully characterise the test material and to help in the identification of possible correlators between hard to measure parameters, such as the diffusion coefficient, and simpler geotechnical/mineralogical data. It is also hoped that this high level of pre- and post-test characterisation will help to contextualise data, so the impact of heterogeneity on material properties can be better understood. However, at the time of writing much of this data, as presented in Table 1.7, was unavailable and unfortunately could not be included in the report.

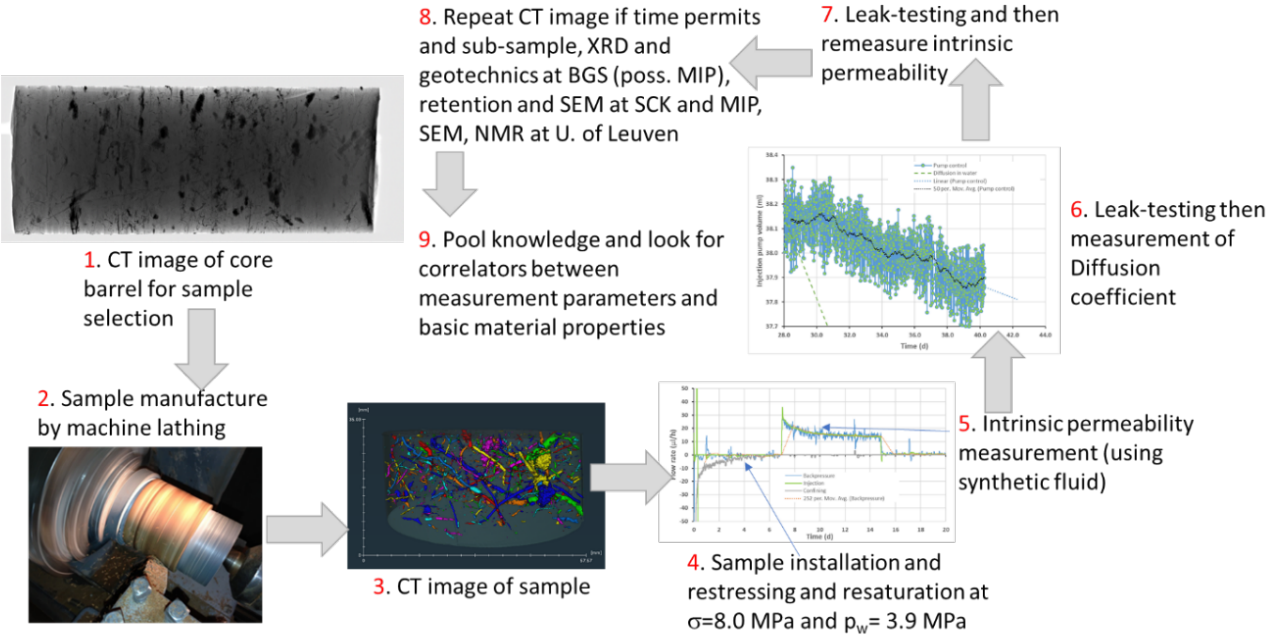

Figure 1.14: Schematic showing the general testing protocol. Note, not all tests in Table 1.4 have followed each step of this protocol as it has been developed at BGS during the project.

Sample ID	Material	Illite (% of clay)	Chlorite (% of clay)	Kaolinite (% of clay)	Illite / Smectite (% of clay)	Surface Area (m^2/g)
FPR-21-011	BC	51.00	4.00	17.00	29.00	251.00
FPR-21-055	BC	39.64	4.96	27.70	27.70	191.68
FPR-21-040_S	Synthetic	19.00	N/A	16.00	65.56	319.00
FPR-22-013	BC	35.77	4.71	27.53	32.00	202.61

Sample ID	Material	Illite (% of clay)	Chlorite (% of clay)	Kaolinite (% of clay)	Illite / Smectite (% of clay)	Surface Area (m^2/g)

Table 1.7: Partial XRD data for samples in this report. Each XRD test contains the clay percentage by mineral as well as the illite to smectite ratio, and a Brunauer-Emmet-Teller surface area analysis of the grains in the sample.

1.2.6. Results

1.2.6.1. Natural clay samples: tests FPR-19-006, FPR-21-011, FPR-21-028, FPR-21-055 and FPR-22-013

Sample Overview Five laboratory-scale samples of Boom Clay and one sample of the Eigenbilzen sand have been tested with the results presented in Table 1.8. In addition, four laboratory-scale tests were also performed on synthetic samples with varying mineralogical compositions, Table 1.5, with the results presented in Table 1.9. In discussion with ONDRAF/NIRAS and COVRA, it was agreed samples should be tested at a greater depth of burial equivalent to around 400 m. As such, unless otherwise stated, tests were performed at a confining stress of 8.0 MPa and a porewater pressure of 3.9 MPa, giving an effective stress of 4.1 MPa.

In the first sample of Boom Clay tested, FPR-19-006, it was only possible to determine intrinsic permeability through numerical analysis of the consolidation transient (see Appendix A). This yielded a value of 5.1x10^{-19} m^2. All attempts to measure the diffusion coefficient were unsuccessful, due to excess leakages from the testing system. Improvements to the apparatus were made, including modification of the pre-charge vessel housing the gas permeant for diffusion testing, the introduction of face-seal metal to metal gaskets on 'make and break' connections to the pressure vessel head and finally the addition of a high precision differential transducer (rated 0-100 kPa) to minimise gas gradients across the sample, that allowed diffusion coefficients to be measured.

In addition to the above changes in apparatus design, the diffusivity of different sheathing/combination of sheathing materials were measured, Figure 1.15, in order to minimise gas losses from isotropic confinement. Heat shrink Teflon was found to have an effective diffusion coefficient of around 2.2x10^{-10} m^2/s. In contrast, a sheath made from polyvinylidene fluoride, PVDF (a highly non-reactive thermoplastic fluoropolymer used in the drinks industry) yielded only minor gains in gas losses, with a measured effective diffusion coefficient of around 1.8x10^{-10} m^2/s. These values were both high in comparison to the apparatus, which based on leakage yielded an equivalent effectie diffusion coefficient of around 8x10^{-12} m^2/s. As Teflon was easier to use and cheaper than PVDF, a combination of aluminised foil and heat shrink Teflon was subsequently tested, yielding a effective diffusion coefficient of around 4.9x10^{-11} m^2/s. It should be noted that this value probably reflects the leakage properties of the membrane holder used to test the various sheathing materials, Figure 1.15, rather than that of the foil and Teflon. However, even this value was more than sufficient for the purposes of this study, so diffusion measurement could be made on natural materials for the rest of the study.

Intrinsic permeability of natural clay samples In test FPR-21-011, performed on a section of Boom Clay which had already been consolidated to the target effective stress (i.e., 4.1 MPa), intrinsic permeability for flow perpendicular to bedding was measured using three ascending, followed by two descending, constant head tests, with pressure differentials of 140, 288, 388, 288 and 140 kPa respectively (Figure 1.16). Measured permeability values were very consistent, resulting in an average value of 1.15x10^{-19} m^2 with a standard deviation of 3.97x10^{-21} m^2, indicating permeability was not sensitive to the magnitude of the differential pressures (i.e., head gradient) applied during this test. However, the value of 1.15x10^{-19} m^2 is significantly lower than that obtained for FPR-19-006, though the latter was based on analysis of the

Figure 1.15: Photo of the membrane holder used to estimate the diffusion coefficients of different sheathing materials. Values obtained are conservative, representing upper leakage values.

consolidation stage where all porosity is assumed to play a role. Based on CT analysis of major features within each sample (Table 1.6), FPR-19-006 has the highest volume of features above 0.5 mm^3. It is possible these play a role in the permeability value determined for the sample and thus may account for the higher value observed for sample FPR-19-006.

In test FPR-21-028A and B, performed parallel to bedding on core material pre-conditioned to the correct effective stress, intrinsic permeability was measured before (test [A]) and after (test [B]) the first diffusivity measurement. The diffusion measurement was then repeated which formed part of test [B]. Interestingly, a significant reduction in permeability value was observed dropping from 5.11x10^{-19} m^2 to 3.68x10^{-19} m^2. The reason for this change is not clear, but appears to be real, given the subsequent reduction in diffusion coefficient when remeasured after the second intrinsic permeability test [B]. Post-test examination of the sample yielded no obvious cause for the reduction in permeability observed in the test. Indeed, the sample actually increased very slightly in volume resulting in the apparent drop in bulk density observed in Table 1.4.

Test FPR-21-055 was performed perpendicular to bedding (on material which had already been pre-compacted to the target effective stress) and based on the average value from two constant head steps, Figure 1.16, yielded a permeability value of 1.13x10^{-19} m^2. This number is very similar to that from sample FPR-21-011, even though there was around 4.4m separation between the samples when taken from within the same borehole. As with test FPR-21-028, intrinsic permeability was remeasured following protracted measurement of the diffusion coefficient. Unlike the afore mentioned test, intrinsic permeability of FPR-21-055 increased slightly following the measurement of diffusion, rising from 1.13x10^{-19} m^2 to 1.70x10^{-19} m^2. While this small change is within the resolution of the apparatus the cause for it remains unclear.

In contrast to some of the previous tests, sample FPR-22-013 (performed parallel to bedding) was not pre-conditioned to the target effective stress. As such, the sample was initially stressed to Mol conditions (i.e., confining and backpressure 4.4 and 2.2 MPa respectively) and the hydraulic conductivity measured, bottom left graph Figure 1.16. This yielded a value of 8.17x10^{-19} m^2. The sample was then stressed to the target effective stress (i.e., confining and backpressure 8.0 and 3.9 MPa respectively) and the permeability remeasured. Upon retesting, permeability had dropped to 6.69x10^{-19} m^2. This is a relatively small decrease and is consistent with the Boom Clay moving along a rebound-reconsolidation line with relatively small gradient. Following diffusion testing, the permeability was measured for a third time, yielding a value of 4.06x10^{-19} m^2 (Table 1.8).

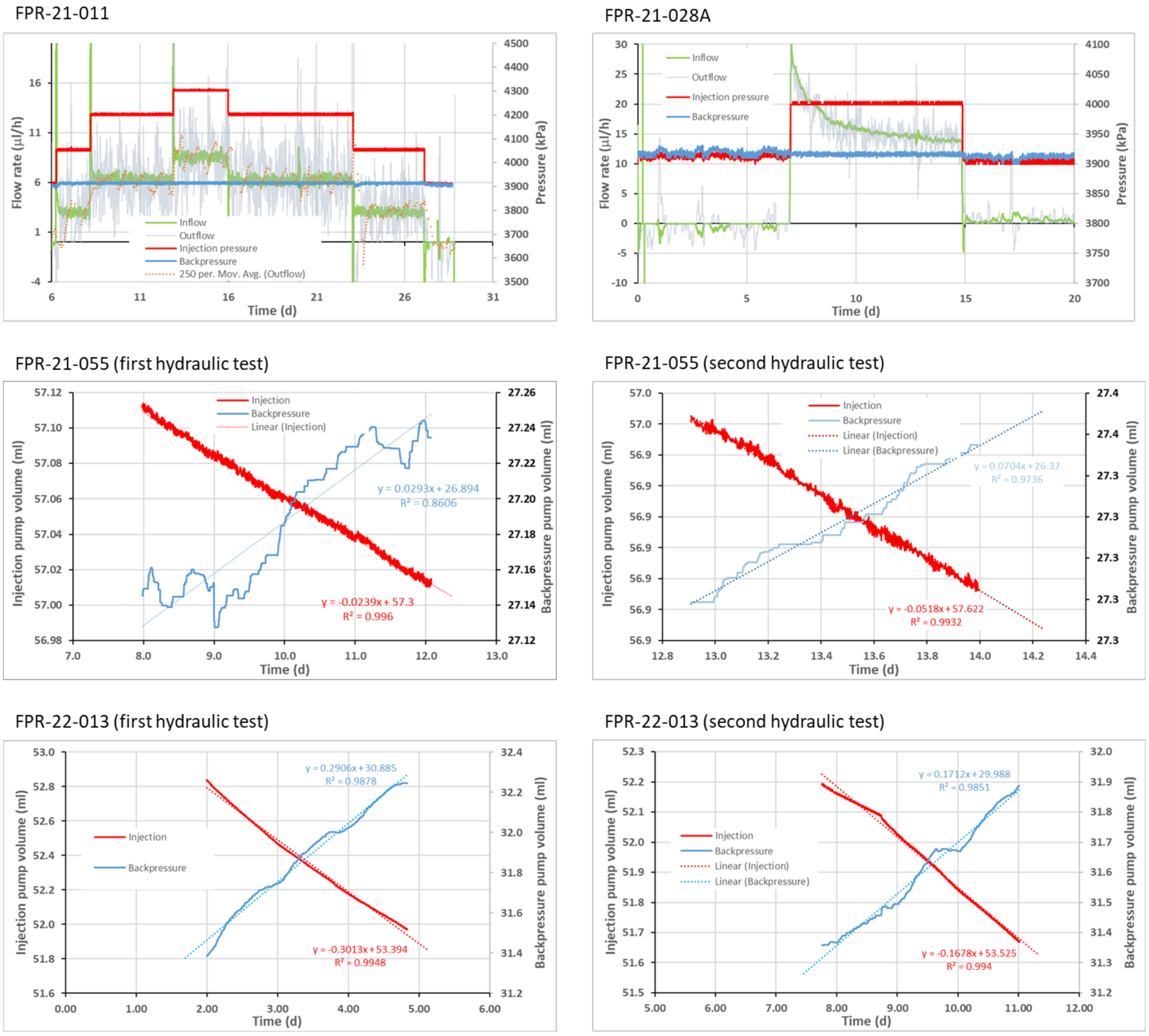
FPR-21-011

FPR-21-028A

FPR-21-055 (first hydraulic test)

FPR-21-055 (second hydraulic test)

FPR-22-013 (first hydraulic test)

FPR-22-013 (second hydraulic test)

Figure 1.16: Hydraulic test data for tests performed on natural clay samples prior to gas testing. Top left shows inflow, outflow, injection pressure and backpressure data for test FPR-21-011. The outflow data appears noisy because the data has been oversampled (logged every 30 seconds). Top right shows similar data for test FPR-21-028A. Here, the injection flow rate exhibits a protracted transient the cause of which is unclear but may be linked to the reduction in permeability of the sample observed during the test. The remaining images are for tests FPR-21-055 and FPR-22-013 showing the change in volume of the injection and backpressure pumps. The gradient from this data can be used to calculate flux and subsequent permeability.

Intrinsic permeability of natural sand samples At the request of SCK CEN and ONDRAF/NIRAS, a sample of Eigenbilzen sand, no. FPR-22-038, was tested. As in test FPR-22-013, the permeability was initially measured under in situ conditions (i.e., with confining and back pressure values of 3.05 and 1.45 MPa respectively) based on data from SCK CEN. This yielded a value of 9.70x10^{-16} m^2 (Table 1.10). Following measurement of the diffusion coefficient the permeability was remeasured, this time yielding a value of 2.22x10^{-17} m^2 (Table 1.10). This represents nearly an order of magnitude decrease in permeability. Confining and backpressure values were then increased to 8.0 and 3.9 MPa respectively and the permeability remeasured. This gave a similar value of 1.79x10^{-17} m^2, suggesting collapsed of the pore structure may have occurred sometime between the first and second hydraulic tests (Figures 1.17A and 1.17B).

Sample Number	Test material	Sample orientation	Permeability, k_i (m^2) prior to diffusion testing	Permeability, k_i (m^2) after to diffusion testing
FPR-19-006	Boom Clay	Perpendicular	5.14×10^{-19}	-
FPR-21-011	Boom Clay	Perpendicular	1.15×10^{-19}	-
FPR-21-028A	Boom Clay	Parallel	5.11×10^{-19}	-
FPR-21-028B	Boom Clay	Parallel	3.68×10^{-19}	-
FPR-21-055	Boom Clay	Perpendicular	1.13×10^{-19}	1.70×10^{-19}
FPR-22-013	Boom Clay	Parallel	6.69×10^{-19}	4.03×10^{-19}
FPR-22-038A	Eigenbilzen sand	Perpendicular	9.70×10^{-16}	2.22×10^{-17}
FPR-22-038B	Eigenbilzen sand	Perpendicular	1.79×10^{-17}	-

Table 1.8: Summary of intrinsic permeability, k_i, before and after gas diffusion measurements were made. Note, test FPR-21-028 was split into two measurement phases each yielding a different value for permeability. Test FPR-22-038 was performed at two different confining stress and backpressure values i.e., 4.4 and 2.2 MPa, and 8.0 and 3.9 MPa for tests A and B, respectively.

Intrinsic permeability of synthetic samples The hydraulic properties of four synthetic samples were measured as part of this study (Table 1.5). Each sample had a different mineralogical composition so that the coupling between permeability, diffusion and mineralogy could be explored. Intrinsic permeability was measured in a similar manner to that of previous natural samples, i.e., by constant head steady state testing.

In test FPR-21-040_S, the permeability was measured twice prior to gas testing, yielding values of 9.03 and 9.00 x 10^{-18} m^2 (Figure 1.18). Following diffusion testing, the permeability of the sample was remeasured. During this latter stage data processing was complicated by a small leak but yielded an estimated value of 3.36 x 10^{-18} m^2. This represents a large drop in permeability and is similar to the behaviour observed for samples FPR-22-013 and FPR-22-038.

In tests FPR-23-008_S, FPR-23-010_S and FPR-23-037_S intrinsic permeability was measured before and after diffusion testing (Table 1.9). Inspection of the data shows that permeability values vary between test samples, which is discussed in a later section, see section 1.2.6.3 Diffusion and permeability correlations. In two of the tests (samples FPR-21-040_S and FPR-23-008_S) the permeability value measured after diffusion testing is significantly lower than the value prior to testing. Sadly, the test protocol developed as part of this study meant the sample was quartered following removal from the apparatus. This complicated measurement of the geotechnical properties. At the time of writing, partial data only was available and could not be used to explain the changes in permeability observed. Further post-mortem work is required to explain this observation.

1.2.6.2. Diffusion properties of natural and synthetic materials

The diffusion coefficient to helium was measured in all tests except that of FPR-19-006 and the data has been tabulated in Table 1.10. In tests FPR-21-028 intrinsic permeability and the diffusion coefficient were measured on two separate occasions, both yielding slightly different values (Table 1.8), suggesting some time dependent evolution of the sample. In test FPR-22-038 the intrinsic permeability and diffusion coefficient were measured at two confining and backpressures. Figure 1.19 shows the change in the injection pump volume for two tests as gas slowly diffused through each sample. The difference in the apparent noise in the data between tests FPR-21-011 and FPR-21-028B (Figure 1.19), is caused by the introduction of a high accuracy differential pressure transducer. Unfortunately, this unit wasn't available at the start of the test programme which had to rely on the less sensitive pump transducers. The high accuracy device, accurate to +/- 0.1 kPa was used to control the injection pump to minimise the chance of developing an excess gas pressure, and thus unwanted gas advection. This level of accuracy meant that the injection pump constantly adjusted its position to compensate for the loss of gas by diffusion and expansion/contraction of gas caused by any minor changes in temperature. However, sampling across multiple days allowed trends in data to be identified and thus the diffusion coefficient to be calculated. In some tests it was necessary to apply a leak correction which was determined either before testing, when the system was checked to see if it was leak tight, or after testing, to check the system remained leak tight.

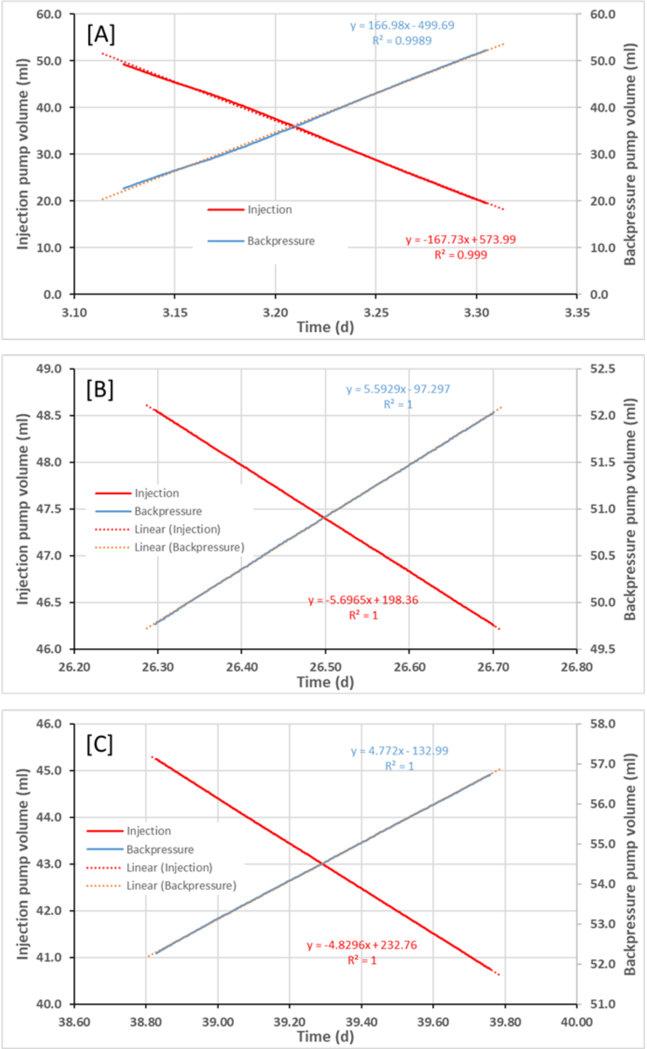

Figure 1.17: Data showing the volume loss and gain from the injection and backpressure pumps respectively during hydraulic testing of sample FPR-22-038. [A] hydraulic test under in situ conditions prior to diffusion testing. [B] hydraulic test following under in situ condition following diffusion measurement. [C] hydraulic test under target effective stress conditions of 8.0 MPa confining pressure and 3.9 MPa backpressure.

Sample Number	**Test material**	**Sample orientation**	**Permeability, k_i (m^2) prior to diffusion testing**	**Permeability, k_i (m^2) after to diffusion testing**
FPR-21-040_S	Synthetic	None	9.00×10^{-18}	3.36×10^{-18}
FPR-23-008_S	Synthetic	None	5.51×10^{-18}	7.25×10^{-19}
FPR-23-010_S	Synthetic	None	1.00×10^{-19}	1.36×10^{-19}
FPR-23-037_S	Synthetic	None	3.41×10^{-17}	3.18×10^{-17}

Sample Number	Test material	Sample orientation	Permeability, k_i (m^2) prior to diffusion testing	Permeability, k_i (m^2) after to diffusion testing

Table 1.9: Summary of intrinsic permeability values for synthetic samples before and after gas diffusion measurements were made.

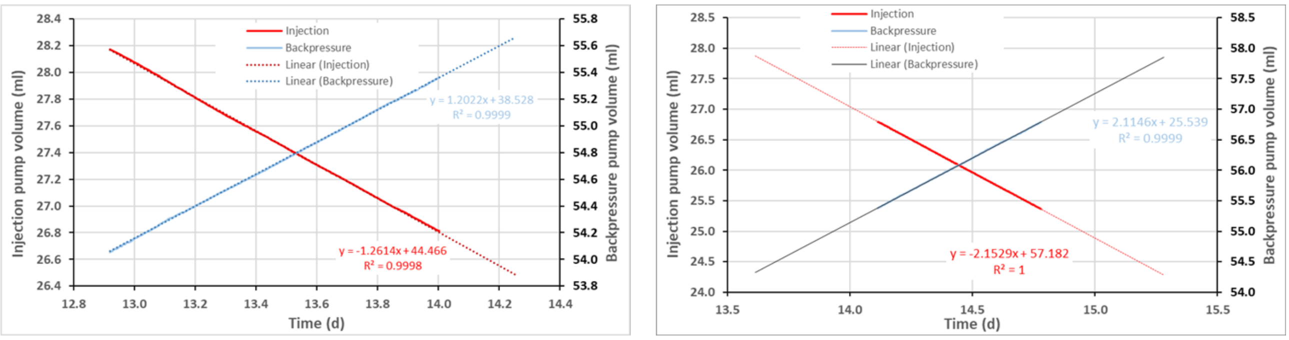

Figure 1.18: Example of volume loss and gain from injection and backpressure pumps respectively during hydraulic testing of a synthetic sample, in this case FPR-21-040.

The data presented in Table 1.10 indicates the Boom Clay and the synthetic samples have lower diffusivities than those of the Eigenbilzen sand. This is not surprising given the highly porous nature of the latter sample. Values for Boom Clay are broadly similar with those published by Jacops et al. (2020b), with the lowest diffusion coefficient measured on a Boom Clay sample cut perpendicular to the bedding (FPR-21-055). While there is a paucity of data, based on the information presented in Table 1.10 and Figure 1.20, gas appears to preferentially diffuse parallel to bedding, with nearly 60% of the diffusional capacity of the Boom Clay moving within the bedding planes.

Sample Number	Test material	Sample orientation	Effective diffusion coefficient (m^2/s)	Comment
FPR-19-006	Boom Clay	Perpendicular	-	-
FPR-21-011	Boom Clay	Perpendicular	3.26×10^{-10}	Leak tight
FPR-21-028A	Boom Clay	Parallel	3.82×10^{-10}	Leak tight
FPR-21-028B	Boom Clay	Parallel	3.71×10^{-10}	Leak tight
FPR-21-055	Boom Clay	Perpendicular	2.57×10^{-10}	Leak correction applied
FPR-22-013	Boom Clay	Parallel	4.71×10^{-10}	Leak correction applied
FPR-22-038A	Eigenbilzen sand	Perpendicular	4.04×10^{-09}	Leak tight
FPR-22-038B	Eigenbilzen sand	Perpendicular	1.05×10^{-09}	Leak correction applied
FPR-21-040	Synthetic	Composition 7	5.10×10^{-10}	Leak tight
FPR-22-008	Synthetic	Composition 8	2.86×10^{-10}	Leak tight
FPR-23-010	Synthetic	Composition 2B	1.12×10^{-10}	Leak correction applied
FPR-23-037	Synthetic	Composition 3B	6.48×10^{-10}	Leak tight

Table 1.10: Summary of diffusion coefficient values from the test study for both natural and synthetic samples. Note, test FPR-21-028 was split into two measurement phases [A] and [B] each yielding a different value for permeability and diffusivity. Test FPR-22-038 was performed at two different confining stress 3.05 and 8.0 MPa for tests [A] and [B] respectively.

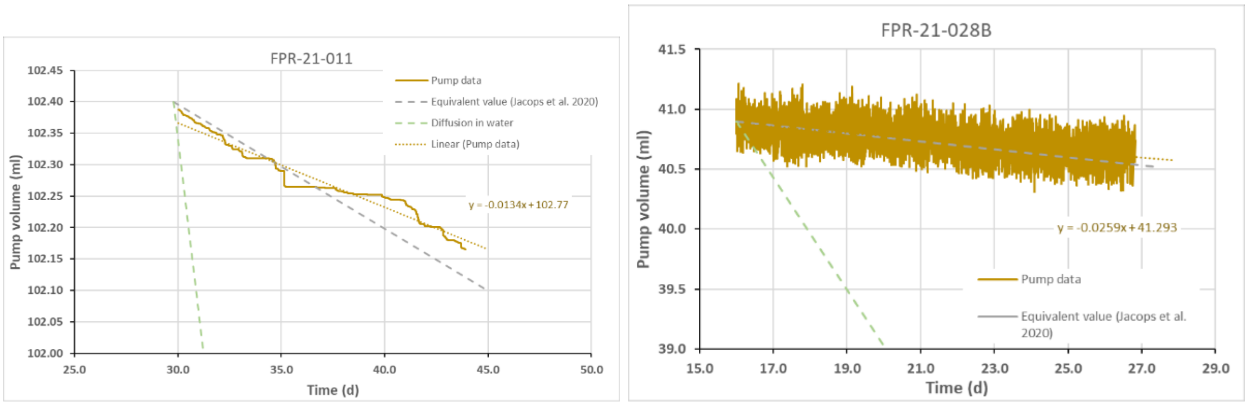

Figure 1.19: Example plots showing the volume loss from the injection pump while measuring diffusion of helium in tests FPR-21-011 and FPR-21-28B. The dotted green line is the equivalent response if the system was measuring the diffusion of gas in water (i.e., assumed to be 6.7×10^{-09} m^2/s). The dotted grey line is the equivalent response from Jacops et al. (2020b) and is based on the average values for diffusion into Boom Clay (i.e., 4.82×10^{-10} m^2/s).

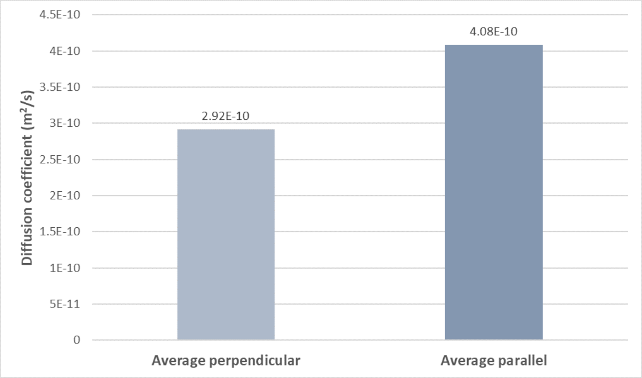

Figure 1.20: Bar chart showing average diffusion coefficients perpendicular and parallel to bedding. Data suggests gas diffuses preferentially parallel to bedding.

1.2.6.3. Diffusion and permeability correlations

While there is a paucity of data, based on the limited values presented in Table 1.10 (excluding the value for FPR-19-006 as this was derived from analysis of the consolidation transient rather than by direct constant head testing), the Boom Clay has a hydraulic anisotropy ratio of around 4.5. While this value will certainly change as more data becomes available, it is, at present, higher than previously measured values, possibly reflecting the higher degree of compaction of the test material within this study, i.e., compacted to 400m equivalent depth of burial.

Data suggests that gas will preferentially diffuse parallel rather than perpendicular to bedding. However, while this statement is true (based on a very limited dataset available), when the diffusion coefficient is cross plotted against permeability a more fundamental relationship emerges (Figure 1.21A). While there is some noise in the data, as would be expected with natural materials, the Boom Clay data when plotted in log-linear space, represented by the blue dots on the graph, indicates a fundamental linkage between diffusion and pre-test intrinsic permeability. While diffusion is an omnidirectional process, the bias towards higher permeability zones within the clay seems intuitively correct as gas, like water, will find it easier to move within larger pores. It is also interesting to note that these same log-normal type relationships were reported for Boom Clay linking changes in permeability to changes in effective stress caused by the application of the test hydraulic gradient, Horseman and Harrington (1994).

The coupling between diffusion coefficient and permeability is demonstrated in the synthetic sample data which extends the relationship over three orders of magnitude. The synthetic sample data shows that mineralogy, diffusion coefficient and permeability are fundamentally linked, and by changing the mineralogy the transport coefficients of the material are altered. However, because mineralogy and composition are controlled in the synthetic samples, the dispersion in the data around the trend line shown in Figure 1.21A is significantly reduced. The fact the two trend lines have similar gradients suggests the same processes governing flow occur in each sample and because of this, for unlithified clays, the synthetic sample approach is a legitimate way of exploring such fundamental couplings.

While changes in microstructure between the natural and synthetic samples may play a role, the offset between the two trend lines in Figure 1.21A suggests the compaction pressure may have been a little high when preparing the synthetic samples[2]. While this speaks to the likely importance of compaction/burial history and its influence on permeability and diffusion coefficient, this was beyond the scope of this study. However, this is less important as the aim of the study was to explore the potential use of analogue (synthetic) samples to explore and define fundamental relationships governing difficult to measure parameters such as the diffusion coefficient. Indeed, as the gradients between the two datasets are so similar and the synthetic sample data extends beyond the likely range of permeabilities that might be encountered in the Boom Clay formation, then it seems reasonable that the trend line derived for Boom Clay could be partially extended (representing the distribution of permeability values for the Boom Clay) to predict likely values of the diffusion coefficient for a given permeability. However, this would need to be confirmed by performing more tests with formation outliers to verify whether the coupling between diffusion coefficient and permeability remains consistent with the existing data.

If one was able to define the distribution in permeability values (in any direction) within an unlithified material then the synthetic sample approach could be used to quickly and accurately define the likely coupling between diffusion and permeability across the likely range of compaction states and mineralogical compositions. Obviously, such relationships may only hold true over certain ranges of mineralogical composition and compaction states. This is demonstrated in Figure 1.21B where data from the test performed on the Eigenbilzen sand has been added and the graph replotted with logarithmic scales. The in situ value plots in the top right of the graph, well beyond the ranges of the Boom Clay and synthetic samples. However, when the sample was compacted to the target depth of 400m, the permeability and diffusivity drop considerably and are more in line with the Boom Clay and synthetic sample datasets. When viewed in this way across multiple orders of magnitude, the noise in the experimental data is compressed somewhat, and the Eigenbilzen sand and Boom Clay data could be represented by a single power law function. However, while this suggests some commonality between the two datasets and the processes occurring therein, great care must be exercised in the application of such broad extrapolations, which require additional experimental verification before they should be used.

In Figure 1.22 the pre-test bulk density values are plotted against the diffusion coefficients for [A] Boom Clay and [B] synthetic samples. As can be seen, the data in Figure 1.22A exhibits considerable noise reducing the apparent strength of the linear trend. Test FPR-21-055 (with a diffusion value of $2.57\text{x}10^{-10}$ m^2/s) plots significantly below the trend line, which otherwise would have been much stronger. However, at the time of writing, no obvious reason as to why this value plotted below those of the other data was available. However, it should be noted that pre-test bulk density values are very susceptible to the degree of saturation, so, if test FPR-21-055 have lost moisture during sample preparation and installation then it would plot with a low bulk density. That said, a cursory look at the post-test values of bulk density from Table 1.4 (which should be water saturated) do not improve the correlation. Sadly, XRD data was also not available at the time of writing so correlations to clay type and clay content could not be made.

In contrast, Figure 1.22B shows a stronger coupling to bulk density than that seen for Boom Clay. It is helped by the fact that densities vary across a much larger range of values than those for natural materials

---

[2] If necessary it should be a simple matter to adjust the compaction pressure to yield synthetic samples with a similar permeability to the unlithified material under investigation.

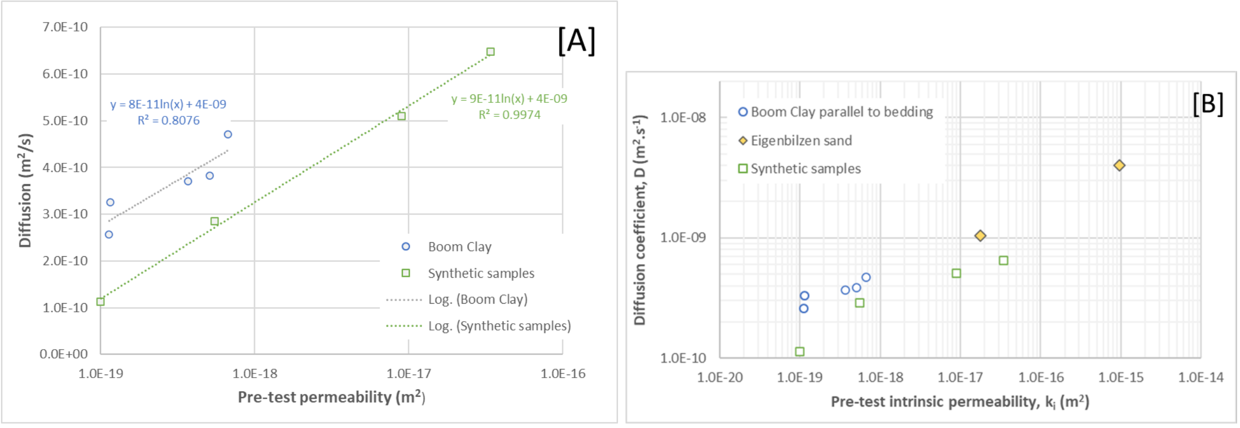

Figure 1.21: [A] Cross-plot of diffusion coefficient against pre-test intrinsic permeability for Boom Clay samples compacted to a pressure equivalent to 400 m depth of burial and synthetic samples comprise of different mineralogical compositions. The graph suggests a fundamental relationship between exists between these two coefficients, with the offset between natural and synthetic samples probably linked to the compaction pressure of the sample. [B] log-log graph including the Eigenbilzen sand data, the values of which are relatively high and should be checked against future measurements.

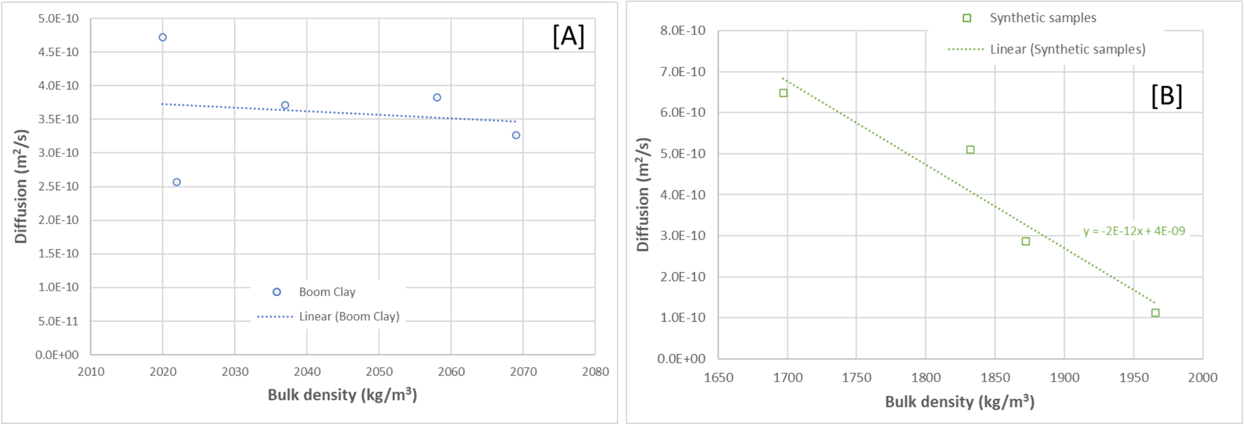

Figure 1.22: [A] Cross-plot of diffusion against pre-test bulk density. The blue dot with a diffusion value of 2.57 x 10^{-10} m^2/s) is from test FPR-21-055. At the time of writing no reason why this value plotted so low was available. It must be noted that bulk density values are very susceptible to saturation so it test FPR-21-055 have lost most it would plot with a low bulk density. [B] same data as [A] but for synthetic samples. Here, bulk densities varied considerably due to the different mineralogical compositions of the samples but exhibit a general linear trend for the sample densities tested.

looked at in this study. While this coupling is most interesting, more data is required to verify the results and to check values remain consistent. It may be that this coupling significantly changes as more data becomes available. Similarly for Boom Clay, more data and better post-test characterisation of the samples allowing geotechnical values to be determined would be most beneficial and allow the strength of the coupling to density to be determined[3].

As bulk density is linked to compact state it seems likely that diffusion values may also change as the density of the clay increases with burial. This is potentially seen in Figure 1.21A and may account for the offset observed between the natural and synthetic sample lines. The strong coupling seen in Figure 1.22B also alludes to the likely coupling between bulk density (which would increase with depth) and the diffusion

---

[3] Note, post-test geotechnical measurement were made difficult as the samples were sections while wet to be sent to SCK.CEN and the University of Leuven.

coefficient.

While analysis of the mineralogical data remains incomplete, a plot of illite/smectite ratios (Table 1.7) against diffusion coefficients (Table 1.10) for the Boom Clay samples shows a preliminary relationship between these two quantities. As only three data points were available at the time of writing, the relationship cannot be used for anything other than an indicator for a possible correlation. Clearly more data is required to check the validity of this correlation.

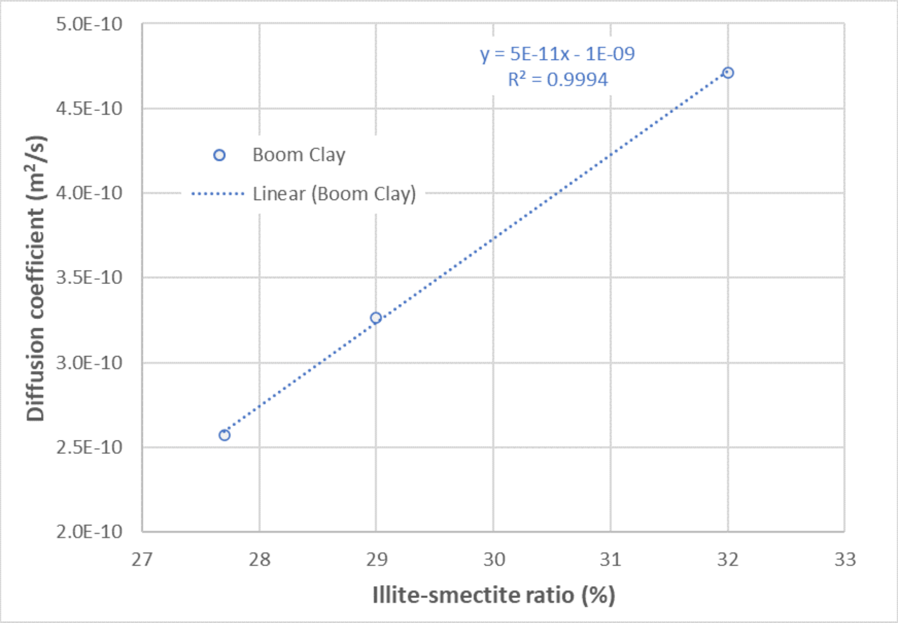

Figure 1.23: Initial cross-plot of diffusion coefficient against illite/smectite ratio. As only three data points were available at the time of publication, this relationship must be treated with caution, but suggests diffusivity in Boom Clay may be linked to the clay ratio.

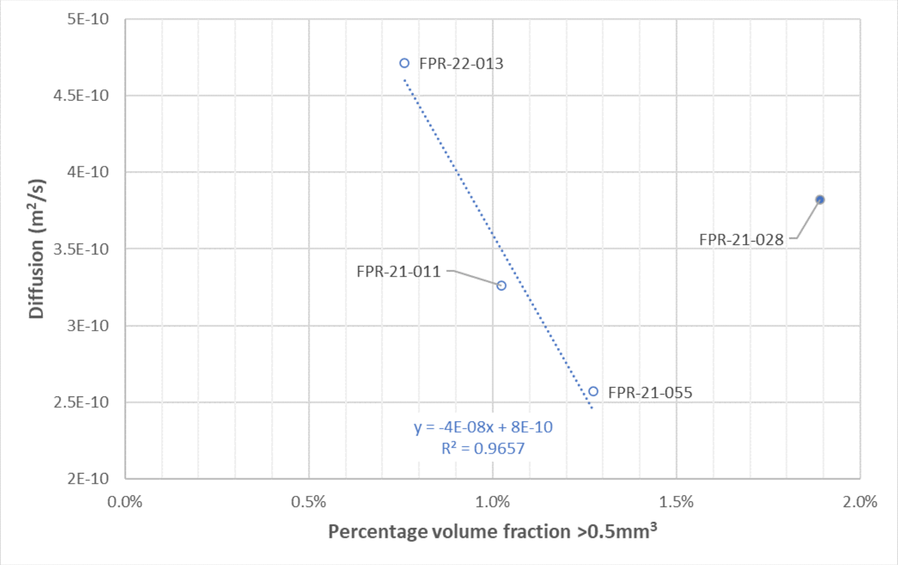

Figure 1.24: Cross plot of diffusion coefficient against percentage volume fraction of features with a volume greater than 0.5 mm^3.

Analysis of the X-ray CT data for natural samples of Boom Clay yields an interesting correlation. By cross plotting the percentage volume fraction[4] of features with a volume greater than 0.5 mm^3 (Table 1.6) against

---

[4] Note, plotting percentage values removes any variability which would be introduced as sample volume between tests.

the diffusion coefficients (Table 1.10), an interesting correlation emerges (Figure 1.25). Examination of the graphs suggests an inverse correlation between the diffusive capacity of the sample and the volume of features greater than 0.5 mm^3, suggesting in general such features in Boom Clay are less conductive.

However, sample FPR-21-028 does not follow this trend. Examination of the pre- and post-test X-ray CT data suggests differences exist between this sample and the other natural clay materials tests. Unlike every other sample in this study, the features in FPR-21-028 are more strongly preferentially orientated about 30º off the vertical. In Figure 1.25 the data from FPR-21-028 and FPR-21-011, both cut parallel to bedding, is presented and visually shows this difference. While most other samples have burrows, these largely are XY planar (horizontal) in nature and more random in direction. FPR-21-028 is also the only sample to show open fractures prior to testing, Figure 1.25A. Whether these differences account for the fact sample FPR-21-028 plots outside the trend for the other three tests is unclear. However, such trends in behaviour may become apparent if more samples are tested.

1.2.7. Summary

A robust methodology has been developed to determine the intrinsic permeability and gas diffusion behaviour of both natural and synthetic sample material under representative repository stress conditions. A methodology has also been developed to manufacture synthetic samples which can be used to explore fundamental couplings between material properties without the complications of material variability. Even so, synthetic and natural Boom Clay samples were found to have commonalities in behaviour with both showing a coupling between intrinsic permeability and the diffusivity. Intuitively this coupling seems reasonable as gas diffusion and the permeability of a sample will always be biased by the connectivity and aperture of larger pores.

While there is a paucity of data, data suggests Boom Clay has a hydraulic anisotropy ratio of around 4.5 for samples tested at the target depth of 400m. While this value will change as more data becomes available, it demonstrates the potential impact of stress history and burial depth.

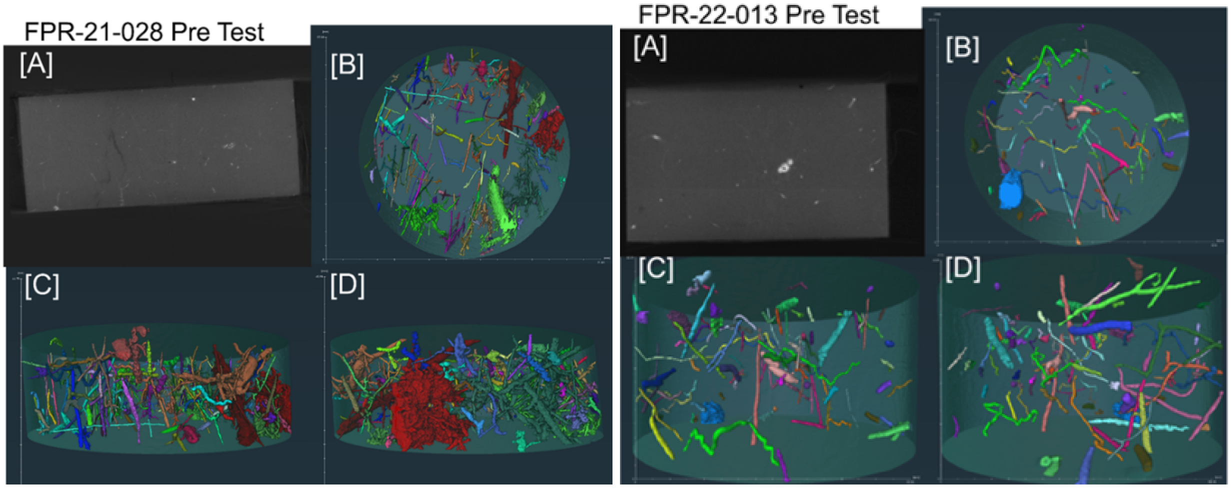

Figure 1.25: Pre-test X-ray Ct data for sample FPR1-21-028 (left image) and FPR-22-013 (right image). Both samples were cut parallel to budding but sample FPR-22-013 shows significantly less burrows and no initial fracturing.

Data suggests gas will preferentially diffuse parallel rather than perpendicular to bedding and appears fundamentally linked to intrinsic permeability. Over the data ranged tested a semi-log relationship was found to exist, like that found by Horseman and Harrington (1994), which links permeability to changes in effective stress. The coupling between intrinsic permeability and diffusion coefficient was much clearer in the synthetic sample data, showing mineralogy, diffusion coefficient and permeability are fundamentally linked. The fact the two trend lines have similar gradients suggests the same processes governing flow (advection or diffusion) occur in test materials. Given this commonality, it seems reasonable that the trend line derived for Boom Clay could be extended to predict likely diffusion coefficient values for higher/lower permeability samples. However, to do this robustly and with confidence would need more experimental information than was available for this study.

Figure 1.26 shows a composite plot of all the data measured in this study. By plotting on logarithmic scales, the data from the Eigenbilzen sand and Boom Clay appear to follow similar trends. This could be coincidence as could the fact data from natural materials and synthetic samples also share very similar power law relationships. However, such relationships should be used with caution. More experimentation is required to check the validity of these relationships which remain tentative.

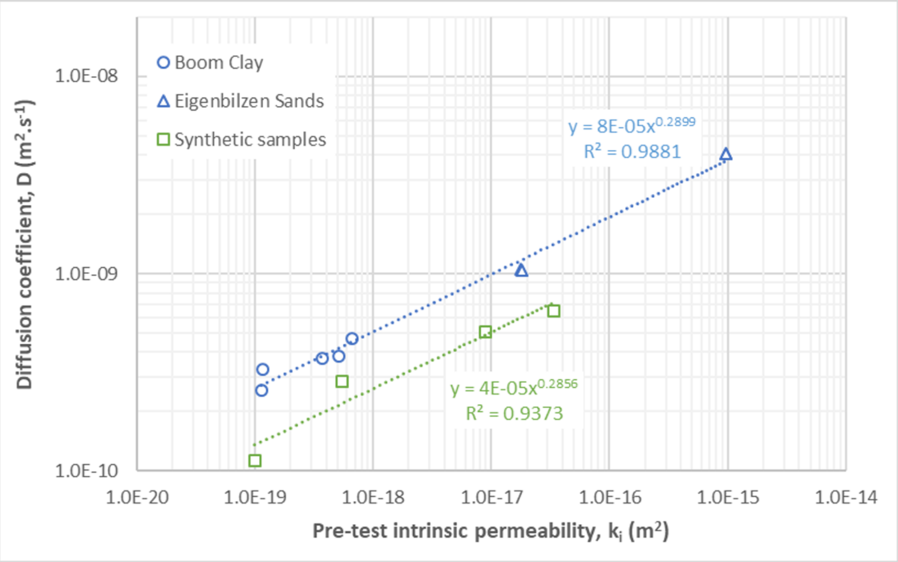

Figure 1.26: Compilation of data from this study for Boom Clay, Eigenbilzen sand and synthetic samples.

A tentative relationship between diffusion coefficient and bulk density also emerges from this study. This relationship is particularly strong for the synthetic samples whose mineralogy and therefore bulk density changed considerably compared to that of the Boom Clay samples. As above, while the data alludes to existence of this relationship, more experiments are required to add confidence and bound the validity of any equations used to predict the diffusion coefficient based on bulk density. As the latter will change as a function of burial depth, it seems likely diffusion coefficients will also decrease accordingly. Sadly, insufficient XRD data was available at the time of writing this summary so any correlations to clay type and clay content could not be made.

Analysis of the X-ray CT data for natural samples of Boom Clay indicates diffusion coefficient could also be linked the percentage volume fraction of features with a volume greater than 0.5 mm^3. The data in Figure 1.24 indicates an inverse correlation between the diffusive capacity of the sample and the volume of features greater than 0.5 mm^3 exist, suggesting in general such features in Boom Clay are less conductive than the surrounding matrix.

1.2.8. Key learning points

1.2.8.1. New knowledge acquired

This study has successfully measured the permeability and diffusion coefficients for Boom Clay, a sample of the Eigenbilzen sand under two different stress regimes, and a range of synthetic samples manufactured with different mineralogical compositions, all adding to the knowledge pool for these materials.

For the first time, tests on Boom Clay have been performed at an equivalent depth of burial of 400m thus providing new data which, in time, can be used to assess the impact of burial history on the diffusion properties of Boom Clay.

While the role of microstructural differences between the synthetic and natural samples needs further consideration and probably accounts for much of the noise in the data for natural samples, this study highlights the potential use of synthetic samples. These materials could, with a bit of tweaking, be manufactured with similar transport characteristics to Boom Clay, and therefore could be used to define important correlations between hard to measure parameters (such as the diffusion coefficient). Synthetic samples benefit from being 'pure' systems (without the complicating aspects (which can lead to dispersion/noise) of natural materials) and can be used to elucidate fundamental relationships more easily.

Diffusion of helium was also shown to occur preferentially along bedding planes with approximately 60% of the diffusional capacity of Boom Clay moving parallel to bedding (which was a key research aim for the project). However, of greater importance was the observed coupling between diffusion and intrinsic permeability which was very clear in the synthetic sample data.

Based on the limited set of data from this study, the anisotropy ratio for the intrinsic permeability of Boom Clay increases with burial depth and was estimated to be around 4.5 with flow moving preferentially parallel to bedding.

Preliminary correlations between diffusion coefficient and hydraulic permeability have been defined along with correlations between diffusion coefficients and bulk densities. The data also suggests the diffusion coefficient can be linked to other factors including X-ray CT data (e.g., the percentage volume of features above 0.5 mm^3). However, all these relationships required further experimental verification.

Examining the data as a whole suggests a fundamental relationship exists between permeability and diffusivity, and when plotted in logarithmic scale the Boom Clay and Eigenbizen sand fall on a common projection. If correct, such relationships could be used to predict diffusivity across a range of material and permeability scales. However, before this can occur substantially more experimental evidence is required to improve/disprove these correlations for different material types.

1.2.8.2. Impact of acquired knowledge

This study has identified important couplings between the diffusion coefficient and intrinsic permeability. With additional verification, this could be used to predict the diffusion coefficient based solely on easier to measure parameters. The importance and usefulness of synthetic test samples to identify and elucidate fundamental relationships has been demonstrated. These relationships can be used to guide future research studies and act as mechanisms to explore possible corelations between key parameters.

1.2.8.3. Remaining knowledge gaps

This study has identified potential correlations between diffusion coefficients and more easily measured parameters such as intrinsic permeability and possibly bulk density. The study lacks sufficient data to provide confidence in these relationships but should be regarded as the first step in highlighting key parameters which could be used to predict diffusivity. This is important as the diffusion coefficient is difficult to measure. This study demonstrates the possibility of such couplings and the importance they could have in the quantitative treatment of repository gas in safety assessment. The correlation between diffusion and mineral composition is complicated and while alluded to in Figure 1.23, it has not been adequately elucidated as part of this study. Additional tests, using a range of synthetic samples, are therefore required to provide a broader quantitative framework for interpretation.

1.2.8.4. Recommendations for the future

Additional diffusion and intrinsic permeability tests are required (both parallel and perpendicular to bedding) to provide a statistically meaningful data set, which can be used to strength the correlations suggested in this study, along with detailed pre- and post-test characterisation of test materials (including X-ray CT data, XRD analyses and measurement of geotechnical parameters).

A systematic study using synthetic samples should also be undertaken to identify and strengthen fundamental correlations, which can be used to highlight couplings or relevance in the quantitative prediction of diffusivity.

References

Horseman, S.T. and Harrington, J.F., 1994. Migration of repository gases in an overconsolidated clay. British Geological Survey, British Geological Survey, Technical report WE/94/7.

Jacops E., Rogiers B., Frederickx L., Swennen R., Littke R., Krooss B.M., Amann-Hildenbrand A. and Bruggeman C. 2020. The relation between petrophysical and transport properties of the Boom Clay and Eigenbilzen Sands. Applied Geochemistry, 114, 104527. doi: 10.1016/j.apgeochem.2020.104527.

Thomson, P.R., Aituar-Zhakupova, A. and Hier-Majumder, S., 2018. Image segmentation and analysis of pore network geometry in two natural sandstones. *Frontiers in Earth Science*, *6*, p.58.

Appendix A

Numerical model: linear elastic skeletal deformation

The fluid flow through a compressible porous medium may be described by Biot's model [1], where the governing equation for flow is obtained by combining Darcy's law with the mass conservation equation. Thus,

$$\nabla \bullet \left(\frac{k}{\mu}\nabla p\right) = \phi\beta\frac{\partial p}{\partial t} + \frac{\partial}{\partial t}(\nabla \bullet \mathbf{u}) \quad (1)$$

where $\mathbf{u}$ is the solid displacement [m], p is the fluid pressure [Pa], k is the intrinsic permeability [m^2], μ is the dynamic viscosity of the fluid [Pa•s], ϕ is the porosity [-] and β is the compressibility of the fluid [Pa^{-1}]. Note that an isotropic permeability, represented by the scalar k, is here assumed.

In this work, an elastic deformation of the matrix is assumed. Hence,

$$\nabla \bullet \tau + \mathbf{f} = \mathbf{0} \quad (2)$$

where $\mathbf{f}$ is the body force per unit volume of the medium [N/m^2] and τ is the total stress on the medium [Pa], which can be expressed as

$$\tau = \sigma - \alpha p \mathrm{I} \quad (3)$$

where σ is the effective stress tensor [Pa], α is the Biot's coefficient [-] and I is the identity tensor. Note that, under the assumption of small strains and an isotropic linear elastic material, the effective stress tensor takes the form

$$\sigma = \lambda \mathrm{tr}(\varepsilon)\,\mathrm{I} + 2G\varepsilon \quad (4)$$

where λ is the first Lamé's constant [Pa], G is the shear modulus [Pa] and tr stands for the trace operator. For the sake of simplicity, $\alpha = 1$ is here assumed. This is a reasonable assumption for a saturated porous medium and leads to the equation

$$\frac{E}{2(1+\nu)(1-2\nu)}\nabla(\nabla \bullet \mathbf{u}) + \frac{E}{2(1+\nu)}\nabla^2\mathbf{u} - \nabla p = -\mathbf{f} \quad (5)$$

where E is the Young's modulus [Pa] and ν is the Poisson's coefficient [-]. Note that the relationships $\varepsilon = \nabla^s\mathbf{u}$, $\lambda = \frac{E\nu}{(1+\nu)(1-2\nu)}$ and $G = \frac{E}{2(1+\nu)}$ have here been used.

Finite element formulation

Following standard procedures, the numerical solution of Biot's model is solved using the Galerkin finite element method. Hence, the coupled-system of discretized equations

$$L^T\frac{du}{dt} + Hp + S\frac{dp}{dt} = -F_p \quad (6.1)$$

$Ku^{n+1} - Lp^{n+1} = F_u$ (6.2)

is solved. By using the backward Euler finite difference time scheme, system (6) becomes

$$\begin{bmatrix} K & L \\ L^T & -\Delta t H\text{-}S \end{bmatrix} \bullet \begin{bmatrix} u^{n+1} \\ p^{n+1} \end{bmatrix} = \begin{bmatrix} F_u \\ L^T u^n - Sp^n + \Delta t F_p \end{bmatrix} \quad (7)$$

with the matrices defined in Table 1.11.

Matrix	**Symbol**	**Expression**
Flux matrix	F_p	$F_p = \int_{\Gamma_p} N^T q d\Omega$, where q is the flux vector prescribed on the boundary Γ_p.
Load matrix	F_u	$F_u = \int_{\Gamma_u} N^T t d\Omega$, where t is the traction vector prescribed on the boundary Γ_u.
Permeability matrix	H	$H = \int_\Omega (\nabla N)^T \frac{k}{\mu} \nabla N d\Omega$
Soil stiffness matrix	K	$K = \int_\Omega B^T C B d\Omega$, where B is the matrix of shape function derivatives and C is the elastic stiffness tensor.
Coupling matrix	L	$L = \int_\Omega B^T m N d\Omega$, where $m=[1,1,1,0,0,0]^T$.
Compressibility matrix	S	$S = \int_\Omega N^T \phi \beta N d\Omega$

Table 1.11: Block matrices of the discretized Biot's system of equations.

Model parametrisation: Young's modulus and permeability estimation for FPR-19-006

The coupled system of equations (7) is solved to estimate the rock properties (namely the hydraulic permeability and the Young's modulus) of geological materials subjected to a consolidation test. Due to the nature of this problem, a two-dimensional axisymmetric finite element model is used here. As detailed in [4], the facts that (a) the Young's modulus mainly determines the total volume of fluid expelled (line 11) and (b) the permeability mainly determines the rate at which fluid is expelled (line 12) are used to estimate the two parameters.

This algorithm provided reasonable theoretical flow-time curves (Figure 1.27) for the Boom Clay sample, with input parameters summarised in Table 1.12 and a fitted Young's modulus of 316 MPa and a fitted permeability of 5.1×10^{-19} m^2.

Meaning	**Symbol [units]**	**Value**
Radius of the sample	r [mm]	24.96
Length of the sample	L [mm]	42.67
Poisson's coefficient	ν [-]	0.125 (1)
Dynamic viscosity	μ [Pa • s]	2.32×10^{-3}

Table 1.12: Geometrical and material parameters used in the numerical fittings for the Boom Clay specimen. Note that (1) the Poisson's coefficient reported by Barnichon and Volckaert (2003) and Bésuelle et al. (2013) is used here.

References

[1] Biot, M.A. (1941). General Theory of Three-Dimensional Consolidation. *Journal of Applied Physics,* 12(2), 155-164. DOI: 10.1063/1.1712886.

[2] Barnichon, J.D. and Volckaert G. (2003). Observations and predictions of hydromechanical coupling effects in the Boom clay, Mol Underground Research Laboratory, Belgium. *Hydrogeology Journal*, 11(1), 193-202. doi: 10.1007/s10040-002-0240-6.

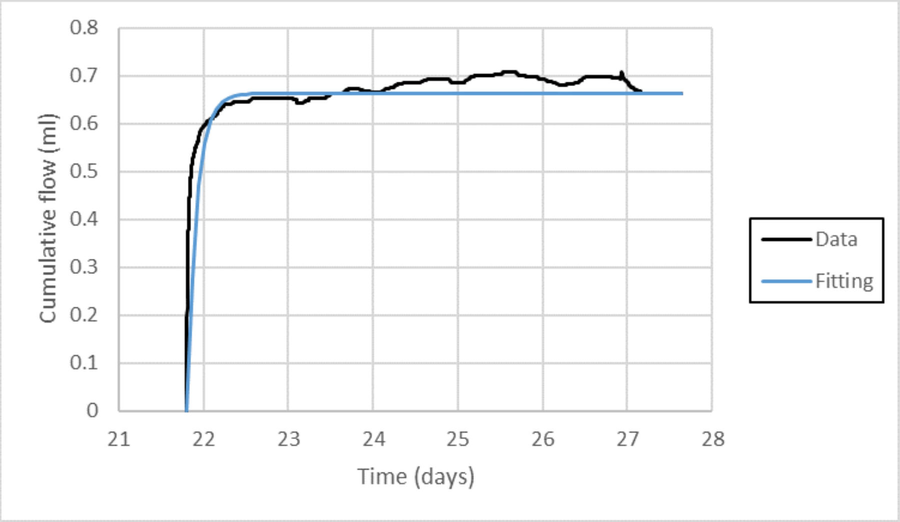

Figure 1.27: Boom Clay specimen: comparison of model to flow data.

[3] Bésuelle, P., Viggiani, G., Desrues, J., Coll, C. and Charrier, P. (2013). A Laboratory Experimental Study of the Hydromechanical Behavior of Boom Clay. *Rock Mechanics and Rock Engineering*, 47(1), 143–155. doi: 10.1007/s00603-013-0421-8.

[4] Tamayo-Mas E., Harrington J.F., Graham C.C. (2018). On modelling of consolidation processes in geological materials. *International Journal of Engineering Science*, 131, 61 – 79. DOI: 10.1016/j.ijengsci.2018.05.008

.

Belgian Nuclear Research Centre (SCK CEN)

1.3. Gas diffusion in unsaturated clay (SCK CEN)

1.3.1. Introduction & Objectives

Deep geological disposal has been widely regarded as the most efficient form of waste disposal for high and long lived intermediate level nuclear wastes. Clays have been conceptualized to host nuclear wastes in quite a few countries (Grambow, 2016). Belgium has recently declared that geological disposal is the way forward and that the current radioactive waste stockpile of high level and long lived intermediate level nuclear waste could potentially be disposed of in poorly indurated clay layers. Extensive research has been done on one such clay based rock called Boom Clay. Boom Clay is a thick plastic clay unit, naturally found in the Northern part of Belgium (Vandenberghe et al., 2014).

The presence of metallic components in HLW (high level waste) and LL-ILW (long-lived intermediate level waste) and the application of metal canisters in the repository will unescapably lead to anaerobic corrosion and hence the imminent generation of gases (hydrogen) as byproducts. It has been established by previous studies that the transport of gases in Boom Clay is dominated by diffusion (Jacops et al., 2013a). If the rate of this diffusive transport is not fast enough however, there would exist an imbalance between gas generation and gas dissipation by diffusion, which in turn, could lead to the formation of a free gas phase. This could lead to damage in the form of fractures in the host rock and the engineered barriers immediately surrounding the nuclear waste, hence paving potential pathways for a fast transport of radionuclides through the barriers. Hence, it is imperative that there is a good understanding of the diffusion process of gases in the host rock as well as on the most suitable method to measure the diffusion coefficients of gases in barrier materials. SCK CEN has already studied the diffusive behavior of gases in fully saturated clay samples from different host rocks (Boom Clay, Opalinus Clay, Callovo-Oxfordian) and materials used in the engineered barrier (bentonite, cementitious materials) (Jacops et al., 2017c). However, the diffusion of gases (or RN) under *partly saturated* conditions is still relatively unknown. Partial saturation is predicted to exist (Tsang et al., 2015) during the lifetime of the repository and therefore it is important to understand how partially saturated conditions could affect the rate of gas transport. There has been some work in measuring the rate of diffusion of ionic species and radioactive tracers (Savoye et al., 2010a) in partially saturated clays but thus far no measurements on gas diffusion, for which there could exist alternate mechanisms for transport. The motivation for performing this task, and by extension the knowledge gap that is tackled, is that partially saturated conditions may come to exist during the lifetime of the repository. Natural ventilation will occur during the excavation of the nuclear waste repository, which could lead to partial desaturation of the host rock. But the gas generation by anaerobic corrosion itself, could also cause the desaturation of the host rock and engineered barriers in the repository (King, 2012).

Hence, it is important to gain understanding on the process of how partial saturation in clay based materials, along with the effect of a change in pore structure, will affect the rate of gas transport. This is done by measuring the diffusion coefficients of gases in clays under varying conditions of:

- Water saturation
- Mineralogical composition – which corresponds to the pore structure of the test materials.

The overall objective is to come up with a comprehensive analysis of all the factors that influence gas diffusion under unsaturated conditions and link the most important factors and the properties that could play a part in the safety assessment during the post closure phase of a geological disposal facility.

It is worth noting that the overall water content of the partially saturated zones within the radioactive waste repository is not expected to be strongly below full saturation. Therefore, an interest range of 70-100% water saturation has been fixed to study the effects of desaturation on gas diffusivity.

1.3.2. Experimental setup

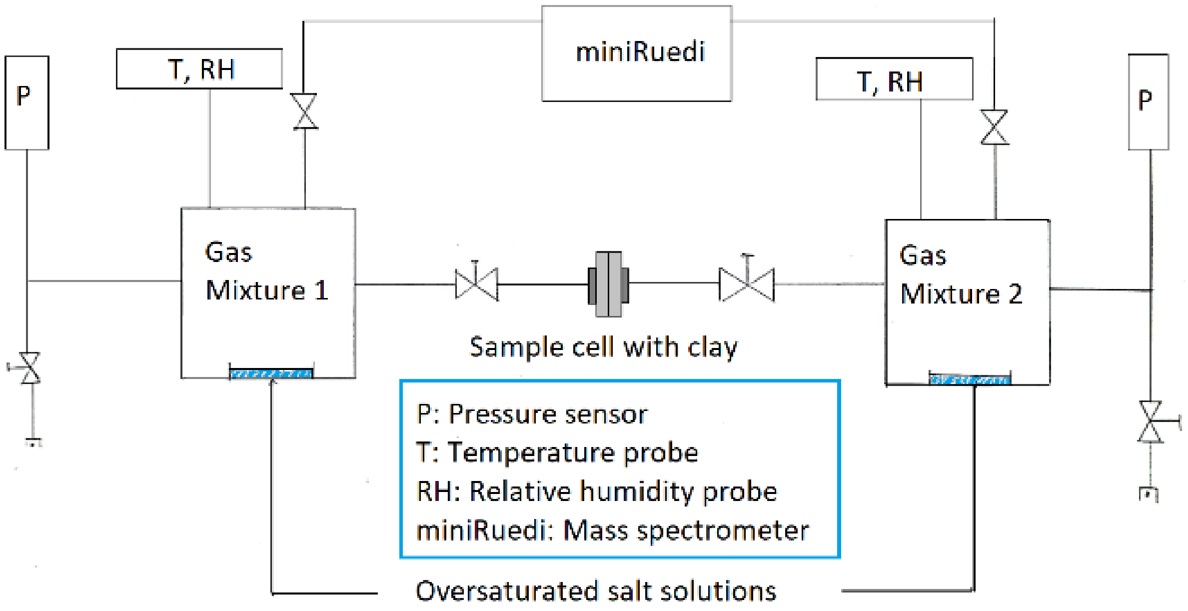

Figure 1.28: Description of experimental setup

1.3.2.1. Description of apparatus

Jacops et al. (2013b) developed a double through diffusion methodology with dissolved gases to determine the diffusion coefficients of a suite of dissolved gases in Boom Clay and other potential barrier materials including concretes and bentonites under fully saturated conditions.

For the purpose of measuring gas diffusion coefficients in partially saturated clays, an approach different from the conventional dissolved gas transport is proposed. The approach is envisioned to be able to conduct experiments in a pure gas phase, to keep the saturation of the clay sample constant, without wetting or drying it during the experiment. A novel setup has been designed and assembled to make diffusivity measurements in purely gaseous conditions under controlled RH, while following the same double through diffusion methodology as described in (Jacops et al., 2013b) .

It consists of two reservoirs which contain the bulk gases which will diffuse through the clay sample. The bulk gases in the upstream reservoir are not continuously circulated by any means other than natural convection. The entire setup is designed to work at ambient pressures and temperatures. The setup is depicted in Figure 1.28.

All diffusion experiments are performed at pressures at or marginally above ambient pressure, with concentration gradients being the only driving force for the transport process. The relative humidity in the reservoirs is maintained by using selected saturated salt solutions, thus keeping the moisture content of the clay sample constant throughout the experiment.

The initial design of the setup was made so as to have venting options in the tubing from the reservoir to the cell as well as the tubing which lead to the sampling ports for at each reservoir. This is shown in Figure 1.29.

This was later adapted to a less tortuous setup in the sense that the vents were removed and any unnecessary metal joints and connections were removed, thus reducing the total amount of material consumed in the construction of the setup while keeping the same functionality. This led a more compact and less leak prone setup. This is shown in Figure 1.30. The setups are equipped with temperature and Druck DPS 5000 CANBus pressure probes, which also have thermometers and one of the setups (Figure 1.29) is also additionally equipped with Vaisala indigo 520 humicap relative humidity sensors.

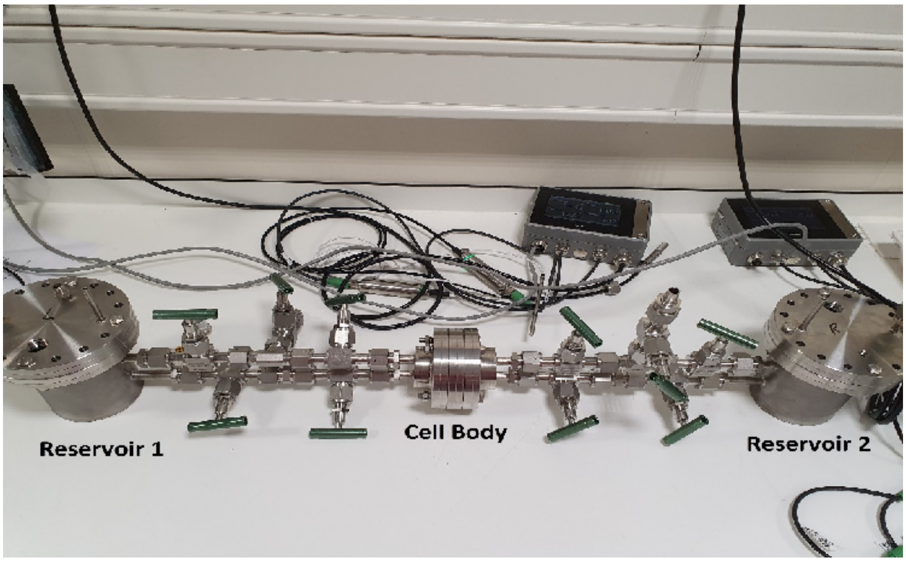

Figure 1.29: First prototype of experimental setup

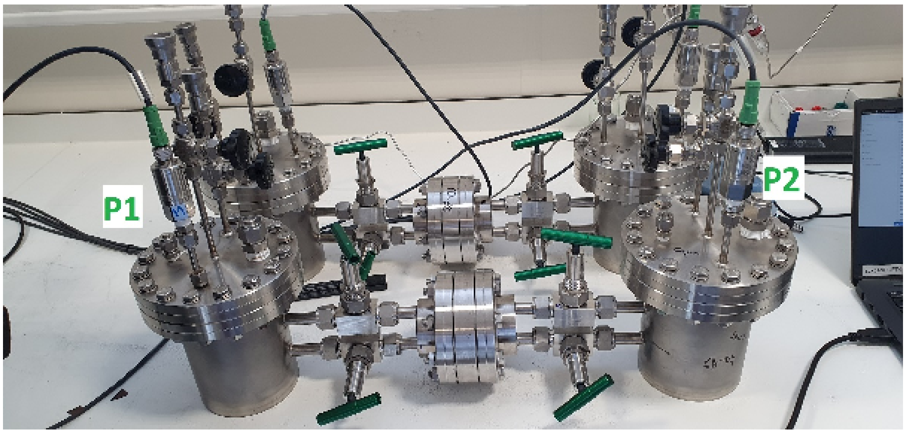

Figure 1.30: Prototype 2 experimental setup; P1, P2 are pressure probes.

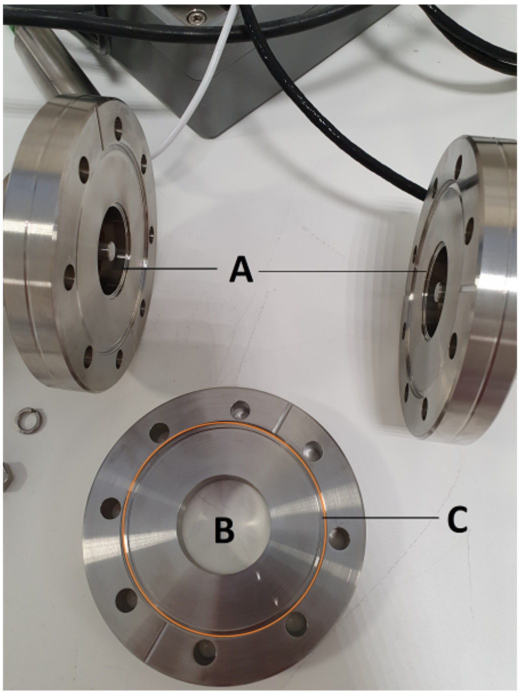

Figure 1.31: dismountable sample cell for cylindrical test samples A: space for gas exchange and filters, B: space for test sample. C: Copper gasket space

The sample is emplaced inside a dismountable cell body as shown in Figure 1.31. Sintered stainless steel filters are used in the space A mentioned in Figure 1.31 to ensure that the test sample in confined and cannot move in during the pressure tests. It consists of a removable flange to house the test sample. To ensure tightness of the sample and to avoid conductive pathways along the stainless steel – sample interface, a layer of moulding eco latex (Vosschemie VSure) is first applied all along the inner surface of B. The samples are then pressed in using a hydraulic press and the flanges are connected and the cell is sealed using copper gaskets to ensure gas tightness. The latex occupies any potential gas pathways and is allowed to harden to ensure good sealing. All diffusion test samples are 38mm diameter x 20mm height.

The gas analysis makes use of mass spectrometry (MS), which is performed using a miniRUEDI (Gasometrix GmbH, Switzerland). This is a portable gas analyser, equipped with a quadrupole mass spectrometer (Standford Research Systems RGA200), with two types of detectors, namely, the electron multiplier and the Faraday cup detectors. The working principle of the mass spectrometer is based on ion currents peaks measured by the detectors, which is then mapped to partial pressures of different gas species present in a mixture relative to a reference or standard gas mixture whose composition is known and defined. The instrument is shown in Figure 1.32.

The pumps are used to maintain vacuum, which is essential to the working of the mass spectrometer. The inlet selector valve is used to indicate to the QMS the correct port from which it must draw in gases to analyse or calibrate. The QMS is a highly sensitive instrument which is equipped with a Faraday cup detector and an electron multiplier detector (for measurement of gases in extremely small concentrations). However, for this study, the F detector will be used for all measurements. Since the QMS in miniruedi is quite sensitive, the diffusion experiments can be carried out at near ambient pressures, which is why there are no diffusion tests under high pressures.

1.3.2.2. Calibration

In order to perform accurate analyses of gas diffusion coefficients in partially saturated clay materials, the method of analysis, in this case, Mass spectrometry, has to be calibrated. For the calibration of MiniRUEDI, we make use of standard gases of known compositions. The details of all the standard gases are provided

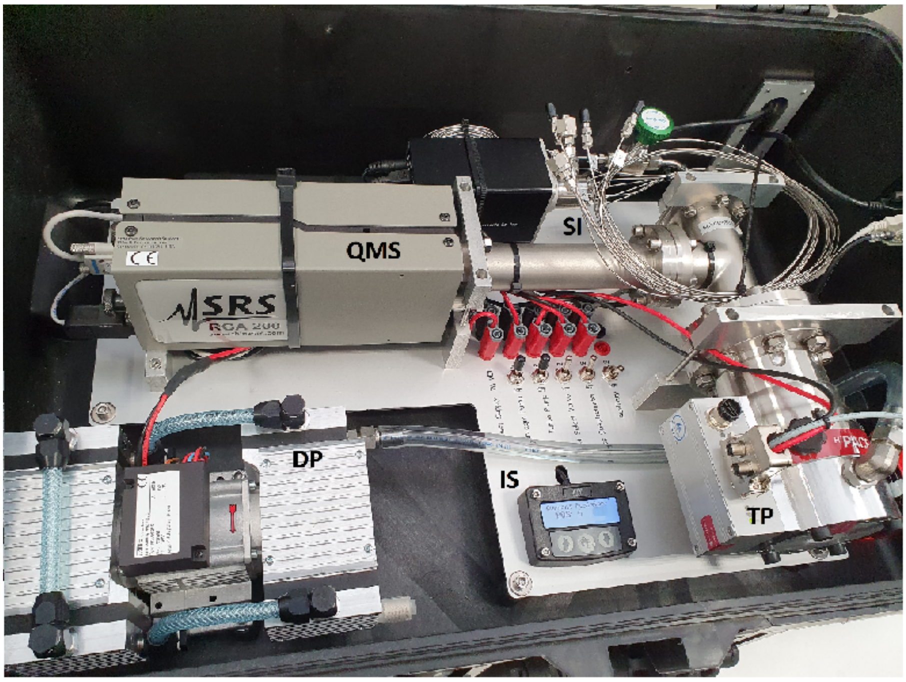

Figure 1.32: MiniRUEDI gas analyser (legend- QMS: quadrupole mass spectrometer, DP : Diaphragm pump, TP: Turbo pump, IS: Inlet selector valve, SI: Sample inlet capillaries)

in Tables 1.13 and 1.14. A single point calibration based on a standard gas of known composition is done, with 5 repetitions per standard measurement. This allows the mass spectrometer to determine the compositions of gases in real time, in terms of partial pressures, by mapping them to a known value of ionisation currents measured from the standard gases. Standard gases can be run straight from the source cylinder to miniRuedi through a pressure valve. However, this is not recommended as it is best to keep all standard and sample analyses using miniRuedi as close to ambient pressure as possible. Thus, all standard gases are filled in Cali-5-Bond gas bags, near ambient pressure.

The mass spectrum scan of a standard gas containing 99.9% Argon is shown in Figure 1.33. The x-axis shows the m/z value, which is the molecular mass to fragmentation charge ratio of the different peaks. For example, the base peak of Argon seen in Figure 1.33 is at m/z =40. However, it also fragments into a smaller, less intense peak at m/z = 20. The intensities shown on the Y-axis are the measured ion currents (A) by the Faraday cup detector. This is then mapped to partial pressures of the standard gas (which is a user input) based on a known composition of standard gas (also a user input). The MS then measures the intensities of currents measured at the targeted m/z ratios of the sample gas for accurate analysis. The standard measurements are generally run once every 5 repetitions of a sample gas analysis to account for higher accuracy in terms of gas analysis.

1.3.2.3. Testing fluids and gases

The gases used in the diffusion studies cover a significant range of molecular sizes. For the initial tests and validation experiments, mixtures of 4 gases (50% helium + methane and 50% ethane + xenon) were used. However, due to technical difficulties, the mixture of 4 gases were substituted with a binary diffusion system for the experiments in unsaturated conditions. The main reason that the mixture of four gases was eventually given up was because of interfering fragments in the mass spectra of methane and ethane. The quantification of both gases in tandem was impossible due to lack of sufficient deconvolution information with regard to resolution of interfering peaks of ethane and methane (Brennwald et al., 2020; Crunelle et al., 1997).

All the gases used in the study are reported in Tables 1.13 and 1.14. All test and flushing gases were

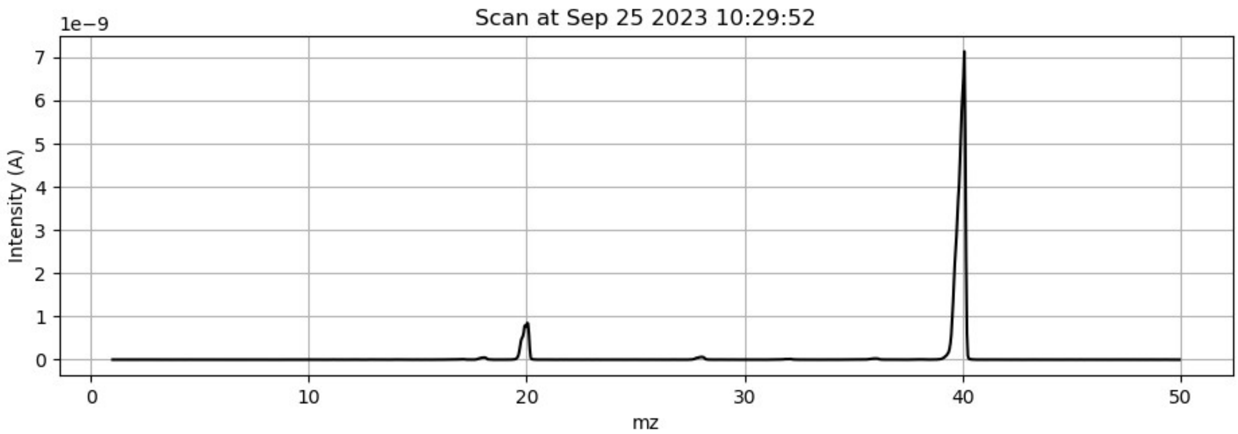

Figure 1.33: Scanned mass spectrum of a calibration gas of 99.9% Argon

obtained from Air Products. The flushing gas used in all experiments is 100% Nitrogen.

Test gases for validation experiments:

Table 1.13: Gases used in validation experiments

Reservoir	Test gas(es)	Standard gases
Chamber 1	50% Helium + 50% Methane	0.1% Xenon and Ethane in 49.9% Helium and Methane
Chamber 2	50% Xenon + 50% Ethane	0.1% Methane and Helium in 49.9% Xenon and Ethane

Test gases used in all other experiments:

Table 1.14: Gases used in diffusion experiments

Reservoir	Test gas(es)	Standard gases
Chamber 1	100% Helium	0.1% Argon in 99.9% Helium
Chamber 2	100% Argon	0.1% Helium in 99.9% Argon

1.3.3. Material properties (pre-test and post-test characteristics)

To validate the diffusion setup, a test sample is selected with characteristics similar to those in reference literature with available diffusivity values (Jacops et al., 2017). A sandy clay material called Eigenbilzen Sand is used, which is a glauconite-rich, fine to medium grained sandy clay found in the layer just above Boom Clay, in Belgium (Vandenberghe et al., 2014). The sandy clay sample, is a subsample from core ON-Mol-2A-189, retrieved from the borehole ON-Mol-2A (November 2014, Mol, Belgium), drilled perpendicular to the bedding plane and comes from a depth of nearly 296 metres.

The sample was extracted from the drill core and shaped to dimensions 38 mm in diameter and 20 mm in height. This was done using a dedicated cutting tool, with the help of a hydraulic press. The sample was shaped and smoothened by hand with a knife and then pressed into the sample cell, which was subsequently fitted into the setup. This particular sample of Eigenbilzen sand was chosen for the test because of the availability of abundant gas diffusivity data in literature. The sample is shown in Figure 1.34. A cropped out section showing the location of the Eigenbilzen sand formation is also shown in the figure.

The samples used in the actual diffusion experiments in unsaturated conditions are synthetic clay based samples prepared in collaboration with the British Geological Survey under EURAD GAS. They are ternary mixtures of sand, silt and clay materials as shown in Figure 1.35. The compositions used in this study are shown in Table 1.15. The synthetic samples are shown in Figure 1.36. The synthetic clay samples were chosen because they are quite close to the mineralogy of some natural clays which are potential host materials in various countries. These host rocks include the Callovo-Oxfordian (France), Boom Clay (Belgium) and the Opalinus Clay (Switzerland) formations (Frederickx et al., 2021; Kneuker et al., 2023; Pellenard & Deconinck, 2006).

Table 1.15: Composition of synthetic samples used in the study

Composition	MX80 Bentonite (63-125 µm) % g/g	Quartz sand (63-125 µm) % g/g	Kaolinite (63-125 µm) % g/g	Muscovite mica (<63 µm) % g/g
7	48	20	12	20
5A	48	35	12	5
6A	48	10	12	30

While it is hard to reproduce the exact microstructure of natural materials, changing mineral composition will have an effect on the pore structure (Pore size distribution) which is an important controlling factor in gas transport and also in the saturation/desaturation.

The vapour equilibrium technique is used to lower the saturation of clay samples for the experiments in partially saturated conditions (Le et al., 2008).

The artificial samples are preferred over natural clay samples in this study because the variability between different samples is better controlled, which enables a better process understanding . Thus, it is possible to design an experimental scheme where we can test the interplay of mineralogical composition of clay based materials on the rates of gas diffusivity and link them to the differences in pore structure to determine what the effect of a changing pore structure, along with partial saturation could be on the rate of gas transport. Furthermore, these artificial materials contain no heterogeneities which could affect the physical integrity of the test samples when subject to suction under desiccated conditions.

The presence of fissures or artefacts in the test sample plugs could provide an alternate pathway for gases and is not ideal for testing gas diffusion coefficients. The synthetic samples have been shown to produce no visible artefacts on dehydration as shown by the CT scans in Figure 1.37.

The two X-ray CT scans in Figure 1.37 depict different slices or areas of interest within the same sample. The images also portray the homogeneity of the samples with regard to distribution of sand, silt and clay particles throughout the sample. It is possible that during the preparation phase, there are minor regions where clay particles can tend to clump together given their cohesive nature and the nature of preparation of the sample powders. The mixing and the dicing is done manually. However, these clusters of clay rich regions are not as prominent when visualised under the CT scanner. All the samples used thus far have been shown in Table 1.16.

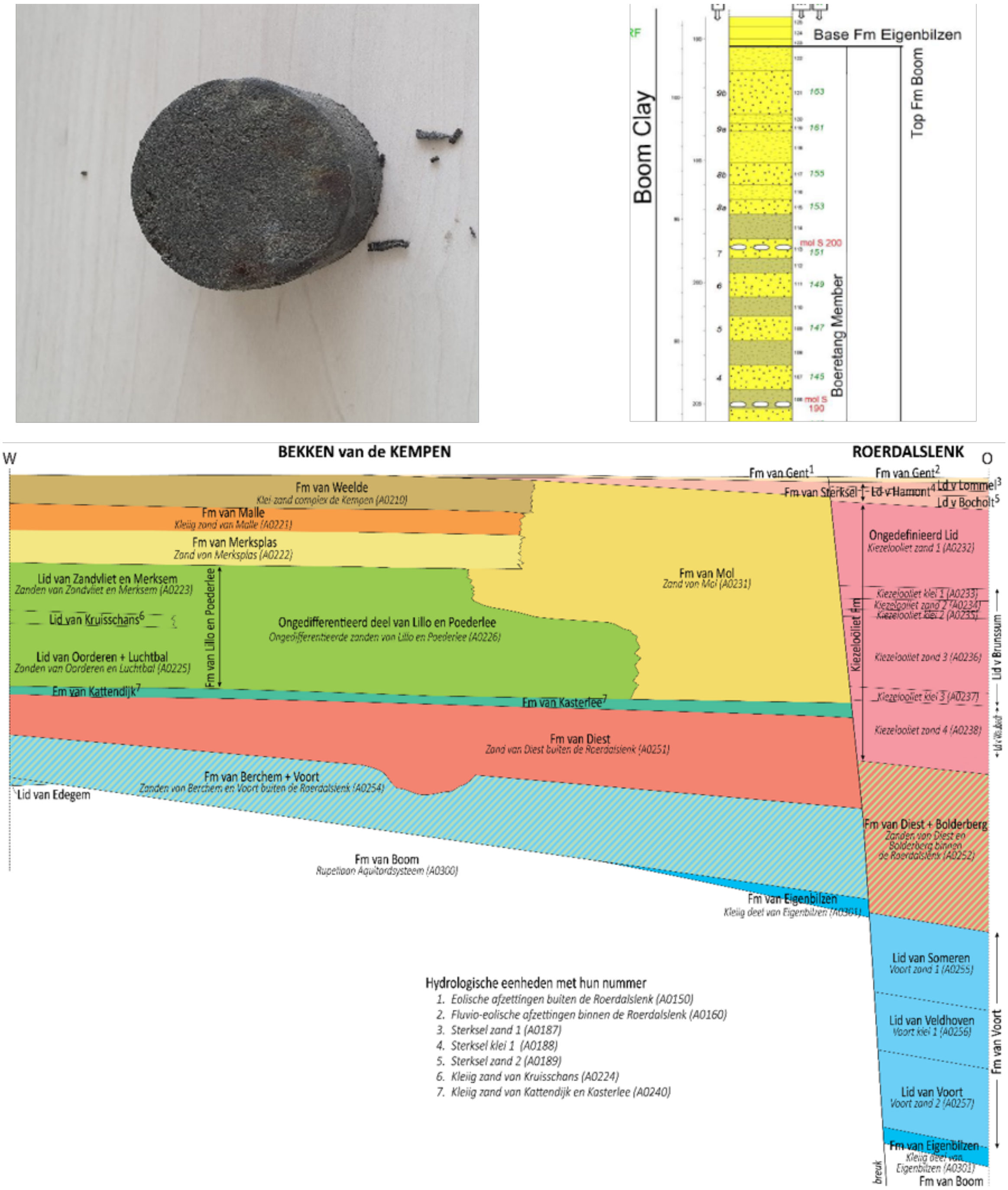

Figure 1.34: Sample Mol-2A-189b (Eigenbilzen sand) and its relative geological depth (Vandenberghe et al., 2014) (https://dov.vlaanderen.be/page/geologisch-3d-model-g3dv3)

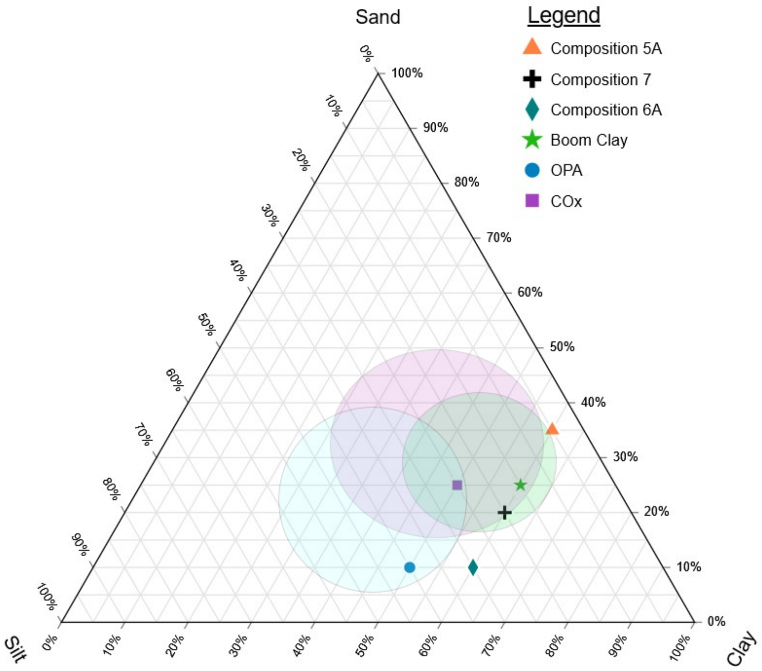

Figure 1.35: Ternary plot of synthetic clays used in the EURAD GAS diffusion project

Figure 1.36: plugs of synthetic clay samples for diffusion tests. (Legend: 5A-01 – composition 5A, 6A08-composition 6A, 61- composition 7.)

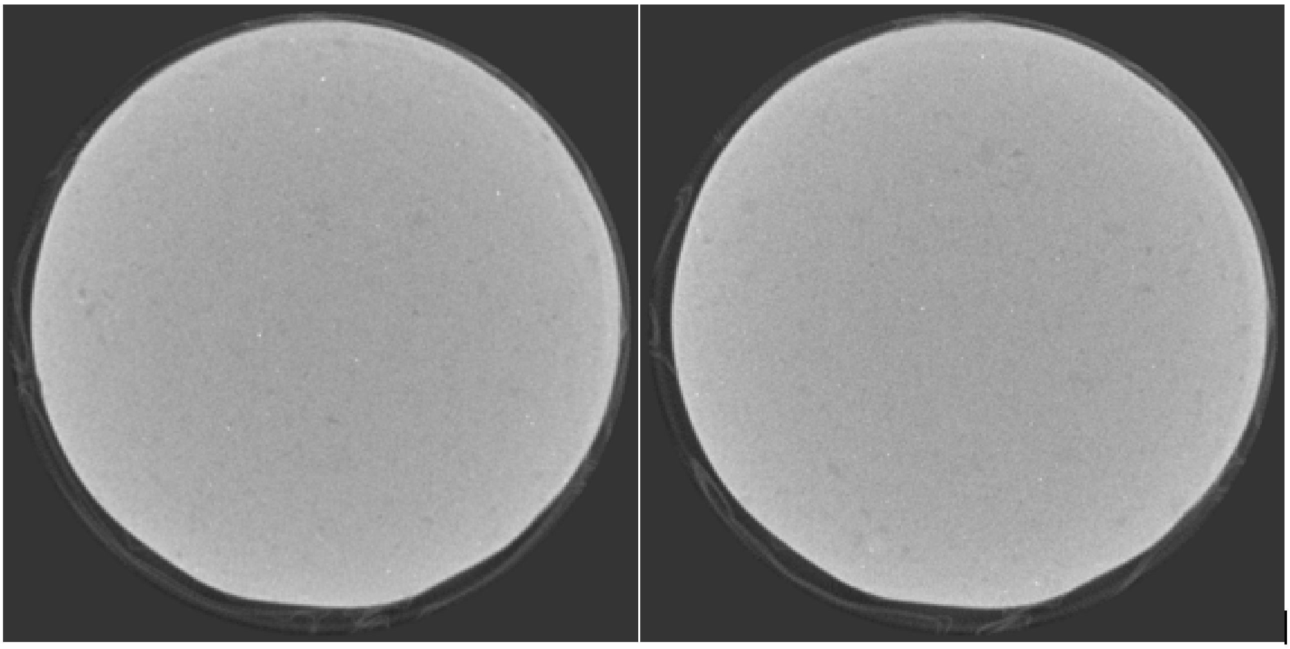

Figure 1.37: X-ray CT images of a sample of composition 5A after desiccation at 3 MPa for 1 month

Table 1.16: Catalogue of samples used in the study

Sample Name	Composition	Density (sp. Gravity)	Porosity
FPR-22-056 to 070	7	1.912	0.42
5A-01 to 09	5A	1.948	0.42
6A-01 to 09	6A	1.862	0.45
Mol-2A-189b	Eigenbilzen sand	-	0.40

1.3.4. Testing protocol

1.3.4.1. Sample conditioning

After the samples have been prepared in required dimensions for diffusion testing, they are placed in sealed environments (desiccators) under constant, fixed relative humidity conditions using oversaturated salts to produce suction corresponding to specific relative humidity values. This is the vapour equilibrium technique and has been described in a study by Le et al. (2008) . The study used the technique to determine the soil water retention curve (SWRC) for Boom Clay. It is a useful tool in estimating the saturation of a clay sample at a specific relative humidity condition. The saturated salt solutions used for conditioning of test samples are shown in Table 1.17. For the salts which produce very high relative humidity (above 90%), the measurement was done using the Vaisala indigo dew-point sensor, which is calibrated to perform at extreme conditions of relative humidity. All measurements are done in air conditioned environments where the temperature is maintained at 20 ± 1 C.

Table 1.17: Salts used for sample conditioning

Saturated salt solution	Measured relative humidity (RH) (%)	Literature RH (%) (Delage et al., 1998)	Suction from Kelvin's law (Delage et al., 1998) (MPa)
Water	100	100	0

Saturated salt solution	Measured relative humidity (RH) (%)	Literature RH (%) (Delage et al., 1998)	Suction from Kelvin's law (Delage et al., 1998) (MPa)
$CuSO_4$	97.9 ± 0.3	98	3
K_2SO_4	95.6 ± 0.7	96	6
KNO_3	93.7 ± 0.3	93	9
NaCl	75	76	39
NaBr	60	58	70

The RH measurements done in Table 1.17 for the very high RH salts are carried out by noting the highest and lowest values measured by the device over a period of 24 hours in a desiccator with a certain saturated salt. The median value is then used to calculate the suction from Kelvin's law as described in Delage et al. (1998). The calculated suction is then rounded to the nearest whole number for easy interpolation from the SWRC. For the salts which are of lower relative humidity (high suction), pinpoint accuracy is less essential and home devices to measure RH are accurate enough. For this, the Testo 174H mini humidity logger was used.

The water retention curves are drawn up by measuring the amount of moisture lost at each step in the drying path using oversaturated salts of different suction values. The total water content is calculated by oven drying a fully saturated sample at 105˚C until mass stabilization. Thus, the water saturation degree at each suction step can be calculated using this vapour drying technique. It is important to mention that in this study, all samples treated as "fully saturated" are done so also by the vapour technique by placing the samples in desiccated chambers at 100% relative humidity until mass stabilisation. Other methods of saturation, such as direct contact with water under a pressure gradient are avoided. This is done for consistency.

1.3.4.2. Diffusion experiments

Once the samples have been conditioned to the target relative humidity conditions, the samples are removed from the desiccator and placed in the diffusion cell. The diffusion cell is then mounted onto the sample rig, this is shown in figure 1.30 .

The setup is then leak and pressure tested at the same time using pure nitrogen gas. This is done using a pressure differential of 0.1 bar across the two reservoirs and is allowed to equilibrate overnight. If the pressures converge, this means that there is a preferential pathway for gases and thus, diffusion results cannot be reliable. On the other hand, if there is loss in total pressure from either of the reservoirs, this means that there is a leak in the system. Thus, this is a crucial step in the diffusion test setup.

Once the pressure tests are successful, the reservoirs are filled with the test gases after sufficient flushing. The experiment is then started when the readings at time t=0 are taken. Sampling of the downstream reservoirs is done once a week for the first 4 weeks then twice a week for the next four. The experiment is stopped when there are enough data points in the steady state regime to allow fitting a linear trend line of concentration of diffusing gas vs time. This step is determined by a linear fit of concentration of the gas at the downstream compartment vs time. A summary of scientific research suggests that if a strong correlation exists between linearly dependent variables, a regression coefficient (R^2) value of greater than 0.9 is desired (Plonsky & Ghanbar, 2018). However, this is purely convention since there are other metrics which also exist to determine the goodness of a fit. However, for this study, since an analytical solution of Fick's first law is being used to determine diffusion coefficients, the R^2 >0.9 is the preferred option.

Therefore, the estimation of diffusion coefficients is based on the following equation:

$$N_A = \left(\frac{D_{\text{eff}} P}{RTz}\right) \ln\left(\frac{1 - y_{A2}}{1 - y_{A1}}\right)$$

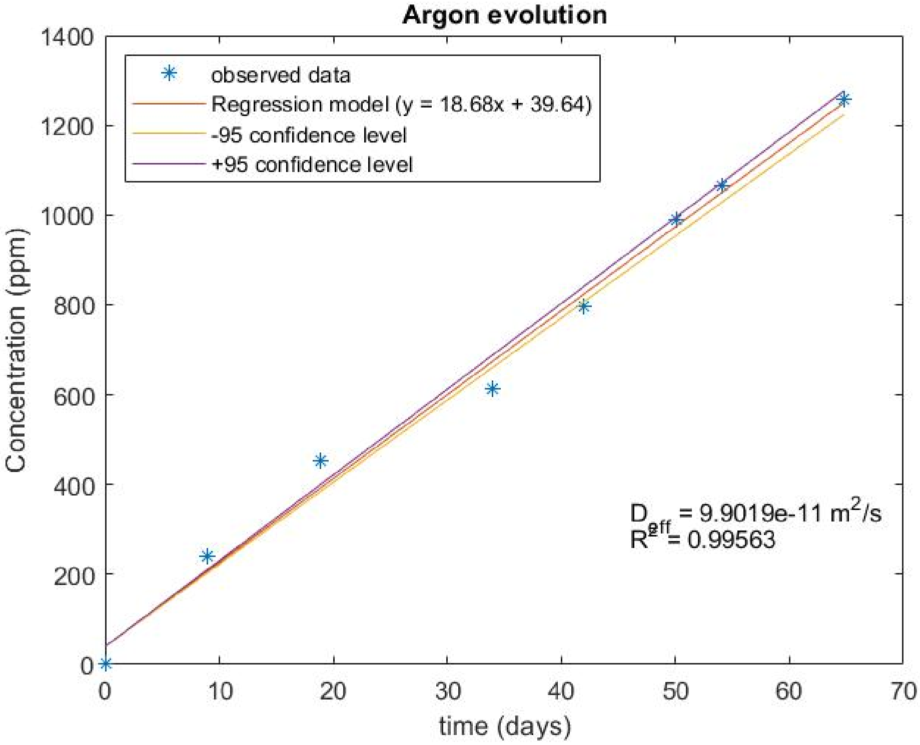

Figure 1.38: Argon measurements in the downstream reservoir in a diffusion experiment

In the above equation, D_{eff} stands for diffusivity (m^2 s^{-1}), N_A is the gas flux (kmol m^{-2} s^{-1}), P is the total pressure (kPa), R (m^3 kPa kmol^{-1} K^{-1}) is the gas constant, T (K) is the absolute temperature and z (m) is the diffusion distance. y_{A2} and y_{A1} are the concentration values (in terms of mole fraction) of the diffusing species in the downstream and upstream reservoir, respectively. In equation (1), the term D_{eff} represents the effective diffusion coefficient of gases across the porous sample. The evolution of gas concentration at the downstream end is used to calculate Flux, which in turn, is used to determine the effective diffusion coefficient, as shown in Figure 1.38. The widely accepted 95% confidence intervals (Sim & Reid, 1999) are also displayed. The uncertainties shown in the results section are calculated based on this approach.

1.3.4.3. Sample characterisation techniques

Sample characterization is important to understand the process of diffusion and how changes on a pore scale can affect gas transport. Thus, to draw links between microstructure and gas transport, it is important to visualise and quantify the pore network of the test samples. A host of characterization methods have been envisioned to achieve this purpose.

Mercury intrusion Porosimetry Mercury intrusion porosimetry (MIP) is used to determine porosity and pore size distribution on various solid and powdered materials. It has been used quite effectively in porosity and PSD determination of cementitious materials (Abell et al., 1999). However, the recommendations on the use of MIP for PSD determination on clays is rather limited (Yuan et al., 2020).

However, MIP is used as a comparative technique to understand the difference between the three different compositions of synthetic samples being studied.

X-Ray µCT X- Ray CT is used as a tool to probe the internal structure of the test samples. Therefore, a thorough scan of the samples would reveal the homogeneity of the sample in terms of material distribution. All the CT scans are done using a TEScan UNITOM XL with a 30-230 kV voltage range at 300W maximum power, with a minimum resolution of 3µm. It is equipped with a greyscale 2856x2856 (8 megapixels) camera with a 430 mm^2 field of view.

4.3.3 Density and Porosity measurements by drying Density measurements are carried out on the test samples by immersion in a fluid of known density. The tests are carried out using an organic liquid Soltrol 130, which has a specific gravity of 0.762 at 20^{O}C. The densities are then calculated by simple relative weight measurements.

Knowing the bulk density of the samples also helps us calculate the porosity by drying, based on difference in densities of the saturated and the dry samples. This is described in Savoye et al. (2018). The results are shown in Table 1.16.

4.3.4 Nitrogen adsorption Nitrogen adsorption is done to probe the porosity of the synthetic clays in the very small pore size range and has been shown to be quite effective in the sub 50nm range (Sing, 2001).

N_2 adsorption measurements are done using a Micromeritics TriStar II 3020. The pore size distribution analysis from Nitrogen adsorption is then complimented with the MIP results and the two are combined to have a better comparative quantitative analysis of the pore size distributions of the synthetic clay based materials used in this study.

1.3.5. Results

1.3.5.1. Water retention properties

The water retention curves of all three compositions of clay-based samples have been shown in Figure 1.39. The different salts used to achieve the different steps have also been mentioned. The differences in different compositions of clay can be seen. However, it is worth mentioning that the interest range in this study is in the 70-100% saturation range and the differences are minute. The water retention curves provide a good estimate on the response of different materials to drying. It can also help interpolate the moisture content of a material when exposed a certain relative humidity environment to prolonged periods. The data is displayed in Table 1.18.

Table 1.18: Saturation levels for different synthetic samples at different suction levels. The clay/silt/sand composition for samples 5A/6A/7 are as follows: 60/5/35; 60/30/10; 60/20/20

		% Water Saturation		
Salt	Suction	Composition 5A ; M = 21.43%	Composition 6A ; M = 23.48%	Composition 7 ; M = 21.9%
Water	0	100	100	100
$CuSO_4$	3	94	93	91
K_2SO_4	6	86	84	82
KNO_3	9	78	75	73
NaCl	39	51	47	47
NaBr	70	35	38	30

The saturation calculations were done based on the determination of the total moisture content of clay subsamples of the same material at full saturation W_s, the dry mass of the subsample after oven drying at 105 ^{O}C till mass stabilisation W_D, which helps determine the total amount of moisture content of the clay sample at full saturation (M). The water saturation S_w is then determined from the measured weight of the sample at each suction step W and the weight of the sample at full saturation W_{Sat} (2). Here, W_{Sat} and W correspond to the mass of the clay plug which is used in the water retention testing (desiccators). W_D and

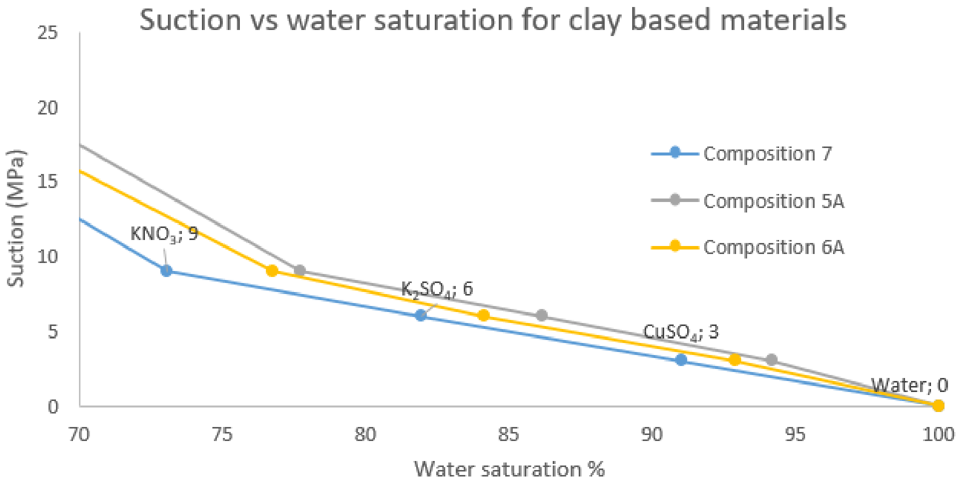

Figure 1.39: Soil water retention curves (SWRC) for different materials in the range of experimental interest

W_s are masses from different clay subsamples which have been dried out in the oven. The measurements are repeated with subsamples to determine the water percentage [which is expressed as M = (W_s-W_D)/W_s] of each composition. M is the total moisture content at saturation. All masses are in grams. The Sw measurements are done in duplicate at each suction step and the average values are reported in Table 1.18.

$$\frac{S_w}{100}(\%) = \frac{\{M \times W_{\text{Sat}}\} - \{W_{\text{Sat}} - W\}}{\{M \times W_{\text{Sat}}\}};\ M = \left(\frac{W_s - W_D}{W_s}\right)$$

1.3.5.2. Scoping pore network modelling

In brief, the objective is to simulate a pore structure for the reference materials and numerically simulate gas flow through the material to assess the impact of desaturation on the rate of gas flow as a means to support understanding of the experimental observations. The basic principle is to make use of existing diffusivity data of gases in water and air and establish the gas flux through the gas-liquid network system using Fick's law of diffusion and a mass balance approach. The idea is that the largest pores will dry out first as a result of desaturation. Starting from the largest pores (tubes), sequential draining is carried out until the required saturation level is reached. A square system is selected and automated using a basic connectivity model. The simulation is carried out in MATLAB. So far, the modelling has only been carried out using a uniformly distributed range of random numbers within the pore size distribution. This may not be the most representative PSD (pore size distribution) for the given material but for the sake of calculation, it is preferred as seeding (storing randomly generated values) is a lot more straightforward in a uniform distribution as opposed to a normal distribution.

The gas flow versus saturation is plotted for varying degrees of saturation between 100 to 20%. This is shown in Figure 1.40 for the case of diffusion of Helium. The data for gas flow at full desaturation has been omitted because it is a few orders of magnitude above the rest and flattens the whole curve towards the x-axis. One seed (Uniformly generated random values of porous properties in a range) was used. The trend indicates that the effect of desaturation is quite low until the 40% range and the flow rate starts to increase by significant amounts only in desaturation degrees below 35%. It is worth noting that the simulations have been performed with a fixed concentration gradient of 5000 ppm.

The results from Figure 1.40 have been checked for repeatability using different seeds for the case of Helium diffusion. The two lines for the same network topology are nearly coincident until the 50% saturation mark. The implications of this could be that desaturation may only really play a significant role in altering

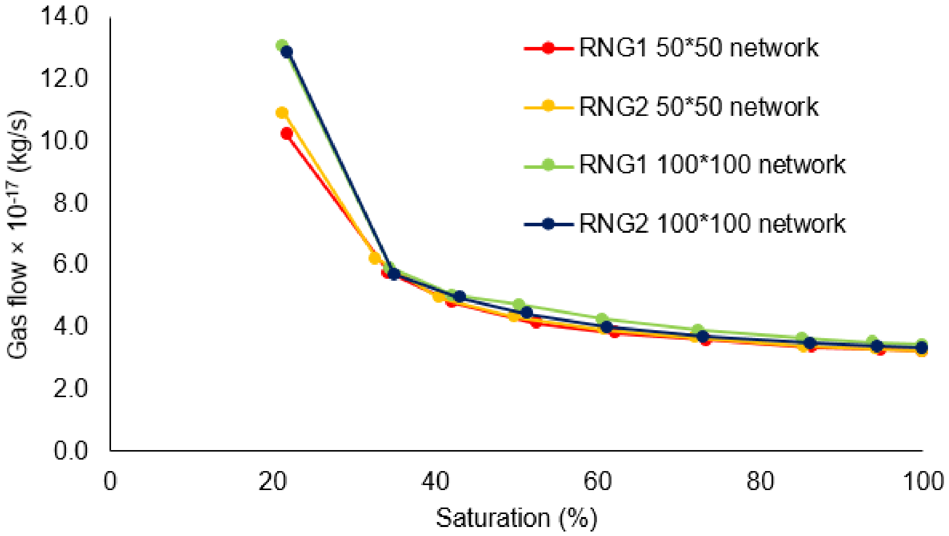

Figure 1.40: He diffusion in a simulated pore network with different networks

the rate of gas transport at very low desaturation values below 40%.

The Random Number Generators (RNGs) were then seeded so that they can be re-invoked if needed to test for repeatability. The program was found to be consistent with the seeding. Multiple different RNGs were studied for the same gases and the result is the same in all the cases, with nearly all the trend lines coinciding until the 40% saturation mark. Two different seeds (RNGs) have been compared for the purpose of illustration.

Figure 1.41 depicts the prediction made by the pore network modelling code. The program predicts that there is little impact of desaturation in the natural range (70-100%), which is the main area of interest. The increase in gas diffusion at around 60% saturation is roughly 20% relative to the full saturation gas diffusion. In that respect, it is worth noting is that these somewhat minor impacts may fall below the range of experimental precision. Therefore, the pore network modelling was a good start to get a basic idea on what to expect from the diffusion experiments.

Thus, the model predicts that at high saturation (above 75%), the gas diffusion coefficients are still not much higher than those in fully saturated conditions.

Gas diffusion experiments

As the novel pure gas phase diffusion setup and experimental methodology differs considerably from the one used for fully saturated systems, it needed validation. The first experiment performed with the new setup was a validation experiment with a sample of Eigenbilzen sand, Mol-2A-189b, which is a naturally occurring sandy silt clay found at the geological level above that of Boom Clay. The results are shown in Table 1.19. This particular sample was chosen owing the availability of previously published reference data to make a comparison (Jacops et al., 2017). The results show comparable values for diffusivities of helium and methane. The minor differences could be attributed to variations in the physical structure given that they are natural samples. D_{eff} is the effective diffusivity determined in the experiment. η was measured by drying.

Table 1.19: Diffusion results for the validation experiment

Eigenbilzen sample name	Porosity η (-)	D_{eff} ($\times 10^{-10}$ m^2 s^{-1})		
		He	CH_4	Xe

ON-Mol-1-39b K17 (Jacops et al., 2017)	0.4	5.82 ± 0.11	2.44 ± 0.05	-
Mol-2A-189b (new set-up)	0.4	4.67 ± 0.17	1.94 ± 0.11	2.01 ± 0.08

Once the setup and experimental methodology were validated, the diffusion experiments on unsaturated clay samples were performed. Gas diffusion experiments have been performed at four different suction levels. Namely, 0, 3, 6 and 9 MPa respectively. This covers the range of saturation degrees defined in the targets, mentioned in the objectives of the study. This is also confirmed in Figure 1.39.

An overview of gas diffusion coefficients for samples of composition 7 (refer Figure 1.35) are shown in Table 1.20 and Figure 1.42.

Table 1.20: Diffusion coefficients overview for synthetic clays of composition 7

Sample	**Suction (MPa)**	**% saturation (based on WRC)**	**D_{eff} * 10^{-10} m²/s**		
			He	**Ar**	**Xe**
FPR056	0	100	1.86 ± 0.03	-	0.31 ± 0.02
FPR056	0	100	1.85 ± 0.07	0.92 ± 0.08	-
FPR056	0	100	1.80 ± 0.22	0.94 ± 0.07	-
FPR057	3	91	1.74 ± 0.17	0.94 ± 0.06	-
FPR059	3	91	1.88 ± 0.10	1.02 ± 0.03	-
FPR060	6	82	1.88 ± 0.12	1.02 ± 0.05	-
FPR063	9	73	2.00 ± 0.20	1.08 ± 0.17	-
FPR064	9	73	2.07 ± 0.03	1.09 ± 0.04	-

An overview of gas diffusion coefficients for measurements made on samples of composition 6A are shown in Table 1.21.

The results point to the increase of gas diffusion coefficients with desaturation over the interval of 0-9 MPa suction. The linear model can be explained as

$$D_{\text{eff}} = aS_w + b$$

Where 'a' is the slope of the curve in Figure 1.42 and b is the intercept. 'b' can be interpreted as the diffusivity at zero saturation i.e., totally dry conditions. However, it seen from Figure 1.41 that the scoping model suggests that there will be a bending point at lower saturations where the diffusivity increases drastically. However, this is not to be seen in the linear model presented in Figure 1.42. Therefore, a model requiring a more representative increase in terms of the rate of transport at lower water saturation is required. A modified variant of Archie's law as descried in several studies (Hu & Wang, 2003; Sébastien Savoye et al., 2010) was used to correlate the effect of water saturation on gas diffusivity. S_w is the water saturation and Φ is the porosity of the test sample. M and n are fitting parameters called the cementation exponent and the saturation index respectively.

$$\frac{D_{\text{eff}}}{D_0} = S_w^n \varnothing^m$$

Figure 1.43 shows a comparison between the linear model presented and the modified form of Archie's power law. It can be seen that the power law fit in Figure 1.43 bears a close resemblance to the trend predicted by the model in Figure 1.41.

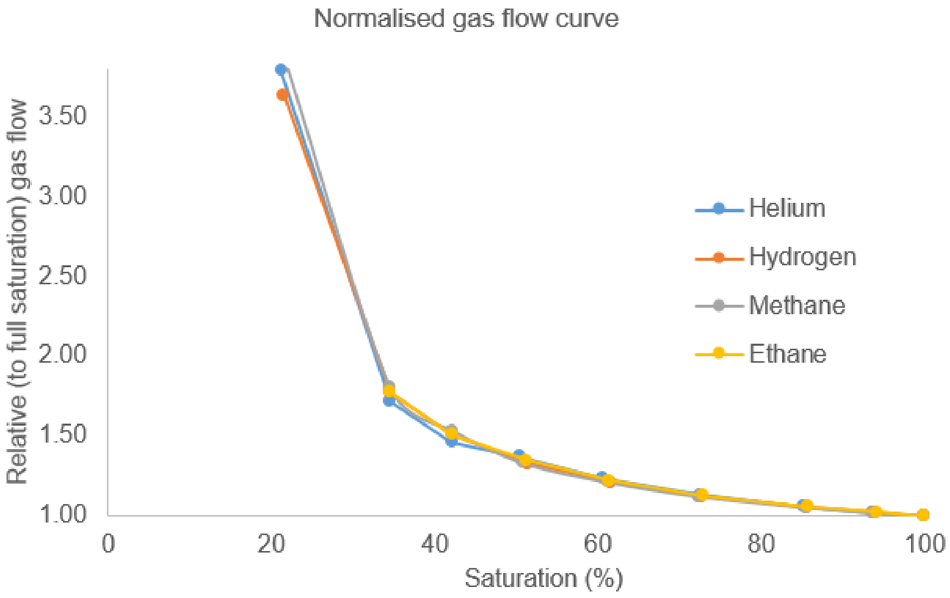

Figure 1.41: Gas diffusion as a function of water saturation for different gases

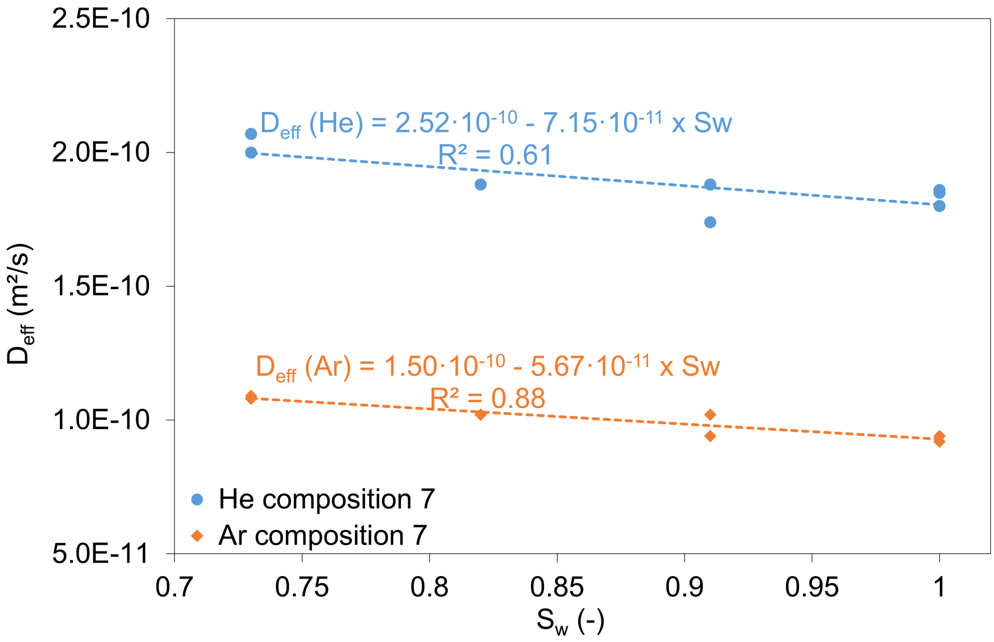

Figure 1.42: Diffusion coefficients overview for synthetic clays of composition 7

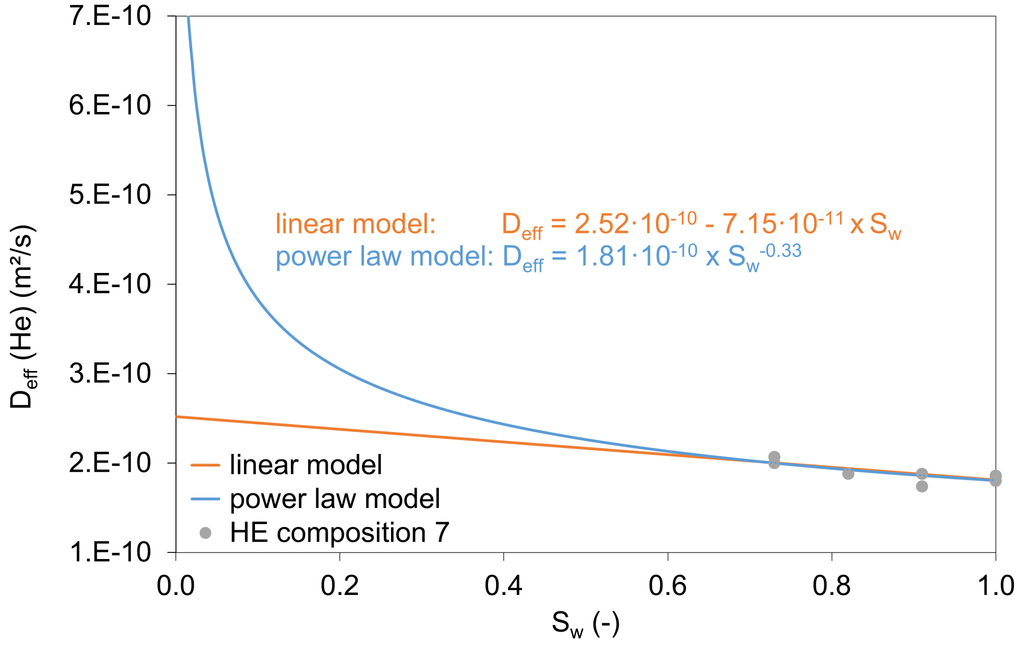

Figure 1.43: Evolution of effective diffusivity with saturation according to two models

The m values are determined from the full saturation case where S_w =1. The model is then fitted for n values to determine the rate of change of effective diffusivity with change in water saturation.

Table 1.21: Gas diffusion coefficients overview - composition 6

Sample	**Suction (MPa)**	**% saturation (based on WRC)**	D_{eff} * 10^{-10} (m^2/s)	
			He	**Ar**
6A09	0	100	1.92 ± 0.13	0.85 ± 0.05
6A02	3	93	1.97 ± 0.20	0.94 ± 0.07
6A05	6	84	2.06 ± 0.14	0.99 ± 0.07
6A06	9	75	2.23 ± 0.08	1.02 ± 0.05

The m factor or the cementation exponent for the two tracers from the intercept of the graph agrees with values reported in literature for expansive soils, where m values for diffusing tracers HTO and I^- have been found to be in range of 2.5 to 3 for both Opalinus clay and COx samples (Savoye et al., 2010; Van Loon et al., 2003) However, this law has not been utilized before with gaseous tracers to correlate diffusivity with saturation, thus the saturation exponent of n deviates from dissolved ionic and radioactive tracers which report n values in between 1 and 2 (Savoye et al., 2010).

This is shown in Figure 1.44. Thus, it becomes important to incorporate the differences in transport mechanisms between dissolved solutes and gaseous tracers.

The behaviour of the gases in these experiments is opposite to what has been observed in dissolved tracers (Savoye et al., 2010 and 2012). Diffusion of gases in clays at partial saturation is a relatively more unhindered phenomenon compared to dissolved tracers and is less effected by a change in saturation in the 73-100 % water saturation (9-0 MPa) range. It reflects on the dual nature of gases: gases diffuse as both a dissolved species (solubility controlled by Henry's constant) and are also capable of diffusing as gas in the gaseous phase. However, ionic and dissolved tracers are limited to being able to diffuse only in the aqueous phase and this has been confirmed by the study performed by (Savoye et al., 2010) where there was found to be a decrease in effective diffusivity with a decrease in saturation.

1.3.5.3. Characterization results

For the time being, X-Ray µCT, MIP and N_2 porosimetry have been used.

X-Ray CT provides information on the homogeneity of the artificial samples, but lacks resolution for a full

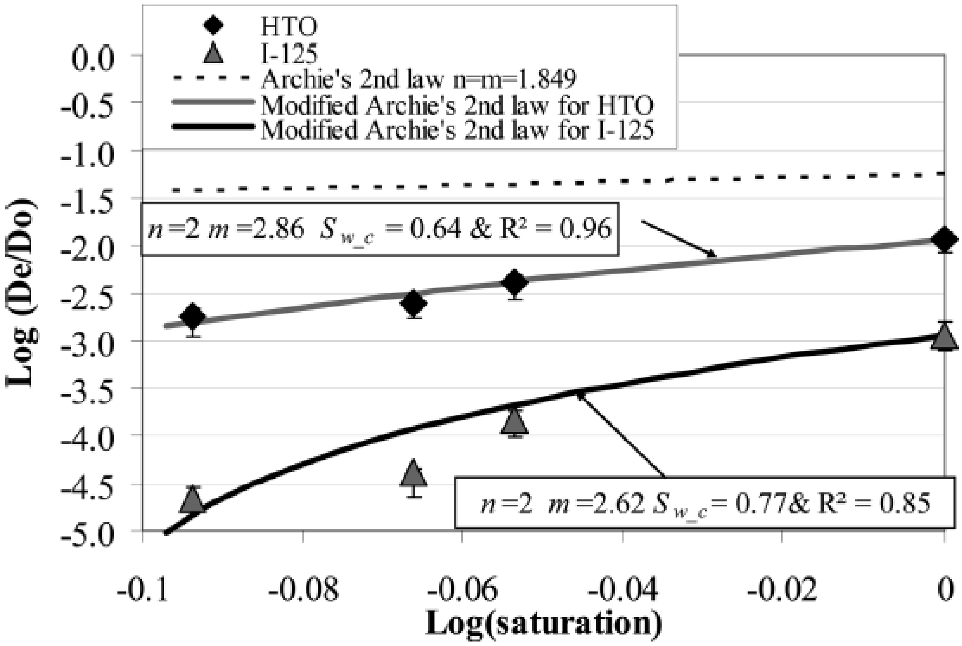

Figure 1.44: Power law fits for ionic tracers, taken from Savoye et al. (2010)

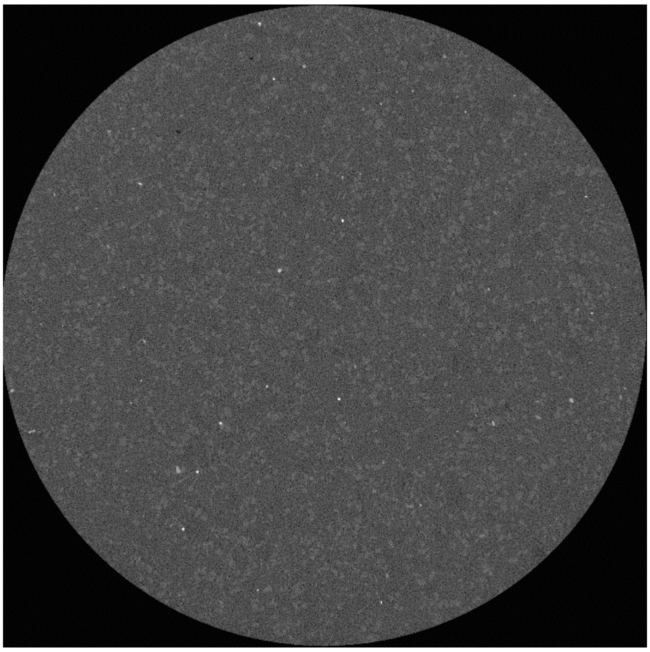

Figure 1.45: Raw image of a CT scan of a 1cm cylindrical sample of composition 7 synthetic clay

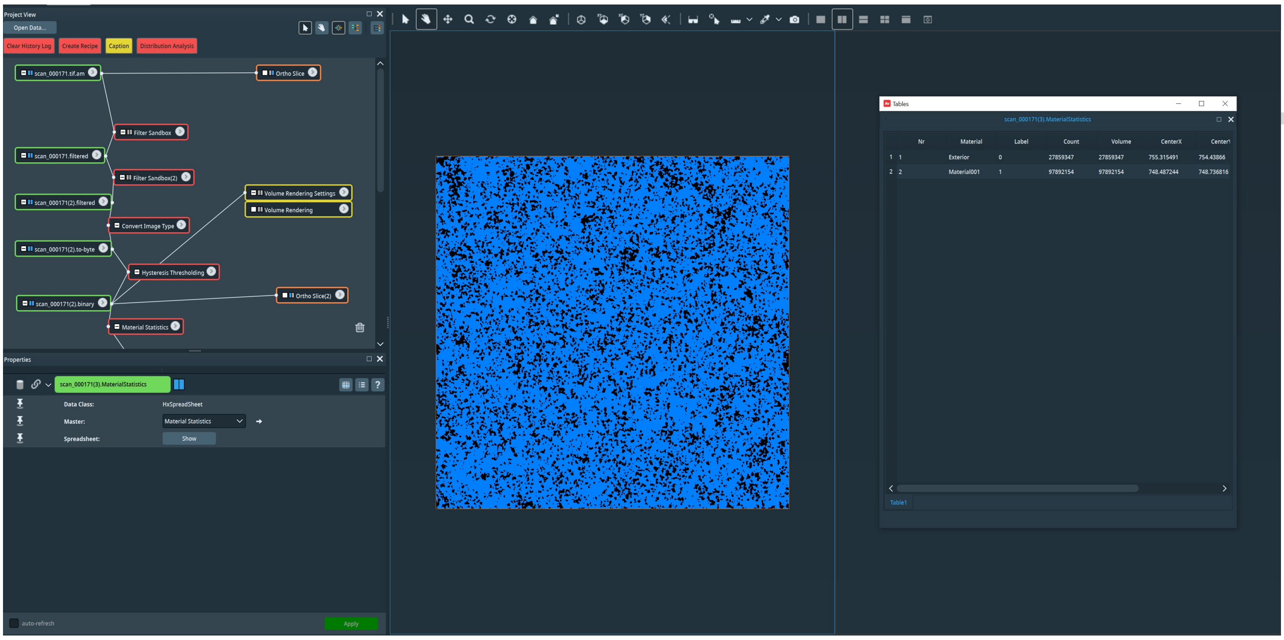

scan_000171(3).MaterialStatistics

Data Class: HxSpreadSheet

Master: Material Statistics

Spreadsheet: Show

scan_000171(3).MaterialStatistics

	Nr	Material	Label	Count	Volume	CenterX	CenterY
1	1	Exterior	0	27859347	27859347	755.315491	754.43866
2	2	Material001	1	97892154	97892154	748.487244	748.736816

Figure 1.46: CT image slice after filter postprocessing and thresholding

space after “hysteresis thresholding”, which just means the segregation of darker pore spaces (black) from all of the actual material (blue) in the sample. The sum of the entire area of the image covered in black, divided by the total area gives the porosity of the sample from image segmentation.

Thus, it can be concluded that X-ray CT resolution is insufficient to probe the total porosity of the synthetic clay based materials. However, it is also worth noting that there is strong evidence of oversegmentation in Figure 1.46 since a porosity of 20% should not correspond to what the resolution of the CT is capable of probing. This is shown in a later section.

However, X-ray CT is also useful in trying to map the homogeneity in terms of material distribution within the samples. This includes particles of sand, silt, clay and water. It is done by means of grey level analysis on the samples of different compositions at varying levels of saturation. The samples are conditioned in the same manner as they would be in the experimental scheme and are scanned at every suction step after equilibrating for about a month. A sample scan is shown below in Figure 1.47 for the sample 5A-01 (composition 5A).

The x-axis shows the number of the slice and the y-axis shows the max(count) of a certain grey level from the histogram of grey levels. The scans are performed in the axial direction. This is assumed to be the contribution from dense material to the matrix since the void spaces are extremely small in comparison to the amount of dense material. Here, dense material could refer to particles of sand, silt or clay.

The peak in the centre is an artefact caused by a Gaussian filter on one of the slices and was included to show the effectiveness of grey level analysis.

Scans on materials of different compositions yield similar results with a flattening in terms of grey values towards the centre of the sample. Thus, it can be concluded that the material distribution (potentially including moisture) is quite even as we move along the sample in the axial direction. However, it would be a premature conclusion and requires more input.

Mercury Intrusion Porosimetry Mercury injection was performed using samples of the three different compositions to give an estimate on the pore spaces within the samples. The results shown in Figure 1.48 show the relative pore size distributions of the different samples. The samples have been oven dried prior

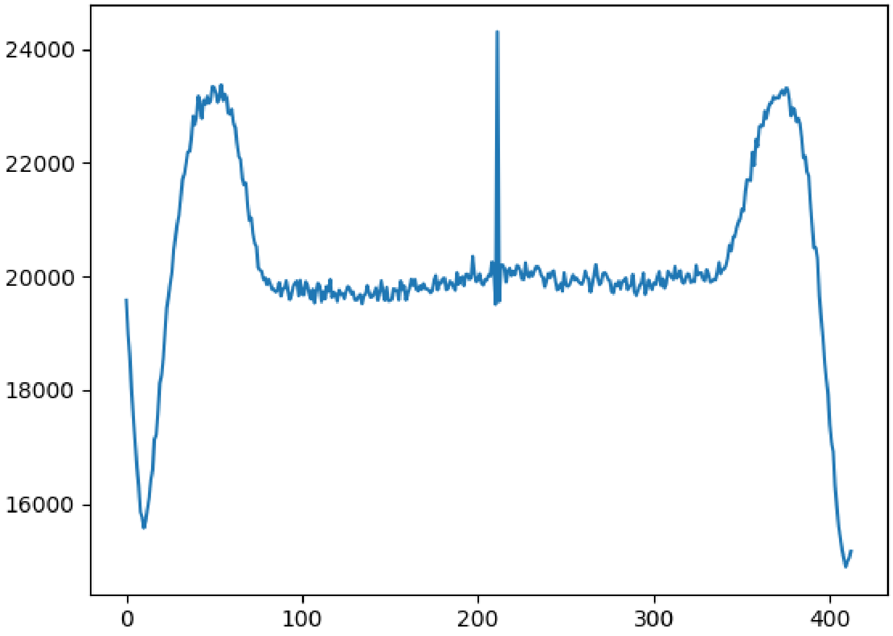

Figure 1.47: Grey level analysis of 5A01 after the 3MPa suction step (x –axis : slice number, y-axis : count of max value of the histogram of grey levels)

to MIP measurements. Conventionally, this is not the best method and MIP may have to be re attempeted using freeze dried samples to preserve their structural integrity better.

It can be seen that the relative PSDs of the different compositions vary between groups (compositions) but not within groups. This shows that different subsamples of the same composition have the same textural properties as each other. The variations between groups can be explained by the presence of higher or lower sand/ silt content. It can be seen that samples with higher mica (6A) content display a distinct distribution in the 200-500 nm range. This could be explained by the fact that the sub 63µm muscovite mica particles could occupy the inter aggregate porosity and this can be further enhanced by the injection of mercury at high pressures. The sample of 5A with very low mica content doesn't display the same trend. This is because of the presence of a high amount of quartz sand (35% by weight), which is a more dense material than mica and the potential higher contribution towards inter aggregate porosity. The samples of higher mica content have one less distinct region of distribution (peaks) than the sample of 5A with a very low mica content.

While MIP provides a decent comparative estimate between the different compositions, it must be worth noting that the injection of high pressure mercury may have caused some compression artefacts because of the quite fragile nature of the synthetic clays, especially in their dry state. This is illustrated in Figure 1.49.

While the total cumulative intrusion must have been about the same since the density and porosity values of the different compositions are similar, it can be seen that this is not the case in Figure 1.49. Thus, high pressure mercury injection is not a good quantitative measure of pore size distribution given the potential for compression artefacts.

Nitrogen Adsorption Nitrogen adsorption was done complimentary to MIP to observe the pore spaces in the sub 10nm range. Nitrogen adsorption has been combined with MIP in studies before to have a better overview of the pore size distribution of porous materials (Labani et al., 2013). The Nitrogen adsorption

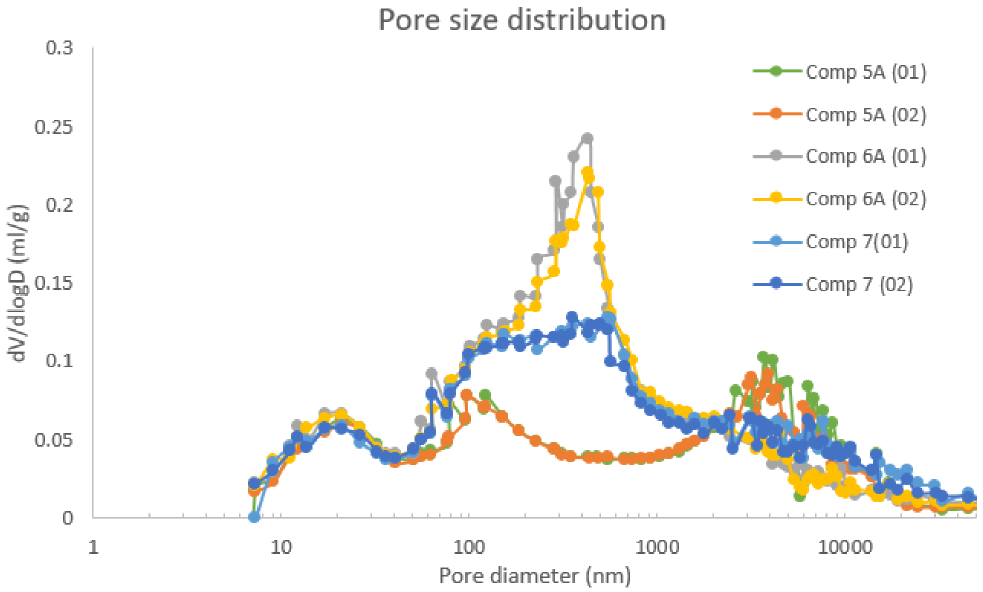

Figure 1.48: MIP PSD of synthetic samples used in the study

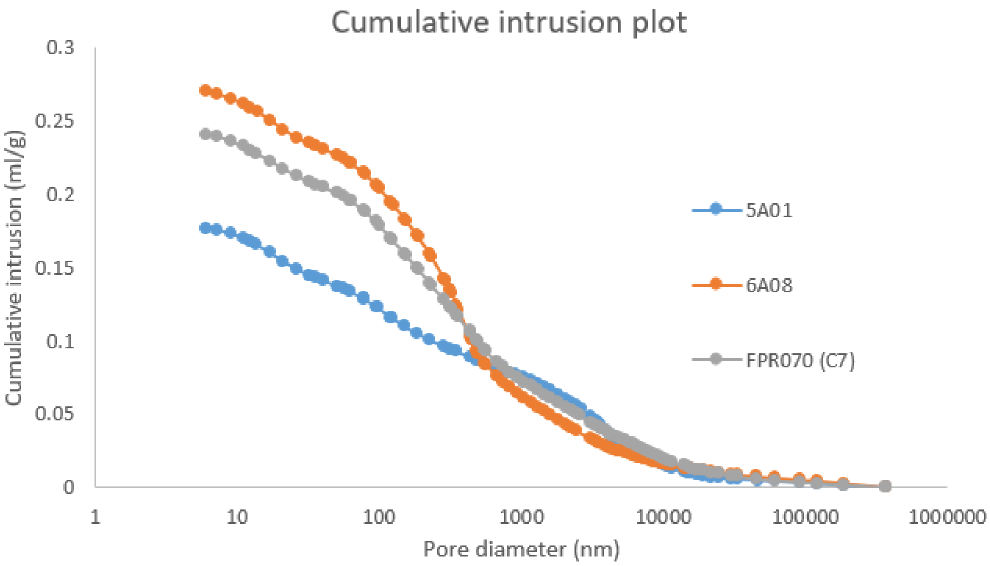

Figure 1.49: Cumulative intrusion plots – MIP (blue = composition 5A, orange = composition 6A, grey = composition 7)

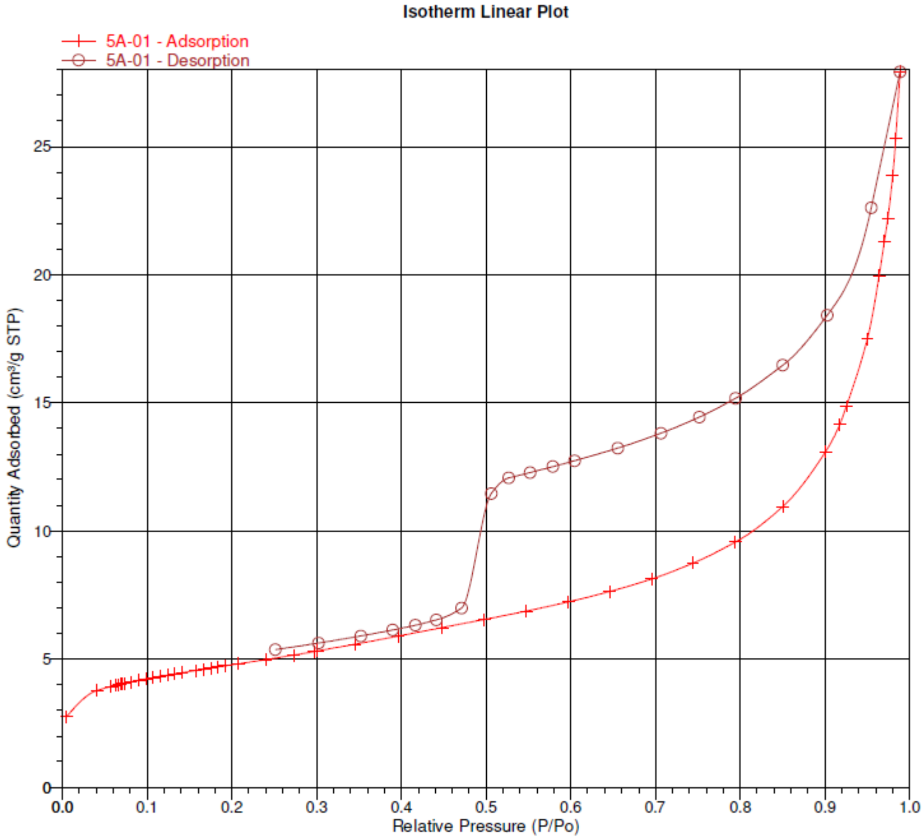

Figure 1.50: Nitrogen adsorption isotherm for sample of composition 5

isotherm is given in Figure 1.50. While the isotherm provides data that can be used to obtain a pore size distribution using Kelvin's law, which is used to evaluate pore width from pore filling pressures, it has also been shown that this is not entirely reliable for pores under 7.5nm (Sing, 2001). Therefore, The BJH (after authors (Barrett et al., 1951)) method is a procedure for calculating pore volumes and pore size distributions from experimental isotherms, using the Kelvin equation. The method is described in detail in (Bardestani et al., 2019).

The comparative pore size distributions are shown in Figure 1.51.

When the PSD from nitrogen adsorption is combined with MIP, it provides a more comprehensive comparative overview of the PSDs of the different materials. This is shown in Figure 1.52.

It can be concluded that in the small pore range (sub 50nm), the differences between the compositions is quite minimal. This is due to the fact that this range of pore sizes is mainly located in the clay matrix and has been reported in previous studies as well (Sammartino et al., 2003). The differences are more enunciated at higher pore dimensions. A potential explanation has been offered in the previous section.

1.3.6. Summary

An overview of gas diffusion coefficients measured experimentally at different levels of saturation in synthetically prepared clay based materials has been provided in this report. The general trend is that diffusivity increases with a decrease in saturation. The observed effects in the two compositions tested so far (composition 7 and 6A) are limited. Data set will be complemented with data from the diffusion experiments on samples of composition 5A. However, thus far, the composition of the samples tested (6A and

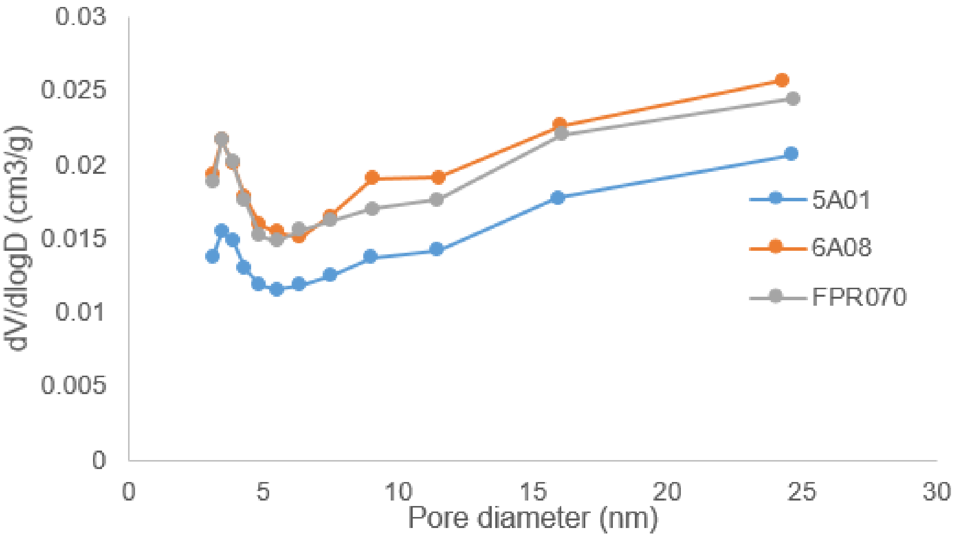

Figure 1.51: Comparative PSDs for different compositions using Nitrogen adsorption

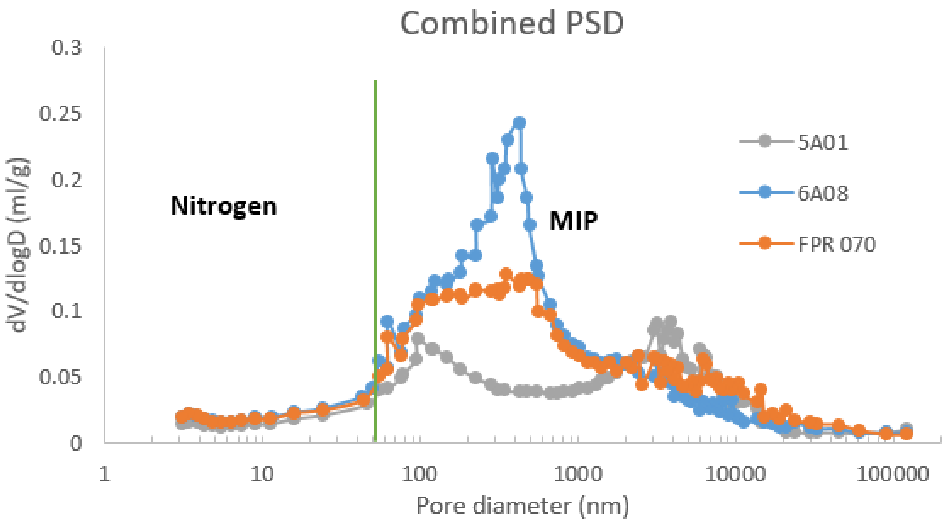

Figure 1.52: combined PSDs

7) seems to not play much of a major role in affecting the rate of gas diffusion through the clay samples either. However, this was along expected lines as the total clay content of all the samples is kept constant.

The characterization of the samples to obtain PSDs have been investigated. While the methods may not be entirely perfect for exact quantitative analysis of individual specimens, they do offer good comparative plots to visualise the differences in the porosity of the samples of different compositions. However, even this should be subject to a bit of scrutiny because of the different physical responses of different composition samples to the injection of high pressure mercury or nitrogen.

Therefore, there is a need for more robust quantitative analysis of the microstructure of each of these different compositions of test samples.

Looking at the diffusion data, it may be possible to conclude that even at 85 or 75% water saturation, the controlling factor is still the transport of gases as a dissolved species in moisture filled pore spaces. While the samples are partially saturated, the saturation is still quite high and this means that even the potential presence of continuous gas pathways, however unlikely (from experimental data), have a negligible impact on the total rate of gas transport through the partially saturated clay samples.

Additionally, a model has to be developed to explain the diffusive behaviour of gases in the two potentially distinct phases which may exist in the pore space of the clay based materials. Coming up with an effective model based on combinations of models that exist in theory for gas diffusion in the dissolved form as well as diffusion in the air spaces would offer a more clear explanation of the entire process.

A comparison of two data fitting models, namely, linear and exponential have been explored and it can be concluded that in the range of experimental testing (high saturation), there are no considerable differences between a linear and an exponential fit. However, the power law bears a closer resemblance to the numerical model. Therefore, this is an avenue which could be explored further by experimental and modelling work.

1.3.7. Key learning points

1.3.7.1. New knowledge acquired

The new knowledge acquired has mainly to do with the methodology behind conducting gas diffusion experiments in partially saturated porous samples. Thus far, the methodology for measuring gas diffusivities as a dissolved tracer with continuous water circulation has been used for effective measurements of gas diffusion coefficients. However, there were certain conditions that needed to exist in order to make those measurements. For instance, high gas pressures and water circulation were essential in the classical dissolved gas diffusion setup. The new setups designed in this work have been used to characterize gas transport in the gaseous phase. Thus, there is no water circulation and the need for higher pressure systems since the miniRUEDI gas analyser is perfectly capable of working well at ambient conditions. The methodology has been validated and used in measuring gas diffusion coefficients for a range of gases. One of the knowledge gaps was the effect of partial saturation (which is predicted to exist for a while post closure) on the rate of gas transport. The data collected so far points to the fact that the rate of gas transport is marginally increased in partially saturated clay based materials as opposed to rates of ionic tracers, which decrease with desaturation.

1.3.7.2. Impact of acquired knowledge

The context of the work detailed in this report are under EURAD-GAS. The objective is to have a detailed account of the processes that could proceed the gas generation phase of a geological disposal facility. The experimental data points to the fact that in the zones of a repository which may be potentially unsaturated, the rate of gas dissipation by diffusion is slightly higher than a fully saturated system. This could have net positive implications, however slight, in the safety assessment in terms of the gas problem.

1.3.7.3. Remaining knowledge gaps

One of the main remaining knowledge gaps is the break through point in terms of a sudden overall increase in gas flux with desaturation. The model presented here predicts that this is not likely to happen until very low values of saturation are encountered (sub 40%). This is also confirmed by a theoretical model (4) in the range of high saturations tested so far. While this may not be directly applicable in a real life nuclear waste repository, it is still worth exploring for the process understanding.

Furthermore, the impact of different compositions with extremely high clay content (which could be interesting for countries looking to host their radioactive wastes in dense, clay rich rocks, or for instance, a material with a high sand content. Again, like the range of water saturations, this study is limited to mild changes in terms of mineralogy of the test materials. More extreme variations have not been designed yet. However, again, this could be quite interesting to understand and model the process and the controls behind gas transport.

Additionally, effective quantitative methods for probing the exact PSD of the synthetic materials used in this study is not available yet. For this, a new technique involving C-14 autoradiography using PMMA as a carrier has been envisioned. This study will be performed in collaboration with University of Helinki to try and resolve the microstructure of the synthetic clays used in the study.

1.3.7.4. Recommendations for the future

As mentioned in the previous section, the entire study has been limited to samples that are in the 70-100% water saturation range and the clay content in the test materials has been fixed at 60% by weight. A further step would be to test gas diffusivities in more dry samples (<50% water saturation). Also, testing gas diffusivities at higher sand/clay contents could yield interesting results. However, there are limitations on the kind of samples that can be manufactured at the moment given the method of preparing synthetic mixtures from powders is still quite novel. With time and better understanding of the materials, these synthetic clays could provide a sustainable and effective alternative to using natural samples for transport testing.

References

Abell, A. B., Willis, K. L., & Lange, D. A. (1999). Mercury Intrusion Porosimetry and Image Analysis of Cement-Based Materials. *Journal of Colloid and Interface Science*, *211*(1), 39–44. https://doi.org/10.1006/JCIS.1998.5

Bardestani, R., Patience, G. S., & Kaliaguine, S. (2019). Experimental methods in chemical engineering: specific surface area and pore size distribution measurements—BET, BJH, and DFT. *The Canadian Journal of Chemical Engineering*, *97*(11), 2781–2791. https://doi.org/10.1002/CJCE.23632

Barrett, E. P., Joyner, L. G., & Halenda, P. P. (1951). The Determination of Pore Volume and Area Distributions in Porous Substances. I. Computations from Nitrogen Isotherms. *Journal of the American Chemical Society*, *73*(1), 373–380. https://doi.org/10.1021/JA01145A126/ASSET/JA01145A126.FP.PNG_V03

Brennwald, M. S., Tomonaga, Y., & Kipfer, R. (2020). Deconvolution and compensation of mass spectrometric overlap interferences with the miniRUEDI portable mass spectrometer. *MethodsX*, *7*, 101038. https://doi.org/10.1016/J.MEX.2020.101038

Cooper, D., Turinsky, A., Sensen, C., & Hallgrimsson, B. (2007). Effect of voxel size on 3D micro-CT analysis of cortical bone porosity. *Calcified Tissue International*, *80*(3), 211–219. https://doi.org/10.1007/S00223-005-0274-6/TABLES/3

Crunelle, B., Surdyk, D., Pauwels, J. F., & Sochet, L. R. (1997). Experimental study of low-pressure premixed methane and ethane flames by molecular beam sampling and mass spectrometry analysis. *Journal de Chimie Physique*, *94*(3), 433–459. https://doi.org/10.1051/JCP/1997940433

Delage, P., Howat, M. D., & Cui, Y. J. (1998). The relationship between suction and swelling properties in a heavily compacted unsaturated clay. *Engineering Geology*, *50*(1–2), 31–48. https://doi.org/10.1016/S0013-7952(97)00083-5

Frederickx, L., Honty, M., De Craen, M., & Elsen, J. (2021). Evaluating the quantification of the clay mineralogy of the Rupelian Boom Clay in Belgium by a detailed study of size fractions. *Applied Clay Science*, *201*, 105954. https://doi.org/10.1016/j.clay.2020.105954

Grambow, B. (2016). Geological Disposal of Radioactive Waste in Clay. *Elements*, *12*(4), 239–245. https://doi.org/10.2113/GSELEMENTS.12.4.239

Hu, Q., & Wang, J. S. Y. (2003). Aqueous-phase diffusion in unsaturated geologic media: A review. *Critical Reviews in Environmental Science and Technology*, *33*(3), 275–297. https://doi.org/10.1080/10643380390814488

Jacops, E., Aertsens, M., Maes, N., Bruggeman, C., Swennen, R., Krooss, B., Amann-Hildenbrand, A., & Littke, R. (2017). The Dependency of Diffusion Coefficients and Geometric Factor on the Size of the Diffusing Molecule: Observations for Different Clay-Based Materials. *Geofluids*, *2017*. https://doi.org/10.1155/2017/8652560

Jacops, E., Volckaert, G., Maes, N., Weetjens, E., & Govaerts, J. (2013). Determination of gas diffusion coefficients in saturated porous media: He and CH4 diffusion in Boom Clay. *Applied Clay Science*, *83–84*, 217–223. https://doi.org/10.1016/j.clay.2013.08.047

King, F. (2012). Gaseous hydrogen issues in nuclear waste disposal. *Gaseous Hydrogen Embrittlement of Materials in Energy Technologies: The Problem, Its Characterisation and Effects on Particular Alloy Classes*, 126–148. https://doi.org/10.1533/9780857093899.1.126

Kneuker, T., Dohrmann, R., Ufer, K., & Jaeggi, D. (2023). Compositional-structural characterization of the Opalinus Clay and Passwang Formation: New insights from Rietveld refinement (Mont Terri URL, Switzerland). *Applied Clay Science*, *242*, 107017. https://doi.org/10.1016/J.CLAY.2023.107017

Labani, M. M., Rezaee, R., Saeedi, A., & Hinai, A. Al. (2013). Evaluation of pore size spectrum of gas shale reservoirs using low pressure nitrogen adsorption, gas expansion and mercury porosimetry: A case study from the Perth and Canning Basins, Western Australia. *Journal of Petroleum Science and Engineering*, *112*, 7–16. https://doi.org/10.1016/J.PETROL.2013.11.022

Le, T. T., Delage, P., Cui, Y. J., Tang, A. M., Lima, A., Romero, E., Gens, A., & Li, X. L. (2008). Water retention properties of Boom clay: A comparison between different experimental techniques. *Unsaturated Soils: Advances in Geo-Engineering - Proceedings of the 1st European Conference on Unsaturated Soils, E-UNSAT 2008*, 229–234. https://doi.org/10.1201/9780203884430-32/WATER-RETENTION-PROPERTIES-BOOM-CLAY-COMPARISON-DIFFERENT-EXPERIMENTAL-TECHNIQUES-LE-DELAGE-CUI-TANG-LIMA-ROMERO-GENS-LI

Pellenard, P., & Deconinck, J. F. (2006). Mineralogical variability of Callovo-Oxfordian clays from the Paris Basin and the Subalpine Basin. *Comptes Rendus Geoscience*, *338*(12–13), 854–866. https://doi.org/10.1016/J.CRTE.2

Plonsky, L., & Ghanbar, H. (2018). Multiple Regression in L2 Research: A Methodological Synthesis and Guide to Interpreting R2 Values. *The Modern Language Journal*, *102*(4), 713–731. https://doi.org/10.1111/MODL.1250

Sammartino, S., Bouchet, A., Prêt, D., Parneix, J. C., & Tevissen, E. (2003). Spatial distribution of porosity and minerals in clay rocks from the Callovo-Oxfordian formation (Meuse/Haute-Marne, Eastern France)—implications on ionic species diffusion and rock sorption capability. *Applied Clay Science*, *23*(1–4), 157–166. https://doi.org/10.1016/S0169-1317(03)00098-X

Savoye, S., Beaucaire, C., Fayette, A., Herbette, M., & Coelho, D. (2012). Mobility of cesium through the callovo-oxfordian claystones under partially saturated conditions. *Environmental Science and Technology*, *46*(5), 2633–2641. https://doi.org/10.1021/es2037433

Savoye, S., Rajyaguru, A., Macé, N., Lefèvre, S., Spir, G., & Robinet, J. C. (2018). How mobile is tritiated water through unsaturated cement-based materials? New insights from two complementary approaches.

Applied Radiation and Isotopes, *139*(April), 98–106. https://doi.org/10.1016/j.apradiso.2018.04.019

Savoye, Sébastien, Page, J., Puente, C., Imbert, C., & Coelho, D. (2010). New experimental approach for studying diffusion through an intact and unsaturated medium: A case study with callovo-oxfordian argillite. *Environmental Science and Technology*, *44*(10), 3698–3704. https://doi.org/10.1021/es903738t

Sim, J., & Reid, N. (1999). Statistical Inference by Confidence Intervals: Issues of Interpretation and Utilization. *Physical Therapy*, *79*(2), 186–195. https://doi.org/10.1093/PTJ/79.2.186

Sing, K. (2001). The use of nitrogen adsorption for the characterisation of porous materials. *Colloids and Surfaces A: Physicochemical and Engineering Aspects*, *187–188*, 3–9. https://doi.org/10.1016/S0927-7757(01)00612-4

Tsang, C. F., Neretnieks, I., & Tsang, Y. (2015). Hydrologic issues associated with nuclear waste repositories. *Water Resources Research*, *51*(9), 6923–6972. https://doi.org/10.1002/2015WR017641

Van Loon, L. R., Soler, J. M., Jakob, A., & Bradbury, M. H. (2003). Effect of confining pressure on the diffusion of HTO, 36Cl- and 125I- in a layered argillaceous rock (Opalinus Clay): diffusion perpendicular to the fabric. *Applied Geochemistry*, *18*(10), 1653–1662. https://doi.org/10.1016/S0883-2927(03)00047-7

Vandenberghe, N., De Craen, M., & Wouters, L. (2014). The Boom Clay Geology from sedimentation to present-day occurrence - a review. *Memoirs of the Geological Survey of Belgium*, *60*(3), 76.

Yuan, S., Liu, X., & Buzzi, O. (2020). Technical aspects of mercury intrusion porosimetry for clays. *Https://Doi.Org/10.1680/Jenge.16.00039*, *8*(4), 255–263. https://doi.org/10.1680/JENGE.16.00039

.

Belgian Nuclear Research Centre (SCK CEN)

1.4. In-situ diffusion experiment with dissolved neon in Boom Clay NEMESIS (SCK CEN)

1.4.1. Introduction & Objectives

SCK CEN has extensively studied gas diffusion in saturated porous media in the lab resulting in a large database of gas diffusion coefficients in Boom Clay (Jacops et al. 2013, Jacops et al. 2015, Jacops et al. 2016, Jacops et al. 2017a, Jacops et al. 2017b, Jacops 2018, Jacops et al. 2020a, Jacops et al. 2020b, Jacops et al. 2023). These lab tests were performed at small scale (centimetre scale) so the question arises whether the diffusion coefficients measured at lab scale are also valid on larger (meter) scale. To validate the data obtained in the lab, ONDRAF/NIRAS, SCK CEN and EURIDICE (who manages and operates HADES URL) will conduct an *in situ* diffusion experiment in the HADES URL: NEMESIS (Neon diffusion in MEGAS *In situ*).

The main goal of the *in situ* gas diffusion experiment is to validate that upscaling of diffusion data for dissolved gases obtained on lab (cm) scale to more relevant large (m) scale is possible.

Previous *in situ* gas injection experiments showed the importance of limiting the disturbed stress field for transport experiments. Therefore, it has been decided to re-use the MEGAS E5 piezometers drilled in the Test Drift in 1992. This installation consists of 4 horizontally oriented piezometers in a 3D configuration (Figure 1.53 and Figure 1.54). Each piezometer is 15 m deep and equipped with several filters. As detailed in Volckaert et al. (1995) and in Ortiz et al. (2002), this setup was used in 1994 to perform a gas breakthrough experiment by injecting gas (helium) in filter 20. In 1998, a new gas breakthrough experiment was performed in filters 13 and 14, followed by a tracer diffusion experiment in which HTO (tritiated water) was injected in filter 13 and monitored in the surrounding filters. To avoid interaction with the previous experiments performed on the MEGAS piezometers, another tracer gas, neon, will be used for the NEMESIS experiment. The neon will dissolve in water and will be in contact with the Boom Clay from filter 17. Three neighbouring filters located in horizontal and vertical planes will serve as gas monitoring filters by measuring how the neon gas concentration evolves over time (filters 9, 18 and 22, Figure 1.54). This configuration will allow the investigation of the diffusion of neon in three dimensions and determine the anisotropic diffusion coefficients of dissolved neon. Neon is selected because it is 1/ considered as a good proxy for H_2 (the main gas generated in a GDF) (Jacops et al. 2017a) and 2/ not naturally present in the Boom Clay (no interference for detection). Under real repository conditions, H_2 might be converted into CH_4 by microbes. As this conversion makes it impossible to obtain reliable diffusion coefficients, and given the fact that the main aim of the research is to study the upscaling of diffusion, we selected neon as a proxy for H_2.

The NEMESIS setup to measure diffusion *in situ* is a modification of the setup which has been used to measure diffusion of gases in the lab, which is described in detail in Jacops et al. (2013). This setup consists of one injection circuit (source – connected to filter 17) and three monitoring circuits (target 1, 2 and 3 – connected to respectively filters 9, 18 and 22) (Figure 1.54 and Figure 1.55).

As mentioned above, HTO has been injected in filter 13 (Ortiz et al. 2002). The HTO diffusion plume has reached filters 9, 10, 11, 12, 13, 14, 15 and 16 and their concentration of HTO is followed for more than 20 years. In 2019, during the preparation phase of NEMESIS, the pore water contamination around all the other filters was measured. Because these filters around filter 13 are HTO contaminated, the test with Neon will be done as much as possible outside of this zone to avoid major contamination of the setup.

1.4.2. Experimental setup

Description of apparatus

A schematic overview of the setup is shown in Figure 1.55. During the experiment, filter 17 is connected to the source circuit. One tube of the filter is connected to the inlet of the source gas system (V100). The

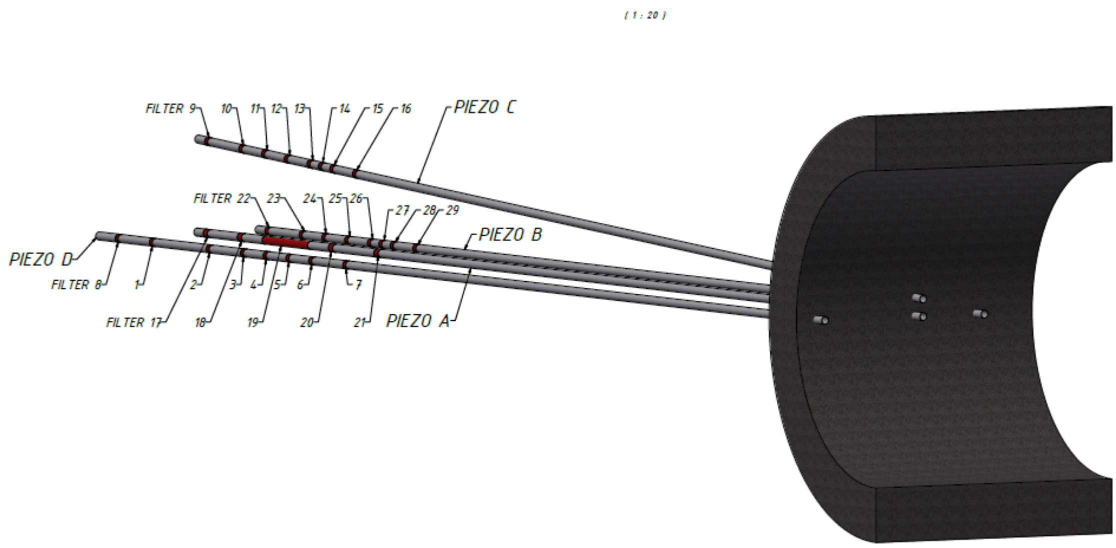

Figure 1.53: Overview of the 4 MEGAS piezometers (A to D) and their filters (1 to 29)

inlet is connected via V102 to the upper connector of a vessel of 1 litre (B100) of which half the volume is filled with water and half with Neon (pressurized at the same pressure as the *in situ* measured pore water pressure). The lower connector of the vessel is directly connected to the inlet (V104) of a magnetically

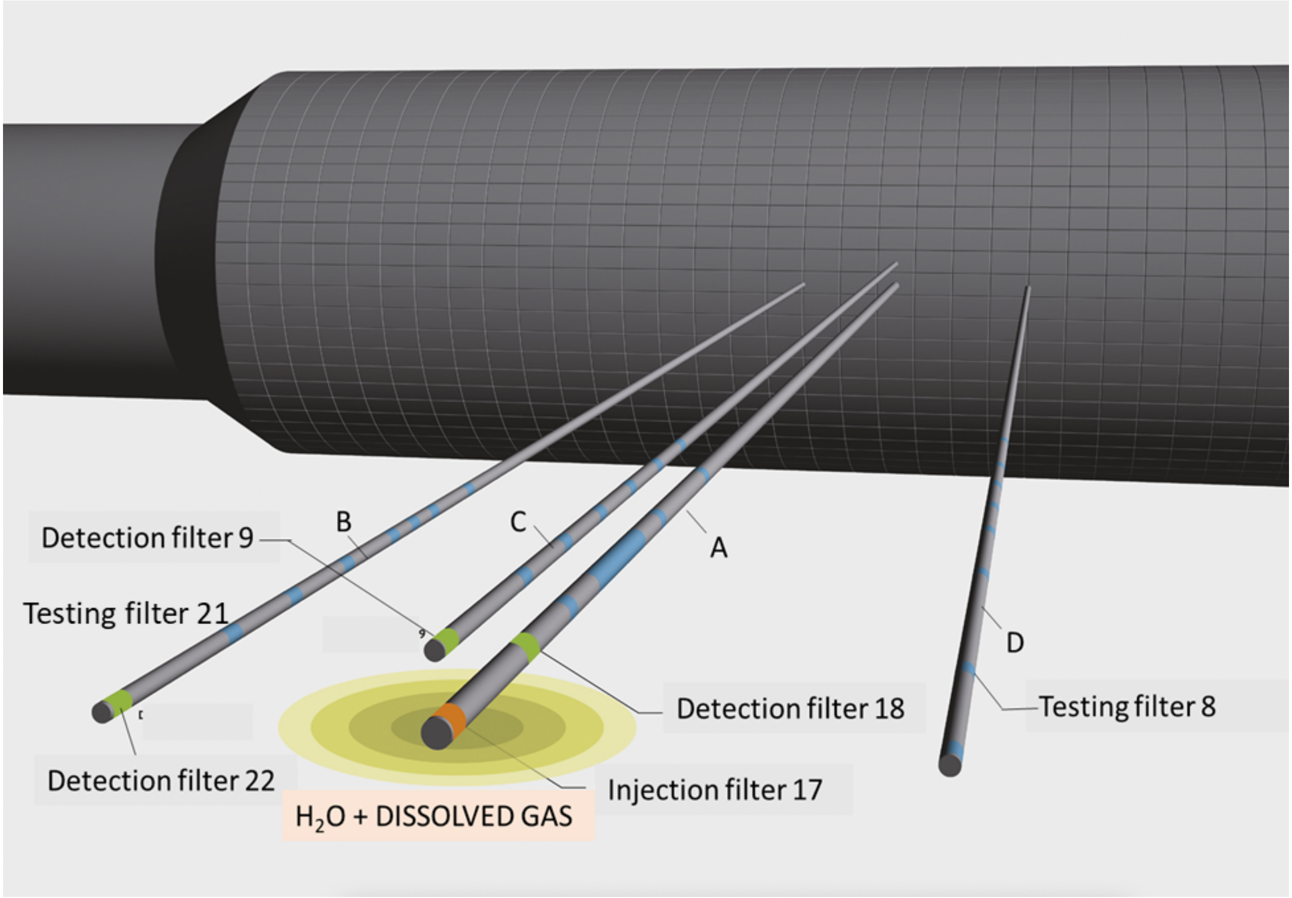

Figure 1.54: 3D view of the NEMESIS diffusion experiment

coupled gear pump (P100), which pumps around the water and speeds up the homogenization of the dissolved gas in the water in the source gas system and the water in the filter, filter chamber and two micro tubes connected to the filter. The outlet of the pump (V105) is connected to the outlet of the source circuit (V106), and the latter is connected to the other tube of the filter which allows the water to return to the filter. Also a bypass between the inlet and the outlet of the source gas system is foreseen (V101). This bypass allows the source gas system to be internally flushed, pressurised, etc. without influencing the filter itself and thus the *in situ* conditions. Through a 10 mm wide connection (V108), this circuit is connected to the gas analyser. In order to monitor the water level in the vessel, an extra tube (B101) with level sensor (U100) is installed in parallel with the vessel. The volume of water in each vessel is an essential parameter to estimate the diffusion coefficient, and is measured by the level sensors. The circuit is pressurized through a female quick connector which is closed off by V107. The water flow in the circuit is monitored by a flow meter (FI 100) which is installed between the outlet of the vessel and the inlet of the pump (V103). As pump failure might slow down the diffusion process, sufficient water flow has to be ensured over the full course of the experiment. Therefore, water flow is continuously monitored by flow sensors.

Filters 9, 18 and 22 are connected to the monitoring systems. The monitoring systems are identical to the source circuit, but are directly connected to the gas analyser. Gas can be sampled directly from the top part of the vessel as a sample line is going directly to the gas analyser (via V128/148/168).

Gas from all three monitoring systems can be analysed automatically, using a gas analyser (CGC4 Compact Gas Chromatograph 4 , Interscience). The gas analyser is equipped with a multi position valve which allows automated sampling.

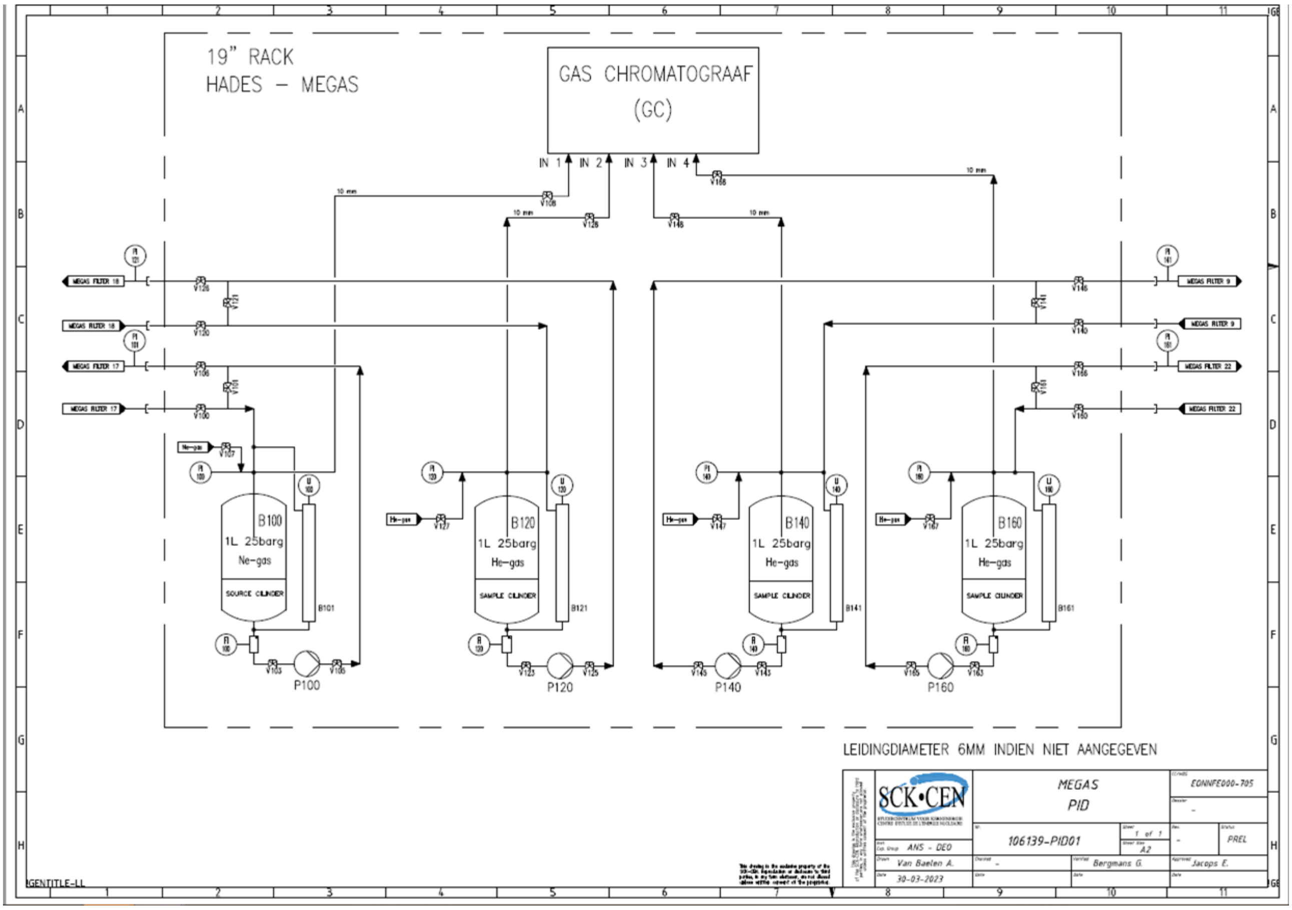

Figure 1.55: Schematic view of the setup with 1x injection/source circuit (S – on the left) and 3x monitoring circuit (T1, T2 and T3)

Note that the first version of the setup, which was commissioned early 2020 did not contain a system to monitor the water level and a connection to respressurize the setup after sampling. As both components were considered to be essential for a successful experiment, the setup was modified accordingly. The construction of MEGAS 2.0 was finished in December 2020.

An overview of all used sensors is given in Table 1.22.

parameter	Brand	type sensor	range	accuracy	resolution
Pressure before pump	Druck	UNIK 5000	0 -18 bar abs	0.2 % FS	
Level	Sick	LFP0300-G1NMB	0 – 300 mm	± 5 mm	2 mm (approx. 12 ml)
Flow	Keyence	FD-XC8M	0 – 3000 ml/min	0.3% FS	0.1 ml/min
Pressure after pump	Druck	PTX1400	0 – 25 bar abs	0.2 % FS	
Temperature	Digikey	JS8746B-0.15	-40 – 125 ℃	0.1 ℃	

Table 1.22: Overview of used sensors

Calibration

Several steps were taken to test, calibrate and validate the setup, including:

- Validation and calibration of the gas analyser for neon measurement
- Leak testing of setup
- Determination of the total volume of the setup
- Calibration of the level sensors
- Calibration of the pressure sensors
- Optimisation of the pump rate and verification of the flow sensors
- Measuring the head loss due to pumping
- Measuring impact of gas sampling on the pressure in the injection and monitoring circuits
- Testing of the setup by performing a diffusion experiment with neon on a Boom Clay core placed between the source and target 1 circuit
- Checking the validity of Darcy's law under low pressure gradient
- Performing preliminary in diffusion experiment in filters 8 and 21

All calibration and validation steps are described in an internal report of SCK CEN (R-9349) by Jacops, Chen et al. (2023) and information is available upon request.

Testing fluids

The used fluid in the *in situ* experiment is synthetic Boom Clay pore water (De Craen et al. 2004), which is prepared under anoxic conditions. The composition of the water is given in Table 1.23.

salts	*Theoretical mass (mg) for 1 L*
$NaHCO_3$	*1168*
H_3BO_3	*43*

salts	Theoretical mass (mg) for 1 L
KCl	25
$MgCl_2.6H_2O$	22
NaF	11
NaCl	10
$FeSO_4.7H_2O$	7
Na_2SO_4	0.3
$CaCO_3$	1000

Table 1.23: Composition of the synthetic Boom Clay pore water

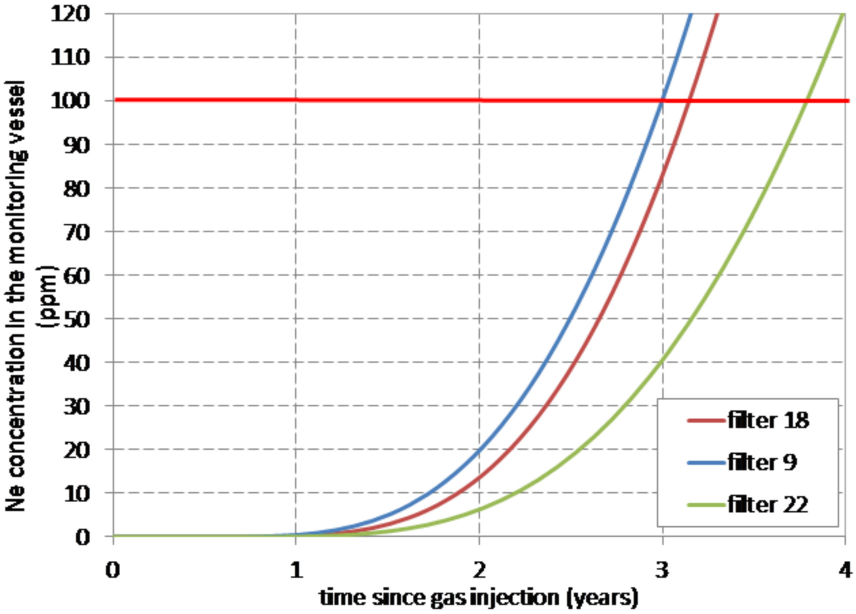

Figure 1.56: Zoom of Ne concentration in the gas phase (in ppm) to indicate when the detection limit of 100ppm is passed considering a total gas pressure of 15.8 bar in the monitoring vessel

Scoping calculations

Scoping calculations are described in detail in Jacops et al. (2020). Updated scoping calculations show that, as expected, filters 9, 18 and 22 are most interesting to monitor. As diffusion is a slow process, the upper detection limit of 100 ppm Ne will be passed only after 3 years, while the more realistic lower detection limit of 50 ppm is passed after 2.5 year (Figure 1.56).

1.4.3. Material properties (pre-test and post-test characteristics)

For the Boom Clay around MEGAS/NEMESIS, some parameter values are used in the models but the values are discussed in the modelling-related sections.

1.4.4. Testing protocol

Types of diffusion experiments

Figure 1.57 summarizes some standard types of diffusion experiments. The corresponding setups are basically one dimensional (1D) and are all modeled by 1D models.

In through diffusion experiments, the clay is placed between two water reservoirs (Figure 1.57, b). One of these reservoirs, the high-concentration reservoir or inlet, is initially doped with a tracer (C_0). The other reservoir, the low-concentration reservoir or outlet, is initially tracer-free. The clay is initially tracer free as well. By measuring the time evolution of the tracer concentration in the low-concentration and/or the high-concentration reservoir (C_b decrease) and/or the tracer concentration in the clay at the end of the experiment (C as function of the position x), the diffusion parameters can be calculated by using a mathematical model with the appropriate boundary conditions and formalisms (see Bourg and Tournassat (2015) and Aertsens (2011)).

In in diffusion experiments (Figure 1.57, c), clay is placed in contact with a water reservoir which is doped with a concentration of the tracer of interest (C_0). The concentration decrease of the tracer in the water reservoir (C_b) is measured as a function of time. At the end of the experiment, also the tracer profile in the clay can be determined. Clearly, in diffusion can be considered as the initial phase of through diffusion.

Verification at laboratory and *in situ* scale

Before starting the through diffusion experiment, verification of the setup was performed at two different scales. First, a through diffusion experiment was performed in the surface laboratory, using a Boom Clay sample which was confined in a diffusion cell. Next, the performance of the setup was verified by performing in *in situ* in diffusion experiment in filter 8 and 21.

Testing of the setup with a Boom Clay sample (within the surface laboratory)

In order to test whether the designed setup is able to measure diffusion coefficients, a diffusion experiment with a Boom Clay sample was performed within the lab. The sample (ON-Mol-1 core 112a, 260.84-261.04 m below drilling table) was loaded into a standard diffusion cell (sample confined under constant volume), and hydraulic conductivity was measured by applying a constant pressure head. Next, one side of the sample cell was connected to the source circuit, and the other side was connected to the target circuit. The source circuit was filled with 750 ml of degassed water and ~16 bar Ne, while the target circuit was filled with 750 ml of degassed water and ~16 bar He. The concentration increase of Ne in the target vessel was measured as a function of time.

3D in diffusion experiment in filters 8 and 21 (*in situ* conditions)

Rationale for the 3D in diffusion test Once the long-term gas diffusion test has started, there will be no chance for interruption or remediation. As a result, thorough and rigorous test preparations are required before the start of the formal test. Performing *in situ* a 3D in diffusion test gave us a great opportunity to rapidly gain an insight in the working principles of the test set up.

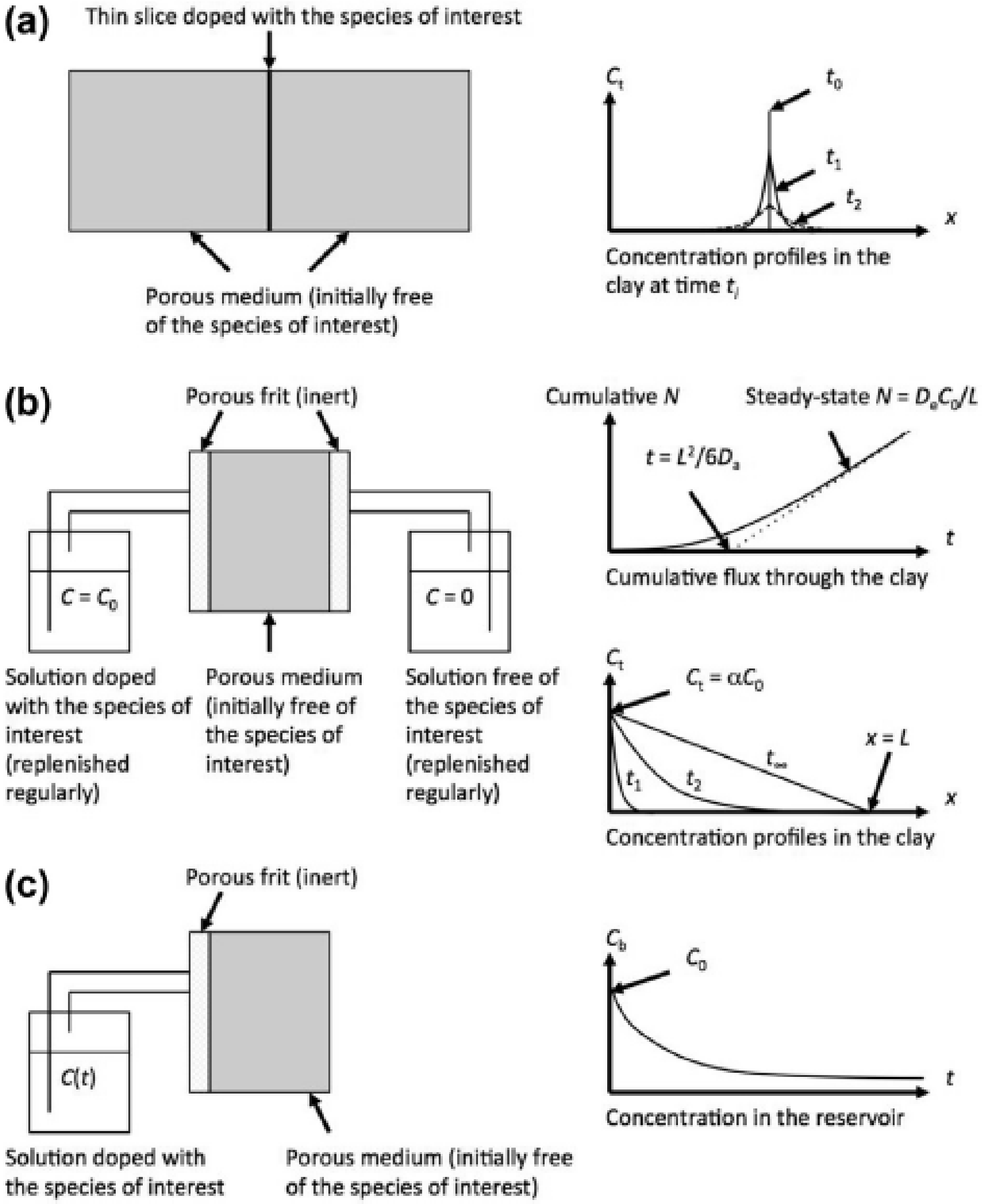

Figure 1.57: Schematic description of 3 methodologies commonly used to obtain diffusion coefficients in clay materials: (a) closed cell, (b) through diffusion and (c) in diffusion. After Bourg and Tournassat (2015)

During the preparation phase, one of the circuits was pressurized with helium, and the circuit was put in contact with filter D8. During this test, we observed a pressure decrease over time – related to the diffusion of helium into the pore water around filter D8. In the laboratory diffusion test, both gas and water pressures in the vessel can be strictly controlled to prevent water flow. In the *in situ* diffusion test, mass exchange between the clay and filter and pressure variations in the vessel happen automatically. However, detailed interpretation of the pressure decrease related to the diffusion process in this test may be difficult because some of the boundary conditions are complex. For instance, diffusion of dissolved gas into the clay leads to a gas pressure drop in the circuit. If this pressure drop is lower than the local pore water pressure, one could expect water flowing from the formation into the circuit. From a theoretical point of view, this water flow should follow Darcy's law. But from the experimental point of view, it may be not clear if water flows back or not, and if Darcy's law is perfectly followed. Models for interpretation of test results can be useful to confirm these hypotheses and to check if they are well controlled in the diffusion test.

A properly performed 3D in diffusion test is indeed of importance to provide relevant information on the boundary conditions of the setup and surrounding host rock, and check the validity of the currently available model and its parameters. This is a prerequisite for the *in situ* through diffusion test that is supposed to run for years.

Protocol for the 3D in diffusion test Two 3D in diffusion tests were respectively performed on filter A21 and D8 of the NEMESIS setup. Notice that filter A21 has a surface area which is about 2.4 times larger than that of filter D8.

The following steps were followed:

- Filter twin tubes were connected to a vessel in the cabinet respectively;
- Each vessel was partly filled with water, and the rest with helium;
- The helium in the vessel was pressurized to a certain pressure (i.e. P_i) in order that the pressure at the location of the connected filter was the same as the *in situ* intact pressure (i.e. P_0) after the test started with pumping around the gas saturated water solution in the filter;
- In order to ensure good circulation, water with dissolved gas was pumped around with a given flow rate of 25 ml/minute;
- The pressure variation with time in the vessel, P(t) was measured.

In the above tests, helium was dissolved into the vessel under pressure and with pumping, the dissolved gas was circulated to the filter through the twin tubes. The dissolved helium diffused into the Boom Clay surrounding the filter under the concentration gradient of the dissolved helium.

Because of the diffusion process, the gas pressure in the vessel decreased with time, P(t), and under the pressure gradient $\Delta P = P_0 - P(t)$, Boom Clay water around the filter flowed into the vessel through the twin tubes. It means that the pressure in the vessel varied with time as a consequence of two processes: diffusion of dissolved gas into host Boom Clay and Darcian flow of Boom Clay pore water into the vessel.

Based on the measurement of P(t) and the Boom Clay permeability around the filter and by considering pore water inflow into the vessel, the diffusion coefficient of the near-field Boom Clay could be derived by numerical modelling.

Initial pressure setting at the vessels To perform the 3D in diffusion test, it was considered to have an initial pressure at the location of the filter in the circuit to be the same as the *in situ* intact pressure. Therefore, it was necessary to determine two factors: 1/ the *in situ* intact pressures around filter A21 and D8 and 2/ the water pressure head loss along the twin-tubes under the water flow rate of 25 mL/min.

The *in situ* intact pore water pressure around A21 was 12.76 bar, while it was 14.65 bar around filter D8. Based on *in situ* measurements, under the water flow rate of 25ml/min, the average water pressure head loss along the twin tube was 0.245 bar for filter A21, while it was 0.303 bar for filter D8.

Consequently, the initial pressure in the vessel was set at 12.76-0.245/2=12.64 bar at the vessel connected to A21, while it was set at 14.65-0.303/2=14.50 bar at the vessel connected to D8. Due to difficulties in very precise controlling the vessel pressure, the actual value was initially set at 12.62 bar at vessel connected to filter A21 which was only 0.02 bar higher than the target value, while it was initially set at 14.53 bar at the vessel connected to filter D8 which was only 0.03 bar higher than the target value. After opening the valves between the setup and the clay formation and turning on the pump, pressure was monitored as a function of time.

NEMESIS: a 3D through diffusion experiment

NEMESIS is an *in situ* diffusion experiment carried out in the HADES underground research laboratory (URL) which corresponds to a 3D version of a closed cell gas diffusion experiment. Dissolved neon is injected in a central spot, the injection filter 17. Because the injection filter, as well as all other filters, are in contact with the surrounding clay, the dissolved neon diffuses away from the source into the surrounding clay. Where in the 1D closed cell experiment the tracer concentration is determined at several positions at a fixed time, here it is measured at some positions (the monitoring filters) for a large number of times. Depending on the positions of the monitoring filters, this type of experiment allows the apparent diffusion coefficient(s) parallel and/or perpendicular to the bedding plane (Aertsens et al. 2023) to be estimated.

Prior to the start of the NEMESIS 3D diffusion experiment, all circuits were emptied and flushed with inert gas. The source circuit was filled with ± 500 ml synthetic pore water, while the target vessels were filled with ± 750 ml. A gas phase was added (Ne for the source, He for the targets) up to a pressure about 1 bar above the planned starting pressure. A leak test was performed, and the target circuits were checked for the absence of neon. In a last stage, the head loss of each circuit was measured, and the results were used to set the exact starting stable pressure in the vessel (Table 1.24). After setting all vessels to the exact, predefined value, the valves between the circuits and the Boom Clay were opened, pumps were turned on and the experiment was started on September 5, 2023 at 10:13 CET (GMT +2).

Note that the small pressure difference between the pressure target stable value and actual stable value is caused by temperature fluctuations in HADES URL.

	Pore water pressure (bar)	Head loss (bar)	Target initial stable value in vessel (bar)	Actual initial stable pressure in vessels (bar)
Source	15.15	0.323	14.99	15.09
Target 1	15.18	0.331	15.01	15.07
Target 2	14.68	0.335	14.51	14.56
Target 3	15.21	0.318	15.05	15.10

Table 1.24: Relevant pressure values for the start of NEMESIS

1.4.5. Results

Test case with Boom Clay sample

In order to test whether the designed setup is able to measure diffusion coefficients, a diffusion experiment with a small sample (from core ON-Mol-1, 112a – diameter 80 mm, length 30 mm) was performed in the lab. The sample was taken from the ON-Mol-1 core 112a which originates from the Mol-1 drilling, and was retrieved from a depth between 260.84 and 261.04 m below drilling table. the sample with diameter 80 mm and length 30 mm was loaded into a constant volume cell. Prior to the diffusion test, the hydraulic conductivity of the sample was measured by using constant pressure head, and the measured K was 1.7 x 10^{-12} m/s. The fluid injection also resaturated the sample.

The porosity obtained afterwards from sample drying was 40% and specific surface area 46 m^2/g.

Based on the concentration change over time (Figure 1.58), the calculated diffusion coefficient is D_{eff} = 1.59 ± 0.02 x 10^{-10} m^2/s which is very much in line with the value of 1.75 x 10^{-10} m^2/s reported for another Boom Clay sample (sample ON-Mol1-84b – also referred to as “K2”) oriented perpendicular to bedding plane, as reported by Jacops (2018).

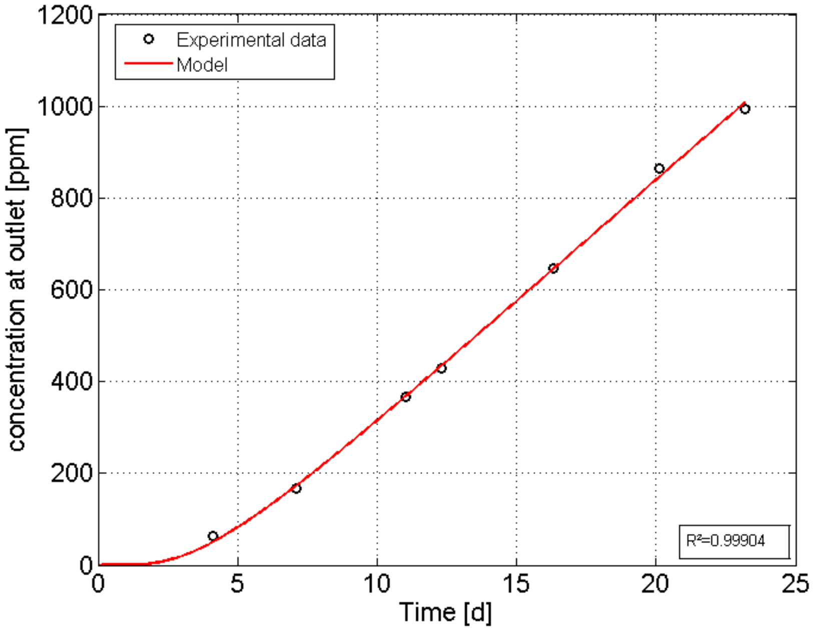

Figure 1.58: Neon concentration increase as a function of time in the downstream vessel (target 1)

Main 3D in diffusion test results

Two 3D in diffusion tests started on Oct. 24, 2022, and the measured pressure drops, dP(t)=P_i-P(t), are presented in Figure 1.59. In the vessel connected to filter A21 and filter D8, a steady pressure drop of about 0.16 bar and 0.29 bar could be observed respectively. Some abnormal pressure variations of dP observed in Figure 1.59 were due to the abnormal temperature changes in the gallery induced by incidents such as ventilation failure.

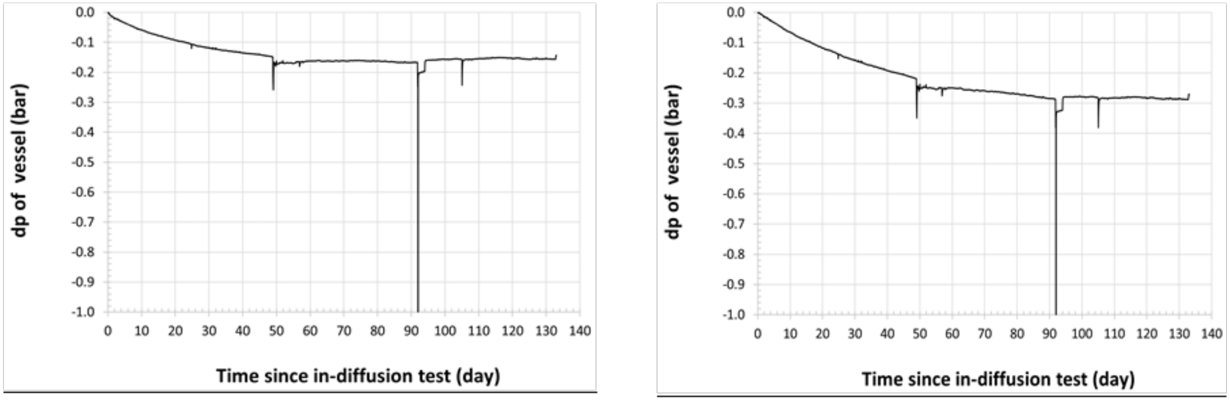

(a) Filter A21

(b) Filter D8

Figure 1.59: The pressure drops in both vessels (A21 left, D8 right) from the two 3D in diffusion tests

The three-month measurements follow well the prediction curves (see next section on data analysis for details). The good agreement between model results and field measurements confirms our lab scale test results. It also implies the good understanding of the *in situ* experimental system, which lays a good foundation for the long-term neon *in situ* diffusion experiment afterwards.

Data analysis of the 3D in diffusion experiment in filters 8 and 21

Modelling of the 3D in diffusion experiments in D8 and A21 The test procedure is described earlier. The pressure set in both vessels accounts for the water pressure head loss before and after the pump. Head loss refers to the total pressure losses sustained by the fluid as it flows from the suction point to the discharge point. So the pump has to generate pressure, which compensates for the losses, so that the fluid can keep running through the system. Figure 1.60 shows the layout and the initial pressure of A21 and D8. If there is no water exchange between the filter and vessel, the water and gas volume in the vessel will keep constant at their initial values of 750mL. With the diffusion of He into Boom Clay, the concentration of He in the water and the gas pressure in the vessel will decrease with time. With the diffusion going on and pressure dropping, water will flow back into the vessel, thereby compressing the gas in the vessel. The compression of gas induces increase of the gas pressure, which in turn prevents water flowing back. Therefore, the diffusion process is automatically adjusted by the balance between the gas-water phases in the vessel. This implies that we need to include the Darcy flow module in the model to simulate such a dynamic process. Unfortunately, measurement of the water volume in the vessel is only possible with limited accuracy (uncertainty of ± 12 ml).

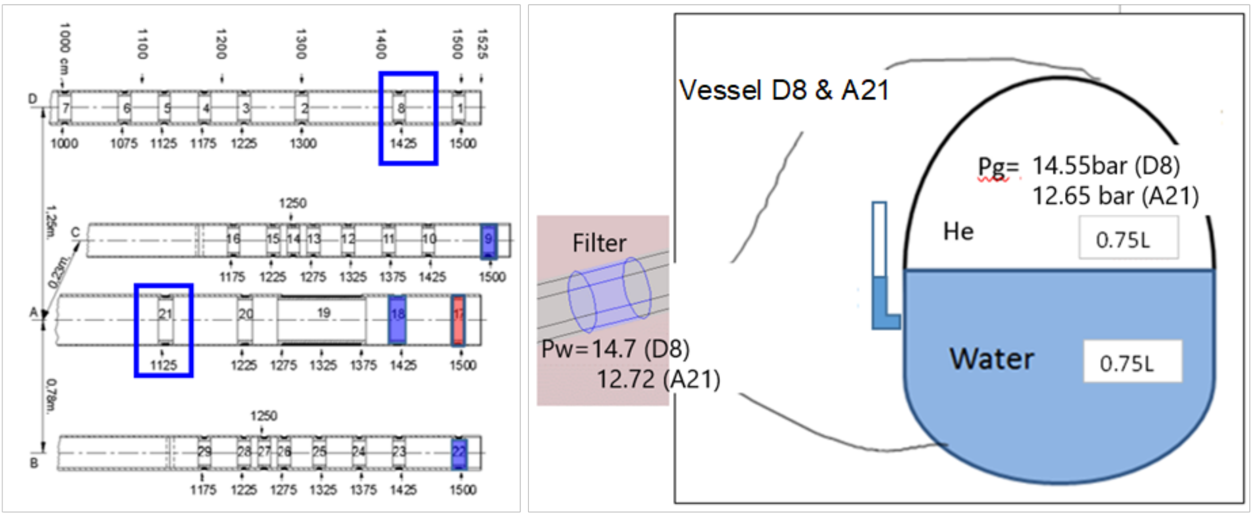

Figure 1.60: Layout and the initial state of filters A21 and D8

The commercial software COMSOL is used to calculate the pressure variations in the vessels for a duration of 300 days. The COMSOL model is illustrated in Figure 1.61. The initial conditions and main parameter values used for the 3D in diffusion tests are listed in Table 1.25.

	D8	A21
Surface area [m^2]	0.01	0.025
Vessel pressure [bar]	14.55	12.65
***In situ* water pressure at filter [bar]**	14.7	12.77
Initial V_{water} (vessel and tube) [mL]	916	929
Initial V_{gas} [mL]	750	
D_{0_water} [m²/s]	4 x 10^{-9}	
$D_{e\_H\_He}$ [m²/s]	74.7 x 10^{-11} (from lab test)	
$D_{e\_V\_He}$ [m²/s]	$D_{e\_H\_He}$ /1.3	
Porosity [-]	0.38	

	D8	A21
K_H [m/s]	4.5 x 10^{-12}	
K_v [m/s]	2.1 x 10^{-12}	

Table 1.25: Main parameter values for the numerical model

The 3D in diffusion test is modelled for two cases: i) without water flowing (case 1) and ii) with water flowing (case 2). A Darcy's flow module is coupled with the diffusion module in case 2. The total amount of gas (in mole) diffused into the clay is denoted as $M_{gas\_diffused\_into\_clay}$ that is both the time and surface integral of the gas flux J_{gas} at the filter surface. The gas pressure in the vessel is calculated as:

$$P_g[bar] = \frac{(Initial\ He\ in\ the\ vessel - M_{gas\_diffused\_into\_clay}(t))\ [mol]}{Henry's\_constant[\frac{mol}{L\bullet bar}] \times V_{water}(t)[L] + \frac{V_{gas}(t)[L]\times 100}{8.314[\frac{J}{Kmol}]\times 293{,}15K}}$$

Where the volume of gas and water in the vessel is updated based on the amount of water flowing back into the vessel.

Predictions for the 3D in diffusion test are shown in Figure 1.62 for both cases. Figure 1.62 clearly indicates that without water flowing, the gas pressure in the vessel continuously decreases, while with water flowing back into the vessel, the gas pressure approaches to a constant value. Another prediction is that the surface area of the filter influences the amount of gas diffused into the clay and water inflow to the vessel, but does not impact the final gas pressure drop in the vessel much when there is water inflow. These observations are based on the assumption that the Boom Clay is homogeneous around the two filters.

The measured pressure drops in both vessels are compared with the predictions, as shown in Figure 1.63. First, both vessels follow the case considering water flow, i.e. approaching a steady value. This implies that water inflow to the vessel plays an important role in adjusting the vessel pressure. Second, gas pressure drop in vessel A21 is very close to the prediction (red curve), while gas pressure drop for D8 is larger than the prediction. In the following section, some sensitivity modelling has been carried out to investigate the possible reasons for these deviations.

Sensitivity analysis

Impact of temperature variations In the modelling presented above, the temperature is assumed to remain constant at 20 ºC. However, the vessel pressure measurements in Figure 1.63 show sudden pressure drops on day 49 and on Jan. 24 2023 due to the heating power off at EURIDICE. These short-term incidents had significant impact on the pressures in the vessels and consequently affected the 3D in diffusion tests. Figure 1.64 illustrates the sudden temperature drop of 2.2 ºC in 6 hours on day 49 caused by the heating power off in the gallery, and a steady temperature decrease with a rate of 0.3 ºC in 49 days during the winter.

The historical temperature measurements in the vessel cabinets in Figure 1.65 indicate that the seasonal temperature increase in summer and decrease in winter follow approximately the rate of 0.3-0.5ºC in 49 days.

To investigate the impact of seasonal temperature variations on the vessel pressure drop, a continuous temperature decrease or increase in five months are considered for A21. Results in Figure 1.66 indicate that the seasonal T variations (the case with ±0.5ºC in 49 days) cause no more than 6% disturbances to the pressure drop after 5 months.

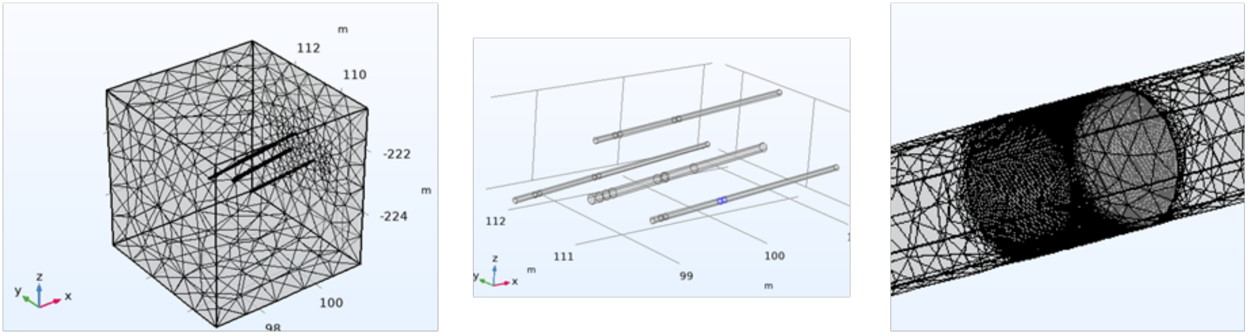

Geometry of the model Piezometers and filters Detailed mesh of the filter D8

Figure 1.61: COMSOL model for 3D in diffusion test

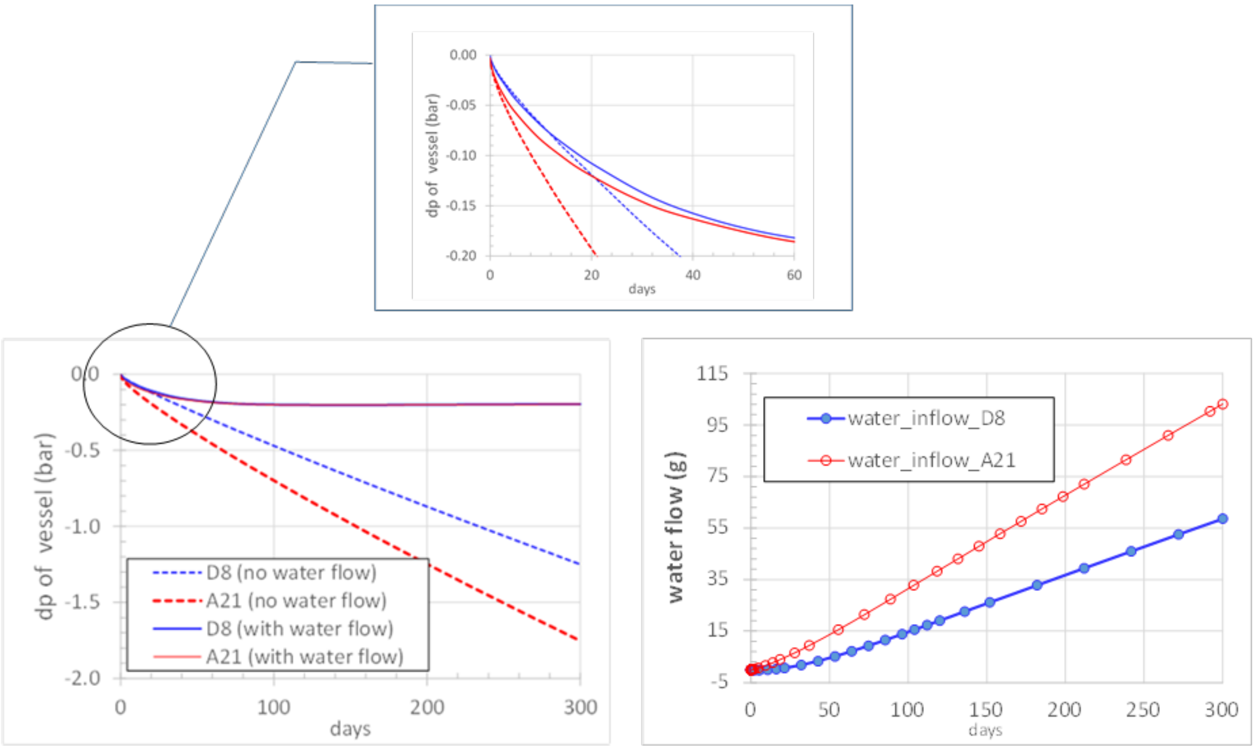

Figure 1.62: Model prediction for two cases: without water flowing and with water flowing back into the vessel: gas pressure drop in the vessel (left) and amount of water flowing back to the vessel (right)

Impact of diffusion coefficient D In this section, a range of diffusion coefficient values are tested for the clay around the filter A21, as shown in Figure 1.67. Among them, the base case refers to the diffusion values listed in Table 1.25: D_{eff_H}=7.47 x 10^{-10} [m^2/s] and D_{eff_H}/D_{eff_V}=1.3. Results indicate that a smaller diffusion coefficient decreases the diffusion process and thus the pressure drop in the vessel. As a result, less water is flowing back to the vessel. Overall, there is a linear dependence of pressure drop and water inflow on D values Figure 1.68.

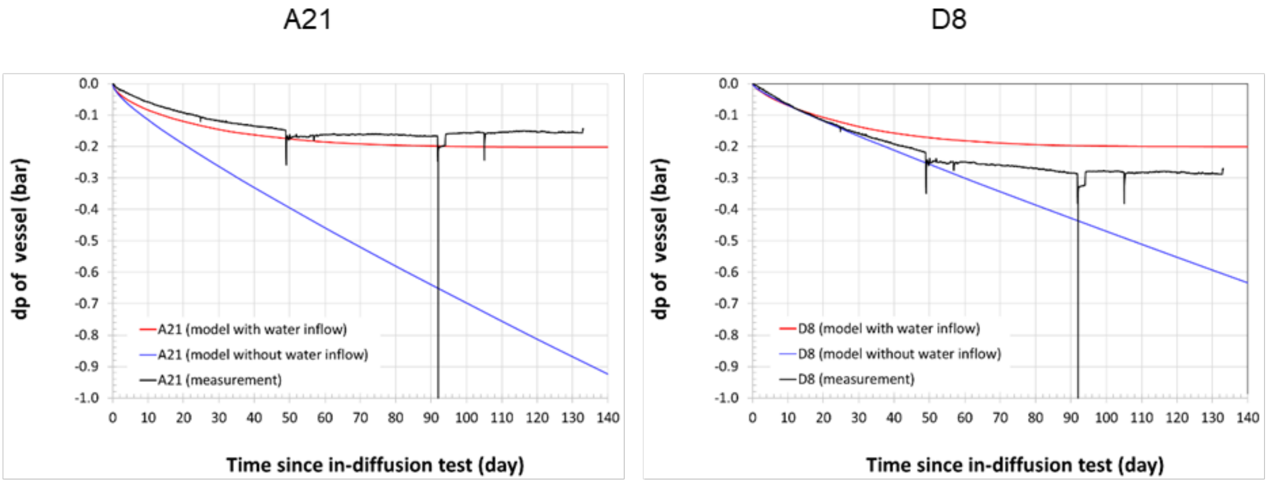

Figure 1.63: Comparison between the measured and modelled pressure drops in both vessels.

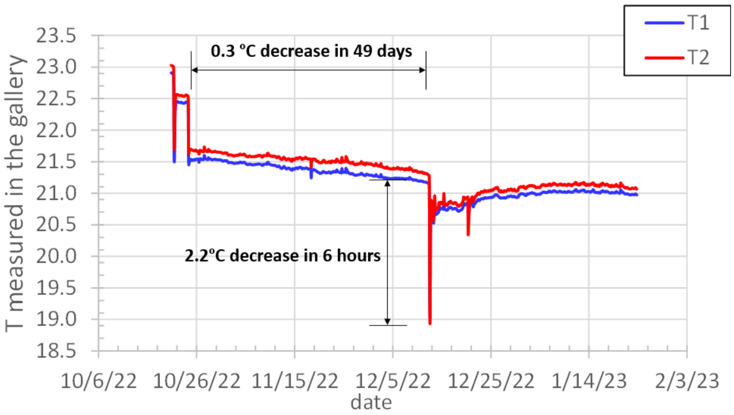

Figure 1.64: The temperature drop measured on day 49 in the cabinet due to heating power off in the gallery. T2 is for D8 and T1 is for A21.

Impact of hydraulic conductivity K A range of hydraulic conductivity values are tested in this section for the clay around the filter A21, as shown in Figure 1.69. Among them, the base case refers to the hydraulic conductivity values listed in Table 1.25 : K_H=4.5 x 10^{-12} [m/s] and K_v=2.1 x 10^{-12} [m/s]. Logically, hydraulic conductivity has opposite effects as compared to the diffusion coefficient: a smaller hydraulic conductivity makes it more difficult for the water to flow back to the vessel, thus fastens the pressure drop in the vessel. There is a linear dependence of pressure drop and water inflow on 1/K (Figure 1.70)

The opposite effects of K and D on the pressure drop is are combined in Figure 1.71.

Impact of anisotropy ratio of D_{eff_H}/D_{eff_V} The anisotropic ratio of 1.3 is used in the base case for calculating D_{eff_V}, while the anisotropic ratio of 1.63 was measured for the diffusion coefficient of He in the laboratory using confined apparatus. The impact of these two anisotropic values is presented in Figure 1.72. When D_{eff_H} is fixed, larger anisotropic ratio makes smaller D_{eff_V}, thus less pressure drop in the vessel.

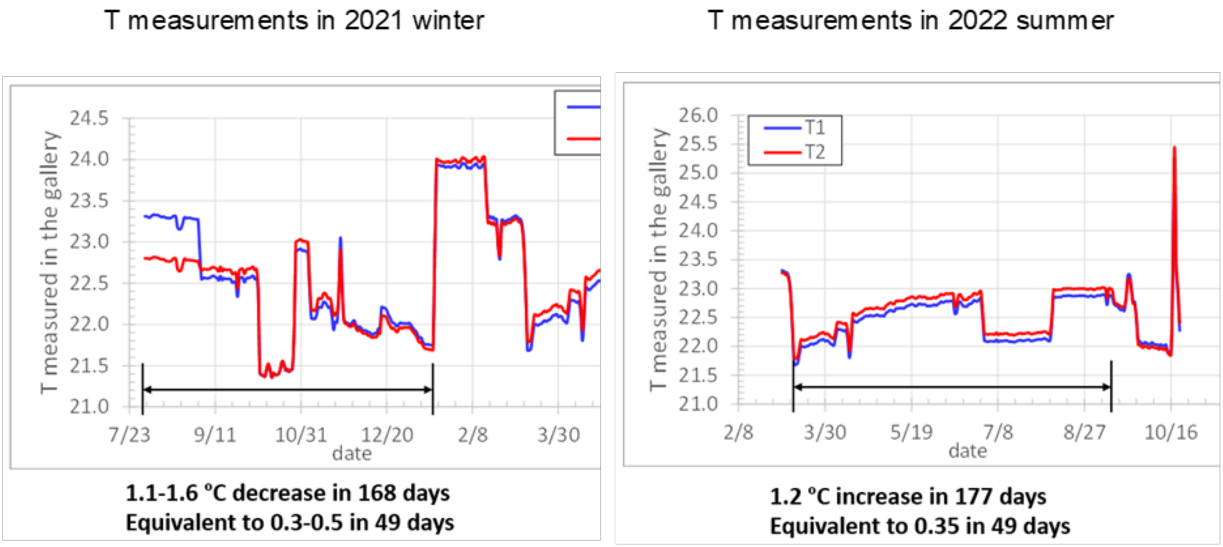

Figure 1.65: Historical temperature measurements in the vessel cabinets in 2021 and 2022.

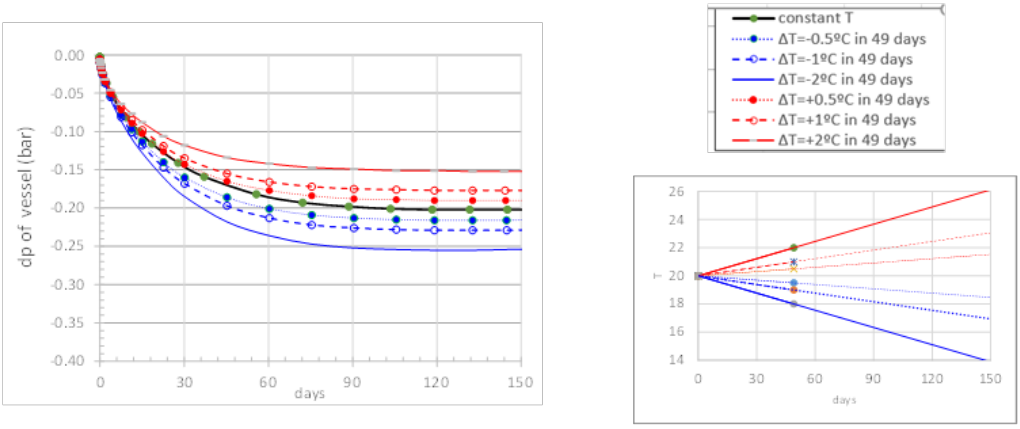

Figure 1.66: Impact of seasonal temperature variations on the vessel pressure drop of A21

Fitting the 3D in diffusion test In the 3D in diffusion test, at the moment the pump was on and water started to flow in the circuit, there was a sudden pressure drop in the vessel, although the water head loss is accurately considered and verified. The dropped pressure was 14.53 bar for D8 and 12.65 bar for A21. In this section, these two actual pressures are updated in the model as the initial pressure of the respective vessel. Furthermore, the actual temperature variations as the yellow dots in Figure 1.73 are used in the updated model. For the base case, the rest of the parameters are the same as listed in Table 4.

The updated model results are shown in Figure 1.74. For the base case, measured pressure drop is lower than modelling results for A21 and higher for D8. For A21, decreasing the diffusion coefficient or increasing anisotropy ratio makes the fitting better. It was found that by decreasing the diffusion coefficient to 0.8 x the reference value makes the modelling results very close to the measurements. For D8, increasing the diffusion coefficient to 1.45 x the reference value or decreasing the hydraulic conductivity (0.5x reference value) fits the measurements better. But decreasing K makes it difficult for the pressure to reach a steady

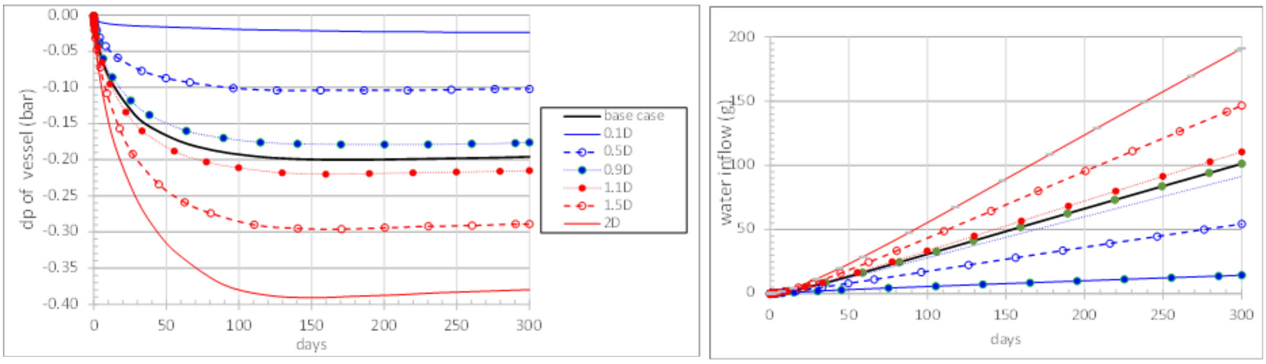

Figure 1.67: Impact of diffusion coefficient of the clay on the vessel pressure drop of A21 (left) and water inflow to the vessel (right). Same legend applies for both figures.

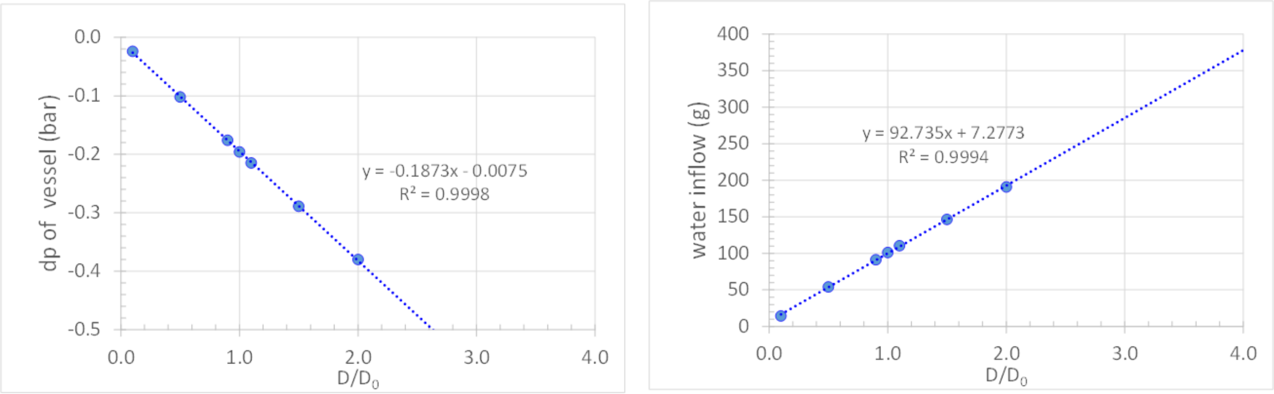

Figure 1.68: Linear dependence of pressure drop in the vessel (left) and water inflow to the vessel (right) on the diffusion coefficient of the clay. The results at 300 days are used for the graph.

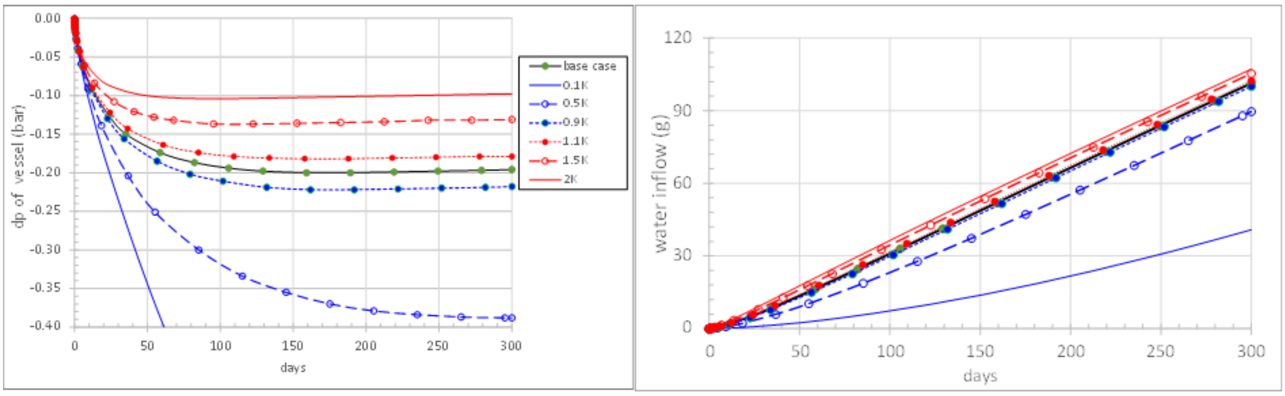

Figure 1.69: Impact of hydraulic conductivity of the clay on the vessel pressure drop of A21 (left) and water inflow to the vessel (right). Same legend applies for both figures.

state and seems to not match the real situation.

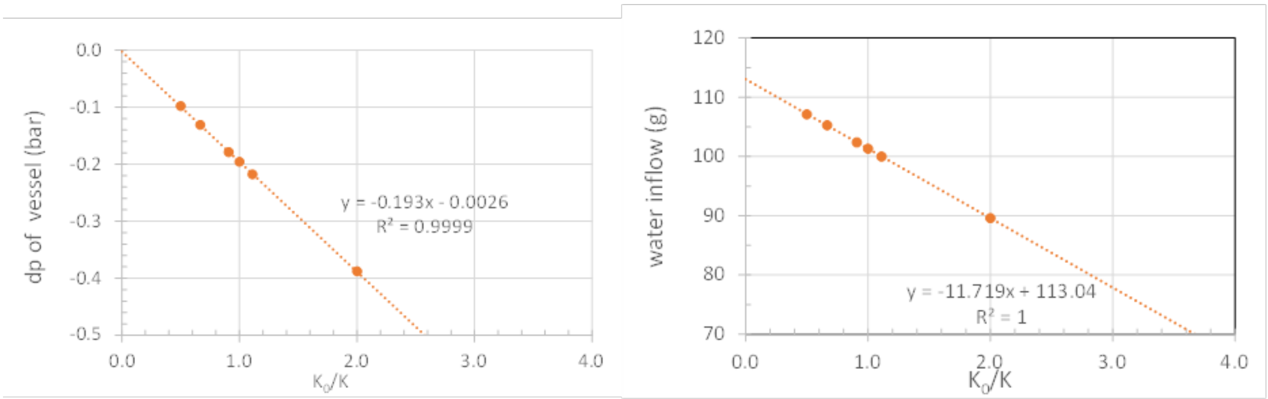

Figure 1.70: Linear dependence of pressure drop in the vessel (left) and water inflow to the vessel (right) on the hydraulic conductivity of the clay. The results at 300 days are used for the graph.

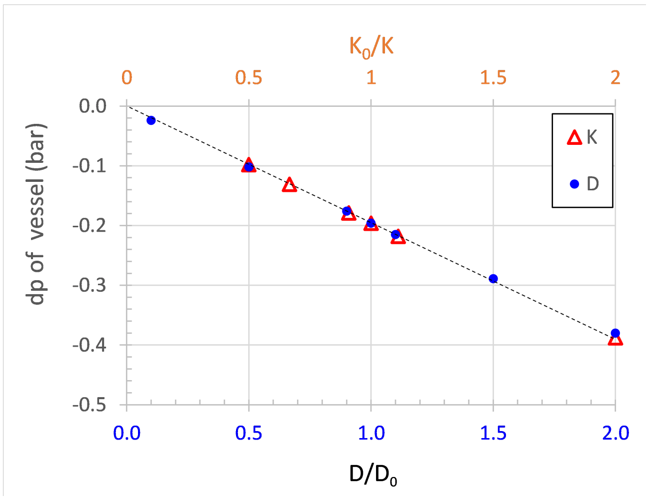

Figure 1.71: Impact of D and K on pressure drop in the vessel.

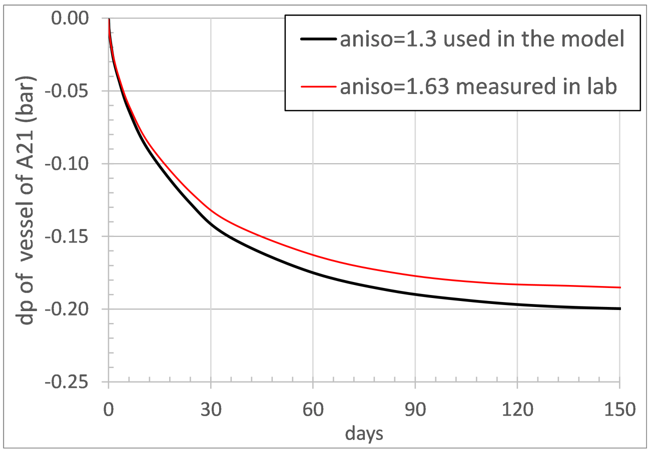

Figure 1.72: Impact of anisotropic ratio of the diffusion coefficient on pressure drop in the vessel.

1.4.6. Summary

This report describes the preparation phase of the NEMESIS *in situ* experiment. The first stage of the preparation phase started after the construction of the setup, and includes mainly leak testing, determina-

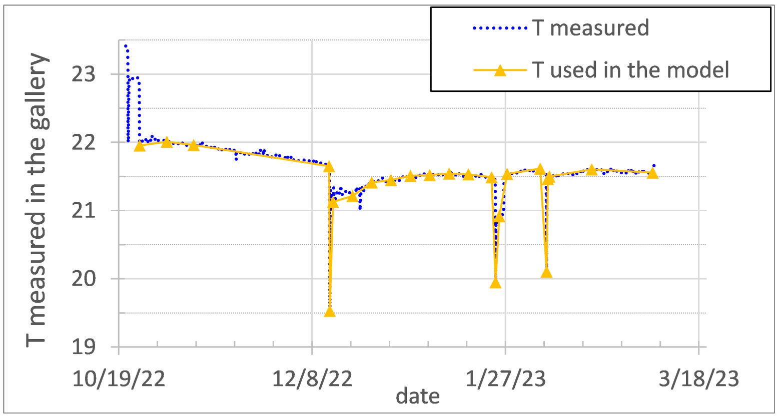

Figure 1.73: Temperature variations used in the updated modelling.

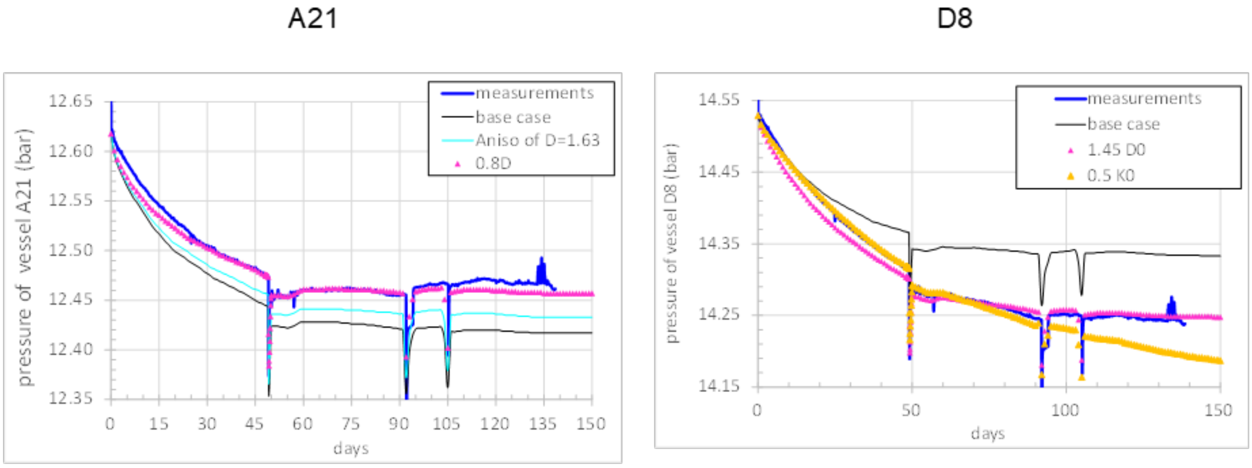

Figure 1.74: Attempts to fit the pressure drop measurements by varying model parameters

tion of the total volume of the setup, calibration of all sensors, optimization of the flow rate of the pumps, the connection of the tubes from the involved piezometer filters, calibration and validation of the gas analyser. Two “validation” tests have been performed. The first test was a diffusion test with a small clay sample which was loaded in a standard gas diffusion cell and which was placed between the source and a target circuit, filled with neon and helium, respectively. During the test, neon diffused from the source circuit, through the sample towards the target circuit. The diffusion coefficient was estimated based on the concentration change in the target circuit, measured as a function of time. As the measured diffusion coefficient was similar to previous measured values, obtained from diffusion experiments in the validated gas-diffusion tests, the setup was considered to be suited for measuring diffusion of dissolved gas. The second validation test was a 3D in diffusion experiment, performed in 2 filters (D8 and A21) which are not involved in the final NEMESIS experiment. The experiment consisted of filling 2 circuits with synthetic pore water and helium at a pressure equal to the pore water pressure, and pumping around the dissolved helium. As helium diffused into the surrounding clay formation, pressure decreased as a function of time and the pressure decrease allowed the assessment of the diffusion parameters and the validity of the available diffusion model. The fitted diffusion coefficient for filter A21 was 80% of the value measured in the gas lab, while it was 145% for D8 - which is considered to be a good result. Together with the 3D in diffusion test, also the head loss due to pumping was measured and the validity of Darcy’s law (water flow under very small pressure gradient) was measured. After all these preparation steps, we considered the setup and the model almost ready to be started.

In the final preparation stage, the pressure of all tubes was monitored as the initial pore water pressure should be recovered, the setups were brought to a pressure slightly above the pore water pressure, the composition of the gas phases was measured and the head loss due to pumping was assessed. Finally, the pressure in the vessels was set correctly (compensating for the head loss) and the valves towards the piezometer filters were opened. The pumps were turned on and the diffusion started on September 5, 2023 at 10:13 CET. The composition of the gas phase in the target circuits will be measured every 3 months in the first year, afterwards the sampling frequency will be increased up to 1/month. The experiment is assumed to run for 5 years.

1.4.7. Key learning points

1.7.1 New knowledge acquired

For now, the key learning points from NEMESIS are mainly technical. During the preparation phase, we were confronted with many technical issues which had to be solved. The total process of designing, constructing and validating the experiment was very complex and time consuming. The two in diffusion experiments provided valuable insights in the performance and response of the setup and allowed validation of the diffusion model.

1.7.2 Impact of acquired knowledge

As the NEMESIS experiment started only recently, only the results for the 2 in diffusion tests are available at the end of EURAD-GAS. As the pressure drop due to in diffusion for filter A21 could be matched in the diffusion model with a value at 80% of the lab-diffusion coefficient, while for filter D8 this value was 145%, there is a first indication that the lab-scale data are in line with *in situ* data. Though, this can only be confirmed when sufficient data points from the 3D diffusion test are available.

1.7.3 Remaining knowledge gaps

As the NEMESIS experiment started only recently and the first results are expected in 2026, diffusion coefficients on larger scale are not yet available.

1.7.4 Recommendations for the future

It is recommended to continue the NEMESIS experiment for the coming years. The leassons learned from the preparation of the NEMESIS experiment should be taken into account when future gas diffusion *in-situ* experiments are planned.

References

Aertsens, M. (2011). Migration in Clay: experiments and models. SCK-CEN ER-165. Mol, Belgium.

Aertsens, M., E. Weetjens, J. Govaerts, N. Maes and S. Brassinnes (2023). "CP1 and Tribicarb-3D: unique long-term and large-scale in situ migration tests in Boom Clay at the HADES Underground Research Laboratory." Geological Society, London, Special Publications **536**(1): SP536-2022-2041.

Bourg, I. C. and C. Tournassat (2015). Chapter 6 - Self-Diffusion of Water and Ions in Clay Barriers. Developments in Clay Science. C. Tournassat, C. Steefel, I. Bourg and F. Bergaya, Elsevier. **Volume 6:** 189-226.

De Craen, M., L. Wang, M. Van Geet and H. Moors (2004). Geochemistry of Boom Clay pore water at the Mol site. SCK-CEN BLG-990. Mol, Belgium.

Jacops, E. (2018). Development and application of an innovative method for studying the diffusion of dissolved gases in porous saturated media. PhD thesis., KU Leuven.

Jacops, E., M. Aertsens, N. Maes, C. Bruggeman, B. M. Krooss, A. Amann-Hildenbrand, R. Swennen and R. Littke (2017). "Interplay of molecular size and pore network geometry on the diffusion of dissolved gases and HTO in Boom Clay." Applied Geochemistry **76**: 182-195.

Jacops, E., M. Aertsens, N. Maes, C. Bruggeman, R. Swennen, B. Krooss, A. Amann-Hildenbrand and R. Littke (2017). "The Dependency of Diffusion Coefficients and Geometric Factor on the Size of the Diffusing Molecule: Observations for Different Clay-Based Materials." Geofluids **2017**: 16.

Jacops, E., G. Chen, L. Yu, A. Vanleeuw, D. Nackaerts and M. Aertens (2023). NEMESIS progress report 2023; SCK CEN R-9349; Mol, Belgium.

Jacops, E., N. Maes, C. Bruggeman and A. Grade (2016). "Measuring diffusion coefficients of dissolved He and Ar in three potential clay host formations: Boom Clay, Callovo-Oxfordian Clay and Opalinus Clay." Geological Society, London, Special Publications **443**.

Jacops, E., B. Rogiers, L. Frederickx, R. Swennen, R. Littke, B. M. Krooss, A. Amann-Hildenbrand and C. Bruggeman (2020). "The relation between petrophysical and transport properties of the Boom Clay and Eigenbilzen Sands." Applied Geochemistry **114**: 104527.

Jacops, E., R. Swennen, N. Janssens, T. Seemann, A. Amann-Hildenbrand, B. M. Krooss, R. Littke, N. Maes and C. Bruggeman (2020). "Linking petrographical and petrophysical properties to transport characteristics: A case from Boom Clay and Eigenbilzen Sands." Applied Clay Science **190**: 105568.

Jacops, E., G. Volckaert, N. Maes, E. Weetjens and J. Govaerts (2013). "Determination of gas diffusion coefficients in saturated porous media: He and CH_4 diffusion in Boom Clay." Applied Clay Science **83-84**: 217-223.

Jacops, E., K. Wouters, G. Volckaert, H. Moors, N. Maes, C. Bruggeman, R. Swennen and R. Littke (2015). "Measuring the effective diffusion coefficient of dissolved hydrogen in saturated Boom Clay." Applied Geochemistry **61**(0): 175-184.

Jacops, E., L. Yu, G. Chen and S. Levasseur (2023). "Gas transport in Boom Clay: the role of the HADES URL in process understanding." Geological Society, London, Special Publications **536**(1): SP536-2022-2042.

Jacops, E., L. Yu and N. Maes (2020). A new in situ gas diffusion experiment: objectives, design and experimental protocol. SCK CEN Reports, SCK CEN.

Ortiz, L., G. Volckaert and D. Mallants (2002). "Gas generation and migration in Boom Clay, a potential host rock formation for nuclear waste storage." Engineering Geology **64**: 287-296.

Volckaert, G., L. Ortiz, P. De Cannière, M. Put, S. Horseman, J. Harrington, V. Fioravante and I. M (1995). MEGAS Modelling and experiments on gas migration in repository host rocks. Final Report Phase 1. EUR-16235. Luxembourg.

.

IRSN

1.5. Studying the onset of desaturation process in argillites (IRSN)

1.5.1. Introduction

Clay rocks are considered as potential host rock for radioactive waste deep repositories namely for their low hydraulic conductivity and high sorption capacity. The transport and transfer properties of these rocks are extensively studied experimentally and theoretically. However, the spatial connectivity of the pores is controlled by throats smaller than micrometer, which induces long characteristic time for transient experiments and makes them persistently complicated. Such nano-size pores are difficult to observe, preventing from getting direct insight into pore-scale processes. Amongst them, the transfer properties of nearly saturated clays are of great interest since gases are expected to be produced within repositories and to desaturate partially neighbouring portions of the host rock. A particular issue is related to the inset of the drainage process where an important dispersion of experimental data has been noticed. Mostly, the unsaturated samples are being prepared by equilibration within an atmosphere with a given relative humidity, where the final state is defined following the mass change of the sample. It is then supposed that the desaturation is homogeneous within the sample, i.e., the biggest pores are desaturated first within the whole sample volume, while small pores remain water saturated. This hypothesis is employed to establish suction curves which are then used for macroscopic simulations of gas migration.

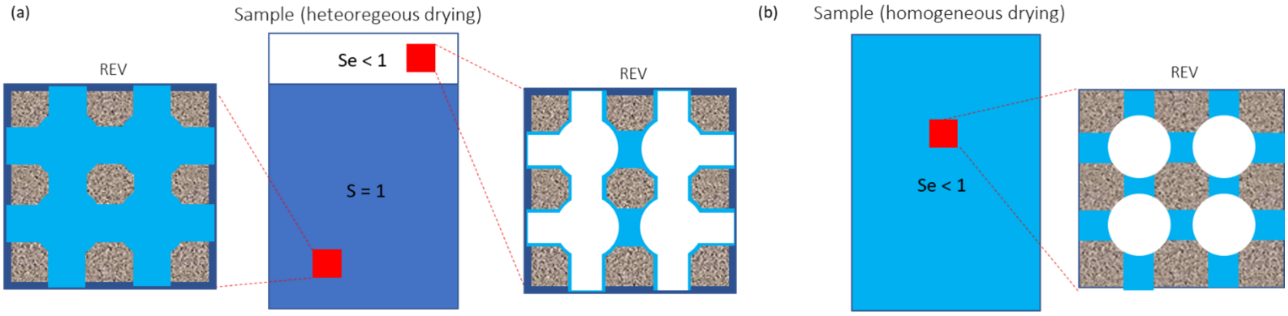

Figure 1.75: Example of (a) heterogeneous drying and (b) homogeneous drying

Many X-ray microtomography studies on clays rocks were reported, with voxel sizes in micrometer range (for example 14 µm (Lenoir et al., 2007) or 0.7 µm (Robinet, 2008)), where the mineralogy and macroporosity could be characterized. To our knowledge there are very limited studies aiming at imaging water-air distribution in clay rock. For example, in (Stavropoulou et al., 2020), only the biggest cracks with few pixels were visible under their adopted resolution of 42 µm and neutron tomography had to be used to differentiate between water and air. Nevertheless, the 3D µCT imaging data are of high interest also as inputs for developing pore-scale numerical simulations, for example the analysis of advective gas and diffusive solute transport within partially saturated clay (Genty et al., 2017a; Pazdniakou and Dymitrowska, 2018b).

IRSN proposed to use X-ray micro- and nano- tomography to characterize the pore network of different clay materials (Toarcian, Sand of Eigenbilzen, synthetic materials from BGS) at different saturation levels. This requires an acquisition of 3D images of chosen clay at several levels of saturation and a subsequent development of image analysis tools for segmentation of low contrast domains in order to be able to distinguish between water, gas and clay phases. The aim is to assess the hypothesis of the uniformity, Figure 1.75, of the desaturation process, with the direct visualisation of water and gas filled macropores by X-ray tomography. We want to characterize the water-air distribution as a function of radial distance from the sample border. If the desaturation is homogeneous and due to the strong capillarity and small pores sizes, we expect that the biggest macro and meso pores (sub-micron scale in geoscience terms), will dry first and thus it is sufficient to observe them at submicron scale all over the sample.

The acquired 3D imaging data will be shared with the EURAD WP6 GAS partners to be used to build synthetic pore network models that will allow for example to numerically determine the effective diffusion coefficients as function of the water saturation. Such values can be tested against those determined in the diffusion experiments by SCK CEN and BGS, and in modelling by PSI.

1.5.2. Experimental set-up

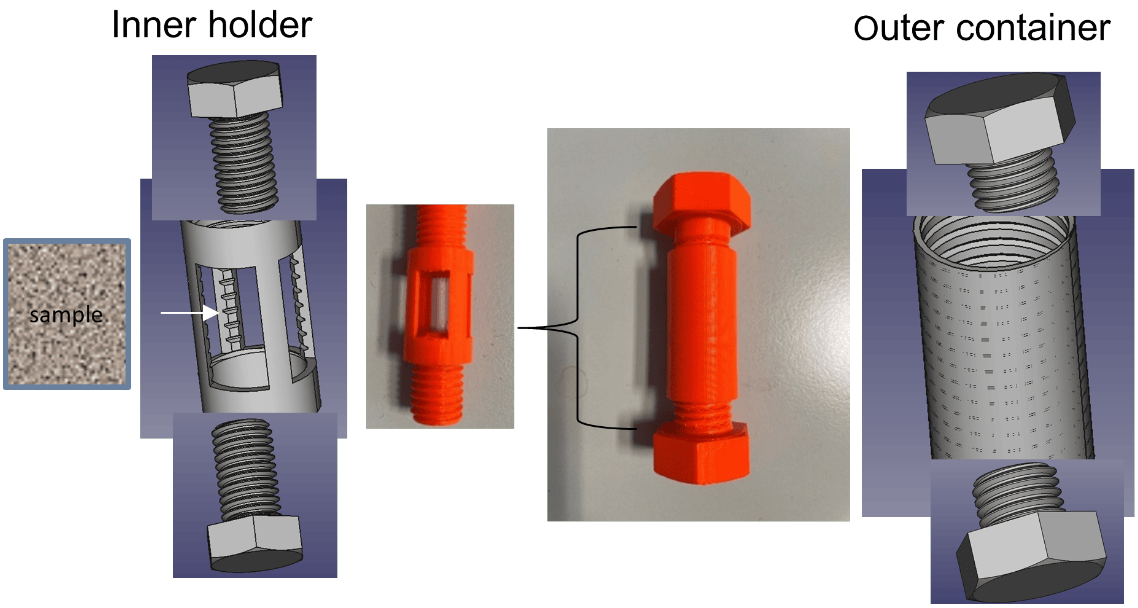

Figure 1.76: 3D printed axial confinement cell and the outer container for transfer and scanning.

The diameter of cylindrical samples should be below 10 mm to achieve the resolution of about 0.5 μm in imaged sub-volumes. First the samples will be placed in controlled atmosphere chamber on a high sensitivity balance and equilibrated at given relative humidity using saturated saline solutions. For transfer and scanning, they will be placed in vapour tight capsules or wrapped in parafilm. Some attempts will be made to stabilize the sample temperature during scanning to avoid spurious evaporation effects. The drainage path is followed starting at full water saturation, however we do not go down to water saturations lower than 80%, since in this range the desiccation effects are expected to dominate over vapour diffusion. We work with bore argillite samples in order to get quicker stabilization at different saturation levels. To avoid swelling and shrinking of clay-rich materials some tests are done with radially constrained samples, Figure 1.76.

1.5.3. Material properties (pre-test and post-test characteristics)

1.5.3.1. Materials and samples

Three rock material candidates are: Toarcian argillite, Sand of Eigenbilzen, and BGS synthetic clay. For Toarcian samples, they were taken from Tournemire URL (Gallery East 03, see Figure 1.77(a)), with the borehole (depth 1-2m) perpendicular to the bedding (and parallel to the bedding for statistical and comparison purpose); samples were trimmed on site (lathe machine) right after coring (Figure 1.77(b)).

The Toarcian argillite has a low porosity of about 11% or lower, with most of the pore sizes in the nanometer range, which makes the direct observation of pore fluids very challenging. To test our methodology, it is preferable to work on more porous materials. Thus, we have chosen the Eigenbilzen Sands, a sandy layer above the Boom Clay, presenting an increased quartz content and thus much higher permeability, but almost the same porosity. SCK CEN prepared for us two series of 10mm dia. cylinders from two different cores of Eigenbilzen Sand:

- Eigenbilzen Mol2A core 188a (borehole drilled November 2014), 295.00 - 295.52m (94 cm); green-grey very fine clayey sand (Eigenbilzen Sands (SCK CEN)) – cores are parallel to bedding

- Eigenbilzen Mol2A core 189 - cores are perpendicular to the bedding.

Only a very limited (on 2 samples) petrophysical analysis was done on this material due to restricted number of samples. The overall measured porosity was 37.0%, initial suction 0.24 MPa and saturation 94.4%. Further pore space analysis is available from SCK CEN and BGS.

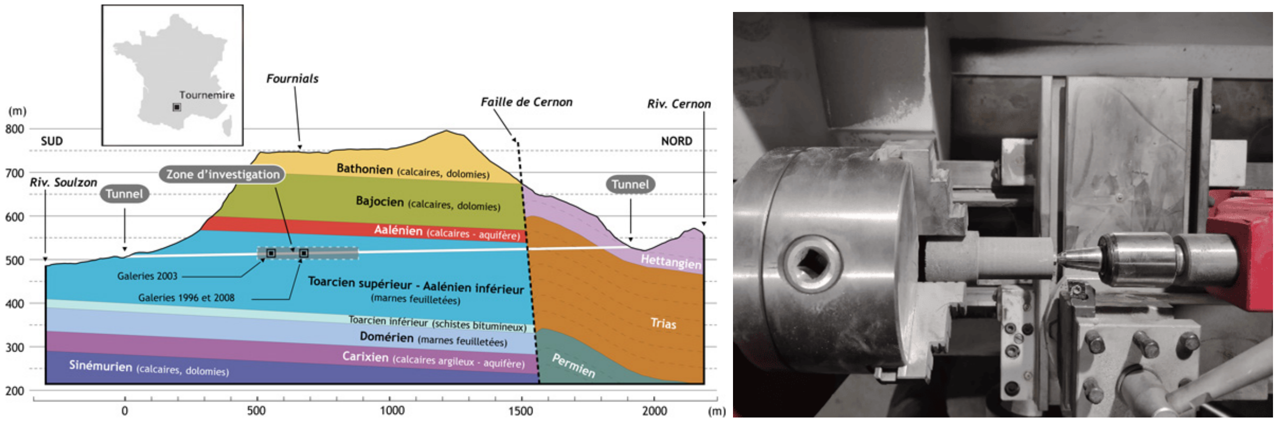

Figure 1.77: Geological repository of Toarcian argillite (a) site (b) trimming

The general porosity values of the Toarcian argillite are provided in Table 1.26 and for Eigenbilzen Sand they were assessed to be of 40±2% , Jacops et al. (2020b).

Table 1.26: Overall porosity of Toarcian argillite

Overall porosity	**Source**
6% - 9%	Hedan et al. (2012, 2014)
7.8 % -10.2 %	Matray et al. (2007)
6–8% (<10% all cases)	Boisson et al. (2001)
9.6% - 10.5%	Savoye et al. (2008)
6.5% - 7.1%	Cabrera (2001)
8.0% -10.6%	Altinier et al. (2007)

The synthetic clays provided by the British Geological Survey are composed of various proportions of clay, silt and sand. Type 1 and 8 (see Figure 1.78) to have both external contents of clay, and thus of microporosity. As the first trial material of the synthetic clay, composition 8 contains 80% clay, 10% silt and 10% sand., was assessed.

For such synthetic clay, mineralogy is distributed homogeneously and that the samples are fully saturated at initial condition; the specimens are in the form of cylinders with 1cm diameter and the height of 5-6 cm on delivery.

1.5.3.2. Specimen for SRCT scans

Synchrotron scans were planned on Toarcian and Sand of Eigenbilzen specimens, as BGS synthetic clays were not available during the scanning time slots. As a statistical interest, samples both perpendicular and parallel to the bedding at three different saturation levels are studied (Table 1.27); particular for Toarcian, perpendicular samples consists of both axial restraint and unrestraint conditions and they have been re-saturated to approach their in-situ condition (Figure 1.79). BGS synthetic clay samples were attempted on Zeiss Xradia 510 Versa 3D X-ray Tomography machine (theoretical resolution down to 0.7μm) later. Figure 1.80 shows the axial restraint condition using a bespoke 3D printed container, and Figure 1.81 shows the three different materials under the restraint condition.

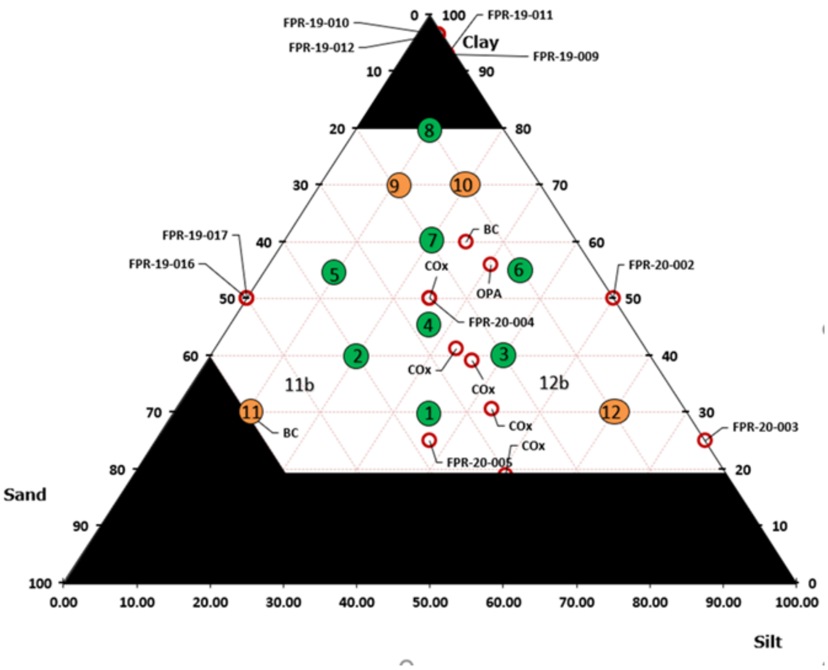

Figure 1.78: Ternary diagram for BGS synthetic clays

Table 1.27: Host rocks specimens prepared for scanning.

Theoretical suction	Sand of Eigenbilzen (//)	Sand of Eigenbilzen (⊥)	Toarcian argillite (//)	Toarcian argillite (⊥)
3.3 MPa	Unrestraint	Axial restraint	Unrestraint	Axial restraint (resat) Unrestraint (resat)
9 MPa	Unrestraint	Axial restraint	Unrestraint	Axial restraint (resat) Unrestraint (resat)
21.8 MPa	Unrestraint	Axial restraint	Unrestraint	Axial restraint (resat) Unrestraint (resat)

Note: data of Toarcian argillite samples which are // to bedding are yet to be processed, thus their results are not provided in this report.

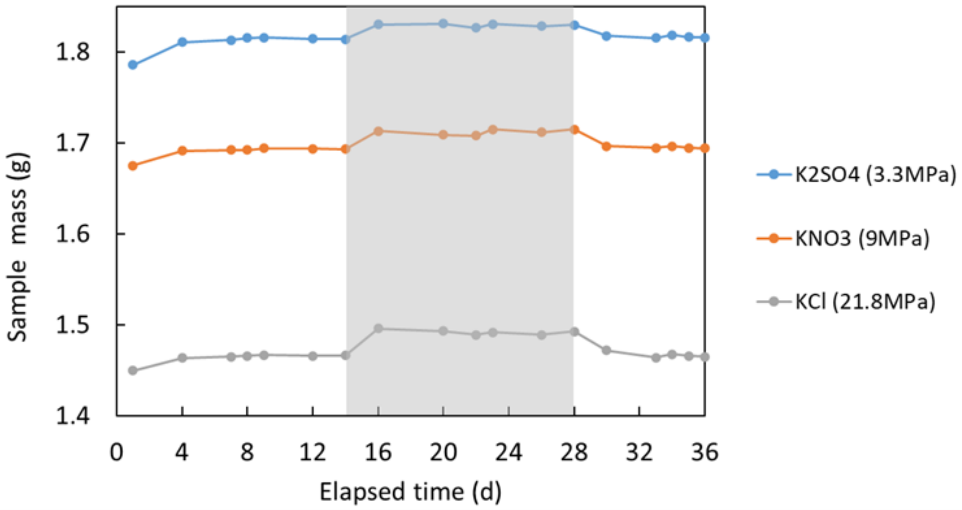

Figure 1.79: Example of regular mass monitoring for Toarcian (shaded regions represents the re-saturation step)

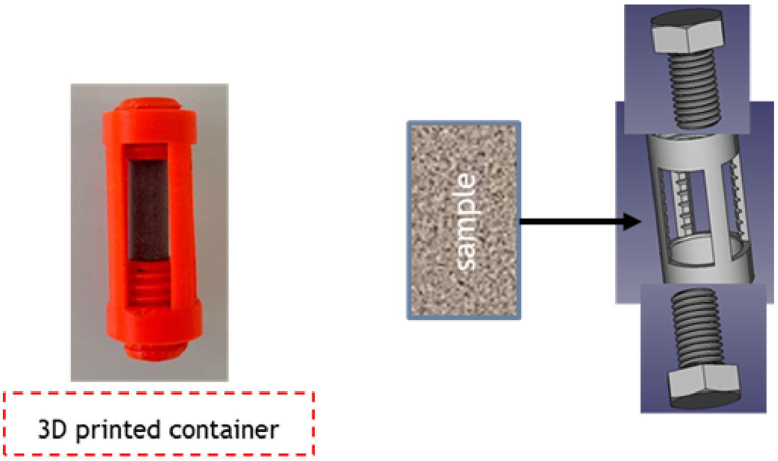

Figure 1.80: Specimen conditioning in axially constrained cells

1.5.3.3. Petrophysical analysis of Toarcien

Toarcian argillite is not very well characterized due to its variability over the Tournemine URL. Thus we started by making a series of petrophysical analysis. Several small argillite Toarcian samples of 6-10 mm diameter and 20-35 mm length were prepared from freshly drilled cores perpendicular to the bedding, Figure 1.77(b). They were transferred to the laboratory and some initial tests were done using the basis of each sample to obtain their porosity and dry density. In the first series of small cores excavated from the depth of -3.5m to -4.5m under the level of URL, we obtained a correlation between the depth and the petrophysical parameters as can be seen in Figure 1.82.

After a short quest we have realized that we probably met a dolomitic-rich layer with a significant drop in porosity, which is known from neighbouring locations at depths from 3 and 4 meters, but which has a dip of 5-10° towards the direction N173°. Therefore, we have performed another vertical drilling with cores taken much closer the URL level (-70 cm to -210 cm). This time the petrophysical parameters obtained were homogeneous within in the sampling zone, see Figure 1.83. The mean porosity calculated for this location was of 11.3±0.4% and the initial state corresponding to the 45.9±2.4MPa of suction and saturation of 72.7±5%.

Petrophysical analysis for Toarcian was conducted following the protocol from Figure 1.84. A number of

Figure 1.81: Specimens of the three clays in containment cells

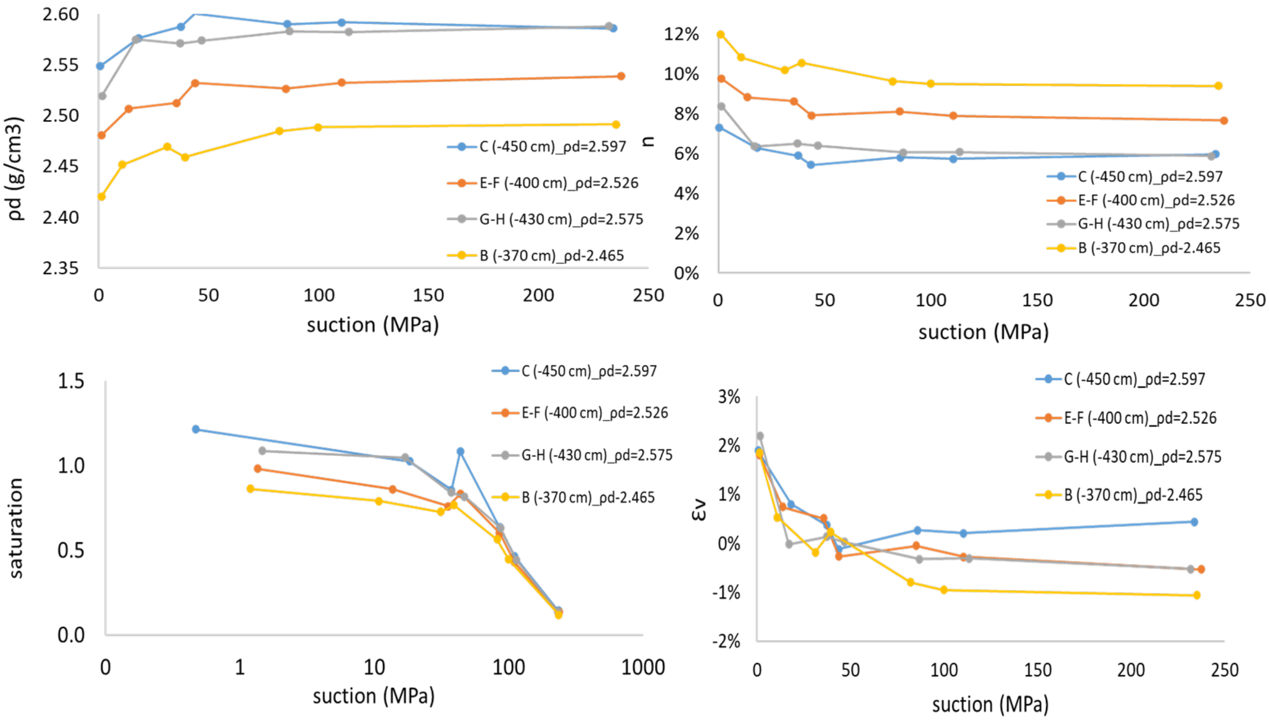

Figure 1.82: Petrophysical analysis of first series of Toarcian samples excavated from -370 to -450cm

small samples was put in desiccators with different RH conditions after the initial condition was determined (Figure 1.85) and mass was checked regularly until stabilised (Figure 1.86).

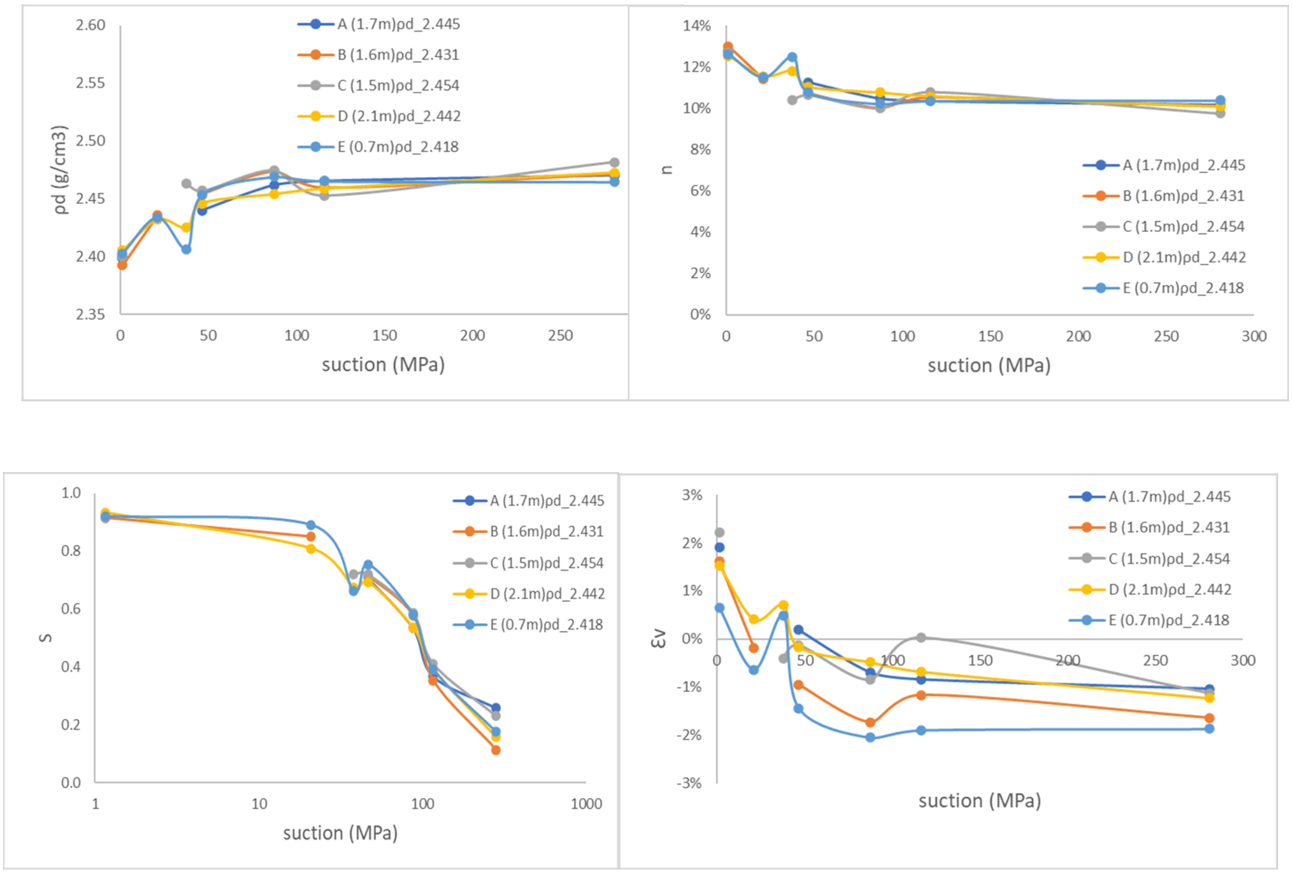

Figure 1.83: Petrophysical analysis of the second s of Toarcian samples excavated from -70 to -210cm.

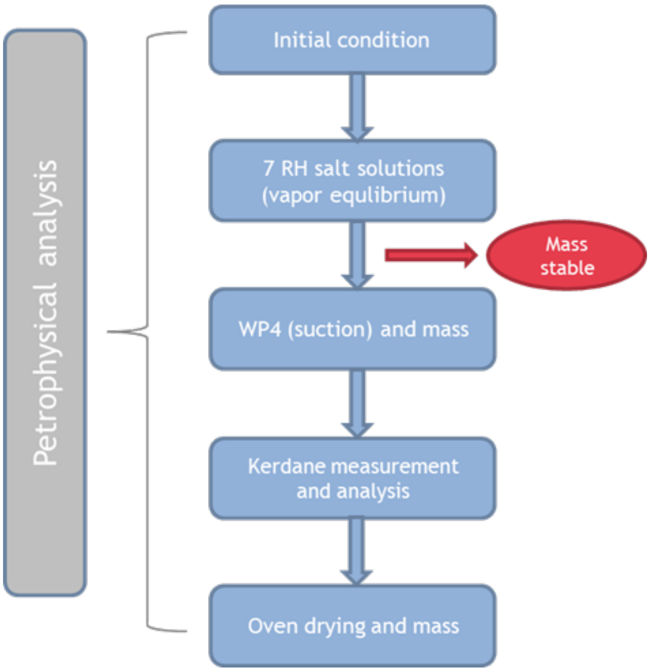

Figure 1.84: Protocol for petrophysical analysis of argillite samples

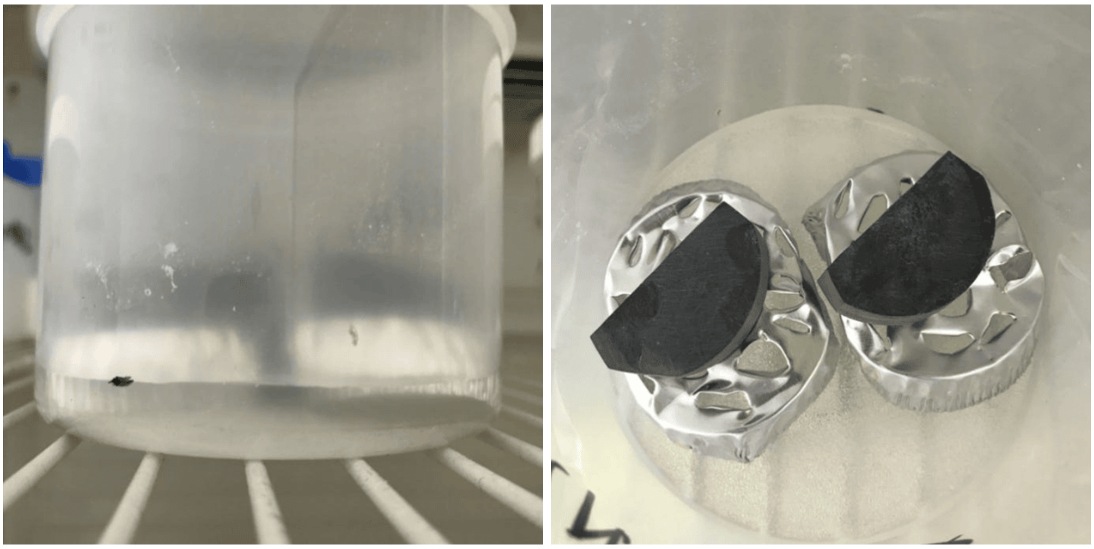

Figure 1.85: Sample conditioning in desiccator under prescribed RH (aiming at defined saturation level)

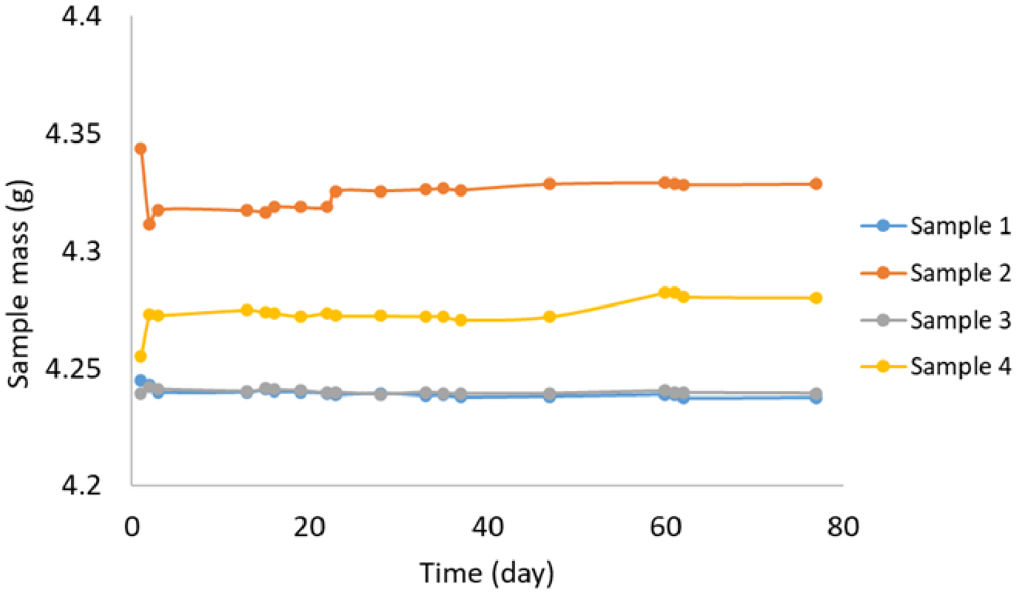

Figure 1.86: Follow-up of mass changes during RH conditioning at saturated vapour conditions

The characteristics of the Toarcian argillite are presented in Figure 1.87; all the properties show a sensible correlation against the imposed suction (saturation level), that the sample tended to become denser, drier and shrink. The properties at the initial condition were also determined (quantitatively in Table 1.28) and graphically presented together with the data for various saturated samples. Accordingly, soil water retention characteristics curve (SWCC, Figure 1.88) was also determined, which was presented together with the data from previous researchers which confirm the experimental results to be reliable.

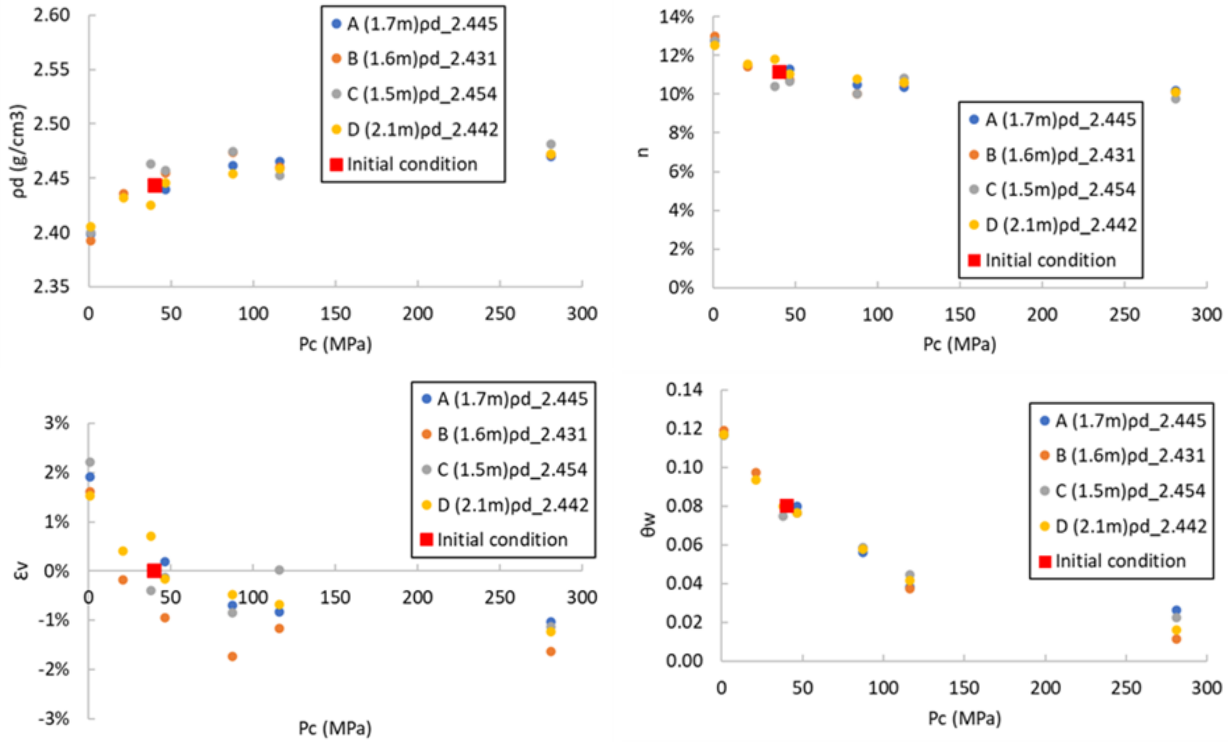

Figure 1.87: Characteristics of Toarcian: dry density (ρd), porosity (n), volumetric strain (εv), volumetric water content (Θw)

Table 1.28: Initial condition of Toarcian argillite

Suction (MPa)	θw	n	S	ρd
40	8.1% 7.7%	10.9% 10.6%	74.8% 72.5%	2.451 2.459

Although the characteristics were not conducted for Sand of Eigenbilzen, its initial condition was determined via two samples, as presented in Table 1.29.

Table 1.29: Initial condition of Eigenbilzen Sand

Suction (MPa)	θw	n	S	ρd
0.24	35.1% 34.8%	37.2% 36.8%	94.4% 94.5%	1.677 1.687

The properties of the BGS synthetic clays of composition 8, see Figure 1.28, were characterised, with its initial condition presented in Table 1.30 and characteristics at various saturation/suction levels graphically presented in Figure 1.89. Likewise, all the properties show a sensible correlation against the imposed

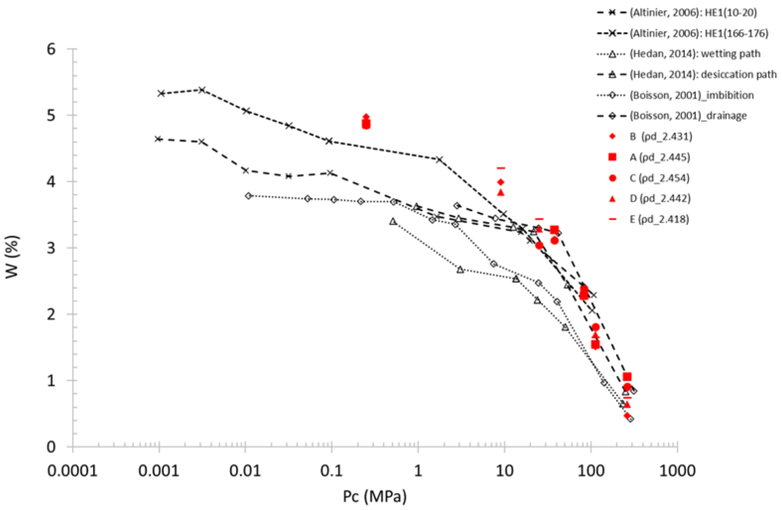

Figure 1.88: Measured suction curve for Toarcian as compared to literature data

suction (saturation level), that the sample tended to become denser, drier and shrink. SWRC was also determined (Figure 1.90).

Table 1.30: Initial conditions of BGS synthetic clay

Suction (MPa)	θw	n	S	ρd
	40.7%	45.9%	88.5%	1.384
2.4 - 3 MPa	38.9%	45.9%	84.6%	1.384
	38.4%	46.3%	83.0%	1.375

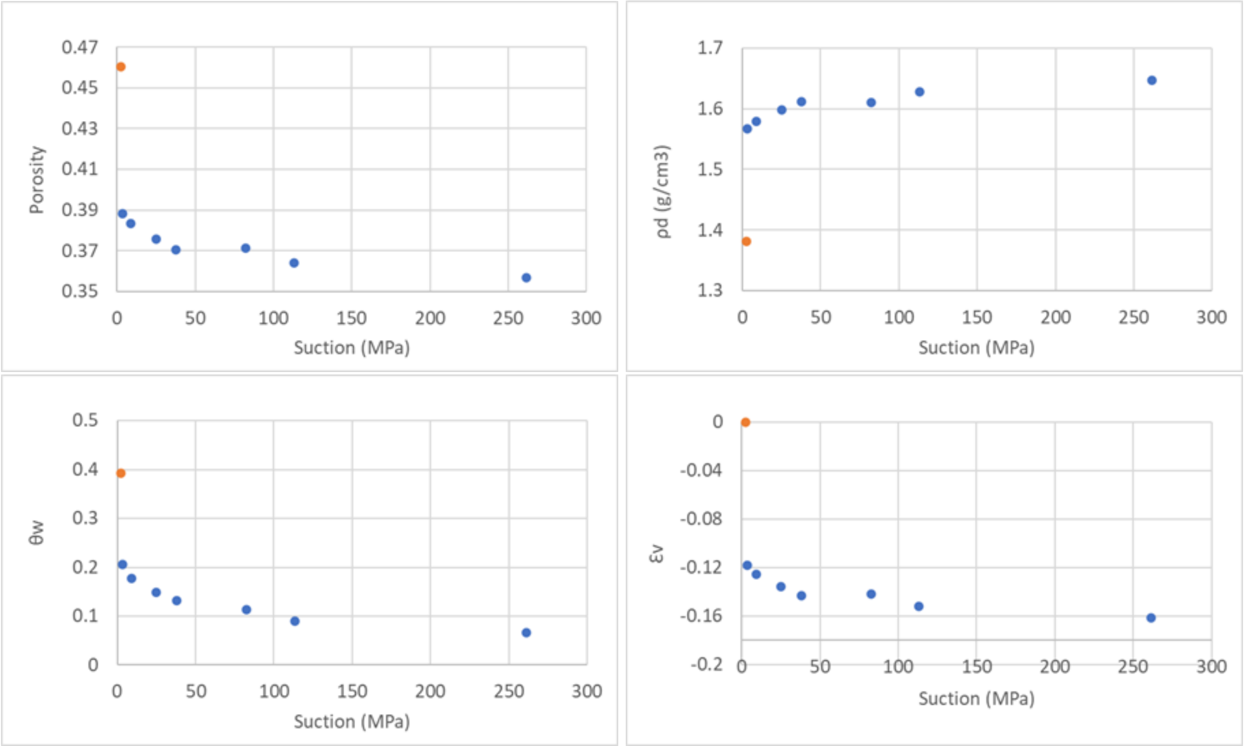

Figure 1.89: Properties of BGS synthetic clay: porosity, dry density, volumetric water content, volumetric strain

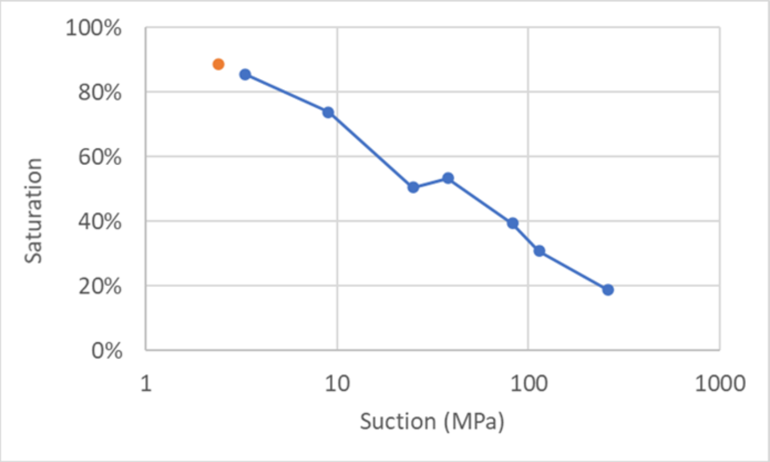

Figure 1.90: SWRC of BGS synthetic clay

1.5.4. Testing protocol

For each material of interest (Toarcian, Sand of Eigenbilzen and synthetic) small cylindrical samples with 6-10 mm dia. were manufactured and equilibrated at different RHs, see Table 1.30, via vapour equilibrium approach at constant temperature (20℃). For half of samples perpendicular to the bedding, axial swelling was restrained by using a 3D sample holder (Figure 1.80), the other half as well as samples parallel to bedding were conditioned unrestricted. Their mass change was followed daily. Usually 7-10 days were needed to stabilize the sample mass, see Figure 1.91. For transport, the samples were placed in vapour tight acrylic/plastic (3D printed) cylindrical containers.

Table 1.31: Saturated salt solutions used for vapour equilibration of clay samples

salt solution (20 ℃)	KCl	KNO_3	K_2SO_4	Distilled Water
RH	84%	95%	98%	100%
Suction [MPa]	23.4	8	3.2	0

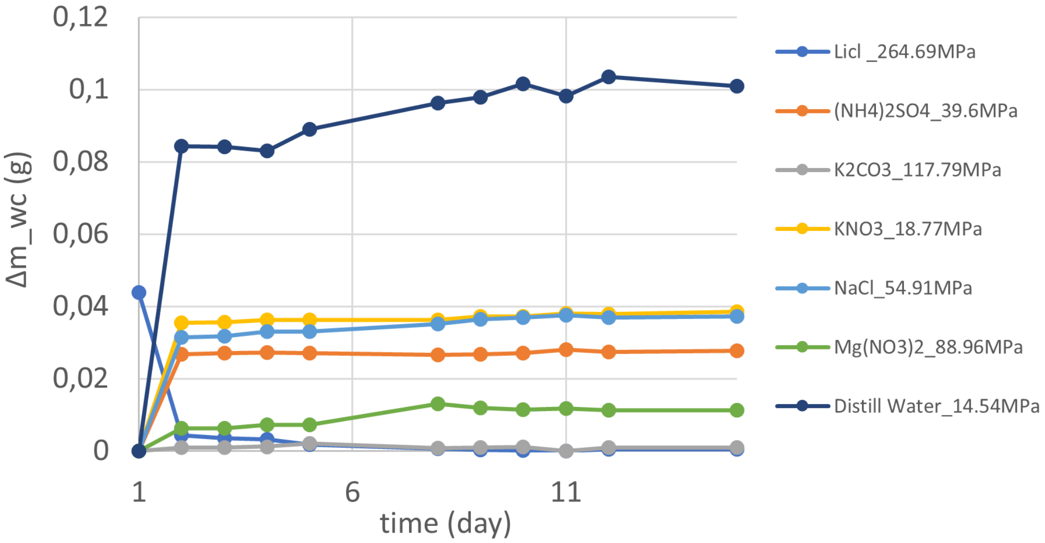

Figure 1.91: An example of vapour equilibration of Toarcian samples.

1.5.5. Results

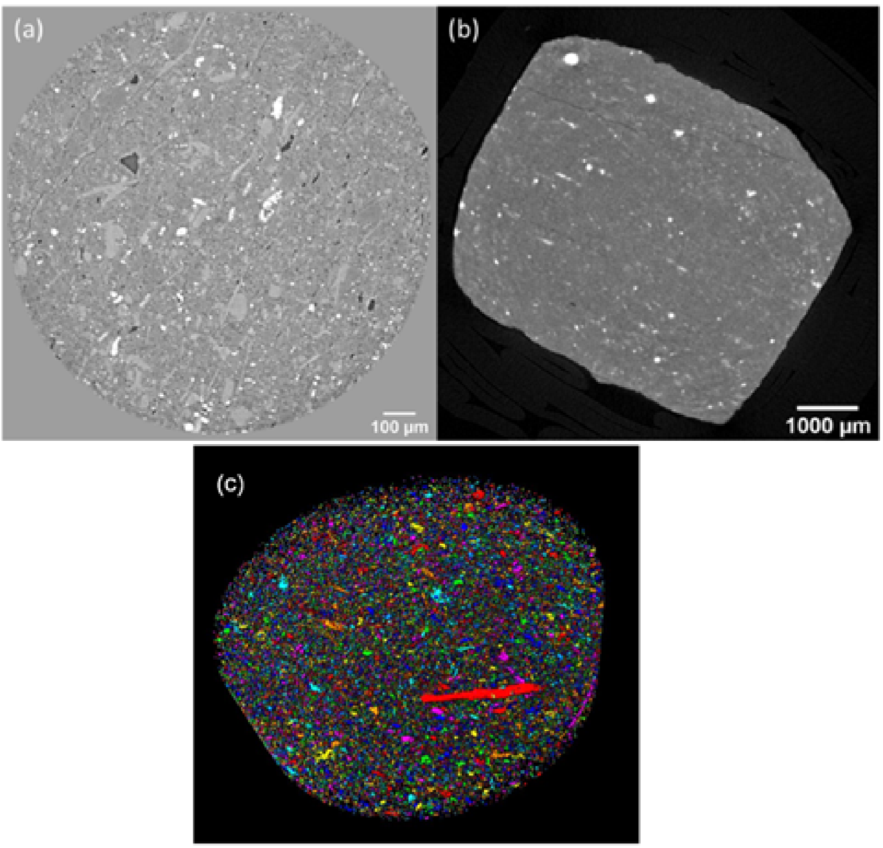

Figure 1.92: Example images of a dry Toarcian argilite; scanned from (a) Soleil Anatomix (b) in-lab Skyscan1173; segmented pores in 3D volume from Soleil Anatomix (c)

To assess the possibility of conducting our study in the laboratory CTscan (Skycan1173) we made some test scans on Toarcian samples and compared them with these acquired by courtesy of Synchrotron Soleil staff at Anatomix line; see Figure 1.92.

See Table 1.32 for scan settings in both cases. As expected, the scans from lab CT facility resulted in image quality limited in both spatial resolution for resolving smaller pores and contrast between gas/water phases. Synchrotron CT facilities with a transmission X-ray target have the advantage to boost the contrast between phases (particularly with similar attenuation coefficients) via phase-contrast imaging as well as allowing a better spatial resolution.

For example, a dried Toarcian argillite rock was imaged at Soleil Synchrotron via phase-contrast imaging (see Figure 1.92), with the data quality allowing the segmentation of pores bigger than 0.7μm. However due to its uncontrolled saturation state, it was obviously not possible to conclude about the possibility to distinguish water and air the macro-pores.

Thus, we have scanned another Toarcian sample equilibrated with Mg(NO3)2 (82.4 MPa) to the saturation of 72.4%, Figure 1.93. We were able to detect a porosity of 2.4% (26% of the poral volume equal to 9% - this was a sample from our first series). This value should be compared to 0.4% porosity obtained in lab CT. It means that the 27.6% of pore volume was filled with air. It can be observed that the sample presented macroscopic desiccation cracks, which probably facilitated uniform desaturation and thus also in this case we were unable to directly observe gas and water filled pores. It is clear from this example that we need to restrict our work to still higher saturations and RH.

Table 1.32: Properties and settings of scans in facilities used for this study

	SkyScanner1173 (John)	Synchrotron Soleil, Anatomix line
Scan settings	85keV, 82 μA	40 keV, 500 mA 2000 projections parallel beam
Pixel size	7.2 μm	0.65 µm detector size: 2k x 2k (offset: 4k x 4k available)
Duration	duration 3h12m	10 minutes
Sample diameter	7mm	up to 10 mm

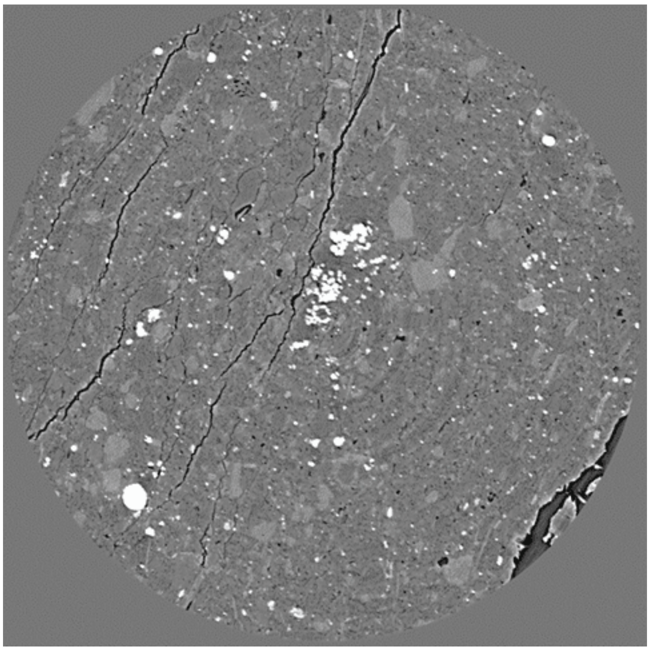

Figure 1.93: Partially saturated Toarcian sample imaged in Synchrotron Soleil

On the basis of the trial scans in Synchrotron Soleil we have requested beamtime on Anatomix line to be able to test more systematically several samples equilibrated at different RH, including Toarcian and Sand of Eigenbilzen. The project was granted a slot on April 12-15, 2022. We were able to register more than 100 sub-volume scans on 15 Toarcian and 12 Sand of Eigenbilzen samples. For each sample we have scanned three locations starting from the centre of the sample and going radially towards the lateral surface (voxel size of 0.65 µm and FOV of 1.3 mm^3).

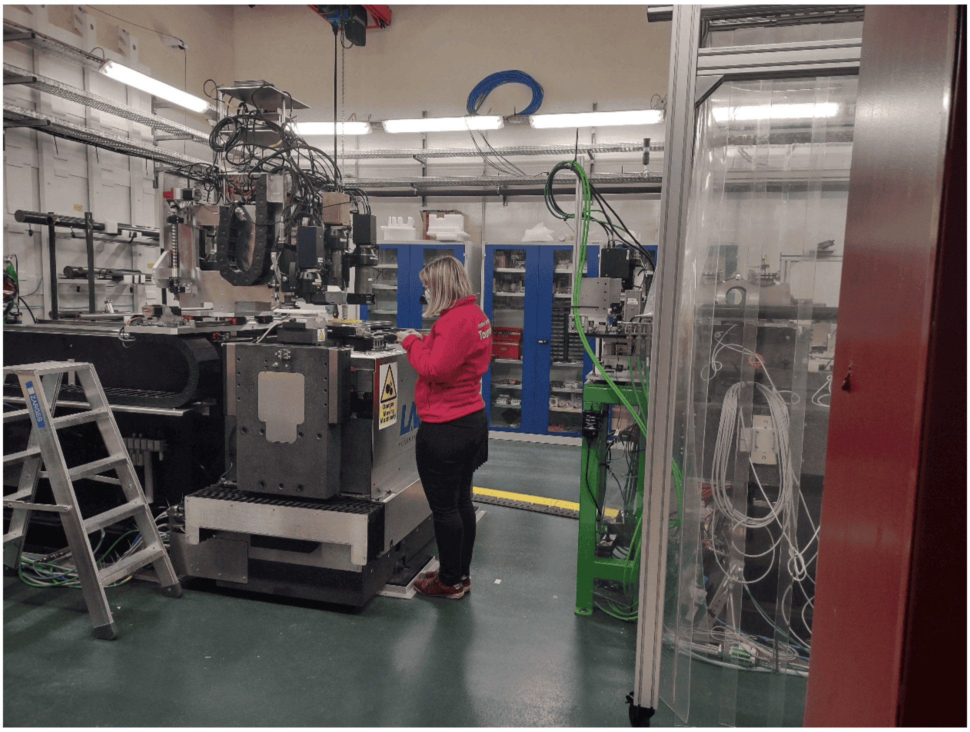

Figure 1.94: Installing a sample in the scanning hutch of Anatomix line of Synchrotron Soleil

1.5.5.1. Synchrotron µCT imaging

1.5.5.2. SRCT facility and sampling

Following the approved beamtime allocated from SOLEIL Synchrotron Centre, Toarcian and Sand of Eigenbilzen samples were prepared and scanned using the ANATMOIX beamline, which could provide good imaging data at a pixel resolution of 0.65 µm for the target clay materials.

Given the fact that the specimens have a dimension of 10mm in diameter, the white beam micro-tomography mode on ANATOMIX beamline was decided to be used. The setups of the facility and the specimen are presented in Figure 1.95.

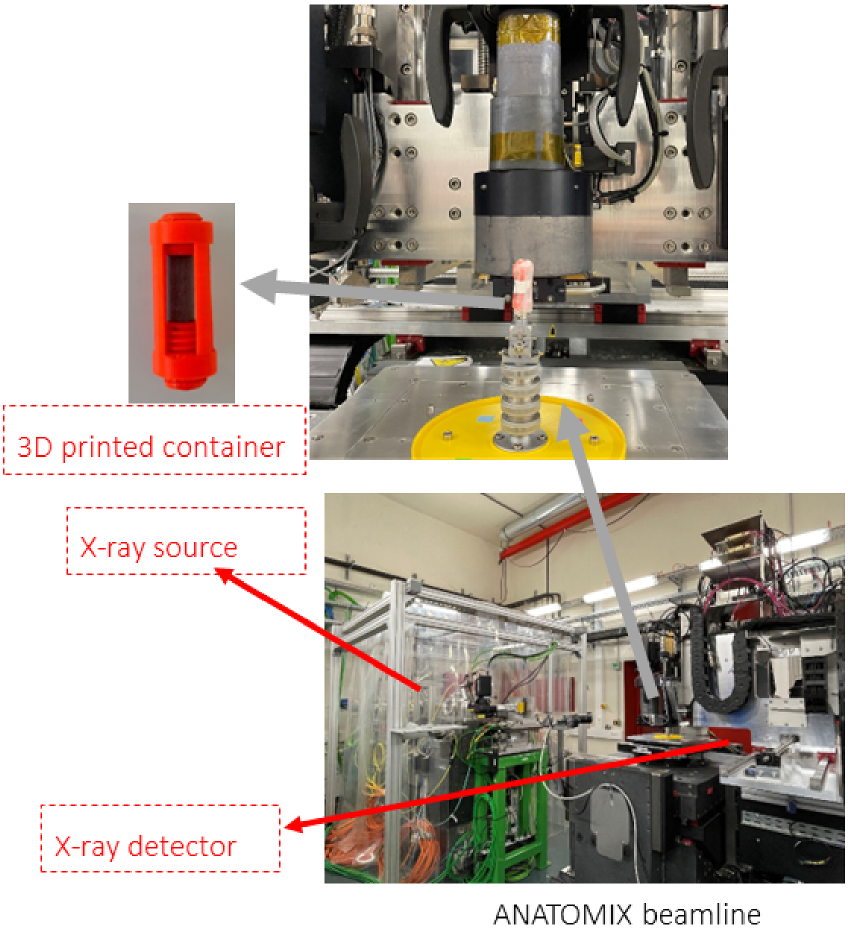

Figure 1.95: Synchrotron Soleil, Anatomix line: facility and setups

The scan settings are illustrated as follows:

1. The effective white beam X-ray energy was about 40 keV; 2000 projections; the storage ring current was 500 mA; pixel size is 0.65 µm.
2. Full scan rotation is 180 degrees.
3. The first scan was done in the center of the sample and the following moved them in 1 mm steps outwards. The field of view is 1.3 mm x 1.3 mm x 1.3 mm.

1.5.5.3. Data pre- and post-processing

1.5.5.4. Scan protocol and region of interest (ROI)

Three scans were operated for each specimen, following a spatial arrangement in radial direction. Schematics are presented in Figure 1.97. A rectangular ROI (Figure 1.98) was selected for the subsequent image processing and analysis.

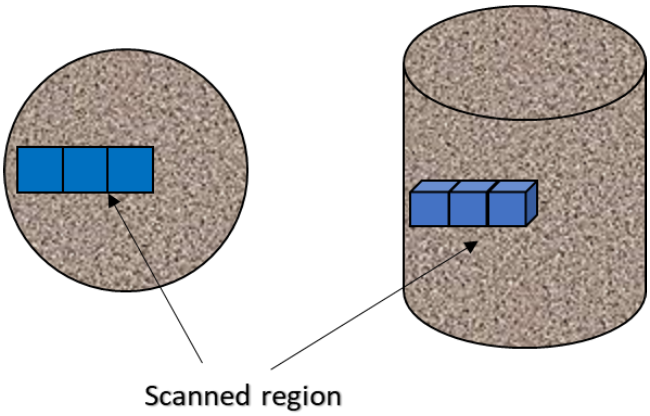

Figure 1.96: Schema of scan regions for SRCT imaging

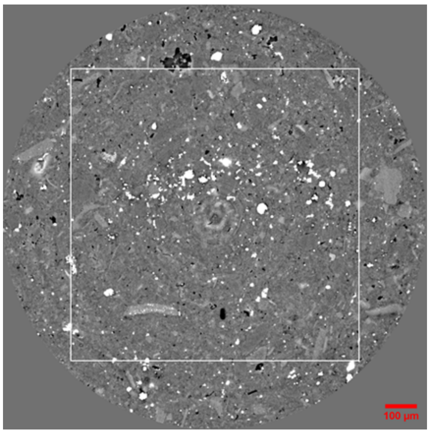

Figure 1.97: ROI for image analysis

1.5.5.5. Image acquisition, reconstruction, and segmentation

After the image acquisition, reconstruction for 3D volume data was carried out. Seeing the advantage of the propagation phase-contrast imaging at SRCT beamline, Paganin filter was applied, with a kernel of 25 pixels, to reduce the overshooting at the material phase edges and increase the spacing between phases. This allows an easier segmentation since the phase edges are less enhanced. An example for the reconstructed image before and after applying the Paganin filter was presented in Figure 1.99. The GV profiles of a straight line across various materials show the enhanced contrast by Paganin filter.

Image segmentation is usually achieved by two approaches; one is the standard thresholding method based on greyscale, and the other is the machine learning method which takes into account both the greyscale and object features. After evaluating the data quality, Trainable Weka Segmentation (TWS) was adopted, although this would significantly occupy the computational resource and the associated increased time on data processing.

The training features that were adopted in the phase classification process of TWS are Hessian, Structure, Variance, Mean.

The 32-bit raw data were first consistently converted to 8-bit type to spare time of data processing. A

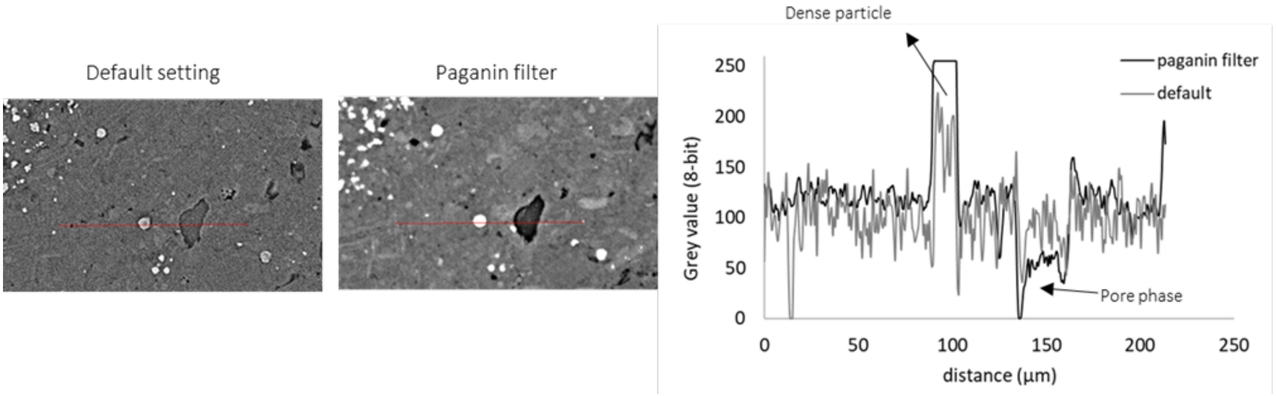

Figure 1.98: Example of the image with and without applying Paganin filter

small image stack was used for the creation of the classifiers for different materials/phases. A number of small regions from different locations of the scan data were drawn and classified to each corresponding material. For the data of host rock candidate, pore phase and solid material were the target, as a fact that the water/air interface cannot be differentiated at the currently scan resolution.

Then, the classifier was trained and the quality of the segmentation was checked until satisfactory results were obtained. An example showing the data processed from the TWS segmentation is given in Figure 1.100. The segmented pore phase would be binarized (examples in Figure 1.101), for the subsequent pore related analysis.

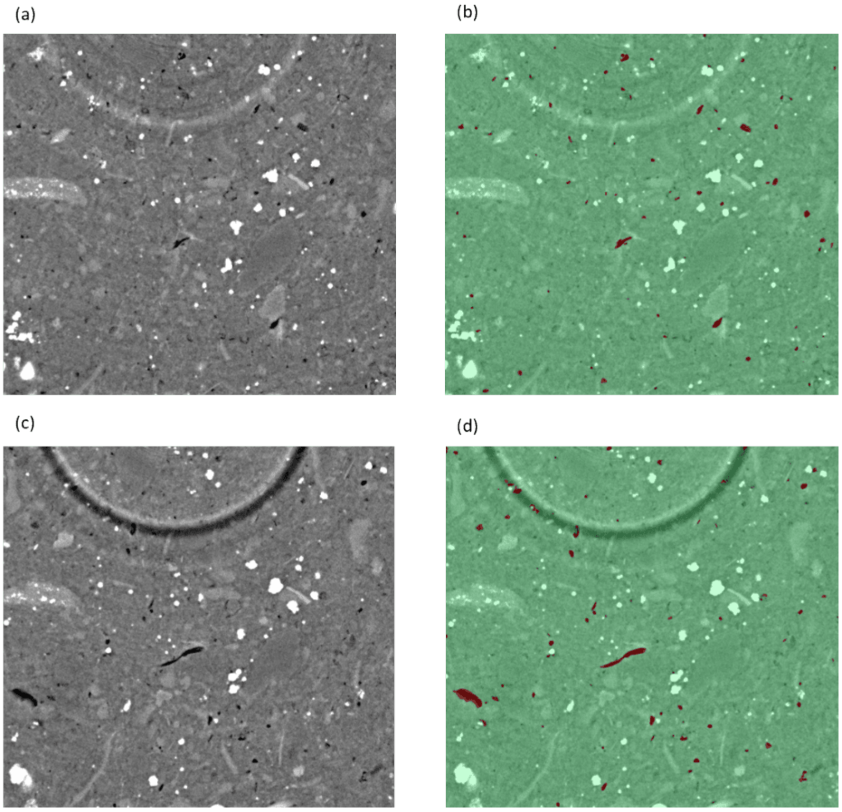

Figure 1.99: Example of image segmentation by TWS; (a) original image with only isolated pores, (b) segmented image with only isolated pores, (c) original image with pores and ring artefact, (d) segmented image with pores and ring artefact

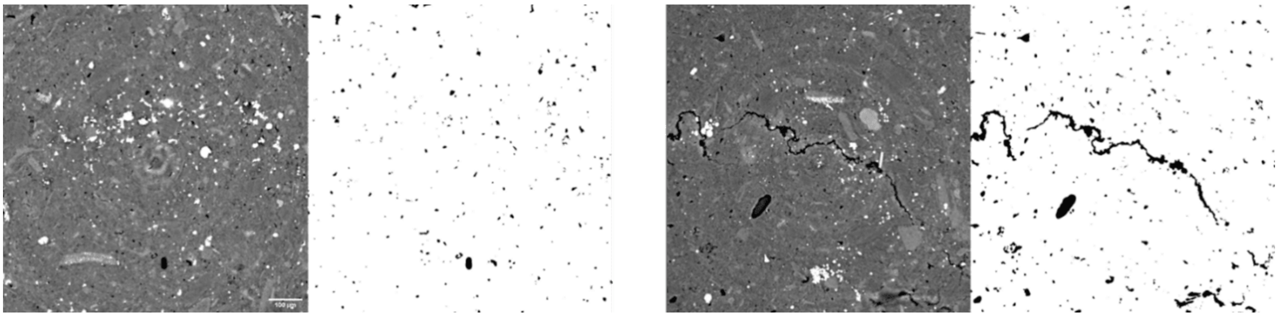

Figure 1.100: Two examples of original images and their binarized pore phase from a specimen with a suction of 3.3MPa; only pores (left) and pores and cracks (right).

1.5.5.6. Analysis and results of Toarcian argillite

Table 1.33: Porosity under SRCT analysis

Toarcian argillite samples	Axial restraint	Unrestraint	From characterisation
K_2SO_4 (4 MPa)	1.74%	1.75%	11% (initial conditions, 45MPa)
KNO_3 (9 MPa)	1.13%	1.73%	10% (LiCl, 261MPa)- lower bound
KCl (21 MPa)	1.13%	1.74%	12.7% (Distill water)-upper bound

For the SRCT data of Toarcian argillite, the pore related results, i.e., porosity and pore size distribution were determined. The average porosity, without distinction of filling fluid, for the specimens at different saturation levels was determined, as given in Table 1.33 and also plotted in Figure 1.102 for comparisons against the spatial distance. A comparison of mean porosity between restraint and unresistant specimen was also produced (Figure 1.103).

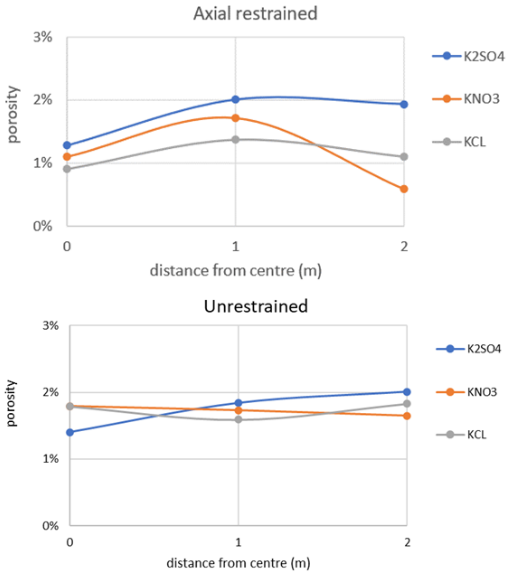

Figure 1.101: Porosity against radial distance for Toarcian ⊥ specimens equilibrated at different RH; IC stands for Initial Conditions

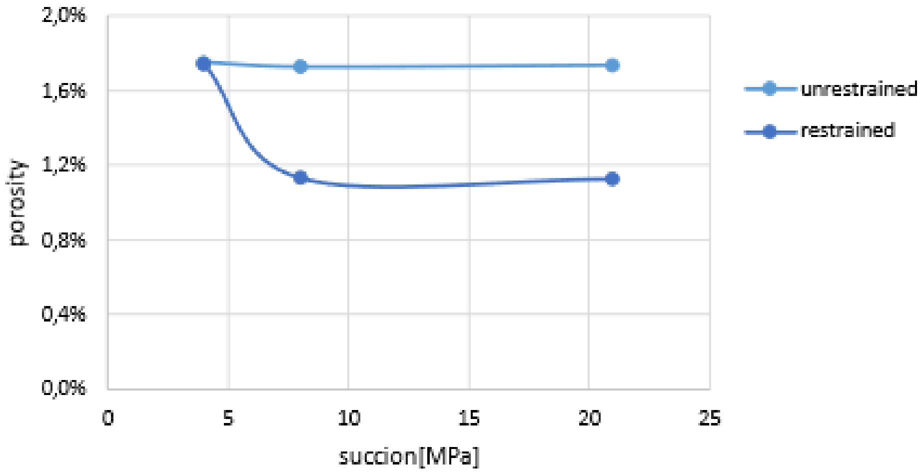

Figure 1.102: Comparison between restraint and unrestrainet mean porosity in Toarcian ⊥ specimens

The results show that global porosity is 11-12 % as obtained from the characterization, this means the CT determined porosity for the pore with the size over 0.65 µm is about 10 % of the total porosity, close/lower than the S_{air} (air saturation of these samples). A correlation between RH (saturation) with porosity can be obtained, which indicates the swelling potential of the material. The more porous condition has been proved in unrestrained samples. On the other hand, the results indicate a correlation between porosity and radial distance, more obviously shown from the data of the unrestrained samples.

Importantly, the results (e.g. Figure 1.104(top)), also infer, although may not be significantly, a uniform drying in radial direction (with RHs), but this could be further verified. And cracks can be indicated from the results of porosity distribution where the overall porosity was derived (e.g. the sudden jump in Figure 1.104(bottom)). However, if the zones with string increase of porosity are eliminated, the overall behaviour doesn't change significantly, even though the mean porosity becomes lower, see.

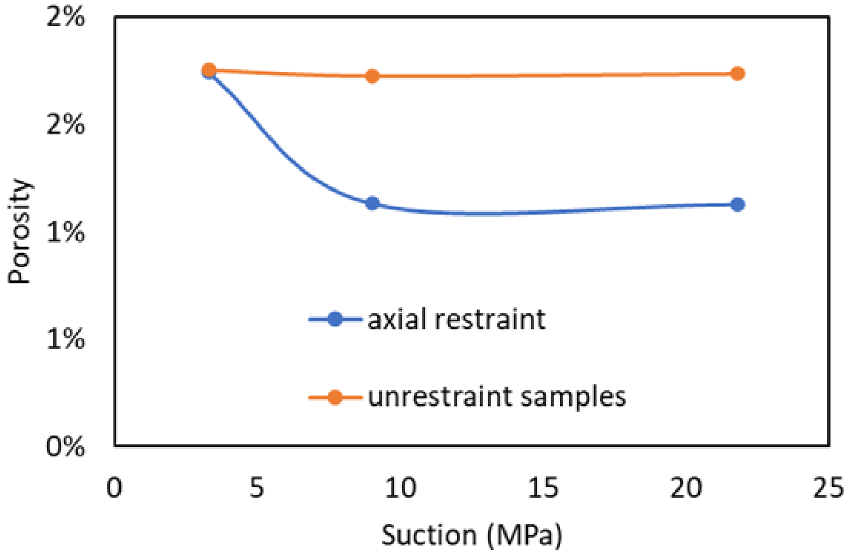

Figure 1.103: Porosity profiles and the associated mean porosity against radial distance in (top) restraint (bottom) unrestrained samples.

Analysis was also carried out for the pore size distribution of the segmented pore phase in each specimen. This is achieved from Avizo using the label analysis function (e.g. Figure 1.105), in 3D spatial domain.

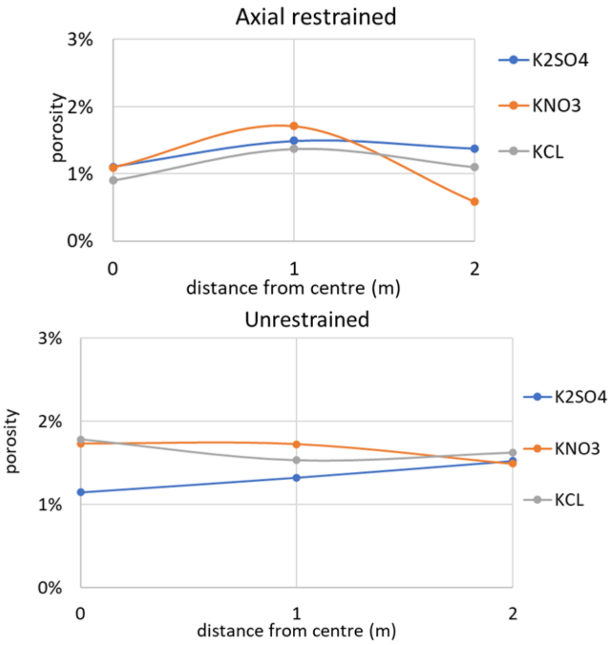

Figure 1.104: Mean porosity when "crack" zones are excluded, to be compared with Figure 1.103

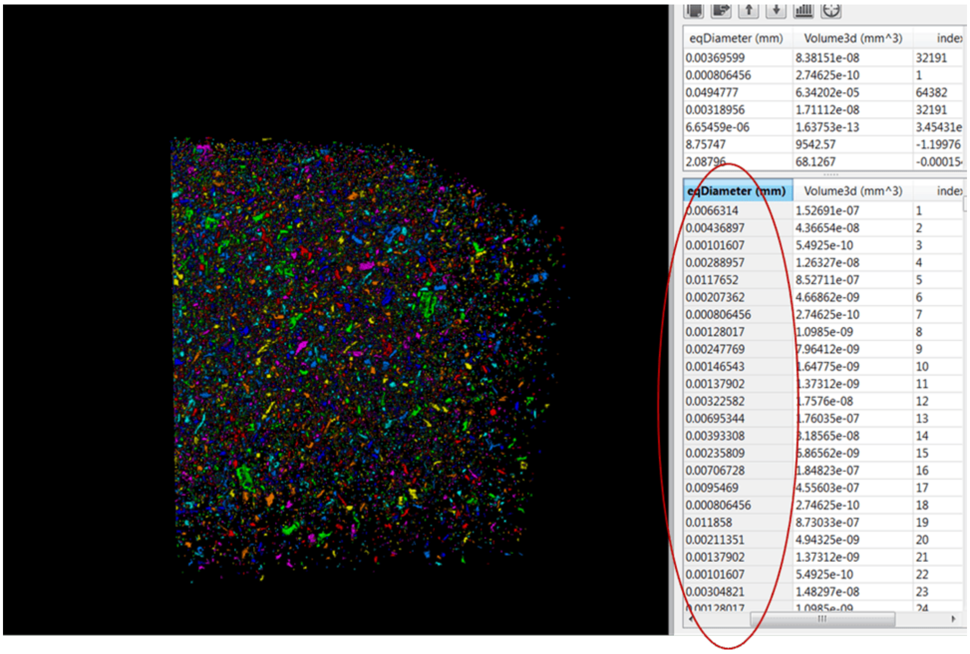

eqDiameter (mm)	Volume3d (mm^3)	inde
0.00369599	8.38151e-08	32191
0.000806456	2.74625e-10	1
0.0494777	6.34202e-05	64382
0.00318956	1.71112e-08	32191
6.65459e-06	1.63753e-13	3.45431e
8.75747	9542.57	-1.19976
2.08796	68.1267	-0.00015

eqDiameter (mm)	Volume3d (mm^3)	inde
0.0066314	1.52691e-07	1
0.00436897	4.36654e-08	2
0.00101607	5.4925e-10	3
0.00288957	1.26327e-08	4
0.0117652	8.52711e-07	5
0.00207362	4.66862e-09	6
0.000806456	2.74625e-10	7
0.00128017	1.0985e-09	8
0.00247769	7.96412e-09	9
0.00146543	1.64775e-09	10
0.00137902	1.37312e-09	11
0.00322582	1.7576e-08	12
0.00695344	1.76035e-07	13
0.00393308	3.18565e-08	14
0.00235809	5.86562e-09	15
0.00706728	1.84823e-07	16
0.0095469	4.55603e-07	17
0.000806456	2.74625e-10	18
0.011858	8.73033e-07	19
0.00211351	4.94325e-09	20
0.00137902	1.37312e-09	21
0.00101607	5.4925e-10	22
0.00304821	1.48297e-08	23
0.00128017	1.0985e-09	24

Figure 1.105: Schematics of label analysis for PSD

The PSD results are presented in the way of histogram graphs for statistical purpose (Figure 1.106, Figure 1.107 and Figure 1.108). Two main conclusions can be drawn from here:

- The pore with the smallest size played a dominant role
- There is a general trend that the scanned region near the sample border possessed a more porous condition.

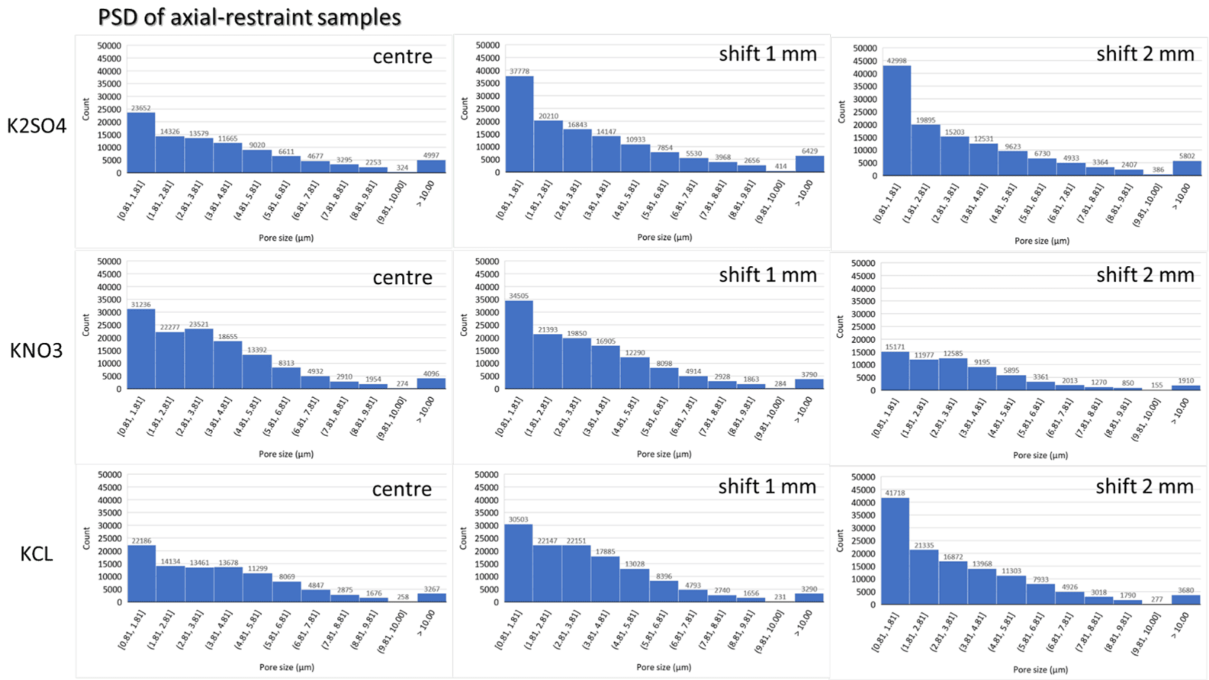

Figure 1.106: PSD of restraint samples

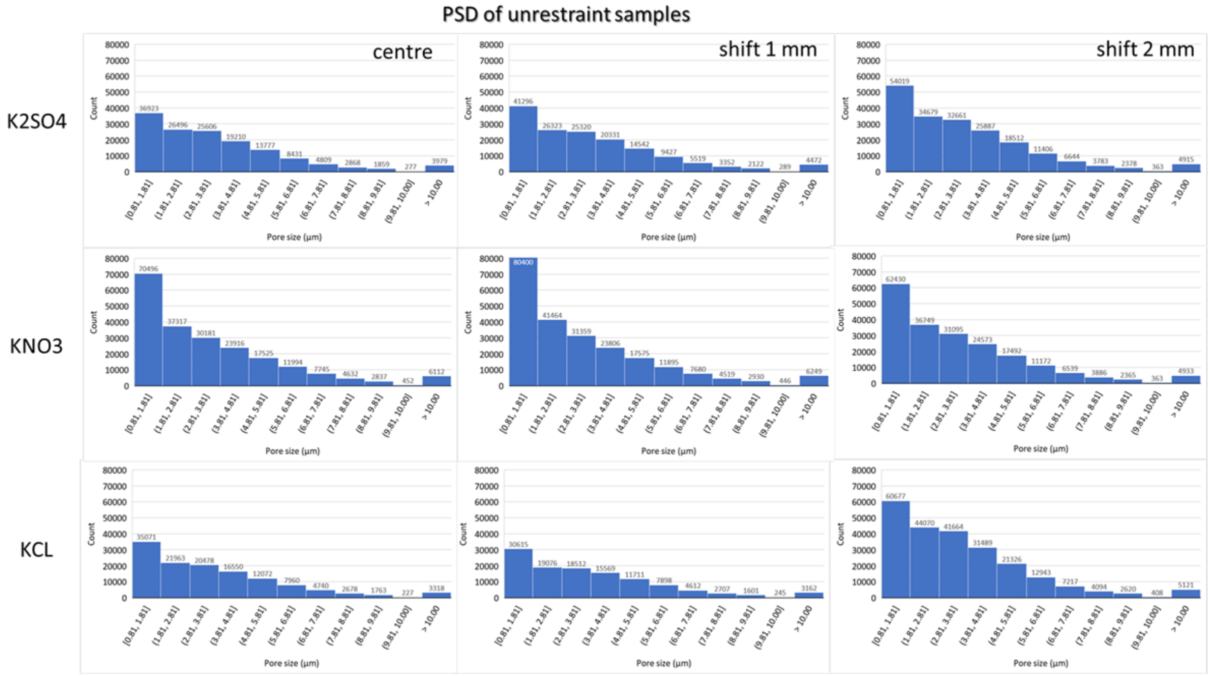

Figure 1.107: PSD of unrestraint samples

1.5.5.7. Discussion on Toarcian results

The above results do not explicitly show the aspect on water-air distribution, as no obvious water phase has been detected. The following analysis based on Laplace law was conducted (Figure 1.109).

So in order to be able to see pore water from the current adopted CT imaging technique (indicating the homogeneous drying condition), the suction has to be not greater than 0.448 MPa.

The pore size (d) & saturation (Se) indicate that:

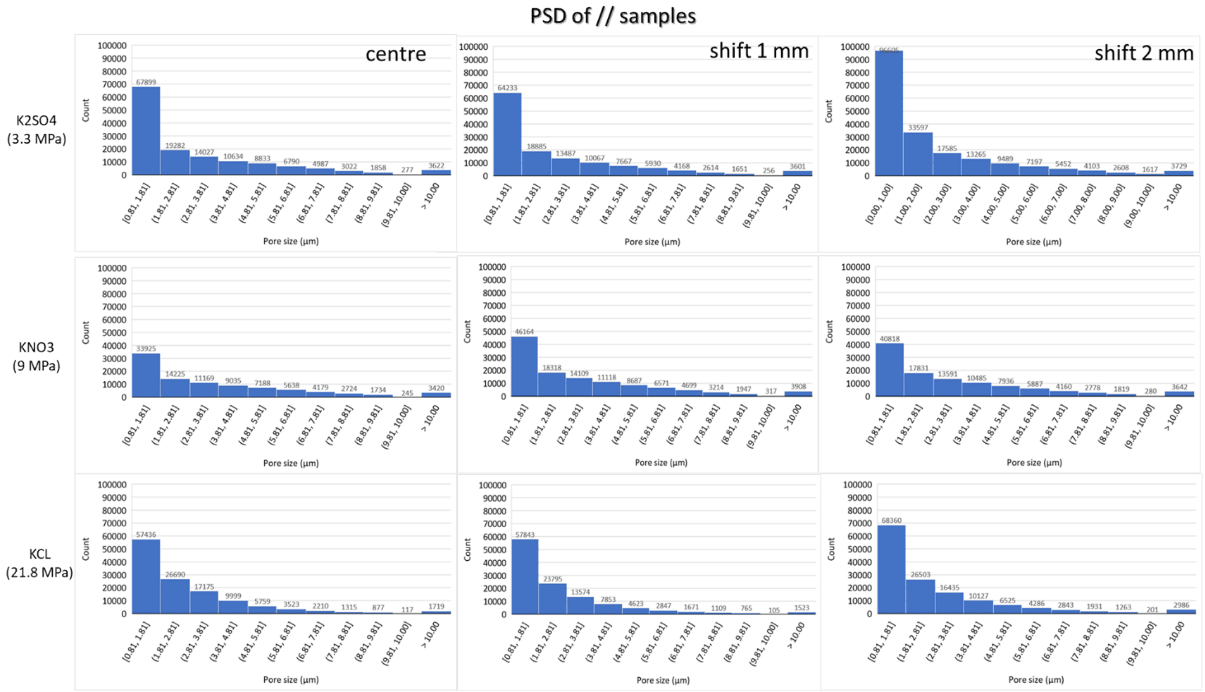

Figure 1.108: PSD of samples parallel to bedding

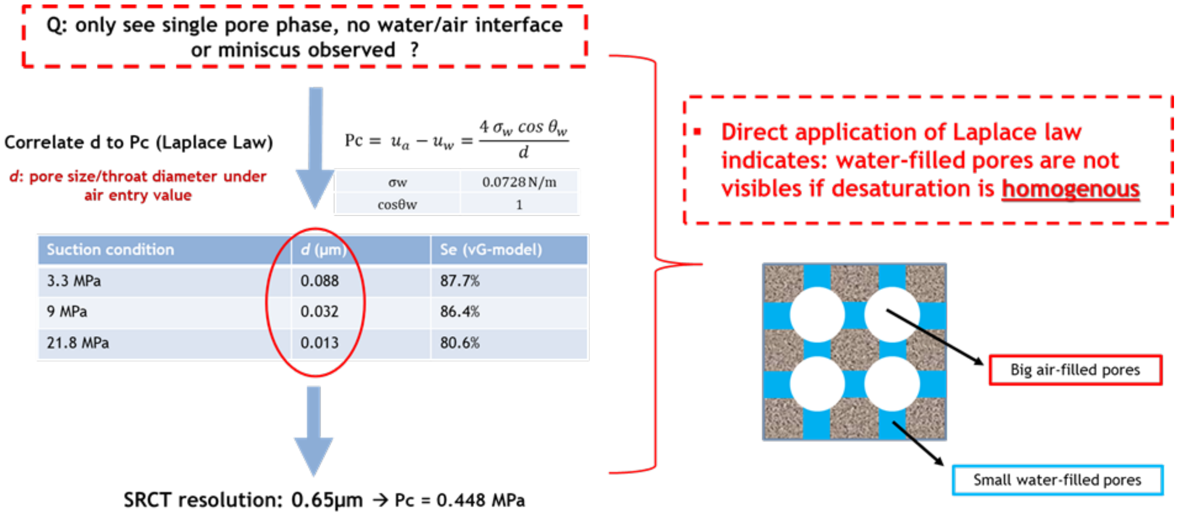

Q: only see single pore phase, no water/air interface or miniscus observed ?

Correlate d to Pc (Laplace Law)

d: pore size/throat diameter under air entry value

$$\mathrm{Pc} = u_a - u_w = \frac{4\,\sigma_w \cos\theta_w}{d}$$

σw	0.0728 N/m
cosθw	1

Suction condition	d (µm)	Se (vG-model)
3.3 MPa	0.088	87.7%
9 MPa	0.032	86.4%
21.8 MPa	0.013	80.6%

SRCT resolution: 0.65µm → Pc = 0.448 MPa

- Direct application of Laplace law indicates: water-filled pores are not visibles if desaturation is homogenous

Figure 1.109: Verification of the drying pattern via Laplace law

- The detectable water-filled pores from the scanned samples are much smaller than the SRCT resolution
- The saturations of the samples are smaller than the value corresponding to the capillary pressure (Pc) when water-filled pores can be resolved by SRCT scans
- The results also infer that a very small portion of the pores whose size is in the detectable range (> 0.65µm)

1.5.5.8. Analysis and results of Sand of Eigenbilzen

Similar protocol was implemented for the analysis on the SRCT data of Sand of Eigenbilzen, except including an extra filtration step that a median filter of 3 pixels was applied (Figure 1.110).

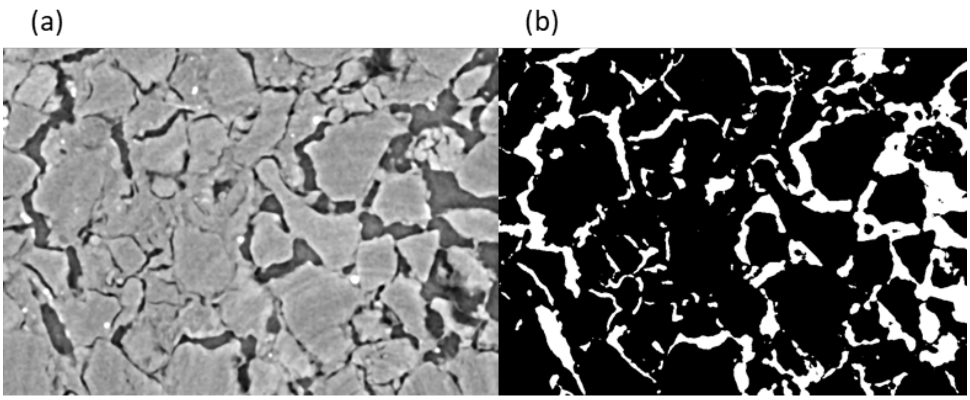

Figure 1.110: Example of Sand of Eigenbilzen data (a) original with median filter (b) segmented data

The porosity distribution results for the Sand of Eigenbilzen samples perpendicular and parallel to the bedding are presented in Figure 1.111 which generally show uniform characteristics, with no obvious cracks noticed.

Also, the current results do not explicitly show the relationship between the suction/saturation levels with the porosity, while the values are in a sensible range when compared to the literature (Table 1.26).

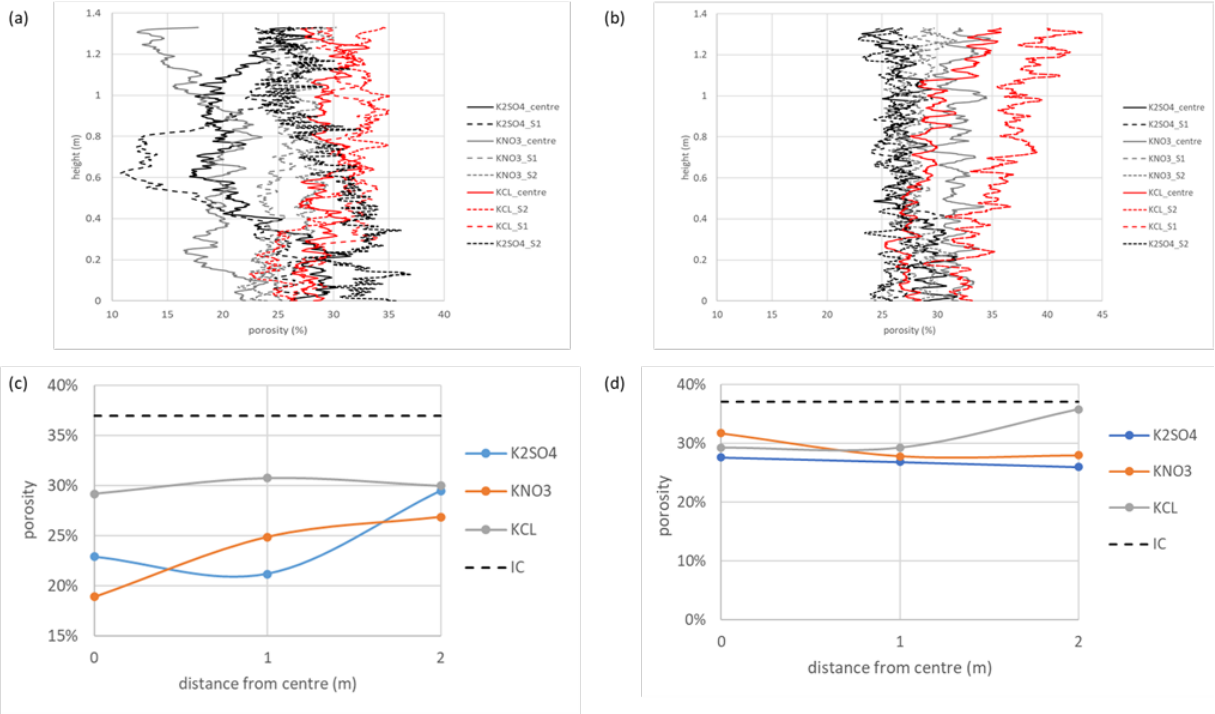

Figure 1.111: Porosity result of Sand of Eigenbilzen profile and mean values of perpendicular (left: a and c) and parallel (right: b and d)samples.

Results of the pore size distribution (PSD) were also assessed for the Sand of Eigenbilzen CT data (Figure 1.112) for samples perpendicular to bedding and Figure 1.113 for samples parallel to bedding), where a few conclusive points were drawn:

- a trend that the region of the sample near the sample border is more porous
- similar to Toarcian argillite, the smallest pore played the dominant role

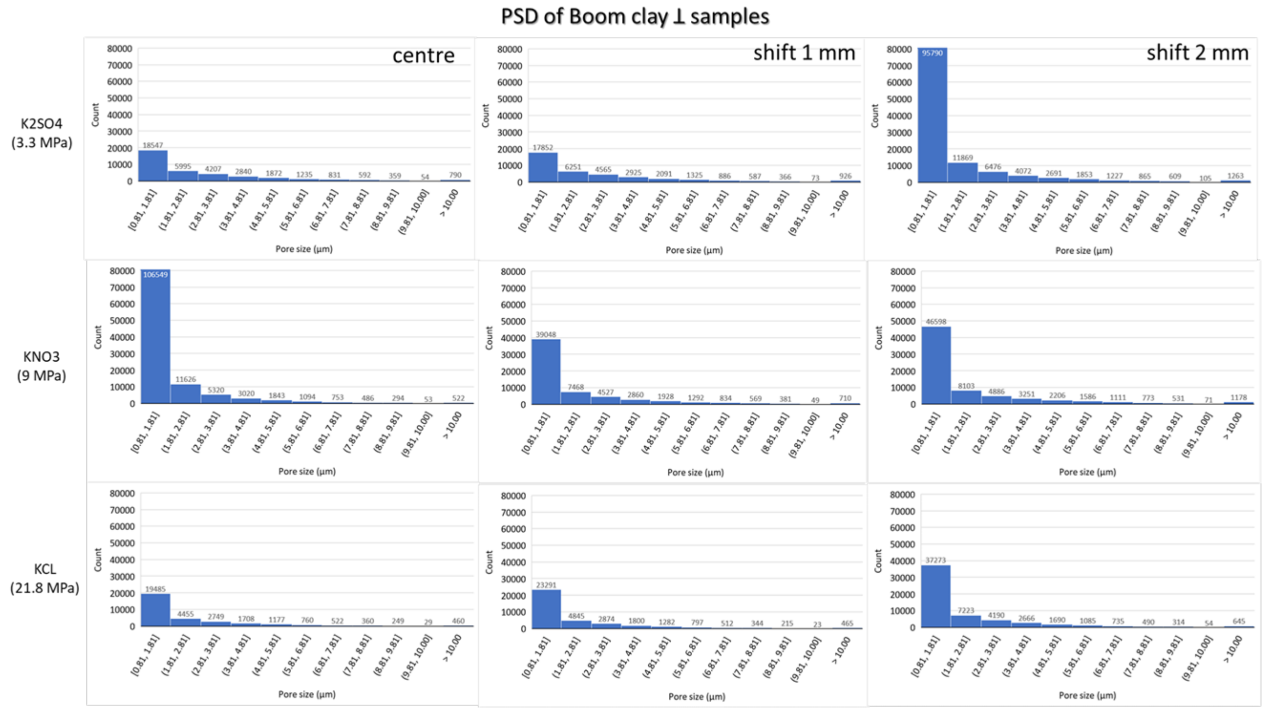

Figure 1.112: PSD of Sand of Eigenbilzen perpendicular to bedding

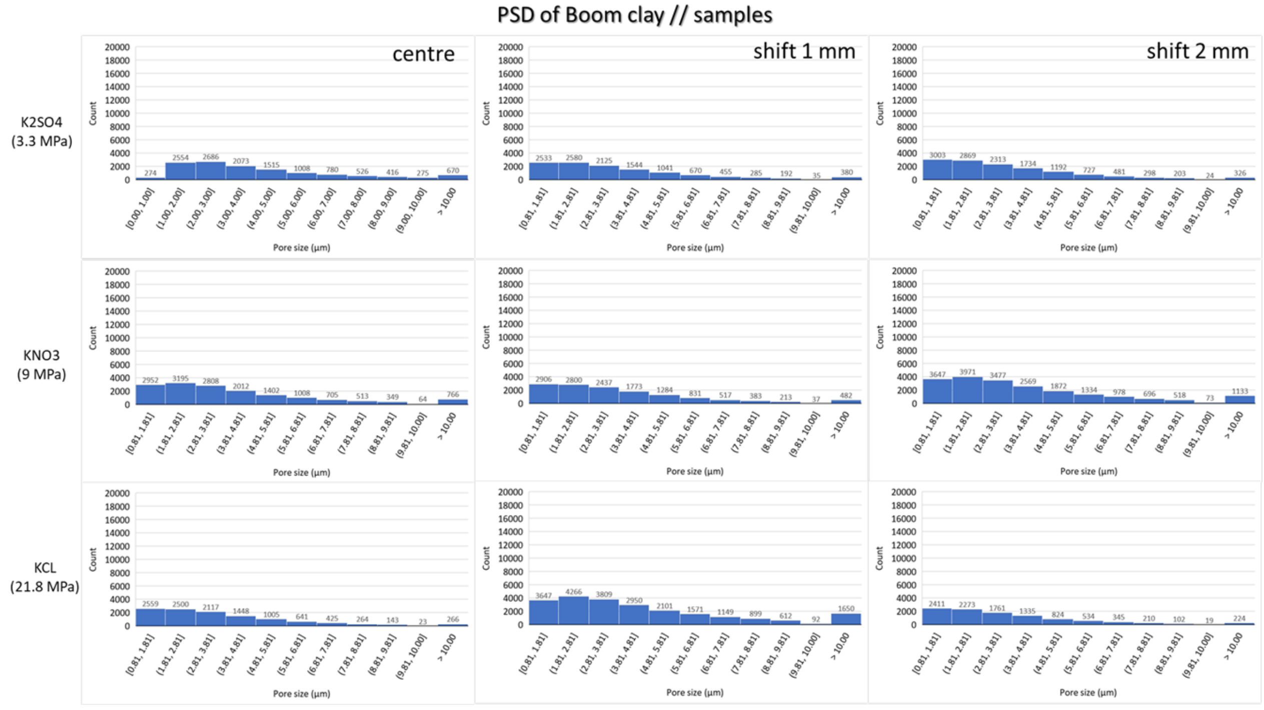

Figure 1.113: PSD of Sand of Eigenbilzen parallel to bedding

1.5.5.9. EXCITE Network

BGS synthetic clays were also investigated, although not on synchrotron, using the X-ray CT facility under the framework of the H2020 EXCITE project (Grant Agreement no. 101005611); we have collaborated with University of Granada, registered at Cuesta del Hospicio s/n 18007 Granada (Spain), providing Transnational Access (TNA) to the following research facility 05- (UGR) - CIC - X-ray μ-CT (ZEISS Xradia 510

Versa), Campus Universitario de Fuentenueva, Paseo Prof. Juan Ossorio, s/n, 18003 Granada (SPAIN). 9 days were allocated between 01/07/2022 and 14/07/2022.

1.5.5.10. Exploration of scan setting

Six scans were conducted: all scans from 1 to 4 at location 1, near the edge of the cylinder. The scan name Sample 1-Zone 2 is located in the second region (a region shifted inside). The scan settings on the scans of the BGS samples are presented in Table 1.34.

Table 1.34: General scan settings (exposure time varies for different scans)

Energy	Power	Pixel resolution	Exposure time	Projection count
80kV	7W	0.7µm	22s/35s/50s	3201

Also, the details and situation of the scan condition are summarised as (Table 1.35).

Table 1.35: Scan exposure and situation

Scan title	Exposure time	Situation/condition
S1-S1	35s	movement issue
S1-S2	35s	tighten the container
S1-S3	22s	slight movement issue, without a container
S1-S4	35s	without a container (holder trying to improve the quality of the results, avoiding movements and vibrations whilst the sample is turning during the scan); a sheet of dough at the base of the holder to hold the sample in the best way and it increased the volume around the sample (a little bit). The voxel size decreased some tenths.
S1-Z2	55s	more distance for phase contrast, but beam hardening issue, which cannot be avoided because a lower kilovoltage is to be used but it would increase the exposure time (52h)
S5-S1	22s	New sample, without a container

The issues and challenges noticed from the Versa scans (examples images given in Figure 1.114 on our BGS clay materials:

- movement of the sample
- the sample is larger than the recommended size for this type of scan, a worse signal-to-noise ratio is always achieved than if the sample is small
- components of very different densities and surrounding water are not differentiated in the sample.
- The scans are taking 33-36 hours because the system requires a high exposure time per projection to achieve the required voxel size considering the densities and sample size.
- impossible to apply the phase contrast because these samples are larger and denser than the required to apply 40kV.

1.5.6. Summary

The aim of this work was to study water-air distribution during onset of desaturation in argillaceous rock to confirm when small scale samples can be considered to be homogeneously desaturated, an assumption which is often made for further evaluation of unsaturated transport properties (suction, diffusion, . . .).

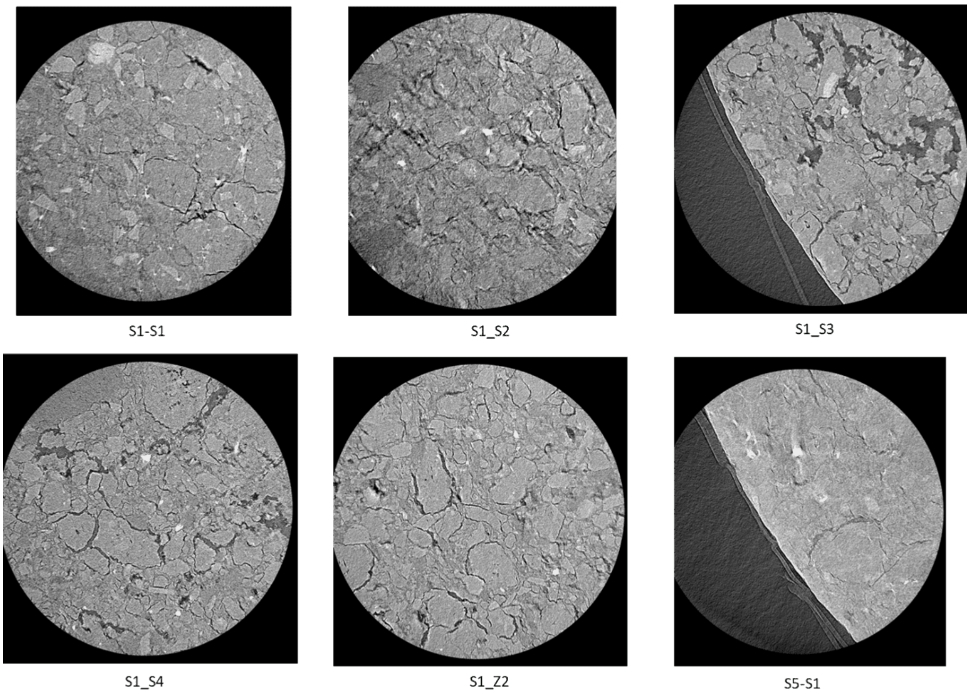

S1-S1 S1_S2 S1_S3

S1_S4 S1_Z2 S5-S1

Figure 1.114: Example images from different scan settings

This project used the advanced X-ray Synchrotron imaging and lab-based CT facilities, to investigate the pore scale information about the desaturation process of the host rock candidates (Toarcian, Sand of Eigenbilzen) at a sub-micron scale. For this purpose, small cylindrical samples with dia. 6-10mm were prepared in different RH conditions (RH> 90%). Some of them, cut perpendicularly to the rock bedding plane, prior to resaturation and during RH equilibration where conditioned in 3D-printed axial confinement cells to prevent dominant swelling. From each sample, three adjacent sub-volumes of 1mm^3 were imaged: one in the center of the sample and the other two placed radially towards sample external surface. After acquisition, the 3D reconstruction was conducted using Paganin filter to enhance grey value distance between phases and Trainable Weka Segmentation was applied to extract the pore space.

For host rocks, Toarcian argillite and Sand of Eigenbilzen, the main observations are:

- no direct detection of water/gas-filled pores was achieved, under the current submicron (0.65µm pixel resolution) via CT synchrotron imaging facility.
- The current CT resolution may be insufficient for the samples with the RH-imposed saturation levels to directly observe water-air menisci.
- The porosity results indicate the homogeneity of drying in host rock candidates, that large pores dry first ahead of the small pores.
- The results of the porosity versus RH also suggest a homogenous desaturation.
- The results of PSDs infer the dominance of smaller pores (0.65 and 2 micron) and show that they are more present near samples surfaces.

Only about one third of imaged samples was threated up to now, but the work is ongoing and should be completed before the end of the project EURAD-GAS in June 2024.

1.5.7. Key learning points

New knowledge acquired

We have shown with this project that it is possible to manufacture very small diameter cylinders of fresh argillaceous rocks by simple lathing of larger samples. This was possible on both samples that were perpendicular and parallel to the bedding plane with very limited damage to the samples.

Although with X-ray microtomography it is still difficult to directly distinguish between water and air-filled pores, it is possible to obtain some pore-scale properties (porosity) profile through the whole sample on the scale of several millimetres.

Porosity profile observation indicates that desaturation may be homogeneous within sub-centimetre sized samples, even close to the full water saturation.

Comparison of sub-volumes situated in the center and near the surface of the samples indicates however some variations in porosity and PSD which are not trivial to interpret.

Impact of acquired knowledge.

This work will help to initiate similar research projects on small scale solid hostrocks' samples and moving away from using powder ersatz, using which may modify obtained material properties.

Several recent experiments search for satisfactory explanations for observed discrepancies in effective transport properties of unsaturated argilites. Our work helps to highlight the issue of water-air distribution in experimental set-ups.

The extensive set of 3D images of Toarcian and Sand of Eigenbilzen acquired within this project are available to Eurad and wider scientific community as a base for pore-scale simulations and homogenisation approaches.

Remaining knowledge gaps

In spite of the fact that were not able to directly distinguish between water and air-filled pores in argillites and that the calculated porosity profiles seem to indicate that desaturation process is homogeneous within the studied samples, we believe that further steps are required to support the statement that the desaturation distribution can be considered as homogeneous on centimetre size samples:

- improvement and complementary analysis can be carried out on already obtained synchrotron data of Toarcian and Sand of Eigenbilzen in particular in terms of grey level distribution within the pore space to check if different fluids can be distinguished by statistical methods. In particular it is necessary to correct for the over-sharpening of pores edges without losing information about the grey levels in the centre of pores.

- smaller-size samples and higher resolution, or higher saturation levels can be attempted for the observation of air/water interface in host rock materials

Recommendations for the future

Unfortunately, and due to schedule differences, in this project we did not follow the sample preparation protocol that was developed in common work by teams within EURAD; we would recommend repeating this analysis on samples prepared and followed by X-ray microtomography to reject damaged/fractured samples.

Modelling

.

Paul-Scherrer-Institute (PSI)

1.6. Modeling gas diffusion in saturated and unsaturated conditions (PSI)

1.6.1. Motivation

In a geological system, a hierarchy of scales exists, comprising the molecular scale, pore-scale, and large geological/continuum scale, with each scale corresponding to different pore sizes. The Geological Scale is of interest in achieving the ultimate goal of gas transport in a deep geological repository. Molecular Dynamics can be used to study diffusion at the molecular scale, while Pore Scale Modelling can be employed to investigate fluid transport through diffusion and advection. Continuum numerical modeling can simulate large geological scales, where the complex porous media is represented by a continuum and averaged over all the properties of the media within a certain volume. In material studies, a certain Representative Elementary Volume (REV) is usually selected. The REV is the smallest volume that can yield a measurement representative of the whole. At smaller sampled volumes, there are fluctuations in material properties, while at larger volumes, properties become constant. In continuum modeling, domains are typically discretized into smaller volumes, and the smallest volume represents the REV. Thus, continuum models are unable to capture complex behavior below the REV, as the properties within the REV are averaged. Therefore, to obtain a more realistic understanding and prediction of gas transport in a deep geological repository, a comprehensive approach spanning across multiple scales (from the molecular to the continuum scale) is necessary. However, transitioning from the microscale to the continuum scale has been a great challenge over the years. The main focus of the project conducted at PSI is part of a PhD Thesis Owusu (2023) to gain a better understanding of diffusion in porous clay media. To achieve this, two kinds of simulations were performed: molecular dynamics and pore-scale simulations. The molecular dynamics simulations investigate diffusion within small pores, while the pore scale simulation examines the effect of porosity, connectivity, and arrangement of particles on microscopic diffusion. The microscopic transport parameters obtained from the pore scale simulation can be used in other models at the continuum scale. To obtain a more comprehensive understanding of diffusion in porous clay media, an upscaling method is applied in pore-scale simulations which incorporate behaviors occurring below the REV. This approach considers both the pore-scale properties and complexities, as well as the local clay interaction properties (i.e., the local diffusive coefficients obtained from molecular dynamics simulations). The successful validation of this approach for water diffusivity was achieved through a comparison of the 3D simulations of water transport in complex porous geometry obtained by molecular dynamic simulations (including full interatomic interactions) with the upscaling approach, using random walk simulation of non-interacting particles and lattice-based representation of pore geometry Churakov and Gimmi (2011a). It should be noted that during the construction phase of the repository, it is expected that the host rock will undergo local de-saturation, necessitating a temporary re-saturation period estimated to range between $10^3 - 10^4$ years before achieving full saturation. Therefore, different degrees of saturation are expected to occur in the pores. According to Kelvin's equation, big pores are expected to desaturate first, followed by small pores as relative humidity reduces. Our model is expected to capture the flow of gases at different saturation states. To better understand diffusive transport, we aim to answer the following questions: (a) What is the preferential diffusion pathway of gas in porous clay media, interlayer or micropore, and how does the diffusion coefficient vary with pore size and geometry? (b) In the context of gas transport in porous clay media, what is the spatial distribution and partitioning of gas phases, and how do they relate to the complex pore geometry and interlayer/micropore structures? This study presents a comprehensive investigation of the transport properties of gas in smectite clay. Equilibrium molecular dynamics simulation was applied to understand the diffusion mechanism of dissolved gases in a smectite clay nanopore. The influence of pore size, gas species, and temperature on the molecular scale diffusive transport was further explored. Equilibrium molecular dynamics was used to understand the diffusion of gases in a partially saturated smectite clay nanopore and how gas partitions between the gas-rich phase and the water phase in the nanopore. Furthermore, non-equilibrium molecular dynamics was applied to investigate the dynamics of viscous gas flow in the nanopore. It has been shown by studies that the dissolution of solutes in saturated porous clay materials can change the swelling behavior of the clay materials, which, in turn, can change the porosity and thereby change the transport properties. An upscaling approach was performed where local diffusion coefficients were implemented in a random walk and lattice Boltzmann simulations to understand pore scale diffusivity.

1.6.2. Numerical Model

Numerical modeling of gas transport in porous clays involves using mathematical equations and computer simulations to study how gases move through clay formations. The modeling process typically involves developing mathematical models that describe the transport of gases through the porous clay matrix, taking into account factors such as the permeability of the clay, the properties of the gas, and the geometry of the porous media. These models can be solved using numerical methods, such as finite element or finite difference methods, which can accurately simulate the complex behavior of gases in porous media. Numerical modeling can also be used to investigate the impact of various factors on gas transport, such as changes in temperature, pressure, and fluid saturation. This information can be used to develop better strategies for managing gas migration in subsurface environments.

Numerical modeling of gas transport in nuclear repositories is essential because it provides a more comprehensive understanding of the complex processes occurring in these systems. While experimental results are crucial and provide valuable data, numerical modeling allows the simulation of a wider range of conditions, scenarios, and timescales that might not be possible to investigate experimentally. Additionally, numerical models can help us identify the critical parameters that influence the gas transport processes, which is challenging to achieve solely through experiments. Furthermore, numerical modeling can help to interpret and understand experimental results by providing a framework to test hypotheses and validate observations. By combining both experimental results and numerical modeling, we can improve our confidence in predicting the behavior of gas transport in nuclear repositories, which is crucial for ensuring the safe and reliable management of nuclear waste.

The finite element or finite volume discretization approach on a continuum scale is often used for numerical modeling of reactive transport processes at the repository scale. In order to achieve this, the computational domain is partitioned into small voxels (elements or volumes) that are many orders of magnitude larger than the pore diameter. Transport characteristics are homogenized and smoothed out within these voxels, and macroscopic parameters including porosity, tortuosity, diffusivity, and permeability are used to describe the pore space. This method, however, neglects the small-scale geometrical properties and heterogeneities of porous materials, which may cause numerical results to be dependent on spatial grid discretization.

To overcome this limitation, three approaches can be used. Firstly, well-defined laboratory experiments can be conducted to provide the missing information. Secondly, pore-level solvers can be coupled with macroscopic ones in a multiscale simulator to account for pore geometry and connectivity. Thirdly, appropriate correlations can be extracted from pore-level simulations to provide the necessary microscopic feedback.

Pore-level simulations require an explicit representation of pore geometry and connectivity. Representative structures can be generated computationally or obtained via X-ray/ion-beam microtomography techniques. The diffusivity of molecular species in nano-pores can be obtained through molecular dynamics simulations. These effective pore scale diffusion coefficients can be used by pore-level methods, such as random walk, Brownian dynamics, and Lattice Boltzmann, to account for pore space connectivity and mineralogical heterogeneities. This approach can obtain sample-specific effective transport parameters for macroscopic simulations.

1.6.2.1. Molecular dynamics simulation

Molecular dynamics (MD) simulations are computational tools that allow for the study of the equilibrium and non-equilibrium behavior of molecules over time. These simulations rely on the integration of Newton's equations of motion to simulate the motion of atoms and molecules within a system. The equation of motion takes into account the mass of the molecule, potential energy, force on the molecule, position of the reference particle, and distance between the reference molecule and neighboring molecules. Newton's equation is given by:

$$M_k \frac{d^2 R_k}{dt^2} = -\frac{\partial V(R^n)}{\partial R_k} = f_k(R^n) \tag{1.1}$$

where M_k is the mass of the molecule, V is the potential energy, f_k is the force on the molecule, R_k is the position of the reference particle and R^n is the distance between the reference molecule and the neighboring molecules.

To conduct MD simulations, force potentials are required to describe intermolecular interactions within the system. These force potentials, also known as force fields, typically consist of mathematical functions that describe the potential energy between atoms or molecules as a function of their positions and orientations. Different types of force potentials used in MD simulations include empirical, semi-empirical, and ab initio potentials. Empirical force fields are commonly used due to their computational efficiency and ability to accurately capture the behavior of various substances at a wide range of conditions.

The total potential energy (U) in an MD simulation can be described as the sum of Van der Waals energy (υ^{LJ}), Coulombic energy ($\upsilon^{\mathrm{Coulomb}}$), and bonded interaction ($\upsilon^{\mathrm{Bonded}}$) potential term. The Van der Waals energy is represented by the Lennard-Jones (LJ) energy and distance parameters. The Coulombic energy is dependent on the charges of the atoms and their distance apart, with the Lorentz-Berthelot combination rules used to predict interatomic interactions between unequal atomic species. The total potential energy is mathematically written as:

$$U = \upsilon^{LJ} + \upsilon^{Coulomb} + \upsilon^{Bonded} \tag{1.2}$$

with

$$\upsilon^{LJ}(r_{ij}) = 4\epsilon_{ij}\left[\left(\frac{\sigma_{ij}}{r_{ij}}\right)^{12} - \left(\frac{\sigma_{ij}}{r_{ij}}\right)^{6}\right] \tag{1.3}$$

$$\upsilon^{Coulomb}(r_{i,j}) = \frac{Q_i Q_j}{4\pi\epsilon_0 r_{ij}} \tag{1.4}$$

$$\upsilon^{Bonded} = \frac{1}{2}\sum_{bonds} k_{i,j}(r_{i,j} - r_{eq})^2 \tag{1.5}$$

where atoms i and j are r_{ij} apart, ϵ_{ij} and σ_{ij} are the Lennard-Jones (LJ) energy and distance parameters, respectively. Q_i is the charge of atom i, Q_j is the charge of atom j and ϵ_0 is the vacuum permittivity. $k_{i,j}$ is the harmonic force constant and r_{eq} is the equilibrium bond distance.

Macroscopic diffusion observed in concentration gradient is the consequence of stochastic dynamics of molecules at an atomistic scale. At equilibrium condition, as simulated by Molecular Dynamics simulations, the self-diffusion of molecules in fluid and gas phase is triggered by collision of particles. Accordingly, the diffusion coefficients of water and gaseous molecules D can be derived from the slope of a plot of the mean square displacement of particles $\langle l^2 \rangle$ using the Einstein relation in the limit of sufficiently long simulation time:

$$D = \frac{1}{2n}\lim_{t\to\infty}\frac{d\langle l^2\rangle}{dt} \quad (n = order\ of\ dimension) \tag{1.6}$$

The asymptotic long time limit was approximated by calculating the slope $\langle l^2 \rangle$ versus t for the probe time scale τ = 100 ps for which linear relationship is fullfilled. The $\langle l^2 \rangle$ was calculated in all three dimensions in the bulk aqueous system (n =3). In the clay nanopore, only the x and y components of the trajectory were used (n =2), and they describe the two-dimensional diffusion parallel to the interlayer nanopore.

1.6.2.2. Molecular dynamics simulation code

Numerous molecular dynamics codes have been developed for molecular dynamics simulations. Specifically, for the present study, two such codes were implemented:

- **LAMMPS:** The LAMMPS package Plimpton (1995) was employed to conduct the simulations. LAMMPS is an open-source classical molecular dynamics code with a focus on materials modeling. The acronym LAMMPS stands for Large-scale Atomic/Molecular Massively Parallel Simulator. This software is suitable for simulating particles at various scales, including atomic, meso, or continuum levels, and can serve as a parallel particle simulator.
- **GROMACS:** GROMACS Bekker et al. (1993) (GROningen MAchine for Chemical Simulations) is a widely used open-source software package for molecular dynamics simulations of biomolecules, such as proteins, lipids, and nucleic acids. It is designed to perform a range of simulation types, including energy minimization, equilibration, and production runs, with support for a variety of force fields and algorithms. GROMACS is particularly well-suited for high-performance computing environments, with scalable parallelization and optimization for different hardware architectures. The software is freely available under the GNU Lesser General Public License (LGPL) and is actively maintained by a large community of developers and users.

In this study, the rigid SPC/E water model for H_2O was chosen because it is able to reproduce the D-value of bulk water, the vapor-liquid equilibrium, and the swelling behavior of clays Bourg and Sposito (2010); Errington and Panagiotopoulos (1998); Guillot (2002); Ferrage et al. (2011); Marry et al. (2011).

Molecular dynamics simulations have been widely used to study fluid, solute, and gas interactions, as well as transport mechanisms Gimmi and Churakov (2019a); Torgersen et al. (2004); He et al. (2015); Gadikota et al. (2017a); Jiang and Lin (2018a); Zhu et al. (2018a); Kosakowski et al. (2008a); Botan et al. (2011, 2013). These simulations involve modeling the behavior of individual atoms and molecules over time to understand how they interact with each other and their surroundings. In fluid systems, molecular dynamics simulations have been used to study phenomena such as viscosity, diffusion, and flow behavior Kosakowski et al. (2008a); Botan et al. (2011, 2013); Zhu et al. (2018a); Torgersen et al. (2004). In solute systems, simulations can help predict solubility, partitioning, and adsorption behavior Jiang and Lin (2018a); Gadikota et al. (2017a); Sarkisov and Monson (2001); Campos et al. (2009). In gas systems, simulations have been used to study gas dynamics, coordination, and mobility. Overall, molecular dynamics simulations provide a powerful tool for investigating complex interactions and transport phenomena in fluid, solute, and gas systems.

1.6.2.3. Random walk simulations

Random walk (RW) simulations are a valuable tool for effectively studying the diffusion of chemical species within clays. These simulations provide insights into the intricate network of pores and channels, enabling a better understanding of the complex behavior of particles in a porous clay medium at the pore scale. By tracking the random movements of molecules within the clay's porous structure, random walk simulations capture the heterogeneous nature of pore-scale diffusion. To enhance the accuracy and applicability of these simulations, they can be combined with other modeling techniques. For example, coupling random walk simulations with computational fluid dynamics (CFD) techniques allows for a more comprehensive analysis of coupled diffusion and advection processes Mofakham and Ahmadi (2020); Dehbi (2011); Forsyth et al. (2016). By integrating CFD, it becomes possible to simulate the flow of fluid within the porous medium, providing a deeper understanding of the transport behavior of substances. One of the significant advantages of random walk simulations is their ability to account for the complex and tortuous diffusion paths within the porous clay medium. With its wide range of pore sizes, shapes, and connectivity, the clay medium poses challenges for accurately predicting diffusion behavior. Random walk simulations overcome this challenge by incorporating probability distributions that reflect the likelihood of particles traversing different types of pores Churakov and Gimmi (2011a); Gimmi and Churakov (2019b); LaBolle et al. (1998, 1996). This capability is instrumental in assessing the effective diffusion properties of substances within the porous medium.

In a random walk method, particles known as random walkers move stochastically with random displacements and directions defined by a probability distribution function. If these random walkers encounter impermeable boundaries, specific reflection conditions are implemented. By applying appropriate statistical treatment, the random walk model can reproduce Fick's equation, which describes diffusion. Figure 1.115 illustrates a 2-dimensional system where a domain ($S_{i,j}$) within the material is examined, with 'i' and 'j' representing the dimensions in the x and y directions, respectively.

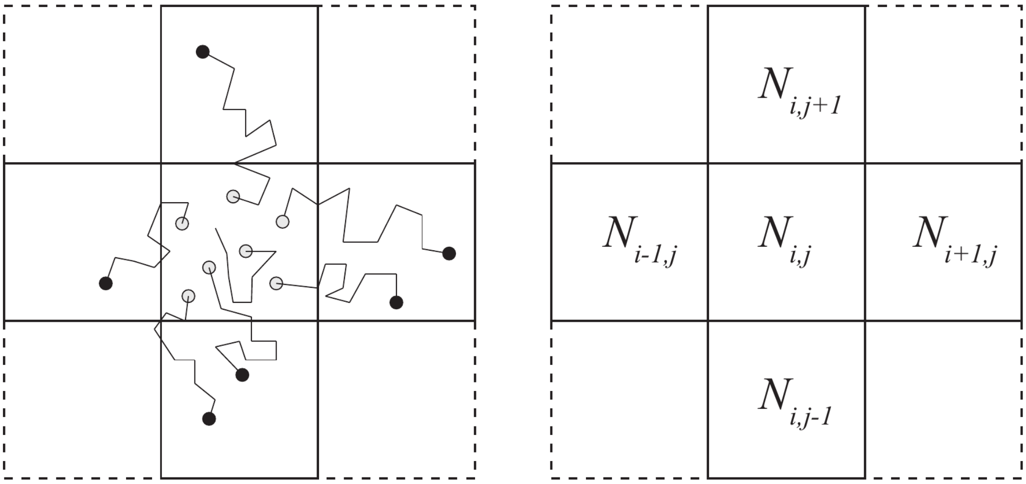

Figure 1.115: Illustration of the motion of random walkers and the number of random walkers per box.

By considering the number of particles entering and leaving the domain, we can establish a mass balance equation. Assuming the probability of particle movement or exiting the domain as $p = R^p\Delta t$, we can express the mass balance equation after a time step of Δt as follows:

$$N_{i,j}(t+\Delta t) = N_{i,j}(t) + R^p\Delta t(-2N_{i,j}(t) - 2N_{i,j}(t) + N_{i-1,j}(t) + N_{i+1,j}(t) + N_{i,j-1}(t) + N_{i,j+1}(t)) \quad (1.7)$$

To simplify and further analyze this equation, we can rearrange the terms and introduce Δx^2 and Δy^2, representing the step distances in the x and y directions within the system, respectively:

$$\begin{aligned}\frac{N_i(t+\Delta t) - N_i(t)}{\Delta t} = (R^p\Delta x^2)&\frac{(N_{i+1,j}(t) - 2N_{i,j}(t) + N_{i-1,j}(t)}{\Delta x^2} + \\ (R^p\Delta y^2)&\frac{(N_{i,j+1}(t) - 2N_{i,j}(t) + N_{i,j-1}(t))}{\Delta y^2}\end{aligned} \quad (1.8)$$

This equation represents the discrete form of a partial differential equation with respect to $N_{x,y}(t)$, which denotes the number of particles at position x, y at time t. Therefore, we can express it as:

$$\frac{\partial N}{\partial t} = (R^p\Delta x^2)\frac{\partial^2 N}{\partial x^2} + (R^p\Delta y^2)\frac{\partial^2 N}{\partial y^2} \quad (1.9)$$

Alternatively, if we describe the system in terms of the number of particles per box, represented as $C_{i,j}(t) = N/V_b$ (where V_b is the volume per box), we can derive the diffusion equation as follows:

$$\frac{\partial C}{\partial t} = D_{xx}\frac{\partial^2 C}{\partial x^2} + D_{yy}\frac{\partial^2 C}{\partial y^2} \tag{1.10}$$

Here, D_{xx} and D_{yy} denote the effective diffusion coefficients in the x and y directions, respectively. When D_{xx} equals D_{yy}, the diffusion coefficient can be expressed as:

$$\frac{\partial C}{\partial t} = D_e\left(\frac{\partial^2 C}{\partial x^2} + \frac{\partial^2 C}{\partial y^2}\right) \tag{1.11}$$

where D_e is the effective diffusion coefficient.

1.6.2.4. Lattice Boltzmann modeling

Lattice Boltzmann Modeling (LBM) is a computational fluid dynamics method used to simulate single and multiphase fluids at the pore scale. It is a relatively new approach compared to traditional computational fluid dynamics (CFD) methods such as finite difference and finite element methods. This technique has proven to be effective in replicating the behavior of real fluids in various applications. The Lattice Boltzmann Modeling approach offers a diverse range of dynamic phenomena that can be simulated with relative ease, such as unsteady flows, phase separation, evaporation, condensation, cavitation, solute and heat transport, buoyancy, and surface interactions Genty and Pot (2013); Boek and Venturoli (2010); Spaid and Phelan Jr (1997); He and Luo (1997); Qin et al. (2019); Sukop and Or (2004); Chen et al. (2011b); Ezzatneshan (2017); Walsh and Saar (2010); Peng et al. (2011); Yin et al. (2011); Rosén et al. (2012); Zhou et al. (2004); Chen et al. (2009); Li et al. (2014); Zhang (2011). Furthermore, persistent metastable states can be effectively achieved using this method Sukop (2006).

The LBM method is based on the Boltzmann equation, which describes the behavior of a gas as a function of its velocity distribution function. The conceptual framework of the model is based on a particle perspective, in which collisions, streaming, and interactions between particles, as well as between particles and surfaces, are considered the fundamental components. The Boltzmann equation is solved on a lattice, hence the name Lattice Boltzmann Modeling.

Model concept: Boltzmann proposed that a gas can be viewed as a collection of particles that interact with each other according to classical mechanics. However, due to the vast number of particles involved, a statistical treatment is necessary. In the lattice Boltzmann framework, the gas molecules kinetics is simplified to two basic operations: **streaming of fictitious particles through space** and **colliding at specific grid locations on the lattice**. The Boltzmann distribution function describes the probability distribution of particle velocities in a gas at thermodynamic equilibrium, and it is derived based on the assumption that the gas particles undergo random collisions with each other at their maximum entropy state. In a gas, the particles are in constant motion and undergo collisions with each other. These collisions result in the exchange of energy between the particles, which causes the particle velocities to be distributed according to the Boltzmann distribution. At thermodynamic equilibrium, the probability of finding a particle with a given velocity is described by the Boltzmann distribution function (1.12).

$$f(v) = \left[\frac{m}{2\pi k_b T}\right]^{3/2} 4\pi v^2 exp\left(-\frac{mv^2}{2k_b T}\right) \tag{1.12}$$

where f(v) is the Maxwell-Boltzmann equilibrium distribution function for velocity (v). The mass of the particle is denoted as m, T denotes the temperature and k_b is the Boltzmann constant.

Lattice Boltzmann models take Boltzmann's initial conceptual view of gas kinetics and simplify it even further, allowing for the simulation of fluid behavior using even fewer parameters. Instead of considering an infinite number of possible particle positions and momenta, the lattice model reduces them to just a few discrete positions and momenta. This is achieved by discretizing time and space into a regular Cartesian grid, where particles at a given time step exist within the nodes of the lattice. In the 2D model case, the number of possible momentum variations is also significantly reduced, to just 8 directions, 3 magnitudes. The model is referred to as D2Q9, given its two-dimensional nature and the inclusion of nine discrete velocities Qian et al. (1992). By reducing the complexity of the fluid dynamics problem, Lattice Boltzmann models are able to simulate fluid behavior with high accuracy while requiring less computational resources than traditional methods which aim at solving the Boltzmann Equation. In a typical dimensionalization, the LBM models utilize the lattice unit (lu) as the fundamental measure of length, and time steps (ts) are employed as the unit of time. This approach provides a standard framework for LBM simulations, facilitating comparison and reproducibility of results across different studies.

The typical Lattice Boltzmann Method (LBM) implementation simplifies the Boltzmann collision integral by a relaxation to equilibrium, namely the BGK approximation of the Boltzmann equation He et al. (1997):

$$\frac{\partial f}{\partial t} + \xi \cdot \nabla f + F \cdot \nabla_{\xi} f = -\frac{f - f^{eq}}{\tau} \tag{1.13}$$

where the single-particle distribution function in the phase space $(\mathrm{x}, \xi, \mathrm{t})$ is represented by $\mathrm{f}(\mathrm{x}, \xi, \mathrm{t})$, while the corresponding Maxwell-Boltzmann distribution function is denoted as $\mathrm{f}^{\mathrm{eq}}(\mathrm{x}, \xi)$. Here, x refers to the position vector, ξ represents the microscopic velocity, $\mathrm{F}(\mathrm{x}, \mathrm{t})$ is a body force, and τ is the relaxation time.

The lattice BGK method (i.e. the fully discretized Boltzmann equation with the BGK collision operator Bhatnagar et al. (1954)) employs a discrete distribution function, $\mathrm{f_i}$, to represent the velocity distribution of fictitious particles of the fluid. This distribution function satisfies the Lattice Boltzmann equation as follows He et al. (1997):

$$f_i(x + e_i \Delta t, t + \Delta t) = f_i(x, t) - \frac{1}{\tau}(f_i(x, t) - f_i^{eq}(x, t)) + S_i(x, t) \tag{1.14}$$

where $\mathrm{f_i}(\mathrm{x}, \mathrm{t})$ denotes the velocity distribution function related to the discrete velocity direction i, $\mathrm{f_i^{eq}}$ is the equilibrium distribution function (Maxwell-Boltzmann distribution function), τ is the relaxation time and $\mathrm{S_i}(\mathrm{x}, \mathrm{t})$ is the source term added to the standard Lattice Boltzmann equation.

Equation 1.14 can be decomposed into two distinct parts that are performed in succession:

- The first part is collision (or relaxation)

$$f_i^*(x, t) = f_i(x, t) - \frac{\Delta t}{\tau}(f_i(x, t) - f_i^{eq}(x, t)) \tag{1.15}$$

  where $\mathrm{f_i^*}$ represents the distribution function after the collision and $\mathrm{f_i}$.
- The second part is streaming (or propagation)

$$f_i(x + c_i \Delta t, t + \Delta t) = f_i^*(x, t) \tag{1.16}$$

The equilibrium distribution function $\mathrm{f_i^{eq}}(\mathrm{x}, \mathrm{t})$ can be calculated as Luo (1998):

$$f_i^{eq}(x, t) = \omega_i \rho \left[1 + \frac{e_i \cdot u}{c_s^2} + \frac{(e_i \cdot u)^2}{2c_s^4} - \frac{(u)^2}{2c_s^2}\right] \tag{1.17}$$

with

$$\rho = \sum_i f_i \tag{1.18}$$

and

$$u = \frac{1}{\rho} \sum_i f_i e_i \tag{1.19}$$

In Equation (1.14) and (1.17), the e_i denote the discrete velocities, and ω_i represent their respective weights listed in Table 1.36. The macroscopic density and macroscopic velocity vector are denoted by ρ and u respectively. Discrete velocity models are typically denoted as DnQm, where n refers to the number of dimensions in space, and m indicates the total number of velocities.

Table 1.36: Summary of weighting coefficients and sound speeds

Model	w_i	c_s^2
D2Q7	1/2 (i=0), 1/12 (i=1, ... , 6)	$c^2/4$
D2Q9	4/9 (i=0), 1/9 (i=1, 2, 3, 4), 1/36 (i=5, 6, 7, 8)	$c^2/3$
D3Q15	2/9 (i=0), 1/9 (i=1, ... , 6), 1/72 (i=7, ... , 14)	$c^2/3$
D3Q19	1/3 (i=0), 1/18 (i=1, ... ,6), 1/36 (i=7, ... , 18)	$c^2/3$

Figure 1.116 illustrates the widely used 2D and 3D discrete velocity models, namely D2Q7, D2Q9, D3Q15, and D3Q19. Specifically for the D3Q19 model Wolf-Gladrow (2004), the discrete velocities are given in Table 1.36. In the Table 1.36, the discrete velocities are multiplied by the parameter c, which is the lattice speed and is defined as $c = \Delta x/\Delta t$

Table 1.37: D3Q19 discrete velocities

e_0	e_1	e_2	e_3	e_4	e_5	e_6	e_7	e_8	e_9	e_{10}	e_{11}	e_{12}	e_{13}	e_{14}	e_{15}	e_{16}	e_{17}	e_{18}
0	1	-1	0	0	0	0	1	-1	1	-1	1	-1	1	-1	0	0	0	0
0	0	0	1	-1	0	0	1	1	-1	-1	0	0	0	0	1	-1	1	-1
0	0	0	0	0	1	-1	0	0	0	0	1	1	-1	-1	1	1	-1	-1

In conclusion, Lattice Boltzmann modeling is a computational technique that has been widely used to simulate fluid transport in porous media, including porous clay materials Gao et al. (2017, 2014); Froning et al. (2013); Zhang et al. (2014); Wang et al. (2016a); Chen et al. (2013); Akai et al. (2020); O'Brien et al. (2002); Yin et al. (2019a); Ghanbarian et al. (2015). In the context of shale gas extraction, the Lattice Boltzmann method has been applied to study the transport of fluids in the nanopores of shale rocks, which is crucial for the productivity of gas wells Zhang et al. (2014); Wang et al. (2016a). The technique has also been used to investigate the geochemical reactions that occur in clay materials during CO_2 sequestration, which can provide important insights into the long-term stability of geological CO_2 storage sites Gao et al. (2017). Furthermore, Lattice Boltzmann modeling has been employed in geotechnical engineering to investigate the flow of fluids through compacted clay liners Kutay et al. (2006), which are commonly used as barriers to prevent contamination of groundwater. In addition to these applications, Lattice Boltzmann modeling with coupled chemical reaction can also be used to simulate fluid transport in clay-based porous media for geochemical applications such as the diffusion, adsorption, and desorption of contaminants in soils and sediments Akai et al. (2020); Chen et al. (2013); O'Brien et al. (2002); Yin et al. (2019a); Ghanbarian et al. (2015). By accurately simulating fluid transport in porous clay materials, the Lattice Boltzmann method can help to understand the mechanisms of transport and facilitate the development of efficient and sustainable solutions for various practical problems in geoengineering and environmental science.

1.6.3. Results for Saturated System

Equilibrium molecular dynamics simulations reported below were conducted for saturated montmorillonite pores at different pore size distribution, temperature and concentrations of gases and published in Owusu

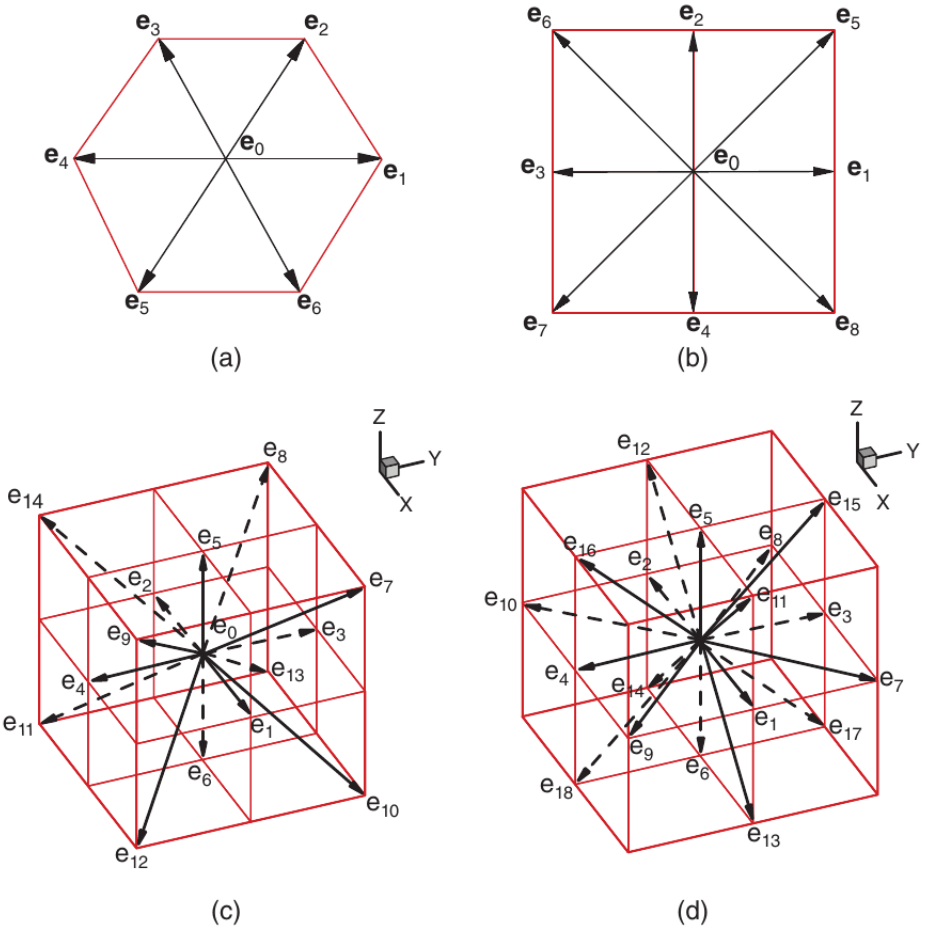

Figure 1.116: "Discrete velocity models (a) D2Q7 (b) D2Q9 (c) D3Q15 (d) D3Q19." Reproduced with permission Huang et al. (2015a)

et al. (2022a).

1.6.3.1. Diffusion in bulk liquid water

Due to hydrodynamic correlations in finite size systems, the diffusion coefficient obtained by molecular dynamic simulations with periodic boundary condition D_{PBC} are inversely proportional to the system size. In order to verify our model parameters and thus accurately determine the influence of clay particles on the diffusion coefficient and activation energy of water and gases in the macroscopic limit, we first examined the ability of our MD simulations to reproduce the values of the self-diffusion coefficient (D_0) and activation energy (E_a) values of bulk water and dissolved gas molecules. Figure 1.117 shows the D_{PBC} of bulk water as a function of inverse simulation cell size (L^{-1}) for systems with 512, 1331, 3375, 6859 water molecules.

The dashed line illustrates the linear regression of the plotted data for each temperature. A size-corrected D_0 value was obtained by extrapolating the D_{PBC} against L^{-1} values by linear regression to 1/L = 0. Holmboe et al. Holmboe and Bourg (2014) applied a similar method to MD simulations of water and compared the size dependence of the D_0 values from the extrapolated fit with that obtained from the Green-Kubo method. They performed separate simulations from the fitted data and obtained an SPC/E viscosity (η) for each temperature by applying the Green-Kubo relations to the autocorrelation function of the stress tensor elements. It was concluded that Yeh and Hummers' equation accurately predicts the size dependence of D_0 at 298 K, but slightly overestimates the temperature dependence of this size dependence.

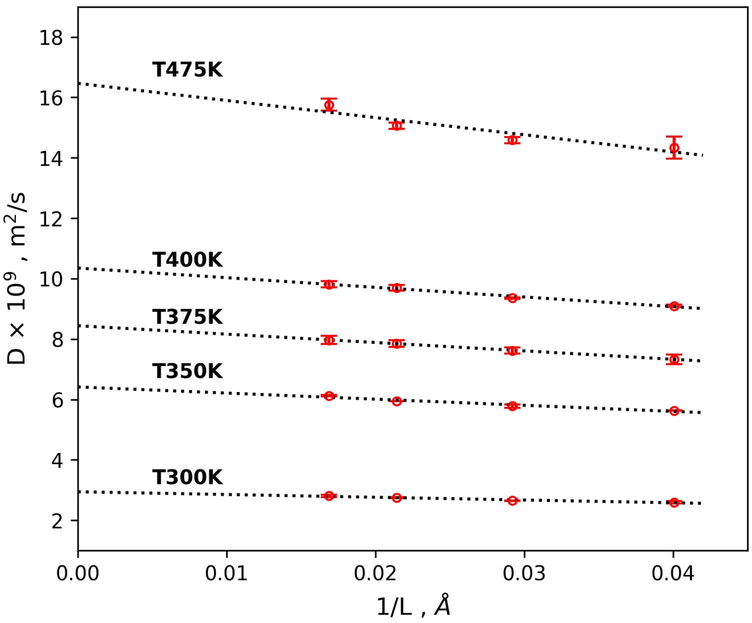

Figure 1.117: D_{PBC} values for bulk water as a function of inverse simulation cell size (for simulations with 512, 1331, 3375, and 6859) at different temperatures. The size-corrected diffusion coefficient D_0 is determined by linear regression (black dashed line) to 1/L = 0.

In this simulation, a corrected D_0 value of $2.92 \pm 0.03 \times 10^{-9}$ m^2/s was obtained for water at ambient conditions. This value overestimates the D_0 value from experiments Tsimpanogiannis et al. (2019). (2.65 $\times 10^{-9}$ m^2/s) by about 21%. This is consistent with the studies of Tsimpanogiannis et al. (2019), who performed a critical review of the classical molecular studies of bulk water. In their studies, they calculated the deviation of the relative self-diffusion coefficient from the experimental value at ambient conditions for different force fields. They calculated that the deviation of the SPC/E water model is about 30% from the experimental values.

It was also found that the resulting D_0 values from the SPC/E water model from this work underestimate the E_a values of the bulk water by ΔE_a = 4.9 kJ mol^{-1} (about 30% deviation), as shown in Table 1.38. This is probably because most interatomic potentials used in MD simulations have been parameterized to describe the system of interest at a particular temperature, and sometimes perform poorly when applied at very different temperatures. To determine if this effect is solely due to the SPC/E model underestimating the temperature dependence of viscosity (η), the calculated η values from the MD simulation were compared to the experimental values. The results show a less significant deviation of the simulated η values from those of the experiment (at least at temperature $>$ 350 K), as shown in Figure 1.118. Therefore, viscosity alone cannot fully account for the deviation between experimentally measured and predicted E_a values.

Studies by Yeh and Hummer Yeh and Hummer (2004), Holmboe et al. Holmboe and Bourg (2014), and Medina et al. Medina et al. (2011) show that the viscosity of the SPC/E water model is insensitive to the size of the simulation cell. However, the difference in E_a could be due to the fact that the water density of SPC/E from MD simulations was not equated with the experimentally measured bulk density of water. The density of the SPC/E water was then compared to the experimental density and it can be seen from Figure 1.118 that the SPC/E water model in our simulations underestimates the density of the water by 0.82 - 5.8% (with increasing temperature). The observed underestimation of the density could explain the corresponding underestimation of the activation energy for diffusion.

The diffusion coefficients and activation energy of diffusion of gases in bulk water obtained by molecular dynamic simulations at ambient conditions are shown in Figure 1.119 and Table 1.38. The results are in

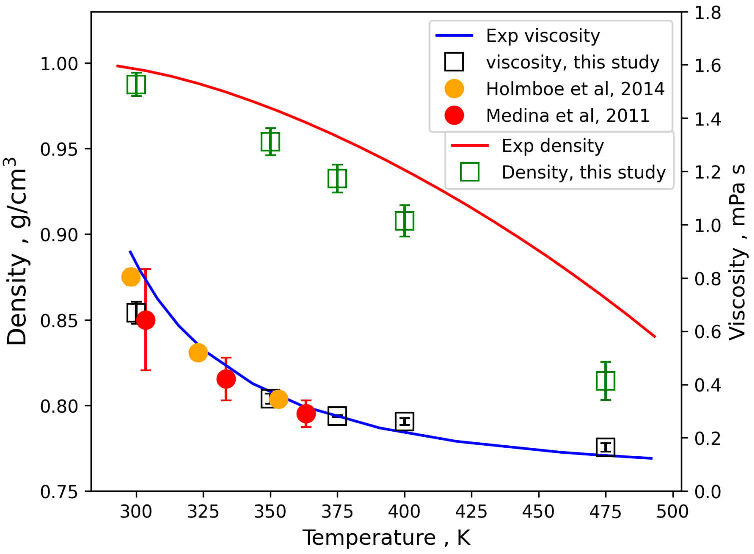

Figure 1.118: Comparison of the density of the SPC/E water model from this study (green markers) and the experimental water density (red line) Sengers and Watson (1986). The right-hand axis indicates our simulated (black markers) and the experimental (blue line) shear viscosities Kestin et al. (1985). Red and yellow circles represent shear viscosities predicted by other MD studies Holmboe and Bourg (2014); Medina et al. (2011).

*Table 1.38: MD simulation predictions of the self-diffusion coefficients D (**10^{-9} m^2/s**) and activation energy of diffusion (kJmol^{-1}) values for dissolved gas in bulk water*

	He	H_2	CO_2	Ar	CH_4	H_2O
T [K]						
300	8.52 ± 0.53	6.35 ± 0.26	2.64 ± 0.06	2.86 ± 0.10	2.61 ± 0.08	2.95 ± 0.01
350	16.11 ± 0.7	11.05 ± 0.78	5.11 ± 0.11	6.32 ± 0.31	5.59 ± 0.15	6.41 ± 0.05
375	20.79 ± 1.28	13.61± 0.44	6.57 ± 0.21	8.95 ± 0.34	6.96 ± 0.23	8.44 ± 0.11
$E_{a,MD}$	11.13 ± 0.00	9.54 ± 0.00	11.41 ± 0.00	14.16 ± 0.00	12.44 ± 0.04	11.58 ± 0.12
$E_{a,EXP}$	11.70 [a]	16.06 [a]	19.51 [a]	19.81 [a]	18.36 [a]	16.50 [b]

[a] Boudreau (1997) Boudreau (1997). and Jähne et al. (1987). Jähne et al. (1987a).
[b] Ioannis et al. (2019) Tsimpanogiannis et al. (2019).

general agreement with the experimental data Boudreau (1997); Jähne et al. (1987a). An average deviation of about 26% is observed and could be related to the inability of the SPC/E-gas model to accurately predict the experimental value of the diffusion coefficient. For example, Moultos et al. Moultos et al. (2014) have done extensive work on the diffusivity of CO_2 gas by combining different CO_2 and H_2O force field models. In their work, they have a D_0 value of $2.7 \pm 0.5\ 10^{-9}m^2/s$ for CO_2 in the SPC/E-EPM2 model at 1 bar and 298.15 K. This is in agreement with the experimental value of the diffusion coefficient. This agrees with the value predicted in this work ($2.80 \pm 0.30\ 10^{-9}m^2/s$ at 1 bar and 300 K). They concluded from their work that the combination of the TIP4P/2005 H_2O model with the EPM2 CO_2 model (approximately 2% deviation) accurately predicts the experimental diffusion coefficient of CO_2 in bulk water.

As expected, the D_0 values increase with increasing temperature (Table 1.38). The directly proportional relationship between the diffusion coefficient and temperature is a well-known concept from a theoretical and experimental understanding of diffusion Longsworth (1954); Han and Bartels (1996); Krynicki et al. (1978). Furthermore, the D_0 values were fitted to the Stokes-Einstein relation . Figure 1.119 shows that D_0 generally decreases as the size (hydrodynamic radius) of the gas molecule increases, and it asymptotically reaches zero. It can also be seen that MD deviates slightly from the experiment, which represents the overestimation of the MD simulation compared to the experiment. Similar to water, the E_a values for gases are also underestimated with an average deviation of about 30%. A correction value is calculated which is added to the E_a values from the MD simulations gases in clay.

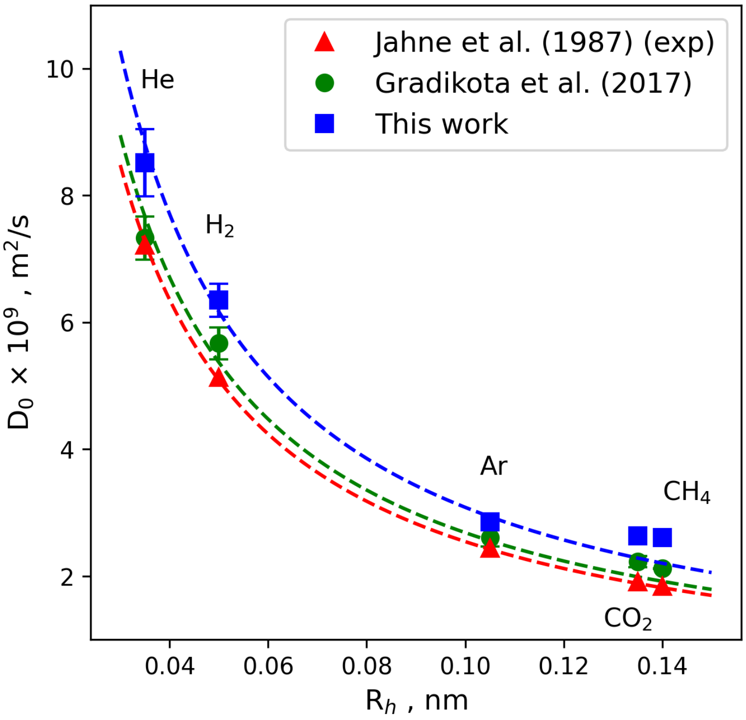

Figure 1.119: Self-diffusion coefficients of gas solutes in bulk water as a function of the solute hydrodynamic radius from MD predictions from our results and other results obtained from experiments and previously reported MD predictions Gadikota et al. (2017a); Jähne et al. (1987a).

1.6.3.2. Pore size effect on the diffusion of gases

To investigate the dependence of the mobility of gases in Na-MMT interlayer nanopores on pore size and temperature, a series of molecular dynamics simulations were performed for 5 gases (He, H_2, CO_2, Ar, CH_4) at 7 different nanopore sizes (with an average increase in base distance of about 0.265 nm). Molecular dynamics simulations were performed in a slit pore setup in which water with gas molecules at the solubility limit concentration is confined between montmorillonite particles at temperatures 300, 350, and 375 K. In the results, an increase in the D value of gases with increasing temperature is observed in the clay nanopore. This is similar to the behavior observed in the bulk simulations, experimental and theoretical studies. However, for different pore sizes, the D value of the gases increases at different rates. For example, when the temperature increases from 300 to 350 K, the D value for He gas increases from 2.59×10^{-9} to 5.18×10^{-9} m^2/s for a pore size of 1.0 nm, an increase of about 2 times, while it is only about 1.5 times higher for a pore size of 2.6 nm.

It is also observed that the self-diffusion coefficient of He at a pore size of 1.0 nm, for example, is $2.59 \pm 0.14\ 10^{-9}$ m^2/s at 300 K. However, when the pore size is increased to 2.6 nm at the same temperature, an approximately 3-fold increase in diffusivity is observed with a resultant value of $7.46 \pm 0.67\ 10^{-9}$ m^2/s at 300 K. A similar increase is observed in all other gas simulations with an average factor of about 2.5 times. It can be concluded that the diffusion coefficient of gases confined in Na-MMT increases with increasing pore size and shows different rates at different temperature-pore size pairs. This relationship is also supported byprevious studies Wang et al. (2018); Yuan et al. (2014); Kim et al. (2015). For example, Wang et al. (2018) reported in their MD simulation that the self-diffusion of CH_4 in Ca-MMT increases with increasing interlayer pore size in the range of 1.8 - 50 nm. Experimental diffusion methods used

Table 1.39: $D_{0,f}$ and k_c fitting parameters from the fit of the MD simulation

		He	H_2	CO_2	Ar	CH_4
	T [K]					
$D_{0,f}$	300	9.85	7.02	2.58	2.91	2.22
	350	15.86	12.58	5.05	64.44	4.57
	375	18.82	15.14	6.25	6.81	8.80
k_c	300	0.67	0.69	0.74	0.71	0.71
	350	0.68	0.73	0.76	0.71	0.71
	375	0.67	0.71	0.75	0.70	0.70

byYuan et al. (2014) on a shale rock also show that gas diffusion is higher in micrometer-sized pores than in nanometer-sized pores. Furthermore, Kim et al. (2015) concluded in their experimental studies that the Knudsen diffusion coefficient of gas increases with increasing pore radius.Wang et al. (2016c,b) sufficiently characterized the pressure-driven flow behavior of hydrocarbons and carbon dioxide in shale nanopores by the slip-corrected Poiseuille equation and derived that the slip length depends exponentially on the pore size.

A power curve given by eq 1.20 was fitted to the MD simulation results to model the behavior of the diffusion coefficient of gas as a function of pore size:

$$D = D_{0,f} - \frac{k_c}{h} D_{0,f} \tag{1.20}$$

where h is the pore width (expressed as pore diameter in nm) of the clay, $D_{0,f}$ is the diffusion coefficient in bulk water from the fit, and k_c is a fitting parameter relating to the clay surface. $D_{f,0}$ and k_c values from the fit are listed in Table 1.39.

Figure 1.120 shows the results for the diffusion of gases in Na-MMT at temperatures of 300, 350, and 375 K, fitted with eq 1.20. The $D_{0,f}$ values obtained from the fitting agree with the D_0 values measured in the bulk MD simulations. k_c values range from 0.67 - 0.76 nm with an average of 0.71 nm. A similar trend in diffusion behavior with respect to pore size is observed for all gases, with the D value increasing with increasing pore size. It is also observed that for the same pore size, the size of the gas affects the diffusion coefficient in a similar way as observed in the bulk simulations. For example, it can be observed that He gas with the smallest size is the fastest (black curve in Figure 1.120) and CH_4 gas with the largest size is the slowest (blue curve in Figure 1.120).

Gadikota et al. (2017a) studied the hydrophobic solvation of gases (CO_2, CH_4, H_2, noble gases) in interlayer clay nanopores. In their simulation, the predicted diffusion coefficient of the studied gases at ambient conditions is about 1.5 times larger than the values obtained in this work for a 2W hydrated layer system. This difference can be attributed to the charge of the clay layer used in their studies and also to the fact that their clay layer was simulated as a rigid body. In this work, the clay layer was simulated as a fully flexible body. Nevertheless, the D value for CH_4 from the MD simulation of Hu et al. (2021) (0.43×10^{-9} m^2/s) is close to the value determined in this work (0.49×10^{-9} m^2/s) for a 2W hydrated layer system. In the study by Myshakin et al. (2013), they give simulation values for the diffusion of CO_2 in hydrated Na-MMT. They obtained a D value of 0.82 ± 0.05 10^{-9} m^2/s, which agrees with the value obtained in this work (0.60 $\pm$ 0.10 10^{-9} m^2/s) for a 2W hydrated layer at 300 K and 1 bar. The slightly lower value can be attributed to the different concentrations of CO_2 in the hydrated nanopore in the two studies (molar ratio of 0.2 in their work and 0.01 in this study). From their work, they deduced that the diffusion coefficient for CO_2 increases with increasing concentration due to the associated expansion of the interlayer nanopore.

To investigate the influence of the clay layer on the diffusion of the interlayer species, the diffusion coefficients of the gas in the clay layer nanopore were normalized by the diffusion coefficient of the gas in the

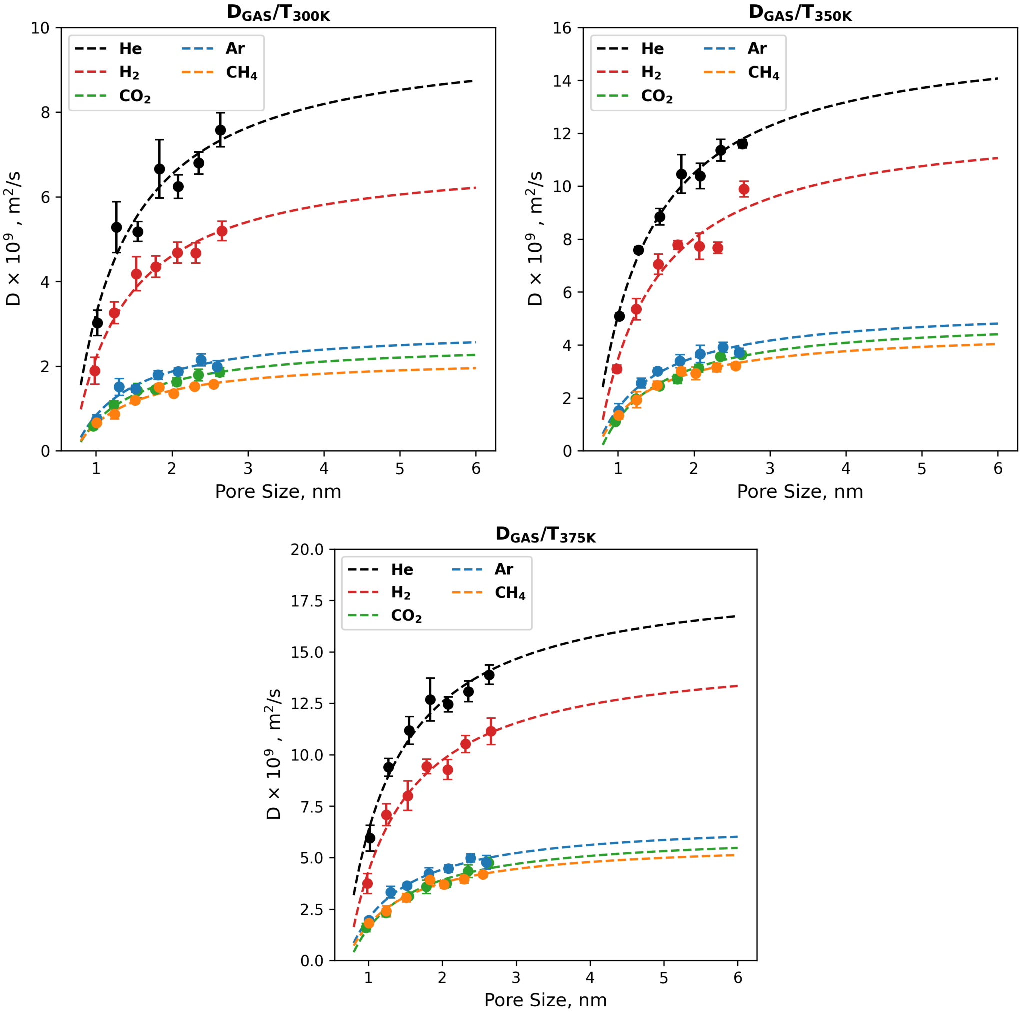

Figure 1.120: Diffusion coefficient of gases in saturated Na-MMT as a function of pore size fitted with eq 1.20 at temperatures (a) 300 K (b) 350 K and (c) 375 K.

bulk water (D_0) predicted by our MD simulation. The normalized values could then be fitted to the function in eq 1.21 by a simple rearrangement of eq 1.20.

$$\frac{D}{D_0} = 1 - \frac{k_c}{h} \tag{1.21}$$

The curve in Figure 1.121 represents an average value for all temperatures and follows the conclusion ofWang et al. (2016c), that the ratio at different temperatures almost converges to a single curve as a function of pore spacing, indicating an empirical correlation. Due to the limited transport space, diffusion of entrapped species through the clay layers is hindered. Therefore, the diffusion coefficients of gases are slower under confinement than in bulk. As the size of the nanopores increases, the D of the gases shows a monotonically increasing trend and asymptotically approaches the value of the bulk. However, this behavior is different for all gases, so that H_2 approaches the bulk value faster than, for example, CH_4. This shows that the effect of confinement is different for different gases. One could argue that this difference could be due to the nature of the interactions between the gas, liquid, and clay layer. This will be further investigated in the next sections.

From the fit, we could derive a more robust equation relating the diffusion coefficient to the pore size for all types of gases by inculcating macroscopic variables. To achieve this, eq 1.21 was further expanded by applying Bourg et al. Bourg and Sposito (2010) formulation which connects molecular scale diffusion to continuum scale (eq 1.22). With this formulation, we are able to calculate the apparent diffusion coefficient of gases in clay medium for variable pore sizes as described by eq 1.23.

$$D_a = \frac{q_{nano}}{G} D_0 \tag{1.22}$$

$$D_a = \frac{D_0}{G}\left(1 - \frac{k_c}{h_{av}}\right) \tag{1.23}$$

where D_a is the apparent diffusion coefficient of the gas, D_0 is the diffusion coefficient of the gas in bulk water, q_{nano} is the relative diffusion coefficient (D/D_0) from MD simulation, G is the geometric factor and h_{av} is average pore width.

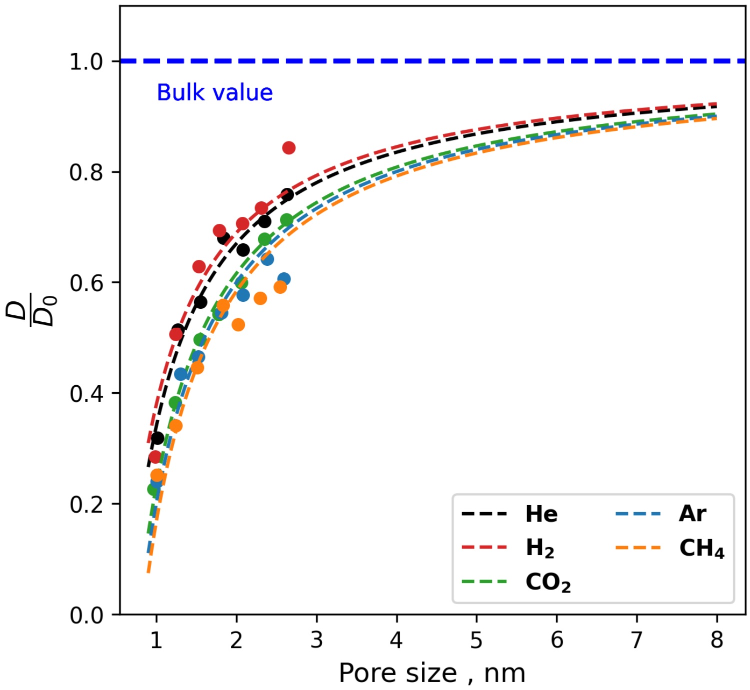

Figure 1.121: A fit showing the relative diffusion coefficient of gases (D/D_0) in clay nanopores as a function of pore size. The marker dots represent averaged D/D_0 for temperatures of 300, 350, and 375 K. The lines represent the fit of D/D_0 with eq 1.21.

In most diffusion experiments, a single effective or pore diffusion coefficient is given, which is an average sum over all pore sizes. These simple formulations, such as eq 1.21 and eq 1.23, are useful for testing theories and explaining experimental results by providing a microscopic view. In addition, they provide a basis for easy incorporation into an up-scaling framework, such as Lattice Boltzmann, which can be advantageous in linking nanoscale simulations with macroscale measurements.

Comparison of MD simulation with experimental investigations: In general, direct experimental measurement of gas diffusion coefficients in clay nanopores is not possible Gadikota et al. (2017a). Therefore, a direct one-to-one mapping of simulation to experimental data is not easily achieved. The reason is that the experimental measurements are performed at a macro scale, where all the complex geometry of the clay matrix such as heterogeneity, pore network, pore distribution, and tortuosity is taken into account. Therefore, observing the relative trends in the experimental and theoretical data is more appropriate for validating the simulation. Nevertheless, it is possible to compare the simulation results for the bulk fluid. A cross-comparison of simulations and experimental data as a function of macroscopic parameters such as temperature and porosity could also be performed.

In order to compare our simulations with the experimental results, eq 1.23 was used to calculate the apparent diffusion coefficients (D_a). The D_a obtained from the formulation is then compared to the D_a measured directly from the double-through diffusion experiment of Jacops et al. (2017d). They calculated geometric factors for gases in Boom clays. They also reduced the pore size distribution to a single pore size (R_{pore}) calculated by fitting their data to a single pore size hydraulic conductivity model obtained from hydraulic conductivity experiments. Using the geometric factors and pore sizes from their experiments as input parameters for eq 1.23 we can reproduce the apparent diffusion coefficients measured directly from the experiments.

Figure 1.122 shows a plot of the apparent diffusion coefficients obtained from experiments with gases in three different types of Boom clay having varying porosity and pore size distribution Jacops et al. (2017d). It also shows a plot of apparent diffusion coefficients as a function of hydrodynamic radius predicted with eq 1.23 using molecular diffusivity of gaseous molecules calculated by molecular dunalic simulations and average pore size fitted to the experimental data of Jacops et al. (2017d). . It can be seen from the plots that the values obtained from experiments agree with those obtained from eq 1.23 Jacops et al. (2017d). Although Jacops et al. Jacops et al. (2017d) had some challenges in their measurements, the plots show that with accurate values for the geometric factor and dominant pore size, it is possible to reproduce the experimental results of the apparent diffusion coefficient for clays with eq 1.23.

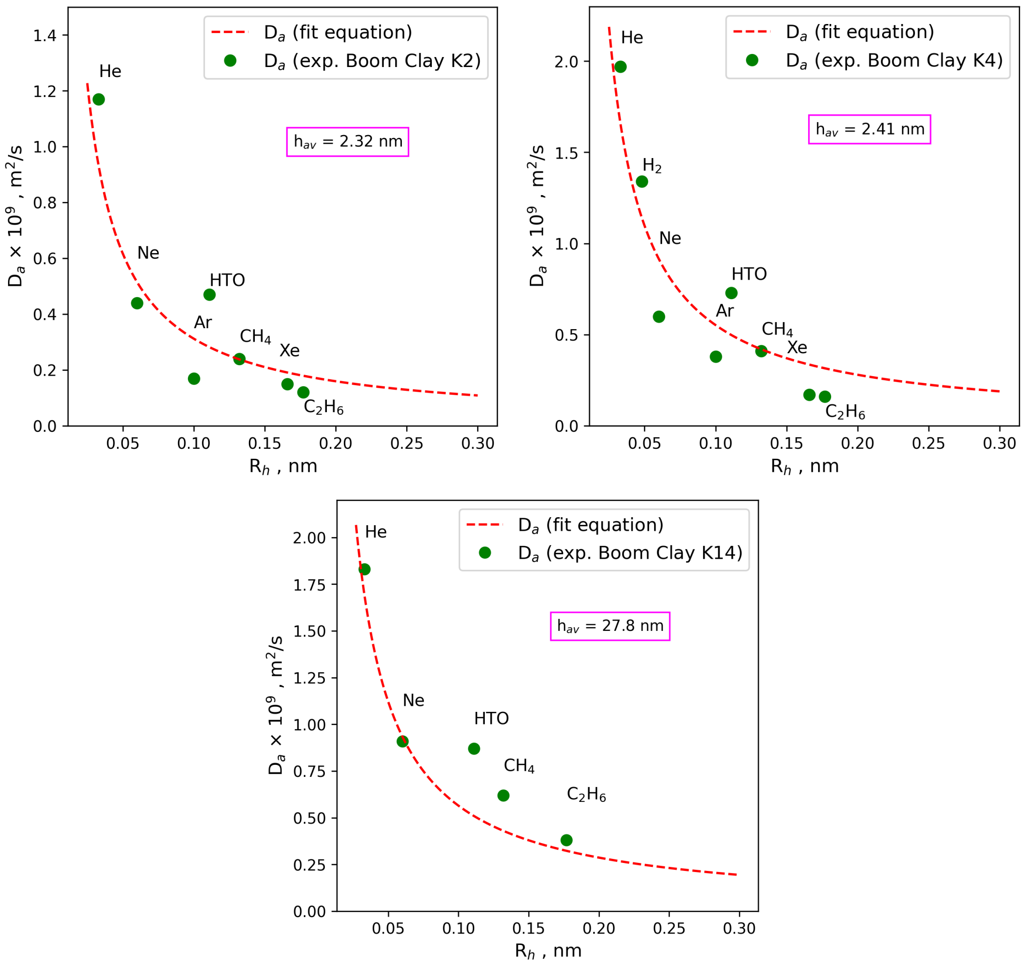

Figure 1.122: Apparent diffusion coefficients obtained from experiments of gases in three different Boom clays with varying pore size distribution and porosity, as well as apparent diffusion coefficients calculated with eq 1.23 fitted as a function of the hydrodynamic radius

1.6.3.3. Pore size and water-gas mixture effect on diffusion of water

To investigate the degree of influence of the clay layer on the self-diffusion of water in the water-gas mixture, the diffusion coefficients of water in the clay layer nanopore were normalized by the diffusion coefficient of water (D_0) in the bulk water predicted by our MD simulation procedure.

Figure 1.123 shows a plot of the D/D_0 values of water in Na-MMT nanopores as a function of pore size, calculated for each hydration state of the water-gas mixture and averaged over all temperatures (fitted with eq 1.21). It can be observed that confinement has a significant effect on the diffusion of water in the Na-MMT nanopores, with an increase in pore size leading to a corresponding increase in D values. This behavior is similar to that observed in previous studies for water and ion diffusion from MD simulations Holmboe and Bourg (2014); Tsimpanogiannis et al. (2019); Botan et al. (2011); Ngouana W and Kalinichev (2014a); Wang et al. (2006). Holmboe and Bourg (2014) investigated the diffusion of water through MD simulations in Na-MMT nanopores and found that confinement significantly affects the diffusion of bulk water by a reduction factor of about 20-90% at different pore sizes. In the studies of Botan et al. (2011), the D value of diffusion of SPC/E water in Na-MMT pores is reduced by about 70% compared to the bulk value due to the higher density and surface effects near the clay walls. Other types of clays have also been studied for their confining effect on water dynamics: Zhou et al. Zhou et al. (2016) showed that the self-diffusion coefficient of water in montmorillonite is faster than that of water in an Mg-rich clay. Ngouana et al. Ngouana W and Kalinichev (2014a) studied the structure and dynamics of hydrated Cs-montmorillonite and found that the mobility of Cs ions and H_2O diffusion coefficients increased with increasing water content and distance from the clay surface. They observed the typical structuring of water molecules due to their increased concentration at the surface of the clay layer with increasing water content, indicating a hydrophilic nature of water at the clay surface. Wang et al. Wang et al. (2006) applied molecular dynamics simulations to study the properties of interfacial water on surfaces of brucite, gibbsite, hydrotalcite, etc. They found that the differences in structural charge on the octahedral layer, the cation occupancies and distributions, and the orientations of the OH groups affect the surface water structure. From the atomic density profiles, they were able to determine that the structural properties of the water at the surface of talc and muscovite are different. The water exhibits a hydrophobic property at the talc surface and hydrophilic properties at the muscovite surface Wang et al. (2006). The smectite interactions in this study show high hydrophilicity. This could be observed from the high-density water structure at the surface of the Na-montmorillonite (see Figure 1.124). This is consistent with a comprehensive study by Szczerba et al. Szczerba et al. (2020). They applied molecular dynamics simulations to quantify the hydrophobicity and hydrophilicity of charged smectite-siloxane surfaces. They found that the hydrophobicity and hydrophilicity of smectite surfaces depend on the consideration of counterions in the integral part of the surface. They concluded that a smectite surface without counterions is hydrophobic or moderately hydrophilic. However, when counterions are included, the surface is strongly hydrophilic Szczerba et al. (2020).

In the work ofTsimpanogiannis et al. (2019), they evaluated the self-diffusion of confined water for a variety of confinement systems representing materials that differ in chemical nature, shape, size, and surface charge distribution. These features significantly affect the structural and transport properties of the confined fluid near the interface. They observed differences in the confinement effects of carbon compounds, minerals, biomolecules, and other confining media. From this, they concluded that the type of confining material plays an important role in affecting water diffusion Tsimpanogiannis et al. (2019) . At mineral surfaces, in particular, the presence of water leads to interactions between the water and the surface. Thus, water with hydrophilic mineral surfaces can form hydrogen bonds at the interface, which can divide the water in the pore into so-called water layers and thus cause a reduction in diffusion Ou et al. (2014).

1.6.3.4. Activation energy of diffusion

To determine the temperature dependence of gases and water in Na-MMT, Arrhenius plots of diffusion coefficients were constructed and fitted with a least squares regression line. In this way, the activation energy (E_a) of the diffusion of water (in the water-gas mixture) and of gases could be determined. Corrected

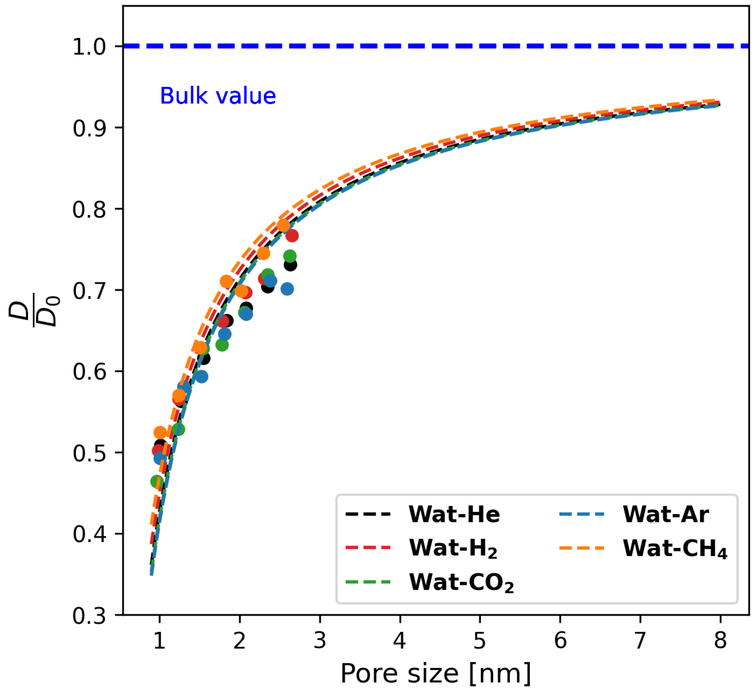

Figure 1.123: Relative diffusion coefficient (D/D_0) of water in a water-gas mixture in clay nanopores as a function of water content/pore size. The marker dots represent D/D_0 for temperatures 300, 350, and 375 K, respectively. The lines represent the fit of D/D_0 with eq 1.21.

E_a values of 8.8, 15.7, 19.0, 16.6, 18.3, and 18.54 were obtained for He, H_2, CO_2, Ar, CH_4, and water respectively.

In general, our results show that the E_a values for water are influenced slightly by the confinement. This effect is due to the structuring of the water molecules near the clay surface, which is more pronounced in the first two layers of water near the surface and decreases thereafter. The average activation energy for water in the Na-MMT is about 18.54 ± 0.31 kJ/mol. This agrees with values obtained by experiments for pure water in clay Van Loon et al. (2002); Sánchez et al. (2009). Van Loon et al. Van Loon et al. (2002) investigated the activation energy of water in Opalinus clay by diffusion and neutron spectroscopy experiments and obtained a value of 22 kJ/mol. Sanchez et al. Sánchez et al. (2009) performed macroscopic and microscopic diffusion experiments on different types of clay materials. In particular, for Na-MMT they obtained values of 20.78 and 11.57 kJ/mol for macro and micro experiments, respectively Sánchez et al. (2009).

On average, the E_a values of water in the confined state are about 11% higher than in the bulk, which is consistent with experimental observations Van Loon et al. (2002); Sánchez et al. (2009). This increase in E_a values is due to the fact that the interaction of water molecules with their neighbors in bulk water is largely based on hydrogen bonds. Therefore, when the environment of a water molecule changes, e.g. water in a Na-MMT, the interactions of the molecule with the clay surface can greatly increase the E_a value from the bulk.

Similarly, for water, confinement has a slight influence on the E_a values of gases. As far as we know, the activation energy of dissolved gases in saturated clay nanopores has not yet been studied. From our results, the monoatomic gases (He, Ar) in the Na-MMT confinement have E_a values deviating about 20% below that of the bulk water, while the polyatomic gases in the Na-MMT confinement have E_a values deviating about 3% below that of the bulk water. One could argue that He and Ar are spherically symmetric, non-polar gases, so we do not expect strong interactions with the clay surface. However, the water itself in the water-gas mixture interacts with the clay surface, changing the dynamics of the water so that the monoatomic gases can move more freely from one water cage to another than is the case in the bulk. In the case of polyatomic gases, a much stronger interaction with the clay surface and with the water is possible, therefore gases are not able to move freely as compared to monoatomic gases. Nevertheless, the E_a for gases in clay can be taken as that of the E_a obtained in bulk water.

1.6.3.5. Structure of gas and aqueous fluids in clay interlayer

To further investigate the structure of the intercalated gas-water mixture, atomic density profiles, and radial pair correlation calculations were performed. Atomic density profiles for pore sizes 1.0 and 2.1 nm are presented in this section.

1.6.3.6. Atomic density profiles

The average density profile of the gases in the interlayer region along the vertical axis is shown in Figure 1.124. Regions 1 and 2 show the regions of inner- and outer- spheres defined by Vasconcelos et al. Vasconcelos et al. (2007) at a distance from the siloxane surface. The water molecules in Region 1 on both surfaces form hydrogen bonds with oxygen atoms on both surfaces and are therefore strongly oriented. The shoulder peaks of Hw (hydrogen of water) at about 15.0 and 9.8 Å (pore size 1.0 and 2.1 nm respectively) on the z-axis indicate the orientation of the Hw molecules on the siloxane surface. The presence of the surface strongly influences the distribution of the water molecules up to a distance of about 5 Å from the clay surface. From this point on, the water molecules are distributed rather randomly, as is to be expected in the bulk and as can be seen from the almost flat central area of the profile in Figure 1.124b. This is not the same for pore size at 1.0 nm as molecules tend to be distributed only at the surface of the clay. Although the negatively charged clay surface attracts the Na^+ ions, as can be seen from the two peaks near the surface, Na^+ tends to form outer-sphere complexes due to its hydrophilic nature and the orientation of the water molecules.

In all seven cases where the pore size varies between 1.0 and 2.6 nm, gases have two distinct peaks near the two clay surfaces, indicating that gases have a fairly strong affinity for the clay surface. He and H_2 have a broader peak whose tails extend closer to the siloxane surface than the other gases (see Figure 1.124). This is probably due to the small size of the gas molecules. It appears that He and H_2 have a large mobility parallel to the clay surface. Ar, CO_2, and CH_4, on the other hand, have peaks in the density overlapping with high-density water regions due to their large size.

Radial distribution functions: The RDF values are summarised in Table 1.40. To fully understand the interaction strength of the gas-liquid and gas-surface structure, we calculated the average coordination number of oxygen atoms around a gas particle.

Table 1.40 shows the coordination numbers of Ow and Ob around gases at a pore size of 2.1 nm. The total number of oxygen atoms surrounding the gases was calculated as Nt_O, which is the sum of the coordination numbers of the oxygen of the water and the oxygen of the siloxane surface. The values are in agreement with the results reported in previous studies Gadikota et al. (2017a); Koh et al. (2000); De Jong et al. (1997); Broadbent and Neilson (1994). As for the gas-oxygen (water) coordination number, our results are in agreement with the values obtained by neutron diffraction (CH_4, 19 ± 2 De Jong et al. (1997); Ar, 16 ± 2 Broadbent and Neilson (1994)). The results show that the least coordinated gas has the highest mobility and vice versa. It can be concluded that as the interaction with the water and the clay surface increases, the mobility of the gases decreases.

1.6.4. Results for Partially Saturated System

Equilibrium and non-equilibrium molecular dynamics simulations reported below were conducted for partially saturated montmorillonite pores at different pore size distribution, temperature and concentrations of gases and published in Owusu et al. (2023).

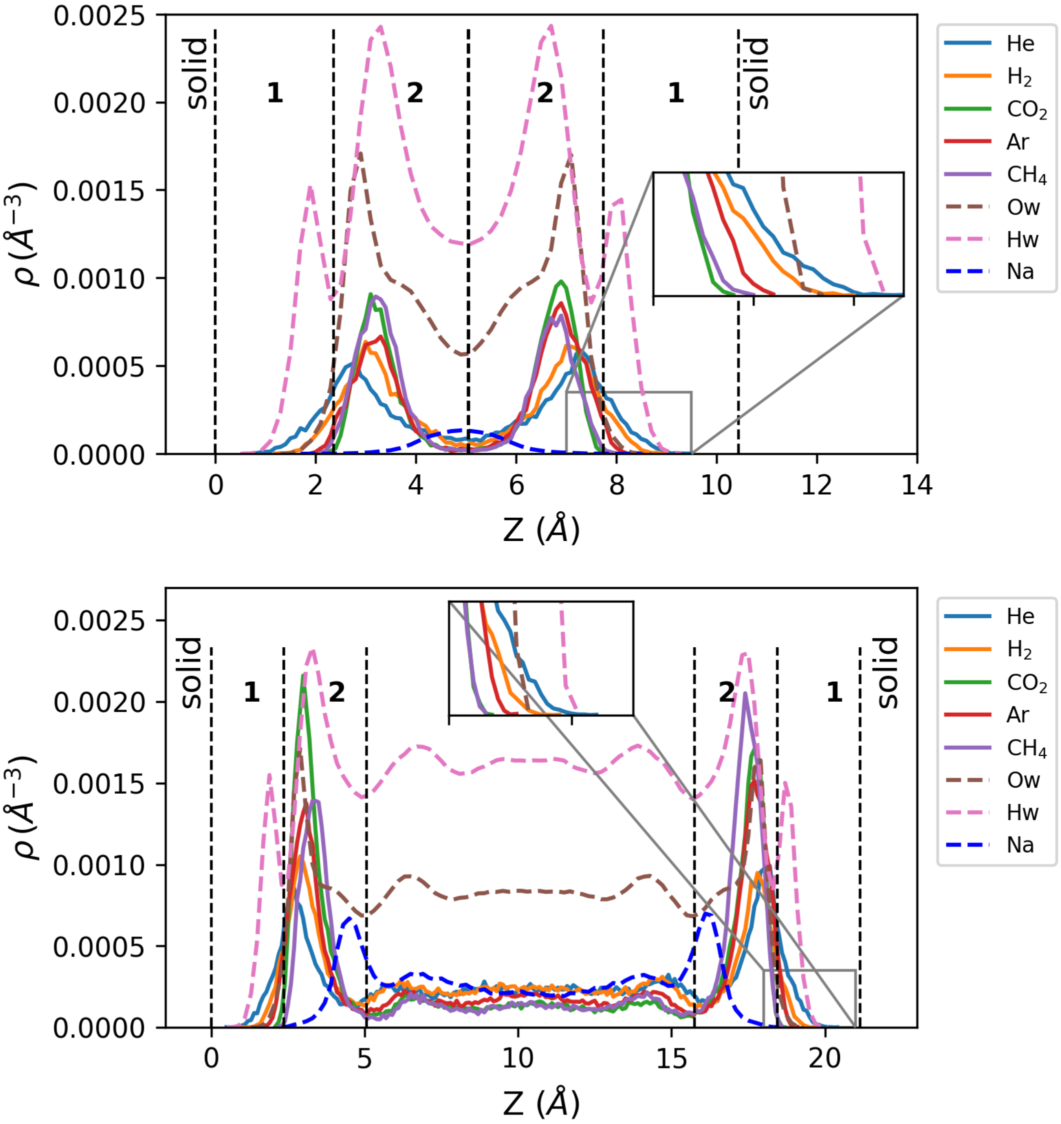

Figure 1.124: Density profiles of gases, water, and Na^+ ions at a pore size of (a) 1.0 and (b) 2.1 nm. The values of Ow and Hw are scaled down to 5% for better visualization

1.6.4.1. Self-diffusion of gas molecules

The self-diffusion coefficients of gas molecules were first studied by simulating a system of 1000 gas molecules at temperatures of 300 K and 330 K and a pressure of 12 MPa for each type of gas. The system was equilibrated in the NVE ensemble for 200 ps. A further equilibration of 1 ns was performed in the NPT ensemble. This was followed by a production run of 5 ns in the NVT ensemble to calculate the self-diffusion coefficients. Table 1.41 shows the values of the self-diffusion coefficients of gas molecules from the MD predictions.

To verify and validate the model parameters and the values of the self-diffusion coefficients, the results of the MD simulations were compared with experimental data Woessner et al. (1969); Robb and Drickamer (1951); Groß et al. (1998); Chen et al. (2001) and also evaluated using an empirical procedure Slattery and Bird (1958); Stiel and Thodos (1965); Lamb et al. (1981). Both data sets agree very well with the empirical relationships. Calculations from the kinetic theory of gases have been used in the past to estimate the diffusion coefficient, viscosity, and thermal conductivity of dilute gases using their intermolecular forces Hirschfelder et al. (1964). This approach was extended by Slattery et al. Slattery and Bird (1958)

Table 1.40: Coordination numbers of water and clay oxygen around gases at pore size 2.1 nm

	$Nt_O{}^a(O_w, O_b)$	$r_{max}{}^b$	$r_{min}{}^c$
He	13.8 (11.8, 2.0)	3.00	4.42
H_2	16.8 (14.3, 2.5)	3.23	4.65
Ar	17.3 (14.3, 3.0)	3.52	4.80
CO_2	19.7 (15.0, 4.7)	3.82	5.10
CH_4	20.2 (15.3, 3.7)	3.67	4.96

[a] Nt_O is the total coordination number of oxygen around gases.
[b] r_{max} is the maximum peak distance of first coordination shell.
[c] r_{min} is the minimum peak distance of first coordination shell.

Table 1.41: Predicted self-diffusion coefficients of gas molecules D (10^{-6} m^2/s) at 12 MPa

	H_2	He	CH_4	Ar	CO_2
T [K]					
300	1.470	1.257	0.164	0.134	0.040
330	1.511	1.486	0.217	0.161	0.069

by developing a relation from dimensional analysis considerations and experimental diffusivities using Enskog's kinetic theory for dense gases. Their formulation can predict the self-diffusion coefficients of dense non-polar gases. Based on the work of Slattery and Bird. Slattery and Bird (1958) , Stiel et al. Stiel and Thodos (1965) developed a comprehensive relation for calculating the self-diffusion coefficient of polar, non-polar, and binary gas mixtures for dense gases.

In this study, the density of gas molecules at equilibrium was used to predict the self-diffusion coefficients using the empirical formulation of Stiel et al. Stiel and Thodos (1965) (Eq 1.24 and Eq 1.25) and Slattery et al. Slattery and Bird (1958) (Eq 1.26). Equation 1.24 and Eq 1.25 apply to Ar, H_2, CO_2, and CH_4 gas, while Eq 1.26 applies to He gas:

$$(\rho D)\xi = 0.464 \times 10^{-5} [1.391\, T_R - 0.381]^{2/3} \;\; for T_R < 1.5 \tag{1.24}$$

and

$$(\rho D)\xi = 0.488 \times 10^{-5}\, T_R{}^{0.777} \;\; for T_R >= 1.5 \tag{1.25}$$

and

$$(pD)\frac{M^{1/2}}{P_c^{2/3} T_c^{5/6}} = 3.882 \times 10^{-4}\, T_R{}^{1.823} \tag{1.26}$$

where ρ is the gas density, D is the diffusion coefficient, $\xi = T_c^{1/6}/M^{1/2}P_c^{2/3}$, p is system pressure, T_c is critical temperature of gas, P_c is critical pressure of gas, M is the molecular weight and Tr is the reduced temperature (T/T_c).

Figure 1.125 shows a plot of the self-diffusion coefficients of gas molecules as a function of gas density from MD predictions. The graph also shows the values calculated from the empirical procedure and experiments. From Figure 1.125 it can be seen that the self-diffusion coefficient of gas molecules is inversely proportional to the gas density. The fitting line in Figure 1.125 represents a fitting of the diffusion coefficients at low densities using the Chapman-Enskog theory described by Chapman and Cowling Chapman and Cowling (1990).

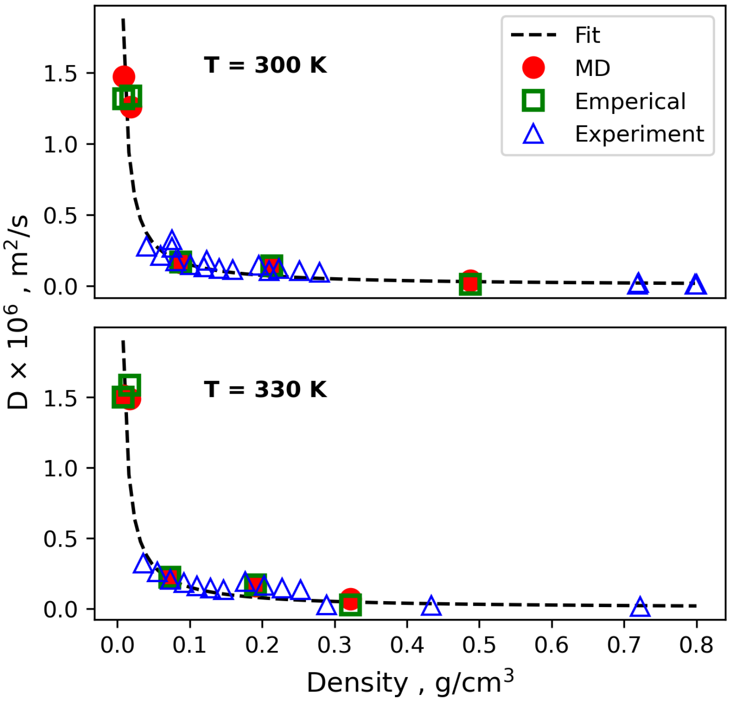

Figure 1.125: Predicted self-diffusion coefficients for gas molecules as a function of equilibrium gas density at 12 MPa from MD simulations. The graph includes experimental values Woessner et al. (1969); Robb and Drickamer (1951); Groß et al. (1998); Chen et al. (2001) as well as predictions based on empirical relations. The fitting line shows diffusion coefficients predicted using the Chapman-Enskog theory, described by Chapman and Cowling Chapman and Cowling (1990).

1.6.4.2. Gas partitioning

The distribution of the gas molecules in the water-rich phase was determined from the density profiles (Figure S2-S11) of the gas in the water-rich phase. The partition coefficient (K) and the free energy difference (ΔG) associated with the transfer of the gas molecules into the water-rich phase are obtained. Figure 1.126 illustrates the density distribution of water on the external surface of the clay as a function of gas-filled pore width. At a smaller gas-filled pore width, the density profile shows three highly structured layers of water at distances of 0.3, 0.6, and 0.9 nm from the surface of the clay. This behavior is typical of what can be expected under fully saturated conditions Churakov (2013a); Owusu et al. (2022a). Further away from the surface $>$ 1.0 nm, the density distribution is constant and the water shows a bulk-like behavior.

Taking into account the structuring of the liquid near the clay surface, the partition coefficients and Gibbs free energy of gas transfer were determined for two regions: (a) the partitioning of gas molecules to the solid-liquid interface and (b) the partitioning to the bulk-like water-rich region. These regions are indicated in Figure 1.126 by the colors cyan and pink respectively (insert). The values of gas molecules at the solid-liquid interface (K_I, ΔG_I) and in the bulk-like water region (K_B, ΔG_B) are given in Table 1.42. For a wide range of saturation, the K and ΔG values are essentially constant within the statistical uncertainties of the simulation. Therefore, the results in Table 1.42 represent averaged values over several simulations with different gas-filled pore widths. It is important to note that, in the context of partitioning in the bulk-like water region, our averaging calculations were limited to a range of gas-filled pore widths between 1.8 and 3.3 nm. This restriction was implemented as the region in question is no longer present beyond a gas-filled pore width of 3.3 nm. Similarly, for partitioning at the solid-liquid interface, our results were limited to a range of gas-filled pore widths between 1.8 and 4.3 nm. This was done in accordance with our trajectory analysis, which indicated that for gas-filled pore widths exceeding 4.3 nm (in the case of thin water films),

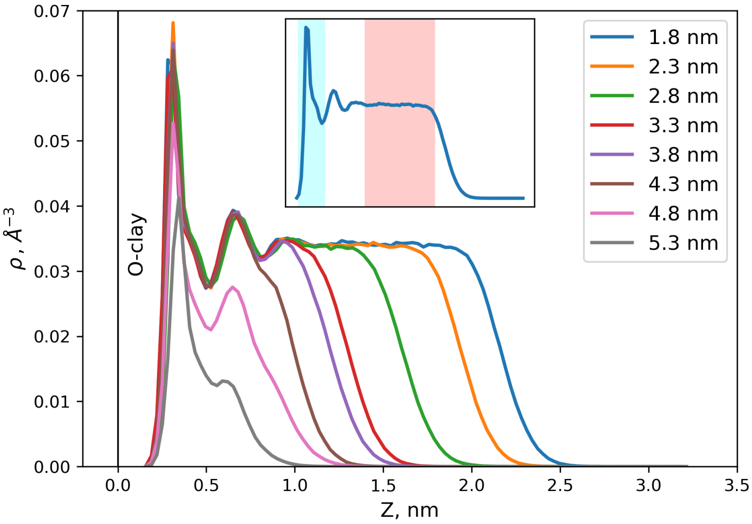

Figure 1.126: Density distribution of water on the external surface of the clay (half pore width). (insert) The cyan-colored area on the density plot shows the solid interface characterized by strong structuring of fluid. This domain is used for the analysis of gas partitioning to the solid-liquid interface. The pink-colored area shows the domain occupied by the bulk-liquid-like phase.

the water molecules tend to cluster around the Na ions, resulting in discontinuous coverage of the clay surface by the water film. As a consequence, gas-filled domains make direct contact with the clay surface.

The results indicate that K_B and K_I increase as the temperature is raised. Moreover, the particle density of the gas molecules was found to impact gas partitioning. CO_2 and Ar, which have molecular masses of 44 and 39.95 g/mol, respectively, exhibit significantly higher partitioning coefficients than He, H_2, and CH_4. Interestingly, despite He having a smaller molecular mass than CH_4, its small molecular size allows for easier penetration into the interstitial spaces between water molecules, resulting in greater partitioning. Prior research has demonstrated a direct relationship between partition coefficient and molecular weight Shimmo et al. (2004); Smedes et al. (2009), as well as polarizability Staikova et al. (2004); Chenzhong and Zhiliang (1998); Raevsky et al. (2009); Lewis (1989).

Table 1.42: Partitioning coefficients K (10^{-7}) and Gibbs free energy of transfer G (kJ mol^{-1}) of gas molecules at the solid-liquid interface and at the bulk-like water region

		H_2	He	CH_4	Ar	CO_2
T [K]						
300						
	K_B	0.97 ± 0.46	2.45 ± 1.30	1.51 ± 0.82	7.90 ± 1.49	138.97 ± 26.29
	K_I	1.22 ± 0.58	2.56 ± 1.02	1.34 ± 0.66	7.26 ± 2.80	142.14 ± 21.72
	G_B	40.64 ± 1.46	38.29 ± 1.23	39.52 ± 1.24	35.09 ± 0.48	27.94 ± 0.50
	G_I	40.07 ± 1.45	38.06 ± 1.00	39.68 ± 0.99	35.53 ± 1.29	27.87 ± 0.41
330						
	K_B	10.94 ± 3.95	20.06 ± 4.44	10.05 ± 4.32	53.02 ± 7.21	389.24 ± 58.56
	K_I	9.15 ± 3.80	20.12 ± 3.46	9.83 ± 5.24	49.03 ± 7.46	392.30 ± 78.15
	G_B	37.84 ± 1.00	36.07 ± 0.64	38.16 ± 1.21	33.35 ± 0.36	27.89 ± 0.41
	G_I	38.35 ± 0.97	36.03 ± 0.50	38.44 ± 1.73	33.57 ± 0.39	27.89 ± 0.55

1.6.4.3. Effect of saturation on the diffusion of gases

The self-diffusion coefficient of gas molecules in the gas phase at temperatures of 300 K and 330 K as a function of the gas-filled pore width, normalized to the diffusion coefficient in the bulk (D_0), is shown in Figure 1.127. It should be noted that gas-filled pore widths below 1.8 nm were excluded from this study because a larger quantity of gas molecules was required to keep the pore space open for gas-phase diffusion. This behavior is likely due to dispersive interactions between opposing water platelets that result in a net attractive force between closely spaced platelets. As the gas-phase pore size increases, this effect diminishes.

The results show that the diffusion coefficient increase with pore size and asymptotically converges towards the value in the bulk state. It was originally believed that a constant value (D_0) over a wide range of pore widths would be obtained by using the survival probability method to calculate the diffusion coefficient associated exclusively with the gas phase in the bulk and that this would eliminate the effects of confinement. However, the opposite was found. The results showed that He gas specifically, was strongly affected by confinement compared to other gases; possibly due to the Knudsen effect. To investigate this, the mean free path of the gas molecules was calculated based on the collisions in the trajectories of the molecular dynamics simulations, and compared with the calculations of the mean free path performed with kinetic theory, which agreed well. Table 1.43 shows the values for the mean free path from molecular dynamics calculations and from kinetic theory for temperatures of 300 and 330 K.

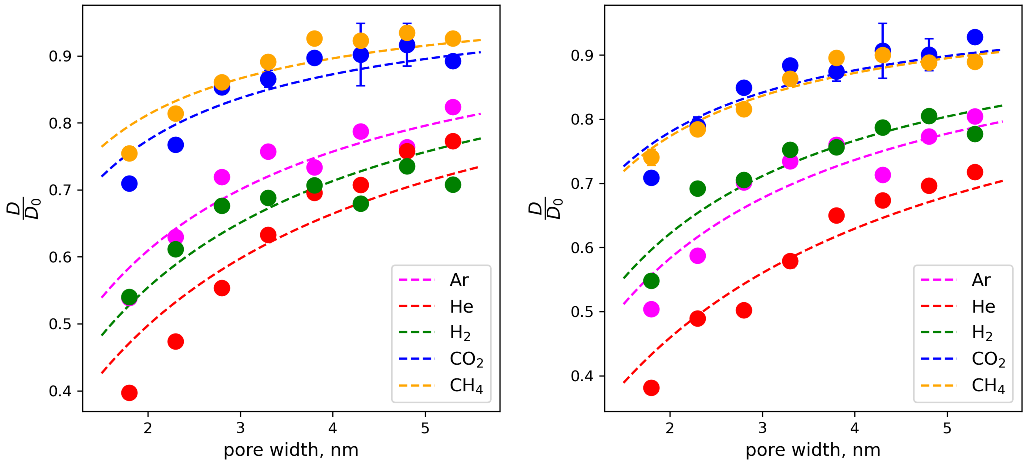

Figure 1.127: Diffusion coefficient (D (10^{-6} m^2/s)) of gas molecules in the bulk gas phase in Na-MMT at 12 MPa as a function of gas-filled pore width (a) 300 K (b) 330 K.

Table 1.43: Mean free path of gas molecules (nm) from MD simulations (λ_{MD}) with $\sigma_{col} = \sigma_{gas}$ and kinetic theory (λ_{KT})

	300 K		330 K	
Gas	λ_{KT}	λ_{MD}	λ_{KT}	λ_{MD}
H_2	8.45	10.47	9.13	12.02
He	10.40	10.91	11.65	11.89
Ar	6.23	6.01	6.87	6.31
CH_4	4.98	4.76	6.09	5.93
CO_2	3.01	3.04	4.59	5.20

σ_{col} is the collision diameter and σ_{gas} is the diameter of the gas molecule which is the Lennard-Jones collision diameter (σ)

In general, it can be observed that the maximum gas-filled pore size is still smaller than the mean free path for most gas molecules. Consequently, the diffusion coefficient is reduced due to collisions with the water interface, which results in gas molecules having a shorter mean free path under confinement. Strong influence is exerted on the He gas because it has the largest mean free path compared to the other gases.

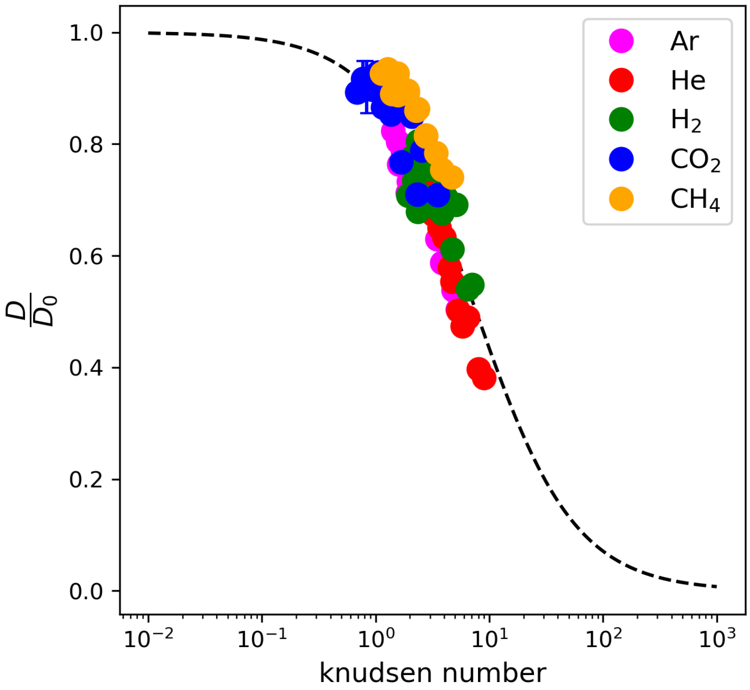

Figure 1.128: Average diffusion coefficient of gas molecules normalized to the diffusion coefficient in a pure bulk system as a function of the Knudsen number and fitted with eqn 1.27. The curve shift observed in this study is attributed to the specific physicochemical conditions considered, which differ from the simplified conditions assumed in the original Bosanquet approximation.

The Knudsen number was calculated from the mean free path and the gas-filled pore sizes. A diagram showing the relationship between the diffusion coefficient and the Knudsen number is shown in Figure 1.128. A mathematical equation developed from the graph after the Bosanquet approximation Pollard and Present (1948); Krishna and van Baten (2012) is given as:

$$D = D_0 \left(\frac{1}{1 + \alpha_d \left(\frac{\lambda}{h - 2t_w} \right)} \right) \tag{1.27}$$

and

$$Kn = \left(\frac{\lambda}{h - 2t_w} \right) \tag{1.28}$$

where D_0 represents the bulk diffusion coefficient in the gas phase at 12 MPa, λ denotes the mean free path of the gas at 12 MPa, h is the width of the pore, t_w is the thickness of the adsorbed water film, which varies with the degree of saturation. The parameter α_d is the Bosanquet correction parameter obtained through fitting and has a value of 0.2.

Based on the work of Yin et al. Yin et al. (2019b) , the identification of three gas diffusion regimes can be made in a porous media, determined by the local Knudsen number. The regimes are characterized by Kn values of ≤ 0.1, $0.1 < \text{Kn} < 10$, and $\text{Kn} \geq 10$. In the case of molecular diffusion ($\text{Kn} \leq 0.1$), intermolecular collisions are dominant. When Knudsen diffusion occurs ($\text{Kn} \geq 10$), the dominant collisions are between molecules and a solid wall. In the case of transition diffusion ($0.1 < \text{Kn} < 10$), significant intermolecular collisions and collisions between molecules and the solid wall occur. The Knudsen number ranges from 0.6 to 6 in our results, indicating that diffusion is in the transition regime, and not purely molecular.

Several studies have shown that the original Bosanquet formula can approximate gas diffusion well in the transition regime Pollard and Present (1948); Guo et al. (2019); Tomadakis and Sotirchos (1993); Ruthven et al. (2012). Guo et al. Guo et al. (2019) used the Boltzmann transport equation to study gas diffusion, and found a Bosanquet correction parameter, α_d of 0.9, where the Knudsen number was determined using the method of the largest sphere. The Knudsen diffusivity derived from the kinetic theory of gases yielded an α_d of 1.8, which underestimated the value obtained by Guo et al. Guo et al. (2019). In this study, we obtained an α_d of 0.2, which appears to overestimate the other predictions. It is worth noting that the original Bosanquet approximation was developed from empirical studies and relies on several idealized conditions. The current system exhibits non-ideal gas behavior due to the high pressure. In addition, the gas-wall collisions may not be perfectly elastic since the wall consists of water molecules. Hence, surface phenomena such as adsorption and water vapor mobility at the gas-water interface may not be captured by the original Bosanquet approximation. Chen et al. Chen and Zhou (2023) investigated the validity of the Bosanquet approximation using equilibrium molecular dynamics simulations and concluded that further modifications to the Bosanquet approximation are necessary to account for the intermolecular forces of fluid molecules and the smoothness of the pore walls.

Experimental data regarding gas diffusion coefficients in partially saturated smectite micropores as a function of gas-filled pore width are currently unavailable. However, a previous investigation of gas diffusion in saturated smectite incorporated a geometric factor and utilized an empirically derived function from a molecular dynamics study Owusu et al. (2022a). This approach produced predictions that closely matched experimental gas diffusion data in Boom clay. Therefore, we propose to adopt a similar methodology in our current study and modify eqn 1.27 accordingly.

$$D = \frac{D_0}{G}\left(\frac{1}{1+\alpha_d\left(\frac{\lambda}{h_{av}-2t_w}\right)}\right) \tag{1.29}$$

where G is the geometric factor and $\mathrm{h_{av}}$ is the average pore width. The geometric factor refers to an empirical parameter accounting for the reduction of the diffusive transport of species in porous media in comparison with the bulk phase due to the geometric complexity of pore space Churakov and Gimmi (2011a). The geometric factor takes into account the tortuosity of diffusion paths, pore constrictivity, and the overall complexity of the clay pore structure. In general, the tortuosity and constrictivity can not be measured independently and are thus often lumped in a single parameter referred to as a geometric factor. This equation allows to predict the gas phase diffusivity for general conditions based on the geometric properties of porous media, mean pore size, and the partial water pressure via the corresponding parameters, G, $\mathrm{h_{av}}$, $\mathrm{t_w}$. A further effect of temperature can be considered following the approach described in our previous study Owusu et al. (2022a).

1.6.4.4. Flow dynamics

The study of fluid behavior necessitates a fundamental understanding of dynamic viscosity. As such, non-equilibrium molecular dynamics simulations were conducted in order to address this objective. A constant force acting on each fluid atom in the direction parallel to the clay surface initiated a fluid flow. Subsequently, the steady-state velocity profiles were analyzed to determine the dynamic viscosity of gas in partially saturated Na-MMT. The Navier-Stokes equation predicted a parabolic (Poiseuille) velocity profile assuming constant viscosity and density. The dynamic viscosity was then obtained. These findings provide valuable insights into the properties of fluids in confined spaces.

Method validation: To validate the simulation setup, non-equilibrium molecular dynamics simulations were conducted for water flow in fully saturated Na-MMT. The resulting velocity and density profiles are shown in Figure 1.129. The density profile of water at the center of the pore remains constant at 1 g/cm^3, indicative of bulk water behavior. Close to the surface, notable fluctuations in water density are observed within a 1 nm region, with a maximum density of approximately 2 g/cm^3. The calculated dynamic viscosity for water in a 6 nm nanopore is 0.634 cP, a value that is in agreement with prior research on the dynamic viscosity of bulk water Botan et al. (2011), flow simulations in a 6 nm Na-MMT nanopore Botan et al. (2011), and experiments with bulk water Haynes (2004), which reported values of 0.66 cP, 0.68 cP, and 0.891 cP, respectively. In contrast to the findings of Botan et al. Botan et al. (2011), deviations from the parabolic flow profile near the surface were not significant in this study. This may be due to the use of a constant force, which is approximately one magnitude of order higher than that utilized in their study Botan et al. (2011). A higher force leads to greater water mobility, thereby diminishing the impact of water-surface interactions. The sliding velocity at the surface was roughly 75 m/s, indicating higher mobility than the study by Botan et al Botan et al. (2011), which reported a velocity of about 4 m/s Botan et al. (2011).

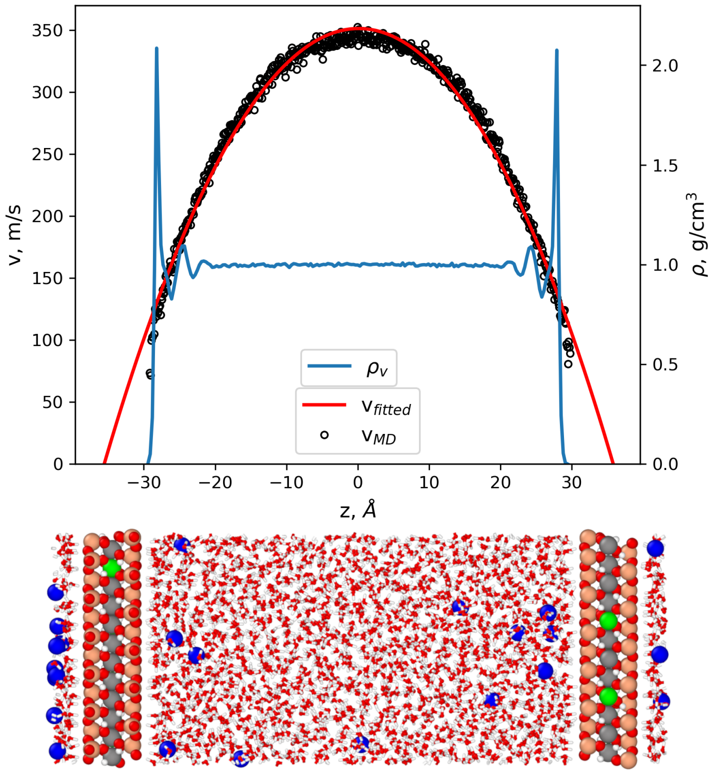

Figure 1.129: Steady-state velocity profile of water flow in Na-MMT. The force is acting parallel to the surface on each fluid atom in the x-direction. This diagram also shows the mass density profile of water. The black markers represent the velocity values from the MD simulation, the red line is the parabolic fit of the Poiseuille flow extrapolated here to the velocity at zero, and the blue line represents the mass density profile of the water.

The boundary condition responsible for the parabolic profile at the center of the pore is a crucial parameter that has been extensively studied Squires and Quake (2005). The slip boundary condition has conventionally been assumed for continuum-scale fluids. In their review on microfluidics, Squire et al. Squires and Quake (2005) demonstrated that the no-slip boundary condition is not valid for gas within distances smaller than the mean free path from the wall. They also showed that non-continuum effects play a role in the boundary conditions of fluids confined to a molecular scale. Experimental techniques used to study microfluidic behavior generally indicate that wetting (hydrophilic) surfaces follow the no-slip boundary condition, whereas non-wetting (hydrophobic) surfaces follow a slip boundary condition Squires and Quake (2005). To reveal the appropriate boundary conditions best applicable to the system and estimate the slip at the solid-liquid and liquid-gas interface the slip length was calculated for each interface. The slip length is defined as the distance within the surface/wall at which the (extrapolated) fluid velocity would be stationary; this can be expressed as:

$$L_s = \pm \frac{v_x(z_{surf})}{\left(\frac{dv_x}{dz}\right)_{z_{surf}}} \tag{1.30}$$

where L_s is the slip length, v_x is the slip velocity at the liquid-solid or gas-water boundary, z_{surf} is the location of the slip surface, and $\left(\frac{dv_x}{dz}\right)_{z_{surf}}$ is the derivative of the slip velocity at the slip surface.

The simulation resulted in a slip length value of 5.00 ± 0.45 Å for flow water in Na-MMT. Although there are no experimental determinations of the slip length, our value is in agreement with the value of 6 Å obtained by Marry et al. Marry et al. (2003) when studying electro-osmosis in Na-MMT.

Gas dynamics in slit pore: As an initial approach, the bulk viscosity of gas species was determined through bulk equilibrium molecular dynamics simulations, utilizing the Green-Kubo method at a temperature of 300 K and pressure of 12 MPa. The obtained results, presented in Table 1.44, indicate good agreement with the experimental values obtained at a temperature of 300 K and pressure of 0.1 MPa. It is thereby demonstrated that the dependence of viscosity on pressure is moderate. Nevertheless, the molecular weight presents a strong influence on the viscosity values.

Table 1.44: Average dynamic viscosity (centipoise) slip length (Å) values for gas dynamics

Gas	μ_0	${}^a\mu_{exp}$	μ_{dry}	Div [%]	L_{DGPD}	L_{CGWPD}	L_{dry}
H_2	0.009	0.009	0.007	-24.4	3.94 ± 1.02	4.29 ± 0.52	41.78
He	0.018	0.020	0.013	-29.2	3.16 ± 0.34	4.24 ± 0.67	54.14
Ar	0.028	0.023	0.021	-1.3	1.24 ± 0.32	1.81 ± 0.35	2.98
CH_4	0.010	0.011	0.004	-5.0	0.65 ± 0.19	0.94 ± 0.45	8.58
CO_2	0.033	0.015	0.014	83.3	0.74 ± 0.13	2.06 ± 0.47	0.65

[a] μ_{exp} is experimental dynamic viscosity values Vogel (2010); May et al. (2007); Cencek et al. (2012); Laesecke and Muzny (2017b,a). μ_0 denotes the viscosity of gas from the bulk gas system using the Green-Kubo method. μ_{dry} is the viscosity of gas in a dry pyrophyllite. L_{DGPD} denotes the slip length for gas in the DGPD. L_{CGWPD} denotes the slip length for gas in a CGWPD. L_{dry} denotes the slip length for gas in the dry pyrophyllite. The symbol Div represents the percent difference between the relative viscosities (μ/μ_0) in the dry pore width and in the maximum partially saturated gas-filled pore width.

Two distinct methodologies have been developed for investigating the dynamics of gas species, as depicted in Figure 1.130: Decoupled Gas Phase Dynamics (DGPD) and Coupled Gas and Water Phase Dynamics (CGWPD). In the DGPD system (Figure 1.130a), the adsorbed water film experience no external forces but rather undergoes weak traction at the gas-water interface due to the coupling of shear stresses resulting from the flow of gas species.

The dynamic viscosity of the gas species is shown in Figure 1.131 as a function of the Knudsen number for DGPD and CGWPD. The findings demonstrate that the viscosity behavior remains unchanged in both DGPD and CGWPD, indicating that dynamic viscosity is an inherent property of the gas. However, a strong dependence of viscosity on the Knudsen number is observed. This means that the pore size and the mean free path of a gas under confinement are crucial in determining the viscous behavior of the gas. By analogy with the successful simulations of diffusion processes, the geometric factor G is added to provide extrapolation from single pore model to macroscopic system using a Bosanquet-type approximation that

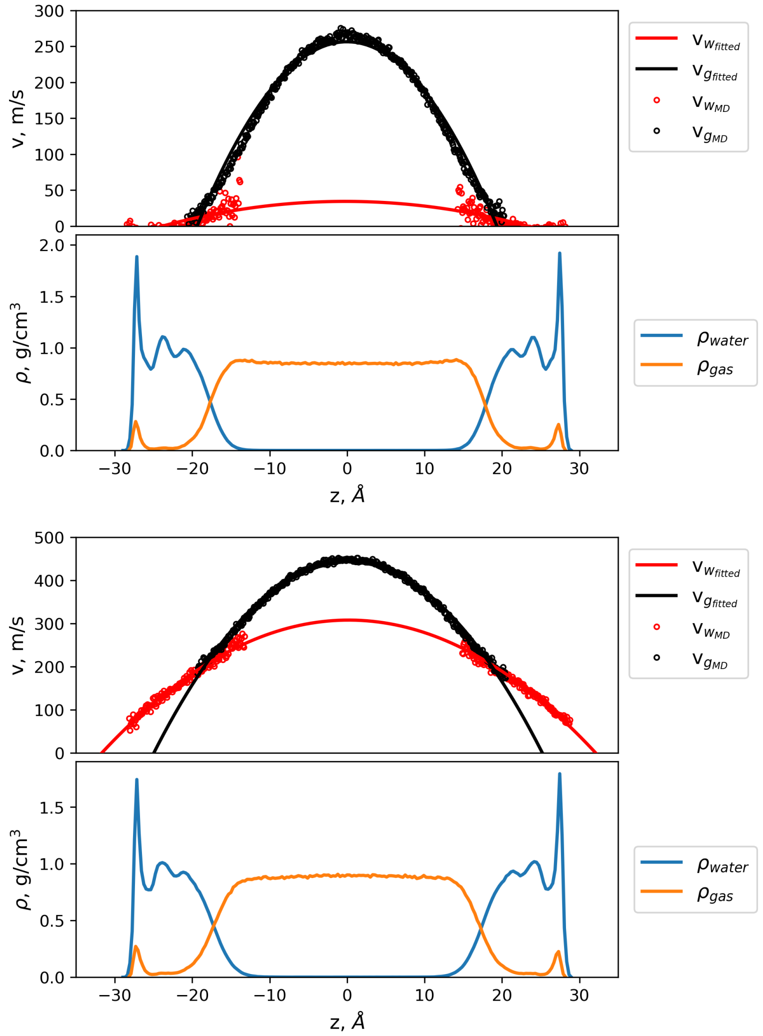

Figure 1.130: Velocity and density profiles of CO_2 gas in steady state at a pore width of 3.3 nm. The red line fits the velocity profile of water, the black line fits the velocity profile of CO_2 gas, the blue is the density profile of water and the orange is the density profile of CO_2 gas. (a) DGPD (b) CGWPD.

satisfactorily describes the Knudsen number dependence of the viscosity:

$$\mu = \frac{\mu_0}{G}\left(\frac{1}{1 + \alpha_v\left(\frac{\lambda}{h_{av} - 2t_w}\right)}\right) \tag{1.31}$$

where μ_0 represents the bulk dynamic viscosity of the gas, λ denotes the mean free path of the gas, h_{av} is the average width of the pore, t_w is the thickness of the adsorbed water film, which varies with the degree of saturation, α_v is the Bosanquet correction parameter obtained through fitting and has a value of 0.5.

Based on the Knudsen number, four flow regimes are recognized by a widely used empirical classification of gas flow in rarefied conditions Barber and Emerson (2006). The Navier-Stokes equation is the best tool to describe flow when $\mathrm{Kn} < 10^{-3}$ because the continuum assumption is valid and is supported by the no-slip boundary condition at the walls. With slip-velocity and temperature-jump boundary conditions, the continuum equations' applicability can be expanded for the regime of $10^{-3} < \mathrm{Kn} < 10^{-1}$ (also known as the slip-flow regime) Agrawal and Prabhu (2008); Dongari et al. (2009). The transition regime $10^{-1} < \mathrm{Kn} < 10^{1}$, is the most challenging to handle. Intermolecular collisions for $\mathrm{Kn} > 10^{1}$ become negligible, and the kinetic theory is typically used to describe the so-called free-molecular flow regime Michalis et al.

(2010).

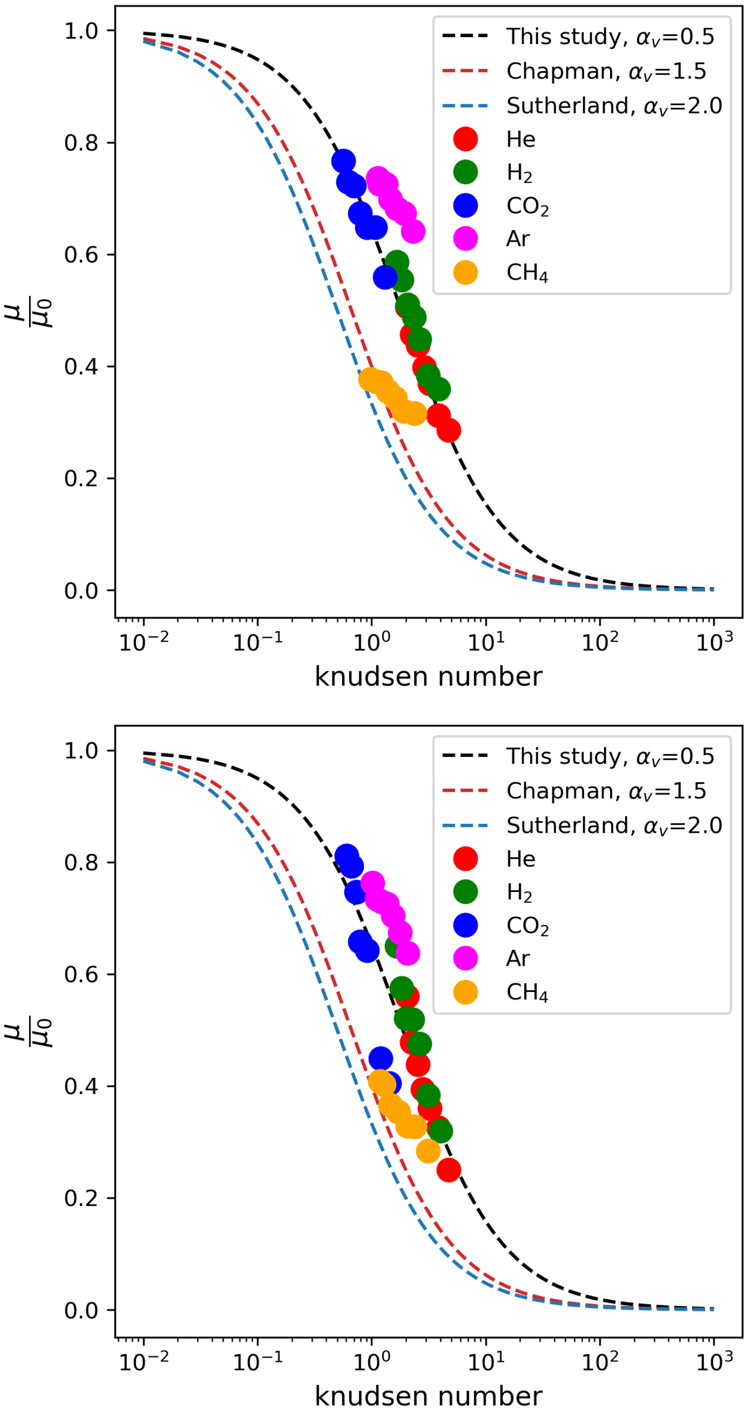

Figure 1.131: Dynamic viscosity of gas molecules in Na-MMT as a function of the Knudsen number(a) DGPD (b) CGWPD.

This study investigates the transition regime of the viscous flow of gas species. The rarefaction (correction) parameter α_v for this study is found to be 0.5, which differs from the values reported in previous studies, such as 1.5 and 2.0 Michalis et al. (2010). This deviation is attributed to the same underlying factor as that discussed for diffusion(see: Effect of saturation on the diffusion of gases). To explore the impact of pore wall type on viscosity, gas flow simulations were conducted in a dry pyrophyllite. The viscosity values and the corresponding percentage deviation of the relative viscosities (μ/μ_0) from the maximum partially saturated gas-filled pore width are presented in Table 1.44. The observed deviation values (Div) of the gas species indicate a pronounced influence of the interacting surface on the dynamic viscosity of the confined gas molecules. Specifically, He, H_2, CH_4, and Ar exhibit a higher affinity towards the liquid wall compared to the solid wall, resulting in reduced relative viscosities, upon contact with water molecules. He and H_2 with lower molecular weights show a much stronger affinity. Conversely, CO_2 exhibits the opposite trend, with a very strong affinity for the clay solid wall.

Table 1.44 presents the slip length values (L_{DGPD}, L_{CGWPD}, and L_{dry}) for gas flow in DGPD, CGWPD, and dry pyrophyllite. The results demonstrate that both DGPD and CGWPD exhibit a marginal slip condition at the liquid surface, with CGDW exhibiting slightly higher slip length values than DGPD. This observation may be attributed to the presence of water molecules moving tangentially to the gas flow at the gas-water interface, resulting in dynamic stresses exerted on the gas surface due to relative motion, which leads to additional traction. The gas flow characteristics of dry pyrophyllite exhibit a more pronounced slip condition compared to those in contact with water, which is an intriguing finding. The slip length is notably larger for helium (He) and hydrogen (H_2), and this trend correlates well with the divergence (Div) values. He and H_2 have less affinity for the solid surface, leading to their greater mobility at the interface, resulting in higher slip velocity and subsequently increased slip length. Conversely, CO_2 exhibits a strong affinity for the solid surface, resulting in a considerably lower slip length.

1.6.4.5. Viscosity of water in two-phase flow

The present study investigates the dynamic viscosity of the water film under partially saturated conditions for CGWPD. Figure 1.132 displays the dynamic viscosity as a function of the number of adsorbed water layers, which indicates the thickness of the adsorbed water film. The data in the plot are averaged for several film length to assess the statistical uncertainty of the data . The findings reveal that the dynamic viscosity of water increases with decreasing thickness of the adsorbed water film. This is consistent with the hypothesis that water molecules near the clay surface have lower mobility, which leads to a higher dynamic viscosity due to interaction with the clay surface. At 3.5 to 1.8 water layers, the dynamic viscosity increases to about 2.0 cP, which is approximately twice the value observed in bulk water. This increase in viscosity is attributed to the fact that, in thin water films, water is more influenced by the clay surface, and mobility is lowered. These findings provide insights into the impact of adsorbed water thickness on water phase mobility near the clay surface and their effect on the dynamic viscosity of water in a CGWPD.

1.6.5. Results - Pore Scale Modelling

The pore scale modeling results reported below were conducted as a part of a PHD thesis, published in Owusu (2023).

1.6.5.1. Validation of pore-scale simulation methodology

To validate our different upscaling approaches, we compared the results of the large-scale molecular dynamics (MD) simulation with the random walk (RW) simulations. Both MD and RW simulations were conducted for a total simulation time of 72 ns, and the mean square displacement (MSD) was calculated using the particle trajectories throughout the entire simulation period.

Figures 1.133a and 1.133b compare the mean square displacement (MSD) plots obtained from MD simulations and RW simulations (A1 and A2 approaches). In A1, a constant bulk water diffusion coefficient of 2.3 $\mathrm{nm}^2/\mathrm{ns}$ was uniformly applied throughout the entire pore domain. However, in A2, local diffusion coefficients obtained by MD simulations for various slit pore size (see Pore size effect on the diffusion of gases) were assigned to different regions of the pore space based on their proximity to the clay surface. The results reveal a noticeable difference between the MD simulations and A1/A2 simulations, with A1 and A2 exhibiting a considerably steeper slope. This difference suggests that the particle mobility in A1 and A2 is significantly higher than in the MD simulations, indicating that A1 and A2 fail to accurately capture molecular-scale dynamics. Merely incorporating local diffusion coefficients based on surface behavior is

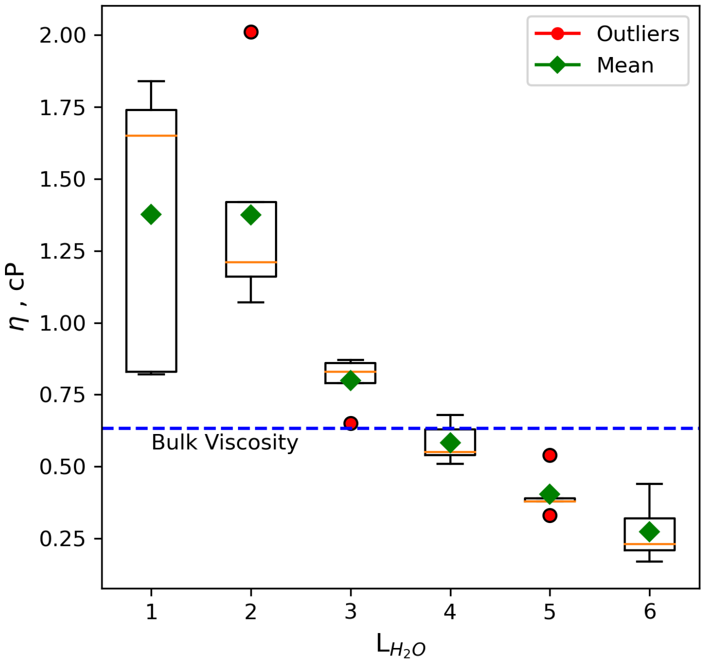

Figure 1.132: Dynamic viscosity of water films confined in Na-MMT clay slit pore as a function of the number of adsorbed water layers.

inadequate to fully replicate the particle dynamics observed in the MD simulations within the RW simulations. To properly take into account the slow water dynamics in small interlayer pores, the diffusion coefficients should by derived from MD simulations in 1, 2, and 3 water layer thick slit pores Owusu et al. (2022a).

Figure 1.133c presents a comparison of the mean square displacement plots between the MD simulation and the RW approach A3 simulation. In the model A3, the diffusivity in larger pores is considered in the same manner as in the model A2, whereas the diffusivity in the interlayer pores (e.g. smaller then 1 nm corresponding to 3, 2 or 1 water layers) were assigned based on data from MD simulations conducted on systems with 1, 2, or 3 water layers. The results demonstrate that the mean square displacement curves of the MD and A3 simulations are nearly parallel, indicating that the retention of particles at the clay surface and within clay interlayers is accurately captured.

Generally, it is widely observed that particle displacement along the layering of clay particles (x- and y-direction) is faster compared to displacement perpendicular to the layering (z-direction), as shown in Figure 1.133c. The mean square displacement (MSD) curves exhibit an initial ballistic regime, extending up to 20 ns in the RW simulation and up to 10 ns in the MD simulation. These differences in the short-time behavior of the MSD curves are due to the differences in the short-range interaction between MD and RW particles. This short time dynamics however is irrelevant to the macroscopic diffusion.

Comparison of 2D lattice Boltzmann and 2D RW simulation: A 2-dimensional representation of the clay pore structure was obtained by extracting a slice from the 3D geometry. Minor adjustments were made to improve connectivity in the 2D plane, with minor interventions. The resulting 2D geometry used for the lattice Boltzmann (LB) simulation is shown in Figure 1.134.

The upscaling approach A1 and A2 were implemented in the lattice Boltzmann (LB) simulation. Figure 1.135 shows a 2D slice through 3D domain considered in previous chapter and used for the lattice Boltzmann simulation, the distribution of local diffusion coefficients ($\mathrm{nm}^2/\mathrm{ps}$) within the pore space based on

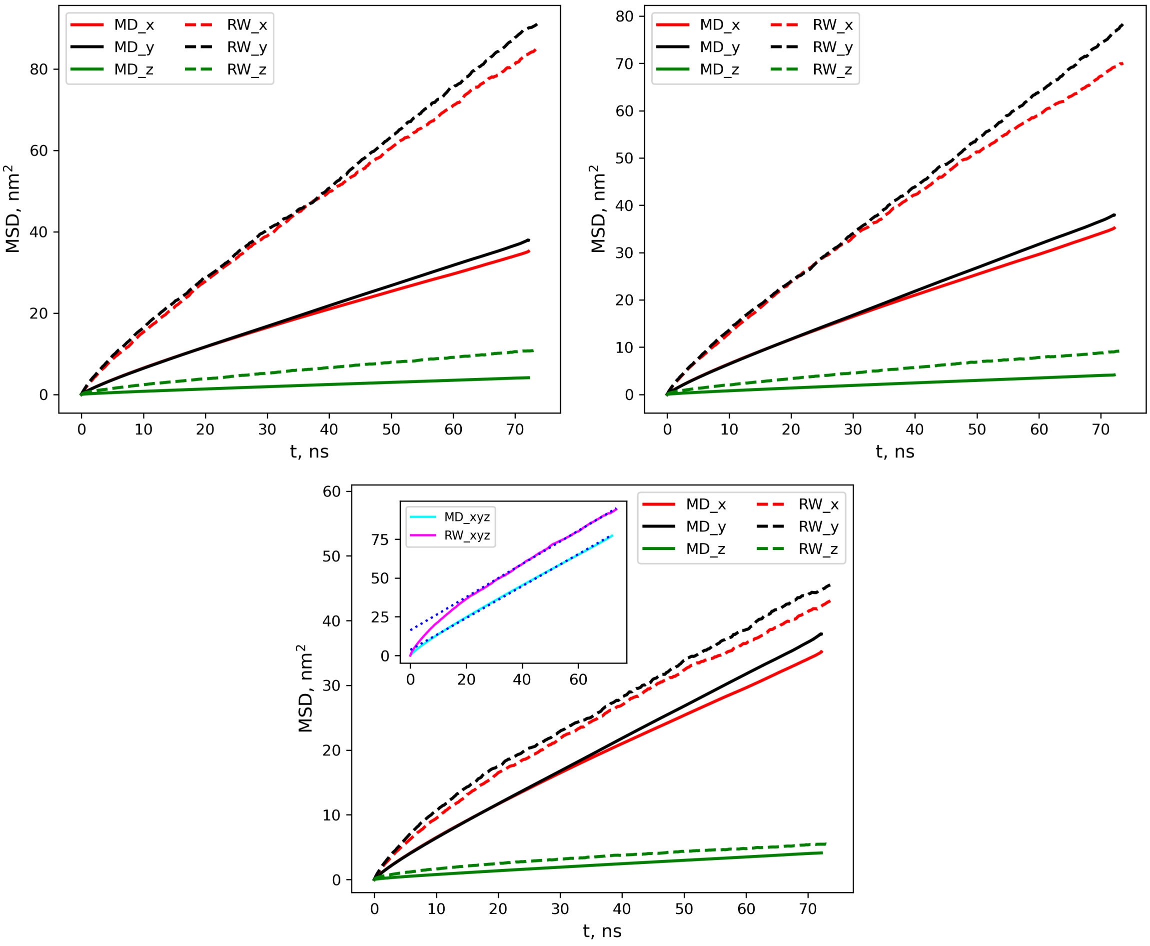

Figure 1.133: Comparison of the mean square displacement obtained in large-scale MD and RW simulations from approach (a) A1 (b) A2 (c) A3

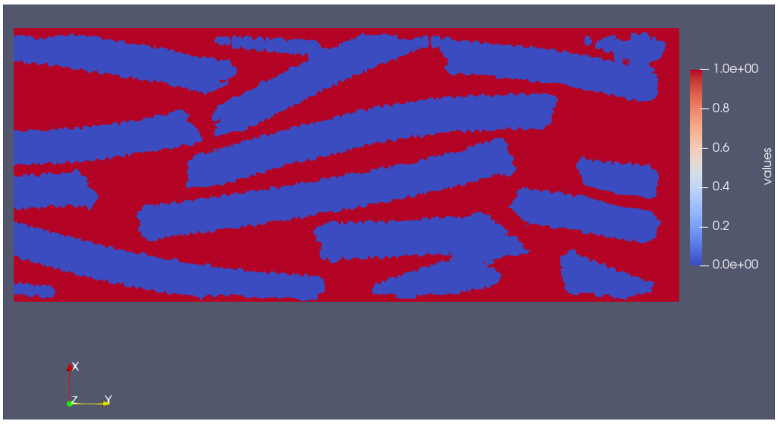

Figure 1.134: Configuration of the 2D clay structure for lattice Boltzmann modeling. Clay particles and pore space are represented by blue and red regions, respectively.

proximity to the clay surface is shown with color gradient.

The 2D lattice Boltzmann modeling involves measuring a species concentration transport rate at a steady state under the given concentration gradient. This rate is then compared to the diffusion coefficient of the species in bulk water, resulting in the determination of the effective diffusion coefficient (D_e). To further compare the lattice Boltzmann modeling with random walk simulation, a random walk simulation was

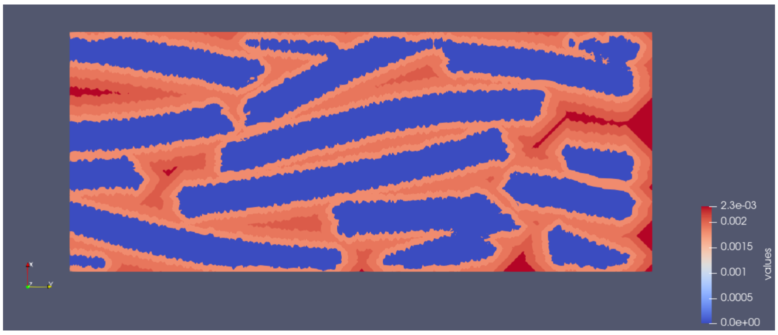

Figure 1.135: Snapshot of the lattice Boltzmann system configuration showcasing the spatial distribution of diffusion coefficients ($\mathrm{nm}^2/\mathrm{ps}$) within the pore space based on proximity to the clay surface.

conducted using the same 2D clay structure as the lattice Boltzmann model. Table 1.45 presents the D_e values obtained from both the lattice Boltzmann (LB) and random walk (RW) simulations.

Table 1.45: Effective diffusion coefficients derived from 2D LB and RW simulations in direction parallel and perpendicular to the bedding of clay particles. See Figure 1.135

	diffusion coefficients [10^{-10}, m^2s^{-1}]	
	$D_{e\parallel}$	$D_{e\perp}$
LB-2D-A1	3.13	0.84
LB-2D-A2	2.27	0.63
RW-2D-A1	3.44	0.79
RW-2D-A2	2.75	0.59

The results demonstrate a good agreement between the random walk (RW) simulation and the lattice Boltzmann (LB) modeling with a deviation factor of about 1.1. As we proceed, our future work aims to extend the LB modeling approach to encompass a three-dimensional (3D) model, thereby enhancing the accuracy and applicability of our findings. The actual wall time for the simulations in a 1 CPU core is 8.2×10^1 seconds for the RW simulation and 4.3×10^5 seconds for the LB simulation. It is worth noting that the RW simulation offers a computational advantage compared to the LB and MD simulations, however, the advantage of LB is that it can be extended to simulate ions transport.

1.6.5.2. Diffusion of water in highly compacted smectite clay

The effective diffusion coefficient for water in the model clay sample was determined for the large-scale MD and 3D-RW simulations, respectively. The simulated structure consisted of 30 hexagonal clay particles compacted within a simulation cell measuring 24 × 24 × 7 nm^3, with a dry density of 1.67 $\mathrm{g/cm}^3$ and a porosity of 0.45. The individual clay particle used was a Na-montmorillonite, characterized by the stoichiometry $Na_{0.8}[Al_{3.2}Mg_{0.8}]Si_8O_{20}(OH)_4$. Isomorphous substitutions of Mg^{2+} with Al^{3+} in the octahedral sheets were randomly distributed while maintaining the constraint of no adjacent substitutions. To achieve charge neutrality, the resulting negative structural charge was counterbalanced through adsorbed Na ions. Two dimensional slice through the 3D setup is shown in Figure 1.134. The calculation excluded the ballistic regime and focused on the linear part of the slope to determine the effective diffusion coefficient at 25℃. The obtained effective diffusion coefficients for the MD and RW simulations are presented in Table 1.46.

The effective diffusion coefficient values reveal that A1 and A2 simulations overestimate the diffusion coefficient compared to the MD simulation by factors of approximately 2.45 and 1.99, respectively. In contrast, A3 shows a close agreement with the large-scale MD simulation, differing by only 4%. These results highlight the significance of incorporating both surface diffusion and interlayer diffusion behavior in pore-scale random walk simulations to accurately determine the effective diffusion coefficient and validate the proposed model, RW-MD for estimation of the sample-scale diffusion coefficients. It is also worth

Table 1.46: Effective diffusion coefficients derived from large-scale MD and RW simulations for clay sample with density 1.67 g/cm^3 and a porosity of 0.45.

	diffusion coefficients [10^{-10}, m^2s^{-1}]			
	$D_{e\parallel}$	$D_{e\perp}$	$G_{\parallel}$ [-]	$G_{\perp}$
MD	2.33	0.26	9.87	88.46
RW-A1	5.66	0.64	4.06	35.82
RW-A2	4.61	0.52	4.99	43.98
RW-A3	2.20	0.24	10.45	97.45

mentioning that computational resources necessary for the estimation of water diffusion in MD are almost 10^5 orders of magnitude larger than the ones needed for the combined MD-RW approach. Furthermore, the RW-MD approach can rely on existing MD data for clay minerals conducted in the past.

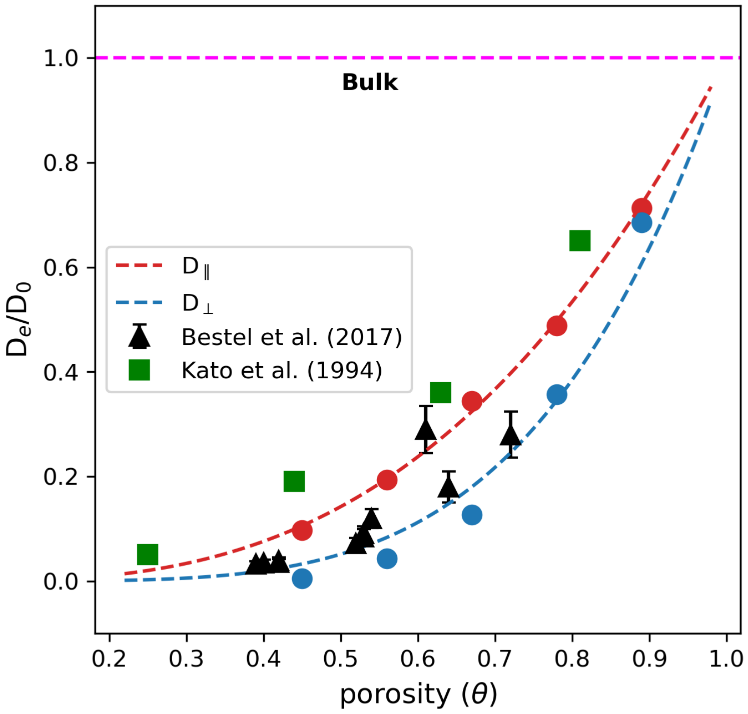

Figure 1.136: Relative effective diffusion coefficients of water as a function of clay porosity. Red and blue markers represent values obtained from this study for diffusion parallel and perpendicular to clay layering respectively. Black and green markers represent experimental data obtained for Na-montmorillonite Benson and Trast (1995) and Na-bentonite Kato et al. (1994) respectively.

1.6.6. Summary

This report investigates the transport mechanisms of gas in porous clay materials and explores the relationships between the structural properties of the clay minerals and the mobility of small gaseous molecules. Specifically, it focuses on smectite-rich clay rocks, which are considered suitable host rocks for deep geological repositories of nuclear waste. A thorough comprehension of gas transport behavior and related processes within these repositories is essential to ensure the safe and reliable design of waste storage systems.

Conventionally, experimental studies are conducted to investigate the behavior of fluids in porous media, with the goal of obtaining their transport parameters. These parameters are crucial for assessing the suitability of host rocks and designing effective barrier materials. However, laboratory and field experiments may not fully capture the long-term evolution of transport processes and the changes in thermo-hydro-mechanical-chemical conditions specific to the subsurface environment. Consequently, numerical and computer simulations have emerged as invaluable tools for investigating transport mechanisms and examining system behavior beyond the limitations of experimental methodologies. Moreover, numerical and computer simulations offer a unique opportunity to comprehend experimental results, explore scales and processes that are not detectable through experiments alone, and enhance our understanding of the underlying transport mechanisms. In this study, molecular dynamics simulations have been employed to observe fluid behavior at the nanoscale, and a methodology has been developed to upscale the results to a pore scale using pore-scale simulations. By integrating these simulation techniques, a more comprehensive understanding of gas transport in porous clay materials can be achieved.

We have conducted a comprehensive investigation of gas diffusion behavior at the nanoscale using molecular dynamics simulations. Our main objective was to gain insights into the mobility of gases within clay nanopores and interlayer spaces. Gas mobility is influenced by several factors, including pore size, degree of saturation, pressure, temperature, and the specific interaction between the gas molecule and mineral surfaces. To this aim, the mobility of gases (Ar, He, H_2, CH_4, and CO_2) was investigated in fully saturated and partially saturated slit pores of smectite particles using classical molecular dynamics simulations. In the fully saturated system, gas molecules were dissolved into the water and the pore size was varied at a constant molar ratio of gas to water. By analyzing simulation results, a general relationship between the mobility of gases and their fundamental molecular properties was established. Our findings revealed that the diffusion of gases is significantly influenced by three key factors: the mineralogy of the confinement (specifically, the type of clay), the size of the clay nanopore, and the hydrodynamic radius of the gas molecule (which indicates the gas type). Based on these results, we derived an equation that effectively connects these parameters. This equation will be invaluable for macro-scale numerical modeling and laboratory experiments. The repository is expected to undergo a temporal desaturation process that will require a significant amount of time for the system to re-saturate. Gas mobility in this case will be in partial saturation. Consequently, a two-phase model was setup containing a hydrated surface of smectite particles and gas-filled porosity. By varying the water film thickness, different degrees of saturation in the system were emulated. In such a setup the gas migration takes place both in the gas-rich and liquid-rich phases. At the partially saturated conditions, the advective transport in the gas phase can be a dominant transport mechanism. Accordingly, both gas diffusion and gas dynamics were investigated under partial saturation. The simulation results suggest that the gas-diffusive behavior in this system exhibits a transition regime characterized by a combination of molecular diffusion and Knudsen diffusion. As a result, Fick's law, which is commonly used to describe diffusion processes, is not suitable in this case. Our findings highlighted that gas diffusion is influenced by multiple factors, including the thickness of the water films, the mean-free path of the gas molecules, and the average available pore width. A Bonsanquet-type approximation was successfully applied to establish a relation between these parameters and the diffusion coefficient. When a pressure gradient is applied, gas under partial saturation begins to flow as a free phase, and the transport of the gas phase is controlled by the dynamic viscosity of the gas. This emphasizes the significance of the second approach, which focuses on gas dynamics under partial saturation. To investigate the viscosity of gases confined between water films in a clay nanopore, classical non-equilibrium molecular dynamics simulations were conducted. Similar to diffusivity, the viscosity evolution as a function of pore size exhibits a transition regime, being controlled by the thickness of the water films, the mean-free path of gas molecules, and the average available pore width. In the same way, the relationships between these parameters and viscosity could be approximated by the Bosanquet-type approximation.

Molecular dynamics simulations provide insight into fluid behavior at the nanoscale to microscale. However, when it comes to designing clay barriers, the actual parameters used are based on macroscopic observations. In order to bridge the gap between molecular and continuum behavior, an intermediate scale (pore scale) simulation was implemented. This simulation incorporates the molecular interactions between the fluid and mineral surfaces, thus connecting them to the larger continuum behavior. Large-scale molecular dynamics simulations can achieve this as well, but they require significant computational resources. In this study, two pore-scale simulation approaches; random walk (RW) and lattice Boltzmann (LB) simulations were benchmarked. These simulations enabled us to calculate the effective diffusion coefficient of water in a compacted porous smectite clay sample. The results were then compared with large-scale molecular dynamics simulations performed on the same clay sample. A very good agreement between the 3D RW simulation and the large-scale MD simulations, as well as between 2D lattice Boltzmann modeling and 2D random walk simulations was observed. This work highlights also the consistency and transferability of results between the different computational methods. Overall, the results demonstrated a close agreement with experimental work conducted on Na-montmorillonite and Na-bentonite, and a relationship between the effective diffusion coefficient and the microstructural changes was established.

Although molecular dynamics allows for the exploration of numerous molecular properties, this study simplified certain steps. Specifically, we focused on a basic Na-montmorillonite clay with Mg substituting for Al in the octahedral sheet. However, it's important to note that in natural montmorillonite, Al can also replace Si in the tetrahedral sheet. This substitution leads to variations in the clay's surface charge and surface charge distributions. Previous studies have demonstrated that the specific distribution of these substitutions affects the hydrated montmorillonite's structural and dynamic properties, including the mobility of aqueous species, swelling behavior, and interlayer structure (Liu et al. (2008a); Ngouana W and Kalinichev (2014a); Kosakowski et al. (2008a); Sun et al. (2016). Therefore, the transport parameters and swelling pressure calculations obtained in this study are limited to our simplified clay model and may not precisely capture the behavior of other clay structures. Nonetheless, they provide a valuable initial approximation.

The concentration of gas plays a significant role in determining the diffusion coefficient, making gas solubility an essential parameter to consider Benazzouz et al. (2022a); Jähne et al. (1987b); Wise and Houghton (1966a). Moreover, studies have revealed that confinement enhances gas solubility, particularly in the case of methane Benazzouz et al. (2022a). Typically, at ambient conditions, gases exhibit low solubility, resulting in an insufficient number of molecules for accurate molecular dynamics simulations. In our study, we employed a gas concentration of 0.5 mol/L, which exceeds the typical gas solubility limit observed in bulk water under ambient conditions. Despite this higher solubility limit, our model successfully replicated experimental results for self-diffusion coefficients. To accurately quantify gas diffusion under varying conditions, a recommended approach involves conducting a Grand Canonical Molecular Dynamics simulation to accurately estimate gas solubility. Subsequently, diffusion computations can be performed.

The assumptions made in partial saturation simulations, such as considering planar thin films of water adsorbed to slit clay nanopores, may oversimplify the gas phase transport process. Clay nanopores, however, exhibit diverse morphologies including spherical or cylindrical shapes, which can deviate from perfect planarity Strangfeld (2021); Guo et al. (2015). These variations in pore size and geometry can significantly influence pore saturation. Furthermore, gas transport may not occur as a continuous phase along the thin water film, but rather as gas bubbles enveloped by water, leading to curvature in the water layer. Thus, to accurately describe the behavior of gas in actual clay materials, it is crucial to consider the influence of pore morphology on gas diffusion and the diffusion of gas bubbles through the water.

Pore-scale simulations of water diffusion in porous clay smectite structures successfully provided insights into the diffusion process. It should be acknowledged, however, that this study solely considered a saturated system, neglecting the possibility of partial saturation where some pores are fully filled, while others may be dry or partially filled. In the case of partial saturation, the transport of water or gas species becomes more complex. In order to provide a more comprehensive understanding of the transport phenomena within the clay structures, specific transport processes due to the saturation of the pore must be described. The 2D lattice Boltzmann model was successfully applied and compared to the 2D random walk simulation. It was however challenging, from the side of the computational resources to apply a full 3D lattice Boltzmann simulation of a finely resolved complex structure of clay's tortuous characteristics. Consequently, there is a need for an enhanced lattice Boltzmann simulation in a 3D environment to accurately assess the applicability and limitations of the lattice Boltzmann method.

1.6.7. Key Learning Points

A semi-empirical equation connecting effective diffusivity of dissolved gas molecules in clay rocks with their molecular mobility in bulk water (available experimentally), interaction with clay mineral surface (obtained by molecular simulation as function of inter particle distance), and "geometry factor" (experimentally available from HTO measurements with clay rocks) has been established. This empirical equation can be used to assess gas molecule's mobility in clay rocks, if no direct experimental data are available, as well as for interpolation of experimental data in THMC modelling.

The boundary conditions for transition between Knudsen and molecular diffusion of gases in partially saturated conditions was evaluated by molecular dynamics simulations. Further, the viscosity of the gas and water in fully and partially saturated conditions were evaluated. These data could be relevant for the macroscopic modelling of advective gas transport in porous media.

An upscaling concept combining the animistic simulations and pore scale modelling has been developed which is capable to predict the diffusive mobility of solutes in complex porous media. The analysis of data and model performance indicate that the most critical parameter in this upscaling approach is the accurate and realistic description of the particle arrangement.

1.6.8. References

.

Belgian Nuclear Research Centre (SCK CEN)

BGR (OGS Team)

1.7. Modeling gas diffusion in saturated conditions (BGR)

1.7.1. SCK CEN experiment

The SCK CEN gas diffusion experiment has been analysed by BGR using latest OGS model development by UFZ (section 2.12.2).

In the scope of Task 2 in the work package GAS, the Belgian Nuclear Research Centre (SCK CEN) performs an experiment focusing on the dissolution and diffusion of dissolved gas. The experimental setup is described in Jacops et al. (2015) as well as in previous EURAD milestone reports such as MS99-100. This experiment features a cylindrical Boom Clay sample, which is fully liquid saturated. It is designed in such a way that dissolved gas concentration gradients across the sample can be applied without inducing a liquid pressure gradient at the same time (Fig. 1.137). Thus, it is guaranteed that gas transport across the sample occurs exclusively via the diffusive process as opposed to advection of dissolved gas in the liquid phase. Since the sample is fully liquid saturated, there is no advection of gas in a free gas phase. Therefore, the mode of gas transport investigated in this experiment can be attributed to the leftmost mode in the gas transport concept (cf. Fig. 2.293).

The experiment features two boundaries at the faces of the cylindrical sample, each of which are connected to a liquid and gas filled and pressurized vessel. Initially, the gas phase in the first vessel is composed exclusively of helium (called the helium upstream vessel henceforth), whereas the gas phase in the second vessel contains only methane (called the methane upstream vessel hereinafter). Consequently, there are two opposing concentration gradients created across the sample, one gradient for each gas species. Because the total pressures in each vessel are almost identical, there is no liquid or gas pressure gradient created across the sample. During the course of the experiment, both gas species diffuse through the sample, driven by their respective concentration gradients in the liquid phase. Consequently, the concentration in the respective opposing vessel increases. For the helium, the methane upstream vessel serves as the helium downstream vessel and visa versa. The increase of concentration of each gas species in the respective downstream vessel leads to an increase of the partial pressure in the gas phase of that vessel, according to Henry's law. This partial pressure or concentration increase is measured by gas chromatograph and numerically predicted by the modelling code. The numerical setup features a quasi-one-dimensional bar, in which the two gas species diffuse. The volume of the injection filters, and tubing is neglected and it is assumed that any gas entering or exiting the sample arrives instantaneously in the respective downstream vessel. It is furthermore assumed that the gas arriving in the downstream vessel is always at an instant equilibrium with the partial pressure in the gas phase of the respective vessel, according to Henry's law. The total pressure in each upstream vessel serves as Dirichlet boundary condition for the numerical model and is applied to each of the faces of the cylinder. The time-dependent value of this boundary condition is depicted in Fig. 1.137. These boundary conditions are time-dependent, because the total pressure changes each time a sample is taken for evaluation in the gas chromatograph. Finally, Fig. 1.138 shows the comparison of experimental measurements and the numerical predictions in the right plot as well as numerically predicted mass fluxes in the left plot. Both results are shown for the

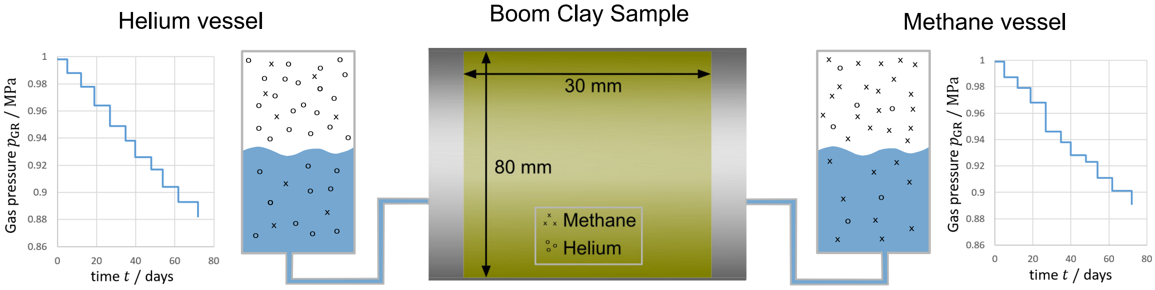

Figure 1.137: Experimental setup of the double diffusion experiment Pitz et al. (2023b).

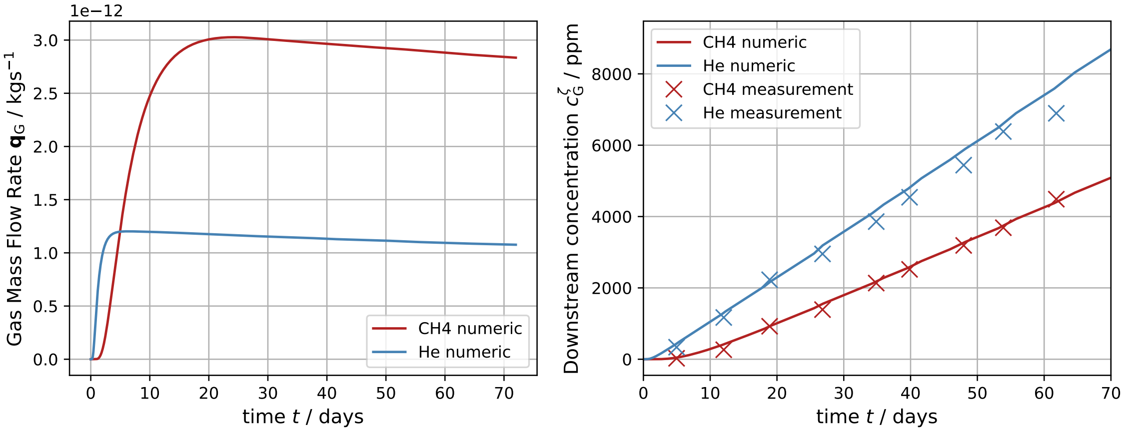

Figure 1.138: Comparison of experimental and numerical results for the double diffusion experiment. Pitz et al. (2023b)

helium and methane species. Firstly, it can be seen that the results agree well. Thus, the double diffusion experiment conducted at SCK CEN serves as a valuable experiment for the validation and verification of the implementation of the gas dissolution and diffusion process in OGS-6 (TH^{2}M model). The results can be interpreted as follows: The left plot shows that there is generally a higher mass flux of the methane compared to the helium mass flux. This is likely due to higher molar mass of methane in contrast to the relatively low molar mass of helium, which has the higher diffusivity and thus the higher diffusion velocity at equal concentration gradients. Over time, the mass flux of both gas species decreases, likely as a consequence of the time-dependent (decreasing) upstream partial gas pressures. Although the mass flux of helium is lower than that of methane, its rate of concentration increase in the downstream vessel is higher than that of methane (cf. right plot Fig. 1.138). This is due to the faster diffusion velocity and due to the fact that according to the ideal gas law, the ratio of partial gas pressures depends on the number of gas particles rather than the ratio of gas mass present in the gaseous phase. It can also be seen that the helium signal arrives faster in the downstream vessel, when compared to the methane. This is due to the higher diffusivity as well as the higher Henry coefficient of methane, which leads to a higher storage capacity, which in turn delays the arrival of the signal. Over all, the experimental and numerical results match very well, thus increasing confidence in the numerical model. An extensive description of the experimental work can be found in Jacops et al. (2015) and a detailed description of the numerical modelling and results is conducted in Pitz et al. (2023b). Fig. 1.139 presents the results of a sensitivity analysis of predicted methane concentration in the downstream vessel gas phase with regard to porosity, diffusion coefficient and Henry coefficient and shows the highest sensitivity in relation to the Henry coefficient.

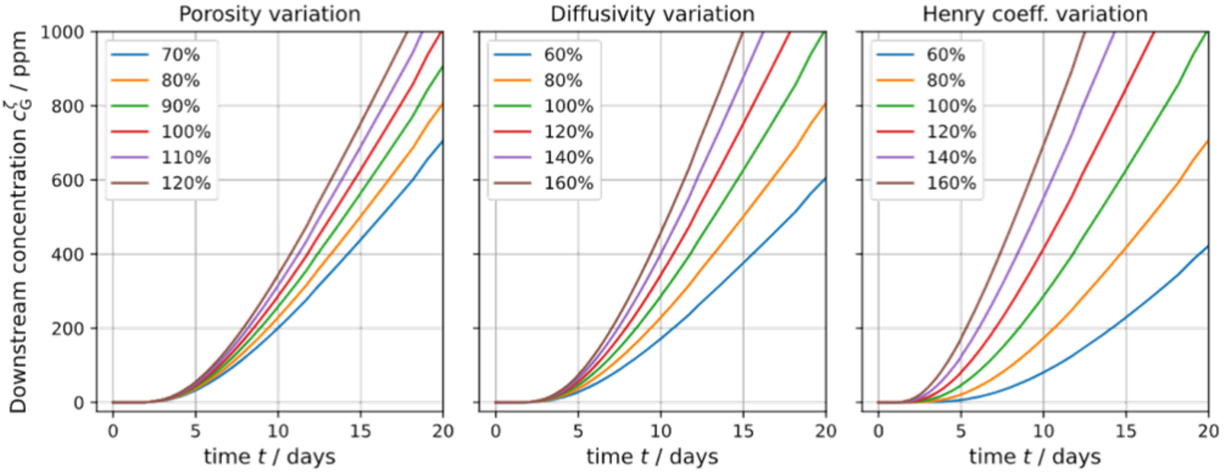

Figure 1.139: Impact of selected parameters on diffusion as modelled in the SCK-CEN gas diffusion experiment.

.

Subtask 2.2:
Advection processes

2. Subtask 2.2: Advection processes

Experiments

.

Belgian Nuclear Research Centre (SCK CEN)

2.1. Long term gas injection under controlled loading (SCK CEN)

2.1.1. Introduction & Objectives

2.1.1.1. Description of the research questions

In the Boom Clay, transport of gas can occur either by diffusion as dissolved species, or by the formation of conductive pathways through the clay matrix. When the gas pressure is low, transport occurs only by diffusion. When the gas pressure is close to the total stress of the clay matrix, conductive gas pathways can be formed through the clay matrix by pathway dilation or fracturing.

Diffusion of dissolved gases in Boom Clay is studied experimentally by SCK CEN, leading to a large data set with diffusion coefficients of different gases, for different orientations w.r.t. bedding plane and for different lithological subunits. Formation of conducting pathways in Boom Clay is studied under controlled mechanical conditions at BGS (UK), UPC (Spain) and at Ecole Centrale de Lille (France) – see for instance Horseman, Harrington et al. (1999), Harrington, Milodowski et al. (2012), Gonzalez Blanco (2017), Gonzalez-Blanco, Romero et al. (2021).

The transition between the two transport mechanisms in low permeability clay host formations is known to be both pressure and time dependent. Most of the research focuses on the influence of gas injection (at various levels and rates) on breakthrough behaviour, without taking into account the effect of time. The dependency on time of the limits of diffusive transport of dissolved gas and the possible transition from diffusive transport to free gas flow is still unclear.

To fill the knowledge gaps, SCK CEN, in collaboration with ONDRAF/NIRAS, proposed to perform long-term, slow gas injection tests under isostatic conditions at gas pressures slightly inferior to the confinement pressure in order to:

1/ Validate under controlled loading the mechanisms of diffusion of dissolved gas in Boom Clay (previous tests have been done in constant volume conditions).

2/ Investigate the limits of diffusive transport of dissolved gas and a possible transition to free gas flow during a long gas injection time.

Jacops, Yu et al. (2020) described the set-up and protocol to perform the long-term slow gas injection tests. Jacops, Maes et al. (2022) described the preparation and construction phase, which started in 2020 and ended in 2021. This report summarizes the results of the first experiment and provides recommendations for future experiments.

2.1.1.2. Strategy to answer the research question(s)

The proposed experiment is a modified version of the lab set-up in which diffusion of dissolved gas is measured in clay samples which are confined in a constant volume cell (Jacops, Volckaert et al. 2013). For the experiments described in this report, the clay sample was not placed in a constant volume cell, but loaded in an isostatic cell where an isotropic stress was loaded onto the sample (Figure 2.1). During the first phase, diffusion of dissolved gases was measured. Each side of the clay sample was connected to a vessel, which was filled half/half with water/gas. Water, containing the dissolved gas was circulated over the filters of the sample cell with a pump. Due to the concentration gradient, the dissolved gas diffused through the clay sample and ended up in the vessel at the opposite side where it equilibrates between the gas and water phase. On a regular basis, gas samples were taken from the gas phase in each vessel, and the diffusion coefficient could be calculated from the concentration change in time. This set-up allowed us to validate the diffusion coefficients for gases, for conditions of uncontrolled loading towards conditions of controlled loading.

During the second phase, the water in the injection vessel was replaced by pure gas and thus the injection side of the sample was only in contact with wet gas (Figure 2.2, right side). The downstream side of the

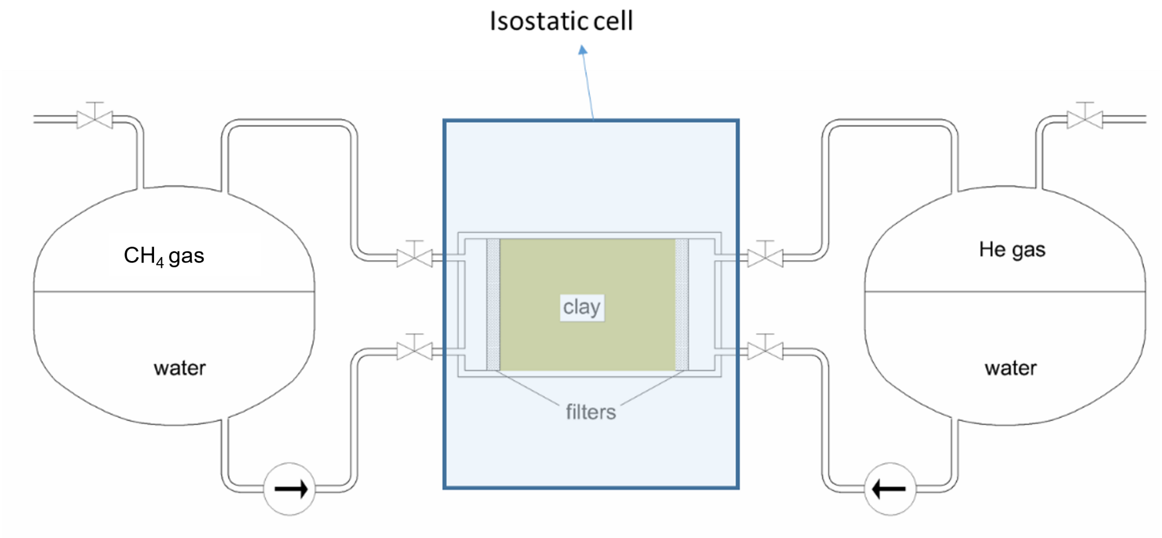

Figure 2.1: Diffusion of dissolved gas under controlled loading – phase 1

sample was still in contact with gas equilibrated water that was circulated continuously. Gas samples were taken from the gas phase in the downstream vessel regularly (Figure 2.2, left side) and the concentration evolution in time was registered, which allowed calculating the gas flux through the clay. Once the flux was stable for at least 6 weeks, gas pressure in the upstream vessel was increased and the new flux was measured. Based on the concentration change in time during the different pressure steps, the evolution of the gas flux could be assessed. When approaching the minimum principal stress, gas pressure was increased with very small steps (0.1 bar), allowing the system enough time to adapt to the changing boundary condition and studying the response of the Boom Clay to the gas pressure.

It should be noted that the performed scoping calculations (e.g. in Jacops, Maes et al. (2022)) are based on Fick's diffusion theory. When the gas pressure goes beyond 5 bar, the pore network within the clay matrix starts to play a role, which will contain large uncertainties. Theoretically, when the difference between the water pressure and gas pressure is lower than gas entry value, which is considered around 30 bar, there will be no desaturation of the sample and diffusion in full saturated conditions still holds.

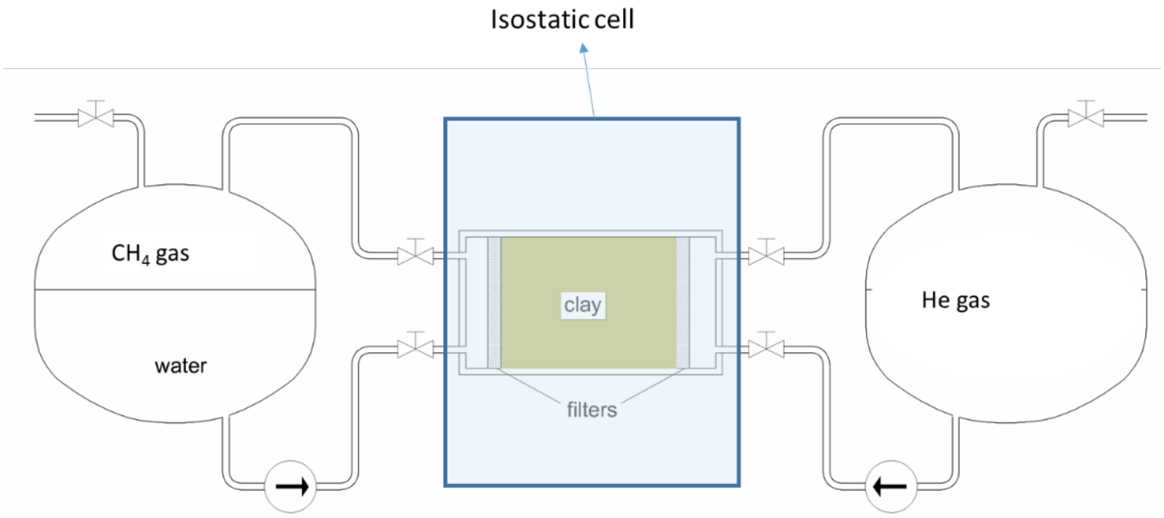

Figure 2.2: Diffusive and advective gas flow by using a pure gas phase in the injection vessel (right) – phase 2

However, this concept is valid from macroscopic point of view. When considering the heterogeneity of the material, some local minuscule water surfaces with larger pore radius may break earlier. This local behaviour is believed to deviate gas transport behaviour from pure diffusion. Given long enough time and very slow gas injection, such subtle variations are hoped to be observed with the current experimental design. Furthermore, when and under which gas pressure, a connected dilation and/or fracture pathway could finally be formed, is today an open question and a potential outcome in this study.

The aim of this experimental programme is so to monitor 1/ how the gas inflow changes when pressure increases by monitoring the pressure at the injection side, and 2/ how the outflow changes by measuring the concentration increase over time and to assess at which point (near the total stress) a change in the process can be notified.

2.1.2. Experimental set-up

2.1.2.1. Description of apparatus

The apparatus consists of an isostatic cell and an upstream and downstream circuit (Figure 2.3). The isostatic cell is used to apply isotropic stress on the sample. The bottom side of the sample is connected to the upstream circuit, while the top is connected to the downstream circuit. Each circuit consists of a vessel, pump, pressure transducer and sampling port. During the first phase, both vessels are filled with water and gas, and water with dissolved gas is pumped around at both sides. During the second phase, the upstream circuit is filled with gas only and no pumping occurs at this side. Each vessel is equipped with a connector, which allows taking a sample of the gas phase, in order to monitor the concentration evolution over time. High precision pressure transducers are connected to the vessels to monitor the pressure evolution over time.

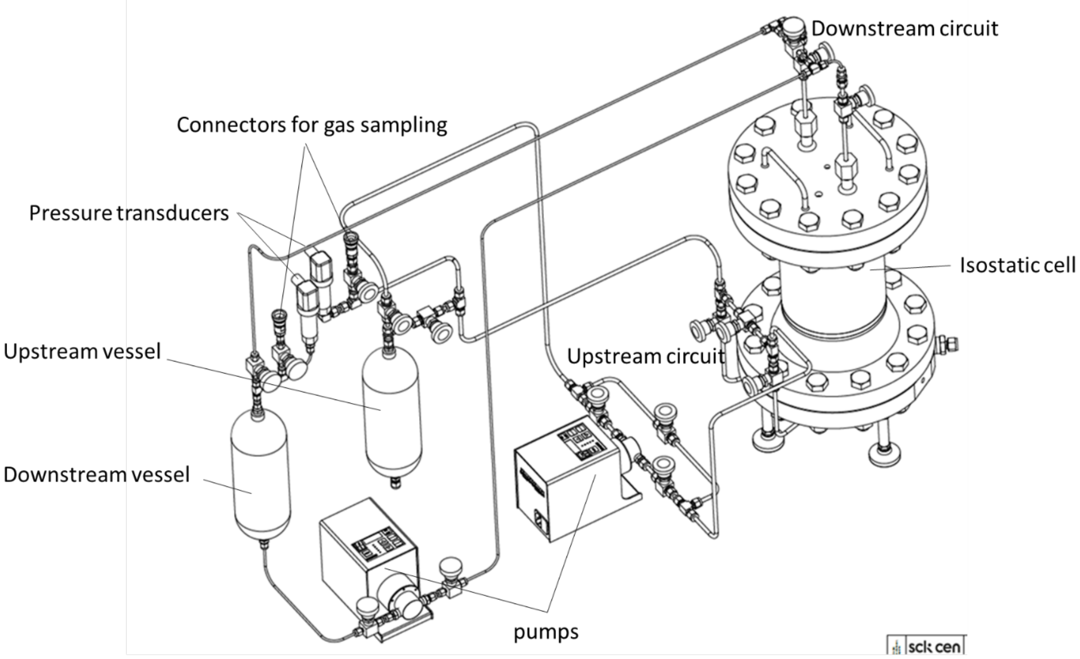

Figure 2.3: As-built schema of the experimental set-up

Pumps and pump heads Water is pumped around using an ISMATEC (Switzerland) Reglo-Z digital gear pump, combined with a MICROPUMP GA pump head (type GA-T23-JFS-B). The pump is a magnetically coupled gear pump: it has rotating magnets, on top of which the pump head is mounted. The spinning of the magnets leads to the spinning of 2 gears inside the pump head which makes the water flow through the pump head. Thus, the pump and pump head are fully isolated.

Pump head GA-T23-JFSB has a flow rate between 4.6 and 460 ml/min. The maximum pressure difference is 5.2 bar, while the maximum system pressure is 22 bar. Gears are made from PEEK. In past diffusion experiments, gears from graphite have been used, but these were too sensitive to wear.

Swagelok material All swagelok components are made of stainless steel (AISI 316). The used valves are stainless steel bellow sealed valves (type SS-2H or SS-6H, depending on the tube connection). The body-to-bonnet seal is welded which ensures good leaktightness.

Pressure sensors Pressure in the upstream and downstream vessel is measured using DRUCK DPS8000 high accuracy pressure sensors. These sensors make use of the new TERPS technology. TERPS is a resonant silicon pressure sensor technology platform that provides an order of magnitude higher accuracy and stability than current pressure measurement technologies available. The sensors have a range of 0 – 35 bar abs, with an accuracy 0.01% full scale. Temperature compensation is foreseen in the range -10 to 50℃.

The pressure sensor in the isostatic cell is a DRUCK DPS5000 CANbus pressure sensor. The sensor has a range of 0 to 50 bar abs with an accuracy of 0.1% full scale. Temperature compensation is foreseen in the range -20 to 80℃.

Isostatic cell The cell (Figure 2.4) is approximately 540 mm high and 317 mm in diameter. In the bottom flange, 2 in- and outlets are foreseen that connect to the sample which can be mounted in the cell. Two extra in- and outlets allow to fill and empty the cell. In the top flange, again 2 in-and outlets are foreseen which connect directly to the sample. Two additional connections are foreseen to mount a pressure sensor and to remove accumulated gas.

The cell is CE-certified for a maximum pressure of 50 bar g and a maximum temperature of 50℃.

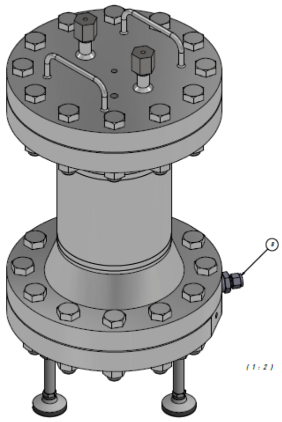

Figure 2.4: Design of the isostatic cell

2.1.2.2. Calibration

Measuring the total volume of the upstream and downstream circuits In order to know the exact boundary conditions, the total volume of each circuit has to be known. In order to calculate the total volume, the pressure in the circuit is registered. The circuit was pressurised at a known (high) pressure, and connected to the vessel with known volume (at low, known pressure). The equilibration pressure is measured, and the volume of the circuit is calculated, considering that ΔP1xV1 = ΔP2xV2.

The volume measurement was repeated 3x for each circuit and the results are shown in Table 2.1 and Table 2.2. The average volume is 1046 ml for the upstream circuit and 1012 ml for the downstream circuit.

	volume vessel (ml)	before expansion (bar a)	after expansion (bar a)	circuit before expansion (bar a)	circuit after expansion (bar a)	calculated volume circuit (ml)
replicate 1	1000	0	4.180	7.661	3.668	1046
replicate 2	1000	1.047	4.358	7.015	3.845	1044
replicate 3	1000	1.068	4.258	6.884	3.843	1046

Table 2.1: Results of the volume measurement of the upstream circuit

$V_{avg,system\ right}$= 1046 ± 1 ml

	volume vessel (ml)	before expansion (bar a)	after expansion (bar a)	circuit before expansion (bar a)	circuit after expansion (bar a)	calculated volume circuit (ml)
replicate 1	1000	1.025	4.232	6.908	3.745	1014
replicate 2	1000	0.996	2.734	3.745	2.026	1011
replicate 3	1000	1.026	3.817	6.186	3.426	1011

Table 2.2: Results of the volume measurement of the downstream circuit

$V_{avg,\ system\ left}$= 1012 ± 2 ml

Measuring diffusion of helium through membrane materials When performing long term gas experiments under isotropic loading, diffusion of gas from the sample into the confining fluid can become significant. Therefore, it is important to measure the diffusion coefficients of gases through the membrane materials.

Together with BGS, SCK CEN tested 3 membrane materials: PVDF, heat shrink Teflon and heat shrink Teflon combined with one layer of aluminium foil. Diffusion of He was measured through a membrane disc of 2 cm (Teflon) or 9 cm (PVDF) diameter and 0.5 mm thickness. The measured pore diffusion coefficients (D_p) are listed in Table 2.3. Diffusion of He through heat shrink Teflon with aluminium foil is five times slower than without aluminium foil, and eight times slower than in PVDF. Diffusion of methane is even much lower, with values < 1 x 10^{-11} m²/s. As heat shrink Teflon and aluminium foil are easy to handle and least permeable to gas, these materials have been used in the experiment described in this report.

The average value for D_p, for He in a clay-rich Boom Clay sample is 1.2 x 10^{-11} m²/s, which implies that diffusion through the membrane cannot be neglected.

	D_p (He) (10^{-11} m²/s)	D_p (CH_4) (10^{-11} m²/s)
PVDF	30	
Heat shrink Teflon	20	
Heat shrink Teflon + aluminium foil test 1	4	0.2
Heat shrink Teflon + aluminium foil test 2	4	0.05

Table 2.3: Overview of measured diffusion coefficients for He and CH_4 in PVDF and heat shrink Teflon with and without aluminium foil

2.1.2.3. Testing fluids

During the experiment, synthetic Boom Clay pore water (containing 0.014 M $NaHCO_3$) was used. Helium and methane gas were used in respectively the upstream and downstream circuit.

Material properties (pre-test and post-test characteristics)

The tested sample originates from core ON-Mol-1 116b, which has been taken from a depth of 264.69-264.79 m below drilling table (drilling table located at 29.83 mTAW[1]).

The porosity, calculated from sample drying at 105℃ is 35%.

Visual inspection of the sample pre-testing showed a rather homogeneous sample, without cracks or major pyrite inclusions. The texture of the sample was clayey.

After unloading the sample, it was inspected post-test. The sample was not dehydrated (soft and plastic clay), no cracks were observed (Figure 2.5).

Mineralogical composition (XRD) or specific surface area (by N_2-adsorption) have not been measured for this sample.

2.1.3. Testing protocol

2.1.3.1. Sample preparation

The first test specimen was sampled from core ON-Mol-1 116b. A plug of 50 mm diameter and 20 mm length was cut with a cutting edge. Next, the sample was placed between the two flanges (like a hamburger), and the "hamburger" was wrapped with 3 layers of aluminium foil and covered with one sleeve of heat shrink Teflon (Figure 2.6). Note that we encountered a problem with the first delivery of Teflon, which lead to strong heating of the sample. This might have affected the clay plug in some way, but in the sample dismantling no abnormal features were observed. After finishing the sample preparation (2021-09-27), final sample loading in the isostatic cell took 3 months because of technical issues. Finally, early December 2021, the sample was loaded in the isostatic cell and pressurised to a pressure of 30 bar.

---

[1] TAW = 'Tweede Algemene Waterpassing" - second general levelling

Figure 2.5: Post-test images of the sample, showing no major heterogeneities at the sample surface (left = bottom, right = top of the sample)

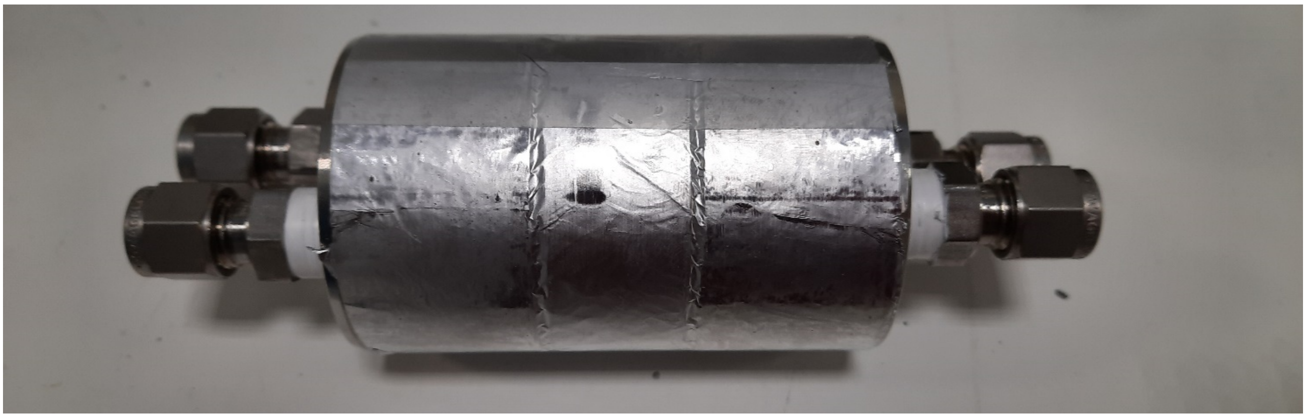

Figure 2.6: Sample with flanges and several layers of aluminium foil

2.1.3.2. Setup preparation

After loading the sample in the isostatic cell, a leak test was performed. All components were tested, except those located beyond the valves (towards sample) which isolate the sample from the upstream and downstream circuit. Next, the isostatic cell was filled with water and connected to a syringe pump. The syringe pump was set at low injection rate, and pressure increased gradually – up to a value of 30 bar. During the pressurization, the valves between the upstream and downstream circuit and the sample cell were open. The pressure in the isostatic cell was monitored regularly, but remained stable over time.

2.1.3.3. Experimental testing scheme

The experiment has been performed in 5 phases in total, which are summarized in Table 2.4. The details of experimental phase are listed in the results section of each phase, as it is too complex to separate the experimental phase from its results. The confining pressure was maintained at 30 bar over the entire duration of the experiment.

Phase number	P upstream (bar)	P downstream (bar)	remark
Hydraulic conductivity testing	7.3	4.5	Both vessels filled with water + N_2
Phase 1	5	5	Both vessels filled with water + He/CH_4
Phase 2	5	5	Upstream vessel filled with He, downstream vessel filled with water + CH_4
Phase 3	10	5	Upstream vessel filled with He, downstream vessel filled with water + CH_4
Phase 4	15	5	Upstream vessel filled with He, downstream vessel filled with water + CH_4
Phase 5	20	5	Upstream vessel filled with He, downstream vessel filled with water + CH_4

Phase number	P upstream (bar)	P downstream (bar)	remark

Table 2.4: Overview of the different experimental phases, which are more detailed in the "results" section

2.1.4. Results

2.1.4.1. Hydraulic conductivity measurement

Prior to the hydraulic conductivity measurement, the setup was flushed with nitrogen to remove all air. Three cycles of flushing 5x with nitrogen and connecting to the vacuum pump were performed.

Next, the setup was filled with synthetic Boom Clay pore water, containing mainly 0.014 M $NaHCO_3$ (De Craen, Wang et al. 2004). The water was prepared in a glovebox under nitrogen atmosphere. Each vessel was connected to a syringe pump, and the upstream vessel was pressurized at 7.3 bar, while the downstream vessel was at 4.5 bar. In the upstream vessel, both water inflow (Figure 2.7) and pressure were registered. The downstream vessel was disconnected from the syringe pump, and only pressure was measured. Given the low accuracy of the built-in pressure transducers of the syringe pumps, all pressures are measured by the pressure transducers installed in the set-up (DRUCK TERPS 8000). After 6 weeks, the hydraulic conductivity measurement was stopped, and a stable value of 1.9 ± 1 x 10^{-12} m/s was obtained.

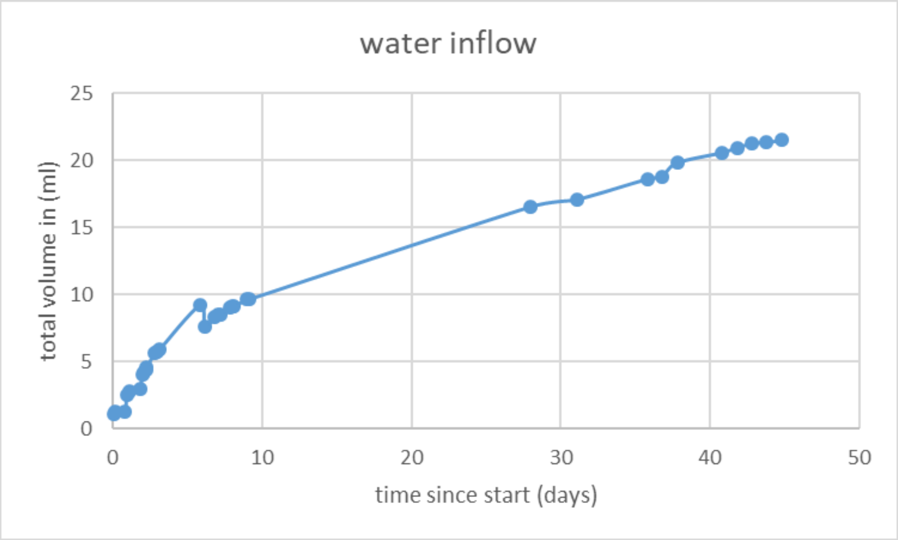

Figure 2.7: Water inflow into the sample in the upstream vessel, measured with the upstream syringe pump. K is calculated based on the pressure measured inside the setup and the inflow from the syringe pump connected to the upstream vessel.

2.1.4.2. Diffusion phase 1

The diffusion phase with dissolved gas at equal pressure (5 bar) started in February 2022. During the preparation phase, both vessels were filled with approximately 500 ml of synthetic Boom Clay pore water (0.014 M $NaHCO_3$) which was prepared in a glovebox with N_2 atmosphere. Filling was done by using water transfer vessels, and the exact transferred water volume is obtained by weighing the vessels before and after transfer. The gas phase was flushed several times with He (upstream vessel) and CH4 (downstream vessel) to remove the nitrogen as much as possible. The water flow rate of the pumps was set at 10 ml/min. The upstream vessel was finally filled with 497 ml He at 5 bar, while the downstream vessel was filled with 496 ml CH_4 at 5 bar. Both gas phases were analysed at t=0, and no He or CH_4 were measured in respectively the downstream and upstream vessel. The eventually remaining N_2 is considered to be non-interfering in the diffusion test. The diffusion test started on February 7, 2022.

Gas samples were taken on a regular basis from both the upstream and downstream vessel, and the concentration increase of He and CH_4 was measured as a function of time. The diffusion coefficients were fitted from the measured flux by using the one-parameter fit (ηR fixed at 0.38, D_p fitted) and the two-parameter fit (ηR + D_p fitted) (see Figure 2.8 and Table 2.5). More information on diffusion fitting can be found in Jacops, Aertsens et al. (2017). For phase 1, the D_{eff} values (D_{eff} = n D_p) from both fitting strategies are very similar, but lower than the reference value (Table 2.5).

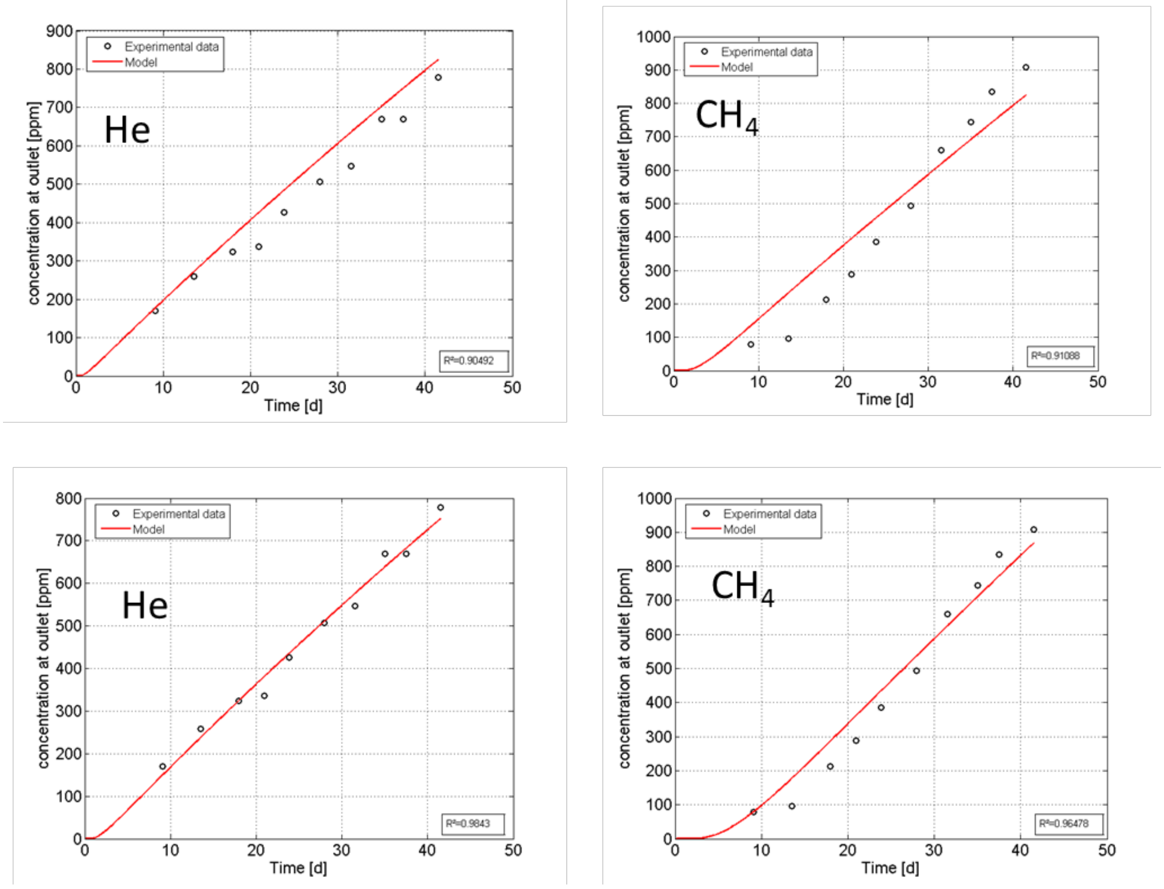

Figure 2.8: Concentration increase of He (left) and CH_4 (right) as a function of time, including the 1-parameter fit (top) and 2-parameter fit (bottom).

Experimental results

	D_{eff} (1 pm fit) (10^{-10} m²/s)	ηR (-)	D_p (10^{-10} m²/s)	D_{eff} 2 pm fit (10^{-10} m²/s)	ref value D_{eff} (10^{-10} m²/s)
He phase 1	2.8	0.59	4.4	2.6	5
He phase 2	2.3	0.23	10	2.3	5
He phase 3	5.3	1.05	5.3	5.6	5
He combi phase 1+2	2.8	0.54	5.1	2.8	5
CH_4 phase 1	9.1	1	1.1	1.1	0.9

Table 2.5: Fitted diffusion coefficients for the different phases, reference values from Jacops, Aertsens et al. (2017)

Modelling result for phase 1 **Test observations :** The test observations are shown Figure 2.9.

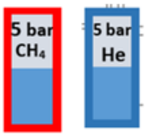

- **Dissolved gas** at both ends
- Equal pressure at both ends: 5 bar
- 7th Feb-21th March (42 days):

- Gas pressure in the upstream vessel decreases from 5.07 bar to 4.26 bar in 42 days with Δp=5.07-4.26=0.81 bar.
- Gas pressure in the downstream vessel decreases from 5.11 bar to 4.38 bar in 42 days with Δp=0.73 bar.
- Gas pressure decrease in both vessels are due to 10 times of sampling. Each sampling induces around 0.07 bar pressure drop.
- He concentration increases 779 ppm in the downstream vessel.
- CH_4 concentration increases 908 ppm in the upstream vessel.

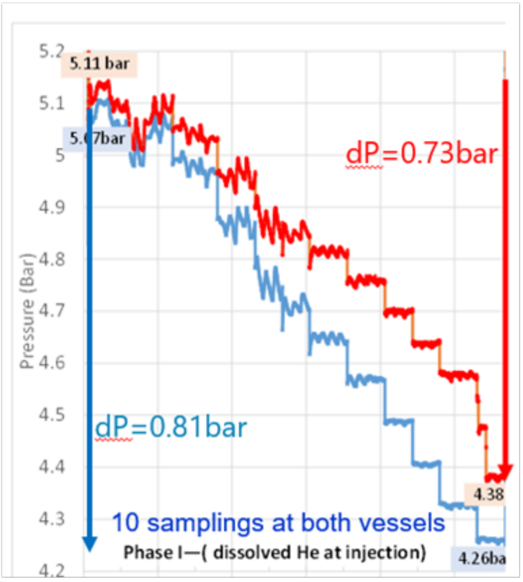

Figure 2.9: Test observations in phase 1, with dissolved gas in both vessels at equal pressure of 5 bar.

Modelling results:

Diffusion of dissolved He and CH_4 is calculated using a 2D axi-symmetrical COMSOL model considering a diffusive sleeve. The clay sample has a diameter of 5 cm and a height of 2 cm. The sleeve is modelled as a porous media with a porosity of 1. The top and bottom filters have a diameter of 3 cm. Except the filters and the sleeve, all the rest boundaries are considered impermeable. The measured gas pressures at both vessels are used as the boundary condition.

Apparent diffusion coefficients of He and CH_4 are 1.22×10^{-9} and 2.42×10^{-10} [m²/s], respectively. Henry's coefficients of He and CH_4 are 0.00037 and 0.0014 [mol/L/bar], respectively. Effective diffusion coefficients of sleeve for He and CH_4 are 4×10^{-11} and 3×10^{-13} [m²/s], respectively. Porosity of clay sample is set a reference value of 0.37, which is a typical value for Boom Clay.

Numerical results (see Figure 2.10) show that besides the 7.7×10^{-5} mol He which enters the downstream vessel, the amount of He which diffused into the isostatic cell through the sleeve is around 1.3×10^{-4} mol. For CH_4, besides the 7.4×10^{-5} mol CH_4 which entered the downstream vessel, the amount of CH_4 diffused into isostatic cell through the sleeve is around 8.3×10^{-6} mol.

Gas concentration was measured for both gases in their respective downstream vessel, and the measurements agree very well with the modelling results (see Figure 2.11).

2.1.4.3. Diffusion phase 2

Experimental results Phase 2 is characterized by injecting pure gas (helium) at 5 bar instead of dissolved gas. In order to change the injection mode, following detailed procedure was applied:

- Close valves of cell
- Release pressure in upstream vessel and release pressure at upstream side of sample
- Remove water by opening the vessel (bottom) + use helium to push out remaining water

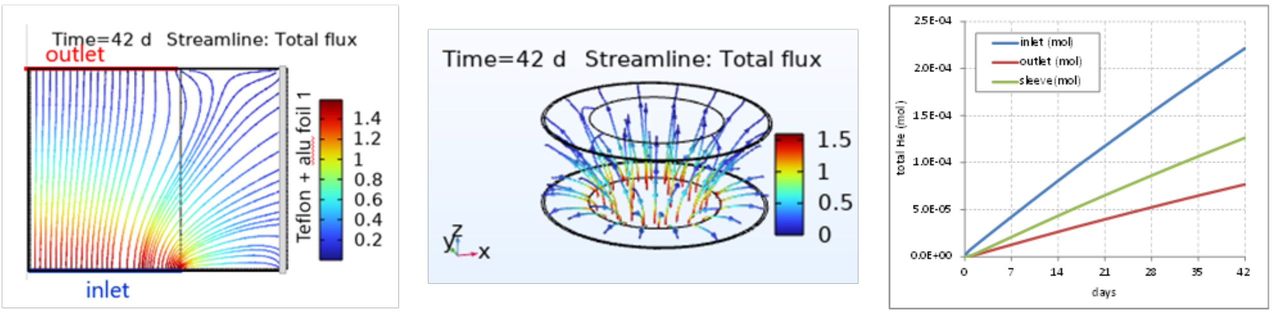

Figure 2.10: Modelling results for He transport in phase 1: streamline in 2D-axi model (left), 3D streamline (middle) and accumulated He at inlet, outlet and through the sleeve (right).

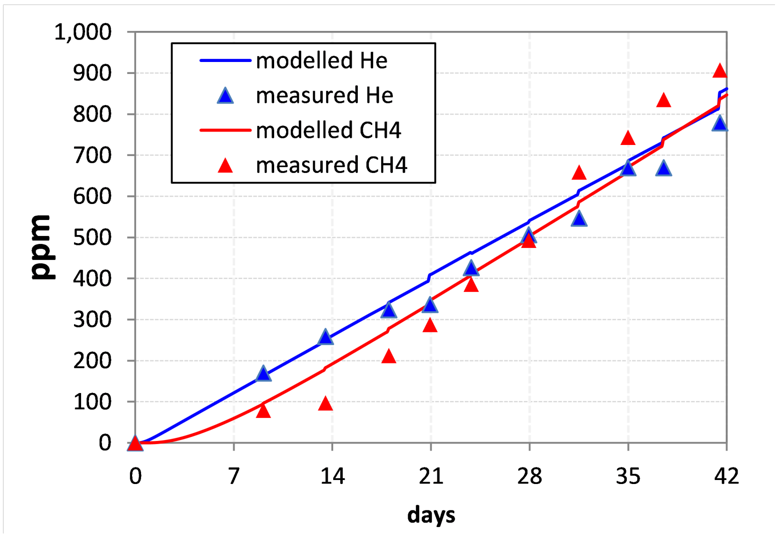

Figure 2.11: Comparison between the modelled gas concentration and measurements in both vessels.

- Flush also over the sample inlet
- Close the vessel again
- Now check the volume of gas available for gas by gas expansion
- Add a bit of water to the upstream vessel to give the gas phase some moisture
- Flush upstream side (incl. sample) 10x with He at 5 bar
- Pressurize upstream side at 5.3 bar
- Isolate sample again
- Perform short leak test
- Repressurise downstream vessel with CH_4 from 4.384 bar to 5.92 bar and down to 5.55 bar
- Turn on pump in downstream circuit to mix water and gas
- Take sample t=0 for phase 2
- Set pressure at both sides at same value: He = 5.08 bar and CH_4 = 5.11 bar
- At He side: close valves of pump and open bypass
- Restarted 24/3/2022 15:00

After starting the second phase, a small leak was observed in the upstream compartment, which was solved. The sampling is clearly visible by the pressure drops, once the pressure of the downstream vessel dropped below the value of the upstream vessel, the downstream vessel was repressurized (Figure 2.12).

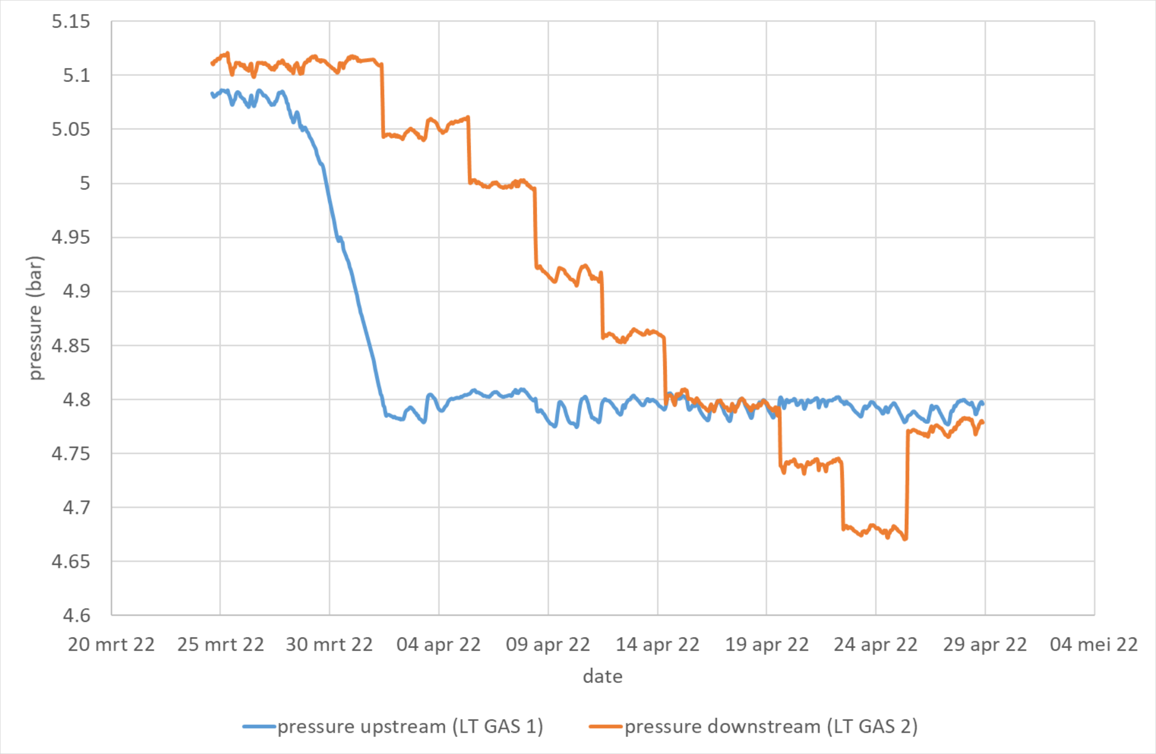

Figure 2.12: Pressure evolution in the upstream and downstream vessel, clearly showing the leak (blue line) in the upstream part (= LT gas 1) and the effect of sampling (orange line, LT gas 2) in the downstream vessel.

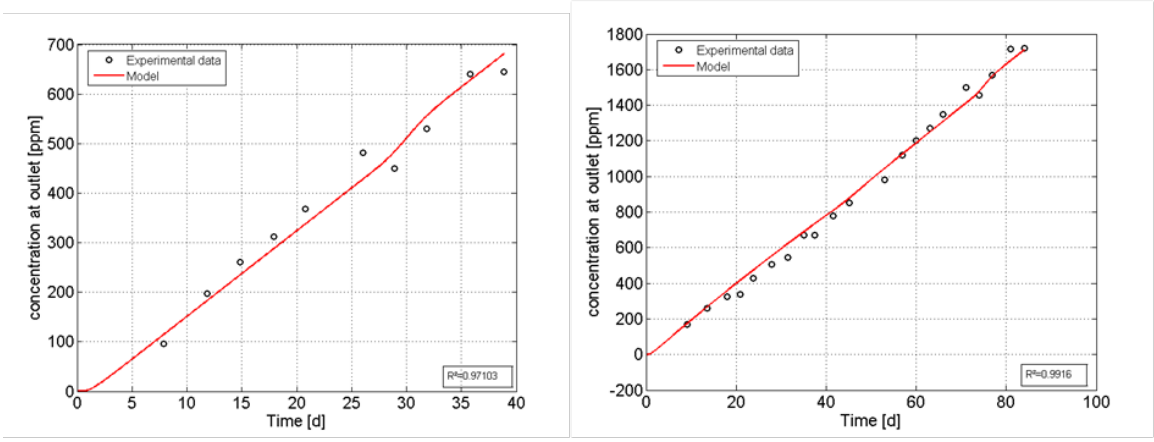

Figure 2.13: Net concentration increase of He in phase 1 (left) and in combined phase 1 + 2 concentration increase (right) as a function of time, using the 1-parameter fit

The concentration increase of helium as a function of time has been obtained (see Figure 2.13). The concentration change of CH_4 in the upstream vessel was no longer monitored, in order to keep the pressure in the upstream vessel constant.

In order to fit the diffusion coefficient of phase 2 with the model which is currently available, the net concentration increase was used. As the pressure of the gas in the downstream compartment has to be quasi constant (around 5 bar), the vessel is repressurized regularly. As adding gas leads to a dilution of the helium, the measured concentrations are corrected for all repressurisation/dilution steps. The fitted diffusion coefficients for phase 2 and combined phase 1 + 2 are shown in Table 2.5.

The difference between all measured D_{eff} values (phase 1, 2 and combined) and the different diffusion fitting strategies (1 parameter vs. 2 parameters) is small. It was observed that there is no significant difference between gas diffusion by using dissolved gas or pure gas.

Modelling results for phase 2 **Test observations :** A summary of the test observation is shown in (see Figure 2.14).

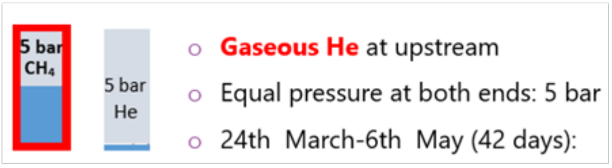

- **Gaseous He** at upstream
- Equal pressure at both ends: 5 bar
- 24th March-6th May (42 days):

- Leakage at upstream was found and repaired on April 1st.
- Pressure in the upstream vessel decreases from 4.8 bar to 4.79 bar during 35 days ;
- He increased from 981 to 1856 ppm in downstream vessel: 1856-981=875 ppm

Figure 2.14: Test observations in phase 2, with gaseous He at upstream with equal pressure at both vessels of 5 bar.

Modelling results:

The transport of He is modelled with the measured gas pressure in the upstream vessel as the boundary condition at the inlet. The modelled He concentration increase in the downstream vessel is very close to the ppm measurement in the first 28 days, as shown in Figure 2.15. Whereas after 28 days, the measured ppm deviates from the predicted line and becomes lower than the expected values.

Based on the diffusion modelling of He, the total He leaving the upstream vessel is calculated to be 1.9 10^{-4} mol in the last 35 days, which corresponds to a pressure drop of 0.05 bar, while the measured pressure drop is only 0.01 bar in the last 35 days. This is consistent to the measured lower ppm after 28 days. In the modelling, we don't differentiate between the gaseous He at inlet and the dissolved He at inlet. Whether this induces the small deviation needs further investigation. In general, in both phase 1 and phase 2, the measured data differs not much from the model results.

2.1.4.4. Diffusion phase 3

Experimental results Pressure was increased on May 10, 2022 from 5 to 10 bar, concentration increased steadily but the outflux was clearly increased compared to phase 1 and 2 (Figure 2.16) . When looking at the net concentration in helium in this phase (Figure 2.17) and fitting the diffusion coefficient, D_{eff} is now 2.3 times higher than at 5 bar, leading to D_{eff} ~5.3 x 10^{-10} m²/s (1 pm fit) or 5.6 x 10^{-10} m²/s for the 2 pm fit (Table 2.4).

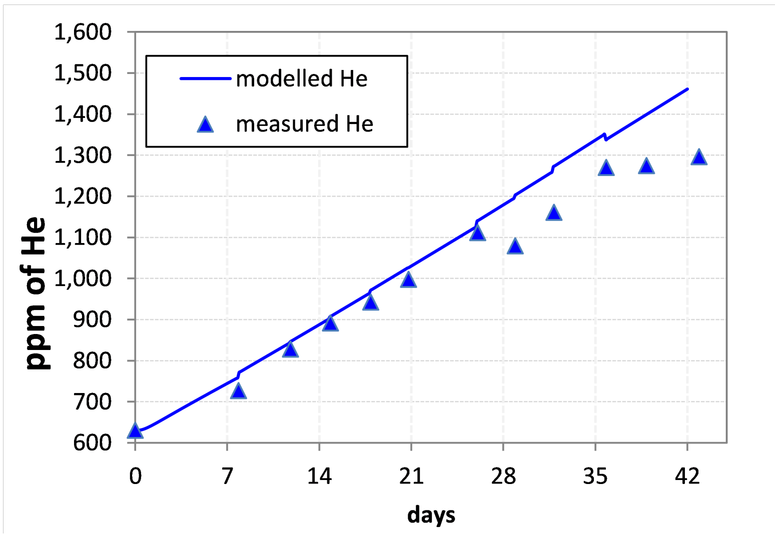

Figure 2.15: Comparison between the modelled He concentration in the downstream vessel and measurements.

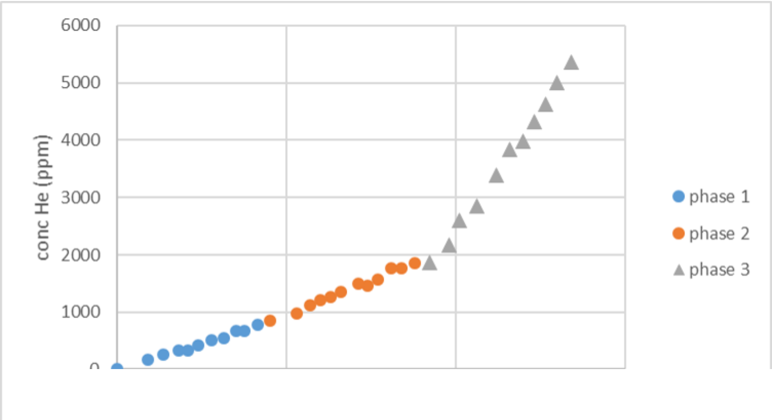

Figure 2.16: Conce

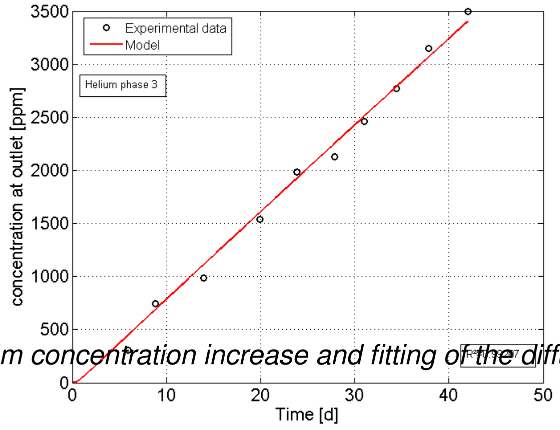

Figure 2.17: Net helium concentration increase and fitting of the diffusion coefficient in phase 3

Modelling results for phase 3 **Test observations :** Test observations are shown in Figure 2.18.

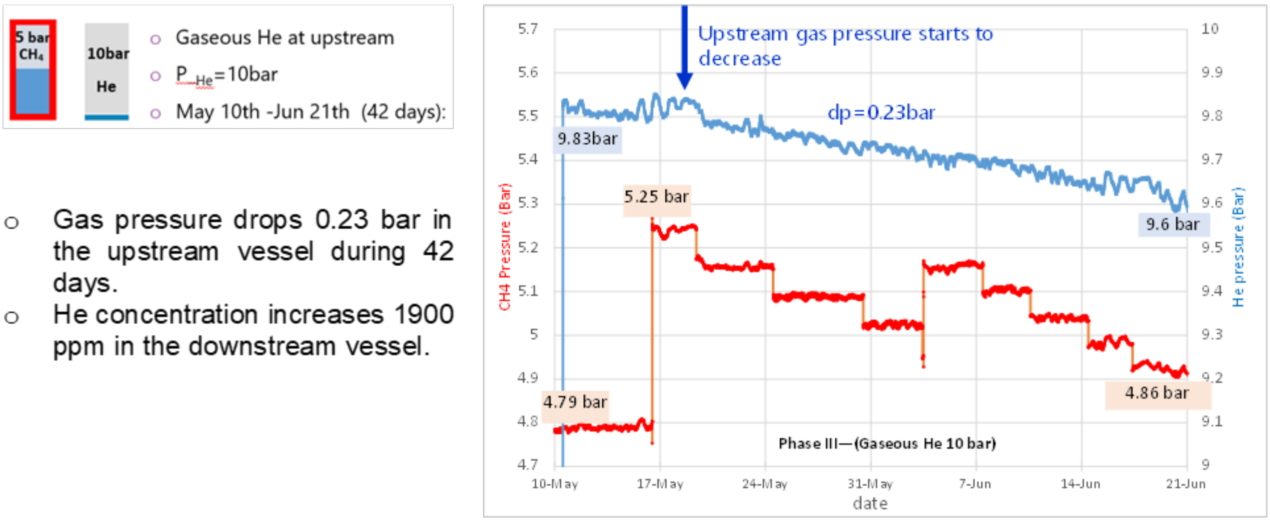

- Gas pressure drops 0.23 bar in the upstream vessel during 42 days.
- He concentration increases 1900 ppm in the downstream vessel.

Figure 2.18: Test observations in phase 3, with gas pressure of He at upstream increasing to 10 bar (red line for downstream vessel pressure corresponding to the left Y axis, and blue line for upstream vessel pressure corresponding to the right Y axis).

Modelling results:

Using the gas pressure measured in the upstream vessel as the boundary condition at inlet, the modelled He concentration increase in downstream vessel is close to the ppm measurement for the first 28 days, as shown in Figure 2.19 (top). After 28 days, measured ppm becomes larger than the expected values. By the end of phase 3, the measured He concentration is 1900 ppm while 1600 ppm is obtained from the modelling results. The total He out of the upstream vessel is calculated to be 4.6 x 10^{-4} mol, which corresponds to a pressure drop of 0.012 bar. This is much lower than the measured pressure drop of 0.23 bar.

A pressure drop of 0.23 bar means 0.009 mol He flowing out of the upstream vessel, see Figure 2.19 (bottom). An increase of 1900 ppm of He in the downstream vessel corresponds to 0.0002 mole He entering the downstream vessel. Besides, about 0.00026 mol He may diffuse through the sleeve into the isostatic cell. From the mass balance point of view, these values imply that 95 % gaseous He (about volume of 20 ml at 10 bar) is “lost” somewhere.

2.1.4.5. Diffusion phase 4 + 5 and further

Experimental results In phase 4, pressure was gradually increased from 10 to 15 bar. Phase 4 started on June 24, 2022 and ended July 15, 2022. The helium concentration in the inlet vessel increased strongly, with a net increase of almost 31 000 ppm over 20 days (Figure 2.20). The concentration increase is much larger than what would be expected from modelling calculations. Also, pressure in the upstream vessel decreased with 0.5 bar, which is more than the total amount of helium which diffused into the downstream vessel. So a part of the helium is “lost”. Later phases (pressure increase to 20 bar) showed similar results, with much higher flux through the sample, and a larger pressure decrease in the upstream vessel than the mass balance calculations would expect. Pressure was even increased to 20 bar, with similar results. An attempt to repeat the experiment with an upstream pressure of 5 and 10 bar failed. As we do not have a clear explanation for these results, they are not further discussed. In the future, the experiment will be repeated with other samples, which should increase the insight and understanding .

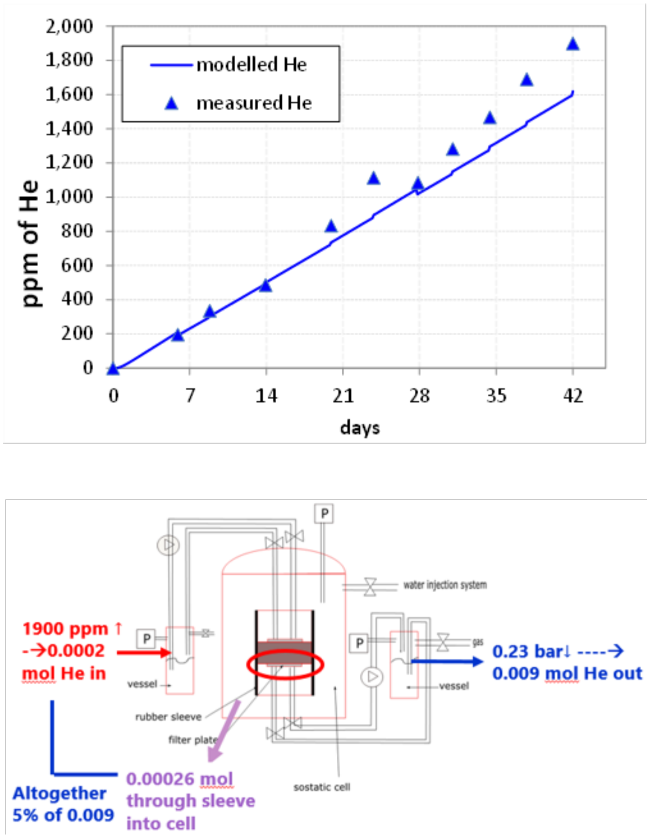

Figure 2.19: (top) Comparison between the modelled He concentration in the downstream vessel and measurements; (bottom) mass of He in the circuit.

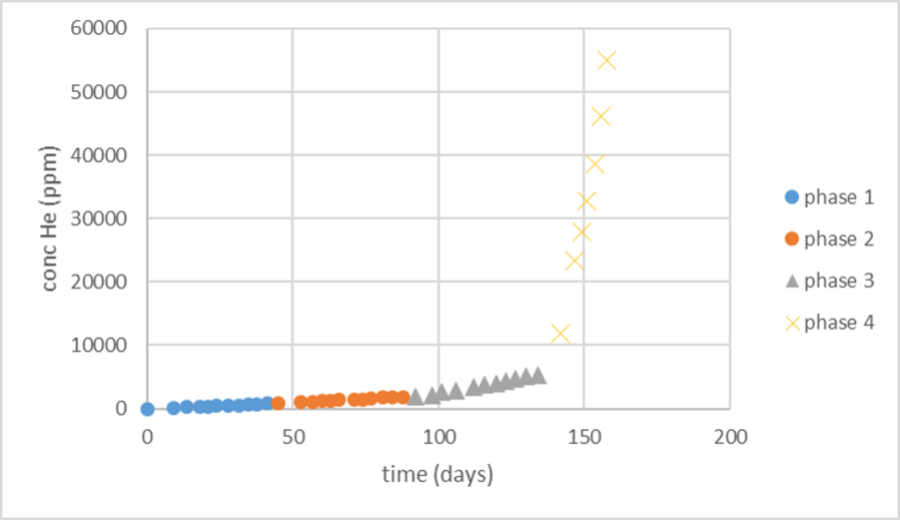

Figure 2.20: Concentration increase of helium in the downstream vessel in phase 1, 2, 3 and 4

2.1.4.6. Post-test CT scanning

A CT scan was performed on the post-test sample (Figure 2.21). When starting to look at the sample from bottom (injection side) to top, some features can be observed from the bottom on, indicating some black spots (= less x-ray attenuation so less dense material) which are considered to be (former) cracks. The cracks are mainly located at the centre of the sample, where the gas injection took place. For slice 266, the cracks have moved to the upper right corner, while they disappeared in slice 356. Around slice 375, a new crack appears, again located at the centre and also in slice 395 the crack is located at the centre but in a different quadrant. More towards the top, e.g. around slide 450, the sample looks homogeneous again, except for some small pieces of pyrite. So there is no trace of a continuous gas pathway over the full length of the sample, but especially at the lower part of the sample, there are indications for fracturing.

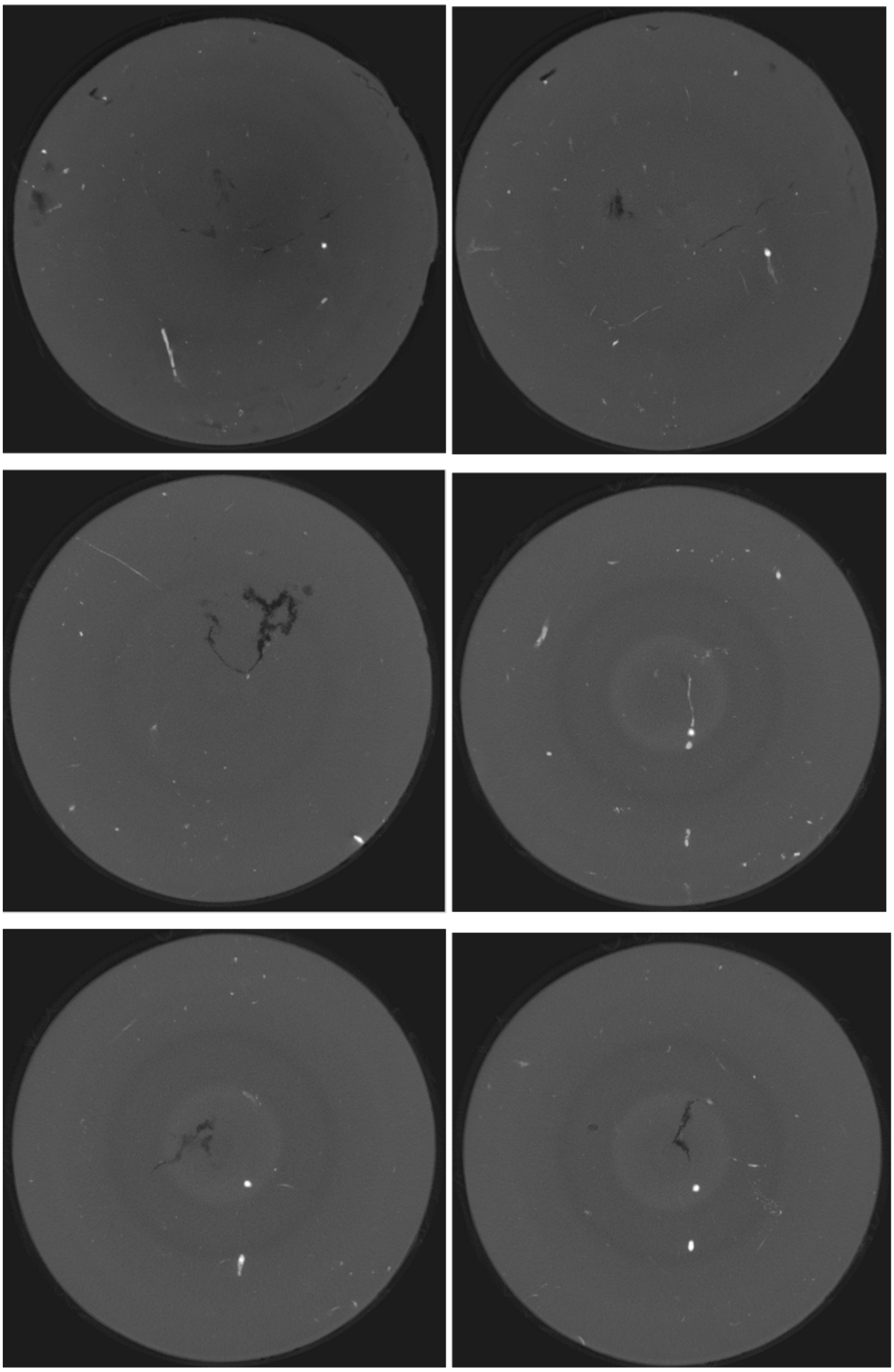

Figure 2.21: CT images of the sample. Black spots indicate less x-ray attenuation and thus less dense material (fractures). 6 representative slices are shown in this figure. Slice numbering starts from the bottom (injection side) of the sample. Top row: slice 195 and 207, middle row 266 and 356, bottom row 375 and 395

2.1.5. Summary

This chapter describes the result of the first long term gas injection experiment with a Boom Clay sample. The experiment started with sample preparation and sample loading to return the sample to in situ stress conditions. Next, the sample was resaturated and hydraulic conductivity was measured.

The diffusion-part started with diffusion of dissolved gases (He and CH_4) at 5 bar, where diffusion coefficients for He and CH_4 were obtained. Next, the injection side of the clay sample was exposed to pure He gas at 5 bar, and again the diffusion coefficient of He was measured. The diffusion coefficient for gaseous He was similar to the diffusion coefficient of dissolved He, indicating that the way the sample is exposed to gas (pure gas or dissolved gas) does not influence the outcome of a diffusion experiment.

In the following stage, the helium pressure upstream was increased to 10 bar, while the downstream pressure remained at 5 bar and again the diffusive outflux was measured and the diffusion coefficient was calculated but turned to be 2.5 times higher than in the previous stage. Next, the upstream pressure was increased to 15 bar, a strong increase in flux was observed, together with a continuous decrease in pressure (larger than the influx) in the upstream vessel. Currently, there is no clear explanation for the increase in helium flux at the outlet and the significant decrease in pressure at the inlet. Post-analysis testing of the sample by CT scanning showed the presence of potential gas fractures. Though, many questions and uncertainties remain. Therefore, proper interpretation of the advective phase of this experiment is not possible. A new experiment is started.

2.1.6. Key learning points

2.1.6.1. New knowledge acquired

Together with BGS, SCK CEN managed to measure the diffusion coefficient of helium through several sleeves, such as PVDF, heat shrink Teflon and a combination of heat shrink Teflon and aluminium foil. Diffusion of helium through heat shrink Teflon with aluminium foil is 5x slower than without foil. So adding foil reduces the loss of helium into the confining fluid. Diffusion of CH_4 is even much more reduced, so it can be considered to perform the diffusion experiment with CH_4 instead of He – in case leakage of gas into the confining fluid would complicate the interpretation of the experiment. The diffusion coefficients, measured in the preparation phase have been used later in the experiment to calculate the gas loss into the confining fluid.

The current experiment

- enabled us to verify if diffusion of dissolved gas is influenced by the confining method (within the pressure range of interest)
- illustrated that either performing tests with pure gas or dissolved gas provides same results

Impact of acquired knowledge

Two main objectives were formulated at the start of the EURAD-GAS project.

- Validate under controlled loading the mechanisms of diffusion of dissolved gas in Boom Clay (previous tests have been done in constant volume conditions).
- Investigate the limits of diffusive transport of dissolved gas and a possible transition to free gas flow during a long gas injection time.

The first objective has been met, as the results of the first test indicates only minor differences between diffusion under constant volume versus isotropic loading conditions.

Regarding the second objective, no conclusions can be drawn yet as the interpretation of results of the current experiment, when using a pressure gradient, are not clear enough for the moment. Experiments need to be repeated to improve understanding and gain confidence in the results.

2.1.6.2. Remaining knowledge gaps

The limits of diffusive transport of dissolved gas and a possible transition to free gas flow during a long gas injection time are still unknown. As only one sample was studied for now, the impact of sample morphology/heterogeneity is still unknown.

2.1.6.3. Recommendations for the future

It is strongly recommended to repeat the experiment, taking into account some improvements such as

- CT scanning of the sample prior to use, to avoid large heterogeneities such as pyrite inclusions which could lead to preferential gas pathways
- Improved leak testing, including all connections inside the isostatic cell
- Use of CH_4 instead of He, as CH_4 is less prone to leakage and diffusion through the membranes is slower
- Use of a detailed standard protocol for this type of test

References

De Craen, M., L. Wang, M. Van Geet and H. Moors (2004). Geochemistry of Boom Clay pore water at the Mol site. SCK-CEN BLG-990. Mol, Belgium.

Gonzalez-Blanco, L., E. Romero, P. Marschall and S. Levasseur (2021). "Hydro-mechanical Response to Gas Transfer of Deep Argillaceous Host Rocks for Radioactive Waste Disposal." Rock Mechanics and Rock Engineering.

Gonzalez Blanco, L. (2017). Gas Migration in Deep Argillaceous Formations: Boom Clay and Indurated Clays, Universitat Politècnica de Catalunya.

Harrington, J., A. Milodowski, C. Graham, J. Rushton and R. Cuss (2012). "Evidence for gas-induced pathways in clay using a nanoparticle injection technique." Mineralogical Magazine **76**(8): 3327-3336.

Horseman, S., J. Harrington and P. Sellin (1999). "Gas migration in clay barriers." Engineering Geology **54**(1-2): 139-149.

Jacops, E., M. Aertsens, N. Maes, C. Bruggeman, B. M. Krooss, A. Amann-Hildenbrand, R. Swennen and R. Littke (2017). "Interplay of molecular size and pore network geometry on the diffusion of dissolved gases and HTO in Boom Clay." Applied Geochemistry **76**: 182-195.

Jacops, E., T. Maes, A. Vanleeuw and H. De Soete (2022). Long term gas injection in Boom Clay, SCK CEN.

Jacops, E., G. Volckaert, N. Maes, E. Weetjens and J. Govaerts (2013). "Determination of gas diffusion coefficients in saturated porous media: He and CH_4 diffusion in Boom Clay." Applied Clay Science **83-84**: 217-223.

Jacops, E., L. Yu and A. Vanleeuw (2020). Long-term slow gas injection experiment under isostatic conditions in the Boom Clay: design of the setup and experimental protocol Status 2020 SCK CEN R-7363, Belgian Nuclear Research Center.

.

British Geological Survey (BGS)

2.2. Triaxial tests (BGS))

2.2.1. Introduction & Objectives

To accurately predict the movement of gas through argillaceous materials it is first necessary to define the correct conceptual model that best represents the empirical data. In a clay-based GDF four primary phenomenological models can be defined to describe gas flow as proposed by Marschall et al. (2005; *Figure 2.22*): (i) gas movement by solution and/or diffusion governed by Henry's and Fick's Laws respectively within interstitial fluids along prevailing hydraulic gradients; (ii) gas flow in the original porosity of the fabric governed by a generalised form of Darcy's Law, commonly referred to visco-capillary (or 2-phase) flow; (iii) gas flow along localised dilatant pathways (micro-fissuring), which may or may not interact with the continuum stress field, the permeability of which is dependent on an interplay between local gas pressure and the effective stress state; and (iv) gas flow along macro fractures similar in form to those observed in hydrofracture activities during reservoir stimulation, where fracture initiation occurs when the gas pressure exceeds the sum of the minor principle stress and tensile strength.

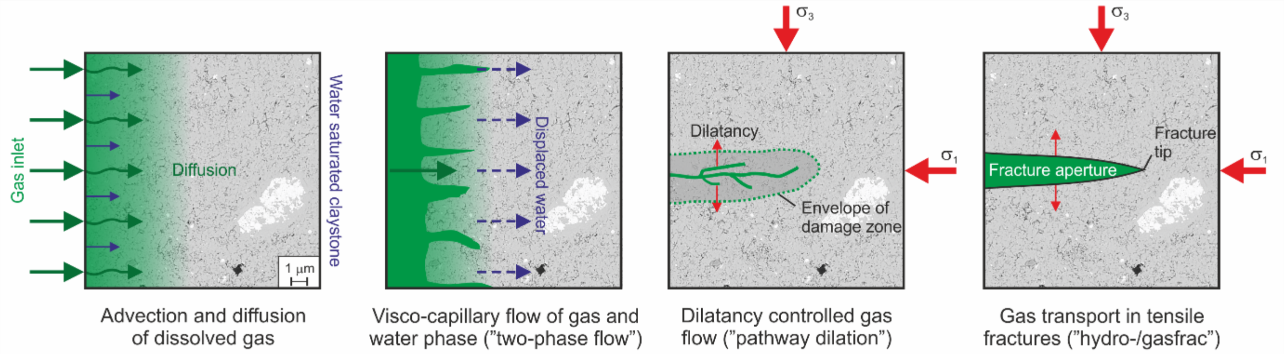

Advection and diffusion of dissolved gas

Visco-capillary flow of gas and water phase ("two-phase flow")

Dilatancy controlled gas flow ("pathway dilation")

Gas transport in tensile fractures ("hydro-/gasfrac")

Figure 2.22: Description of the four main processes of gas movement in clays (after Marschall et al., 2005)

Two primary modes for advective gas transport through natural mudrocks are therefore proposed; (i) visco-capillary flow, where capillary forces must be overridden to allow displacement of the wetting phase, by migrating gas and (ii) the formation of discrete gas-filled pathways, by localised consolidation of the clay matrix. The potential for one specific mechanism to prevail is dependent on a range of factors, including the saturation state of the clay and the amount of clay present. Natural heterogeneity within clay-hosted repositories may also play an important role in the migration of gas and the mitigation of peak gas pressure. For fully saturated, pure clay bentonite materials, such as those used in engineered barriers, experimental evidence indicates that gas flow by pathway dilation is the preferred mode of transport. In such cases, significant hydromechanical coupling is observed, which cannot be satisfactorily explained by visco-capillary flow processes. This hydromechanical coupling between the immiscible phase, the interstitial fluid, and the total stress, remains unclear.

To address these issues, an experimental study was proposed examining the fundamental mechanisms governing gas flow through intact mudrocks and the petrographic controls on the transition between displacement and dilatant flow. The use of a bespoke triaxial apparatus under different boundary conditions aimed to identify both the primary transport mechanism for each material and commonalities in behaviour. Tests were conducted on Boom Clay (BC) and Callovo-Oxfordian claystone (COx) at both a "low" and "high" stress conditions.

2.2.2. Experimental set-up

2.2.2.1. Description of apparatus

The study utilizes a modified version of a triaxial apparatus used on previous studies of Opalinus Clay (Cuss et al., 2007), Boom Clay (Harrington et al., 2017), and reservoir rocks (Harrington et al., 2018). The modification brought the apparatus up to the same operational capacity as the Stress Path Permeameter used on the EU FORGE project (Cuss et al., 2014).

The triaxial apparatus (Triax Rig) consisted of 5 main components (*Figure 2.23*, *Figure 2.24*):

1. The sample, placed in a flexible Hoek sleeve within the main pressure vessel.
2. An axial loading system consisting of a single Enerpac hydraulic ram which was pressurised by a Teledyne Isco series 260D syringe pump. The axial ram was connected to a Linear Variable Differential Transformer (LVDT) with an accuracy of 0.001 mm.
3. A confining pressure system using a Teledyne Isco series 260D pump.
4. An injection and backpressure system using one 260D (Back pressure) and 500D (injection) Teledyne Isco syringe pumps. This allowed fluid (water or gas) injection and for the measurement of porewater displacement from the sample.
5. A custom designed data acquisition system which allows remote monitoring and controlling of all experimental parameters.

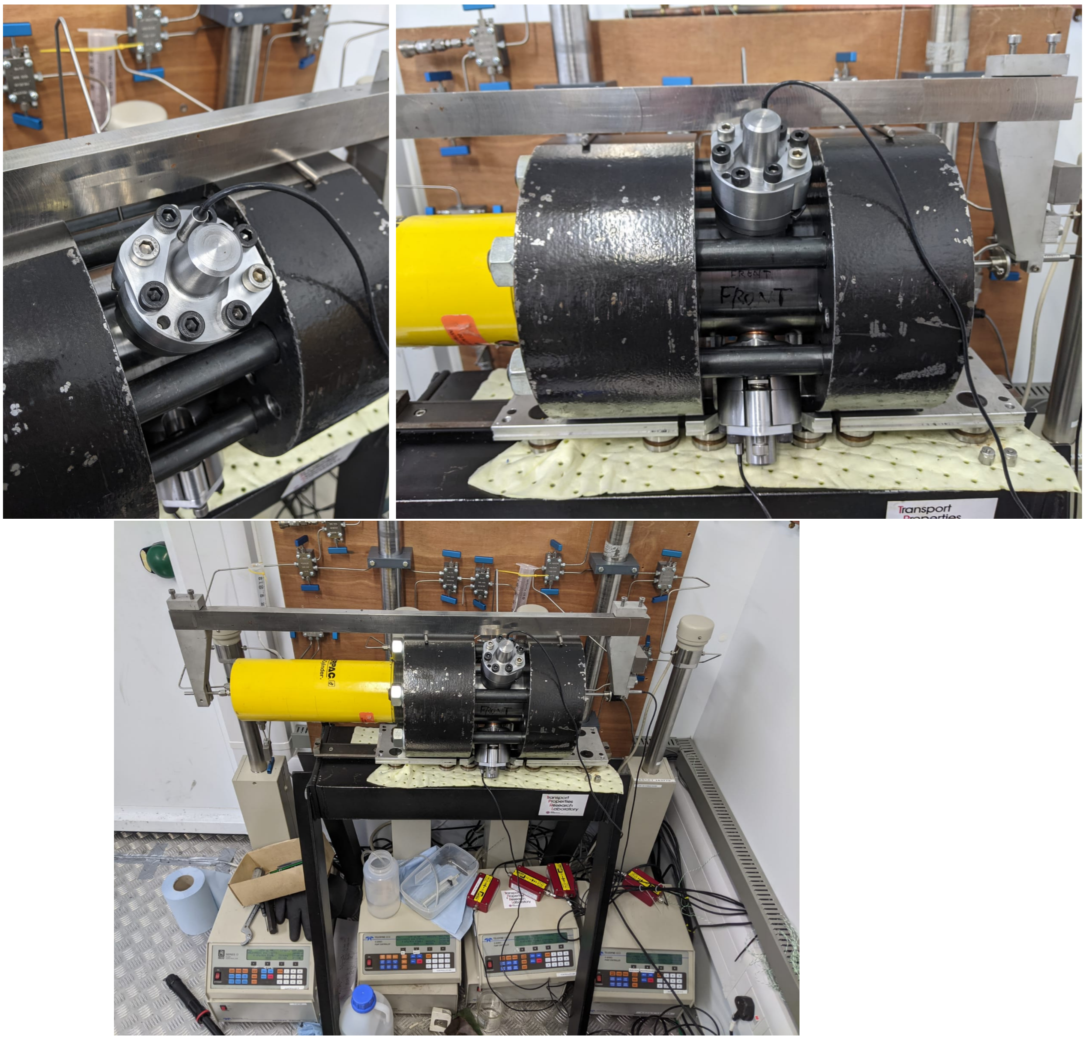

Figure 2.23: Photographs of the modified Triax apparatus.

The existing apparatus was modified for the current study to give radial strain measurement (*Figure 2.23*, *Figure 2.24*). The pressure vessel of the apparatus was modified by the addition of three radial strain measurement devices. These were spaced by 120° at the mid-plane of the sample and were an existing proven design as used in the BGS Elastimeter apparatus. These pressure balanced devices had steel rods in direct contact with the outer diameter of the Hoek sleeve. Three 10mm diameter brass plates were cemented to the outer edge of the Hoek sleeve in order to reduce the force the push-rods imposed on the sample surface. The push rods extended to the outside of the pressure vessel, where high precision LVDTs were used to measure the displacement of the sample diameter. The LVDTs could measuring sub-micron displacements. Because of the dimensions of the Triaxial apparatus used, compared with the existing Elastimeter, the sealing mechanism of the radial devices needed to be modified.

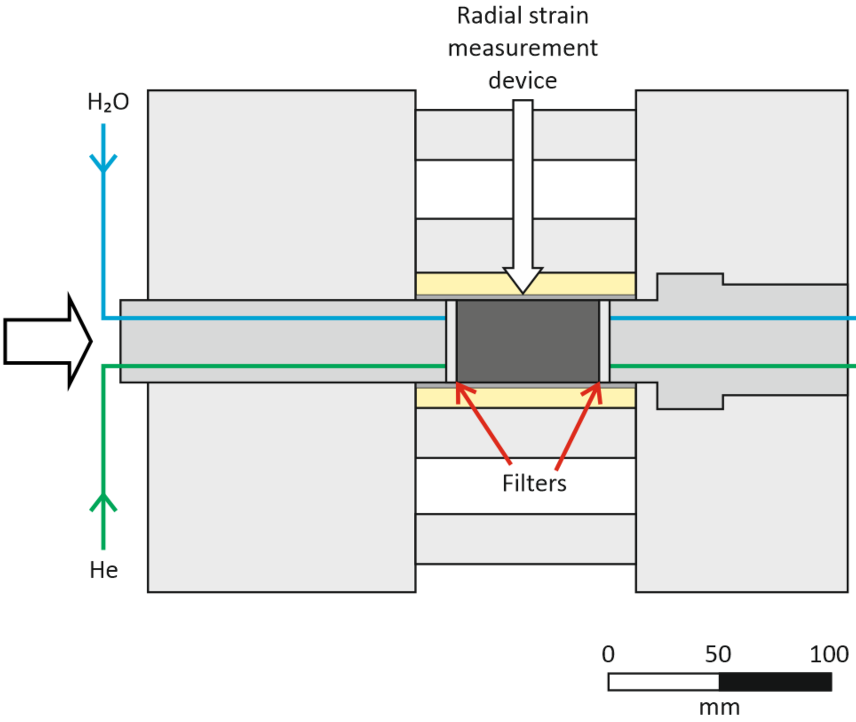

Figure 2.24: Schematic of the triaxial apparatus.

Prepared samples (Figure 2.25a) were placed within the Hoek sleeve, which was then housed within the main pressure vessel (Figure 2.25bc). The pressure vessel had an o-ring at each end, which was in contact with the widest part of the Hoek sleeve. These o-rings ensured that the confining fluid (glycerol) did not come into contact with the sample. Porous filters were added to each end of the sample and the pressure vessel was placed in the Triax rig (Figure 2.25de). Each end of the sample was held in contact with the stainless-steel platens, which applied the axial load from the Enerpac ram. Retaining collars and axial tie-rods locked the system components together so that the apparatus could not move during testing. Each of these assembly steps are shown in Figure 2.25.

All tests were conducted at two confining pressures, denoted high and low. For Boom Clay this corresponded with depths of interest within the Netherlands and Belgium (400m) and the HADES URL in Belgium (220m). For Callovo-Oxfordian claystone one stress state corresponded to the depth of sample extraction (450m), with the second stress state moderately higher.

The following parameters were recorded directly: Starting dimensions of the sample; Starting weight of the sample; Confining pressure; Axial stress; Injection pressure; Back pressure; Axial strain; Radial strain ×3; Volume and pressure of the injection pump; Volume and pressure of the axial pump; Volume and pressure of the injection pore pressure pump; Volume and pressure of the back pressure pump; Temperature of the laboratory; End dimensions of the sample; End weight of the sample; End weight of the sample after drying; and Time. From these parameters, the following were determined: Saturation state of the starting material; Porosity and void ratio of the starting material; Axial strain; Radial strain; Volumetric strain; Volumetric strain from volume of the confining system; In flow; Out flow; Timing of major events giving a velocity of gas movement through the sample; Saturation state of the end material; and Porosity and void ratio of the end material.

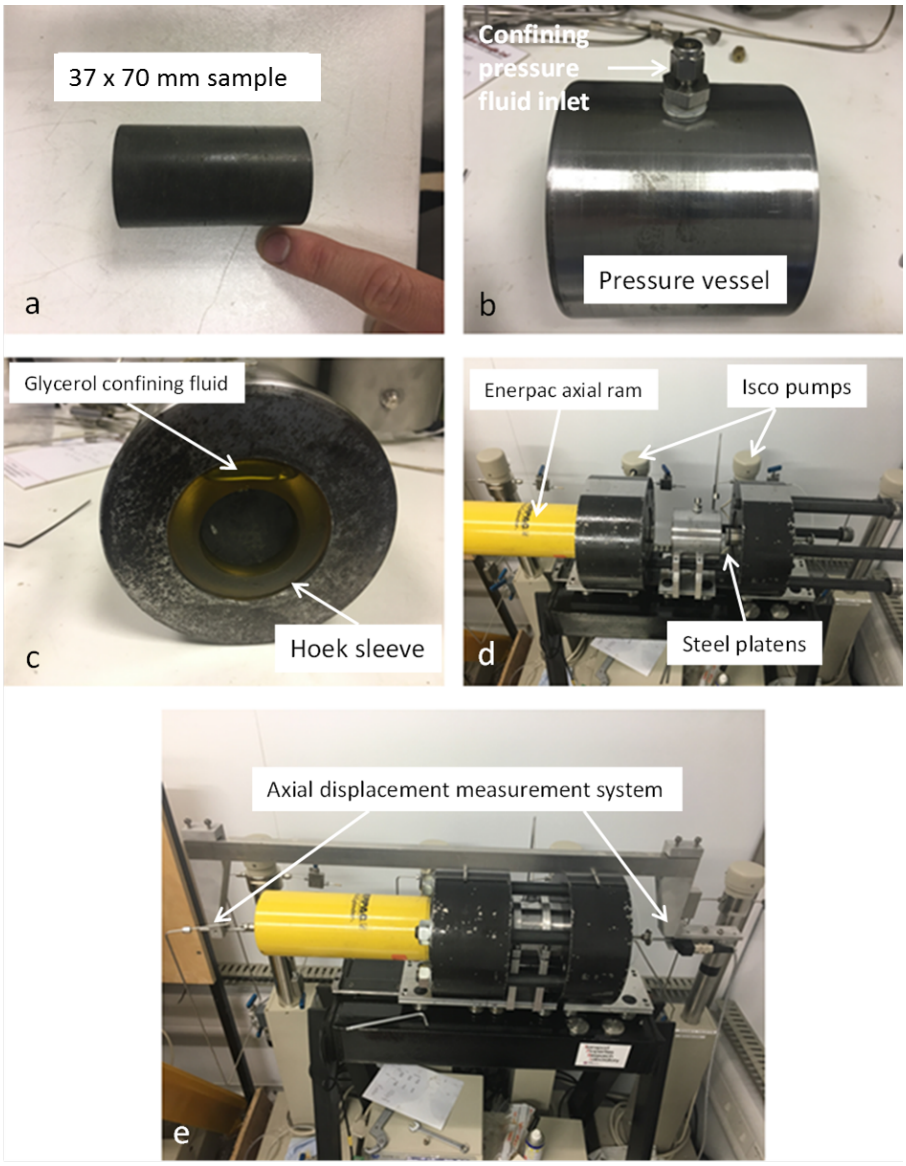

Figure 2.25: Assembly of the triaxial apparatus a) Test sample and size used; b) Pressure vessel showing confining pressure inlet; c) Sample within Hoek sleeve and confining fluid surrounding; d) Test set-up showing pumps and Enerpac axial ram; e) Final test set-up with axial ram and axial displacement measurement system mounted. Note: Apparatus shown in pre-modified state

2.2.2.2. Calibration

The apparatus comprised four syringe pumps, four Gems pressure transducers, and four Linear Variable Differential Transformers (LVDT). Each type of device had a different calibration routine and/or cycle between repeat measurements.

The four displacement LVDT devices were only re-calibrated at the end of the experimental programme. For all four devices the manufacturer supplied calibration was initially assumed. Re-calibration was performed using calibration blocks, which were manufactured to high standard and allowed the devices to be displaced by known distances. By using multiple calibration blocks over a range of lengths, it was possible to confirm calibration of all four devices.

The syringe pumps and pressure transducers were calibrated after each test. The confining pressure, injection pressure, and back pressure syringe pumps (and corresponding pressure transducers) were pressurised at 0 (atmospheric), 2, 4, 6, 8, 10, 12, 14, 16, 18, 20, 18, 16, 14, 12, 10, 8, 6, 4, 2 and 0 MPa. The axial syringe pump and pressure transducer were pressurised at 0 (atmospheric), 0.1, 0.25, 0.5, 1, 2, 3, 4, 5, 7.5, 10, 7.5, 5, 4, 3, 2, 1, 0.5, 0.25, 0.1 and 0 MPa. At each stage the pressure reading of a Fluke pressure calibrator was noted to give precise pressure measurement. The Fluke calibrator was itself re-calibrated by the manufacturer on an annual basis to industry standards.

The Triax Rig does not have a direct measure of load on the sample. However, the pressure in the axial ram is known, which can be converted to load knowing the area of the end of the sample. To confirm this, a calibration was performed at the start and end of the experimental program by replacing the pressure vessel assembly with a calibration load cell. This load cell was itself calibrated annually by the manufacturer to industry standards. The load cell was loaded over a range of steps and the electrical output noted against the load reading of the calibration device. This calibration was used to convert the pressure in the axial ram to force, allowing axial stress to be determined.

For all calibration data the slope, intercept, and R^2 was calculated, the latter being used to ascertain whether the calibration had been of sufficient quality, with R^2 expected to be close to unity. As well as R^2, graphs of the calibration data were also inspected. Where necessary, calibration was repeated if R^2 was not acceptable. During the experimental programme, no device showed significant deviation from the initial calibration.

2.2.2.3. Testing fluids

All tests were conducted with helium as the gas permeant. Given the importance of fluid chemistry on the behaviour of clay-rich materials, it is crucial that transport and mechanical testing is conducted using water in equilibrium with the test material. For the hydraulic stage of the experiment, synthetic pore water was manufactured to ensure the water was chemically balanced with the test samples.

Boom Clay synthetic pore fluid

A detailed analysis of pore fluid data for the Boom Clay formation was conducted by De Craen et al. (2004) and a reference pore water composition defined for HADES (*Table 2.6*). Synthetic solutions were mixed in batches approximately every 6 months, depending on the amount of testing being conducted.

Table 2.6: Reference Boom Clay pore water after De Craen et al. (2004).

Ion	mg/l	mmol/l	Ion	mg/l	mmol/l
Ca	2.0	0.05	**Al**	0.6×10^{-3}	2.4×10^{-5}
Fe	0.2	0.003	**Total S**	0.77	0.02
Mg	1.6	0.06	**Cl -**	26	0.7
K	7.2	0.2	**SO_4^{2-}**	2.2	0.02
Si	3.4	0.1	**HCO_3 -**	878.9	14.4
Na	359	15.6			

Callovo-Oxfordian claystone synthetic pore fluid

The hydrochemistry of the interstitial fluid was provided by Andra (*Table 2.7*). A stock solution comprised of the following components was used as the aqueous test fluid in all hydraulic test stages: Ca^{2+} (227 mg l^{-1}); Mg^{2+} (125 mg l^{-1}); Na^+ (1012 mg l^{-1}); K^+ (35.7 mg l^{-1}); SO_4^{2-} (1266 mg l^{-1}); S_i (4.59 mg l^{-1}); S_iO^2 (9.83 mg l^{-1}); S_r (13.5 mg l^{-1}); total S (423 mg l^{-1}); total Fe (0.941 mg l^{-1}).

Table 2.7: Synthetic pore fluid geochemistry for Callovo-Oxfordian claystone.

Ion	mg/l	Ion	mg/l
NaCl	1950	**MgSO4, 7H20**	1020
NaHCO3	130	**CaCl2, 2H2O**	80
KCl	35	**Na2SO4**	700
CaSO4, 2H2O	630		

2.2.3. Material properties (pre-test and post-test characteristics)

Boom Clay

The geological and hydrogeological setting of the Boom Clay in northern Belgium has been summarised by Beerten & Leterme (2012) and in the Netherlands by Vis & Verweij (2014). The Boom Clay (usually referred to as the Rupel Clay in the Netherlands) is of lower Oligocene (ca 28 to 34 Ma) age and forms part of the Rupel Formation. In the Netherlands the Rupel Formation has been subdivided into the Vessem, Rupel Clay and Steensel members (Wong et al., 2007). These members are diachronous, with both the basal Vessem and the overlying Steensel members being sandy marine deposits (Vis & Verweij; 2014) laid down close to the palaeo-shorelines. The Boom Clay is a pyritic, grey to dark brown marine clay with septarian (carbonate rich) concretions. Towards the basin margins the clays grade into sands. The formation reaches a maximum thickness of up to 250 m, with a mean thickness of around 65 m, and dips gently towards the north-east at between 1 and 2°.

The core material used in the current study was taken from the HADES underground research laboratory at Mol in Belgium. Here, the Boom Clay consists mainly of mixed clay and silt, with additional minor sand (Bernier & Bastiaens, 2007). Mineralogical composition of the Boom Clay is widely reported, predominantly assessed using XRD. The clay content is generally reported to vary from between 23 and 60 % of the bulk material composition and is predominantly made up of illite, smectite, and kaolinite, which is often seen in interlaminated zones (Blanchart et al., 2012; Dehandschutter et al., 2004; Wemaere et al., 2008; Yu et al., 2012). The non-clay fraction of the Boom Clay primarily consists of quartz, again widely reported to vary between 23 and 60 %. The remaining percentage of the non-clay fraction consists of feldspars, calcite, and pyrite. Honty & De Craen (2011) report the composition to be 22-77 % quartz, 0-6.3% albite, 0.4-17.3% k-feldspar, 0-1.5% siderite, 0-4.6% calcite, 0-2% apatite, 0.3-5% pyrite, 5-37% illite/muscovite, 6.8-35% smectite + illite/smectite, 2-16% kaolinite, and 14-4% chlorite. This demonstrates the variability of Boom Clay. Cores of Boom Clay were acquired from EURIDICE (Belgium) from the HADES URL from a depth of 220m.

Callovo-Oxfordian claystone

The Callovo-Oxfordian claystone (COx; 150-160 Ma) was deposited under marine basin conditions during a period in which the Paris Basin, France, was variously linked to the Atlantic and Tethyan Oceans, as well as to the London Basin and North Sea (Rousset & Clauer, 2003). Clay sedimentation is therefore considered to have two primary inputs; continental and oceanic. The claystone is over- and underlain by Oxfordian and Bathonian shelf limestones. It is primarily clayey at its base, then becomes increasingly silty and then increasingly calcareous at its top (Gaucher *et al.*, 2004). A maximum clay content zone within the clayey base has been identified; this is interpreted to mark the inflection point (and interval of maximum flooding) from a lower transgressive sequence to an upper regressive sequence (Gaucher *et al.*, 2004).

The UA variety of the COx occurs at repository depth and can be considered to be the clay-rich part of the unit. The samples used came from the Meuse/Haute-Marne underground research laboratory at Bure in France. Yven *et al.* (2007) report three main mineral phases; clay minerals, quartz, and calcite. Secondary mineral phases include dolomite, feldspar, pyrite, hematite, and traces of siderite. Calcite and quartz represent 40 – 55 % of the rock. Clay represents 20 – 55 %, with secondary minerals forming less than 5 %. Clay minerals include illite and illite-smectite with subordinate kaolinite and chlorite. Wenk *et al.* (2008) reports clay 25-55 wt%, 23-44% carbonates and 20-31% silt (essentially quartz + feldspar). Clay minerals are reported to include illite and illite-smectite with subordinate kaolinite and chlorite. In the upper half of the formation the illite-smectite is disordered and contains 50-70% smectite interlayers, whilst in the lower half the illite-smectite is ordered (R=1 type) with lower contents (20-40%) of smectite interlayers (Wenk *et al.*, 2008). Beds can contain common organic matter. Other authors report compositions similar to these. Wileveau & Bernier (2008) quote values for quartz (18%), calcite (25%), clay minerals (55%; illite-smectite ~65%, illite 30%) and kaolinite and chlorite (2%) with subordinate feldspars, pyrite, and iron oxides (2%). Esteban *et al.* (2006) report 35-60% clay minerals with the remaining shared by calcite and silt. Armand *et al.* (2017) report that the UA unit makes up two-thirds of the total geological layer thickness.

Upon receipt of preserved T-cell core barrels from Andra, the material was catalogued and stored under refrigerated conditions of 4 ℃ to minimize biological and chemical degradation. The preserved core barrels consisted of a multi-layered arrangement designed to re-stress the core to *in situ* stress and to environmentally seal it to reduce chemical, biological, and drying effects. Samples were tested within 12 months of the core being extracted from the Meuse/Haute-Marne URL.

Sample Preparation

Callovo-Oxfordian claystone arrived at BGS in a pre-stressed state in a T-cell. The Boom Clay samples were stored in an unstressed state in vacuum packed foil. Once extracted from the storage arrangement (T-cell or foil), approximately 300mm of core was available, which was subsampled for testing.

During the sub-sampling process a section of core approximately 80 mm in length was cut using a diamond saw. This cut length of core was then trimmed on the lathe (*Figure 2.26*) to the sample dimensions of 37 mm in diameter and 70 mm in length; during this process care was taken to ensure the face of the sample was perpendicular to the length of the sample. This process was done as quickly as possible to reduce the time the sample was exposed to the atmosphere and therefore maintain, as much as possible, the in-situ properties of the core. Both the cut sample for testing, as well as the remains of the large core were then wrapped in cling film and vacuum packed for storage.

Figure 2.26: Callovo-Oxfordian Claystone sample being cut on a lathe during the careful sample preparation process.

Pre- and post-test analysis

Geotechnical data were collected for all sample pre- and post-test. These are summarised in *Table 2.8*.

Table 2.8: Geotechnical data.

	COx1	**COx2**	**BC1**	**BC2**
Diameter pre-test (mm)	38.61	37.85	36.67	37.99
Diameter post-test (mm)	36.86	37.72	36.86	38.35
Length pre-test (mm)	62.01	65.07	67.09	60.73
Length post-test (mm)	67.25	65.35	67.25	61.39
Weight pre-test (g)	177.34	178.22	143.96	139.4
Weight post-test (g)	176.61	179.19	145.52	140.89
Moisture content pre-test	0.066	0.071	0.231	0.230
Moisture content post-test	0.061	0.077	0.245	0.243
Bulk density pre-test (kg/m^3)	2443	2434	2032	2025
Bulk density post-test (kg/m^3)	2462	2416	2010	2004
Dry density pre-test (kg/m^3)	2292	2273	1650	1647
Dry density post-test (kg/m^3)	2319	2243	1615	1612
Grain density (kg/m^3)	2710	2710	2670	2670
Porosity pre-test	0.154	0.161	0.382	0.383
Porosity post-test	0.144	0.172	0.395	0.396
Void ratio pre-test	0.182	0.192	0.618	0.621
Void ratio post-test	0.168	0.208	0.653	0.656
Saturation pre-test	0.978	1.02	0.999	0.988
Saturation post-test	0.988	1.01	0.999	0.988

2.2.4. Testing protocol

The test program was designed to perform several experiments in a similar manner. To be able to compare test results, it was not possible to significantly deviate from the set test protocol. The only variations were related to the length of each stage or the magnitude of stress at when stages were considered complete. Below is a general description of the adopted protocol.

1. **Preparation:** The sample was prepared, photographed, weighed, and measured. Thorough notes taken on any specific features seen in the sample.
2. **Apparatus construction:** The sample was loaded into the apparatus ensuring that when the tensioning rods were pre-tensioned that no load was placed on the sample. This usually meant that the axial ram had to be withdrawn sufficiently that the sample was shorter than the distance between the two loading platens. The apparatus was re-constructed with a tension of 300 Nm on all the six tie rods.
3. **Initial sample loading:** The axial load syringe pump was set to a constant pressure of 200 kPa. This usually took several minutes to achieve as the axial ram had to close the gap between the sample and platens. Once a pressure of 200 kPa was achieved, the pressure in the injection and back-pressure filters was drained to atmospheric. A confining pressure of 200 kPa was then created. This also took several minutes as the Hoek sleeve arrangement resulted in a small volume of trapped air. Although the confining and axial pumps were set to the same pressure, the load on the sample is 3.7 greater than the pressure in the ram. Therefore, there was no risk of leakage from the confining system into the sample.
4. **Pressurisation stage 1:** The confining and axial systems were increased to effective stress levels over a 24-hour period using the Programme Function of the syringe pump. The effective stress was determined to be the confining/axial stress – pore pressure.
5. **Pressure holding:** Pressure was held constant for around one hour to make sure the sample was not creeping. In all tests, the flow of the confining and axial pump quickly stabilised to a low flow and the axial and radial LVDT instruments indicating that there was minimal drainage/creep of the samples.

6. **Pressurisation stage 2:** The injection and back-pressure systems were connected, and synthetic pore fluid was injected into the porous filters using a constant pressure of 200 kPa. The filters were drained of air to ensure minimal residual air was left in the filters. All four syringe pumps (confining, axial, injection, back-pressure) were increased to starting operating conditions over a 24-hour period using the Programme Function of the syringe pumps.
7. **Monitoring:** The flow of the injection system was monitored once the boundary conditions had been reached. Flow generally reduced to less than 1 µl/h within 7 days, often within 24 hours. At this time, the injection and back-pressure systems were isolated from one another.
8. **Hydraulic testing:** A hydraulic test was conducted by raising the pore pressure of the injection system and lowering the pressure in the back-pressure system by the same magnitude. Initially, the pore pressure pumps were changed by ±250 kPa to give a 500 kPa differential across the sample. If this was insufficient to generate steady state flow, it was increased to a gradient of 1000 kPa or 2000 kPa. The gradient was maintained for at least 7 days, depending on whether stead state flow had been achieved. At the end of the hydraulic test, the gradient across the sample was removed and flow was monitored for a further 7 days until flow in/out of the sample had stopped.
9. **Gas injection ramp 1:** The interface vessel was filled with a known volume (~100ml) of helium. Water was injected into the base of the interface vessel to generate a gas pressure. The interface vessel was filled with water until the volume of the pump was empty. In refilling the pump, the water level in the interface vessel retracts. In this way, there was no chance of water being injected into the sample (which could result in hydrofracture) and the volume of the interface vessel occupied by gas was known. The interface vessel was then filled with gas at the pore pressure. The connecting pressure lines to the apparatus and the porous filters were drained using the gas at pressure. This ensured that water was expelled from the filters with a minimal reduction in pore pressure. A small decrease in gas pressure was inevitable and therefore the interface vessel was recharged with helium at the starting gas pressure. The syringe pump was then set to constant pressure to achieve steady gas pressure. After a few hours, the syringe pump was set to constant flow. As water was injected into the base of the interface vessel at a constant rate, the volume occupied by the gas reduced and the gas pressure increased. This resulted in a non-linear increase in gas pressure. The injection rate of the syringe pump was set to raise pressure from pore pressure to ~¾ of the way to confining pressure in 21 days.
10. **Pressure hold:** The syringe pump controlling the injection system was changed to constant pressure once the target pressure was achieved. Flow was monitored for between 7 and 14 days. This stage aimed to observe any flow into the system at a pressure below the minimum principal stress.
11. **Gas injection ramp 2:** If necessary, the interface vessel was refilled with helium. The syringe pump was set to constant flow, aiming to reach the minimum principal stress (confining pressure) in 14 days.
12. **Gas entry:** Once gas entry had occurred and a clear gas peak pressure achieved, the injection pump was continued to inject at the same rate. Post-peak behaviour was observed for up to 4 weeks.
13. **Depressurisation:** The gas injection pressure was lowered to the pore pressure over a one-hour period. The injection and back-pressure systems were then connected. This allowed all four syringe pumps to be reduced to a magnitude of 200 kPa over a six-hour period.
14. **Dismantling of apparatus:** The apparatus was depressurised the final 200 kPa to atmospheric pressure over a period of minutes. The apparatus was then dismantled, and the sample was measured, weighed, photographed, and vacuum sealed for interim storage.

The test protocol is summarised visually in *Figure 2.27* for an idealised test program and in *Table 2.10*. The test program is summarised in *Table 2.9*. Further test will be conducted up until the end of the project.

Table 2.9: Test program. HY = hydraulic test; GE = gas entry; PP = post peak pressure; // = sample long-axis parallel with bedding; ⊥ = sample long-axis perpendicular to bedding.

Test	Rock type	Test name	Stages	Boundary condition	Bedding direction
1	Callovo-Oxfordian	COx1	HY, GE, PP	In situ	//
2	Boom Clay	BC1	HY, GE, PP	In situ (220m)	⊥
3	Boom Clay	BC2	HY, GE, PP	In situ (400m)	⊥
4	Callovo-Oxfordian	COx2	HY, GE, PP	In situ +	//

Table 2.10: Test protocol.

Stage	Title	Description	Days
1	Preparation	Measurement of sample	0.04
2	Apparatus construction	Assembly of apparatus with sample	0.04
3	Initial sample loading	Loading to 200 kPa confining pressure	0.04
4	Pressurisation stage 1	Increasing confining and axial systems to effective stress	1
5	Pressurisation holding	Monitoring for creep	0.04
6	Pressurisation stage 2	Increasing to test boundary conditions	1
7	Monitoring	Re-saturation and stabilisation of flow	7
8	Hydraulic testing	Two stage hydraulic test	14
9	Gas injection ramp 1	Increasing gas pressure to ¾ of confining pressure	21
10	Pressure hold	Monitoring for flow at stress lower than minimum principal stress	7
11	Gas injection ramp 2	Increasing gas pressure to minimum principal stress	14
12	Gas entry	Monitoring behaviour post gas entry	28
13	Depressurisation	Reducing boundary conditions to atmospheric	0.3
14	Dismantling	Removal of the sample from the apparatus	0.04

2.2.5. Results

At the time of reporting, a total of four tests had been completed. The initial plan was for tests to last 3 months. However, delays imposed by the Covid-19 pandemic and time limitations of the experiments, it was difficult to complete experiments in just three months. The experimental programme also suffered from samples of Callovo-Oxfordian claystone where hydraulic flow was difficult to achieve and in two samples, could not be initiated. This issue added a significant delay to the experimental programme. Early in the experimental programme it was decided to run experiments for enough time as opposed to limiting each experiment to a three-month limit.

Test COx1: FPR_21_043 Callovo-Oxfordian, parallel to bedding, in situ stress

The first test conducted was performed on Callovo-Oxfordian claystone with a sample prepared parallel to bedding (Figure 2.28). This test would be a repeat of one conducted as part of the EU FP7 Fate of Repository Gases (FORGE) project and allow the behaviour of the apparatus to be determined in comparison with the existing triaxial experiments conducted in the Stress Path Permeameter (SPP).

The boundary conditions of the experiment were established in two parts (*Figure 2.29*). The first brought the sample up to effective stress over a 24-hour period. The sample was then held for 24 hours, before a second part increased the boundary conditions to be that of in situ over another 24 hours. *Figure 2.29*b shows the resultant strain of increasing confining and axial strain. It should be noted that the apparatus has not been designed to measure absolute strain and is optimised to observe changes of strain once

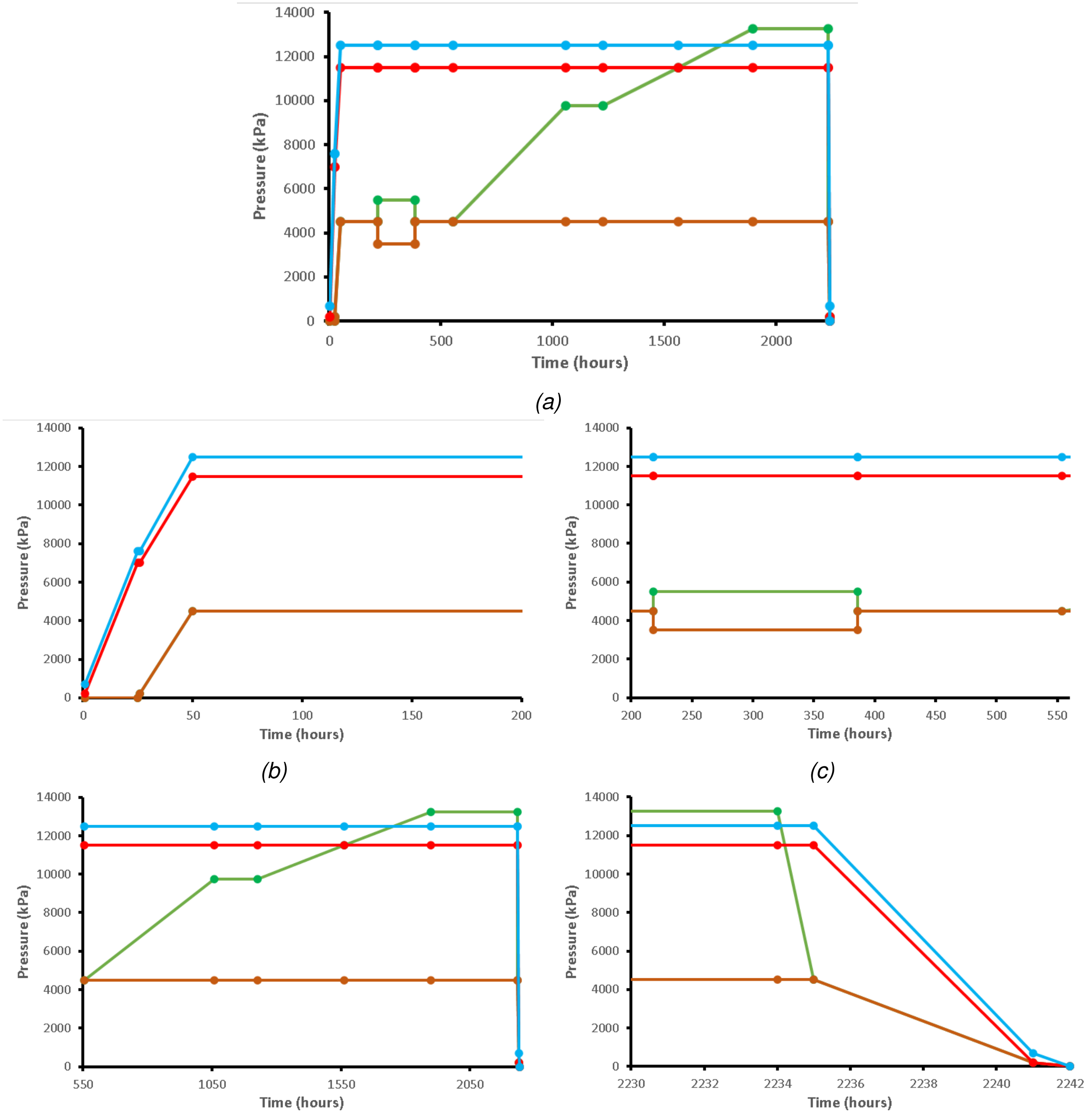

(a)

(b)

(c)

(d)

(e)

Figure 2.27: Idealised test protocol. a) Full test history; b) Initial pressurisation; c) Hydraulic testing; d) Gas testing; e) de-pressurisation. Note: Blue = axial stress, red = confining pressure; brown = back pressure, and green = injection pressure.

boundary conditions are static. Careful calibration is not sufficient to know with certainty what the absolute strain of the sample was in the initial pressurisation, i.e., in the first 2 to 3 hours.

The first stage of the test comprised a hydraulic test, as shown in *2.30*. Two stages of flow were conducted with a gradient of 1 and 2 MPa across the sample (*Figure 2.30*a). Table 2.11 summarises the achieved hydraulic data with *Figure 2.30*b showing the flow data. As seen, the average permeability was 5.34 × 10^{-21} m^2. This is within the accepted range of permeability for Callovo-Oxfordian claystone. The permeability at the backpressure end of the sample was lower than at the injection end. This was caused by the sample being under-saturated, which is highlighted by the sample still undergoing strain prior to the initiation of the hydraulic gradient (*Figure 2.30*c). However, the initial gradient resulted in axial strain of the sample. The

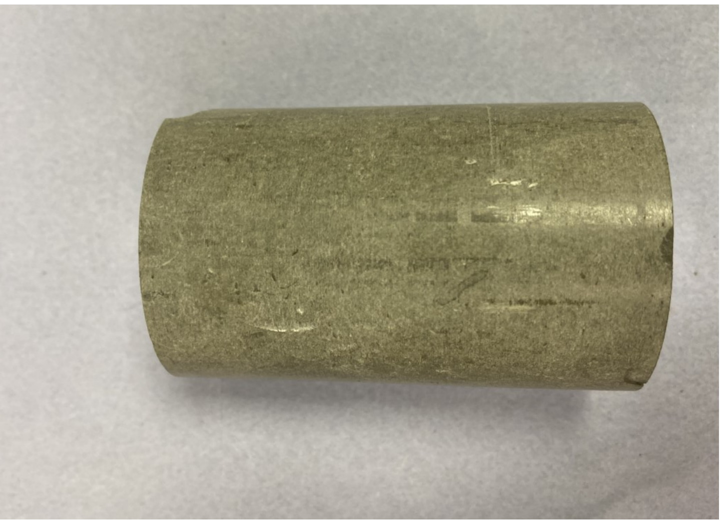

Figure 2.28: Sample of Callovo-Oxfordian claystone prepared by machine lathing.

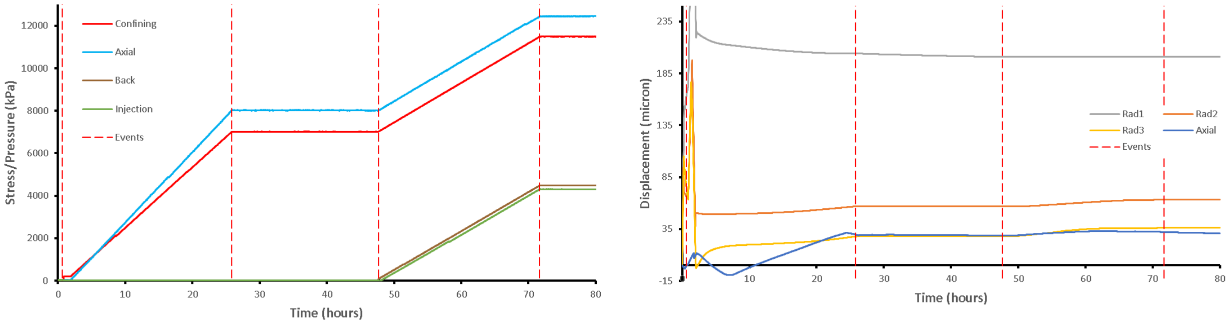

(a) (b)

Figure 2.29: Pressurisation of test COx1. a) Boundary conditions; b) Strain.

second event line shows the establishment of the 2 MPa gradient on the sample. This shows that radial strain was seen in the sample with a reduction in axial strain. As the hydraulic gradient across the sample was increased, the permeability reduced (*Figure 2.30*d).

Table 2.11: Hydraulic data for Callovo-Oxfordian claystone.

	Pressure gradient (kPa)	Hydraulic conductivity (m s^{-1})	Permeability (m^2)
Inflow	984	7.49×10^{-14}	7.65×10^{-21}
Outflow	984	4.32×10^{-14}	4.41×10^{-21}
Average	**984**	$\mathbf{5.91 \times 10^{-14}}$	$\mathbf{6.03 \times 10^{-21}}$
Inflow	1954	5.09×10^{-14}	5.20×10^{-21}
Outflow	1954	3.99×10^{-14}	4.08×10^{-21}
Average	**1954**	$\mathbf{4.54 \times 10^{-14}}$	$\mathbf{4.64 \times 10^{-21}}$
AVERAGE		$\mathbf{5.23 \times 10^{-14}}$	$\mathbf{5.34 \times 10^{-21}}$

The test was conducted as a two-stage constant flow gas ramp experiment. *Figure 2.31* shows the results from the first pressure ramp. Gas pressure was increased from 4.6 to 11.5 MPa in 580 hours (24 days), with gas pressure then held constant for 668 hours (27 days). As a result of increased gas pressure (*Figure 2.31*a), there was outflow from the sample (*Figure 2.31*b), i.e. fluid was expelled from the

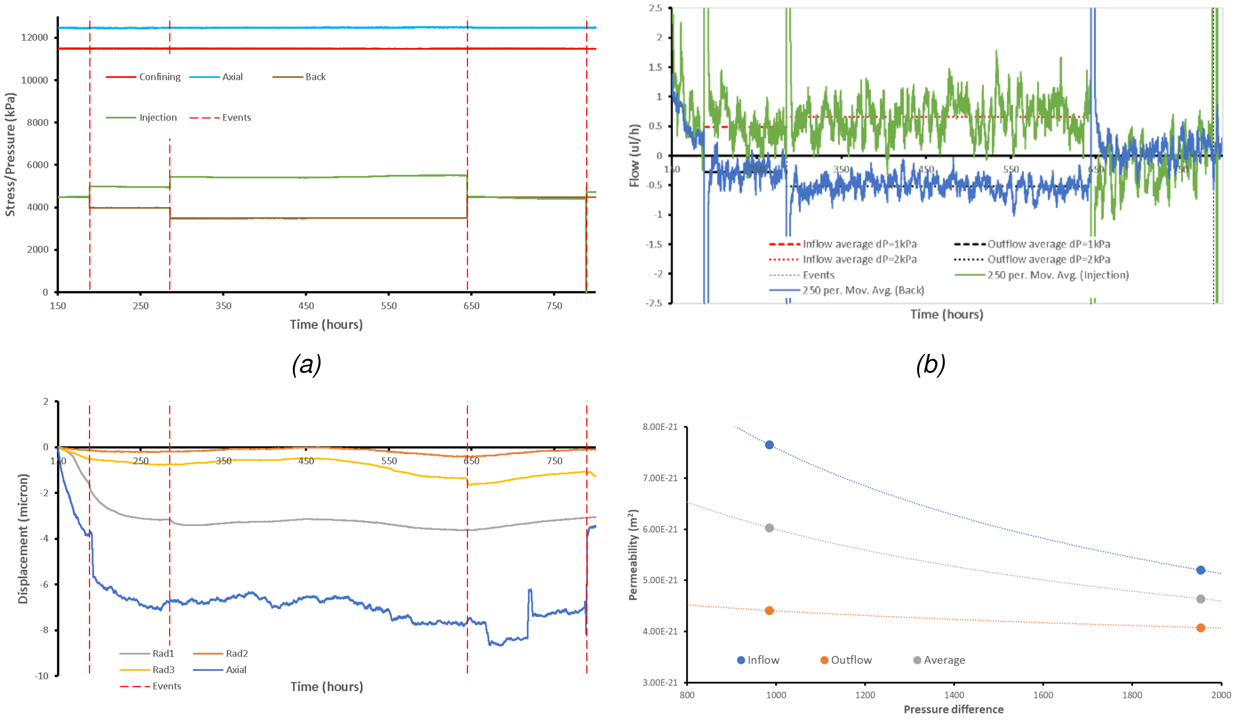

(a) *(b)*

(c) *(d)*

Figure 2.30: Hydraulic test stage of COx1. a)
Boundary conditions; b) Flow response; c) Strain; d) Permeability result.

sample. Coincidentally, the sample dilated (*Figure 2.31*c), with dilation stopping when gas pressure was held constant. This response is attributed to the expulsion of excess fluid from the injection filter. It is not interpreted that advective gas flow was occurring, as confirmed by outflow returning to zero flow during the pressure hold stage.

The second stage of constant flow gas injection took the sample through gas entry (*Figure 2.32*). Three events have been identified, as shown by three event lines in *Figure 2.32*b. The first event line identified in Figure 11b at 2560.52 hours corresponds with a change in volume of the sample, as identified by the volume of the confining system. The second event line at 2567.79 hours shows radial and axial disturbance of the sample, as shown in *Figure 2.32*ef. The largest of these strains was seen in Radial 2, with only 4 microns change in sample radius. At the third event line at 2587.37 hours, gas pressure reduced instantaneously by 150 kPa (*Figure 2.32*b) and from then onwards the gas pressure remained relatively constant. Gas peak pressure was around 100 kPa below the minimum principal stress, confining pressure. Coincident with the pressure reduction was the outflow from the sample, *Figure 2.32*cd. Flow was relatively steady and showed 150 µl/h outflow. *Figure 2.32*g shows gas flow into and out of the sample at STP conditions. This shows that following a high peak in outflow, the flow out of the sample quickly equalled the flow into the sample (steady state flow).

Figure 2.33 shows that the sample was de-pressurised over a period of around four hours. Following the decommissioning of the experiment, small fractures were seen within the sample (Figure 2.34). At the end of the test the water content of the sample was found to be 6.5 %, compared with a starting water content of 6.6 %. Accounting for the change in sample volume, the end saturation of the sample was 97.5 % compared with a starting saturation of 97.8 %. This decrease in saturation is not thought to be significant and could be a result of errors in the measurements taken.

Test COx2: Callovo-Oxfordian, parallel to bedding, higher stress

The fourth test conducted was performed on Callovo-Oxfordian claystone with a sample prepared parallel

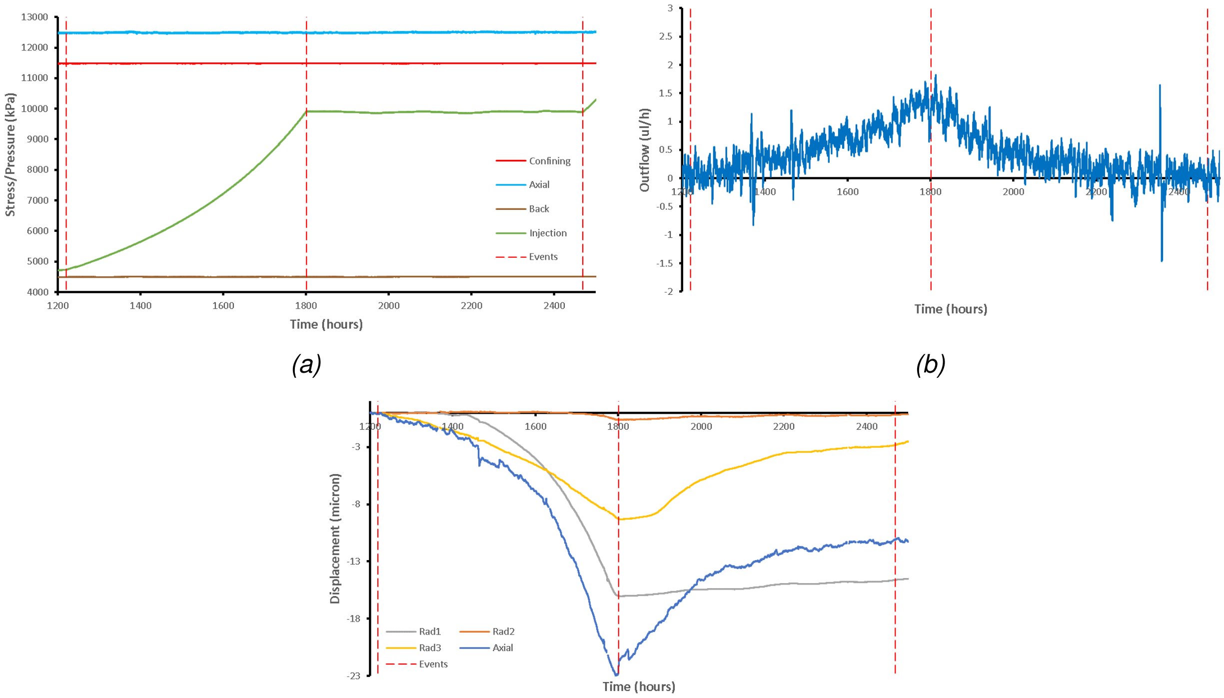

(a)

(b)

(c)

Figure 2.31: Gas ramp 1 of test COx1. a) Boundary conditions; b) Outflow from the sample; c) Strain.

to bedding (*Figure 2.35*). This test was conducted at a higher stress condition that test COx1.

The boundary conditions of the experiment were established in two parts (*Figure 2.36*). The first brought the sample up to effective stress over a ~24-hour period. The sample was then held for 2 hours, before a second part increased the boundary conditions to be that of in situ over another 24 hours. *Figure 2.36*b shows the resultant strain of increasing confining and axial strain. It should be noted that the apparatus has not been designed to measure absolute strain and is optimised to observe changes of strain once boundary conditions are static. Careful calibration is not sufficient to know with certainty what the absolute strain of the sample is in the initial pressurisation.

The first stage of the test comprised a hydraulic test, as shown in *Figure 2.37*. Three stages of flow were conducted with a gradient of 1, 2 and 3 MPa across the sample (*Figure 2.37*a). *Table 2.12* summarises the achieved hydraulic data with *Figure 2.37*b showing the flow data. As seen, the average permeability was 6.85×10^{-21} m^2. This is within the accepted range of permeability for Callovo-Oxfordian claystone. The calculated permeability at the backpressure end of the sample was generally lower than that at the injection end and true steady-state flow was not seen. However, little strain occurred during the hydraulic stage suggesting that swelling was not evoked by the change in pore pressure (*Figure 2.37*c). However, the second gradient resulted in axial strain of the sample, the reasons for this are uncertain. As the hydraulic gradient across the sample was increased, the permeability reduced (*Figure 2.37*d). However, this could also show that the permeability was changing with time as the sample re-hydrated. This was not confirmed by a reduction in hydraulic gradient.

Table 2.12: Hydraulic data for Callovo-Oxfordian claystone test COx2.

	Pressure gradient (kPa)	**Hydraulic conductivity (m s^{-1})**	**Permeability (m^2)**
Inflow	966	7.89×10^{-14}	8.06×10^{-21}
Outflow	966	7.03×10^{-14}	7.18×10^{-21}

Average	**966**	**7.46 × 10^{-14}**	**7.62 × 10^{-21}**
Inflow	1968	6.31 × 10^{-14}	6.45 × 10^{-21}
Outflow	1968	6.79 × 10^{-14}	6.94 × 10^{-21}
Average	**1968**	**6.55 × 10^{-14}**	**6.69 × 10^{-21}**
Inflow	2993	6.26 × 10^{-14}	6.40 × 10^{-21}
Outflow	2993	5.95 × 10^{-14}	6.08 × 10^{-21}
Average	**2993**	**6.11 × 10^{-14}**	**6.24 × 10^{-21}**
AVERAGE		**6.71 × 10^{-14}**	**6.85 × 10^{-21}**

The test was conducted as a two-stage constant flow gas ramp experiment. *Figure 2.38* shows the results from the first pressure ramp. Gas pressure was increased from 4.75 to 14.5 MPa in 574 hours (24 days), with gas pressure then held constant for 174 hours (7 days). As a result of increased gas pressure (*Figure 2.38*a), there was outflow from the sample (*Figure 2.38*b), i.e. fluid was expelled from the sample. Coincidentally, the sample elongated (*Figure 2.38*c) with some dilation about the centre of the sample. This strain ceased when gas pressure was held constant. This response is attributed to the expulsion of excess fluid from the injection filter. It is not interpreted that advective gas flow was occurring, as confirmed by outflow returning towards zero flow during the pressure hold stage.

The second stage of constant flow gas injection took the sample through gas entry (*Figure 2.39*). Many events have been identified from changes in strain and/or flow, as shown by event lines in *Figure 2.39*b. The first event line at 1785.84 hours corresponds with a small change in outflow (*Figure 2.39*c) and the start of subtle radial strain (*Figure 2.39*d). Two events at 1808.4 and 1812.8 hours both show strain in Radial 1 and have corresponding changes in outflow, although it has to be noted that this change in outflow was close to the limit of resolution of the syringe pumps used. The fourth event line at 1830 hours shows a peak in gas pressure (*Figure 2.39*b) and the simultaneous increase in outflow from the sample (*Figure 2.39*c). This event does not correspond with any strain at the midplane of the sample (*Figure 2.39*d) and the temperature variation within the laboratory was making identification of axial strain difficult (*Figure 2.39*e). The response of flow and gas pressure was dynamic following gas peak pressure. Gas pressure decreased and then increased, reaching a second peak at the sixth event line at 1858.83 hours. Out flow from the sample (*Figure 2.39*c) showed three episodes of increasing and decreasing flow. This caused the rate of gas pressure change to alter. During this period little strain occurred, although episodes of outflow did correlate with changes in radial 1 strain, as highlighted by the last 6 event lines. Gas pressure reached a near asymptote of 15250 kPa, a reduction in gas pressure of 425 kPa from the maximum gas pressure experienced. Following the final event line at 2049.18 hours, gas pressure and outflow became erratic, with a distinct difference in behaviour. It should be noted that the maximum strain seen at the midplane of the sample was of the order of only 1 micron (*Figure 2.39*d).

*Figure 2.39*f shows the inflow and outflow of the test converted to STP conditions. In previous tests, the peak in gas pressure corresponded with a peak in gas flow. In the current test, this peak was absent, with outflow less than inflow. Around 1900 hours, outflow had increased to be greater than inflow and this corresponds with the most rapid reduction in gas pressure. In test COx2 it took around 70 hours for outflow to exceed, and then approximate, inflow. Average outflow can be seen to be smaller than inflow, resulting in a reduction in gas injection pressure.

*Figure 2.40*a shows that the sample was de-pressurised over a period of 24 hours, with the main de-pressurisation happening over around four hours. Initially, gas pressure at the injection end of the sample was lowered to equal the backpressure.

Following the decommissioning of the experiment, small fractures were seen within the sample. The sample was placed on the laboratory worktop for dimension measurement and was seen to fracture. *Figure 2.41*a shows the sample soon after measurement after the fractures appeared to develop. *Figure 2.41*b shows that the sample broke in half with a clear fracture surface. Fossils were apparent in the plane of failure. *Figure 2.40*b shows the radial strain during the unloading stage. As seen, gas pressure stopped

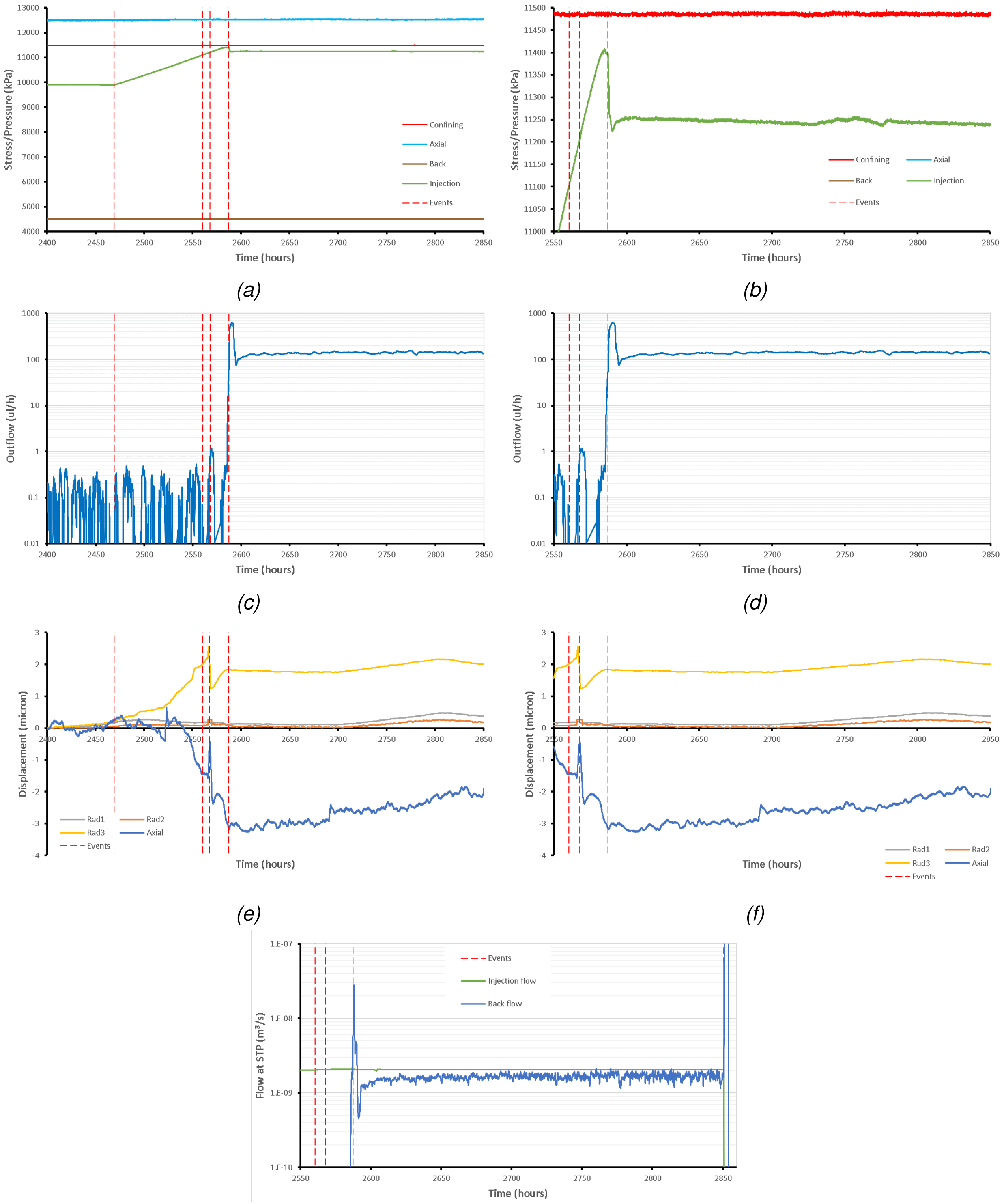

(a)

(b)

(c)

(d)

(e)

(f)

(g)

Figure 2.32: Gas ramp 2 of test COx1. a) Boundary conditions; b) Detail of gas pressure at gas entry; c) Outflow from the sample; d) Detail of the outflow from the sample; e) Strain; f) Detail of strain around the time of gas entry; g) Flow into and out of the sample at STP conditions.

reducing at 2234 hours when the pump controlling pore pressure filled and could no longer reduce pressure. As a result, gas pressure matched the greatest principal stress and the sample gas fractured, as seen by dilation in Radial 2 and Radial 3 in *Figure 2.40*b. Therefore, the fracturing seen was the result of excessive gas pressure during depressurisation. Additionally, it is possible that trapped gas within the

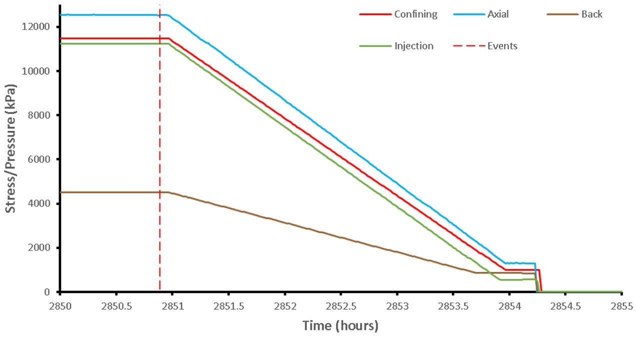

Figure 2.33: Unloading of sample COx1.

Figure 2.34: Photos of the sample (COx1) after removal from the apparatus with small fractures highlighted.

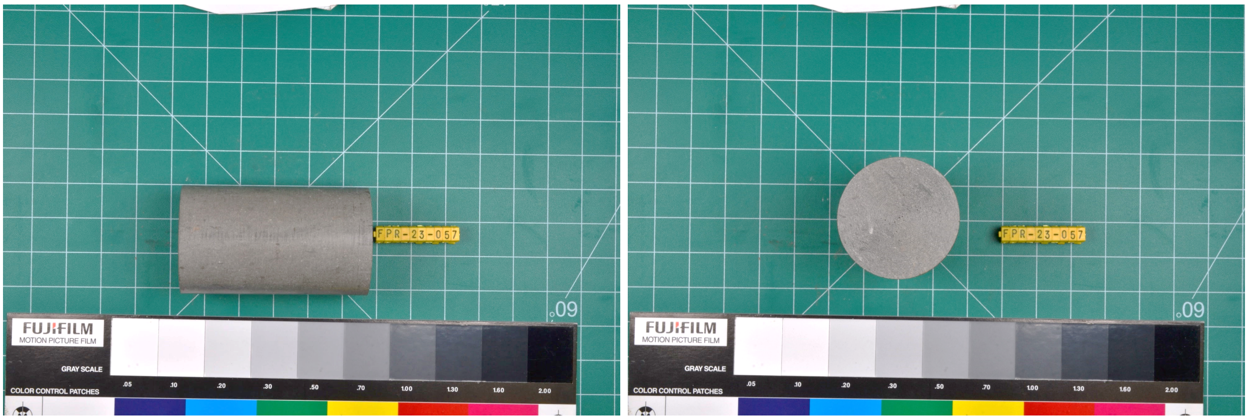

(a) (b)

Figure 2.35: Sample of Callovo-Oxfordian claystone prepared by machine lathing.

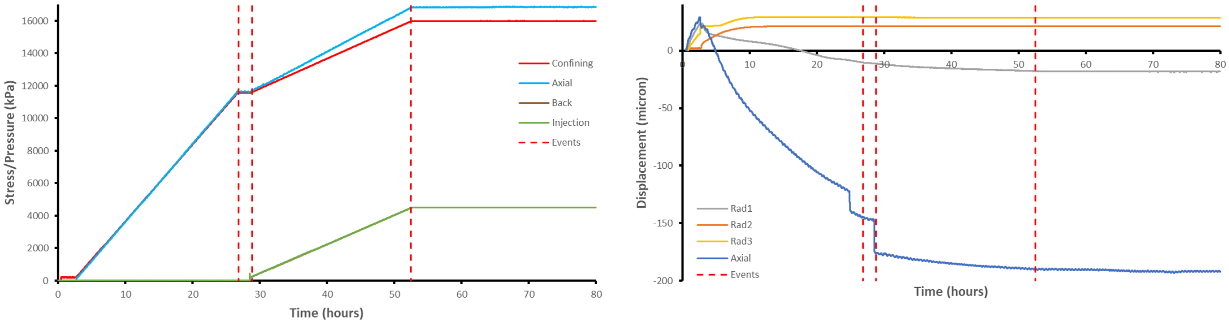

(a) (b)

Figure 2.36: Pressurisation of test COx2. a) Boundary conditions; b) Strain.

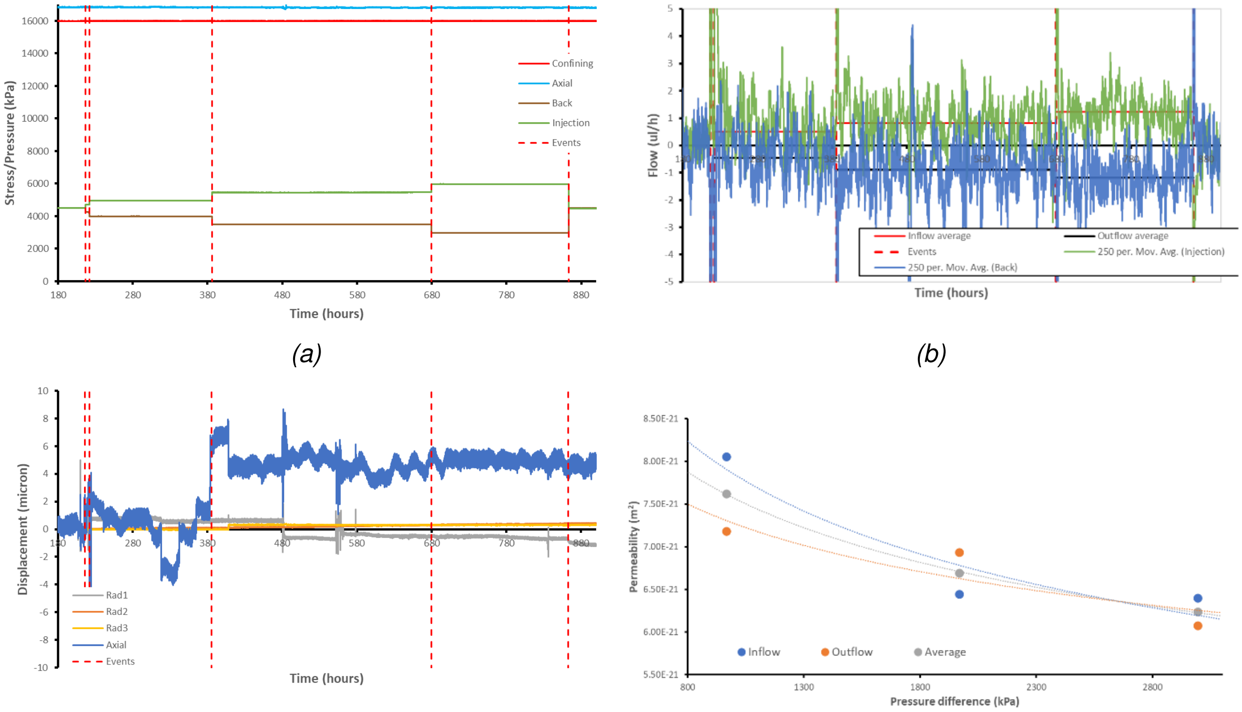

(a) (b)

(c) (d)

Figure 2.37: Hydraulic test stage of COx2. a) Boundary conditions; b) Flow response; c) Strain; d) Permeability result.

sample expanded and exploited a bedding-parallel weakness. At the end of the test the water content of the sample was found to be 7 water content of 7.1 . The starting saturation was 100 saturation being 98

Test BC1: FPR_22_026 Boom Clay, perpendicular to bedding, in situ stress

The second test conducted was performed on Boom Clay with a sample prepared perpendicular to bedding (*Figure 2.42*). This test would be similar to test COx1 with boundary conditions representing the HADES URL in Belgium where the core material had been taken. As shown in *Figure 2.42*, a small ring was accidentally lathed into the sample. This had minimal depth and was not as deep as the photograph suggests.

The boundary conditions of the experiment were established in two parts (*Figure 2.43*). The first brought the sample up to effective stress over a 24-hour period. The sample was then held for 48 hours, before a second part increased the boundary conditions to be that of in situ over another 24 hours. During the initial

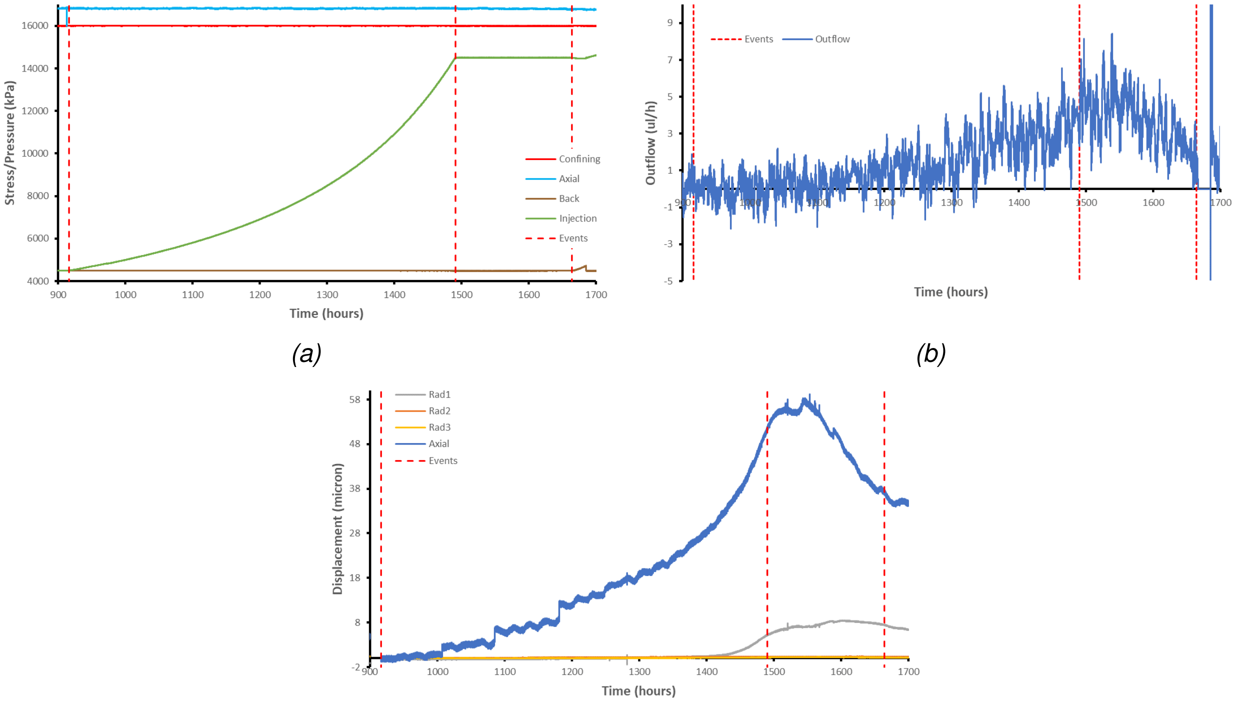

(a) (b)

(c)

Figure 2.38: Gas ramp 1 of test COx2. a) Boundary conditions; b) Outflow from the sample; c) Strain.

pressurisation stage there were periods when confining pressure was greater than axial stress. The data were scrutinised, and it was deemed that the sample had not been compromised. *Figure 2.43*b shows the resultant strain of increasing confining and axial strain. It should be noted that the apparatus has not been designed to measure absolute strain and is optimised to observe changes of strain once boundary conditions are static. Careful calibration is not sufficient to know with certainty what the absolute strain of the sample is in the initial pressurisation, i.e., in the first 3 hours.

The first stage of the test comprised a hydraulic test, as shown in *Figure 2.43*. Two stages of flow were conducted with a gradient of 0.5 and 1 MPa across the sample (*Figure 2.43*a). *Table 2.13* summarises the achieved hydraulic data with *Figure 2.43*b showing the flow data. As seen, the average permeability was 1.59×10^{-19} m^2, with little difference between the two different hydraulic gradients used. The achieved permeability is within the accepted range of permeability for Boom Clay. The permeability at the back-pressure end of the sample was lower than at the injection end. This was caused by the sample being under-saturated. However, the initial gradient resulted in radial strain of the sample. The second event line shows the establishment of the 1 MPa gradient on the sample. This shows that radial strain was seen in the sample. As the hydraulic gradient across the sample was increased, the average permeability increased marginally, although this may be because of creep of the sample and increased hydration (*Figure 2.43*d).

Table 2.13: Hydraulic data for Boom Clay test BC1.

	Pressure gradient (kPa)	**Hydraulic conductivity (m s^{-1})**	**Permeability (m^2)**
Inflow	520	1.58×10^{-12}	1.61×10^{-19}
Outflow	520	1.53×10^{-12}	1.56×10^{-19}
Average	**520**	$\mathbf{1.55 \times 10^{-12}}$	$\mathbf{1.58 \times 10^{-19}}$
Inflow	1011	1.57×10^{-12}	1.60×10^{-19}
Outflow	1011	1.55×10^{-12}	1.58×10^{-19}

Average	**1011**	**1.56×10^{-12}**	**1.59×10^{-19}**
AVERAGE		**1.56×10^{-12}**	**1.59×10^{-19}**

The test was conducted as a two-stage constant flow gas ramp experiment. *Figure 2.45* shows the results from the first pressure ramp. Gas pressure was increased from 2.2 to 3.4 MPa in 502 hours (21 days), with gas pressure then held constant for 141 hours (6 days). As a result of increased gas pressure (*Figure 2.45*a), there was outflow from the sample (*Figure 2.45*b), i.e. fluid was expelled from the sample. Coincidentally, the sample strained (*Figure 2.45*c). This response is attributed to the expulsion of excess fluid from the injection filter. It is not interpreted that advective gas flow was occurring, as confirmed by outflow returning to zero flow during the pressure hold stage.

The second stage of constant flow gas injection took the sample through gas entry (*Figure 2.46*). Six events have been identified, as shown by six event lines in *Figure 2.46*. The first event line identified in *Figure 2.46*b at 2043.61 hours corresponds with the start of axial strain and occurred when the gas injection pressure was being held constant, with gas injection restarting at 2064.09 hours. This latter time corresponds with a change in axial strain (*Figure 2.46*d). The next two event lines at 2093.01 and 2130.48 hours correspond with minor strains seen in Radial 1. The final two event lines show gas entry. The first at 2181.45 hours shows the start of a decrease in gas pressure, with the second at 2182.29 hours showing the first outflow from the sample. Therefore, if the pressure drop is representative of gas entry, it took around 50 minutes for gas to flow end to end of the sample. The decrease in gas pressure totalled around 200 kPa. At the time of reduction in gas pressure, Radial 1 showed dilation of around 1 micron (*Figure 2.46*d). This corresponded with a large spike in outflow from the sample (*Figure 2.46*c), which was short lived, with flow quickly stabilising to around 40 μl/h. *Figure 2.46*e shows flow into and out of the sample at STP conditions. As seen, stable flow was achieved, however flow into the system was greater than flow of the sample. This resulted in a slow increase in gas pressure, as seen in *Figure 2.46*b.

Figure 2.47 shows that the sample was de-pressurised over a period of around seven hours. Following the decommissioning of the experiment, a couple of features are worthy of note (*Figure 2.48*). The sample appears to have a small amount of diameter variation, with the ends of the sample appearing wider than the central part of the sample. A series of fine fractures are seen parallel with the sample long-axis. These are also apparent in the end of the sample, with hairline features seen within 1 to 2 mm of the sample edge. At the end of the test the water content of the sample was found to be 24.5 %, compared with a starting water content of 23.1 %. Accounting for the change in sample volume, both starting and end saturation was 99.9 %. Therefore, no desaturation of the sample occurred as a result of gas movement.

Test BC2: FPR_22_089 Boom Clay, perpendicular to bedding, high stress

The third test conducted was performed on Boom Clay with a sample prepared perpendicular to bedding (*Figure 2.49*). This test would be similar to test BC1, but with boundary conditions representing the stress state expected in the Netherlands.

The boundary conditions of the experiment were established in two parts (*Figure 2.50*). The first brought the sample up to effective stress over a 24-hour period. The sample was then held for 24 hours, before a second part increased the boundary conditions to that desired over another 24 hours. *Figure 2.50*b shows the resultant strain of increasing confining and axial strain. It should be noted that the apparatus has not been designed to measure absolute strain and is optimised to observe changes of strain once boundary conditions are static.

The first stage of the test comprised a hydraulic test, as shown in *Figure 2.51*. One stage of flow was conducted with a gradient of 1 MPa across the sample (*Figure 2.51*a). *Table 2.14* summarises the achieved hydraulic data with *Figure 2.51*b showing the flow data. As seen, the average permeability was 9.92×10^{-20} m^2. This is within the accepted range of permeability for Boom Clay. The permeability at the backpressure end of the sample was lower than at the injection end. The establishment of a pressure gradient across the sample resulted in axial strain and the start of dilation of Radial 2. The second event line shows when

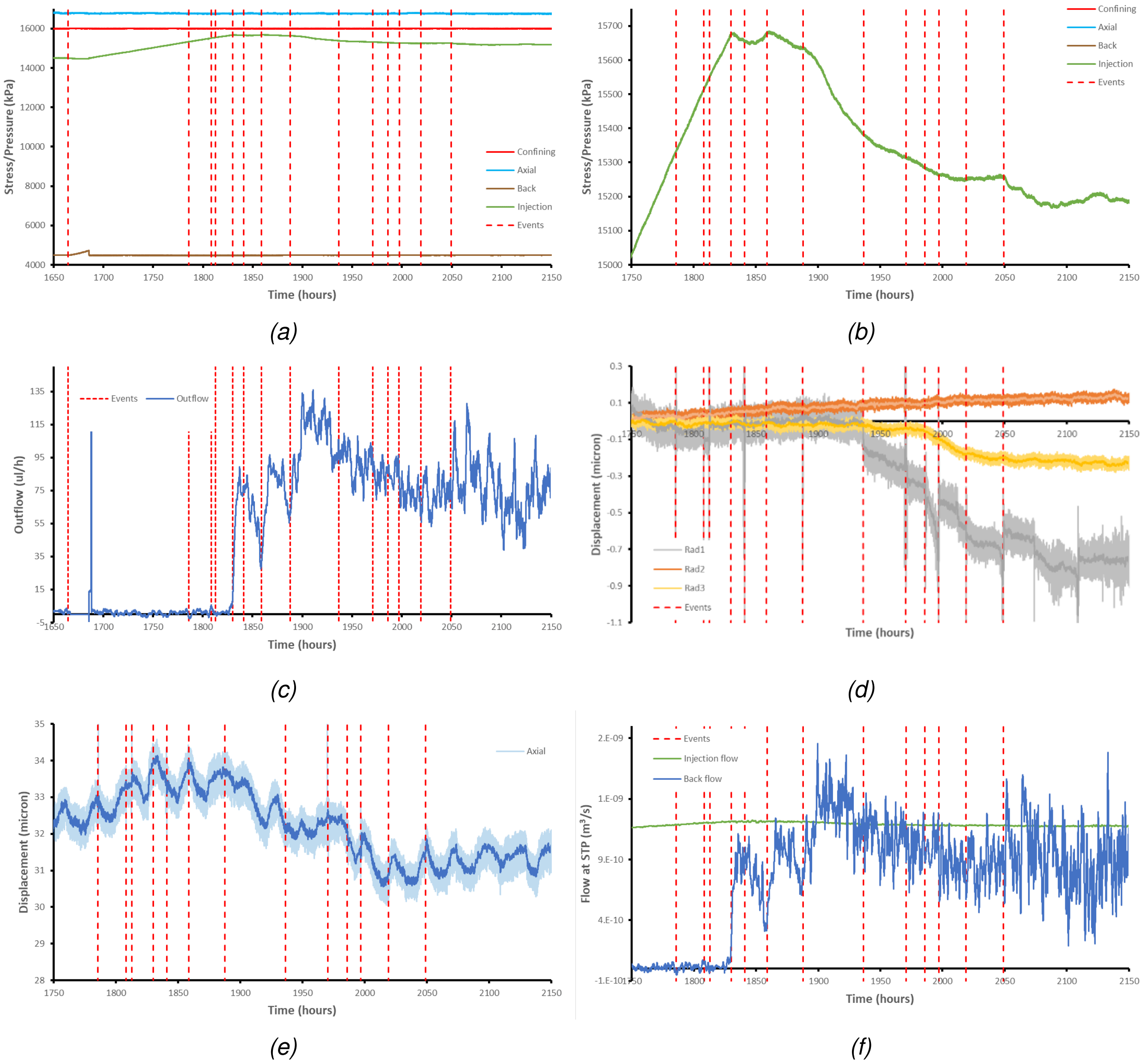

(a) (b)

(c) (d)

(e) (f)

Figure 2.39: Gas ramp 2 of test COx2. a) Boundary conditions; b) Detail of gas pressure at gas entry; c) Outflow from the sample; d) Radial strain; e) Axial strain; f) Flow into and out of the sample at STP conditions.

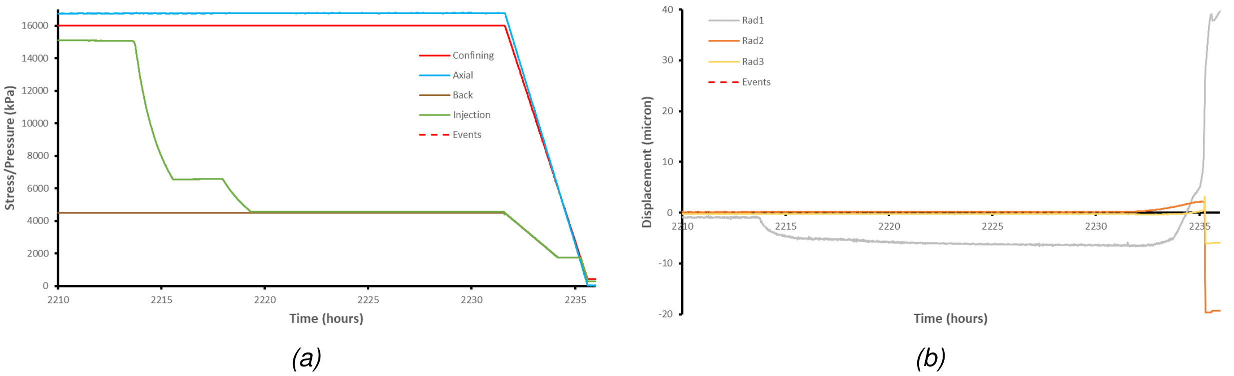

(a) (b)

Figure 2.40: Unloading of sample COx2. a) Boundary conditions; b) Radial strain.

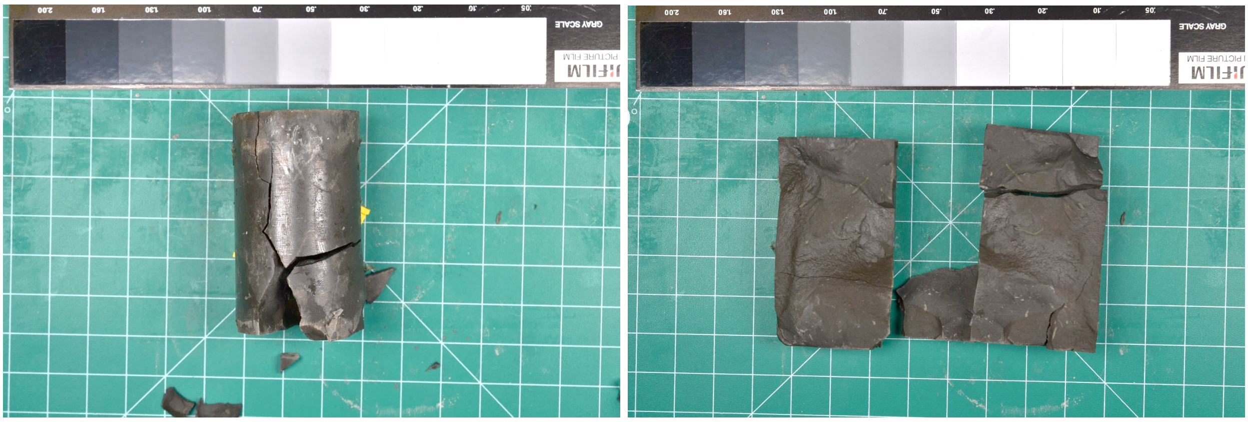

(a) (b)

Figure 2.41: Photos of the sample after removal from the apparatus with fractures visible.

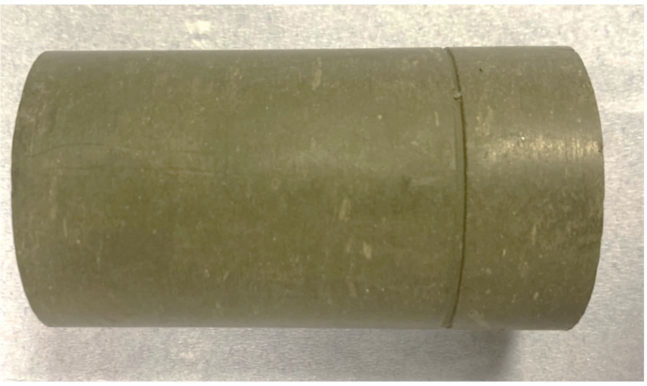

Figure 2.42: Sample of Boom Clay prepared by machine lathing for test BC1.

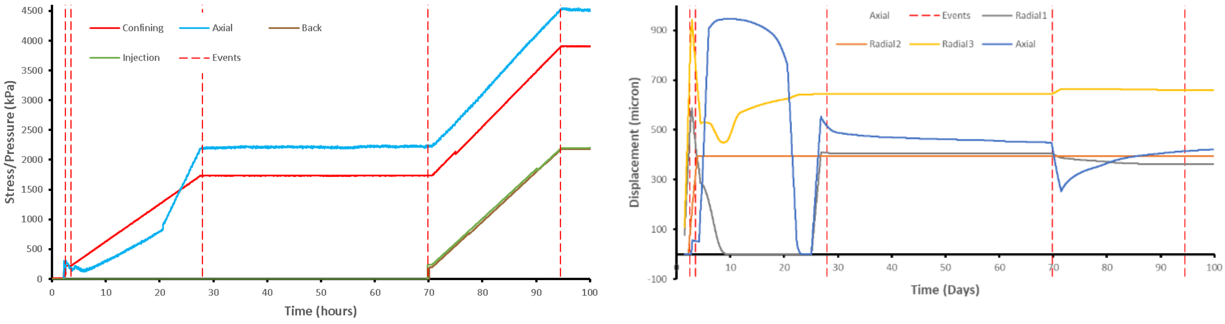

(a) (b)

Figure 2.43: Pressurisation of test BC1. a) Boundary conditions; b) Strain

boundary conditions were changed so that no gradient existed across the sample. This time, dilation in Radial 2 started to accelerate and Radial 3 showed several microns of compression (*Figure 2.51*c).

Table 2.14: Hydraulic data for Boom Clay test BC2.

	Pressure gradient (kPa)	**Hydraulic conductivity (m s^{-1})**	**Permeability (m^2)**
Inflow	1007	9.79×10^{-13}	1.00×10^{-19}
Outflow	1007	9.63×10^{-13}	9.84×10^{-20}

Average	**1007**	**9.71×10^{-13}**	**9.92×10^{-20}**

The test was conducted as a two-stage constant flow gas ramp experiment. *Figure 2.52* shows the results from the first pressure ramp. Gas pressure was increased from 4.9 to 7.4 MPa in 478 hours (20 days), with gas pressure then held constant for 144 hours (6 days). As a result of increased gas pressure (*Figure 2.52*a), there was outflow from the sample (*Figure 2.52*b), i.e. fluid was expelled from the sample. Little strain of the sample occurred (*Figure 2.52*c). However, as flow started to reduce, the sample started to strain. Two sensors showed compression and one showed dilation, suggesting that the sample may have shifted laterally. The initial increase in outflow is attributed to the expulsion of excess fluid from the injection filter. It is not interpreted that advective gas flow was occurring, as confirmed by outflow returning to zero flow during the pressure hold stage.

The second stage of constant flow gas injection took the sample through gas entry (*Figure 2.53*). Ten events have been identified, as shown by ten event lines in *Figure 2.53*b. Around 1128 hours, outflow started to increase (*Figure 2.53*c). Around this time, Radial 2 started to dilate, while the axial strain started to contract (*Figure 2.53*d). The first event line at 1154.77 hours showed considerable hydromechanical coupling. At this time, gas pressure rapidly reduced by 130 kPa (*Figure 2.53*b), Radial 2 dilated by around 5 microns, axial strain reduced by less than 1 micron (*Figure 2.53*d), and outflow from the sample peaked at over 2000 μl/h (*Figure 2.53*c). This peak was short lived and gas pressure started to increase again (*Figure 2.53*b). The remaining nine event lines all show a saw-toothed pressure response, with rapid reductions in gas pressure (*Figure 2.53*b). At each of these events, outflow from the sample peaked at around 1000 μl/h. However, no significant strain was seen for any of these events (*Figure 2.53*d). This suggests that permanent strain was created by the first event and that subsequent breakthrough events did not create any new strain of the sample. *Figure 2.53*f shows that each subsequent peak in gas pressure reduced until a steady peak pressure was established. After the final pressure decrease event at 1241.84 hours, gas pressure remained constant, with flow increasing to a steady 300 μl/h. The response observed appears similar to fault valve behaviour. Flow was episodic until a fully open pathway was achieved sustaining constant flow through the sample. *Figure 2.53*e shows that inflow increased as a result of the spikes in inflow, with the short-lived spikes stopping when inflow was equal to outflow, i.e., steady state flow.

Figure 2.54 shows that the sample was de-pressurised over a period of around 24 hours. Following the decommissioning of the experiment, small fractures were seen within the sample parallel with the bedding direction (*Figure 2.55*). However, *Figure 2.54*a shows that gas pressure exceeded confining pressure during depressurisation as the pore pressure pump filled. Around this time, Radial 2 and Radial 3 show dilation. Therefore, some of the fractures could be the result of gas fracture. At the end of the test the water content of the sample was found to be 24.3 %, compared with a starting water content of 23.0 %. Taking into account the change in sample volume, both starting and end saturation was 98.8 %. Therefore, no desaturation of the sample occurred as a result of gas movement.

Comparing tests

Figure 2.56 compares the results for the two tests conducted in Callovo-Oxfordian claystone. The two tests were conducted at different stresses. The first test (COx1) was tested at similar stresses to in situ. The second test was conducted at a higher stress, with less differential between the maximum (axial) and minimum (confining) principal stresses. Given the difference in boundary conditions, the results are consistent. Both tests showed outflow from the sample during the first gas ramp. In both tests, this reduced back to a condition of no flow when gas pressure was held constant. This is interpreted as the expulsion of excess water from the injection filter and is not evidence of gas movement, confirmed by a condition of zero flow when the gas pressure was held constant. Differences were seen in the strain responses. The expulsion of water from the filter caused COx1 to dilate through swelling. However, COx2 showed compressional deformation. This shows that this sample was contracting as a result of the higher stress condition.

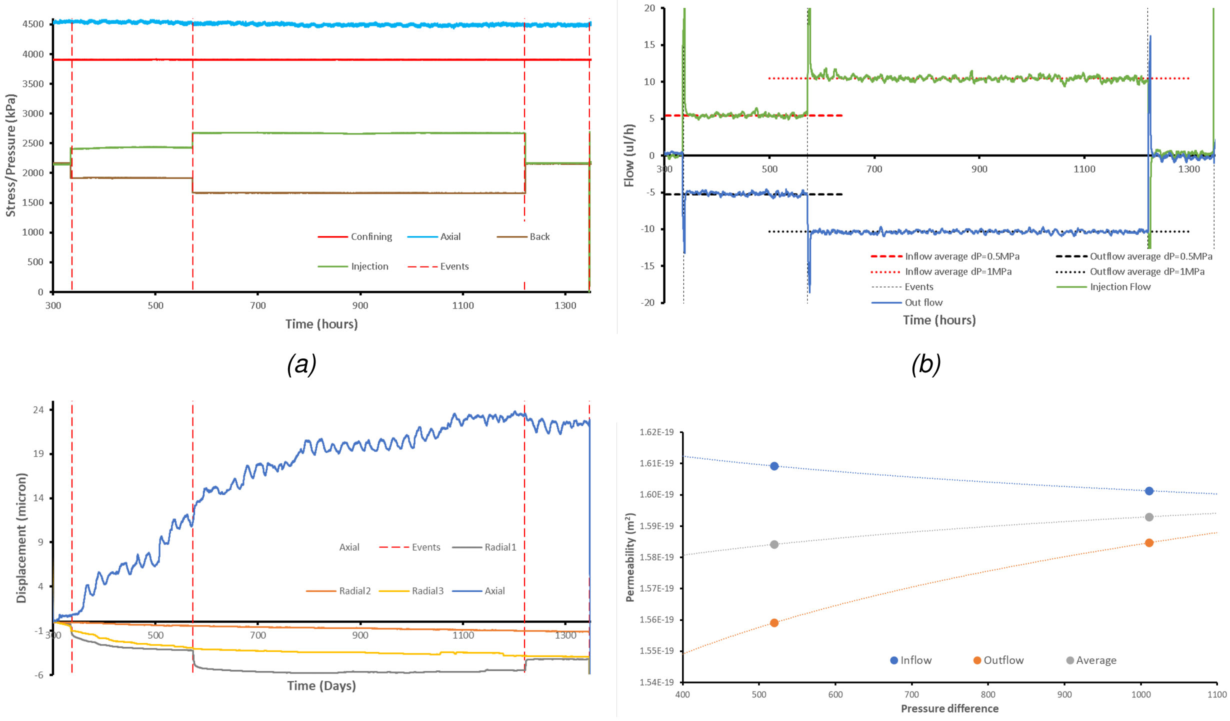

(a) (b)

(c) (d)

Figure 2.44: Hydraulic test stage of BC1. a) Boundary conditions; b) Flow response; c) Strain; d) Permeability result.

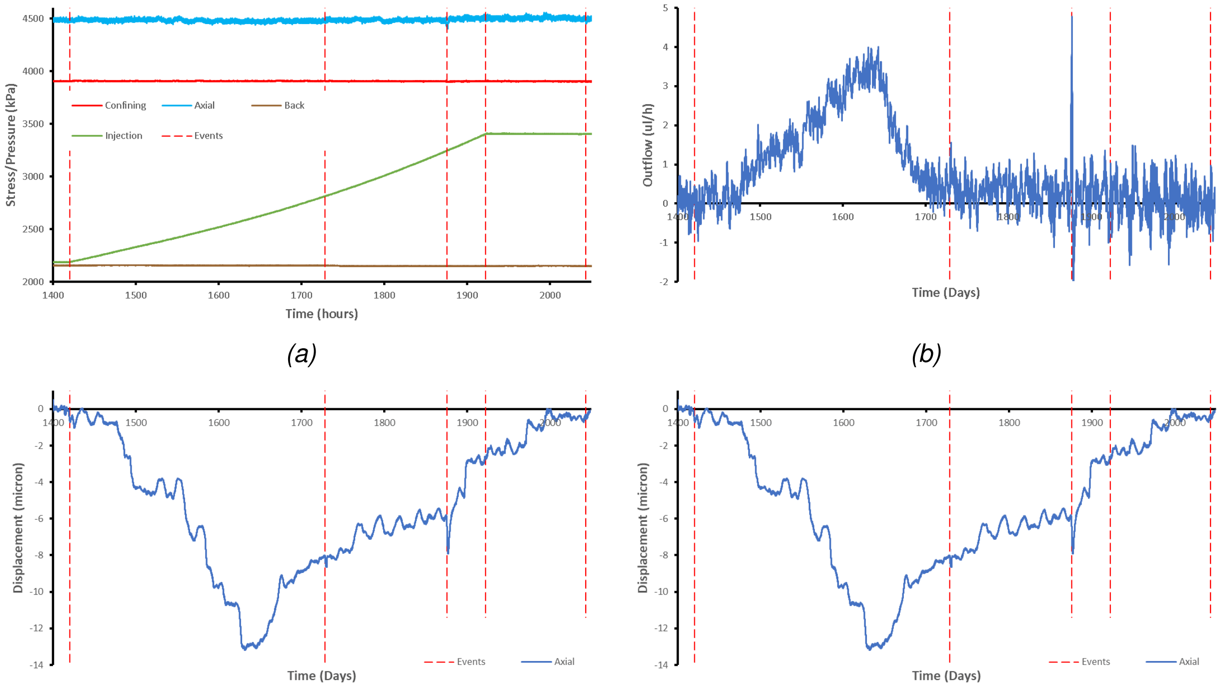

(a) (b)

(c) (d)

Figure 2.45: Gas ramp 1 of test BC1. a) Boundary conditions; b) Outflow from the sample; c) Radial strain; d) Axial strain.

In both tests, gas entry occurred at a pressure below the minimum principal stress. Gas pressure never

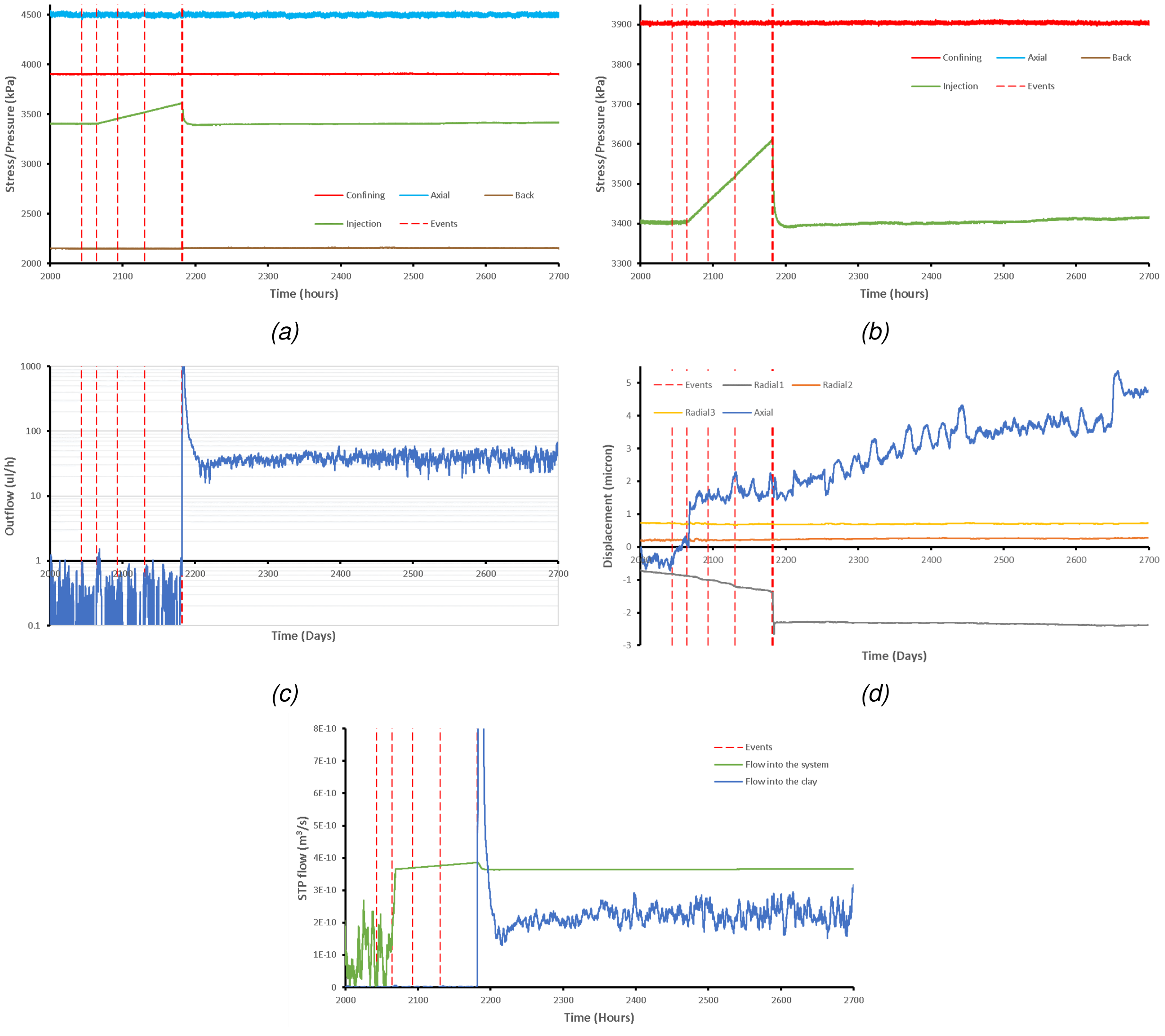

(a) (b)

(c) (d)

(e)

Figure 2.46: Gas ramp 2 of test BC1. a) Boundary conditions; b) Detail of gas pressure at gas entry; c) Outflow from the sample; d) Strain; e) Flow into and out of the sample at STP conditions.

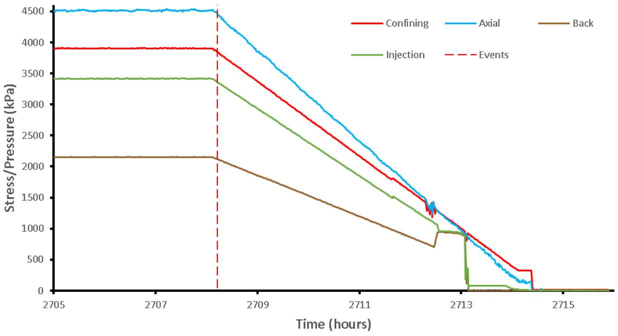

Figure 2.47: Unloading of sample BC1.

exceeded confining pressure, and steady state flow was established at a stress considerably below confining pressure. The maximum gas pressure is therefore related to the minimum principal stress. The behaviour at peak pressure differed between the tests. In COx1, gas pressure rapidly reduced as a result


(a) (b)

Figure 2.48: Photos of sample BC1 after removal from the apparatus.

Figure 2.49: Sample of Boom Clay prepared by machine lathing for test BC2.

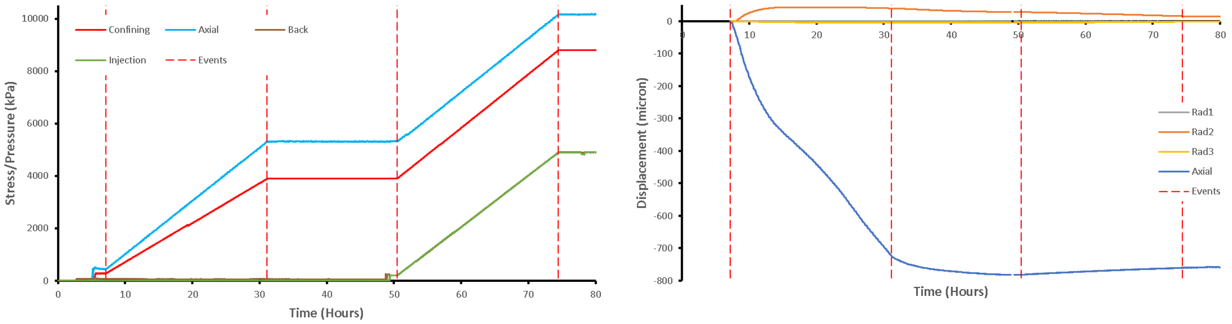

(a) (b)

Figure 2.50: Pressurisation of test BC2. a) Boundary conditions; b) Strain.

of a short-lived peak in flow into the sample. Steady-state flow was quickly established. Dilation of the sample was seen, although of the order of a micron in magnitude. At the higher stress condition, the gas pressure peaked and developed over many days before reaching an asymptote. No singular large peak in flow was seen, with more sustained flow events. Little dilation was noted at gas entry, with small dilational features seen in just one radial sensor. Therefore, while both tests showed gas movement as pressures less than the minimum principle stress, what occurred as gas became mobile appears different in the two

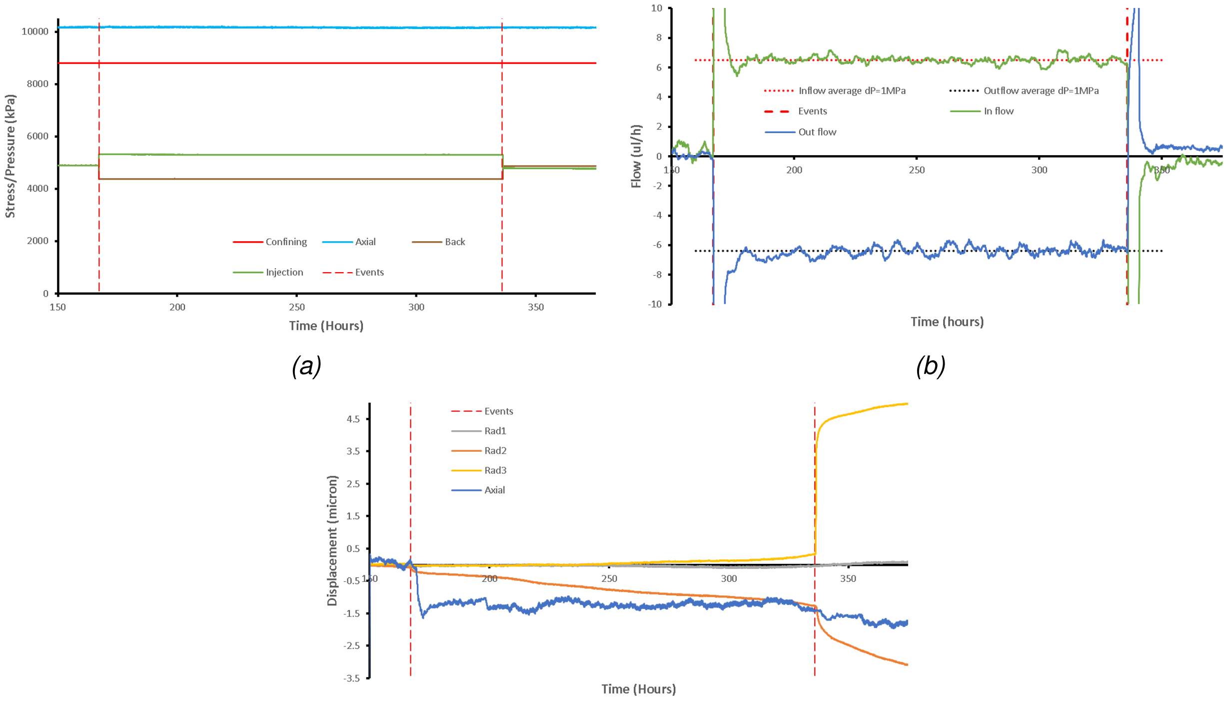

(a) (b)

(c)

Figure 2.51: Hydraulic test stage of BC2. a) Boundary conditions; b) Flow response; c) Strain.

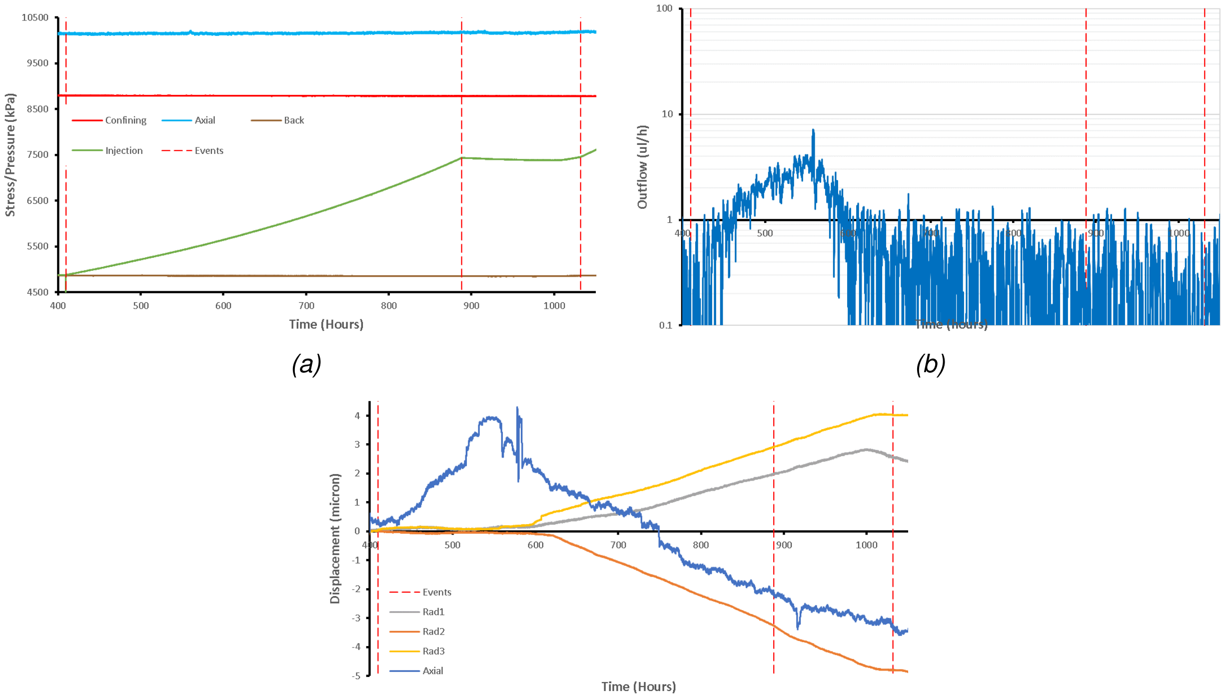

(a) (b)

(c)

Figure 2.52: Gas ramp 1 of test BC2. a) Boundary conditions; b) Outflow from the sample; c) Strain.

tests.

Figure 2.57 compares the two tests conducted in Boom Clay. The first test (BC1) was conducted at a stress state relevant to Belgium, while the second test (BC2) represented a stress state applicable to

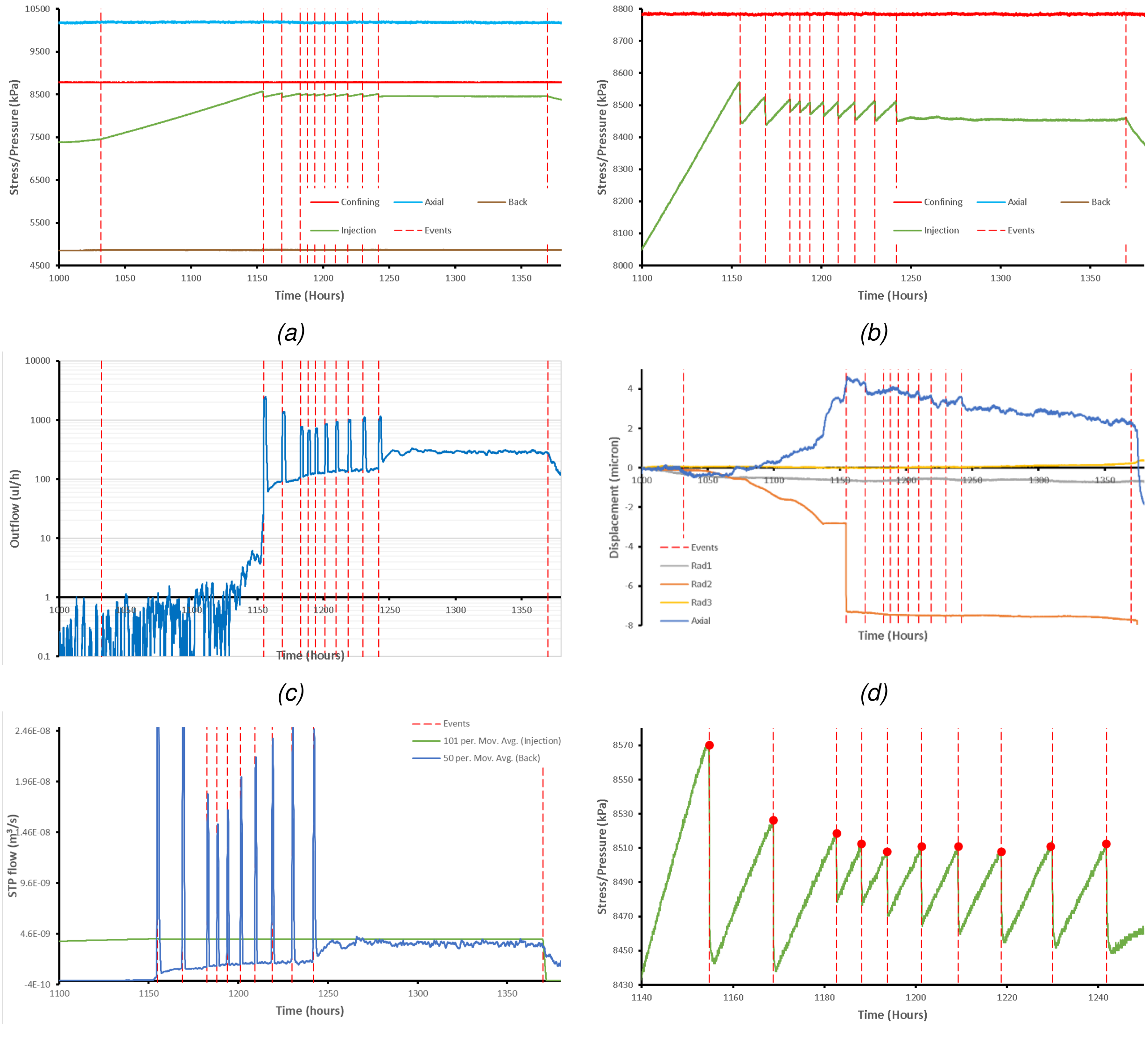

(a) (b)

(c) (d)

(e) (f)

Figure 2.53: Gas ramp 2 of test BC2. a) Boundary conditions; b) Detail of gas pressure at gas entry; c) Outflow from the sample; d) Strain; e) Flow into and out of the sample at STP conditions; f) Saw-tooth gas pressure response.

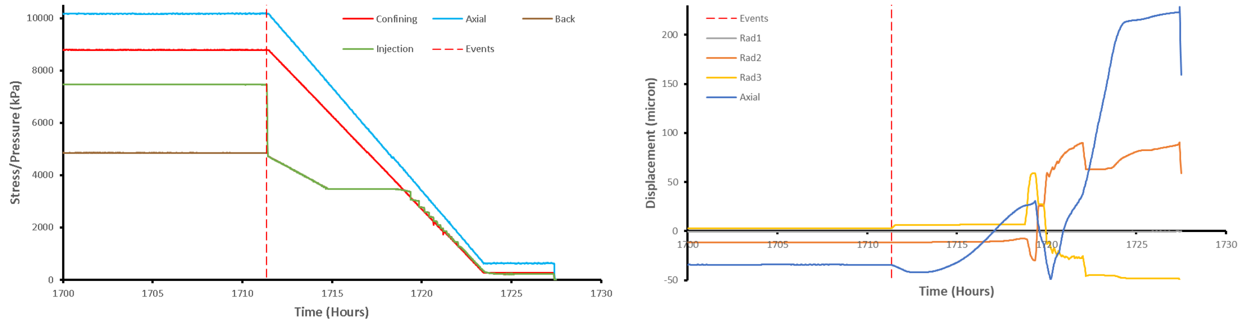

(a) (b)

Figure 2.54: Unloading of sample BC2. a) Boundary conditions; b) Strain.

Figure 2.55: Photo of sample BC2 after removal from the apparatus with small fractures seen parallel with bedding.

the Netherlands. The general features of the two tests correspond closely. Both tests showed outflow early in the first gas ramp. However, the higher hydraulic conductivity compared with Callovo-Oxfordian claystone meant that the flow was short-lived and outflow returned to zero during the gas ramp, not as a consequence of pausing the increase in gas pressure. In both tests, gas pressure peaked at a pressure below the minimum principal stress. Gas pressure rapid reduced as a short-lived peak in flow occurred. At the peak in gas pressure, dilation was seen in one of the radial sensors. Note that the single sensor was different in the two tests demonstrating that no failure of the sensors occurred to minimise the strain observed. The strain was highly localised and of the order of 2 – 5 microns.

In test BC1 (*Figure 2.57*) flow quickly became near-steady state, with a small increase in gas pressure. In test BC2 a "saw-tooth" response was seen, with multiple peaks in gas pressure seen. Each gas peak was lower than the previous event. This response appears similar to fault valve behaviour. After multiple events, gas flow became steady state. These two tests suggest that in BC1 a well-established dilatant gas pathway was created at peak pressure. This open feature conducted gas and did not evolve much, although there may have been elastic recovery of the pathway resulting in a small increase in pressure. In test BC2, a non-continuous dilatant gas pathway formed, with episodic flow eventually forming an open pathway. In both tests, only the initial gas peak resulted in detectable dilatant deformation. In both tests, steady flow was achieved with a gas pressure significantly below the minimum principal stress.

Comparing with previous tests

The aim of the first test conducted, COx1, was to replicate the results achieved as part of the EU FORGE project (Cuss et al., 2014), as shown in *Figure 2.58*. In FORGE, strains of the orders of 10's microns, up to 50 microns, was seen. These strains were slow in becoming established, taking several days to become steady. Flow showed similar features, with the first evidence of gas outflow being around 40 days after the first evidence of gas entry into the sample. Even taking into account the difference in sample size, the strain seen in FORGE was significantly greater than seen in the current study, the establishment of strain was much slower, as was the rate of gas movement through the sample. Consistency also exists between the studies, with all tests seeing gas flow at a pressure below the minimum principal stress, developing to a steady pressure significantly below confining pressure.

Figure 2.59 summarises results in Boom Clay as obtained as part of Covra's OPERA study (Harrington et al., 2017). This was a test conducted at a depth representative of the stress state in the Netherlands, i.e., at the same stress state as test BC2. As shown, strains were of the order of 10s of microns and these took some time (hours) to develop. The outflow from the test also took similar time to develop. This

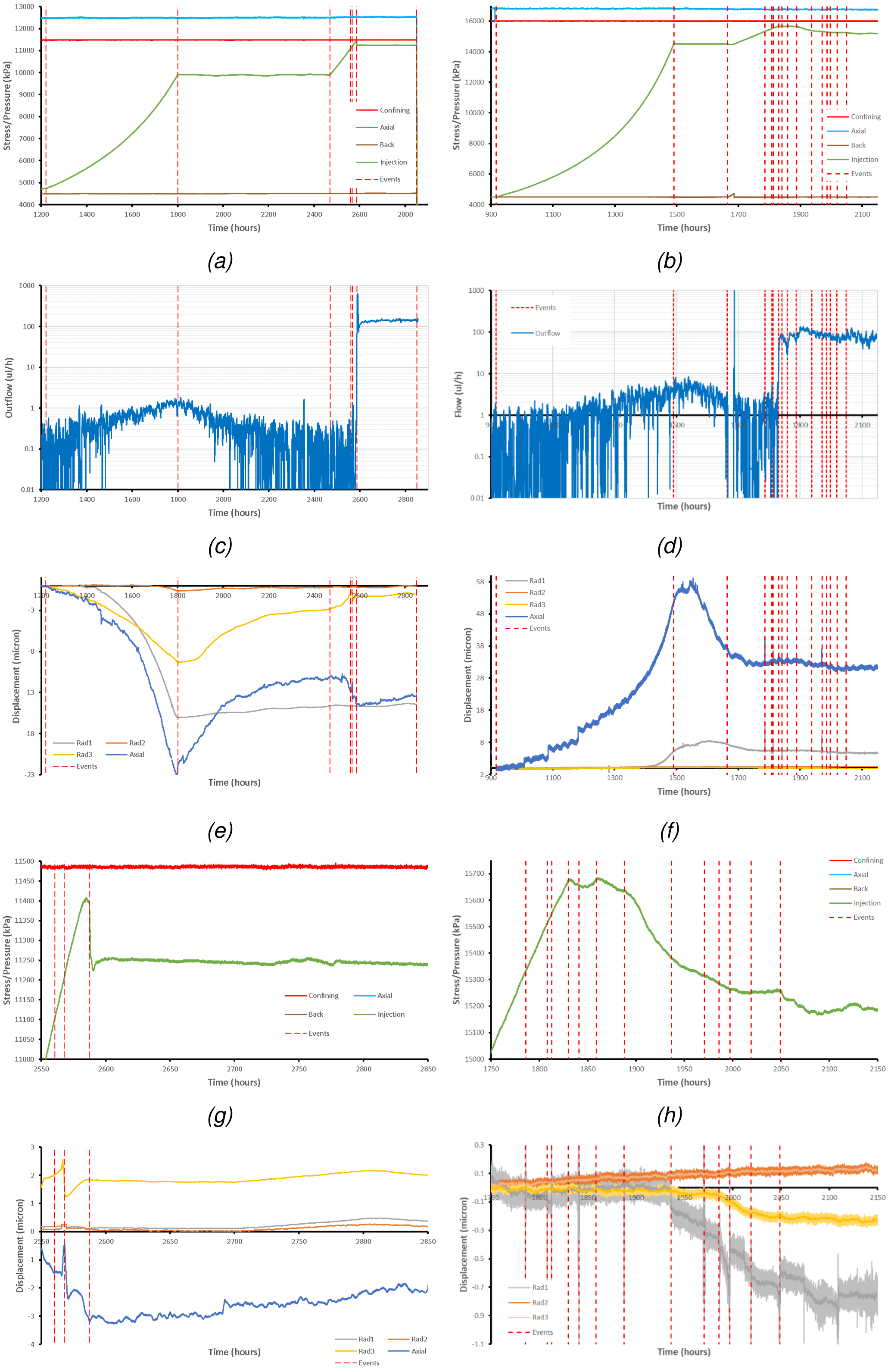

(a) (b)

(c) (d)

(e) (f)

(g) (h)

(i) (j)

Figure 2.56: Comparison of tests conducted in Callovo-Oxfordian claystone. a/b) Gas injection test boundary conditions; c/d) Outflow; e/f) Displacement (sample strain); g/h) Detail of gas pressure at peak pressure; i/j) Detail of strain at gas peak pressure. Note: COx1 on left, COx2 on right

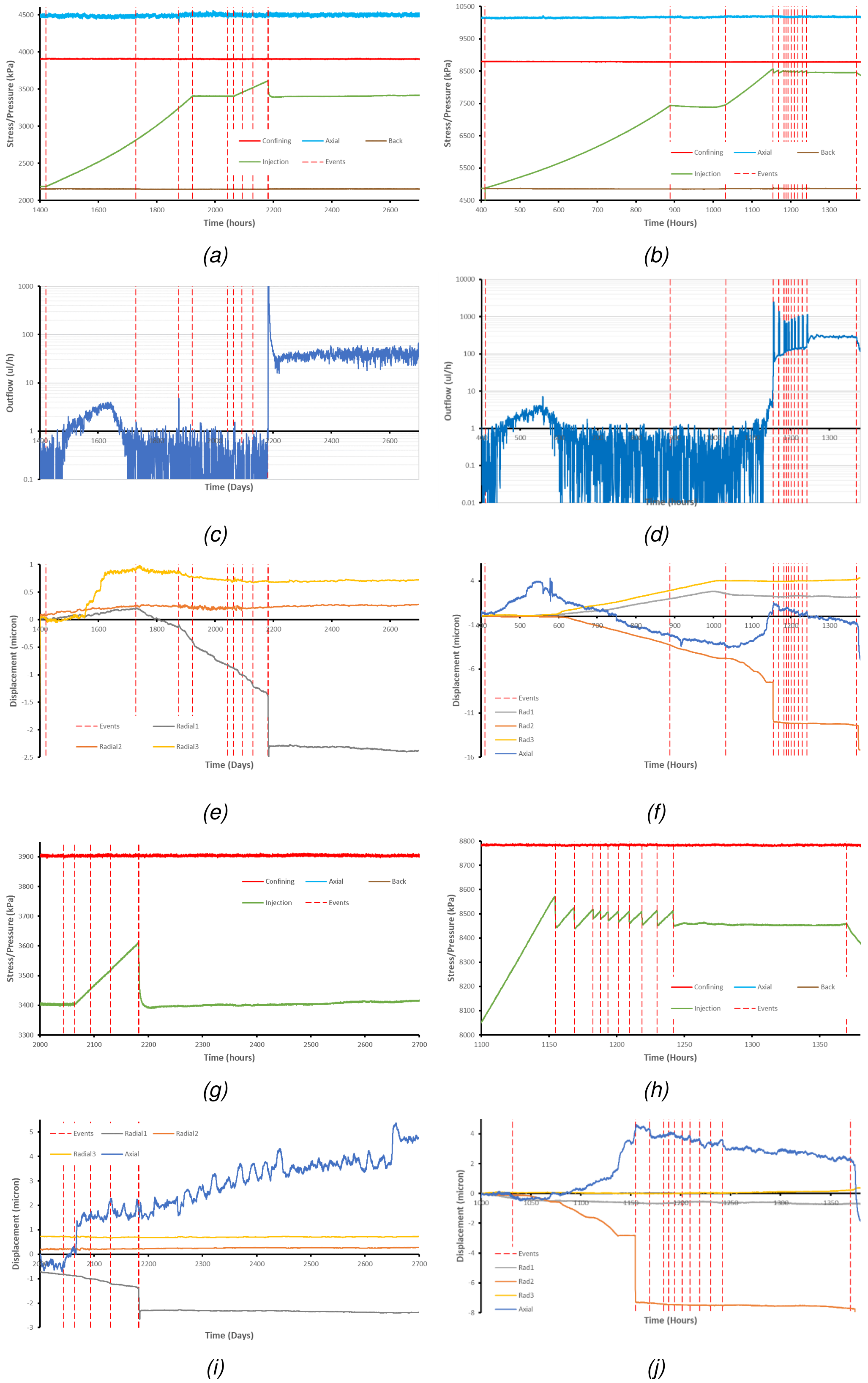

(a) (b) (c) (d) (e) (f) (g) (h) (i) (j)

Figure 2.57: Comparison of tests conducted in Boom Clay. a/b) Gas injection test boundary conditions; c/d) Outflow; e/f) Displacement (sample strain); g/h) Detail of gas pressure at peak pressure; i/j) Detail of strain at gas peak pressure. Note: BC1 on left, BC2 on right

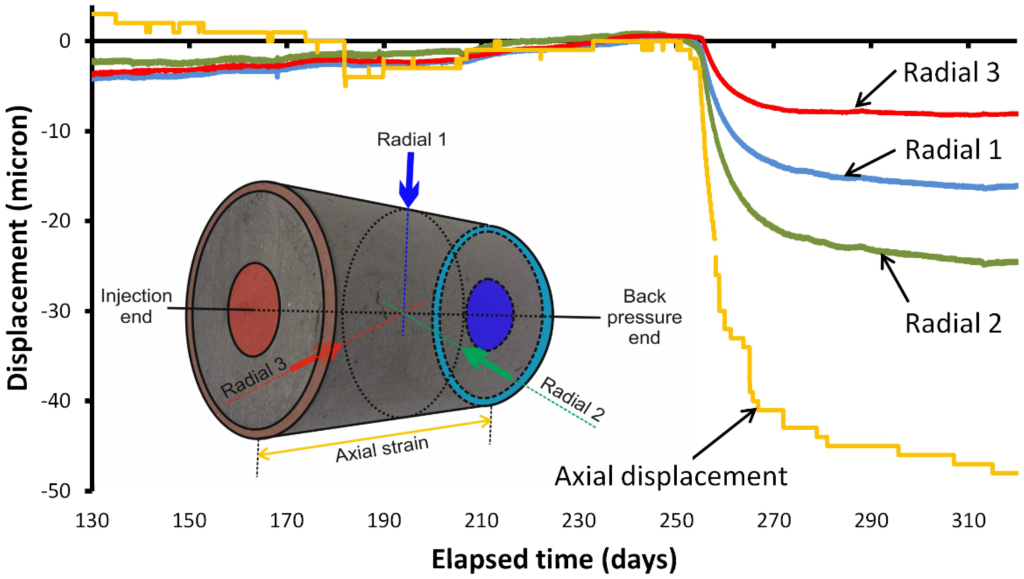

Figure 2.58: Summary of results seen in Callovo-Oxfordian claystone as part of the EU FORGE project (From Cuss et al., 2014).

contrasts with the results from the current study with almost instantaneous outflow from the sample as the gas pressure peaked, and with strain of only a few microns that occurred instantaneously. Therefore, as with Callovo-Oxfordian claystone, considerable differences are seen in the magnitude of the strain, and the rate of strain and flow development. However, in all tests, gas was seen to peak at a stress below the minimum principal stress and developed an asymptote at a pressure significantly below the confining pressure.

Both Callovo-Oxfordian claystone and Boom Clay show significant differences in the magnitude of strains and the rate that strains and flow developed. The difference between the current study and results achieved in the FORGE and OPERA projects is problematic and required careful consideration.

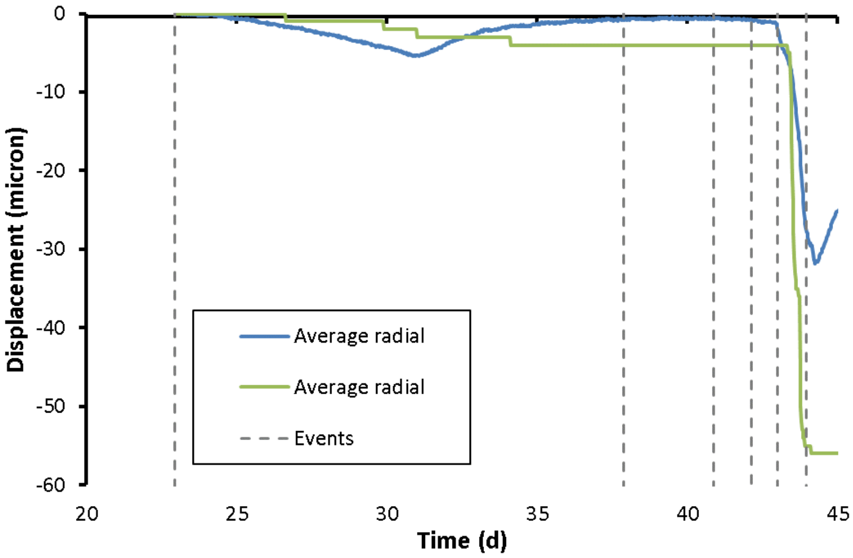

Figure 2.59: Summary of results seen in Boom Clay as part of the OPERA project (From Harrington et al., 2017).

The FORGE and OPERA studies were conducted using the Stress Path Permeameter with samples of 56 mm diameter. The current study used a similar apparatus, but with samples of 38 mm diameter. Initially it was considered whether the differences were simply the result of using different apparatus. It was considered that the strain measurement in the Triax apparatus was at fault. However, as the two tests in Boom Clay showed, different strain sensors detected deformation in the two tests. This gives confidence that the strains were localised and that all sensors were working as expected. The next consideration was the experimental geometry. In FORGE and OPERA, the injection and back-pressure filters were not of full diameter, whereas in the current experimental geometry, full-face filters were used. This should not alter the physics of gas flow significantly but had to be considered. Unpublished test results for Callovo-Oxfordian claystone conducted at BGS using the Elastimeter apparatus also utilised full diameter filters. Strain and flow results were more aligned with the current study than seen in FORGE. We also considered other data achieved in other rocks. As part of the Mont Terri Consortium Gas Transfer (GT) project, four laboratory gas injection tests were conducted in Opalinus Clay (Cuss et al., 2022). These experiments achieved results consistent with FORGE and utilised small injection filters. Therefore, it was noted that full face filters tended to achieve rapid strain and flow development, with limited localised flow. In contrast, partial end filters resulted in the slow development of much greater strain, with outflow taking considerable time to develop.

The Stress Path Permeameter was constructed with partial end filters and “guard-rings” so that sidewall flow could be discounted from gas flow experiments. However, this test geometry makes modelling much more complicated, and it was requested to use full-face filters. This has clearly changed the response of the rock. We therefore have to consider whether the current tests are simply observing sidewall flow. As part of the GT experiment, a gas injection experiment was conducted with a sample of tungsten to force sidewall flow. Whilst this test showed localised strain with small displacements, gas flow did not begin until a pressure greater than confining pressure. While sidewall flow cannot be ruled out entirely, the response seen in the current study is not fully consistent with the sidewall flow test conducted in GT (Cuss et al., 2022). Therefore, the conceptual model shown in *Figure 2.60* was proposed and discussed at EURAD GAS meetings. It was proposed that full face filter experiments exploit features around the periphery of the sample. Even though test samples are made as careful as possible using machine lathing, it is still possible that parallel features are created with the sample boundary. It was hypothesised that the full width filter meant that these features were accessible and easily exploited. With small end filters, gas must enter the intact interior of the sample as opposed to exploiting the edge of the sample. It was intended to x-ray CT the samples, although the technique suffers from edge effects that often means that the area of interest is difficult to definitively study. However, time was not available to do so before reporting.

Compelling evidence in support of the hypothesis is shown in *Figure 2.61*. Photos taken of sample BC1 following gas injection shows fine features within 1-3 mm of the sample periphery. If these are exploited by gas the deformation will be much more localised than if gas moved through the body of the sample. Therefore, it is suggested that the test geometry is influencing the results.

2.2.6. Summary

This package of work conducted four triaxial gas injection experiments on Boom Clay and Callovo-Oxfordian claystone. Each test was conducted in an identical way, with six stages; 1) The sample was carefully loaded over a period of around 48 hours to first get the boundary conditions to the effective stress, and then to the desired test boundary conditions. 2) A hydraulic test of between one and three steps that was conducted by raising pore water pressure at the injection end of the sample and lowering pressure at the backpressure end by the same amount to create a pressure gradient across the sample but while maintaining a constant average pore-pressure. 3) A gas ramp to increase injection pressure to around ¾ of the way between pore-pressure and confining pressure. 4) A holding stage, where gas pressure was held constant to observe whether gas was mobile within the system. 5) A second gas ramp to take the sample through to gas entry and breakthrough. 6) Depressurisation of the sample over a 4-24 hour period to allow sample extraction from the apparatus. For each rock type, two tests were conducted at two different boundary conditions. The first represented the in situ conditions of sample coring from either the Meuse/Haute-Marne underground laboratory at Bure in France, or the HADES underground laboratory at

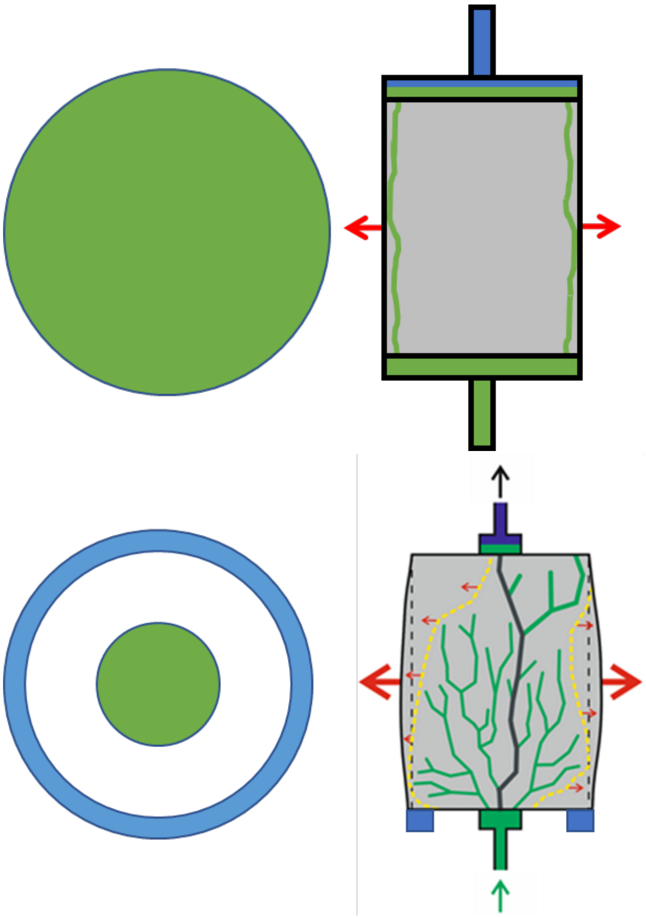

Figure 2.60: Conceptual model of gas flow being influenced by the size of the injection filter.

Figure 2.61: Fine features seen around the periphery of the sample in test BC1.

Mol in Belgium. The second test represented an increased stress state. For Boom Clay, this approximated the stress state expected in the Netherlands. For Callovo-Oxfordian claystone the second stress state was a higher stress than the first test, with a much-reduced differential between axial and confining pressures. The aim of the study was to observe whether stress was a control on the transition from visco-capilary flow to dilatant pathway formation. Tests in Callovo-Oxfordian claystone were oriented parallel with bedding, while Boom Clay samples were oriented perpendicular to bedding.

Callovo-Oxfordian claystone

The two tests conducted in Callovo-Oxfordian claystone gave consistent results, even though they were conducted at different stresses. Both tests showed outflow from the sample during the first gas ramp. In both tests, this reduced to a condition of no flow when gas pressure was held constant. This is interpreted as the expulsion of excess water from the injection filter and is not evidence of gas movement, confirmed by a condition of zero flow when the gas pressure was held constant. Differences were seen in the strain responses. The expulsion of water from the filter caused COx1 to increase in volume through swelling. However, COx2 showed compressional deformation. This shows that this sample was contracting because of the higher stress condition.

In both tests, gas entry occurred at a pressure below the minimum principal stress. Gas pressure never exceeded confining pressure, and steady state flow was established at a stress considerably below confining pressure. The maximum gas pressure is therefore related to the minimum principal stress. The behaviour at peak pressure differed between the tests. In COx1, gas pressure rapidly reduced because of a short-lived peak in flow into the sample. Steady-state flow was quickly established. Dilation of the sample was seen, although of the order of a micron in magnitude. At the higher stress condition, the gas pressure peaked and developed over many days before reaching an asymptote. No singular large peak in flow was seen, with more sustained flow events. Little dilation was noted at gas entry, with small dilational features seen in just one radial sensor. Therefore, while both tests showed gas movement at pressures less than the minimum principal stress, what occurred as gas became mobile appears different in the two tests.

The aim of the first test conducted, COx1, was to replicate the results achieved as part of the EU FORGE project. In FORGE, strains of the orders of 10's microns, up to 50 microns, was seen. These strains were slow in becoming established, taking several days to become steady. Flow showed similar features, with the first evidence of gas outflow being around 40 days after the first evidence of gas entry into the sample. Even taking into account the difference in sample size, the strain seen in FORGE was significantly greater than seen in the current study, the establishment of strain was much slower, as was the rate of gas movement through the sample. Consistency also exists between the studies, with all tests seeing gas flow at a pressure below the minimum principal stress, developing to a steady pressure significantly below confining pressure.

Boom Clay

The first test (BC1) was conducted at a stress state relevant to HADES URL in Belgium, while the second test (BC2) represented a stress state applicable to the Netherlands. The general features of the two tests correspond closely. Both tests showed outflow early in the first gas ramp. However, the higher hydraulic conductivity compared with Callovo-Oxfordian claystone meant that the flow was short-lived, and outflow returned to zero during the gas ramp, not as a consequence of pausing the increase in gas pressure. In both tests, gas pressure peaked at a magnitude below the minimum principal stress. Gas pressure rapidly reduced as a short-lived peak in flow occurred. At the peak in gas pressure, dilation was seen in one of the radial sensors. Note that the single sensor was different in the two tests demonstrating that no failure of the sensors occurred to minimise the strain observed. The strain was highly localised and of the order of 2 – 5 microns. In test BC1 flow quickly became near-steady state, with a small increase in gas pressure. In test BC2 a "saw-tooth" response was seen, with multiple peaks in gas pressure. Each gas peak was lower than the previous event. This response appears similar to fault valve behaviour. After multiple events, gas flow became steady state. These two tests suggest that in BC1 a well-established dilatant gas pathway was created at peak pressure. This open feature conducted gas and did not evolve much, although there may have been elastic recovery of the pathway resulting in a small increase in pressure. In test BC2, a non-continuous dilatant gas pathway formed, with episodic flow eventually forming an open pathway. In both tests, only the initial gas peak resulted in detectable dilatant deformation. In both tests, steady flow was achieved with a gas pressure significantly below the minimum principal stress.

Test BC2 was conducted similarly to tests conducted as part of Covra's OPERA study. The latter saw strains of the order of 10s microns and these took some time (hours) to develop. The outflow from the test also took similar time to develop. This contrasts with the results from the current study with almost instantaneous outflow from the sample as the gas pressure peaked, and with strain of only a few microns that occurred instantaneously. Therefore, as with Callovo-Oxfordian claystone, considerable differences are seen in the magnitude of the strain, and the rate of strain and flow development. However, in all tests, gas was seen to peak at a stress below the minimum principal stress and developed an asymptote at a pressure significantly below the confining pressure.

Comparing both rock types

Both Callovo-Oxfordian claystone and Boom Clay show significant differences in the magnitude of strains and the rate that strains and flow developed compared with previous studies. The FORGE and OPERA studies were conducted using the Stress Path Permeameter with samples of 56mm diameter. The current study used a similar apparatus, but with samples of 38 mm diameter. Initially it was considered whether the differences were simply the result of using different apparatus, considering that the strain measurement in the Triax apparatus was at fault. However, as the two tests in Boom Clay showed, different strain sensors detected deformation in the two tests. This gives confidence that the strains were localised and that all sensors were working as expected. The next consideration was the experimental geometry. In FORGE and OPERA, the injection and back-pressure filters were not of full diameter, whereas in the current experimental geometry, full-face filters were used. This should not alter the physics of gas flow significantly but had to be considered. Unpublished test results for Callovo-Oxfordian claystone conducted at BGS using the Elastimeter apparatus also utilised full diameter filters. Strain and flow results were more aligned with the current study than seen in FORGE. As part of the Mont Terri Consortium Gas Transfer (GT) project, four laboratory gas injection tests were conducted in Opalinus Clay. These experiments achieved results consistent with FORGE and utilised small injection filters. Therefore, it was noted that full face filters tended to achieve rapid strain and flow development, with limited localised flow. In contrast, partial end filters resulted in the slow development of much greater strain, with outflow taking considerable time to develop. While sidewall flow cannot be fully discounted, it is not believed that the current tests were simply because of sidewall flow as gas became mobile at a pressure below confining pressure and developed to a pressure significantly below confining pressure. The identification of fine features, possibly fractures, around the periphery of one of the Boom Clay tests supports the hypothesis that the gas exploited weaknesses created by the sample preparation technique. Therefore, the test geometry was playing a strong control on the observed results once gas became mobile.

In all tests, gas became mobile at a pressure below the minimum principal stress. While dilatancy was not as strong as seen in previous tests, localised dilatancy was seen. In test COx2 the sample was accidentally gas-fractured during depressurisation as the pore pressure pump ran out of volume to reduce pressure. This resulted in a highly fractured sample. Therefore, unintentionally, clear differences were observed between gas fracturing and dilatant pathway formation. In the other tests, pervasive fractures did not form.

2.2.7. Key learning points

2.2.7.1. New knowledge acquired

The primary aim of the study was to determine whether stress controls the transition from visco-capiliary flow to dilatancy controlled flow. No evidence of visco-capiliary flow was seen, with all tests showing dilatancy, albeit small, at the time of gas entry.

In all tests, gas became mobile at a pressure less than the minimum principal stress (confining pressure) and developed to a pressure significantly below confining pressure. If test samples were simply fracturing, or if flow was by simple sidewall flow, this would not occur at a pressure below the minimum principal stress.

Significant differences have been seen between tests of different geometry. In tests conducted with small injection filters, gas moves through the body of the sample and results in the slow development of strain and out flow. The use of full-face filters allowed gas to exploit weaknesses in the sample, resulting in highly localised dilatant strain, instantaneous outflow at gas peak pressure, and the quick establishment of steady-state flow. Comparison with other test programmes confirms that the observations are test geometry dependent and not apparatus or sample size related.

Gas fracture results in the pervasive fracturing of the sample, not seen in samples where dilatant pathway formation has occurred. It is therefore seen that dilatant pathways are not fracture related.

2.2.7.2. Impact of acquired knowledge

The current study questions whether the use of full-face filters is appropriate and whether discrepancies seen between laboratories is the result of filter geometry selection. This may mean that uncertainty exists in the interpretation of experiments conducted with full-face filters.

Dilatant pathway formation was the only mechanism seen during gas injection. The control of the gas entry pressure is the minimum principal stress.

2.2.7.3. Remaining knowledge gaps

It is still not proven fully that stress is a control on the physics of gas flow and whether there is a transition from visco-capiliary flow to dilatant pathway formation. This will require many more experiments.

A clear difference exists between dilatant pathway formation and gas fracturing. The transition from one to the other is likely to be gas pressurisation rate. This requires further consideration.

2.2.7.4. Recommendations for the future

Confirmation tests are required to observe whether smaller filter in the current experimental geometry result in similar results seen in the FORGE and OPERA projects for Callovo-Oxfordian claystone and Boom Clay respectively.

References

Armand, G., Conil, N., Talandier, J. and Seyedi, D.M. (2017) Fundamental aspects of the hydromechanical behaviour of Callovo-Oxfordian claystone: from experimental studies to model calibration and validation. *Computers and Geotechnics*, *85*, pp.277-286.

Beerten, K, Leterme, B (2012) *Physical geography of north-eastern Belgium – the Boom Clay outcrop and sub-crop zone SCK-CEN report* ER-202 12/Kbe/P-2 60p.

Bernier, F, Li, XL, and Bastiaens, W (2007) *Twenty-five years' geotechnical observation and testing in the Tertiary Boom Clay formation,* Géotechnique 57(2) 229–237.

Blanchart, P, Faure, P, De Craen, M, Bruggeman, C, and Michels, R (2012) *Experimental investigation on the role of kerogen and clay minerals in the formation of bitumen during the oxidation of Boom Clay,* Fuel 97, 344–351.

Cuss, R.J., Harrington, J., Giot, R., and Auvray, C. (2014) Experimental observations of mechanical dilation at the onset of gas flow in Callovo-Oxfordian claystone. In: *Clays in Natural and Engineered Barriers for Radioactive Waste Confinement*; Norris, A., Bruni, J., Cathelineau, M., Delage, P., Fairhurst, C., Gaucher, E.C., Hohn, E.H., Kalinichev, A., Lalieux, P, and Sellin, P. (Eds), **400,** *Geological Society Special Publications*: London, United Kingdom, Geological Society of London, pp. 507-519, doi:10.1144/SP400.26

Cuss, R.J., Harrington, J.F., Noy, D.J., Birchall, D.J., and Marschall, P. (2007) Consolidation and rebound properties of Opalinus clay: A long-term, fully-drained test. *In:* Clays in Natural & Engineered Barriers for Radioactive Waste Confinement. 3rd International Meeting, September 17th to 20th 2007, Lille, France.

Cuss, RJ, Wiseall, AC, and Sentis, M (2022) Evaluation of gas transport models and of the behaviour of clay rocks under gas pressure: GT Experiment. Mont Terri Technical Meeting TM-39. Porrentruy, Switzerland, January 2022.

De Craen, M, Wang, L, Van Geet, M, Moors, H (2004) *Geochemistry of Boom Clay pore water at the Mol site,* SCK-CEN-BL-990 04/MDC/P-48, SCK-CEN.

Dehandschutter, B, Vandycke, S, Sintubin, M, Vandenberghe, N, Gaviglio, P, Sizun, JP Wouters, L, (2004) *Microfabric of fractured Boom Clay at depth: a case study of brittle-ductile transitional clay behaviour,* Applied Clay Science, 26(1-4) pp.389-401.

Esteban, L., Bouchez, J.L. and Trouiller, A., 2006. The Callovo-Oxfordian argillites from the eastern Paris Basin: Magnetic data and petrofabrics. *Comptes Rendus Géoscience*, *338*(12-13), pp.867-881.

Gaucher, E., Robelin, C., Matray, J.-M., Négrel, G., Gros, Y., Heitz, J.-F., Vinsot, A., Rebours, H., Cassagnabère, A. and Bouche, A.T. (2004) ANDRA underground research laboratory: interpretation of the mineralogical and geochemical data acquired in the Callovo-Oxfordian formation by investigative drilling, Phys. Chem. Earth 29, pp. 55–77.

Harrington, J.F., Cuss, R.J., Wiseall, A.C., Daniels, K.A., Graham, C.C., and Tamayo-Mas, E. (2017) Scoping study examining the behaviour of Boom Clay at repository depths of interest to OPERA. *OPERA-PU-BGS523&616*, 215pp.

Harrington, J.F., Graham, C.C., Dobbs, M.R., Cuss, R.J., Daniels, K.A., Wiseall, A.C., Parkes, D., Paluszny, A., Zimmerman, R.W., Salimzadeh, S., Tsaparli, V., Tempone, P., Thomas, R.N., Xenias, D., and Whitmarsh, L. (2018) CONTAIN D11: Integrated final results and conclusions. *CONTAIN Report* **D11**, 72pp.

Honty, M, and De Craen, M. (2011) *Boom Clay mineralogy – qualitative and quantitative aspects,* SCK CEN contract: CO-90-08-2214-00 NIRAS/ONDRAF contract: CCHO 2009-0940000, Research Plan Geosynthesis.

Marschall P., Horseman S., Gimmi T. (2005) Characterisation of Gas Transport Properties of the Opalinus Clay, a Potential Host Rock Formation for Radioactive Waste Disposal, Oil & Gas Science and Technology – Rev. IFP, 60, 1, pp 121-139.

Rousset, D. and Clauer, N. (2003) Discrete clay diagenesis in a very low-permeable sequence constrained by an isotopic (K–Ar and Rb–Sr) study. *Contributions to Mineralogy and Petrology*, *145*(2), pp.182-198.

Vis, GJ, and Verweij, JM. (2014) *Geological and geohydrological characterization of the Boom Clay and its overburden,* OPERA-TNO 411 Technical Report.

Wemaere, I, Marivoet, J, and Labat, S (2008) *Hydraulic conductivity variability of the Boom Clay in north-east Belgium based on four core drilled boreholes,* Physics and Chemistry of the Earth, Parts A/B/C 33 24-36.

Wenk, H.-R., Voltolini, M., Mazurek, M., Van Loon, L.R. and Vinsot, A. (2008) Preferred Orientations and Anisotropy in Shales: Callovo-Oxfordian Shale (France) and Opalinus Caly (Switzerland), Clays and Clay Minerals, 56, pp 285-306.

Wileveau, Y. and Bernier, F. (2008) Similarities in the hydromechanical response of Callovo-Oxfordian clay and Boom Clay during gallery excavation. Physics and Chemistry of the Earth, Parts A/B/C, 33, pp.S343-S349.

Wong, T, Batjes, DAJ, and de Jager, J, (Eds.; 2007) *Geology of the Netherlands*. Herent: Royal Netherlands Academy of Arts and Sciences.

Yu, HD, Chen, WZ, Jia, SP, Cao, JJ, and Li, XL (2012), *Experimental study on the hydro-mechanical behaviour of Boom clay,* International Journal of Rock Mechanics and Mining Sciences 53 159-165.

Yven, B., Sammartino, S., Géraud, Y., Homand, F., and Villiéras, F. (2007) Mineralogy, texture and porosity of Callovo-Oxfordian argillites of the Meuse/Haute-Marne region (eastern Paris Basin). *Mémoires de la Société géologique de France*, **178**, pp.73–90.

.

British Geological Survey (BGS)

2.3. Lasgit (BGS)

2.3.1. Executive Summary

Lasgit was a full-scale demonstration experiment conducted at a depth of 420m at the Äspö Hard Rock Laboratory. The experiment started following the closure of the deposition hole on 1^{st} February 2005 and logged data for a total of 5782 days, finally being decommissioned by mid-February 2021.

The main objectives for the Lasgit experiment were fully achieved during the 17-year project, allowing the upscaling of laboratory-derived process understanding to the field scale. The findings provide fundamental information that addresses key questions relating to the treatment of gas in safety assessment and the resulting implications for the evolution of the buffer in the event of a deposition hole containing a defective canister. The main conclusions were: 1) In all tests, regardless of initial gas volume, the movement of gas occurred at a pressure very close to the local total stress; 2) No signs of localised consolidation of the bentonite were observed; 3) The measured peak gas pressures should not lead to any mechanical damage to the buffer or to other barrier components in the repository; 4) Peak gas pressure is linked to the hydraulic permeability of the buffer and the ease at which gas can exit a deposition hole; 5) Gas is transported through a limited number of dilatant pathways. The pathways are expected to be small, in relation to the total volume of the buffer, and temporally variable; 6) No desaturation of the bentonite buffer as a result of gas transport was observed; 7) Over the timescale of the project, pathway closure was only partially successful; 8) The gas pathways are expected to slowly close at a finite “shut-in” pressure; 9) Gas migration through a bentonite is highly unlikely to alter the favourable hydromechanical properties of the barrier; 10) The impact of emplaced and long-lived persistent heterogeneities within the bentonite on gas pressure remains unclear.

The results from GT1 through GT6 and the FCT show gas transport processes are scale invariant when compared with laboratory experiments and insensitive to the initial upstream gas volume. This may have been expected but had never been tested, beyond laboratory scales, prior to Lasgit. The role of water and the maturity (i.e. state of pore-pressure, hydraulic conductivity, and stress homogenisation of the buffer in the time-frame of the experiment) have been shown to strongly impact gas flow in the buffer. Given the similarities in behaviour between individual tests and those performed in the laboratory, it is reasonable to assume that while peak gas pressures would increase as the buffer continued to mature and reach a state of hydraulic equilibrium, any change would be relatively small, linked to increases in swelling and porewater pressure. The absence of high peak gas pressures such as those sometimes observed during laboratory testing is an important outcome from Lasgit. While gas-induced consolidation may not have been directly observed, the similarities in gas migration behaviour at both scales indicate that it can be further investigated in the laboratory.

Advection (displacement versus dilatant gas flow): Upscaling of laboratory-scale observations using Lasgit as a test facility – UKRI-BGS

2.3.2. Introduction & Objectives

In the Swedish KBS-3 repository concept for spent nuclear fuel (SKB, 2009), copper/steel canisters containing spent fuel will be placed in large diameter (~1.8m) boreholes drilled into the floor of the repository tunnels. The space around each canister will be filled with pre-compacted bentonite blocks, which over time, will draw in the surrounding groundwater and swell, closing any remaining construction gaps. Once hydrated, the bentonite will act as a low permeability diffusional barrier, severely limiting the migration of any radionuclides released from the canister after closure of the repository. While the copper/steel canisters are expected to have a very substantial life, from a performance assessment perspective, it is important to consider the possible impact of groundwater penetrating a canister. Under certain conditions corrosion of the ferrous insert of each canister under anoxic conditions will lead to the formation of hydrogen. Radioactive decay of the waste and the radiolysis of water will produce some additional gas. Depending on the gas production rate and the rate of diffusion of gas molecules in the pores of the bentonite, it is possible that gas will accumulate in the void-space of each canister (Horseman, 1996; Horseman et al., 1997; 1999; Weetjens & Sillen, 2006; Ortiz et al. 2002; Wikramaratna et al., 1993; SKB, 2011). Gas will then enter the bentonite when the gas pressure exceeds some critical entry pressure specific to this material. Since water penetration of the canister is a prerequisite for the generation of hydrogen gas in the buffer, the timing of gas movement in the clay might coincide with that of radionuclide release into the buffer.

The quantitative treatment of gas migration in compact clays is a highly complex issue (Rodwell et al, 1999). The state of knowledge pertaining to the movement of gas in initially saturated buffer bentonite prior to Lasgit was based on small-scale laboratory studies (Donohew *et al.*, 2000; Harrington & Horseman, 1999; Horseman *et al.*, 1999; 1997; Hume, 1999; Pusch *et al.*, 1987; 1985; Tanai *et al.*, 1997). Laboratory tests have demonstrated the importance of the boundary condition on gas migration (Harrington & Horseman, 2003; Horseman *et al.*, 2004). Gas penetration is strongly dependent on the degree of water saturation of the bentonite. At water saturations less than 70% (Tanai et al., 1997) to around 80 – 90% (Hume, 1999), clay, such as bentonite, contains an interconnected network of air voids resulting in little or no pressure threshold for gas flow. As full saturation is approached, gas entry and breakthrough pressures increase rapidly (Gray et al., 1996; Hume, 1999). Gas flow is accompanied by local dilation of the buffer clay (Horseman et al., 1999). Porewater pressure and total stress acting within the clay are strongly affected by the passage of gas. The maximum gas pressure attainable during a discharge event, in part, relates to the geometry and spatial distribution of both the gas pathways within the buffer and the characteristics of the fractures distributed along the walls of the emplacement borehole. The transmissivity and hydrostatic pressure of these features will affect the maximum gas pressure that can be generated within the buffer.

While significant improvements in our understanding of the gas-buffer system had taken place prior to Lasgit (Harrington & Horseman, 2003), laboratory work had highlighted a number of uncertainties (Horseman et al., 2004), notably the sensitivity of the gas migration process to experimental boundary conditions and possible scale-dependency of the measured responses. As determined by Sellin & Harrington (2006), these issues were best addressed by undertaking a **La**rge-**S**cale **G**as **I**njection **T**est, or "Lasgit"; where large refers to a full-scale KBS-3 demonstration.

The Large Scale Gas Injection Test (Lasgit) was in continuous operation between February 2005 and December 2020, being fully decommissioned by February 2021. During this time the highly instrumented full-scale KBS-3 mock-up underwent natural and artificial hydration. *Table 2.15* outlines the full test history. The start of the Eurad GAS project occurred on Day 5232 of Lasgit. Prior to the start of the EURAD project a total of four gas injection tests had been completed. These occurred through two different injection filters on the surface of the copper canister to mimic a defect. The final phase of experimentation conducted as part of Eurad GAS included two gas injection tests, one each in the same two filters as previous investigations. The final test, known as the Full Canister Test, investigated the role of gas volume on advective movement. This test involved the pressurization of the void space within the canister and offered a unique perspective on buffer performance. Following the completion of the Full Canister Test the experiment was decommissioned, including thorough sampling of the buffer to determine saturation and evidence of gas pathways. The aim of the Lasgit experiment in EURAD Gas was to enable the upscaling of laboratory scale observations of the mechanisms governing advective gas flow to a full-scale KBS3 demonstration.

Stage	Description	Filter	Date	Day
0	Start of Lasgit		1/2/2005	1
1	Natural and artificial hydration phase 1	All	1/2/2005 – 25/5/2007	1 – 813
2	Gas injection test 1	FL903	25/4/2007 – 16/2/2008	813 – 1110
3	Natural and artificial hydration phase 2	All	16/2/2008 – 2/1/2009	1110 – 1430
4	Gas injection test 2	FL903	2/1/2009 – 13/8/2010	1430 – 2064
5	Gas injection test 3	FU910	13/8/2010 – 20/7/2012	2019 – 2726
6	Gas injection test 4	FL903	20/7/2012 – 15/4/2014	2726 – 3360
7	Hydraulic testing of filters	Most	15/4/2014 – 1/12/2014	3360 – 3590
8	Natural and artificial hydration phase 2	Most	1/12/2014 – 15/5/2015	3590 – 3755
9	Natural hydration	Most	15/5/2015 – 30/9/2020	3755 – 5720
10	Gas injection test 5	FU910	12/4/2019 – 29/5/2019	5183 – 5220
11	Gas injection test 6	FL903	29/5/2019 – 29/7/2019	5230 – 5264
12	Full Canister Test	FCT	29/7/2019 – 30/9/2020	5291 – 5720
13	Decommissioning		1/10/2020 +	5721 +

Table 2.15: Complete test history of Lasgit.

The question of upscaling from laboratory observations was addressed in two ways. Firstly, the qualitative comparison of the six gas injection experiments conducted during Lasgit at a field scale with the laboratory experiments conducted previously on small samples of bentonite. Secondly, the influence gas volume has on the post entry behaviour was investigated by the Full Canister Test. Laboratory experiments are limited to a gas volume of one litre, gas injection tests in Lasgit are limited to five litres, and the full canister test has 1.5 m^3 volume of gas. This final test phase gave direct comparison observations based on large gas volumes.

2.3.3. Experimental set-up

2.3.3.1. Description of apparatus

The Lasgit experimental setup is described in detail in SKB Technical Report TR-22-06 (Cuss et al., 2022). The key features of the experiment are summarized below.

Lasgit was a full-scale demonstration experiment operated by Svensk Kärnbränslehantering AB (SKB) at the Äspö Hard Rock Laboratory (HRL) at a depth of 420 m (*Figure 2.62*). The installation phase of Lasgit was undertaken from 2003 to early 2005 and consisted of the design, construction, and emplacement of the infrastructure necessary to perform the experiment. The experiment was initiated on 1st February 2005 following the closure of the deposition hole.

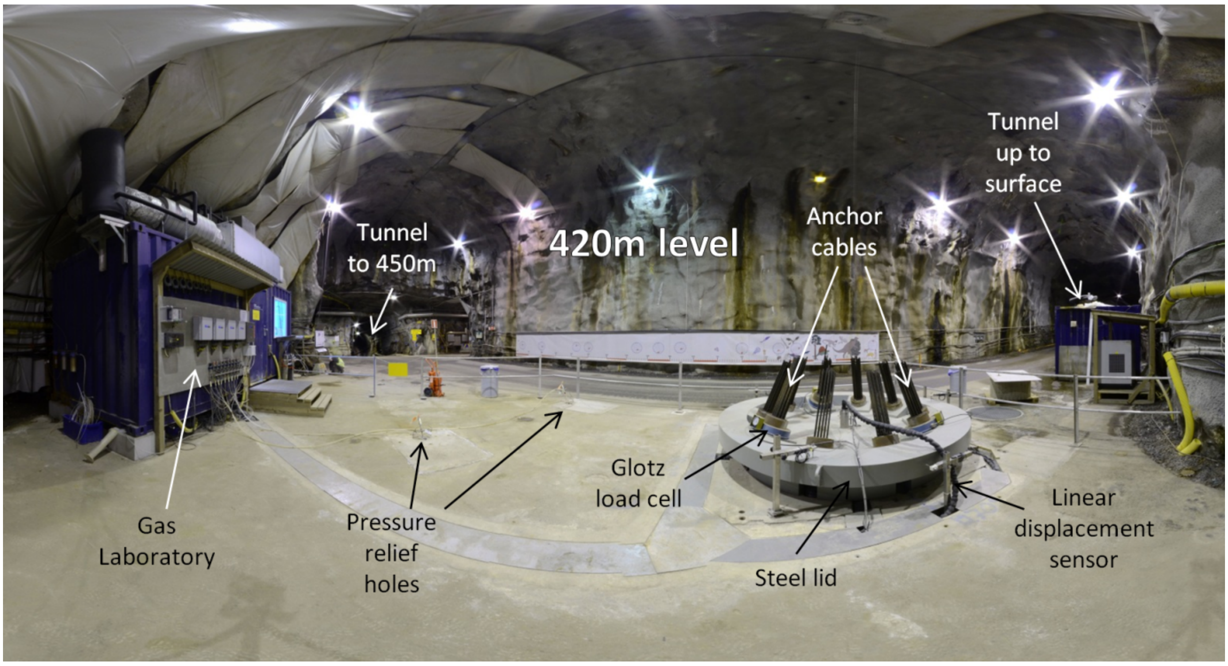

Figure 2.62: A panoramic view of the Lasgit test site located 420m below ground at the Äspö Hard Rock Laboratory in Sweden. The photo shows the position of the deposition hole, gas laboratory, pressure relief holes (containing a series of packered intervals in order to monitor porewater pressure in the surrounding fracture network) and some of the instrumentation attached to the steel lid.

The Lasgit experiment was commissioned in deposition hole DA3147G01, which was the first emplacement borehole to be drilled at the Äspö HRL. The deposition hole was vertical, and had a length of 8.5 m and a diameter of approximately 1.75 m. Prior to the emplacement of Lasgit, the deposition hole was fully mapped. The deposition hole was filled with pre-compacted bentonite blocks and a copper canister. The hole was capped by a conical concrete plug retained by a reinforced SS2172 carbon steel lid capable of withstanding over 5,000 kN force. A full-scale KBS-3 copper canister with iron insert was modified for the Lasgit experiment with thirteen circular filters of varying dimensions located on its surface in three separate arrays (*Figure 2.63*) to provide point sources for gas injection simulating potential canister defects. These filters could also be used to inject water during the hydration stages to help locally saturate the buffer around each test filter. Filter mats were placed in strategic positions both within the buffer and on the rock-wall to aid hydration. The canister was surrounded by specially manufactured pre-compacted bentonite blocks, all of which had initial water saturations in excess of 95 %. In the engineering void between the pre-compacted bentonite rings and the rock-wall, bentonite pellets were used. As the bentonite system began to saturate these swelled to fill the construction gaps and form a seal around the canister.

The deposition hole, buffer, and canister were equipped with instrumentation to measure the total stress, pore-water pressure and relative humidity in 32, 26 and 7 positions respectively (see *Figure 2.63*). Additional instrumentation continually monitored variations in temperature, relative displacement of the lid and canister, and the restraining forces on the rock anchors. The experiment was monitored and controlled from a temperature-controlled gas laboratory that allowed remote control and monitoring of the test. *Figure 2.62* shows a photograph of the test site following the installation stage.

The experimental set-up was highly instrumented with:

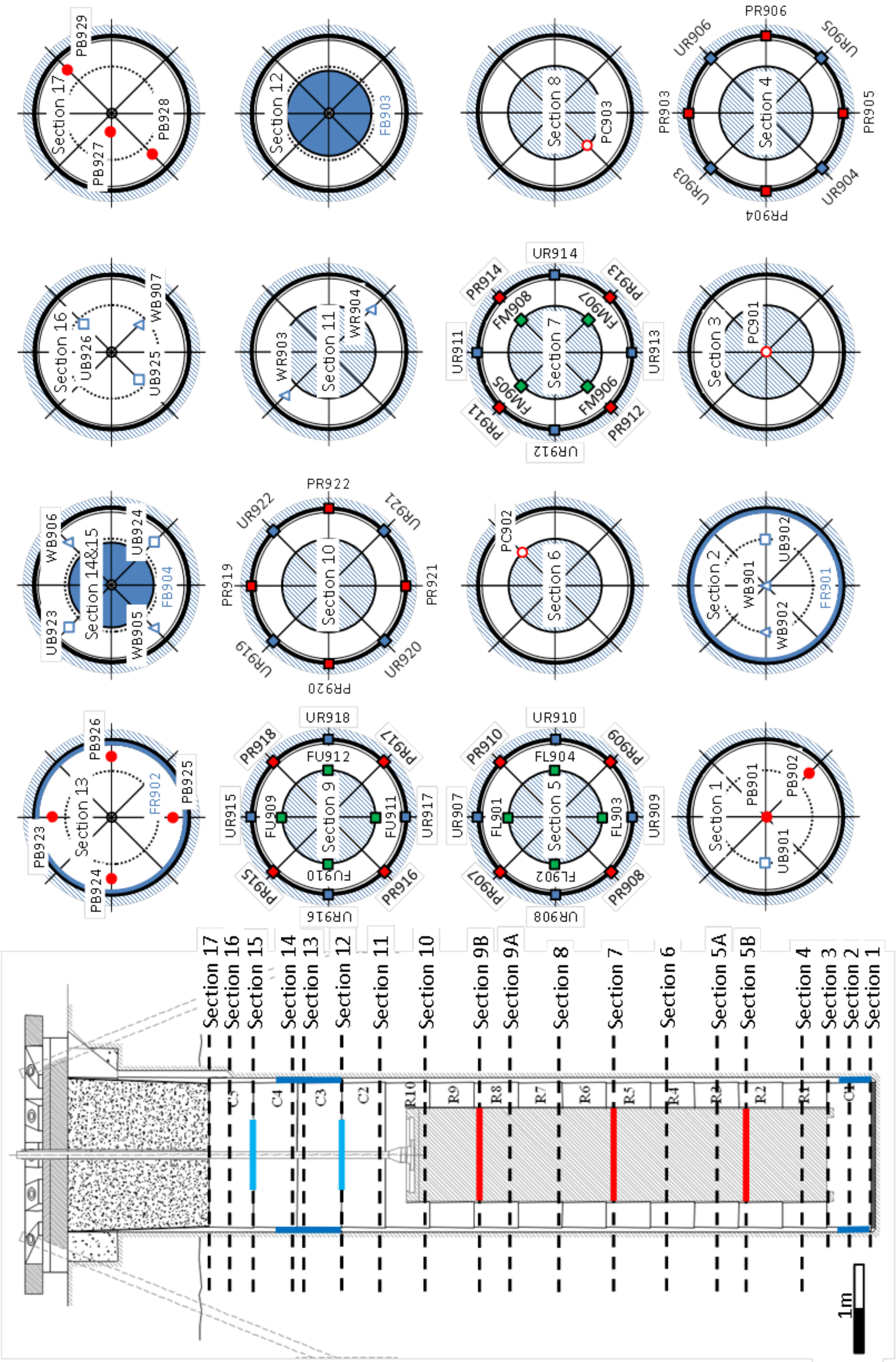

Figure 2.63: Schematic of the layout of the Lasgit experiment showing the locations of sensors. Sensors are placed in 14 of a total of 17 sections, filter mats for artificial water saturation in 4 sections and gas injection filters in 4 sections (UB9xx = pore-pressure sensor within the bentonite buffer; UR9xx = pore-pressure sensor at the rock wall; FL90x = injection filter on the lower array; FM90x = injection filter on the mid-plane array; FU9xx = injection filter on the upper array; Cx = bentonite block; Rx = bentonite ring).

- 17 pore pressure sensors rated to 25MPa on each of the 12 canister filters (FU9xx, FM9xx, FL9xx – where U denotes upper array, M mid-plane, and L lower array filters on the canister surface), canister pressure (FC9xx) and filter mats (FR9xx and FB9xx – where R denotes the filter mats on the rock wall and B denotes the filter mats placed between bentonite blocks).
- 20 Geokon pore pressure sensors on the deposition hole wall (UR9xx).
- 6 Geokon pore pressure sensors within the bentonite buffer (UB9xx).
- 20 Geokon radial stress sensors on the deposition hole wall (PR9xx).
- 9 Geokon total stress sensors within the bentonite buffer (PB9xx).
- 3 Sensotec stress sensors on the canister surface (PC90x).
- 7 Wescor psychrometer sensors within the bentonite buffer (WB9xx).
- 7 linear displacement sensors to measure the movement of the canister lid and relative position of the canister (DP9xx).
- 3 Glötzl load cells measuring load on three of the rock anchors holding the canister lid in place (LP9xx).
- 9 pore pressure sensors measuring water pressure in 9 intervals in two pressure-relief holes (U9xx).
- 5 thermocouples measuring the temperature in the canister (TC9xx), laboratory (TL9xx), office (TO(xx), and tunnel above the Lasgit experiment (TA(xx).
- 2 pore pressure sensors measuring the pressure of gas in the lab (RH9xx) and compressed air pressure (RA9xx).
- 4 syringe pumps recording pump pressure, volume, and flowrate.

Figure 2.63 shows the distribution of all sensors within the deposition hole. In total, over 150 instrument outputs were monitored and recorded by a customised data acquisition graphical interface based on National Instruments LabVIEW^{TM} software. The data acquisition system, located in the office area of the Gas Laboratory, operated on a PC that was connected to the SKB local area network (LAN) providing real-time data acquisition and control. The LabVIEW software performed two primary functions. The first was to log all device outputs from both the depositional hole and the experimental apparatus (excluding the RH sensors which were monitored by existing equipment attached to another experiment at the HRL). The second function of the system was to provide remote control of key experimental systems such as the ISCO syringe pumps and automated servo-controlled valve work. Proximity sensors mounted on each valve provided continuous feedback to the control system identifying the current status of a particular valve. This facility enabled staff at BGS Headquarters in Keyworth, UK, to change pump settings and/or open/close any of the 68 actuated valves housed within the gas laboratory, remotely in real-time in order to initiate test sequences. Automated alarm systems embedded in the Lasgit software were configured to provide both e-mail notification and, under certain circumstances shutdown the ISCO pump systems if required.

The boundary conditions of the experiment were those dictated by the pressures and stresses built up naturally within the bentonite buffer during re-hydration. The canister lid had been pre-stressed to 1300 kN to impose a similar force comparable with that which would be generated by the back-fill placed within the gallery above each deposition hole in a geological disposal facility. The experiment was conducted at ambient temperatures.

2.3.3.2. Calibration

The complete Lasgit setup could be divided into two sets of sensors; those that were accessible and those that were buried within the deposition hole and therefore inaccessible. Those two sets of sensors were calibrated in different ways.

For the inaccessible sensors, the factory calibrations were used. These were calibrated against known standards to ensure accurate and comparable outputs during the experimental programme. The inaccessible sensors were of Geokon or Glötzl instruments. Some sensors were retrieved during decommissioning and re-calibrated to compensate for sensor drift over time. Where necessary, a linear drift was assumed.

The majority of the accessible transducers measured pressure, with additional sensors measuring lid displacement and temperature. These were re-calibrated at regular intervals, aimed at every 6 months, but in practice the interval was more like annual. Calibrations were conducted at Days 0, 393, 481, 854, 1000, 1109, 1180, 1288, 1444, 1577, 1967, 2206, 2458, 2969, 3283, 3640, 4242, 4529, 4900, 5061, 5264, and 5748. During each calibration, the sensors were isolated from downhole. A Fluke pressure calibrator was attached to the system, itself having annual calibration during an annual service. For canister and filter mat transducers an ISCO syringe pump was used to pressurise the calibration line of the apparatus at 0 (atmospheric), 2.5, 5, 7.5, 10, 7.5, 5, 2.5, and 0 MPa stages. At each stage the pressure reading of the calibrator was noted along with the voltage of all sensors. The four syringe pumps were calibrated in a similar manner. The pressure sensors of the pressure relief holes were of lower rating and therefore the calibration steps were 0, 0.8, 1.6, 2.4, 3.2, 4, 3.2, 2.4, 1.6, 0.8, and 0 MPa. The final regular calibration was that of temperature. Here a heated bath was used with a calibrated temperature probe, measuring digital readings of temperature at 10, 20, and 30 °C. For temperature it was not deemed necessary to perform calibration steps both up and down the scale.

For all calibration data the slope, intercept, and R^2 was calculated, the latter being used to ascertain whether the calibration had been of sufficient quality, with R^2 expected to be close to unity. As well as R^2, graphs of the calibration were also inspected. Where necessary, calibration was repeated if R^2 was not acceptable.

As well as determining whether individual calibration steps had been successful, it was necessary to quality control the complete calibration dataset. A problem was noted for the pressure within the canister (PXGOFC901). Throughout the history of the experiment, the canister was vented to atmosphere, therefore the calibrated result for this sensor should read atmospheric. Yet, between the calibrations at Day 3640 and 4242 the pressure was recorded as reaching nearly -200 kPa. This could not be possible as the sensors used were not designed to record a vacuum and indicated a calibration error. *Figure 2.64* shows the calibration data for PXGOFC901 and clearly identifies the calibration at Day 4242 as erroneous. Re-examination of the calibration data at this time showed a good R^2 value, indicating that the calibration had been performed as expected. The reason for the error was likely to be an issue with the Fluke pressure transducer at the time. Careful consideration was given to the correction of the calibration data, with regression used to “smooth” the calibration data, or to just remove the single problematic data point. It was decided to discount the calibration at Day 4242 and to assume linear drift between the calibrations at Day 3640 and 4529. This was done for all canister and filter mat pressure sensors. During data processing, a linear drift was assumed for all sensors between calibration times.

Data reduction during gas testing also requires an accurate determination of the total system volume during any particular test stage. Where possible the total volume of each test circuit from the syringe pump to injection filter was measured prior to the start of testing.

To minimise possible errors introduced into the data from instrumentation drift caused by the extended test duration of the Lasgit experiment, recalibration of laboratory pressure transducers and thermocouples was performed every 6-12 months, the exact date of which, was based on convenience to the test programme. As such, Lasgit data were processed in six monthly.

Error checking of Lasgit data

The Lasgit experiment lasted 5782 days, resulting in 432,314 data records of 175 channels; a total of 75,654,950 data points. However, taking in account of data “drop-outs” and following full QC of the data, a total of 69,752,457 data were accepted.

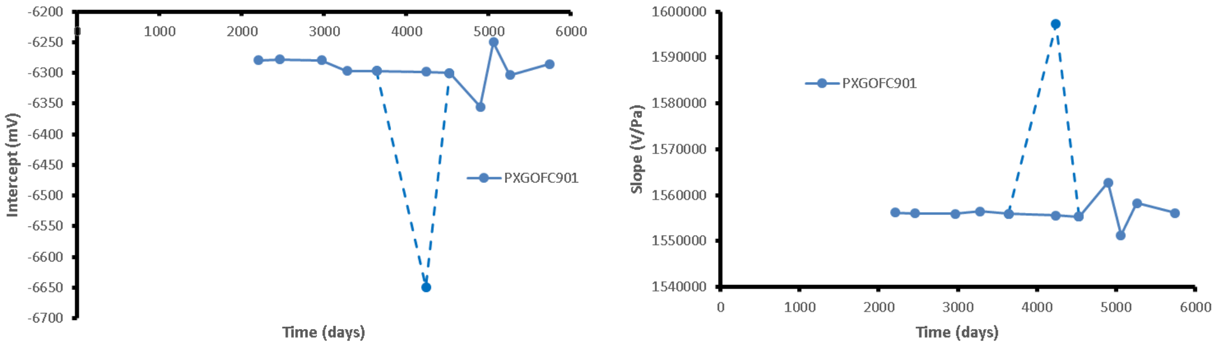

(a) *(b)*

Figure 2.64: Calibration data for canister pressure (PXGOFC901).

Data were generally transferred three times a week from Äspö Hard Rock Laboratory to BGS Keyworth using the remote Citrix server link (later replaced by a TeamViewer link). Once the data had been transferred to the UK, it was visually checked in a text editor program to ensure that the data were not corrupt. A check was made that data were not missing by comparing the time stamp of the new data with that from the previous data transfer. Once these initial checks had been conducted the data was imported to an Excel spreadsheet that contained all of the unprocessed (raw) data.

All data were processed in a second spreadsheet, which was linked to the raw data sheet. Here, data were converted from raw to scaled units ready for graphing and interpretation. Graphs of all parameters of interest were available for viewing and allowed on-going quality control (QC) of the data. The daily QC procedure was modified in 2008 with every sensor being checked in individual graphs displaying the last 10 days' worth of data. This allowed events that created subtle changes in values to be observed. Events could be identified by their elapsed time and were plotted on all other graphs, this allowed cross-correlations of sensors to be identified much easier and offered new insight into the hydro-mechanical response of the Lasgit system. At this time, the processing procedure was also improved. Initially, data were logged on an hourly basis, but this was changed at first to 30-minute intervals, and then 15-minute intervals. The latter being the fastest the Geokon logger could achieve. With 15-minute intervals it was possible to filter the data over 3 or 5 records and to automatically highlight erroneous data.

Data processing and traceability

There were a number of issues that arose in the recorded data. These included data synchronisation, erroneous values, loss of data during servicing or interruptions to logging system, and transducer drift. However, a number of QC methodologies were routinely employed to ensure both the quality and traceability of the collected Lasgit data. On a six-monthly basis, all data were thoroughly QC checked. This was performed using a series of conditional formatted Excel spreadsheets. Data were thoroughly checked for erroneous values or "outliers", with every anomaly examined and an informed decision made whether to remove, edit, or retain the data point in question. To ensure a coherent and traceable process a log was made of each change to the data sheet. No changes were made to the raw data files. The QC procedures were also repeated at the end of the experiment on the complete dataset to achieve the definitive dataset. All identified anomalies with the dataset were investigated.

2.3.3.3. Testing fluids

Natural hydration of the buffer occurred through the inflow of natural Äspö pore water through the fractures intersecting the deposition hole. Prior to installation of the buffer, inflow was measured to be between 10 and 20 litres of water per day over a small area of the hole, estimated to be 240 litres per day into the deposition hole. This natural water therefore accounted for a significant proportion of hydration fluid.

In the early days of the Lasgit experiment, water extracted from the bedrock close to the Lasgit experiment was used for artificial hydration of the filters on the canister surface and the filter mats. This led to issues of precipitation within the syringe pumps, which damaged the barrel of the pumps resulting in leakage. It was decided to use local “tap water” instead and this solved the issues. The exact chemical composition of the water was not determined.

The experiments conducted during the duration of the Eurad GAS project were performed using helium or nitrogen gas, with two-stage head tests conducted using tap water.

2.3.4. Material properties

The Lasgit experiment was commissioned in deposition hole number DA3147G01, which was the first emplacement borehole to be drilled at the Äspö Hard Rock Laboratory (HRL). The experiment was located within the Tunnel Boring Machine (TBM) assembly hall on the 420m-level of the tunnel system (*Figure 2.65*). The tunnel system at Äspö is comprised of an underground access ramp approximately 3600m long. It is initially straight but between sections 1600 – 3100m turns into a spiral.

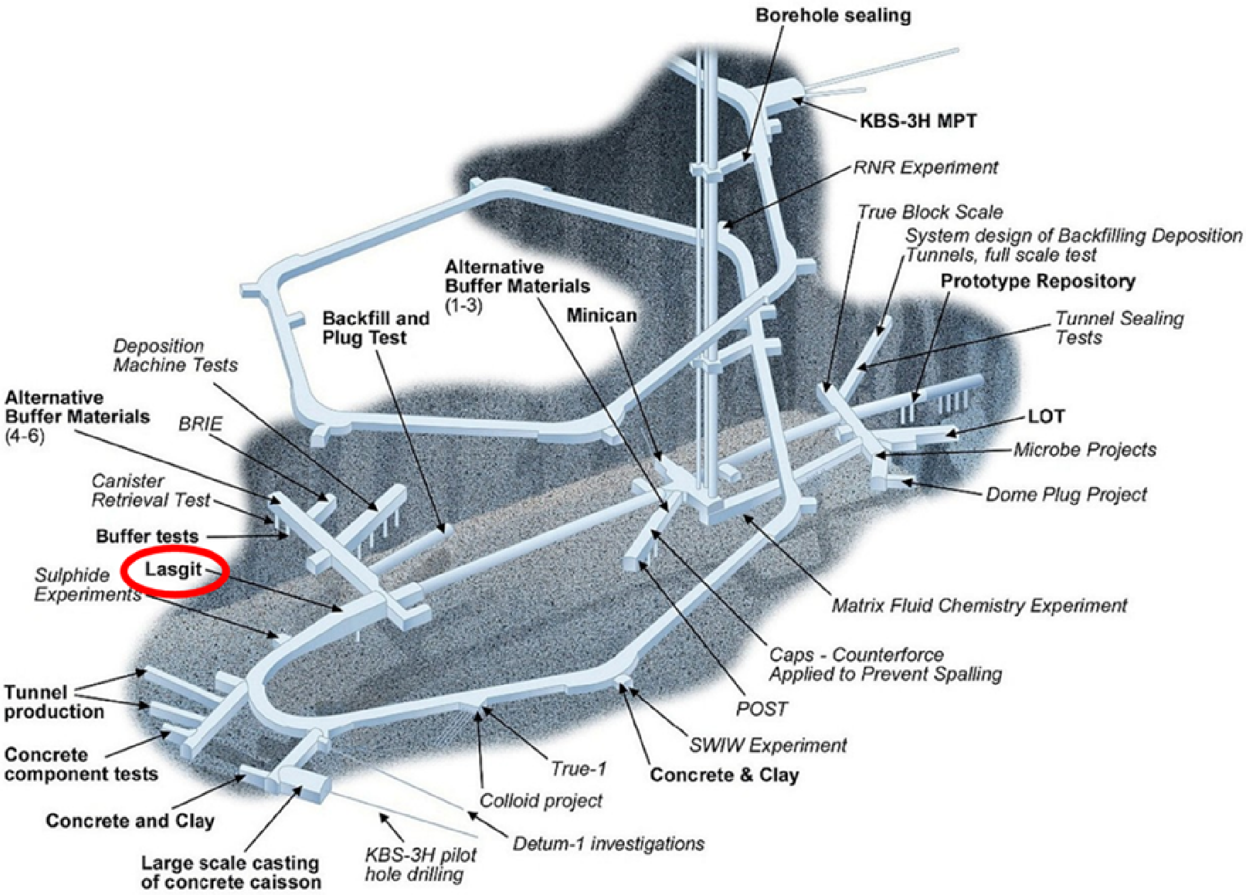

Figure 2.65: Location of Lasgit at 420 m depth in the Äspö Hard Lock Laboratory.

The DA3147G01 deposition hole had a length of 8.5 m and a diameter of around 1.75 m and was mostly within Äspö diorite. In addition, greenstone, fine-grained granite, and pegmatite make up the wall rock. The fractures within the wall rock have been comprehensively mapped, with conductive fractures identified.

A full scale KBS-3 canister was modified for the Lasgit experiment with twelve circular filters of varying dimensions located on its surface to provide point sources for gas injection, mimicking potential canister defects This design consists of a 50mm thick outer copper skin, which acts as a corrosion barrier in the oxygen-poor groundwater of the crystalline rock selected for disposal, and a nodular iron insert to provide strength and rigidity. Each canister weighs up to 27 tonnes (including the fuel rod assemblies), is 4.835 metres long and has a diameter of 1.05 metre.

Bentonite buffer – starting properties

Figure 2.66 shows a sketch cross-section through the deposition hole, giving dimensions of the individual elements of the KBS-3V concept. The space around the canister was filled with pre-compacted bentonite blocks, which, once hydrated, act as a low permeability diffusional barrier. The unique physicochemical properties of the bentonite depend on its colloidal behaviour and enormous specific surface. These include high sorption capacity, very high plasticity and excellent fracture self-sealing characteristics, severely limiting the migration of any radionuclides released from a canister after closure of the repository.

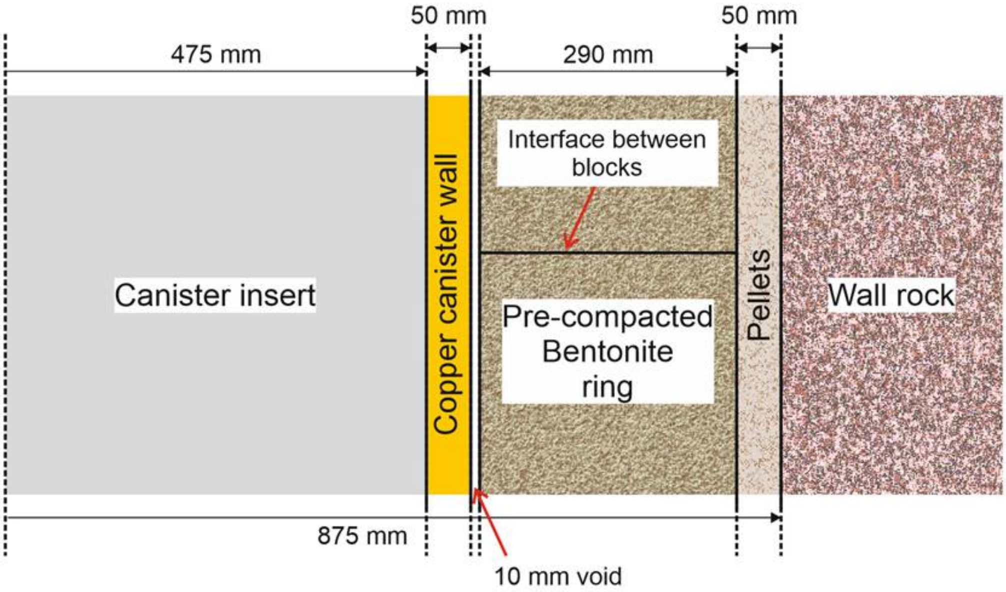

Figure 2.66: Cross-section sketch through the Lasgit deposition hole showing the canister, engineered void, pre-compacted bentonite ring, pellets, and wall rock.

The bentonite used was MX-80 (Johannesson, 2003) with a water content of 22 % (for the ring-shaped blocks) and 26 % (for the cylindrical blocks). The natural water content of MX-80 is 10 %, therefore water had to be added to the starting bentonite powder to achieve the desired water content and a saturation of > 95 %. Blocks were manufactured from bentonite powder that was pre-checked to meet the required specification. The quality-control included tests of natural water content, free swelling, liquid limit, and grain size distribution for each of the delivered Big-Bags. Variable water content is common and varies between 8 and 13 %, although the water content of each delivery tends to be very small. The grain size distribution test used a sieve to determine the size of the granules of clay particles. This test was performed to avoid deliveries with very fine powder, which might be hard to both mix and compact.

To achieve a high degree of saturation, water of a specific quantity was mixed with the powdered bentonite using an Eirich mixer at Hackman-Rörstrand AB. Once mixed, the water content of the mix was determined by drying a sample at 105 ℃ for 24 hours, with the rest of the bentonite placed in plastic bags to avoid desiccation during transportation and storage. The mixed bentonite was transported to Hydroweld AB in Ystad for pre-compaction. The mixture was poured into a rigid mould for either a complete block or a ring and was compacted vertically using a 30,000-ton press. Limited clearance in the press meant that the sample was compressed in three stages, adding more pistons as the sample compressed. Throughout the compaction the mould was connected to a vacuum pump to de-air the powder/block. Full compression took ~10 minutes to reach 50 MPa (10734 ton for segments and 6159 ton for rings), with maximum load held for 60 minutes. Unloading took a further 10 minutes with the blocks then removed from the mould and checked for dimension and weight and that the desired density had been achieved. Up to three blocks

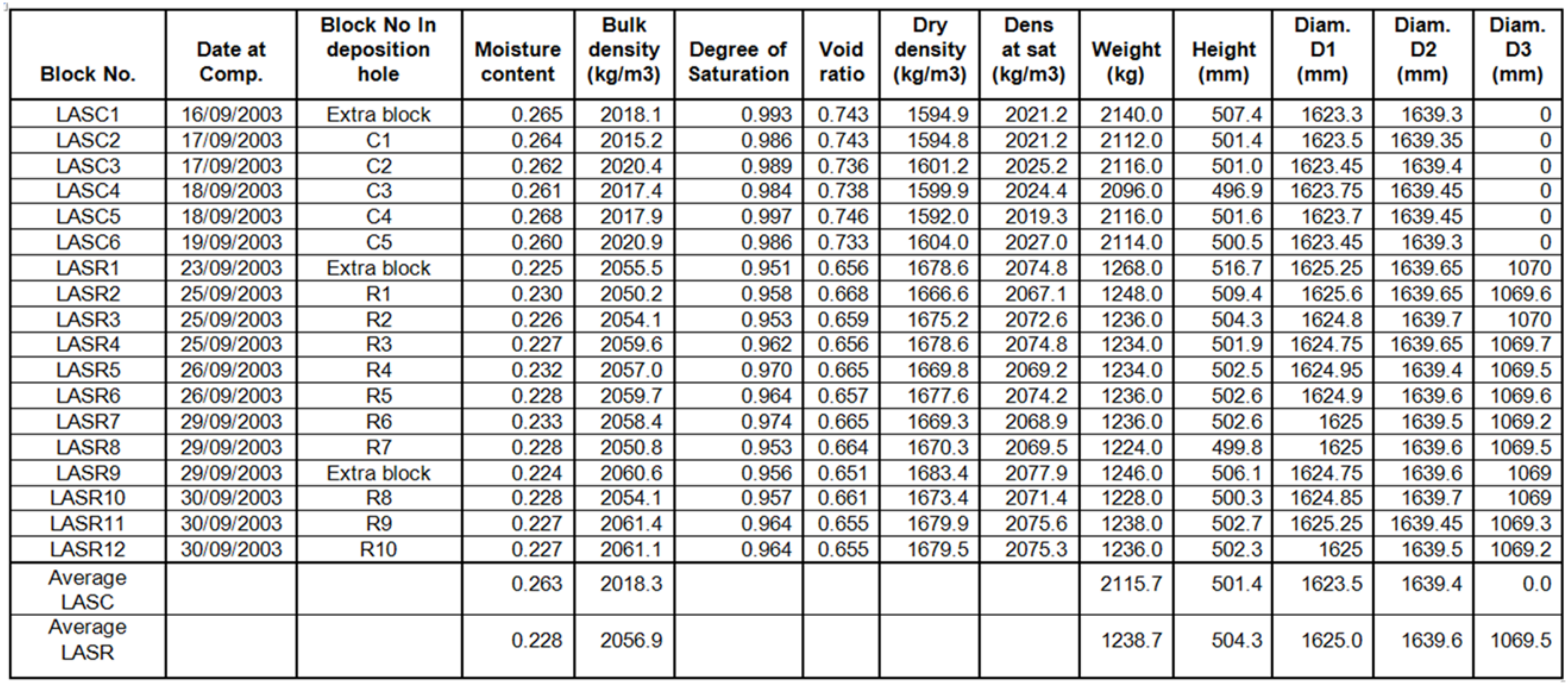

Block No.	Date at Comp.	Block No In deposition hole	Moisture content	Bulk density (kg/m3)	Degree of Saturation	Void ratio	Dry density (kg/m3)	Dens at sat (kg/m3)	Weight (kg)	Height (mm)	Diam. D1 (mm)	Diam. D2 (mm)	Diam. D3 (mm)
LASC1	16/09/2003	Extra block	0.265	2018.1	0.993	0.743	1594.9	2021.2	2140.0	507.4	1623.3	1639.3	0
LASC2	17/09/2003	C1	0.264	2015.2	0.986	0.743	1594.8	2021.2	2112.0	501.4	1623.5	1639.35	0
LASC3	17/09/2003	C2	0.262	2020.4	0.989	0.736	1601.2	2025.2	2116.0	501.0	1623.45	1639.4	0
LASC4	18/09/2003	C3	0.261	2017.4	0.984	0.738	1599.9	2024.4	2096.0	496.9	1623.75	1639.45	0
LASC5	18/09/2003	C4	0.268	2017.9	0.997	0.746	1592.0	2019.3	2116.0	501.6	1623.7	1639.45	0
LASC6	19/09/2003	C5	0.260	2020.9	0.986	0.733	1604.0	2027.0	2114.0	500.5	1623.45	1639.3	0
LASR1	23/09/2003	Extra block	0.225	2055.5	0.951	0.656	1678.6	2074.8	1268.0	516.7	1625.25	1639.65	1070
LASR2	25/09/2003	R1	0.230	2050.2	0.958	0.668	1666.6	2067.1	1248.0	509.4	1625.6	1639.65	1069.6
LASR3	25/09/2003	R2	0.226	2054.1	0.953	0.659	1675.2	2072.6	1236.0	504.3	1624.8	1639.7	1070
LASR4	25/09/2003	R3	0.227	2059.6	0.962	0.656	1678.6	2074.8	1234.0	501.9	1624.75	1639.65	1069.7
LASR5	26/09/2003	R4	0.232	2057.0	0.970	0.665	1669.8	2069.2	1234.0	502.5	1624.95	1639.4	1069.5
LASR6	26/09/2003	R5	0.228	2059.7	0.964	0.657	1677.6	2074.2	1236.0	502.6	1624.9	1639.6	1069.6
LASR7	29/09/2003	R6	0.233	2058.4	0.974	0.665	1669.3	2068.9	1236.0	502.6	1625	1639.5	1069.2
LASR8	29/09/2003	R7	0.228	2050.8	0.953	0.664	1670.3	2069.5	1224.0	499.8	1625	1639.6	1069.5
LASR9	29/09/2003	Extra block	0.224	2060.6	0.956	0.651	1683.4	2077.9	1246.0	506.1	1624.75	1639.6	1069
LASR10	30/09/2003	R8	0.228	2054.1	0.957	0.661	1673.4	2071.4	1228.0	500.3	1624.85	1639.7	1069
LASR11	30/09/2003	R9	0.227	2061.4	0.964	0.655	1679.9	2075.6	1238.0	502.7	1625.25	1639.45	1069.3
LASR12	30/09/2003	R10	0.227	2061.1	0.964	0.655	1679.5	2075.3	1236.0	502.3	1625	1639.5	1069.2
Average LASC			0.263	2018.3					2115.7	501.4	1623.5	1639.4	0.0
Average LASR			0.228	2056.9					1238.7	504.3	1625.0	1639.6	1069.5

Table 2.16: Properties and dimensions of the bentonite buffer. Diameter D1 and D2 are measured widths of the blocks measured orthogonal to one another, D3 is the inner diameter of the annular rings.

were manufactured a day.

Table 2.16 shows the dimensions and starting physical properties of the pre-compacted bentonite rings and blocks. As shown, a high degree of saturation (between 95.1 % and 99.7 %) was achieved, with bulk densities ranging between 2018 kg.m^{-3} and 2061 kg.m^{-3}. *Table 2.17* shows the expected density and swelling pressure after saturation at different sections of the deposition hole. This predicts a swelling pressure of between 3970 kPa and 4368 kPa within the Lasgit depositional hole, with greater pressure achieved above and below the canister.

The four upper most segments required a centre hole to be drilled using a seam drill to accommodate the Monel pipe, added to allow pressure lines and cables to lead to the copper canister. The bottom (C1) block was machined to accommodate the bottom of the canister with a track of 1070 mm outer diameter and 830 mm inner diameter to a depth of 85 mm. This was done using a drilling device for hole-drilling in concrete. Certain blocks were also prepared for mounting transducers. This was done using ordinary drills and grinding machines.

The space between the bentonite rings and wall-rock was in-filled using bentonite pellets, manufactured by Saut-Conreursin in France. Each pellet was pressed from bentonite and had dimensions of 16.3 × 16.3 × 8.3 mm, a water content of about 17 % and an expected density of a single pellet of about 2050 kg.m^{-3}. The expected bulk density of the fillings was approximately 1230 kg.m^{-3}.

Table 2.17: Expected density and swelling pressure after saturation at different sections of the deposition hole. Calculation does not take into account the engineered gap or pellet region and represent the maximum possible swelling pressure.

Section	Density at saturation (kg.m^{-3})	Void ratio	Dry density (kg.m^{-3})	Expected swelling pressure (kPa)
C – above and below canister	1972	0.831	1518	4368
R – at canister	1964	0.846	1506	3970

Bentonite buffer – final properties

The bentonite buffer was comprehensively sampled during decommissioning. It took approximately 5 months to sample and dismantle all of the bentonite. The work was mainly carried out by two workers, one who worked down in the deposition hole and one who took care of samples, disposal of material, handled lifting and so on. Working hours were Monday to Friday, 8 hours a day. Prior to weekends or planned interruptions in the dismantling, measures were taken to minimize the effect of the inflow of water from the surrounding rock mass, for example water-absorbing agents which were then removed when the work was resumed. On longer breaks such as Christmas and New Year, work was done on some holidays to prevent the bentonite from being exposed to water for longer periods of time.

The entire buffer stack was sampled by core drilling (*Figure 2.67*a) each block layer according to a pre-determined pattern, the template used in the drilling is shown in *Figure 2.67*b. For **complete blocks (C)** at angles of 0, 90, 180, and 270° samples were taken every 50 mm between 75 and 825 mm from the centre of the hole. An additional sample was taken at 850 mm within the pellet zone. In order to achieve a separation of 50 mm the cores were taken on alternate sides of the centre. At angles of 45, 135, 225, and 315° samples were taken at 100 mm separation between 575 and 850 mm from the centre of the hole. For **ring blocks (R)** at angles of 0, 90, 180, and 270° samples were taken every 50 mm between 575 and 825 mm from the centre of the hole. An additional sample was taken at 850 mm within the pellets. At angles of 45, 135, 225, and 315° samples were taken at 100 mm separation between 575 and 850 mm from the centre of the hole. Cores were drilled through the full height of each block with a height of ~500 mm. Immediately after drilling, the cores were packaged in plastic and labelled with their unique position before being sent for analysis. From each core, two samples were sawn, both were analysed for water content and dry density at the Äspö Laboratory.

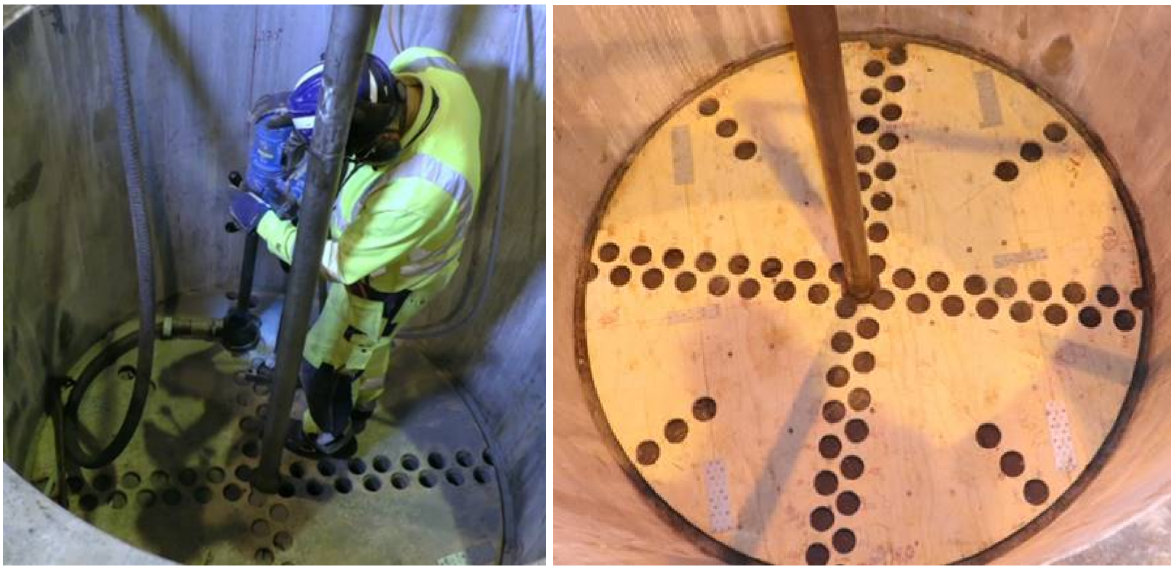
(a) (b)

Figure 2.67: Sampling of the bentonite buffer during decommissioning. a) core drilling of the buffer; b) Drill template for complete blocks showing the pattern of sampling.

When all cores had been drilled in the block layer, the remaining bentonite was removed and disposed of. The work of removing the bentonite was very time-consuming, as the bentonite had saturated and a swelling pressure had thus formed. This made it impossible to lift the canister before the surrounding bentonite had been removed. To remove ring R-blocks, personnel had to work in a gap between the rock and the canister that was no wider than 350 mm. The saturated bentonite blocks were hard and difficult to remove, the best method was to use an electric chisel hammer to break it into small pieces. To bring removed material to the surface, a specially adapted basket was used that fitted in the gap around the canister.

Final geotechnics of the buffer

All samples were analysed at the Äspö laboratory to determine geotechnical properties. A total of 1800 samples were tested between the 21st September 2020 and 16th February 2021. By oven-drying the samples at 110°C, each sample had water content (ratio of the weight of water to the weight of the solids in a sample), bulk density, and dry density determined. From these, simple calculations were made to determine void ratio and saturation (ratio of full saturation to measured saturation). These measures could be compared with the geotechnics determined for the individual bentonite blocks before emplacement.

Horizontal profiles of geotechnical data through the buffer

Figure 2.68 shows a typical profile for the bottom segment (C1) of bentonite located in the base of the deposition hole below the canister. Only the data oriented 0/180° is shown. *Figure 2.68*a shows the measured water content. This shows that water content increased compared with that determined for the block prior to emplacement. Water content also increased towards the outside of the deposition hole, but also shows a region of lower water content roughly below where the canister would have been. This may have been as a result of compression when supporting the canister. Dry density (*Figure 2.68*b) shows the opposite to water content. Dry density has decreased compared with that for the block prior to emplacement. Saturation is shown in *Figure 2.68*c. The saturation state has been increased and averages close to unity, i.e. full saturation. However, at the edges of the deposition hole the buffer was over-saturated. It should be noted that the saturation calculation is very sensitive to small errors in measured values and can easily give estimates of over-saturation. The void ratio (*Figure 2.68*d) increased towards the margins of the deposition hole and had increased since manufacture of the blocks. It should be noted that the vales greatly increase/decrease close to the edge of the deposition hole, especially where the pellets were located.

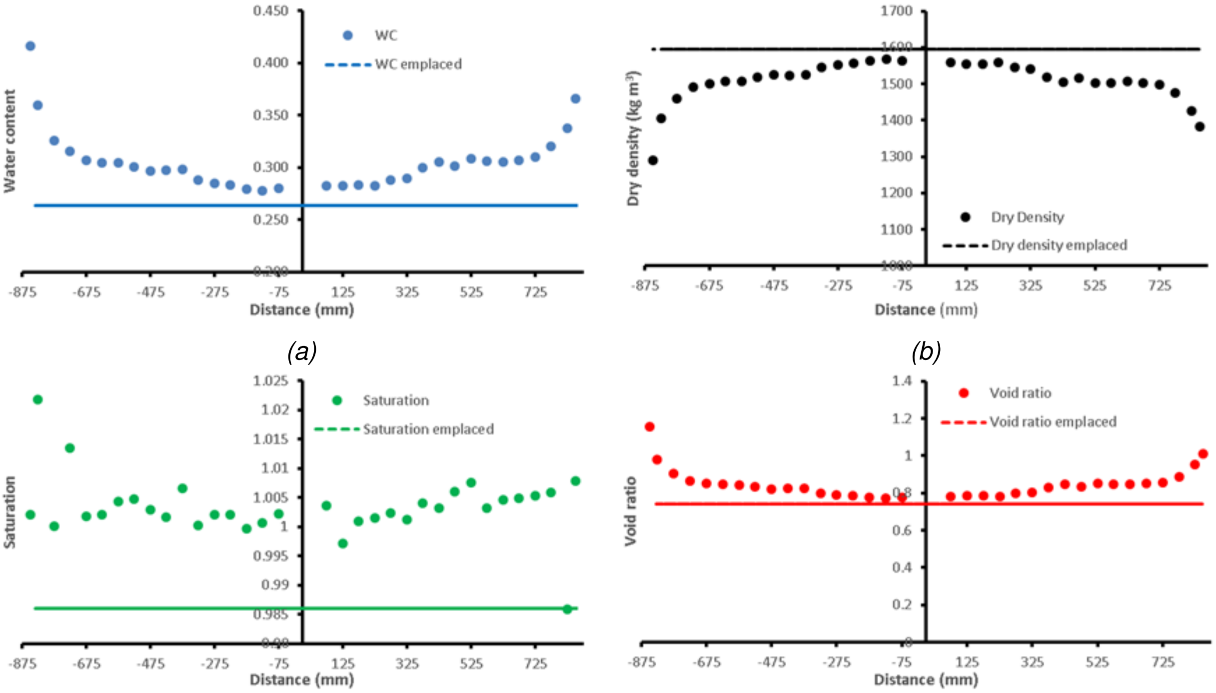

(a) (b)

(c) (d)

Figure 2.68: Profiles of geotechnical properties within the bottom bentonite segment (C1) oriented at 0/180°. a) Water content; b) Dry density; c) Saturation; d) Void ratio.

Figure 2.69 shows an example of geotechnical data at the level of one of the injection filter arrays (height 176.63 cm) on the canister surface, with the lower filter array shown. Water content (*Figure 2.69*a) of the bentonite ring had increased since emplacement and increased towards the outside of the deposition hole, especially within the pellets. In addition, water content also increased towards the inner buffer surface close to the canister. This may be as a result of swollen bentonite as it closed the engineered void or may be as a result of artificial hydration through the canister filters. Dry density (*Figure 2.69*b) showed the opposite with a decrease since emplacement, with decreases more towards the outside of the deposition hole and towards the canister. Saturation of the bentonite had increased since emplacement (*Figure 2.69*c) and was close to unity, i.e., full saturation. Void ratio showed different behaviour (*Figure 2.69*d). Generally, void ratio had decreased since emplacement, with increases seen within the pellets.

The final example of profile data is given at a height of 627.7 cm, near to the level where many pore pressure (UB) and stress sensors (PB) were located in the buffer (*Figure 2.70*). Water content of the block had increased since emplacement (*Figure 2.70*a) with water content higher towards the outside of the buffer, especially within the pellets. However, water content had also increased on the inside of the block where the hole was located to allow the Monel pipe to feed through and allow pressure lines and cables to connect with the canister. This may be either as a result of swelling of the bentonite to fill the engineered void or suggests that water was transported along the Monel pipe surface. Dry density shows the opposite general response (*Figure 2.70*b). Dry density had reduced since emplacement and reduced towards the outside of the deposition hole and the inside of the block where the Monel pipe was located. The saturation state of the block had been increased since emplacement (*Figure 2.70*c) and averaged around unity, showing it was fully saturated. On one side of the canister, saturation was increased towards the margins of the buffer. Void ratio increased within the block since emplacement (*Figure 2.70*d), with

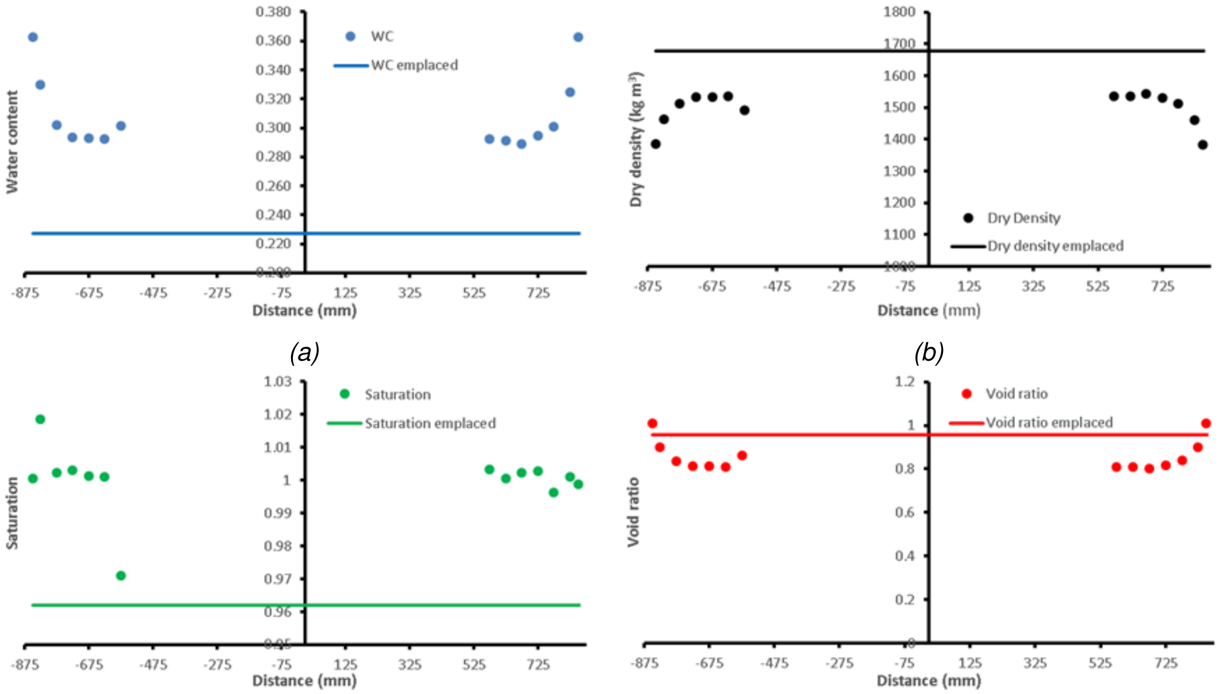

(a) *(b)*

(c) *(d)*

Figure 2.69: Profiles of geotechnical properties at the level of the lower canister filter array oriented 90/270°. a) Water content; b) Dry density; c) Saturation; d) Void ratio.

increases towards the outside of deposition hole and at the inside of the block where the Monel pipe was located. The data from this level was close to a filter mat within the buffer and did not show the variation seen in *Figure 2.70* for the bottom bentonite segment. This suggests that the reduction/increase seen where the canister was located was not created by swelling pressure vertically within the deposition hole and was as a result of the weight of the canister.

Vertical profiles of geotechnical data through the buffer

Geotechnical data can also be considered in a vertical context to see how properties change with depth. This is particularly interesting in Lasgit as a pore pressure and stress gradient was seen along the length of the deposition hole.

Figure 2.71 compares the data across the full width of the buffer in the 180° direction for 75, 325, 575, 725, and 850mm distance from the centre. What can be seen is the difference in geotechnical properties seen for segments (C) and rings (R) before the blocks were emplaced. Water content, void ratio, and saturation were lower in rings, while dry density was higher. Water content determined from decommissioning shows a relatively consistent water content along the length of the deposition hole. The differences seen before emplacement had disappeared. Water content did increase with depth. The data from along the length of the canister (50.1 to 533.1 cm height) was more varied, possibly as it would have included zones of increased hydration from the canister filters and because this region would have swelled to close the engineered gap. For water content (*Figure 2.71*a) there doesn't appear to be much variation in the pattern of results, except for the results seen in the pellet region. However, subtle difference can be seen. Below the canister, water content is lowest at the centre of the segment, whereas above the canister it is higher than at 325 mm. This suggests at both of these areas water is moving from the outside of the buffer inwards, with the Monel pipe assisting hydration above the canister. Similar can be seen in dry density (*Figure 2.71*b), with the highest dry density in the centre of the buffer. Little variation in dry density is seen, except in the pellet region. Saturation (*Figure 2.71*c) shows little variation with distance from the centre of the buffer, with the whole buffer in the direction of 180° close to full saturation. Void ratio data

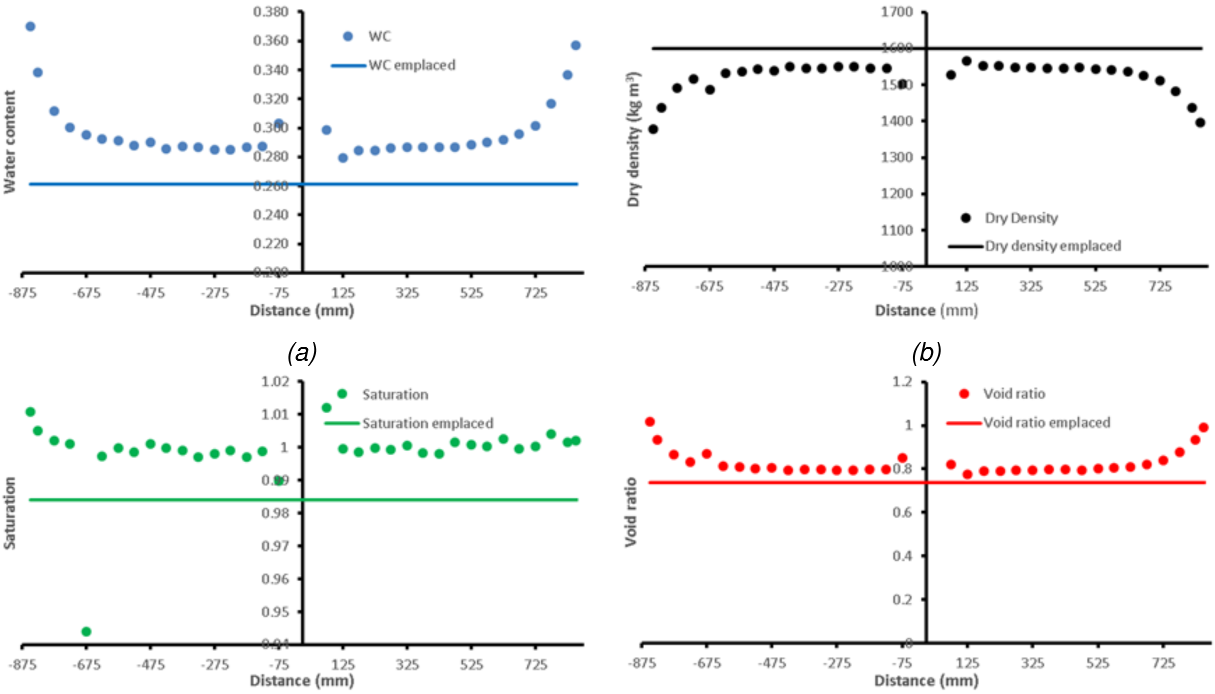

(a) *(b)*

(c) *(d)*

Figure 2.70: Profiles of geotechnical properties at a height of 627.7cm towards the top of the deposition hole. a) Water content; b) Dry density; c) Saturation; d) Void ratio.

(*Figure 2.71*d) are more complicated, but similar to water content. At the base of the buffer void ratio clearly increase from the centre of the buffer to the outside. Similar can be seen above the canister, although the data close to the Monel pipe shows elevated void ratio.

Distribution of geotechnical properties in plan

The distribution of geotechnical properties can also be considered in plan to look for zones of variation. It is important though to consider effects of interpolation. The distribution of data points show a high spread of data in two orthogonal directions, with a lesser spread of data at 45°. This distribution is not well suited to many interpolation algorithms, with minimum curvature prone to artefacts. All gridding methods in Surfer v22 were considered, with the radial basis function appearing most appropriate for the distribution of data points. This still resulted in artefacts that need considering when interpreting the results.

Figure 2.72 shows the distribution of geotechnical properties at a height equivalent to the lower canister filter array, including FL903. Water content (*Figure 2.72*a) generally increased towards the outside of the deposition hole. However, at FL903 (180°) water content also increased towards the canister. This is not the case for all eight sampling directions, but is for most, with the lowest water content generally midway between the canister and the deposition hole wall. The inverse is seen in dry density (*Figure 2.72*b) with a general decrease towards the deposition hole wall, with the highest dry density midway between the canister and the wall. Saturation is generally close to unity for the entire area, but does show an area of lower saturation at 270° where FL902 was located and a slight over-saturation at 180° where FL903 was located. Void ratio (*Figure 2.72* d) generally increased towards the deposition hole wall, with a low approximately halfway between the canister and the wall. In detail, a gradient of water content, dry density, and void ratio can be seen from 45° to 225°, showing that the buffer was not fully equilibrated and this may be reflected in the distribution of radial stress seen.

Figure 2.73 shows the distribution of geotechnical properties at a height of 627 close to the height of stress (PB) and pore pressure (UB) sensors above the canister. Water content (*Figure 2.73*a) shows an offset circular pattern with water content increasing towards the outside of the deposition hole. However, the minimum water content occurs non-centrally. Dry density (*Figure 2.73*b) decreased from the centre of the hole towards the outside. The Monel pipe created an anomaly at the centre. Saturation (*Figure 2.73*c) was relatively constant throughout the segment and was close to unity. There were localised anomalies in places. Void ratio (*Figure 2.73*d) increased from the centre of the hole, although it was also raised as a result of the Monel pipe.

A total of 1800 samples gave a good description of the geotechnical properties of the buffer. The re-

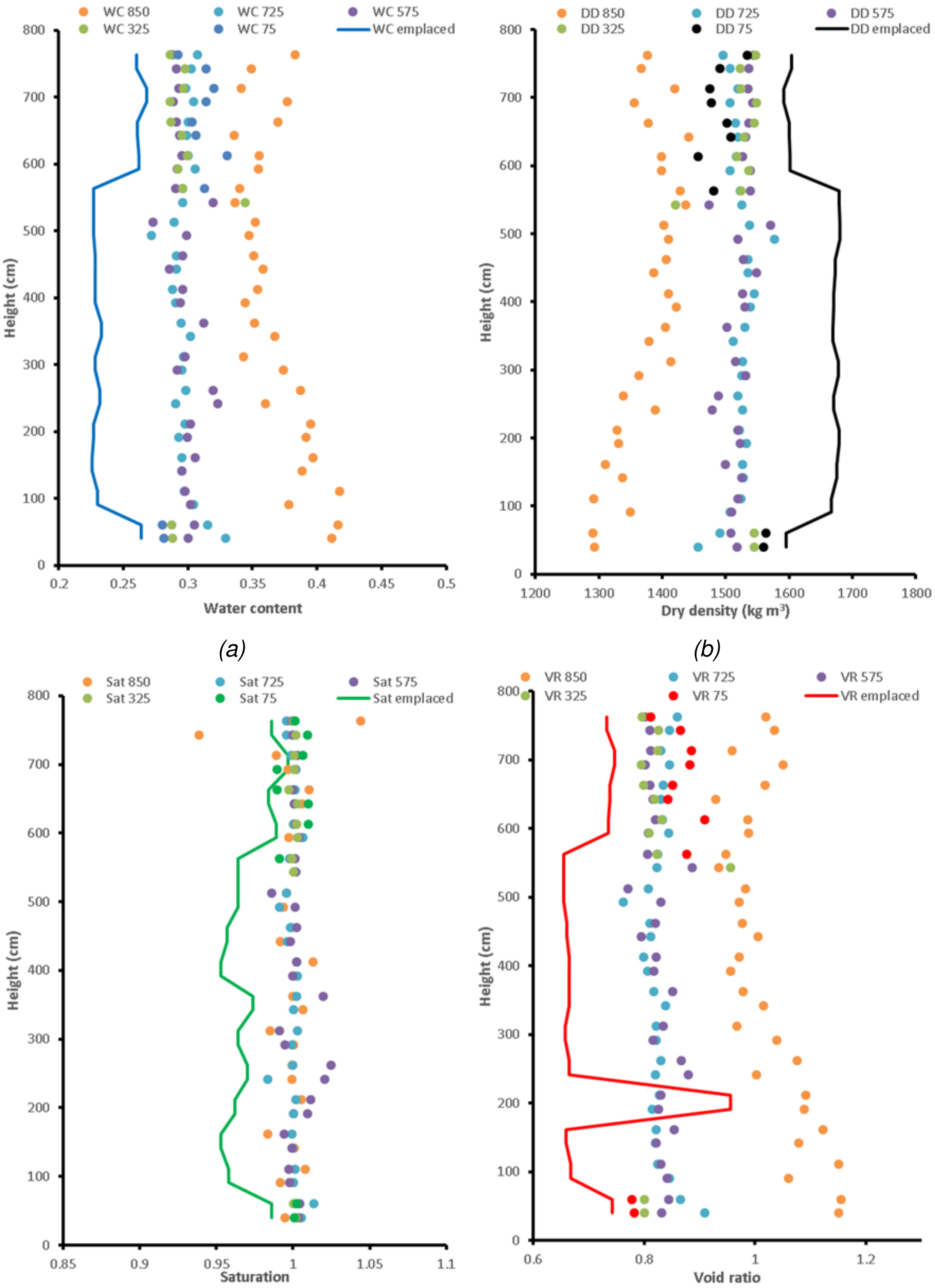

(a) (b)

(c) (d)

Figure 2.71: Vertical profiles of geotechnical properties at different distances from the centre of the hole at an orientation of 180°. a) Water content; b) Dry density; c) Saturation; d) Void ratio.

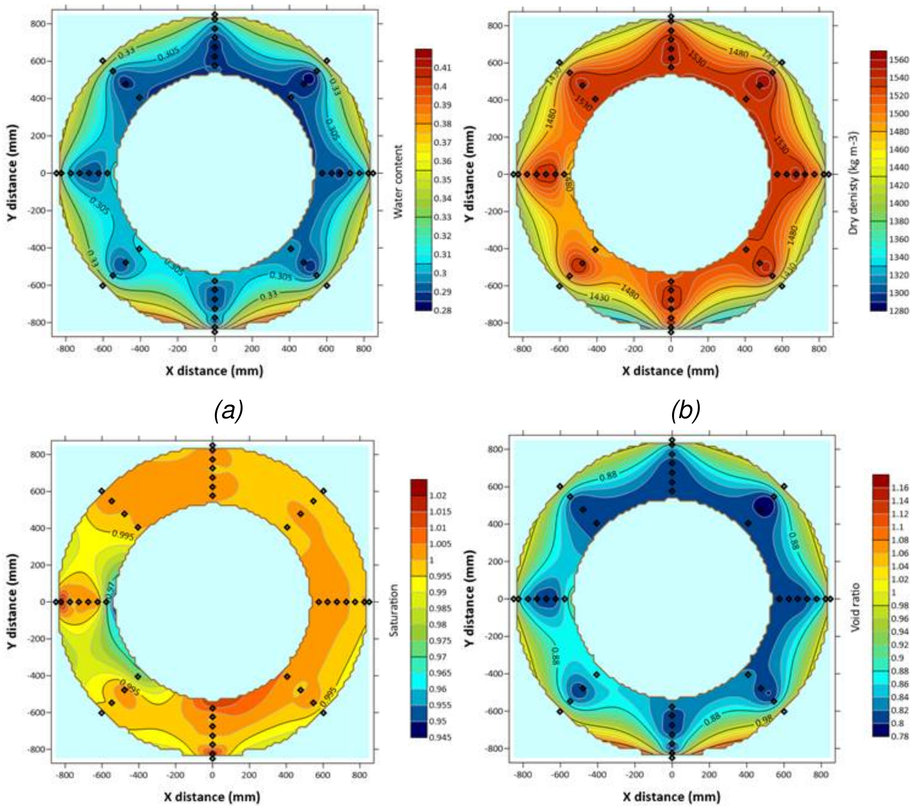

(a) (b)

(c) (d)

Figure 2.72: Distribution of geotechnical properties at a height of 176 cm from the bottom of the deposition hole. a) Water content; b) Dry density; c) Saturation; d) Void ratio.

sults show that the properties had greatly modified since the manufacture of the bentonite blocks. Pre-installation there was a significant difference between the properties of the full segments and the annular bentonite rings. By the end of Lasgit, these differences were no longer apparent, as the buffer had modified to give a smooth variation in geotechnical properties with depth. In general, the data presented shows that the buffer was close to full saturation, with some zones of over-saturation (saturation > 1), which may result from the way the geotechnical properties are calculated. The average saturation for all samples within the bentonite blocks was 0.999. The buffer itself was relatively homogenous, with increases in water content and void ratio, and decreases in dry density, towards the outside of the buffer, especially where pellets were located. More variation was seen within the pellets, with water content and void ratio increasing towards the bottom of the hole and towards the concrete plug at the top of the buffer. In the zone closest to the canister, greater variation was seen in results. This was probably as a result of the buffer swelling to fill the engineered gap. This may also have been as a result of artificial hydration from the canister filters. The data also showed that the Monel pipe had an influence on geotechnical properties, with an increased water content and decreased dry density. The distribution of properties showed that as well as variation from centre to outside, a variation existed around the hole from 45 to 225°. The geotechnical properties show that the bulk of the pre-compacted bentonite blocks were homogenous, with the outsides of the blocks varying. This was as a result of the use of pellets and/or the swelling of the blocks to fill engineering voids. It is likely that gas would have exploited these zones if the properties meant that the movement of gas was easier. Dry density within the whole deposition hole reduced from emplacement values. This was as a result of swelling to fill the engineered gap and the pellet zone. This may have been greater than expected as a small amount of clay was flushed from the hole early in the test history, although compared with the total volume of clay this mass loss would have been minor. It should be noted that during the removal of the buffer all segment interfaces were still well defined and that no signs of self-healing were observed.

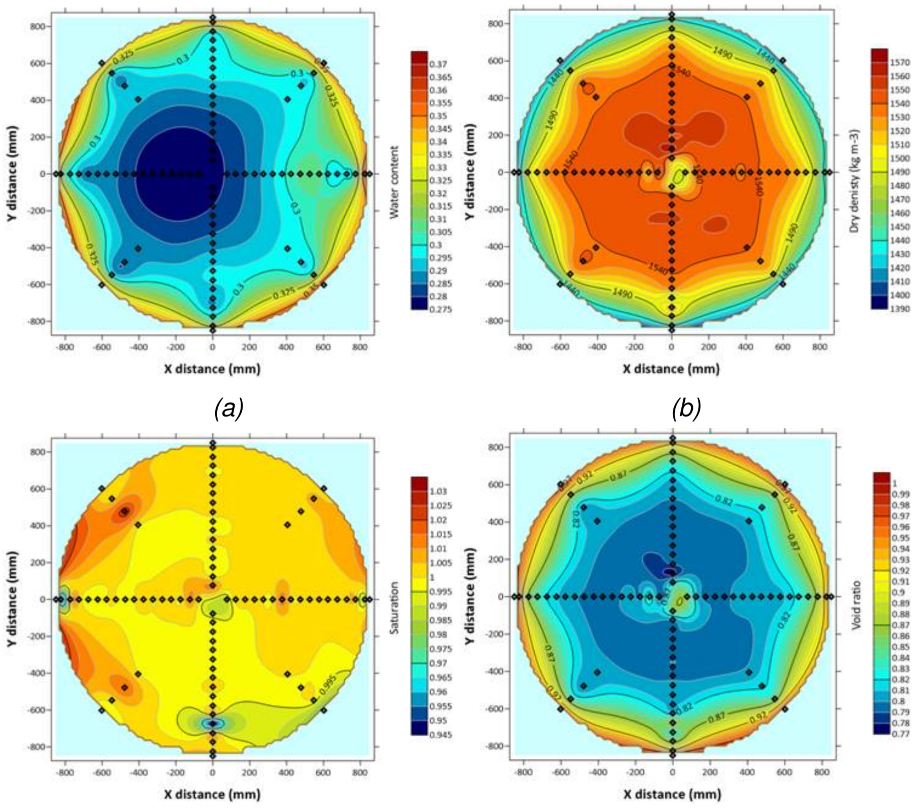

(a) (b)

(c) (d)

Figure 2.73: Distribution of geotechnical properties at a height of 627 cm from the bottom of the deposition hole. a) Water content; b) Dry density; c) Saturation; d) Void ratio.

2.3.5. Testing protocol

Boundary conditions

The boundary conditions of the experiment were those dictated by the pressures and stresses building up naturally within the bentonite buffer during re-hydration (natural and artificial). The canister lid had been pre-stressed to 1,300 kN to impose a similar force comparable with that which would be generated by the back-fill placed within the gallery above each deposition hole in a geological disposal facility. The experiment was conducted at ambient temperatures.

Two-stage hydraulic tests

At several times during the full test history, hydraulic properties were investigated at the canister filters using two-stage constant head tests (*Table 2.18*). *Figure 2.74* shows an example test prior to gas injection test 1. The filter to be investigated was isolated (i.e. hydration paused at that location) and the pore pressure was allowed to equilibrate. Pore pressure was then increased using one syringe pump set to constant pressure. The flow of water into the filter was monitored by observing the volume of the syringe pump. Generally, pore pressure was raised for 28 days, followed by a further period of constant pressure at the equilibrated pore pressure first observed before the initial raised pressure step. The two stages were then modelled to establish hydraulic conductivity and storage. The initial high-pressure stage saw a flow of water into the buffer, where the second stage saw water flow back out of the buffer.

Two-stage hydraulic tests were conducted before and after most gas injection tests to investigate changes in hydraulic response as a result of gas movement. At filters FL903 and FU910, which were tested 4 and 2 times each, repeat testing also showed variations in hydraulic properties over longer periods of the Lasgit experiment. Prior to the final round of gas testing (Gas test 5, Gas test 6, and full canister test), the hydraulic properties of all canister filters was investigated.

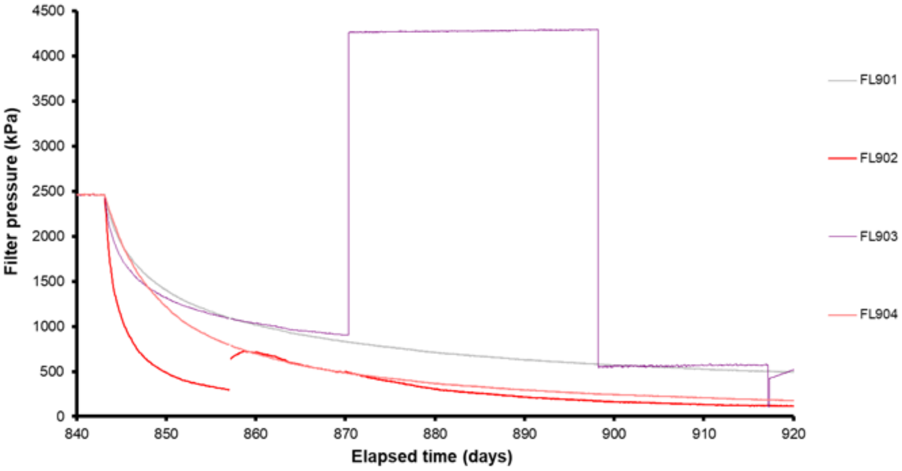

Figure 2.74: Example two-stage constant head test conducted to determine hydraulic properties of the buffer

Table 2.18: Description of two-stage constant head tests.

Stage	Description	Pressure
Shut in	Reduction in pore pressure from hydration pressure to equilibrated pressure	Local pore pressure (starting pressure)
High pressure stage	Raise pore pressure for 28 days	4250 kPa
Low pressure stage	Reduce pore pressure for 28 days	Starting pressure
Recovery	Recovery of pore pressure	Local pore pressure

Gas injection tests

The six conventional gas injection tests were conducted in a similar manner, with distinct differences. Here, we describe the general procedure.

Gas injection tests used one of two interface vessel each with a volume of 5 litres. Gas pressure was generated by injecting water into the base of the interface vessel, compressing a volume of gas. At the start of each gas injection test, the interface vessel was filled with water and this water level was reduced by a known amount using a syringe pump on refill mode. For gas injection 1 this was approximately 1,250 ml of gas at the starting pressure. The injection filter was then flushed of water with using the drain for the test filter. Once drained, the drain was closed, and gas pressure was established at the desired starting pressure. In most tests, a secondary test of gas volume was made by changing the volume of the interface by a known amount and observing the change in gas pressure. From this, initial gas volume could be estimated. At this point, gas pressure was established in the injection filter and the system was ready to start gas injection.

Gas injection ramps (*Figure 2.75*) were created by injecting water at a defined flow rate into the bottom of the 5-litre gas interface vessel. This created an increasing gas pressure as the gas was compressed. Note: the pressure increase was non-linear because of the constant flow feed of water to the interface vessel. The aim of the gas injection ramps was to raise gas pressure from in situ pore water pressure up to a pressure sufficient to result in gas entry in up to four steps. At defined gas pressures, the mode of the injection syringe pump was changed to constant pressure to investigate the flow properties at pressure below that necessary to cause gas entry. The example gas injection test in *Figure 2.75* shows that up to four gas ramps were employed to raise gas pressure up until gas entry. Once gas entry had been detected, the flow of water into the interface vessel was maintained for varying lengths of time. *Table 2.19* gives a description of typical test conditions, while *Table 2.20* shows the gas ramps of the six gas injection tests. Note, it was necessary to refill the interface vessel with gas on some tests. This was done using the same procedure outlined above.

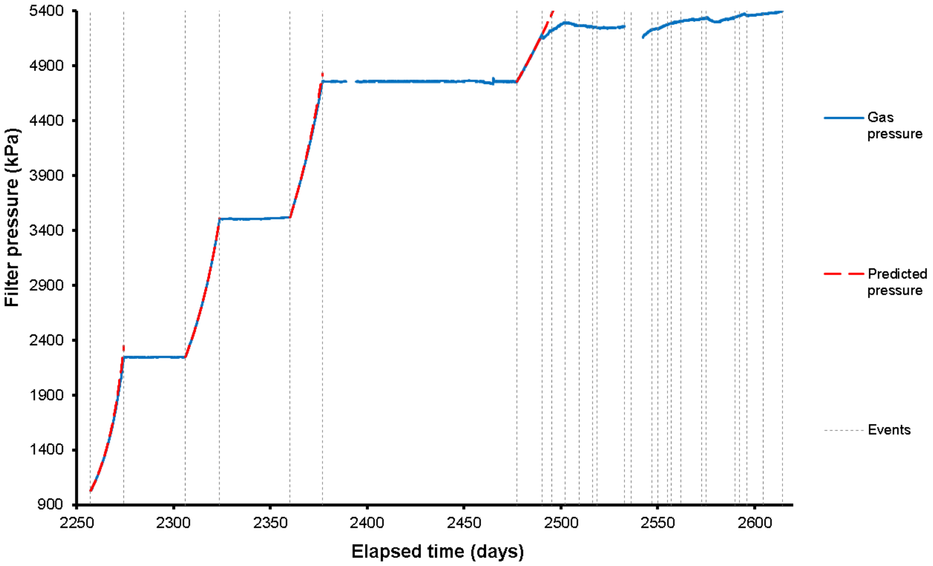

Figure 2.75: Example gas injection test (GT3).

Table 2.19: Description of gas injection tests. # - interface vessel re-filled with gas if necessary.

Stage	Description	Pressure
Filling of interface vessel with gas	Filling of interface vessel with a known volume of gas, flushing of the injection filter, and equilibration of filter with gas in solution.	In situ pore water pressure
Gas ramp 1	Raise gas pressure by at least 1 MPa in 14-28 days	Raise by 1 MPa+
Constant pressure 1	Keep gas pressure constant for ~28 days#	Constant Pressure 1
Gas ramp 2	Raise gas pressure by at least 1 MPa in 14-28 days	Raise by 1 MPa+
Constant pressure 2	Keep gas pressure constant for ~28 days#	Constant Pressure 2
Gas ramp 3	Raise gas pressure by at least 1 MPa in 14-28 days	Raise by 1 MPa+
Constant pressure 3	Keep gas pressure constant for ~28 days#	Constant Pressure 3
Gas ramp 4	Raise gas pressure through to gas entry	Up to gas entry
Post gas entry	Continue gas injection and observe gas pressure	Monitor gas pressure

Table 2.20: Gas injection ramps used during gas injection tests.

Gas test	Ramp 1 (kPa)	Ramp 2 (kPa)	Ramp 3 (kPa)	Ramp 4 (kPa)	Comments
GT1	425-1840	1850-5660	-	-	2-stage test
GT2	1300-2540	2540-3780	3770-5060	5090-5870	4-stage test
GT3	1020-2250	2250-3500	3520-4760	4760-5190	4-stage test
GT4	1870-2870	2870-3860	3870-4850	4850-6170	4-stage test
GT5	4230-5350	-	-	-	Single stage test from high starting pressure

GT6	4830-6470	-	-	-	Single stage test from high starting pressure
FCT	4930-6500	6500-7090	-	-	2-stage test

Full Canister Test

The Full Canister Test (FCT) was the final gas test to be conducted and required modification of the Lasgit laboratory. All of the previous gas injection tests were conducted using a limited volume of gas. The Lasgit set-up included two interface vessels of 5 litres volume each in the laboratory. This limited the gas volume to 5 litres at the start of gas injection or whenever the interface vessel was re-charged as the two interface vessels were on separate parts of the injection system. The Full Canister Test aimed to investigate whether the volume of gas played a role in gas migration. In effect, the 5-litre interface vessel was replaced by the copper canister, with an internal volume initially estimated to be greater than one cubic metre (1000 litres). The test would also be conducted differently, with new gas added from the interface vessel to a constant volume (canister) to increase gas pressure, as opposed to a fixed quantity of starting gas being compressed to increase pressure. During a normal test at gas entry, the limited volume of gas in the interface vessel was increased as pathways formed. This resulted in a reduction in gas pressure. Assuming that the FCT would result in the formation of dilatant pathways of similar volume to that seen in GT1 to GT6, there would be no noticeable reduction in gas pressure at peak conditions. In other words, in GT1 to GT6 the pathway volume was significant compared with the volume occupied by the gas in the interface vessel, whereas the pathway volume in the FCT is very small, and therefore insignificant, compared with the volume of gas in the canister. The Full Canister Test would examine whether this changed the dynamics of pathway propagation.

In order to conduct the Full Canister Test a number of important modifications were needed to the existing Lasgit Laboratory. 1) A large supply of gas was needed and this was achieved by adding a pallet of 12 J-cylinders of Nitrogen to the system (see *Figure 2.76*). This was a sufficient volume of gas to raise the pressure in the canister up to the expected gas entry pressure. 2) A reliable supply of water was needed in order to use the existing interfaces vessels to get an accurate estimate of gas pumped into the canister. 3) An additional pressure sensor in the interface vessel circuit to measure the pressure of the interface vessels. 4) Re-plumbing of the system to facilitate the test. 5) The addition of two one-way valves to add safety in the Lasgit laboratory.

A schematic of the modified laboratory is shown in *Figure 2.77*. The following will outline the modifications and how the test was operated:

1) The first modification was to allow both interface vessels to be used in series, meaning that 10 litres of pressurised gas could be added to the canister in one go and mean that the refilling of the interface vessels would occur less frequently. This gave 10 litres of volume per refill. A pore pressure sensor (labelled P) was added so that the pressure in the interface vessels was known.

2) The second modification was the addition of the gas pallet (as shown in *Figure 2.76* and green square in *Figure 2.77*) to the end of the interface vessel circuit through valve V056.

3) The third modification was the addition of two one-way valves to the system to add safety to the ISCO pumps. If the ISCO pump was to leak, it could mean that the contents of the interface vessel could discharge through the pump/refill circuit. At certain times in the pressurisation procedure, it could mean the contents of the interface vessel or gas supply could leak through the pump. Therefore, two one-way valves were added near valves V002 and V016 (as shown by arrows in *Figure 2.77*) to prevent backflow.

4) The fourth modification was the addition of the water bowser (see *Figure 2.77*) to the water inlet of the syringe pumps.

Operation of the Full Canister Test

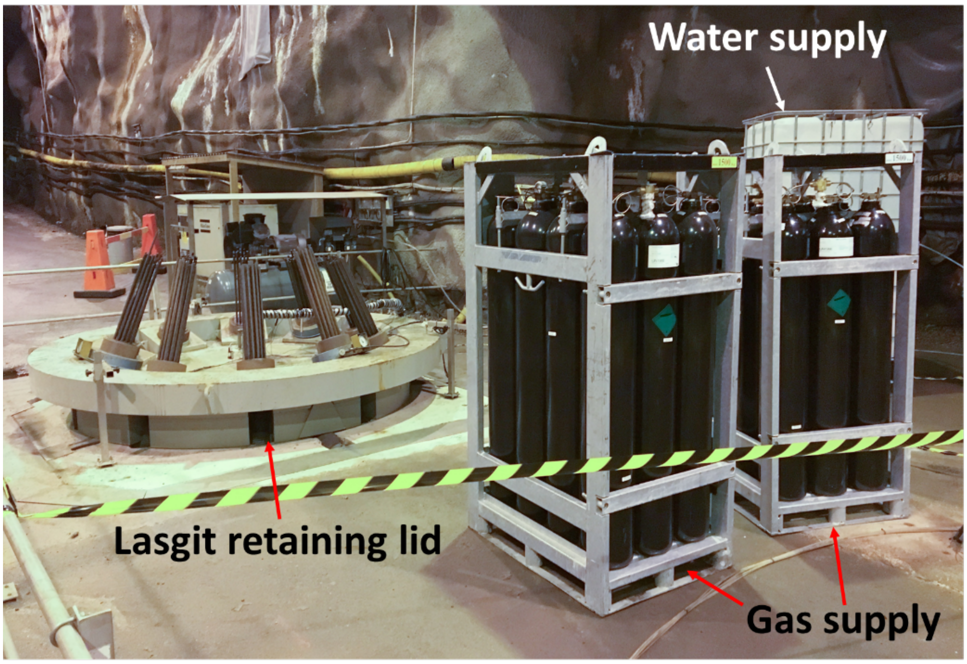

Figure 2.76: The addition of a pallet of 12 J-cylinders of gas and a water bowser to the Lasgit experiment in order to perform the Full Canister Test.

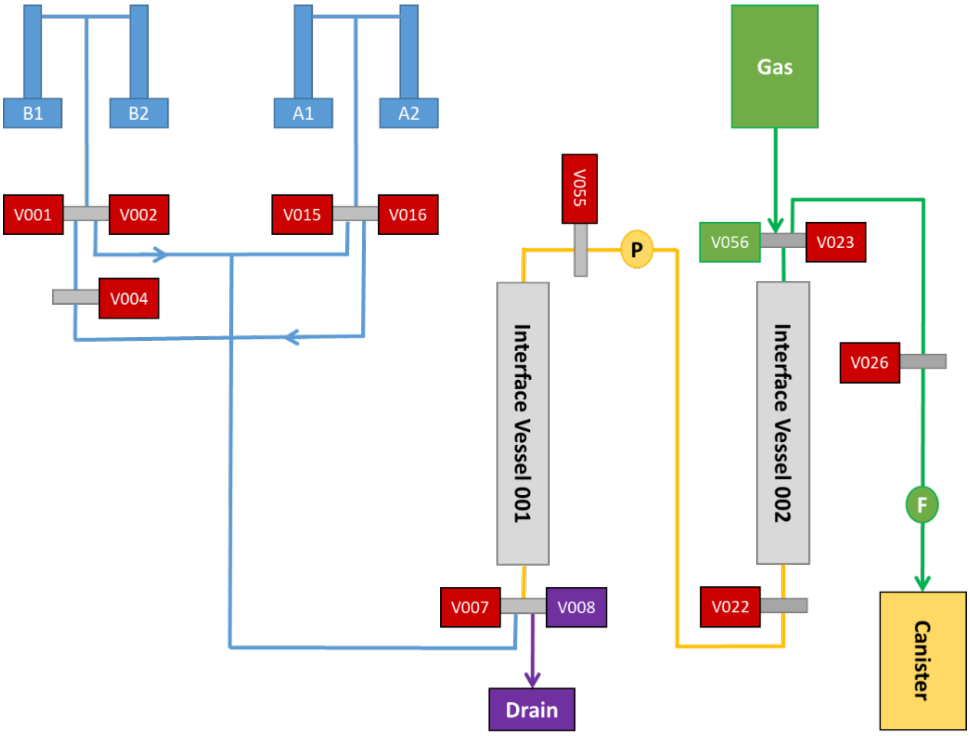

Figure 2.77: Schematic of the modifications made to the Lasgit laboratory to allow the Full Canister Test to be conducted. Blue lines are water; green lines are gas; yellow lines are water or gas depending on refill state.

The following describes how the Full Canister Test was conducted:

1. The gas supply was used to directly fill the canister to a starting pressure of around 5000 kPa, this took nearly 24 hours as filling was slow being limited by the small diameter of the pressure lines.

2. With valve V023 closed (canister isolated from system), and valve V007 closed (pump system isolated), valve V008 was opened to drain the interface vessel. Once this was fully drained, V008 was closed.
3. The interface vessel was filled by opening valve V056. The pressure of the interface vessel was monitored at P until the pressure was approximately equal to the pressure in the canister. Valve V056 was closed and the starting interface vessel pressure was noted once pressure was stable.
4. Valve V023 was opened, re-connecting the interface vessel with the canister. The pressure of the interface vessel and canister were noted.
5. Valve V007 was then opened and either pump-set A or B was started.
6. The pumps, operating in reciprocating mode, would then fill the interface vessel with water, adding gas to the canister. If would take 20 pump refills to fully empty the interface vessels of gas, as each pump's volume was only 0.5 l, so 19 full refills were aimed for.
7. Valve V007 was closed to isolate the pump and the pump was stopped and the volume of the pump noted. Valves V026 and V023 were closed to isolate the interface vessel from the canister. Valve V008 (drain) was opened and the pressure of the interface vessel was monitored. The small (~1 litre) remaining volume of gas pushed out the water from the interface vessels. The rate of pressure decay was relatively slow and when the water was expelled, the rate of change would increase as it was easier for gas to drain through the narrow pressure tube-work. Once the rate of change was detected, valve V008 was closed. It took around 20-25 minutes to drain the interface vessel, depending on the pressure and volume of the remaining gas.
8. The procedure was repeated by performing stages 3-7. For each re-fill procedure, the total volume of water pumped into the interface vessel was calculated.

The procedure was timed so that refilling occurred between 12 and 24 hours, with most occurring on a 12-hour interval. Throughout the pressure ramp, a total of 55 refills were performed.

At the end of the experiment it was necessary to reduce the pressure of the canister in a controlled and safe manner. This was done in a similar way to filling. Valve V026 was opened to fill the interface vessel with gas and closed when full, as indicated by a stable pressure. Valve V026 was then closed and V008 opened to drain the contents of the interface vessel. The pressure of the interface vessel was observed and indicated when it was empty. Valve V008 was then closed and the procedure repeated. It took 55 emptying cycles until the pressure was such that the remaining volume of gas could be directly vented. Each single cycle took between 15 and 50 minutes depending on the pressure of the canister.

2.3.6. Results

The full test results are comprehensively reported in Cuss et al., 2022. Here, a brief outline of the significant results is given.

Hydraulic testing

Many two-stage hydraulic tests were conducted during the Lasgit experiment. The majority were in filters FL903 and FU910, with tests conducted before each gas injection test and after most. This allowed the hydraulic properties and specific storage to be examined as each test represented a snapshot of the state of the buffer. Around Day 3500, most of the canister filters were tested. While these were a single snapshot of the hydraulic properties, it gave an indication of the variation in properties around the canister. The data were modelled using a simple 1-D model with flow assumed to be along a pipe of diameter equivalent to the filter diameter, with the pore pressure at the deposition hole wall used to define the boundary conditions.

Figure 2.78 shows the evolution of hydraulic properties for filters FL903 and FU910. For canister filter FL903, the hydraulic properties of the buffer reduced over the course of the test history (*Figure 2.78*a). At Day 870, hydraulic conductivity was 1.3 x 10^{-12} m s^{-1}, decreasing to 1.7 x 10^{-13} m s^{-1} at Day 5266.

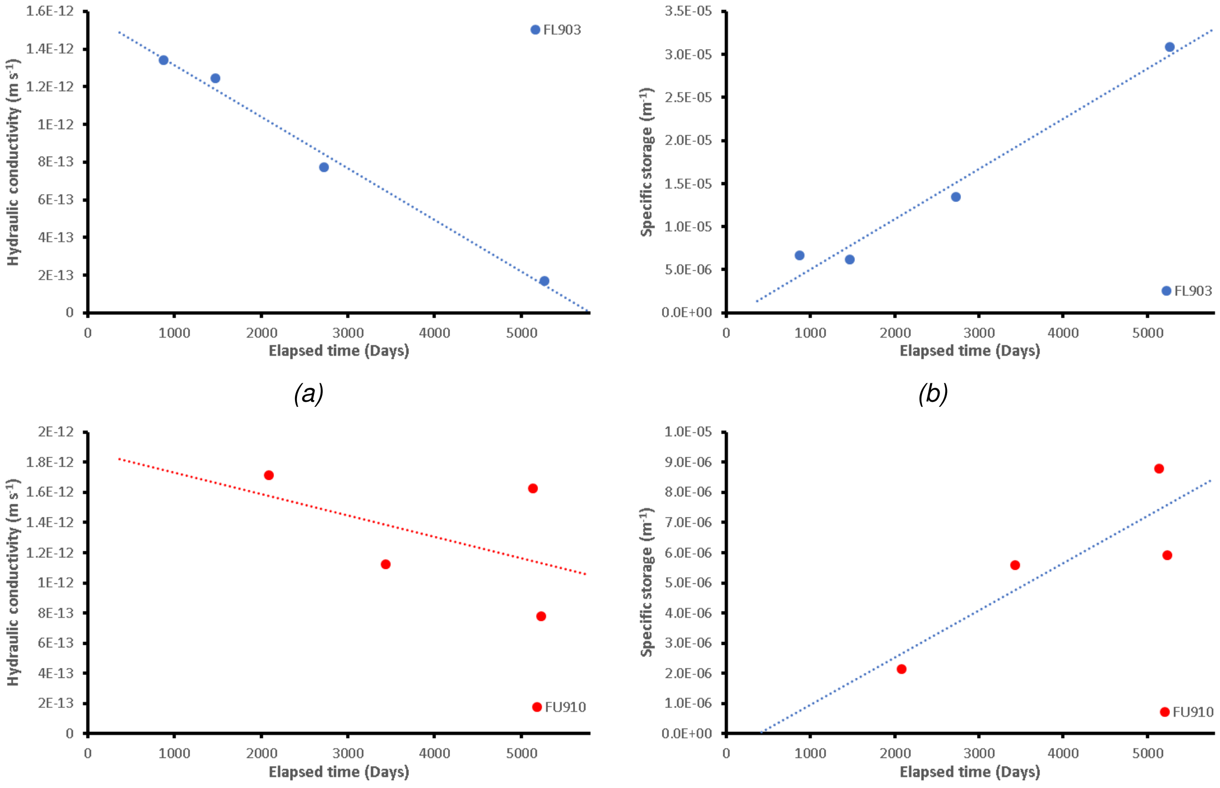

(a) *(b)*

(c) *(d)*

Figure 2.78: Evolution of hydraulic properties at FL903 and FU910. a) Hydraulic conductivity of FL903; b) Specific storage of FL903; c) Hydraulic conductivity of FU910; d) Specific storage of FU910.

This represents a near order of magnitude reduction in conductivity over the 12-year period. However, it should be noted that the modelled data is quite variable. Specific storage increased over the same period (*Figure 2.78*b), from 6.7 x 10^{-6} m^{-1} at Day 870 to 3.1 x 10^{-5} m^{-1} at Day 5266. For canister filter FU910, hydraulic conductivity also decreased from 1.7 x 10^{-12} m s^{-1} at Day 2086 to 7.8 x 10^{-13} m s^{-1} at Day 5235 (*Figure 2.78*c). This was considerably less of a reduction than seen at FL903 and with great spread in the results. Over the same period specific storage increased from 2.1 x 10^{-6} m^{-1} to 8.8 x 10^{-6} m^{-1} (*Figure 2.78*d). These data show that the hydraulic properties of the buffer were continuing to evolve and reduce at the injection filter locations as the buffer matured. The system was far from attaining hydraulic equilibrium, even though the geotechnical data showed that the buffer was close to, or at, full saturation.

Figure 2.79 shows the hydraulic properties for seven two-step hydraulic tests conducted between Day 3360 and Day 3478. These are single snapshots of the properties of the buffer but show the heterogeneity around the canister. Filter FU911 showed the lowest hydraulic conductivity of 7.1 x 10^{-13} m s^{-1} with FU909 showing the highest conductivity of 4.2 x 10^{-12} m s^{-1} (*Figure 2.79*a). This shows a six-fold variation in hydraulic conductivity. Specific storage varied between a minimum of 6.3 x 10^{-6} m^{-1} for FM908 and a maximum of 1.1 x 10^{-5} m^{-1} for FM907 (*Figure 2.79*b). This shows limited variation. This snapshot of the buffer shows considerable variability around the canister and highlights that the zone surrounding the canister was variable in terms of the transport properties.

Gas Injection Tests in canister filter FL903

Four tests were conducted in canister filter FL903 on the lower array of canister filters at a height of 1709 mm in the deposition hole. The first test, Gas Injection Test 1 (GT1) was conducted between Day 917 and Day 1010; Gas Injection Test 2 (GT2) between Day 1577 and Day 1967; Gas Injection Test 4 (GT4) between Day 2988 and Day 3283; while the final test, Gas Injection Test 6 (GT6) was conducted between

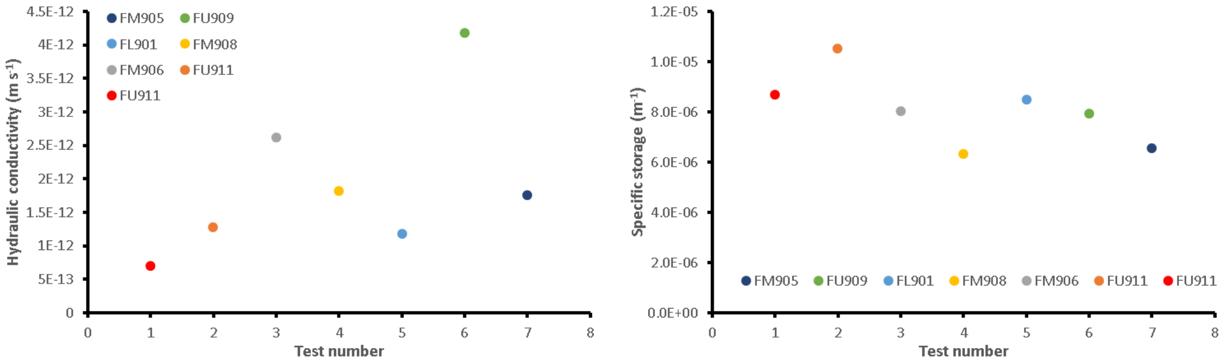

(a) *(b)*

Figure 2.79: Hydraulic properties of the buffer determined between Day 3360 and 3478. a) Hydraulic conductivity; b) Specific storage.

Day 5230 and Day 5263. This means there was 917 days between the start of Lasgit and GT1; 567 days between GT1 and GT2; 1020 days between GT2 and GT4; and 1947 days between GT4 and GT6. The main data relating to the tests conducted in filter FL903 are summarised in *Table 2.21*.

Table 2.21: Data relating to gas injection tests conducted in canister filter FL903.

No.	Test	Gas ramps	Start (Days)	End (Days)	Time gap (Days)	Peak pressure (kPa)	Time at peak (Days)	Gas entry pressure (kPa)
1	GT1	2	917.32	1010.03	917.32	5666	972.24	-
2	GT2	4	1577.40	1967.98	567.36	5868	1769.65	-
3	GT4	4	2988.08	3283.02	1020.11	6174	3205.31	6141
4	GT6	1	5230.29	5263.95	1947.26	5827	5235.96	6382

Figure 2.80 compares the gas pressure and flow data for all four tests conducted in FL903, with the gas pressure compared in more detail in *Figure 2.81*. *Figure 2.80* shows that the gas flow into the system was different for the four tests. This potentially means that the results could have varied if the processes controlling gas entry were dependent on the rate of pressurisation. Variations in flow rate can derive from difference in the starting volume and if processes are also dependent on the volume of the gas, this could introduce a further variation to the data. However, the volumes of gas were not significantly different and the variation in pressurisation rate was only around 14.5 times faster in GT1 compared with GT2. For significant variation in behaviour, it would be expected that orders of magnitude variation in flow rate would be required to observe different behaviour as gas fracturing has not be seen in the laboratory at similar pressurisation rates (Mechanism 4; Marschall *et al.*, 2005). This must be the case, otherwise the rate employed during laboratory testing or during Lasgit would be un-representative since the pressure increase rate used in the tests conducted here were several orders of magnitude greater than that expected during gas generation in the canister.

Figure 2.80 shows difference in response for flow into the clay. In GT1, flow into the clay slowly increased during the final gas ramp. This suggests that gas started to enter the clay but could also represent the loss of gas through diffusion and solution. In the other gas injection tests, flow into the clay was generally low and only increased around the time of peak pressure. As GT1 was the first test that was conducted in FL903, the difference might be related to gas saturation of the clay around the injection filter. The buffer would have been unsaturated with respect to the gas, and the first test would have had more gas going into solution than in subsequent tests. GT1 showed a pre-cursor flow event, which was largely absent from the repeat tests. This suggests that gas started to enter the buffer at a lower pressure than peak pressure but that pathways soon became unstable and stopped propagating as gas pressure continued to increase at a rate similar to that seen before the pre-cursor flow event.

At peak pressure, flow greatly increased and peaked. In GT1 two peaks were seen, a similar pa was observed in GT2. However, GT4 only had a single peak in flow, while GT6 showed at least 3 peaks. In GT1 and GT2, the initial peak was the greatest flow into the buffer, whereas in GT6, the three peaks

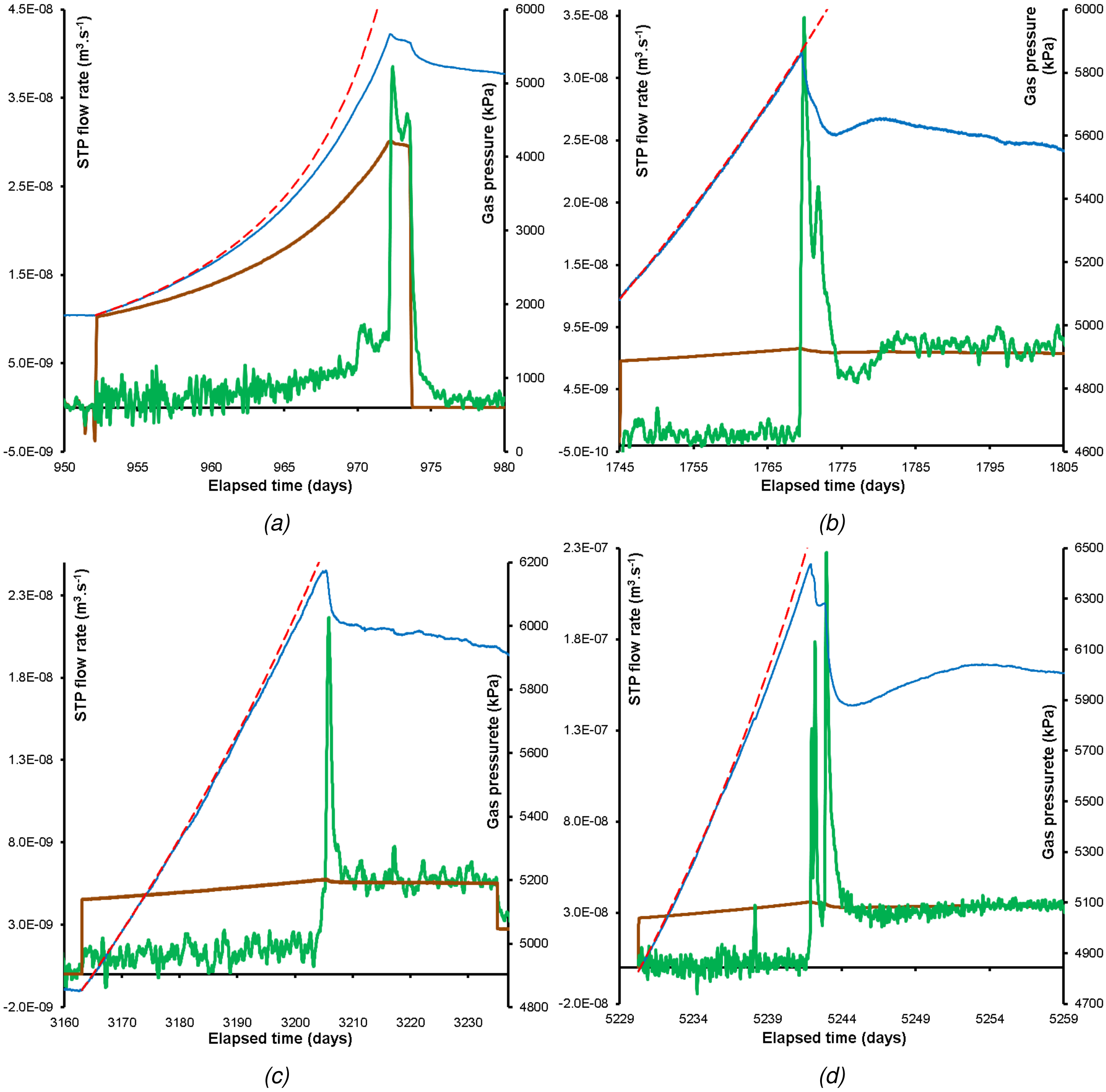

(a) *(b)*

(c) *(d)*

Figure 2.80: Comparison of gas entry behaviour for the four tests conducted in canister filter FL903. a) Gas Injection Test 1; b) Gas Injection Test 2; Gas Injection Test 4; Gas Injection Test 6.

and buffer. This means that the bentonite in contact with the canister had swelled and will have had slightly different properties to that of deep within the buffer. This was observed in differences in geotechnical properties close to the canister compared to within the middle of the annular rings. Therefore, gas was more likely to move within this region at, or near, the canister/buffer interface. However, to exit the KBS-3 system, it had to either propagate through the buffer, or exploit an interface between individual rings. It was interpreted in GT1 that gas moved initially down the canister following the prevailing stress gradient, before exiting the deposition hole through the interface between rings R1 and R2. The first peak seen in GT1 thus represents the formation of pathways and movement along the canister/buffer zone, while the second peak represents the pathways exploiting weaknesses between bentonite rings.

During decommissioning, it was noted that negligible self-healing had occurred between bentonite blocks and during excavation, clean surfaces were created when the buffer had been extracted. One interface was cored so that it could be tested in the laboratory, but it was impossible to core the buffer interface without the two sides detaching. In Lasgit, it was expected that initial formation of pathways would require the greatest energy and that the propagation of pathways would be easier. GT6 suggests that the initial formation of pathways resulted in new pathway formation that encountered two weaknesses or sinks. It is likely that the second peak occurred as a pre-existing open pathway was intercepted, with the third peak because of intercepting an interface between two rings. This third peak in flow resulted in considerable loss of pressure suggesting that gas had exited the deposition hole.

GT2 and GT6 had similar characteristics, that match flow responses in the laboratory. Flow into the clay rapidly decreased as gas pressure loss slowed, with the flowrate into the clay becoming lower than the flowrate into the system, i.e., gas pressure increased. This over- and under-shooting of flow has been seen in laboratory-scale experiments (e.g., Harrington & Horseman, 2003; Harrington et al., 2017). With time, flow into the clay matched flow into the system, meaning that steady-state flow was established. Test GT1 was not conducted for long enough to know whether it would have seen the same behaviour. However, GT4 just showed a single peak in flow, resulting in a loss of gas pressure followed by a stable reduction of gas pressure. This suggests that pathways formed in previous tests were re-activated with relative ease.

The qualitative gas flow behaviour shown in *Figure 2.80* was similar for all four tests, apart from the differences that have been accounted for above. GT2 was conducted using neon as a tracer, instead of the usual helium. There was no significant difference for GT2 to suggest that the type of gas used had an influence on the gas transport behaviour.

Figure 2.81 compares the gas pressure result for all four tests conducted in FL903. The data have been normalised so that peak pressure occurred at a time of 0 days. The individual gas tests have then been transposed about the y-axis to compare the response in *Figure 2.81*a. This figure highlights the differences in pressurisation rate, as shown by the different slopes seen for the four tests up until the time of peak pressure. However, comparisons can still be made. After peak pressure, the gas pressure rapidly reduced and in three of the tests this occurred in two events, the exception being GT4 with just a single reduction event. In GT2 and GT6 gas pressure recovered after an initial drop in pressure. This could be explained by propagating pathway(s) reaching the outside of the deposition hole or that pathway propagation continued along new paths. The pressurised pathway would propagate until it reached the outside of the buffer, resulting in the loss of gas, the pressure in the conductive pathway reducing and the pathway contracting slightly. This results in less gas movement and the gas pressure increases until the pathway dilates sufficiently that gas flow is steady-state and the pressure reduces at a constant rate. Eventually, gas pressure will reduce to a point that the gas pathway is unstable and closes, resulting in an increase in gas pressure once more until with the pathway is re-opened or a new pathway is formed.

*Figure 2.81*b shows the pressure data corrected for pressurisation rate. Data were corrected so that all tests had the same slope of pressure increase up until peak gas pressure. To achieve this, time was adjusted by multiplying by 14.5, 1.08, and 5 for GT1, GT4, and GT6 respectively so that tests showed the same pressurisation rate as GT2. This shows that GT2, GT4, and GT6 progressed to a similar rate of pressure loss as shown by the black dashed line. This was the pressure loss of a pathway from FL903 to the surrounding wall rock in the deposition hole. Test GT1 has a similar slope, although the data is limited. This suggests that the processes governing flow along a conductive pathway were not pressurisation rate dependent. Comparing *Figure 2.81*a and *Figure 2.81*b shows an additional pressurisation-rate independent feature. *Figure 2.81*a shows that the pressure decrease and recovery in GT2 and GT6 both took about 10 days to create a secondary peak in pressure, irrespective of pressurisation rate. When the data were corrected for flow rate (*Figure 2.81*b), the features now had considerable different forms, with GT2 recovering in 10 days compared with 60 days in the corrected data for GT6. *Figure 2.81*b shows that GT1 did not see the same initial pressure decrease as the subsequent gas injection tests. This suggests that GT2, GT4, and GT6 exploited pathways formed by GT1 and that the buffer had not fully self-healed following the first gas test.

Figure 2.82 compares the response seen in selected pore pressure (UR) sensors around the time of peak stress and gas entry. Test GT1 (*Figure 2.82*a) saw a distinctive form in UR906. Pressure started to increase, before a secondary feature resulted in a much greater pressure increase. This relatively quickly

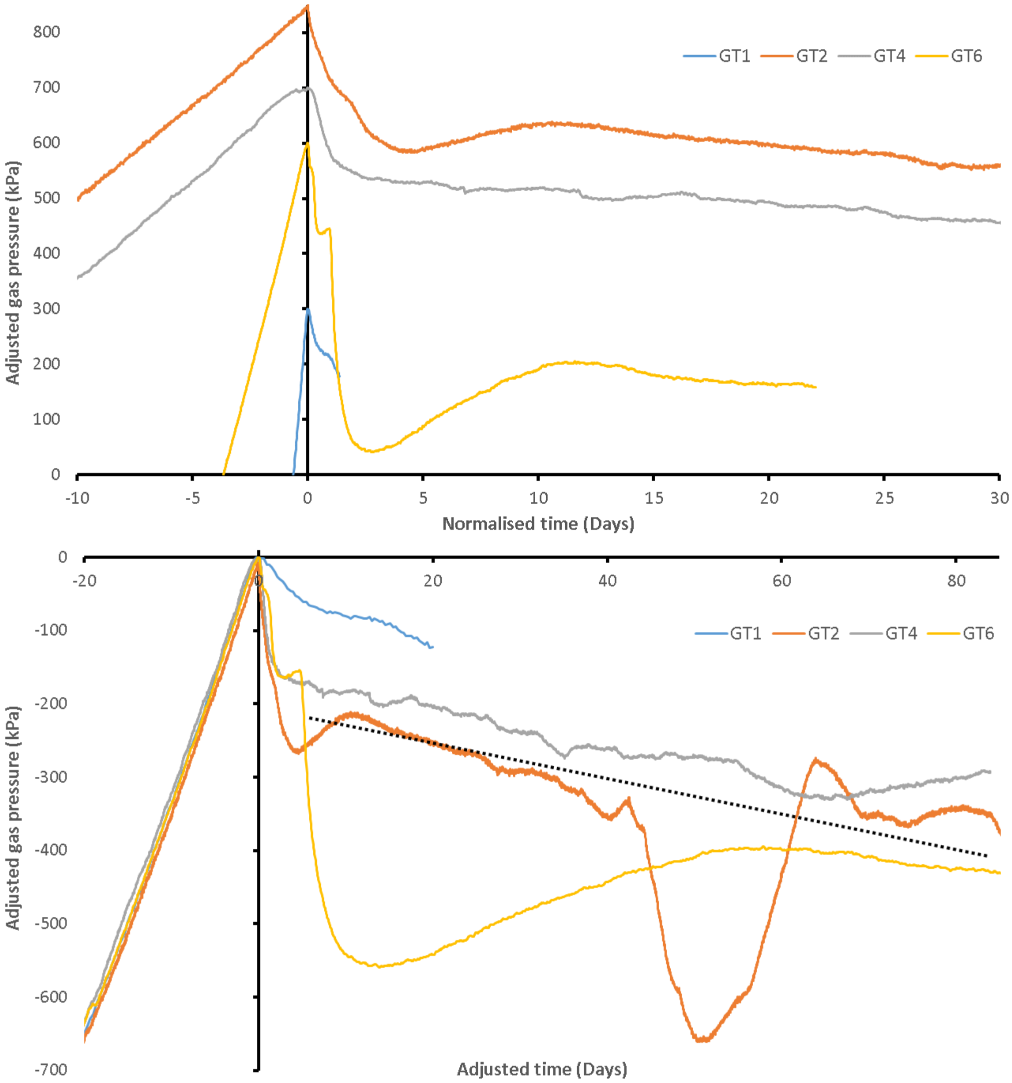

Figure 2.81: Comparison of gas pressure for the four tests conducted in canister filter FL903. a) Gas pressure around peak pressure for all four tests; b) Gas pressure adjusted to correct for different pressurisation rates.

peaked and then decayed back to the starting pressure over several days. Several other sensors showed a single peak of similar form to the initial pressure rise seen in UR906, while UR909 saw a pressure decrease. During GT2 (*Figure 2.82*b), the form of UG905 was very similar, with a pressure increase like that seen in GT1. Sensor UR909 also decreased, as seen in GT1. However, the pressure increase at other locations was largely absent. This may suggest that GT1 showed virgin formation of pathways, with GT2 re-activating these pathways. Test GT4 showed a different response (*Figure 2.82*c). Small steps in pore pressure were seen in UR905, with UR908 showing the greatest increase in pore pressure. This suggests that GT4 showed different propagation response than GT1 and GT2 and that some new pathways formed. Test GT6 (*Figure 2.82*d) then showed similar response to GT1 and GT2, with some comparison to GT4. UR905 was again the dominant pore pressure response but as in GT4, UR908 also showed pressure increase. This suggests that features formed in GT1 and reactivated in GT2 were again reactivated but additional features formed in GT4 were also reactivated. The form of the response for GT6 is more like GT1 and may suggest that a degree of self-sealing had occurred.

Figure 2.83 compares the response observed in selected radial stress (PR) sensors around the time of peak pressure and gas entry. In GT1, PR905 and PR906 showed the dominant response (*Figure 2.83*a). Stress increased over nearly a day, until peaking and then taking several days to decay. The response

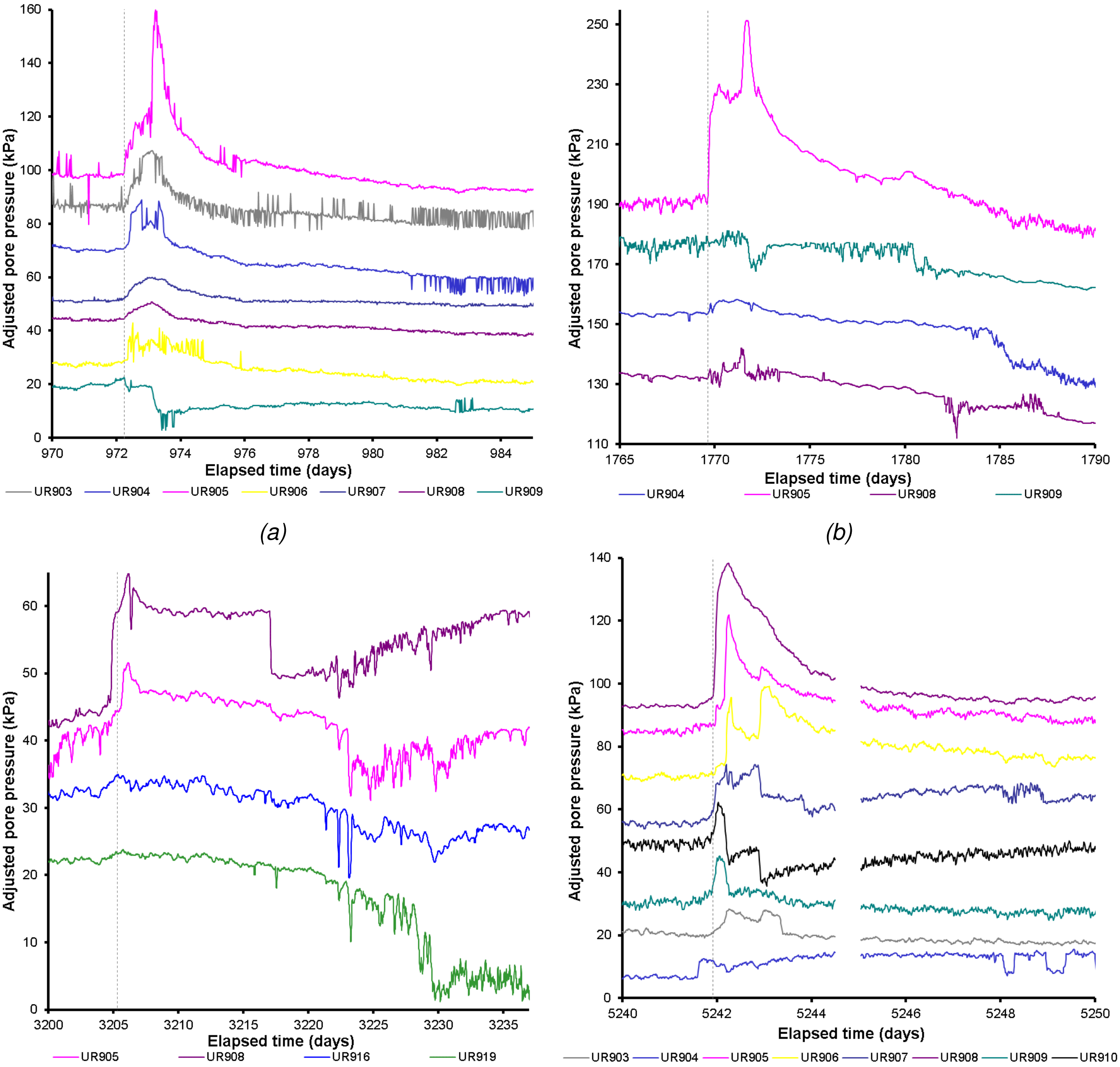

(a)

(b)

(c)

(d)

Figure 2.82: Pore pressure observed in a selection of sensors close to FL903 around peak gas pressure. a) Gas Injection Test 1; b) Gas Injection Test 2; c) Gas Injection Test 4; d) Gas Injection Test 6. Each sensor has been adjusted about the y-axis for display purposes. Gas peak pressure is highlighted as a dashed event line.

was seen in several locations, with PR909 showing a decrease in stress. Similarities were seen in GT2 (*Figure 2.83*b), with PR906 now being the dominant feature, with UR905 also showing considerable stress increase. However, the form of the result was subtly different, with a sharper peak and more rapid stress drop compared with the gradual reduction in stress seen in GT1. As with GT1, PR909 decreased in stress. As with pore pressure, radial stress showed a different form in GT4 compared with GT1 and GT2 (*Figure 2.83*c). Stress increases were considerably lower in magnitude with a more step-like response for PR906. Sensor PR907 showed a response and as with pore pressure, suggests that the direction of gas migration was different for this gas test. In the final gas test, GT6 (*Figure 2.83*d), the response was different to that seen in GT1 and GT2. For pore pressure, the responses of GT1, GT2, and GT6 were similar but for radial stress, GT6 differs from GT1 and GT2. This time, a stepped response in stress was seen, with little stress decay after the increase. Sensors PR905 and PR906 showed the dominant response as seen

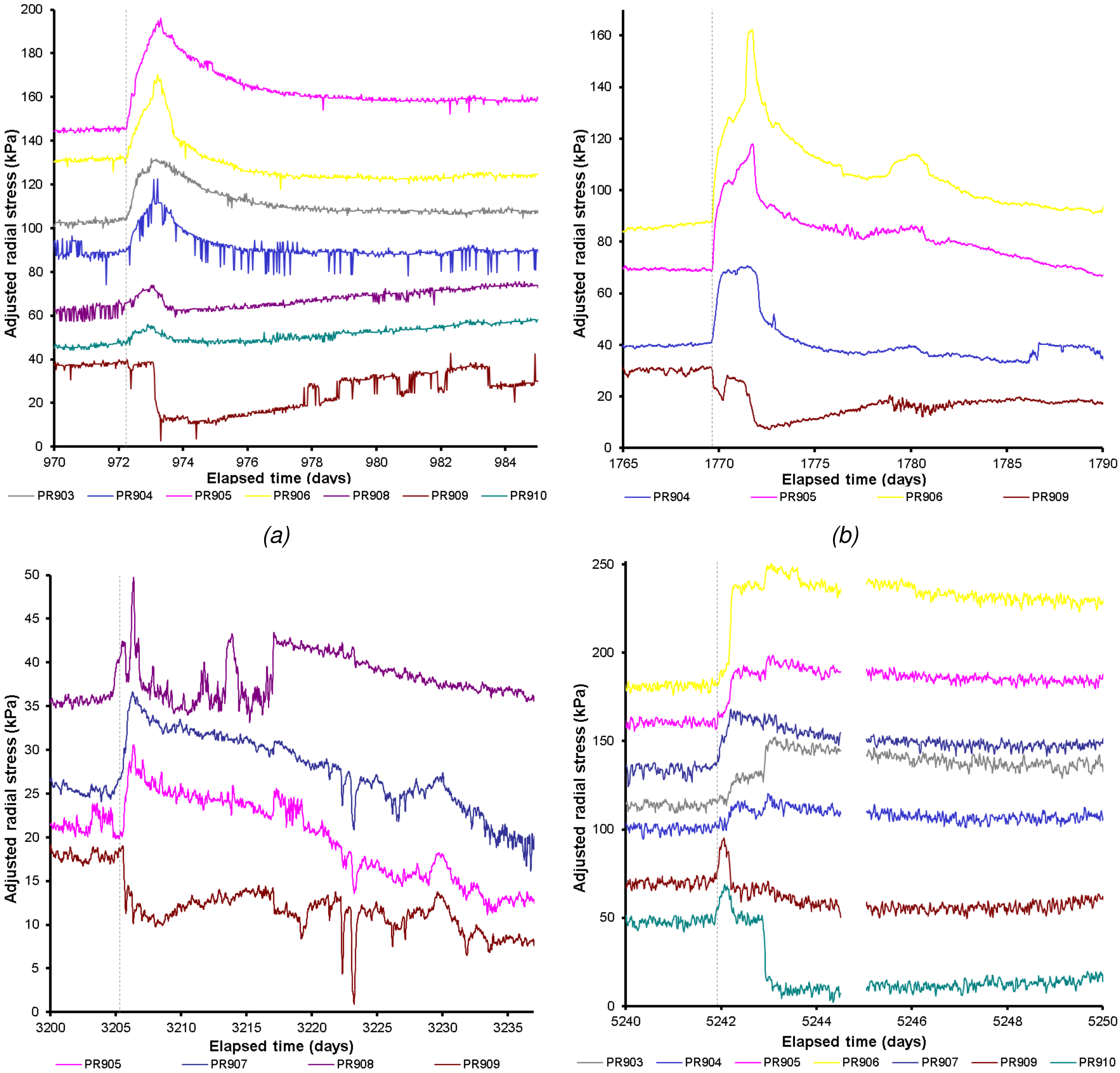

(a) *(b)* *(c)* *(d)*

Figure 2.83: Radial stresses observed in a selection of sensors close to FL903 around peak gas pressure. a) Gas Injection Test 1; b) Gas Injection Test 2; c) Gas Injection Test 4; d) Gas Injection Test 6. Each sensor has been adjusted about the y-axis for display purposes. Gas peak pressure is highlighted as a dashed event line.

in GT1 and GT2 but with the additional response of PR904, as seen in GT4. For this test, PR909 showed a stress increase and peak, whereas in the other gas injection tests this location saw a stress reduction. This time, PR910 showed the stress reduction.

The pore pressure and radial stress responses (*Figure 2.82*, *Figure 2.83*) show that in GT1 new pathways formed in the buffer. Certain characteristics suggest that gas pathway propagation was in a similar direction, possibly re-opening pathways. However, GT4 showed a different response and that gas movement was in a different direction to GT1 and GT2 and not just through the re-establishment of pathways formed in the previous tests, i.e. pathways had self-sealed. The final gas injection test then showed gas propagation in the directions that match all three previous gas injection tests and may show that pathways formed in these tests were re-established.

Figure 2.84 shows additional features for GT2 and GT4 that are relevant to the test comparison. In GT2, flow was continued after gas entry for much longer than in GT1 (*Figure 2.84*a). This shows a series of over- and under-shoots of flow into the clay, with periods of pressure decay, recovery, and peak behaviour. The red area shown in *Figure 2.84*a signifies when a leak occurred as an air actuated valve failed to operate. It is possible that the pressure decay around Day 1810 may have been a similar event, but it is unlikely, it is probable that a prominent gas pathway had formed, resulting in a loss of gas pressure. The reducing pressure resulted in the pathway closing, either partially or completely, resulting in an increase gas pressure, before a secondary peak suggests the re-establishment of the pathway out of the buffer, or the formation of a new pathway within the buffer. Following the experimental artefact around Day 1865 and the re-establishment of gas pressure, the pressure started to rise, until another peak was encountered. It is worth noting that the gas peaks around Day 1832 and Day 1898 were of similar magnitude and the reductions in pressure at Day 1770 following peak stress, Day 1815, and Day 1900 all have similar slope. Therefore, the re-establishment of a gas pathway occurred at the same pressure, and the rate of pathway growth was similar. This shows that the physics driving gas pathway formation and propagation is repeatable.

*Figure 2.84*b shows the flow result for Gas Injection Test 4. This test had a single peak in flow and the system quickly established steady state flow, with gas pressure slowly reducing at a constant rate. Flowrate into the system was approximately halved, with flow into the clay quickly reducing to match flow into the system. This changed the slope of the pressure decay in filter FL903, becoming almost level. Flow into the system then reduced for a second time. So that flow into the clay again was almost the same as flow into the system. Again, the slope of the gas injection pressure changed, and this time gas pressure started to increase. This suggests that the aperture of the conductive pathways was flow rate dependent. As flow was reduced, the pathways contracted sufficiently that the flow into the clay was less than the flow into the system. The degree of dilation of the pathways being flow rate dependent is a fundamental observation.

In GT1, it was interpreted that gas had moved down the outside of the canister following the prevailing stress gradient, before exiting the deposition hole, most likely along the interface between bentonite rings R1 and R2 and/or C1 and R1 (*Figure 2.86*a). *Figure 2.85*a,b and *Figure 2.86* shows that gas directly migrated to two sensor locations within the deposition hole during GT2. Analysis of the data suggested that gas migrated around the canister and was first detected 180° around the canister to filter FL901. *Figure 2.85*b shows that gas movement to FL901 occurred through a series of events, raising pressure towards the gas injection pressure in at least 6 separate events. Gas also propagated downwards towards the bottom of the deposition hole and reached sensor UB902 in a single event. It is possible that gas was able to flow along cable runs in the bentonite to reach UB902. *Figure 2.85*a shows that the injection filter, FL901, and UB902 were all directly connected and that the drop in gas pressure along the pathway was relatively small. However, when pressure dropped, this connection was lost, and was only re-established around the time gas pressure peaked for a second time. This suggests that the peak in pressure occurred when the pathway was re-opened. When pressure reduced because of leakage in the laboratory, connection was lost again but this time was not re-established by increases in pressure and another gas peak. This demonstrates the dynamic nature of the gas pathways and that multiple pathways existed. In time, gas migrated up the deposition hole towards the top of the canister. Gas sampling in the pressure relief holes showed that gas had escaped the deposition hole.

It is uncertain where gas migration occurred in Gas Injection Test 4. Gas pathways did not intercept any other sensor location in the system. The stress response at gas entry was small which suggests that the test exploited pre-existing flow-paths in the system that were still open, or easy to open. It is possible that the test exploited the gas pathway network created either during GT1 or GT2 from FL903, or more likely the network created by test GT3 in FU910, which had resulted in the migration of gas to filter FL904 on the same level of the canister as FL903. *Figure 2.86*c shows a possible interpretation of gas movement in GT4. Gas Injection Test 6 showed that gas quite rapidly directly reached canister filter FL901 (*Figure 2.85*c, *Figure 2.86*d). Migration was through a few discrete events, but pressure quickly rose to match the gas injection pressure. Gas had therefore migrated 180° around the canister without intercepting either of the

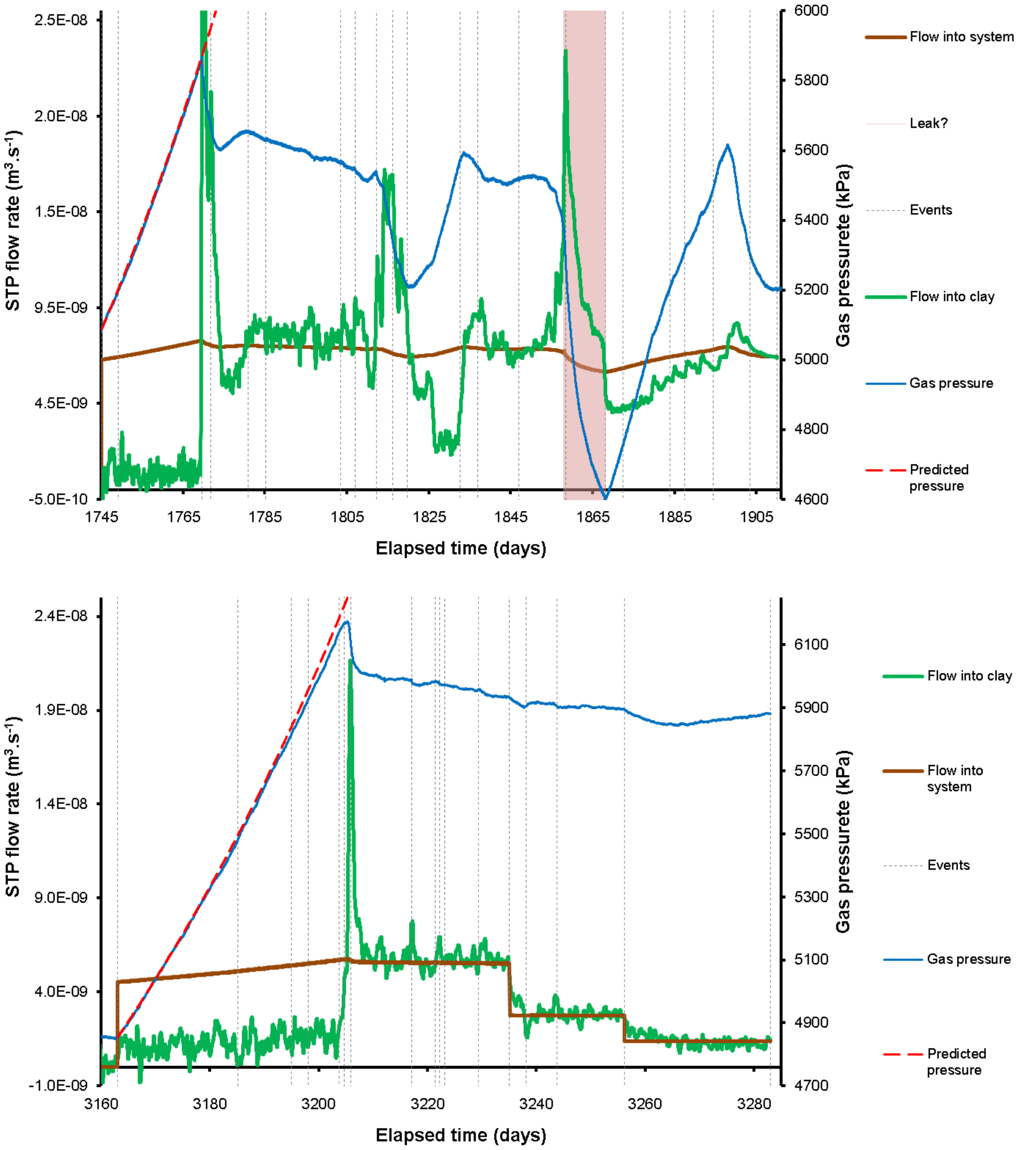

Figure 2.84: Additional features of flow of gas into the system and the clay during. a) Gas Injection Test 2; b) Gas Injection Test 4.

two injection filters in between (FL902 or FL904). Gas then moved towards the bottom of the canister. From here, the gas found a pathway out of the deposition hole, most likely along the interface between bentonite rings R1 and R2, or R1 and C1 at the level of the bottom of the canister.

There is evidence that subsequent gas injection tests behaved similarly and that pathways may have re-activated. However, it is clear that the migration of gas was not identical between tests, with new pathways forming. The formed pathways self-sealed, at least partially.

Gas Injection Tests in canister filter FU910

Two tests were conducted in canister filter FU910 on the upper array of canister filters at a height of 4124 mm in the deposition hole. The first test, Gas Injection Test 3 (GT3) was conducted between Day 2257 and Day 5183, Gas Injection Test 5 (GT5) was conducted between Day 5183 and Day 5220. This means there was 2490 days between the start of Lasgit and GT3, and 2568 days between the end of GT3 and the start of GT5. The main data relating to the tests conducted in filter FL903 are summarised in *Table 2.22*.

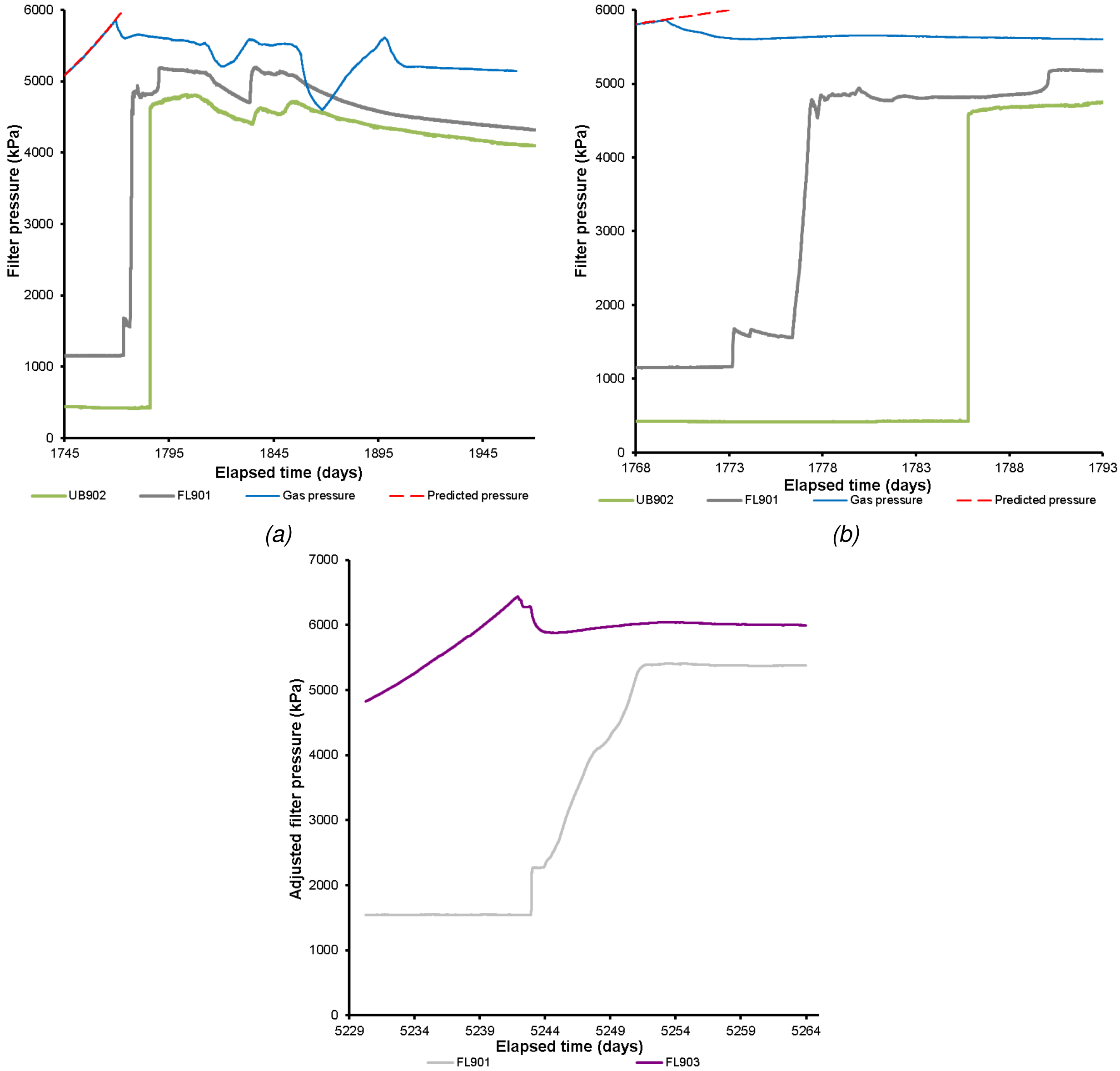

(a) *(b)*

(c)

Figure 2.85: Detail of sensors that showed evidence of gas pressurisation during Gas Injection Tests. a) Gas Injection Test 2; b) Detail of Gas Injection Test 2; c) Gas Injection Test 4.

Table 2.22: Data relating to gas injection tests conducted in canister filter FU910.

No.	**Test**	**Gas ramps**	**Start (Days)**	**End (Days)**	**Time gap (Days)**	**Peak pressure (kPa)**	**Time at peak (Days)**	**Gas entry pressure (kPa)**
1	GT3	4	2257.23	2614.46	2257.23	5192	2490.37	-
2	GT5	1	5183.27	5220.47	2568.82	5347	5202.57	4919

Figure 2.87 compares the gas pressure and flow data for the two tests conducted in FU910 (GT3 and 5), with the gas pressure compared in more detail in *Figure 2.88*. *Figure 2.87* shows that the gas flow into the system was different for the two tests. This potentially means that the results could have been affected if the processes controlling gas entry were dependent on the rate of pressurisation. In GT3, flow into the

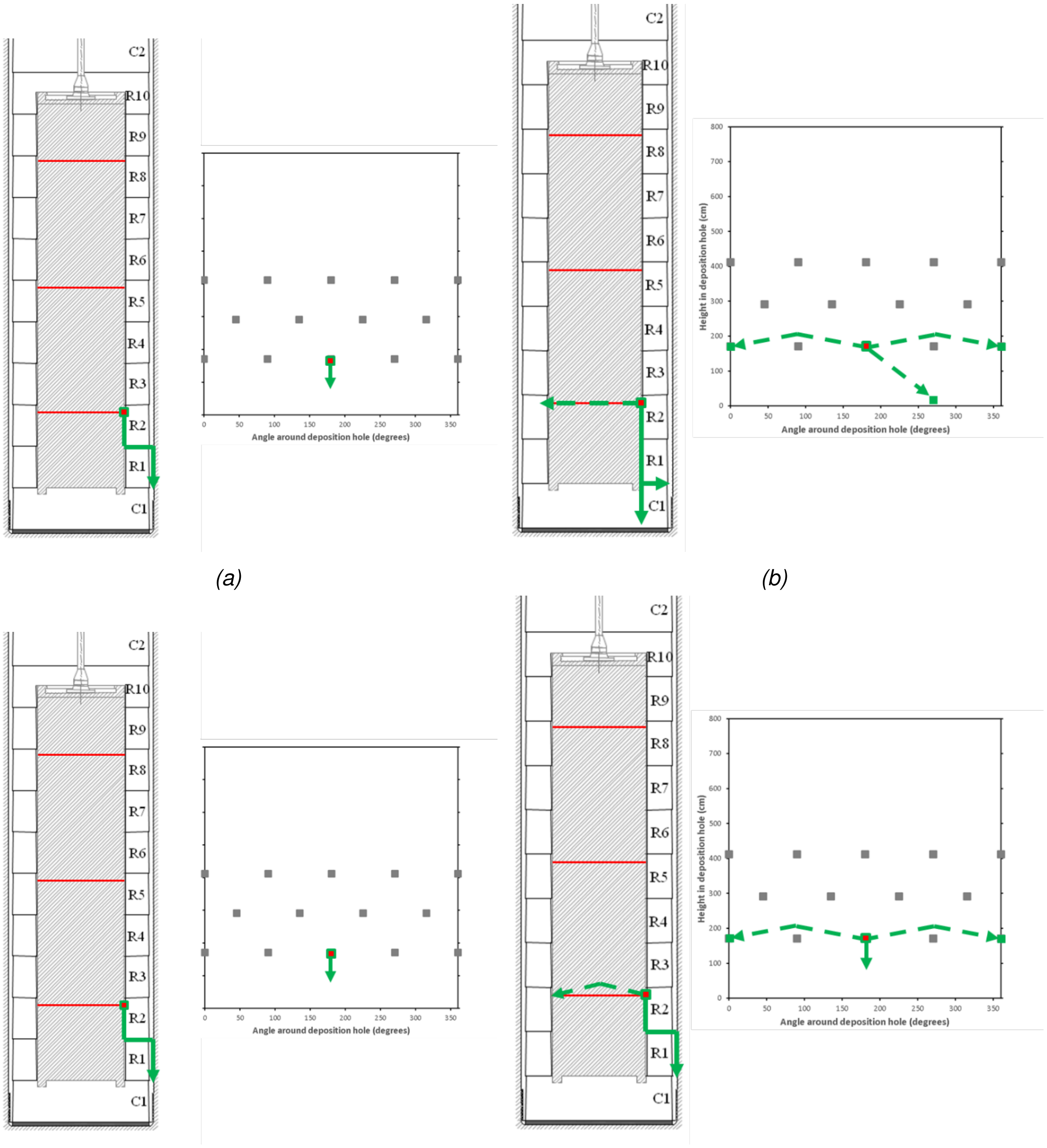

(a)

(b)

(c)

(d)

Figure 2.86: Schematic of the direction of gas flow during gas testing in lower filter FL903. a) Flow in Gas Test 1; b) Flow in Gas Test 2; c) Flow in Gas Test 2; d) Flow in Gas Test 2.

clay was low, up until the sudden increase in flow at around peak pressure. There were no pre-cursor flows and a single peak in flow was formed, reducing gas pressure rapidly. The peak in flow was short lived and flow into the clay quickly reduced to below that of flow into the system and as a result gas pressure started to rise again. Similar behaviour was seen in GT5. There was no pre-cursor flow and a rapid increase in flow with a single short-lived spike. However, in GT5 flow into the clay did not reduce below the flowrate into the system for some time so gas pressure slowly increased. In both cases, gas entry saw a rapid propagation of pathways, lowering gas pressure. These pathways either became unstable or the gas flow encountered a baffle in the system, resulting in an increase in gas pressure. In both tests, gas pressure had a secondary peak, which this time was broader compared with the instantaneous pressure drop seen at initial peak pressure. In both tests pressure increased above, or very close to, the initial peak pressure.

This contrasts with what was seen in FL903, with peak pressure being followed by reducing gas pressure. At FU910, this suggests that continued propagation of pathways was more difficult higher in the canister or that an easy route out of the system was not achieved. In both tests, during the initial recovery of gas pressure there was a change of slope, suggesting that pathway propagation increased. This change in slope was more obvious in GT5 but is present in GT3 as well. In both tests, this event also corresponded with a short-lived spike in flow, although in GT3 there was a break in data recording that may have masked the feature. The qualitative gas flow behaviour shown in *Figure 2.87* shows a similar behaviour and form for both gas pressure and flow, with short lived spike in flow resulting in steady-state movement of gas as flow into the clay matches flow into the system.

Figure 2.88 compares the gas pressure result for the two tests conducted in FU910. The data were normalised so that peak pressure occurred at a time of 0 days. The individual gas tests have then been transposed along the y-axis to compare the response in *Figure 2.88*a. This figure highlights the differences in pressurisation rate, as shown by the different slopes seen up until the time of peak pressure, although the difference is not excessive. At peak pressure, the gas pressure rapidly reduced. In GT3 a reduction of ~40 kPa was seen, with GT5 reducing ~180 kPa. This suggests that GT5 re-activated existing pathways in the system quite easily. In GT3 pressure recovered to create a secondary, broad, peak, while in GT5 a second instantaneous pressure drop was seen at a gas pressure similar to the initial peak gas pressure. This behaviour suggests that gas pathways were continuing to grow and that gas had not been able to exit the deposition hole, at least until the secondary peaks occurred. Correcting the data for differences in flow rate into the system (*Figure 2.88*b) shows that the pressure recovery had a similar slope. In GT3 this resulted in a secondary peak, but in GT5 at a similar adjusted time there was a change in slope. This suggests slight differences between the propagation of pathways in the two tests. The rapid loss of more pressure in GT5 suggests that the repeat test exploited features formed during GT3 and that the buffer had not fully self-healed following the first gas test.

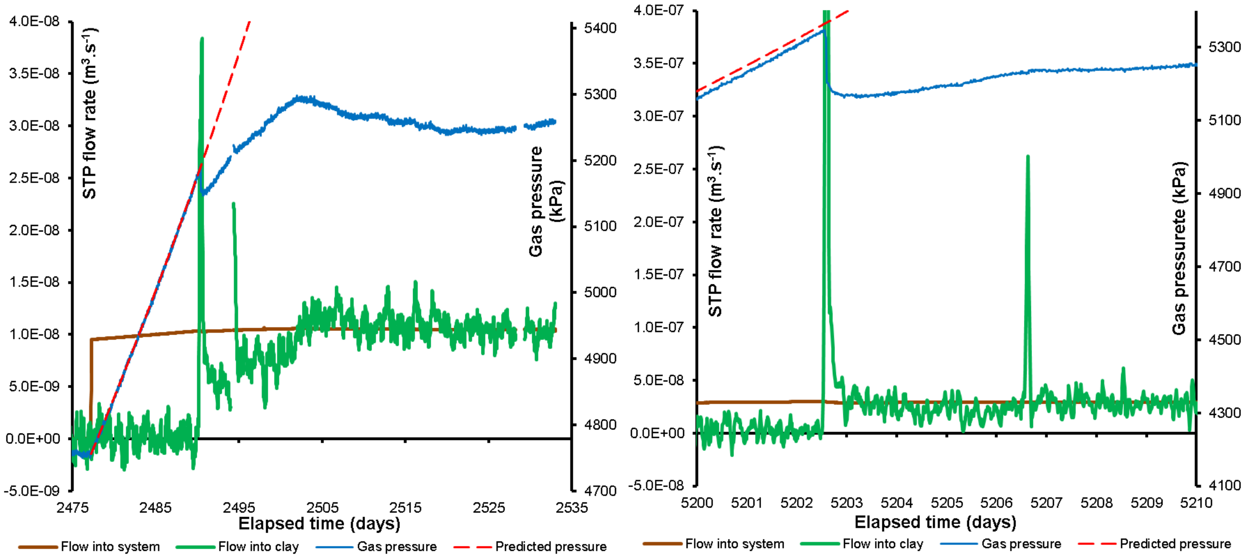

(a) (b)

Figure 2.87: Comparison of gas entry behaviour for the two tests conducted in canister filter FU910. a) Gas Injection Test 3; b) Gas Injection Test 5.

Figure 2.89 compares the response observed in selected pore pressure (UR) sensors around the time of peak stress and gas entry. For test GT3 (*Figure 2.89*a) peak pressure occurred at Day 2490.37. Note that UR916 was situated opposite the injection filter on the outer edge of the bentonite buffer. This sensor saw little variation at the time of peak pressure but was considerably noisy. Instantaneous pressure increases were seen in UR915 and UR921, suggesting that initial gas movement was in the general direction of these sensors, along the canister surface. It is noted that few pore pressure sensors registered a change at peak gas pressure, which is surprising given the instantaneous drop in gas pressure. For test GT5 (*Figure 2.89*b) peak pressure occurred at Day 5202.57. Again, FU916 directly opposite the injection filter recorded only a minor pressure reduction. Pore pressure greatly increased in at least five locations, but with varying form. Three sensors showed an instantaneous pressure increase followed by a slow pressure decay, one sensor showed a pressure increase in a series of steps, and one sensor showed a gradual slow pressure increase. The form of the response of pore pressure in tests GT3 and GT5 was very different. However, GT5 was like that seen in most of the tests conducted in filter FL903.

Figure 2.90 compares the response seen in selected radial stress (PR) sensors at the time of peak gas pressure. No radial stress sensors were located opposite the injection filter. Sensors PR915 and PR916 were situated at the same level as FU910 but 45° around the canister in both directions. PR911 and PR912 were situated below PR915 and PR916 respectively, with PR921 situated above the injector at the same orientation. Peak pressure occurred in GT3 at Day 2490.37 (*Figure 2.90*a). At this time, PR915 and PR917 increased in stress, with PR919 increasing around five days later. This suggests that gas moved in this general direction along the canister surface. Radial stress increased at PR911 some 100 days later. This suggests that gas movement was transient throughout this test. For GT5 (*Figure 2.90*b), gas peak pressure occurred at Day 5202.57 and this was accompanied by an increase in almost all PR sensors. A stepped response was seen, with some sensors showing a delayed response. As with pore pressure, the radial stress data suggest the slow formation of pathways in GT3, which were reactivated in GT5. In sensor PR917 the form of the response was similar between tests, with PR915 also superficially being similar, although the response was more complex in GT3 and the amplitude of variation in GT5 was significantly greater. In both tests, PR919 saw a delayed increase of stress as gas moved.

The pore pressure and radial stress responses (*Figure 2.89*, *Figure 2.90*) show that GT3 saw the slow formation of virgin pathways in the buffer. Certain features of GT5 suggest that gas pathway propagation was in a similar direction, probably re-opening pathways extant from the earlier gas injection test. This suggests that pathways had not fully self-sealed and were easily reactivated, but near the injection filter the system had self-sealed, probably because of the two-step hydraulic tests conducted.

Figure 2.91 shows additional features for GT3 and GT5 that are relevant to the discussion. In GT3, flow was continued for considerable time after gas entry (*Figure 2.91*a). Generally, flow into the clay quickly equalled flow in the system and steady-state flow was established. By Day 2530, the pressure in FU910 had peaked twice, troughed twice, and was increasing for a third time. Shortly after, a system failure in the lab halted gas injection and when it was re-started gas pressure had reduced but it quickly recovered and by around Day 2555 was increasing at a rate similar to that seen at Day 2534 before the shut-in. A series of pressure decreases then occurred demonstrating that either new pathways were forming, or that gas venting from the deposition hole was episodic. When the test was halted, gas pressure was at its highest and was continuing to increase. It was approximately 200 kPa higher than the initial peak pressure event. The data suggest that pathway formation continued.

*Figure 2.91*b shows the flow result for Gas Injection Test 5. This test had a single peak in flow and showed the system quickly established near steady-state flow, with gas pressure slowly increasing at a constant rate. Flow into the clay was only marginally lower than the flow into the system, resulting in a slow increase in pressure. When gas pressure approached that of the peak pressure, a second peak was seen with instantaneous pressure loss. The slope of this linear pressure increase was similar to that seen in GT3 when the data were corrected for differences in flow rate (*Figure 2.88*b). This suggests that the physics governing the increasing pressure was repeatable and scaled with flow rate.

In both gas injection tests, pathways were seen to directly propagate to other sensors within the deposition hole, as shown in *Figure 2.92* and *Figure 2.93*. In GT3 (*Figure 2.92*a,b, *Figure 2.93*a), gas first moved to FU909/FU912 in a series of pressure events. Following GT3, it was found that FU909 and FU912 were wrongly connected within the Lasgit laboratory, meaning that filter FU912 was not connected to the laboratory and therefore FU909 had been the pressurised filter. This was corrected before GT5. Gas then arrived at FU911, again in a series of pressure increases, albeit over a longer period. Next, gas reached

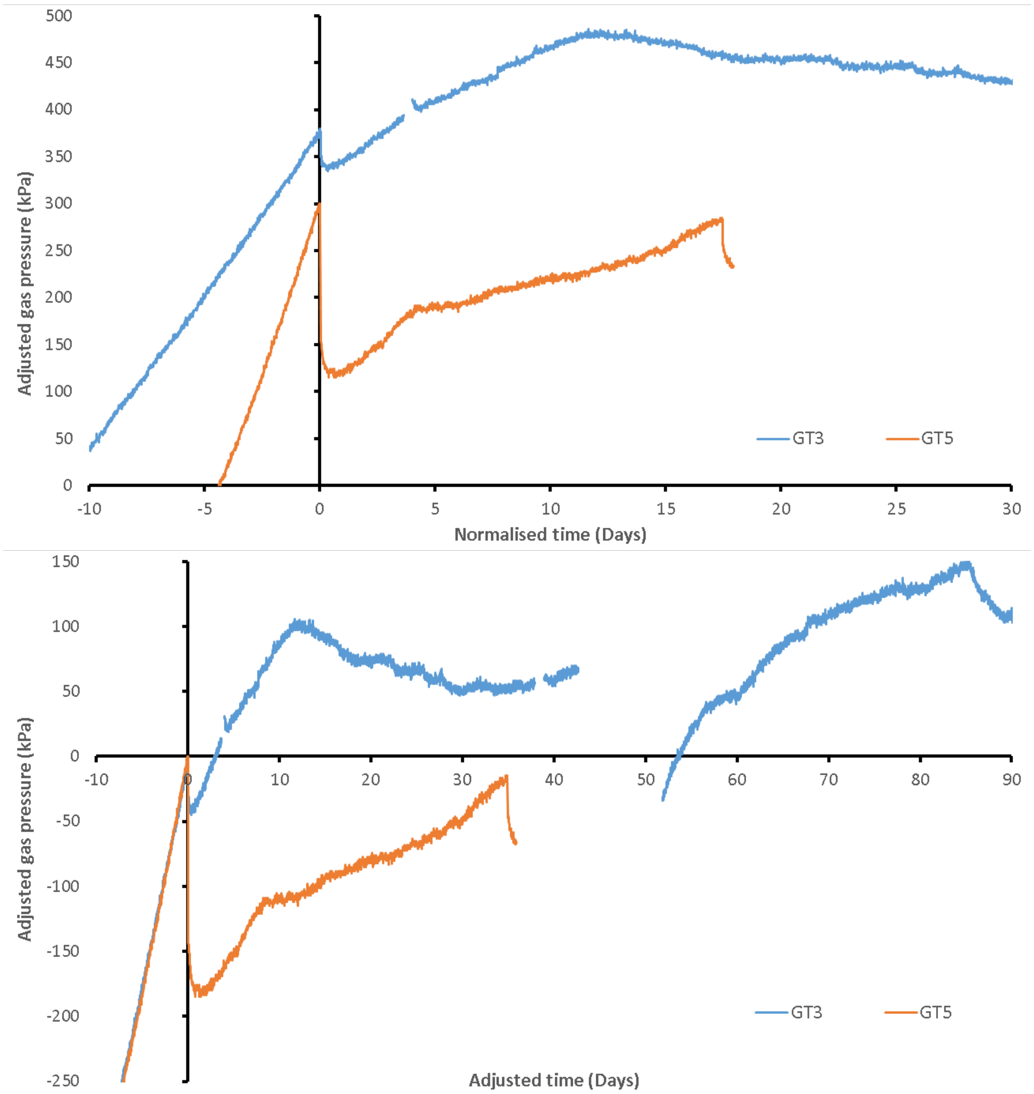

Figure 2.88: Comparison of gas pressure for the two tests conducted in canister filter FU910. a) Gas pressure around peak pressure for both tests; b) Gas pressure adjusted to correct for different pressurisation rates.

PC903, and finally reached FL904 towards the bottom of the canister. *Figure 2.92*d shows the location of these sensors on the canister surface. For GT5 (*Figure 2.92*c, *Figure 2.93*b), at peak gas pressure, pressure at FU909 and PC903 increased instantaneously. This confirms that pathways created during GT3 were re-opened at peak pressure during GT5 and shows that limited sealing of the existing pathway network occurred in the ~2500 days between the two tests. Gas did not reach FU911 or FL904, showing that at least some of the pathway network was not reactivated and may have even self-sealed. It should be noted that both FU911 and FL904 were hydraulically tested between the two gas injection tests, and this may have aided self-sealing. However, FU909 was also hydraulically tested and this was not self-sealed. It is not certain whether gas managed to escape the deposition hole as pathways were still forming or developing in GT3.

There is evidence that subsequent gas injection tests behaved similarly and that pathways were reactivated. However, the migration of gas was not identical between tests, with new pathways forming or at least some existing pathways not reactivating. The formed pathways self-sealed, at least partially.

The Full Canister Test

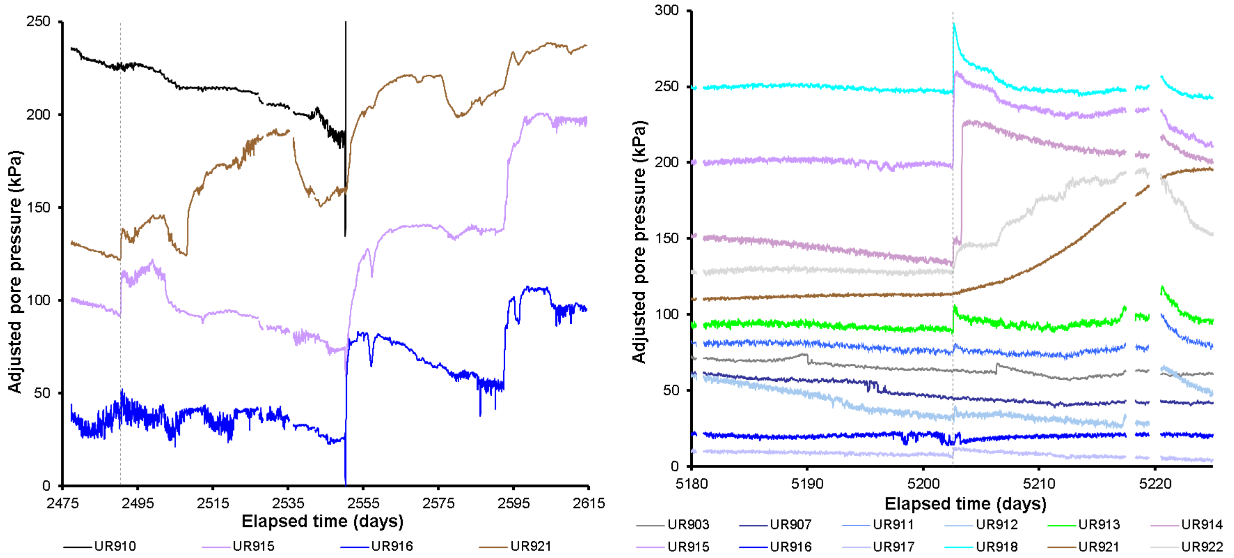

(a) (b)

Figure 2.89: Pore pressure observed in a selection of sensors close to FU910 around peak gas pressure. a) Gas Injection Test 3; b) Gas Injection Test 5. Each sensor has been adjusted about the y-axis for display purposes. Gas peak pressure is highlighted as a dashed event line.

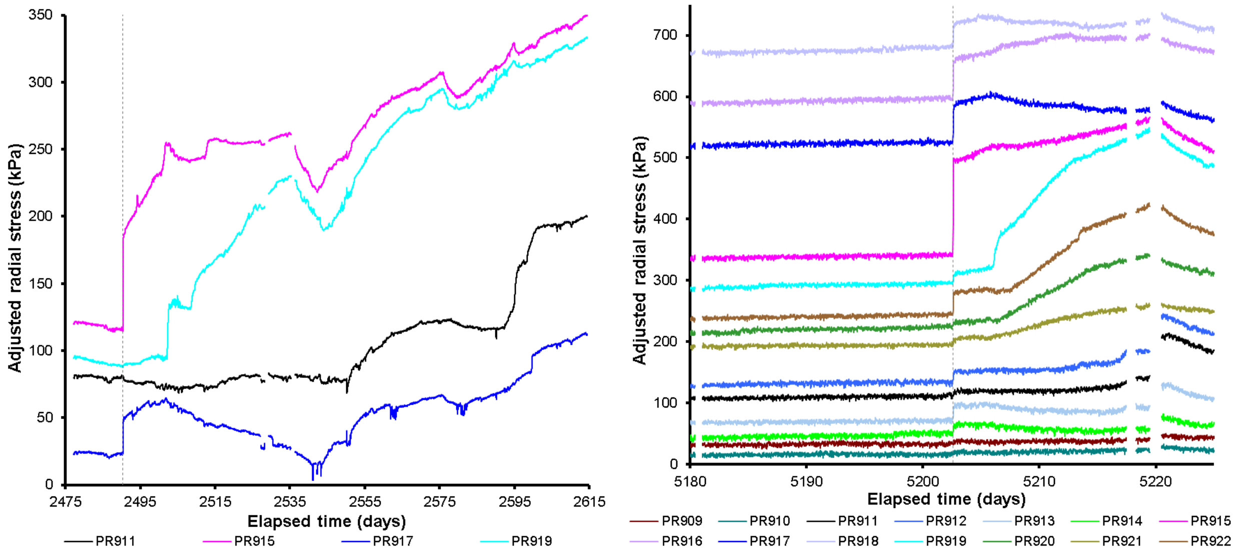

(a) (b)

Figure 2.90: Radial stresses observed in a selection of sensors close to FU910 around peak gas pressure. a) Gas Injection Test 3; b) Gas Injection Test 5. Each sensor has been adjusted about the y-axis for display purposes. Gas peak pressure is highlighted as a dashed event line.

The Full Canister Test reached gas entry in a different manner than for the six gas injection tests. Gas pressure was held constant at a magnitude a little higher than gas entry was expected while water in the canister slowly drained through the FCT filter. Had the gas ramp been increased it was likely that the buffer would have been hydrofractured by the water in the filter, something that was of no interest to Lasgit. All previous tests had gas entry at a pressure close to the local stress. The Full Canister Test filter (FCT) was located close to the axial stress sensor on the bottom of the canister, PC901. This meant that gas entry was expected ~7000 kPa. When pressure reached 7100 kPa (*Figure 2.94*), it was kept constant to allow the FCT filter to drain of water and to wait until gas entry occurred. It was estimated that 7100 kPa was

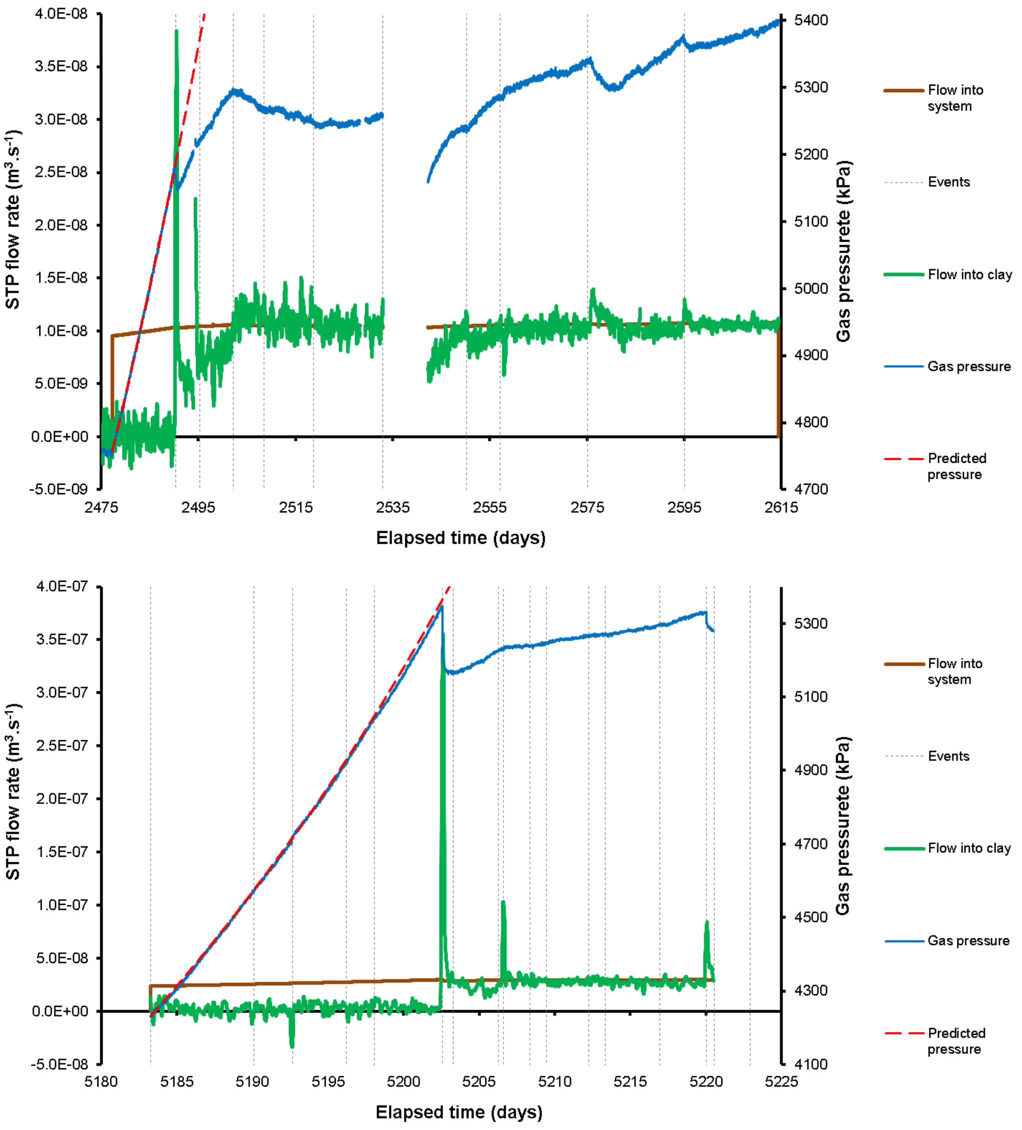

Figure 2.91: Additional features of flow of gas into the system and the clay during gas injection testing. a) Gas Injection Test 3; b) Gas Injection Test 5.

sufficient for gas entry to occur, but would not be high enough that the bentonite would be gas fractured.

Figure 34 shows the radial stress and pore pressure results for the FCT test for selected sensors. It should be noted that the sensor array was optimised for testing in the canister filters and that the coverage at the base of the canister was limited. However, gas entry was observed. The form of the pore pressure (*Figure 2.95*a) profile was different from that seen in all the other gas injection tests. Pore pressure increased and then when it peaked, quickly dropped. This is almost the opposite behaviour to that seen in the previous tests where pore pressure tended to rise instantaneously and take time to decay. However, the general form has similarities to that seen at FL903. The rapid decrease in pore pressure suggests that gas moved into the buffer and relieved the loading of the deposition hole wall. Radial stress had a similar form to pore pressure (*Figure 2.95*b), which had similarities to that seen in GT2. This may mean that the FCT test exploited pathways formed in previous gas injection tests and simply re-activated extant pathways. The data may also suggest that the buffer was “inflated” by the gas and that the reduction in pore pressure and stress was this “balloon” being deflated as a pathway reached the outside of the deposition hole and gas could exit the system.

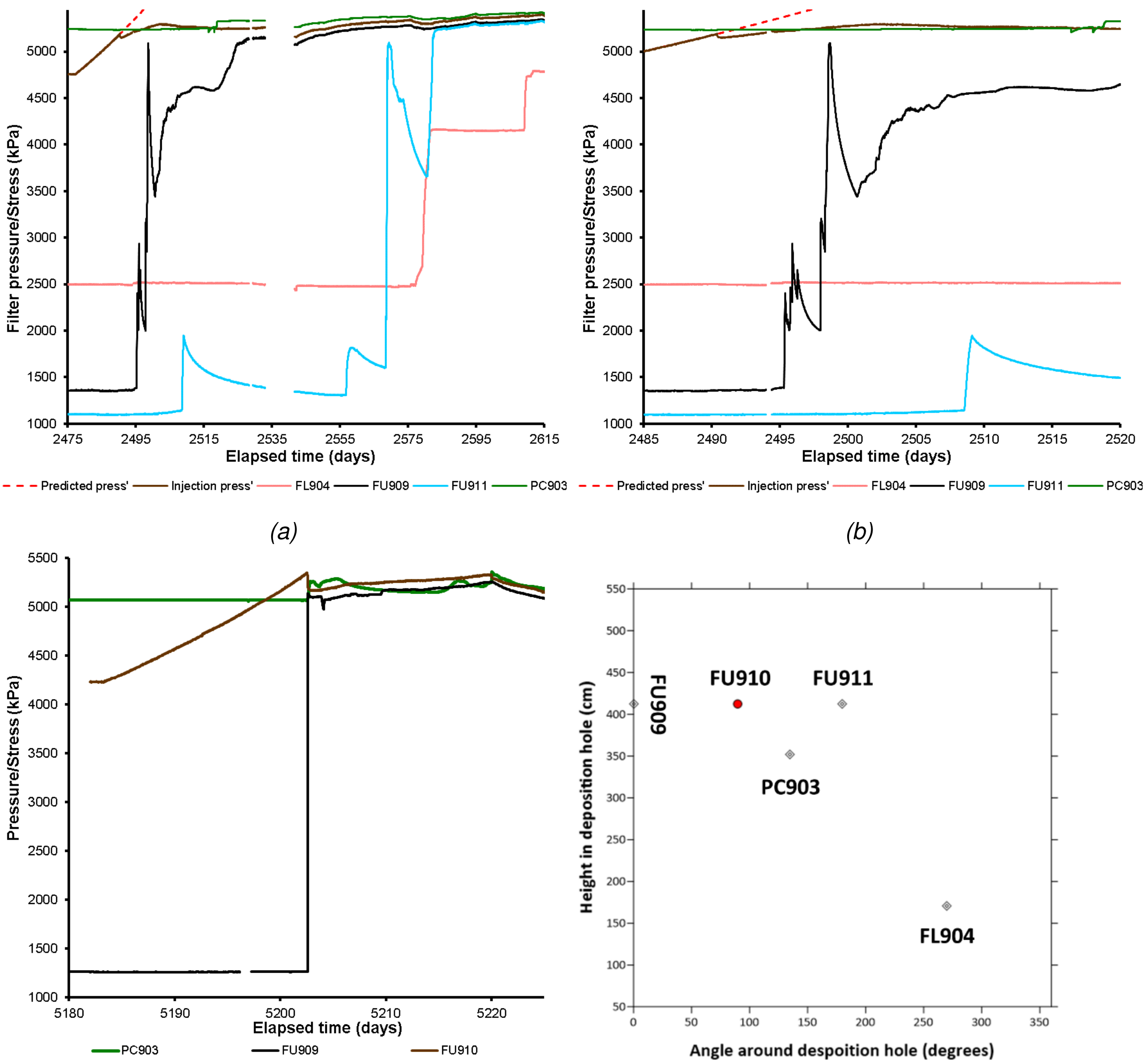

(a) (b)

(c) (d)

Figure 2.92: Detail of sensors that showed evidence of gas pressurisation during Gas Injection Tests in FU910. a) Gas Injection Test 3; b) Detail of Gas Injection Test 3; c) Gas Injection Test 5; d) Location of sensors in the deposition hole.

Figure 2.96 shows that gas migrated within the KBS-3 system and directly intercepted the canister filter FL901 and pore pressure sensor UB902 within the bentonite, near to the FCT filter. The gas took at least two pressure events to fully pressurise UB902. Once both sensors registered pressurisation they had similar pore pressure, and both decayed for the remainder of the test period at a similar rate to that of the FCT gas pressure. This pressure decay showed chaotic response, before eventually resulting in a slow and steady reduction in pressure. Both FL901 and UB902 were clearly in direct open communication with one another. However, the pressures recorded at UB902 and FL901 were considerably lower than the canister pressure which suggests that the connection between the canister and sensors was not complete. The slow pressure decay of the canister pressure at FL901, and UB902 is thought to have occurred as gas exited the deposition hole. It should be noted that FL901 was pressurised in both GT2 and GT4 and UB902 was pressurised in GT2 when testing from canister filter FL903. It is probable that the FCT test exploited pre-existing features in the clay from this earlier testing. It is evident that the significantly larger volume of gas used in the FCT had not altered the gas propagation behaviour, except that an initial gas

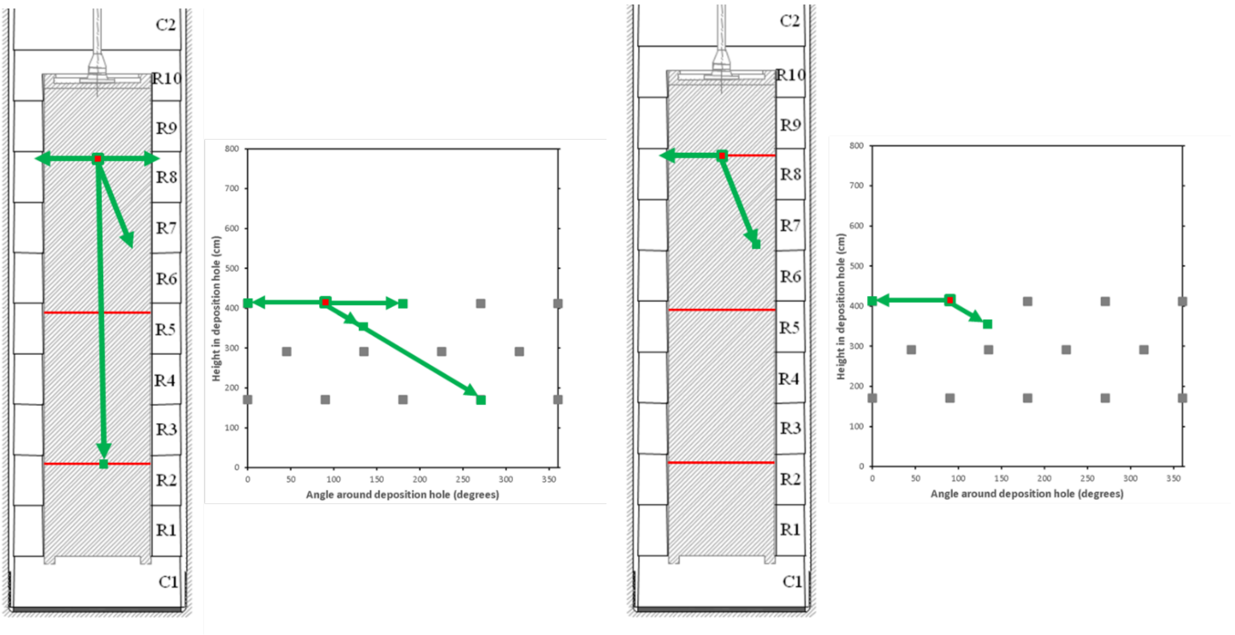

(a)

(b)

Figure 2.93: Schematic of the direction of gas flow during gas testing in upper filter FU910. a) Flow in Gas Test 3; b) Flow in Gas Test 5.

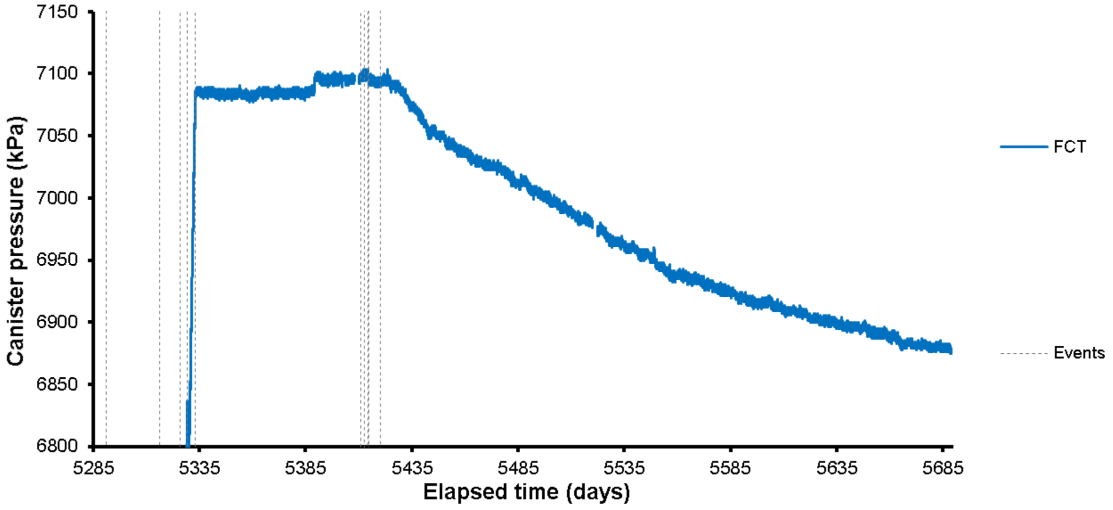

Figure 2.94: Pressure of the canister during the Full Canister Test.

pressure reduction was not seen in the FCT test as gas entered the bentonite buffer.

Conceptual model of gas movement

The following conceptual model of gas movement has been devised from all observations from all gas injection tests. The interface between the canister and buffer played an integral role in gas movement. In several gas injection tests the gas reached isolated points within the deposition hole (various sensors/filters). In GT2 gas moved 180° around the canister surface from filter FL903 to FL901 whilst no pressure change was observed in filters FL902 or FL904. This demonstrated that the entire interface was not conductive. It is possible that gas entered the buffer. However, it is improbable that whilst migrating in the buffer that it managed to intercept FL901 on the opposite side of the canister. Therefore, it is likely that localised gas pathways formed that moved around the canister surface intercepting a limited number

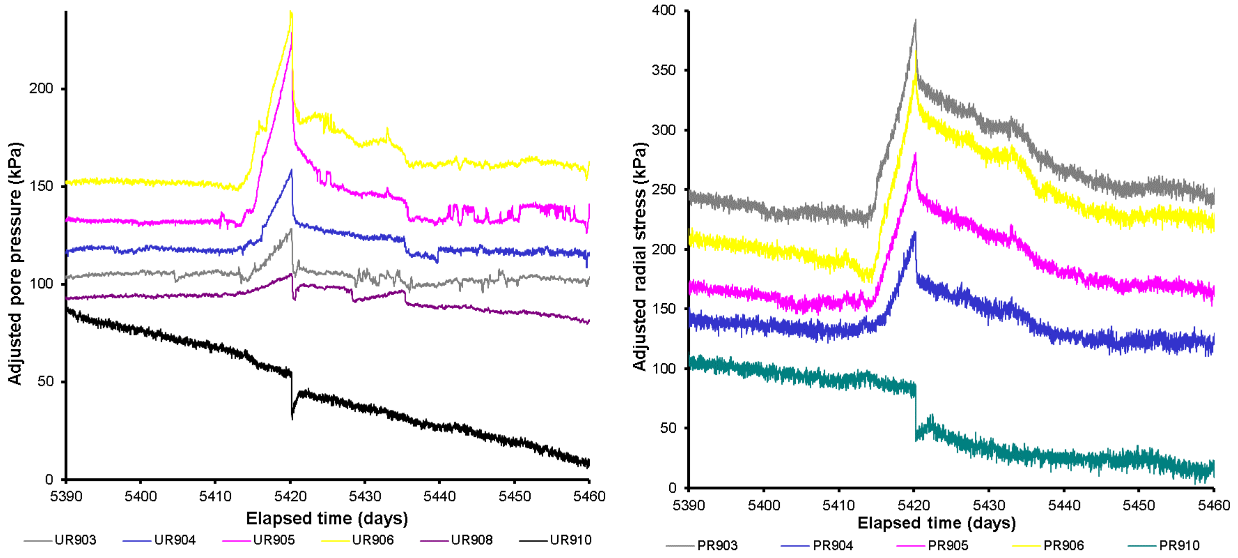

(a) (b)

Figure 2.95: Detail of radial stress and pore fluid pressure at the rock wall around the time of gas entry. a) Pore pressure at the deposition wall; b) Radial stress on the deposition wall.

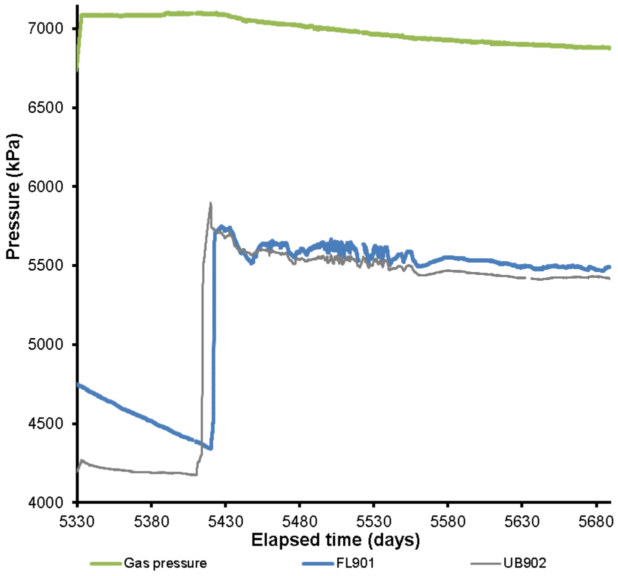

Figure 2.96: Detail of sensors that showed evidence of gas pressurisation during the Full Canister Test.

of sensors. In test GT3, the gas injection stage was prolonged. This showed that movement occurred on multiple pathways. A single pathway could not have seen the pressurisation of sensors over a series of pressure increase events. Therefore, multiple pathways were forming at the same time, even once a predominant pathway had formed allowing gas to exit the deposition hole. Test GT3 also showed behaviour of episodic flow. Many sensors increased to the gas injection pressure through a series of pressure increases. This shows that the pathways that formed were not continuously open, and that gas movement was like the propagation of bubbles. This may suggest that pathways became unstable as they grew, i.e., as they lengthen there was sufficient energy to keep the pathway open. Therefore, pathways were not simple tensile fractures in the bentonite.

Figure 2.97 shows a general model to describe gas movement. At the start of the experiment there was a nominal 10mm gap between the canister and the bentonite rings (*Figure 2.97*a). Water started

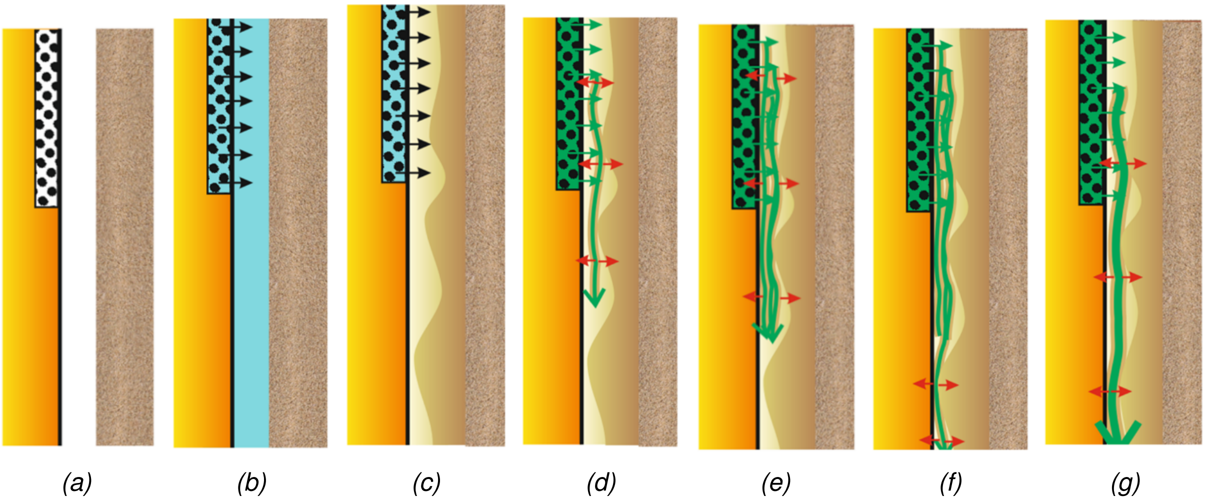

Figure 2.97: Conceptual model of gas flow. See text for full description.

to hydrate the buffer and pellets from the outside of the deposition hole resulting in swelling and the slow closure of the engineered gap. Water was also carefully introduced from the canister filters to aid swelling of the buffer (*Figure 2.97*b). This resulted in the formation of a zone close to the canister that filled the engineered gap that was of variable density (*Figure 2.97*c). In general, this zone was relatively homogenous as shown by the geotechnical results, but a clear zone of different properties was formed close to the canister. The radial stress at the deposition hole wall was seen to be heterogeneous and this may derive from variations in the properties of the pellet zone, which will have resulted in variations in the properties of the canister/buffer interface. This is shown schematically in *Figure 2.97*c. As gas injection occurred, gas entered the low-density interface zone resulting in mechanical opening of pathways seen as increases in radial stress (*Figure 2.97*d). As shown in *Figure 2.97*d, the gas pathway propagated as far as it could, reaching a zone of higher density that it could not pass. This may explain the pre-cursor flow event seen in GT1. More gas pathways formed (*Figure 2.97*e) or the single formed pathway increased in size. This continued until sufficient energy was available to overcome the obstruction identified in *Figure 2.97*d and the pathway started to grow (*Figure 2.97*e). This resulted in the formation of a dominant pathway (*Figure 2.97*f) which ultimately found a way out of the buffer. *Figure 2.97* shows the concept for a single pathway. All evidence suggests that multiple localised pathways formed coincidently. Therefore, the feature that stops one pathway continuing may result in other pathways forming as more gas entered the system. However, GT3 shows that pathways that demonstrated episodic flow re-opened with time.

In most tests it was evident that gas had found a way out of the deposition hole, most notably GT2 when the injection of neon was detected in the pressure-relief holes. The conceptual model for gas movement suggests that the interface between the canister and buffer was exploited. It would be difficult for gas to leave the low-density interface zone and enter the higher-density buffer to propagate to the deposition hole wall. Therefore, it was interpreted that gas moved along the interface between two blocks/rings in the deposition hole. During decommissioning, this interface was seen to be still prominent with limited self-healing. Axial stress in the deposition hole was seen to be high as shown by the PB9xx sensors. The interfaces would have been mechanically closed by the stress field, but the interface was likely to have properties favourable to gas movement compared with the internal body of each bentonite block/ring. Movement along the interface was likely to be similar to the conceptual model introduced in *Figure 2.97*.

Peak pressure evolution

One of the primary reasons for repeating the gas injection tests was to see if the gas transport properties changed with time, as the buffer matured. Conducting four gas injection tests in the same filter offered a good insight into the controls on the gas injection pressure. It has been shown that stress was considerably heterogeneous within the deposition hole. Considerable variation was seen at the deposition hole wall in the 20 sensors, as was axial and radial stress on the canister surface at just 3 locations. Unfortunately, stress was not measured at each canister filter and therefore local stress had to be estimated. The radial sensor array was positioned such that no sensor was directly opposite FL903 on the rock wall, had testing occurred in the mid-plane canister filters then there would have been radial stress sensors opposite the injection filter. This meant that the closest sensors were 45° around the canister at PR908 and PR909 on the same level as the injector, at 45° at PR912 and PR913 on the next level above the injector, and directly below the injector at PR905. From these, and stress sensor PC902, which was on the level above the injector but 135° around the canister surface, local stress was estimated. The heterogeneity seen in the canister stress data means that this estimate of stress at FL903 may be inaccurate.

Figure 2.98 shows gas peak pressure increased throughout the history of the full test. The data is shown with a logarithmic best-fit, which describes the increase in peak pressure well. *Figure 2.98* shows the interpolated estimate of radial stress. This also increased during the Lasgit test and is also shown with a logarithmic fit. However, the fit to the data is not as good. Also shown is the value of radial stress at the surface of the canister at PC902. This was shown to increase with time and is also shown with a logarithmic fit. As with interpolated radial stress, the fit is not perfect. Displayed is the periods of when artificial hydration was active, with grey showing when artificial hydration was paused. The end of artificial hydration resulted in radial stress levelling and the stress at PC902 reducing. It is apparent that the ending of hydration greatly impacted the local stresses in the system. However, no such affect is seen in the gas peak pressure. *Figure 2.98*b shows the results for interpolated radial stress and for PC901 for only the first three tests prior to the ending of artificial hydration. This shows a good logarithmic fit. However, the form of the slope was much steeper for both radial stress and PC901 than for the gas peak pressure. These observations suggest that gas peak pressure was not solely dependent on the stress within the system.

Hydraulic conductivity determined from the two-stage constant head tests showed that the hydraulic properties reduced in filter FL903 over the life of the Lasgit test. This data was also independent of artificial hydration. *Figure 2.99* shows the relationship between hydraulic conductivity and the peak gas pressure. This shows that peak pressure increased in FL903 as the hydraulic conductivity reduced. This is not surprising as the buffer matured in response to hydration and increasing stress on the system.

Comparing all gas injection tests

Figure 2.100 shows gas peak pressure for the six gas injection tests. Peak pressure increased for tests conducted in filter FL903 as described by a logarithmic fit. Peak pressure at FU910 was at a lower pressure and is also shown with a logarithmic fit, for consistency with FL903. Neither filter showed an influence from artificial hydration ending, even though stress had reduced in the system as a result. It appears that gas peak pressure was independent of this boundary condition. Previously, it had been suggested that stress was the primary controller of gas peak pressure. *Figure 2.101* shows the relationship between gas peak pressure and stress for the seven tests in Lasgit and for laboratory tests (Graham *et al.*, 2016). The dashed line in *Figure 2.101* represents unity, when stress on the canister would be equal to the gas peak pressure. One test in FU910 and the FCT were close to this condition. However, most tests in FL903 occurred at a pressure up to 600 kPa above local stress. This may be as a result in inaccurate estimates of stress at the filter but may represent a need for a slight excess pressure to cause peak conditions. It should be noted that gas peak pressure was not significantly above local stress, as had been seen in a limited number of laboratory-scale experiments (*Figure 2.101*b). Therefore, stress was the primary control on gas migration but hysteresis in the system meant that a reducing stress field had not altered the gas peak pressure.

Figure 2.102 shows the relationship between hydraulic conductivity determined from two-stage constant head tests with peak gas pressure. All the data suggest that peak gas pressure scales with hydraulic conductivity and as the buffer matured, the peak pressure increased as hydraulic conductivity reduced. This isn't surprising as both hydraulic and gas properties will be dependent on the pore network of the buffer, and as the buffer matured, porosity would reduce, and water and gas flow would become more difficult. The progress of hydraulic properties appears independent of, or at most affected only very slightly by the ending of artificial hydration. It is suggested that hydraulic conductivity evolution was a secondary

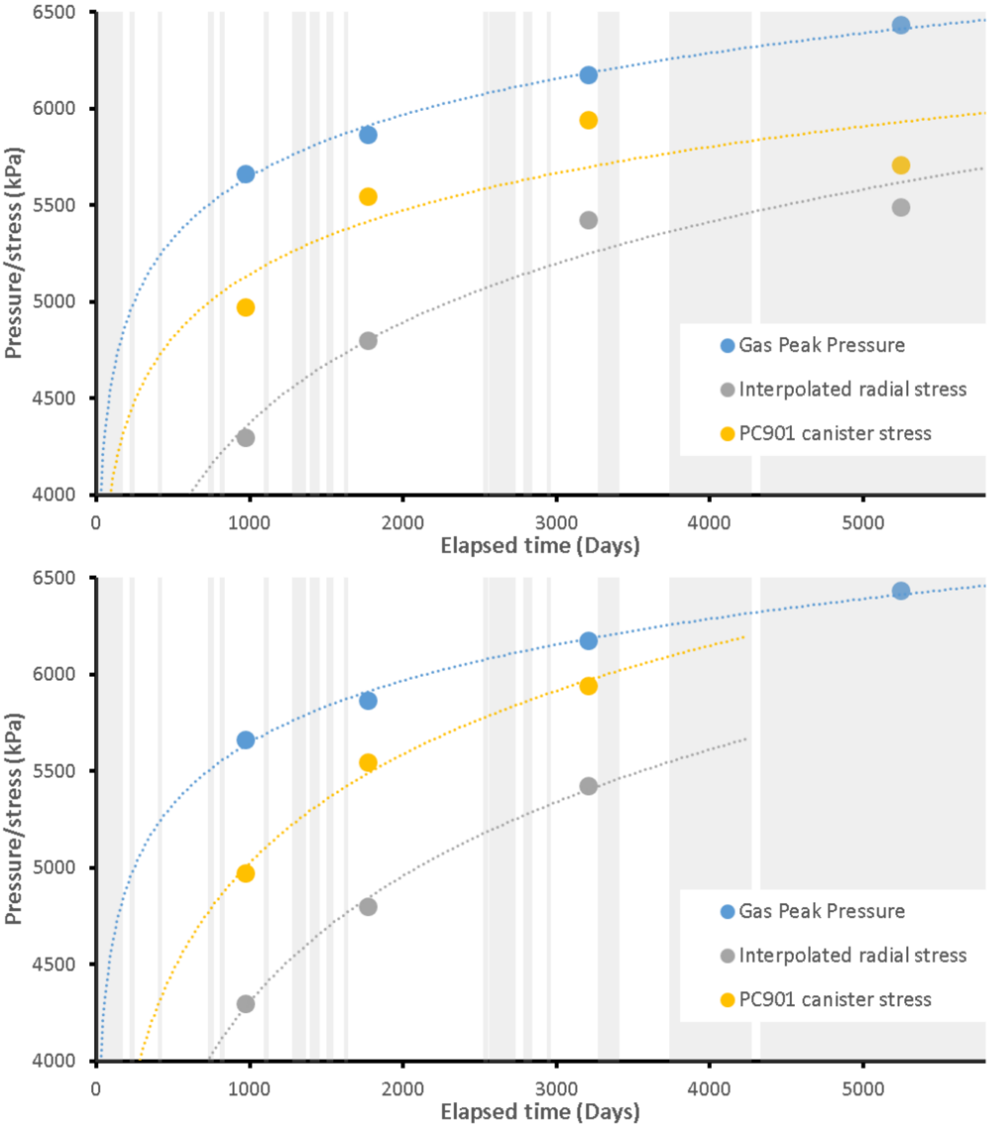

Figure 2.98: Increase in peak pressure, interpolated radial stress, and canister stress for the four gas injection tests in FL903. a) All test results; b) Estimated stress only up until the end of artificial hydration.

control on gas peak flow, although this is a proxy for the maturity of the buffer. This control was partly dependent on the stress field.

2.3.7. Summary

Comment on maturation of the buffer

Ideally, the KBS-3 system should mature to full saturation, with limited heterogeneity in the deposition hole in terms of stress and pore pressure. Net pressure should evolved to a small finite value, as should suction. The saturation of the bentonite should reach unity and not vary significantly within the deposition hole. This was not the case. It was impractical to run Lasgit for longer and the gradual failure of experimental components showed that the system was slowly failing. However, even within this, non-ideal, context clear conclusions could still be drawn.

The definitive observations of buffer maturity come from the results of hydraulic testing and this can be compared with the geotechnical observations. Hydraulic conductivity of repeat testing at canister filters showed a reduction with time. At Day 870, hydraulic conductivity was 1.3 x 10^{-12} m s^{-1}, decreasing to 1.7 x 10^{-13} m s^{-1} at Day 5266. This represented a near order of magnitude reduction in conductivity over a 12-

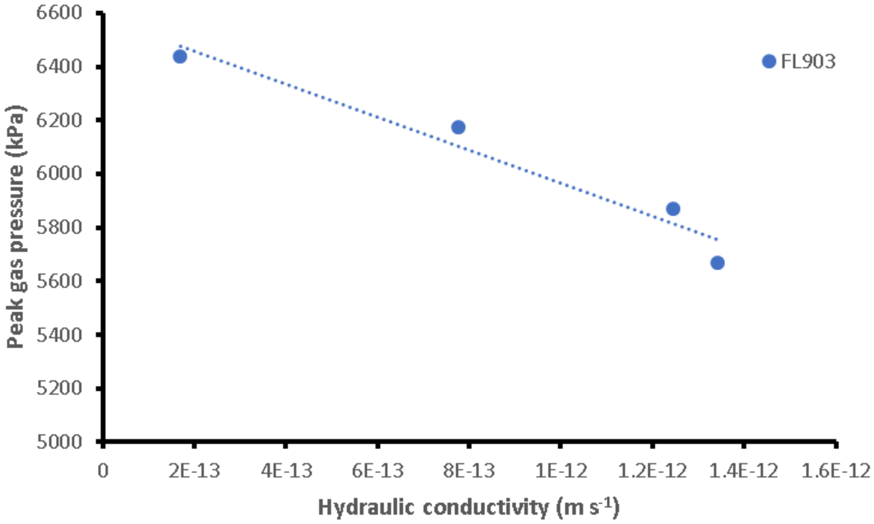

Figure 2.99: Relationship between hydraulic conductivity and peak gas pressure.

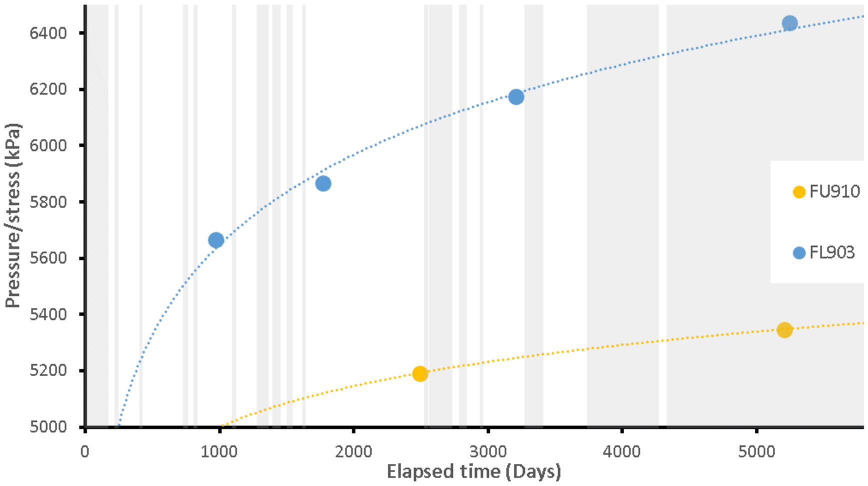

Figure 2.100: Gas peak pressure evolution with time for six gas injection tests in Lasgit.

year period. For injection filter FU910 the reduction was not as great, reducing from 1.7 x 10^{-12} m s^{-1} at Day 2086 to 7.8 x 10^{-13} m s^{-1} at Day 5235. Over the same period, specific storage increased at both locations. There is limited data and considerable scatter in the results but there does not appear to be a defined asymptote to the changes as the buffer continued to mature. Most of the canister filters were hydraulically tested around Day 3500. This showed a variable result with hydraulic conductivity between 7.1 x 10^{-13} m s^{-1} and 4.2 x 10^{-12} m s^{-1}. This showed that the transport properties close to the canister were varied over a 6-fold range. Considerable variation was seen in the geotechnical properties close to the canister and in the pellet region. This may reflect the hydraulic conductivity heterogeneity. However, the geotechnical data showed that the average saturation for the 1522 samples in the buffer was 0.999, meaning that the buffer was nearly fully saturated. The geotechnical data also showed a distinct difference between the properties of segments and rings before emplacement, which at the end of the test had homogenised. Therefore, the bentonite buffer appeared to be in equilibrium, but was not in hydraulic or stress equilibrium and was continuing to mature.

Summary of gas injection testing

All four tests conducted in canister filter FL903 showed a similar pressure response at peak gas pressure, which was different to that seen in FU910. At FL903 pressure rapidly reduced at peak pressure, with

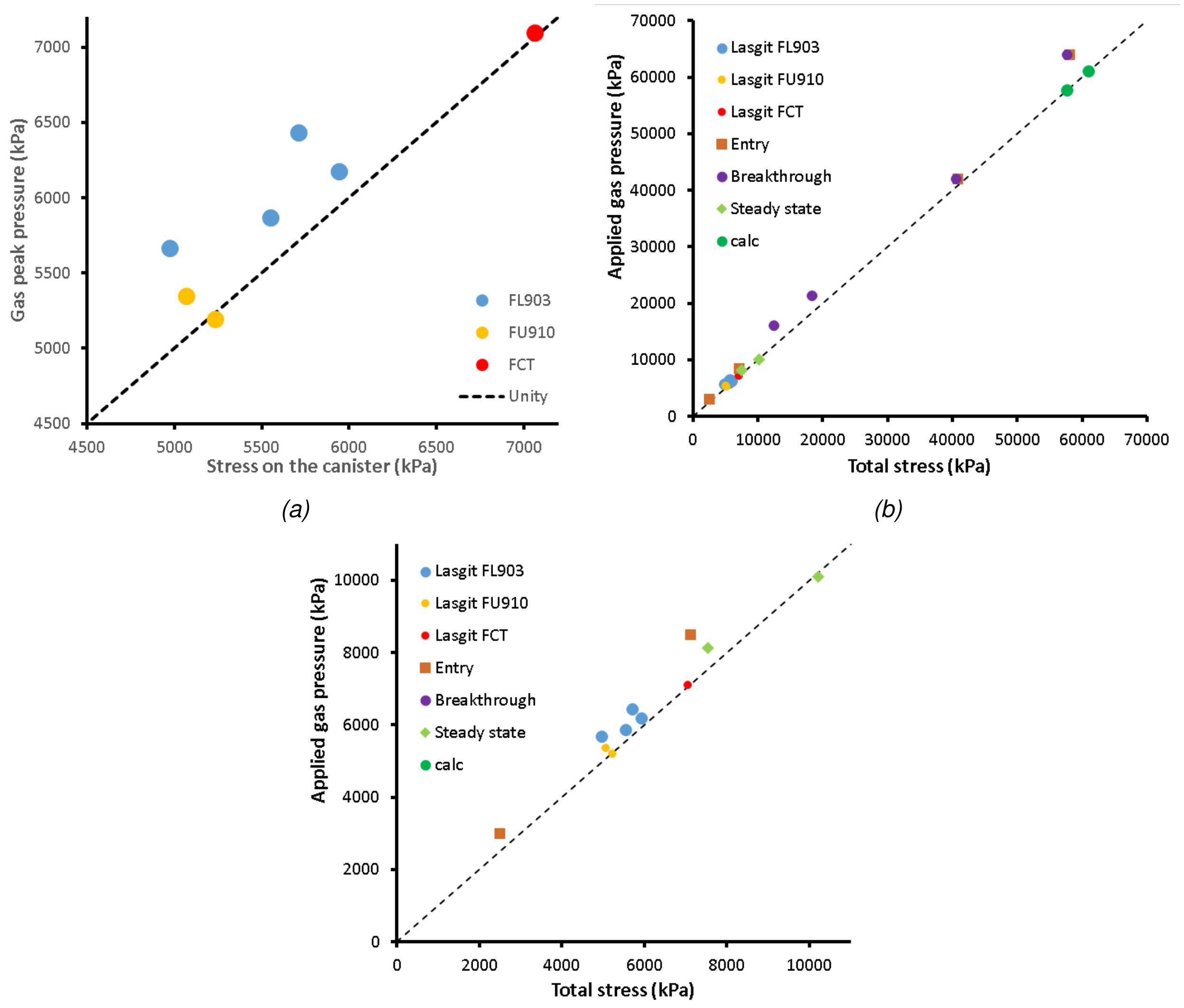

(a)

(b)

(c)

Figure 2.101: The relationship between gas peak pressure and radial stress on the canister for all gas injection tests in Lasgit. a) Data from Lasgit; b) Compilation of data from tests in bentonite; c) Detail of data compilation.

generally two events occurring during the initial pressure reduction. Pressure recovered to a single slope of pressure reduction when the data were corrected for differences in injection flow rate. In tests conducted at FU910, the initial pressure reduction at peak gas pressure was followed by a recovery in pressure and a secondary peak either at a similar or higher pressure to the initial peak. The pressure reduction in the first test was smaller than observed in subsequent tests at both filter and this was related to the difference between formation of new pathways and the re-opening of existing pathways in repeat tests.

In the first test conducted at FL903, a pre-cursor flow event was observed, followed by a spike in flow. Most tests in FL903 saw one or more spikes in flow, showing that pathway formation was progressing in stages. After the short-lived spike in flow, the flow into the clay decreased to be lower than the flow into the system and gas pressure started to increase. This continued until a secondary peak in pressure was seen and the flow into the clay was then marginally greater than flow into the system and pressure slowly decreased. A similar flow response was seen at FU910. However, the initial peak in flow was greater and the flow into the clay reduced to be less than flow into the system for much longer, resulting in an increasing pore pressure. No pre-cursor flow events were seen at this filter.

Extended testing gave useful insights into gas flow. In GT2 a series of pressure reductions and recovery

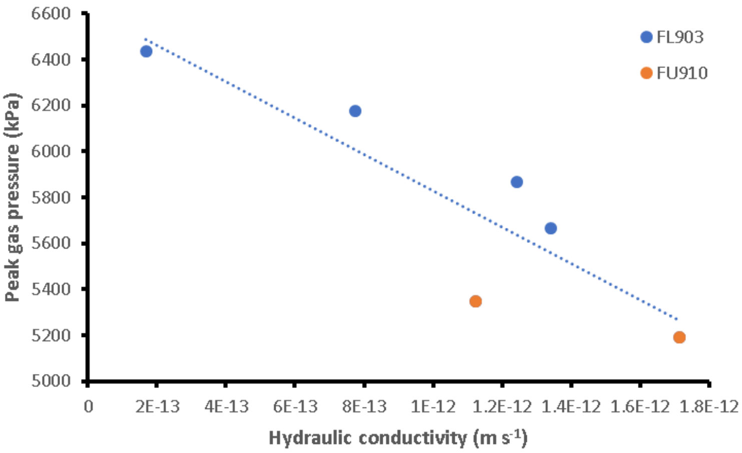

Figure 2.102: The relationship between gas peak pressure and hydraulic conductivity six gas injection tests in Lasgit.

were seen. This suggests that flow paths were developing with time. The pressure reduction occurred as a conductive feature(s) allowed gas pressure to reduce, probably due to gas leaving the deposition hole. This pathway partially closed as gas pressure reduced and as a result, the conductivity of the pathway also reduced, and gas pressure increased until the pathway was re-opened and pressure reduced once more. The results from GT4 confirm this. Gas flow into the system was reduced in two steps, once stable flow had been established, each approximately halving the flow of the previous step. On the third step, pressure started to increase, suggesting that the force required to keep pathways open was flow-rate dependent. As flow was reduced, the pathway partially closed, decreasing conductivity and thus increasing pressure. In GT3 and GT5, prolonged gas injection resulted in a series of peaks in gas pressure. This behaviour is similar to that seen in 'fault valve behaviour' or episodic flow, where the conductivity of a feature gets reactivated at a given pressure, allowing fluid to flow and pressure to decrease. In the two tests conducted at FU910, this may mean that the pathway connecting the gas to the wall rock was acting as a valve and that the pathways were unstable.

The primary control of gas peak pressure was local stress. This was difficult to determine in filters FL903 and FU910 with a high degree of certainty. However, estimates of the local stress show that gas peak pressure occurred at, or a little above, local stress. The maximum difference between the local stress and peak pressure was ~600 kPa. A secondary control on gas peak pressure was the maturity of the buffer, which was linked to the development of stress. The ending of artificial hydration resulted in stresses in the system being reduced, yet gas peak pressure continued to increase. The buffer continued to mature even though stress had reduced. This was confirmed in the hydraulic conductivity data that showed continued reduction independent of whether artificial hydration was occurring. The results from Lasgit show that gas peak pressure was related to the modelled hydraulic conductivity determined from two-stage constant head tests.

The movement of gas was inferred from the array of pore pressure and radial stress sensors at the rock wall, and from the direct movement of gas to sensors during the test. In the first test in FL903 (GT1), the data indicate that the gas moved downwards along the outside of the canister and then along the interface between two bentonite blocks. In test GT2, the gas moved 180° around the canister, before migrating to the base of the canister and later finding a way from the deposition hole, most likely between bentonite blocks. This may have exploited the same features formed in GT1. In GT4, gas also moved to FL901 and it is likely that this test re-activated features formed in GT2.

In the first test conducted in FU910 (GT3), considerable movement was seen. The gas first moved 90° around the canister to FU909, before intercepting FU911, the filter 90° the other way around the canister. Gas then moved downwards, intercepting a stress sensor (PC903), before reaching FL904, the filter on the lower array of the canister filters. In GT5, this repeat test immediately reached FU909 and PC903. This showed re-activation of some of the pathways formed in GT3, but not the re-activation of all. In the Full Canister Test, gas reached UB902 and FL901, pathways that had been established in previous tests using FL903. Therefore, there was evidence that subsequent gas injection tests behaved similarly and that pathways may have re-activated. However, the migration of gas was not identical between tests, with new pathways forming. The formed pathways then, at least partially self-sealed.

Gas injection tests were conducted from canister filters FL903, FU910, and the FCT filter. In all seven tests, gas injection occurred around the peak pressure and it appeared that gas found a pathway out of the deposition hole. This resulted in the careful venting of pressurised gas in a controlled manner that had little to no long-term effect on the physical properties of the buffer. Repeat gas testing suggested that pathways were extant for prolonged periods and were sometimes re-activated by subsequent tests in the same filter. Moreover, testing in filters may have intercepted pathways created in previous tests at other filters.

2.3.8. Key learning points

2.3.8.1. New knowledge acquired

All observations from Lasgit support and give argument to the handling of gas transport through compact buffer bentonite in the manner presented at the beginning of this section:

1. In all tests, regardless of initial gas volume, the movement of gas occurred at a pressure very close to the local total stress.
2. While not specifically tested, no signs of localised consolidation of the bentonite were observed.
3. The measured peak gas pressures should not lead to any mechanical damage to the buffer or to other barrier components in the repository.
4. Peak gas pressure is linked to the hydraulic permeability of the buffer and the ease at which gas can exit a deposition hole.
5. Gas is transported through a limited number of dilatant pathways. The pathways are expected to be small, in relation to the total volume of the buffer, and temporally variable.
6. No desaturation, of the bentonite buffer, as a result of gas transport was observed.
7. Over the timescale of the project, pathway closure was only partially successful in the absence of injected water.
8. The gas pathways are expected to slowly close at a finite “shut-in” pressure.
9. Gas migration through a bentonite is highly unlikely to alter the favourable hydromechanical properties of the barrier.
10. The impact of emplaced and long-lived persistent heterogeneities within the bentonite on gas pressure remains unclear.

The results from GT1 through GT6 and the FCT show gas transport processes are scale invariant and insensitive to the initial upstream gas volume. This may have been expected but had never been tested, beyond laboratory scales, prior to Lasgit. The role of water and the maturity (i.e. state of homogenisation of the buffer) have been shown to strongly impact gas flow in the buffer. While the Lasgit system was not in hydraulic equilibrium, given the similarities in behaviour between individual tests and those performed in the laboratory, it is reasonable to assume that while peak gas pressures would increase, and any change would be relatively small, linked to increases in swelling and porewater pressure. The absence of high peak gas pressures such as those sometimes observed during laboratory testing is an important outcome from Lasgit. While gas-induced consolidation may not have been directly observed, the similarities in gas migration behaviour at both scales indicate that it can be further investigated in the laboratory.

2.3.8.2. Impact of acquired knowledge

The main objectives for the Lasgit experiment were fully achieved during the 17-year project, allowing the upscaling of laboratory-derived process understanding to the field scale. The findings provide fundamental information that addresses key questions relating to the treatment of gas in safety assessment and the resulting implications for the evolution of the buffer in the event of a deposition hole containing a defective canister. The main conclusions of the project have already been incorporated into the safety case submitted by SKB for disposal in Sweden. The findings will continue to feed into research into properties of bentonite in disposal concepts. The full-scale Lasgit experiment showed similar behaviour to laboratory experiments. As such, further knowledge can be obtained from targeted laboratory experiments as opposed to complex field-scale experiments.

2.3.8.3. Remaining knowledge gaps

Taken in their totality, the observations from Lasgit support the idea that gas is mainly transported through dilatant pathways (mechanism 3) in a saturated buffer bentonite. The presence of emplacement and long-lived persistent heterogeneities within the bentonite are likely to impact both gas pressure and the size, position and number of gas pathways. However, the impact of this observation is unclear at the present time and remains an open question.

2.3.8.4. Recommendations for the future

Targeted laboratory-scale experiments can be used to close the remaining open questions. These questions include, but are not limited to:

- The influence of temperature on the long-term properties of the buffer
- Homogenisation and the prevalence of heterogeneities within the buffer
- The number, size, and distribution of dilatant gas pathways
- The long-term properties of interfaces between bentonite blocks

References

Cuss, R.J., Harrington, J.F., Tamayo-Mas, E., Noy, D.J., Birchall, D.J., Sellin, P., and Nord, M. (2022) Large scale gas injection test (Lasgit) performed at the Äspö Hard Rock Laboratory. Final report. Svensk Kärnbränslehantering AB (SKB) Technical Report TR-22-06, SKB, Stockholm, Sweden. Pp.529. https://www.skb.com/publication/2501822

Donohew, A.T., Horseman, S.T. and Harrington, J.F. (2000). Gas entry into unconfined clay pastes between the liquid and plastic limits. Chapter 18. In: Environmental Mineralogy - Microbial Interactions, Anthropogenic Influences, Contaminated Land and Waste Management (eds J.D. Cotter-Howells, L.S. Campbell, E. Valsami-Jones and M. Batchelder), Mineralogical Society, London, Special Publication No. 9, 369-394.

Graham, C.C., Harrington, J.F. and Sellin, P. (2016) Gas migration in pre-compacted bentonite under elevated pore-water pressure conditions. *Applied Clay Science*, **132**, pp.353-365.

Gray, M., Kirkham, T.J., Lin, A.W.-L., and Graham, J. (1996). On the gas breakthrough resistance of engineered clay barrier materials proposed for use in nuclear fuel waste disposal. In: Proc. CNS Int. Conf. on Deep Disposal of Radioactive Waste, Canadian Nuclear Society, Winnipeg, Manitoba, 16-19 Sept.

Harrington, J.F. and Horseman, S.T. (1999). Gas transport properties of clays and mudrocks. In: *Muds And Mudstones: Physical And Fluid Flow Properties* (eds A.C.Aplin, A.J. Fleet, and J.H.S. Macquaker). Geological Society of London, Special Publication No. **158**, 107-124.

Harrington, J.F. and Horseman, S.T. (2003). Gas migration in KBS-3 buffer bentonite: Sensitivity of test parameters to experimental boundary conditions. *Report* **TR-03-02**. Svensk Kärbränslehantering AB (SKB), Stockholm, Sweden.

Harrington, J.F., Graham, C.C., Cuss, R.J. and Norris, S., (2017). Gas network development in a precompacted bentonite experiment: Evidence of generation and evolution. *Applied Clay Science*, **147**, pp.80-89.

Horseman, S.T., Harrington, J.F. and Sellin, P. (1997). Gas Migration In Mx80 Buffer Bentonite. In: *Proc. Scientific Basis For Nuclear Waste Management XX, Boston, 2-6 Dec., 1996* (eds W.J. Gray And I.R. Triay), MRS Symposia Proceedings, Vol. 465, Materials Research Society, Warrendale, Pennsylvania, 1003-1010.

Horseman, S.T., Harrington, J.F. and Sellin, P. (1999). Gas migration in clay barriers. In: Pusch, R. and Yong, R.N. (eds) *Microstructural Modelling of Natural and Artificially Prepared Clay Soils with Special Emphasis on the Use of Clays for Waste Isolation* (1999 Special Edition), Engineering Geology, Vol 54, pp139-149, Elsevier, Amsterdam.

Horseman, S.T., Harrington, J.F. and Sellin, P. (2004). Water and gas flow in Mx80 bentonite buffer clay. In: Symposium on the Scientific Basis for Nuclear Waste Management XXVII (Kalmar), Materials Research Society, Vol. 807. 715-720.

Horseman, S.T. (1996). Generation and migration of repository gases: Some key considerations in radioactive waste disposal. In: Proc. Int. 2-Day Conference, London, 21-22 Nov. 1996, IBC Technical Services, Energy Division, 26 pp.

Hume, H.B. (1999). *Gas breakthrough in compacted Avonlea bentonite*. MSc thesis, Department of Soil Science, University of Manitoba, Winnipeg, Canada.

Johannesson, L.-E. (2003) Djupförvarsteknik: Large Scale Gas Injection Test: Manufacturing of buffer for the large scale gas injection test. *Technical Document* **TD-04-01**. Svensk Kärnbränslehantering AB (SKB), Stockholm, Sweden

Marschall, P., Horseman, S. and Gimmi, T., 2005. Characterisation of gas transport properties of the Opalinus Clay, a potential host rock formation for radioactive waste disposal. *Oil & gas science and technology*, **60**(1), pp.121-139.

Ortiz, L., Volckaert, G. and Mallants, D. (2002) Gas generation and migration in Boom Clay, a potential host rock formation for nuclear waste storage. Engineering Geology, 64, 287-296.

Pusch, R., Hökmark, H. and Börgesson, L. (1987). Outline of models of water and gas flow through smectite clay buffers. *SKB Technical Report* **87-10**, Stockholm, Sweden.

Pusch, R., Ranhagen L. and Nilsson, K. (1985). Gas migration through Mx-80 bentonite. *Nagra Technical Report* **NTB 85-36**, Wettingen, Switzerland.

Rodwell, W.R., Harris, A.W., Horseman, S.T., Lalieux, P., Müller, M., Ortiz Amaya, L. and Pruess, K. (1999). Gas migration and two-phase flow through engineered and geological barriers for a deep repository for radioactive waste. EC/NEA Status Report EUR 19122EN, European Union, Luxembourg.

Sellin, P. and Harrington, J.F. (2006). Large-Scale Gas Injection Test (Lasgit) Current Status. American Nuclear Society High Level Waste Meeting, Las Vegas.

SKB (2009) Design premises for a KBS-3V repository based on results from the safety assessment SR-Can and some subsequent analyses. Technical Report TR-09-22. Svensk Kärnbränslehantering AB (SKB), Stockholm, Sweden

SKB (2011) Long-term Safety for the Final Repository for Spent Nuclear Fuel at Forsmark: Main Report of the SR-Site Project. SKB Technical Report TR-11-01. Svensk Kärnbränslehantering AB (SKB), Stockholm, Sweden.

Tanai, K., Kanno, T., and Gallé, C. (1997). Experimental study of gas permeabilities and breakthrough pressures in clays. In: Scientific Basis for Nuclear Waste Management XX, Boston (eds W.J. Gray And I.R. Triay), MRS Symposia Proceeding Vol. 465, Materials Research Society, Warrendale, Pennsylvania, 1003-1010.

Weetjens, E. and Sillen, X. (2006) Gas Generation and Migration in the Near Field of a Supercontainer-Based Disposal System for Vitrified High-Level Radioactive Waste, Proc. 11th Int. High-Level Radioactive Waste Management Conf. (IHLRWM), Las Vegas, Nevada, April 30–May 4, 2006.

Wikramaratna, R.S., Goodfield, M., Rodwell, W.R., Nash, P.J. and Agg, P.J., 1993. A preliminary assessment of gas migration from the copper/steel canister (No. SKB-TR--93-31). Swedish Nuclear Fuel and Waste Management Co.

.

British Geological Survey (BGS)

2.4. Pathway closure and sealing processes - FracVis (UKRI-BGS)

2.4.1. Introduction & Objectives

As part of the FORGE project, Cuss et al. (2014) proposed the conceptual model of gas flow in Callovo-Oxfordian claystone shown in Figure 2.103. A dendritic pattern of dilatant pathways was suggested, these grow until a dominant pathway(s) allows flow to exit the sample.

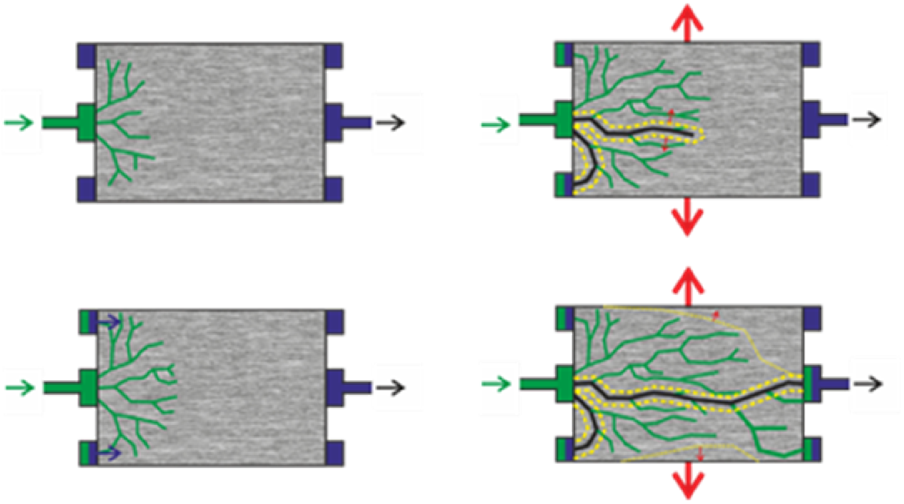

Figure 2.103: Conceptual model of gas flow in Callovo-Oxfordian claystone.

In compact clay-rich material, the nano-scale dimensions of gas pathways make real-time imaging of gas movement exceptionally challenging. Postmortem examination of samples yields limited information because of the transient nature of the pathways (self-sealing). This necessitates the use of nano-particulates or analogue systems to make observations that can confirm experimental data. BGS developed a bespoke Fracture Visualization Rig (FVR; Wiseall et al., 2015) capable of directly observing the initiation, propagation, coalescence, sealing etc of gas pathways in clay pastes under load. To date, all observations have confirmed conceptual models of gas pathway propagation from triaxial systems and continue to expand our knowledge of the processes governing dilatant pathway propagation. In addition, results gained from the FVR show gas pathways can seal and on re-pressurisation new pathways form (Cuss et al., 2017). The FVR uses analogue clay samples, either as pre-compacted samples from crushed material or a clay paste, which are then confined in an oedometer-type geometry up to a normal stress of 3 MPa. This limit is governed by the strength of the quartz-fused glass window that allows direct observation of the sample during gas flow.

Analogue tests allow direct observation of pathway growth and are quick to perform, meaning that a comprehensive study with as many as 100 tests can be performed as quickly as a single test in competent rock. With that in mind, an experimental programme of around 50 experiments was devised to answer specific research questions:

- Laboratory tests have shown variation in parameters. This leads to questions about repeatability and whether pathway formation is stochastic. Performing tests in an identical manner five times allows the qualitative and quantitative comparison of pathway growth and helps in determining whether pathway growth is random or controlled by other factors, such as material fabric and the presence of pre-exiting weaknesses.
- Qualitatively, similar results of gas flow are seen in triaxial tests in Boom Clay, Callovo-Oxfordian claystone, Opalinus Clay, and pre-compacted bentonite. Repeat testing in each of these materials would also allow comparison to be made between the pathway formation in the different clays.

- Moisture content has been seen to be a control on gas flow properties. A study of gas flow in a range of water contents would allow qualitative and quantitative statements to be made on the role of moisture content on the physics governing gas flow.
- The self-sealing properties of clay-rich rocks has been shown to be an effective mechanism reducing the flow properties of fractures, faults, and gas pathways. It is uncertain what happens during a second episode of gas injection. Therefore, the FVR can be used to answer whether pre-existing pathways are re-opened or whether new pathways form.
- If gas is formed in a repository that is sufficient in magnitude to result in advective gas transport, episodic flow is likely. This leads to questions of what happens if gas supply changes, stops, and/or re-starts. Questions also exist whether pathway growth would continue at a constant pressure or whether it would stop. The FVR is well placed to run experiments to directly observe the physics and to make inferences of what happens in competent rock.
- It has been speculated that pressurisation rate plays a role in gas movement. This is difficult to observe in the laboratory where experiments are slow yet are still orders of magnitude quicker than would be expected in a full-scale repository. Analogue tests run in much shorter time scales, with a test performed within 2 hours in a clay paste compared with tests that takes 3-months under triaxial conditions, also conducted by BGS as part of EURAD-GAS. Therefore, it is much easier to perform tests over different timescales, with three orders of magnitude planned. This will aim to answer whether there is a difference in the physics driving gas flow related to pressurisation rate.
- Back filling of repository galleries is proposed using a sand/bentonite mix. The gas flow properties are likely to vary as the sand/bentonite ratio changes. The FVR allows direct observation over a range of mixtures and could determine at what mixture the physics driving gas flow transitions from dilatancy to two-phase flow. We know that gas movement in pure sand is by two-phase flow and that movement in pure clay is by dilatancy. It is an aim to determine at what point there is a transition from one to the other.

The test programme therefore aimed to answer fundamental questions about gas flow in clay-rich rocks.

2.4.2. Experimental set-up

2.4.2.1. Description of apparatus

The experimental programme was designed to perform at least 43 experiments using the Fracture Visualization Rig (FVR; Figure 2.104). This apparatus was designed and manufactured by the Transport Properties Research Laboratory at the BGS (Wiseall *et al.*, 2015; Cuss et al., 2017). The FVR consists of a 150 mm diameter, 50 mm thick fused silica glass window held rigidly in place by a 230 mm diameter steel collar, resulting in a 110 mm diameter viewing window. The collar has twelve bolts spaced at 30° intervals that when tightened can impose a normal stress of up to 3 MPa. The thin clay sample was located between the lower steel platen and the glass window and was held laterally in place by a porous plastic filter. This allowed excess water to drain from the clay paste but retained the clay within the 150 mm diameter area. A paper gasket was placed between the steel collar and the glass window to protect the silica fused glass.

Gas or water was injected into the clay paste at the centre of the lower platen through a 3 mm porous steel filter. The permeant was injected and controlled by a high precision Teledyne ISCO-260D syringe pump, which was connected to a gas-water interface vessel. The syringe pump could achieve an injection pressure ranging from 0.2 to 13 MPa. Although the glass window only had a maximum rating of approximately 3 MPa, the localised nature of pressurisation meant that injection pressure could safely exceed the stress rating of the materials used. This had been modelled to ensure safe operation.

Early in the study, all twelve bolts were tightened to a known torque to impose the normal load. Under three of the bolts, oriented at 120° intervals, were load cells to confirm the stress imposed and to register changes in stress as gas injection occurred. However, comparison of tests showed that the recorded

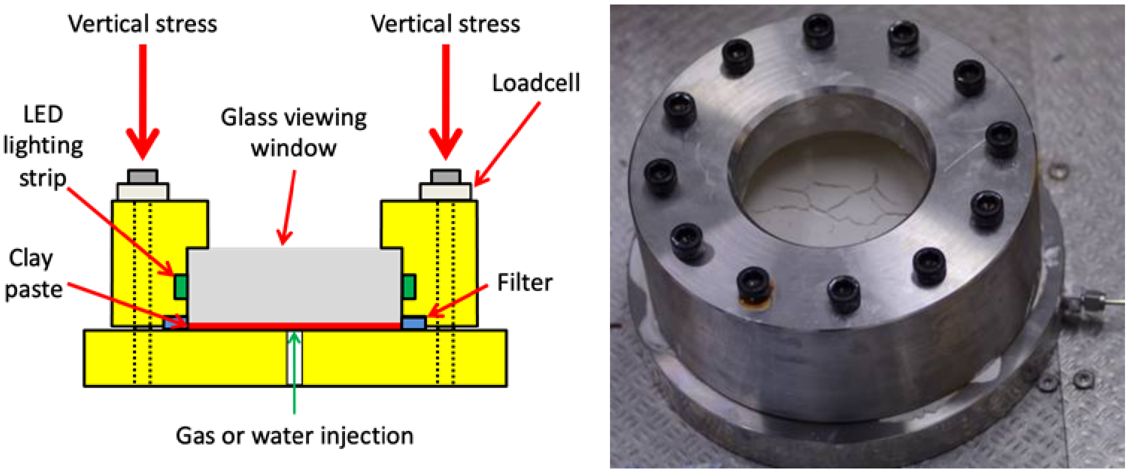

(a) (b)

Figure 2.104: The Fracture Visualisation Rig (FVR); a) schematic of the apparatus; b) photo of the FVR.

normal load was not consistent with the torque applied. This resulted in a study that showed that torque on the bolt was not a perfect proxy for applied normal load. As a result, only 3 of the 12 bolts were used and these were tightened to a known normal load as determined by the 3 load cells. This modified approach meant that the first 10 experiments were repeated.

Data recorded were of two forms. The first was the visual data recorded by the digital camera. The second was the output from the syringe pump, the three load cells, and a single pore pressure sensor.

For gas injection experiments, where gas pathway propagation was relatively slow, it was possible to record the experiment using time-lapse photography. For time-lapse, a Nikon D800 Digital Single-Lens Reflex (DSLR) camera with Nikkor AF 60 mm f2.8D Micro lens captured images every three seconds. The camera was mounted on a tripod with ball-head mount to allow the camera to be located directly above the centre of the viewing window. Images were captured at a resolution of 7360 × 4912 (36 megapixels), with time-lapse controlled by an intervalometer. All images were recorded as RAW/NEF format and were batch processed using Adobe Lightroom software into optimized greyscale to aid feature identification. Images were exported from Adobe Lightroom as Jpeg format for further processing using Matlab and for making timelapse videos.

Several modifications were made to the existing FVR to aid feature identification. The use of timelapse photography meant that the viewing window had to be well illuminated. In previous studies, the reflection of light from the steel baseplate would in certain locations be seen as white and in others black, especially when converted to monochrome. To give pathways a consistent colour, the baseplate of the rig was powder coated in a light blue colour. This was specifically chosen as it would provide contrast to the testing material and therefore aid in the visualisation of pathways and in the image analysis post-test. However, the powder coating was found to be easily scratched and started to delaminate from the baseplate. As a result, all powder coating was removed up unto and including the recess for the porous plastic filter. The lighting of the viewing window from above had also been found to not give an even illumination because of internal reflections within the glass. To remedy this, a recess was machined into the steel retaining collar to accommodate LED strip lighting. This lighting was centred 25 mm up the glass window and created an even illumination. The LEDs could be set to any colour, but in practice were set to white. The low angle of illumination to the pathways meant that the base plate was not illuminated when gas pathways formed and as such all pathways appeared black, meaning that powder coating of the base plate wasn't necessary and removing it did not have a detrimental influence on ability to identify features.

2.4.2.2. Calibration

The apparatus comprised one syringe pump, three load cells, one pore pressure sensor, and one camera. Each type of device had a different calibration routine and/or cycle between repeat measurements.

The syringe pump was calibrated at regular intervals by pressurising at 0 (atmospheric), 2.5, 5, 7.5, 10, 7.5, 5, 2.5, and 0 MPa. At each stage the pressure reading of a Fluke pressure calibrator was noted to give precise pressure measurement. The Fluke calibrator was itself re-calibrated by the manufacturer on an annual basis to industry standards. A similar approach was used for the pore pressure transducer; however, it was pressurised at 0, 0.8, 1.6, 2.4, 3.2, 4, 3.2, 2.4, 1.6, 0.8, and 0 MPa.

The load cells were calibrated using a hydraulic load-frame. Each load cell was placed one at a time in series with a calibration load cell device. The load cells were loaded over a range of steps and the electrical output was noted against the load reading of the calibration device. The latter was re-calibrated annually by the manufacturer to industry standards.

The camera was calibrated for time. At the start of each test the time of the camera was checked against the time of the logging PC. This allowed the photos to be synchronised with the experimental data.

For all calibration data the slope, intercept, and R^2 was calculated, the latter being used to ascertain whether the calibration had been of sufficient quality, with R^2 expected to be close to unity. As well as R^2, graphs of the calibration were also inspected. Where necessary, calibration was repeated if R^2 was not acceptable. During the experimental programme, no device showed significant deviation from the initial calibration.

2.4.2.3. Testing fluids

All tests were conducted with helium as the gas permeant. Given the importance of fluid chemistry on the behaviour of clay-rich materials, it is crucial that transport and mechanical testing is conducted using water in equilibrium with the test material. Synthetic pore water was used during the mixing of the clay paste to ensure the water was chemically balanced.

Boom Clay synthetic pore fluid

A detailed analysis of pore fluid data for the Boom Clay formation was conducted by De Craen et al. (2004) and a reference pore water composition defined for the HADES Underground Research Laboratory (*Table 2.23*). Synthetic solutions were mixed in batches approximately every 6 months, depending on the amount of testing being conducted. The recipe for making the pore fluid is described in *Table 2.24*.

Callovo-Oxfordian claystone synthetic pore fluid

The hydrochemistry of the interstitial fluid was provided by Andra (*Table 2.25*). A stock solution was used when mixing all clay pastes.

Opalinus Clay synthetic pore fluid

A detailed analysis of the pore fluid chemistry of the Opalinus Clay was reported by Pearson et al. (2003), the so-called Pearson Water. *Table 2.26* shows the recipe of the pore fluids used in the current study.

Bentonite synthetic pore fluid

To reduce the effect of swelling, the bentonite paste needed to be mixed with a mild saline fluid. It was decided to use Boom Clay synthetic pore fluid.

Table 2.23: Reference Boom Clay pore water after De Craen et al. (2004).

Ion	mg/l	mmol/l	Ion	mg/l	mmol/l
Ca	2.0	0.05	**Al**	0.6×10^{-3}	2.4×10^{-5}

Table 2.23: Reference Boom Clay pore water after De Craen et al. (2004).

Ion	mg/l	mmol/l	Ion	mg/l	mmol/l
Fe	0.2	0.003	**Total S**	0.77	0.02
Mg	1.6	0.06	**Cl -**	26	0.7
K	7.2	0.2	**SO_4^{2-}**	2.2	0.02
Si	3.4	0.1	**HCO_3 -**	878.9	14.4
Na	359	15.6			

Table 2.24: Recipe for making Boom Clay synthetic pore water.

Chemical	mg/l	Chemical	mg/l	Chemical	mg/l
$NaHCO_3$	1209	**$FeSO_4$**	0.456	**KCl**	14.91
Na_2SiO_3	12.2	**$MgSO_4$**	2.046	**NaCl**	18.35
$CaCl_2$	5.55	**$MgCl_2$**	4.094	**NaOH**	27.44

Table 2.25: Recipe for making Calloxo-Oxfordian claystone synthetic pore water.

Ion	mg/l	Ion	mg/l	Ion	mg/l
$CaSO_4,2H_2O$	930	**NaCl**	1724	**$NaHCO_3$**	344
$MgCl_2,6H_2O$	915	**$SrCl_2,6H_2O$**	53		
KCl	45	**Na_2SO_4**	1023		

Table 2.26: Pore-water chemistry used as test fluid on all Opalinus Clay samples, from Pearson et al. (2003).

Ion	mg/l	Ion	mg/l
NaCl	7598	**$CaCl_2,2H_20$**	816
KCl	231	**Na_2SO_4**	1420
$MgCl_2,6H_20$	511	**Na_2CO_3**	33

2.4.3. Material properties (pre-test and post-test characteristics)

Boom Clay

The geological and hydrogeological setting of the Boom Clay in northern Belgium has been summarised by Beerten & Leterme (2012) and in the Netherlands by Vis & Verweij (2014). The Boom Clay (usually referred to as the Rupel Clay in the Netherlands) is of lower Oligocene (ca 28 to 34 Ma) age and forms part of the Rupel Formation. In the Netherlands the Rupel Formation has been subdivided into the Vessem, Rupel Clay, and Steensel members (Wong et al., 2007). These members are diachronous, with both the basal Vessem and the overlying Steensel members being sandy marine deposits (Vis & Verweij; 2014) laid down close to the palaeo-shorelines. The Boom Clay is a pyritic, grey to dark brown marine clay with septarian (carbonate rich) concretions. Towards the basin margins the clays grade into sands. The formation reaches a maximum thickness of up to 250 m, with a mean thickness of around 65 m, and dips gently towards the north-east at between 1 and 2°.

The core material used in the current study was taken from the HADES underground research laboratory at Mol in Belgium. Here, the Boom Clay consists mainly of mixed clay and silt, with additional minor sand (Bernier, 2007). Mineralogical composition of the Boom Clay is widely reported, predominantly assessed using XRD. The clay content is generally reported to vary from between 23 and 60 % of the bulk material composition and is predominantly made up of illite, smectite and kaolinite, which is often seen in inter-laminated zones (Blanchart et al., 2012; Dehandschutter et al., 2004; Wemaere et al., 2008; Yu et al., 2012). The non-clay fraction of the Boom Clay primarily consists of quartz, again widely reported to vary between 23 and 60 %. The remaining percentage of the non-clay fraction consists of feldspars, calcite, and pyrite. Honty & De Craen (2011) report the composition to be 22-77 % quartz, 0-6.3% albite, 0.4-17.3% k-feldspar, 0-1.5% siderite, 0-4.6% calcite, 0-2% apatite, 0.3-5% pyrite, 5-37% illite/muscovite, 6.8-35% smectite + illite/smectite, 2-16% kaolinite, and 14-4% chlorite. This demonstrates the variability of Boom Clay. Cores of Boom Clay were acquired from EURIDICE (Belgium) from the HADES URL from a depth of 220m.

Callovo-Oxfordian claystone

The Callovo-Oxfordian claystone (COx; 150-160 Ma) was deposited under marine basin conditions during a period in which the Paris Basin, France, was variously linked to the Atlantic and Tethyan Oceans, as well as to the London Basin and North Sea (Rousset & Clauer, 2003). Clay sedimentation is therefore considered to have two primary inputs: continental and oceanic. The claystone is over- and underlain by Oxfordian and Bathonian shelf limestones. It is primarily clayey at its base, then becomes increasingly silty and then increasingly calcareous at its top (Gaucher *et al.*, 2004). A maximum clay content zone within the clayey base has been identified; this is interpreted to mark the inflection point (and interval of maximum flooding) from a lower transgressive sequence to an upper regressive sequence (Gaucher *et al.*, 2004).

The UA (clay-rich) variety of the COx occurs at repository depth and can be considered to be the clay-rich part of the unit. The samples used came from the Meuse/Haute-Marne underground research laboratory at Bure in France. Yven *et al.* (2007) report three main mineral phases; clay minerals, quartz and calcite. Secondary mineral phases include dolomite, feldspar, pyrite, hematite and traces of siderite. Calcite and quartz represent 40 – 55 % of the rock. Clay represents 20 – 55 %, with secondary minerals forming less than 5 %. Clay minerals include illite and illite-smectite with subordinate kaolinite and chlorite. Wenk *et al.* (2008) reports clay 25-55 wt%, 23-44% carbonates and 20-31% silt (essentially quartz + feldspar). Clay minerals are reported to include illite and illite-smectite with subordinate kaolinite and chlorite. In the upper half of the formation the illite-smectite is disordered and contains 50-70% smectite interlayers, whilst in the lower half the illite-smectite is ordered (R=1 type) with lower contents (20-40%) of smectite interlayers (Wenk *et al.*, 2008). Beds can contain common organic matter. Other authors report compositions similar to these. Wileveau & Bernier (2008) quote values for quartz (18%), calcite (25%), clay minerals (55%; illite-smectite ~65%, illite 30%) and kaolinite and chlorite (2%) with subordinate feldspars, pyrite and iron oxides (2%). Esteban *et al.* (2006) report 35-60% clay minerals with the remaining shared by calcite and silt. Armand *et al.* (2017) report that the UA unit makes up two-thirds of the total geological layer thickness.

Upon receipt of preserved T-cell core barrels from Andra, the material was catalogued and stored under refrigerated conditions of 4 ℃ to minimize biological and chemical degradation. The preserved core barrels consisted of a multi-layered arrangement designed to re-stress the core to *in situ* stress and to environmentally seal it to reduce chemical, biological and drying effects. Samples were tested within 12 months of the core being extracted from the Meuse/Haute-Marne URL.

Opalinus Clay

The Opalinus Clay (OPA) is a Jurassic (Aalenian, ~180 Ma) shallow marine clayshale found in Switzerland. The formation, named after the ammonite Leioceras opalinum, consists of indurated dark grey micaceous claystones (shales) that are subdivided into several lithostratigraphic units. Some of them contain thin sandy lenses, limestone concretions, or siderite nodules. The clay-mineral content ranges from 40 – 80 wt% (9 – 29 % illite, 3 – 10 % chlorite, 6 – 20% kaolinite, and 4 – 12 % illite/smectite mixed layers in the ratio 70/30). Other minerals are quartz (15 – 30 %), calcite (6 – 40 %), siderite (2 – 3 %), ankerite (0 – 3 %), feldspars (1 – 7 %), pyrite (1 – 3 %), and organic carbon (<1 %). The total water content ranges from 4 – 19 % (Gautschi, 2001). At the Mont Terri underground research laboratory, three facies can be distinguished; a shaly facies in the lower half of the sequence, a 15 metre thick sandy, carbonate-rich facies in the middle of the sequence and a sandy facies interstratified with the shaly facies in the upper part. For the current study, samples from the shaly facies were used. The OPA at Mont Terri is an over-consolidated shale with a maximum burial depth of 1,200m and is presently around 280m depth. All core material used in the current study came from the shaly facies at the Mont Terri underground research laboratory. Core material derived from borehole BFI-4, a borehole drilled parallel to bedding.

Bentonite

The bentonite clay is a mixture of Ca- or Na-montmorillonite (>90%) with smaller amounts of feldspar, calcite and quartz. The bentonite used was MX-80 (Johannesson, 2003) with a natural water content of 15 %. The clay was supplied to BGS by SKB. MX-80 is the commercial name given to the specific artificial bentonite, and the VOLCLAY^{TM} MX-80 used in this study was a fine-grained sodium bentonite from Wyoming. The MX-80 had the following chemical formula $(Na,Ca)_{0.33}$ $(Al_{1.67}Mg_{0.33})$ Si_4O_{10} $(OH)_2$. nH_2O and a mineralogical composition of SiO_2 (63.02%), Al_2O_3 (21.08%), Fe_2O_3 (3.25%), FeO (0.35%), MgO (2.67%), Na_2O (2.57%), CaO (0.65%), Trace (0.72%) and LOI (5.64%). The bentonite had been milled to a grain size of no larger than 30 microns, with the smallest grain size expected to be 16 microns.

Sand

The sand used was derived from high purity quartz sand supplied by Lochaline Quartz Sand Ltd, which had been sieved to obtain particles in the range 63-125 microns.

Sample preparation

Clay pastes were created by mixing known quantities of ball-milled clay powder with synthetic pore fluid. The proportions for the clay/water mix varied for each clay type, as summarised in *Table 2.27*. The water and clay mixture were thoroughly mixed until a consistent paste had been achieved. This was then smeared onto the surface of the glass of the FVR as evenly in thickness and distribution as possible. The application of torque to the bolts of the FVR then created a uniform thickness of gouge. The time between mixture and assembly of the apparatus was minimised to ensure that no significant drying of the paste occurred. The amount of clay mixed was enough to create a 1mm thick clay sample with 2 - 3 g surplus used to determine water content.

Table 2.27: Mixture of clay and water used to make clay pastes.

Clay	Clay weight (g)	Water weight (g)	Water content (%)
Callovo-Oxfordian	40	22	37
Boom Clay	40	27	42
Opalinus Clay	40	27	41

Geotechnical properties

Table 2.28 summarises the geotechnical properties of the tests conducted. A total of 25 tests were conducted, giving 5 repeat tests each of Boom Clay (BC), Callovo-Oxfordian claystone (COx), and Opalinus Clay (OPA). The other tests were conducted to achieve a reliable test result with varying mixes of clay and water, as well as one test conducted on pure kaolinite. Only water content is given. A small proportion of the clay mixture was collected after mixing and after the test from near injection filter in the centre of the sample, therefore before and after gas injection. The clay paste was weighed and then dried for 24 hours at 105° and re-weighed. This gave the water content of the samples.

Table 2.28 shows that the starting water content is consistent for each of the five repeat tests. The water content of Callovo-Oxfordian clay paste was an average of 37.52±0.06%, for Boom Clay paste was 42.24±0.03%, and for Opalinus Clay paste of 41.30±0.06%. Following gas injection, the average water content was 34.37±0.29% for Callovo-Oxfordian clay paste, 40.26±0.17% for Boom Clay paste, and 38.64±0.15% for Opalinus Clay paste. This shows a reduction of 3.15% for Callovo-Oxfordian clay paste, 1.98% for Boom Clay paste, and 2.67% for Opalinus clay paste. It is uncertain whether this reduction in water content was because of de-water during compression of the paste when the experiment is setup or whether it was a drying effect of gas movement. This will be investigated at a later stage.

Table 2.28 suggests that consistent clay pastes were created, and that no geotechnical variation is apparent that could result in differences between gas injection experiments.

Table 2.28: Geotechnical properties of the clay pastes used in the current study. Note: Kaol = kaolinite, COx = Callovo-Oxfordian, BC = Boom Clay, OPA = Opalinus Clay. Used tests are icluded in the reference studies.

	Test number	Clay	Used test	Date of test	Weight of clay (g)	Weight of clay+water (g)	Water content start (%)	Water content end (%)
1	FPR-23-068	Kaol	/	17/04/2023	40.09	62.02	/	/
2	FPR-23-069	COx	/	17/04/2023	40.08	62.16	/	/
3	**FPR-23-070**	**COx**	**COx1**	**18/04/2023**	**40.00**	**62.00**	**37.57**	/
4	**FPR-23-071**	**COx**	**COx2**	**18/04/2023**	**40.03**	**62.15**	**37.25**	**34.52**
5	**FPR-23-072**	**COx**	**COx3**	**19/06/2023**	**40.02**	**62.03**	**37.59**	**33.33**
6	**FPR-23-073**	**COx**	**COx4**	**19/06/2023**	**40.07**	**62.10**	**37.71**	**34.20**
7	**FPR-23-074**	**COx**	**COx5**	**20/06/2023**	**40.00**	**62.02**	**37.49**	**35.45**
8	FPR-23-075	BC	/	20/06/2023	40.01	62.14	37.46	/
9	FPR-23-076	BC	/	21/06/2023	40.00	67.00	42.20	40.94
10	FPR-23-077	BC	/	21/06/2023	40.01	62.09	37.36	/
11	FPR-23-078	BC	/	22/06/2023	40.01	57.04	31.94	29.74
12	**FPR-23-079**	**BC**	**BC1**	**22/06/2023**	**40.01**	**67.02**	**42.17**	/
13	**FPR-23-080**	**BC**	**BC2**	**26/06/2023**	**40.01**	**67.11**	**42.21**	**40.64**
14	**FPR-23-081**	**BC**	**BC3**	**26/06/2023**	**40.01**	**67.03**	**42.31**	**39.69**
15	**FPR-23-082**	**BC**	**BC4**	**27/06/2023**	**40.02**	**67.04**	**42.23**	**40.54**
16	**FPR-23-083**	**BC**	**BC5**	**27/06/2023**	**40.02**	**67.04**	**42.30**	**40.17**
17	FPR-23-084	OPA	/	04/07/2023	40.01	62.16	36.49	34.80
18	FPR-23-085	OPA	/	04/07/2023	40.00	67.05	41.36	/
19	FPR-23-086	OPA	/	05/07/2023	40.01	67.02	41.33	38.17
20	FPR-23-087	OPA	/	06/07/2023	40.01	67.00	41.39	38.72
21	**FPR-23-088**	**OPA**	**OPA1**	**06/07/2023**	**40.00**	**67.00**	**41.35**	**38.90**
22	**FPR-23-089**	**OPA**	**OPA2**	**10/07/2023**	**40.01**	**67.01**	**41.15**	**38.37**
23	**FPR-23-090**	**OPA**	**OPA3**	**10/07/2023**	**40.01**	**67.01**	**41.42**	
24	**FPR-23-091**	**OPA**	**OPA4**	**11/07/2023**	**40.01**	**67.01**		
25	**FPR-23-092**	**OPA**	**OPA5**	**11/07/2023**	**40.02**	**67.05**		

2.4.4. Testing protocol

Table 2.29 summarises the test programme, with six individual studies planned. These aimed to answer the following research questions:

- **Repeatability:** Do we see similar behaviour (gas entry pressure, pathway network etc) for five repeat tests?
- **Clay types:** Do we see similar behaviour between different clay pastes? [as part of Repeatability study]

- **Moisture content:** Do we see differences in behaviour for variations in moisture content?
- **Self-sealing:** Do we see evidence of self-sealing of gas pathways?
- **Pathway-growth:** What happens if gas supply stops?
- **Pressurisation rate:** Do we see any change in behaviour with pressurisation rate?
- **Sand/bentonite:** Do we see any change in behaviour over a range of sand:bentonite mixes?

To answer these questions with certainty, a minimum of 43 experiments was required. In practice, some experiments were repeated, and additional tests were conducted to fine-tune the water content of the paste and the starting gas pressure to give reliable results.

Please note: The glass viewing window of the Fracture Visualisation Rig was accidentally point-loaded after the completion of 25 experiments. A small fragment of glass chipped off the glass and ended up between the gasket and the glass window. When applying load to the steel collar, the stress was concentrated on this small shard of glass, point loading the main glass window and resulting in it breaking. A replacement was ordered; however, it would not arrive in time for reporting. As described in *Table 2.29*, only repeat studies in COx, BC, and OPA were complete by the time of reporting. All tests will be completed by the end of the EURAD-GAS project.

Table 2.29: Plan of the tests to be conducted to answer 6 research questions.

Investigation	Test protocol	Paste	Number of tests	Status
Repeatability	Standard	COx	5	**Complete**
		OPA	5	**Complete**
		BC	5	**Complete**
Moisture content	Standard	Mx80	5	To complete
		Mx80	5	To complete
Self-sealing	Sealing	COx	1	To complete
		OPA	1	To complete
		BC	1	To complete
		Mx80	1	To complete
Pathway growth	Paused	Mx80	4	To complete
Pressurisation rate	Standard	Mx80	5	To complete
Sand/bentonite	Standard	Mx80/sand	5	To complete

Table 2.29 shows that there were three different test protocols used during the experimental programme. These are described below.

Standard test protocol

1. Once the clay paste had been mixed, around ¾ of the paste was smeared on the bottom of the glass viewing window. The window and collar arrangement were then turned over, and the rig assembled. The porous plastic filter acted as a location ring and once in place the collar and glass were slowly lowered on the base plate. The collar was then rotated to line up with the bolt hole. Three long bolts were added first. These screwed through the base plate and into the table below the apparatus. This held the apparatus securely when tightening the three main bolts. Note, these three long bolts did not place any load on the steel collar or the clay paste. Three bolts and load cells were then placed at 120° separation. The torque on the bolts were sequentially increased in steps up to the desired normal load over a period of around five minutes. The load cells were read from the logging PC. The reading was noted, and the system was left for 15 minutes and the load was recorded and re-torqued if necessary. The load was also recorded after a further 15 minutes and re-torqued. If load had stopped reducing, then the experiment could start.

Load reduced because the clay paste was settling and potentially draining. The use of a porous plastic filter meant that the system was able to drain.

2. The syringe pump delivered water to the base of a water/gas interface vessel. At the start of each experiment, the interface vessel was put into refill mode to a volume of approximately 50 ml. The system was set so that full discharge of the syringe pump into the water/gas interface vessel would not result in the discharge of water from the interface vessel into the apparatus. The pumping of water into the apparatus could result in hydrofracture of the glass. Therefore, refilling the pump by 50 ml created a 50 ml volume for the gas to occupy. The interface vessel was then filled with helium gas to the required starting pressure. The syringe pump was set to constant flow, which for most experiments was 25 ml/h, meaning that the full volume of gas was discharged in two hours, meaning most experiments were less than two hours in duration. The exception was the pressurisation rate experiments that used a different flow rate. The time-lapse camera was started, the valve between the interface vessel and the apparatus was opened, and the pump was started. The time, starting pressure, and starting volume were noted.

3. In the standard protocol, the experiment was run until gas breakthrough had been achieved. Observations were noted after 30, 60, 90, and 120 minutes of the gas pressure and whether any features had formed. Once gas breakthrough had been achieved, the time-lapse camera was stopped, and the apparatus was dismantled. A small amount of clay was retrieved from the surface of the baseplate for geotechnical properties.

A total of 35 of the 43 experiments were planned using the Standard Protocol. Of these, 30 were conducted identically, with 5 being performed at different pressurisation rates to give a total test duration of 0.1, 1, 10, 100, and 1000h.

Sealing test protocol

The sealing test protocol followed the standard test protocol for stages 1 and 2. The first stage of the sealing test protocol followed standard protocol stage 3; however, gas breakthrough was not achieved. Once a substantial gas pathway network had been achieved, gas injection was stopped and gas pressure relieved. This tended to close most of the pathways. Synthetic pore water was then injected at a low pressure for at least 24 hours. This aimed to re-saturate the clay paste and to self-seal the pathways. After 24 hours of hydration, the injection filter was flushed and a second gas injection test was conducted, this time through to breakthrough. This test protocol aimed to observe self-sealing of the pathways and whether repeat gas injection exploited the existing gas network or created a new network of pathways.

Paused test protocol

Two similar test protocols were devised to investigate episodic gas supply. Both protocols were similar and followed the standard test protocol for stages 1 and 2. Stage 3 of the standard protocol was followed, but soon after gas entry and the formation of a limited number of pathways the test was "paused." For two experiments, this meant stopping the syringe pump and seeing whether pathway growth stopped or continued as the gas pressure started to decay. In the two other experiments, the syringe pump was switched from constant flow to constant pressure to see how this changed the pathway growth rate. Depending on what happened, gas injection was restarted and run until gas breakthrough occurred.

All tests were dismantled in the same manner, with a small amount of clay recovered, weighed, and oven dried for 24 hours at 105° to determine water content.

2.4.5. Results

Description of test COx2 (FPR-23-071)

Figure 2.105 shows a series of images from test COx1 (FPR-23-070) from the first formation of gas pathways (Figure 2.105a) to just before gas breakthrough (Figure 2.105n). This test was the second of five repeat gas injection tests conducted on paste of Callovo-Oxfordian claystone. The time between each photo is 55 seconds, or 18 frames of time-lapse. The total time shown by Figure 2.105 is 708 seconds, or 235 time-lapse frames.

There are features of note in Figure 2.105a that need discussion relating to sample preparation. As can be seen, a series of features can be seen in the image prior to the formation of gas pathways. During the set-up of the experiment a few areas of trapped air were common in tests. As the glass window was lowered onto the clay paste it was very difficult to not trap air. This was previously solved by producing pre-compacted samples of around 0.5mm height. However, initial calibration tests showed that injected gas in Boom Clay tended to migrate between the pre-compacted clay and the glass window, or between the baseplate and the pre-compacted clay out of view of the camera. As a result, the decision was taken to use clay paste as these had been shown to visualise pathways within the clay, as required. However, clay paste tends to trap air bubbles. Initial calibration tests showed that certain procedures could be adopted to reduce the numbers of bubbles, but that they could not be eliminated fully. In test COx1, the first frame shown in Figure 2.105a occurred around 54 minutes into the experiment. Therefore, this time represents around 2 hours from when the clay paste was first loaded. As a result, some of the pressurised gas bubbles resulted in localised gas pathway formation and several of the bubbles seen in Figure 2.105a show "tails" that are resultant from the pressure within the bubbles. These should not be confused with gas pathways created by the controlled experiment. It must be noted that the start clay paste therefore has a texture that is not easily controlled and has been minimised as much as possible.

*Figure 3*ab show that the initial pathway formation resulted in pathways moving in two directions, 180° degrees opposed to one another. As these grew, both are seen to branch in Figure 2.105c, resulting in 4 growing features (Figure 2.105de). Initially, the features shown to the right of the injection point in the centre of the photos preferentially grew. As each branch of pathway reached a critical length they branch into two pathways, creating a dendritic pattern. By the time shown in Figure 2.105j, the pathways to the left of the injection point began to preferentially grow, meaning that by the end shown in Figure 2.105n the distribution left and right of the injection point appears to be relatively even. The only difference seems to be more pathways seen above the injection point compared with below. This may be dominated by a region towards the bottom of the view where pathways did not form. However, it is clear from Figure 2.105 that multiple gas pathways formed. At times, certain pathways grew preferentially, these paused at a certain length and then other pathways within the dendritic network of pathways took over.

It must be noted that the full area of clay is not visible. The shoulder of the steel retaining collar means that the outer 20 mm of the clay is not visible. In a simple system, it would be expected that a single pathway grows from the centre of the view to the outside, where gas pressure would escape through the plastic filter. Figure 2.105 clearly shows that pathways have a critical length that result in branching and the pressure loss along a pathway means that as gas pathways form further away from the injection point their growth becomes unstable and other pathways then grow as a consequence.

Detail of test COx3 (FPR-23-072)

Figure 2.106 and Figure 2.107 show the results of test COx3 (FPR-23-072), which was the third of five repeat gas injection tests conducted on paste of Callovo-Oxfordian claystone.

Figure 2.106 shows the results of test COx3. Figure 2.106a shows the resultant gas pressure, with the six highlighted circles representing the time-lapse frames shown in Figure 2.106d-i. Gas pressure increased as an exponential as water was injected into the base of the interface vessel at a constant volumetric rate. The first event highlighted in Figure 2.106a at 1650 seconds is the interpretation of when gas entry occurred, viewed as a deviation from the predicted gas pressure from the ideal gas law. At this time, the stress measured by the three load cells started to increase, as shown in Figure 2.106b. This is interpreted as the formation of dilatant pathways and the dilation of the clay resulting in an increase in stress. While the majority of observed strain occurs in the plane of the sample, resulting in strain in the perpendicular direction to accommodate the addition of gas. Pressure continued to increase until a significant change in slope, as highlighted by the second event at 2250 seconds. At this time, stress on the sample decreased and flow into the clay (Figure 2.106c) increased. However, the time-lapse frames shown in Figure 2.106d-i at a time interval of 12 minutes and highlighted circles on Figure 2.106a-c show that gas entry occurred at a time earlier than interpreted from the test results and that the majority of gas pathways had formed by the second circle at time 2187 (Figure 2.106g).

Figure 2.107 shows greater detail of initial gas entry into the clay with time-lapse frames shown on a 3-minute interval and greater detail of the test results. As can be seen, the majority of gas pathways had formed by Figure 2.107h, which was around the time of maximum stress, but before the change in gradient of the observed gas pressure (Figure 2.107i). Comparing Figure 2.107h and Figure 2.107i does show that some pathways had closed, and therefore the change in gradient of the gas pressure corresponds well with the escape of gas from the system and the closure of some features.

Figure 2.107 shows that the interpretation of first gas entry is very difficult from test results. The interpreted gas entry was later than the first entry seen in the time-lapse. The first gas entry does correspond with

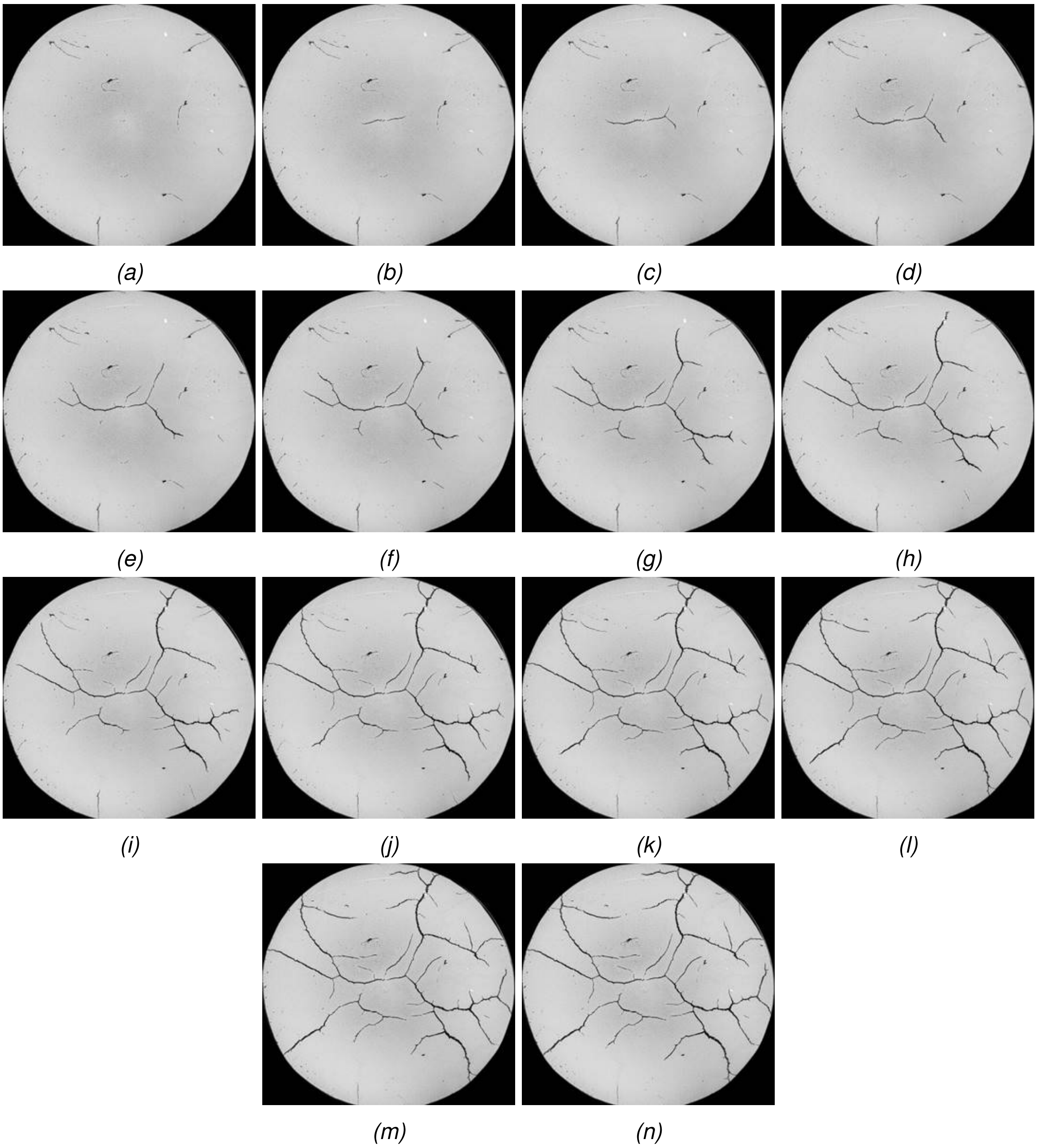

Figure 2.105: Detail of test COx1.

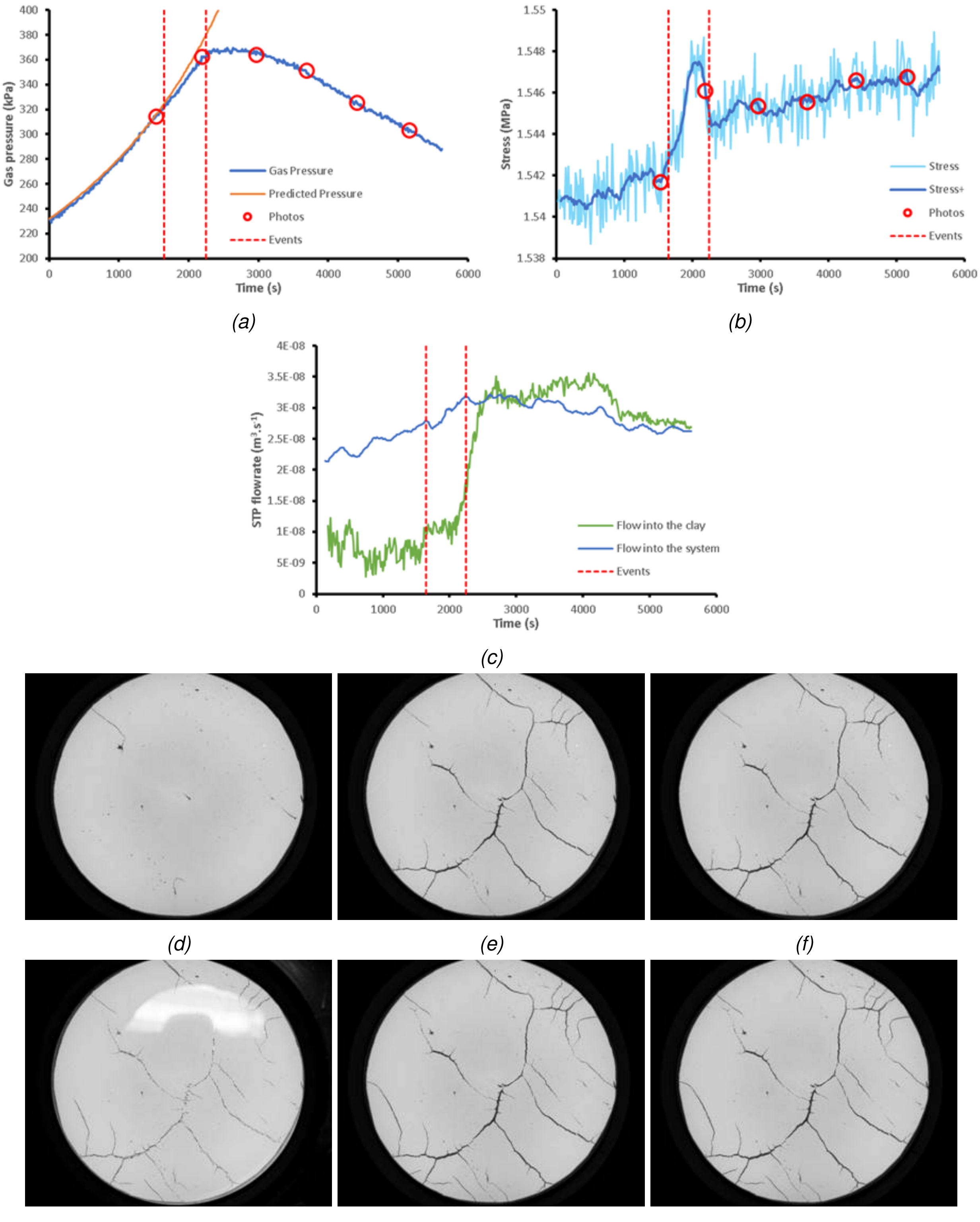

(a)

(b)

(c)

(d)

(e)

(f)

(g)

(h)

(i)

Figure 2.106: Results of test COx3 around the time of gas entry. a) Gas pressure; b) stress; c) flow into the clay; d-i) Corresponding time-lapse frames.

the start of increase of stress on the sample, but the noise level of the data meant that a later time was picked as the time of gas entry at 1650 seconds. At this time (Figure 2.107b) a considerable population of features had already formed.

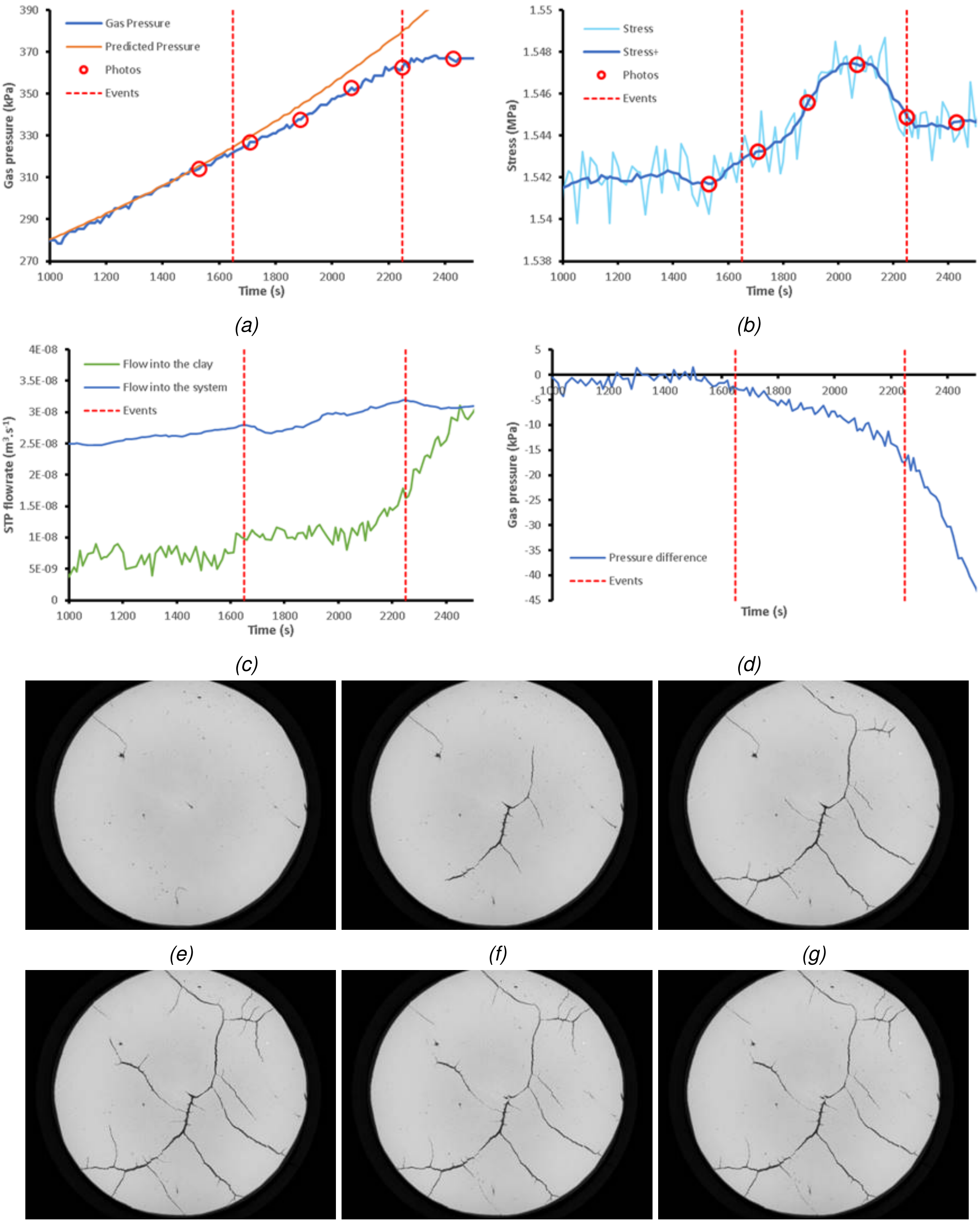

(a) (b)

(c) (d)

(e) (f) (g)

(h) (i) (j)

Figure 2.107: Detail of test COx3 around the time of gas entry. a) Gas pressure; b) stress; c) flow into the clay; d) difference between predicted and observed gas pressure; e-j) Corresponding time-lapse frames.

Repeatability study

For each clay paste, five tests were conducted as close to identical as possible. The final frame before breakthrough is shown for Boom Clay in Figure 2.108, Callovo-Oxfordian claystone in Figure 2.109, and

Opalinus Clay in Figure 2.110.

Boom Clay repeatability

Five tests were conducted at as close to identical conditions as possible using pastes of Boom Clay (tests BC1-5). The time-lapse frames for the five tests are shown in Figure 2.108 at a time just before gas breakthrough and closure of pathways. Several similarities can be seen, as well as clear differences. The most significant anomaly is seen in Figure 2.108d, where pathways were very fine and several did not break the surface, i.e. the pathway was not the full height through the clay. Fine traces are seen under these conditions, with a darkening of greyscale. Although not immediately obvious in Figure 2.108d, a similar dendritic pattern of pathways formed. Therefore, all five tests showed a similar pattern of pathways. Differences were seen in the width of pathways, with test BC4 showing very fine pathways (Figure 2.108d) and test BC5 showing several broad features (Figure 2.108e). The distribution of pathways appears even around the sample, although test BC3 (Figure 2.108c) shows pathway formation generally in the upper half of the sample, and test BC1 (Figure 2.108a) shows pathways forming more to the right of the viewing area. Generally, all five tests showed the formation of a dendritic pattern of pathways from the central injection point with pathways of varying width. There is a stochastic nature to the formation of pathways.

Callovo-Oxfordian claystone repeatability

Five tests were conducted at as close to identical conditions as possible using pastes of Callovo-Oxfordian claystone (tests COx1-5). The time-lapse frames for the five tests are shown in Figure 2.109 at a time just before gas breakthrough and closure of pathways. Generally, the repeatability of the pathways is good with a stochasticity to the distribution. In all tests, long pathways form with multiple off-shoot pathways from these main features, this is clearly seen in tests COx4 (Figure 2.109d) and COx5 (Figure 2.109e), although it can be seen in all five tests. One difference that can be highlighted is a difference in distribution of features related to the early formation of pathways. In test COx4 (Figure 2.109d) two gas pathways formed 180° to one another, both of which quickly branched into four pathways approximately 90° from one another. This created four populations of features evenly distributed throughout the sample. This can be contrasted with test COx3 (Figure 2.109c), where although two pathways also formed from the central injection point, these were not 180° from one another and did not quickly branch into four evenly distributed populations of pathways. In this test, two populations of pathways can be better defined. Two populations are easier to identify in COx5, with three populations in COx1 and COx2. Therefore, the early history of pathway formation dictates the number of populations of pathways and the end distribution of all features. Test COx5 (Figure 2.109e) also showed some features of much greater width than the other tests. Generally, all five tests showed the formation of a dendritic pattern of pathways from the central injection point with a stochastic distribution. Early pathway formation dictated the end distribution of pathways.

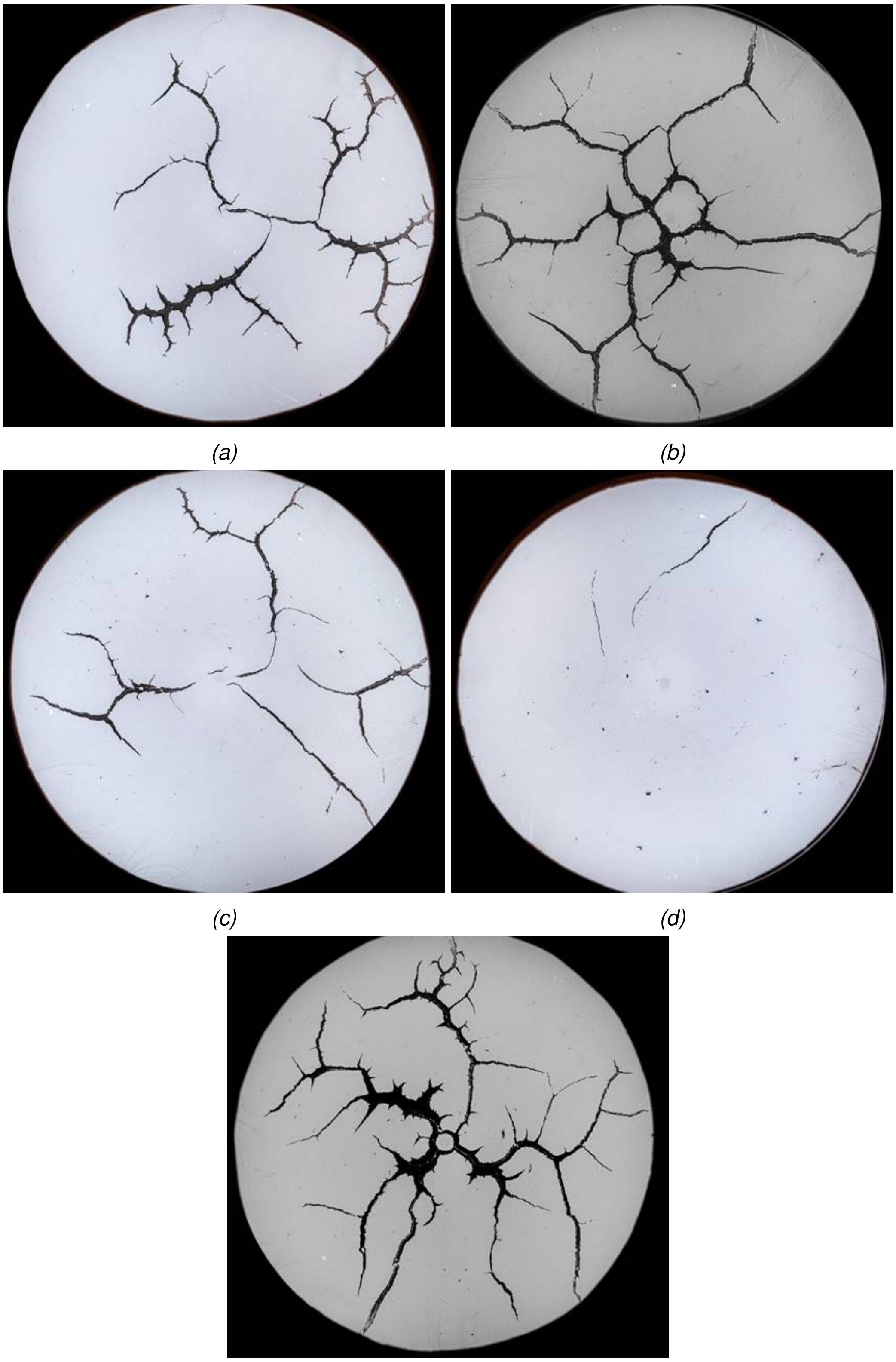

(a) (b)

(c) (d)

(e)

Figure 2.108: Repeatability of Boom Clay. a) BC1 – FPR-23-079; b) BC2 – FPR-23-080; c) BC3 – FPR-23-081; d) BC4 – FPR-23-082; e) BC5 – FPR-23-083.

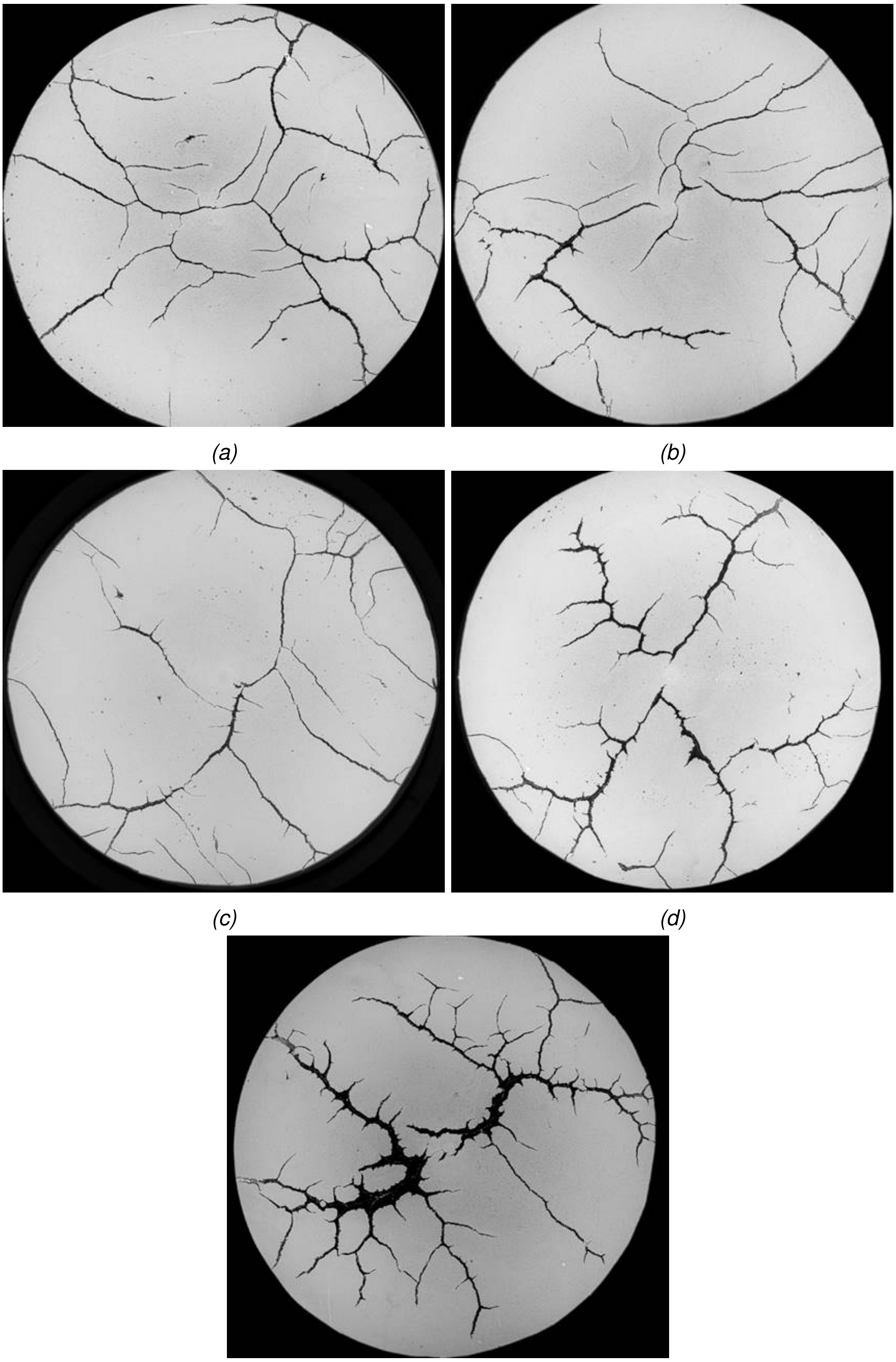
(a)
(b)
(c)
(d)
(e)

Figure 2.109: Repeatability of Callovo-Oxfordian claystone. a) COx1 – FPR-23-070; b) COx2 – FPR-23-071; c) COx3 – FPR-23-072; d) COx4 – FPR-23-073; e) COx5 – FPR-23-074.

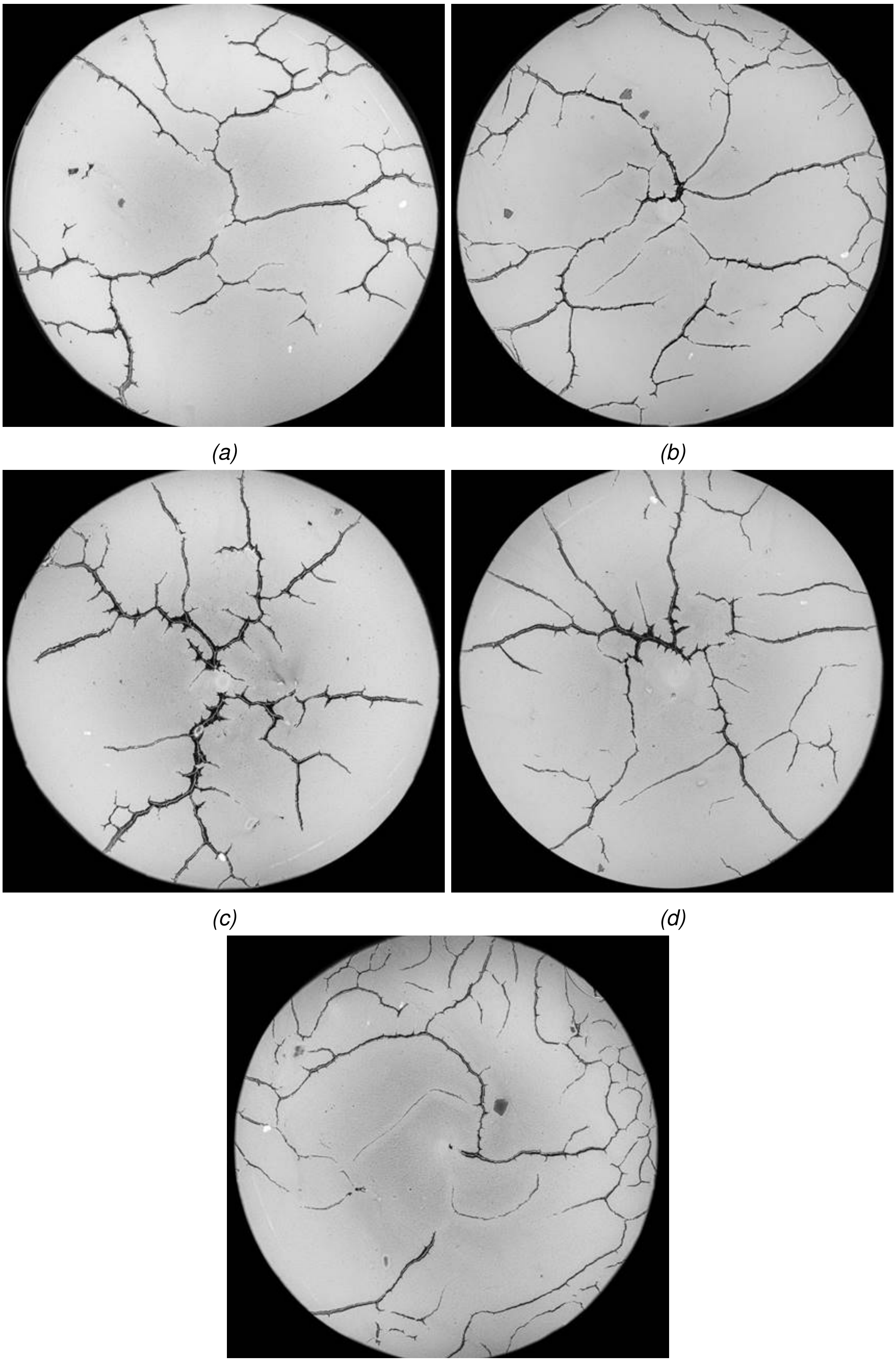
(a) (b) (c) (d) (e)

Figure 2.110: Repeatability of Opalinus Clay. a) OPA1 – FPR-23-088; b) OPA2 – FPR-23-089; c) OPA3 – FPR-23-090; d) OPA4 – FPR-23-091; e) OPA5 – FPR-23-092.

Opalinus Clay repeatability

Five tests were conducted at as close to identical conditions as possible using pastes of Opalinus Clay (tests OPA1-5). The time-lapse frames for the five tests are shown in Figure 2.110 at a time just before gas breakthrough and closure of pathways. Generally, the repeatability of the pathways is good with a stochasticity to the distribution. As with Callovo-Oxfordian claystone, the general distribution of pathways was dictated by the early formation of pathways. Tests OPA1 (Figure 2.110a), OPA3 (Figure 2.110c), and OPA4 (Figure 2.110d) shows four initial pathways creating four distinct populations. In test OPA2, initially five or six pathways formed resulting in at least five populations of pathways. All these four tests resulted in a relatively even distribution of pathways within the sample. It should be noted that test OPA3 (Figure 2.110c) showed the formation of much broader pathways, with some wider pathways also noted in test OPA4. The anomalous sample was OPA5 (Figure 2.110e). Here, the initial growth of pathways started predominantly towards the right and top of the sample. This resulted in a considerable population of pathways forming at the edge of the viewable area all along the sample on the upper half of the viewable area. The history of pathway formation showed one pathway propagating directly to the right of the injection point and when this approached the outside of the sample it branched both upwards and downwards to create a complex network of pathways. The second initial feature started to propagate towards the top of the sample from the central injection point and arced to the left, before splitting. As with the other

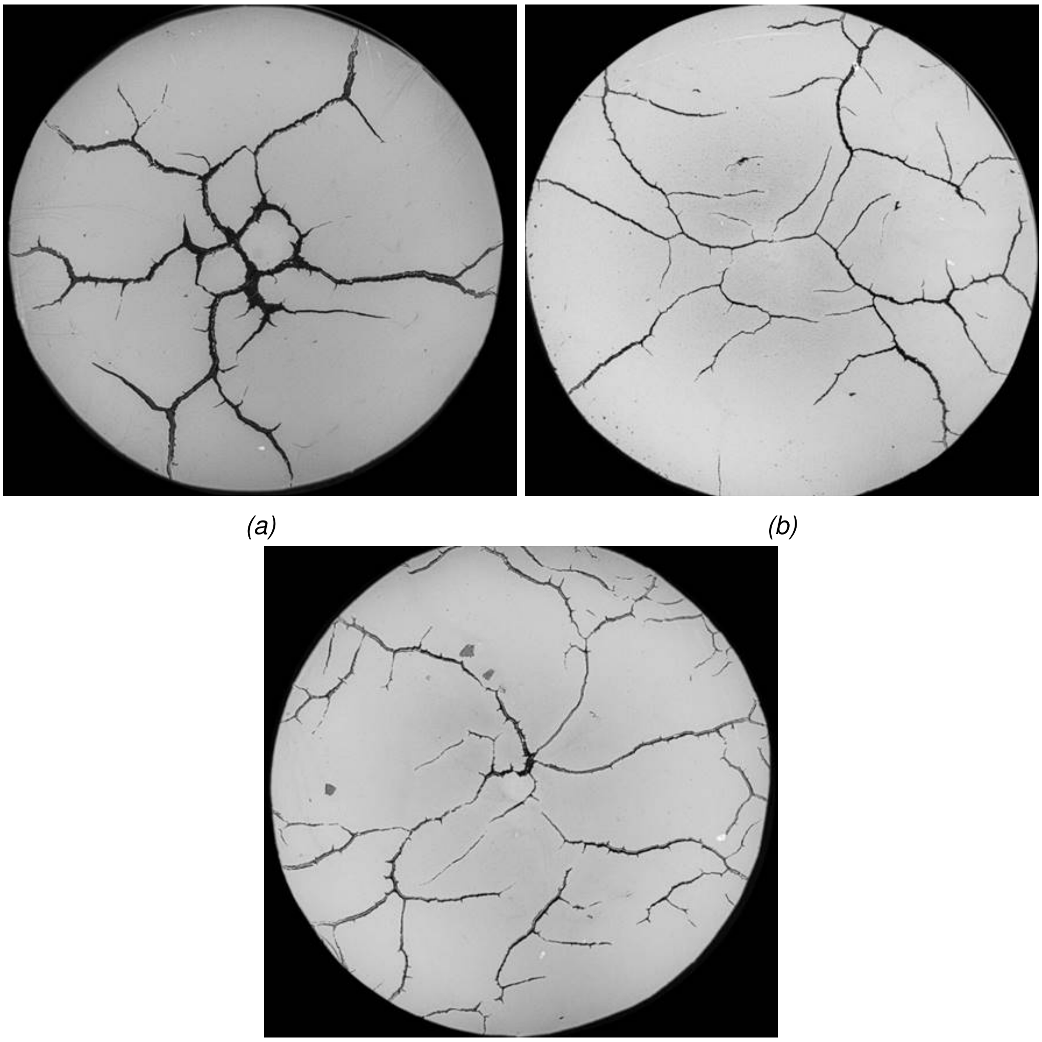
(a) (b)

(c)

Figure 2.111: Comparison of pathway formation in paste of Boom Clay (BC), Callovo-Oxfordian claystone (COx), and Opalinus Clay (OPA). a) test BC2; b) test COx1; c) test OPA2.

population of pathways, this resulted in many pathways forming along the edge of the view area. Only a minor population of pathways formed towards the bottom of the sample from the central injection point. Generally, all five tests showed the formation of a dendritic pattern of pathways from the central injection point with pathways of varying width. There is a stochastic nature to the formation of pathways.

Comparison of clay types

Figure 2.111 compares the results for the three types of paste investigated. In all three pastes, dilatant pathways formed with a stochastic distribution. The pathways seen in Boom Clay tended to be much broader than those seen in Callovo-Oxfordian claystone and Opalinus Clay. In all three paste types, pathways branched and created a dendritic distribution of pathways. The end distribution was dictated by the initial formation of pathways and how many populations of pathways formed close to the injection point. In the examples shown, multiple populations of pathways can be identified. The results of Figure 2.111 show that no significant difference was seen in the physics creating pathways in clay paste. As discussed later, there are controls on paste properties that dictate the width of pathways and that may explain the difference seen in Boom Clay. It is therefore concluded that all three clay types showed the formation of a dendritic pattern of pathways from the central injection point with a stochastic distribution. Early pathway formation dictated the end distribution of pathways.

Pathway formation in detail

Figure 2.112 shows the detail of pathway formation for test COx2. A linear pathway is seen to form in Figure 2.112a. The edges of this pathway are not smooth and can be seen to be made up of a series of curved surfaces. This initial feature branched into two, as seen in Figure 2.112b. For some unknown reason, the left-hand branch predominated and preferentially grew. This branch also branched into two, with other off shoots forming along this main feature. In Figure 2.112c the left-hand branch continued to preferentially grow, although the initial right-hand branch was also growing at a much slower rate. Further offshoot features formed. Figure 2.112d-e show this general behaviour, with the main feature preferentially growing and the off-shoots and initial branch continuing to grow at a much slower rate. It can be noted that minor branches resulted in a minor change in direction of the main pathway. Figure 2.112f-i show the main pathway reaching the edge of the view, but the width of the main feature increased. All the offshoots and branches slowly grew with one offshoot moving towards the top of the frame in the opposite direction to its parent, the main pathway in view. The remaining frames (Figure 2.112j-l) show that the offshoot feature starting around the centre of the view propagated out of the frame of view and becomes a secondary pathway. As this feature grew it did not create any offshoots or branches, neither did any of the other branches/offshoots. Therefore, this suggests that only the broad main pathways result in the formation of branches or offshoots. This might indicate that the opening ahead of a main feature results in the “cracking” of the pathway wall in a similar manner to geological rifting. Figure 2.112 shows that the mid-point of the main pathway is seen as a small trace of clay was left on the baseplate of the apparatus.

Further insight is gained on pathway migration by considering the feature shown in Figure 2.113 of test OPA5. When the time-lapse photo is processed, it is possible to see a light halo around some of the pathways (Figure 2.113a). This is most apparent when the view is blurred, as shown in Figure 2.113b. The blur removes the detail of the high frequency of the sample fabric and highlights the broad features. Using ImageJ, a profile was drawn to observe the grey-scale values of the image, as shown in Figure 2.113c. The pathway itself is highlighted as a clear black (low value of greyscale), while the halo around the pathway is seen as an elevated value of greyscale compared with the background. This shows that the halo is much broader than the pathway itself.

The halo is interpreted as a compression of the clay surrounding the pathway. This is confirmed by observing the central injection point in all tests. Figure 2.110 shows that Opalinus Clay results in a light greyscale at the injection point, this is clearest in Figure 2.110b. As gas pressure increases at the injection filter it results in the compression of the clay. This results in raising density and/or de-watering. Therefore, compression of the clay paste results in a lightening of greyscale. The halo highlighted by Figure 2.113

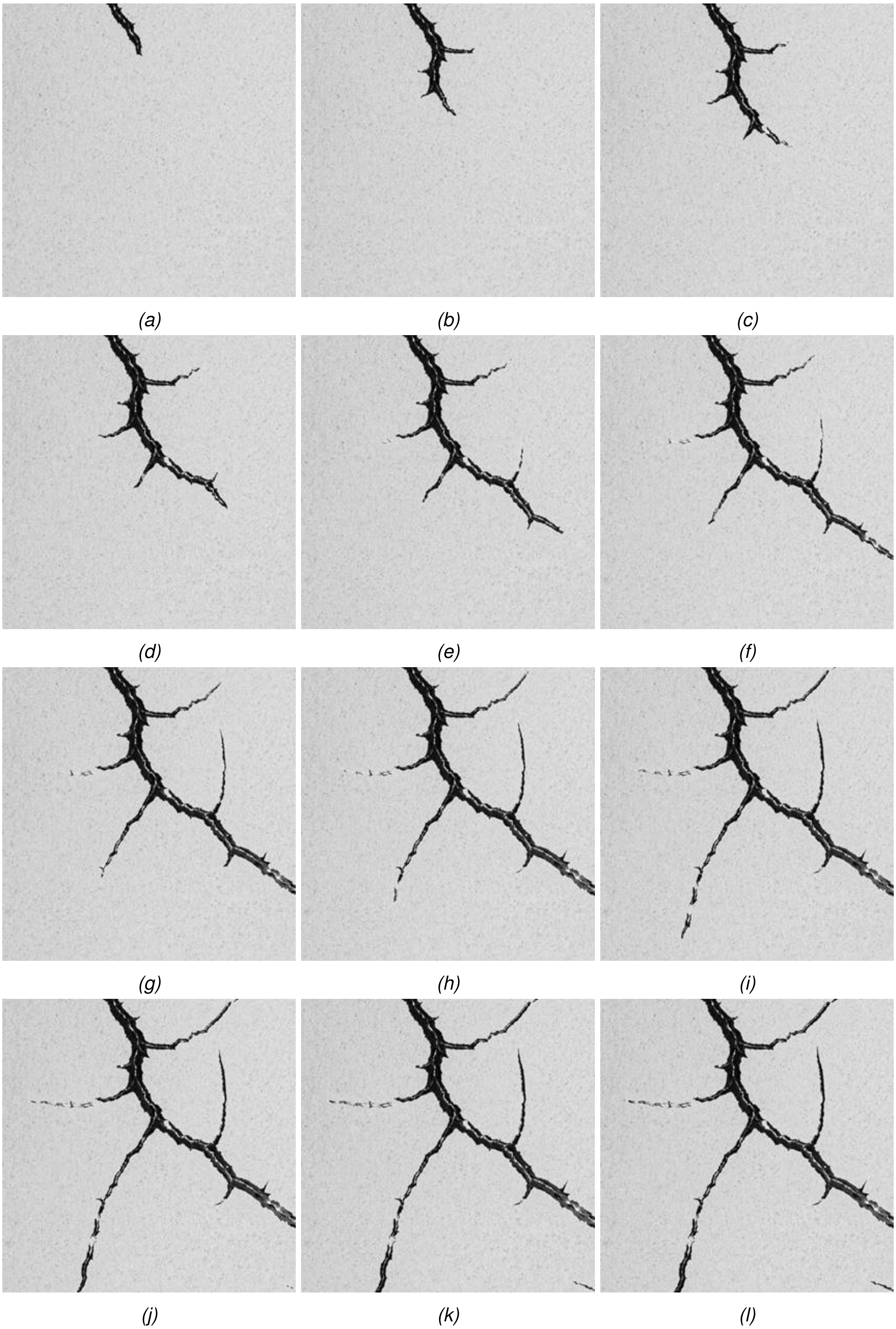

Figure 2.112: Detail of pathway formation. Test COx2 (FPR-23-0071).

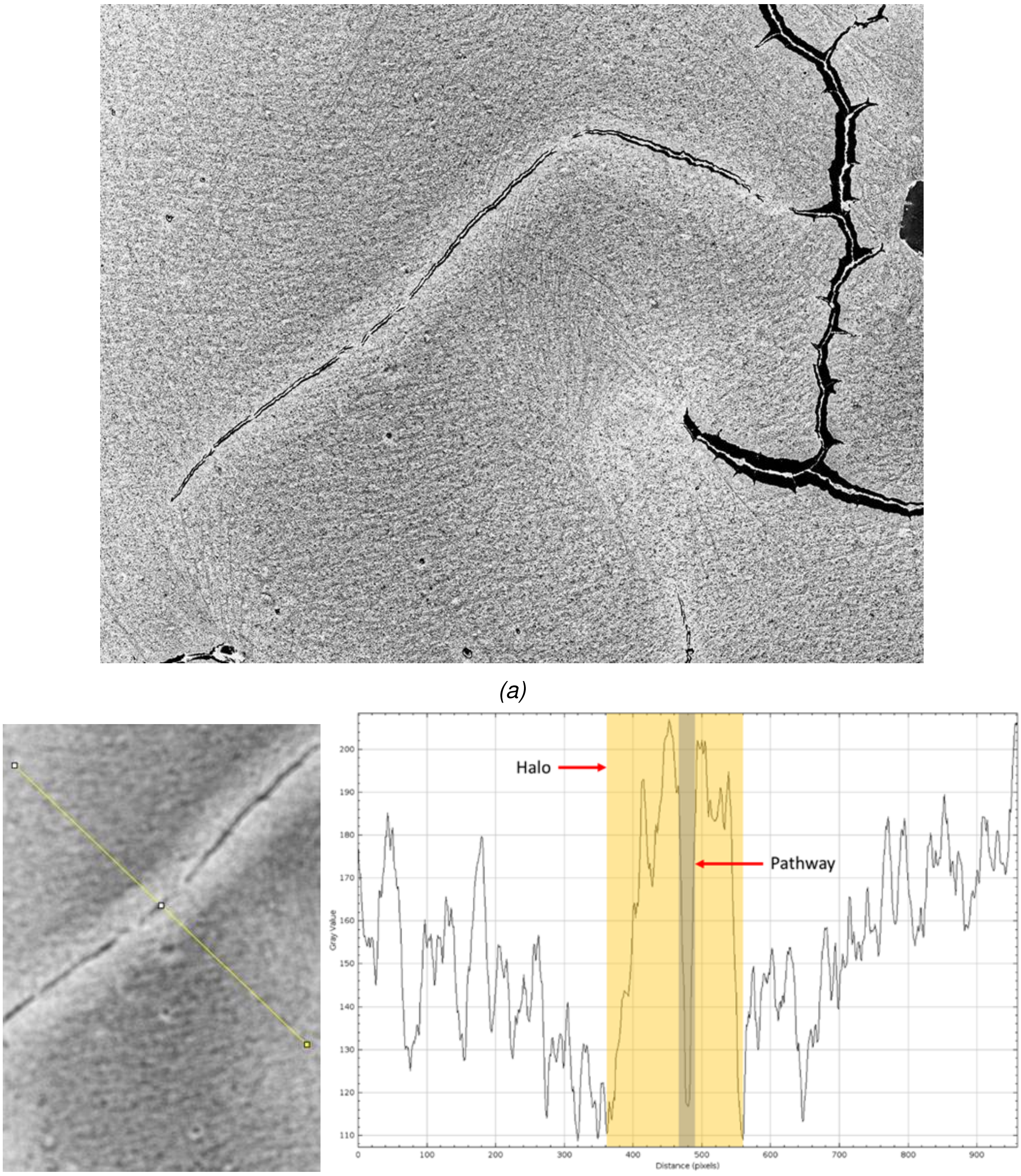

(a)

(b)

(c)

Figure 2.113: Halo features seen around pathways in detail.

therefore shows compression of the clay paste in the walls of the pathway. This has been inferred as a mechanism in pathway dilatancy and is confirmed in fracture visualisation experiments.

Further insight on pathway physics can also be gained by considering pathway closure, as shown in Figure 2.114 for test OPA4. When gas pressure is relieved as a pathway migrates as far as the outer filter of the apparatus, pressure is therefore reduced within all pathways. Figure 2.114 shows two consecutive timelapse frames separated by 3 seconds. In Figure 2.114a a pathway is clearly seen about the centre of the view. As gas pressure reduced, this feature closed completely, as seen in Figure 2.114b. A faint trace of the pathway can be seen as a slightly darker grey lineation. Closure of this feature resulted in the opening of two features that paralleled the closed feature. An air bubble also opened as the feature pathway closed. This shows that the compressed clay either side of the feature pathway was elastically opened and once pressure reduced the elasticity resulted in the closure of the pathway. Some pathways

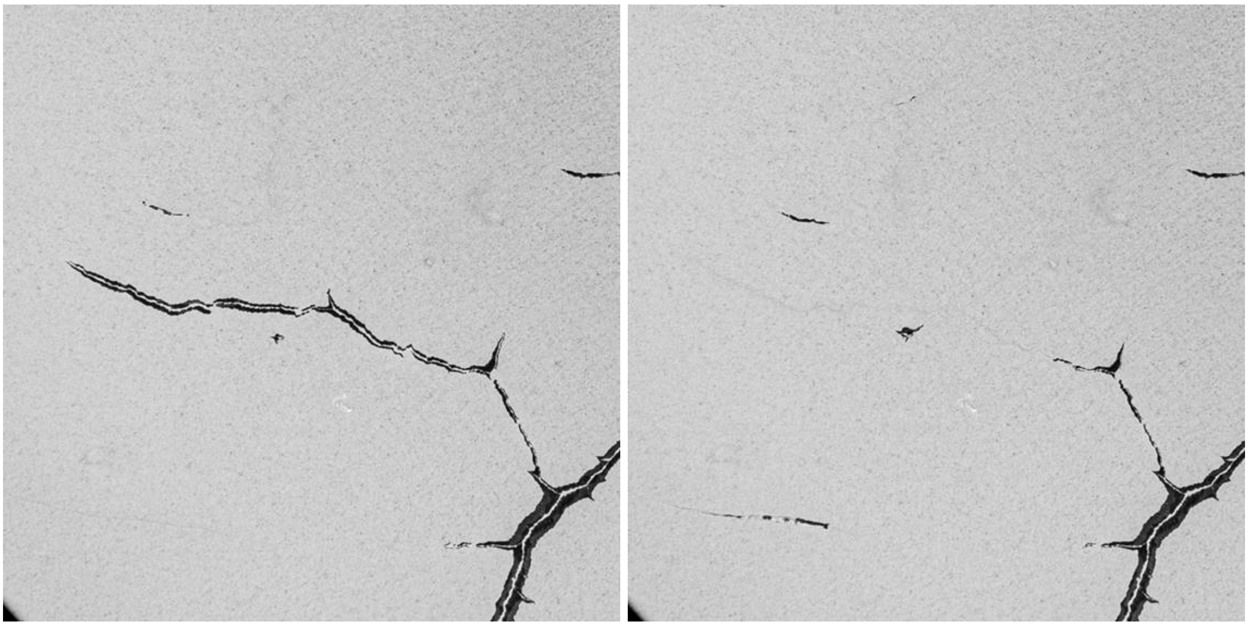

(a) (b)

Figure 2.114: Detail of the closure of pathways as seen in test OPA4.

remain opened, but this is likely to result from friction between the clay and/or steel baseplate. Figure 2.114 confirms the inferred physics of pathway dilation.

Variation with water content

The experimental programme included dedicated experiments on the role of water content on pathway formation in bentonite. However, these experiments have yet to be completed as a result in breakage of the glass within the apparatus. However, all clay pastes started by conducting tests at varying water content until pathway formation was that expected. Whilst these experiments were not as robust as the experiments that will be conducted later in the study, they do offer insight into the role water content has on pathway formation.

Figure 2.115 shows three tests conducted in Boom Clay for a range of water contents between 32 and 42%. As seen, the highest water content resulted in thin pathways, whereas the lower water content resulted in very broad features. The length of the experiment also greatly varied. At the lowest water content (32%), it took less than two timelapse frames to progress from gas entry to breakthrough, i.e., less than 6 seconds. For the intermediate water content (37%) it took 5 time-lapse frames to progress from gas entry to breakthrough, i.e., 15 seconds. However, for a water content of 42% it took around 18 mins to reach breakthrough. Therefore, water content controls the size of the pathways and the velocity of pathway propagation. At lower water content, the paste behaved more explosively, while at higher water content it behaved as expected with slow propagation of dilatant pathways. At a higher water content there was more closure of the pathways once gas pressure had been relived.

Evidence of self-sealing

Dedicated experiments were planned to investigate self-sealing issues, and these have yet to be completed because of breakage of the glass viewing window. However, two experiments showed self-sealing processes. Figure 2.105 showed the detail of test COx1 up until breakthrough. This test did not have the sort of breakthrough that most tests had. *Figure 14* shows a continuation of Figure 2.105, with the last timelapse frame shown in Figure 2.105 being the first frame shown in Figure 2.116

A secondary set of pathways were formed following breakthrough, as shown in Figure 2.116. This created a new set of pathways that did not match the initial population of pathways. Figure 2.117 compares the

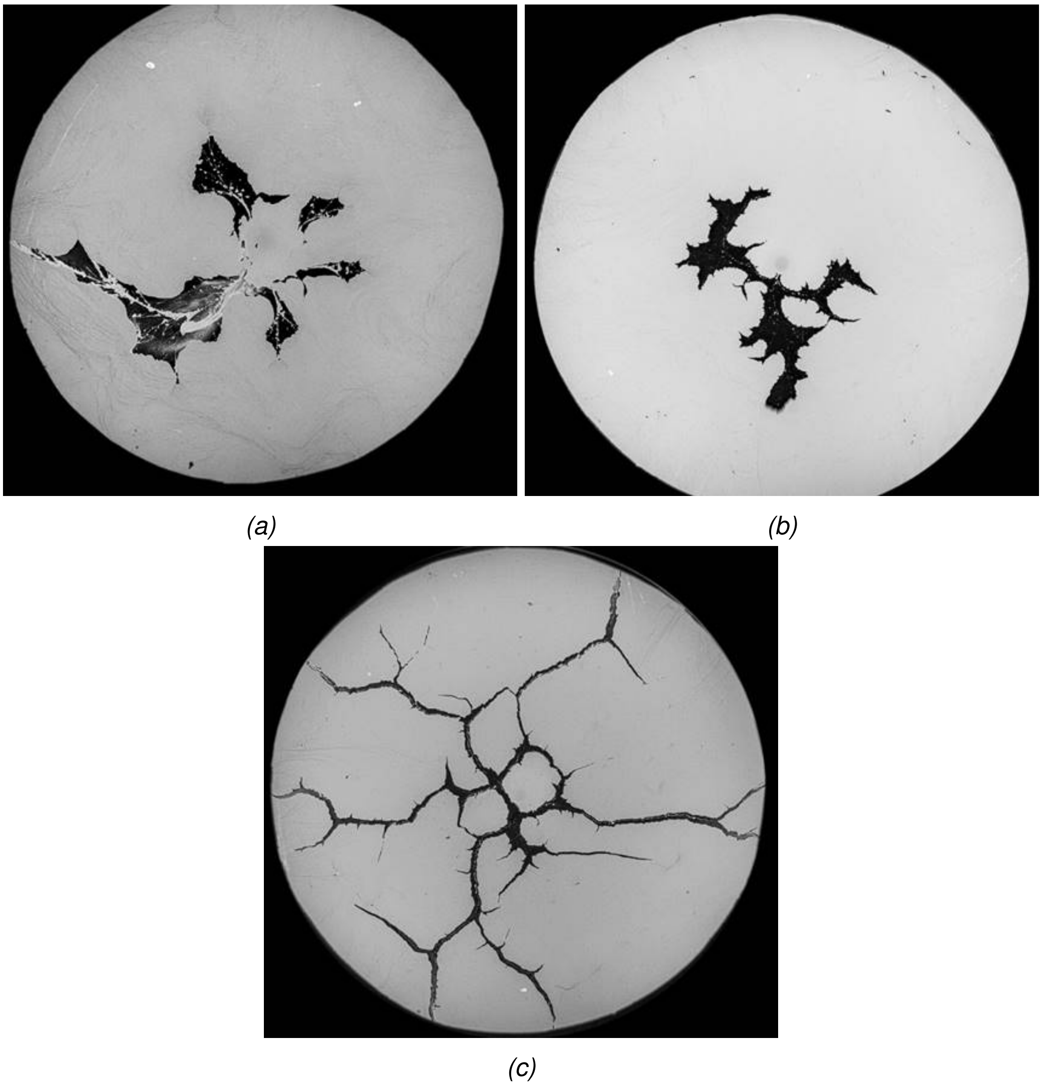

Figure 2.115: Water content of Boom Clay. a) Water content of 32%; b) Water content of 37%; c) Water content of 42%

two populations of pathways with the initial set of pathways shown in blue and the secondary set shown in green. This clearly shows that most of the secondary set of pathways did not match the primary set. The closure of the pathways at the centre of the sample resulted in a new set of pathways forming once pressure was sufficient. As stated previously, the new second set of initial pathways then dictated the distribution of the secondary set of pathways. Figure 2.116b shows that the tip of the propagating pathways resulted in the compression of the clay ahead of the pathway. This closed the existing pathway network and meant that few pathways reached the existing pathways with the latter being in an open state. Figure 2.117 also shows that some of the secondary pathways cut directly across the existing pathways. This meant that the pathways had self-healed and did not represent a mechanical weakness for the propagating pathways to exploit. The time-lapse video of the experiment suggests that the primary set of pathways played no role in the distribution of the secondary set, and the latter formed as if the former had never formed. However, towards the periphery of the viewed area, some of the secondary paths appear to have connected with the primary set of pathways (these pathways appear almost black), although this could just mean that the pathway shown as secondary were not closed at breakthrough or were not re-pressurised by the growth of the secondary set of pathways.

Quantification of pathway growth

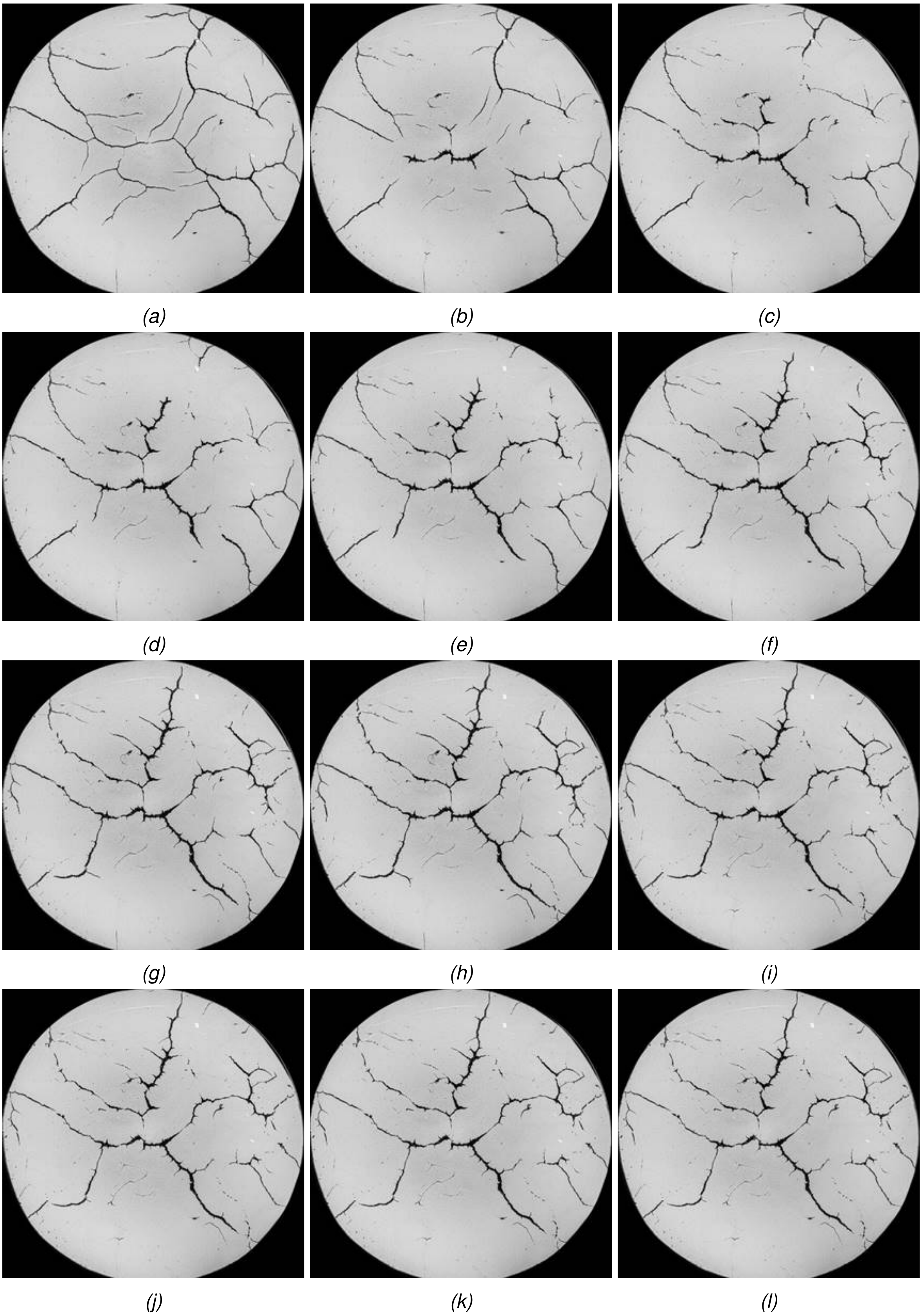

Figure 2.116: Evidence of self-sealing seen in test COx1.

The experimental programme has not been completed by the time of reporting. The intention is to complete the experiments as soon as replacement glass is delivered. Once all tests have been completed, a study

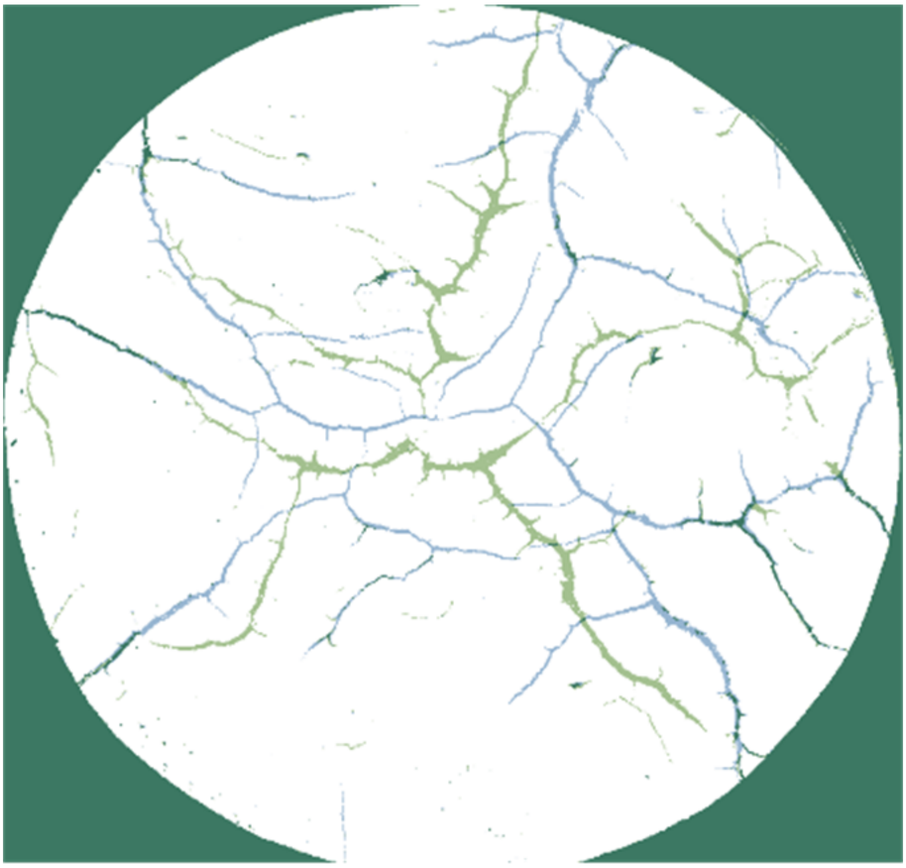

Figure 2.117: Comparison of pathway population 1 (blue) and 2 (green) showing evidence of self-sealing in COx1.

aimed to quantity pathway growth will then occur. Therefore, at the time of reporting we do not have quantitative data on pathway volume, velocity, or growth.

2.4.6. Summary

At the time of reporting, a total of 25 experiments had been conducted. This meant that 15 of the planned 43 experiments had been completed. Breakage of the glass viewing window of the apparatus had resulted in a significant delay to the experiments as the component is made to order. Additionally, quantitative analysis of the conducted experiments was also not complete.

The study aimed to answer several key questions about gas flow in clay-rich materials. This included research questions such as: 1) Do we see similar behaviour (gas entry pressure, pathway network etc) for five repeat tests? 2) Do we see similar behaviour between different clay pastes? 3) Do we see differences in behaviour for variations in moisture content? 4) Do we see evidence of self-sealing of gas pathways? 5) What happens if gas supply stops? 5) Do we see any change in behaviour with pressurisation rate? 6) Do we see any change in behaviour over a range of sand:bentonite mixes? The 25 experiments conducted mean that answers to question 1 to 4 could, at least in part, be made for Boom Clay, Callovo-Oxfordian claystone, and Opalinus Clay.

The use of clay paste resulted in an unavoidable fabric in each test sample. Experience had established a methodology where the fabric was minimised and did not impact experiments adversely. However, it was difficult to not result in trapped air bubbles within the clay, that when the sample was loaded resulted in air pressure sufficient to form dilatant pathways from the bubbles. These were not seen to impact the experiment or influence the direction that pathways propagated. It must be noted that the start clay paste therefore has a texture that is not easily controlled and has been minimised as much as possible.

All experiments showed similar pathway formation. In all three pastes, dilatant pathways formed with a stochastic distribution. The pathways seen in Boom Clay tended to be much broader than those seen in Callovo-Oxfordian claystone and Opalinus Clay. In all three paste types, pathways branched and created a dendritic distribution of pathways. The end distribution was dictated by the initial formation of pathways and how many populations of pathways formed close to the injection point. In the examples shown, multiple populations of pathways could be identified. Comparison of each test showed that no significant difference was seen in the physics creating pathways in clay paste. It is therefore concluded that all three clay types showed the formation of a dendritic pattern of pathways from the central injection point with a stochastic distribution. Early pathway formation dictated the end distribution of pathways.

Detailed examination of pathway migration showed a main pathway, with the formation of branches and offshoots from this dominant feature. As pathways migrated, branches formed at a critical length and one branch dominated more than the other. The main pathway propagated at a much greater velocity than the smaller offshoots and branches. In the highlighted example, one small offshoot propagated in the opposite direction of the main pathway, highlighting that pathway formation was not simply from the centre of the sample to the outside. It was noted that only the main pathway resulted in branching and offshoots. This might indicate that the opening ahead of a main feature resulted in the “cracking” of the pathway wall in a similar manner to geological rifting.

For each clay paste type, five repeat tests were conducted as identical as possible. In Boom Clay, all five tests showed a similar pattern of pathways. Differences were seen in the width of pathways, with one test showing very fine pathways and another showing several broad features. Generally, all five tests showed the formation of a dendritic pattern of pathways from the central injection point with pathways of varying width. There was a stochastic nature to the formation of pathways. In Callovo-Oxfordian claystone, generally all five tests showed the formation of a dendritic pattern of pathways from the central injection point with a stochastic distribution. Multiple populations of pathways were seen, and the number of the populations varied between the five tests. The early formation of pathways near to the injection point dictated the number and distribution of the populations of pathways, which varied between two and four. In Opalinus Clay, all five tests showed the formation of a dendritic pattern of pathways from the central injection point with pathways of varying width with a stochastic nature to the formation of pathways. Some variation in the width of pathways was seen, with two tests showing broader features in places. As with Callovo-Oxfordian claystone, the early formation of pathways dictated the distribution and populations of features. Between three and five distinct populations could be identified. The final test conducted in Opalinus Clay showed a different distribution of pathways, with a considerable number forming at the periphery of the viewable area.

It must be noted that the full area of the clay was not visible. The shoulder of the steel retaining collar meant that the outer 20 mm of the clay was not visible. In a simple system, it would be expected that a single pathway grew from the centre of the view to the outside, where gas pressure would escape through the plastic filter. This was not seen with multiple pathways forming, with many pathway tips growing at the same time. Pathways tended to have a critical length that resulted in branching and the pressure loss along a pathway meant that as gas pathways formed further away from the injection point their growth became unstable and other pathways then grew as a consequence.

Close examination of pathways showed a halo feature around some pathways. The compression of the clay near the injection port resulted in a lightening of the greyscale, meaning that compressed clay lightened in greyscale. Therefore, the halo showed that the wall of the clay either side of the pathways compressed to accommodate the dilating pathway. The halo was around five times the width of the pathway on both sides. This confirms the conceptual model of dilatant pathway migration with the compression of pathway walls. This is further confirmed by observing the closure of pathways. As gas pressure reduced, some pathways elastically closed completely, leaving a faint trace of the pathway as a darker grey lineation. Closure of the pathways also resulted in the opening of other features, such as gas bubbles or pathways. This demonstrated that the compressed clay either side of the feature pathway was elastically opened and once pressure reduced the elasticity resulted in the closure of the pathway. Some pathways remain opened, but this is likely to result from friction between the clay and/or steel baseplate.

Results were introduced comparing the experimental parameters with the time-lapse photographs. The time when the first gas pathways were seen corresponded with the approximate time when a deviation between the observed gas pressure and the predicted gas pressure was observed. At this time, stress on the sample increased as the clay dilated to accommodate the forming network of pathways. Gas pressure continued to increase until a clear change in slope was seen. At this time, some pathways closed indicating that gas breakthrough had occurred, and gas had started to exit the clay. Stress on the sample also started to decrease as gas pressure within the pathways reduced. The data presented suggests that the interpretation of first gas entry is very difficult from test results. The interpreted gas entry was later than the first entry seen in the time-lapse images. The first gas entry did correspond with the start of increase of stress on the sample, but the noise level of the data meant that a later time was picked as the time of gas entry. At this time a considerable population of features had already formed. Therefore, the interpretation of gas injection experiments in competent rock may not identify the time of the first gas entry.

Experiments were initially conducted in each clay type at different water content to determine the ideal water content. In Boom Clay, the geometry and velocity of pathway formation was seen to be strongly influenced by water content. For a high water content of 42%, thin pathways formed that took around 18 minutes to reach breakthrough. At a lower water content of 37% it took around 15 seconds to reach breakthrough and the width of pathways was very broad compared with those that formed at a water content of 42%. At the lowest water content of 32%, it took less than 6 seconds to reach breakthrough and very broad pathways formed. Therefore, water content controls the size of the pathways and the velocity of pathway propagation. At lower water content, the paste behaved more explosively, while at higher water content it behaved as expected with slow propagation of dilatant pathways. At a higher water content there was more closure of the pathways once gas pressure had been relived.

Self-sealing was seen in two experiments. Midway through the pathway propagation phase, gas pressure was relieved as a pathway reached the outside of the sample. This resulted in the elastic closure of pathways, especially at the centre of the sample. A secondary set of pathways then formed which did not match the primary set. As stated earlier, the new second set of initial pathways then dictated the secondary set of pathways. As the pathways propagated, the clay ahead of the pathway compressed, resulting in further closure of the existing pathways. As a result, some of the secondary pathways cut directly across the existing pathways, meaning that the primary pathways had self-healed and did not represent a mechanical weakness for the propagating pathways to exploit. The time-lapse video of the experiment suggests that the primary set of pathways played no role in the distribution of the secondary set, and the latter formed as if the former had never formed. However, towards the periphery of the viewed area, some of the secondary paths appear to have connected with the primary set.

2.4.7. Key learning points

2.4.7.1. New knowledge acquired

The use of carefully designed analogue tests using clay pastes have confirmed key aspects of the dilatant pathway gas flow mechanism. These were previously inferred from interpretation of experiments on competent rock samples where direct observation was not possible.

The current tests have confirmed that multiple pathways form at the same time, and these vary in size and distribution within the sample. The velocity of pathway growth varies between pathways, with some pathways migrating quicker and others at a slow rate. The distribution of pathways is stochastic, with the distribution dictated early in the experiment by the initial formation and branching of pathways. It was seen that some pathways paused in their growth and restarted to grow later. It is an important observation that multiple pathways form at the same time.

Pathway formation is by the creation of dilatant pathways as opposed to fracture formation as a fracture would propagate at the speed of the sonic velocity of the clay if sufficient water was at the crack tip. Secondly, gas entry occurs at a pressure considerably below the stress imposed, therefore gas pathways are not traditional fractures.

The dendritic pattern of pathways resulted in distinct populations of pathways. The number of these populations is set early in the migration process.

The current experiments confirmed that the walls of a dilatant pathway elastically compress to accommodate the pathway. As a result, stress on the sample increases as seen in the load cell data, in the same way as seen in triaxial experiments. The width of the compression zone is many times the width of the pathway and this is likely to relate to the competence of the material. Ahead of a moving pathway the clay is also compressed. This means that pathways close existing fabric or pre-existing pathways.

As gas pressure reduced because of breakthrough, the elastically compressed pathway walls rebound and close the pathways. Only a small trace was seen. This explains why post-mortem analysis of samples of Boom Clay have failed to identify any gas pathways. The current results suggest that pathways will elastically close to an extent that they cannot be identified in SEM analysis.

Main features resulted in branching and formation of offshoots in a similar manner to geological rifting. Smaller, finer pathways did not branch to the same extent.

Water content controls the width and velocity of pathway propagation. This suggests that pathway migration in competent clay will also be dictated by water content.

Self-sealing was observed, with a secondary set of pathways forming that did not correspond with the primary features. Secondary pathways were seen to cross primary features as if they did not exist, meaning a self-healing of the pathways. Without self-healing, the primary features would have represented a mechanical weakness that would have been easy to transmit gas. However, pre-existing features were not seen by the formation of a secondary set of features.

No variation in the physics of gas pathway formation was seen between the three clay types tested.

Repeatability was good between the tests conducted under identical conditions with only minor variations. Repeat tests showed the stochastic nature of pathway formation.

Interpretation of gas entry from analysis of gas pressures and stress measurements results in an estimate of initial gas entry later than seen. Therefore, interpretation of triaxial experiments may not properly identify initial gas entry.

2.4.7.2. Impact of acquired knowledge

The experimental results have confirmed the existing conceptual model of dilatant pathway migration. It has shown the process of dilatant pathway formation and confirms that the changes in stress observed in triaxial experiments is because of dilatant pathway formation. Observations of pathway closure have confirmed why post-mortem analysis of triaxial experiments has not identified any pathways, which has been interpreted by others as evidence of visco-capillary flow.

Observations of self-sealing suggest that pre-existing dilatant pathways will not impact future episodes of gas flow. Therefore, successive episodes of gas movement are not likely to result in changes in the gas migration capacity of the rock.

Changes in water content are likely to change the properties of gas pathway migration, most notably the size and velocity of pathways.

The experimental programme has confirmed the usefulness of simple analogue tests in confirming key assumptions of process. This approach in the future could significantly increase our understanding of several processes relevant to radioactive waste disposal.

2.4.7.3. Remaining knowledge gaps

The experimental programme has not been completed at the time of reporting because of breakage of a key component of the apparatus. By the time of the end of EURAD-GAS project, it is anticipated that all the research questions aimed to be investigated by the study will have been answered. This will highlight where remaining gaps exist. The experimental programme aimed to answer a limited number of research questions. This can be broadened to look at other topics, such as salinity, stress, layering of rocks, heterogeneity, the influence of voids, interfaces between clay and other materials, hydration, and different types of bentonite.

2.4.7.4. Recommendations for the future

The current study has been a useful first step in investigating gas flow in clay using a visualisation approach. Further experiments can be conducted to look at specific problems as listed above. Experimental results can be modelled in the future, although the stochastic nature of pathway growth shows that deterministic modelling the distribution of pathways will have limited usefulness.

References

Armand, G., Conil, N., Talandier, J. and Seyedi, D.M. (2017) Fundamental aspects of the hydromechanical behaviour of Callovo-Oxfordian claystone: from experimental studies to model calibration and validation. *Computers and Geotechnics*, *85*, pp.277-286.

Beerten, K, and Leterme, B (2012) *Physical geography of north-eastern Belgium – the Boom Clay outcrop and sub-crop zone SCK-CEN report* ER-202 12/Kbe/P-2 60p.

Bernier, F, Li, XL, and Bastiaens, W. (2007) *Twenty-five years' geotechnical observation and testing in the Tertiary Boom Clay formation,* Géotechnique 57(2) pp.229–237.

Blanchart, P, Faure, P, De Craen, M, Bruggeman, C, and Michels, R (2012) *Experimental investigation on the role of kerogen and clay minerals in the formation of bitumen during the oxidation of Boom Clay,* Fuel 97, 344–351.

Cuss, R.J., Harrington, J., Giot, R., and Auvray, C. (2014) Experimental observations of mechanical dilation at the onset of gas flow in Callovo-Oxfordian claystone. In: *Clays in Natural and Engineered Barriers for Radioactive Waste Confinement*; Norris, A., Bruni, J., Cathelineau, M., Delage, P., Fairhurst, C., Gaucher, E.C., Hohn, E.H., Kalinichev, A., Lalieux, P, and Sellin, P. (Eds), **400,** *Geological Society Special Publications*: London, United Kingdom, Geological Society of London, pp. 507-519, doi:10.1144/SP400.26

Cuss, R.J., Wiseall, A.C., and Hough, E. (2017) An experimental study of the influence of bedding and pre-existing fractures on the propagation of hydraulic fractures. M4ShaleGas report D1.3, British Geological Survey, Nottingham, UK, 86pp. www.m4shalegas.eu

De Craen, M, Wang, L, Van Geet, M, and Moors, H (2004) *Geochemistry of Boom Clay pore water at the Mol site,* SCK-CEN-BL-990 04/MDC/P-48, SCK-CEN.

Dehandschutter, B, Vandycke, S, Sintubin, M, Vandenberghe, N, Gaviglio, P, Sizun, JP, and Wouters, L, (2004) *Microfabric of fractured Boom Clay at depth: a case study of brittle-ductile transitional clay behaviour,* Applied Clay Science, 26(1-4) pp.389-401.

Esteban, L., Bouchez, J.L. and Trouiller, A. (2006) The Callovo-Oxfordian argillites from the eastern Paris Basin: Magnetic data and petrofabrics. *Comptes Rendus Géoscience*, *338*(12-13), pp.867-881.

Gaucher, E., Robelin, C., Matray, J.-M., Négrel, G., Gros, Y., Heitz, J.-F., Vinsot, A., Rebours, H., Cassagnabère, A. and Bouche, A.T. (2004) ANDRA underground research laboratory: interpretation of the mineralogical and geochemical data acquired in the Callovo-Oxfordian formation by investigative drilling, Phys. Chem. Earth 29, pp. 55–77.

Gautschi, A. (2001) Hydrogeology of a fractured shale (Opalinus Clay): Implications for deep geological disposal of radioactive wastes. *Hydrogeology Journal,* **9,** pp.97–107

Honty, M, and De Craen, M (2011) *Boom Clay mineralogy – qualitative and quantitative aspects,* SCK CEN contract: CO-90-08-2214-00 NIRAS/ONDRAF contract: CCHO 2009-0940000, Research Plan Geosynthesis.

Pearson F. J., Arcos D., Boisson J.-Y., Fernandez A. M., Gäbler H.-E., Gaucher E., Gautschi A., Griffault L., Hernan P. and Waber H. N. (2003) *Mont Terri Project — Geochemistry of Water in the Opalinus Clay Formation at the Mont Terri Rock Laboratory*. Geology Series No. 5. Swiss Federal Office of Water and Geology, Bern.

Rousset, D. and Clauer, N. (2003) Discrete clay diagenesis in a very low-permeable sequence constrained by an isotopic (K–Ar and Rb–Sr) study. *Contributions to Mineralogy and Petrology*, *145*(2), pp.182-198.

Vis, GJ, and Verweij, JM. (2014) *Geological and geohydrological characterization of the Boom Clay and its overburden,* OPERA-TNO 411 Technical Report.

Wemaere, I, Marivoet, J, and Labat, S. (2008) *Hydraulic conductivity variability of the Boom Clay in north-east Belgium based on four core drilled boreholes,* Physics and Chemistry of the Earth, Parts A/B/C 33 24-36.

Wenk, H.-R., Voltolini, M., Mazurek, M., Van Loon, L.R. and Vinsot, A. (2008) Preferred Orientations and Anisotropy in Shales: Callovo-Oxfordian Shale (France) and Opalinus Caly (Switzerland), Clays and Clay Minerals, 56, pp 285-306.

Wileveau, Y. and Bernier, F. (2008) Similarities in the hydromechanical response of Callovo-Oxfordian clay and Boom Clay during gallery excavation. Physics and Chemistry of the Earth, Parts A/B/C, 33, pp.S343-S349.

Wiseall, A.C., Cuss, R.J., Graham, C.C., and Harrington, J.F. (2015) The visualization of flow paths in experimental studies of clay-rich materials. *Mineralogical Magazine*, **79**(6), pp.1335-1342. DOI: 10.1180/minmag.2015.079.06.09.

Wong, T, Batjes, DAJ, and de Jager, J, (Eds.; 2007) *Geology of the Netherlands*. Herent: Royal Netherlands Academy of Arts and Sciences.

Yu, HD, Chen, WZ, Jia, SP, Cao, JJ, and Li, XL (2012) *Experimental study on the hydro-mechanical behaviour of Boom clay,* International Journal of Rock Mechanics and Mining Sciences 53 (2012) 159-165.

Yven, B., Sammartino, S., Géraud, Y., Homand, F., and Villiéras, F. (2007) Mineralogy, texture and porosity of Callovo-Oxfordian argillites of the Meuse/Haute-Marne region (eastern Paris Basin). *Mémoires de la Société géologique de France*, **178**, pp.73–90.

.

British Geological Survey (BGS)

2.5. Advection processes (UKRI-BGS)

2.5.1. Laboratory scale testing of synthetic materials (UKRI-BGS)

Over the lifetime of a GDF, gases may be generated by the waste itself, corrosion of the waste canisters and microbial action (IAEA, 1997). Hydrogen, in particular, is a likely product, although other gases may also be relevant, depending on the nature of the waste. Evaluation and management of the interaction between these gases, the EBS and the hostrock is, therefore, required to assess repository safety (Sellin et al., 2013).

Very low hydraulic permeabilities, a relatively deformable matrix and a low tensile strength are key characteristics of clay-rich materials, which strongly influence their gas flow properties (Neuzil, et al., 1994; Marschall et al., 2005). Gas migration in clays can occur by 4 primary mechanisms (Marschall et al., 2005): (i) dissolution of gas into porewater (governed by Henry's Law) and diffusion (governed by Fick's law), (ii) advection after overwhelming pore network capillary forces, resulting in the displacement of water through preexisting porosity, (iii) advection through the creation of new voidage, via deformation of the matrix, or (iv) macroscale hydrofracture. The first of these mechanisms will always occur, but if the diffusion of gas is not sufficient to match its generation rate, then pressure will build until advection (ii or iii) eventually occurs. Which advection mechanism will dominate depends on whether the pore throat radii are sufficiently large to allow water displacement at pressures below those necessary to deform the clay matrix (Marschall et al., 2005; Harrington et al., 1999). Findings from the EC FORGE project, indicated that lower clay contents and lower saturation states (which are expected to vary during repository lifetime) may favour the former, whilst higher clay content and higher saturations may increase the likelihood of deformation (Sellin et al., 2013; Graham et al., 2014b). However, the conditions for this transition and the understanding necessary to select the correct conceptual model for a given clay-material remain poorly constrained (Graham et al., 2014b; Birkholzer et al., 2019).

Multiple experimental programmes document the occurrence of gas flow in clays, above a critical threshold (Graham et al., 2014b; EURAD, 2020; Pusch et al., 1985; Tanai et al., 1997; Gallé et al., 1998; Horseman et al., 1997; Horseman et al., 1999; Graham et al., 2016; Shimura et al., 2017), which has been shown to relate to the internal stress state of the clay, σ_{ij}, (Gallé et al., 1998; Horseman et al., 1999; Graham et al., 2016). This behaviour has been attributed to gas advection via deformation of the matrix (iii), also termed 'pathway dilatancy'. In such cases, gas migration is accompanied by complex hydromechanical coupling, which has proven challenging but necessary for comprehensive numerical simulation of the process (Birkholzer et al., 2019; Guo and Fall, 2021). Nevertheless, insufficient information is available to populate gas flow models incorporating these features (e.g., spatial and temporal distribution of pathways), limiting the development of predictive simulations in this field (Guo and Fall, 2021; Rutqvist et al., 2021).

This information remains limited for clay-rich materials because: (i) the narrow pore throats (Nelson, 2009) and gas pathway apertures involved (>50nm; Harrington et al., 2012) hinder the use of conventional analytical and imaging methodologies on a representative scale (Busch et al., 2017; Godinho et al., 2019), (ii) gas pathways close on depressurisation and cannot be distinguished from damage using standard petrological/analytical techniques Harrington et al. (2012), (iii) clay-rich materials are highly attenuating to acoustic energy (Tosaya, 1982), limiting the success of conventional approaches, such as the monitoring of acoustic emissions to distinguish deformation mechanisms and locations. Recent attempts to image gas pathways in natural clay using microCT analysis may provide an insight into the distribution of residual pathways after gas injection (Gonzalez-Blanco et al., 2017). However, the large scale of these features and their persistence after testing is inconsistent with previous observations (Harrington et al., 2012) and is suggestive of permanent sample damage, potentially due to desaturation or depressurisation of gas after testing. Such post-test methodologies are also limited in that they do not provide real-time information relating to pathway development under pressurised conditions and are likely to detect only the largest features.

As such, this test programme has been designed to examine the role of clay content (in relation to other constituents) on the favoured gas advection mechanism and the resulting distribution of transported gas within these flow regimes. A methodology has been developed to create compacted clays samples with a controlled composition. These samples have then been subjected to gas injection experiments in a constant volume cell after an initial rehydration and swelling phase. An array of 24 stress sensors has been used to monitor the mechanical response of the clay in detail and provide additional insight into the mechanisms and distribution of gas flow in these experiments. This represents the first truly quantitative assessment of deformation in real-time during gas migration and provides a new opportunity to inform predictive simulation of gas advection models in bentonite.

In the following sections a detailed description of the apparatus, the test procedure and results obtained to date are presented. Additional testing will be conducted before the end of the EURAD project and will be reported in the literature when complete. Initial findings from this study have also been published in Graham and Harrington (2023).

2.5.2. Experimental set-up

2.5.2.1. Description of apparatus

BGS custom-designed apparatus (*Figure 2.118*) has six main components: (1) a thick-walled, dual-closure Invar[2] pressure vessel; (2) an injection pressure system; (3) a backpressure system; (4) 24 total stress gauges to measure radial and axial total stresses; (5) two porewater pressure monitoring filters; and (6) a microcomputer-based data acquisition system based around a National Instruments Compact Rio set-up.

The pressure vessel comprises of a dual-closure tubular vessel manufactured from Invar, which is pressure-tested up to 70 MPa. Each end-closure is secured by eight high tensile cap screws which could be used to apply a small pre-stress to the specimen if required. The vessel is mounted vertically with injection of gas through a rod mounted in the lower end-closure (*Figure 2.118*) the dimensions of which are presented in *Figure 2.119*.

The 60 mm internal bore of the pressure vessel is honed and hard-chromed to give a highly polished surface. Two pore pressure filters, labelled F1 and F2 () are mounted in the lower end-closure and used to provide local measurements for pore pressure during the course of the experiment. The total stress sensors are located in a regular geometric pattern, Table 2.30, with 4 radial arrays, each comprised of four sensors, spaced evenly along the sample. Each end-closure also contains four axial total stress sensors, mounted in a square configuration, visible in *Figure 2.118* and *Figure 2.119* [C] and [D].

The central or injection filter is embedded at the end of a 6.4 mm diameter stainless steel tube and is used to inject helium during gas testing. The end of the filter is profiled to match a standard twist drill to minimise voidage around the injection tip.

Table 2.30: Sensor locations. Sensor prefixed with the letter A=axial, R=radial and F=Filter. Radius equates to the centre line of the vessel running axially along its length. Height (z) is the distance from the base of the sample. Surface area relates to the circular size of the sensor/filter, see Figure 2.118.

Sensor name	Rotation (degrees)	Radius (mm)	Height, z (mm)	Surface area (mm^2)
A1	0	20	0	50.27
A2	90	20	0	50.27
A3	180	20	0	50.27
A4	270	20	0	50.27
R1	0	30	12	50.27
R2	90	30	12	50.27
R3	180	30	12	50.27

---

[2] Invar, also know as Alloy 36, is a nickel-iron alloy with a low thermal expansion coefficient.

Table 2.30: Sensor locations. Sensor prefixed with the letter A=axial, R=radial and F=Filter. Radius equates to the centre line of the vessel running axially along its length. Height (z) is the distance from the base of the sample. Surface area relates to the circular size of the sensor/filter, see Figure 2.118.

Sensor name	Rotation (degrees)	Radius (mm)	Height, z (mm)	Surface area (mm^2)
R4	270	30	12	50.27
R5	45	30	24	50.27
R6	135	30	24	50.27
R7	225	30	24	50.27
R8	315	30	24	50.27
R9	0	30	36	50.27
R10	90	30	36	50.27
R11	180	30	36	50.27
R12	270	30	36	50.27
R13	45	30	48	50.27
R14	135	30	48	50.27
R15	225	30	48	50.27
R16	315	30	48	50.27
A5	0	20	60	50.27
A6	90	20	60	50.27
A7	180	20	60	50.27
A8	270	20	60	50.27
F1	135	24	0	28.27
F2	315	24	0	28.27

Pressure and flow rate of the test fluids is controlled using two ISCO-260, Series D, syringe pumps, operating from a single digital control unit. Given the potential for gas leakage past the injection pump seal, a constant flow rate is generated by displacing gas from a pre-charged cylinder (interface vessel) by pumping water into its base. This also facilitates water-saturation of the helium prior to injection, reducing the potential for desiccation. A second pre-charge vessel is placed in the backpressure circuit to collect the gas as it is discharged from the sample. The ISCO pump controller is connected to the National Instruments Compact Rio data logger via an RS232 serial port connection. Test data is over-sampled at an acquisition rate of one scan per 10 seconds. Test data is then smoothed in test history figures, to reduce noise levels, unless additional resolution is required.

2.5.2.2. Calibration

A pressure calibration for one of the ISCO pumps is conducted using a regularly calibrated standard device, by applying ascending and descending incremental steps in constant pressure. The calibrated pump is then used to apply similar, but multiple automated, ascending and descending incremental pore water pressure cycles over at least a 24-hour period, allowing all pressure sensors to be calibrated and the absence of hysteresis ascertained.

Conventionally a linear least-squares regression is used to determine calibration parameters. However, with the sensors used in this apparatus and at the low pressures which testing was conducted at, a non-linearity was detected in the tail of the calibration curve in some cases. This non-linearity was found to increase substantially with every test and, therefore, efforts were made to improve the fitting approach. Residuals were compared when applying 3 different models: (i) a standard linear fit, (ii) a piecewise 2-slope linear fit, and (iii) a piecewise linear-quadratic fit. A Bayesian Information Criterion (BIC) analysis was used to find most valuable changepoint for each sensor response. A substantial improvement has

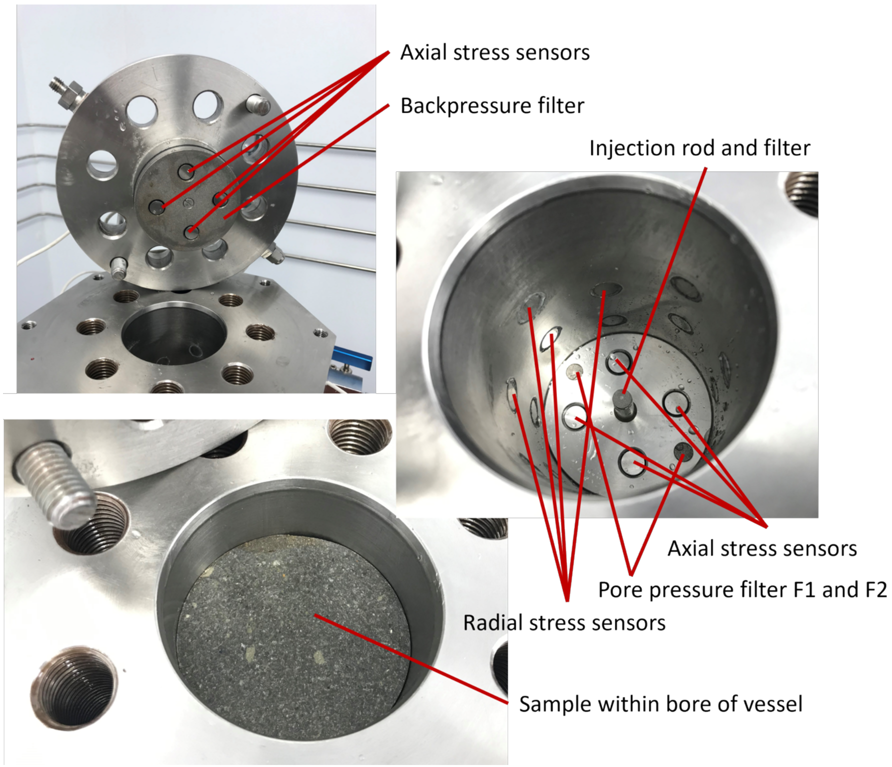

Figure 2.118: Photos of the apparatus and a sample installed within the bore of the vessel.

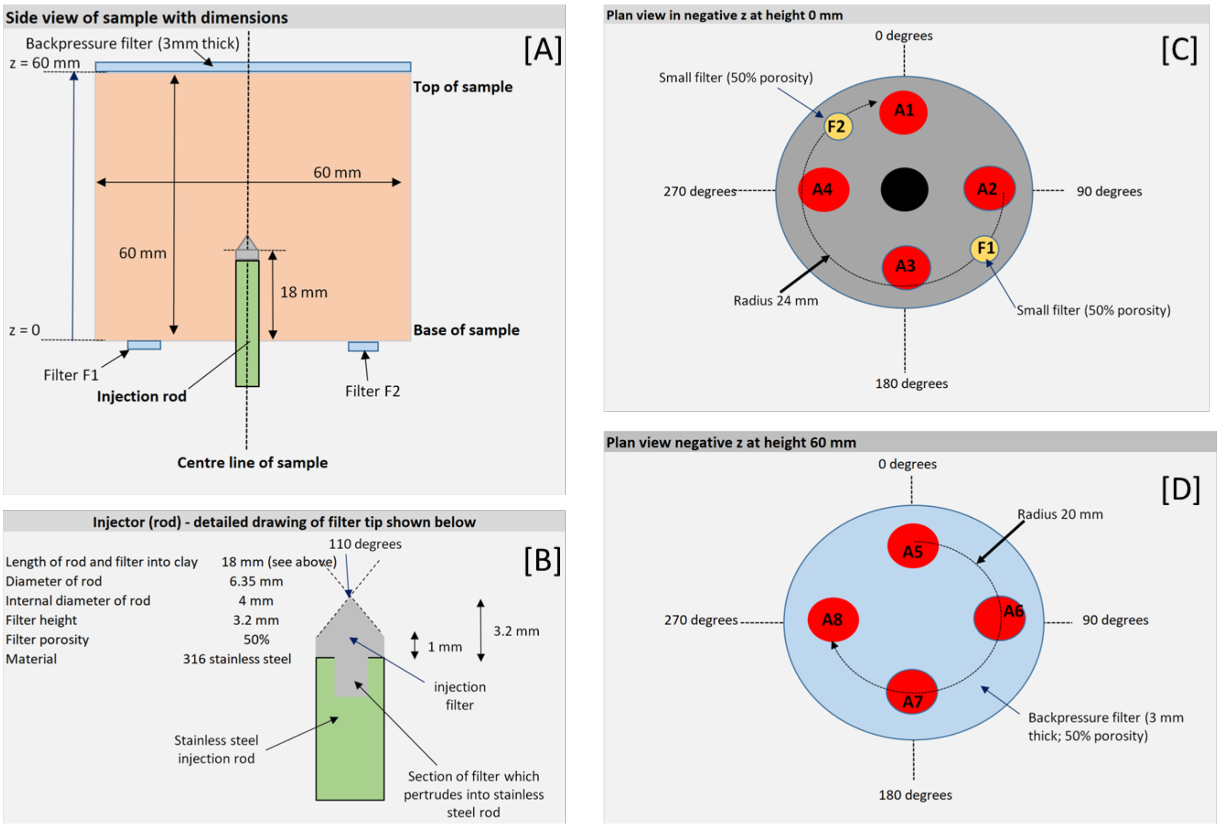

Figure 2.119: Schematic of the apparatus. [A] shows the dimensions of the sample and filters. [B] shows the dimensions of the injection filter. [C] and [D] show the location of the axial sensors in contact with the base and top of sample respectively.

	g/L
NaCl	1.950
$NaHCO_3$	0.130
KCl	0.035
$CaSO_4,2H_2O$	0.630
$MgSO_4,7H_20$	1.020
$CaCl_2,2H_2O$	0.080
Na_2SO_4	0.700

Table 2.31: Chemical composition of the synthetic COx solution used for the synthetic samples in this test programme.

been found be the use of this latter function ($\approx$ 97% error reduction with respect to the initial value; *Figure 2.120*) and, where a non-linearity was observed during calibration, test data will be back-calculated using this new calibration approach going forward.

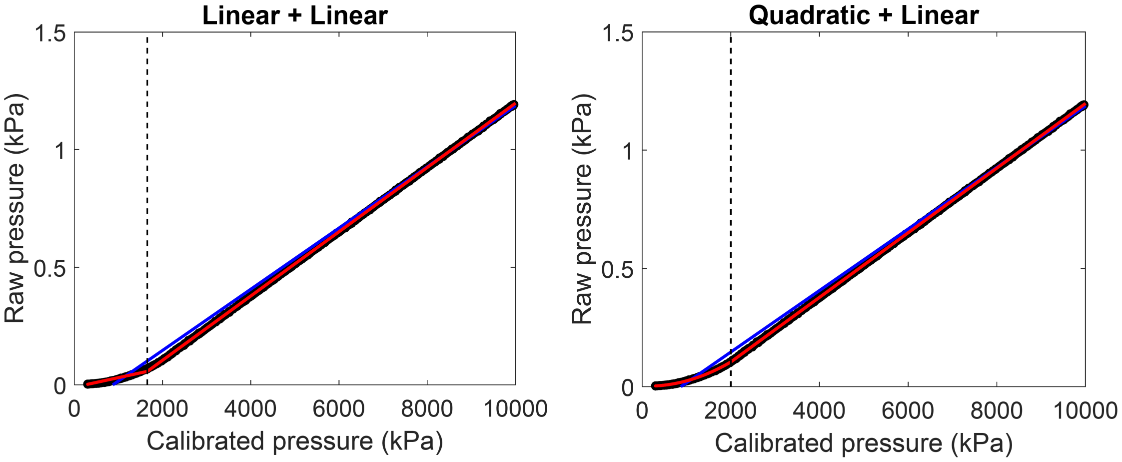

Figure 2.120: Comparison of calibration curve fitting models, with direct measurements shown in black and a standard linear fit shown in blue. Significant deviation occurs at lower pressures. The calculated changepoint used for piecewise fitting is indicated by the dashed black line. Left: A 2-slope linear-linear fit, shown in red ($\approx$ 95% error reduction with respect to the initial value). Right: A 2-slope quadratic-linear fit, shown in red ($\approx$ 97% error reduction with respect to the initial value).

2.5.2.3. Testing fluids

Initial testing (FPR-21-004 and FPR-22-024) was conducted on Mx80 bentonite. Testing of these samples was conducted using deionised water. With the transition to testing on synthetic clay samples (FPR-22-024), a synthetic pore fluid solution has been and continues to be used for the remainder of the project, in order to limit swelling. Since there are no specific *in situ* conditions for such synthetic samples, the reference composition for the Callovo-Oxfordian at the Meuse/Haute Marne Underground Research Laboratory has been selected, as provided by Andra (Table 2.31). It was chosen as a relatively 'generic' pore fluid, which is not expected to encourage substantial swelling, but also not to drastically inhibit swelling either.

2.5.3. Material properties (pre-test and post-test characteristics)

Testing has been conducted on clay mixtures compacted at the BGS, the procedure for which is given in 'Milestone 99 and 100: Experimental progress report of task 2.1 and 2.2'. After pressing samples are turned on a lath and trimmed to diameter and length both of 60mm. Samples FPR-21-004 (Test 1) and FPR-21-034 (Test 2) were composed of 100% Mx80 bentonite. All other experiments have been conducted on synthetic clay samples with varying compositions, consisting of 3 major components: sand, clay and silt. The clay component of each sample is an 80/20% mixture of MX80 bentonite and kaolinite. The bentonite has been milled to a grain size of no larger than 30 microns. The silt fraction is pure muscovite mica and the sand fraction is derived from high purity quartz sand supplied by Lochaline Quartz Sand Ltd, which has been sieved to obtain particles in the range 63-125 microns. *Figure 2.120* shows the synthetic sample composition matrix, with planned compositions marked with a purple circle and associated number. The findings from testing composition 4b (Test 6) have been used to inform the decision to run composition 2b (over composition 3b) as the final test. Sample preparation is now underway and testing will be completed by the end of the project. Composition number 7 is the closest in composition to the natural composition of the Boom Clay (*Figure 2.121*). A sample with this composition (FPR-22-024) was used in Test 4. All test sample numbers and compositions are listed in *Table 2.32*, alongside the test stages applied to the samples. Test samples were lathed to a diameter fractionally below the interior diameter of the vessel, to ensure the sample wasn't damaged during installation.

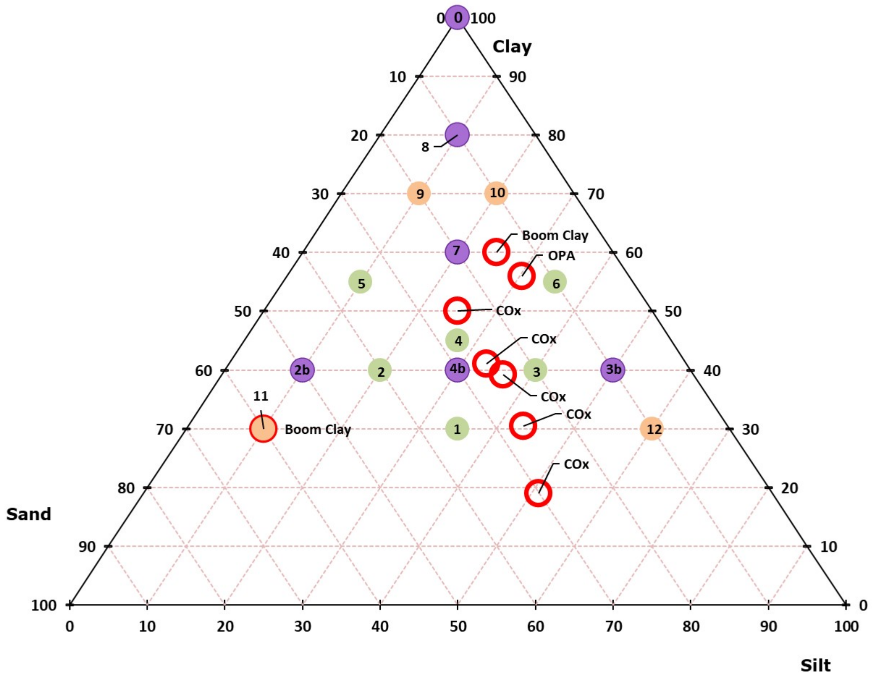

Figure 2.121: Test compositions for the duration of the project. The red circle highlights the end-member clay sample (BC=Boom Clay) and the purple circles show the approximate intended testing compositions. The findings from testing compositions 4b inform a decision on whether to run composition 2b or 3b as the final test.

Table 2.32: Test numbers, sample names and associated compositions, as well as test stages conducted. Eq=equilibration, Hyd=hydration/swelling, GCF=Gas injection Constant Flow rate and Shut-in=stopping of injection pump and pressure decline.

Test	Sample number	Material	Stages
1	FPR-21-004	100% Mx80	Eq, Hyd, Eq, GCF, Shut-in
2	FPR-21-034	100% Mx80	Eq, Hyd, Eq, GCF
3	FPR-22-024	60/20/20% Clay/silt/sand (7)	Eq, Hyd, early decommissioning
4	FPR-22-027	60/20/20% Clay/silt/sand (7)	Eq, Hyd, Eq, GCF

Table 2.32: Test numbers, sample names and associated compositions, as well as test stages conducted. Eq=equilibration, Hyd=hydration/swelling, GCF=Gas injection Constant Flow rate and Shut-in=stopping of injection pump and pressure decline.

Test	**Sample number**	**Material**	**Stages**
5	FPR-22-073	40/10/50% Clay/silt/sand (2b)	Eq, Hyd, early decommissioning
6	FPR-23-033	40/30/30% Clay/silt/sand (4b)	Eq, Hyd, Eq, GCF
7	FPR-23-xxx	40/10/50% Clay/silt/sand (2b)	Due to start

A target dry density of 1.5 g/cm^3 was selected for all test samples. However, pre- and post-geotechnical measurements have also been made for test samples and will be included when findings are published.

2.5.4. Testing protocol

All test samples are subjected to the following test stages: (1) ambient swelling/equilibration with the hydrated filter discs, (2) resaturation and hydration, (3) equilibration and (4) gas injection (stage 4). In addition, sample FPR-21-004 was also subjected to a shut-in phase to examine self-sealing. This wasn't conducted for the synthetic samples to limit imbibition of water after gas breakthrough, so that post-test saturation measurements might provide an indication of any potential desaturation during gas flow.

After calibration all test pipework (excluding the gas injection rod) were flushed with water before testing was started. The top end-closure filter and bottom spot filters (F1 and F2) were also flushed with water before installation of the sample. The test sample was then allowed to slide into the vessel interior and the end-closure bolts tightened until a small change in the lower axial stress sensors was detected, indicating that the sample had come into contact with the base of the vessel. Water from the filters was kept at atmospheric pressure, allowing a brief period of suction into the clay (~24 hrs), so as to limit the likelihood of erosion after pressurisation. The initial hydration phase was then conducted by applying a constant water pressure to the sample. Whilst an applied water pressure of 1MPa was used for the bentonite tests, this was lowered to 250kPa for the synthetic samples after the first synthetic sample (Test 3) was found to generate substantially lower pressures. Selection of a lower applied water pressure was, therefore, decided to be necessary to ensure that the subsequent gas injection phase was not initiated at a pressure already close to the swelling pressure of the sample. Water pressure was supplied through all filters except the injection rod, where an equivalent gas pressure was applied to ensure water could not enter the injection filter.

Hydration was assumed to be complete after the observed stresses generated by the clay were seen to asymptote (e.g., Figure 2.122). Gas injection was next conducted at a constant flow rate of 180μl/h, through the central injection rod. Helium gas was used as a proxy for Hydrogen, so as to inhibit mass changes due to methanogenesis, as well as reducing safety complexities introduced by using this gas (Mijnendonckx et al., 2019). Helium represents a suitable proxy due to its similar atomic size and because the primary process under consideration is mechanical in nature, it is reasonable to assume no significant differences in gas migration behaviour are likely. Test histories for each sample are given in Table 2.32.

2.5.5. Results

Experimental observations – Test 1 (FPR-21-004)

This test was also conducted on a 100% Mx80 bentonite sample. A detailed description of this experiment is given in the Milestone 173: Task 2.2 Experimental progress report. Additional analysis is also presented in Graham and Harrington (2023). Following installation of the sample, a small backpressure of 250 kPa was simultaneously applied to the backpressure filter and both F1 and F2 filters, Figure 2.118. On day 3.1, pressure in all three filters was increased to 1.0 MPa, and the sample allowed to hydrate. The subsequent development of axial stresses is shown in *Figure 5*. At the same time, water pressure was increased and the gas (helium) pressure in the injection filter was also incremented to match the change in water pressure. This was done in order to prevent accidental water flow into the filter and thus remove the possibility of slug flow (i.e. gas displacement of water from the filter ahead of gas entry into the sample) during gas injection. By the end of the swelling test stage, an average axial stress of 7.5 MPa at the bottom had been generated, compared to 8.5 MPa at the top of the sample.

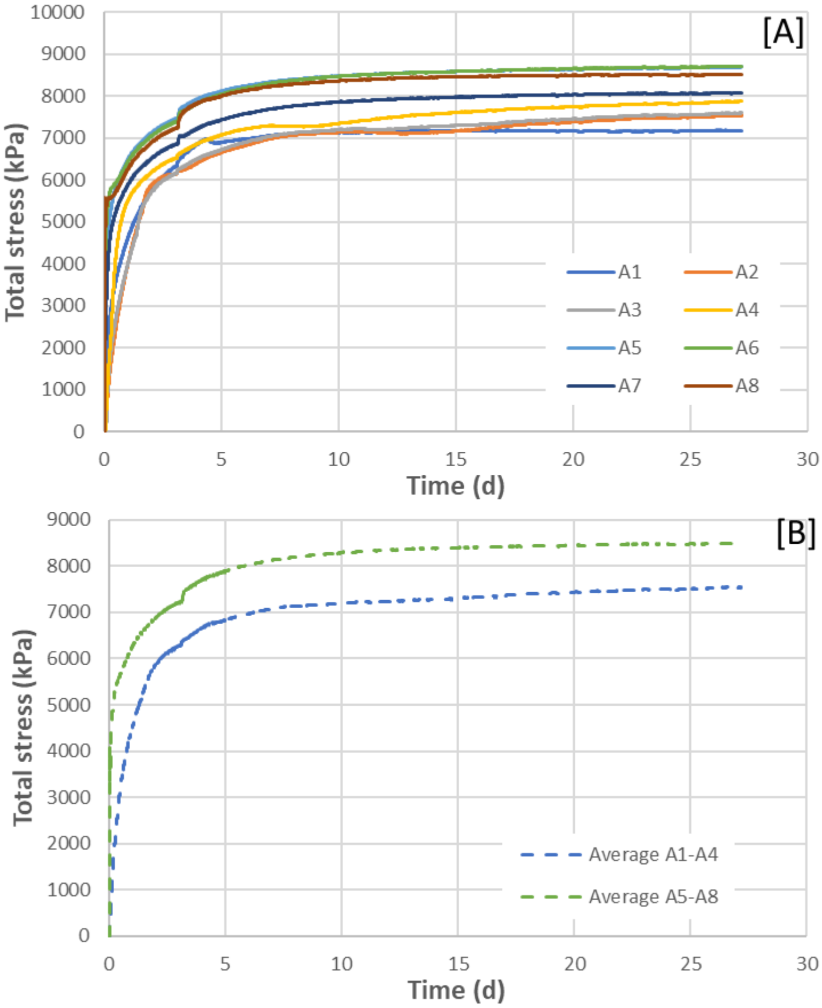

Figure 2.122: Test 1 (FPR-21-004) showing the development of axial stress during hydration and swelling. In [A] each sensor is shown and in [B] the average stress is shown: sensors A1 to A4 (located at the base of the sample) and A5 to A8 (positioned on the top face of the sample).

Following a brief period of further equilibration, gas testing began on day 28.4 with the injection pump set at a constant displacement rate of 180 μl/h. Gas pressure gradually increased for the following 49.4 days, reaching a peak value of 12.36 MPa at day 77.8 (*Figure 2.123*). This was followed by a spontaneous negative pressure transient leading to a quasi-steady state around day 84.9. At this point, the injection pump was stopped, (test stage 5 = shut in), and the pressure allowed to slowly decay. Gas pressure continued to decline until the test was stopped at day 117.

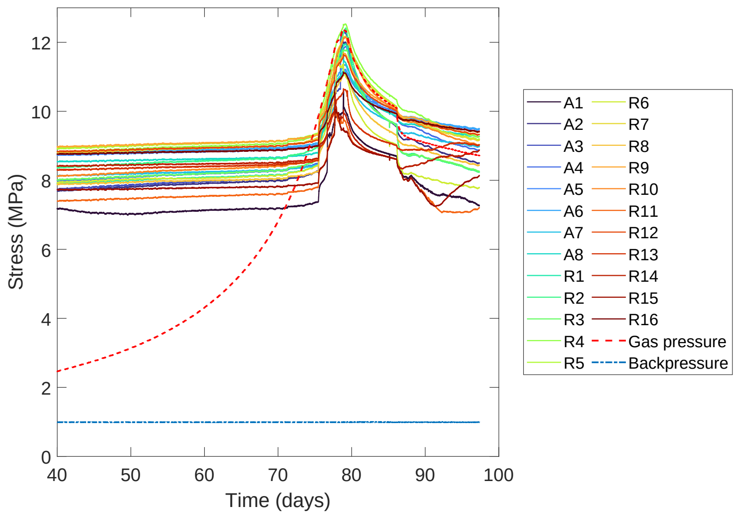

Figure 2.123: Test 1 (FPR-21-004) showing the development of gas pressure, axial stresses (A1-A8) and radial stresses (R1-R16). Gas pressure and back pressure are indicated by the dashed red and blue lines. The gradual increase in most sensors from day 40 to 70 can be attributed to continued hydration of the bentonite.

Closer inspection of the axial stress data (*Figure 2.124*) suggests a small gas entry event occurred around day 70.1, shortly after gas pressure exceeded the lowest value of axial stress. However, inspection of the outflow data shows no obvious sign of discharge. In the absence of a suitable sink, gas pressure continued to increase, finally resulting in a major gas entry event around day 74.3 at a gas pressure of around 9.84 MPa.

Gas breakthrough did not occur until day 75.5, at which point, outflow rapidly increased and was associated with a series of spontaneous changes in the stress field (*Figure 2.124* [A]). However, the initial development of permeability was short-lived, as from day 76.1 to 76.5 outflow reduced to pre-major breakthrough levels and was accompanied by further increases in gas pressure and stresses within the sample, as gas tried to reconnect with the backpressure filter. Outflow from the sample spontaneously increased for a second time at day 76.5 and was again associated with complex changes in the stress field (*Figure 2.124* [B]).

Figure 2.125 shows the evolution of axial stress in response to the development of flow out of the sample. Gradual and abrupt changes in stress were observed, similar to those ascribed to the development of flow paths in previous experiments using a similar experimental set-up (Harrington et al., 2017; Harrington et al., 2019). Following major gas breakthrough, outflow, stress and gas pressure were observed to fluctuate in synchrony, indicating coupled behaviour. While the peak gas pressure response was more rounded in shape compared to the that of outflow, peak gas pressure occurred prior to peak outflow. This suggests a degree of time-dependent behaviour in the development of gas pathways and thus permeability within the sample. However, by the end of the test stage at day 84.9 (*Figure 2.125*), inflow and outflow were approximately equal, signifying the test was approaching a near steady-state condition.

As soon as the injection pump was stopped, gas pressure, axial stress and outflow from the sample rapidly decreased (*Figure 2.126*). For the first time, gas pressure dropped below axial stresses A2 and A5 through

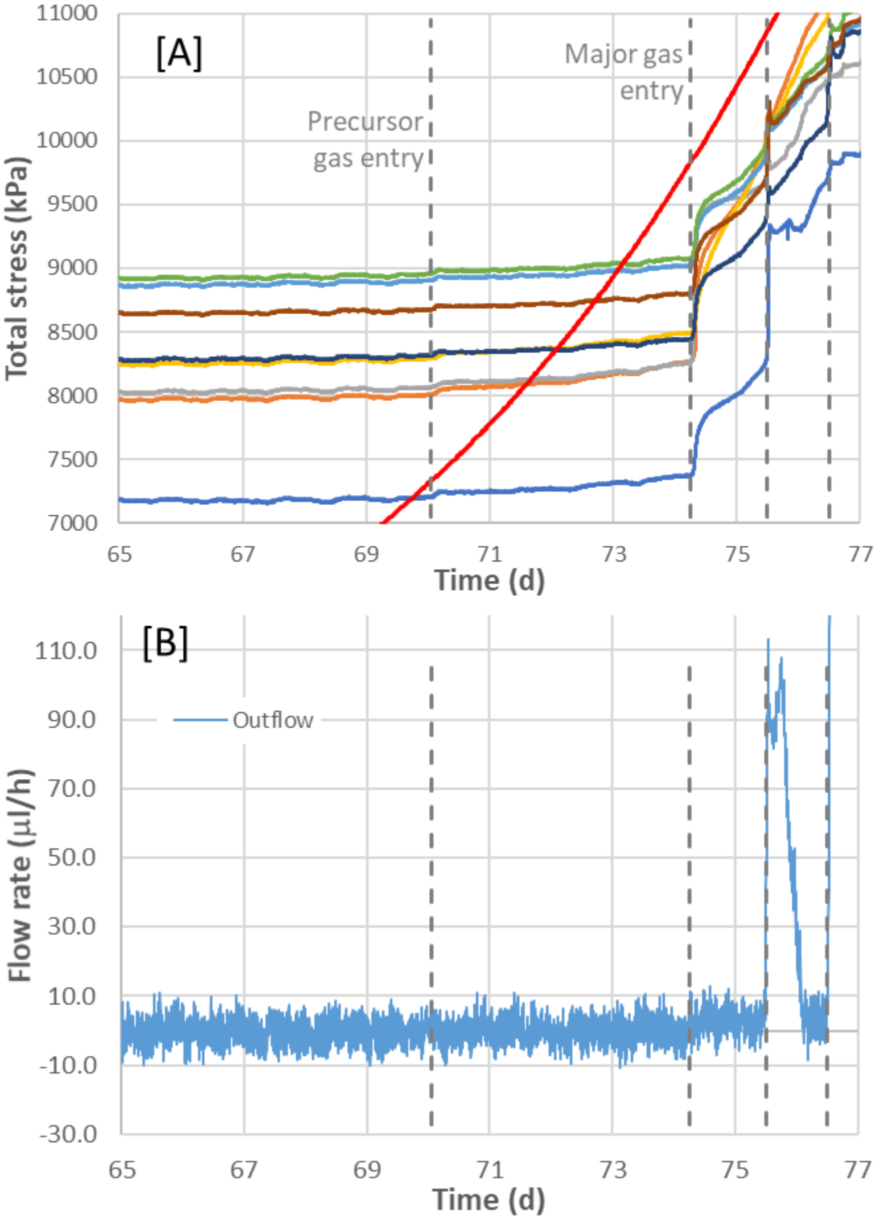

Figure 2.124: Data from part of stage 4 of Test 1 (FPR-21-004) with dotted lines denoting significant events. [A] expanded view of gas pressure and axial stress data showing precursor gas entry around day 70.1 followed by major gas entry at day 74.3. Line colours are the same as those on Figure 2.124. [B] shows time averaged outflow data under experimental conditions with major gas outflow occurring at day 75.5.

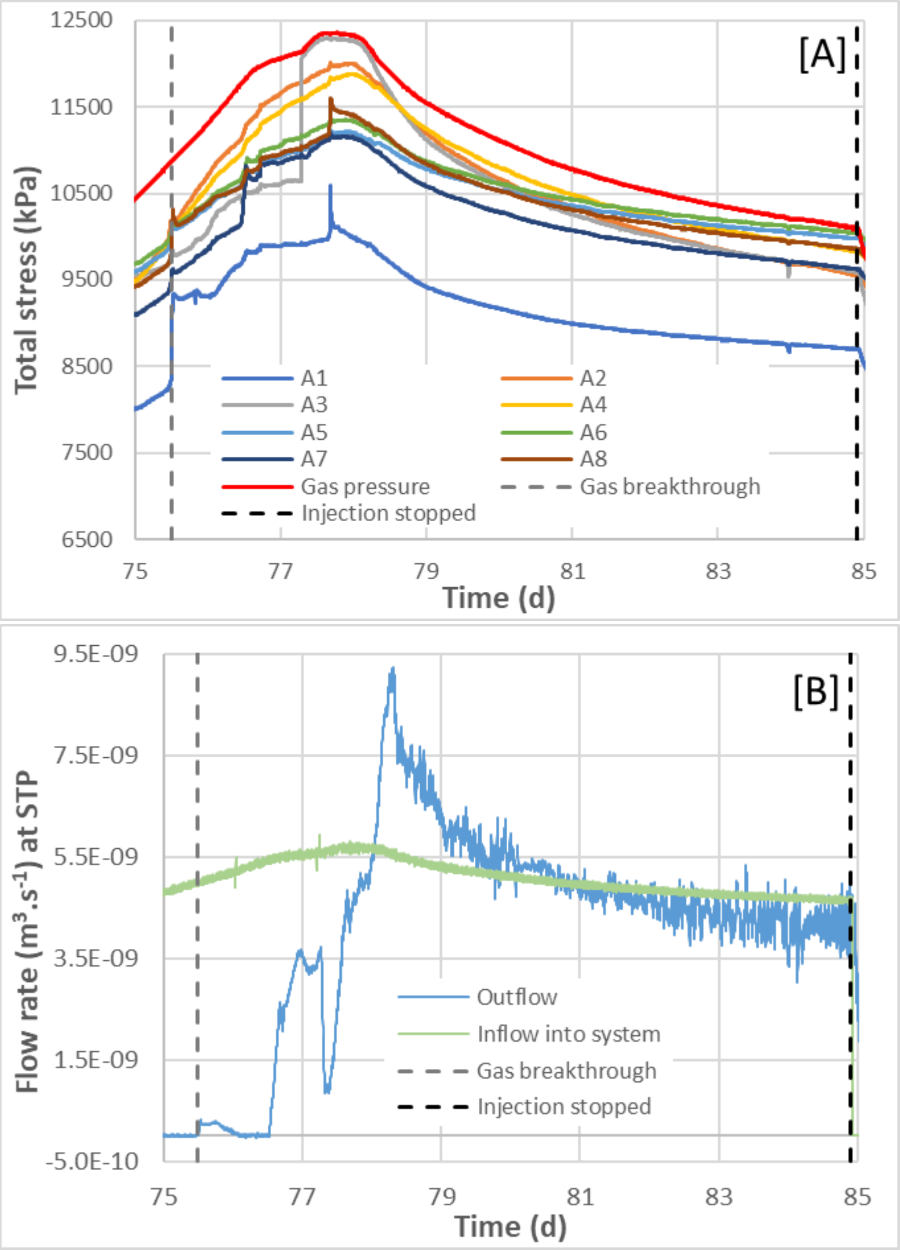

Figure 2.125: Data from part of stage 4 of Test 1 (FPR-21-004). [A] development of axial stress and [B] evolution of inflow and outflow data at STP, from day 75-85.

A8, suggesting depressurisation of some pathways and trapping of residual gas in others. From day 87, a more gradual decline in gas pressure and axial stress was observed. By the end of the stage, gas pressure was over 1.0 MPa lower than axial stress at sensors A5 and A6.

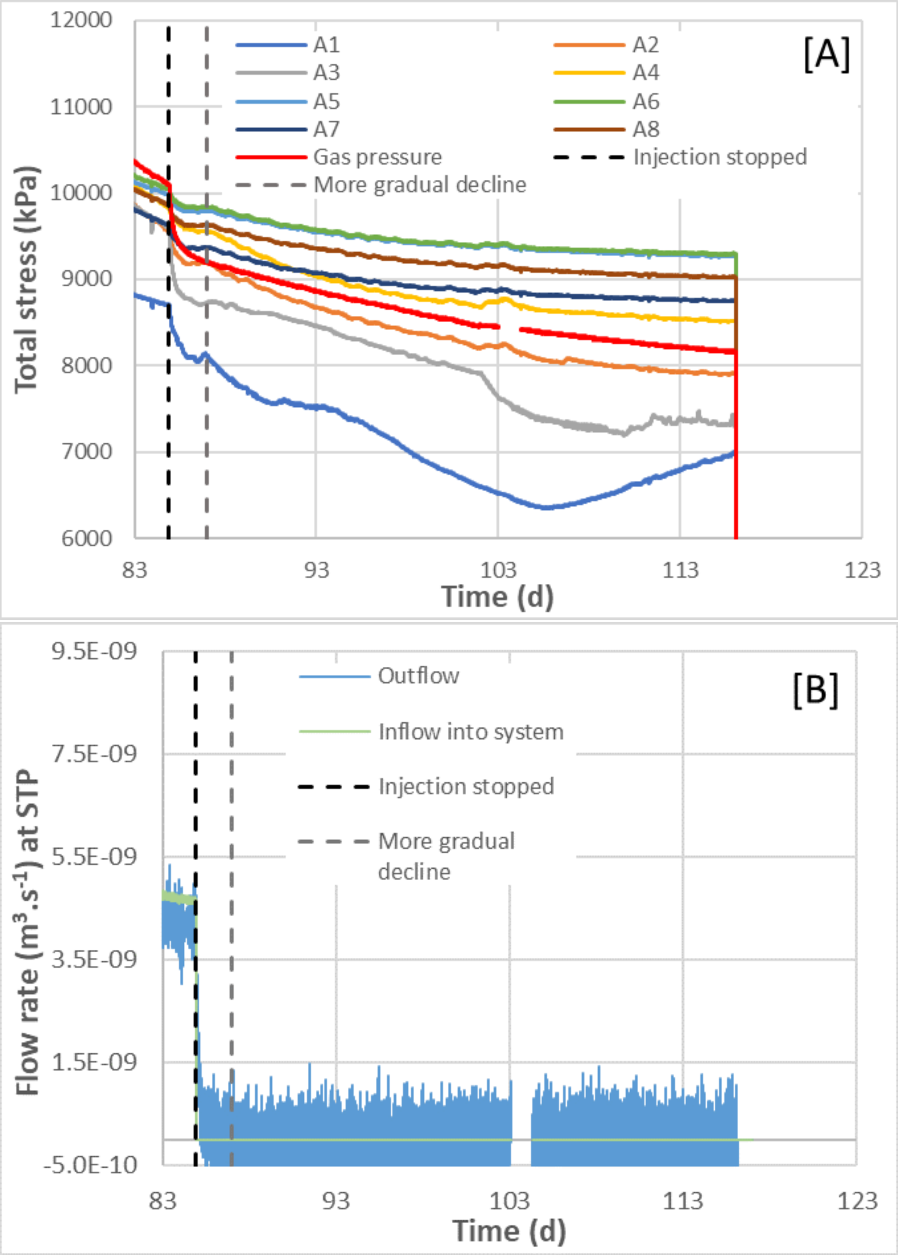

Figure 2.126: The shut-in phase of testing for sample FPR-21-004. [A] change in gas pressure and axial stress and [B] evolution of outflow (at STP) following the cessation of pumping at day 84.9 (the missing data at day 103 relates to a temporary logging failure).

Experimental observations – Test 2 (FPR-21-034)

This test was also conducted on a 100% Mx80 bentonite sample. Due to a temporary malfunction in stress sensors reporting at the base of the vessel, a higher pre-stress was applied to the sample to ensure sample contact with the lower platen (and stress sensors). Unfortunately, this resulted in an average stress ~3 MPa greater than in Test 2 (FPR-21-004). Whilst non-ideal, the dataset provides an opportunity to compare gas migration behaviour in a scenario where compressibility of the clay is reduced.

As before, the sample was initially allowed to hydrate from atmospheric pressure, using water present in the backpressure filter and filters F1 and F2 after flushing. After stress development was seen to level off the same filters were then used to apply a water pressure of 1MPa to the clay. At the same time, the gas (helium) pressure in the injection filter was also incremented to match the change in water pressure. This was done in order to prevent accidental water flow into the filter and thus remove the possibility of slug flow (i.e. gas displacement of water from the filter ahead of gas entry into the sample) during the gas injection phase. The resulting swelling of the sample occurred in a similar fashion to Test FPR-21-004 (*Figure 2.122*), reaching a plateau with an average stress value of 11.1MPa.

Once stresses reached steady values, filters F1 and F2 were isolated from the backpressure pump and the injection pump was used to apply gas through the central road at a constant flow rate of 180 μl/h. Gas pressure gradually increased as a result and at day 11.4 and a gas pressure of 11.1MPa, the monitored stresses displayed a rapid change in slope (*Figure 2.127*; *Figure 2.128*). Significant disruption was apparent in the stress field from this point onwards (*Figure 2.128*), three main outflow events correlating with declines in gas pressure (*Figure 2.129*). At day 16.9 gas pressure reached an initial peak value of 19.8MPa. This was followed by a brief negative pressure transient and a return to increasing gas pressure. A secondary gas pressure peak of 20.5 MPa then occurred at day 17.7, followed by a further negative transient, correlating with major gas outflow. At this point, the injection pump was stopped and the test was decommissioned.

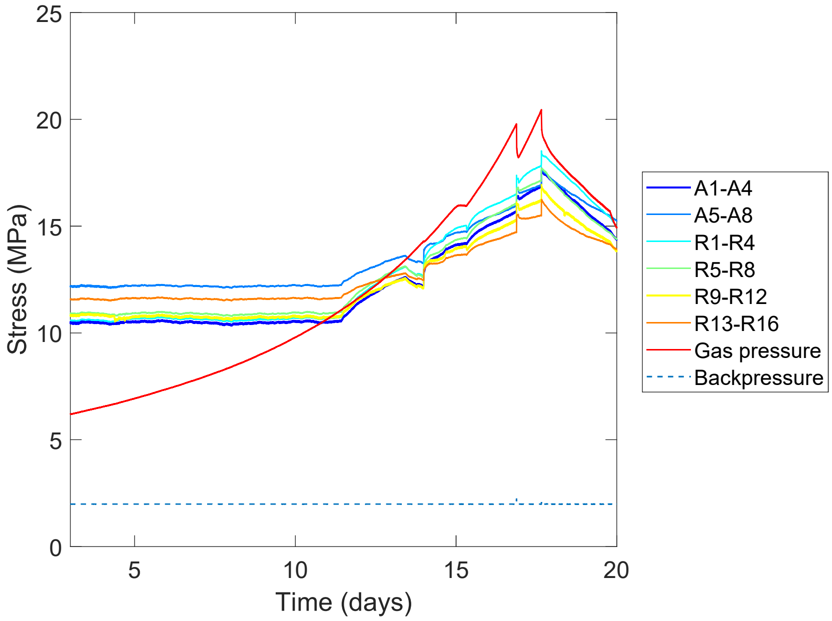

Figure 2.127: Average stress at each plane of measurement along the sample axis FPR-21-034 (Test 2).

Whilst, in this test, gas entry occurred at a greater gas pressure than for Test 1 (FPR-21-004), this behaviour is consistent with a large number of studies indicating that gas entry occurs after gas pressures are greater than the local stresses in the clay at the point of entry (Harrington and Horseman, 2003; Graham et al., 2012). The rapid escalation in stress field development indicates that gas entry occurred at the same pressure as the average stress measured in the clay (11.1MPa) and continued until a gas network had formed that was sufficient to allow gas to escape and pressures to decline as a result. Observations

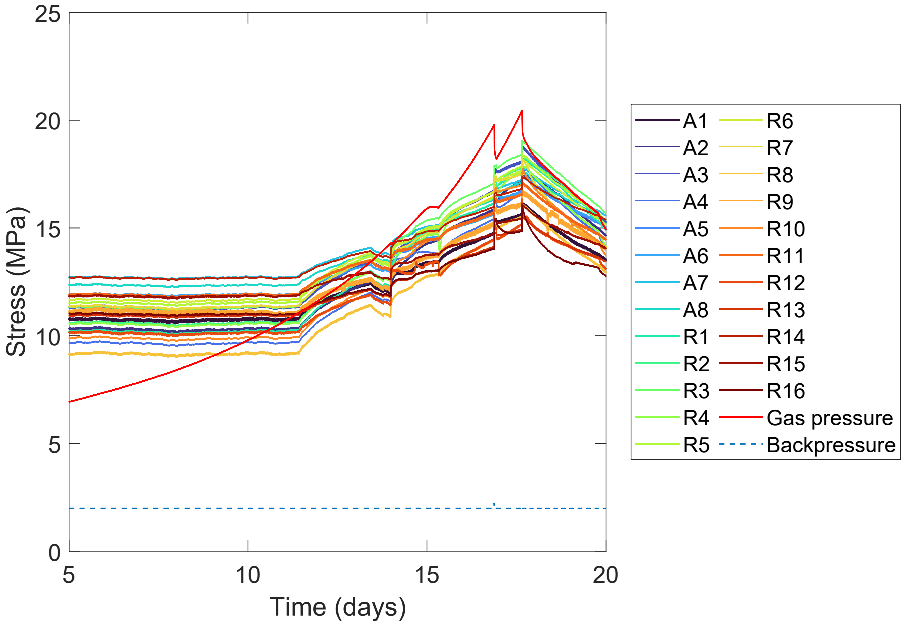

Figure 2.128: All monitored stresses from the onset of gas entry to gas breakthrough, for sample FPR-21-034 (Test 2).

of a double-peak (or more) in gas pressure have previously been interpreted as a being a consequence of the self-sealing capacity of the clay, whilst the gas pathway network evolves towards a more stable state (Graham et al., 2014; Harrington et al., 2017; Harrington et al., 2019).

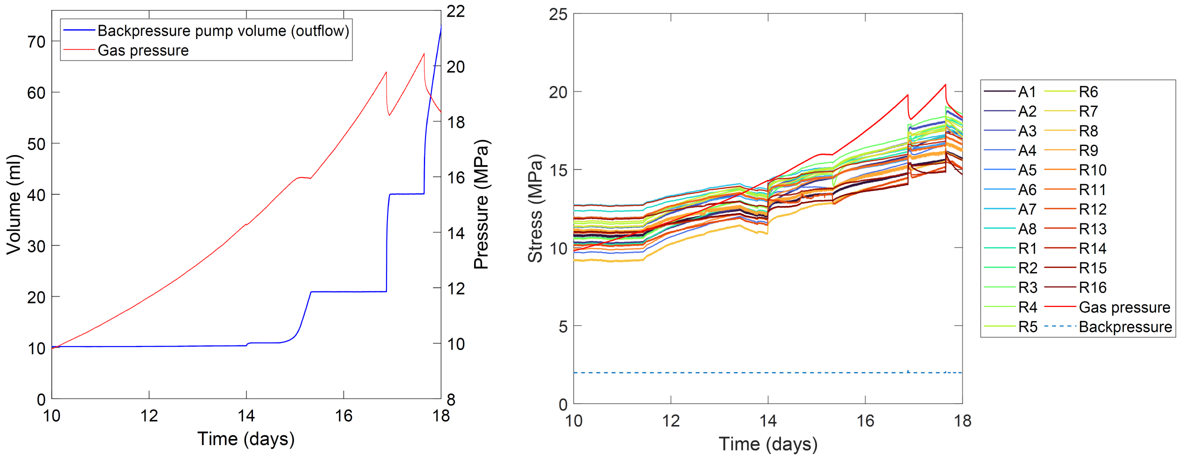

Figure 2.129: Test 2 (FPR-21-034) gas pressure evolution (red) during entry and breakthrough against: (Left) outflow detected by backpressure pump volume (blue) and (right) all monitored stresses.

Experimental observations – Test 3 (FPR-22-024)

This test was conducted on a synthetic clay sample relatively close in composition to the Boom Clay within the ternary text matrix (Composition 7; Section 1.3). As with the previous tests, the sample was allowed to initially hydrate from atmospheric pressure, using water present in the backpressure filter and filters F1 and F2 after flushing of the system. After a period of just under 5 days, the same filters were used to apply a water pressure of 1MPa to the clay. As before, the gas (helium) pressure in the injection filter was also incremented at the same time to match the change in water pressure.

The resulting stresses in the clay were observed to respond much more rapidly to hydration (*Figure 2.130*) than for the pure bentonite samples, which is intuitive, given the lower content of swelling clay and the associated higher permeability of the clay. A spread in measured stresses ~1MPa was observed, with an average stress ~1MPa. This latter value is reassuringly consistent with the swelling pressure of the Boom Clay at Mol, though it should be noted that this has previously been measured using a different pore fluid chemistry (OPERA, 2017). Unfortunately, after the initial swelling phase, a routine update in the laboratory logging software resulted in a step change to sensor outputs that could not be resolved without recalibration. The test was decommissioned as a result. It should be noted that hydration was conducted at 1 MPa to remain consistent with Test 1 and 2. However, given the substantially lower swelling pressures observed in this test, it was decided that a lower applied water pressure would be necessary for subsequent samples using a synthetic clay/sand/silt mixture, to ensure that when matched with an initial applied gas pressure, the conditions necessary for flow were not immediately met. An applied water pressure of 0.25 MPa was, therefore, used for all subsequent tests.

Experimental observations – Test 4 (FPR-22-027)

This test was conducted on a synthetic clay sample with a composition, relatively close to within the ternary text matrix to the Boom Clay (Composition 7; Section 1.3). As with the previous tests, the sample was allowed to initially hydrate from atmospheric pressure, using water present in the backpressure filter and filters F1 and F2 after flushing of the system. After a period of ~1 day, the same filters were used to apply a water pressure of 0.25 MPa to the clay. Again, an equivalent gas pressure was applied at the gas injection rod to ensure water could not enter the injection filter during the hydration phase. The sample displayed a typical swelling response, with change in stress reducing substantially by day 4 at an average stress value

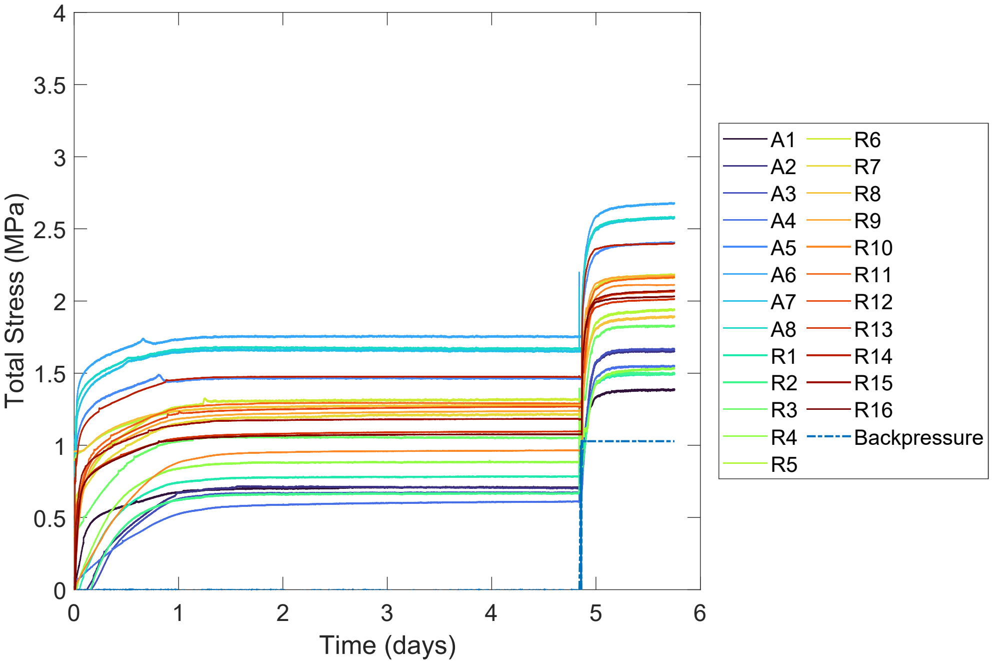

Figure 2.130: Initial stress development in Test 3 (FPR-22-024).

of ~1.4 MPa. Just before day 5, filters F1 and F2 were isolated and injection of helium through the gas injection rod was initiated at a constant flow rate of 180 μl/h. A gradual, but sustained increase in measured stresses began at ~ 10.8 days (and Pg ~ 1.1 MPa), which was followed by a gradual increase in outflow (*Figure 2.131*; *Figure 2.132*; *Figure 2.133*). At ~ 11.7days, a notable increase in outflow began, which was seen to correlate with the peaking of gas pressure. As with previous tests, after the first escalation in observed stresses was detected, significant disruption of the stress field was apparent (*Figure 2.132*). At day 12.7 the backpressure pump reached capacity and could not be immediately vented, resulting in a very small increase in pressure at the downstream end of the sample. However, a constant rate of outflow had already been reached and the test was decommissioned.

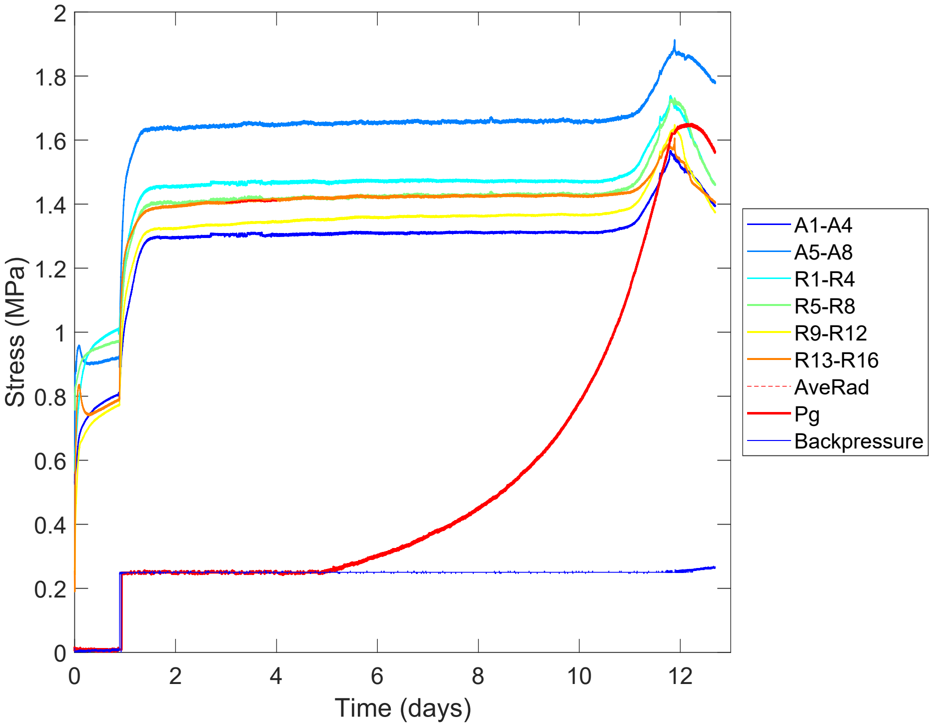

Figure 2.131: Average stress at each plane of measurement along the sample FPR-22-027 (Test 4).

Experimental observations – Test 5 (FPR-22-073)

This test was conducted on a synthetic clay sample with a clay/silt/sand composition of 40/10/50% (Composition 2b; Section 1.3). Following the general test procedure, the sample was allowed to initially hydrate from atmospheric pressure, using water present in the backpressure filter and filters F1 and F2 after flushing of the system. After a period of just under ~ 1 day, the same filters were used to apply a water pressure of 0.25 MPa to the clay and an equivalent gas pressure was applied at the injection filter to match the change in water pressure. As with Test 3, the resulting stresses in the clay were observed to respond much more rapidly to hydration (*Figure 2.134*) than for the pure bentonite samples (Tests 1 and 2). Using a standard linear calibration (see Section 1.2.2) resulted in multiple sensors reporting values substantially above zero (up to ~ 1 MPa) before hydration began (*Figure 2.134*). It was, therefore, decided to apply a 2 slope linear-linear calibration, resulting in a marked improvement in the zero value of the measured stresses. However, these values also indicated a swelling pressure close to zero. Unfortunately, it became apparent at this time that an error made in the compaction procedure for this batch of test samples had occurred, suggesting that the lack of detected swelling was the result of an abnormally low sample dry

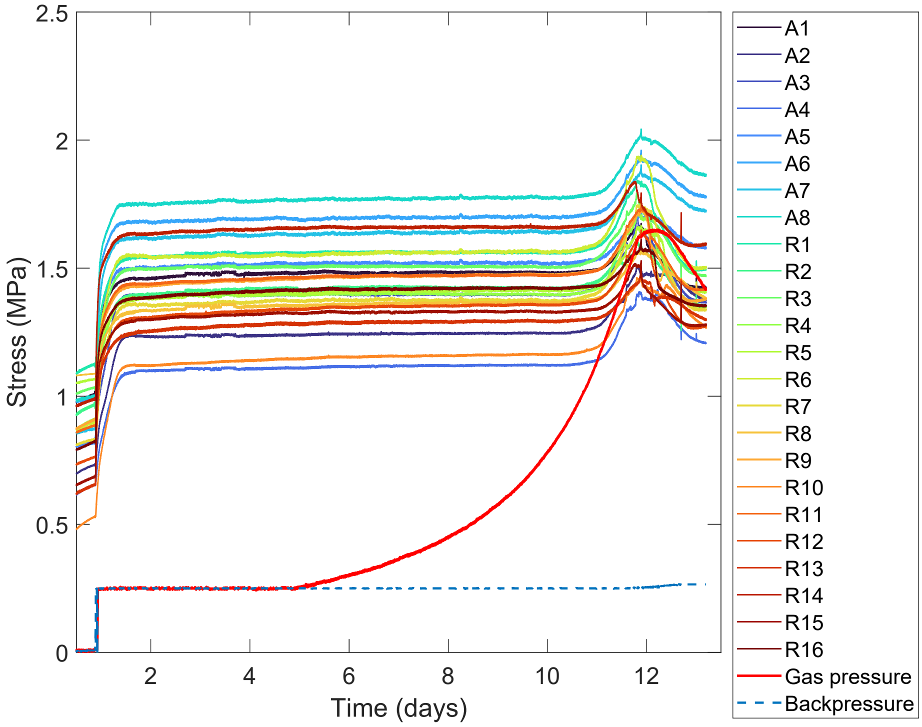

Figure 2.132: All monitored stresses from the onset of gas entry to gas breakthrough, for sample FPR-22-027 (Test 4).

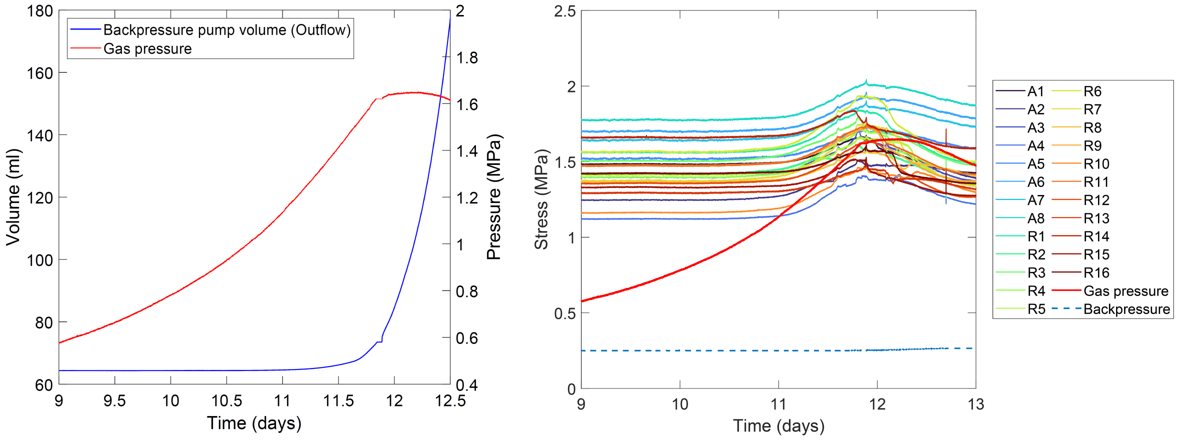

Figure 2.133: Test 4 (FPR-22-027) gas pressure evolution during entry and breakthrough against, Left: backpressure pumps volume (outflow) in blue, Right: All monitored stresses.

density. Rather than continue, without certainty, the test was decommissioned.

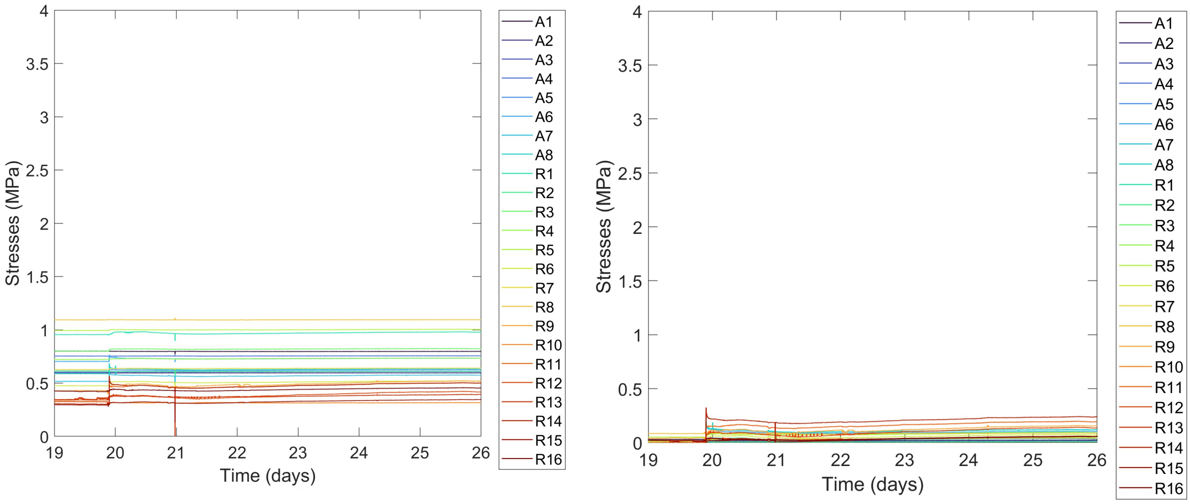

Figure 2.134: All monitored stresses from the onset of gas entry to gas breakthrough, for sample FPR-22-073 (Test 5). Left: Estimated stresses using a single slope linear calibration. Right: Estimated stresses using a 2-slope linear-linear calibration. This latter approach provides a more realistic reflection of the true sensor response. The increase in stress observed just before day 20 reflects initiation of hydration at a constant applied water pressure of 0.25 MPa, but indicates minimal sample swelling as a result.

Experimental observations – Test 6 (FPR-23-033)

This test was conducted on a synthetic clay sample with a clay/silt/sand composition of 40/30/30% (Composition 4b; Section 1.3). As in previous tests, the sample was allowed to initially hydrate from atmospheric pressure, using water present in the backpressure filter and filters F1 and F2 after flushing of the system (*Figure 2.135*; *Figure 2.136*). After a period of ~ 6 days, the same filters were used to apply a water pressure of 0.25 MPa to the clay. An equivalent gas pressure was applied at the injection filter 2 days later. This approach was adopted given the low clay content of the sample, to reduce the likelihood of gas escaping along the side of the sample before clay swelling could progress. Stresses in the sample were then allowed to develop and asymptote, with an average value ~ 0.9 MPa by the end of the test stage. It should be noted, however, that only a standard linear calibration has been applied to this dataset to date. Final stress values may, therefore, differ somewhat after the piecewise calibration approach described in Section 1.2.2 is applied. An electrical issue was also identified with a group of stress sensors R8-R16 being logged on the same card, resulting in minor 'on-off' DC-like fluctuations in the observed stress values.

At day 22.3, injection of helium through the gas injection rod was initiated at a constant flow rate of 180 μl/h. Unlike in previous tests, monitored stresses were not observed to increase substantially as gas pressure approached a similar value (*Figure 2.137*). Instead, a small but much more rapid increase in measured stresses was noted at day 64.6, coincident with a small drop in the applied gas pressure (from 0.9 MPa), followed shortly after by a return of stresses to their previous levels and a recovery in gas pressure (*Figure 2.138*). First outflow from the sample was also detected during this episode of elevated stresses and ceased after they returned to their previous values. Gas pressure continued to increase after this, with a gradual increase in outflow occurring approximately one day later. The gas pressurisation rate began to reduce at this time and peaked at around day 68.8, by which time a relatively constant outflow rate had been established. A small but notable reduction in monitored stresses was also apparent for multiple stress sensors at this time.

On day 77.8 the gas reservoir was depleted and the injection pump stopped. Rather than allow a shut-in phase at this stage, the test was then decommissioned. Care was taken to depressurise the sample very slowly, over a period of more than 5 hours, to ensure fracturing of the sample was not induced by rapid expansion of residual gas within the sample. This was considered of particular importance for lower clay content samples, where the presence of fractures after testing might be considered to relate to previously dilatant pathways. Unfortunately, radial sensors display electrical disruption throughout testing (including the swelling phase of testing). This behaviour began before gas testing was initiated but could not be eliminated during testing. Nevertheless, the other stress sensors continued to produce substantially quieter outputs (*Figure 2.137*). Axial stresses remained relatively quiescent between gas entry and breakthrough and significant gradual increases in either radial or axial stresses over a period of several days were not observed.

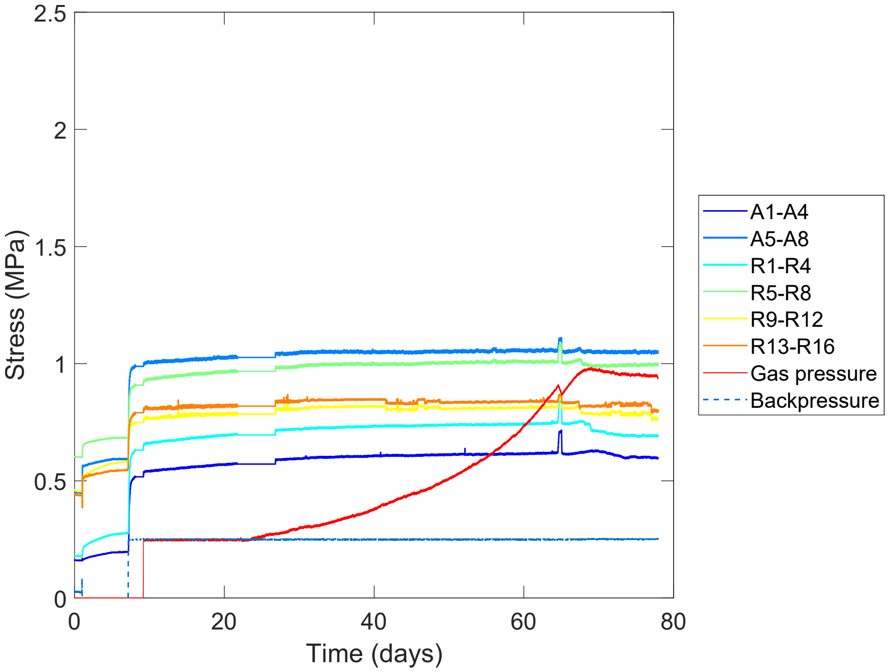

Figure 2.135: Average stress at each plane of measurement along the axis of sample FPR-23-033 (Test 6).

Test overview

In all tests, as swelling development stage was conducted, while the sample was allowed to hydrate and internal stresses were developed as a result of swelling under constant volume boundary condition. Using this data, a final average swelling pressure, π, was estimated from the average of all monitored stresses, σ_{Ave}, towards the end of the test stage, such that:

$$\pi = \sigma_{Ave} - p_w$$

Resulting values are shown as a function of clay content and combined sand+silt content in *Figure 2.139*. Tests 2 and 5 have been excluded due the additional pre-stress applied during commissioning of the former and concerns around the compaction pressure used to manufacture the test sample in the latter. Whilst further expansion will improve an assessment of the form of the relationship, a clear correlation is

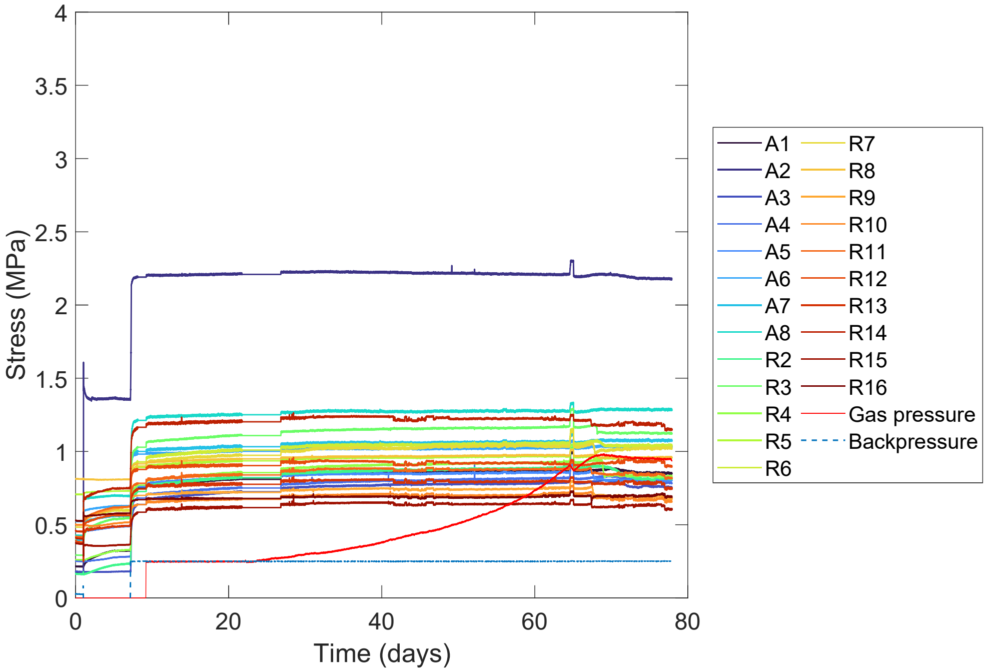

Figure 2.136: All monitored stresses from the onset of gas entry to gas breakthrough, for sample FPR-23-033 (Test 6).

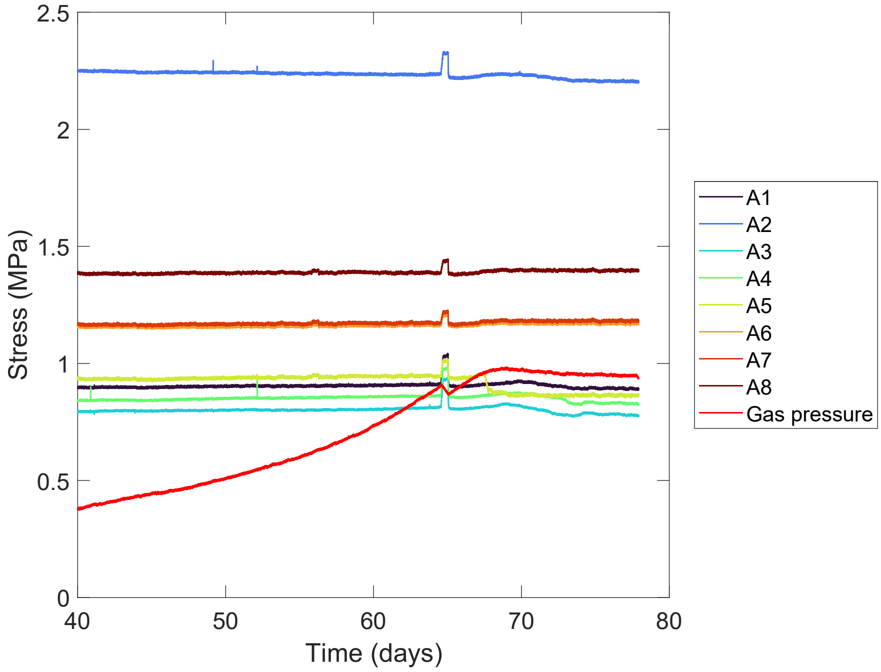

Figure 2.137: Axial stresses from the onset of gas entry to gas breakthrough, for sample FPR-21-034 (Test 6). Although Radial sensors display electrical disruption throughout testing (including swelling phase; see Figure 2.136), axial stresses remained relatively quiescent between gas entry and breakthrough and in both cases a significant increase in stresses over a period of several days was not observed, unlike in previous tests.

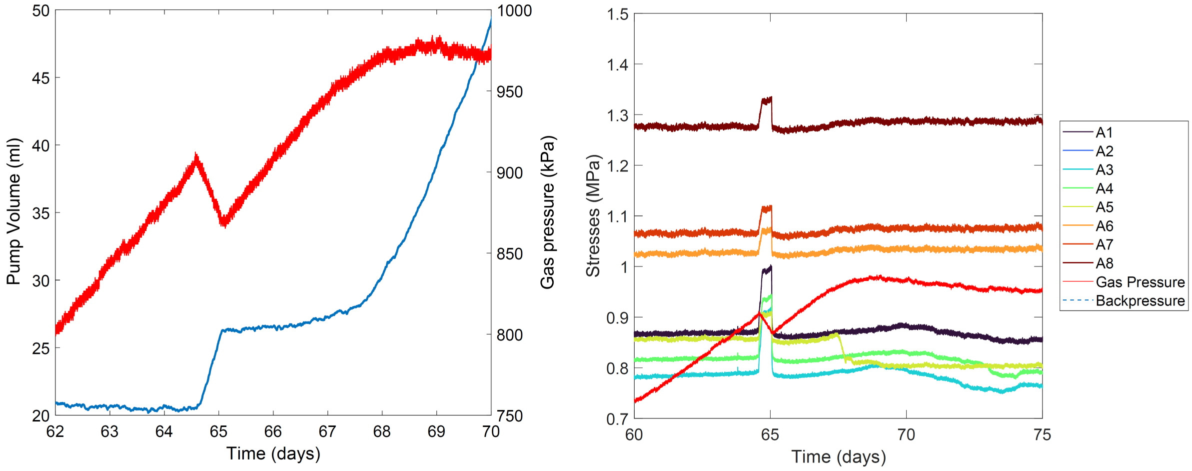

Figure 2.138: Test 6 (FPR-23-033) gas pressure evolution during entry and breakthrough against, Left: backpressure pumps volume (outflow) in blue, Right: Axial stresses.

apparent between the clay content and the measured swelling pressure, as would be expected. Additional data on Boom Clay from the OPERA programme (Harrington et al., 2017b), also highlights the similarity in generated swelling pressure between this natural material and the composition 7 synthetic sample (which was closest in its composition).

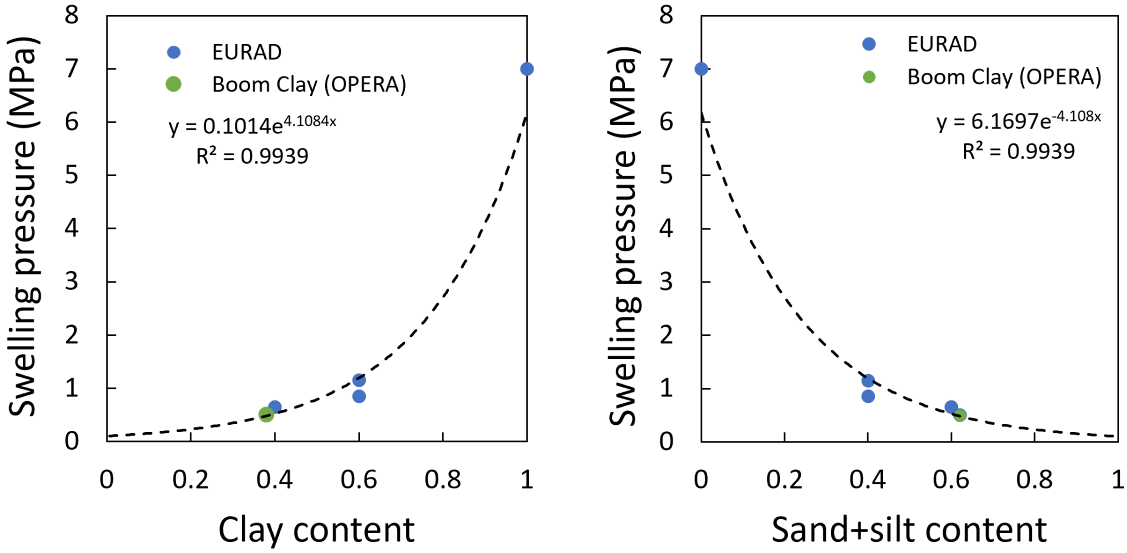

Figure 2.139: Relationship between swelling pressure and clay versus non-clay content. Composition 7 displays similar properties to the Boom Clay.

Multiple experimental programmes document the occurrence of gas flow in clays above a critical threshold (Graham et al., 2014b; EURAD, 2020; Pusch et al., 1985; Tanai et al., 1997; Gallé et al., 1998; Horseman et al., 1997; Horseman et al., 1999; Graham et al., 2016; Shimura et al., 2017), which has been shown to relate to the internal stress state of the clay, σ_{ij}, (Gallé et al., 1998; Horseman et al., 1999; Graham et al., 2016). *Figure 2.140* shows this association for constant volume gas injection experiments conducted on bentonite in EC FORGE (Graham et al., 2014b). Gas tests conducted at the large-scale gas injection test in the Äspö Underground Research Laboratory in Sweden, displayed a similar association (SKB, 2022). Data from this study (Tests 1, 2, 4 and 6) also show this same relationship, including those conducted on synthetic clay/sand/silt mixtures. This is in line with the conceptual model for pathway dilatancy developed before and during EC FORGE (Harrington and Horseman, 2003; Graham et al., 2012; Graham et al., 2014b).

An overview of Tests 1, 2, 4 and 6 is shown in *Figure 2.141* (a-d), showing gas pressure and stress development in the lead up to and following peak gas pressure. In all 4 tests, gas pressure increases nonlinearly, whilst flow cannot occur, as pumping continues at a constant flow rate. In all cases, outflow occurred with a reduction in the slope of the gas pressure curve. In Tests (a)-(c), this is (i) accompanied by a marked and sustained increase in the monitored stresses within the material and (ii) is followed by a marked decline in gas pressure. However, in Test 6 (*Figure 2.141* d) a qualitatively dissimilar stress response is observed. Whilst gas breakthrough still occurs relatively close to the average stress (lowest gas entry pressure on *Figure 2.140*), there is markedly less large-scale stress field disruption than for the other tests. Instead, only a rapid and brief disturbance is observed, which correlates with the first gas outflow and a slight drop in several stress measurements is noted as gas pressure peaks. Furthermore, after gas pressure peaks, only a minimal decline in gas pressure is noted.

These observations, therefore, indicate the following:

- The behaviour observed during gas injection in Tests 1, 2 and 4, is best explained by localised

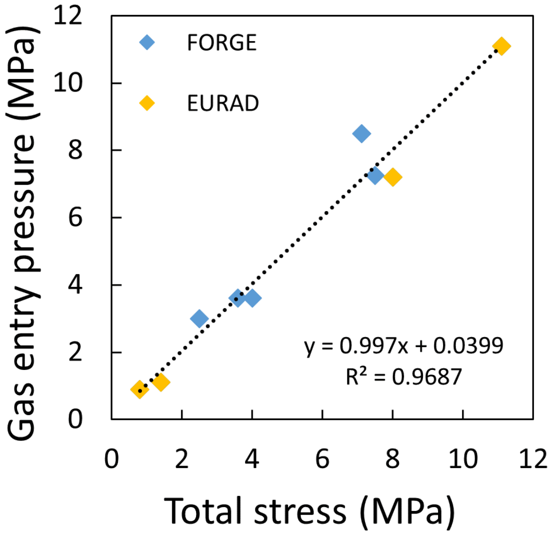

Figure 2.140: Gas entry pressure vs total stress for gas constant volume tests on compacted clays in FORGE and this study (EURAD).

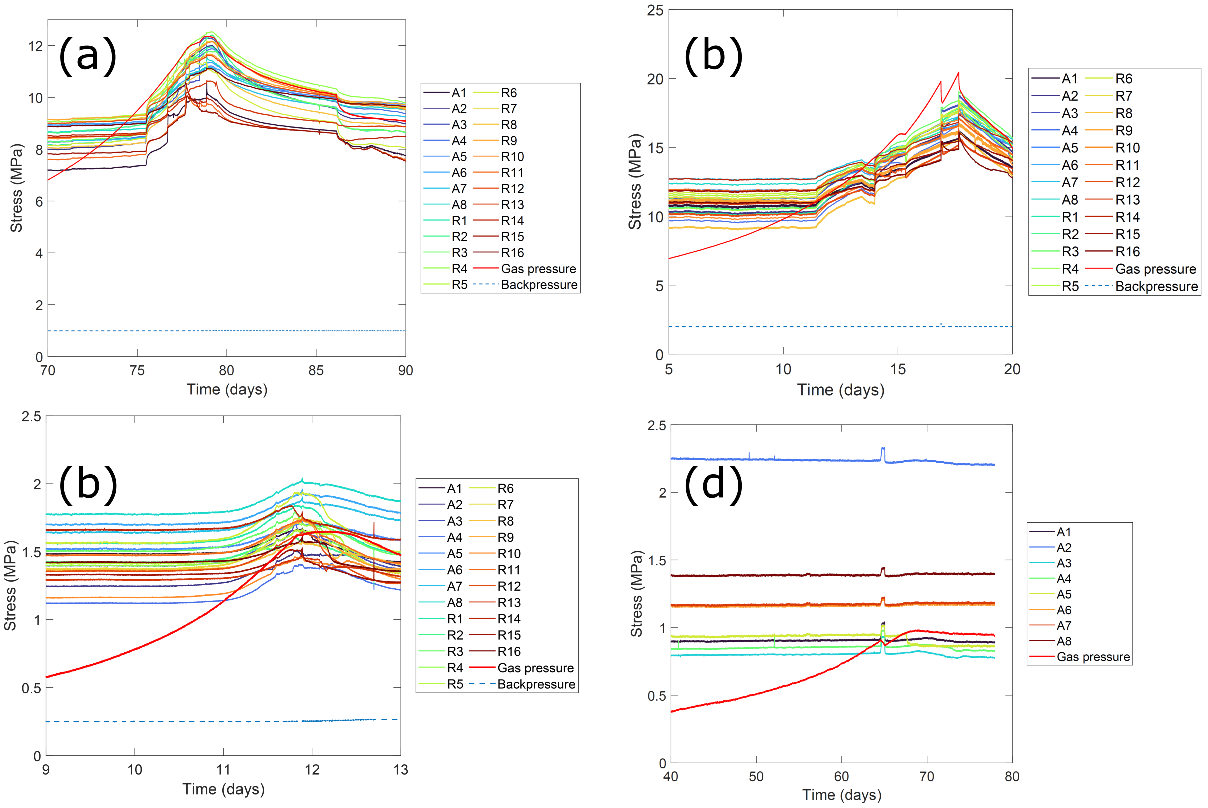

Figure 2.141: Comparison of gas pressure and stress evolution in the lead up to and following peak gas pressure, for Tests 1 (a), 2 (b), 4 (c) and 6 (d). Markedly different stress evolution was observed in Test 6.

deformation of the clay (pathway dilatancy). As well as the association between gas entry pressure and local measured stress, these observations include: (i) significant disruption in the stress field in advance of major gas flow, no outflow detected before stress field disturbance takes place and similar characteristics of this disruption to those of fractured systems (see Stress field analysis section below; Graham and Harrington, 2023).

- In the case of Test 4, behaviour consistent with pathway dilatancy was observed, despite a clay content of only 60%.
- Gas flow behaviour in Test 6 is not fully consistent with previous observations of pathway dilatancy, although the occurrence of gas entry still appears to be at least moderately linked to the stress state in the sample.

Figure 2.142 shows the excess gas pressure (gas pressure minus applied water pressure) at the estimated point of gas entry, against the clay content of the test samples (for Tests 1, 4 and 6). Test 2 has not been included in this figure, because the additional pre-stress applied to the sample at the onset of testing, which resulted in a relatively high gas entry value. It should be noted that the inclusion of Test 2 has negligible impact on the point of intersection with the x-axis. Whilst further expansion of this dataset is required (and is ongoing), the substantial reduction in gas entry pressure with clay content is apparent. It is also interesting to note that the intersection of this loosely constrained trend occurs at approximately 40% clay content, matching the composition of the sample used in Test 6. Completion of the final test for this project and further expansion of the dataset will provide additional clarity around these findings, but it is possible that this test has been conducted close to the transition point between gas flow mechanisms.

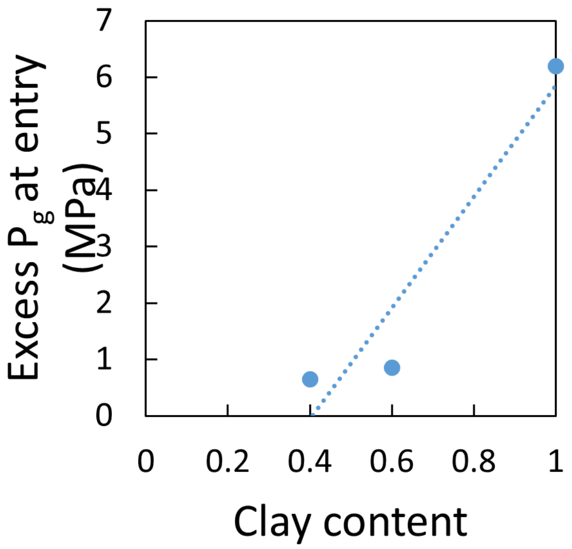

Figure 2.142: Excess pressure at gas entry for samples of differing clay content. The dashed line denotes the simplest possible trend (a linear fit), but expansion of the dataset is required to assess the true relationship.

Stress field analysis

In addition to the experimental results described above, additional work has been conducted to obtain additional information on gas migration mechanisms, by detailed analysis of stress field data. Stress measurements are conventionally made during bentonite swelling tests to assess the equilibration of the sample on hydration, usually in a constant volume or oedometer cell. Harrington and Horseman (2003) monitored the stress field during gas injection through fully saturated Mx80 bentonite, constrained within a constant volume cell. They observed localised and abrupt changes in the stress field in multiple locations and attributed this to mechanical deformation of the clay following gas entry. Similar, localised disruption of the stress field was also observed during multiple gas injection tests at the large-scale gas injection test in the Äspö Underground Research Laboratory in Sweden (SKB, 2022). Recent work has shown that analysis of first order fluctuations in the stress field contain information on deformation due to gas pressurisation (Graham et al., 2012; Harrington et al., 2017; Harrington et al., 2019). In this study, we have developed a more extensive analysis, using data from the more heavily-instrumented stress field monitoring system. Similar automatic algorithms are routinely used in seismology (Leonard and Kennett, 1999) and have proven highly successful in the assessment of micromechanical deformation using acoustic emission data generated during rock deformation testing (Zang et al., 1998; Graham et al., 2010).

Due to the elevated stresses in Test 2 and the electrical noise present on some of the radial sensors in Test 6, this approach is only shown for Tests 1 and 4. Additional filtering of Test 6 will be carried out to enable similar processing in future. First order perturbations in the stress field were detected, or ‘picked’, using an automated algorithm designed to assess their presence above background levels. Any initial offset was removed and the first derivative found, with respect to time, for each stress sensor (*Figure 2.143*). With the greater sensor coverage and higher logging rates used in this study, variable upper and lower noise thresholds could be set, calculated (initially) as ± 2 x the standard deviation (s.d.) across a rolling window. Individual signal peaks and troughs occurring above and below the chosen noise thresholds were then found using a rolling window with a quarterlength overlap. The resulting ‘picks’ were then examined and thresholds varied until a value of 3 x s.d. was found to provide satisfactory results for the exclusion of data below these values. Whilst further events may remain undetected below these thresholds, it was considered better to exclude a few minor events than add many additional ‘false’ events, resulting from the noise thresholds being set too low.

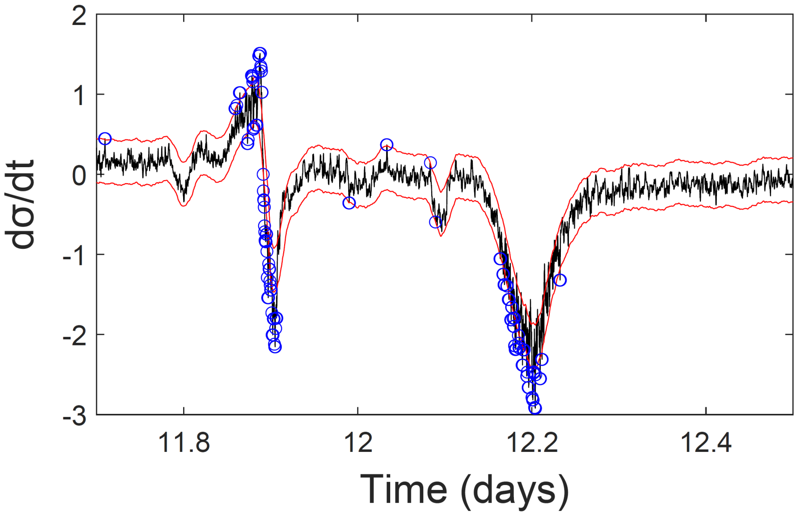

Figure 2.143: First order derivative of stress data from one stress sensor, showing the rolling window threshold (red) and resulting perturbation event ‘picks’ (blue circles).

Selected stress perturbation ‘events’ were next collated into a catalogue of detection times and magnitudes (peak or trough dσ/dt). The cumulative number of events could then be plotted as a function of time for each sensor gas test (*Figure 2.144* a). The associated evolution in gas (injection) pressure for each test is shown in (*Figure 2.144* d). Where detection times were found to correlate across multiple sensors, they were assumed to derive from the same event and counted only once in a ‘cumulative number of unique events curve’ (*Figure 2.144* b). In investigations of acoustic emissions in microfracture, the cumulative number of events with time has been used as a form of internal state variable representing the progressive weakening of rock on the approach to failure Lockner (1993). *Figure 2.144* (b) shows that a similar form of curve is observed in Tests 1 and 4 to typical acoustic emission data (Graham and Harrington, 2023).

Fracturing and faulting phenomenon in rock are routinely studied through a wide range of methodologies.

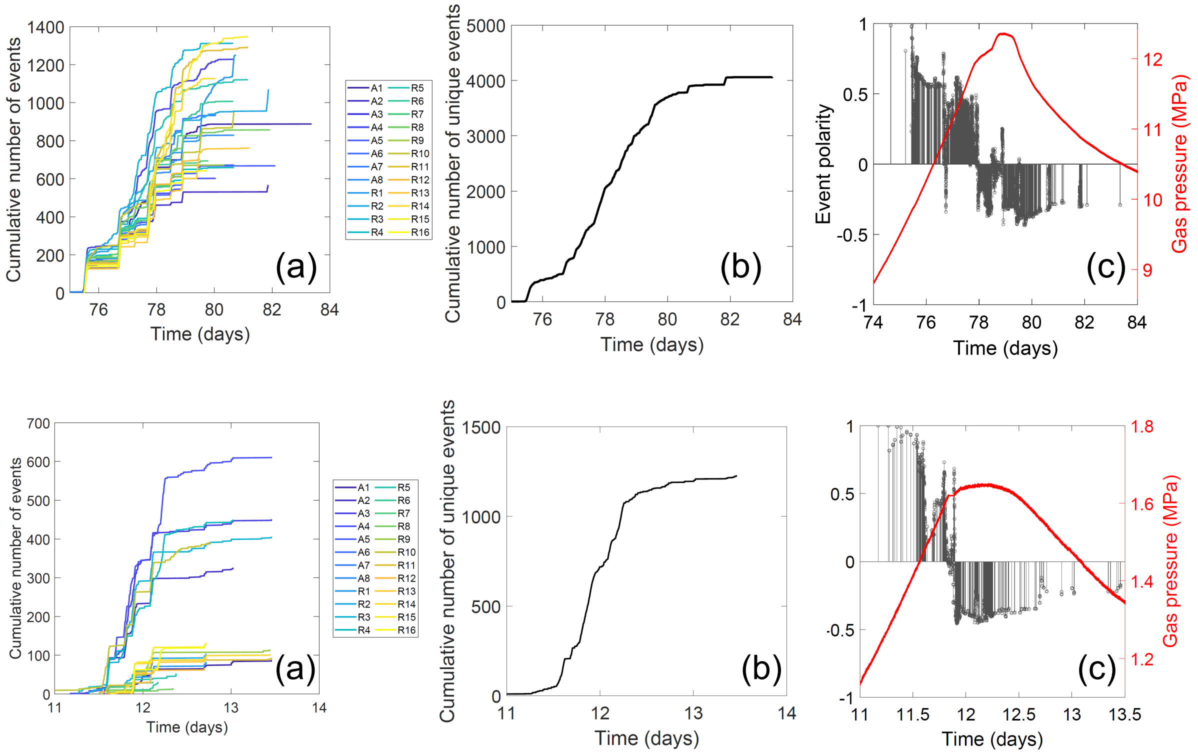

Figure 2.144: Top row: Test 1 (a) Cumulative number of detected stress perturbation events for each sensor, (b) Cumulative number of unique events, (c) calculated polarity of detected events and associated evolution in gas pressure (red). Positive polarity values are associated with an element of 'opening' behaviour and negative events are dominated by 'closing'. Bottom row: Test 4 (a) Cumulative number of detected stress perturbation events for each sensor, (b) Cumulative number of unique events, (c) calculated polarity of detected events and associated evolution in gas pressure (red).

In particular, seismological data provides information relating to the frequency, location, clustering and progression of both slip, on tectonic faults, and fracturing, induced by volcanic activity. Several quantitative approaches used in these fractured systems have, therefore, been applied to detected stress perturbations in these gas tests, to enable comparison of the phenomenon.

Both earthquake and acoustic emission data have been widely shown to exhibit frequency-magnitude distributions that can be represented by power-law relations (Mogi, 1967; Scholz, 1968; Gutenberg,1949; Main and Burton, 1986). The Gutenberg-Richter relation describes the occurrence of earthquakes such that;

$$\log N(M) = a - bM$$

where N is the number of earthquakes of magnitude, M, and a and b are material constants.

Such a relationship is generally considered to be evidence of fractal scaling, where a 'b-value' of b =1 infers a truly scale invariant system (Aki, 1981; Turcotte, 1990; Hatton et al., 1993). In the case of acoustic emission data, M is conventionally calculated from the peak amplitude, A_{peak}, of each detected event (Lockner, 1993; Goebel et al., 2012), such that:

$$M - log\left(A_{peak}\right)$$

In this study, the same approach has been applied to calculate cumulative frequency-magnitude distributions for stress perturbations detected during gas flow in Test 1 (*Figure 2.145*). This was done for two different intervals during the gas entry phase: (i) the first 1000 events detected (early) and the last 1000 events detected before gas breakthrough (late). The results display a similar form to those shown for acoustic emissions in rock fracture experiments (*Figure 2.145*), with relatively linear relationship for magnitudes less than 3, above which a clear break in slope is apparent. Such behaviour is typical and is usually attributed to sample size limiting the size of fracture that can be generated. These findings indicate that deformation associated with gas migration occurs across a range of scales, much like microfracture in triaxial compression tests. The slope, b, of this distribution can also be used to infer the size distribution of such deformation. A change in the slope is also apparent between early and late events, which is also a common observation in acoustic emission datasets generated during microfracture of rock, as the fracture size distribution localises before failure. These findings demonstrate that the distribution of active gas pathways can change between gas entry and gas breakthrough.

In addition, a simple method was used for estimating the predominant deformation behaviour resulting in stress field behaviour, based on a methodology applied to acoustic emissions by Zang et al. (1998). The first motion amplitude, A_i, at k sensors, is used to find an average polarity for each event, according to:

$$pol = \frac{1}{k}\sum_{i=1}^{k} sign\left(A_i\right)$$

This provides an estimate of the net polarity in volume change at the location of the deformation source. Calculated event magnitudes detected during Tests 1 and 4 were used to provide normalised polarity values for stress perturbation events between -1 and +1 (*Figure 2.144* c). Positive polarity values are associated with an element of 'opening' behaviour and negative events are dominated by 'closing'. In both tests positive events were found to occur as gas pressure increased and negative events were detected as gas pressure declined, indicating the occurrence of pathway dilation during gas migration and closure after flow ends. The same technique has also been applied to previous gas datasets during the project, which also show the same behaviour (Graham and Harrington, 2023).

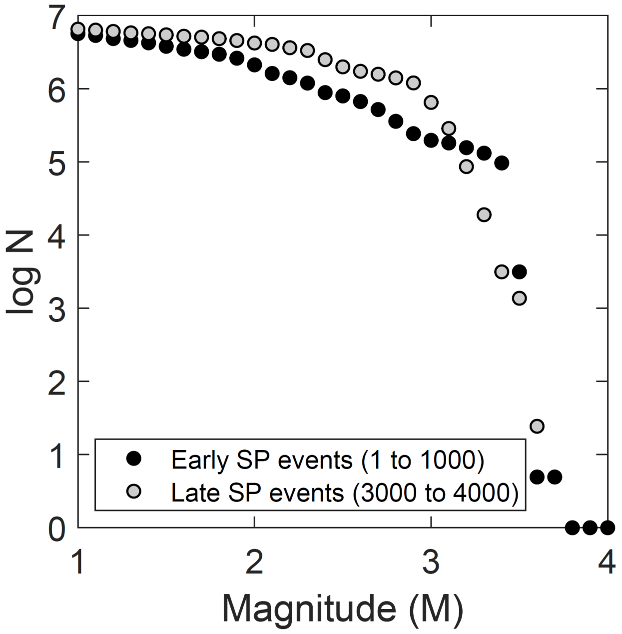

Figure 2.145: Cumulative frequency-magnitude distribution for Test 1.

For Test 1, the cumulative number of events detected events at each sensor throughout the duration of gas entry and breakthrough (*Figure 2.144* a) was plotted as function of sensor location and interpolated, to provide a map the cumulative detection of deformation events about the test sample (*Figure 2.146*). It should be noted that the latter relates purely to the number of events detected at each sensor location, irrespective of source magnitude or distance from the sensor. Nevertheless, a notably localised distribution in event detections is apparent during gas migration, with the first events occurring at the same height as the gas injection point (a filter on a rod, embedded into the middle of the clay at a height=12.5mm). *Figure 2.146* provides insight into the spatial distribution of stress field disruption during gas flow in bentonite. It should be noted that this relates specifically to the number of events, with no weighting for magnitude, but is a reflection of the cumulative degree of deformation detected at each sensor location.

These findings demonstrate that the most significant stress field disruption in the early stages of gas entry occurs close to the injection rod (elevated values are seen in the in the vicinity of x=100mm and height=10mm), indicating a spatial association between gas injection and disruption of the stress field. Since disruption is then observed to grow in a relatively localised fashion towards the downstream end of the sample, without crossing the base of the sample (i.e., sensors in the height=0mm plane would likely all show significant disruption), it is possible to discount interfacial gas flow occurring between the walls of the vessel and the clay. Whilst *Figure 2.146* relates to the stress disturbance experienced around the outer exterior of the clay, this approach provides the first evidence of the spatial progression of deformation during gas migration through bentonite and hints at the potential for further refinement to allow true location analysis to be carried out.

2.5.6. Summary

This test programme was designed to contribute to the following key outcomes for EURAD GAS:

- Improving understanding of the observed gas transport modes and identifying their main controls
- Conceptualisation of transport mechanisms at micro and macro scales

In particular, the intention was to:

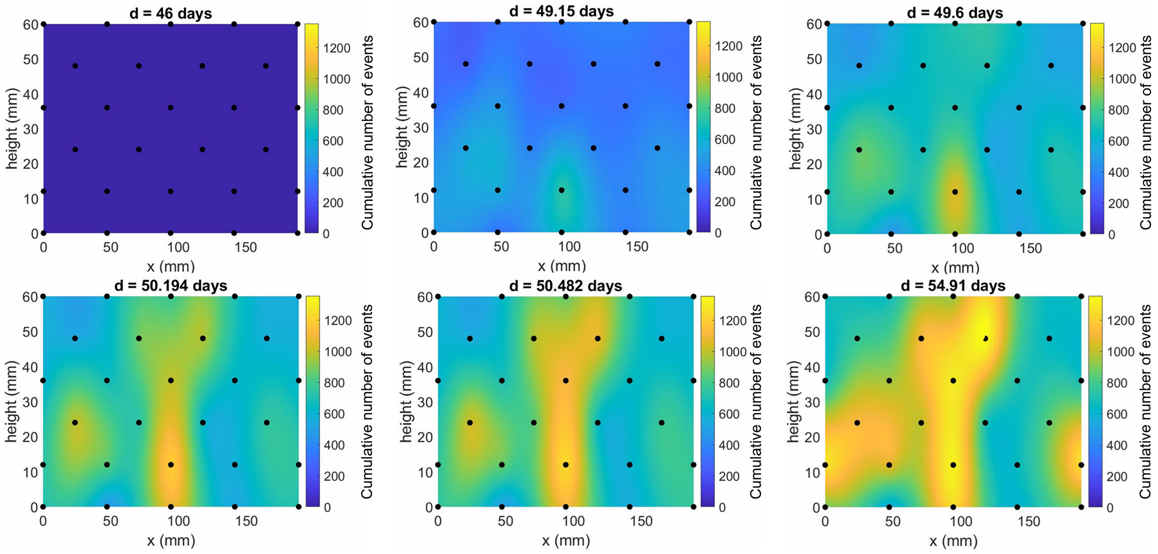

Figure 2.146: Total number of stress perturbation 'events' detected (cumulative number of events) by a given time in days for Test 1. Values have no units and have been interpolated between all sensors (black circles) surrounding the sample. The gas injection rod filter was located at a height=12.5mm. Values are plotted across the exterior surface of the sample, as a function of distance along cylinder axis (height) and distance along cylinder circumference (x) in (mm). The resulting distribution indicates a localised progression of 'deformation' during gas injection.

- Examine the impact of clay content and mineralogy on gas advection behaviour
- Investigate the possibility of a transition between gas advection flow mechanisms
- Improve conceptual understanding of the micromechanical behaviour and potentially the distribution of gas migration in the experiments

Primary outcomes include:

- A heavily instrumented and novel test cell has been designed and constructed.
- A sample compaction procedure has been developed for the creation of synthetic clay samples with a controlled mineralogy
- 6 tests have been conducted in this novel cell, determining swelling pressure and gas flow characteristics in these materials

- New knowledge has been acquired in relation to the presence of a transition between gas advection flow mechanisms and the conceptual understanding of the micromechanical behaviour during gas flow (see Section 1.7)

As such, the primary objectives of the study have been met. Key learning points from this work are outlined in Section 1.7, including a summary of new knowledge and its impact, as well as identification of remaining knowledge gaps and recommendations for the future.

2.5.7. Key learning points

New knowledge acquired

The new knowledge relating to gas flow in clays acquired from this study is summarised as follows:

- As expected, swelling pressure is correlated with clay content in engineered clays and anti-correlated with sand+silt fraction in synthetic mixtures of clay, sand and silt
- Under the conditions used in these tests, evidence indicates that gas flow in all but one experiment only occurred following deformation of the material
    - This was true at high clay contents, but also apparent for a clay content of 60% - this is somewhat lower than previous estimates that visco-capillary flow becomes the dominant flow mechanism for clay contents below 80% (FORGE, 2014). It is possible that the inclusion of silt (with a substantially smaller grain size), has influenced this transition in these tests. However, the previous estimate from FORGE was based on 2 experiments with different experimental set-ups, rather than a systematic study using the same approach.
    - These findings highlight the need to build the experimental database around the position of this transition in order to increase certainty and to assess the repeatability of findings.
    - In these tests (where pathway dilatancy is thought to have occurred), gas entry took place at pressures close to the average stress experienced by test samples (Harrington and Horseman, 2023; Graham et al., 2012; FORGE, 2014), despite the addition of sand and silt. Synthetic samples in particular display a clear one-to-one correlation between these values.
- Under the conditions used in these tests, a test sample with a clay content of 40% displayed markedly different stress field behaviour during gas injection, as compared to samples with a lower clay content.
    - Gas entry was still found to correlate with the stress state of the sample and some limited coupling between outflow and measured stresses was observed, but substantially less than previously seen.
    - One possible explanation is that this test occurred close to the transition between the pathway dilatancy and the visco-capillary flow regimes, though continued expansion and assessment of repeatability will be important to confirm this.
- A correlation was found between gas entry pressure and clay content of test samples, although additional testing will constrain this trend further.
- Stress field data contains information about evolution of deformation resulting from pathway dilatancy and its distribution.
    - A new analysis technique can be used to quantify the degree of deformation occurring during gas injection.
    - This methodology also provides the first real-time evidence of the spatial evolution of deformation, which displays a localised form during pathway dilatancy.
- Deformation shows many similar features to microfracturing in rock compression tests including:
    - A rapid accumulation curve, similar to those used in damage mechanics modelling of macrofracture formation and commonly observed in well-characterised fracture systems.
    - A 'Gutenberg-Richter' frequency-magnitude-type distribution, commonly observed in well-characterised fracture systems
- Unlike rock microfracture in compression, however, source analysis indicates that deformation includes a more significant tensile component, that is consistent with 'opening' and 'closing' of pathways before and after gas pressure reaches a peak.
- The frequency-magnitude distribution of this deformation indicates a network of many pathways (100's-100's), across a range of sizes. Changes in this distribution have also been observed during progression from gas entry to gas breakthrough, demonstrating that the distribution of active gas pathways can change during progression to major outflow. This also suggests that post-test analysis may not provide a true reflection of gas pathway characteristics during gas injection.

Impact of acquired knowledge

The original objectives of this study have been achieved.

Key impacts include the indication that:

- pathway dilatancy can occur at lower clay contents than previously thought, when at fully saturated conditions.
- that a transition between pathway dilatancy and visco-capillary flow may well occur at lower clay contents (~40%).
- the presence of non-clay fractions does not impact the conceptual model that gas entry is predicted by total stress, in situations where pathway dilatancy is expected to occur (at least up to total quantities of 60%).
- clay content appears to directly relate to gas entry pressure.

Findings from this study allow the following progress in particular:

- Frequency-magnitude distributions can now be measured and provide a pathway size distribution that can be used to constrain pathway dilatancy models with a real-time metric under pressurised conditions.
- Two metrics (cumulative number of detected deformation events and deformation polarity) can now be measured and provided as a form of internal state variable representing the progressive increase and decrease in clay permeability as pathways open and close. This should allow a substantial improvement in our capacity to simulate this process.

Remaining knowledge gaps

A number of knowledge gaps remain or have come to light as result of this study. These include:

- Whether the impact of silt on gas flow behaviour differs from that of sand. The final gas test should provide further understanding, although further testing is necessary to fully examine this in detail.
- Whether the minimal coupling of gas flow to the local stress field observed in the lowest clay content test ceases altogether at even lower clay contents and, if so, at what value?
- What impact does compaction history have on the properties of clay mixtures? Test samples were subjected to the same compaction history during testing. Examination of compaction history on gas flow mechanism has yet to be conducted. The preconsolidation pressure is much higher than for natural materials – what impact would lowering this to investigate the influence of the Over Consolidation Ratio (OCR) have?
- How does the introduction of greater levels of heterogeneity impact gas entry behaviour?
- How does the additional influence of cementation impact gas properties? Greater gas pressures are generally considered necessary to overwhelm tensile strength. What are the mineralogical controls on this behaviour?

Recommendations for the future

As a result of the findings in this study, the following recommendations are suggested for the future:

- Additional testing of clay-sand mixes to confirm and better constrain the original identification of the transition between mechanisms (FORGE, 2014) for a 2-mineral system.

- Additional tests examining the impact of dry density and compaction history on the observed gas flow mechanism.
- Further work to assess of the influence of pressurisation rate on the degree and distribution of deformation during pathway dilatancy formation.
- Repeat gas injection experiments with stress field analysis would allow the degree of self-sealing to be quantified for the first time and could be compared in cases where hydration is carried out between gas tests. This could enable an improved understanding of the influence of key controls on the degree of self-sealing that occurs after gas advection.

References

Aki, K. A probabilistic synthesis of precursory phenomena. (Eds. Simpson, D.W. and Richards, P. G.), Earthquake Prediction, 566-574 (American Geophysical Union 1981).

Birkholzer, J.T. et al. 25 years of DECOVALEX-Scientific advances and lessons learned from an international research collaboration in coupled subsurface processes. International Journal of Rock Mechanics and Mining Sciences, 122, 103995 (2019).

Busch, A. et al. Determining the porosity of mudrocks using methodological pluralism. Geological Society, London, Special Publications, 454, 1, 15-38 (2017).

EURAD. Deliverable 6.1: Initial State-of-the-Art on Gas Transport in Clayey Materials. EC FORGE (2020).

Gallé, C. and Tanai, K. Evaluation of gas transport properties of backfill materials for waste disposal: H2 migration experiments in compacted Fo-Ca clay. Clays and Clay Minerals, 46, 5, 498-508 (1998).

Godinho, J.R., Ma, L., Chai, Y., Storm, M. and Burnett, T.L. Mineral precipitation in fractures and nanopores within shale imaged using time-lapse x-ray tomography. Minerals, 9, 8, p.480 (2019).

Goebel, T.H.W. et al. Identifying fault heterogeneity through mapping spatial anomalies in acoustic emission statistics. Journal of Geophysical Research: Solid Earth, 117(B3), (2012).

Gonzalez-Blanco, L., Romero, E., Jommi, C., Sillen, X. and Li, X. Exploring fissure opening and their connectivity in a Cenozoic clay during gas injection. In Advances in laboratory testing and modelling of soils and shales. (Springer International Publishing, 2017).

Graham, C.C. and Harrington, J.F., 2023. Stress field disruption allows gas-driven microdeformation in bentonite to be quantified, Long-term, sustainable solutions to radioactive waste management, Nature Scientific Reports.

Graham, C.C., Stanchits, S., Main, I.G. and Dresen, G. Comparison of polarity and moment tensor inversion methods for source analysis of acoustic emission data. International Journal of Rock Mechanics and Mining Sciences, 47, 1, 161-169 (2010).

Graham, C.C., Harrington, J.F., Cuss, R.J. and Sellin, P., 2012. Gas migration experiments in bentonite: implications for numerical modelling. Mineralogical Magazine, 76(8), pp.3279-3292.

Graham, C.C., Harrington, J.F., Cuss, R.J. and Sellin, P., 2014. Pore-pressure cycling experiments on Mx80 Bentonite. London: The Geological Society of London.

Graham, C.C., Harrington, J.F. and Cuss, R.J. Editors: Sellin, P. and Shaw, R. FORGE D3.38: Chapter 10. Experiments and modelling on the behaviour of EBS (2014b).

Graham, C.C., Harrington, J.F. and Sellin, P. Gas migration in pre-compacted bentonite under elevated pore-water pressure conditions. Applied Clay Science, 132, 353-365 (2016).

Guo, G. and Fall, M. Advances in modelling of hydro-mechanical processes in gas migration within saturated bentonite: A state-of-art review. Engineering Geology, 287, 106123 (2021).

Gutenberg, B., and C. F. Richter. Seismicity of the Earth (Princeton University Press, 1949).

Harrington, J.F., Horseman, S.T., 2003. Gas migration in KBS-3 buffer bentonite: sensitivity of test parameters to experimental boundary conditions. Report TR-03-02. Svensk Kärbränslehantering AB (SKB), Stockholm, Sweden.

Harrington, J.F., Milodowski, A.E., Graham, C.C., Rushton, J.C. and Cuss, R.J. Evidence for gas induced pathways in clay using a nanoparticle injection technique. Mineralogical Magazine, 76, 8, 3327-3336 (2012).

Harrington, J.F., Graham, C.C., Cuss, R.J. and Norris, S., 2017. Gas network development in a precompacted bentonite experiment: Evidence of generation and evolution. Applied Clay Science, 147, pp.80-89.

Harrington, J.F., Cuss, R.J., Wiseall, A.C., Daniels, K.A., Graham, C.C. and Tamayo-Mas, E., 2017b. Scoping study examining the behaviour of Boom Clay at disposal depths investigated in OPERA.

Harrington, J.F., Graham, C.C., Cuss, R.J. and Norris, S., 2019. Gas network development in compact bentonite: key controls on the stability of flow pathways. Geofluids, 2019, pp.1-19.

Hatton, C.G., Main, I.G. and Meredith, P.G. A comparison of seismic and structural measurements of scaling exponents during tensile subcritical crack growth. Journal of structural Geology, 15, 12, 1485-1495 (1993).

Horseman, S.T., Harrington, J.F. and Sellin, P. Gas migration in Mx80 buffer bentonite. In: Symposium on the Scientific Basis for Nuclear Waste Management XX (Boston), Materials Research Society, 465, 1003-1010 (1997).

Horseman, S.T., Harrington, J.F. and Sellin, P. Gas migration in clay barriers. In: Pusch, R. and Yong, R.N. (eds) Microstructural Modelling of Natural and Artificially Prepared Clay Soils with Special Emphasis on the Use of Clays for Waste Isolation (Special Edition), Engineering Geology, 54, 139-149, Elsevier, Amsterdam (1999).

Horseman, S.T., Harrington, J.F. and Sellin, P., 1999. Gas migration in clay barriers. Engineering geology, 54(1-2), pp.139-149.

IAEA (International Atomic Energy Agency). Experience in Selection and Characterization of Sites for Geological Disposal of Radioactive Waste, IAEA TECDOC-991, Vienna (1997).

Kim, K., Rutqvist, J., Harrington, J.F., Tamayo-Mas, E. and Birkholzer, J.T. Discrete dilatant pathway modeling of gas migration through compacted bentonite clay. International Journal of Rock Mechanics and Mining Sciences, 137, 104569 (2021).

Leonard, M. and Kennett, B.L.N. Multi-component autoregressive techniques for the analysis of seismograms. Phys Earth Planet Inter; 113, 1–4, 247–63 (1999).

Lockner, D. The role of acoustic emission in the study of rock fracture. International Journal of Rock Mechanics and Mining Sciences & Geomechanics Abstracts, 30, 7, 883-899, (1993).

Main, I.G. and Burton, P.W. Long-term earthquake recurrence constrained by tectonic seismic moment release rates. Bulletin of the Seismological Society of America, 76, 1, 297-304 (1986).

Marschall, P., Horseman, S. and Gimmi, T. Characterisation of gas transport properties of the Opalinus Clay, a potential host rock formation for radioactive waste disposal. Oil & gas science and technology, 60, 1, 121-139 (2005).

Mijnendonckx, K. et al. An active microbial community in Boom Clay pore water collected from piezometers impedes validating predictive modelling of ongoing geochemical processes. Applied Geochemistry, 106, 149-160 (2019).

Mogi, K., Earthquakes and fractures, Tectonophysics, 5, 1, 35-55 (1967).

Nelson, P.H. Pore-throat sizes in sandstones, tight sandstones, and shales. AAPG bulletin, 93, 3, 329-340 (2009).

Neuzil, C.E. How permeable are clays and shales? Water resources research, 30, 2, 145-150 (1994).

Pusch, R., Ranhagen, L., Nilsson, K. and Geological, S. Gas migration through Mx-80 bentonite. Final report. NAGRA Technical Report, 85-36 (1985).

Scholz, C. H. The frequency-magnitude relation of microfracturing in rock and its relation to earthquakes, Bulletin of the Seismological Society of America, 58, 1, 399-415 (1968).

Sellin, P. and Leupin, O.X. The use of clay as an engineered barrier in radioactive-waste management–a review. Clays and Clay Minerals, 61, 6, 477-498 (2013).

Shimura, T., Takahashi, S., Nishimura, M., Koga, K. and Owada, H. Study on gas migration behavior through bentonite buffer material (2017).

Tanai, K., Kanno, T. and Gallè, C. Experimental study of gas permeabilities and breakthrough pressures in clays. Proceedings of the Fall Meeting of the Material Research Society, Boston, USA, 465, 995-1002 (1997).

Tosaya, C. A. Acoustical properties of clay-bearing rocks. (Stanford University, 1982).

Turcotte, D. L. Implications of chaos, scale-invariance and fractal statistics in geology, Palaeogeography, Palaeoclimatology, Palaeoecology, 89, 301-308 (1990).

SKB, 2022. Large scale gas injection test (Lasgit) performed at the Äspö Hard Rock Laboratory, SKB-TR-22-06, Swedish Nuclear Fuel and Waste Management Co. (2022)

Zang, A. et al. Source analysis of acoustic emissions in Aue granite cores under symmetric and asymmetric compressive loads. Geophys J Int, 135, 1113–30 (1998).

Mogi, K., Earthquakes and fractures, Tectonophysics, 5, 1, 35-55 (1967).

.

CIEMAT

2.6. Characterization of advective gas transport in FEBEX bentonite (CIEMAT)

2.6.1. Introduction & Objectives

The aim of this work programme is to discern the mechanisms controlling advective gas flow in the Spanish reference barrier material (FEBEX compacted bentonite), accounting for the local hydro-mechanical and micro-structural aspects in a range of conditions (density, compaction state, gas pressure, saturation-suction).

Previous research indicates that the formation of discrete gas-filled pathways could explain the transport properties of the compacted bentonite at high saturations ($Sr > .97$). In these quasi-saturated samples, the breakthrough pressure will be determined for different dry densities and confining pressures, generated from bentonite swelling.

Uniaxial compaction of granular bentonite provides cylindrical samples (diameter $38\,\mathrm{mm}$, length $20\,\mathrm{mm}$), at high dry densities (1.5, 1.6 and $1.7\,\mathrm{Mg/m^3}$) with different water contents (from hygroscopic to almost saturated, including 0.18, 0.22 and 0.26). Granulated material is directly compacted in the cell at required dry density. The sample height was limited to $20\,\mathrm{mm}$ expecting to reduce the experiment times by a factor 9 to 16.

The update planning of the project focuses on the characterization of the selected densities in a yearly approach:

- From March 2021 to February 2022: focused on bentonite at dry density 1.5.
- From March 2022 to February 2023: focused on bentonite at dry density 1.6.
- From March 2023 to February 2024: focused on bentonite at dry density 1.7.

The measured gas flow compares to the expected flow to determine the actual gas flow mechanisms (e.g. validity of the concepts applied in high-density compacted clay). The combination of gas flow data and post-mortem analyses of the samples will permit a detailed understanding of the processes. If needed, complementary analyses of the samples will be performed after the tests. Auxiliary data will be taken from existing databases.

2.6.2. Experimental set-up

The descriptions of the experimental setups derive from CIEMAT's technical procedures PT-MA-04-06 (Gas permeability under high-pressure constant load; Carbonell and Gutiérrez (2017)) and PT-MA-04-07 (Gas breakthrough in expansive materials; Gutiérrez (2017)). Modifications done during the development of the project are also included.

Depending on the boundary conditions and gas pressures, two type of equipment permit to evaluate the gas flow through the samples compacted at high dry density with different water contents. Depending on the equipment, gas flow is measure with mass-flow-meters or calculated for pressure-time data series.

The first setup performs steady gas permeability measurements under different gas pressures and two possible confining conditions: an isostatic or triaxial pressure applies on an elastic membrane or a rigid cell (isochoric) assures a perfect contact with the sample and hinders its deformation (so the swelling generates the confining pressure). Mass flowmeters measure gas flow.

The second setup intends to measure the break-through (BT) pressure through fully saturated expansive porous samples; the gas permeability values can also be determined from the estimated gas flow. In this case, only the isochoric cell is standard. Time-pressure data series permit to estimate the gas flow.

Both setups work under high injection pressures, so pairs of absolute pressure sensors measure the differential pressure values of the tests. All pressure values are absolute.

All wetted parts (sintered metal filters, tubing, fitting and valves) are made on SS316.

All tests are performed at a nominal temperature of 22(2) °C in an air-conditioned laboratory.

2.6.3. Description of apparatus

2.6.3.1. High Pressure Steady-State Gas Permeability apparatus

The high-pressure steady-state (HP-S) gas permeability unit was designed to perform steady gas permeability measurements under different gas pressures, allowing the variation of the inlet pressure and the control of confining pressure.

A triaxial (or isostatic) cell confines a cylindrical sample. The setup works as a constant head permeameter that allows the independent control of the injection and confining pressures in the cell, during the time necessary to get a steady flow; and the measurement of the flow, the temperature and the relative humidity of the gas outlet. The backpressure is kept atmospheric.

A gas forward pressure controller manages the injection pressure. Two pressure sensors measure the inlet and outlet pressure of the cell, for redundancy. Three gas mass flowmeters can measure different ranges of the outward flow.

Two independent lines let perform two tests simultaneously. Both lines differ in the maximum confining pressure that can be applied (high confining pressure line, HCP, and low confining pressure line, LCP). The general scheme of both lines is shown in the Figure 2.147 (HCP top, LCP bottom).

The detailed description of the main components of the setup is given below:

Test cell (Figure 2.148). It is a modification of an isostatic cell adapted to measuring the axial load. The standard dimensions of the sample are 38 mm diameter and 76 mm length. These cells have three inputs: one for drainage and outlet pressure, one for injection of pressure to the sample, and one for application of confining pressure. Three valves close the cell ports and an anvil fits the cell head. The tests will not be performed under real triaxial conditions.

Gas reservoirs. A gas sample cylinder (SS-316, 300 cm^3), placed upstream the cell, removes the possible fluctuations induced by the pressure controller in the flow measurement. In addition, it permits to keep gas supply in case of pneumatic fracturing.

Confining pressure system: ensures enough pressure to guarantee the perfect adherence of the membranes to the sample surface. In the high confining pressure line (HCP, Figure 2.147, top), an OLAER high pressure blade accumulator (up to 33 MPa) transmits the nitrogen pressure to the water inside the cell. In the low confining pressure line (LCP, Figure 2.147, bottom), an advanced pressure/volume controller (200 cc) can reach pressures of up to 16 MPa.

Pressure controllers: High pressure forward pressure controllers (double-valve, linearity and hysteresis $\pm 0.5\,\%$ FS, stability $\leq \pm 0.05\,\%$ FS), calibrated to the consigned conditions (N2, 190 bar a, 20 °C), manage the injection pressures. The minimum differential pressure is 7 bar.

Pressure sensors: Sensors (0–35 MPa, $\pm 0.04\,\%$ FS BSL) measure the pressure in the injection port of the cell and in the outlet port of the water/nitrogen separator (confining pressure). Sensors (0–0.7 MPa, $\pm 0.04\,\%$ FS BSL) measure the pressure in outlet of each line (atmospheric pressure).

Gas mass flowmeters. A set of three mass flowmeters (nominal flow ranges: 0.04–2, 0.2–10 and 2–100 STP $\mathrm{cm}^3/\mathrm{min}$) measure the gas outflow rates. The first flow meter has the higher range; the last one, the lower range. The set gives redundant values for the lowest flows and, if needed, as the flow becomes higher, the low-range flowmeters can be isolated from the measurement. The minimum flow value in our current set-up is 0.04 $\mathrm{STPcm}^3/\mathrm{min}$ (2 % FS). Flowmeters operate on a principle of heat transfer by sensing the temperature increment along a heated section of a capillary tube. Although calibrated to the consigned conditions (N2, 70 bar a, 20 °C), a software enables to calculate conversion factors at any different temperature/pressure combination. The accuracy of the conversion factor is always lower than 2.5% in the expected experiment conditions (20 °C $<$ T $<$ 25 °C; 1 bar a $<$ P $<$ 80 bar a). Maximum gas flow value allowed to the experimental device is 130 STPcm^3/min.

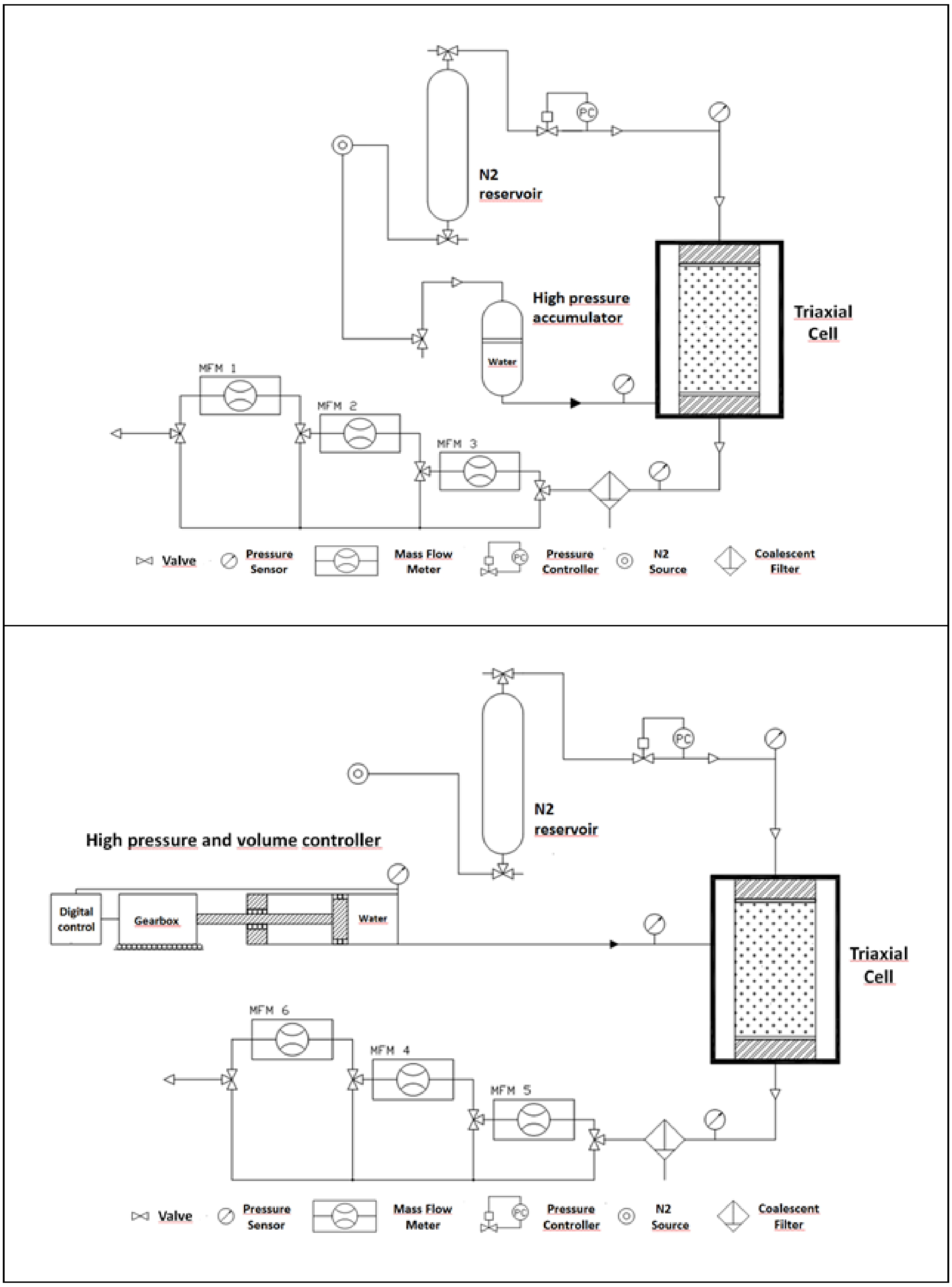

Figure 2.147: Top: Schematic of HP-S (HCP), with triaxial cell and blade accumulator (up to 33 MPa*). Bottom: Schematic of HP-S (LCP) apparatus with triaxial cell and pressure-volume controller (*16 MPa*)*

Temperature sensors. A temperature module provides 8 differential input channels that are software programmable for different sensor types (class B RTDs, in the experiment), with built-in ambient temperature sensor.

RH/T transmitters: to estimate the evolution of the suction in the sample, RH/T transmitters (%RH ±1.8, T ±0.3 °C) measure these variables in the gas outflow.

Data Acquisition System (DAS): A connection box supplies the power to the pressure sensors and flowmeters and sends the control signals. Sensors signals pass through a digital converter (National Inst. ®) that digitized them and sent the values to the control computer. The control program, designed under "LabVIEW 2020" (Figure 2.150 and Figure 2.150), manages all the signals, monitors and records the data.

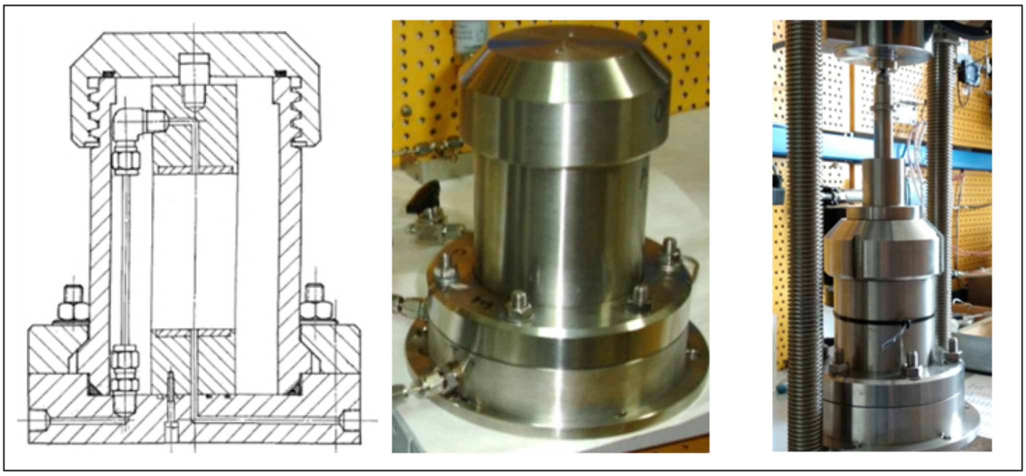

Figure 2.148: Schematic of isostatic cell; pictures of original and modified (triaxial) cells

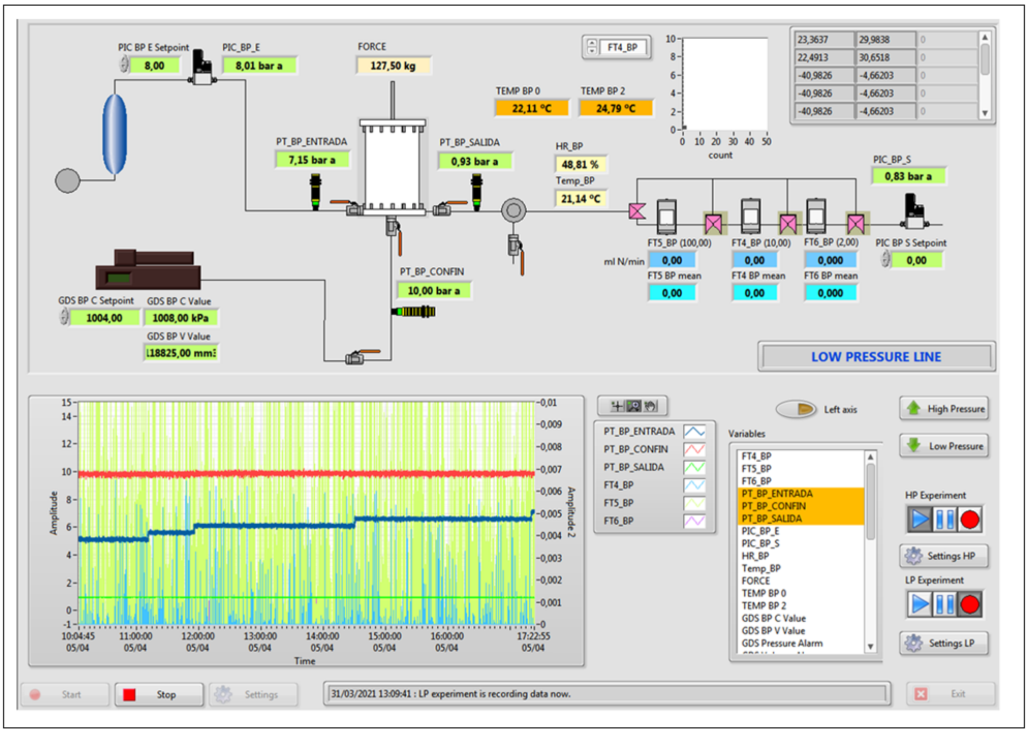

PIC BP E Setpoint 8,00
PIC_BP_E 8,01 bar a
FORCE 127,50 kg
TEMP BP 0 22,11 °C
TEMP BP 2 24,79 °C
PT_BP_ENTRADA 7,15 bar a
PT_BP_SALIDA 0,93 bar a
HR_BP 48,81 %
Temp_BP 21,14 °C
PIC_BP_S 0,83 bar a
FT5_BP (100,00) 0,00
FT4_BP (10,00) 0,00
FT6_BP (2,00) 0,000
PIC BP S Setpoint 0,00
FT5 BP mean 0,00
FT4 BP mean 0,00
FT6 BP mean 0,000
PT_BP_CONFIN 10,00 bar a
GDS BP C Setpoint 1004,00
GDS BP C Value 1008,00 kPa
GDS BP V Value ı18825,00 mm³

23,3637	29,9838	0
22,4913	30,6518	0
-40,9826	-4,66203	0
-40,9826	-4,66203	0
-40,9826	-4,66203	0

31/03/2021 13:09:41 : LP experiment is recording data now.

Figure 2.149: Full screen of management program in LabView® for LP-S equipment: parameters, graphics and controls.

The programs to manage the experiments have been improved including the new measurement devices (Figure 2.149 and Figure 2.150), and fine-tuning both the previous measurements and the new RH/T measurements, with miniaturized sensors, on the gas outlets.

During the project, the improvement of the equipment for measuring gas permeability has continued, incorporating the possibility of including long-term automatic pressure ramps.

At the end, the equipment has been also used to measure BT pressures in 1.7 DD samples (higher than 14 MPa).

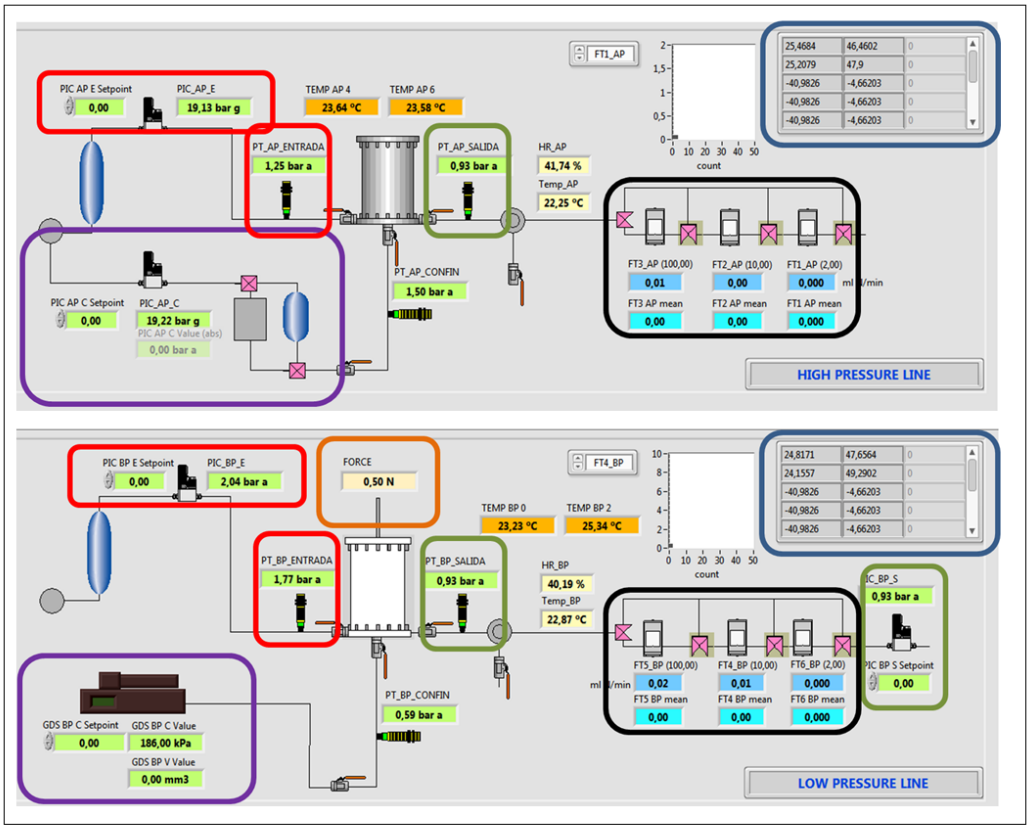

PIC AP E Setpoint 0,00
PIC_AP_E 19,13 bar g
TEMP AP 4 23,64 °C
TEMP AP 6 23,58 °C
PT_AP_ENTRADA 1,25 bar a
PT_AP_SALIDA 0,93 bar a
HR_AP 41,74 %
Temp_AP 22,25 °C
FT1_AP

25,4684	46,4602	0
25,2079	47,9	0
-40,9826	-4,66203	0
-40,9826	-4,66203	0
-40,9826	-4,66203	0

PIC AP C Setpoint 0,00
PIC_AP_C 19,22 bar g
PIC AP C Value (abs) 0,00 bar a
PT_AP_CONFIN 1,50 bar a
FT3_AP (100,00) 0,01
FT2_AP (10,00) 0,00
FT1_AP (2,00) 0,000 ml /min
FT3 AP mean 0,00
FT2 AP mean 0,00
FT1 AP mean 0,000

PIC BP E Setpoint 0,00
PIC_BP_E 2,04 bar a
FORCE 0,50 N
TEMP BP 0 23,23 °C
TEMP BP 2 25,34 °C
FT4_BP

24,8171	47,6564	0
24,1557	49,2902	0
-40,9826	-4,66203	0
-40,9826	-4,66203	0
-40,9826	-4,66203	0

PT_BP_ENTRADA 1,77 bar a
PT_BP_SALIDA 0,93 bar a
HR_BP 40,19 %
Temp_BP 22,87 °C
IC_BP_S 0,93 bar a
PIC BP S Setpoint 0,00
FT5_BP (100,00) 0,02
FT4_BP (10,00) 0,01
FT6_BP (2,00) 0,000
ml /min
FT5 BP mean 0,00
FT4 BP mean 0,00
FT6 BP mean 0,000
PT_BP_CONFIN 0,59 bar a
GDS BP C Setpoint 0,00
GDS BP C Value 186,00 kPa
GDS BP V Value 0,00 mm3

Figure 2.150: Parameters for HP-S and LP-S lines in LabView® program: injection pressure (red), confinig PV control (purple), outlet pressure (green), mass-flow (black), RH/T outflow (blue), axial force (orange), and temperatures.

2.6.3.2. Gas breakthrough apparatus

The setup works as a dynamic fall-out test that allows the independent management of up to eight tests, recording the inlet pressure and the outlet pressure (dynamic back-pressure) in the reservoirs, and the temperature.

Tests differ mainly in the cell diameter, the reservoir volumes, the inlet and outlet gas lines (with valves), and the attached pressure sensors (see 2.6.9.5 for individual description of setups).

A non-deformable (isochoric) cylindrical cell confines a saturated sample, each end connected to a sealed gas reservoir of known volume.

Upstream pressure increases to higher values, by steps, until gas passes through the sample. A sudden pressure increase in the downstream reservoir, usually preceded or accompanied by a pressure drop in the upstream one, indicates the break-through (BT).

The detailed description of the components of the BT setup is given below:

Test cell. A cylindrical stainless steel body (100mm long and 38-50mm inner diameter); and two filters (SS316, SSF), each one supported by one piston (P) confine the sample. Threaded caps (TC) fits the piston at both ends. The covers have a central hole through which the cell is connected to the inlet/outlet gas reservoirs (Figure 2.151, schematic). To fit shorter samples, several stoppers block the pistons against the caps.

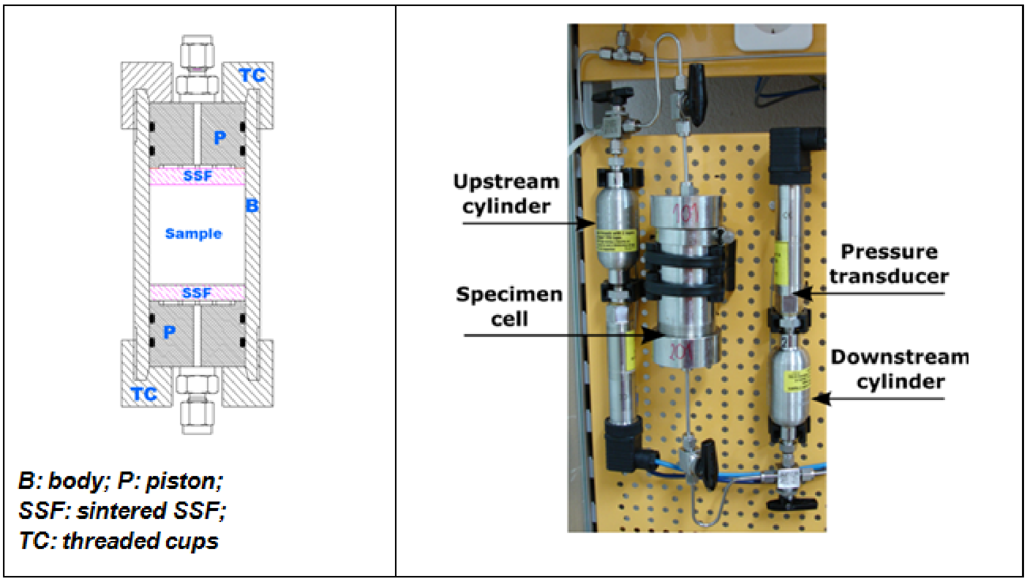

Figure 2.151: Schematic of isochoric cell and picture of the BT apparatus

High-pressure gas supply: From standard pressurized nitrogen cylinder, nitrogen passes to a high-pressure cylinder (300 cc, 34.4 MPa) that prevents fluctuations in the gas supply to the pressure controller (Bronkhorst® EL-PRESS, 34 MPa, ±0.5 % BSL). It has been factory calibrated for nitrogen gas and at room temperature. It is connected to their control interface which, in turn, is linked to the central computer. A pressure multiplier (Sprague®, PowerstarTM 4, double effect) allows all available gas to be used when cylinder pressure falls below test pressure.

Gas reservoirs: Two gas sample cylinders ($\sim$ 150, 75 or 50 cm^3; SS-316), placed upstream and downstream the sample, apply the injection pressure and collect the gas flow, respectively., in different combinations.

Pressure sensors Two pressure sensors, each associated with one gas reservoirs (Figure 2.149)., measure the actual pressure values: sensor (0–35 MPa, ±0.04 % FS BSL) at the inlet ports; and sensor (0–13.5 MPa or 0–7.0 MPa, ±0.04 % FS BSL) at the outlet ports.

Temperature sensors: Miniature thermocouples measure the temperatures of the downstream reservoirs, considered as representative of the each test.

Data Acquisition System (DAS): A connection box supplies the power to the pressure sensors and send their signals to a data logger (Hewlett Packard®, HP34970A), where the signals are digitized and sent to the control computer. The control program, designed under “LabViewTM 2020”, manages all the signals, monitors and records the data.

The program to manage the tests (Figure 2.152 and Figure 2.153) has been improved including the new measurement channels, enhanced management of the tests (files, channels, and frequencies), graphics and time indicator.

In order to calculate the gas flow through the sample, it needs the vessel volumes and the slopes of the pressure-time curves (both inlet and outlet). There are three methods to obtain the slopes: 1) by numerical derivation of obtained data (problematic because of the limited precision of the sensor, especially at low-pressure differences or slower pressure decrease); 2) by polynomial fitting; or 3) by non-linear fitting of a “representative” model of the gas transport mechanisms (with physical meaning).

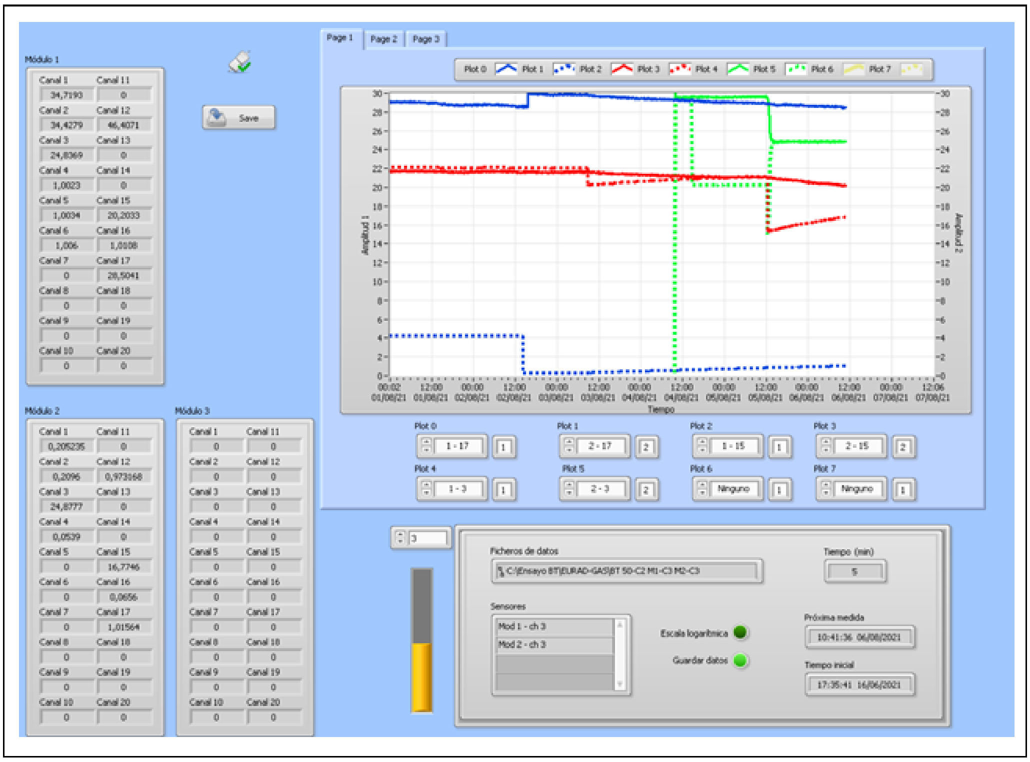

Módulo 1

Canal 1	34,7193	Canal 11	0
Canal 2	34,4279	Canal 12	46,4071
Canal 3	24,8369	Canal 13	0
Canal 4	1,0023	Canal 14	0
Canal 5	1,0034	Canal 15	20,2033
Canal 6	1,006	Canal 16	1,0108
Canal 7	0	Canal 17	28,5041
Canal 8	0	Canal 18	0
Canal 9	0	Canal 19	0
Canal 10	0	Canal 20	0

Módulo 2

Canal 1	0,205235	Canal 11	0
Canal 2	0,2096	Canal 12	0,973168
Canal 3	24,8777	Canal 13	0
Canal 4	0,0539	Canal 14	0
Canal 5	0	Canal 15	16,7746
Canal 6	0	Canal 16	0,0656
Canal 7	0	Canal 17	1,01564
Canal 8	0	Canal 18	0
Canal 9	0	Canal 19	0
Canal 10	0	Canal 20	0

Módulo 3

Canal 1	0	Canal 11	0
Canal 2	0	Canal 12	0
Canal 3	0	Canal 13	0
Canal 4	0	Canal 14	0
Canal 5	0	Canal 15	0
Canal 6	0	Canal 16	0
Canal 7	0	Canal 17	0
Canal 8	0	Canal 18	0
Canal 9	0	Canal 19	0
Canal 10	0	Canal 20	0

Plot 0: 1 - 17 | 1
Plot 1: 2 - 17 | 2
Plot 2: 1 - 15 | 1
Plot 3: 2 - 15 | 2
Plot 4: 1 - 3 | 1
Plot 5: 2 - 3 | 2
Plot 6: Ninguno | 1
Plot 7: Ninguno | 1

3

Ficheros de datos: C:\Ensayo BT\EURAD-GAS\BT 50-C2 M1-C3 M2-C3
Tiempo (min): 5
Sensores: Mod 1 - ch 3; Mod 2 - ch 3
Escala logarítmica ●
Guardar datos ●
Próxima medida: 10:41:36 06/08/2021
Tiempo inicial: 17:35:41 16/06/2021

Figure 2.152: Full screen of management program in LabView® for BT equipment: measurement channels, test management and time bar.

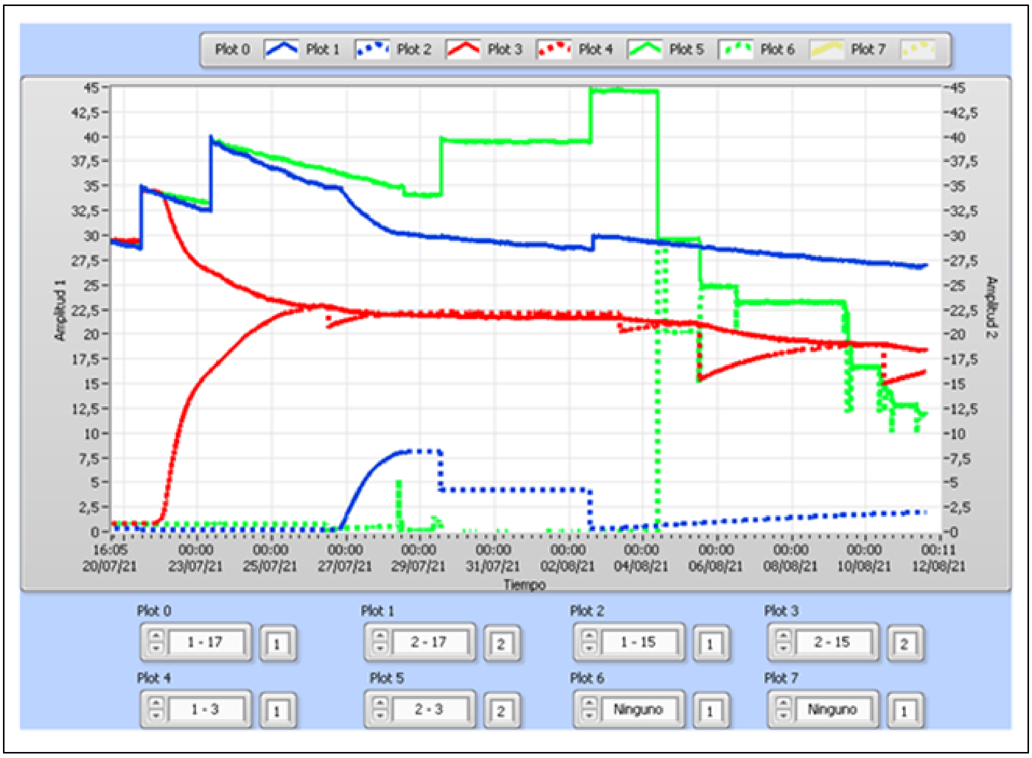

Plot 0: 1 - 17 | 1
Plot 1: 2 - 17 | 2
Plot 2: 1 - 15 | 1
Plot 3: 2 - 15 | 2
Plot 4: 1 - 3 | 1
Plot 5: 2 - 3 | 2
Plot 6: Ninguno | 1
Plot 7: Ninguno | 1

Figure 2.153: Detail of the graphics of management program in LabView® for BT equipment: graphics of selected channels.

2.6.3.3. Calibration

Pressure sensors Calibration of the pressure sensors is made against a Druck DPI 610, portable pressure calibrator, with an accuracy (combined non-linearity, hysteresis and repeatability) of 0.025 % FS (160 bar a). Applied pressure is hydraulic or pneumatic, in this case generated by a high-pressure controller (better than 0.5 % FS, up to 190 bar a).

Known increasing and decreasing pressure steps are applied to the sensor, and the voltage measured by the DAS at each step is noted. The parameters of the linear regression (from VDC-P pairs) are entered into the respective control program.

Reservoir volume The volume of the tanks used as input and output reservoirs for the cells have been calibrated by weighing. The assembly formed by the pressure sensor, the tank filled with deaerated water, and the associated valve has been weighed in the closed position, with three filling pressures: empty, 0.1, 0.6 and 2.0 MPa.

The volume has been calculated by differences and density/temperature corrections. Value and the value at 0.6 MPa has been taken as a reference, used in subsequent calculations.

The rest of the volumes have been calculated from dimensions (tubing, slots and perforations in the closing pistons) or densities (stainless steel filters).

2.6.4. Testing fluids

Gas in the tests is dry nitrogen (**commercial** grade). Nitrogen is a safe, easy to use and inert gas, which ensures the absence of chemical reactions when transported through study materials. When using nitrogen gas with a high degree of purity, the density of the gas will depend only on the applied gas pressure.

The maximal difference of the compressibility factor, Z, with respect to the ideal gas behaviour, in the range of pressure and temperature of our tests, is 0.99364 (20 °C, 48 bar-a). This Z value should indicate an underestimation of 0.64% in the actual density value, when an ideal gas is considered to obtain the flow rate.

2.6.5. Material properties (pre-test and post-test characteristics)

2.6.5.1. FEBEX raw bentonite

The FEBEX bentonite is considered in the Spanish concept for a radioactive waste repository in crystalline rock (AGP Granito, Enresa (2000),Enresa (2006)). Levasseur et al. (2021c) summarise its origin and properties, characterised over the years in various laboratories.

It was extracted from the Cortijo de Archidona deposit (Cabo de Gata area, SE Spain) for the FEBEX large-scale tests in 1996.

The composition consists of more than 90% montmorillonite (actually made up of a smectite-illite mixed layer, with 10–15% of illite layers) with variable quantities of quartz (2 ± 1%), plagioclase (3 ± 1%), K-felspar (traces), calcite (1 ± 1%), and cristobalite-trydimite (2 ± 1%). Ca^{2+} (33 ± 2 meq/100 g), Mg^{2+} (33 ± 3 meq/100 g) and Na^{+} (28 ± 1 meq/100 g) are the main exchangeable cations. The main soluble ions are chloride, sulphate, bicarbonate and sodium.

The material is a granulate bentonite obtained after several processing: homogenisation, on-site air-drying, crumbling, drying in a rotary oven at 60 °C and sieving to size > 5 mm.

The liquid limit of the bentonite is 102 ± 4%, the plastic limit 53 ± 3%, the density of the solid particles 2.70(4) g/cm^3. 67 ± 3% of particles are smaller than 2 µm. The hygroscopic water content in equilibrium with the laboratory atmosphere (relative humidity 50 ± 10%, temperature 21(3) °C, total suction about

100 MPa) is 13.7 ± 1.3%. The external specific surface area is 32(3) $\mathrm{m^2/g}$ and the total specific surface area is around 725 $\mathrm{m^2/g}$.

The saturated hydraulic conductivity and the swelling pressure of compacted bentonite samples are both exponentially related to their dry density. For a dry density of 1.6 $\mathrm{g/cm^3}$, saturated with deionised water at room temperature, the saturated permeability of the bentonite is approximately 5×10^{-14} m/s and the swelling pressure of about 6 MPa.

2.6.5.2. Pre-test characteristics

The granulate bentonite (grain size < 5 mm; water content $\sim$ 14.5%; suction 140 MPa) was mixing with deionised water to obtain the selected water contents (hygroscopic 14.5%, 18%, 22% and 26%). To facilitate a uniform distribution of moisture, mixtures stabilised for several days in closed plastic bags.

Samples 20 mm height have been compacted, at different dry densities (1.5, 1.6, 1.7 $\mathrm{Mg/m^3}$) and initial humidity (from hygroscopic, 14.5%, to saturation –theoretical). They were uniaxial compacted in the test cells to fit exactly their diameter (38–50 mm diameter).

Depending on the dry density, the water content and the grain size, the compaction pressures have ranged from 7 to 43 MPa. Compaction time before unloading the sample was 5–10 minutes; a light unloading is expected before the final reloading induced by the tight closure of the cell.

It is expected that the lower the water content, the better preserved the structure of the aggregates in the samples. Compaction of remoulded clays near-optimum water content causes the aggregates distorted to fill the macro pores, making gas permeability should be essentially zero.

Dimensions, dry density, saturation state, porosity and void ratio For target dry density 1.5, seven samples were tested: four samples (50 mm diameter) with the complete grain size distribution, aimed to study the effect of the initial water content; and three samples (38 mm diameter) with different grain size distribution, aimed to observe the possible effect of remained pore structure after saturation.

For target dry density 1.6, two samples (full grain distribution) were tested; one for each diameter. For 1.7, three samples with complete grain size distribution are being tested, two of them with 50 mm diameter.

Table 2.33 shows the as-compacted characteristics of the samples, sorted by diameter and target dry density. Calculation of degree of satuation (Sr), porosity (n) and void ratio (e) use specific weight of bentonite as 2.7 and water as 1.

Table 2.33: As-compacted sample characteristics (1.5, 1.6 and 1.7 $\mathrm{Mg/m^3}$ *dry density).*

Ref.	Grain size (mm)	Height (mm)	Water content (%)	Dry density ($\mathrm{Mg/m^3}$)	Sr (%)	n	e
50-1	complete	20.2	26.6	1.49	88.0	0.45	0.81
50-2	complete	20.4	22.8	1.46	72.9	0.46	0.85
50-3	complete	20.3	18.4	1.46	58.6	0.46	0.85
50-4	complete	20.6	13.8	1.45	43.7	0.46	0.86
50-5	complete	19.7	21.4	1.59	83.5	0.41	0.70
50-6	complete	19.6	22.3	1.71	103.8	0.37	0.58
38-1	complete	19.7	26.6	1.51	91.8	0.44	0.79
38-2	$1.18 < x < 2.0$	19.6	14.5	1.53	51.4	0.43	0.76
38-3	$2.83 < x < 4.7$	19.8	14.8	1.50	50.1	0.44	0.80
38-4	complete	20.1	21.5	1.61	85.6	0.40	0.68
38-5	complete	19.9	22.2	1.69	101.0	0.37	0.60
38-7	complete	20.1	22.0	1.68	97.6	0.38	0.61

Before gas injection, the samples are saturated and their hydraulic conductivity is determined. Hydration was performed at isochoric condition, with distilled water at 1.6 MPa. In spite of the irreversible modification of the bentonite structure with respect to the as-compacted state, bentonite aggregates remain detectable.

The results corresponding to the complementary analyses of water permeability and MIP are presented in the section of results.

2.6.5.3. Post-test characteristics

Dimensions, dry density, saturation state, porosity and void ratio After complete testing, the samples were extracted from cells and analysed. Table 2.34 shows the as-compacted characteristics of the samples, sorted by diameter and dry density.

Table 2.34: Post-test sample characteristics (1.5, 1.6 and $1.7\ \mathrm{Mg/m^3}$ *dry density).*

Ref.	**Grain size** (mm)	**Height** (mm)	**Water content** (%)	**Dry density** ($\mathrm{Mg/m^3}$)	**Sr** (%)	**n**	**e**
50-1	complete	20.3	29.3	1.47	99.0	0.46	0.84
50-2	complete	20.7	31.5	1.44	106.2	0.47	0.87
50-3	complete	20.7	32.9	1.43	111.0	0.47	0.89
50-4	complete						
50-5	complete	21.1	27.3	1.53	107.2	0.43	0.76
50-6	complete						
38-1	complete	20.0	28.5	1.50	96.3	0.44	0.80
38-2	$1.18 < x < 2.0$	20.0	28.6	1.50	96.6	0.44	0.80
38-3	$2.83 < x < 4.7$	20.1	29.9	1.48	100.8	0.45	0.83
38-4	complete	20.3	26.3	1.54	103.4	0.43	0.76
38-5	complete						
38-7	complete						

The results corresponding to the complementary analyses of water permeability and MIP are presented in the section of results.

2.6.6. Testing protocol

Some changes on the foreseen tests were adopted during the project time and from the beginning: 1) the sample height was limited to 20 mm, expecting to reduce the experiment times by a factor 9 to 16; 2) the number of simultaneous BT tests was increased at the cost of reducing the gas permebilty test; and 3) the experimental protocols have evolved with work as needed.

2.6.6.1. Water saturation protocol: isochoric cell

Main changes in the as-compacted microstructure of the samples (inter-granular and intra-aggregate modes) occur due to liquid water, not to vapour transfer. In order to develop the swelling pressure (that prevent preferential gas flows between the sample and the body cell) and to evolve as much as possible the as-compacted microstructure, samples must be full saturated.

The following protocol tries to enhance the saturation process of the samples:

1. To apply vacuum at both ends of the sample during 2-3 minutes.
2. While applying vacuum to one end, injecting pressurised deionized water (1.6 MPa) to the other end until observing some water in the opposite end (if possible).
3. To inject pressurised water (1.6 MPa) at both ends of the sample during 1 week.

This protocol is related to the water permeability protocol. If the water permeability measurement is not steady, the third point must be repeated.

2.6.6.2. Water permeability protocol: isochoric cell

To measure permeability, after executing the saturation protocol, this protocol tries to reduce the duration of the permeability test. Water volume at test conditions is calculated from water mass collected in an hermetic vial.

1. While injecting pressurised water ($1.6\,\mathrm{MPa}$) at the one end of the sample, collects water outflow at atmospheric pressure in a vial with septum through a needle.
2. Every 24 hours, close the outlet, disconnect the vial and weight the mass of water; then reconnect the vial and open the outlet. This step takes less than five minutes.
3. To repeat the step 3 during a week.
4. If daily water flow becomes stable before, then finish the protocol. If flow does not stabilise, then execute the step 3 of the saturation protocol, and repeat the steps 1 to 3 of this protocol.

The pressure gradient in the test is $\sim 0.8\,\mathrm{MPa/cm}$ ($\sim$ 8,000).

2.6.6.3. Break-through protocol

When the breakthrough pressure is reached, once gas has made its way through the clay, the gas will flow at a rate that is controlled only by the available gas pressure. If some pore throats close or become saturated with decreasing pressure, this gradually reduces the interconnected flow pathways of the gas until flow stops (shut-in pressure), and some gas could be trapped within the pore space. If not, the gas flow goes on up to equalize the pressures.

The objective of this protocol is to determine the gas break-through pressure of an specimen in the experimental set-up (described in 2.6.3.2.). It includes other protocols described before.

Pre-assembly steps:

1. Checking the good condition of the cell (body, pistons, o-rings) to ensure a perfect seal.
2. Checking sintered metal filters are clean and dry.
3. Check the water content of the material well in advance.

Sample preparation:

1. Checking the mass of material to obtain the desired density, taking into account the humidity and the dimensions ($20\,\mathrm{mm}$ in height and 38 or $50\,\mathrm{mm}$ in diameter, depending on the cell).
2. Compact the granular sample uniaxial inside the steel cell closed with the screw cap and the piston assembly (piston, sintered filter and paper filter). Checking the mass and height of the sample indirectly.
3. Closing the cell with the other screw cap and the piston assembly (piston, sintered filter and paper filter) to seal and isolate the sample during the saturation test.

Phase 1. Sample saturation:

1. Executing the water saturation protocol.
2. Executing the water permeability protocol.

Phase 2. Breakthrough test:

1. Disconnecting the cell from the saturation equipment. Reference the cell lengt.
2. Dismounting the cell; extracting wet filters; checking mass and dimensions of the sample.
3. Filter papers and sintered metal filters are changed by dry ones
4. Refitting the cell to its reference length (in less than 20 minutes).
5. Connecting the cell to the experimental equipment, verifying there are no leaks.
6. Set initial pressures: upstream to 500 kPa; downstream to vacuum (3 kPa) or atmospheric pressure ($\sim$ 99 kPa). After stabilization of the pressures, open the valves and the test began. The time of gas filling is negligible in comparison with the pressure response.
7. If there are no changes in pressures during 24 hours, the injection pressure is increased, step by step (500 kPa, at least for 24 h).
8. The previous step is repeated until the gas begins to flow through the sample (BT pressure), producing an increase in the pressure value in the outlet reservoir and a decrease in the pressure value in the inlet reservoir.
9. Let the flow until the inlet and outlet pressure values stabilize.
10. After stabilization, decrease the downstream pressure with the same initial pattern, step by step (500 kPa, at least for 24 h), trying to provoke a new BT.
11. If after decreasing outlet pressure to atmospheric, there is not a BT, increase the upstream pressure again, following the same scheme in step 7, up to reach a new BT.
12. Once producing the considered number of BTs, two new phases of the test (saturation/permeability and BT) can start.

An important issue: Checking the presence of water displaced from the sample in the tubing, before disconnecting the cell.

Sample disassembly:

1. Extracting the samples at the end of the test
2. Checking the mass and dimensions, the water content and the dry density.

2.6.6.4. Gas permeability protocol

The objective of this protocol is to determine the gas permeability of a specimen in the experimental set-up (described in 2.6.3.)

Operation and maintenance conditions:

1. Checking leaks in the gas and water circuits.
2. Checking instrumentation and DAS work correctly.

Pre-assembly steps:

1. Checking the good condition of the cell (body, pistons, o-rings) to ensure a perfect seal.
2. Checking sintered metal filters are clean and dry.
3. Check the water content of the material well in advance.

Sample compaction:

1. Checking the mass of material to to obtain the desired density, taking into account the humidity and the volume of the sample (depending on the cell diameter).
2. Compacting uniaxial the granular sample a mold of adequate dimensions. Depending on the load to be applied to obtain the target density, compaction is carried out either by means of a uniaxial press, or with a hydraulic jack.
3. Desmantling the mold and extract the specimen, registering the mass and dimensions of the sample.

Mounting the sample in the cell:

1. Encasing the sample in an internal latex membrane and an external latex or EPDM membrane, placing a layer of vacuum grease between them.
2. Placing a paper filter on top of the sample and encasing the upper piston within the membranes.
3. Placing a paper filter on the top of the lower piston, mounted on the cell base, and encasing it within the membranes, checking the integrity of the assembly.
4. Connecting the injection pressure port of the upper piston to the cell base port, checking for leakages.
5. Place the top cover –body cell sub-assembly and tighten the nuts of the six screws crosswise until fully tightened.
6. Connecting the confining pressure inlet pipes. Proceed to fill the cell with de-aerated water through the confining pressure inlet of the cell, keeping opened the drill of the load rod. When the drill overflows, stop filling.
7. Insert the load rod in the drill and open the confining pressure inlet. Continue inserting the load rod up to contact the upper piston, and close the three valves (injection pressure, confining pressure and gas outflow).

Connection of the cell to the experimental equipment:

1. Choose the line where testing the sample.
2. Connect the injection pressure and the confining pressure inlets to their respective gas sources, and the gas outlet to the se of flowmeters. Checking for leakages.

Gas permeability: To analyse the effect of injection and confining pressures on gas permeability of unsaturated material, the test consists of several phases. In this test, the confining pressure will be a compromise between the need to avoid the transport of gas along the sample-sleeve contact under the increasing injection pressures applied.

1. Connecting the cell to the experimental equipment, verifying that there are no leaks. Gas outflow is atmosphere.
2. Stablishing the confining pressure, the injection pressure increases in steps (0.5MPa) up to measuring gas flow.
3. Under previously stablished injection pressure, the confining pressure is increased to observe decreasing gas outflow.
4. Stablished the new confining pressure, the injection pressure increased in steps (0.5MPa) up to measuring gas flow again.
5. Decreasing the injection pressure under the constant confining pressure

An important issue: RH sensors let check if there is some moisture in the gas coming from the sample.

Sample disassembly:

1. Extracting the samples at the end of the test.
2. Checking the mass and dimensions, the water content and the dry density.

2.6.7. Results

2.6.7.1. Mercury Intrusion Porosimetry of pre-test samples

In presence of a pressurized gas, the larger connected pores serve as the potential flow pathways, while the smaller pores in the matrix remain saturated. Hence, the analysis of the pore structure of the compacted bentonite, both in as-compacted and saturated states.

Small compacted samples (ϕ-13mm, H-10mm), that fit in the measurement cups of the porosimeter serve as references to compare with the tested samples, after gas injection. A Micromeritics AutoPore IV, with a maximum pressure of $220\,\mathrm{MPa}$ ($\sim$ $7\,\mathrm{nm}$), performed the mercury intrusion porosimetry (MIP) analysis of these samples. They were prepared by freezing drying, which is assumed don't change soil volume in excess.

For these samples, the distribution of the incremental pore volume (log differential intrusion, dV/dlogD) and the cumulative volume vs pore size diameter are presented for samples of different densities and water content (Figure 2.154 and Figure 2.155)

The pore size distribution is clearly bi-modal, with meso pores and macro pores The dominant mesopores values are close to $10\,\mathrm{nm}$, which would correspond to the pores inside clay aggregates that are not affected by the magnitude of the compaction load. The macro pores values, which would correspond to the inter-aggregate pores, are between 20 and $200\,\mathrm{\mu m}$, depend on compaction (and on grain size for a fixed density). The boundary between the two pore size families is located around $200\,\mathrm{nm}$. The boundary between them seems to be around $200\,\mathrm{nm}$. Samples differ mainly in the proportion of macro-pores due to compaction and water content.

These values agree with the observations in Lloret et al. (2003) and Lloret and Villar (2007) for FEBEX bentonite, at different densities, that shown a bimodal pore size distribution in unsaturated compacted bentonites.

Capillary pressures for water can be predicted from MIP measurements. The soil-moisture characteristic curve would be equivalent to the desorption curve (with Sr = 0), taking into account that pore sizes smaller than $7\,\mathrm{nm}$ are not accessible to our instrument. From Kelvin's equation for water, the maximum filled pore radius for 85% relative humidity is about $7\,\mathrm{nm}$. If we consider a "rigid" structure, the pore size distribution is modified by layers of adsorbed water that reduce the effective size of the pores determined by MIP, reducing the gas passage.

2.6.7.2. Mercury Intrusion Porosimetry of tested samples

MIP analyses were performed in samples after gas injection test. The samples were divided in two subsamples, one in the injection zone (S) and other in the outlet part (I).

The log differential intrusion (dV/dlogD) and the incremental volume vs pore size diameter for samples of 1.5 and 1.6 densities and different water contents are presented. Figure 2.156 and Figure 2.157 show some $50\,\mathrm{mm}$ diameter samples; Figure 2.158 and Figure 2.159 show the equivalent ones for $38\,\mathrm{mm}$ diameter.

Observations show the latent inter-aggregate pore size mode (350 and $1{,}100\,\mathrm{nm}$) indicated by Lloret and Villar (2007) for FEBEX bentonite. This mode appears more clearly in some samples at dry density 1.5 (Figure 2.156).

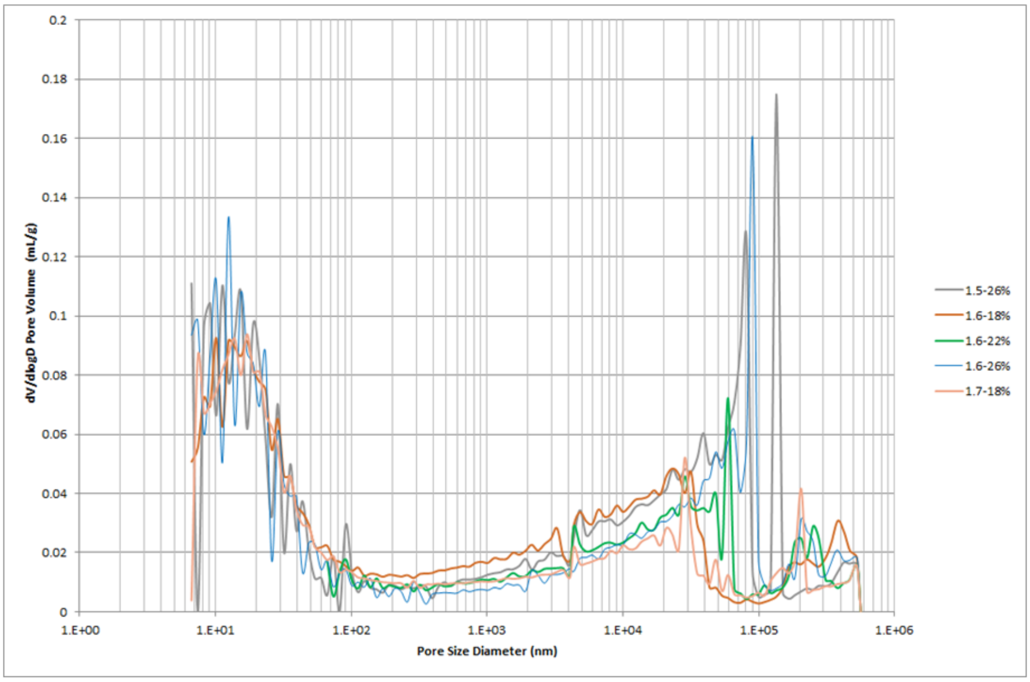

Figure 2.154: dV/dlogD Pore Volume (mL/g) for different as-compacted small samples.

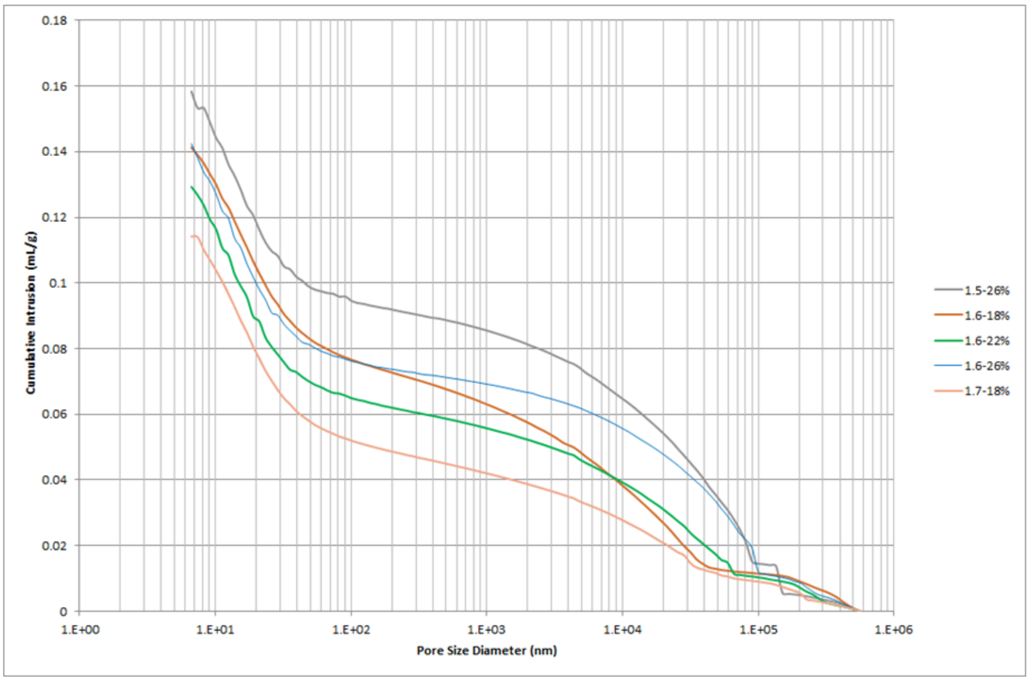

Figure 2.155: Incremental volume (mL/g) for different as-compacted small samples.

2.6.7.3. Water permeability

The water permeability values (Table 2.35; Figure 2.160), obtained from the protocol described above (2.6.6.2), are slightly higher than the referenced values for the FEBEX bentonite at this density Lloret and Villar (2007). This behaviour could be related to the low water volume passed through the sample, which would suppose saline water rather than deionized water. The differences between the permeability values for the first and second phases are not significant, and confirm the utility of the designed protocol.

In the second permeability phase, after the first phase of BTs, a certain gas pressure was detected in

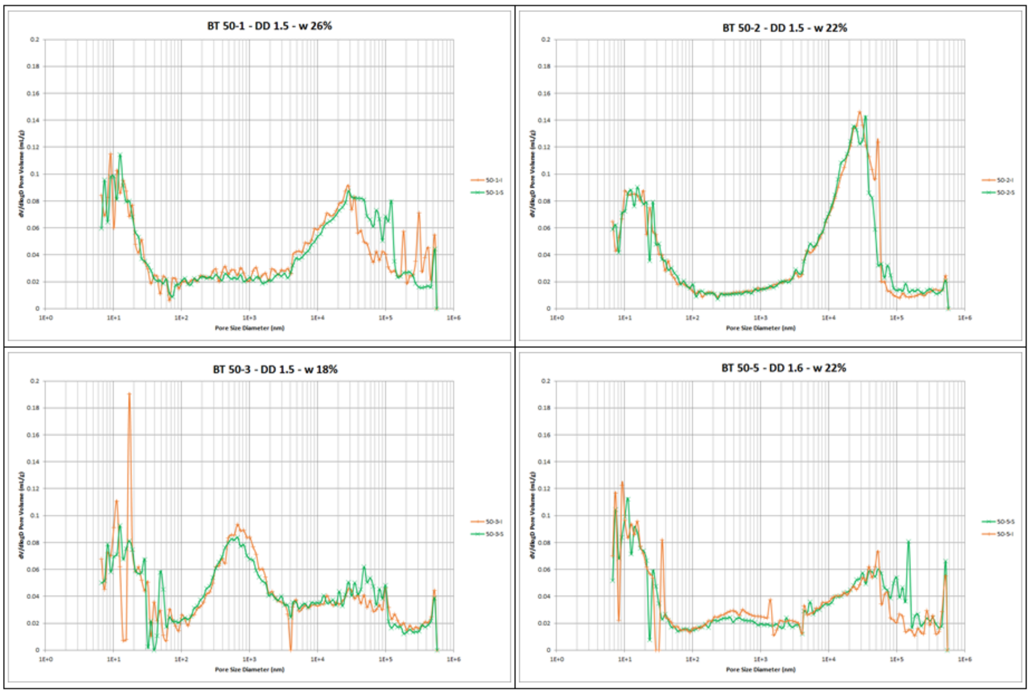

Figure 2.156: dV/dlogD Pore Volume (mL/g) for samples of 50 mm *diameter.*

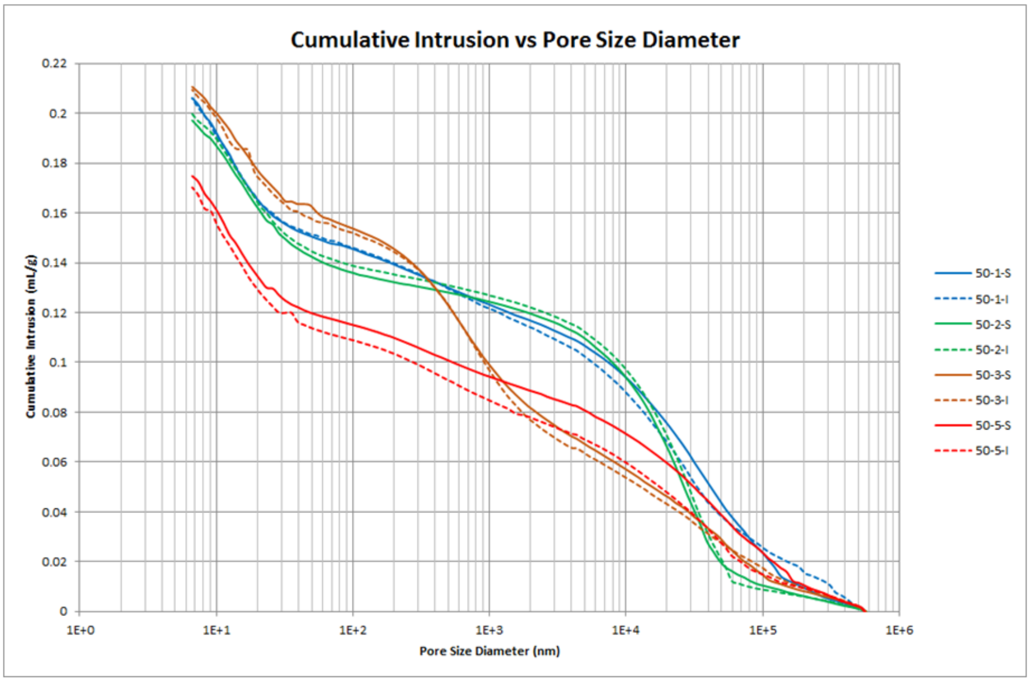

Figure 2.157: Incremental volume (mL/g) for samples of 50 mm *diameter.*

some vials that collect water, during the first few days. Since both ends of the sample saturate at the same pressure, gas trapped during the injection phase or dissolved in the pore water remains in the sample.

During the replacement of the wet filters with dry ones, it can be observed that the the basic microstructural pattern of powder grains from as-compacted state remains, as shown in Figure 2.161 and Figure 2.162, including the segregation of fine particles on the bottom during compaction (top cell in BT test).

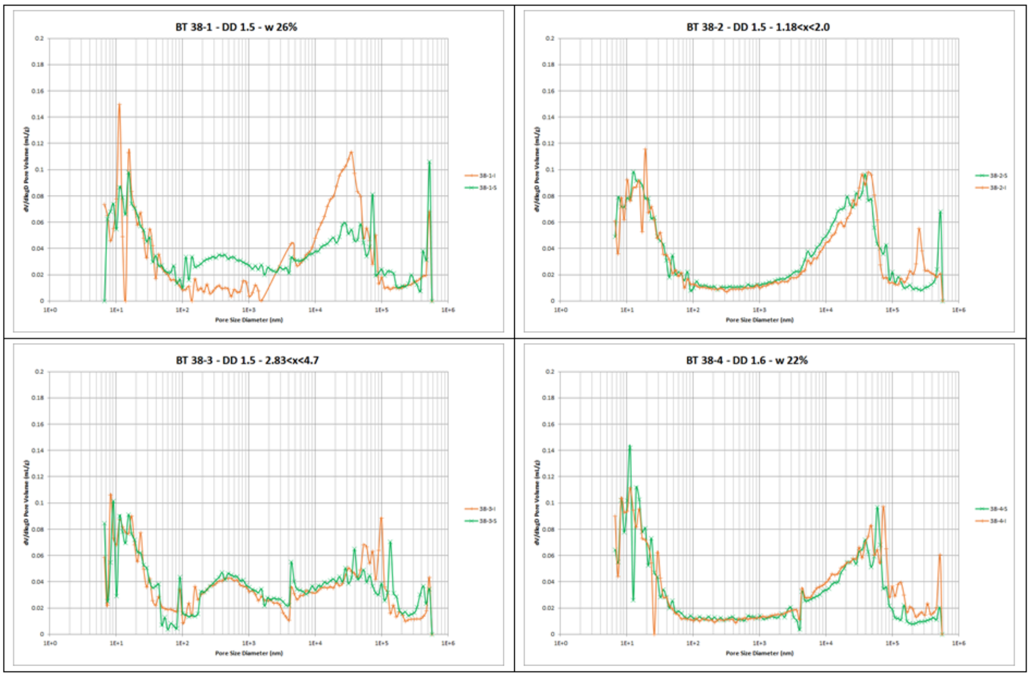

Figure 2.158: dV/dlogD Pore Volume (mL/g) for samples of 38 mm *diameter.*

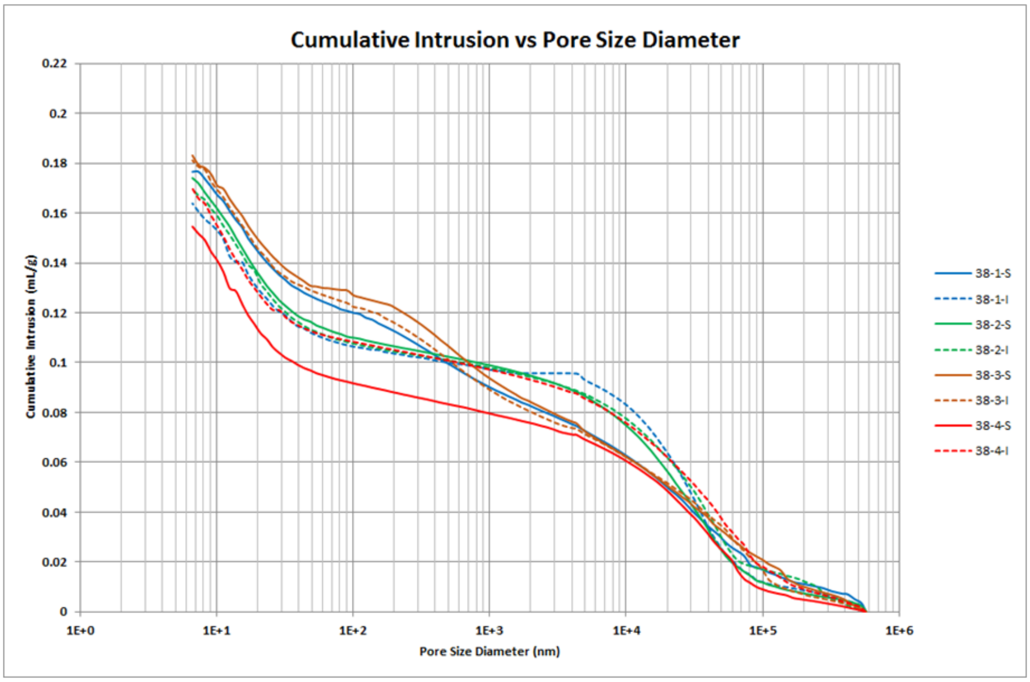

Figure 2.159: Incremental volume (mL/g) for samples of 38 mm *diameter.*

2.6.7.4. Gas permeability on as-compacted samples

The intrinsic permeability of as-compacted material at $w < 22\%$ ($Sr < 0.8$) was so high ($> 1 \times 10^{-14}$ m^2) that flowmeter measurement saturated at very low pressures. Nonetheless, linear relationship of flow with injection pressure was observed.

Table 2.35: Water permeabilities for the first and second saturation phases of the BT tests (at dry density 1.5, 1.6 & 1.7 Mg/m^3)

Ref.	Grain size	Dd Mg/m^3	W ini %	Sr ini %	1st kw ave m^2	2nd kw ave m^2
50-1	complete	1.49	26.6	88.0	1.18×10^{-18}	8.91×10^{-19}
50-2	complete	1.46	22.8	72.9	1.37×10^{-18}	1.45×10^{-18}
50-3	complete	1.46	18.4	58.6	1.80×10^{-18}	2.07×10^{-18}
50-4	complete	1.45	13.8	43.7	2.27×10^{-18}	1.50×10^{-18}
50-5	complete	1.59	21.4	83.5	6.03×10^{-19}	4.54×10^{-19}
50-6	complete	1.71	22.3	103.8	3.07×10^{-19}	–
38-1	complete	1.51	26.6	91.8	8.21×10^{-19}	8.04×10^{-19}
38-2	$1.18 < x < 2.0$	1.53	14.5	51.4	8.91×10^{-19}	–
38-3	$2.83 < x < 4.7$	1.50	14.8	50.1	1.18×10^{-18}	8.60×10^{-19}
38-4	complete	1.61	21.5	85.6	5.39×10^{-19}	6.02×10^{-19}
38-5	complete	1.69	22.2	101.0	2.65×10^{-19}	3.36×10^{-19}
38-7	complete	1.68	22.0	97.6	4.79×10^{-19}	4.31×10^{-19}

2.6.7.5. Break-through test on compacted samples: DD 1.5

Microstructural heterogeneity has a decisive influence on the critical gas pressure, at which gas penetration through the buffer clay begins, along paths of least resistance. From above, we could expect similar behaviours for the samples compacted from the same grain size distribution, unless initial water content modifies the effective pore distribution within the bentonite or affects the swelling pressure that determines the effective (confining) pressure.

For highly plastic clays, at low suctions, the effective stress is equivalent to the swelling pressure under constant volume, preventing preferential gas flows between the sample and the body cell. However, at high suctions, the swelling pressures are smaller than the corresponding applied suctions, so local paths for gas transport could develop through the sample.

Tests differ mainly in the cell diameter, the reservoir volumes, the inlet and outlet gas lines (with valves), and the attached pressure sensors (see appendix A for individual description of setups).

For a better comparison, the test has been grouped by target dry density, as followed from the original plannig: 1.5, 1.6 and 1.7 DD.

BT test: D50-1 W26.6 150/75 1.5 DD In the first phase of injection, inlet and outlet pressures did not equalize after the first BTs (Figure 2.163, Table 2.36), indicating flow channels close when pressure decreases to a certain value. Only after the 5th BT, gas pathways are continuously opened.

The first BT opened at a differential pressure of 5.91 MPa, and closed at a residual differential pressure of 4.04 MPa; while, the second BT opened at a differential pressure of 5.26 MPa. This is compatible with a weakening of the sample after the first B, which reduced the residual pressure to 0.20 MPa.

After 400 hours, a group of BTs (third to fiveth) show similar characteristics: differential pressure around 5.49 MPa and residual pressure higher than 2.7 MPa. The last value would be the minimum BT pressure for this sample, in agreement with the expected swelling pressure for the dry density.

After fifth BT, gas flow is continuous with two phases: the first one up to reach a residual pressure of 2.5 MPa ($\sim$ 3,000 h); the second one from this residual value with a lower rate that does not change much more when increasing differential pressure at $\sim$ 4,300 hours.

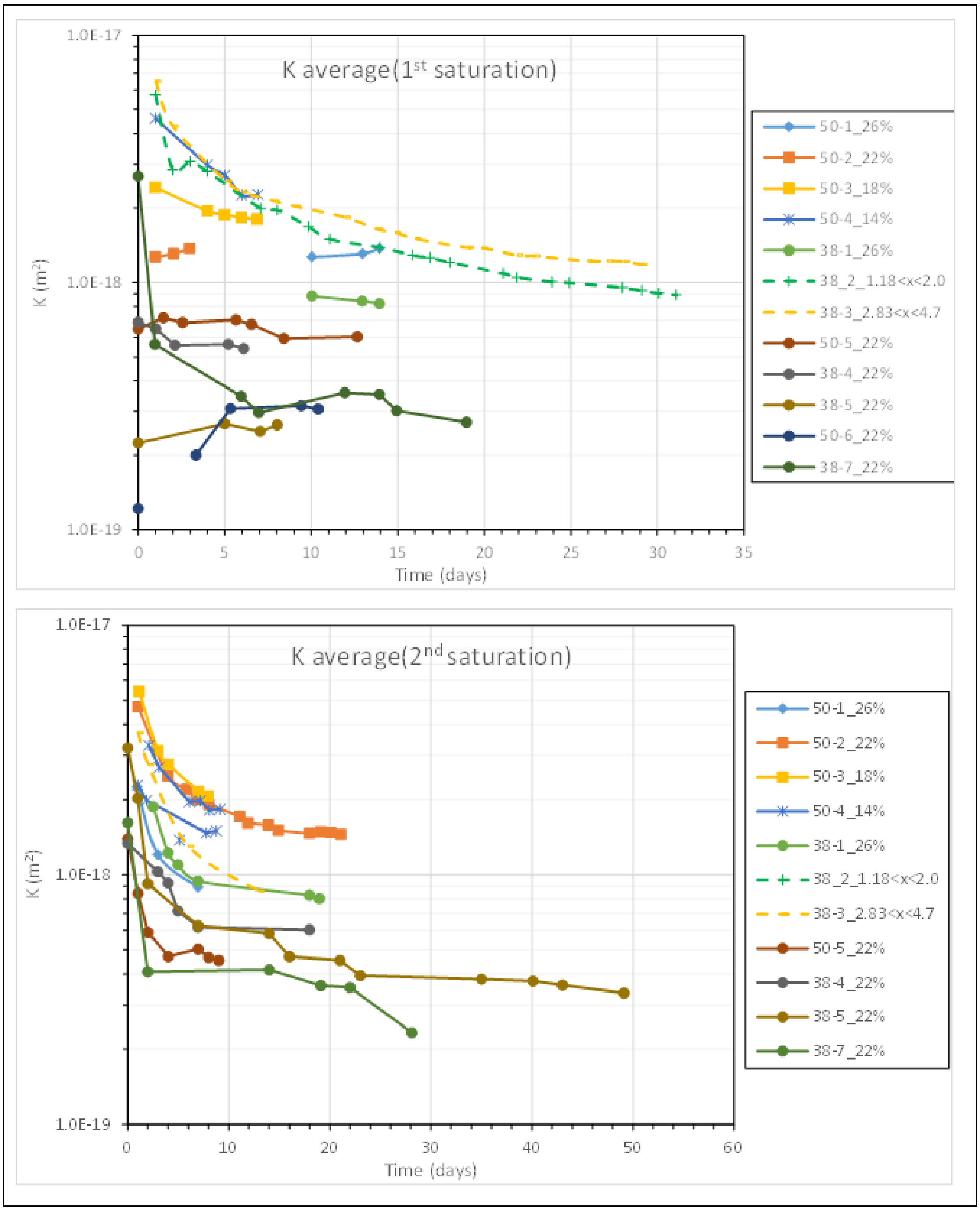

Figure 2.160: Evolution of the average water permeability vs test time: up) 1st water saturation phase of the BT tests; down) 2nd water saturation phase of the BT tests. BT references include: sample diameter, setup number, water content at compaction, and grain size class at compaction (if not full distribution).

In the second phase, after saturation of the sample, the first BT was a "slow" one with a similar value to the equivalent one in the first phase, 6.0 MPa. This BT became "instantaneous" with the next pressure step, indicating that actual value is closer to previous step.. Inlet and outlet pressures equalized and a leakage was detected before the third BT (Figure 2.164, Table 2.37); after, gas flow was continuous during more than 4,400 hours.

Other two BTs were induced over the slight gas flow existent. Pressure values and shapes are similar.

BT test: D50-2 W22 150/75 1.5 DD In the first phase (Figure 2.165, Table 2.38), inlet and outlet pressures equalized after the first BT, in all successive steps, indicating flow channels remained opened during the whole phase. The first and only BT opened at a differential pressure of 4.47 MPa, higher than the

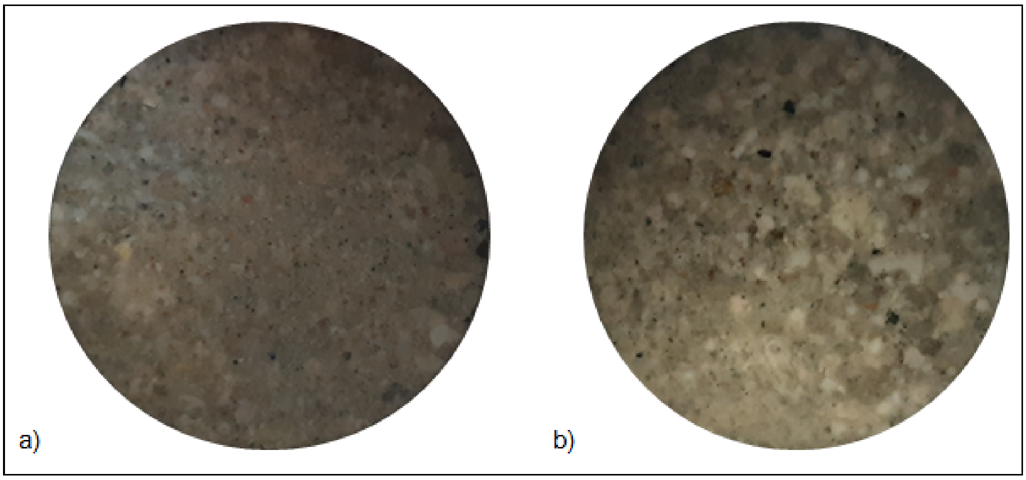

Figure 2.161: BT 50-3 (w.c. 18%): surface views after first permeability a) top; b) bottom

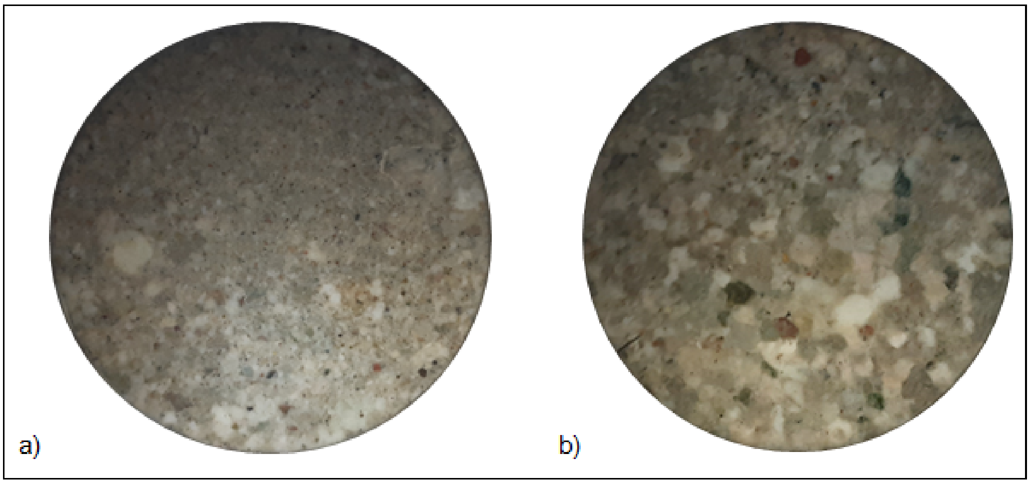

Figure 2.162: BT 50-4 (w.c. 14%): surface views after first permeability a) top; b) bottom

Table 2.36: Characteristics of the BTs in test 50_1_26

1^{st} phase	**P_{inj} max** (MPa)	**P_{out}** (MPa)	**ΔP_{max}** (MPa)	**Time at P_{max}** (hours)	**P_{inj} after** (MPa)	**P_{out} after** (MPa)	**$\Delta P_{residual}$** (MPa)	**Duration** (hours)
1^{st} BT	5.94	0.03	5.91	17	5.30	1.26	4.04	0
2^{nd} BT	5.29	0.02	5.26	6	3.57	3.37	0.20	1
3^{rd} BT	5.48	0.10	5.38	Inst.	4.60	1.80	2.79	1
4^{th} BT	5.49	0.10	5.39	Inst.	4.10	2.76	1.34	0
5^{th} BT	5.49	0.12	5.37	Inst.	4.59	1.86	2.73	1
Gas flow	4.54	0.13	4.41	Inst.	3.85	1.35	2.50	2,593
Gas flow	3.85	0.93	2.92					

expected swelling pressure. All BTs developed instantaneously.

In second phase (Figure 2.166, Table 2.39), after saturation of the sample, the amplitude of the first BT is similar to the equivalent one in the first phase, 4.97 MPa, but the decrease in pressure close the flow channels at a residual pressure of 0.53 MPa.

The second BT opened at a differential pressure of 3.41 MPa. It is compatible with a weakening of the

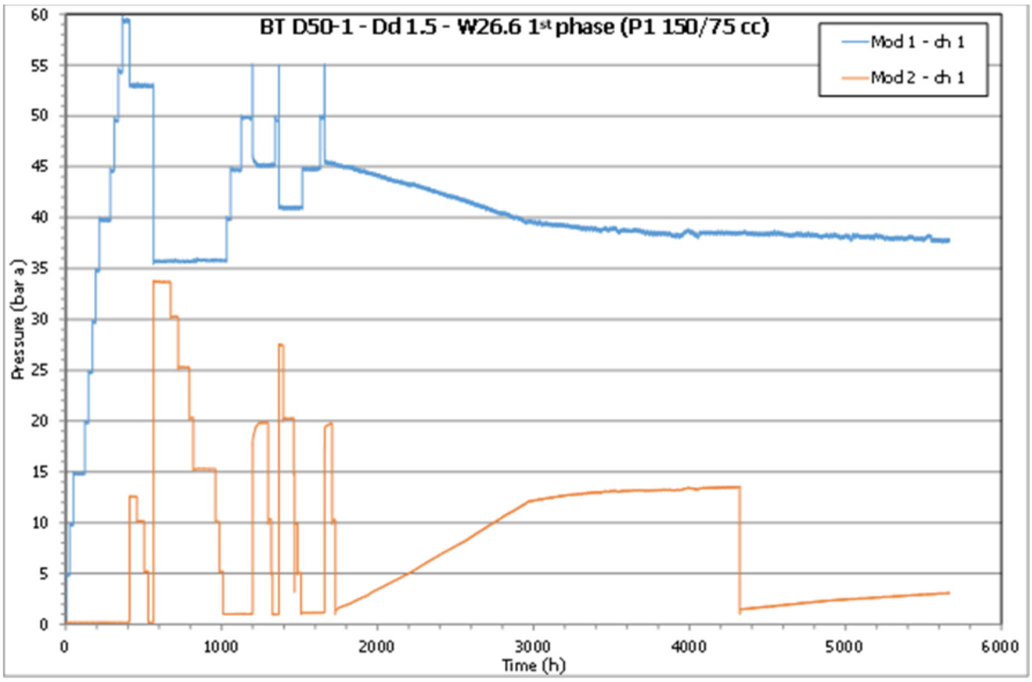

Figure 2.163: Pressure-time curve of BT test 50_1_26: 1st phase

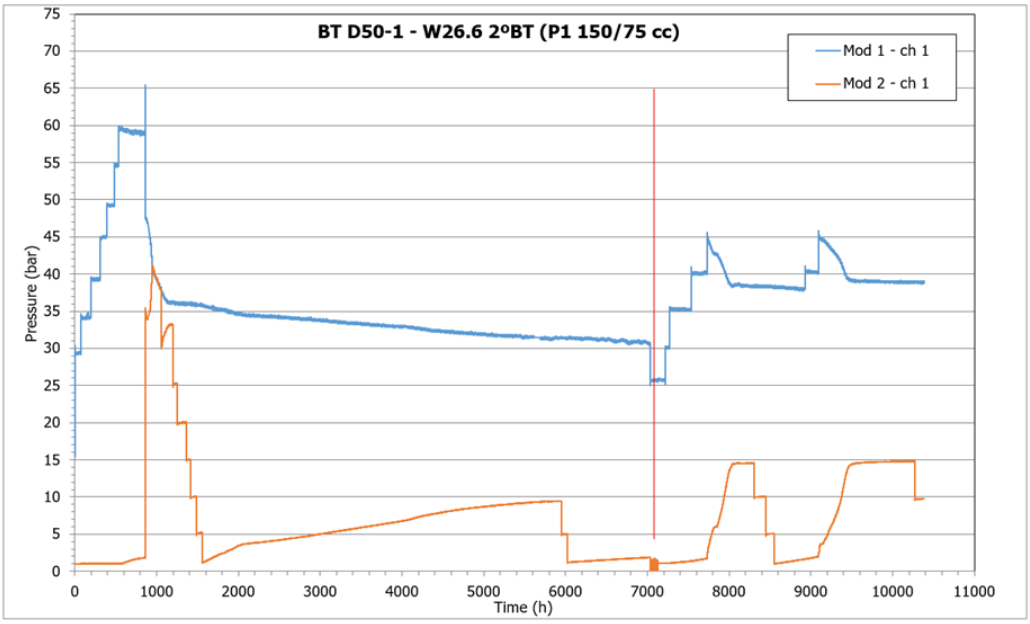

Figure 2.164: Pressure-time curve of BT test 50_1_26: 2nd phase

sample after the first BT, which reduced the residual pressure to 0.20 MPa.

The third BT opened at a lower pressure, 2.48 MPa, but behaviour was quite different. The pressure stabilization took more than 570 hours and the residual pressure was higher than 1.3 MPa. These pressures were maintained more than 1,000 hours before the next pressure steps, probably affecting the next BT. The fourth and fifth BTs show same differential pressure, 2.93 MPa. The residual pressure is higher in the fourth BT, 1.22 MPa (closed to previous one), than in the fifth BT, 0.43 MPa. The slopes were also different.

Finally, after a long stabilization time ($\sim$ 1,000 hours), the sixth BT (at 3.43 MPa) equalized inlet and outlet pressures, indicating flow channels remained opened. This BT pressure is slightly higher than the expected swelling pressure. However, the gas pathways became closed after some time ($<$ 200 hours) and remained

Table 2.37: Characteristics of the BTs in test 50_1_26: 2nd phase

2nd phase	P_{inj} max (MPa)	P_{out} (MPa)	ΔP_{max} (MPa)	Time at P_{max} (hours)	P_{inj} after (MPa)	P_{out} after (MPa)	$\Delta P_{residual}$ (MPa)	Duration (hours)
1st BT	5.46	0.11	5.36	Slow	3.46	2.94	0.53	7
2nd BT	6.51	0.18	6.33	Inst.	3.62	3.32	0.30	334
Leakage	3.58	0.12	3.46	Inst.	3.13	0.94	2.19	570
3rd BT	3.13	0.5	2.63	Slow	4.52	0.2	4.34	200
4th BT	4.52	0.2	4.50	Slow	3.84	1.46	2.38	600
5th BT	4.56	0.2	4.54	Slow	3.90	1.48	2.42	600

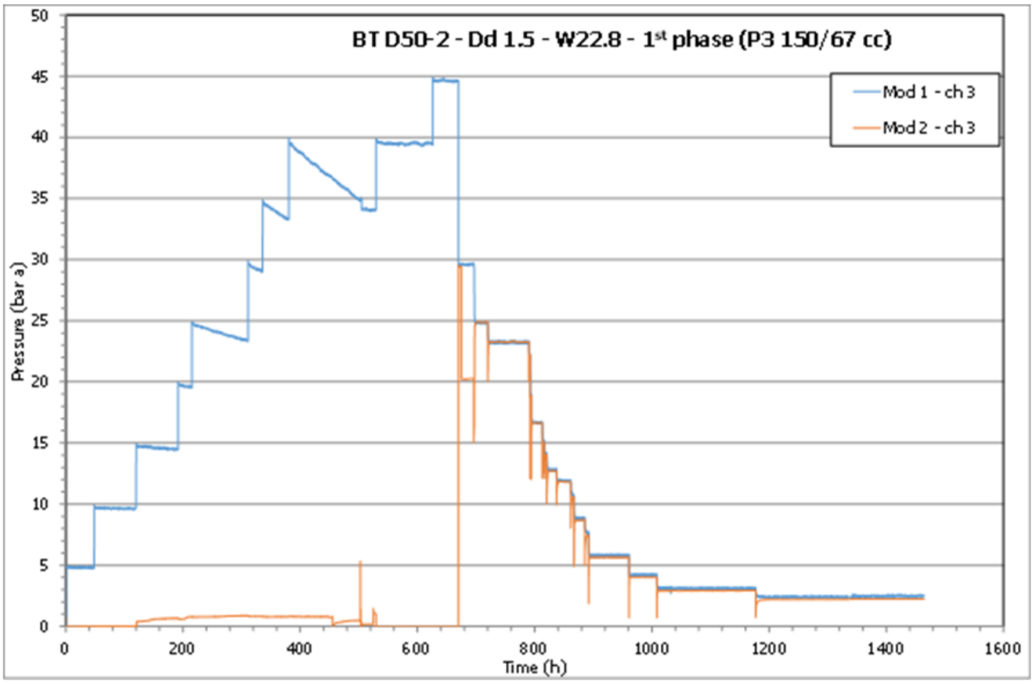

Figure 2.165: Pressure-time curve of BT test 50_2_22: 1st phase

in this condition to the end of the test (> 1,600 hours).

BT test: D50-3 W18 150/75 1.5 DD In the first phase (Table 2.40, Figure 2.167), inlet and outlet pressures equalized after the first BT, in all successive steps, indicating flow channels remained opened during the whole phase. The first and only BT opened at a differential pressure of 3.36 MPa, higher than the expected swelling pressure. All BTs developed instantaneously. Behaviour is similar to the first phase of previous test D50-2 W22.

In second phase (Figure 2.168, Table 2.41), after saturation of the sample, the pressure of the first BT is higher, 3.9 MPa, than the equivalent one in the first phase. After this BT, pressures equalized and the gas flow did not stop, indicating flow channels remained opened and could maintain some gas.

After 600 hours stabilization time, a new BT was tried. This second BT (at 2.55 MPa) let channels opened with a continuous gas flow during more than 1,200 hours, till the outlet pressure was around 1.0 MPa. This lower BT pressure is compatible with a weakening of the sample after the first BT, which reduced the differential pressure needed to shoot the process from 3.90 to 2.43 MPa. From this point, the gas pathways became opened more than 1,600 hours.

The third BT took place at a similar differential pressure, 2.39 MPa. Their characteristics were similar to

Table 2.38: Characteristics of the BTs in test 50_2_22: 1st phase

1st phase	P_{inj} max (MPa)	P_{out} (MPa)	ΔP_{max} (MPa)	Time at P_{max} (hours)	P_{inj} after (MPa)	P_{out} after (MPa)	$\Delta P_{residual}$ (MPa)	Duration (hours)
1st BT	4.46	−0.01	4.47	Inst.	2.94	2.96	−0.01	0.3
Gas flow	2.96	1.50	1.45	Inst.	2.49	2.49	0.00	7.0
Gas flow	2.48	2.00	0.48	Inst.	2.32	2.33	0.00	1.8
Gas flow	2.32	2.00	0.32	Inst.	2.21	2.22	−0.01	1.8
Gas flow	2.21	1.21	1.01	Inst.	1.89	1.89	0.00	2.0
Gas flow	1.89	1.20	0.69	Inst.	1.67	1.67	0.01	2.9
Gas flow	1.66	1.21	0.45	Inst.	1.51	1.51	0.01	3.0
Gas flow	1.51	1.21	0.31	Inst.	1.41	1.40	0.01	2.9
Gas flow	1.41	1.00	0.41	Inst.	1.29	1.27	0.01	3.4
Gas flow	1.27	0.99	0.28	Inst.	1.19	1.19	0.01	5.3
Gas flow	1.19	0.80	0.39	Inst.	1.07	1.06	0.02	3.8
Gas flow	1.07	0.49	0.58	Inst.	0.88	0.87	0.01	3.4
Gas flow	0.88	0.50	0.39	Inst.	0.76	0.75	0.01	6.2
Gas flow	0.76	0.19	0.58	Inst.	0.58	0.56	0.02	2.3
Gas flow	0.57	0.07	0.50	Inst.	0.41	0.40	0.01	0.8
Gas flow	0.42	0.07	0.35	Inst.	0.31	0.29	0.02	2.9
Gas flow	0.31	0.07	0.24	Inst.	0.25	0.22	0.03	10.6

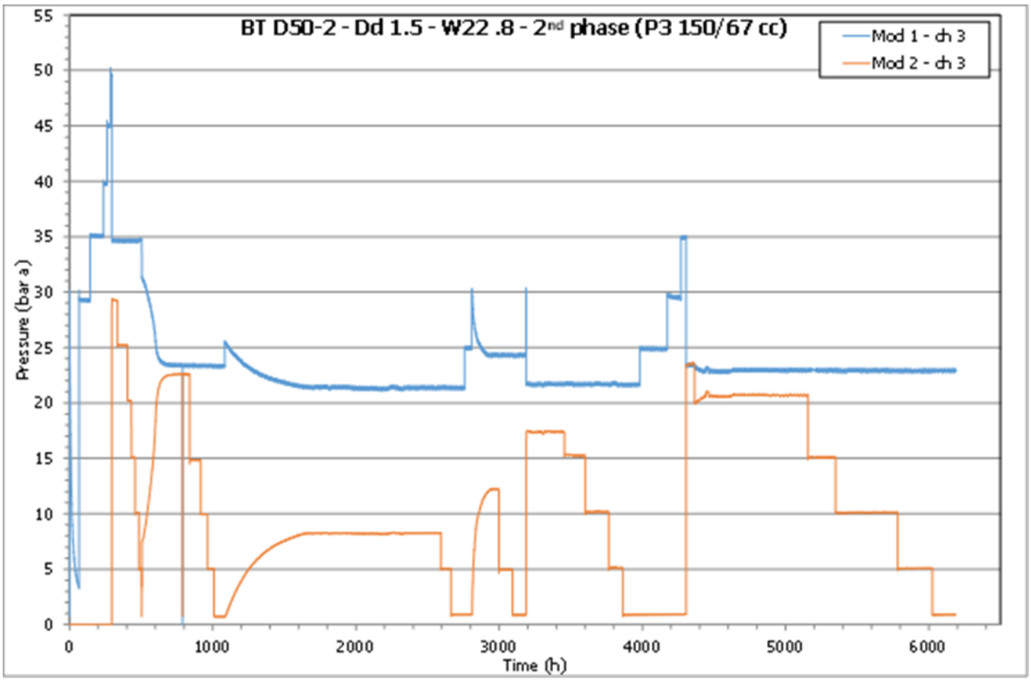

Figure 2.166: Pressure-time curve of BT test50_2_22: 2nd phase

the second one. Gas pathways remained opened more than 3,000 hours.

BT test: D50-4 W14 150/75 1.5 DD Figure 2.169 shows a major problem involved in this long-term experiments: gas leakages. From the beginning of the test, we detected an important gas leakage upstream of the sample but we were unable to correct it during long time. In any case, the BT values are acceptable, although the pertinent corrections will be made to calculate the gas flow from the downstream pressure

Table 2.39: Characteristics of the BTs in test 50_2_22: 2nd phase

2nd phase	P_{inj} max (MPa)	P_{out} (MPa)	ΔP_{max} (MPa)	Time at P_{max} (hours)	P_{inj} after (MPa)	P_{out} after (MPa)	$\Delta P_{residual}$ (MPa)	Duration (hours)
1st BT	4.97	0.00	4.97	2	3.46	2.94	0.53	7
2nd BT	3.48	0.07	3.41	Inst.	2.33	2.25	0.12	334
3rd BT	2.55	0.07	2.48	Inst.	2.15	0.83	1.32	570
4th BT	3.02	0.09	2.93	Inst.	2.44	1.22	1.22	169
5th BT	3.02	0.09	2.93	Inst.	2.17	1.74	0.43	6
6th BT	3.51	0.08	3.43	Inst.	2.33	2.34	−0.01	0

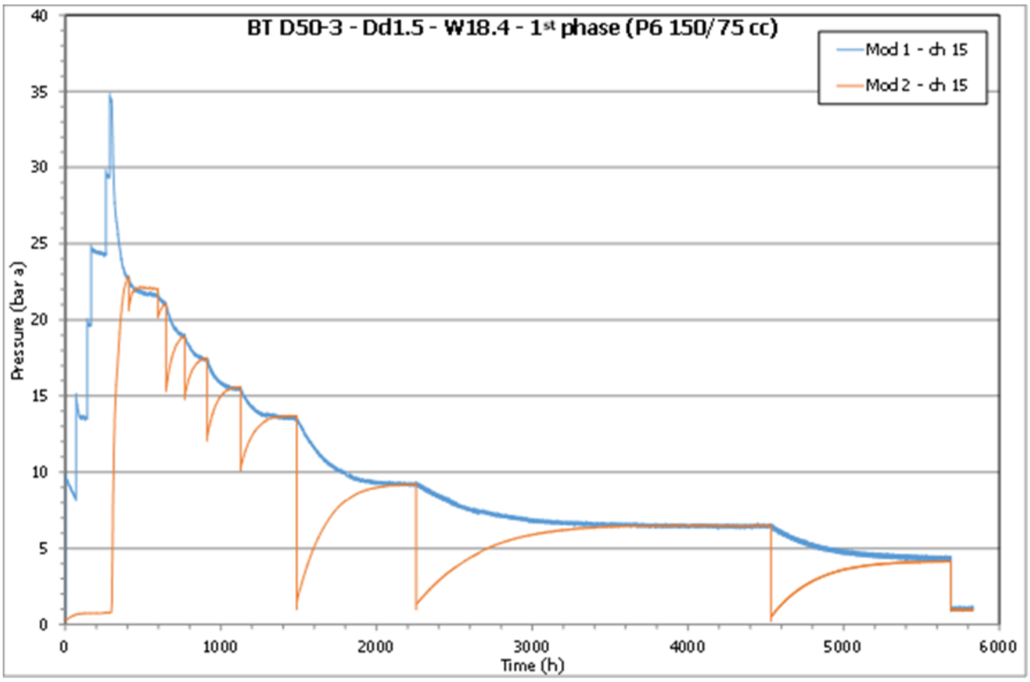

Figure 2.167: Pressure-time curve of BT test 50_3_18: 1st phase

Table 2.40: Characteristics of the BTs in test 50_3_18: 1st phase

1st phase	P_{inj} max (MPa)	P_{out} (MPa)	ΔP_{max} (MPa)	Time at P_{max} (hours)	P_{inj} after (MPa)	P_{out} after (MPa)	$\Delta P_{residual}$ (MPa)	Duration (hours)
1st BT	3.44	0.08	3.36	Inst.	2.28	2.28	0.00	112
Gas flow	2.27	2.06	0.22	Inst.	2.18	2.21	−0.03	67
Gas flow	2.18	2.01	0.17	Inst.	2.11	2.11	0.00	49
Gas flow	2.11	1.55	0.56	Inst.	1.89	1.90	0.00	120
Gas flow	1.90	1.47	0.42	Inst.	1.74	1.75	−0.01	141
Gas flow	1.73	1.24	0.49	Inst.	1.54	1.56	−0.02	211
Gas flow	1.55	1.01	0.54	Inst.	1.36	1.37	−0.01	287
Gas flow	1.35	0.10	1.26	Inst.	0.92	0.92	0.00	764
Gas flow	0.93	0.10	0.83	Inst.	0.65	0.65	0.00	1,387
Gas flow	0.64	0.02	0.62	Inst.	0.42	0.41	0.01	1,130

and volume.

In this test (Figure 2.169, Table 2.42), inlet and outlet pressures did not equalize indicating flow channels

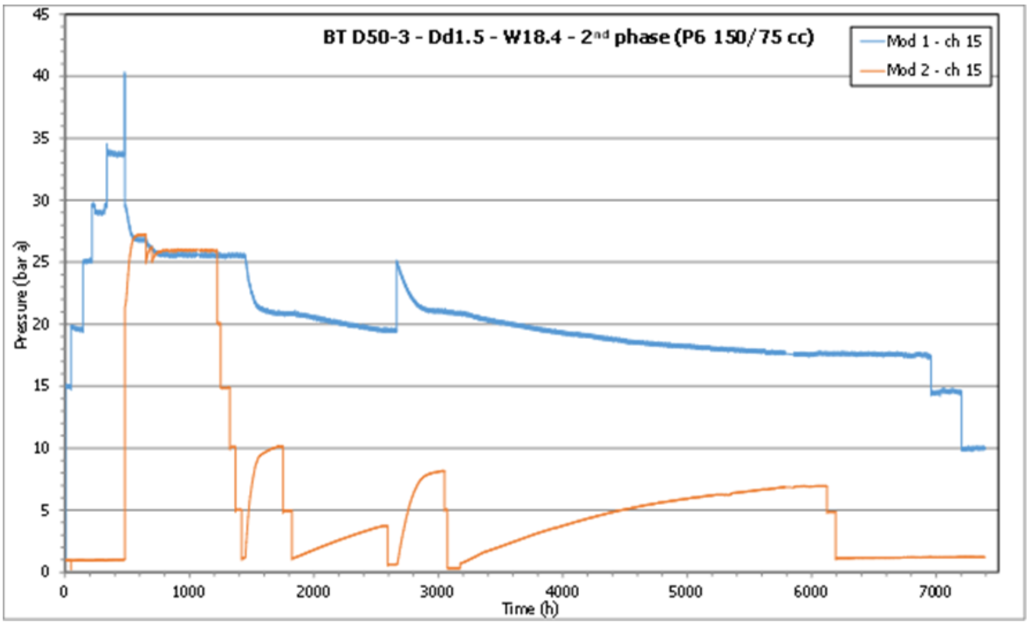

Figure 2.168: Pressure-time curve of BT test 50_3_18: 2nd phase

Table 2.41: Characteristics of the BTs in test 50_3_18: 2nd phase

2nd phase	**P_{inj} max** (MPa)	**P_{out}** (MPa)	**ΔP_{max}** (MPa)	**Time at P_{max}** (hours)	**P_{inj} after** (MPa)	**P_{out} after** (MPa)	**$\Delta P_{residual}$** (MPa)	**Duration** (hours)
1st BT	4.00	0.11	3.90	2	2.95	2.12	0.83	0.8
Slope change	2.95	2.12	0.83	Inst.	2.69	2.72	−0.04	102.9
Gas flow	2.68	2.50	0.18	Inst	2.63	2.62	0.01	44.6
Gas flow	2.60	2.50	0.1	Slow	2.56	2.59	−0.03	103.8
2nd BT	2.55	0.11	2.43	Inst.	2.09	1.01	1.08	273.5
3rd BT	2.50	0.11	2.39	Inst.	2.09	1.01	1.08	400.0
Gas flow	2.09	0.11	1.97	Slow	1.95	0.37	1.58	713.0
No gas flow	1.76	0.11	1.65		1.00	0.12	0.88	1,197.7

close when pressure decreases to a certain value. After the 3rd BT, gas pathways remain opened during more than 3,000 hours.

Table 2.42: Characteristics of the BTs in test 50_4_13: 1st phase

1st phase	**P_{inj} max** (MPa)	**P_{out}** (MPa)	**ΔP_{max}** (MPa)	**Time at P_{max}** (hours)	**P_{inj} after** (MPa)	**P_{out} after** (MPa)	**$\Delta P_{residual}$** (MPa)	**Duration** (hours)
1st BT	3.47	0.02	3.46	50	2.98	0.81	2.17	66
2nd BT	2.98	0.02	2.96	10	2.40	0.24	2.16	824
3rd BT	3.00	0.24	2.76	Inst.	2.59	0.94	1.66	3,487
4th BT	3.48	0.18	3.30	Inst.	2.55	1.92	0.63	548
Gas flow	2.54	1.50	1.04	Inst.				

The first BT opened at a differential pressure higher than 3.46 MPa, and closed at a residual differential pressure of 2.17 MPa. The second BT opened at a differential pressure higher than 2.96 MPa, This value is compatible with a weakening of the sample after the first BT. The residual pressure did not change, 2.16 MPa. The third BT opened at a differential pressure of 2.76 MPa, similar to the previous one, and

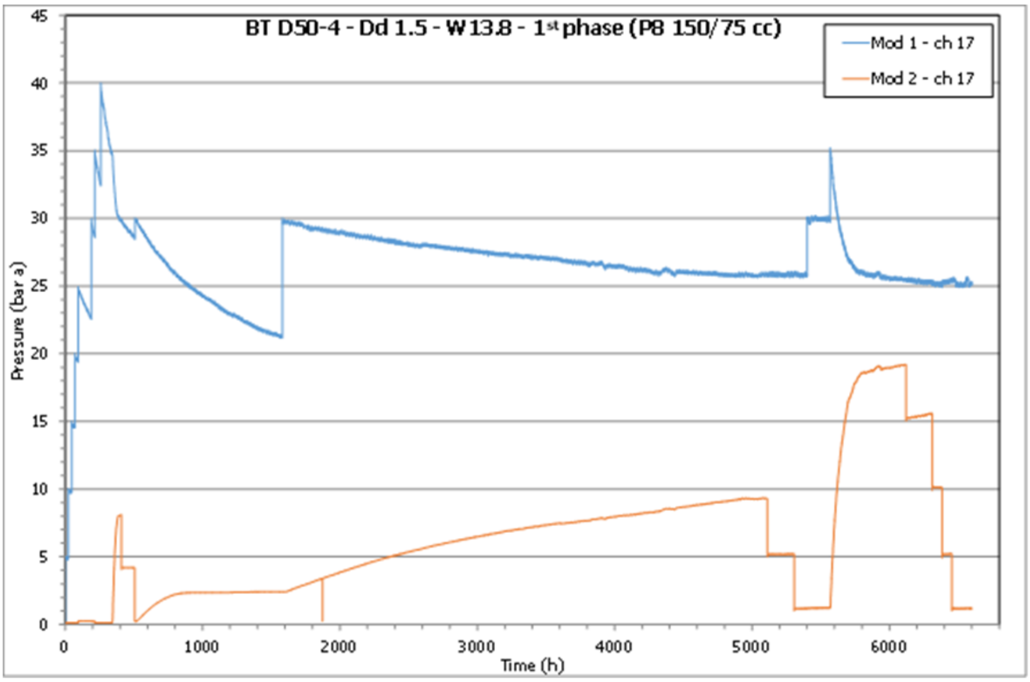

Figure 2.169: Pressure-time curve of BT test 50_4_13: 1st phase

sustained the gas flow up to a residual pressure of 1.66 MPa (2.59 MPa injection). The last BT of this phase opened at a differential pressure of 3.3 MPa, with continuous flow even at residual pressure lower than 0.63 MPa.

In second phase (Figure 2.170, Table 2.43), after saturation of the sample, the first BT opened at a differential pressure slightly higher than in phase 1 and almost equalized the pressures. Following BTs opened at lower pressures with a “slow” behaviour, indicating the weakening of the sample, where gas channels remained opened more than 4,000 hours.

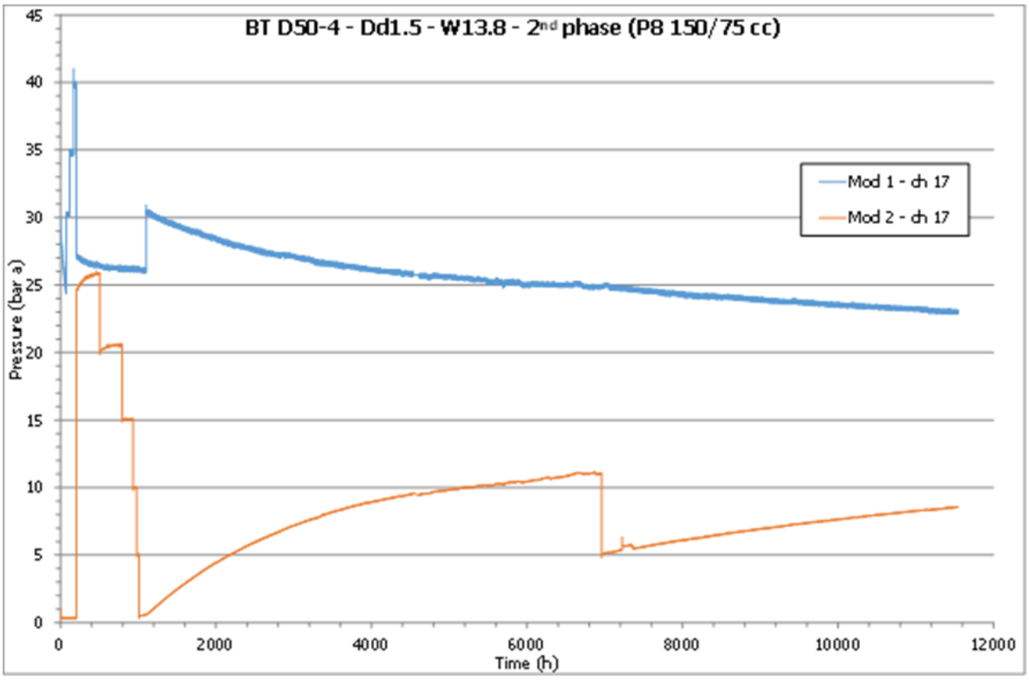

Figure 2.170: Pressure-time curve of BT test 50_4_13: 2nd phase

Table 2.43: Characteristics of the BTs in test 50_4_13: 2nd phase

2nd phase	P_{inj} max (MPa)	P_{out} (MPa)	ΔP_{max} (MPa)	Time at P_{max} (hours)	P_{inj} after (MPa)	P_{out} after (MPa)	$\Delta P_{residual}$ (MPa)	Duration (hours)
1st BT	3.98	0.03	3.95		2.72	2.46	0.26	0.7
Gas flow	3.09	0.06	3.03		2.49	1.10	1.39	5,835
Gas flow	2.48	0.51	1.97					

BT test: D38-1 W26 75/50 1.5 DD This sample in this test is comparable to sample in test D50-1 W26.6, with only minor changes in density (1.49 vs 1.51) and degree of saturation (0.88 vs 0.92) reported (Table 2.33).

In this test (Figure 2.171) there was a huge gas leakage produced after more 500 hours of test.

After the first BTs (Figure 2.171, Table 2.44), pressure did not equalized and stabilized indicating that flow channels closed when pressure decreases to a certain value. Only after the 3rd BT, gas pathways remained opened.

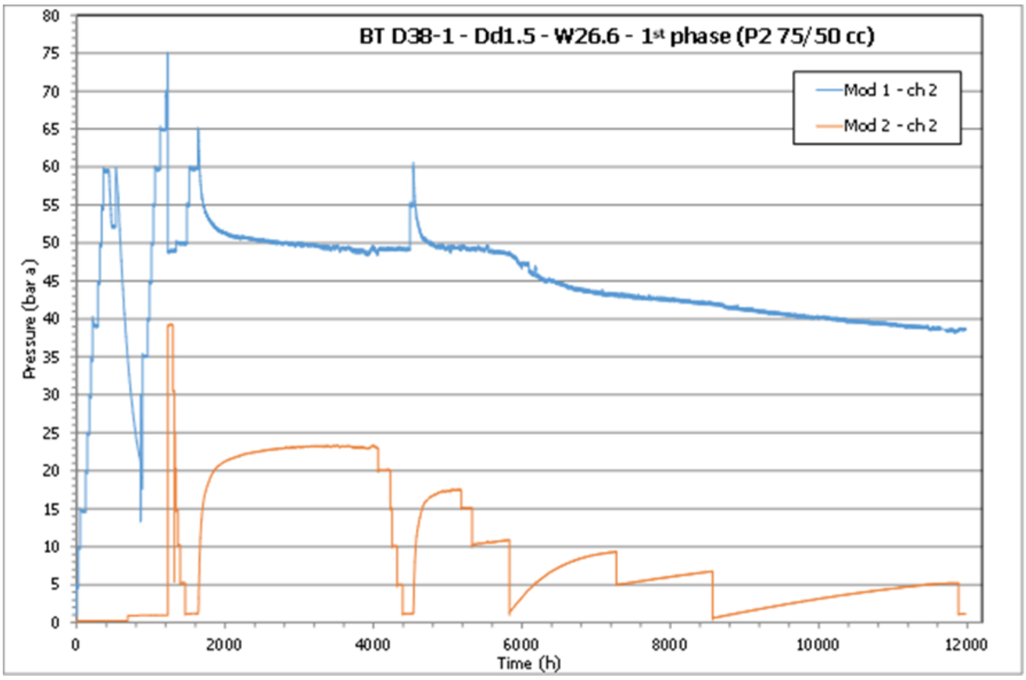

Figure 2.171: Pressure-time curve of BT test 38_1_26: 1st phase

Table 2.44: Characteristics of the BTs in test 38_1_26: 1st phase

1st phase	P_{inj} max (MPa)	P_{out} (MPa)	ΔP_{max} (MPa)	Time at P_{max} (hours)	P_{inj} after (MPa)	P_{out} after (MPa)	$\Delta P_{residual}$ (MPa)	Duration (hours)
1st BT	7.47	0.1	7.37	Inst.	4.89	3.93	0.96	5
2nd BT	6.49	0.12	6.37	Inst.	4.98	2.32	2.65	1,600
3rd BT	6.01	0.12	5.89	Inst.	4.98	2.14	3.22	500
Gas flow	4.93	1.04	3.89	Inst.	4.89	1.09	3.796	370
Gas flow	4.87	1.4	4.73	Inst.				

The first BT opened at a differential pressure of 7.37 MPa, and closed at a residual differential pressure of 0.96 MPa. The second BT opened at a differential pressure of 6.37 MPa, compatible with a weakening of the sample after the first BT. Gas flow continued during more than 2,000 hours at decreasing rate, up to reach a residual pressure to 2.65 MPa.

The third BT was produced at a lower differential pressure, 5.89 MPa. After this BT, gas flow was established and did not stop but the flow rate decreased. So, outlet pressure was decreased in order to obtain different flow rates and a possible BT was produced at 4.93 MPa (3.89 MPa, differential pressure).

In second phase (Figure 2.172, Table 2.45), after saturation of the sample, the pressure of the first BT (7.54 MPa) is equivalent to that of the first phase, This is also case for the other BTs with values around 6.0 MPa, but without establish an observable gas flow.

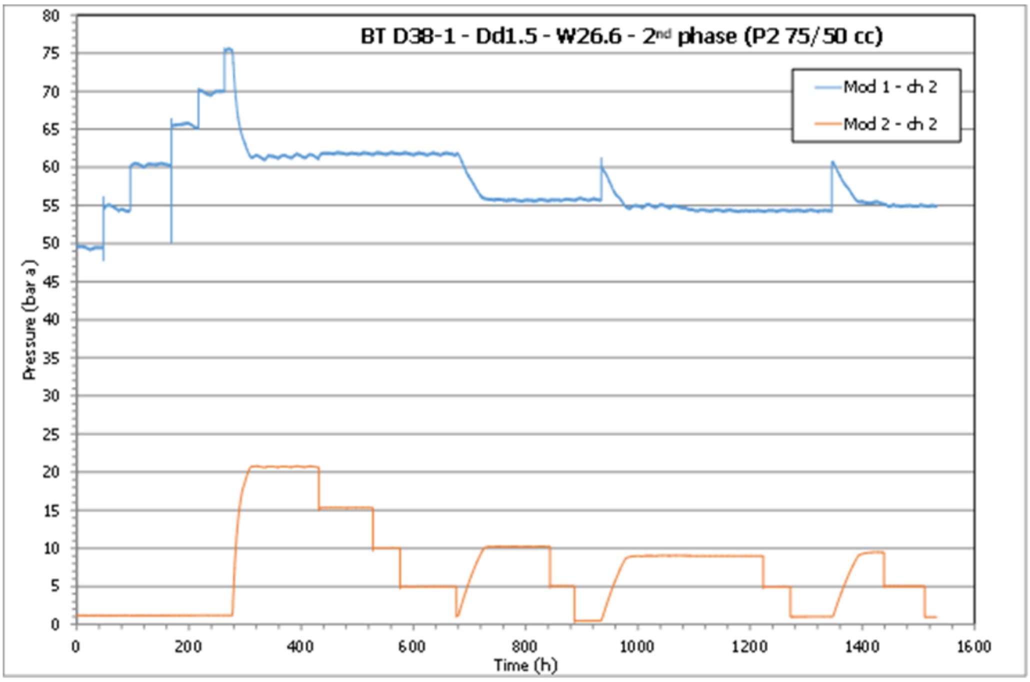

Figure 2.172: Pressure-time curve of BT test 38_1_26: 2nd phase

Table 2.45: Characteristics of the BTs in test 38_1_26: 2nd phase

2nd phase	P_{inj} max (MPa)	P_{out} (MPa)	ΔP_{max} (MPa)	Time at P_{max} (hours)	P_{inj} after (MPa)	P_{out} after (MPa)	$\Delta P_{residual}$ (MPa)	Duration (hours)
1st BT	7.54	0.12	7.42		6.13	2.07	4.06	35
2nd BT	6.18	0.12	6.07		5.59	1.02	4.56	69
3rd BT	6.01	0.05	5.97		5.50	0.90	4.60	102
4th BT	6.07	0.11	5.96		5.54	0.95	4.59	71

BT test: D38-2 W14.5 50/50 1.5 DD This failed test is running to obtain some information on the gas diffusion parameters of FEBEX bentonite. No data are provided.

BT test: D38-3 W14.5 75/50 1.5DD In this test (*Figure 2.173*, Table 2.46), after the first BT at 6.43 MPa, gas flow continues for more than 1,000 hours at very low rate, before stopping at a residual pressure of 2.39 MPa, which indicates the closure of the opened pathways.

The second BT was established at a differential pressure of 4.24 MPa and gas flow continued at a higher flow rate than previous BT. The differential, not residual, pressure was 2.83 MPa. The tendency of the curves seemed to indicate a residual pressure higher than that of the first BT.

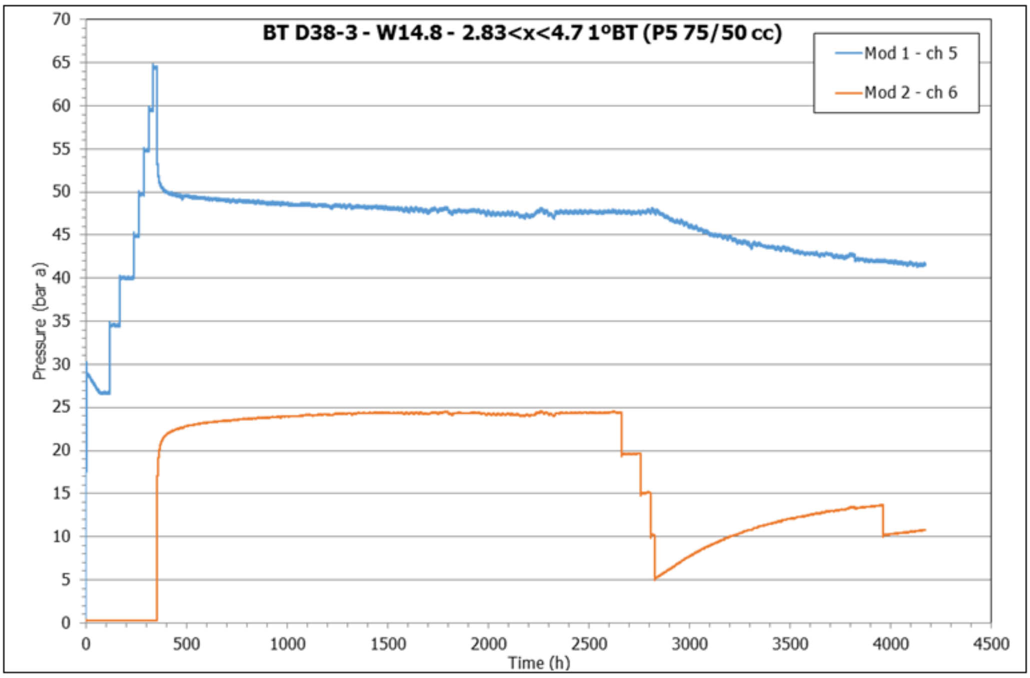

Figure 2.173: Pressure-time curve of BT test 38_3_14.5: grain size $2.83 < x < 4.7$*: 1st phase*

Table 2.46: Characteristics of the BTs in 38_3_14.5: grain size $2.83 < x < 4.7$*: 1st phase*

1st phase	P_{inj} max (MPa)	P_{out} (MPa)	ΔP_{max} (MPa)	Time at P_{max} (hours)	P_{inj} after (MPa)	P_{out} after (MPa)	$\Delta P_{residual}$ (MPa)	Duration (hours)
1st BT	6.46	0.03	6.43	16	4.83	2.44	2.39	1,060
2nd BT	4.76	0.52	4.24	Inst.	4.20	1.36	2.83	930
Gas flow	4.20	1.08	3.12	Inst.				

In the second phase (Figure 2.174, Table 2.47, Table 2.33), after saturation of the sample, the first BT has a similar value to the first phase (6.5 MPa). BT values, decreasing for the following BTs, indicate the changes in the sample.

Table 2.47: Characteristics of the BTs in 38_3_14.5: grain size $2.83 < x < 4.7$*: 2nd phase*

2nd phase	P_{inj} max (MPa)	P_{out} (MPa)	ΔP_{max} (MPa)	Time at P_{max} (hours)	P_{inj} after (MPa)	P_{out} after (MPa)	$\Delta P_{residual}$ (MPa)	Duration (hours)
1st BT	6.50	0.04	6.46	Slow	5.33	1.67	3.67	182
2nd BT	5.97	0.03	5.94	Slow	4.96	1.52	3.44	575
3rd BT	4.97	0.12	4.85	Slow	4.41	0.91	3.50	612
4th BT	5.51	0.06	5.45	Slow	4.80	1.12	3.68	219
5th BT	5.50	0.04	5.46	Slow	4.75	1.16	3.59	514
Gas flow	4.74	0.51	4.23	Slow	4.47	0.90	3.57	1,327
Gas flow	4.47	0.12	2.38	Slow	2.55	0.14	2.40	1,638

2.6.7.6. Break-through test on compacted samples: DD 1.6

BT test: D50-5 W22 150/67 1.6 DD In the first phase (Figure 2.175, Table 2.48, Table 2.46), the first BT occurred at 7.98 MPa and gas flow continued during more than 1,500 hours, till a new BT was generated at 7.41 MPa. The third BT took a similar value but the shape was very sharp, indicating changes in the

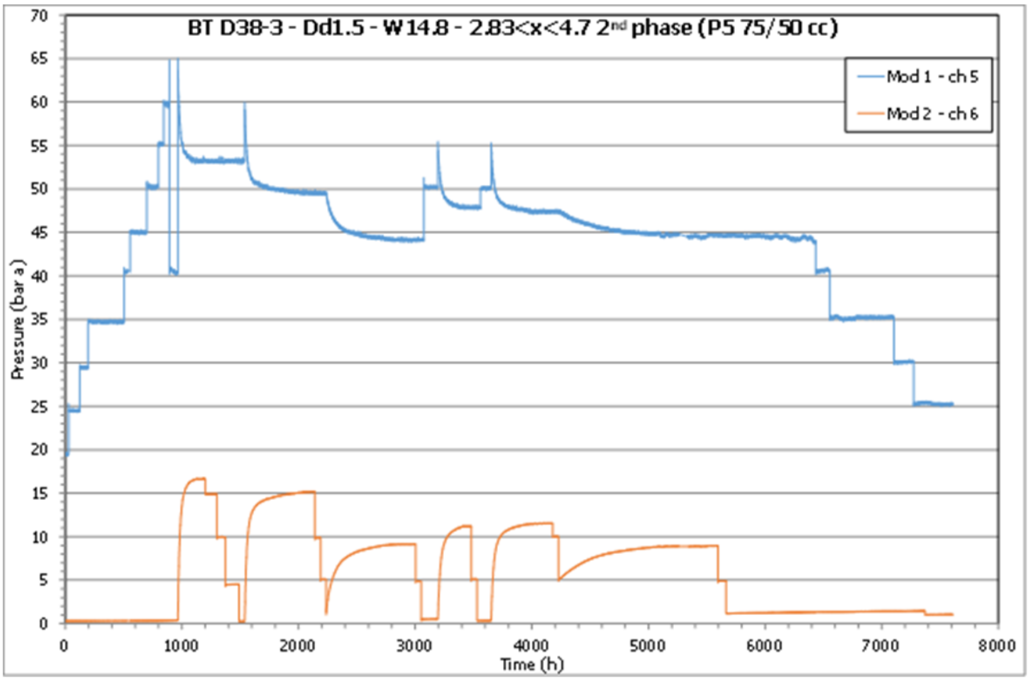

Figure 2.174: Pressure-time curve of BT test 38_3_14.5: grain size $2.83 < x < 4.7$*: 2nd phase*

mechanism of transport. All the values are higher than those of 1.5 DD.

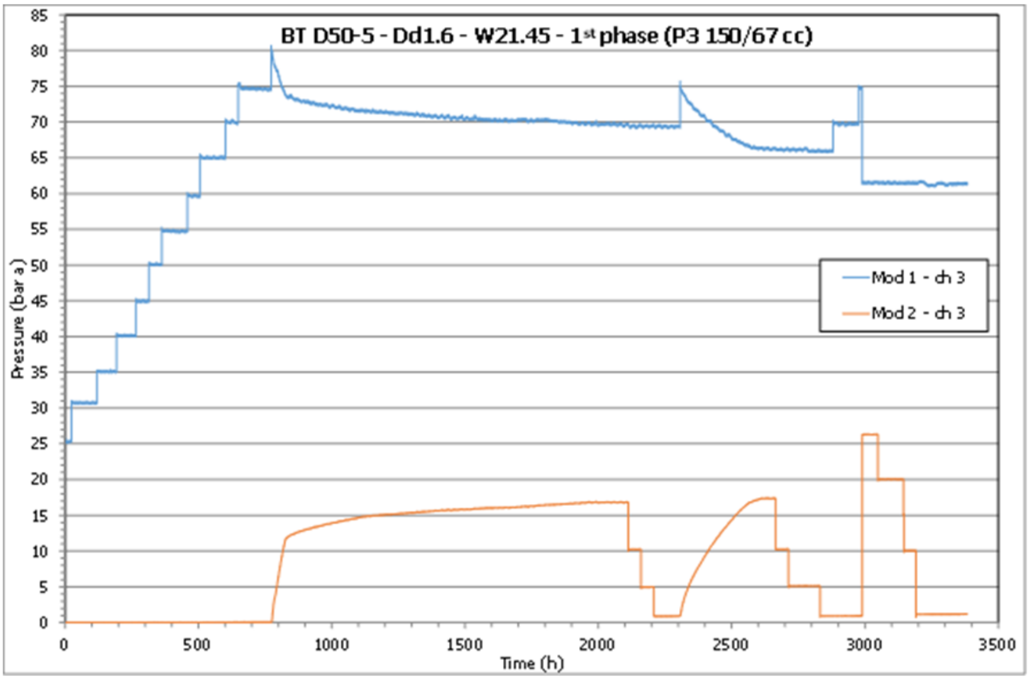

Figure 2.175: Pressure-time curve of BT test 50_5_22: 1st phase

In second phase (Figure 2.176, Table 2.49), after saturation of the sample, the pressure of the first BT was slightly higher than that of the last BT in the first phase (7.46 MPa) and gas flow stopped at 1-MPa residual pressure.

The other three BTs have similar characteristics, both in pressure values and without closing the gas flow up to equalize the pressures. In all the cases, after 300 hours, the sample resealed the channels.

Table 2.48: Characteristics of the BTs in test 50_5_22: 1st phase

1st phase	P_{inj} max (MPa)	P_{out} (MPa)	ΔP_{max} (MPa)	Time at P_{max} (hours)	P_{inj} after (MPa)	P_{out} after (MPa)	$\Delta P_{residual}$ (MPa)	Duration (hours)
1st BT	7.99	0.01	7.98	Slow	6.96	1.68	5.28	1,315
2nd BT	7.50	0.09	7.41	Slow	6.61	1.74	4.88	317
3rd BT	7.47	0.09	7.38	Inst.	6.15	2.63	3.52	2

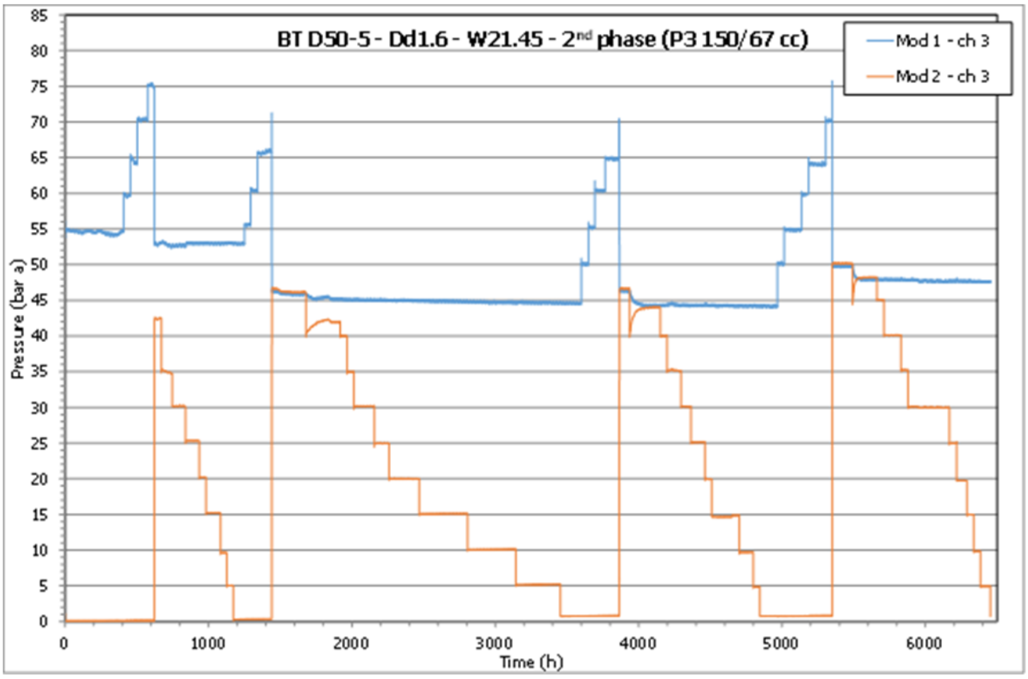

Figure 2.176: Pressure-time curve of BT test 50_5_22: 2nd phase

Table 2.49: Characteristics of the BTs in test 50_5_22: 2nd phase

2nd phase	P_{inj} max (MPa)	P_{out} (MPa)	ΔP_{max} (MPa)	Time at P_{max} (hours)	P_{inj} after (MPa)	P_{out} after (MPa)	$\Delta P_{residual}$ (MPa)	Duration (hours)
1st BT	7.48	0.01	7.46		5.29	4.23	1.06	22
2nd BT	7.03	0.03	6.99		4.64	4.68	−0.03	5
3rd BT	7.02	0.08	6.94		4.63	4.65	−0.02	1
4th BT	7.56	0.08	7.48	Inst	4.97	5.01	−0.03	0

BT test: D38-4 W21.45 75/50 1.6DD In the first phase (Figure 2.177, Table 2.50, Table 2.46), the first BT occurred at 9.94 MPa and pressure stabilized immediately, with a residual pressure higher than 4.1 MPa, The second and third BTs have similar characteristics in BT pressure and slightly different residual pressure.

In the second phase (Figure 2.178, Table 2.51), after saturation of the sample, all the BTs have values around 8.9 MPa and increasing residual pressures.

2.6.7.7. Break-through test on compacted samples: DD 1.7

BT test: D38-5 W22.2 1.7DD In this test, at dry density 1.7, the current pressure limit of the BT equipment (14.0 MPa) was reached. The sample has been transferred to the gas permeability equipment, with a limit set at 19.0 MPa (if no confining pressure is applied, as is the case for BT cells).

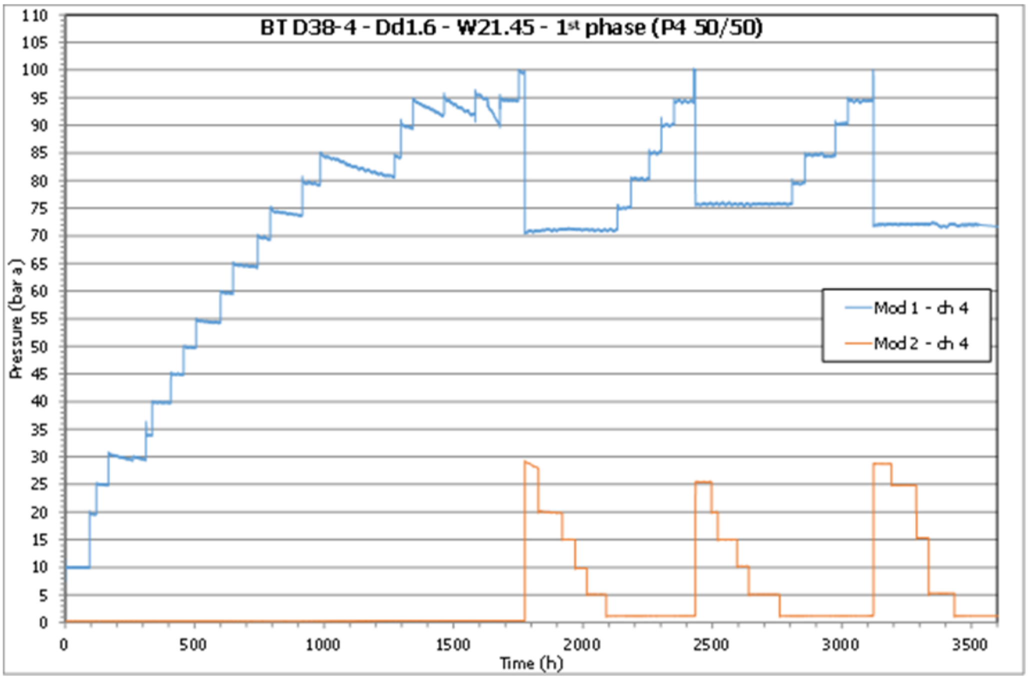

Figure 2.177: Pressure-time curve of BT test 38_4_21.45: 1st phase

Table 2.50: Characteristics of the BTs in test 38_4_21.45: 1st phase

1st phase	**P_{inj} max** (MPa)	**P_{out}** (MPa)	**ΔP_{max}** (MPa)	**Time at P_{max}** (hours)	**P_{inj} after** (MPa)	**P_{out} after** (MPa)	**$\Delta P_{residual}$** (MPa)	**Duration** (hours)
1st BT	9.98	0.03	9.94	Inst	7.04	2.93	4.10	1
2nd BT	10.01	0.12	9.89	Inst	7.54	2.55	4.99	1
3rd BT	9.97	0.12	9.84	Inst	7.18	2.88	4.30	1

Table 2.51: Characteristics of the BTs in test 38_4_21.45: 2nd phase

2nd phase	**P_{inj} max** (MPa)	**P_{out}** (MPa)	**ΔP_{max}** (MPa)	**Time at P_{max}** (hours)	**P_{inj} after** (MPa)	**P_{out} after** (MPa)	**$\Delta P_{residual}$** (MPa)	**Duration** (hours)
1st BT	9.06	0.12	8.94	Inst	5.17	4.01	1.16	1
2nd BT	9.03	0.06	8.97	Inst	5.50	3.57	1.93	50
3rd BT	8.49	0.11	8.38	Inst	5.49	3.14	2.35	16
4th BT	9.02	0.11	8.91		5.79	3.31	2.48	67

A first BT was obtained at a pressure of 16.0 MPa (Figure 2.179, Table 2.52); flow reached the maximum control set-up value (110 STP cc/min) and gas supply was closed, becoming a falling pressure system. Coloured zone in the figure indicates that the signal from flowmeter saturates at 130 STP cc/min.

Table 2.52: Characteristics of the BTs in test 38_4_21.45: 1st phase

1st phase	**P_{inj} max** (MPa)	**P_{out}** (MPa)	**ΔP_{max}** (MPa)	**Time at P_{max}** (hours)	**P_{inj} after** (MPa)	**P_{out} after** (MPa)	**$\Delta P_{residual}$** (MPa)	**Duration** (hours)
1st BT	16.0	0.10	15.9	–	–	–	–	5
2nd BT	10.5	0.10	10.4	–	–	–	–	1.4

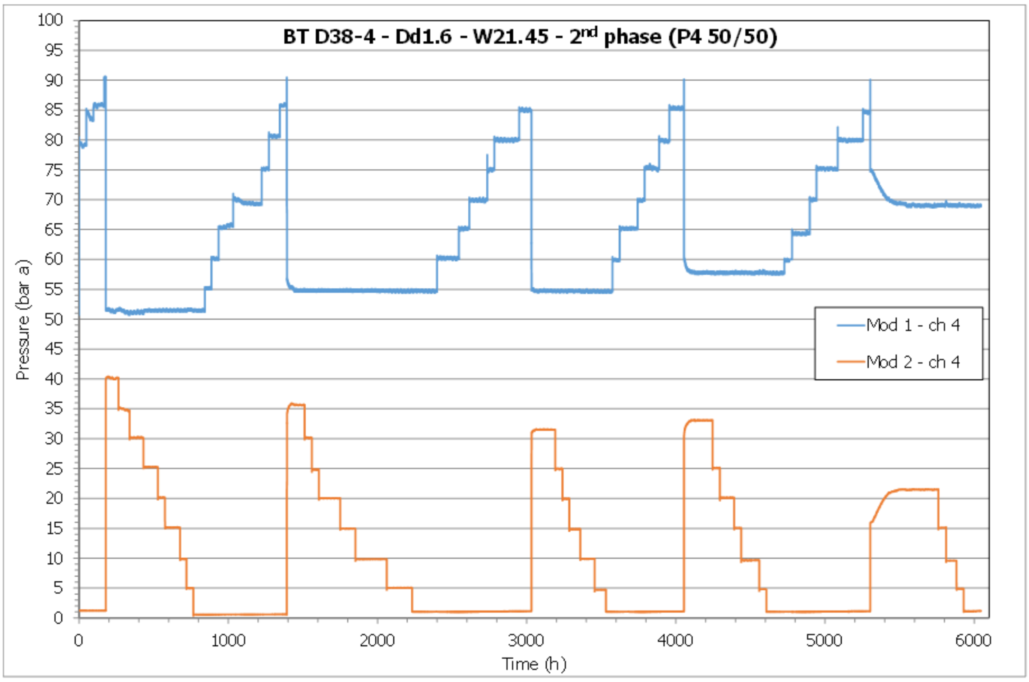

Figure 2.178: Pressure-time curve of BT test 38_4_21.45: 2nd phase

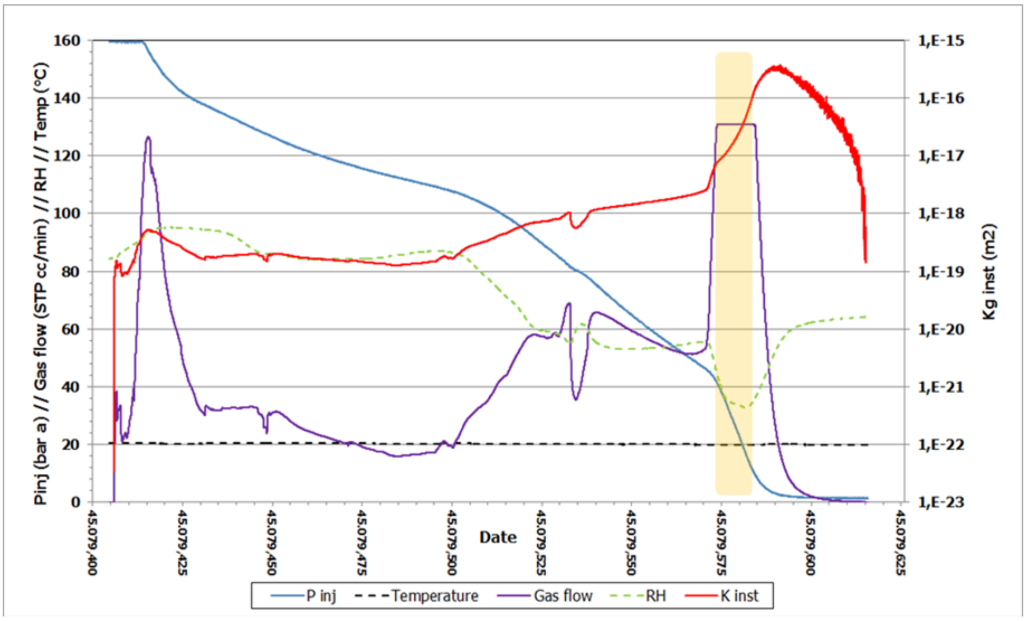

Figure 2.179: Evolution of magnitudes in the first BT in sample 38-5 (1.7 dry density; w22.2%)

A new BT at lower pressure, 10.5 MPa, was induced (Figure 2.180, *Table 2.52*), that reproduced the previous behaviour (high flow, instability and drying).

In the first BT, the intrinsic permeability ranges from initial 10^{-20} to final 10^{-16} m^2, with most values close to 10^{-19} m^2; in the second one, the values ranges from initial 10^{-19} to final 10^{-14} m^2, with most values close to 10^{-18} m^2.

Several common characteristics can be observed:

1. The BT value obtained agrees that the higher the dry density, the higher the BT pressure (from 10 MPa to 16 MPa, for density of 1.6 and 1.7)

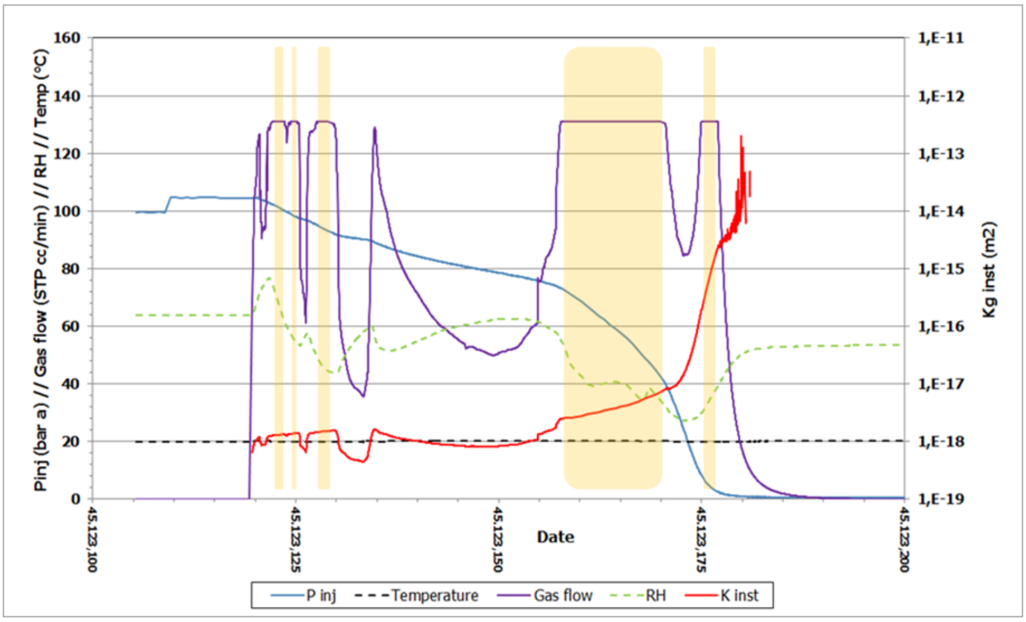

Figure 2.180: Evolution of magnitudes in the second BT in sample 38-5 (1.7 dry density; w22.2%)

2. The unstable behaviour of the flow despite the smooth evolution of the pressure drop; reaching the saturation value of the flow-meter in some periods (coloured zones)
3. The variation in RH, deceasing as a greater amount of dry gas passes through the sample, and stabilizing when the flow does so;
4. Gas flow incorporates vapor water extracted from pathways. The drying process seems to be not compensated by water within the clay, probably due to the low rate transport of liquid water.

2.6.7.8. Analysis of the BT curves

Qualitative analysis of the BT curves The increase of the pressure step magnitude shortened the overall time of the experiment, but at the expense of the accuracy of the BT pressure, whose values became harder to detect.

The BT events on pressure-time curves show some specific characteristics: 1) systematic and consistent repetition of BT values; 2) consistent changes in the slopes; 3) instantaneous vs soft type BTs (different shapes).

Changes in the general shape or the slopes of the pressure-time curves could indicate the onset of the different types of flow. These changes are located in a transitional region, which is below the initially determined BT pressure and positioned at the actual BT pressure. The pressure decay curves will have different shapes if the injection pressure is greater than, close to or less than the actual BT pressure.

So, the BT behaviour is considered a main characteristic for a given liquid-sample system, at a specified temperature (isothermal), related to the pore size distribution and hydro-mechanical state.

Quantitative analysis of the BT curves The BT pressures, grouped by sample and injection gas phase (Figure 2.181), indicate that the BT pressure increases with the dry density of the sample (coloured zone corresponds to 1.6 DD), the initial water content (initial degree of saturation), and the geometrical aspect (ratio length/ diameter).

BT pressures are lower than the air entry pressure, but higher than the upper range of the bulk swelling pressure expected for each considered dry density.

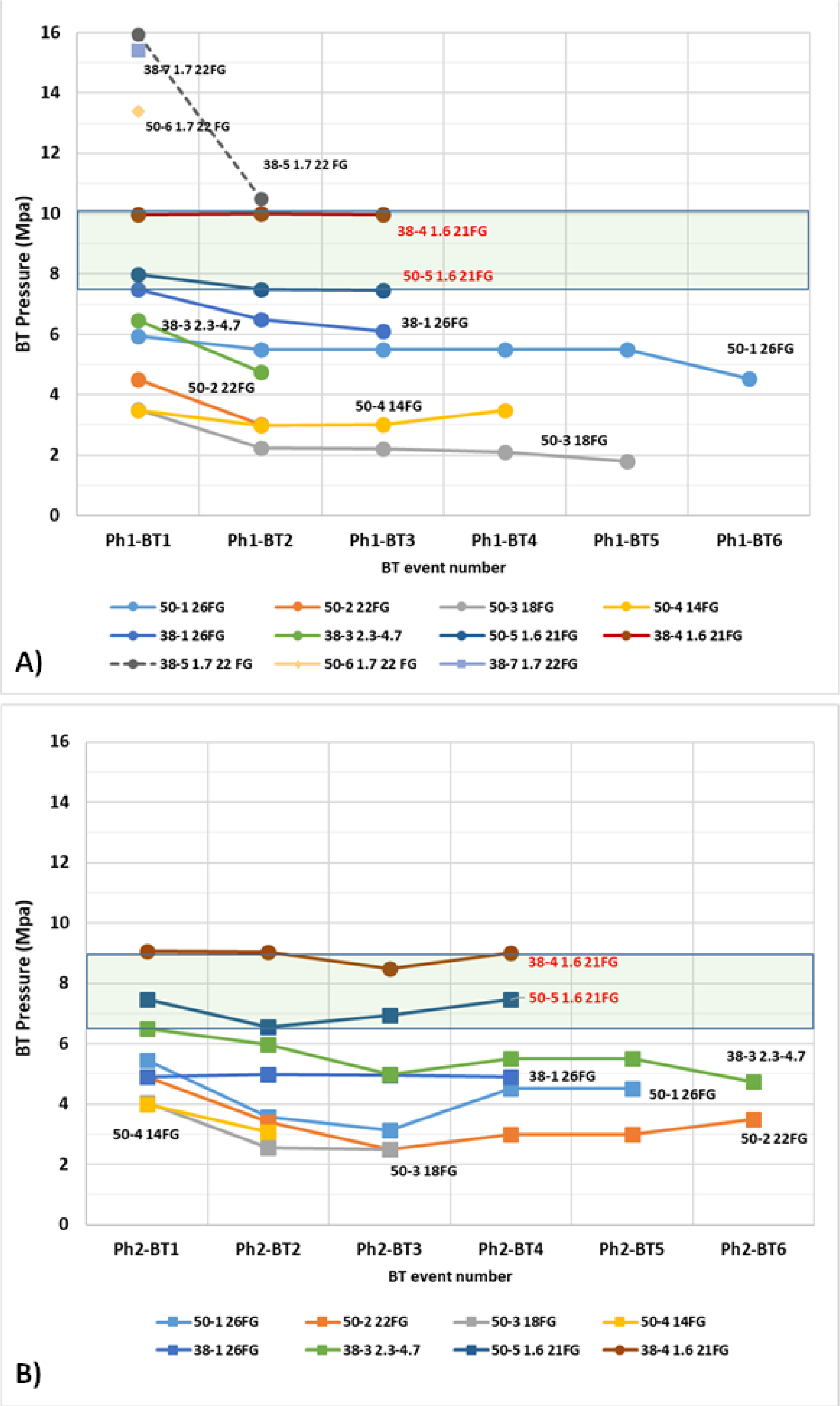

Figure 2.181: BT pressures values vs BT episode number: A) 1st gas injection phase of the BT tests and B) 2nd gas injection phase of the BT tests. BT references include: sample diameter, setup number, initial dry density (DD 1.6 or 1.7, none if DD 1.5), water content at compaction, and grain size at compaction (FG,"full distribution"; other, class size). Coloured zone indicates BT values at DD 1.6; upper zone at DD 1.7; lower zone at DD 1.5.

Considering the pore volume of sample much smaller than the volume of reservoirs, the pressure-time curves of the reservoirs permit calculate the flow rate through the sample. The accuracy of this analysis depends on the assumption that the gas behaved as an ideal gas and that a pseudo-steady state mass-flow is established, *i.e.* gas exiting the high pressure vessel equals gas entering the low pressure vessel.

The registered pressure values reflect oscillations in due to changes in laboratory conditions (temperature) and the inherent uncertainties in the sensors and data acquisition system. To avoid this type of artefacts, it is advisable to fit the pressure-time data to a monotonic and derivable equation. From its derivative, the flow rate is calculated at the most representative instants, and from this, the "apparent" permeability values of the gas phase are calculated from the equations for incompressible media with compressible pore fluids Scheidegger (1974).

For the moment, in the absence of defining the nonlinear fit that best represents the gas transport mechanisms underlying the observed pressure-time curves, simple fitting, lineal or quadratic, were applied to the most stable parts of selected pressure-time curves: first and second phases of BT 38-1_26_1.5 (Figure 2.171 and Figure 2.172); and second phase of BT 38-4_22_1.6 (Figure 2.178).

For 1.5 dry density, the gas permeability comes from 1.6×10^{-19} to 2.2×10^{-22} m^2; with most values in the band 1.6×10^{-19} to 1.6×10^{-20} m^2. For 1.6 dry density, a very stable value around 2.2×10^{-21} m^2 was found. These values arise from long term measurement of the increasing pressure, in opposition to the values obtained for 1.7 dry density, whose gas flow was measured by gas flowmeters, resulting in a majority of values between 10^{-19} and 10^{-18} m^2. This permeability coefficient includes any additional experimental contribution (i.e., cracks or incomplete sealing between sample and body cell). In all cases, the differences of several orders of magnitude among the BT events and the steady state flows indicate the variation in the size/number of the flow channels.

Further analysis of the changes in the shapes and the slopes of the pressure-time curves will be performed, trying to verify the onset of the different types of flow by approximate functions. They are also the best way to smooth the data over time (SYSTAT-SOFTWARE (2002)) and will be applied to most of the pressure-time curves.

2.6.7.9. Other tests: visualization cells

These are 2D cells, already used in other tests with compact samples and/or pellets, whose walls have been modified to generate samples of different thicknesses. The sample is generated by saturation of a sample of specific granulometry, with a maximum size slightly greater than the required thickness, slightly compacted during the assembly of the cell. Figure 2.182 shows a complete cell (thickness 4.5 mm) after closure and the images obtained with back and combined illumination.

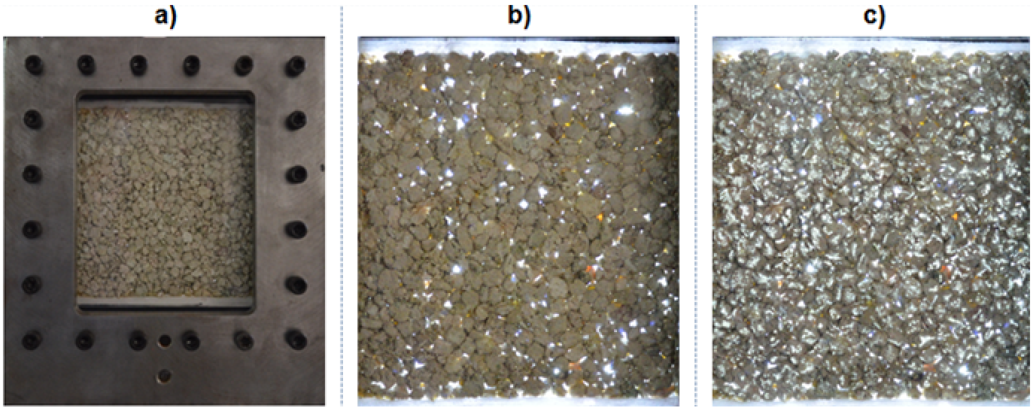

Figure 2.182: Cell view 2D-4.5: a) set; b) back-light (zero porosity zones); c) rear and overhead light (grain/wall contact areas).

After vacuuming from both sides of the sample, hydration is performed from one end, while maintaining

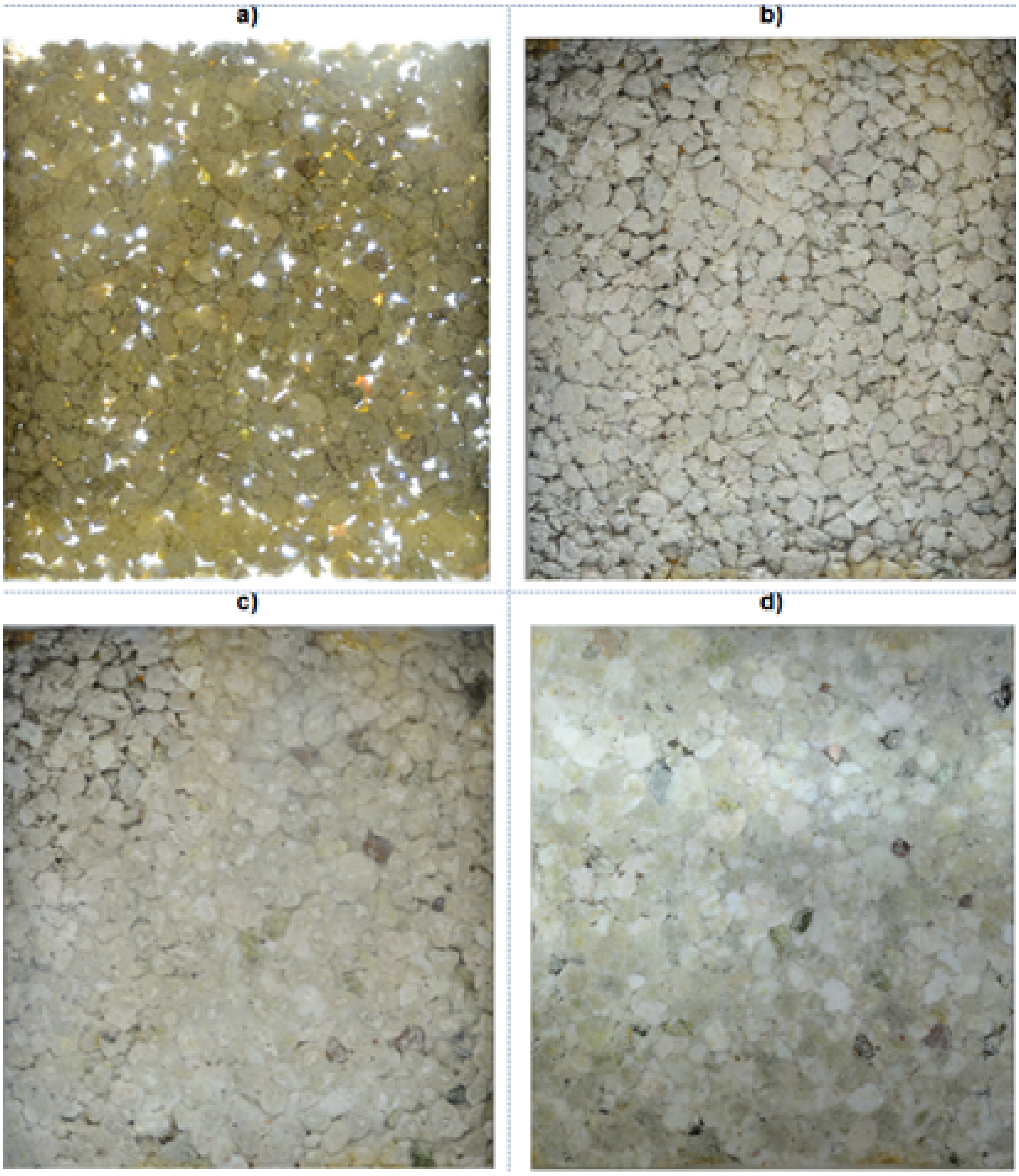

Figure 2.183: Cell 2D-4.5 during saturation: a) initial state (back-light); b, c and d) evolution of saturation (up to 30 minutes).

vacuum at the other end. The selected flow rate allows visual checking of the progress of the hydration front. Once it reaches the opposite end, it is also connected to hydration. Figure 2.183 shows the evolution during saturation, from the initial state to 30 minutes. Figure 2.184 shows the evolution of the closure of the contacts between grains, with back-light.

The objective is the graphic record of the "fracturing" of the material, during the simultaneous injection of gas and water, and the pressures at which it happens, in a 2D type geometry.

Figure 2.185 to Figure 2.188 show the evolution of gas-induced fracturing in a 2D gas injection test on saturated FEBEX bentonite (1.3 DD, w 13,5%) in a "window cell" (120 mm × 120 mm × 20 mm), performed in previous works. Granular material distributed in the cell volume was saturated with deionized water, during several weeks. Then, gas pressure was applied to one inlet of the cell, and increased by-steps. At a pressure around 2 MPa, first indications of gas-induced fractures appeared (Figure 2.185).

Under increasing pressure, new fractures appeared while the previous one became sealed (Figure 2.186). Then, with decreasing pressure, convergence of all generated fractures occurred (Figure 2.187). Under a

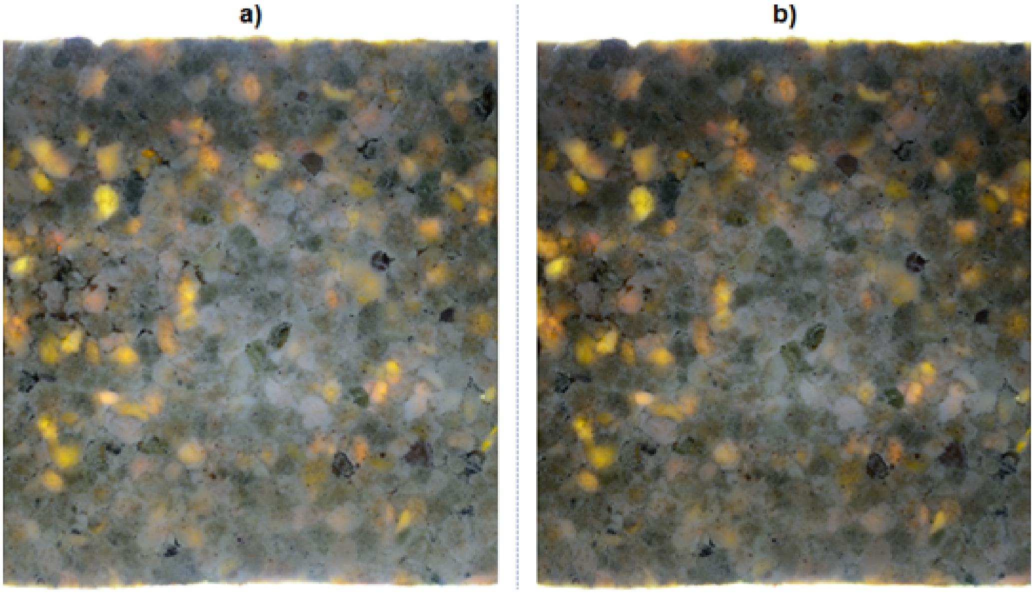

Figure 2.184: Cell 2D-4.5 after 30 minutes of saturation with back-light

new pressurization cycle (Figure 2.188), the previous fractures re-opened and new paths appeared (one in the first location at the beginning of the test). Finally, after 24 hours of pressure decrease, all fractures are sealing even the main one.

The observed behaviour may be attributed to swelling pressure of bentonite (water remobilisation is not considered in this case) compensating the gas pressure at a local level. Extrapolating these effects to long term flow mechanisms in engineered barriers, the effect of this convergence may cease the gas flow in some pathways and may lead to gas inclusions, weakening the material for further pressurization cycles.

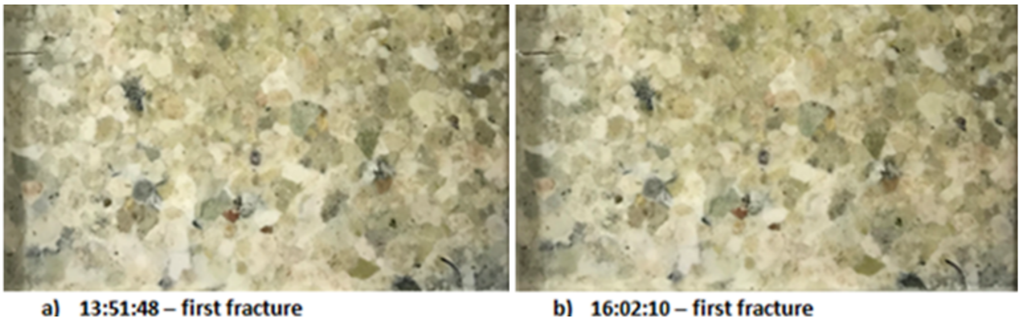

Figure 2.185: Evolution of gas-induced fracturing in 2D sample of FEBEX bentonite (1.3 DD, saturated): a-b) first signs of fracture.

Figure 2.189 shows the detail of the zone where the main fracture is generated. The firstly originated fracture disappears sealing the material (even some fractured grains) when the main fracture expands.

2.6.8. Summary

The gas migration behaviour in buffer material can drastically change with the fraction of bentonite, due to the presence of non-charges particles that decreases the cohesion forces at macro- and microscopic scale, which makes particle bonds weaker and interstitial water more mobile. The proportion of mobile water can vary according to the clay composition (smectite, illite, kaolinite, quartz, . . .).

In pure bentonites, the proportion of mobile water is expected to be less than 1–2% depending on dry density; and the gas migration properties might be correlated with the local geo-mechanical stress conditions (lower local effective stress level). Also, the influence of the state of stress and of stress history

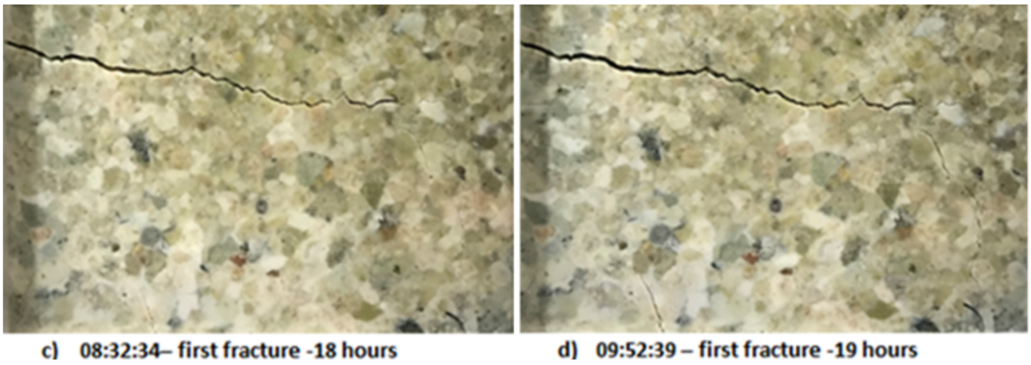

Figure 2.186: Evolution of gas-induced fracturing in 2D sample of FEBEX bentonite (1.3 DD, saturated): c-d) new fractures under increasing pressure.

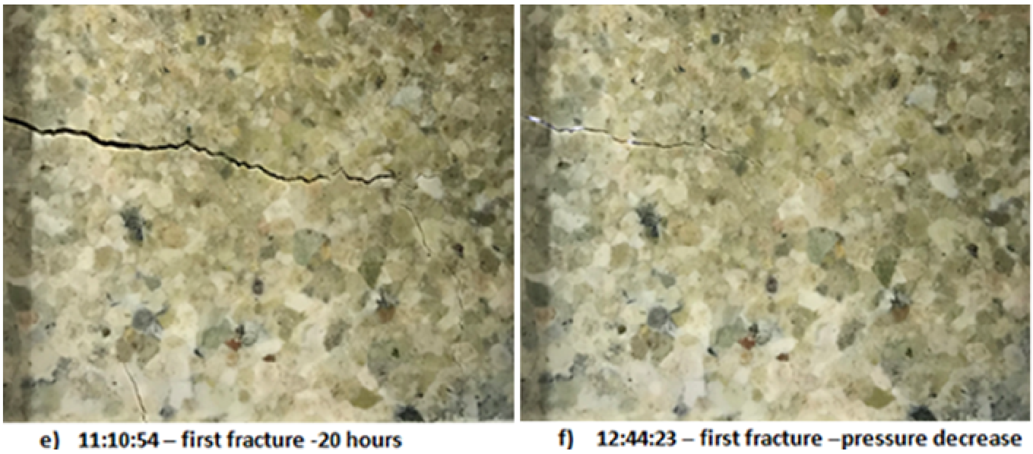

Figure 2.187: Evolution of gas-induced fracturing in 2D sample of FEBEX bentonite (1.3 DD, saturated): e-f) new fractures; f) sealing after decreasing pressure.

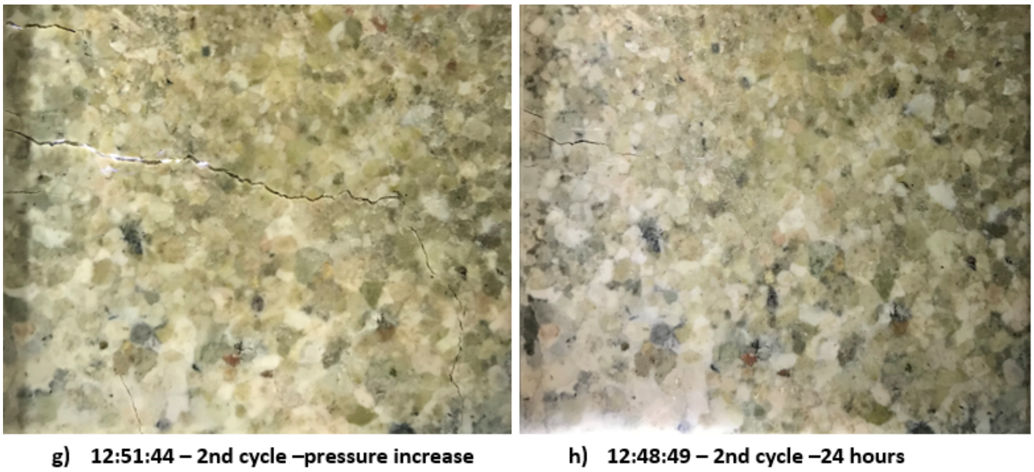

Figure 2.188: Evolution of gas-induced fracturing in 2D sample of FEBEX bentonite (1.3 DD, saturated): g) re-opening of paths under a new pressure cycle; h) resealing of all fractures.

(over-consolidation ratio) on gas transport parameters should be considered.

The Spanish reference clay material, FEBEX bentonite, consists of more than 90% montmorillonite.

Two gas transport mechanisms have been identified, depending on the gas pressure level. Below a value referred as gas entry pressure, the predominant transport mechanism is the diffusion in pore-water. Once

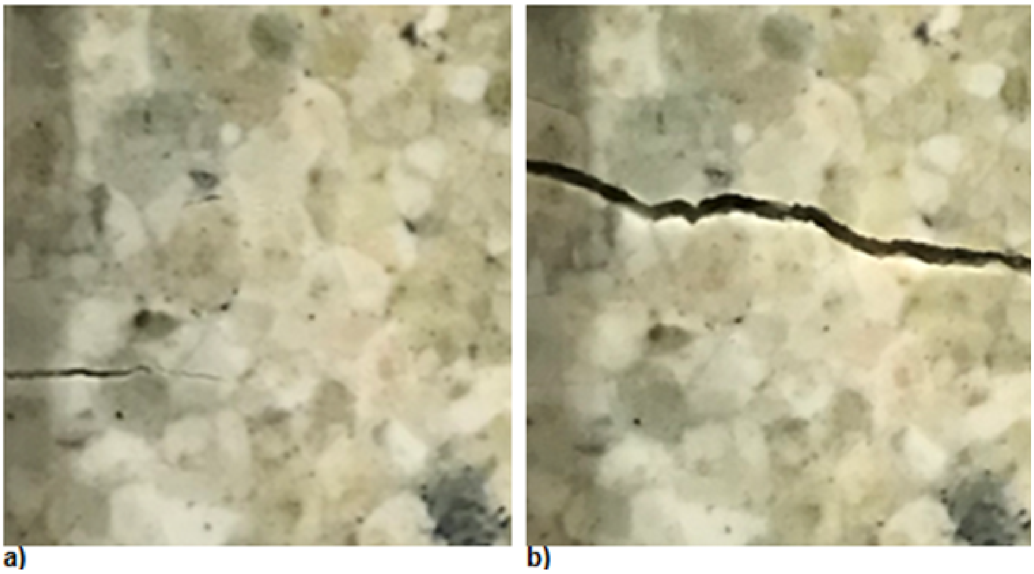

Figure 2.189: Gas-induced fracturing in 2D saturated sample of FEBEX bentonite (1.3 DD, w 13.5%): a) initial fracture; b) main fracture in upper zone and sealing of the previous one.

this gas entry pressure is exceeded, gas flows through existing porosity or flows via self-created and stress-induced pathways. The first type depends on the pore structure of the material, affecting only the most conductive continuous paths (associated with the largest interconnected pores); the second one depends mainly on the current (local) stress state.

Gas displaces the interstitial pore water or push back the clay particles (exceeding the micro shear strength of the material); or both, to create gas-occupied new flow pathways (single gas phase) in the clay during the migration process.

During the time project, five of the seven tests in progress have been completed, and two have been started at density 1.7. Other two test failed. Most of the test are carried out in the BT experimental set-up; while, gas permeability has been used to confirm some results or to achieve higher pressures ($> 14\,\mathrm{MPa}$).

Both experimental set-up, BT and gas permeability, have been improved. In the BT one, more simultaneous tests have been implemented, with temperature measurement, and new pressure sensors. In the gas permeability set-up, digital control and recording have been implemented, as well as a high-pressure controller (up to $19\,\mathrm{MPa}$), and relative humidity and temperatures measurement. In testing procedures, the use of higher pressure steps ($0.5\,\mathrm{MPa}$) shorten overall time (as required) but at the expense of accuracy in BT pressure determination.

All the experiments carried out in this work on initially fully saturated FEBEX bentonite have shown that the gas migration phenomena are only possible if the gas pressure exceeds some threshold value (via self-created and stress-induced pathways controlled by the local stresses). All they showed a high-pressure step (“peak”) in the injection gas pressure followed by a spontaneous negative transient (and their counterpart opposite in the outlet gas pressure).

The BT pressures, grouped by sample and injection gas phase (Figure 2.181), indicate that the BT pressure increases with the dry density of the sample (coloured zones), the initial water content (initial degree of saturation), and the geometrical aspect (ratio length/ diameter).

The BT pressures are lower than the air entry pressure for a given dry density, but higher than the upper range of the bulk swelling pressure expected for each considered dry density. Therefore, pathways for gas transport could be developed through the sample, taking advantage of the local heterogeneities.

Most of the pressure-time curves suggest that gas moves as a discrete phase through a network of pathways formed by the rupture or modification of the clay fabric under the applied high gas pressures (Figure 2.185). Then, gas entry would follow a micro-fracture process, in which the dimensions of the formed pathways adjust in response to changes in gas pressure. The term micro-fracture is used for any type of voids that may exist in the compacted barrier material. Primary micro-fractures (Figure 2.189) depend on the inhomogeneity of the material (the initial structure after compaction) and can be interconnected by induced micro-fractures, depending on the stress field and the gas/water pore pressure.

2.6.9. Key learning points

Previous works with FEBEX bentonite established that:

- Compaction process reduces the total volume of the voids and also decreases the size of the macropore, accordingly, pores can support a higher suction before emptying.
- For lower saturations, given an effective void index, e(1-Sr), the effective permeability, kig·krg, of a material is lower if the particle size is finer (and more homogeneous).
- Gas entry pressure is greater than 15 MPa, which would prevent the capillary process, making it practically impossible for a biphasic flow to take place.
- The BT pressure values were mainly between 1 and 10 MPa, for DD between 1.4 and 1.8
- BT pressure increase with dry density of the sample and is always higher than the swelling pressure.
- Two types of BTs were observed: gradual and instantaneous. A gradual episode is never followed by an instant one, but an instant episode may nevertheless be followed by another instant or a gradual episode.
- The gas pathways in unsaturated bentonite appear to be stable (always open), while in saturated bentonite there is an opening/closing of pathways caused by the changes in gas pressure. This avoids overpressure in the system.

2.6.9.1. New knowledge acquired

The new knowledge, mainly supported by pressure decay curves and postmortem analysis, includes:

- All the experiments on initially fully saturated FEBEX bentonite have shown that the gas migration phenomena are only possible if the gas pressure exceeds some threshold (BT) value.
- The BT pressure values are between 3.5–7.5 MPa for 1.5 DD, 8–10 MPa for 1.6 DD and higher than 15.5 MPa for 1.7 DD. Values are higher than previous ones, probably due to a better control of the target dry density.
- The BT pressures are lower than the air entry pressure, but higher than the upper range of the expected bulk swelling pressure for each considered dry density. Therefore, pathways for gas transport could be developed through the sample, taking advantage of the local heterogeneities.
- BT pressure increases with the dry density and the water content at compaction (initial saturation degree), both affecting the initial pore structure of the material. BT pressure also increases with the geometry of the sample (L/D ratio).
- Some specific characteristics of the pressure-time curves and the BT events are:
  - Systematic and consistent repetition of BT values in both phases on each sample;
  - Consistent shapes, depending on whether the injection pressure is greater than, close to or just less than the actual BT pressure;
  - Consistent changes in the slopes, pointing out the actual BT pressure and, possibly, different types of flow and their underlying physical concept;
  - Presence of instantaneous type and soft type BTs.
- From above, the BT behaviour should be a characteristic of each liquid-sample system related to:

  - The initial state after compaction (pore size distribution, local heterogeneities in composition, stresses and suction),
  - The preservation or modification of the macro- micro-structure of the sample during the test,
  - The specified temperature (in our case, all tests are considered isothermal).
- Changes affecting the initial structure will affect the BT pressure.
- Expulsion of water has been only detected in a single sample. If gas flow is localized, it expected that displaces little water, whatever the mechanism of the initial BT.
- This tendency is more marked if the material is more heterogeneous (at pore scale), as FEBEX granulate is.
- In some tests, the outlet pressure shows an extremely slow and consistent increase that could be associated with some processes other than advective flow.

2.6.9.2. Impact of acquired knowledge

The initial goals were to compare measured vs expected gas flows to determine the actual gas flow mechanisms (e.g. validity of the concepts applied in saturated high-density compacted clay). The combination of gas flow data and post-mortem analyses of the samples should permit to understand the involved processes.

When observed macroscopically, the two foreseen mechanisms, flow of gas through existing porosity and flow of gas stress-induced pathways, appear quite similar, in spite of the different underlying physical processes.

In this phase of the project, there is available a set of pressure-time series from long-term tests (up to 1.5 years), and the previous and subsequent physical characterization (MIP and BET, water permeability) for FEBEX bentonite, in saturated state, for a range of dry densities and conditions.

When completed, the full analysis of these pressure-time curves should improve the understanding of the underlying physical mechanisms to be included in models. Our present interpretation is that gas migration in saturated FEBEX bentonite, at the tested dry densities, occurs by the formation and propagation of dilatant (local) pathways through the sample.

Although mixed modes of gas migration are also possible and share some important features (mechanical coupling in the enlargement of pores by the effects of gas pressure), the huge flows in the first BT events do not seem to indicate transport through a limited number of pores but a fracture-like flow. This aspect needs further verification, although some visualization tests show this type of behaviour.

After the first BTs, the subsequent ones can change their mechanism depending on how the previous one affect the mechanical coupling in the plastic material. In some cases, the reduction of pressure may lead to gas inclusions that increase in the residual permeability of the sample; in other cases, the generation of micro-fractures produces a similar effect on permeability.

The final application is the implementation of this knowledge into the THM models. In the first case, discrete pathways models could probably reproduce better the initial BT phenomena; in the others, the two-phase-flow approach (with random heterogeneous porous media) could reproduce the increase of the residual permeability (flow localization associated with pore-scale heterogeneity).

Does high gas pressure create irreversible damage to the engineered barriers? Pressure-time curves are a good representation of gas seepage as a periodic process: gas accumulates, pressure builds up, cracks open, gas escapes, cracks close, gas accumulates, etc.)

From observations, it is expected, if clay remain saturated, the sealing of the open pathways will occur immediately after the gas release without affecting the barrier integrity, even in the long-term after. This behaviour of the gas paths, which would prevent the overpressure in the barrier system, is supported by:

- Consistent BT pressures in both phases of tests carried out on each sample.
- Estimation of the residual gas permeability is lower than 10^{-24} m^2.
- No noticeable variation in water permeability was found after first phase of BTs.

2.6.9.3. Remaining knowledge gaps

Among other remaining issues, we could highlight:

- Verify the mechanical effect of the rate of pressure increase and/or duration of the pressure steps applied on the saturated material. For example, secondary consolidation could occur due to the gas pressure on the impermeable material; or fracturing of the material, longitudinal or transversal, due to the transmission of pressure by fluids.
- Effect of the over-consolidation of the materials.
- Effect of the cohesion of the material and with the interfaces.
- Effects of the gas inclusions in plastic materials when the gas flow ceases.
- Simultaneous transfer of water, gas and heat: effect of the temperature.
- Upscaling
- To incorporate the results into conceptual models is a major issue.

2.6.9.4. Recommendations for the future

The intensive use of imaging techniques to characterize the initial state after compaction (pore size distribution, local compositional heterogeneities, stresses and suction); and understanding their behaviour and evolution to become pathways for the transport of gas are important issues.

2.6.9.5. Description of break-through setups

Table 2.53: Test BT 50-1: Reservoir volumes and associated pressure sensors: inlet / outlet.

BT 50-1 1,5 26,6%

Ref	Type	Volume	Vol act.
C	DOE-3E 1800	150	148,136
3,1	DOE-3E 1800	75	75,857
Ref/Type	**S/N**	**Channel**	**Range**
UNIK 5000	3402707	M1 - C1	0–350 bar a
PMP 4070	1240394	M1 - C2	0–135 bar a

Table 2.54: Test BT 50-2: Reservoir volumes and associated pressure sensors: inlet / outlet.

BT 50-2 1,5 22,8%

Ref	Type	Volume	Vol act.
B	DOE-3E 1800	150	148,336
D	DOE-3E 1800	75	67,176
Ref/Type	**S/N**	**Channel**	**Range**
UNIK 5000	3402714	M1 - C3	0–350 bar a
PMP 4070	1256283	M2 - C3	0–135 bar a

Table 2.55: Test BT 50-3: Reservoir volumes and associated pressure sensors: inlet / outlet.

BT 50-3 1,5 18%

Ref	Type	Volume	Vol act.
A	DOE-3E 1800	150	147,665
1,0	DOE-3E 1800	75	75,998
Ref/Type	**S/N**	**Channel**	**Range**
UNIK 5000	3401875	M1 - C15	0–350 bar a
PMP 4070	1240395	M2 - C15	0–135 bar a

Table 2.56: Test BT 50-4: Reservoir volumes and associated pressure sensors: inlet / outlet.

BT 50-4 1,5 14%

Ref	Type	Volume	Vol act.
50-4E	DOE-3E 1800	150	144,39
E	DOE-3E 1800	75	75,055
Ref/Type	**S/N**	**Channel**	**Range**
UNIK 5000	3401866	M1 - C17	0–350 bar a
PMP 4070	1246978	M2 - C17	0–70 bar a

Table 2.57: Test BT 50-5: Reservoir volumes and associated pressure sensors: inlet / outlet.

BT 50-5 1,6 21,44%

Ref	Type	Volume	Vol act.
B	DOE-3E 1800	150	148,336
D	DOE-3E 1800	67	67,176
Ref/Type	**S/N**	**Channel**	**Range**
UNIK 5000	3402714	M1 – C3	0–350 bar a
PMP 4070	1256283	M2 – C3	0–70 bar a

Table 2.58: Test BT 50-6: Reservoir volumes and associated pressure sensors: inlet / outlet.

BT 50-6 1,7 22,31%

Ref	Type	Volume	Vol act.
A	DOE-3E 1800	150	147,665
1,0	DOE-3E 1800	75	75,998
Ref/Type	**S/N**	**Channel**	**Range**
UNIK 5000	3401875	M1 – C15	0–350 bar a
PMP 4070	1240395	M2 – C15	0–135 bar a

Table 2.59: Test BT 38-1: Reservoir volumes and associated pressure sensors: inlet / outlet.

BT 38-1 1,5 26,6%

Ref	Type	Volume	Vol act.
3,0	DOE-3E 1800	75	75,346
2,0	DOE-3E 1800	50	50,795
Ref/Type	**S/N**	**Channel**	**Range**
UNIK 5000	3401867	M1 - C2	0–350 bar a
PMP 4070	1247384	M2 - C2	0–70 bar a

Table 2.60: Test BT 38-2: Reservoir volumes and associated pressure sensors: inlet / outlet.

BT 38-2 1,5 14,5% $1,18 < x < 2,0$

Ref	Type	Volume	Vol act.
P3	DOE-3E 1800	50	50,674
P4	DOE-3E 1800	50	50,226
Ref/Type	**S/N**	**Channel**	**Range**
UNIK 5000	3402704	M1 - C4	0–350 bar a
PMP 4070	1247385	M2 - C4	0–70 bar a

Table 2.61: Test BT 38-3: Reservoir volumes and associated pressure sensors: inlet / outlet.

BT 38-3 1,5 14,75% $2,83 < x < 4,7$

Ref	Type	Volume	Vol act.
2,1	DOE-3E 1800	75	75,216
P5	DOE-3E 1800	50	50,421
Ref/Type	**S/N**	**Channel**	**Range**
UNIK 5000	3402712	M1 - C5	0–350 bar a
PMP 4070	1256290	M2 - C6	0–135 bar a

Table 2.62: Test BT 38-4: Reservoir volumes and associated pressure sensors: inlet / outlet.

BT 38-4 1,6 21,45%

Ref	Type	Volume	Vol act.
P3	DOE-3E 1800	50	50,674
P4	DOE-3E 1800	50	50,226
Ref/Type	**S/N**	**Channel**	**Range**
UNIK 5000	3402704	M1 - C4	0–350 bar a
PMP 4070	1247385	M2 - C4	0–70 bar a

Table 2.63: Test BT 38-5: Reservoir volumes and associated pressure sensors: inlet / outlet.

BT 38-5 1,7 22,22%

Ref	Type	Volume	Vol act.
P6	DOE-3E 1800	50	50,501
P7	DOE-3E 1800	50	50,374
Ref/Type	**S/N**	**Channel**	**Range**
UNIK 5000	3402711	M1 - C16	0–350 bar a
PMP 4070	1246979	M2 - C16	0–70 bar a

Table 2.64: Test BT 38-7: Reservoir volumes and associated pressure sensors: inlet / outlet.

BT 38-7 1,7 21,96%

Ref	Type	Volume	Vol act.
3,0	DOE-3E 1800	75	75,346
2,0	DOE-3E 1800	50	50,795
Ref/Type	**S/N**	**Channel**	**Range**
UNIK 5000	3401867	M1 - C2	0–350 bar a
PMP 4070	1247384	M2 - C2	0–70 bar a

.

CTU, SÚRAO

2.7. Gas entry and flow through a bentonite barrier (CTU, SÚRAO)

2.7.1. Introduction & Objectives

The main objectives of the WP GAS are to improve the understanding of the mechanisms of gas transport processes in clay materials, to interrelate gas transport processes with the mechanical behaviour of clays and to determine their influence on the various properties of clays. A further objective comprises the evaluation of the gas transport modes that may occur in the deep geological repository environment and their potential impacts on barrier integrity and the overall reliability of the deep geological repository system.

Laboratory experiments comprise the main tool for obtaining the necessary knowledge and for fulfilling the various objectives. Furthermore, it will be necessary to transfer the knowledge obtained from the experiments so as to address the questions that remain in terms of currently considered repository designs and concepts.

The Czech consortium consists of three institutions. WP 6 involves ÚJV Řež, the CTU in Prague and SÚRAO. Specifically, all these institutions are participating in Subtask 2.2, which concerns displacement versus dilatant gas flow processes in clay-rich materials. The CTU is also a participant in Task 3, which is focusing on barrier integrity. Subtask 2.2 employs an experimental procedure involving an incremental increase in the injection of gas pressure into the sample inlet. This procedure is followed by both of the research institutions so as to allow for the comparison of the test results. In addition to compressed air, ÚJV Řež is also experimenting with hydrogen as the injection gas medium in the experiments (CTU is working only with compressed air) so as to determine if the type of gas affects the test results. A further difference comprises the boundary conditions of the tests due to differences between the measuring apparatuses. The variability of the boundary conditions will allow for the verification of which of the conditions are relevant and to what extent they affect the test results. This contribution contains detailed descriptions of the experiments, laboratory work and measurements for CTU for Subtask 2.2.

2.7.1.1. General description

Subtask 2.2 of the EURAD GAS project is focusing on the advective transport that will occur within the disposal system in the post-closure phase. A free gas phase develops if the gas production rate exceeds the rate at which gas can be dissolved and evacuated via diffusion (Levasseur S. 2020). As gas pressure increases, advective transport occurs. Two primary modes for advective gas transport have been proposed: (i) visco-capillary two phase flow and (ii) the formation of discrete gas-filled pathways. The general objectives of Subtask 2.2 “Advection (displacement vs. dilation)” are to explore which transport mechanisms prevail under which range of conditions, and to form an understanding of how the relationship between gas and liquid phase pressure and solid phase stress impacts the transport of gases.

Based on previous research (including research conducted in connection with the previously performed FORGE EC project - Norris, 2013), two primary modes for advective gas transport through natural mudrocks are assumed; (i) visco-capillary 2 phase flow, where the capillary forces must be overridden in order to allow for the displacement of the wetting phase, via migrating gases and (ii) the formation of discrete gas-filled pathways via the localised consolidation of the clay matrix (Levasseur S. 2020). The potential for one specific mechanism to prevail is dependent on a range of factors, including the saturation state of the clay and the ratio of the clay to sand fraction. For fully saturated, pure clay bentonite materials, such as those used in engineered barriers, experimental evidence indicates that gas flow via pathway dilation is the preferred mode of transport. In such cases, significant hydromechanical coupling is observed, which cannot be satisfactorily explained by means of visco-capillary flow processes. The explanation for the hydromechanical coupling process between the immiscible phase, the interstitial fluid, and the total stress, remains unclear. Understanding these relationships, how they vary from one formation to another, and what impact, if any, they exert on the integrity of the host rock, currently comprises a priority research issue.

2.7.1.2. Research question and strategy

The Czech consortium in the EURAD WP 6 consists of the CTU in Prague and UJV Řež. The CTU is investigating the processes that lead to the entry and flow of gases through a bentonite barrier. This involves, in particular, the investigation of the pressure that leads to gas breakthrough in relation to the swelling pressure, the transport of fluids through the sample prior to breakthrough and the associated development of total pressure.

In order to address the various issues, a series of long-term experiments was planned, involving the slow injection of a gas into a constant volume sample aimed at attaining breakthrough. The slow pressure build-up allowed for the observation of the whole spectrum of processes involved the eventual breakthrough, dilatant flow and the opening and closure of pathways. A specially-designed constant volume cell was used for testing purposes, which allows for the total saturation of the sample and the subsequent determination of the swelling pressure, thus creating a baseline for the injection of a gas into the centre of the sample. A central injection point was chosen so as to reduce the potential for leakages and the creation of preferential pathways along the cell walls. The gradual increase in the gas pressure allowed for the observation of the occurrence of fluid movement (and at which point) inside the sample prior to the breakthrough event via the monitoring of the outflow of water at the top and bottom of the cell. The monitoring of the total pressure assisted in the monitoring of the evolution of stress inside the sample. BCV bentonite was chosen for the experiments since it is in line with the deep geological repository concept proposed by the Czech radioactive waste repository authority (SÚRAO, c2023).

The strategy and experimental set-up is complementary to the work being conducted by UJV, thus allowing for the comparison of the results obtained by the two organisations. The same objectives are being pursued by UJV, the experimental research of which consists of the performance and evaluation of the gas pressure testing (breakthrough testing) of more types of bentonites: BCV and MX-80.

2.7.2. Experimental setup

2.7.2.1. Description of apparatus

The experiments were designed with a view to obtaining the relevant parameters that would allow for the clarification of the behaviour of gas permeation through the bentonite barrier. Both experimental programmes (CTU and UJV) involve the performance and evaluation of gas injection tests on compacted bentonite samples.

The tests are being carried out in specially designed 'permeameter' cells, which basically comprise cylindrical steel chambers (rings) for the housing of the samples (diameter: 30 mm, height: 20-60 mm). The constant volume of the samples is ensured by means of the rigid structure of the experimental cells while allowing for the monitoring of total pressure. The tops and bottoms of the samples have been fitted with sintered steel permeable plates so as to prevent the leaching ('mobilisation') of the material. The pistons and pressure sensors for the measurement of the total (or swelling) pressure of the bentonite are positioned between the upper and bottom flanges of the chamber and the upper and bottom surfaces of the samples. Pressure sensors are connected to a central data logger. The high-pressure constant volume cell is designed to investigate the flow of both water and gases through bentonite samples.

The cell is used in two modes:

- Setup A – water permeability testing and the measurement of total pressure (*Figure 2.190*)
- Setup B – gas breakthrough testing and the measurement of total pressure (*Figure 2.191*)

  The cell is connected to a permeameter during the testing of water permeability (setup A); the setup can be reconfigured to the gas injection mode (setup B) by reversing the flow in the lower flowmeter and by connecting a gas source.

This experiment involves the testing of BCV bentonite. Powdered material (initial water content of approximately 10%) has been uniaxially compacted directly into the cell rings. The target dry density of the material for the first test was set at 1300 kg/m^3, with subsequent tests in the range 1200-1500 kg/m^3. Distilled water is being used as the saturation medium.

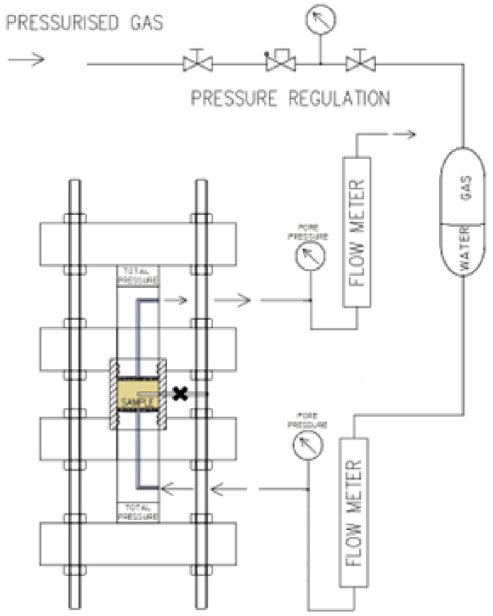

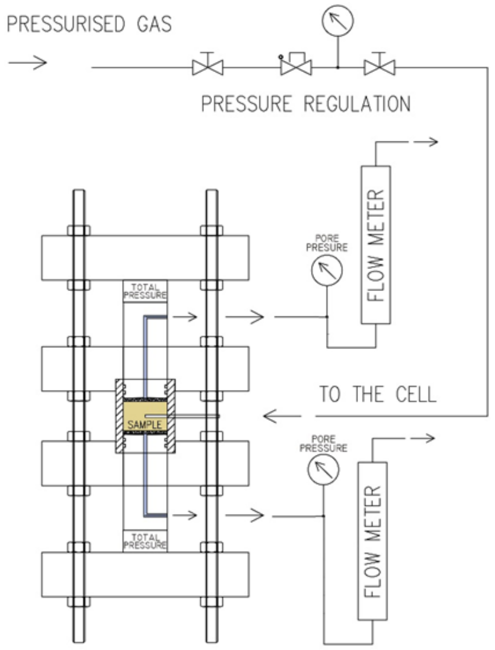

Figure 2.191: Experimental setup B – gas break-
Figure 2.190: Experimental setup A – water perme-through testing and the measurement of total pres-
ability testing and the measurement of total pressuresure

Setup A: The apparatus setup as illustrated in Figure 2.190 is used to investigate water permeability and total pressure during the saturation phases. Distilled water is used as the saturation medium, which is pushed into the material using compressed argon. The water flow is determined manually using a graded capillary tube-based flow meter in the inflow part.

The test is conducted up to the point at which the flow and the total pressure are observed to stabilise. The final water flow values are used for the determination of permeability. The water pressure source is subsequently disconnected so as to allow for the determination of swelling pressure.

Setup B: The apparatus setup as illustrated in Figure 2.191 is used for the performance of gas pressure tests. The principle of the test procedure is to load the sample with a gradual increase in the gas injection pressure until a breakthrough event occurs. The test procedure allows for the monitoring of the injection pressure at the inlet to the sample and the total pressure as measured by the pressure sensors on the pistons (i.e. the total/swelling pressure that is influenced by the injection pressure). The gas outflow at the outlet of the sample is monitored by mass flow meter. In addition, the water outflow at the outlet of the sample can be monitored; however, due to the technical challenges involved (an expected small volume of displaced water from the sample may not be detected by our apparature), this cannot be guaranteed.

The expected outcome of the gas pressure tests comprises the determination of the conditions under which gas enters the material and (possibly) the observation of the desaturation process. The test outcomes will then allow for the description of the ways in which the gas pressure and the geotechnical properties of the bentonite (particularly the total pressure) affect gas permeation through the bentonite barrier.

2.7.2.2. Testing fluids

The gas used for the breakthrough experiments is compressed dry air. Compressed air was chosen for safety reasons and simplicity of handling. Air is compressed using a high-pressure compressor in air cylinders with a capacity of 10 litres or 2 litres. The cylinders are then used in the experiments.

2.7.3. Material properties (pre-test and post-test characteristics)

The material used for testing, its properties and composition is described in detail in the chapter in Milestone 227: Task 2.2 Experimental report + ÚJV Řež (chapter 1.3.1 BCV bentonite).

2.7.4. Testing protocol

2.7.4.1. Preparation of the bentonite samples

The sample is compacted directly into the cell using a piston (uniaxial compaction) to the desired dry density. Powder material with an initial water content of approximately 10% is used as the sample material. A small diameter hole (D=2 mm) is drilled from the side into the centre of the sample into which a stainless-steel needle is inserted. The insertion of the needle prior to saturation allows for efficient sealing around the needle once the bentonite begins to swell during the saturation phase.

2.7.4.2. Phase A – The investigation of saturation, water permeability and swelling pressure

The samples are firstly saturated and their permeability and swelling pressure measured so as to establish the baseline prior to the injection of the gas. Water is pushed from the bottom part under a pressure of 1 MPa. Backpressure is not usually applied (however, it can be used), i.e. the saturation pressure directly determines the hydraulic gradient. Once the flow has stabilised, the permeability is determined, and the water pressure is cut off so as to allow for the equalisation of the sample pore pressure. The swelling pressure is then measured. Depending on the selected boundary condition, water pressure is reapplied in the top and bottom parts followed by a period of equalisation. Once a baseline has been established, gas injection is initiated in the centre of the sample (Phase B).

2.7.4.3. Phase B – Gas injection

Gas (air) is injected with an incremental increase in the injection pressure until a breakthrough event occurs (*Figure 2.193*). At the same time, the pore pressure is regulated according to the pre-determined plan and the water in/outflow from the sample is measured. The gas injection pressure is controlled and increased in increments commencing at 1/3-1/2 of the swelling pressure. It is expected that it will increase by 50 kPa every two to three weeks until a breakthrough event occurs. An initial test was performed with the pore pressure control equal to atmospheric pressure at the top and to around 40 kPa at the bottom (in order to direct the emergence of a gas preferential path in the upward direction). Once the testing is finished, the cells will be dismantled and the water content, density and dry density of the samples are determined using the gravimetric method; alternatively, resaturation will be performed and the hydraulic conductivity and swelling pressure measured.

2.7.4.4. Test procedure

A. Sample preparation and saturation (Setup A)

  i. Compaction of the sample into the cell (ring)
  ii. Drilling of the hole for the needle and needle insertion (the needle port is closed following needle insertion)
  iii. Connection to the permeameter setup (*Figure 2.190*, Setup A)
  iv. Saturation, monitoring of the water flow and total pressure
  v. Permeability measurement (water)
  vi. Cut-off of the saturation pressure

Table 2.65: Overview of the experimental tests on the BCV bentonite samples

sample no.	ρ_d [kg/m^3]	Phase A saturation/ resaturation phase [days]	gas test no.	Phase B gas injection point
P766	1250	168	**PN069**	to the centre
P805	1232	168	**PN077**	to the centre
		50	**PN082**	to base
P815	1394	168	**PN081**	to the centre
		80	**PN092**	to base
P823	1473	168	**PN086**	to base
P840	1471	335	**PN107**	to the centre

vii. Swelling pressure measurement

B. Gas injection test (Setup B)

i. Connection of the cell to the gas injection setup (*2.191*)
ii. Application of a gas injection pressure equal to approx. 1/3 – 1/2 of the swelling pressure using the needle at the centre of the sample
iii. Monitoring of the injection pressure and the total pressure (top and bottom)
iv. 14-day wait for breakthrough or other event to occur
v. If no breakthrough event occurs, increase in the injection pressure to 50 kPa and continue from step B.iii

An overview of the experimental work on the BCV bentonite samples is provided in the table below (Table 2.65)

2.7.5. Results

2.7.5.1. Slow gas breakthrough tests

The original experimental plan set out that the measuring apparatus and the cells would be prepared in the first year, which would be followed in subsequent years by the conducting of five slow pressure tests.

The preparation of the samples, consisting of homogeneous BCV bentonite with a dry density of 1250 to 1470 kg/m^3, took place in August 2020. The saturation phase of the samples lasted for around 168 days (with an applied saturation gradient of 1 MPa). The saturation phase of one of the tests was just 3 months; in this case, the saturation process was accelerated due to the requirement to adhere to the experimental time schedule. It was assumed that most of the changes inside the sample due to saturation would have occurred during this shortened time period. The development of the hydraulic conductivity was recorded during the saturation phase as the constant rate of water outflow. The saturation phase was terminated

Table 2.66: Overview of the slow gas tests performed as part of Subtask 2.2

sample no.	**ρ_d [kg/m^3]**	**gas test no.**	**note**	**Phase B gas injection point**	**total pressure - top sensor [MPa]**	**total pressure - bottom sensor [MPa]**	**initial injection pressure - in first step [MPa]**	**loading step [kPa]/time [days]**
P766	1250	**PN069**	**unsuccessful test** - technical problems with needle at the centre of the sample	to the centre	**0.45**	-	0.6	50/14
P805	1232	**PN077**	**unsuccessful test** - gas passes through testing cell, technical problems with the injection needle	to the centre	**0.40**	-	0.2	50/14
		PN082	resaturation of the sample after unsuccessful test	to base	**0.38**	**0.18**	0.07	50/14
P815	1394	**PN081**	2 months for equipment stabilization (without saturation); **no gas flow detection after BT**	to the centre	**2.21**	**1.14**	0.38	50/14 than 50/7 (after 3rd step)
		PN092		to base	**2.03**	**1.10**	0.57	50/7
P823	1473	**PN086**	simple measuring apparatus (with one piston) and with gas injection from the bottom of the sample	to base	**3.00**	**-**	1.54	50/7
P840	1471	**PN107**	1st step - 2.35 MPa	to the centre	**3.76**	**2.74**	2.35	50/7

via the cessation of the injection of water. The swelling pressure was determined following the stabilisation of the pressure readings provided by the total pressure sensors (positioned at the top and bottom of the sample). Following the completion of Phase A, the experimental setup was reconfigured to allow for the commencement of Phase B. A total of 7 slow gas pressure tests were performed on a total of five samples.

An overview of the complete set of slow gas pressure tests, including the parameters and a description, is provided in Table 2.66.

The pilot gas injection test (PN069) began with an initial loading increment of 6 bars. Breakthrough occurred seven and half hours after the commencement of pressurisation. The results obtained from the slow gas testing of the first sample are shown in graph form in Figure 2.192.

The breakthrough event occurred significantly earlier than expected. Following the dismantling of the sample, it was determined that the test had failed due to technical problems with the injection needle installed in the centre of the sample. The sample was dismantled and a new sample was prepared with the same target dry density (1300 kg/m^3) and an alternative technical approach was applied for the installation of the injection needle in the centre of the sample. Due to the technical problems with the injection needle and the rapid progression of the test, this first test was considered to be unsuccessful.

A second sample with the same dry density was prepared and connected to setup A. The saturation

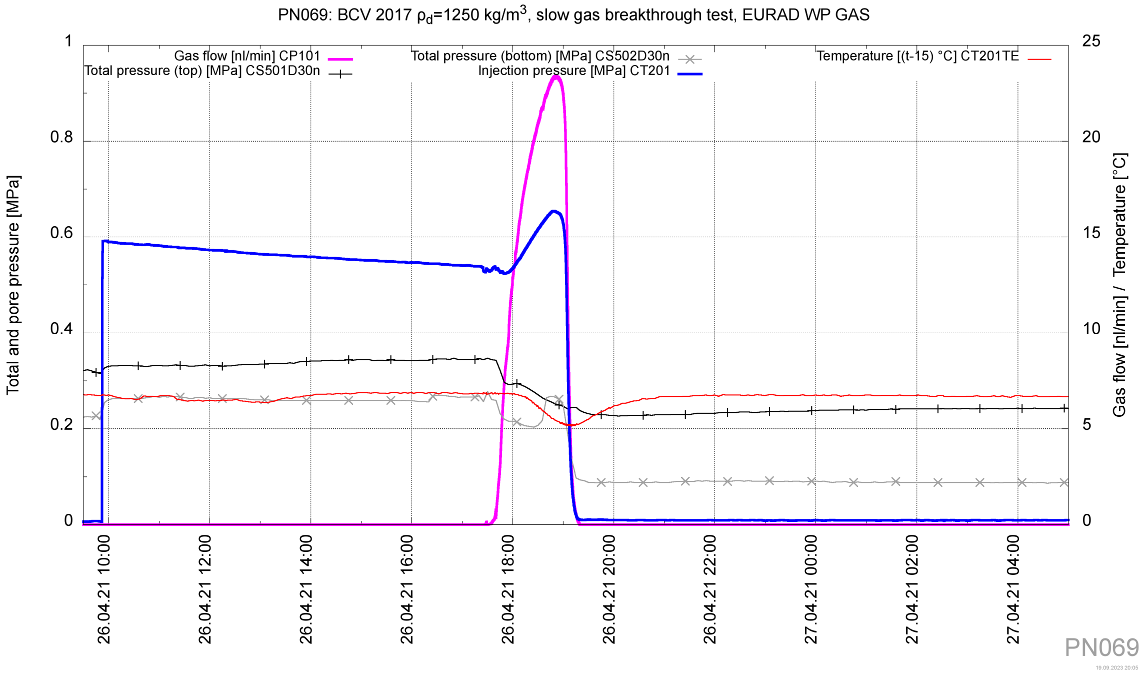

Figure 2.192: The evolution of total pressure, pore pressure, gas injection pressure, gas outflow and temperature during the first slow gas pressure test (PN069) of a sample with a dry density of 1250 kg/m^3

phase lasted 168 days. Following the completion of Phase A, the sample was connected to setup B. The atmospheric pressure was set at the bottom and at the top of the sample. The gas injection test (PN077) commenced on 26 October 2021 and the injection pressure for the first loading increment was set at 0.22 MPa. A decrease occurred in the injection pressure to 0 kPa 6 days following the initiation of pressurisation (during the first loading increment), and no air flow was recorded at the sample outlet. It is suspected that a leakage of the gas occurred around the injection needle.

Due to technical problems with the injection of the gas via the needle into the centre of the sample, the setup of the experiment was modified. It was decided that the gas would be injected from the bottom of the sample for the subsequent gas tests. The sample was connected to setup A and re-saturated for 50 days with a saturation gradient of 1 MPa, whereupon the slow gas test was initiated involving the injection of the gas from the bottom of the sample. The first loading increment was set at half the lower measured total pressure (as evaluated during phase A), which amounted to 0.18 MPa, and was increased in each of the subsequent loading increments by around 50 kPa. The evolution of the slow gas test for the re-saturated sample (PN082) is shown in graph form in Figure 2.193.

Breakthrough occurred when the injection pressure was increased to 0.37 MPa. A very slow gas leak occurred at the outlet of the sample (gas flow rate of 0.1 nl/min) immediately after the pressure was increased. The main breakthrough event (the detected gas flow rate at the outlet of the sample exceeded a value of 25 nl/min) occurred 160 hours following the increase in the injection pressure. This episode is described in more detail in 1.5.3 Breakthrough episodes.

The leakage of the gas and the increasing of the injection pressure were compensated for by the pressure reducing valve, which attempted to maintain the set pressure at a constant 0.37 MPa. Due to the low sensitivity of the pressure reducing valve, the injection pressure fluctuated around the set value (as the leak continued). A “major” breakthrough event occurred 160 hours from breakthrough and the gas flow at the outlet of the sample increased to above a value of 26 nl/min. The cylinder with the compressed air was emptied and the injection pressure decreased to a value of zero. The detailed progression of the breakthrough episode is shown in graph form in Figure 2.194.

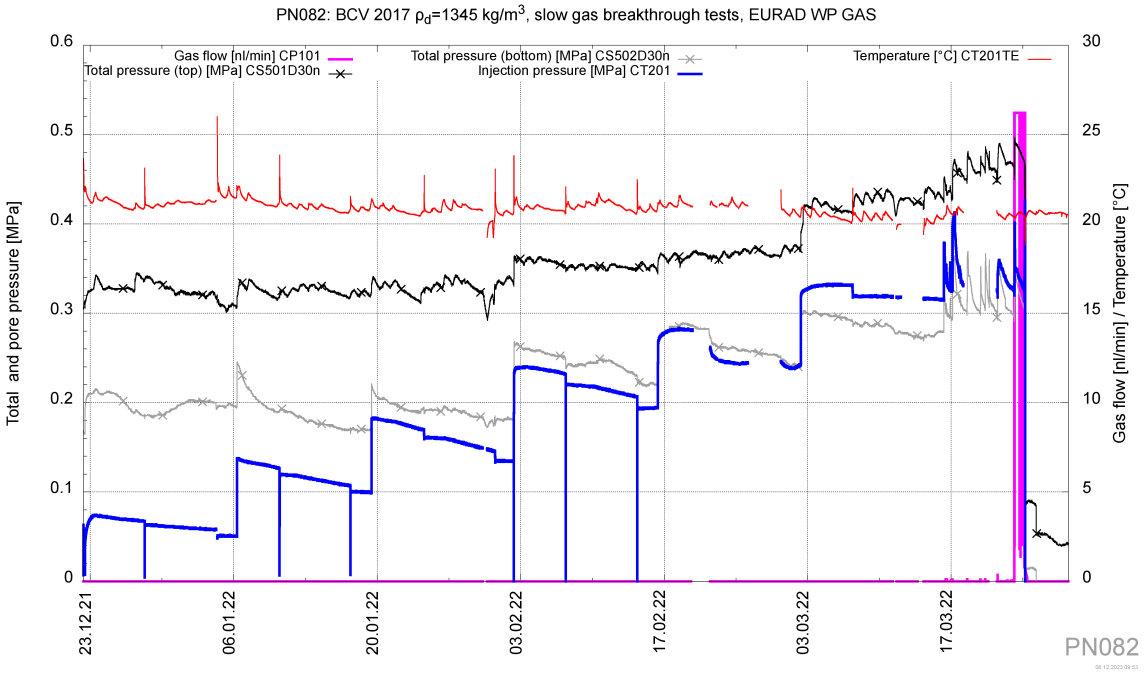

Figure 2.193: The evolution of total pressure, pore pressure, gas injection pressure, gas outflow and temperature during the slow gas pressure test (PN082) of a sample with a dry density of 1230 kg/m^3 after its resaturation

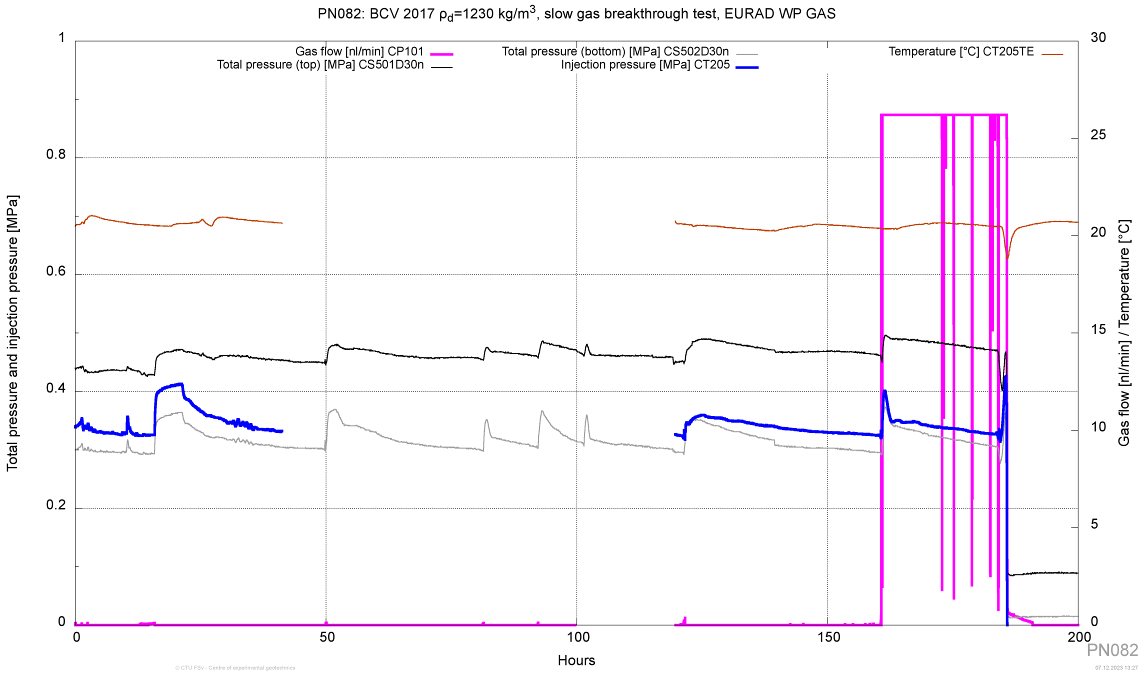

Figure 2.194: The evolution of breakthrough episode PN082: total pressure, gas injection pressure, gas outflow and temperature during slow gas pressure test (PN082) of a sample with a dry density of 1230 kg/m^3 after its resaturation

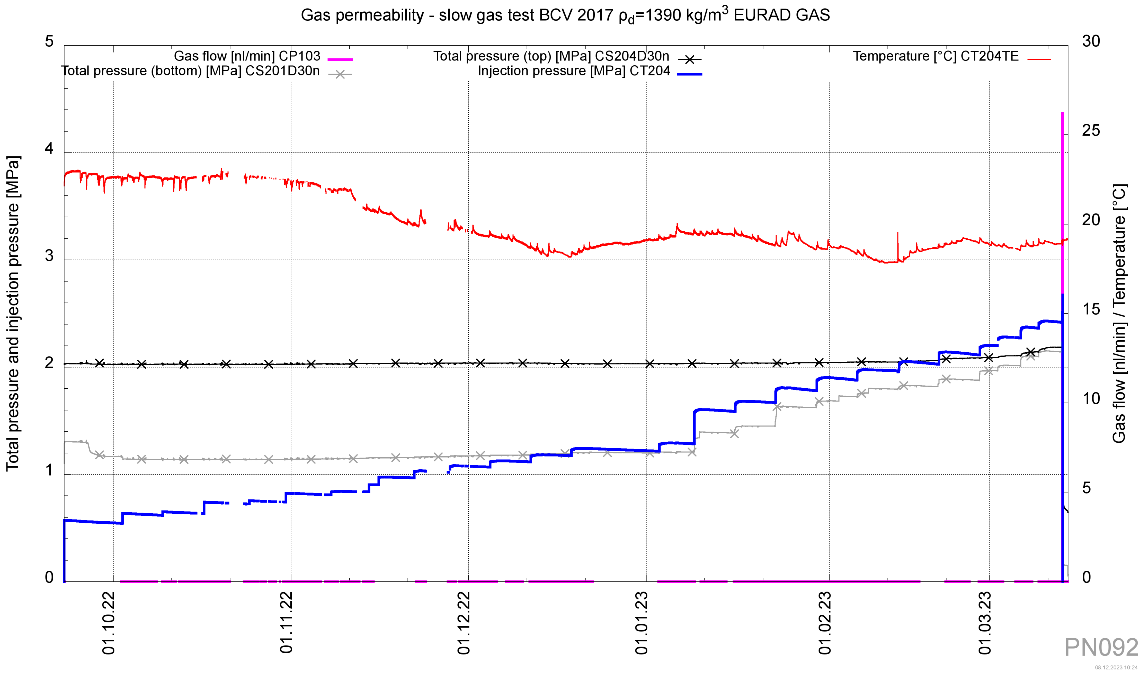

Figure 2.195: The evolution of total pressure, gas injection pressure, gas outflow and temperature during the slow gas pressure test (PN092) of a sample with a dry density of 1390 kg/m^3 after its re-saturation

Aimed at speeding up the test programme, a second apparatus was commissioned and another sample was saturated in parallel with the ongoing test.

A third sample with a dry density of 1390 kg/m^3 was prepared and connected to setup A. The saturation phase lasted 93 days. Following the completion of Phase A, the sample was connected to setup B. Atmospheric pressure was set at the bottom and at the top of the sample. The gas injection test (PN081) commenced on 14 June 2022 and the gas was injected into the centre of the sample (the injection needle was placed within the sample prior to phase A – the saturation phase). The injection pressure for the first loading increment was set at 0.38 MPa. It was decided to reduce the duration of the loading increment so as to accelerate the test. The duration of one loading increment was set at seven days from the third loading step. The value of the increment was the same, i.e. 50 kPa. A decrease occurred in the injection pressure to 0 kPa 98 days following the initiation of pressurisation (during the 8th loading increment – the injection pressure was set at a value of 0.84 MPa), and no air flow was recorded at the sample outlet. It is suspected that a leakage of the gas occurred around the injection needle.

Due to technical problems with the injection of the gas into the centre of the sample, the setup of the experiment was modified once more. The sample was connected to setup A and re-saturated for 80 days with a saturation gradient of 1 MPa, whereupon the slow gas test (PN092) was initiated involving the injection of the gas into the bottom of the sample. The first loading increment was set at half the lower measured total pressure (as evaluated during phase A), which amounted to 1.10 MPa, and was increased in each of the subsequent loading increments by around 50 kPa every 7 days. The evolution of the slow gas test after the resaturation phase (Phase A) for the sample (PN092) with a dry density of 1390 kg/m^3 is shown in graph form in Figure 2.195.

The gas injection test (PN092) commenced on 23 September 2022. A breakthrough event occurred (decrease in the injection pressure and the detection of gas outflow) during the 26th loading increment when the injection pressure was increased to 2.5 MPa.

A fourth sample was then prepared with a dry density of 1470 kg/m^3. Since just two dual cells had been constructed for the conducting of the slow gas tests with gas injection into the centre of the samples and

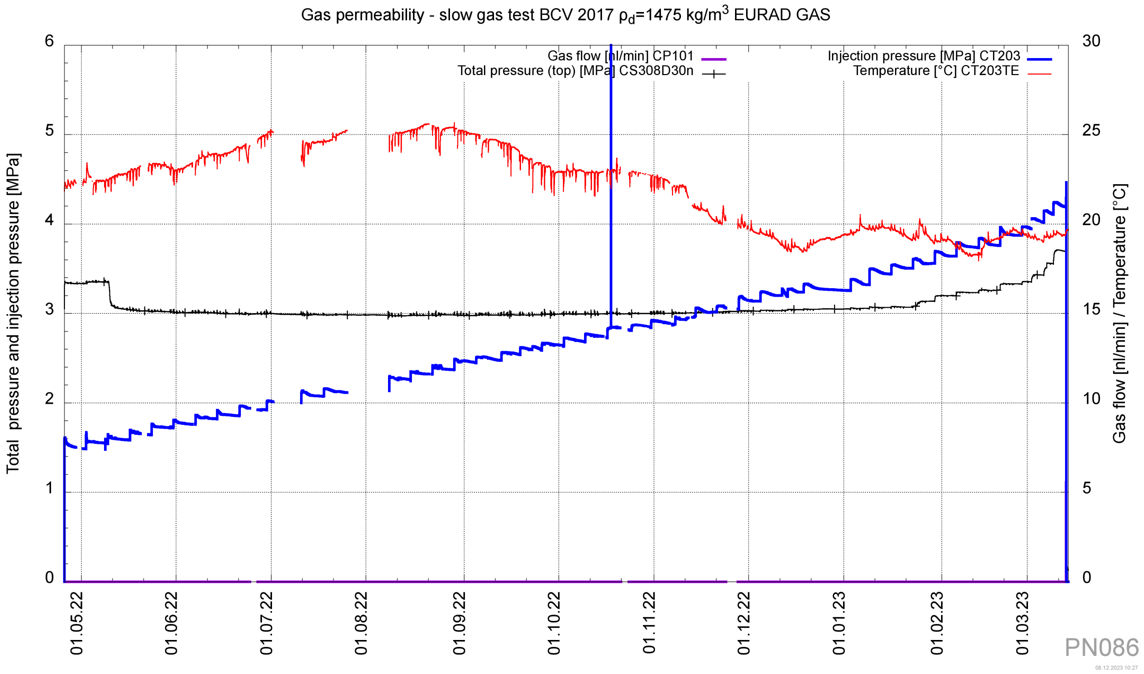

Figure 2.196: The evolution of total pressure, gas injection pressure, gas outflow and temperature during the slow gas pressure test (PN086) of a sample with a dry density of 1475 kg/m^3 in the simple cell (with one piston and one force sensor)

testing was underway using both cells, a single (so-called simple) cell with one piston and one force sensor on top of the piston was used for the testing of the fourth sample. Gas injection was possible only into the bottom of the sample through the sintered plate. The same testing procedure was used as previously. The sample was saturated during Phase A followed by the measurement of the hydraulic conductivity and total stress. The chamber was then disconnected from Phase A and connected to Phase B. The gas injection test (PN086) commenced on 26 April 2023. A breakthrough event occurred during the 46th loading increment (322 days from the initiation of gas injection into the sample) when the injection pressure was increased to 4.43 MPa. The evolution of the slow gas test on the sample (PN086) with a dry density of 1470 kg/m^3 is shown in graph form in Figure 2.196.

The final sample had a dry density of 1470 kg/m^3. The standard experimental setup and procedure were maintained for this sample - a dual cell with two pistons and two force sensors placed on the upper and lower pistons for the measurement of the total pressure. Phase A lasted 168 days and the slow gas test (PN107) commenced on 17 October 2022; the gas was injected into the centre of the sample. The injection pressure for the first loading increment was set at 2.35 MPa, which corresponded to 100% of the measured total pressure value for the bottom force sensor. The increase for the first loading increment was chosen based on experience obtained from the previous tests, concerning which breakthrough always occurred after the exceeding of the measured total stress value. The amount and the interval of the incremental loading procedure were maintained at 50 kPa every 7 days, respectively. This test was the first successful test applying gas injection into the centre of the sample using an injection needle. The evolution of the slow gas test for the sample (PN107) with a dry density of 1470 kg/m^3 is shown in graph form in Figure 2.197.

The reaction of the force sensors (the measurement of total pressure) to the injection pressure once the corresponding values were reached can be observed with respect to all the successful tests. The immediate response of the force sensor to the increase in the injection pressure was evident. This is consistent with the results obtained from a previous study (Hausmannová, 2017) on the impact of saturation pressure on the measured total stress. In the thesis (Hausmannová, 2017) the response of the total stress to the injection pressure increases significantly once the total pressure is exceeded. The total stress increases

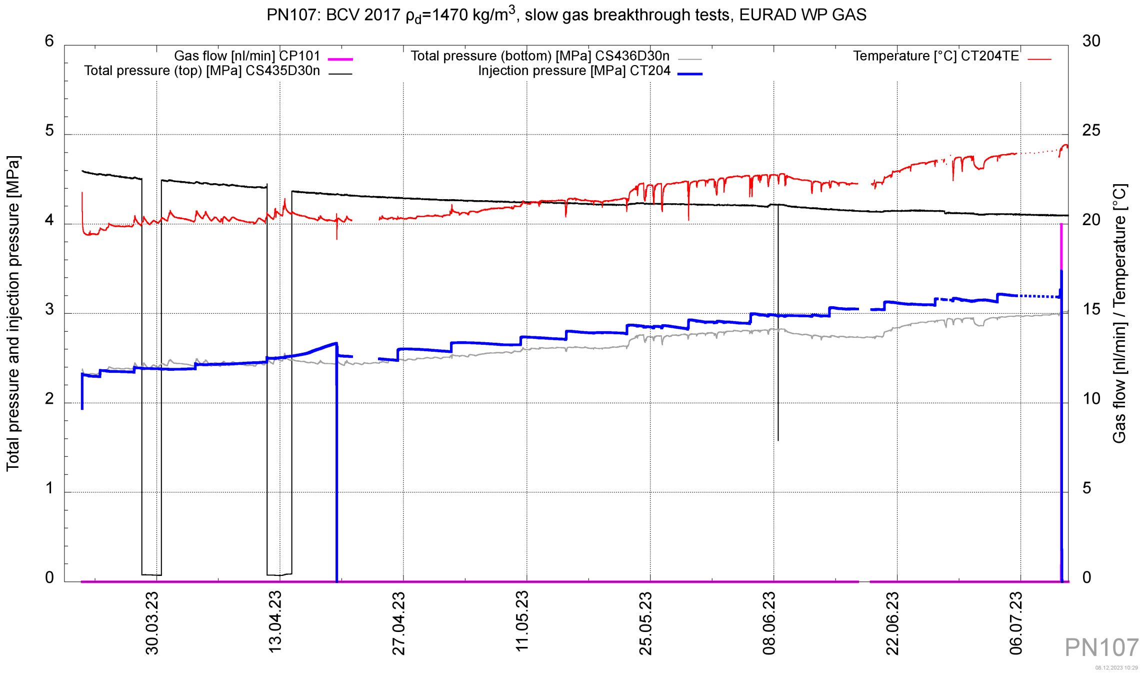

Figure 2.197: The evolution of total pressure, gas injection pressure, gas outflow and temperature during the slow gas pressure test (PN107) of a sample with a dry density of 1470 kg/m^3

by the same value as the injection pressure when the injection pressure is around three times higher than the measured total stress. When the bentonite is constrained under constant volume boundary conditions, the propagation of pathways should result in the significant disturbance of the monitored stress and pore-water pressure (Graham, 2016). This is thought to be due to the activation of frictional effects on the casing, which occurs when the measured total pressure value is exceeded. Alternatively, it is due to a combination of several phenomena, e.g. the activation of frictional forces on the casing and the possible deformation of the bentonite sample. The force sensor responds to all of these effects. If the injection pressure increases continuously above the total pressure, eventually the injection pressure overcomes the casing friction force; the change in the injection pressure is equal to the change in the total pressure. The gas injection pressure decreases, as does the total pressure, following a breakthrough event. The reaction of the bottom force sensor to each increment of the increase in the injection pressure (for the tests in which gas is forced into the bottom of the sample) represents one of the mechanical properties of the experimental cell.

Although these four slow gas breakthrough tests were subjected to slightly different testing procedures, the behaviour of the samples was observed to be very similar. A summary of the results from all the slow gas breakthrough tests is provided in Table 2.67.

Gas injection was performed from the bottom of the samples for three of the tests (PN082, PN092 and PN086) and, in all cases, the breakthrough event occurred following the exceeding of the measured total pressure. Concerning the sample with the lowest dry density (PN082), the breakthrough event occurred at an injection pressure value that was very close to the measured total pressure value. The injection gas pressure had to exceed the measured total pressure by 20 to 50% in order for a breakthrough event to occur. The comparison of the breakthrough pressure values with the theoretical swelling values revealed that breakthrough always occurs within the range of swelling pressure values for defined dry densities.

Concerning the final slow gas breakthrough test on a sample applying gas injection into the centre of the sample, the breakthrough event occurred when the total pressure value measured by the bottom sensor (a lower total pressure value than that measured by the upper force sensor) exceeded the total pressure value by 20%. The difference in the values measured at the lower and upper sensor is due to the distribution

Table 2.67: Overview of the results for all the slow gas breakthrough tests on homogeneous BCV samples

sample no.	**ρ_d [kg/m^3]**	**gas test no.**	**note**	**Phase B gas injection point**	**total pressure - top sensor [MPa]**	**total pressure - bottom sensor [MPa]**	**initial injection pressure - in first step [MPa]**	**loading step [kPa]/time [days]**	**breakthrough pressure [MPa]**	**theoretical swelling pressure [MPa]**
P766	1250	**PN069**	**unsuccessful test** - technical problems with needle at the centre of the sample	to the centre	**0.45**	-	0.6	50/14	---	**0.34 - 0.98**
P805	1232	**PN077**	**unsuccessful test** - gas passes through testing cell, technical problems with the injection needle	to the centre	**0.40**	-	0.2	50/14	**---**	**0.3 - 0.86**
		PN082	resaturation of the sample after unsuccessful test	to base	**0.38**	**0.18**	0.07	50/14	**0.37**	
P815	1394	**PN081**	2 months for equipment stabilization (without saturation); **no gas flow detection after BT**	to the centre	**2.21**	**1.14**	0.38	50/14 than 50/7 (after 3rd step)	**0.84**	**0.89 - 2.57**
		PN092		to base	**2.03**	**1.10**	0.57	50/7	**2.50**	
P823	1473	**PN086**	simple measuring apparatus (with one piston) and with gas injection from the bottom of the sample	to base	**3.00**	**-**	1.54	50/7	**4.43**	**1.56 - 4.54**
P840	1471	**PN107**	1st step - 2.35 MPa	to the centre	**3.76**	**2.74**	2.35	50/7	**3.26**	**1.54 - 4.39**

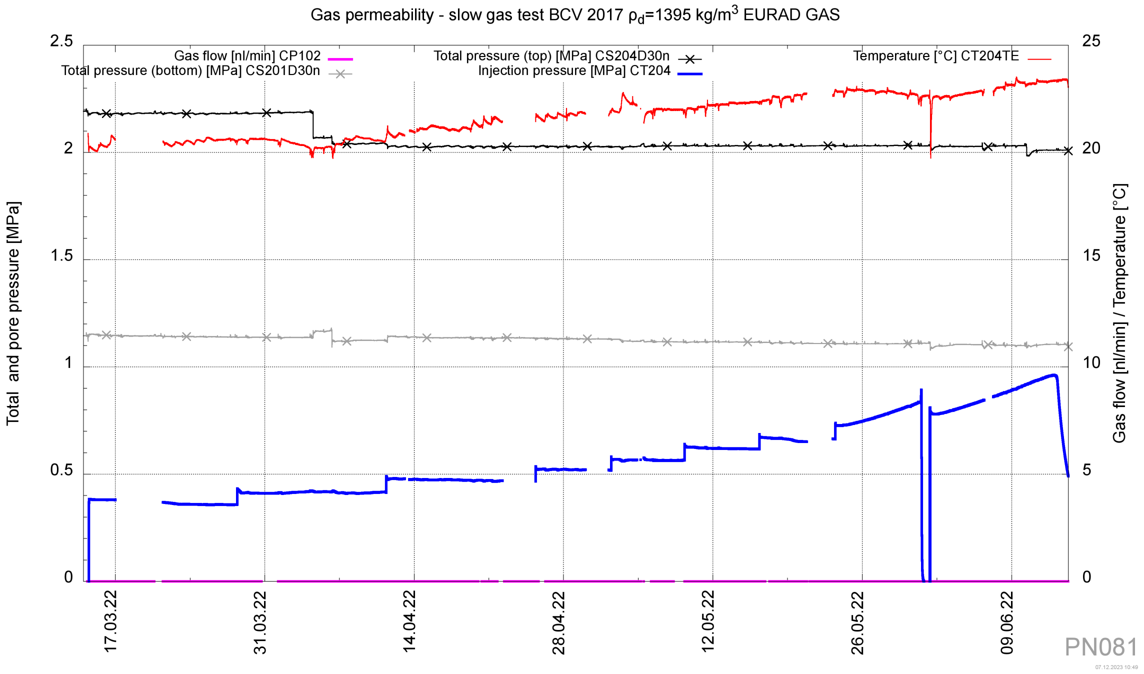

Figure 2.198: The evolution of total pressure, gas injection pressure, gas outflow and temperature during the unsuccessful test (PN081) of a sample with a dry density of 1395 kg/m^3 with the gas injection to the centre of the sample

of forces in the sample. Since the sample is saturated on one side, swelling and expansion of the sample occurs in the cell from the bottom to the top base.

2.7.5.2. Knowledge gained from the unsuccessful tests

Several interesting findings were obtained from the unsuccessful tests. In all cases, these tests involved the injection of gas into the centre of the sample using an injection needle. Concerning the first case, due to technical problems, the measured total stress was exceeded as soon as in the first loading increment and the breakthrough event occurred almost immediately following loading (after 5 hours) (*Figure 2.192*) . In the second case - a second unsuccessful test with gas injection into the centre of the sample (PN077), no air flow was detected at the sample outlet. It is thought that all the air passed along the interface between the needle and the bentonite (due to the imperfect sealing of the needle) and thus out of the sample.

With respect to the third gas breakthrough test applying gas injection into the centre of the sample, a breakthrough event or a drop in the injection pressure (no gas flow was detected at the sample outlet) occurred at a value lower than that of the measured total stress (*Figure 2.198*). Specifically, the breakthrough event occurred at a value of gas injection pressure of 0.84 MPa; the lower measured total pressure value (recorded by the bottom force sensor) amounted to 1.14 MPa.

The presentation of the measured data on the total stress and gas breakthrough pressure for all the tests in the form of a unified graph (*Figure 2.199*) revealed that as the total stress value increases, the gas pressure must be increased above the total stress value in order for breakthrough to occur. The magnitude of the measured total stress increases with the dry density of the bentonite. It can be stated that with the increasing dry density of the bentonite, it is necessary to increase the gas pressure above the total pressure value in order for breakthrough to occur. It is advisable that this suggestion is confirmed by conducting more tests on higher dry density samples (1600 kg/m^3 and above).

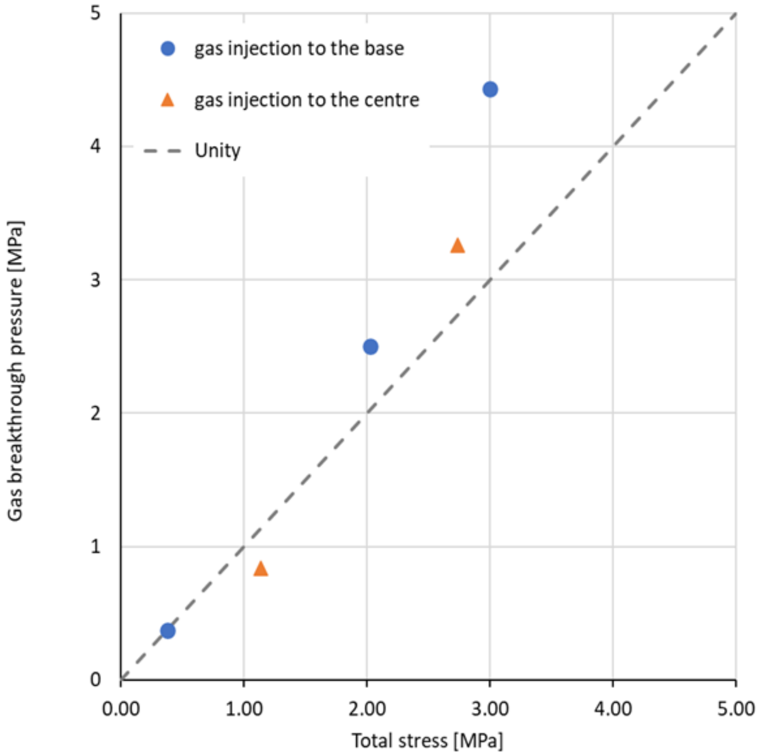

Figure 2.199: Key parameters for the slow gas injection tests. The relationship between the gas breakthrough pressure and the total stress with respect to the gas injection point (from the bottom versus from the centre of the sample). The dotted line represents full conformity

2.7.5.3. Breakthrough episodes

This chapter provides a detailed discussion of the breakthrough episodes of the slow gas tests, especially tests PN082, PN092, PN086 and PN107, the first three of which comprised slow gas breakthrough tests with the injection of the gas from the bottom of the samples. The breakthrough episode refers to the part of the gas test during which the flow of gas is detected at the outlet of the sample and the injection pressure drops (time zero). The monitored parameters comprise primarily the gas injection pressure and the gas flow rate. The evolution of the whole of the episode is monitored from the initial recording of the gas flow to the time at which the gas flow is zero and the injection pressure drops to zero. Such episodes are divided into fast and slow. Fast episodes last up to two hours following breakthrough, whereas slow episodes exceed two hours after breakthrough. The shape of the injection pressure decrease curve following breakthrough may vary. Figure 2.200 illustrates the characteristic pressure waveforms for the gas pressure tests.

In the text following, the breakthrough episodes of slow gas pressure tests are illustrated and discussed in detail. Figures plot the progress of the gas pressure test from the moment the gas flow rate was recorded at the sample outlet (time zero). This point in time has been termed a breakthrough event and the term breakthrough episode is defined as the time period of the gas pressure test from the point of breakthrough to the decrease of injection pressure to zero. The longest breakthrough episode related to the sample with the lowest dry density, i.e. 1230 kg/m^3 (Figure 2.201, Figure 2.203, Figure 2.202). The gas flow rate following breakthrough was very low, i.e. around 0.1 nl/min, and this situation lasted for almost 160 hours at which time repeatedly path closure occurred and the gas flow rate dropped to zero, whereupon breakthrough and a low gas flow rate occurred once more (Figure 2.202). Hence, the gas injection pressure dropped very gradually, indeed almost unnoticeably. Thus, it can be concluded that the preferential path that formed was very narrow and unstable. After around 160 hours from the first recording

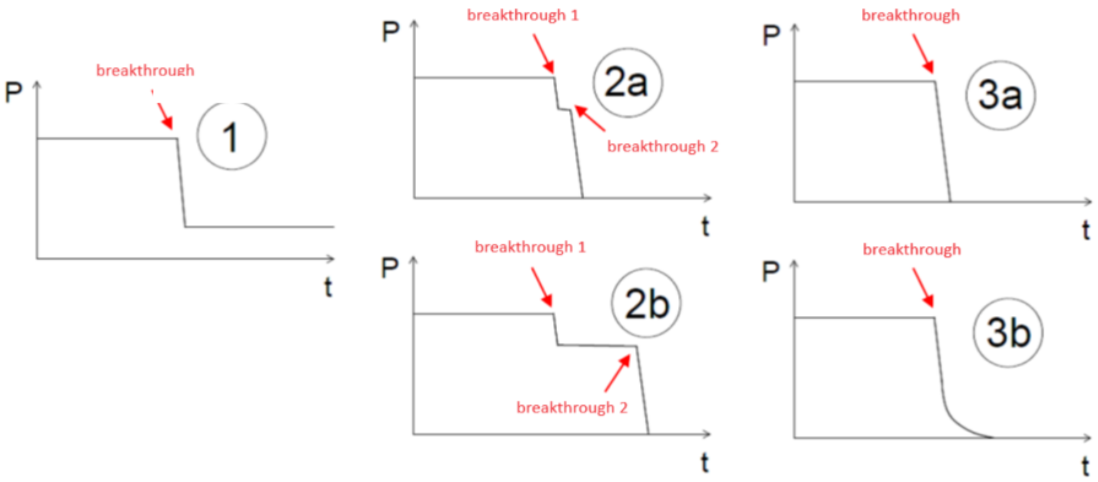

Figure 2.200: Characteristic test patterns

of the gas flow at the outlet of the sample, a significant breakthrough event occurred when the gas flow rate increased rapidly up to in excess of 25 nl/min, and within 30 hours the volume of gas in the cylinder was consumed and the gas injection pressure dropped to zero (Figure 2.203), thus concluding the gas breakthrough episode. Several sharp decreases in the gas flow rate were observed even during the large breakthrough event. Such decreases and increases lasted only a few tens of seconds, during which the resulting dilatation pathway closed and reopened.

The breakthrough episode of gas test PN092 (Figure 2.204) on a sample with a dry density of 1390 kg/m^3 was extremely rapid compared to the previously described test. Immediately after breakthrough, the gas flow rate increased to above 25 nl/min and, within 20 minutes, the gas injection pressure dropped to zero thus concluding the gas breakthrough episode. The preferential dilatant pathway closed and reopened just once during this episode, thus indicating that the dilatant pathway that formed was wider and more stable than that of the sample with a dry density of 1230 kg/m^3.

The breakthrough episode of gas test PN086 on a sample with a dry density of 1470 kg/m^3 evinced a very similar evolution to the test on the sample with a dry density of 1390 kg/m^3 (see above). This episode lasted 3.5 hours. The most significant decrease in the gas injection pressure occurred during the first hour of the gas breakthrough episode, following which the decrease in the injection pressure and the gas flow rate was very slight. The gas flow rate during this episode was low; the maximum value was 9 nl/min. No closure and reopening of the dilatant pathway occurred during this episode and, from the start of the breakthrough episode, the gas passed through the sample without any significant changes in the gas flow rate. Based on these episodes, it can be concluded that the created dilatant pathway was stable and the gradual closure of the pathway occurred until the pressure dropped to zero.

The final test (PN107 – on a sample with a dry density of 1470 kg/m^3 – Figure 2.206) differed from the previously mentioned tests in that the gas was injected into the centre of the sample using an injection needle. The breakthrough episodes in this case evinced a different evolution to those of the previous tests. Initially there was a gentle increase in the gas flow rate without any significant change in the gas injection pressure. After 30 minutes the gas flow rate began to increase rapidly with the occurrence of several rapid decreases and increases, thus indicating the closure and reopening of the created pathway. Following the attainment of the maximum gas flow rate value (20 nl/min), a sharp decrease was evidently followed by a period of relative “stabilisation” (a constant gas flow rate and stable gas injection pressure) until the gas injection pressure began to decrease (due to the depletion of the given volume of gas).

The breakthrough episodes varied from test to test and no general statement can be made concerning how

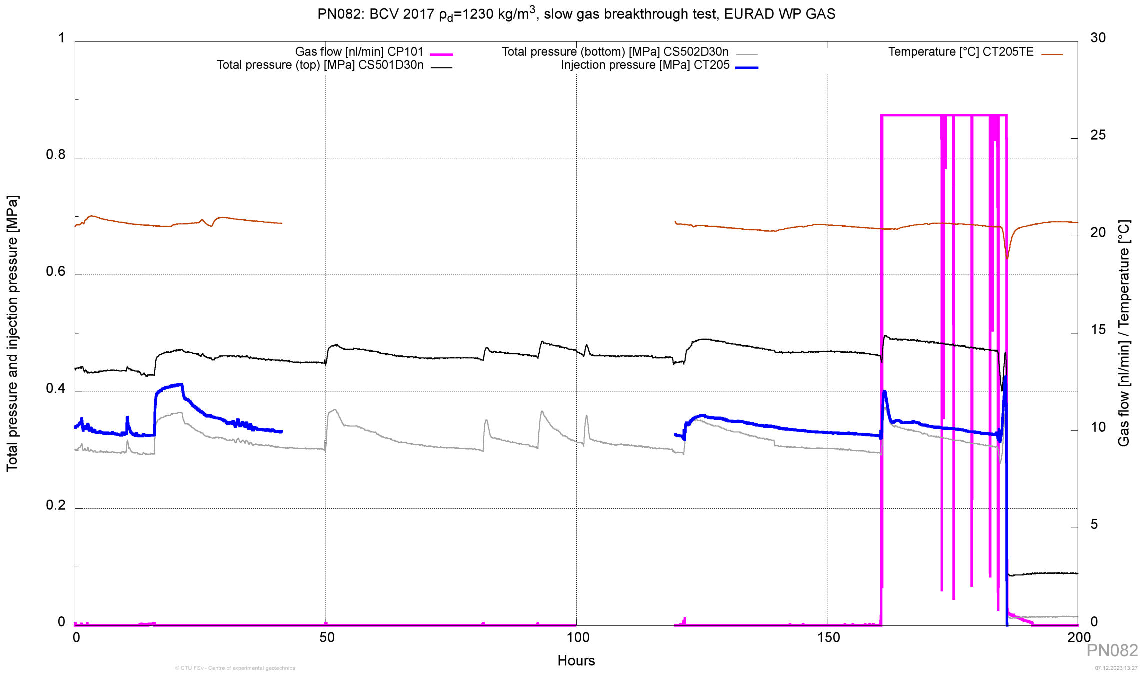

Figure 2.201: The gas breakthrough episode for gas test PN082 on a sample with a dry density of 1230 kg/m^3 with the injection of gas into the bottom of the sample through the sintered plate

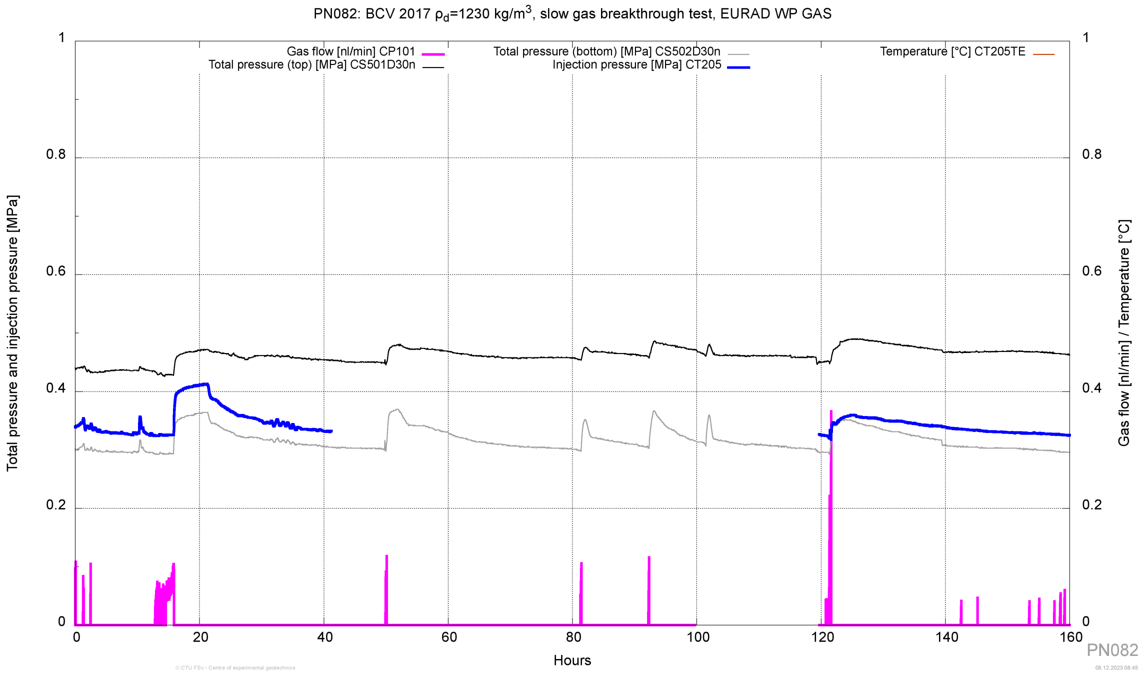

Figure 2.202: Detail of the breakthrough episode for gas test PN082 on a sample with a dry density of 1230 kg/m^3 – a part of the episode up to hour 160 with very low gas flow at the sample output and closing and reopening of the pathway

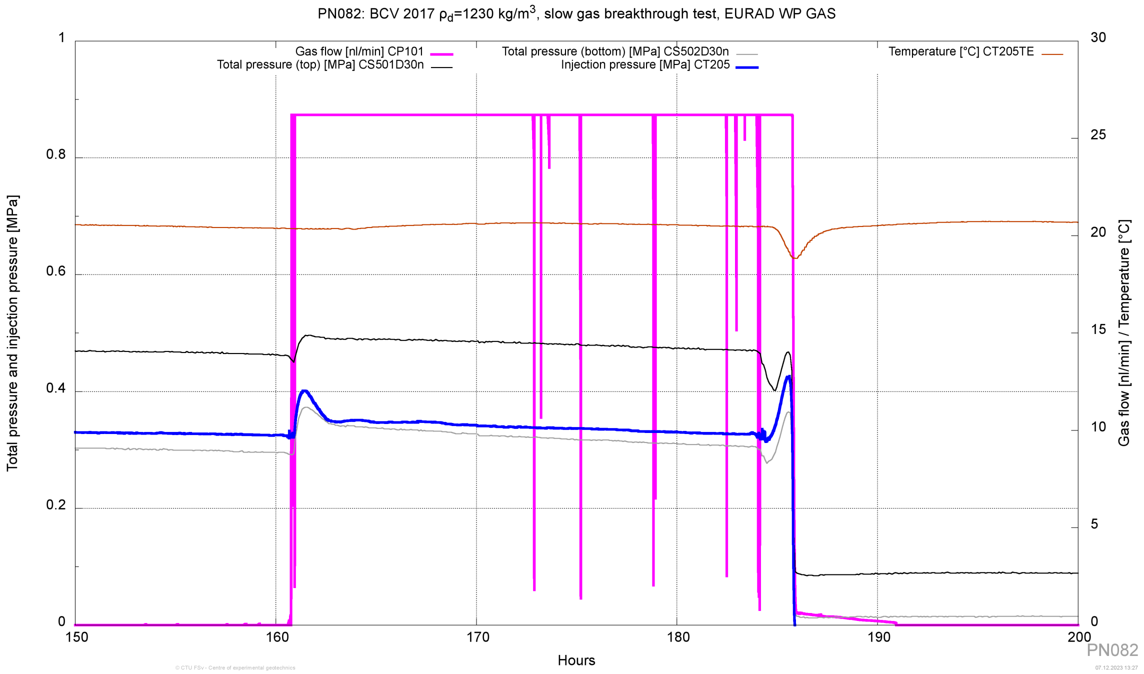

Figure 2.203: Detail of the breakthrough episode for gas test PN082 on a sample with a dry density of 1230 kg/m³ – major breakthrough event with a gas flow rate of over 25 nl/min

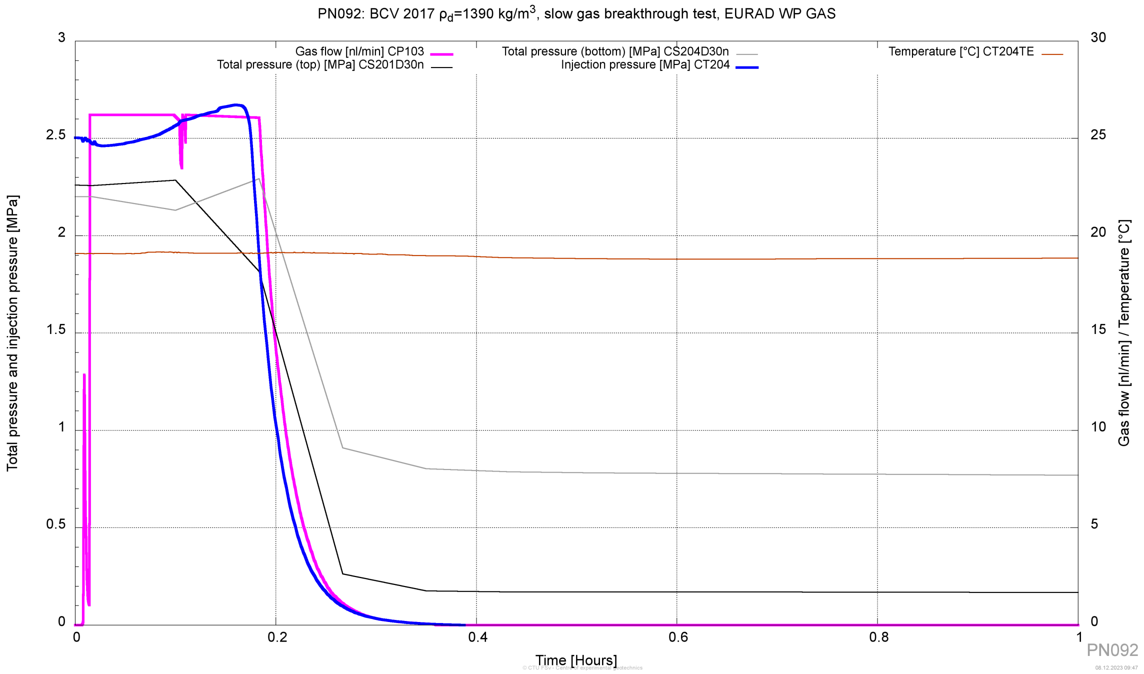

Figure 2.204: The gas breakthrough episode for gas test PN092 on a sample with a dry density of 1390 kg/m³ with the injection of gas into the bottom of the sample through the sintered plate

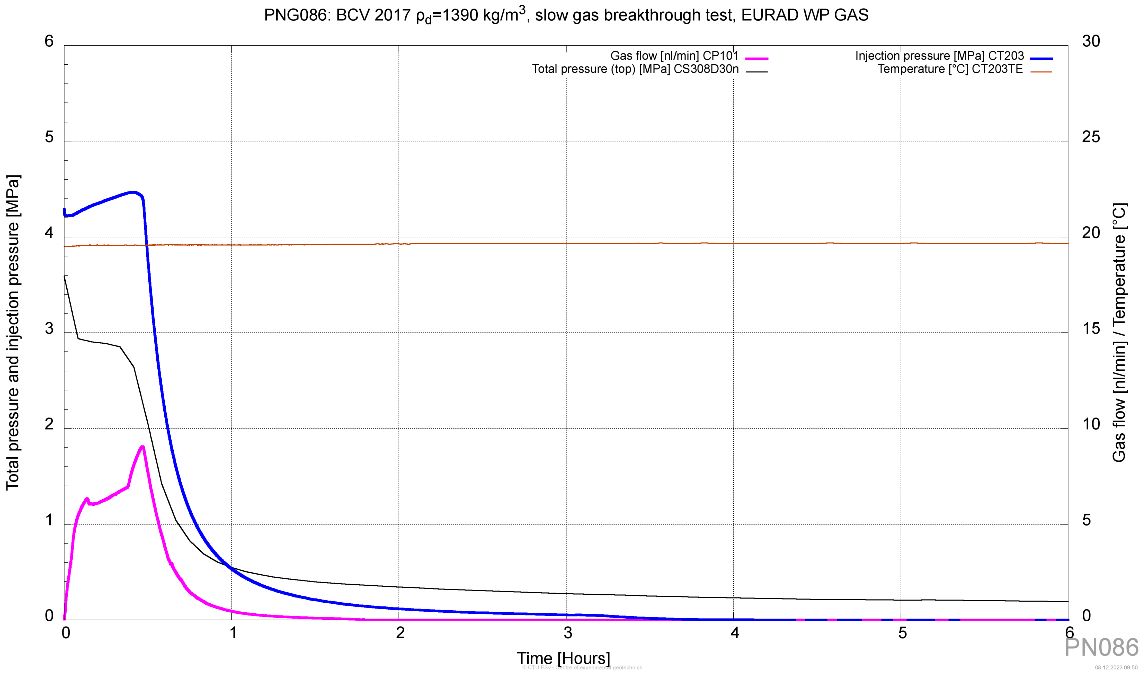

Figure 2.205: The breakthrough episode for gas test PN086 on a sample with a dry density of 1470 kg/m^3 with the injection of gas into the bottom of the sample through the sintered plate

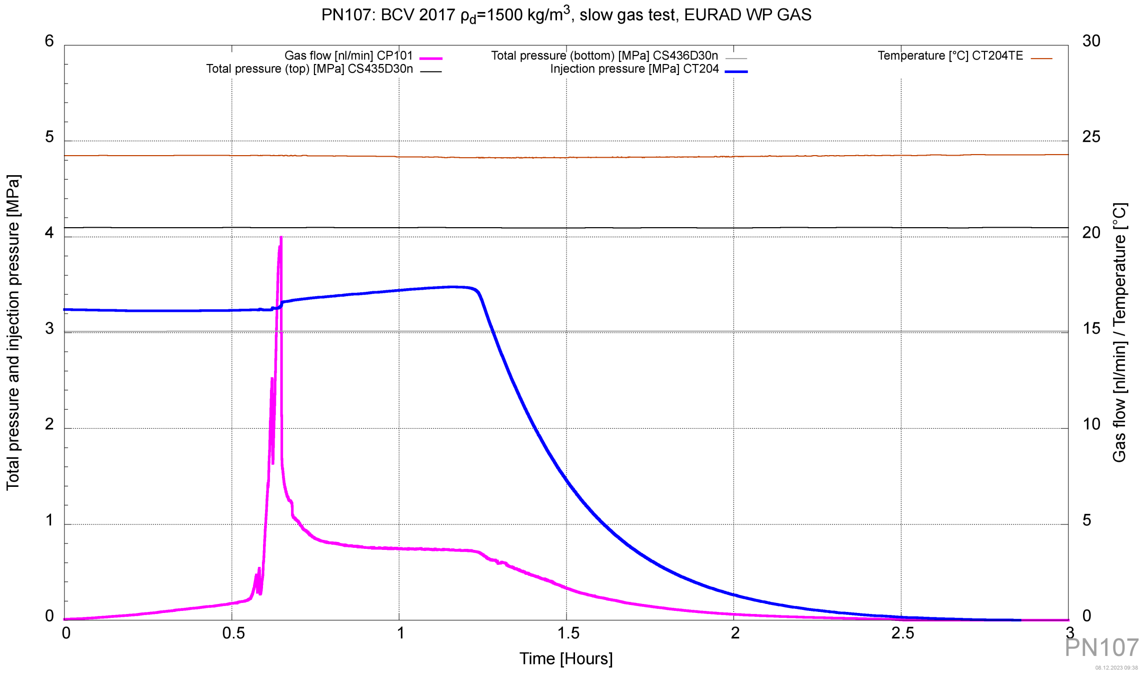

Figure 2.206: The breakthrough episode for gas test PN107 on a sample with a dry density of 1470 kg/m^3 with the injection of gas into the centre of the sample using an injection needle

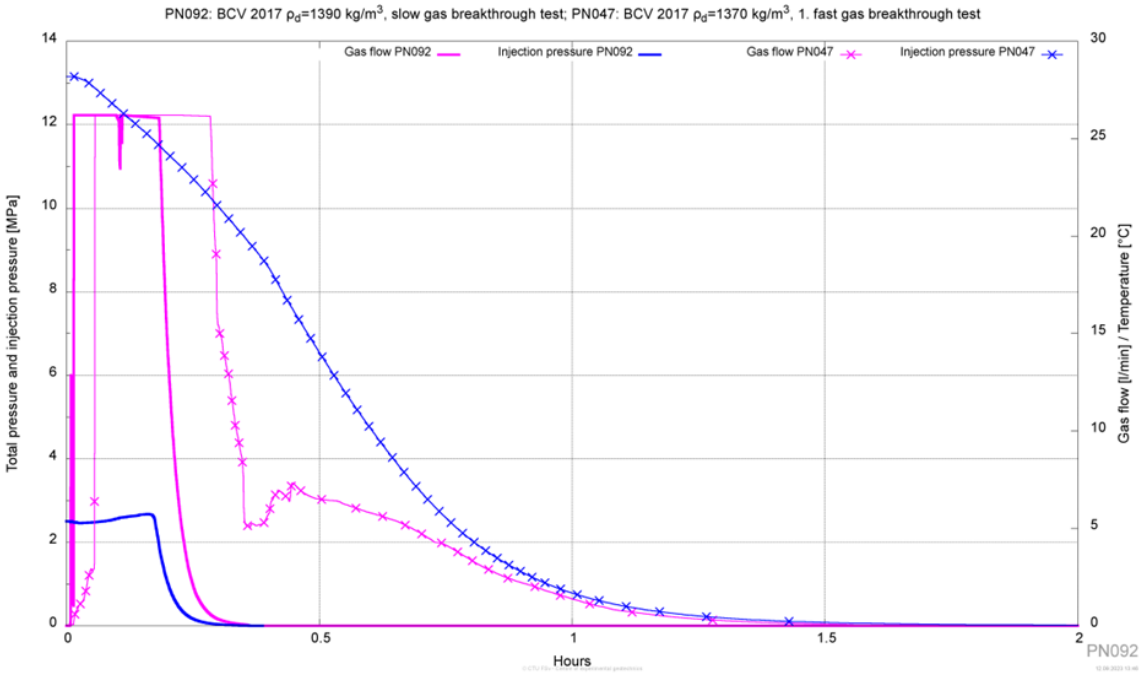

Figure 2.207: Comparison of the gas breakthrough episodes of slow gas test PN092 and fast gas test PN047 with sample dry densities of 1390 kg/m^3 and 1370 kg/m^3, respectively

bentonite with a certain dry density behaves during a gas breakthrough event. It was considered important to compare the episodes determined from the slow gas tests to those observed during the fast gas tests performed as part of Task 3, which were performed on the same equipment and using the same material; only the experimental setup differed. This served to supplement the data available for the analysis and evaluation stage.

The first step involved comparing the episodes determined from the slow gas tests with those from the fast gas tests for samples with similar dry densities. The fast gas tests differed from the slow gas tests in terms of the setting of the gas injection pressure value (13 MPa); moreover, the gas was injected only into the bottom of the samples. The measured parameters of the testing procedure were similar for both types of test. A more extensive assessment of the breakthrough episodes is reported in Task 3, as well as in the final report.

A comparison of the slow and fast gas tests on the samples with very similar dry densities is presented in the following two figures (Figure 2.207, Figure 2.208). The slow gas test PN092 episode and that of fast gas test PN047 are compared; the dry densities of the samples were 1390 kg/m^3 and 1370 kg/m^3 respectively. The courses of the episodes were very similar; increases in the gas flow rate occurred in both cases soon after breakthrough and the duration of the two episodes was almost the same.

The second case relates to the comparison of episodes for slow gas test PN086 and fast gas test PN051, the dry densities of which were 1470 kg/m^3 and 1460 kg/m^3, respectively (Figure 2.208). Once again, the two tests evinced a very similar evolution, and the duration of the episodes was almost identical. The higher gas flow rates in the fast tests (PN047 and PN051) were due to the much higher gas injection pressure. In general, the slow gas tests and fast gas tests were comparable, and it is clear that the magnitude of the gas injection pressure does not affect the gas breakthrough episode pattern.

2.7.5.4. Comparison with the UJV Řež measurements

The similar experimental programme was followed, and a very similar testing setup was used, by the ÚJV Řež team. Therefore, it was decided to compare the results obtained from the two laboratories. The

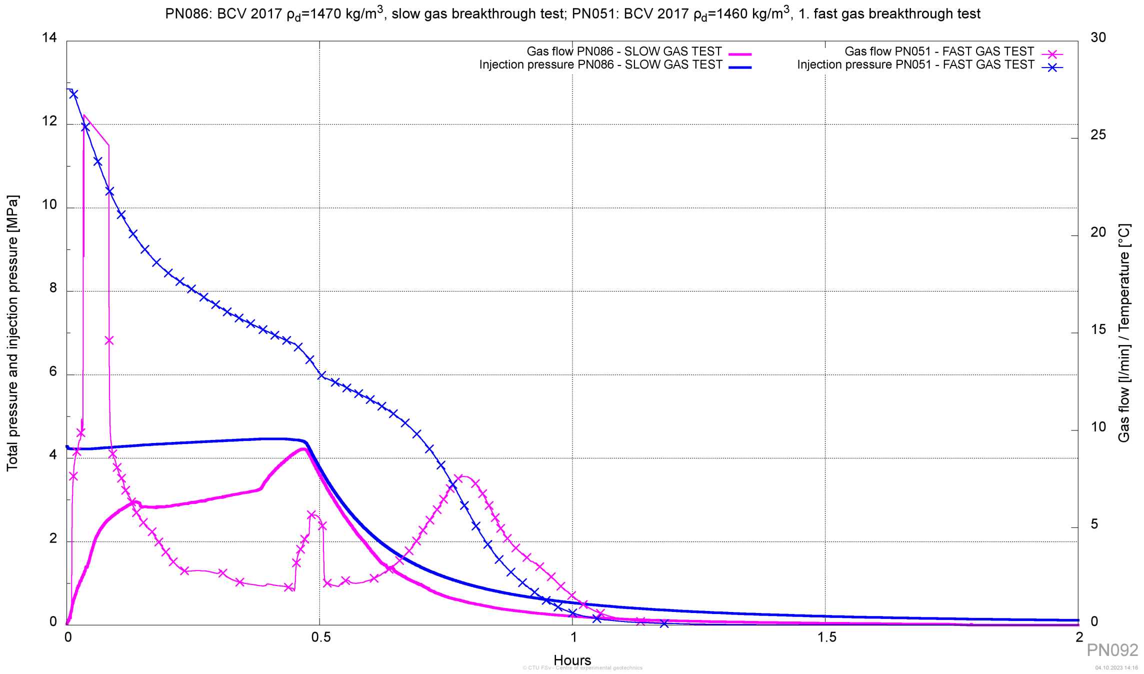

Figure 2.208: Comparison of the gas breakthrough episodes of slow gas test PN086 and fast gas test PN051 with sample dry densities of 1470 kg/m^3 and 1460 kg/m^3, respectively

results of the comparison of the gas breakthrough pressure values (Figure 2.209) revealed that the gas breakthrough pressure values obtained from the hydrogen gas tests (blue triangles in the Figure) and the values from the tests with air (red triangles in the Figure) as the injection gas evinced no significant differences with respect to any of the samples with comparable dry densities. This suggests that the type of gas injected into the sample does not influence the gas breakthrough pressure of the material.

The gas breakthrough pressure results obtained by the ÚJV Řež team usually corresponded to the mean values of the swelling pressure for BCV bentonite. In this case, the swelling ability of the sample and the total pressure were not measured.

The gas breakthrough pressure results determined by the CTU laboratory team were either the same as, or exceeded, the measured axial total pressure. The comparison of the gas breakthrough pressure with the theoretical swelling pressure for a given dry density (Figure 2.209) revealed that the CTU gas breakthrough pressure results were closer to the upper limit of the swelling pressure range. Since the total stress of the test samples was not measured by the ÚJV Řež team, it is not possible to explain this small deviation. In general, the gas breakthrough pressure was higher than the axial total pressure or equal to the theoretical average of the swelling pressure.

2.7.6. Summary

An experimental study was conducted with the objective of investigating the gas breakthrough behaviour of samples of Ca-Mg BCV bentonite with varying dry densities. The purpose of the experiments, which were performed over a period of several years, was to form an understanding of the mechanism involved during slow gas pressure testing and to analyse the parameters that influence the occurrence of breakthrough events. The research was conducted employing a systematic approach and covered bentonite samples with dry densities ranging from 1250 kg/m^3 to 1470 kg/m^3.

The experiments were classified as successful and unsuccessful (attributed to technical issues that required modifications to the experimental setup). Successful breakthrough events were observed when the gas injection pressure exceeded the measured total pressure. The breakthrough pressure was found to

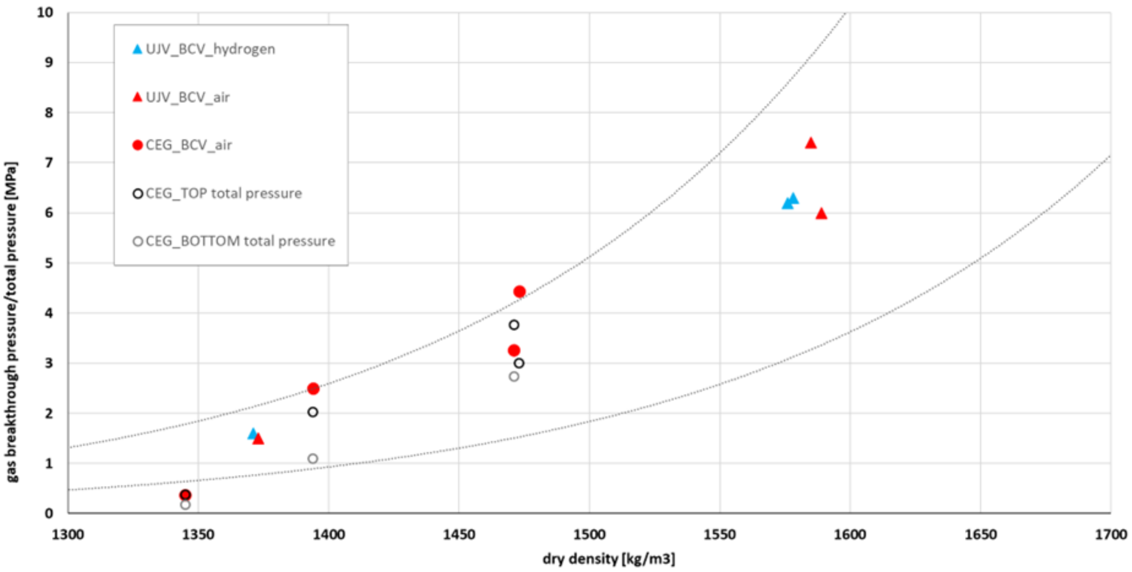

Figure 2.209: Comparison of the gas breakthrough pressure results obtained from the tests at the CTU (CEG) and ÚJV Řež laboratories for BCV bentonite. The dotted lines indicate the swelling pressure range of the BCV material for a given dry density

be dependent on the dry density of the sample, thus indicating a correlation between the two parameters. Moreover, a comparison with the results obtained at the ÚJV Řež laboratory revealed consistent breakthrough pressure values regardless of the type of the injected gas (hydrogen or air) for samples with similar dry densities.

An evaluation of the breakthrough episodes was performed, which included the analysis of their duration, gas flow rates and development patterns. It was observed that the breakthrough episodes varied considerably depending on the dry density and injection point. The comparison of the slow and fast gas tests revealed similarities in terms of the evolution patterns of the breakthrough episodes, thus suggesting that the magnitude of the gas injection pressure does not significantly influence the nature of the breakthrough episode.

In summary, this study involved a comprehensive investigation into the gas breakthrough behaviour of BCV bentonite samples. Via the consideration of variations in the dry density, injection point and type of gas injected, the research succeeded in its aim of enhancing the understanding of gas flow in this type of bentonite. It is anticipated that the findings will contribute to the advancement of research into, and engineering applications related to, the transport of gases in bentonite.

2.7.7. Key learning points

2.7.7.1. New knowledge acquired

By means of the slow gas testing of BCV bentonite samples, we determined the conditions for advective gas flow through this type of bentonite. We already know that Czech Ca-Mg bentonite evinces similar behaviour to bentonites tested in other countries (Mx-80, GMZ) in terms of gas permeability. The formation of dilatant pathways via gas-exerted pressure occurs following the exceeding of the measured axial total stress, which is related to the swelling pressure of the material.

In all cases, the breakthrough pressure was within the swelling pressure range for a given sample dry density. The tests indicated that the source of gas injection (tests employing an injection needle as opposed to tests involving gas injection through the sintered plate) exerts no influence on the breakthrough pressure value. However, the pattern of the test involving the injection of the gas into the centre of the sample and injection from the bottom of the sample differed.

2.7.7.2. Impact of the acquired knowledge

The results obtained from the conducted experiments fully met the objectives set at the beginning of the project. The aim was to form an understanding of the various processes related to the entry and flow of gases through bentonite barriers. The investigation of gas pressure, which leads to gas breakthrough in relation to the swelling pressure and the associated development of total pressure can be considered successful. The findings obtained will contribute significantly to enhancing the understanding of the mechanism of gas transport through bentonite barriers and represent a step forward in the overall research of Czech BCV bentonite. BCV behaves in a similar way to most of the other bentonites (e.g. MX-80, GMZ) investigated in terms of their use in the deep disposal of radioactive waste, the study of which abroad served to inspire the research and the results presented in this report.

2.7.7.3. Remaining knowledge gaps

From the results gained from the experimental testing, and based on discussions with experts in the field, several small improvements were suggested to better understanding gas transport through the bentonite barrier. When comparing breakthrough pressure and total pressure, we observed that it would be useful to monitor the evolution of horizontal total pressure stress during the slow gas test. The knowledge gained would help to better explain how the dilatant pathway formation occurs.

Another knowledge gap is the influence of the interface. We know from various studies (Gutiérrez-Rodrigo, 2021; Liu et al, 2014) that gas often passes at the interface between the bentonite and the test cell during laboratory tests. During CTU testing, post mortem visual analysis was not performed on the bentonite samples, so it cannot be determined where the gas really passed through. To clear out this issue, it is recommended that further gas testing is carried out together with visual analyses (CT scanning). Other solution could be using a guard ring to monitor for side wall flow during gas testing.

As a first step for bentonite gas permeability testing, laboratory testing is ideal. However, we face the limitations of scale and the influence of the test cell on the progress of the tests. The next step should be laboratory verification of the measured results at medium scale and further in-situ conditions.

2.7.7.4. Recommendations for the future

As mentioned in the previous paragraph, the most significant challenge and the next proposed work should be the up-scaling of small-scale laboratory experiments. Up-scaling to medium scale is proposed and subsequently the knowledge generated should be used to design and perform experiments in in-situ conditions and at large scale.

References

Norris, S. (2013). Synthesis Report: Updated Treatment of Gas Generation and Migration in the Safety Case: FORGE Report D31.5R. BGS.

SÚRAO. (c2023). Deep geological repository. SÚRAO. Retrieved December 11, 2023, from https://www.surao.cz/en/de geological-repository/

Liu, J. F., Davy, C. A., Talandier, J., & Skoczylas, F. (2014). Effect of gas pressure on the sealing efficiency of compacted bentonite–sand plugs. Journal of Contaminant Hydrology, 170, 10-27. https://doi.org/10.1016/j.jconhyd.2

Hausmannová, L. (2017). The influence of water pressure on the hydraulic conductivity and swelling pressure of Czech bentonites [dissertation thesis]. Czech Technical University in Prague, Faculty of Civil Engineering.

Gutiérrez-Rodrigo, V., Martín, P. L., & Villar, M. V. (2021). Effect of interfaces on gas breaktrough pressure in compacted bentonite used as engineered barrier for radioactive waste disposal. Process Safety and

Environmental Protection, 149, 244-257. https://doi.org/10.1016/j.psep.2020.10.053

Levasseur, S., Collin, F., Daniels, K., Dymitrowska, M., Harrington, J., Jacops, E., Kolditz, O., Marschall, P., Norris, S., Sillen, X., Talandier, J., Truche, L., & Wendling, J. (2020). Initial State-of-the-Art on Gas Transport in Clayey Materials: Report, Mechanistic understanding of gas transport in clay materials (1st ed.). ONDRAF/NIRAS.

.

ÚJV Řež a.s. / SÚRAO

2.8. Gas breakthrough experiments on different types of bentonites (ÚJV Řež a.s. / SÚRAO)

2.8.1. Introduction & Objectives

The Czech deep geological repository programme anticipates the use of steel-based waste disposal packages without a copper outer layer (SÚRAO, 2023). Therefore, the formation of gases via corrosion processes is of particular importance. The Czech repository will be situated in crystalline rocks, a factor which increases the demands that will be placed on the bentonite barriers. The concept also assumes the use of local bentonites; therefore, one of the long-term objectives concerning the development of the engineered barrier system is to verify the properties and demonstrate the suitability of Czech Ca-Mg bentonite (BCV) for barrier purposes. The ÚJV experimental programme in Task 2 is serving to complement the other activities conducted by the Czech consortium as part of the overall project (CTU programme in Task 2 and Task 3).

The aim of the research is to conduct and subsequently evaluate the gas pressure testing (breakthrough testing) of three types of bentonites: BCV, MX-80 and Kunipia in order to compare Czech BCV bentonite with the bentonite that is most commonly used abroad (MX-80). Moreover, the migration of hydrogen and air through the bentonite samples is studied applying injection pressures that are lower than their respective theoretical swelling pressures.

Prior to the experimental stage, it was necessary to obtain information on the swelling pressures and specific densities of all three types of bentonite; this information was adopted from previously conducted studies. It was necessary to determine the natural water content of each of the materials prior to the preparation of the samples since this parameter varies according to the storage conditions. The experiment commenced with the preparation of the BCV bentonite samples.

The preparation of the samples commenced once the above parameters had been determined. The experimental set-ups for the study of saturation processes and the breakthrough experiments were assembled at the same time.

The bentonite samples were prepared by means of direct compaction according to the target dry density, and the dimensions corresponded to the size of the experimental cell: 3 cm in diameter and 1.5 cm in height. Once this process was completed, the samples were saturated with distilled water in two stages, first in a desiccator and subsequently in a permeameter; in both cases the sample was confined. The hydraulic conductivity was determined once the saturation process was completed.

Three samples were prepared for each target dry density (1400 and 1600 kg/m^3); the first sample was used to determine the porosity and water content following saturation while the second and third samples were used for the gas injection tests and for the determination of the porosity and water content following breakthrough.

Hydrogen or air was injected during the breakthrough tests at constant pressure into the inlet of the experimental cells that contained the saturated bentonite samples. The initial injection pressure applied to the bentonite samples was equivalent to 1/3 or 2/3 of the swelling pressure. Following the stabilisation of the volume of gas/water at the outlet of the cells, the injection pressure was increased in increments of 2-3 bar. This process was repeated until breakthrough was achieved.

A second apparatus was subsequently assembled in order to accelerate the experimental work. The initial injection pressure of some of the tests was closer to the swelling pressure for that dry density than in previous experiments. The tests were completed in March 2021.

Since the experiments with MX-80 bentonite lasted for a very long time period (several months), it was decided to set up a third apparatus for the injection of gas into an MX-80 bentonite sample with a dry density of 1600 kg m^{-3} in March 2022.

The experiments with the BCV and MX-80 bentonites were completed on time; however, the experiments with the Kunipia bentonite are still underway and will not form part of this report.

2.8.2. Experimental set-up

2.8.2.1. Description of the permeameter

The permeameter consists of two DGS ELDPC pumps (GDS Instruments, United Kingdom). Each pump has a tank capacity of 200 ml and one of them is connected to the inlet of the stainless-steel cell for the injection of distilled water at a constant pressure. The second pump is connected to the outlet of the cell for the measurement of the volume of water that flows from the bentonite sample under atmospheric pressure (Figure 2.210). All the data is collected via GDSLab v2.5.4.17 software (GDS Instruments, United Kingdom) at 5-minute intervals.

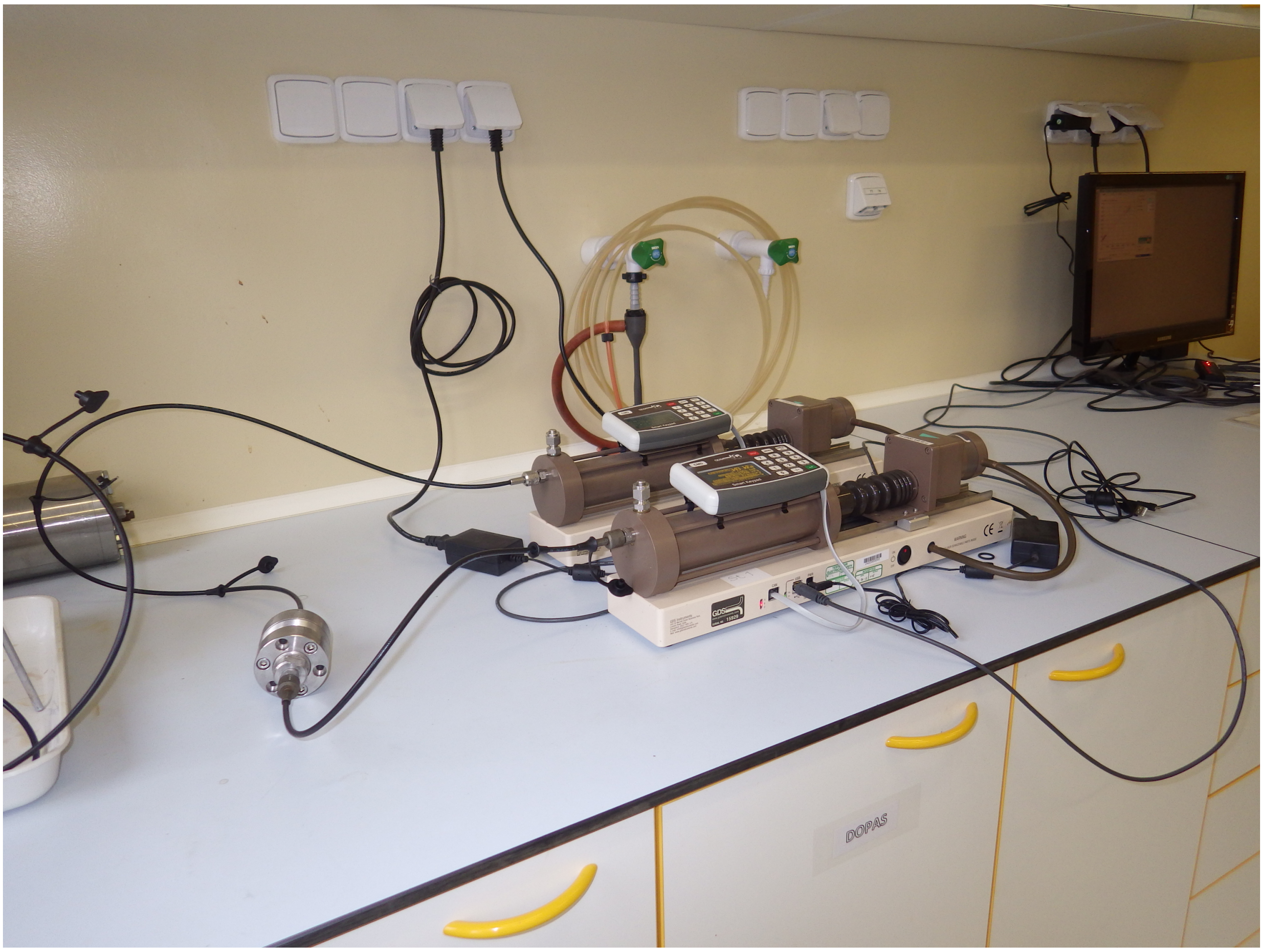

Figure 2.210: Apparatus used for the saturation of the bentonite samples with distilled water

2.8.2.2. Description of the gas injection apparatus

The experimental set-up for the breakthrough experiments using hydrogen is shown in Figure 2.211. The stainless-steel cell is connected to a cylindrical tank (gas exchanger), a pump and a pressure sensor. The inside of the cylindrical tank is divided by a piston and, prior to the start of the gas injection tests, the right side is filled with hydrogen up to a pressure of slightly below the desired injection pressure; once this has been achieved, the tank is disconnected from the external source of hydrogen. The next step comprises the filling of the left side of the tank with air up to the expected injection pressure; in addition, the air helps to maintain the injection pressure at a constant level. During the experiments with air, both sides of the cylindrical tank are filled with air.

The gas injection pressure is measured by a DCP PG1 AK 6287 sensor (pressure range 0-16 MPa; sensor accuracy: ± 0.096 MPa, DataCon, Czech Republic) positioned at the outlet of the gas exchanger. The experimental data is collected every 5 minutes via a DCP PUI 03 5A data-logger (DataCon, Czech Republic).

The volume of fluid that flows through the bentonite sample is measured using a GDS ELDPC pump that is connected to the outlet of the stainless-steel cell. The pump is programmed to measure the volume at atmospheric pressure, and the experimental data is recorded at 5-minute intervals by the GDSLab v2.5.4.17 software (GDS Instruments, United Kingdom).

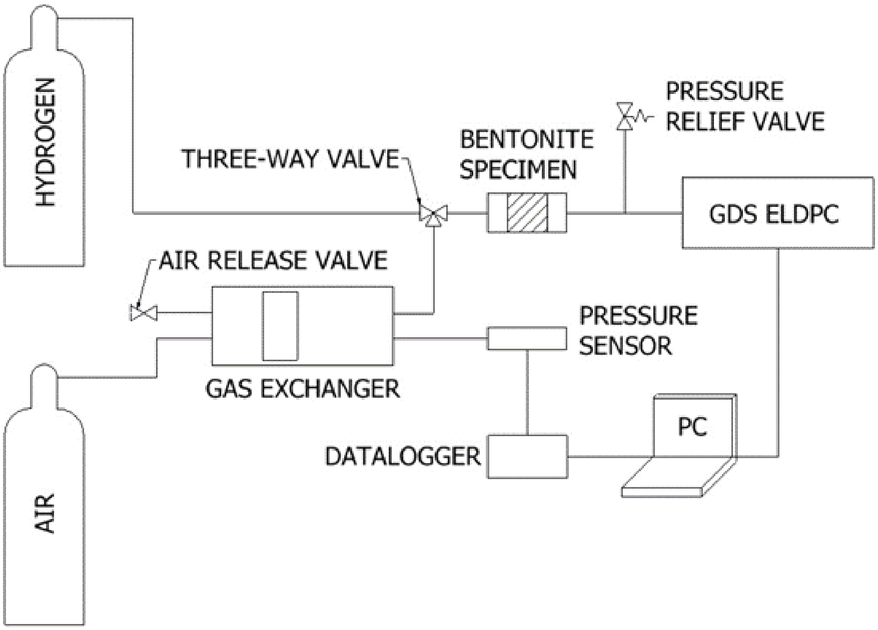

Figure 2.211: Schematic diagram of the apparatus used for the breakthrough experiments

2.8.2.3. Testing fluids

The gases used for the breakthrough experiments comprise hydrogen 5.0 (Linde Gas, Czech Republic) with a purity of $\geq$ 99.999% and compressed air (Linde Gas, Czech Republic) composed of 78.5% N2 and 21.5% O2. The gases were not modified or saturated prior to their use in the experiments.

2.8.3. Material properties (pre-test and post-test characteristics)

2.8.3.1. BCV bentonite

The calcium-magnesium BCV bentonite used in this project was extracted in 2017 from the Černý vrch deposit (KERAMOST a.s., Czech Republic).

The specific density is around 2758 kg m^{-3}. The bulk chemical analysis of the BCV bentonite was performed in the laboratories of Gematest spol. s.r.o. The results are shown in Table 2.68.

Component	% dry wt.
SiO_2	49.75
Al_2O_3	14.80
Fe_2O_3	11.11
TiO_2	3.04
FeO	<0.10
MnO	0.21

Component	% dry wt.
MgO	2.50
CaO	3.10
Na_2O	0.34
K_2O	1.15
P_2O_5	0.86
CO_2	2.29
SO_3 sulphate	0.30
SO_3 total	0.34
H_2O^+	9.71
Total	97.21

Table 2.68: Bulk chemical analysis of Czech BCV bentonite (Červinka et al, 2019)

The semi-quantitative phase analysis of the BCV bentonite was conducted by Červinka et al. (2019). X-ray analyses were performed by three different institutions, i.e. the Institute of Inorganic Chemistry of the Czech Academy of Sciences (Řež), the Czech Geological Survey (Barrandov, Prague), and the Institute of Geology of the Czech Academy of Sciences (Suchdol). The difference in values is due to the different method of determination. The Czech Geological Survey analysed the BCV of bentonite on the <2micrometer fraction. An overview of the results is presented in Table 2.69.

Component	IICCAS, Řež	CGS, Barrandov	IGCAS, Suchdol
Smectite	58.3	86	53,5
K-micas	4.4	N.A.	4
Kaolinite	2.3	1	2.5
SiO_2 phase	8.9	9.5	26.5
Calcite	2.1	2	N.D.
Anatase	4.3	1.5	5.5
Fe oxides, Goethite	10.1	(1-2) [c]	4
Mg-siderite	N.A.	N.D.	2
Ankerite	0.4	N.D.	2
Analcime	0.4	N.D.	N.D.
Amorphous phase	8.8	N.A.	N.A.
Total	100.0	100.0	100.0

Table 2.69: Semiquantitative X-ray powder diffraction results for BCV bentonite: c: the estimate of the amount of goethite was not included in the calculation, N.A: not analysed, N.D: not detected in the bentonite (Červinka et al, 2019)

Červinka et. al (2019) stated that the hydraulic conductivity and swelling pressure of the BCV bentonite (2017) were determined at the CEG CTU. The samples were saturated with distilled water at a constant pressure of 1 MPa. Table 2.70 presents the hydraulic conductivity values depending on the dry density of the samples.

Dry density ρ_d [g.cm^{-3}]	Hydraulic conductivity K [m s^{-1}]
1.391	5.02E^{-13}
1.471	2.26E^{-13}
1.567	1.44E^{-13}

Dry density ρ_d [g.cm^{-3}]	Hydraulic conductivity K [m s^{-1}]
1.633	1.45E^{-13}
1.803	4.55E^{-14}

Table 2.70: Hydraulic conductivity of BCV bentonite 2017 (Červinka et al., 2019)

The graph below shows the swelling pressures obtained in the Czech Republic and published in various reports including Červinka et al. (2019) and Laufek et al. (2021).

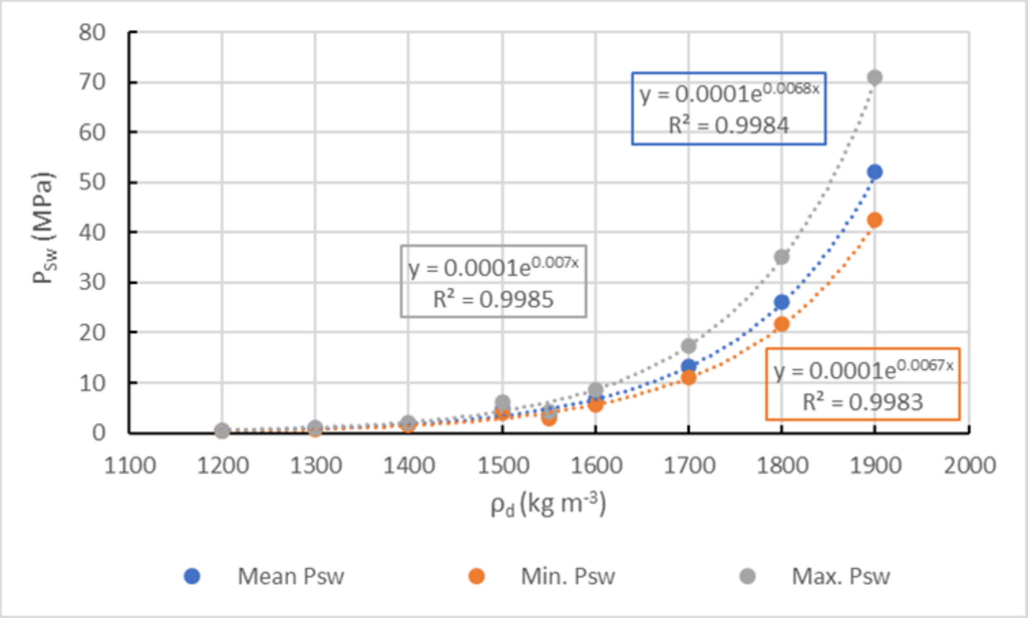

Figure 2.212: Swelling pressures of BCV bentonite

2.8.3.2. MX-80 bentonite

The sodium bentonite used in the experiments was provided by NAGRA (Switzerland) in the form of a mixture of powder and granules, which was homogenised prior to use. The material was subjected to a bulk chemical analysis, the results of which are shown in Table 2.71.

Component	% dry wt.
SiO_2	55.81
Al_2O_3	17.76
Fe_2O_3	3.88
TiO_2	0.15
FeO	0.68
MnO	0.026
MgO	1.30
CaO	2.34
Na_2O	1.25
K_2O	0.56
P_2O_5	0.23
CO_2	0.43
SO_3 sulphate	0.18

Component	% dry wt.

Table 2.71: Bulk chemical analysis of MX-80 sodium bentonite (Dobrev et al., 2017)

The swelling pressure of MX-80 bentonite varies according to different authors. The data published by Karland et al. (2006) and Villar (2005) is shown in the graph below.

2.8.3.3. Natural water content of the bentonites

The natural water content of the bentonites was determined prior to the preparation of the samples.

The determination of the natural water content was carried out according to the Czech version of technical specification CEN ISO/TS 17892-1:2004. Five samples of bentonite powder (each of 2 grams) were dried at 105 ℃ for 24 hours. The weight data was then used to calculate the water content of the samples. The natural water contents of the BCV and MX-80 bentonites are shown in Table 2.72.

Bentonite	Natural water content (%)
BCV	12.3
MX-80	6.5

Table 2.72: Natural water contents of the bentonites used in the ÚJV experiments

2.8.4. Testing protocol

2.8.4.1. Preparation of the bentonite samples

A total of twelve bentonite samples (6 BCV bentonite, 6 MX-80 bentonite) with two target dry densities (1400, 1600 kg m^{-3}) were prepared in cells with dimensions of 3 cm in diameter and 1.5 cm in height.

The stainless-steel cells comprise a central ring (the sample holder) containing an inner ring made of a carbon composite and two lids that cover the tops and bottoms of the samples. Each lid contains a filter support made of a mix of polyether ether ketone (PEEK) and carbon fibres, and two thin stainless-steel disc filters, one made from a fine fabric mesh (322x1900) and the other from a coarser fabric mesh (24x10). The filters are fitted into the filter supports using rubber O-rings (Figure 2.214)

Once the central ring and the bottom lid have been assembled, the bentonite powder is poured into the ring and the cell is placed under a MEGA 11-300 DM1S hydraulic press (Form+Test Seidner+Co GmbH, Germany). The powder is pressed from one side only, i.e., from top to bottom. Once the bentonite powder has been pressed to the desired target dry density, the cell is removed from the hydraulic press and the upper lid is bolted down on top of the sample (Figure 2.215).

2.8.4.2. Hydraulic conductivity of the bentonite samples

All the bentonite samples were saturated with distilled water in two stages, first in a desiccator and then in a permeameter. The second device was used to complete the saturation process and to determine the hydraulic conductivity of the samples.

The hydraulic conductivity of the bentonite samples was determined at various pressure levels depending on the dry density of the sample and at a constant temperature of around 20 ℃. The increase in the saturation pressure depended on the fluctuations in the water flow during the saturation process.

The volume of water was measured at the inlets and outlets of the sample cells via the GDSLab v2.5.4.17 program (GDS Instruments, United Kingdom) that served to record the increase in the water volume over time at the inlets and outlets of the cells in the form of two lines plotted on a graph. Whenever the plotted

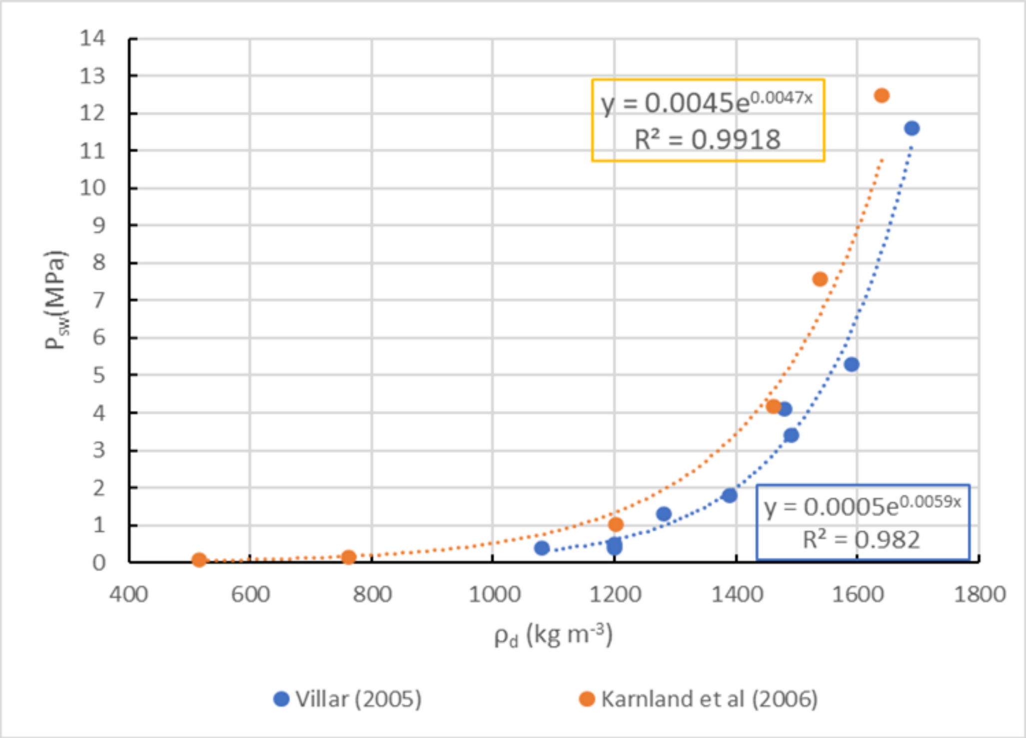

Figure 2.213: Swelling pressures of MX-80 bentonite

Figure 2.214: Open stainless-steel cell

lines were not straight and parallel to each other, the water injection pressure was increased (see Chapter 2.8.2.1). This approach thus allowed for the acceleration of the saturation process.

2.8.4.3. Water content and porosity of the bentonite samples

The water content, density and porosity of the bentonite samples were determined once the bentonite sample was dismantled after the saturation process and after the gas injection tests.

For each series of samples (3 samples with the same target dry densities, i.e., 1400 and 1600 kg m^{-3}), one sample was dismantled immediately following the completion of the saturation process and used for

Figure 2.215: BCV bentonite sample inside the stainless-steel cell

comparison with the samples that were subjected to gas injection testing. The comparison served to provide information on whether desaturation had taken place within the samples subjected to gas injection testing.

Once the bentonite samples had been dismantled, they were cut into slices with a thickness of 0.075 cm. After opening the cells, the central ring that contained the bentonite sample was placed in a device that was used to gradually push the sample out of the ring (in steps of 0.075 cm). The protruding part was then manually removed using a metal blade. Each slice and any crumbs were immediately transferred into an Eppendorf vial so as to avoid the loss of moisture. The slices were then weighed using AND GH-252 (A&D Instruments Ltd, United Kingdom) digital scales before and after being dried at 105 °C for 1 day. The same procedure was followed for the samples used in the gas injection tests. The weight data was then used to calculate the water content and the porosity of the bentonite samples, the latter being calculated as the volume of water in the bentonite sample divided by its total volume. It was observed that the water content did not vary significantly along the lengths of the bentonite samples, the only exceptions being the slices taken from the tops and the bottoms of the samples, where the water content was observed to be slightly higher.

2.8.4.4. Gas injection experiments

The gas injection tests involve the application of a constant gas injection pressure into the bentonite samples at room temperature (around 20 °C). Originally, it was estimated that the initial injection pressure would be at least 1/3 or 2/3 of the theoretical swelling pressure of the specific material and its target dry density. The injection pressure was subsequently increased in steps of 2-3 bar following the stabilisation of the liquid volume that flowed through the bentonite samples. The experiments were terminated once the breakthrough pressure was attained. The bentonite samples were subsequently removed from the stainless-steel cells and dried at 105 °C for 24 hours prior to determining their water content and porosity.

An overview of the experimental work on the BCV and MX-80 bentonite samples is provided in the Table 2.73 below.

Bentonite	Sample	Saturation in desiccator and permeameter	H_2 injection test	Air injection test	Determination of water content after saturation	Determination of water content after gas test
BCV	1400_1	Finished	Not planned	Not planned	Finished	Not planned
	1400_2	Finished	Finished	Not planned	Not planned	Finished
	1400_3	Finished	Not planned	Finished	Not planned	Finished

Bentonite	Sample	Saturation in desiccator and permeameter	H_2 injection test	Air injection test	Determination of water content after saturation	Determination of water content after gas test
MX-80	1600_1	Finished	Not planned	Not planned	Finished	Not planned
	1600_2	Finished	Finished	Not planned	Not planned	Finished
	1600_3	Finished	Not planned	Finished	Not planned	Finished
	1600_2_R	Finished	Finished	Not planed	Not planned	Finished
	1600_3_R	Finished	Not planned	Finished	Not planned	Finished
	1400_1	Finished	Not planned	Not planned	Finished	Not planned
	1400_2	Finished	Finished	Not planned	Not planned	Finished
	1400_3	Finished	Not planned	Finished	Not planned	Finished
	1600_1	Finished	Not planned	Not planned	Finished	Not planned
	1600_2	Finished	Finished	Not planned	Not planned	Finished
	1600_3	Finished	Not planned	Planned	Not planned	Finished

Table 2.73: Overview of the experimental tests on the BCV and MX-80 bentonite samples

2.8.5. Results

2.8.5.1. Hydraulic conductivity of the bentonite samples

Table 2.74 presents the hydraulic conductivities of the samples with two target dry densities (1400 kg m^{-3} and 1600 kg m^{-3}). The hydraulic conductivities decreased with the increasing target dry densities of the samples.

Bentonite	Sample	Target dry density ρ_{td} [kg m^{-3}]	Hydraulic conductivity K [m s^{-1}]	Saturation pressure P [MPa]
BCV	1400_1,	1400	5 x 10^{-13}	0.8
	1400_2,		5 x 10^{-13}	3
	1400_3		4.7 x 10^{-13}	2
	1600_1,	1600	1.1 x 10^{-13}	10
	1600_2,		1 x 10^{-13}	10
	1600_3		1.2 x 10^{-13}	10
	1600_2_R		9.9 x 10^{-14}	10
	1600_3_R		9 x 10^{-14}	10
MX-80	1400_1,	1400	1.9 x 10^{-13}	3
	1400_2,		1.6 x 10^{-13}	3
	1400_3		1.9 x 10^{-13}	5
	1600_1,	1600	7.4 x 10^{-14}	7
	1600_2,		7.3 x 10^{-14}	6
	1600_3		8.5 x 10^{-14}	7

Table 2.74: Hydraulic conductivity of the BCV and MX-80 bentonite samples

2.8.5.2. Water content and porosity of the bentonite samples

The dry density values were determined for each sample during their preparation (based on their known volumes and the water contents of the powder material); the water content and porosity values were determined following the dismantling of the cells once the saturation process or the gas injection testing were completed (Table 2.75).

Bentonite	Sample	Dry density [kg m^{-3}]	Water content [%]	Porosity [-]
BCV	1400_1	1378	37.8	0.5
	1400_2	1371	37.8	0.5
	1400_3	1373	37.1	0.5
	1600_1	1574	29.1	0.4
	1600_2	1578	29.6	0.4
	1600_3	1589	29.6	0.4
	1600_2_R	1576	28,7	0.4
	1600_3_R	1585	27.3	0.4
MX-80	1400_1	1419	36.5	0.5
	1400_2	1391	36.6	0.5
	1400_3	1389	36.9	0.5
	1600_1	1598	28.2	0.4
	1600_2	1595	27.4	0.4
	1600_3	1585	28.9	0.4

Table 2.75: Dry density, water content and porosity of the bentonite samples

2.8.5.3. Gas injection experiments results

Four of the six BCV bentonite samples have been subjected to hydrogen or air injection testing to date. In April 2020, the first hydrogen injection test commenced of a BCV bentonite sample with a target dry density of 1400 kg m^{-3} (BCV 1400_2). Assuming that the theoretical swelling pressure of this material at such a target dry density was around 1.3 MPa, it was decided that the initial hydrogen injection pressure would be set at around 6 bar (0.6 MPa). Breakthrough occurred at 1.6 MPa after 83 days (Figure 2.216). At the beginning of the test, the injection pressure fluctuated before attaining relative stability, which may have been caused by the initial volume changes between the hydrogen and the air inside the gas exchanger.

The second test was carried out by injecting air into a BCV bentonite sample of the same target dry density (BCV 1400_3); the initial injection pressure was the same as in the test using hydrogen. Breakthrough occurred after 217 days (around 7 months) at 1.7 MPa. Figure 2.217 illustrates the evolution of the total volume in the output pump before and after breakthrough. Figure 2.218 serves for the more detailed observation of the progressive increase in the volume measured at the outlet of the experimental cell prior to breakthrough.

The comparison of the hydrogen and air injection tests revealed that the volume measured in the output pump increased more steadily following the injection of air. Hence, the air injection pressure was not increased for several months, which prolonged the duration of the experiment. Moreover, it was observed that it was more difficult to maintain a constant injection pressure during the experiments using hydrogen as a result of the occurrence of small leakages from the apparatus during the testing process.

Following the realisation that the gas injection experiments could continue over several months, it was decided to assemble a second apparatus for the breakthrough experiments in order to speed up the experimental research. The third breakthrough test was performed using this apparatus. Hydrogen was injected into a saturated BCV bentonite sample with a target dry density of 1600 kg m^{-3} (BCV 1600_2). The initial injection pressure was set at 6 MPa, which, compared to the previous tests, is closer to the theoretical swelling pressure (around 6.8 MPa) of this material at this target dry density. This approach was adopted so as to avoid more delays to the project schedule. The test lasted 29 days and breakthrough occurred at 6.3 MPa (Figure 2.219, Figure 2.220).

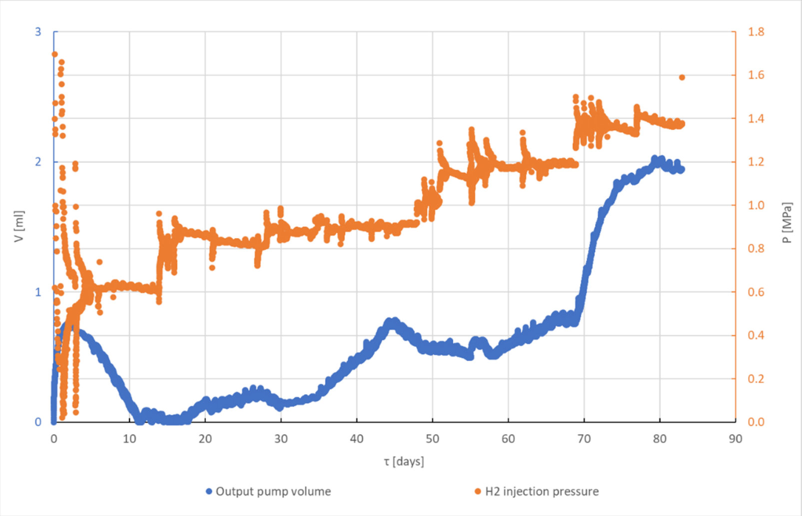

Figure 2.216: Hydrogen injection test on BCV bentonite sample 1400_2

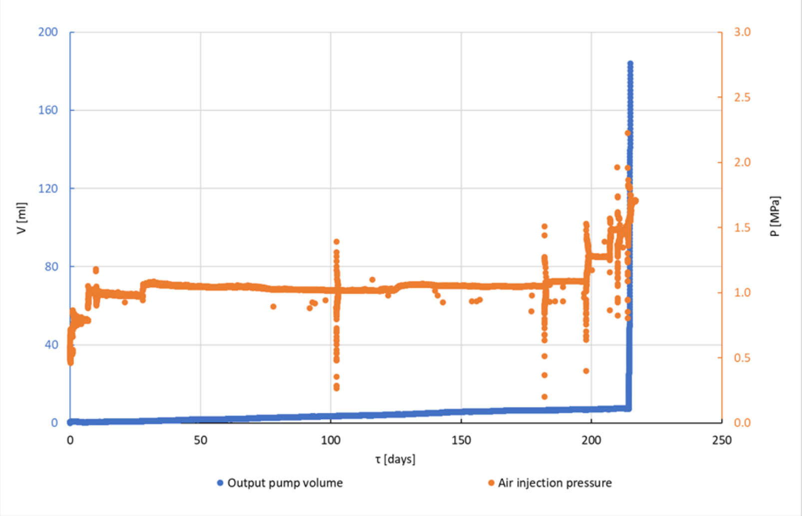

Figure 2.217: Air injection test on BCV bentonite sample 1400_3

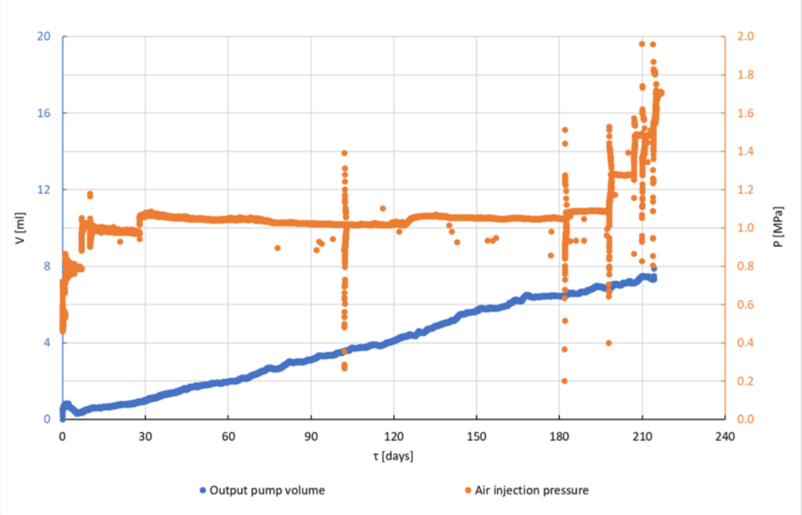

Figure 2.218: Air injection test on BCV bentonite sample 1400_3 prior to breakthrough

The fourth test was carried out by injecting air into a BCV bentonite sample of the same target dry density (BCV 1600_3); the initial injection pressure was the same as in the test using hydrogen. After 10 days, a noticeable decrease was observed in the injection pressure as a result of the depletion of gas in the gas container of the apparatus; the experiment continued once it was refilled. Breakthrough occurred after a total of 11 days at 6 MPa (Figure 2.221, Figure 2.222).

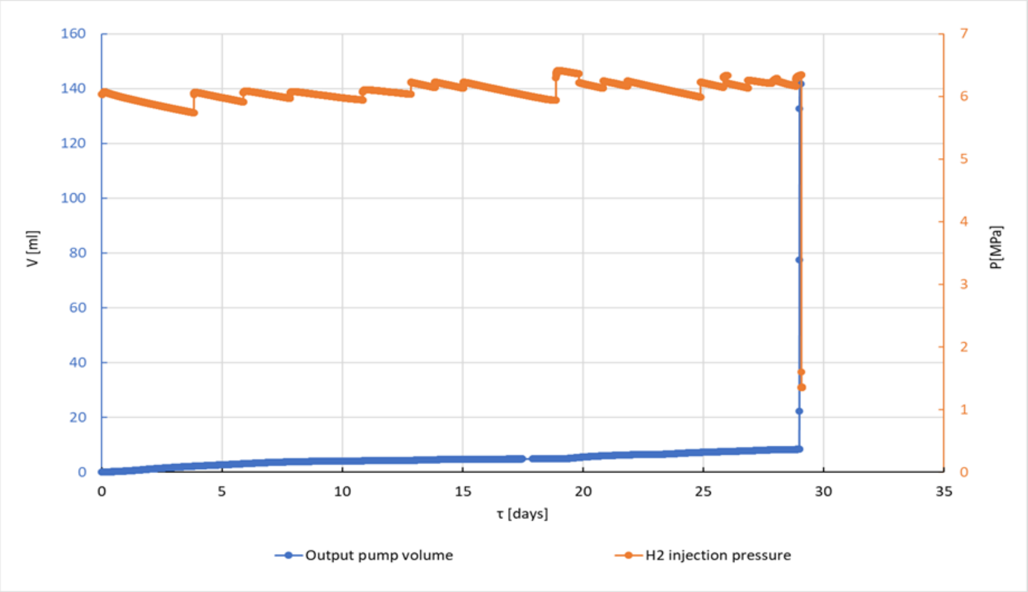

Figure 2.219: Hydrogen injection test on BCV bentonite sample 1600_2

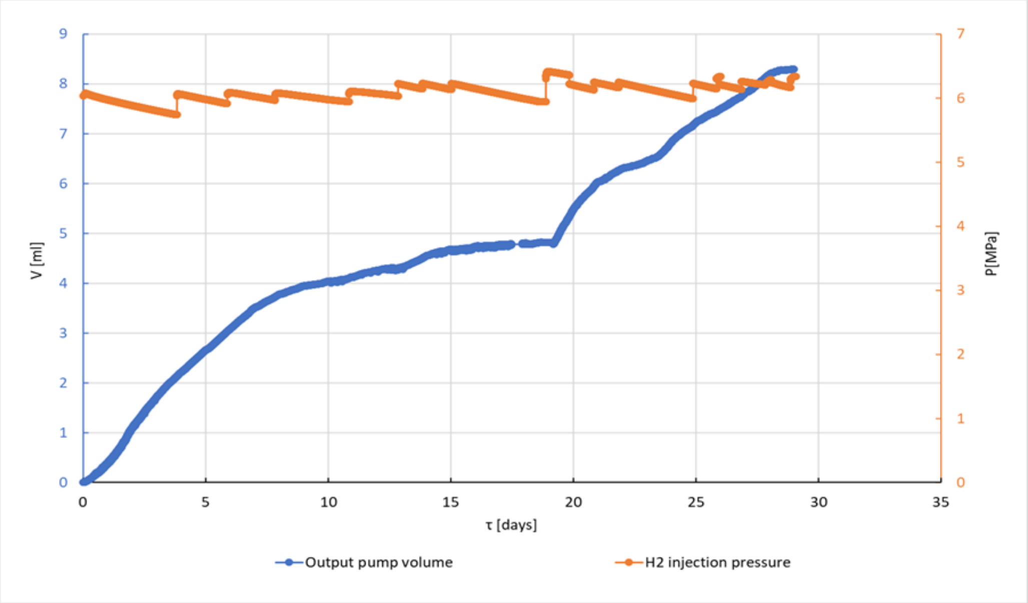

Figure 2.220: Hydrogen injection test on BCV bentonite sample 1600_2 prior to breakthrough

In 2022, the experiments on the BCV bentonite samples with a target dry density of 1600 kg m^{-3} were repeated in order to determine whether breakthrough occurred at the same pressure if the initial injection pressure was lower than in the first experiments. The initial injection pressure for the second set of hydrogen and air injection tests was set at 2 MPa.

The hydrogen experiment (BCV 1600_2_R) lasted for around 5 months (154 days) and breakthrough occurred at 6.2 MPa (Figure 2.223, Figure 2.224), whereas concerning the air injection test (BCV 1600_3_R), breakthrough was observed after almost 8 months (235 days) at 7.4 MPa (Figure 2.225, Figure 2.226).

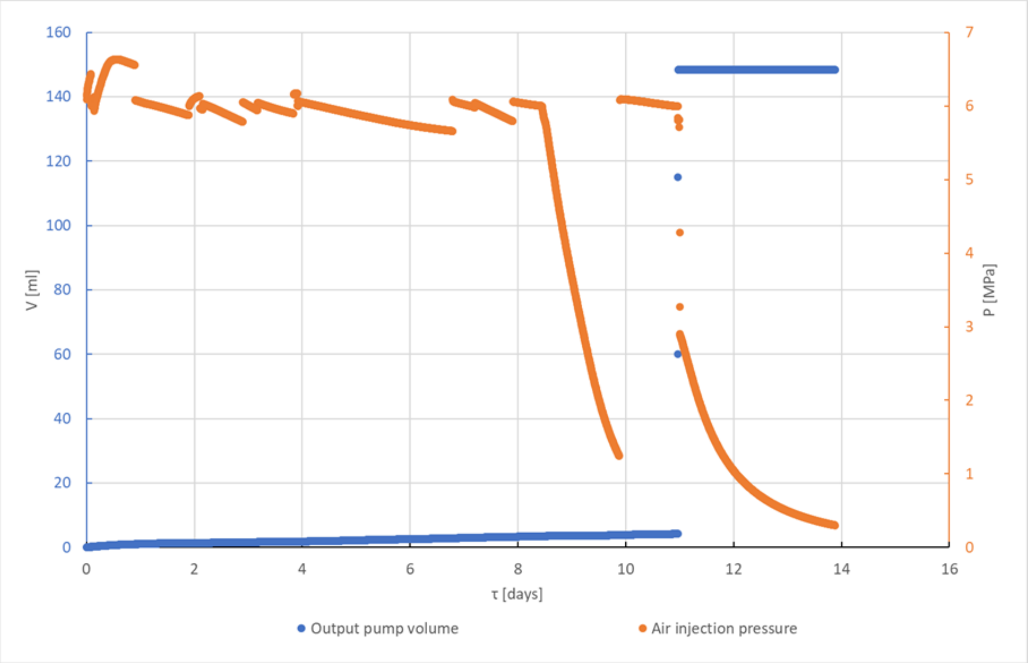

Figure 2.221: Air injection test on BCV bentonite sample 1600_3

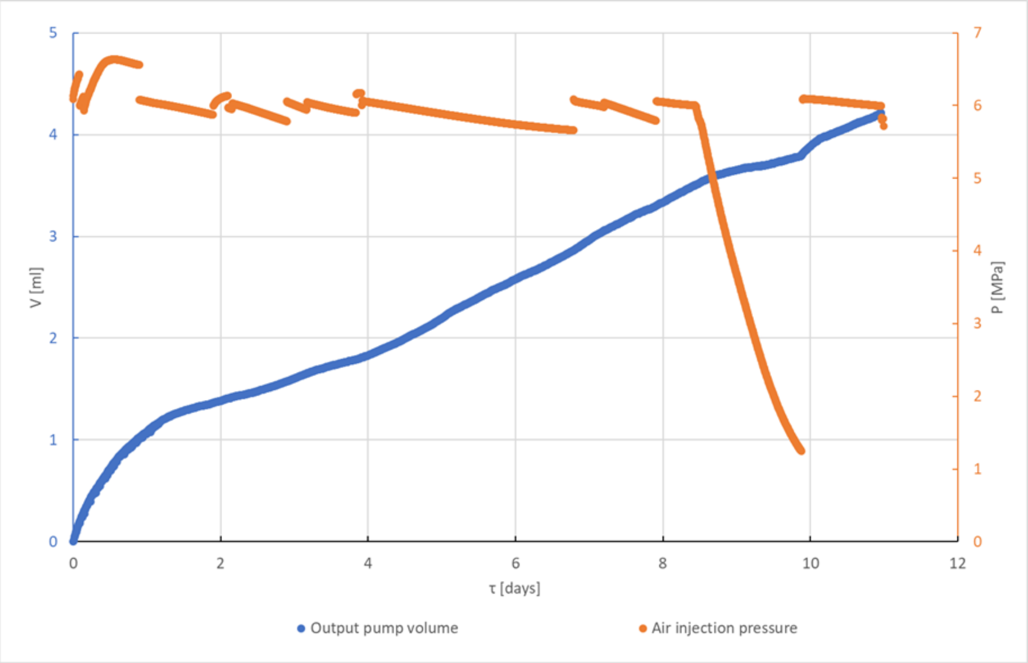

Figure 2.222: Air injection test on BCV bentonite sample 1600_3 prior to breakthrough

The volume of the gas/fluid measured by the pump at the outlets of bentonite samples 1400_2, 1400_3, 1600_2_R and 1600_3_R prior to breakthrough was higher for the air injection experiments than for the hydrogen injection experiments. The only exception was observed in the experiments on bentonite samples 1600_2 and 1600_3, which commenced at a very high initial injection pressure and were conducted over a shorter period than the other experiments.

Prior to the commencement of the MX-80 bentonite gas injection tests, a literature search was performed regarding the theoretical swelling pressures of this material at differing target dry densities. It was observed that the swelling pressures varied depending on the author. According to the extrapolation of data

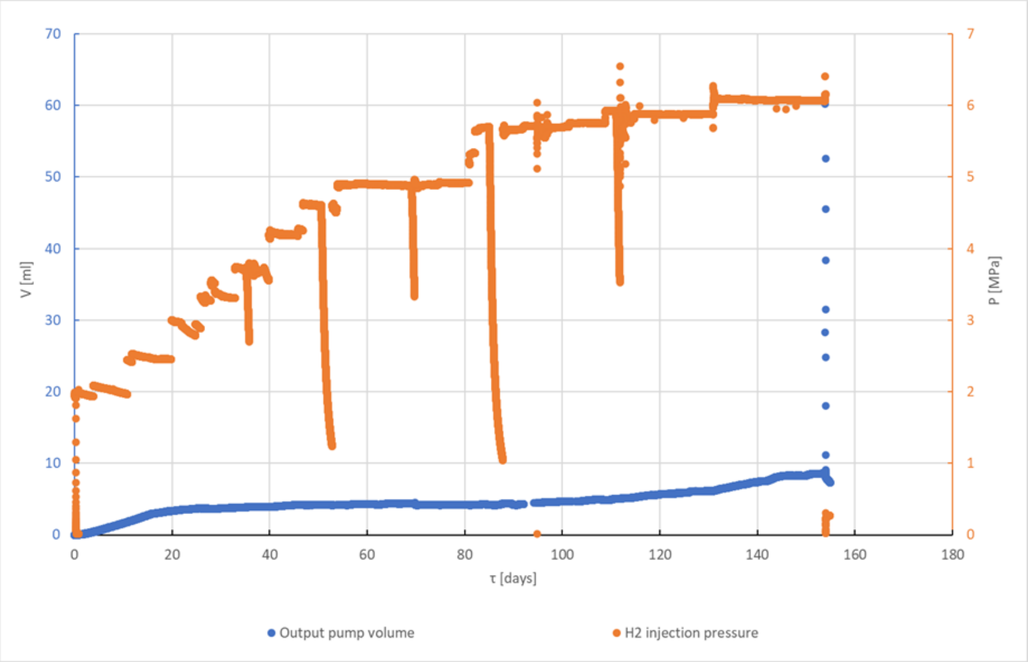

Figure 2.223: Hydrogen injection test on BCV bentonite sample 1600_2_R

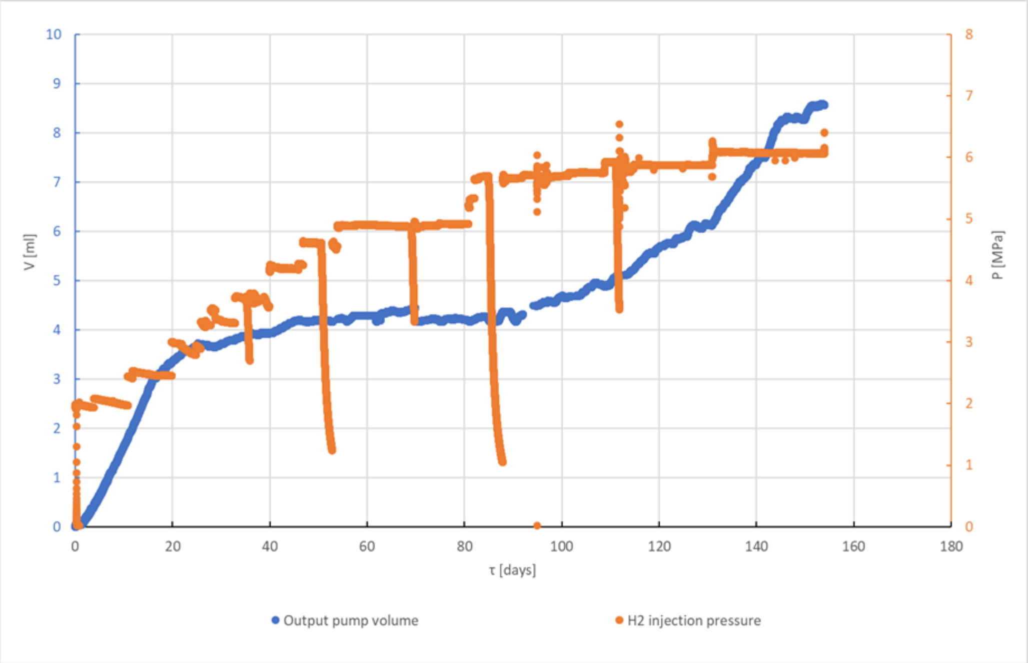

Figure 2.224: Hydrogen injection test on BCV bentonite sample 1600_2_R prior to breakthrough

published by Karnland et al. (2006), the theoretical swelling pressure of a sample with a target dry density of 1400 kg m^{-3} is around 3 MPa, whereas this value is considerably lower (around 1.83 MPa following the extrapolation of the data published by Villar (2005)). Thus, it was decided that the lower swelling pressures would be used to define the initial injection pressure in the hydrogen injection tests. Since the initial injection pressure is considered to be 1/3 of the theoretical pressure, the hydrogen injection tests commenced with an injection pressure of 0.6 MPa.

The first breakthrough experiment on an MX-80 bentonite sample with a target dry density of 1400 kg m^{-3} (MX-80 1400_2, Figure 2.227 and Figure 2.228) commenced in June 2021. The air injection test on a

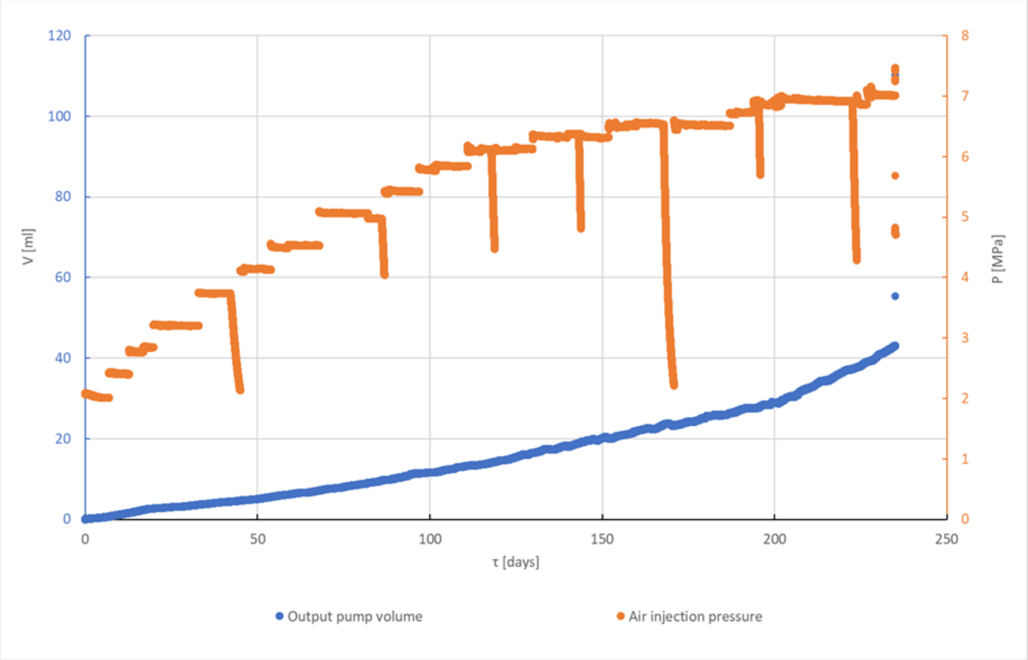

Figure 2.225: Air injection test on BCV bentonite sample 1600_3_R

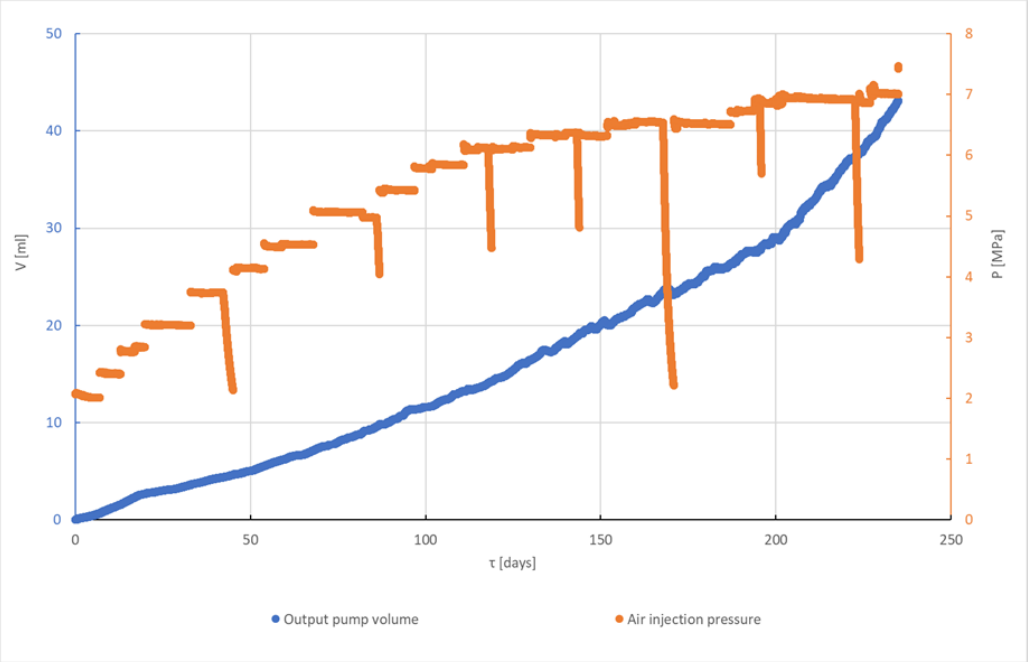

Figure 2.226: Air injection test on BCV bentonite sample 1600_3_R prior to breakthrough

bentonite sample of the same dry density (MX-80 1400_3, Figure 2.229 and Figure 2.230) commenced one month later.

It was observed during the hydrogen experiment that the injection pressure began to oscillate after 208 days; although the cause is uncertain, it was presumed that these abrupt changes were due to technical problems with the pressure sensor. The experiment was terminated after 11 months (341 days) at 3.94 MPa. The air injection test was terminated after 10 months (309 days) at 3.84 MPa. In both cases the breakthrough pressures were slightly above the theoretical swelling pressures determined from the data published by Villar and Karnland.

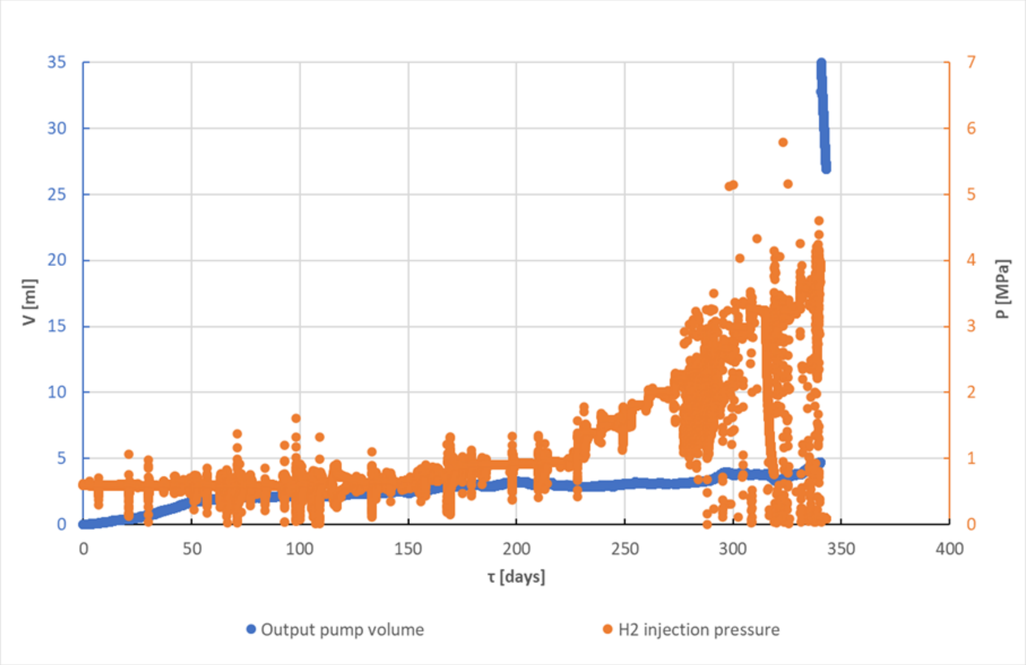

Figure 2.227: Hydrogen injection test on MX-80 bentonite sample 1400_2

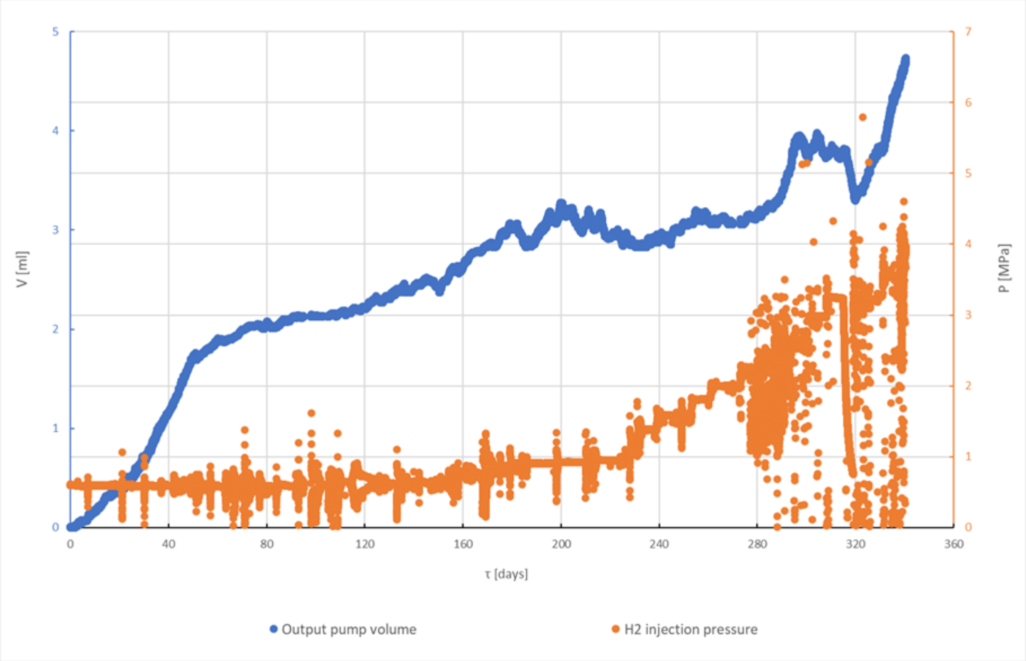

Figure 2.228: Hydrogen injection test on MX-80 bentonite sample 1400_2 prior to breakthrough

In March 2022, a third apparatus was assembled for the injection of hydrogen into a saturated MX-80 bentonite sample with a dry density of 1600 kg m^{-3} (MX-80 1600_2). The swelling pressure of this sample was estimated based on publications by Karnland et al. (2006) and Villar (2005). The swelling pressures were around 8.1 MPa and 6.1 MPa, respectively.

The initial injection pressure of the hydrogen injection test was 2 MPa (1/3 of the swelling pressure estimated from the values published by Villar (2005). The test lasted almost six months (177 days) until breakthrough was observed at 8.5 MPa (Figure 2.231 and Figure 2.232).

The air injection test commenced with an initial injection pressure of 2 MPa and was terminated after 5

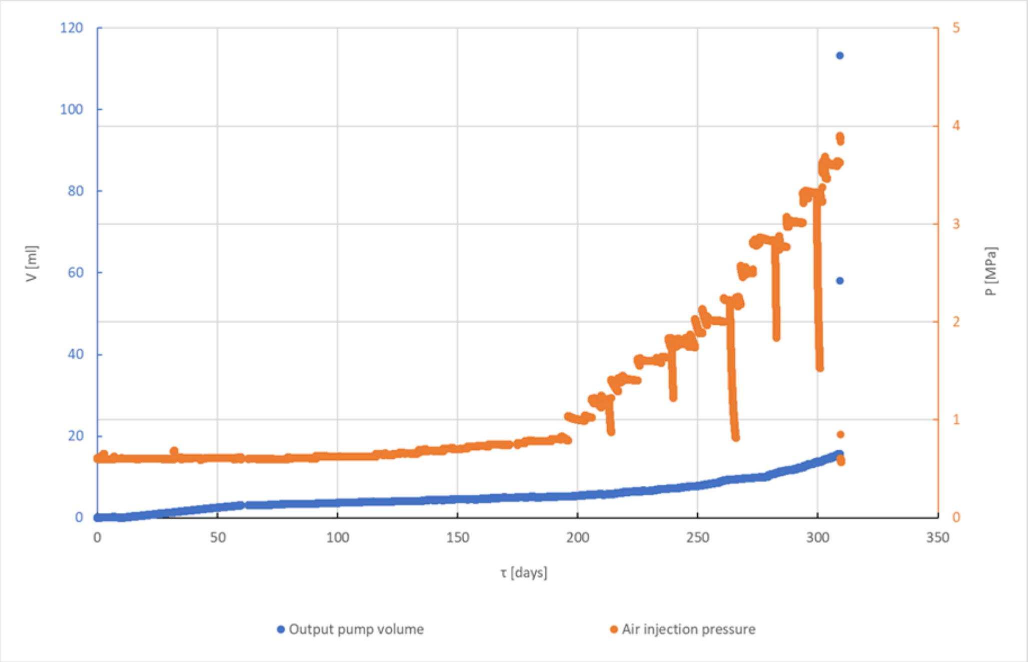

Figure 2.229: Air injection test on MX-80 bentonite sample 1400_3

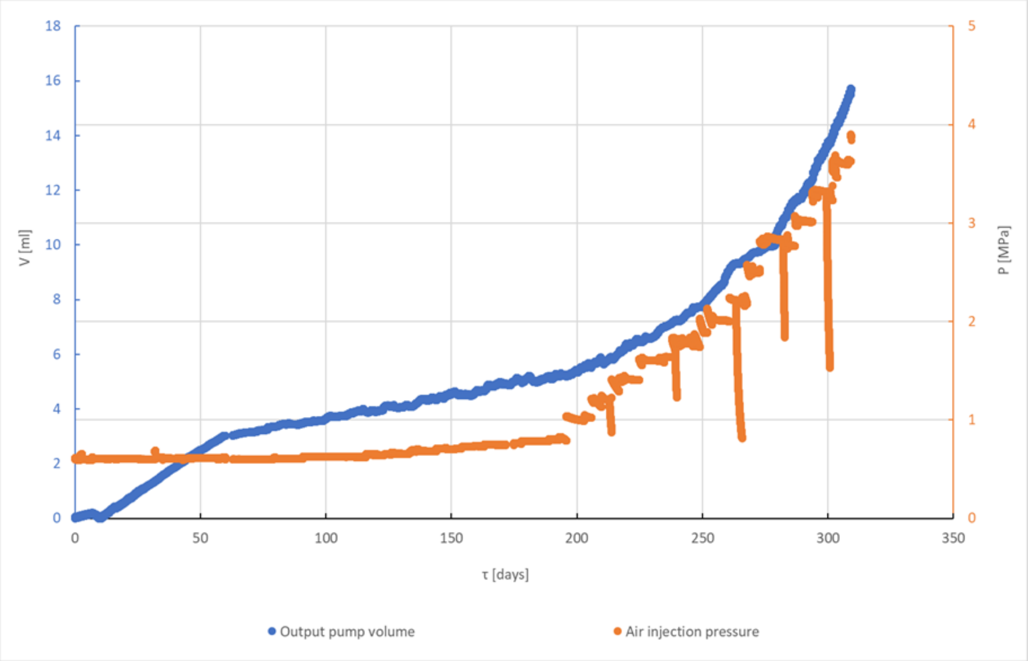

Figure 2.230: Air injection test on MX-80 bentonite sample 1400_3 prior to breakthrough

months (146 days) when breakthrough occurred at 7.2 MPa (Figure 2.233 and Figure 2.234).

The breakthrough pressure in both experiments was close to the theoretical swelling pressure. Moreover, it was observed that concerning the experiment on samples of both dry densities, the cumulative volume of the gas/fluid measured at the outlets of the samples prior to breakthrough was significantly higher in the air injection experiments than in the hydrogen injection experiments.

A further aspect that was observed in most of the experiments concerned a drop in the injection pressure (orange line in the graphs) at various times during the course of the experiments. This was attributed to the depletion of the gas inside the reservoir that was used for the injection of gas into the samples and to maintain a constant injection pressure.

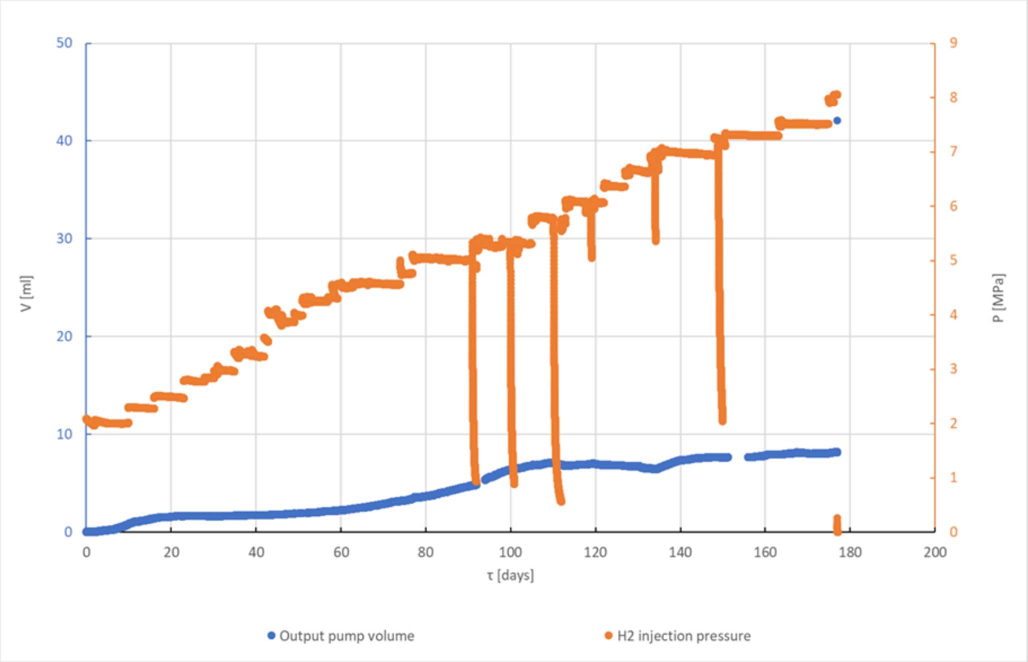

Figure 2.231: Hydrogen injection test on MX-80 bentonite sample 1600_2

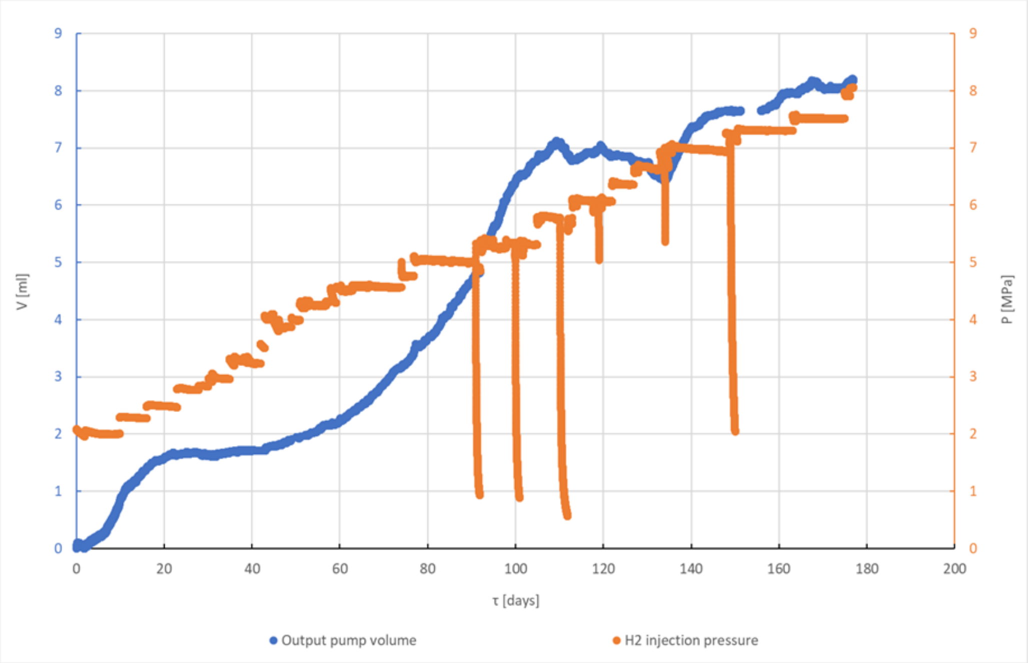

Figure 2.232: Hydrogen injection test on MX-80 bentonite sample 1600_2 prior to breakthrough

1.5.4 Analysis of the breakthrough tests results

A comparison of the breakthrough pressure values and the theoretical swelling pressure of the BCV and MX-80 bentonites is shown in Figure 2.235, Figure 2.236, Figure 2.237, Figure 2.238.

The blue points represent the breakthrough pressures measured during the gas injection tests. The red points represent the theoretical swelling pressures of the BCV bentonite samples according to their dry densities (Červinka et al., 2019 and Laufek et al., 2021). In the case of the MX-80 bentonite tests, the red

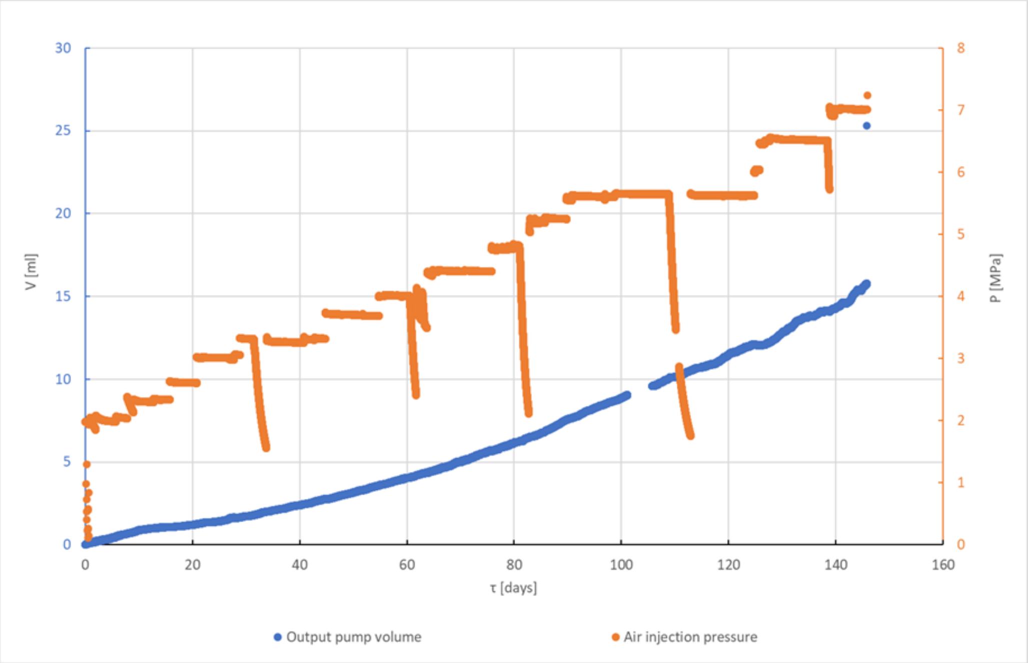

Figure 2.233: Air injection test on MX-80 bentonite sample 1600_3

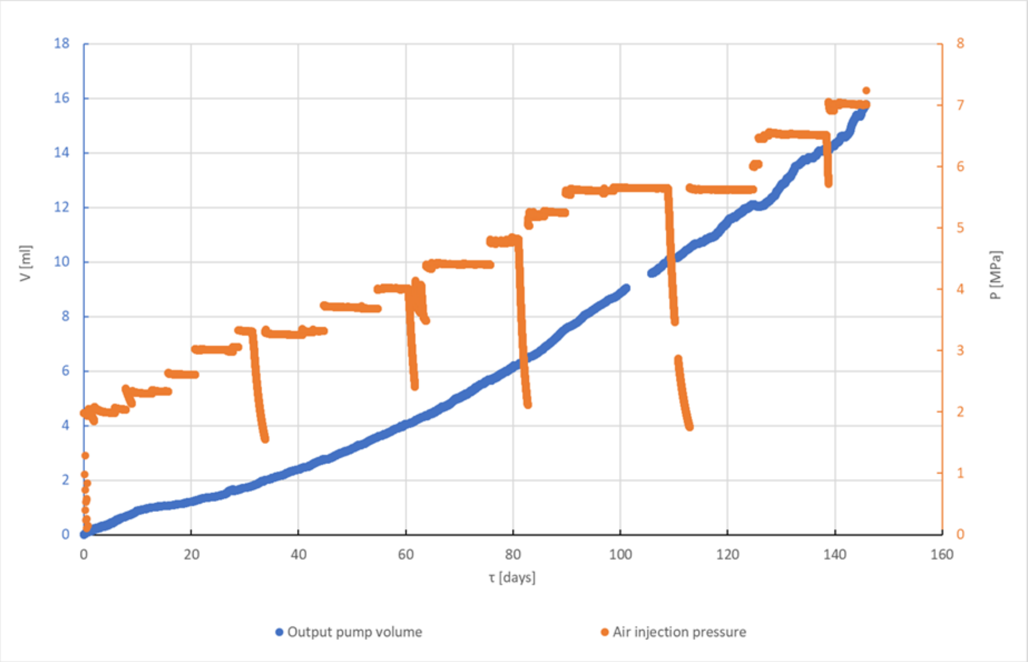

Figure 2.234: Air injection test on MX-80 bentonite sample 1600_3 prior to breakthrough

colour represents the swelling pressures calculated from the data published by Karland et al. (2006). The grey colour represents the swelling pressures based on the data published by Villar (2005).

It is important to point out that the measured breakthrough pressures do not represent the absolute breakthrough pressures, which can only be measured by a constant increase in the injection pressure. The values presented in this paper were influenced by the size of the increments applied to increase the injection pressure.

The breakthrough pressures grew exponentially with the target dry density of the bentonite samples. Lower breakthrough pressures were observed in the experiments on the bentonite samples with a target dry density of close to 1400 kg m^{-3}, whereas higher breakthrough pressures were recorded for the bentonite samples with a target dry density of 1600 kg m^{-3}.

The breakthrough pressures were, in most cases, slightly higher than the swelling pressure of both of the bentonites (Figure 2.235 and Figure 2.237). However, in the case of the bentonite samples with the target dry density (1600 kg m^{-3}), which were injected with air, the breakthrough pressure was slightly lower than, or very close to, the swelling pressure (Figure 2.236 and Figure 2.238). In order to draw a more definitive conclusion, it is suggested that additional injection tests be conducted on samples with the same dry density.

There was no clear evidence that the breakthrough time is directly proportional to the density of the sample; in some cases, this aspect was influenced by other external factors. As mentioned in the previous chapter, in some cases the samples were subjected to higher hydrogen injection pressures so as to obtain results within the project timeframe. In addition, the duration of the gas injection cycles was not the same for all the experiments.

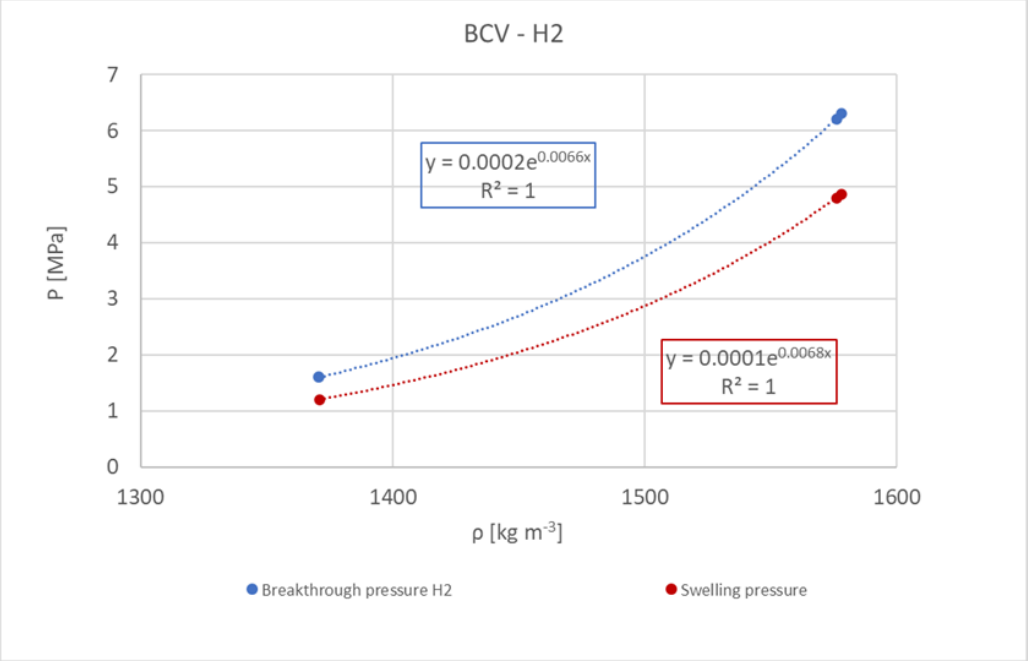

Figure 2.235: Comparison of the hydrogen breakthrough pressures and the swelling pressures of the BCV bentonite samples

In order to determine whether the flow measured at the outlets of the saturated bentonite samples during the breakthrough experiments comprised water or gas, a comparison is provided (see the following table) of the water content of the samples following saturation in the permeameter and following the gas injection tests. The samples were weighed before and after drying at 105℃ for 24 hours so as to determine the volume of water after the saturation and breakthrough tests.

Figure 2.239 and Figure 2.240 illustrate the water content of the samples that were saturated with distilled water but were not subjected to breakthrough testing (blue colour) and the water content of the water-saturated samples that were injected with hydrogen (green colour) and air (red colour).

In contrast to the results reported by Mendoza (2019), which indicated a certain reduction in the water content in the Ca-Mg bentonite samples (BaM), the results of this project showed that the water content did not decrease significantly following the gas injection tests. This suggests that hydrogen and air do not act to desaturate the samples and appear to migrate via small pathways that close following breakthrough. In addition, the volume of the fluid measured by the pump at the outlets of the samples prior to breakthrough was significantly greater than the volume of water lost following the gas injection experiments,

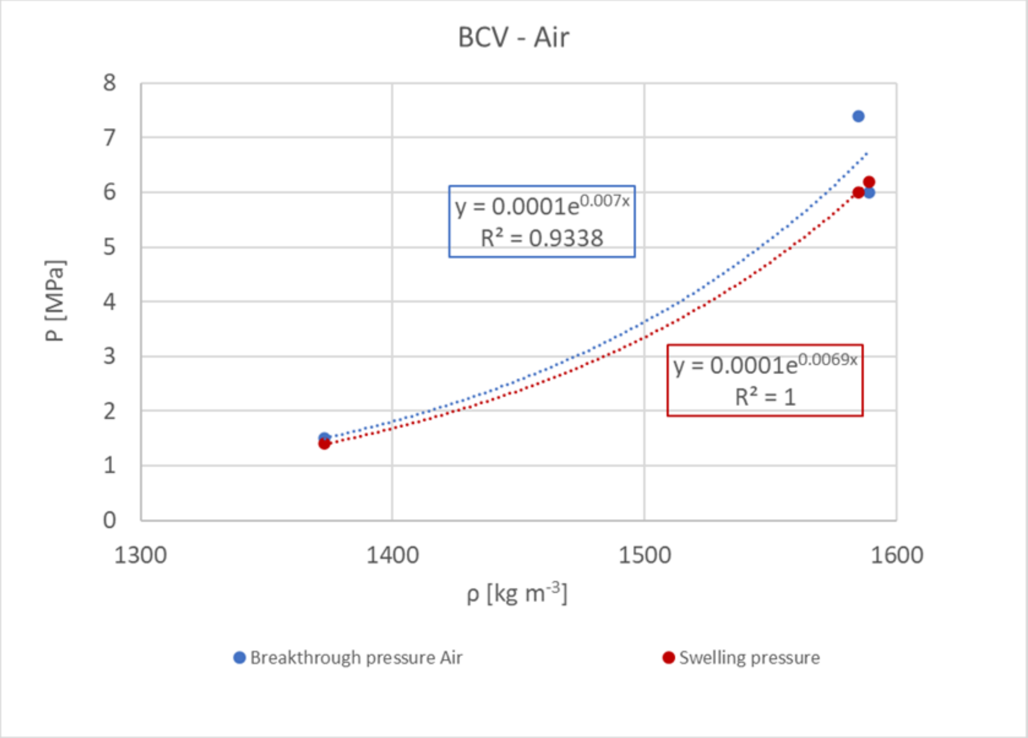

Figure 2.236: Comparison of the air breakthrough pressures and the swelling pressures of the BCV bentonite samples

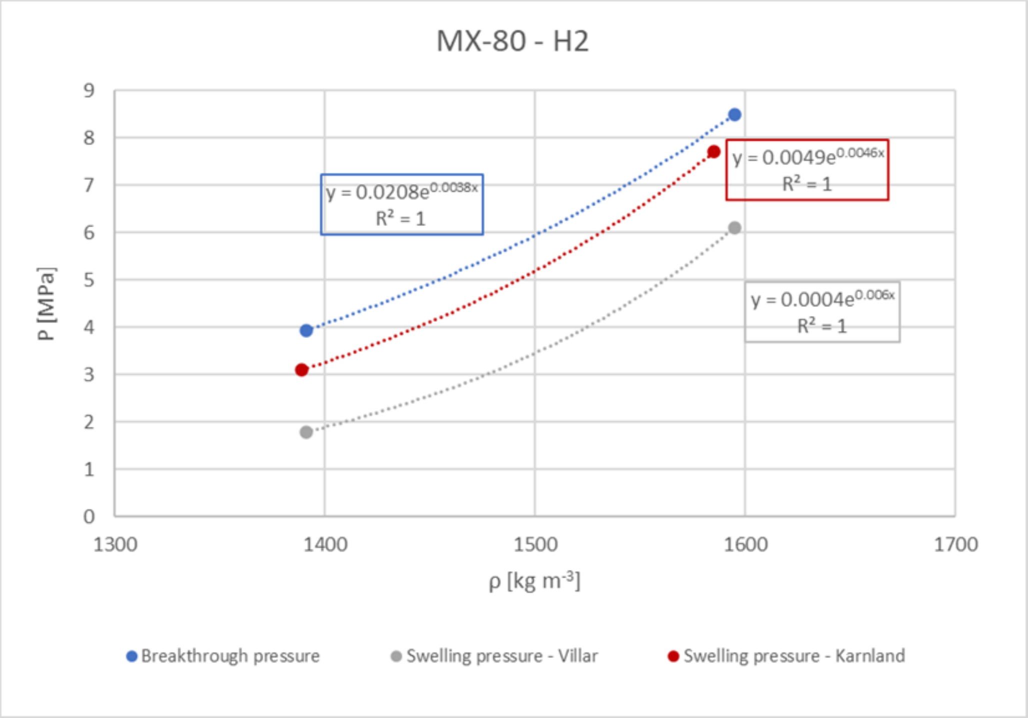

Figure 2.237: Comparison of the hydrogen breakthrough pressures and the swelling pressures of the MX-80 bentonite samples

thus indicating that the flow was composed of hydrogen or air.

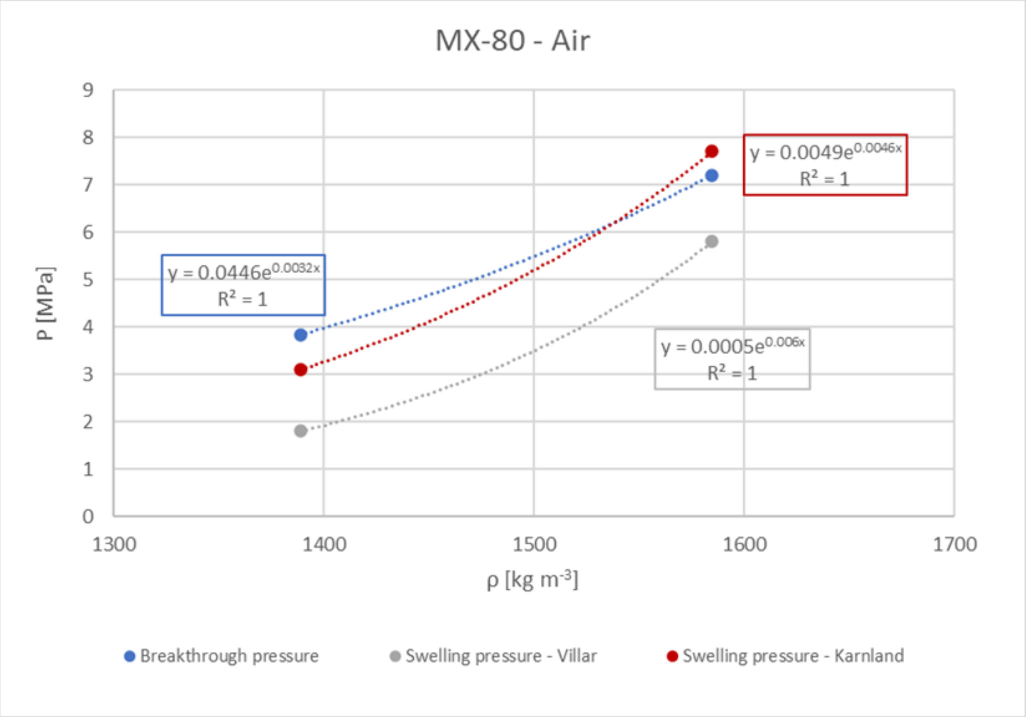

Figure 2.238: Comparison of the air breakthrough pressures and the swelling pressures of the MX-80 bentonite samples

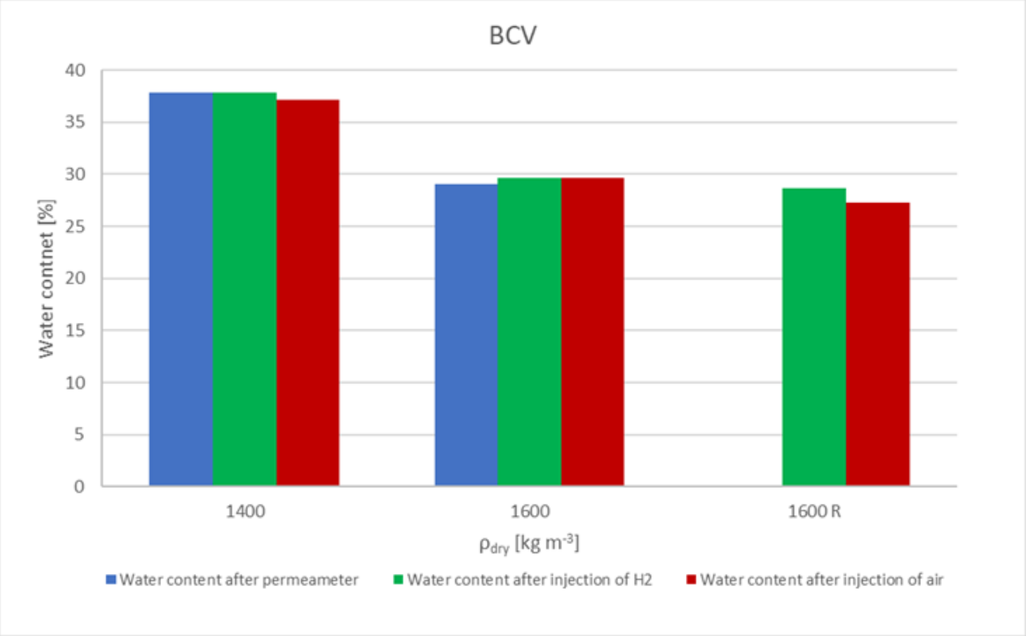

Figure 2.239: Comparison of the water contents of the BCV bentonite samples

Sample	Dry density	Test	Gas injection duration – time until breakthrough	Volume of water before injection of hydrogen V1	Volume of water after breakthrough V2	Loss of water ΔV	Volume measured before breakthrough V3

Sample	Dry density	Test	Gas injection duration – time until breakthrough	Volume of water before injection of hydrogen V1	Volume of water after breakthrough V2	Loss of water ΔV	Volume measured before breakthrough V3
	(kg m^{-3})		(days)	(ml)	(ml)	(ml)	(ml)
1400_1	1378	Water content	-	5.49	-	-	-
1400_2	1371	Hydrogen	83	-	5.59	-0.10	1.95
1400_3	1373	Air	214	-	5.43	0.06	7.33
1600_1	1574	Water content	-	4.85	-	-	-
1600_2	1578	Hydrogen	29	-	4.86	-0.005	8.30
1600_3	1589	Air	11	-	4.87	-0.02	4.22
1600_2_R	1576	Hydrogen	154	-	4.81	0.04	8.56
1600_3_R	1585	Air	235	-	4.43	0.43	43.1

Table 2.76: Comparison of the volumes of water and gas measured following the gas injection tests on the BCV bentonite samples

Sample	Dry density	Test	Gas injection duration – time until breakthrough	Volume of water before injection of hydrogen V1	Volume of water after breakthrough V2	Loss of water ΔV	Volume measured before breakthrough V3
	(kg m^{-3})		(days)	(ml)	(ml)	(ml)	(ml)
1400_1	1419	Water content	-	5.33	-	-	-
1400_2	1391	Hydrogen	341	-	5.36	-0.33	4.73
1400_3	1389	Air	309	-	5.33	-0.002	15.70
1600_1	1599	Water content	-	4.64	-	-	-
1600_2	1595	Hydrogen	177	-	4.47	0.17	8.17
1600_3	1585	Air	146	-	4.76	0.12	15.80

Table 2.77: Comparison of the volumes of water and gas measured following the gas injection tests on the MX- 80 bentonite samples

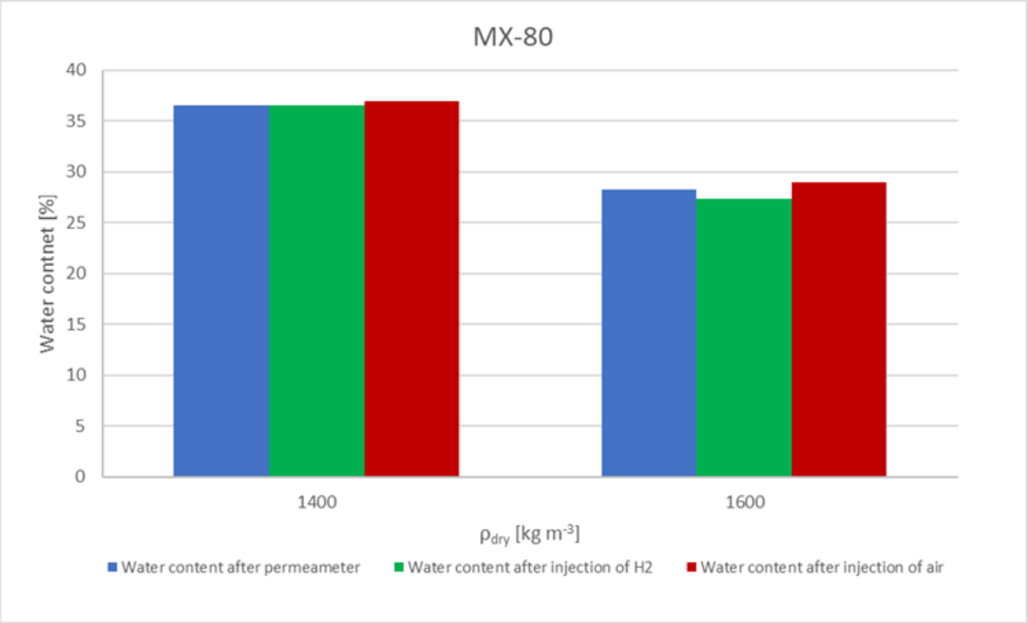

Figure 2.240: Comparison of the water contents of the MX-80 bentonite samples

2.8.6. Summary

The Czech deep geological repository programme anticipates the use of steel-based waste disposal packages (without a copper outer layer). Therefore, the formation of gases via corrosion processes is of particular importance. The Czech repository will be situated in crystalline rocks, a factor which increases the demands that will be placed on the bentonite barriers. The concept also assumes the use of local bentonites; therefore, one of the long-term objectives concerning the development of the engineered barrier system is to verify the properties and demonstrate the suitability of Czech Ca-Mg bentonite (BCV) for barrier purposes. The ÚJV experimental programme in Task 2 is serving to complement the other activities conducted by the Czech consortium as part of the overall project (CTU programme in Task 2 and Task 3, Figure 2.241).

The ÚJV programme was based on the use of existing available equipment without incurring major investment costs for the modification thereof. The first objective was to provide new data on Ca-Mg bentonite and to compare it with data on sodium bentonite MX-80 as the reference material. The key contribution of the research concerned the direct use of hydrogen as the gas injection medium in some of the tests, thus providing unique data for comparison with other gases that are typically used as a surrogate for hydrogen.

The experimental apparatus was equipped with a constant volume cell for compacted bentonite samples of 30 mm in diameter and 15 mm in height. The apparatus enabled the performance of injection tests applying both air and hydrogen. One of the most important parts of the apparatus comprised a sensitive pump which allowed for the measurement of the volume of the liquid that passed through the sample at atmospheric pressure. The project included the conducting of comprehensive series of tests on the two materials (BCV and MX-80 bentonite). Three samples with a target dry density of 1400 kg/m^3 and three samples with a dry density of 1600 kg/m^3 were prepared for each of the materials. One sample was used for air injection testing, the second for hydrogen injection testing and the third as the control sample for the determination of the water content and porosity directly following the saturation process. The procedure for the gas injection testing of the fully water-saturated samples involved the application of pressure increases with increments of 0.2 to 0.3 MPa until gas breakthrough was achieved. Following the completion of the gas injection testing, the samples were dismantled, and their porosity and water contents determined in order to verify whether the samples had been partially desaturated due to the injection of the gas. Table 2.78 and Table 2.79 provide summaries of all the performed tests.

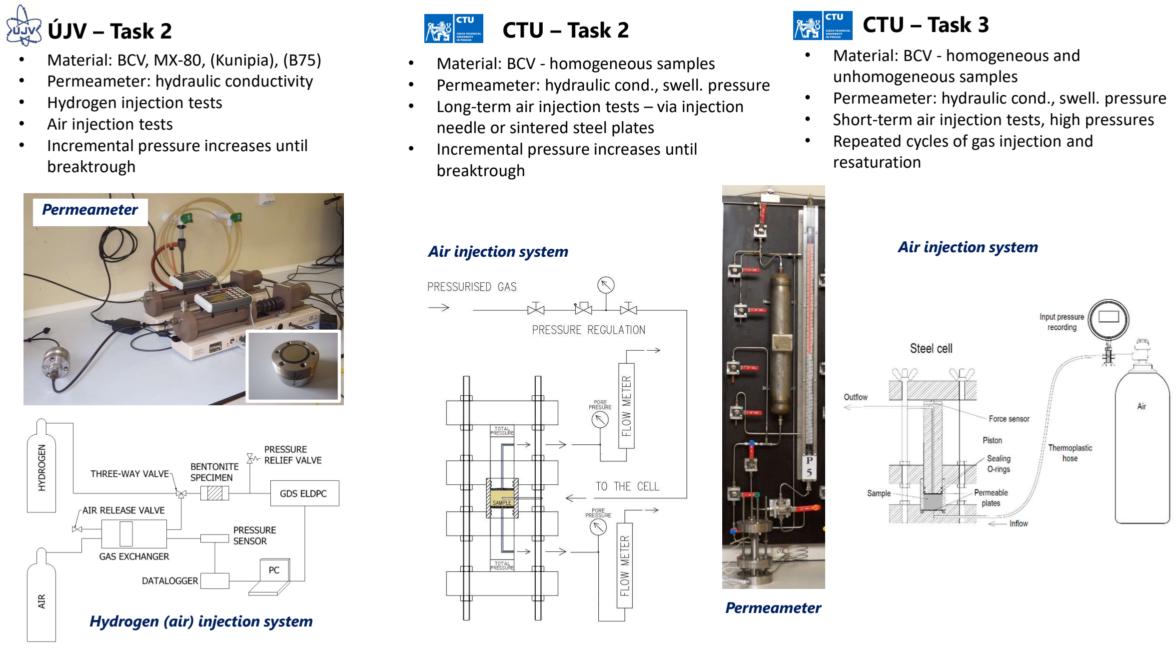

ÚJV – Task 2

- Material: BCV, MX-80, (Kunipia), (B75)
- Permeameter: hydraulic conductivity
- Hydrogen injection tests
- Air injection tests
- Incremental pressure increases until breaktrough

CTU – Task 2

- Material: BCV - homogeneous samples
- Permeameter: hydraulic cond., swell. pressure
- Long-term air injection tests – via injection needle or sintered steel plates
- Incremental pressure increases until breaktrough

CTU – Task 3

- Material: BCV - homogeneous and unhomogeneous samples
- Permeameter: hydraulic cond., swell. pressure
- Short-term air injection tests, high pressures
- Repeated cycles of gas injection and resaturation

Figure 2.241: Overview of the activities of the Czech bentonite cluster

Sample	Dry density [kg m^{-3}]	Test	Time until breakthrough [days]	Initial pressure step (MPa)	BT pressure step (MPa)	Theoretical swelling pressure min – max (average) [MPa]	Water content after dismantling [%]	Saturated water content [%]	Volume in output pump before BT [ml]
1400_1	1378	Water cont.	-	-	-	1.3 – 1.8 (1.5)	37.8	36.2	-
1400_2	1371	Hydrogen	83	0.6	1.6	1.2 – 1.8 (1.4)	37.8	36.6	1.95
1400_3	1373	Air	214	0.6	1.5	1.2 – 1.8 (1.4)	37.1	36.5	7.33
1600_1	1574	Water cont.	-	-	-	4.7 – 7.3 (5.6)	29.1	27.2	-
1600_2	1578	Hydrogen	29	6.0	6.3	4.9 – 7.5 (5.8)	29.6	27.1	8.30
1600_3	1589	Air	11	6.0	6.0	5.3 – 8.1 (6.2)	29.6	26.6	4.22
1600_2_R	1576	Hydrogen	154	2.0	6.2	4.8 – 7.4 (5.7)	28.7	27.1	8.56
1600_3_R	1585	Air	235	2.0	7.4	5.1 – 7.8 (6.0)	27.3	26.8	43.1

Sample	Dry density [kg m^{-3}]	Test	Time until breakthrough [days]	Initial pressure step (MPa)	BT pressure step (MPa)	Theoretical swelling pressure min – max (average) [MPa]	Water content after dismantling [%]	Saturated water content [%]	Volume in output pump before BT [ml]

Table 2.78: Overview of the test results for the BCV samples (BT - Breakthrough)

Sample	Dry density [kg m^{-3}]	Test	Time until breakthrough [days]	Initial pressure step (MPa)	BT pressure step (MPa)	Water content after dism. [%]	Saturated water content [%]	Volume in output pump before BT [ml]
1400_1	1419	Water cont.	-	-	-	36.7	34.9	-
1400_2	1391	Hydrogen	341	0.6	3.94	36.3	36.4	4.73
1400_3	1389	Air	309	0.6	3.84	37	36.5	15.70
1600_1	1599	Water cont.	-	-	-	28.2	27.0	-
1600_2	1595	Hydrogen	177	2	8.05	27.3	27.2	8.17
1600_3	1585	Air	146	2	7.20	28.9	27.6	15.80

Table 2.79: Overview of the test results for the MX-80 samples (BT - Breakthrough)

The first important result concerned the fact that the gas breakthrough event in all cases occurred at pressure levels lying within the theoretical swelling pressure range; this applied for both air and hydrogen injection and both of the studied materials. The facts that the theoretical swelling pressure for higher dry densities lies within a broader interval than lower dry densities, and that the properties of the various batches of material lay within a relatively wide range of variability were taken into account for the purposes of comparing the breakthrough pressure and swelling pressure values. Moreover, no significant difference was observed between the breakthrough pressures of the air and hydrogen.

A further important finding related to the fact that following their dismantling, no major desaturation of the samples was detected. The water contents of the materials were in all cases above the calculated theoretical saturated water content. This result corresponds to the general observation that gas flow through dilatant pathways does not result in significant sample desaturation or that the desaturation is so minor that it cannot be detected by means of standard methods. The comparison of the values of the total volume in the output pump with the theoretical water loss caused by the injection of gas clearly demonstrated that the fluid in the output pump comprised gas. Concerning the gas flow at lower pressure levels, it was observed that a certain flow was registered even during the time of the lowest pressure levels for both types of gases. It was thought that this behaviour was caused by leakages along the cell interface; however, further research will be required in order to reach a definitive conclusion in this respect.

2.8.7. Key learning points

2.8.7.1. New knowledge acquired

The novelty of the results of the Czech programme lies primarily in the provision of new information on the properties of Ca-Mg bentonite. The test methodology employed was of a standard nature and followed procedures that have been applied in the past. The objective was to perform multiple gas injection tests using a relatively simple apparatus that does not allow for the visual checking of the internal structures of the bentonite samples during or after testing. The injection testing procedure included the monitoring of the inlet pressure and the volume of fluid passing through the sample. New knowledge was obtained from the breakthrough pressure data on BCV bentonite (Ca-Mg type) and its comparison with MX-80 (Na type). The experiments confirmed the existing knowledge of gas flow through dilatant pathways as described in previous studies on various types of bentonites. In general, BCV bentonite does not differ from the reference material (MX-80) in terms of gas flow processes. The further added value of the research concerned the acquisition of data from the direct comparison of the behaviour of hydrogen and air, from which it was determined that the type of gas has no effect on the gas breakthrough pressure values, which corresponded to the swelling pressure.

2.8.7.2. Impact of the acquired knowledge

The acquired knowledge is important for the safety assessment of the future Czech deep geological repository, which anticipates the use of steel-based waste disposal packages (carbon steel outer layer) and Ca-Mg-type bentonite for the engineered barrier system. The study performed by ÚJV, which is one of only a small number of studies that have used hydrogen for breakthrough experiment purposes, provided data that is not widely available in the literature. A further important contribution of the Czech cluster concerned the experiments conducted as part of Task 3, which demonstrated the re-sealing capability and integrity of a BCV bentonite barrier. The research allowed for the comprehensive description of gas flow processes in fully saturated compacted bentonite at high gas pressures.

2.8.7.3. Remaining knowledge gaps

The gas injection tests performed simulated an extreme scenario in which a large amount of hydrogen is produced by the corrosion of the waste disposal package and the subsequent accumulation of the gas at the interface between the waste disposal package and the buffer. In such a case, the diffusion capacity of the bentonite buffer is not sufficient to allow for the diffusion of the hydrogen, thus resulting in its accumulation and the loading of the buffer with high pressure. However, the processes that are likely to occur at the interface between the waste disposal package and the buffer, and the amount of hydrogen that is likely to be produced, have not yet been accurately determined.

2.8.7.4. Recommendations for the future

Current recommendations on the issue of gas formation and migration in deep geological repositories using bentonite buffer materials and steel waste packages include the conducting of a comprehensive assessment of the processes that will occur at the interface between the waste package and the bentonite buffer. There is currently a lack of data on the formation of hydrogen and diffusion processes in bentonite. It is not clear how much gas will be produced and how it will evolve over time. Will the gas dissolve in the pore water and diffuse away through the bentonite or will it accumulate in the gaseous form? Experience has shown that it is almost impossible to design a complex in-situ or even laboratory experiment that simulates the conditions expected in the repository and, simultaneously, allows for the study of the formation of hydrogen via corrosion and its transport through the bentonite barrier. Going forward, it is recommended that an assessment is made of whether, and what type of, experiments can be expected to contribute to improving the knowledge of the defined uncertainties.

References

Červinka, R.; Vašíček, R.; Večerník, P.; Kašpar, V. (2019): Complete Characterization of Bentonite BCV. Technical Report 419/2019. - SÚRAO, Prague. In Czech.

Dobrev D., Gondolli J., Mendoza Miranda A N., Steinova J., Zuna M. (2017): Corrosion Test in Natural Granitic Environment. Participation in the material corrosion test (MACOTE) project, part 2 of the contract implementation and evaluation of the MACOTE experiment at the Grimsel Test Site. – Technical Report 194/2017, SURAO, Prague.

Karnland O., Olsson S., Nilsson U. (2006): Mineralogy and sealing properties of various bentonites and smectite-rich clay materials. Technical Report TR-06-30. - SKB Stockholm.

Laufek F., Hanusová I., Svoboda J., Vašíček R., Najser J., Koubová M., Čurda M., Pticem F., Vaculíková L., Sun H., Mašín D. (2021): Mineralogická, geochemická a geotechnická studie BCV 2017 Bentonit – výchozí stav a stav po tepelném zpracování při 200 °C. Minerály 11(8), 871. https://doi.org/10.3390/min11080871. In Czech.

Mendoza A. (2019): Hydrogen transport experiment in bentonite – Final report. Technical Report 383/2019/ENG. - SÚRAO, Prague.

SÚRAO. Deep geological repository. Online. 2023. Available from: https://www.surao.cz/en/deep-geological-repository/. [2023-12-11].

Villar M. V (2005): MX-80 Bentonite. Thermo-Hydro-Mechanical Characterisation Performed at CIEMAT in the Context of the Prototype Project. Technical report 1053. - CIEMAT, Madrid.

.

IC2MP, Univ. Poitiers, CNRS

2.9. Visualization of multiphase flow in nanopores network (IC2MP, Univ. Poitiers, CNRS)

2.9.1. Introduction & Objectives

The aim of the task is to provide an insight into the micro-structural changes inside the claystone (COx) due to gas entry and propagation in the porous network. It intends to contribute to the characterisation of gas transport regimes at the scale of the EDZ and their impact on barrier integrity, accounting for micro-structure changes.

In order to answer this scientific question, CNRS-IC2MP is developing a gas injection test on a sample of small size inside a miniaturised and optimised triaxial cell for high quality in-situ imaging by X-ray tomography. The test was optimised by a full simulation of X-ray beam production and absorption by the sample and the cell. Such an approach with a miniaturised cell allows us to obtain good resolution (close to 1µm) and huge contrast improvement for micro-structure visualisation and gas migration. The small size of the samples considered and cell developed will provide data regarding micro-structural changes inside the claystone. This information may be incorporated in the HM coupled micro-mechanical models that will be used for numerical modelling at the scale of the underground structure.

2.9.2. Experimental set-up

2.9.2.1. Description of apparatus

The new triaxial cell has been designed and built (Figure 2.242a). This new cell is specifically adapted to measure in-situ the volume deformation of sample due to confining pressure, and a gas pressure on the basis of X-ray tomography images. The volume fields of displacement, strains and fractures behaviour are obtained by digital image correlation software adapted for fractured medium (H-DVC, Valle et al. 2019)

In the initial design, the experimental setup is composed of:

- a new triaxial cell,
- a sample with a diameter of a few millimetres (5 mm or less),
- an x-ray µtomography set-up of the University of Poitiers (RX solution©),
- a new injection apparatus made of four HPLC pumps to control confining pressure and stresses applied on the sample.

The challenging key points of the design of the triaxial cell are:

- An improvement quality of contrast for the X-ray tomography volumes allowing to distinguish the mineralogy and local phenomenon (fracture, deformation, porosity evolution) as well as a good speckle for digital volume correlation (DVC). This is achieved by a detailed simulation of the X-ray tomography experiment for back-controlling the triaxial cell design in order to drastically improve the contrast between the different sample components (Figure 2.242b and c). For example, classical large triaxial cell previously used in literature imply exciting voltage 150 kV with associated contrast of around 3cm-1 between clay and water. The miniaturized triaxial cell developed in the framework of this study allows acquisitions at 50 kV only with an improved contrast of 10 cm-1.

- A small size of the cell and the quantity of component composed of four connections (two per pump), two pistons, two caps, a jacket.

- A cell material (PEEK) transparent to X-rays and resistant to aggressive injected resin planed for impregnation under mechanical load.

- A good mechanical strength of the cell enabling to apply the loads up to 20 MPa (gas pressure, confining stress, water pressure). Several designs of the cell were tested by mechanical simulation (with finite

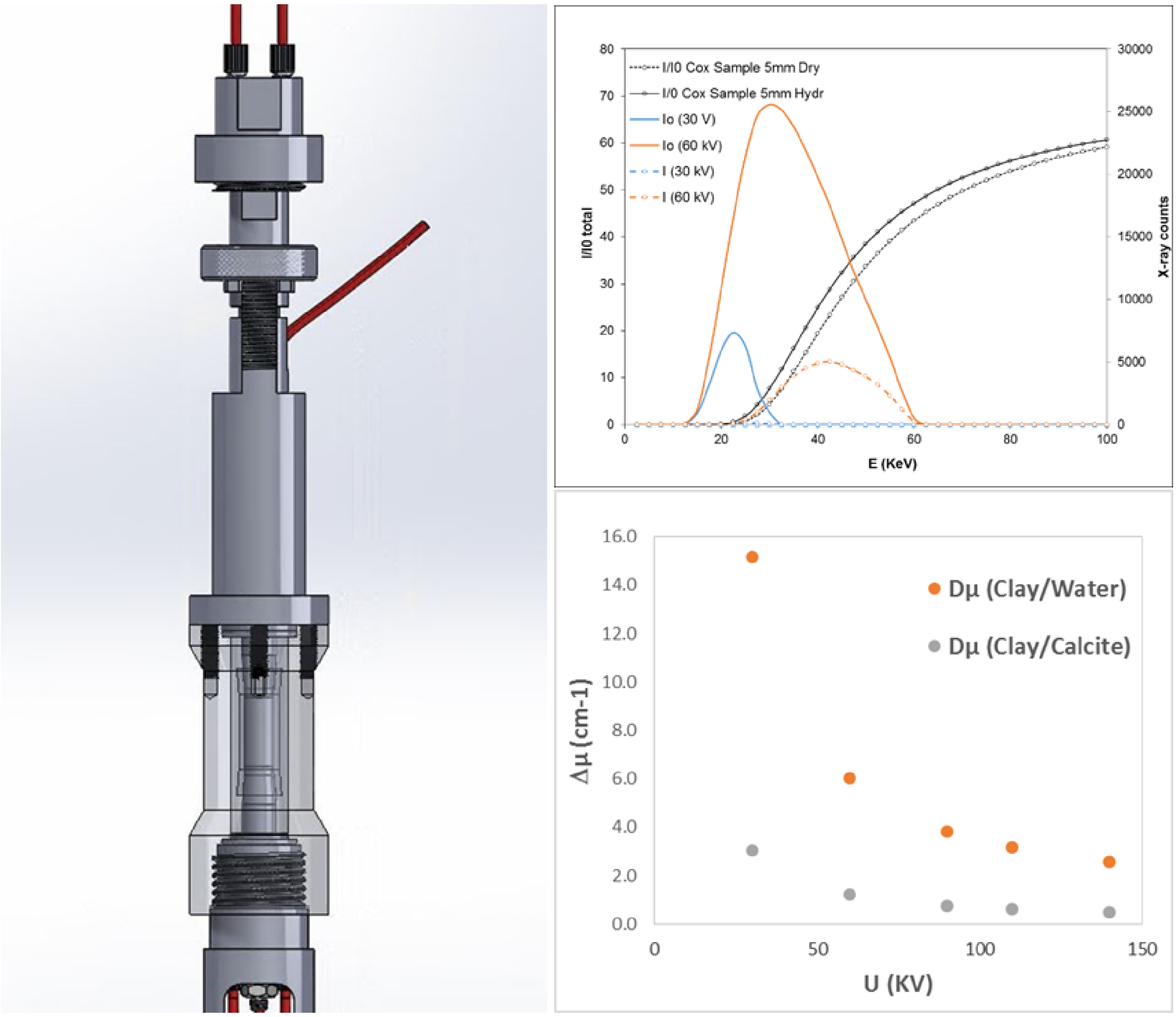

(a) (b)

Figure 2.242: a) New triaxial cell for a 5 mm wide sample. b) Simulation of the X-ray beam production (I0) transmission rate towards the sample into the cell (I/I0) and transmitted beam (I). c) Simulation of the contrast between rock components as a function of accelerating voltage.

element method) to ensure the mechanical resistance of the cell under the applied pressures.

• A gas injection on the top of the sample, which requires to insure that the whole set up is compatible with both gas and solution.

• A good precision of each imposed pressure level and very low injected volume associated to the reduced size of the sample. Choosing a set of accurate pressure sensors and developing specific injection pistons was needed as the total pore volume is only around 20 mm3.

Another difficulty lies in the manufacturing of the small size samples. The apparatus for automatic preparation of the damage-free and small size shale samples is still currently under development (Figure 2.243). It consists of an in-house micro-polishing device allowing to reduce gently the initial core diameter without damaging the sample. After the preparation of the sample, X-ray tomography analysis will be carried out to visualize the microstructure and potential increase of porosity/cracks at the boarder of the sample and further adjust the polish parameters if a damage is observed.

In addition, we developed a new gas injection apparatus made of four HPLC pumps (Figure 2.244). Let us

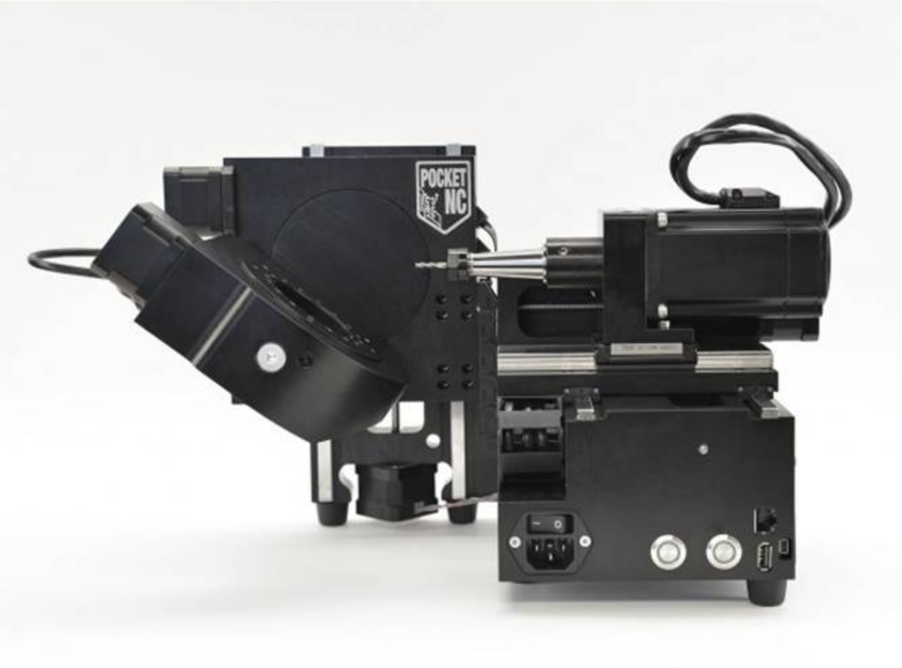

Figure 2.243: House-developed apparatus for automatic preparation of the clay rock samples.

notice that in the initial program, we should have used an existing apparatus but on the one hand it was finally not available and on the other hand it was not accurate enough. This required a significant time and effort.

Figure 2.244: Home-developed gas injection apparatus.

2.9.2.2. Calibration

2.9.2.3. Testing fluids

The sample is initially fully water saturated and insulated at its circumference in order to prevent any gas or water flux. At the base of the sample, two conditions can be tested: insulation, thus no gas and water flow, and drainage, thus gas and water flow allowed. Gas (Argon) will be injected from the top of the sample. Argon was chosen due to its higher density than nitrogen which enables mass flow measurements and its lower water solubility.

2.9.3. Material properties (pre-test and post-test characteristics)

Concerning the materials to be considered, the test will be performed first on a Callovo-Oxfordian claystone. In a second step, once the test has proven its efficiency on the COx, it was also considered to carry out the test on Opalinus Clay. The delay due to the COViD-19 crisis makes it very difficult to consider Opalinus Clay in the framework of the project. Moreover, due to the time consuming and expensive preparation of the few millimetres wide shale cores to be studied, a validation of the set-up was firstly achieved on a compacted powder of illite du Puy at a dry bulk density of 1.6 g.cm-3 with an associated porosity of 42%.

2.9.4. Testing protocol

The principle of the test is to inject a gas, Argon, at the top surface of several samples and to stop the injection at different levels of gas pressure and time for each sample with a systematic 3D imaging by X-ray tomography at the micron scale (1-2.5µm). Once the maximum injection pressure is reached, the sample is imaged by X-ray micro-tomography on the one hand, and then the sample is impregnated by MMA resin mimicking the clay crystal swelling observed with water. After impregnation, the sample will be cut on a plane of interest localised in 3D on the basis of micro-tomography volume and a polished thick section will be prepared in order to be analysed by SEM at the micro-scale. Fluids will be replaced by a resin mimicking water behaviour and a new in-house protocol will be tested to remove water without damaging the samples and insuring to observe differences of micro-structure before and after gas injection. This will allow 2D mineral/porosity maps (BSE-SEM mosaic) on large representative areas with a better contrast and resolution to be obtained. This process will be repeated at different levels of gas pressure in order, particularly above gas entry pressure, to observe the effect of gas penetration and transfer on the microstructure of the claystone. The gas pressure levels will eventually be increased, if possible, until sample breaking. In that way, we will finally observe the evolution of the micro-structure of claystone with the increase of gas pressure and injection time. Regarding the porosity maps obtained, two image resolutions will be used for the SEM mosaics: one for mapping a full core section with a resolution around 60nm, the other around 5nm to detect most of the pores and particles. Only the smallest mesopores and micropores accounting for a minor part of the porous network will not be detected.

Regarding the boundary conditions, the sample will be initially fully water saturated and insulated at its circumference in order to prevent any gas or water flux. At the basis of the sample, two conditions may be tested: insulation, thus no gas and water flow, and drainage, thus gas and water flow allowed. Gas will be injected from the top of the sample. On a mechanical point of view, the sample will be submitted to a triaxial compression state of stress with a water pressure of 5.5 MPa. A confinement around 12 MPa and an axial stress around 16 MPa will be used, to be closed to the state of strain in the COx at the level of the ANDRA underground research laboratory.

2.9.5. Results

The parameters measured are:

• the strain field within the sample by Digital Image Correlation applied on the 3D X-ray tomography volumes: for each deformed state and each domain, all components of strain tensor will be measured and a very good precision on the 3D crack location will be obtained (Valle et al. 2019, https://doi.org/10.1007/s11340-018-0415-2).

- Visualization of the micro-structure of the sample: X-ray micro-tomography and 2D high resolution mineral/porosity map (BSE-SEM mosaic) on large representative areas.
- Pressure of injected gas.
- Downstream water flux measured before the complete gas breakthrough in the downstream reservoir.

Moreover, fracture spacing, fracture aperture and fracture propagation will be probed dynamically by DIC but SEM will provide them also after the experiment with a better resolution. In addition, in order to provide enough information for modelers, to compare and validate numerical models, a sample characterisation before and after subjecting the samples to the gas pressure will be carried out:

- Porosity (evolution).
- Saturation/water content.
- Sample Dimensions.
- Weight.

So far, the setup has been validated for fluid injection and axial/confining pressures up to 20 MPa (Figure 2.245). An overview by orthogonal virtual slice 50μm pixel size was obtained (Figure 2.246) and a large contrast between water, gas and minerals validating the triaxial cell developed. This allows to visualize the distribution of water and gas into the pore network. An acquisition at 2.8µm voxel size was carried out and a virtual horizontal slice is provided on Figure 2.247. In addition, several optimized fast tomography acquisitions were carried out at 30µm(23s), 15µm(36s) and 7µm(3min). A Radiography of 2.5s for live monitoring gas injection (at 2.5bar) was realized but the gas migration through the sample that lasted 5 s was too fast for this live tomography (Figure 2.248).

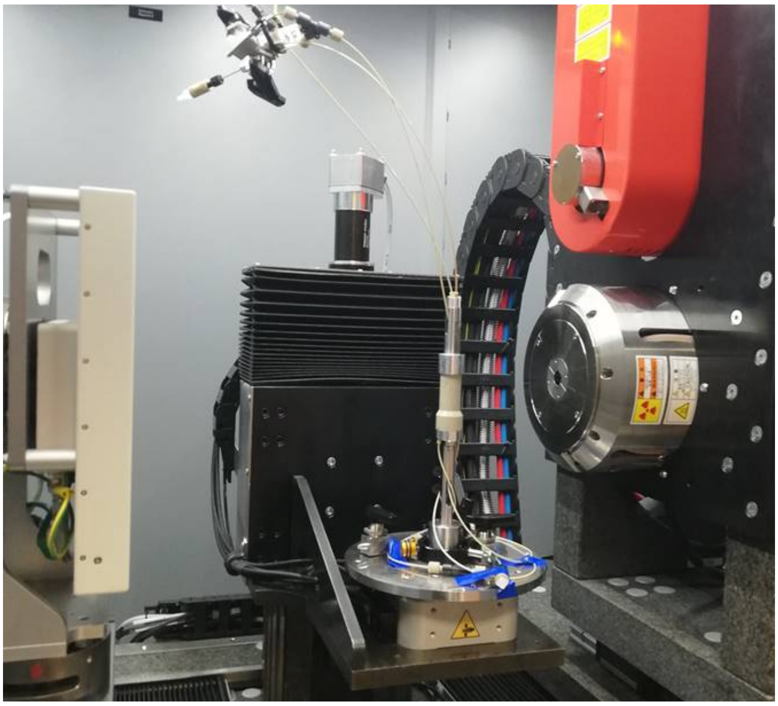

Figure 2.245: New triaxial cell in the X-ray micro-tomography setup.

A first test was carried out on a clayey material, an illite du Puy sample to be more specific. Figures 8 and 9 provide respectively a full sample width by virtual slice at 2.8µm voxel size and a local tomography at 1µm voxel size. It allowed to reach the detection of aggregates and macropores.

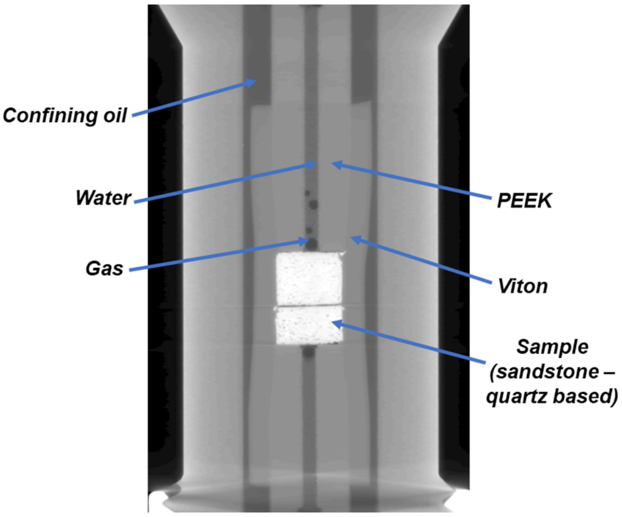

Figure 2.246: Overview by orthogonal virtual slice with a 50μm pixel size.

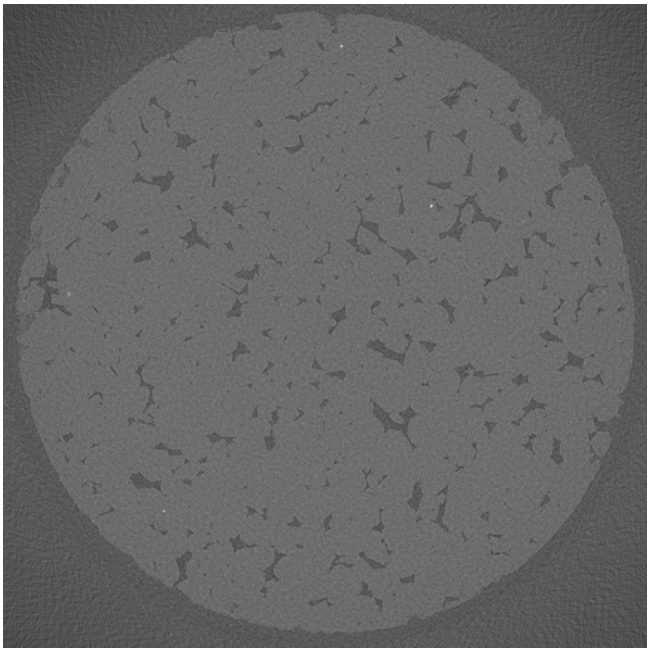

Figure 2.247: Overview by horizonal virtual slice with a 2.8 μm voxel size.

2.9.6. Summary

We intended to provide an insight into the micro-structural changes inside the claystone (COx) due to gas entry and propagation in the porous network in order to contribute to the characterisation of gas transport regimes at the scale of the EDZ and their impact on barrier integrity, accounting for micro-structure changes.

To achieve this aim, CNRS-IC2MP has developed a gas injection test on a sample of small size inside a miniaturised and optimised triaxial cell for high quality in-situ imaging by X-ray tomography. The test was optimised by a full simulation of X-ray beam production and absorption by the sample and the cell. Such an approach with a miniaturised cell allows us to obtain good resolution (close to 1µm) and huge contrast improvement for micro-structure visualisation and gas migration. The small size of the samples and cell allows to obtain data regarding micro-structural changes inside the claystone. In addition, we have developed a new gas injection apparatus, which was not initially planned in the project. Both the gas injection apparatus and the miniaturized cell have been tested and validated, showing encouraging

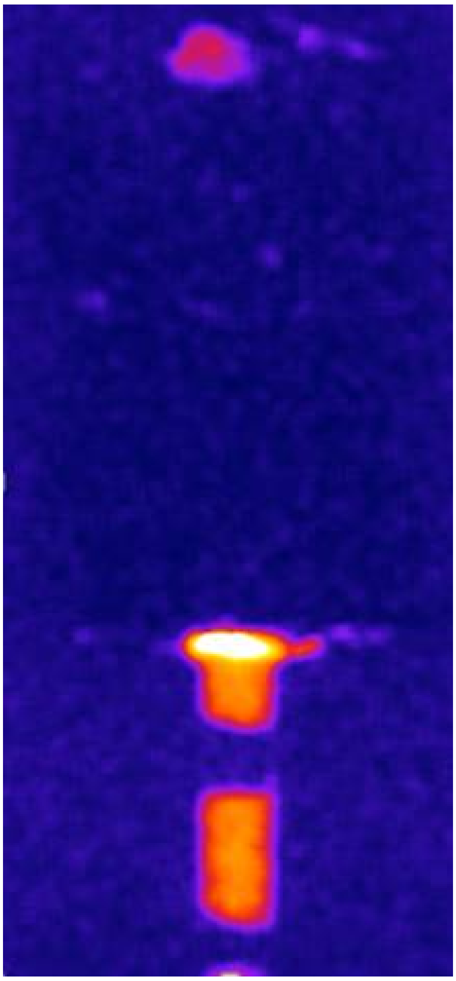

Figure 2.248: Live tomography during gas injection in sandstone (orange and red colours correspond to the presence of gas)

capabilities, on samples of sandstone and Illite du Puy.

In order to apply the full protocol to clayey rock samples of COx, we currently focus on the preparation of the sample, in particular developing our in-house apparatus. We plan to make a test on Cox sample by the end of the year 2023. So we currently have no experimental result on COx. Let say that this is due to several external factor: a long period during which it was not possible to make any experimental developments due to several successive confinements due to COVID, a lot of problems of availability/time of delivery for specific components of the experimental setups. Moreover, the initial setup for mechanical loading and gas injection was supposed to make use of part of CNRS-Georessources experimental material. Nevertheless, due to COVID, it is very difficult to consider the apparatus initially intended because of the shift of the timeline and the necessity of Georessources to use this apparatus for its own program.

2.9.7. Key learning points

2.9.7.1. New knowledge acquired

The knowledge acquired so far essentially concern the technical developments:

- Development and validation of a complete apparatus and protocol for gas injection in clayey materials. Basically the protocol of injection is quite usual but has been successfully adjusted for very low injection volumes associated to the innovative miniaturized triaxial cell.
- Development and validation of a miniaturized triaxial cell.

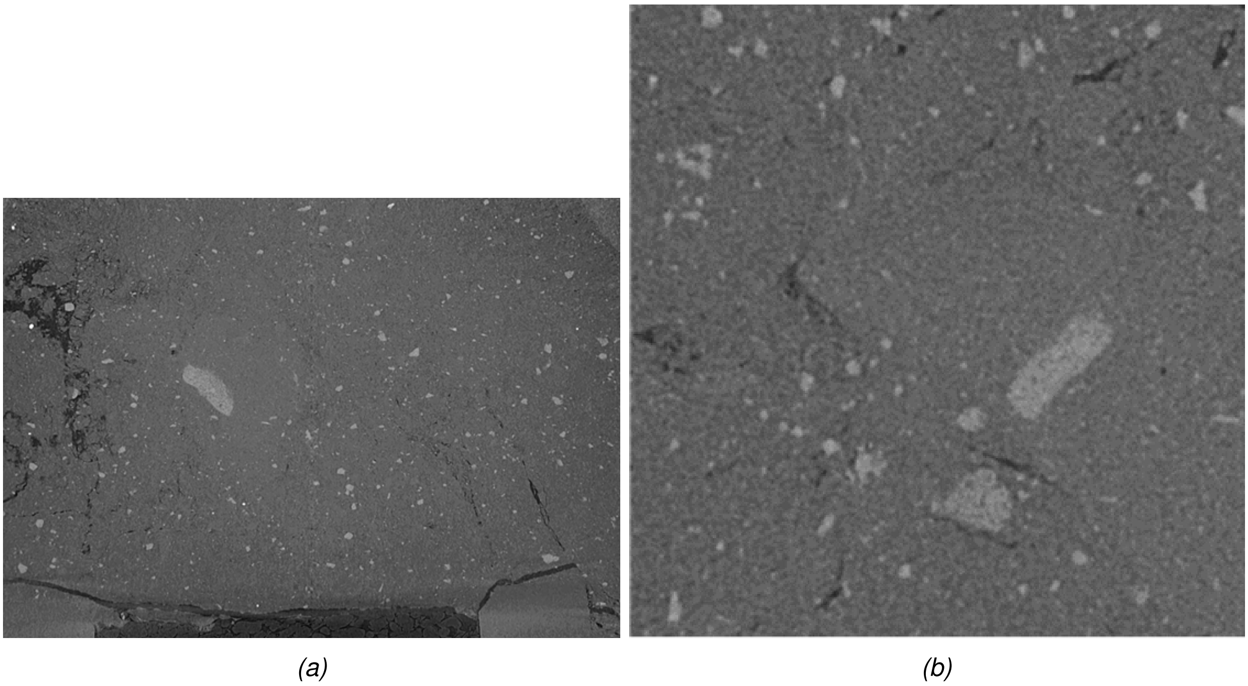

(a) (b)

Figure 2.249: Full sample width by virtual slice at 2.8μm voxel size.

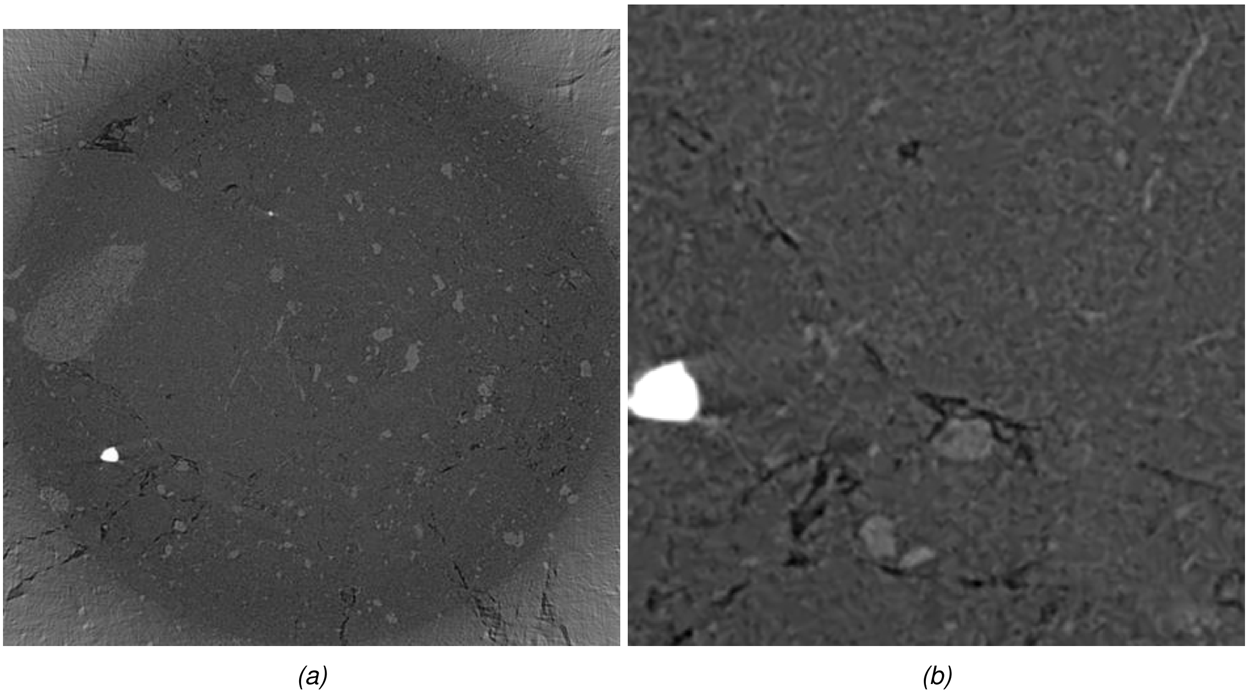

(a) (b)

Figure 2.250: Local tomography at 1μm voxel size.

- Development of an apparatus and protocol for sample preparation which allow to prepare small cores of 5 mm in diameter without usual coring damage.

2.9.7.2. Impact of acquired knowledge

Describe the impact of the knowledge gained – compare it to the initial goals set at the beginning of the project

2.9.7.3. Remaining knowledge gaps

In the work plan timeline, we expect to make a first series of test on COx, at different injection pressure but with the same mechanical loading, by the end of 2023. The samples will then be injected with MMA resin under mechanical loading for high resolution observations by electron microscopy. The strain field evolution upon the gas injection will be assessed in the sample by Digital Image Correlation.

It was not possible to meet the initial objectives in the timeline of the project. There was a long period during which it was not possible to make any experimental developments due to several successive confinements, and we also faced a lot of problems of availability/time of delivery for specific components of the experimental setups (valves, joints, manometers, flowmeters). Moreover, the initial setup for mechanical loading and gas injection was supposed to make use of part of CNRS-Georessources experimental material. Nevertheless, due to COVID, it was very difficult to consider the apparatus initially intended because of the shift of the timeline and the necessity of Georessources to use this apparatus for its own program. So we had to imagine, with the help of Georessources, the new full experimental set up for controlling the confining pressures and injection the fluids.

2.9.7.4. Recommendations for the future

References

Valle, V., Bokam, P., Germaneau, A. *et al.* New Development of Digital Volume Correlation for the Study of Fractured Materials. *Exp Mech* **59**, 1–15 (2019). https://doi.org/10.1007/s11340-018-0415-2

Modelling

.

TU Delft

2.10. Coupled Pneumo-Hydro-Mechanical (PHM) Finite Element (FE) model within the FE code LAGAMINE

2.10.1. Model introduction

2.10.1.1. Introduction

The TU Delft team aims to develop a numerical model capable of reproducing, within a unified framework, the four gas transport mechanisms in initially saturated clays: i) diffusion and advection of dissolved gas, ii) visco-capillary two-phase flow, iii) dilatancy controlled gas flow, and iv) gas fracturing. This model will allow to investigate the factors controlling the onset of each mechanism and the interaction between them in gas injection tests in small samples of few centimetres.

In order to select an appropriate modelling approach, a literature review on experimental characterisation of gas transport mechanisms in water saturated clays and on existing numerical models to simulate this process has been performed. Based on this review, on the available numerical tools and on the experience of the researchers, it was decided to develop a coupled Pneumo-Hydro-Mechanical (PHM) Finite Element (FE) model within the FE code LAGAMINE. Taking advantage of existing capabilities for the simulation of coupled PHM processes in continuum porous media, new developments were implemented to consider discrete fracturing processes via the use of zero-thickness interface elements. For this purpose, the governing equations and FE discretisation of a new type of PHM interface element have been developed and implemented in LAGAMINE, including a set of new mechanical and flow constitutive laws.

In the following section, the background of the proposed modelling approach and the adopted governing equations are described in detail. Section 2.10.1.5 summarises the FE formulation and numerical implementation of the model. The model performance is illustrated with benchmark examples in Section 2.10.2.

This work has been published in the following journal paper: Liaudat, J., Dieudonné, A., & Vardon, P. J. (2023). Modelling gas fracturing in saturated clay samples using triple-node zero-thickness interface elements. Computers and Geotechnics, 154, 105128. https://doi.org/10.1016/j.compgeo.2022.105128

2.10.1.2. Modelling Approach

The gas migration in water saturated clay is modelled in 2D assuming isothermal conditions and using a Pneumo-Hydro-Mechanical (PHM) formulation discretised with FEM. In the proposed modelling approach, continuum elements are used to represent the mechanical and flow processes in the bulk clay material, while zero-thickness interface elements are used to represent existing or induced discontinuities (cracks). The interface elements are introduced a priori in between the continuum elements, thereby providing a set of potential propagation paths for cracks (Figure 2.251). The constitutive laws of the interface elements are such that, as long as they remain closed, they do not have any significant effect on the overall hydro-mechanical response of the modelled clay sample. However, when a certain mechanical threshold is reached (e.g. the tensile strength) and the interface element starts to open, localised mechanical and flow processes are triggered. Similar approaches can be found in the literature for modelling hydraulic fracturing of rocks (Carrier and Granet, 2012; Nguyen et al., 2017; Cordero et al., 2019a,b) and concrete cracking due to chemo-mechanical processes (Idiart et al., 2011a,b; Liaudat et al., 2020). In addition, interface elements can be used to represent interfaces between different materials (e.g., the contact between a clay sample and steel cells used in lab tests) or existing discontinuities (e.g., bedding planes).

This approach has the conceptual advantage of treating the continuum and discontinuities as two separate (though connected) sub-domains within the clay material. In that way, different (though consistent) mechanical and flow constitutive laws can be used for the continuum porous medium and for the induced cracks or pre-existent discontinuities, allowing a more realistic representation of the effect of discontinuities in the clay material. As a negative counterpart, cracks can only develop at the pre-established lines where the interface elements have been inserted. This is a discretisation of a continuum problem. In reality, the

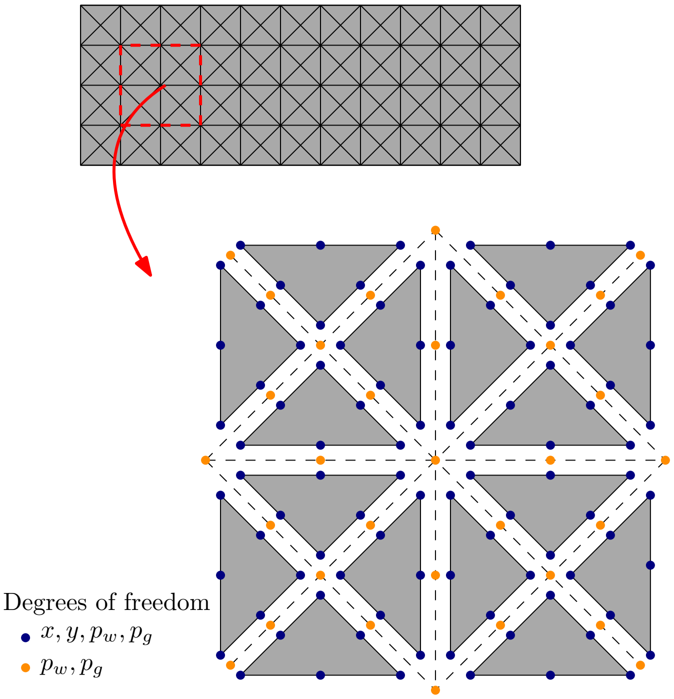

Figure 2.251: Introduction of zero-thickness interface elements in a conventional FE mesh. Adapted from Cordero et al. (2019a).

potential cracking paths for a given boundary value problem are infinite, such that the propagation of cracks will form the pattern that requires exactly the minimum mechanical work. In contrast, with the proposed modelling approach the cracking pattern will be the one that requires the least mechanical work among the set of potential patterns provided by the adopted FE mesh with interface elements. This pattern is not necessarily the one requiring the minimum minimorum mechanical work for the boundary value problem considered, but it will be the closest among the available options. In that way, the refinement of the FE mesh makes it possible to approximate the actual cracking pattern more closely, and, therefore, the proposed modelling approach is mesh convergent. Nonetheless, previous studies of cracking processes with this approach, though considering cement-based materials, suggested that the macroscopic response is not significantly influenced by the precise location of the cracks as long as the initial layout of interfaces is ‘reasonable’, i.e., it includes all major potential cracking paths without excessive tortuosity Carol et al. (2001); Garello (1999); López et al. (2008). In any case, a post-process analysis of the evolution of the stress state in the continuum elements and a mesh sensitivity analysis must be always conducted to assess the suitability of the proposed mesh and propose a new discretisation, if needed.

The interface elements adopted for this model are of the triple-node type (Figure 2.251). The top and bottom face nodes, which are shared with the adjacent continuum elements, have four degrees of freedom (x, y coordinates, liquid phase pressure p_p, and gas phase pressure p_g), while inner nodes have only two (p_p and p_g). (Interface elements of the double-node type are those which only have nodes on the top and bottom faces.) The insertion of these elements in conventional FE meshes is performed with a separate programme which has been developed adapting the algorithm proposed by Nguyen (2014).

The flow problem is treated in the typical theoretical framework for isothermal two-phase flow in porous media, considering two chemical species (water and gas) and two fluid phases (liquid and gas phases). The liquid phase includes both liquid water and dissolved gas species, while the gas phase only comprises gas species, i.e. water vapour is not considered. The mechanical problem is treated with an updated Lagrangian formulation, i.e. geometric non-linearity is taken into account. Finite strain theory is considered for the continuum elements, though small tangential relative displacements are assumed for the discontinuities. In the latter, a node-to-node discretisation of the contact area is used. In a first approach, simple constitutive laws are considered for both types of elements. The continuum medium is assumed to behave linear-elastically, while a simple bilinear elasto-damage law is used for the discontinuities, which is formulated in terms of relative displacements rather than strains. Note that the use of a cohesive-type constitutive relation to represent fracture leads to an automatic regularisation from the viewpoint of objectivity of the mechanical (fracture) problem with mesh refinement Carol et al. (2001), which is a significant advantage of the proposed modelling approach. In establishing the equilibrium equation, quasi-static conditions are assumed, i.e. dynamic forces are neglected. Since the model will be mainly used to simulate injection tests in samples of a few centimetres, body (gravity) forces are neglected.

The coupling between the mechanical and the flow formulations occurs in both directions. On one hand, the fluid phase pressures and the saturation degree are introduced in the mechanical equilibrium equation through the principle of effective stress. On the other hand, the flow properties (gas-entry value, storage capacity, longitudinal transmissivity and diffusivity) vary dramatically, governed largely by the mechanical aperture of the discontinuity. To deal with these strong couplings, a monolithic (fully coupled) numerical implementation is used.

The continuum medium part of the model follows the formulation proposed by Collin et al. (2002a) and Gerard et al. (2008a), without introducing significant changes. In contrast, for modelling the discontinuities a new triple-node PHM interface element has been developed using a node-to-node discretisation of the contact problem. The new interface element borrows concepts from previous works by Segura and Carol Segura and Carol (2004, 2008a,b), who developed a double-node HM interface element with node-to-node contact discretisation, and by Cerfontaine et al. Cerfontaine et al. (2015a) and Dieudonné et al. Dieudonné et al. (2015), who developed a triple-node PHM interface element with segment-to-segment contact discretisation. Although the new interface element is presented in 2D, the formulation developed is valid and readily extensible to 3D.

In the segment-to-segment contact discretisation, the zones at each side of the discontinuity that are going to interact with each other are not defined a priori and may change during the simulation. For that reason, elements with segment-to-segment contact discretisation are able to model large relative displacements properly, although at the expense of a high computational cost. In contrast, in the node-to-node contact discretisation, the interacting zones at each side are defined a priori and are assumed to remain the same during the simulation. This assumption leads to a much lower computational cost, although restricting the applicability of this kind of element to problems with small tangential relative displacements. A brief review on contact discretisation methods can be found in Cerfontaine et al. (2015a).

Note that the systematic use of interface elements all over the mesh, as illustrated in Figure 2.251, has the disadvantage of significantly increasing the number of degrees of freedom in comparison with standard continuum analysis. For the 2D analyses presented in this paper this increase of the computational cost can be afforded, but 3D analysis would require a remedy. For instance, Pandolfi and Ortiz (1998) proposed a procedure based on calculation of inter-element forces to duplicate nodes and insert interface elements as needed.

2.10.1.3. PHM governing equations for the continuum porous medium

Mechanical problem

After neglecting the body forces, the linear momentum balance equation of the continuum porous medium reads as follows:

$$\nabla \cdot \boldsymbol{\sigma} = \mathbf{0} \tag{2.1}$$

where $\boldsymbol{\sigma}$ [Pa] is the Cauchy's total stress tensor. The sign convention of continuum mechanics (i.e. tensile stress is positive) is used in this paper.

The constitutive behaviour of the continuum porous medium is formulated in terms of the effective stress tensor $\boldsymbol{\sigma}'$ and its conjugate strain tensor ε. The material is assumed isotropic and linear elastic, with parameters E [Pa] (Young's modulus) and ν [-] (Poisson's coefficient). The effective stress results from considering the effect of the pore fluid pressures acting on the solid grains of the porous medium via the following expressions:

$$\boldsymbol{\sigma}' = \boldsymbol{\sigma} + bp_s\mathbf{I} \tag{2.2}$$

$$p_s = S_w p_p + S_g p_g \tag{2.3}$$

where b is the Biot's coefficient, $\mathbf{I}$ is the identity tensor, and $\mathrm{p_s}$ [Pa] is the effective pore pressure, and p_π [Pa] and S_π [$\mathrm{m^3/m^3}$] are the pressure and pore saturation degree of the fluid phase π ($\pi = \mathrm{w}$ for the liquid phase and $\pi = \mathrm{g}$ for the gas phase), respectively. The liquid saturation degree is obtained as a function solely of the capillary pressure ($\mathrm{p_c = p_g - p_p}$), as it is described below. Since the pore space is assumed to be fully saturated with the liquid and gas phases, $\mathrm{S_g = 1 - S_w}$.

Flow problem

Mass balance

The mass balance equations of gas and water species in a REV of porous medium are given by:

$$\frac{\partial}{\partial t}\left(nS_w\rho_{\mathrm{w}w}\right) + \nabla\cdot\mathbf{q}_{\mathrm{w}} = 0 \tag{2.4}$$

$$\frac{\partial}{\partial t}\left(nS_w\rho_{\mathrm{g}w} + nS_g\rho_{\mathrm{g}g}\right) + \nabla\cdot\mathbf{q}_{\mathrm{g}} = 0 \tag{2.5}$$

where n is the porosity, $\rho_{\varsigma\pi}$ [$\mathrm{kg/m^3}$] is the mass concentration of ς species in the fluid phase π, and $\mathbf{q}_\varsigma$ [$\mathrm{kg/(m^2\,s)}$] is the average mass flow vector of the ς species. Note that w and g subindexes (in Italic type) are used to denote the liquid and gas phases, while w and g subindexes (in Roman type) are used to denote water and gas species. The storage terms in Eqs. (2.4) and (2.5) couple the mechanical and the flow formulations via the porosity rate, which is obtained with the following expression:

$$\frac{\partial n}{\partial t} = (n-b)\left(C_s\frac{\partial p_s}{\partial t} + \frac{\partial\varepsilon_v}{\partial t}\right) \tag{2.6}$$

where $\mathrm{C_s}$ [1/Pa] is the compressibility (the inverse of the bulk modulus) of the solid grains, and $\varepsilon_\mathrm{v} = \mathrm{tr}(\varepsilon)$ is the volumetric strain of the porous medium.

Equations of state

Only one species is considered in the gas phase, so the density of the gas phase and the density of gas species in the gas phase are the same, i.e. $\rho_{\mathrm{g}g} = \rho_g$. Then, assuming ideal gas behaviour, the density of the gas phase is obtained as follows:

$$\rho_g = \frac{M_\mathrm{g}}{RT}p_g \tag{2.7}$$

where $\mathrm{M_g}$ [kg/mol] is the molar weight of the gas species, $\mathrm{R} = 8.314$ [$\mathrm{(m^3Pa)/(Kmol)}$] is the gas constant, T [K] is the system temperature.

The mass of gas species dissolved per unit volume of liquid phase ($\rho_{\mathrm{g}w}$ [$\mathrm{kg/m^3}$]) is obtained, assuming local equilibrium, with the following Henry's law equation:

$$\rho_{\mathrm{g}w} = H\rho_g \tag{2.8}$$

where H is the dimensionless Henry solubility constant for the gas species in liquid water. It is assumed that the dissolved gas has a negligible effect on the density of the liquid phase, and therefore, it is considered that $\rho_{\mathrm{w}w} = \rho_w$.

The liquid phase density is assumed to depend linearly on the liquid phase pressure according to the following expression:

$$\rho_w = \rho_{w,o}\left[1 + C_w\left(p_p - p_{w,o}\right)\right] \tag{2.9}$$

where $\rho_{w,o}$ [kg/m^3] and C_w [1/Pa] are the water density and compressibility, respectively, at the reference pressure $p_{w,o}$.

Mass flows

The mass flow vectors in Eqs. (2.4) and (2.5) can be expanded as follows:

$$\mathbf{q}_w = \rho_{ww}\mathbf{v}_w \tag{2.10}$$

$$\mathbf{q}_g = \rho_{gw}\mathbf{v}_w + \rho_{gg}\mathbf{v}_g + \mathbf{i}_{gw} \tag{2.11}$$

where $\mathbf{v}_\pi$ [m/s] is the average (Darcy) velocity of the fluid phase π, and $\mathbf{i}_{gw}$ [kg/(m^{2}s)] is the average diffusive flow of gas species dissolved in the pore water.

The average fluid phase velocities are obtained with the following two-phase generalisation of Darcy's law:

$$\mathbf{v}_\pi = -\frac{k_{\pi,r}}{\mu_\pi}\mathrm{k}\nabla p_\pi \quad \text{for } \pi = w, g \tag{2.12}$$

where k [m^2] is the intrinsic permeability tensor of the porous medium, μ_π [Pa s] is the dynamic viscosity of the fluid phase π, and $k_{\pi,r}$ is the dimensionless relative permeability coefficient, which ranges between 0 and 1 as a function solely of S_π.

The average diffusive flow vector of gas species in the pore water is obtained with following generalisation of Fick's law for an unsaturated porous medium:

$$\mathbf{i}_{gw} = -nS_w\tau D_{gw}\rho_w\nabla\left(\frac{\rho_{gw}}{\rho_w}\right) \tag{2.13}$$

where D_{gw} [m^2/s] is the diffusion coefficient of the gas species in bulk water, and τ is a dimensionless coefficient accounting for the effect of the tortuosity of the pore space.

Liquid retention and relative permeability

The retention behaviour of the continuum porous medium has been chosen, for simplicity, to be represented with the standard van Genuchten's model:

$$S_w(p_c) = (1 - S_{wr})\left[1 + \left(\frac{p_c}{p_b}\right)^{\frac{1}{1-\lambda}}\right]^{-\lambda} + S_{wr} \tag{2.14}$$

where S_{wr} is the residual degree of saturation, p_b [Pa] is a parameter related to the gas-entry value, and λ is a parameter that controls the shape of the curve.

The relative permeability coefficients for the liquid and gas phases are considered to be functions of the effective degree of saturation (S_e) according to the following power laws:

$$k_{w,r} = S_e^{n_w}; \quad k_{g,r} = (1 - S_e)^{n_g} \tag{2.15}$$

where n_w and n_g are dimensionless material parameters and

$$S_e = \frac{S_w - S_{wr}}{1 - S_{wr}} \tag{2.16}$$

2.10.1.4. PHM governing equations for the discontinuities

Mechanical problem

The equilibrium condition for a discontinuity is posed for a local basis with direction normal ($\mathbf{e_n}$) and tangential ($\mathbf{e_l}$) to the discontinuity mid-plane, as follows:

$$\frac{\partial \boldsymbol{\sigma}}{\partial l} = \mathbf{0} \tag{2.17}$$

where $\boldsymbol{\sigma} = \begin{bmatrix}\sigma_n & \sigma_l\end{bmatrix}^T$ is the total stress on the discontinuity mid-plane, with components normal (σ_n) and tangential (σ_l) to the discontinuity mid-plane (Figure 2.252).

The constitutive behaviour is formulated in terms of the effective stress $\boldsymbol{\sigma}' = \begin{bmatrix}\sigma'_n & \sigma_l\end{bmatrix}^T$ and the conjugate relative displacement $\mathbf{r} = \begin{bmatrix}r_n & r_l\end{bmatrix}^T$ (Figure 2.252). The effective stress is defined as follows:

$$\boldsymbol{\sigma}' = \boldsymbol{\sigma} + \mathbf{m} p_s \tag{2.18}$$

where p_s [Pa] is the effective fluid pressure at the discontinuity mid-plane, and $\mathbf{m} = \begin{bmatrix}1 & 0\end{bmatrix}^T$.

The effective fluid pressure is obtained as a function of the saturation degree and the fluid phase pressures with the same expression as for the continuum porous medium (Eq. (2.3)). However, here the liquid saturation degree is obtained not only as a function of the capillary pressure, but also of the normal separation (r_n), as it is discussed below. As for the continuum medium, the discontinuity is assumed to be fully saturated with the liquid and gas phases, i.e., $S_g = 1 - S_w$.

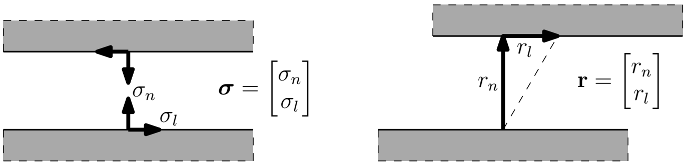

Figure 2.252: Definition of stress and conjugate relative displacement variables for a discontinuity.

In principle, the solid domains at both sides of the discontinuity cannot overlap each other, i.e. the normal relative displacement (r_n) cannot be negative. This strict condition, which would be very demanding for the numerical resolution of the problem, is relaxed by authorising a small interpenetration of the solids in contact using the penalty method. The interpenetration is limited in the constitutive law (see below the formulation of the constitutive law) by assigning a very high normal stiffness for $r_n < 0$.

Constitutive law

The mechanical constitutive behaviour of the discontinuity is modelled using the elasto-damage law proposed by Mi et al. (1998), combined with a Newtonian damper for the normal direction. The response of the elasto-damage law for pure normal (Mode I) and pure shear (Mode II) loading is schematically depicted in Figure 2.253. Three parameters characterise each of these constitutive curves: the maximum tensile/shear strength (σ_{n0}, σ_{l0}), the normal/tangential 'cracking' separation (r_{n0}, r_{l0}) and the normal/tangential debonding separation (r_{nc}, r_{lc}). The dashed lines in Figure 2.253a and b indicate the unloading-reloading path after reaching relative displacements r_n^* and r_l^*, respectively.

In the general (mixed mode) loading condition, normal and tangential stresses are obtained with the following expressions:

$$\sigma'_{n,d} = \begin{cases} (1 - D)\, K_n r_n & \text{if } r_n \geq 0 \\ K_n r_n & \text{if } r_n < 0 \end{cases} \tag{2.19}$$

$$\sigma_l = (1 - D)\, K_l r_l \tag{2.20}$$

where $K_n = \sigma_{n0}/r_{n0}$ and $K_l = \sigma_{l0}/r_{l0}$ are the initial (very high) normal and tangential stiffness, respectively. In the context of this paper, these coefficients should be interpreted as penalty coefficients that must be set to values as high as possible without causing numerical problems, in order to reduce the artificial compliance introduced by the interface elements to negligible values.

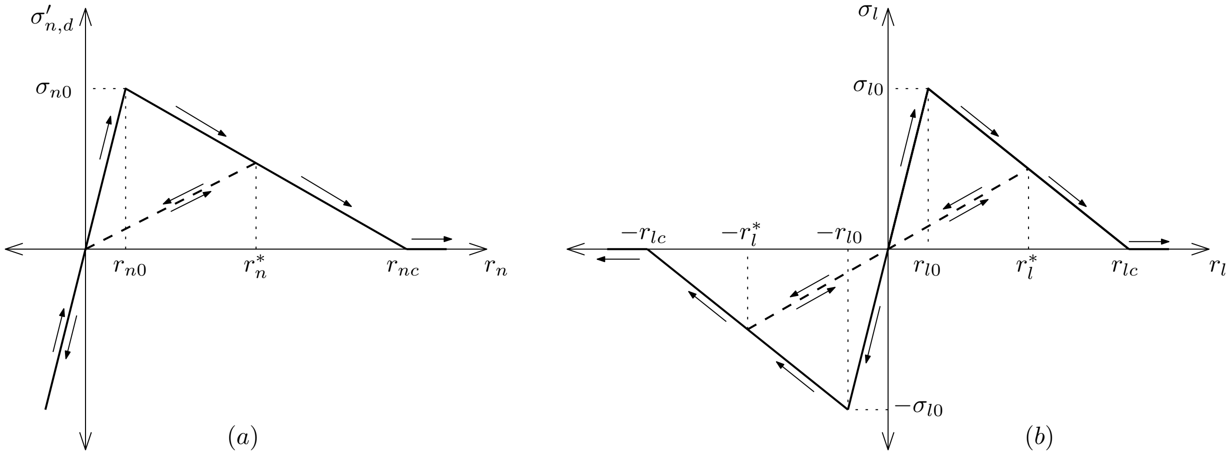

Figure 2.253: Constitutive relationships for (a) pure normal loading and (b) pure tangential loading.

Equations (2.19) and (2.20) are coupled through the damage variable D. The damage variable, which ranges between 0 and 1, accounts for the material softening when the normal and/or the tangential separation goes beyond the cracking separation, and it is obtained from the following expressions:

$$D = \min\left(\frac{\bar{\omega}}{1+\bar{\omega}}\frac{1}{\eta}, 1\right) \tag{2.21}$$

$$\bar{\omega} = \max(\omega) \tag{2.22}$$

$$\omega = \left\langle \left[\left(\frac{\langle r_n \rangle}{r_{n0}} \right)^{\beta} + \left(\frac{|r_l|}{r_{l0}} \right)^{\beta} \right]^{1/\beta} - 1 \right\rangle \tag{2.23}$$

$$\eta = 1 - \frac{r_{n0}}{r_{nc}} = 1 - \frac{r_{l0}}{r_{lc}} \tag{2.24}$$

where ω is a positive scalar that accounts for the mechanical degradation of the discontinuity for a given combination of normal and tangential separations, β is a material parameter that characterises the mixed mode damage and which will generally assume values between 1 and 2 (in this report, $\beta = 1$), $\bar{\omega}$ is a history variable that stores the maximum value reached by ω in the loading history, and $\langle \bullet \rangle = \left(\bullet + |\bullet|\right)/2$ is the Macaulay bracket. The restriction to the material parameter ratios r_{n0}/r_{nc} and r_{l0}/r_{lc} established in Eq. (2.24) guarantees that the tensile and shear strength reach zero simultaneously.

Note in Eq.(2.19) that, under compression loading, the constitutive response is always determined by the (very high) initial stiffness K_n, regardless the damage state of the discontinuity. In that way, the possible overlapping of the solid domains at both sides of the discontinuity under compressive loads is kept small (i.e. the penalty method). Moreover, according to Eq. (2.24), no damage is induced by negative normal separations.

Finally, the effective stress in the normal direction is obtained by adding a viscous component as follows:

$$\sigma'_n = \sigma'_{n,d} + \sigma'_{n,v} \quad \text{with } \sigma'_{n,v} = \zeta \frac{\partial r_n}{\partial t} \tag{2.25}$$

where ζ [Pa s/m] is the viscosity. The viscous term is included to address numerical instabilities that may develop under certain conditions, and which are discussed below in Section 2.10.2.

Flow problem

The formulation of the flow problem is derived by considering a discontinuity of width w [m] surrounded by the continuum porous medium, and a local orthogonal coordinate system defined by the directions tangent ($\mathbf{e_l}$) and normal ($\mathbf{e_n}$) to the discontinuity (Figure 2.254). Flow of the water and gas species may occur both in the longitudinal and in the transversal directions to the discontinuity. For the sake of simplicity, it is assumed that the longitudinal flows depend on the gas and liquid phase pressures at the centre (mid-plane) of the discontinuity width w. Consistently, the remaining parameters/variables of the discontinuity are also computed at the mid-plane, but assumed to be valid across the discontinuity width.

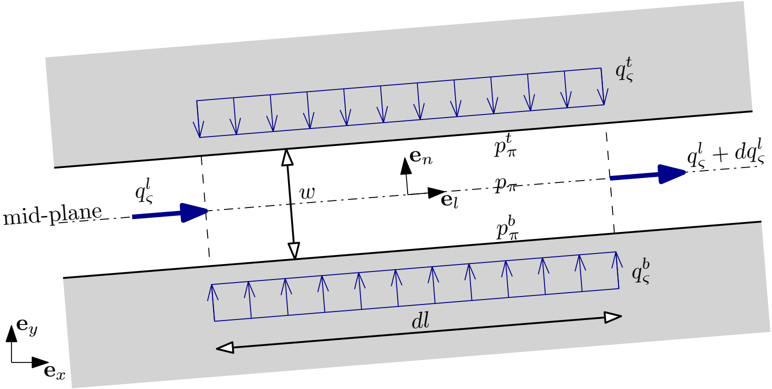

Figure 2.254: Flow problem definition for a 2D discontinuity, for fluid phases $\pi = \mathrm{w}, \mathrm{g}$ *and chemical species* $\varsigma = \mathrm{w}, \mathrm{g}$.

Mass balance

The mass balance of gas and water species is enforced in a differential volume of discontinuity wdl as follows:

$$\frac{\partial}{\partial t}\left(wS_w\rho_{\mathrm{ww}}\right) + \frac{\partial q_{\mathrm{w}}^l}{\partial l} - q_{\mathrm{w}}^b - q_{\mathrm{w}}^t = 0 \tag{2.26}$$

$$\frac{\partial}{\partial t}\left(wS_g\rho_{\mathrm{gg}} + wS_w\rho_{\mathrm{gw}}\right) + \frac{\partial q_{\mathrm{g}}^l}{\partial l} - q_{\mathrm{g}}^b - q_{\mathrm{g}}^t = 0 \tag{2.27}$$

where $\mathrm{q}_\varsigma^\mathrm{l}$ [kg/(m s)] is the longitudinal mass flow of species ς, and $\mathrm{q}_\varsigma^\mathrm{b}$ and $\mathrm{q}_\varsigma^\mathrm{t}$ [kg/(m^2 s)] are the normal mass flows incoming to the discontinuity from the surrounding continuum medium. Densities $\rho_{\varsigma\pi}$ [kg/m^3] are evaluated using the same equations of state as for the continuum medium (Sec. 2.10.1.3). The liquid saturation degree is obtained as a function of the capillary pressure and the normal aperture ($\mathrm{r_n}$), as it is described below. Note that in Eqs. (2.26) and (2.27) the change of the storage capacity due to the possible change of the discontinuity length has been neglected.

The discontinuity width evolves with $\mathrm{r_n}$ as follows:

$$w = \langle r_n \rangle + w_0 \tag{2.28}$$

where $\mathrm{w_0}$ [m] makes it possible to assign an initial storage volume to the discontinuity even if it is mechanically closed.

The mass flows of gas species may be expanded as follows:

$$\begin{aligned} q_{\mathrm{g}}^l &= \rho_g v_g^l + \rho_{\mathrm{gw}} v_w^l + i_{\mathrm{gw}}^l \\ q_{\mathrm{g}}^b &= \rho_g v_g^b + \rho_{\mathrm{gw}} v_w^b + i_{\mathrm{gw}}^b \\ q_{\mathrm{g}}^t &= \rho_g v_g^t + \rho_{\mathrm{gw}} v_w^t + i_{\mathrm{gw}}^t \end{aligned} \tag{2.29}$$

where $\mathrm{v}_\pi^\mathrm{l}$ [m^2/s], $\mathrm{v}_\pi^\mathrm{t}$ [m/s] and $\mathrm{v}_\pi^\mathrm{b}$ [m/s] are the longitudinal and transversal volumetric flows (top and bottom) of phase π, and $\mathrm{i}_\mathrm{gw}^\mathrm{l}$ [kg/(m s)], $\mathrm{i}_\mathrm{gw}^\mathrm{b}$ [kg/(m^2 s)] and $\mathrm{i}_\mathrm{gw}^\mathrm{t}$ [kg/(m^2 s)] are the longitudinal and normal diffusion fluxes of gas species dissolved in the liquid phase.

Similarly, the mass flows of water species are expanded as follows:

$$q_w^l = \rho_w v_w^l; \quad q_w^b = \rho_w v_w^b; \quad q_w^t = \rho_w v_w^t; \tag{2.30}$$

Volumetric fluid phase flows

The longitudinal volumetric fluid phase flows in Eqs. (2.29) and (2.30) are obtained from the following generalised Darcy's law:

$$v_\pi^l = -\frac{k_{\pi,r}}{\mu_\pi} t^l \frac{\partial p_\pi}{\partial l} \tag{2.31}$$

where $\mathrm{k}_{\pi,\mathrm{r}}$ [-] and μ_π [Pa s] are the relative permeability and the dynamic viscosity of the fluid phase π, respectively, and t^l [m^3] is the longitudinal hydraulic coefficient.

Similarly, the transversal volumetric flows are assumed to be proportional to the transversal pressure drops $\check{\mathrm{p}}_\pi^\mathrm{b}$ and $\check{\mathrm{p}}_\pi^\mathrm{t}$ between the discontinuity boundaries and the mid-plane, namely:

$$v_\pi^b = -\frac{k_{\pi,r}}{\mu_\pi} k^b \check{p}_\pi^b \quad \text{for } \pi = w, g \tag{2.32}$$

$$v_\pi^t = -\frac{k_{\pi,r}}{\mu_\pi} k^t \check{p}_\pi^t \quad \text{for } \pi = w, g \tag{2.33}$$

where k^b and k^t [m] are the transversal hydraulic coefficients. The transversal pressure drops are defined as follows:

$$\check{p}_\pi^b = p_\pi - p_\pi^b; \quad \check{p}_\pi^t = p_\pi - p_\pi^t \tag{2.34}$$

where $\mathrm{p}_\pi^\mathrm{b}$, p_π, and $\mathrm{p}_\pi^\mathrm{t}$ [Pa] are the fluid phase pressures at the bottom side, mid-plane and top side of the discontinuity, respectively. With this definition, the transversal flows obtained with Eqs. (2.32) and (2.33) are positive when they go into the discontinuity, regardless of whether they enter through the top or the bottom face.

The hydraulic coefficients t^l, k^b and k^t are considered to be determined by the geometric characteristics of the discontinuity. In this sense, they play the role of the intrinsic permeability in the formulation for the continuum porous medium. The longitudinal coefficient is estimated as a function of the discontinuity normal aperture with the following expression:

$$t^l = \frac{\langle r_n \rangle^3}{12} + t_0^l \tag{2.35}$$

where the first term is given by the Hagen-Poiseuille equation for laminar flow between two parallel plates, and t_0^l makes it possible to assign an initial longitudinal transmissivity to the discontinuity even if it is closed from the mechanical point of view. In contrast, the transversal coefficients k^b and k^t are deemed constant parameters.

Diffusion of gas in the liquid phase

The longitudinal diffusive flow of gas species dissolved in the liquid phase, $\mathrm{i}_\mathrm{gw}^\mathrm{l}$ [kg/(m s)], is obtained with the following generalised Fick's law:

$$i_{gw}^l = -S_w D_{gw} d^l \rho_w \frac{\partial}{\partial l}\left(\frac{\rho_{gw}}{\rho_w}\right) \tag{2.36}$$

where D_gw [m^2/s] is the diffusion coefficient of the gas species in bulk water, and d^l [m] is a coefficient that accounts for the effect of the discontinuity geometry on the the diffusive flux (analogous to the product of porosity and tortuosity in the continuum medium formulation), obtained as a linear function of the normal aperture as follows:

$$d^l = \langle r_n \rangle + d_0^l \tag{2.37}$$

where d^l_0 makes it possible to assign an initial longitudinal diffusivity to the discontinuity even if it is closed from the mechanical point of view. This expression is based on the assumption that diffusion occurs along a clean channel of width $\langle r_n \rangle$ configured by the two faces of the discontinuity.

Considering Henry's law (Eq. (2.8)) and expanding the derivative, Eq. (2.36) can be rewritten in terms of the longitudinal gradients of gas and liquid pressures as follows:

$$i^l_{gw} = -S_w d^l D_{gw} \left(H \frac{\partial \rho_g}{\partial p_g} \frac{\partial p_g}{\partial l} - \frac{\rho_{gw}}{\rho_w} \frac{\partial \rho_w}{\partial p_p} \frac{\partial p_g}{\partial l} \right) \tag{2.38}$$

In addition to the longitudinal diffusive flux, normal fluxes i^b_{gw} and i^t_{gw} [kg/(m^2 s)] from the bottom and top sides of the discontinuity, respectively, are considered. These fluxes are obtained as follows:

$$i^b_{gw} = -S_p D_{gw} \tau^b \left(\rho_{gw} - \rho^b_{gw} \right) \tag{2.39}$$

$$i^t_{gw} = -S_p D_{gw} \tau^t \left(\rho_{gw} - \rho^t_{gw} \right) \tag{2.40}$$

where ρ^b_{gw}, ρ_{gw} and ρ^t_{gw} represent the mass concentration of gas species in the liquid phase at the bottom side, the mid-plane and the top side of the discontinuity, respectively, and τ^b and τ^t [1/m] are constant coefficients that account for the effect of the discontinuity geometry in the effective transversal diffusivities. These expressions are obtained under the assumption that the liquid phase density is constant across the discontinuity. As for the transversal fluid flows, the transversal diffusive flows are positive when they enter the discontinuity.

Finally, considering Henry's law (Eq. (2.8)) and assuming that gas has an ideal behaviour, Eqs. (2.39) and (2.40) can be rewritten in terms of the normal gas pressure jumps (Eqs. (2.32) and (2.33)) as follows:

$$i^b_{gw} = -S_w D_{gw} \tau^b H \frac{\partial \rho_g}{\partial p_g} \check{p}^b_g \tag{2.41}$$

$$i^t_{gw} = -S_w D_{gw} \tau^t H \frac{\partial \rho_g}{\partial p_g} \check{p}^t_g \tag{2.42}$$

Liquid retention and relative permeability

Similarly to the continuum medium, the liquid retention of the discontinuity is also modelled with a van Genuchten curve. However, the assumption of constant curve parameters adopted for the continuum medium is reconsidered for the discontinuities, given the dramatic variations in the fluid-filled 'pore' space with their normal aperture. In order to introduce this effect, Eq. (2.14) is rewritten in terms of functions $\bar{p}_b(r_n)$ and $\bar{S}_{wr}(r_n)$ instead of constant parameters p_b and S_{wr}, i.e.

$$S_w(p_c, r_n) = \left(1 - \bar{S}_{wr}\right) \left[1 + \left(\frac{p_c}{\bar{p}_b} \right)^{\frac{1}{1-\lambda}} \right]^{-\lambda} + \bar{S}_{wr} \tag{2.43}$$

Note that the parameter λ is still deemed to be constant.

In order to obtain functions $\bar{p}_b(r_n)$ and $\bar{S}_{wr}(r_n)$, two possible states of the discontinuity are considered: closed, when $r_n \leq 0$, and open, when $r_n > 0$. As stated above, one of the premises of the proposed modelling approach is that the interface elements representing potential cracking paths must not have any significant effect in the overall behaviour of the modelled material, as long as they remain closed. In other words, in the closed state, the retention curve of the discontinuity must be the same as the one for the continuum medium. This implies that for $r_n \leq 0$, $\bar{p}_b = p_b$ and $\bar{S}_{wr} = S_{wr}$. In contrast, in the open state, the parameter $\bar{p}_b$, which is linked to the gas-entry value, and the parameter $\bar{S}_{wr}$, which accounts for the fraction of the discontinuity volume occupied by immobile (residual) liquid, is expected to decrease for increasing r_n.

In order to derive $\bar{p}_b(r_n)$ in the open state, the Laplace equation to estimate the gas-entry value of the porous medium is first considered:

$$p_{ev} = T_s \left(\frac{1}{R_1} + \frac{1}{R_2} \right) \tag{2.44}$$

where T_s [N/m] is the liquid-gas interfacial tension, and R_1 and R_2 [m] are the curvature radii of the gas-liquid interface. Assuming that $R_1 = R_2 = d/2$, a characteristic pore size of the porous medium can be obtained as $d = 4T_s/p_{ev}$. Likewise, the gas-entry value of an open discontinuity ($\bar{p}_{ev}$) is approximated with the same Laplace equation, but assuming a very large R_1 ($1/R_1 \approx 0$) and $R_2 = d/4 + \bar{r}/2$, i.e.

$$\bar{p}_{ev} = \frac{2T_s}{d/2 + \bar{r}} = \frac{d}{d + 2\bar{r}} p_{ev} \tag{2.45}$$

where $\bar{r}$ [m] represents the effective aperture of the discontinuity. In a strict sense, $\bar{r}$ should be the positive part of r_n. However, in order to prevent numerical problems, $\bar{r}$ is obtained as follows:

$$\bar{r}(r_n) = \langle r_n \rangle - \alpha \left[1 - \exp\left(\frac{-\langle r_n \rangle}{\alpha} \right) \right] \tag{2.46}$$

where the third term gives C^1 continuity to the function $\bar{r}(r_n)$ and makes it possible to smooth the transition between closed ($r_n \leq 0$) and open ($r_n > 0$) states by increasing the positive parameter α. Then, by assuming that $\bar{p}_b$ evolves proportionally to $\bar{p}_{ev}$, the first expression sought is obtained:

$$\bar{p}_b = \frac{d}{d + 2\bar{r}} p_b \tag{2.47}$$

The second expression sought ($\bar{S}_{wr}$) is obtained by assigning an initial volume of immobile liquid phase to the discontinuity in closed state, and assuming that this volume does not grow nor decrease when the normal aperture becomes positive. Considering the pore volume associated to the closed discontinuity is nd, where n is the porosity of the porous medium and d is the above defined characteristic pore size, the volume of immobile liquid phase is estimated as $S_{wr}nd$. Then, considering the updated 'pore' volume of the discontinuity will be $nd + \bar{r}$, the residual saturation degree of the discontinuity evolves as follows:

$$\bar{S}_{wr} = \frac{nd}{nd + \bar{r}} S_{wr} \tag{2.48}$$

Finally, the relative permeabilities are obtained with the same expressions used for the continuum medium (Eq. (2.15)), but introducing the effect of the normal aperture in the residual saturation into the expression of the effective saturation (Eq. (2.48)). This leads to

$$S_e = \frac{S_w - \bar{S}_{wr}}{1 - \bar{S}_{wr}} \tag{2.49}$$

The proposed retention and relative permeability functions are illustrated in Figure 2.255 and Figure 2.256, respectively, which show their evolution for increasing values of r_n. The parameters used were $n = 0.39$, $p_{ev} = 5.0\,\text{MPa}$, $p_b = 10.0\,\text{MPa}$, $S_{wr} = 0.20$, $\lambda = 0.56$, $\alpha = 3{,}000\,\text{nm}$, $n_w = 1.5$, and $n_g = 3.0$. These parameters were calibrated for $r_n = 0$ with experimental data from bulk Boom clay (Gonzalez-Blanco et al., 2016a; Volckaert et al., 1995a). A standard value of $T_s = 72.7\,\text{mN/m}$ corresponding to an air-water interface at 20 °C is adopted (Vargaftik et al., 1983).

2.10.1.5. Numerical model

Finite Element implementation

The model outlined in the previous sections has been implemented in the FE code LAGAMINE. The porous medium equations have been discretised with a large strain element type, which is described in

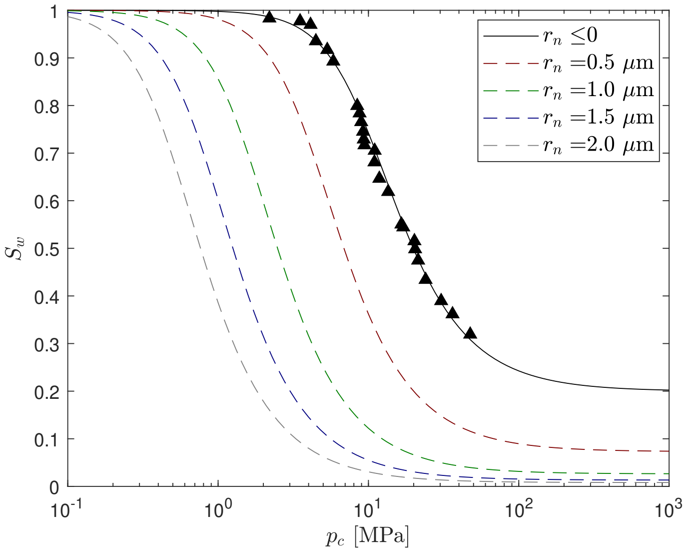

Figure 2.255: Liquid retention curves for discontinuities in Boom clay with different normal aperture. The solid line corresponds to the bulk porous medium or a closed discontinuity ($r_n \leq 0$), while dashed lines correspond to discontinuities with increasing aperture ($r_n > 0$). Markers indicate experimental psychrometer measurements of intact Boom clay from Gonzalez-Blanco et al. (2016a).

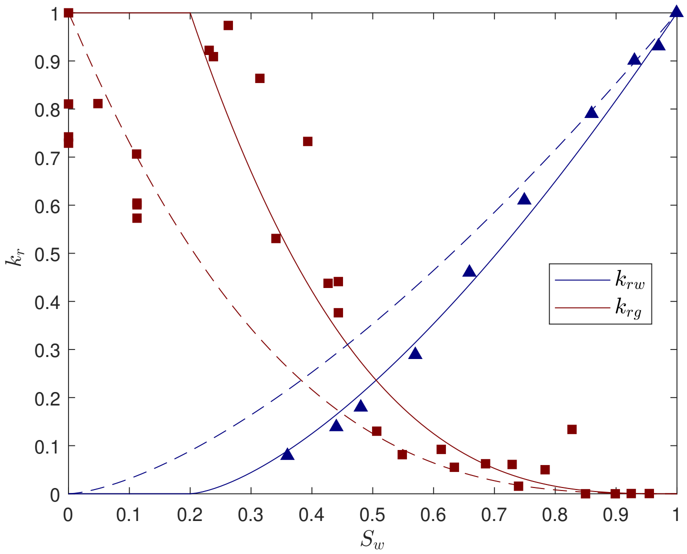

Figure 2.256: Relative permeability functions for discontinuities in Boom Clay. Solid lines correspond to the bulk porous medium or a closed discontinuity ($r_n \leq 0$), while dashed lines correspond to a discontinuity with a large aperture ($r_n = 10\,\mu$m). Markers indicate experimental data from Volckaert et al. (1995a) for intact Boom Clay only.

detail by Collin et al. (2002a). This element has five degrees of freedom at each node (x and y coordinates, liquid pressure, gas pressure and temperature), though the temperature is fixed for the model proposed in this paper. The implementation of this element in LAGAMINE allows the use of shape functions of different order to interpolate the nodal displacements and pore pressures, in order to comply with the Ladyzhenskaya-Babuška-Brezzi stability condition (Arnold, 1990; Brezzi and Bathe, 1990). However, in the simulations performed for this paper the same parabolic shape functions have been used to interpolate displacements and fluid pressures, without observing spurious pressure oscillations or sub-optimal convergence behaviour. The nodal fluxes and forces are obtained after writing the integral forms of Eqs. (2.1), (2.4) and (2.5), and applying the Principle of Virtual Work (Collin, 2003a). To increase the numerical stability, nodal water and gas flows and the corresponding stiffness sub-matrices are always computed in the initial configuration. The so-called tangential stiffness matrix of the coupled element is monolithic, including all the coupling terms and second order effects due to geometry variation (Collin, 2003a).

For the discontinuity equations, a new triple-node zero-thickness interface element has been formulated and implemented in LAGAMINE. The node numbering and nodal degrees of freedom are shown in Figure 2.257 for a quadratic element. Note that the outer nodes (labelled `t` and `b`) are considered for both the mechanical and the flow problems, while the inner nodes (labelled `m`) are only considered for the flow problem. The FE formulation of the mechanical problem is developed with an updated Lagrangian approach and with a node-to-node discretisation of the contact area, by adapting the formulation outlined in Lequesne (2009) for purely mechanical double-node interface elements. In contrast to small displacement formulations, where the normal and tangential components of the relative displacements and stresses are obtained with regard to the original configuration, in the proposed update Lagrangian approach, the position of the mechanical mid-plane, on which the local basis is defined, is updated in each loading increment. For this reason, the proposed element is suitable for problems in which the interface nodes experience large displacements and rotations, although with small tangential relative displacement because of the node-to-node discretisation of the contact area.

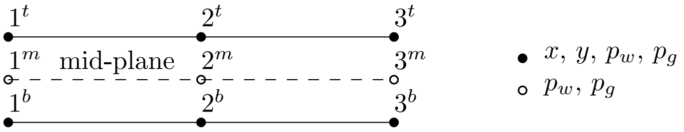

Figure 2.257: Element node numbering and nodal degrees of freedom.

The flow part of the FE formulation has been developed by adapting the coupled HM (single phase) formulation for double-node interface elements proposed in Segura and Carol Segura and Carol (2004, 2008b). In double-node element formulations, the pressure inside the discontinuity is not considered as an independent degree of freedom but assumed to be the average between the pressure at the bottom and top faces. In the following subsection , it is demonstrated that the accuracy of this assumption depends mainly on the longitudinal fluid pressure profiles and the current values of the longitudinal and transversal hydraulic/diffusion coefficients, which in turn depends on the mechanical aperture and the capillary pressure. It is concluded from this analysis, that the error introduced by the average pressure assumption used for double-node elements cannot be estimated a priori. Therefore, developing a triple-node element was preferred to be on the safe side, although at the expense of increasing the computational cost of the model. Moreover, triple-node elements outperform double-node ones in that they allow the user to hydraulically disconnect the continuum medium at one or both sides of the element from the discontinuity channel, just by nullifying the corresponding transversal hydraulic coefficients. In that way, triple-node elements are particularly well-suited for modelling hydraulic interfaces between a permeable medium and an impervious one, e.g. the interface between a clay sample and a metallic testing device. As with the continuum elements, in the proposed interface element the fluid pressure gradients are always computed in the initial configuration.

More comprehensive details of the formulation of the new interface element are presented in the following subsection (‘PHM interface element formulation’).

Finally, after the assemblage of the continuum and the interface element nodal forces and mass fluxes, the mechanical equilibrium and mass balance with the imposed external forces/fluxes is enforced at the end of each time increment, i.e. adopting a backward Euler time integration scheme, using the standard Newton-Raphson method.

The implementation in LAGAMINE of the new interface element and the corresponding constitutive laws has been systematically verified in simple benchmark problems with analytical solutions. A thorough verification of the continuum part of the model can be found in Collin (2003a).

On double- and triple-node interface elements

The formulation of double-node interface elements is developed under the assumption that the fluid pressure inside the discontinuity is approximately equal to the average between top and bottom face pressures, i.e.

$$p_\pi \approx \frac{p_\pi^b + p_\pi^t}{2} \tag{2.50}$$

In order to assess the validity of this assumption, let us consider the mass balance equations Eqs. (2.26) and (2.27) for a steady state:

$$\frac{\partial q_\varsigma^l}{\partial l} - q_\varsigma^b - q_\varsigma^t = 0 \quad \text{for } \varsigma = w, g \tag{2.51}$$

Introduction of Eqs. (2.29) – (2.34) in this expression leads to:

$$\frac{\partial}{\partial l}\left(\rho_\pi T_\pi^l \frac{\partial p_\pi}{\partial l}\right) - \rho_\pi K_\pi^t \left(p_\pi - p_\pi^b\right) - \rho_\pi K_\pi^t \left(p_\pi - p_\pi^t\right) = 0 \quad \text{for } \pi = w, g \tag{2.52}$$

where $\mathrm{T}_\pi^\mathrm{l} = \mathrm{k}_{\pi,\mathrm{r}}\mathrm{t}^\mathrm{l}/\mu_\pi$ and $\mathrm{K}_\pi^\mathrm{t} = \mathrm{k}_{\pi,\mathrm{r}}\mathrm{k}^\mathrm{t}/\mu_\pi$. For the sake of simplicity, the gas dissolved in the liquid phase has been neglected and the bottom and top transversal hydraulic coefficients are assumed to be equal. Finally, after some algebra, the following expression is obtained:

$$p_\pi - \frac{p_\pi^b + p_\pi^t}{2} = \frac{T_\pi^l}{2K_\pi^t}\frac{\partial^2 p_\pi}{\partial l^2} + \frac{1}{2K_\pi^t}\frac{\partial T_\pi^l}{\partial l}\frac{\partial p_\pi}{\partial l} + \frac{T_\pi^l}{2K_\pi^t \rho_\pi}\frac{\partial \rho_\pi}{\partial p_\pi}\left(\frac{\partial p_\pi}{\partial l}\right)^2 \tag{2.53}$$

Note that the significance of the right-hand side terms in this equation determines the accuracy of the average pressure assumption (Eq. (2.50)). From them, it can be concluded, that for a given longitudinal pressure profile, the difference between the results obtained with triple-node elements and the results obtained with double-node elements will be mainly determined by the longitudinal and transversal hydraulic conductivities $\mathrm{T}_\pi^\mathrm{l}$ and $\mathrm{K}_\pi^\mathrm{t}$. The higher $\mathrm{K}_\pi^\mathrm{t}$ and the lower $\mathrm{T}_\pi^\mathrm{l}$, the more similar the results obtained with both kinds of interface elements. A similar conclusion was drawn by Segura and Carol (2004) after comparing the performance of triple- and double-node elements for modelling water flow in a discontinuous medium.

PHM interface element formulation

Nodal unknowns

The nodal unknowns vector $\bar{\mathbf{u}}$ of the interface element depicted in Figure 2.256 is defined as follows:

$$\bar{\mathbf{u}} = \begin{bmatrix} \bar{\mathbf{x}} \\ \bar{\mathbf{p}}_\mathbf{w} \\ \bar{\mathbf{p}}_\mathbf{g} \end{bmatrix} \quad \text{with} \quad \bar{\mathbf{x}} = \begin{bmatrix} \bar{\mathbf{x}}^\mathbf{b} \\ \bar{\mathbf{x}}^\mathbf{t} \end{bmatrix} \quad \text{and} \quad \bar{\mathbf{p}}_\pi = \begin{bmatrix} \bar{\mathbf{p}}_\pi^\mathbf{b} \\ \bar{\mathbf{p}}_\pi^\mathbf{t} \\ \bar{\mathbf{p}}_\pi^\mathbf{m} \end{bmatrix} \tag{2.54}$$

where vectors $\bar{\mathbf{x}}$ and $\bar{\mathbf{p}}_\pi$ ($\pi = \mathrm{w}, \mathrm{g}$) store the nodal coordinates, liquid phase pressures and gas phase pressures, respectively. The superindexes b, t, and m indicate if the nodes correspond to the bottom face, top face or mid-plane of the element. The components of the unknowns vectors are the following:

$$\bar{\mathbf{x}}^b = \left[\mathrm{x}_1^\mathrm{b} \quad \mathrm{y}_1^\mathrm{b} \quad \mathrm{x}_2^\mathrm{b} \quad \mathrm{y}_2^\mathrm{b} \quad \mathrm{x}_3^\mathrm{b} \quad \mathrm{y}_3^\mathrm{b}\right]^\top \tag{2.55}$$

$$\bar{\mathbf{x}}^t = \left[\mathrm{x}_1^\mathrm{t} \quad \mathrm{y}_1^\mathrm{t} \quad \mathrm{x}_2^\mathrm{t} \quad \mathrm{y}_2^\mathrm{t} \quad \mathrm{x}_3^\mathrm{t} \quad \mathrm{y}_3^\mathrm{t}\right]^\top \tag{2.56}$$

$$\bar{\mathbf{p}}_\pi^b = \left[\mathrm{p}_{\pi1}^\mathrm{b} \quad \mathrm{p}_{\pi2}^\mathrm{b} \quad \mathrm{p}_{\pi3}^\mathrm{b}\right]^\top \tag{2.57}$$

$$\bar{\mathbf{p}}_\pi^t = \left[\mathrm{p}_{\pi1}^\mathrm{t} \quad \mathrm{p}_{\pi2}^\mathrm{t} \quad \mathrm{p}_{\pi3}^\mathrm{t}\right]^\top \tag{2.58}$$

$$\bar{\mathbf{p}}_\pi^m = \left[\mathrm{p}_{\pi1}^\mathrm{m} \quad \mathrm{p}_{\pi2}^\mathrm{m} \quad \mathrm{p}_{\pi3}^\mathrm{m}\right]^\top \tag{2.59}$$

In addition to the independent nodal unknowns, dependent unknowns are defined for later convenience. The coordinates of the mid-plane nodes are obtained from the bottom and top coordinates as follows:

$$\overline{\mathbf{x}}^m = \frac{1}{2}\left(\overline{\mathbf{x}}^b + \overline{\mathbf{x}}^t\right) = \frac{1}{2}\begin{bmatrix}\mathbf{I}_6 & \mathbf{I}_6\end{bmatrix}\overline{x} \tag{2.60}$$

where $\mathbf{I}_6$ is the 6×6 identity matrix.

Similarly, the relative displacements between opposites nodes (in the global basis) are given by:

$$\mathbf{a} = \overline{\mathbf{x}}^t - \overline{\mathbf{x}}^b = \begin{bmatrix}-\mathbf{I}_6 & \mathbf{I}_6\end{bmatrix}\overline{\mathbf{x}} \tag{2.61}$$

Finally, the transversal pressure jumps between the bottom and top face nodes and the mid-plane nodes are obtained as follows:

$$\check{\mathbf{p}}_\pi^b = \left(\overline{\mathbf{p}}_\pi^m - \overline{\mathbf{p}}_\pi^b\right) = \begin{bmatrix}-\mathbf{I}_3 & \mathbf{0}_3 & \mathbf{I}_3\end{bmatrix}\overline{\mathbf{p}}_\pi \tag{2.62}$$

$$\check{\mathbf{p}}_\pi^t = \left(\overline{\mathbf{p}}_\pi^m - \overline{\mathbf{p}}_\pi^t\right) = \begin{bmatrix}\mathbf{0}_3 & -\mathbf{I}_3 & \mathbf{I}_3\end{bmatrix}\overline{\mathbf{p}}_\pi \tag{2.63}$$

where $\mathbf{0}_3$ and $\mathbf{I}_3$ are the 3×3 null and identity matrix, respectively.

Local basis

The local axes are defined along the mid-plane between the two discontinuity faces. The axis $\mathbf{e_l}$ is tangent to the mid-plane. The axis $\mathbf{e_n}$ is normal to $\mathbf{e_l}$. In addition, the isoparametric coordinate ξ is defined along the mid-plane such that its value is equal to -1 at the first node, 0 at the central node, and 1 at the last node.

Then, the local axes at a mid-plane point of coordinates $\mathbf{x^m} = [\mathbf{x^m y^m}]^\mathbf{T}$ are given by:

$$\mathbf{e}_l = \frac{1}{|\mathbf{J}|}\frac{\partial \mathbf{x}^m}{\partial \xi} = \frac{1}{|\mathbf{J}|}\begin{bmatrix}\dfrac{\partial \mathrm{x}^\mathrm{m}}{\partial \xi} & \dfrac{\partial \mathrm{y}^\mathrm{m}}{\partial \xi}\end{bmatrix}^\top \tag{2.64}$$

$$\mathbf{e}_n = \frac{1}{|\mathbf{J}|}\begin{bmatrix}-\dfrac{\partial \mathrm{y}^\mathrm{m}}{\partial \xi} & \dfrac{\partial \mathrm{x}^\mathrm{m}}{\partial \xi}\end{bmatrix}^\top \tag{2.65}$$

with

$$|\mathbf{J}| = \sqrt{\left(\frac{\partial x^m}{\partial \xi}\right)^2 + \left(\frac{\partial y^m}{\partial \xi}\right)^2} \tag{2.66}$$

The global coordinates of the mid-plane point of isoparametric coordinate ξ are obtained from the global coordinates of the mid-plane nodes as follows:

$$x^m = \sum_{i=1}^{3} N_i(\xi)x_i^m; \quad y^m = \sum_{i=1}^{3} N_i(\xi)y_i^m \tag{2.67}$$

where $\mathrm{N_i}(\xi)$ is the interpolation function of the mid-plane node i. Therefore,

$$\frac{\partial x^m}{\partial \xi} = \sum_{i=1}^{3}\frac{\partial N_i}{\partial \xi}x_i^m; \quad \frac{\partial y^m}{\partial \xi} = \sum_{i=1}^{3}\frac{\partial N_i}{\partial \xi}y_i^m \tag{2.68}$$

The local basis makes it possible to compute the components of relative displacement vector r from the global coordinates of the bottom and top faces with the following expressions:

$$r_n = e_n \cdot \left(\mathbf{x}^t - \mathbf{x}^b\right) = \mathbf{e}_n \cdot \mathbf{a}; \quad r_l = \mathbf{e}_l \cdot \mathbf{a} \tag{2.69}$$

or with the following equivalent matrix form:

$$\mathbf{r} = \mathbf{Ra}, \quad \text{where} \quad \mathbf{R} = \frac{1}{|\mathbf{J}|}\begin{bmatrix}\dfrac{-\partial \mathrm{y}^\mathrm{m}}{\partial \xi} & \dfrac{\partial \mathrm{x}^\mathrm{m}}{\partial \xi} \\ \dfrac{\partial \mathrm{x}^\mathrm{m}}{\partial \xi} & \dfrac{\partial \mathrm{y}^\mathrm{m}}{\partial \xi}\end{bmatrix} \tag{2.70}$$

Interpolation functions and matrices

The same interpolation functions N_i are employed for the mechanical and the hydraulic problems, namely:

$$N_1 = \frac{1}{2}\xi\left(\xi - 1\right); \quad N_2 = \left(1 - \xi^2\right); \quad N_3 = \frac{1}{2}\xi\left(\xi + 1\right) \tag{2.71}$$

With these functions the following interpolation matrices are constructed:

$$\mathbf{N}^x = \begin{bmatrix} \mathrm{N}_1 & 0 & \mathrm{N}_2 & 0 & \mathrm{N}_3 & 0 \\ 0 & \mathrm{N}_1 & 0 & \mathrm{N}_2 & 0 & \mathrm{N}_3 \end{bmatrix} \tag{2.72}$$

$$\mathbf{N}^p = \begin{bmatrix} \mathrm{N}_1 & \mathrm{N}_2 & \mathrm{N}_3 \end{bmatrix} \tag{2.73}$$

These matrices are used as follows to interpolate the mid-plane coordinates, the relative displacements, the fluid pressures, and transversal pressure jumps, from the nodal unknown vectors $\bar{\mathbf{x}}$ and $\bar{\mathbf{p}}_\pi$:

$$\mathbf{x}^m = \mathbf{N}^x \bar{\mathbf{x}}^m = \frac{1}{2}\mathbf{N}^x \begin{bmatrix} \mathbf{I}_6 & \mathbf{I}_6 \end{bmatrix} \bar{\mathbf{x}} \tag{2.74}$$

$$\mathbf{r} = \mathbf{R}\mathbf{N}^x \bar{\mathbf{a}} = \mathbf{R}\mathbf{N}^x \begin{bmatrix} -\mathbf{I}_6 & \mathbf{I}_6 \end{bmatrix} \bar{\mathbf{x}} = \mathbf{B}^x \bar{\mathbf{x}} \tag{2.75}$$

$$p_\pi^m = \mathbf{N}^p \bar{\mathbf{p}}_\pi^m = \mathbf{N}^p \begin{bmatrix} \mathbf{0}_3 & \mathbf{0}_3 & \mathbf{I}_3 \end{bmatrix} \bar{\mathbf{p}}_\pi = \mathbf{B}^m \bar{\mathbf{p}}_\pi \tag{2.76}$$

$$\check{p}_\pi^b = \mathbf{N}^p \check{\bar{\mathbf{p}}}_\pi^b = \mathbf{N}^p \begin{bmatrix} -\mathbf{I}_3 & \mathbf{0}_3 & \mathbf{I}_3 \end{bmatrix} \bar{\mathbf{p}}_\pi = \check{\mathbf{B}}^b \bar{\mathbf{p}}_\pi \tag{2.77}$$

$$\check{p}_\pi^t = \mathbf{N}^p \check{\bar{\mathbf{p}}}_\pi^t = \mathbf{N}^p \begin{bmatrix} \mathbf{0}_3 & -\mathbf{I}_3 & \mathbf{I}_3 \end{bmatrix} \bar{\mathbf{p}}_\pi = \check{\mathbf{B}}^t \bar{\mathbf{p}}_\pi \tag{2.78}$$

The fluid phase pressure gradients along the mid-plane, which are required to compute the longitudinal mass flows of gas and water species, are obtained with the following expressions:

$$\frac{\partial p_\pi^m}{\partial l} = \frac{\partial \mathbf{B}^m}{\partial l} \bar{\mathbf{p}}_\pi \tag{2.79}$$

where

$$\frac{\partial \mathbf{B}^m}{\partial l} = \frac{1}{|\mathbf{J}|} \frac{\partial \mathbf{N}^p}{\partial \xi} \begin{bmatrix} \mathbf{0}_3 & \mathbf{0}_3 & \mathbf{I}_3 \end{bmatrix} \tag{2.80}$$

Nodal forces and mass flows

The nodal force and mass flow vector $\bar{\mathbf{f}}$ is defined as follows:

$$\bar{\mathbf{f}} = \begin{bmatrix} \bar{\mathbf{f}}_\mathrm{x} \\ \bar{\mathbf{f}}_\mathrm{w} \\ \bar{\mathbf{f}}_\mathrm{g} \end{bmatrix} \tag{2.81}$$

The nodal force vector $\mathbf{f}_\mathrm{x}$ [N] is obtained after applying the Principle of Virtual Work to the integral form of Eq. (2.17):

$$\mathbf{f}^x = \int_{l_{mp}} \left(\mathbf{B}^x\right)^\top \boldsymbol{\sigma}' dl - \int_{l_{mp}} \left(\mathbf{B}^x\right)^\top \mathbf{m} p_s^m dl \tag{2.82}$$

Similarly, the nodal mass flows $\mathbf{f}_\varsigma$ $[\mathrm{kg/s}]$ $(\varsigma = \mathrm{w}, \mathrm{g})$ are obtained from the mass balance equations for water and gas species (Eqs. (2.4) and (2.5)):

$$\mathbf{f}_\varsigma = \int_{l_{mp}} \left(\mathbf{B}^m\right)^\top q_\varsigma^s dl - \int_{l_{mp}} \left(\frac{\partial \mathbf{B}^m}{\partial l}\right)^\top q_\varsigma^l dl - \int_{l_{mp}} \left(\check{\mathbf{B}}^b\right)^\top q_\varsigma^b dl - \int_{l_{mp}} \left(\check{\mathbf{B}}^t\right)^\top q_\varsigma^t dl \tag{2.83}$$

In this expression, $\mathrm{q}_\varsigma^\mathrm{s}$ stands for the mass storage rate of species ς, i.e. for the first terms in Eqs. (2.4) and (2.5).

The numerical integration of Eqs. (2.82) and (2.83) follows the Gauss' scheme with n_{ip} integration points:

$$\mathbf{f}_x = \sum_{i=1}^{n_{ip}} \left(\mathbf{B}^x\right)^\top \boldsymbol{\sigma}' |\mathbf{J}| W_i - \sum_{i=1}^{n_{ip}} \left(\mathbf{B}^x\right)^\top \mathbf{m}\mathbf{B}^m p_s^m |\mathbf{J}| W_i \tag{2.84}$$

$$\mathbf{f}_\varsigma = \sum_{i=1}^{n_{ip}} \left(\mathbf{B}^m\right)^\top q_\zeta^s |\mathbf{J}| W_i - \sum_{i=1}^{n_{ip}} \left(\frac{\partial \mathbf{B}^m}{\partial l}\right)^\top q_\varsigma^l |\mathbf{J}| W_i - \sum_{i=1}^{n_{ip}} \left(\check{\mathbf{B}}^b\right)^\top q_\varsigma^b |\mathbf{J}| W_i - \sum_{i=1}^{n_{ip}} \left(\check{\mathbf{B}}^t\right)^\top q_\varsigma^t |\mathbf{J}| W_i \tag{2.85}$$

where W_i is the weight of the integration point i.

Tangent stiffness matrix

The numerical solution via a Newton-Raphson iterative strategy requires the computation of the following fully coupled tangent stiffness matrix:

$$\frac{\partial \bar{\mathbf{f}}}{\partial \bar{\mathbf{u}}} = \begin{bmatrix} \left.\frac{\partial \bar{\mathbf{f}}_\mathbf{x}}{\partial \bar{\mathbf{x}}}\right|_{12\times 12} & \left.\frac{\partial \bar{\mathbf{f}}_\mathbf{x}}{\partial \bar{\mathbf{p}}_\mathbf{w}}\right|_{12\times 9} & \left.\frac{\partial \bar{\mathbf{f}}_\mathbf{x}}{\partial \bar{\mathbf{p}}_\mathbf{g}}\right|_{12\times 9} \\ \left.\frac{\partial \bar{\mathbf{f}}_\mathbf{w}}{\partial \bar{\mathbf{x}}}\right|_{9\times 12} & \left.\frac{\partial \bar{\mathbf{f}}_\mathbf{w}}{\partial \bar{\mathbf{p}}_\mathbf{w}}\right|_{9\times 9} & \left.\frac{\partial \bar{\mathbf{f}}_\mathbf{w}}{\partial \bar{\mathbf{p}}_\mathbf{g}}\right|_{9\times 9} \\ \left.\frac{\partial \bar{\mathbf{f}}_\mathbf{g}}{\partial \bar{\mathbf{x}}}\right|_{9\times 12} & \left.\frac{\partial \bar{\mathbf{f}}_\mathbf{g}}{\partial \bar{\mathbf{p}}_\mathbf{w}}\right|_{9\times 9} & \left.\frac{\partial \bar{\mathbf{f}}_\mathbf{g}}{\partial \bar{\mathbf{p}}_\mathbf{g}}\right|_{9\times 9} \end{bmatrix} \tag{2.86}$$

2.10.2. Model verification

In this section, the model performance is illustrated with some benchmark examples of increasing complexity. These examples were selected to show the main characteristics of the new PHM interface element and its ability to qualitatively reproduce experimental observations.

In all the following benchmark examples, the gas species considered is hydrogen and the system temperature is $T = 298.15\,\mathrm{K}$. Therefore, the following parameters of the fluid phases/species are common to all the examples: $M_g = 0.002\,\mathrm{kg/mol}$, $H = 0.0193$ (Sander, 2015), $D_{gw} = 5.25 \times 10^{-9}\,\mathrm{m^2/s}$, $\rho_{w,o} = 997\,\mathrm{kg/m^3}$, $p_{w,o} = 0.1\,\mathrm{MPa}$, $C_w = 3.33 \times 10^{-10}\,1/\mathrm{Pa}$, $\mu_w = 8.9 \times 10^{-4}\,\mathrm{Pa\,s}$ (Haynes, 2014), and $\mu_g = 8.92 \times 10^{-6}\,\mathrm{Pa\,s}$ (Haynes, 2014). In the examples where the continuum medium is considered, plane strain is assumed and the following material parameters, representative of Boom Clay, are used: $E = 300\,\mathrm{MPa}$ (Volckaert et al., 2004), $\nu = 0.125$, $n = 0.39$ (Mertens et al., 2004), $C_s \approx 0$, $b = 1$, $k = 3 \times 10^{-19} I_2\,\mathrm{m^2}$ (Arnold et al., 2015) (I_2 is the 2×2 identity tensor), and $\tau = 0.164$ (Jacops et al., 2013b). Unless otherwise stated, the liquid retention and relative permeability parameters of the continuum medium and the discontinuities are the same as given in Section 2.10.1.5 for Figure 2.255 and Figure 2.256.

2.10.2.1. Gas injection in a single interface element

For the first two examples, a single interface element of 1 m length is considered. The displacements of the bottom face of the element are fixed, while a uniform compressive normal load $\sigma_{ini} = -0.4\,\mathrm{MPa}$ is applied on the top face. The initial fluid pressures in all element nodes are $p_w = p_g = 0.1\,\mathrm{MPa}$. In both examples, gas is injected in the mid-plane nodes, while keeping constant the liquid phase pressure.

Case A

In this example, gas is injected at a constant mass rate of $0.1\,\mu\mathrm{g/s}$. The parameters of the mechanical constitutive law are such that the interface behaves linear-elastically with a normal stiffness $K_n = 1 \times 10^{12}\,\mathrm{Pa/m}$ during the injection. Damage is prevented by adopting a large value of r_{n0}. Moreover, no viscosity is considered ($\zeta = 0$). Since there is no tangential loading and the pore pressure only acts in the normal direction, the tangential mechanical parameters are irrelevant. The integration points are considered in coincidence with the mid-plane nodes (Lobatto quadrature). In order to prevent longitudinal fluxes, the gas injection is distributed between the three mid-plane nodes according to the weights of the integration points at the same location.

Figure 2.258 shows the time evolution of selected model variables as gas is injected. The curves are shifted along the time axis to make more visible the values at the beginning of the injection. Initially, the normal aperture is slightly negative ($\mathrm{r_n} = -0.3\,\mu\mathrm{m}$) due to the compressive load. However, the initial width is positive because $\mathrm{w_0} = 1\,\mu\mathrm{m}$ has been adopted. In this way, an initial storage capacity is assigned to the element, which prevents a sudden increase of the gas pressure and the normal aperture in the first time increment.

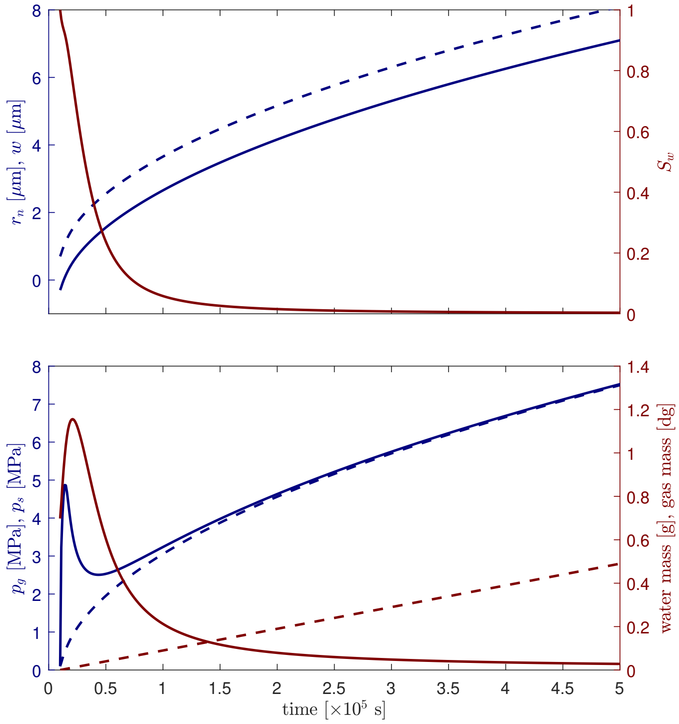

Figure 2.258: Case A – Time evolution of the normal aperture $\mathrm{r_n}$*, the width* w *(dashed line), the liquid saturation degree* $\mathrm{S_w}$*, the gas phase pressure* $\mathrm{p_g}$*, the effective pore pressure* $\mathrm{p_s}$ *(dashed line), and the stored water and gas (dashed line) masses.*

As gas is injected, the effective pore pressure grows monotonically as well as the normal aperture. Both curves hold a proportionality factor of $1/\mathrm{K_n}$. The gas pressure, in contrast, shows a non-monotonic evolution, with a local peak when the normal aperture becomes positive. This peak is explained by the marked effect of the (positive) normal aperture on the retention curve by reducing the gas-entry value (Figure 2.255). As the saturation degree tends to zero, the gas pressure curves converge to the effective pore pressure curve. Note that even when the saturation degree remains practically constant at $\mathrm{S_w} \approx 0$, the relation between the increments of gas pressure and the increments of aperture is still non-linear due to the compressibility of the gas phase.

The constant injection rate is reflected in the linear increase of the stored gas mass. The stored water mass curve, in contrast, shows a peak that is explained by the competing effects of the reduction of $\mathrm{S_w}$ and the increase of $\mathrm{r_n}$ on the storage term of the water mass balance equation. Initially, the positive effect of the increase of $\mathrm{r_n}$ overcomes the negative effect of the decrease of $\mathrm{S_w}$ and water enters the crack, but this behaviour is rapidly reverted after the gas pressure peak, and, from then on, water is expelled.

Figure 2.259 shows the equilibrium path in terms of $\mathrm{p_g}$ versus $\mathrm{r_n}$ as obtained numerically (markers) and analytically (solid lines). The analytical solution is given by the following implicit expression derived from

Eqs. (2.17), (2.18) and (2.3):

$$\sigma'_n(r_n) + p_c S_w(r_n, p_c) - p_g = \sigma_{\text{ini}} \tag{2.87}$$

Note that in this case p_w is fixed, and σ'_n has been reduced to a function of r_n only, since no tangential displacements are possible. This expression has been plotted in Figure 2.259 for three different values of α, in order to show the effect of the second term of Eq. (2.46) on the equilibrium path. Note that for very small or null values of α a sharp peak is obtained at $r_n = 0$. The dashed line in the plot has a slope K_n and reflects the linear elastic response of the interface element to the effective pore pressure. As the interface element is desaturated, the equilibrium path tends to this line.

Note also that although the cracking process will not be modelled using a linear-elastic constitutive law, this example and the following one are representative of the conditions under which an interface element without (or with low) tensile strength opens when confined by linear-elastic continuum elements.

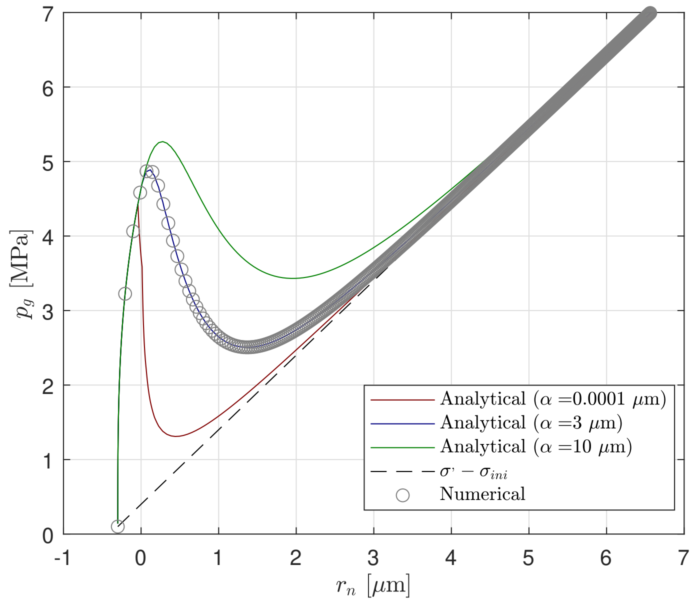

Figure 2.259: Case A – Analytical equilibrium paths for different values of the aperture smoothing parameter α and numerical result for $\alpha = 3\,\mu\text{m}$.

Case B

In this second example, the gas pressure is increased with a constant rate of 3.7×10^{-5} MPa/s until reaching $p_g = 7$ MPa, and then it is reduced, with the same rate, to the initial value.

In Figure 2.260, the red curve shows the model results in terms of p_g versus r_n using the same mechanical parameters as in previous Case A. The blue curve corresponds to the equilibrium path calculated with Eq. (2.87), which is still valid for this case. As the gas pressure is increased, the normal aperture increases following the equilibrium path until reaching the local peak (point A). At this point, a sudden aperture occurs (snap-through instability) until reaching point B on the equilibrium path. Here on, further increase of the gas pressure leads to further normal aperture increase, following the equilibrium path until reaching $p_g = 7$ MPa. The subsequent reduction of the gas pressure is accompanied by the closure of the interface following the equilibrium path until reaching point C, where another aperture jump occurs until reaching the equilibrium path at point D. The initial (negative) aperture is recovered when the gas pressure reaches its initial value $p_g = 0.1$ MPa.

Snap-through instabilities of the type observed in this example (A → B and C → D), which in this case are properly handled by the iterative solving algorithm, have been found to lead to severe convergence problems in more complex boundary value problems. This occurs even when the gas injection is done at a controlled mass rate, because the gas accumulated (stored) in the system may act as a pressure buffer

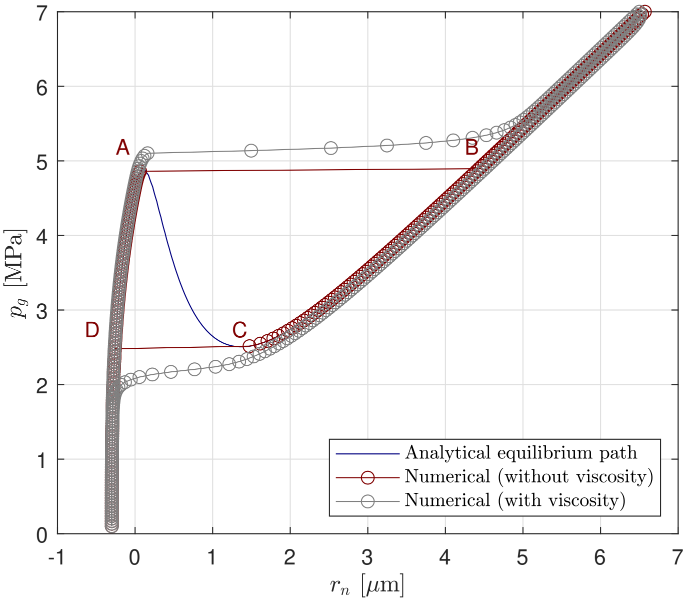

Figure 2.260: Case B – Gas pressure versus normal aperture with and without adding viscous damping to the mechanical constitutive law. The blue line is the analytical equilibrium path obtained with Eq. (2.87).

at the mouth of the opening crack.

One possibility to mitigate this problem is to increase the smoothing parameter α in order to reduce or eliminate the local peak of the equilibrium path, as illustrated in Figure 2.259. Alternatively (or simultaneously), the viscous damper proposed in Eq. (2.25) can be activated. The grey curve in Figure 2.260 shows the stabilising effect of the viscous term with $\zeta = 2 \times 10^5$ Pa s/m. Both numerical parameters α and ζ are tuned by trial and error. Since they introduce a deviation from the intended constitutive behaviour, they should be as small as possible.

2.10.2.2. Gas injection in a clay sample

Case C

This example aims at mimicking, in a simplified manner, a gas injection test in a water saturated clay sample under isochoric conditions. The problem geometry and the FE mesh considered are depicted in Figure 2.261a. A square sample of Boom Clay is placed in between four stiff loading plates. The thicker lines labelled A–E indicate the position of the interface elements. A single, vertical crack propagation path is considered inside the sample (line A). The contact surfaces between the sample and the loading plates are represented by interface elements along lines B, C, D, and E.

The initial stress state of the continuum clay elements is isotropic, with a total stress of -4.5 MPa. The initial stress state of all the interface elements is given by $\sigma_n = -4.5$ MPa and $\sigma_l = 0$ MPa. The initial pore pressures in all the domain is $p_w = p_g = 2.2$ MPa. All the degrees of freedom of the nodes belonging to the loading plates are fixed. Gas is injected at a constant mass rate of 1 µg/s, evenly distributed among all the mid-plane nodes of the interface elements along line B (Figure 2.261a). The gas injection is performed in two stages of 0.6 Ms (1 Ms = 1×10^6 s), with a third stage of 0.6 Ms without injection in between. Time steps range between 1 to 5,000 s, governed by an automatic incrementation algorithm.

The mechanical and flow properties of the clay continuum elements are those given at the beginning of the section. The material parameters of the loading plates continuum elements are irrelevant, since all their nodal degrees of freedom are fixed. The flow and mechanical parameters for the different lines of interface elements are given in Table 2.80. The mechanical parameters of the elements along line A have been estimated in an attempt to make them representative of Boom Clay fracture properties, although

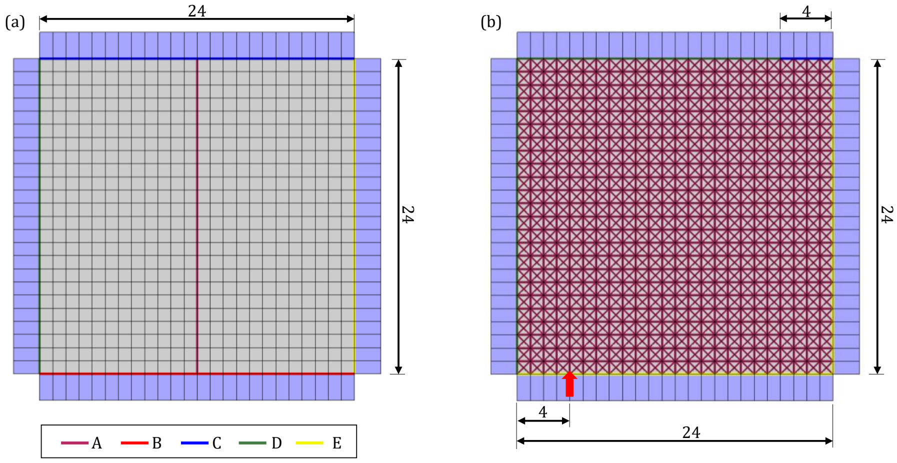

Figure 2.261: Geometry and FE mesh for (a) Case C and (b) Case D. Thick lines indicate the location of the interface elements. The red arrow in (b) indicates the gas injection locus. Dimensions in mm.

the data available in this regard is very sparse. The initial tensile strength and the debonding normal aperture are adopted based on experimental direct tensile tests reported in the literature for different clayey soils (Tang et al., 2015; Trabelsi et al., 2018; Wang et al., 2007). To the best of the authors' knowledge no direct tensile tests on Boom Clay have been reported. Because the adopted mechanical constitutive law is purely cohesive, the increase of shear strength with the confining stress due to friction is not automatically considered. In order to approximate this behaviour, the initial shear strength has been estimated considering the Mohr-Coulomb failure criterion with typical Boom Clay values of $c' = 0.5\,\mathrm{MPa}$ and 18° (Arnold et al., 2015), and an average effective normal stress of $4.5\,\mathrm{MPa}$ during the injection (obtained from preliminary simulations). The initial tensile and shear strength of the clay-plate interfaces (lines B, C,D and E) are assumed to be a tenth of the corresponding values of the bulk clay (line A). In order to use the same penalty coefficients as for line A, the cracking separations (r_{n0}, r_{l0}) are also reduced to a tenth. The snap-through instabilities described in above, are prevented by assigning a viscosity $\zeta = 3 \times 10^{14}\,\mathrm{Pa\,s/m}$ to line A elements.

Table 2.80: Material parameters of the interface elements in Cases C and D (Figure 2.261). The local longitudinal axes of the interface elements are oriented from left to right or from bottom to top.

		Line A	**Line B**	**Line C**	**Line D**	**Line E**
w_0	[m]	0.0	1.0E-5	1.0E-5	0.0	0.0
t^l_0	[m^3]	0.0	1.0E-16	1.0E-16	0.0	0.0
$k^b; k^t$	[m]	1.0E-6; 1.0E-6	0.0; 1.0E-6	1.0E-6; 1.0E-6	1.0E-6; 0.0	0.0; 1.0E-6
d^l_0	[m]	0.0	1E-5	1E-05	0.0	0.0
$\tau^b; \tau^t$	[1/m]	1.0;1.0	0.0;1.0	1.0;1.0	1.0;0.0	1.0;0.0
σ_{n0}	[Pa]	1.5E+5	1.5E+4	1.5E+4	1.5E+4	1.5E+4
$r_{n0}; r_{nc}$	[m]	1.5E-9; 1.5E-4	1.5E-10; 1.5E-5	1.5E-10; 1.5E-5	1.5E-10; 1.5E-5	1.5E-10; 1.5E-5
σ_{l0}	[Pa]	2.0E+6	2.0E+5	2.0E+5	2.0E+5	2.0E+5
$r_{l0}; r_{lc}$	[m]	2.0E-8; 2.0E-3	2.0E-9; 4.0E-4	2.0E-9; 2.0E-4	2.0E-9; 2.0E-4	2.0E-9; 1.0E-4

In addition to representing the mechanical clay-plate interface, lines B and C are also used to simulate the porous filter on top and bottom sides of the sample. With this purpose, non-null values w_0, t^l_0 and d^l_0 have been assigned to them in order to consider the storage capacity and the high permeability/diffusivity of the filters. Moreover, at the gas injection side (line A) the liquid saturation degree has been fixed to $S_w = 0$, while at the back-pressure side (line ???), full liquid saturation is enforced ($S_w = 1$). Note that because of the adopted transversal transport properties, the bottom and lateral plates are hydraulically disconnected from the clay sample.

The liquid retention parameters of lines A, D and E are the same as those used for Figure 2.255, with the exception of the first (bottom) element of line A, where the parameter p_b has been reduced to $1\,\mathrm{MPa}$. This reduction of the gas-entry value is used to represent an imperfection at the sample bottom surface (a void or a cleft), where water can be displaced with lower capillary pressure than in the bulk clay. Otherwise, the gas pressure front would advance homogeneously into the sample precluding the formation of a crack. According to Eq. (2.47), the reduction of p_b from 10 to $1\,\mathrm{MPa}$, corresponds to an increase of the characteristic pore size from $58.1\,\mathrm{nm}$ to $581\,\mathrm{nm}$. Pore size density functions obtained via Mercury Intrusion Porosimetry on Boom Clay samples (Gonzalez-Blanco et al., 2016a) show that features in the order of $500\,\mathrm{nm}$ are not unlikely.

Figure 2.262 shows the time evolution of selected model variables. The gas injection pressure corresponds to the gas phase pressure of the mid-plane nodes of the elements along line B. Due to the high value of t_0^l, the gas pressure at all these nodes is practically the same. The Crack Mouth Opening Displacement (CMOD) is the normal aperture of the first interface element along line A. The gas and water outflows correspond to the mass rates at which a gas and water species leave the clay sample through the top boundary. A negative water outflow indicates that water is being absorbed by the sample. These curves are complemented by Figure 2.263, which shows the deformed geometry and contour plots of gas phase pressure, liquid phase pressure and liquid saturation degree at four characteristic times, namely, when the maximum injection pressure is reached ($0.15\,\mathrm{Ms}$), just before and just after the crack reaches the top plate ($0.236\,\mathrm{Ms}$ and $0.24\,\mathrm{Ms}$), and at the end of the first injection stage ($0.6\,\mathrm{Ms}$).

Between the beginning of the injection and time $0.15\,\mathrm{Ms}$, the gas injection pressure grows monotonically until reaching its maximum value. This pressure increase is accompanied by a separation of the bottom side interface, which occurs at the expense of compressing the clay sample against the top and lateral loading plates, inducing shear stress/displacements along the lateral interface elements. Part of the gas injected during this period is accumulated in the void volume created in that way, while the remaining part invades the clay sample. The gas invasion occurs both into the pore space of the bulk clay (dissolved in the pore water and as a separate phase) and into the crack induced by the gas pressure. The progressive decline of the injection pressure rate is mainly explained by the propagation of the crack, which increases the storage capacity and the overall permeability of the clay sample. The ‘room’ necessary for the formation of the crack and the separation of the bottom side interface is created by reduction of the pore space in the bulk clay material in a consolidation process accompanied by water expulsion.

After the peak, the injection pressure progressively decreases until time $0.236\,\mathrm{Ms}$, when the crack reaches the top plate and a sudden pressure drop occurs. At this time, the crack connects the injection locus at the bottom of the sample with the gas sink at the top, constituting a preferential path for gas flow. Consequently, a sharp raise of the gas outflow is observed, mainly fed by gas previously stored in the bottom contact interface and in the crack. Qualitatively similar sharp break-through events were experimentally observed (Daniels and Harrington, 2017; Graham et al., 2016; Gutiérrez-Rodrigo et al., 2021; Harrington et al., 2019, 2017c; Horseman et al., 1999a).

Because of the gas pressure drop, the bulk clay is decompressed and partially re-saturated, as it is reflected in the negative values of the water outflow curve. The gas and water outflow extreme values are far out of the plotted ranges, reaching values of 8×10^{-8} and $-16 \times 10^{-7}\,\mathrm{kg/s}$, respectively. After this first break-through event, the system goes through a cycle of damped oscillations before smoothly converging to a steady state as the gas outflow converges to the injection rate value. These oscillations are highlighted in the injection pressure plot, but they can also be observed in the gas and water outflow plots. From the mechanical point of view, the oscillations are associated to partial closure and reopening of the crack tip. Notably, oscillatory or intermittent outflows after break-through events are also observed experimentally. Moreover, a detailed analysis of stress perturbation events indicates that the intermittent outflows are correlated with the opening and closing of cracks (Harrington et al., 2019).

The injection shut-off at time $0.6\,\mathrm{Ms}$, leads to a decrease of the gas pressure at the injection locus as gas continues flowing out of the sample through the top side. The gas pressure decrease is accompanied by

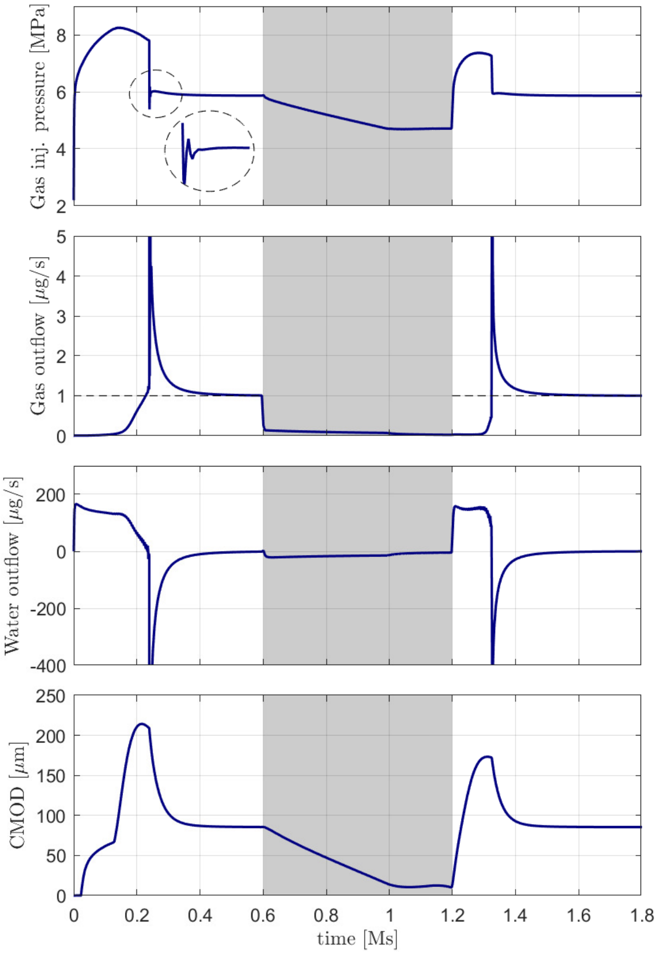

Figure 2.262: Case C – Time evolution of the gas injection pressure, the gas and water mass outflows, and the Crack Mouth Opening Displacement (CMOD).

the progressive closure of the crack. At time 1.0 Ms, when the gas injection pressure reaches $p_g \approx |\sigma_{ini}| = 4.5$ MPa, the crack is almost completely closed and, consequently, the dissipation of the gas overpressure slows down significantly, driven only by the gas transport processes in the continuum elements. Self-sealing of gas pathways following reduction of the injection rate/pressure has been reported in different gas migration tests (Daniels and Harrington, 2017; Graham et al., 2016; Gutiérrez-Rodrigo et al., 2021; Harrington et al., 2019; Horseman et al., 1999a).

At time 1.2 Ms, the gas injection is restarted. In this second injection stage, the evolution curves show features similar to those of the first stage, although with some significant differences. Namely, the maximum injection pressure and the time required to connect the bottom and top plates with the crack are smaller, and the oscillations after the break-through event practically disappear. These differences are attributed to the fact that the initial conditions are different in each case. On one hand, the gas overpressure resulting from the first injection is not completely dissipated during the shut-off stage, and, therefore, less injection time is needed in the second injection stage to reach critical pressure values. On the other hand, the interface elements along lines A, B, D and E offer less or no resistance to opening/sliding during the second injection, since they have been damaged during the first injection stage. Comparable reduction of the break-through pressure in second injections was systematically observed in tests conducted by Gutiérrez-Rodrigo et al. (2021) in compacted bentonite.

Additional simulations were performed with Case C (Figure 2.261a) varying the gas injection rate and the initial stress and pore pressure. Figure 2.264 shows the resulting time evolution of the gas injection

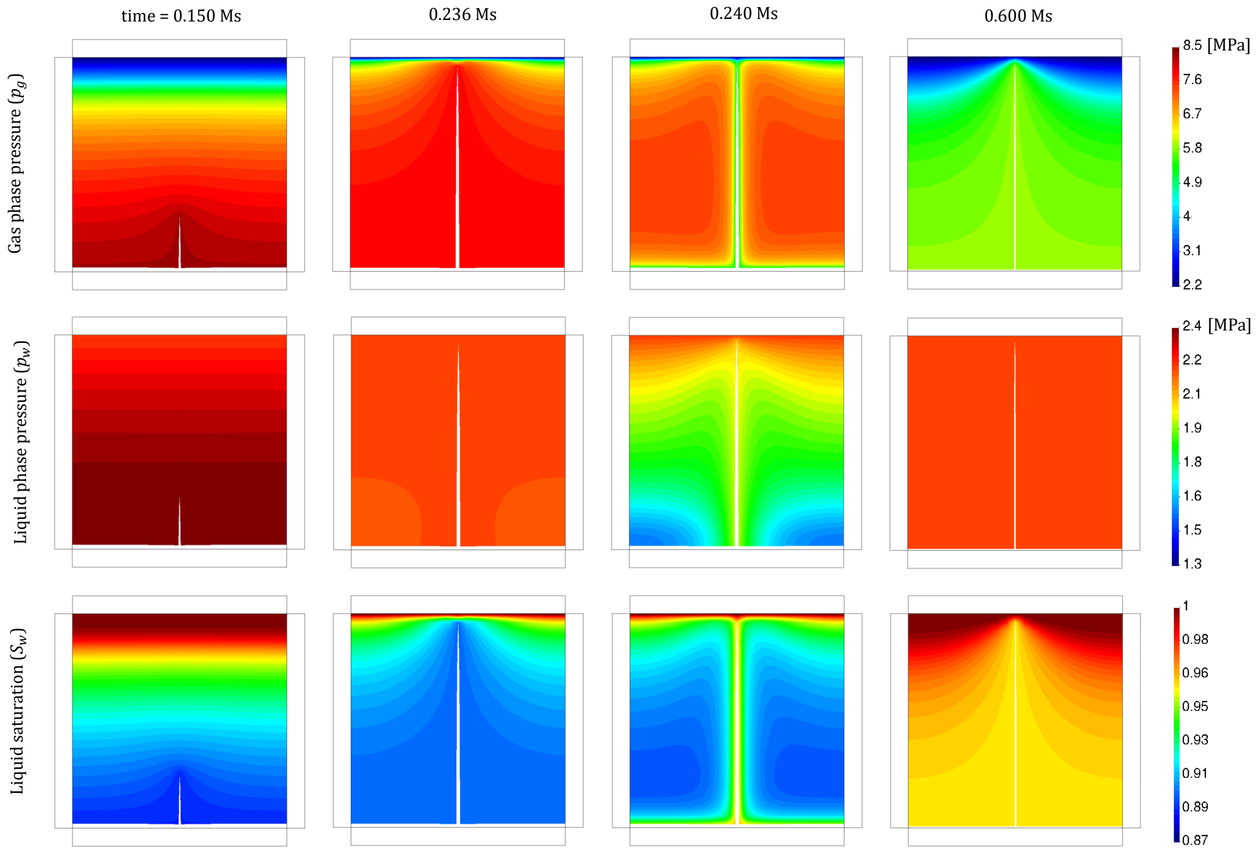

Figure 2.263: Case C – Deformed geometry (scaled $\times 2$), gas phase pressure, liquid phase pressure, and liquid saturation degree at four characteristic times.

pressure, the gas outflow and the water outflow. Note that, in contrast with the previous example, in these additional simulations the gas injection rate remained constant throughout the analysed time.

Figure 2.264a shows the results for three different gas injection rates (f_g), as indicated in the legend, considering the same initial conditions as in the previous simulations ($|\sigma_{ini}| = 4.5$ MPa, $p_w = 2.2$ MPa). Note that for $f_g = 1.00\,\mu g/s$ (blue curves) the results coincide with those shown for the first injection in Figure 2.262. A reduction of the gas injection rate to $f_g = 0.50\,\mu g/s$ leads to results qualitatively similar to those obtained with $f_g = 0.50\,\mu g/s$, although with a reduction in the maximum injection pressure and a significant delay of the gas break-through event. In contrast, further reduction of the injection rate to $f_g = 0.25\,\mu g/s$ leads to a completely different response, without gas fracturing. With this injection rate, the injection pressure tends asymptotically to a steady state condition in which all the injected gas migrates through the specimen via diffusion of dissolved gas and visco-capillary two-phase flow. The latter mechanism has minimal influence due to the low desaturation of the specimen.

Figure 2.264b shows the results for three different initial states, as indicated in the legend, considering the same gas injection rate ($f_g = 0.25\,\mu g/s$). The selected initial conditions were adopted to mimic in-situ conditions at HADES laboratory at 220 m, 195 m and 170 m depth. Note that red curves in Figures 2.264a and b correspond to the same simulation, in which no gas fracturing is developed. However, upon reduction of the initial stress and pore pressure (equivalent to an in-situ depth reduction), break-through events associated to gas fractures are developed. As expected, the lower the equivalent depth, the lower the peak and steady state injection pressure, and the earlier the break-through event occurs.

The previous examples make it possible to appreciate the enrichment of the conventional PHM FE model for bulk clay by the introduction of the new zero-thickness interface elements to represent both macroscopic cracks inside the clay specimen and the distinct behaviour of the interfaces between the specimen and the

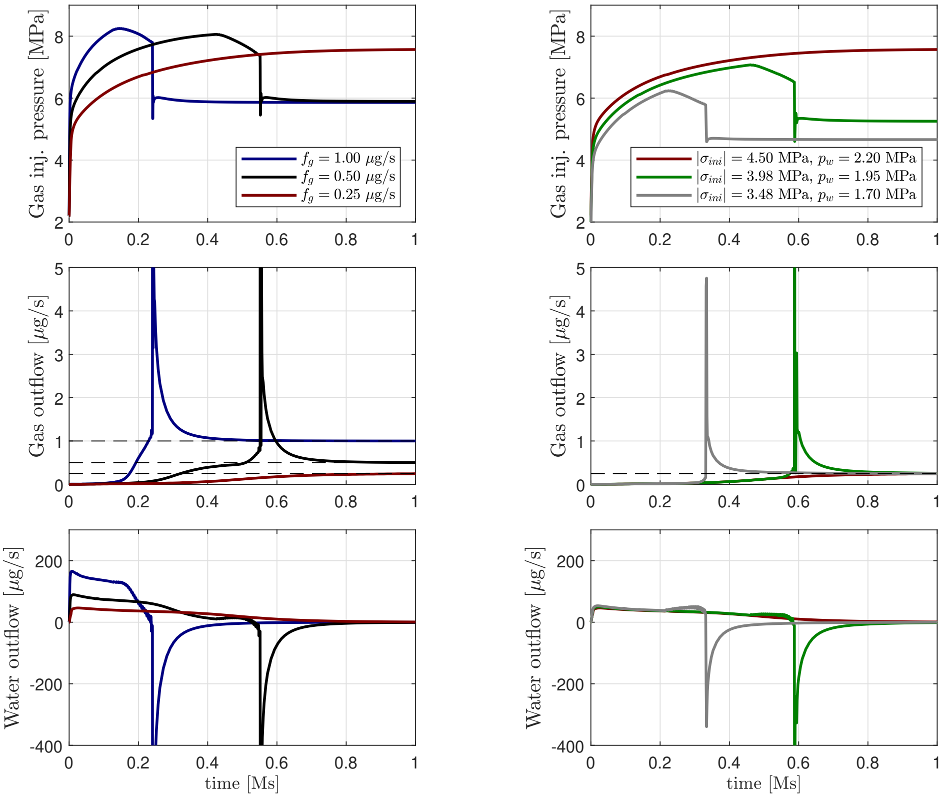

Figure 2.264: Case C – Sensitivity analysis. Left, simulations with the same initial state ($|\sigma_{ini}| = 4.5$ MPa*,* $p_w = 2.2$ MPa*) but different gas injection rate. Right, simulations with the same gas injection rate (*$f_g = 0.25\ \mu g/s$*) but different initial states.*

experimental testing device. Now, in addition to the diffusion/advection of dissolved gas and the two-phase flow mechanisms of the original model, the new model is capable of automatically activating the gas fracturing mechanism when the conditions are met. Moreover, the explicit representation of the clay-device interfaces, which is not possible with any of the modelling approaches reviewed in the introduction, reveals that actual boundary conditions of the clay specimens during gas injection tests may differ significantly from those intended.

Case D

This example aims at demonstrating the ability of the model to reproduce non-straight and branching cracking paths. For this purpose, a similar problem definition as for Case C is considered, but using a different FE mesh and introducing changes in the flow boundary conditions. The new FE mesh is shown in Figure 2.261b, where the labels of the interface element lines correspond to the material parameters given in Table 2.80. Note also in that figure, that that the back-pressure filter has been reduced to the right one-sixth of the top side of the sample (line C in Figure 2.261b), the bottom injection filter has been removed, and that interface elements have been introduced in between all the continuum clay elements. The gas injection is performed with the same mass rate as for Case C ($1\ \mu g/s$), but at a single mid-plane node indicated by a red arrow in Figure 2.261b, instead of uniformly distributed along the bottom side of the sample. Additionally, in order to reduce the computational cost, the liquid pressure is fixed in all the domain.

Since the crack can propagate only along the interface elements, the discretisation of the sample determines the potential cracking paths and, consequently, the geometric characteristics of the FE mesh have an influence on the results. In order to explore the mesh sensitivity of the proposed example, the simulation is repeated using three other FE meshes shown in Figure 2.265. The notation of the meshes indicates the number of elements along one side of the sample, and the structured (s) or unstructured (u) nature of the mesh. Mesh 24s is the same mesh shown in Figure 2.261b. Mesh 24u was obtained by forcing a circular mesh line in the centre of the sample.

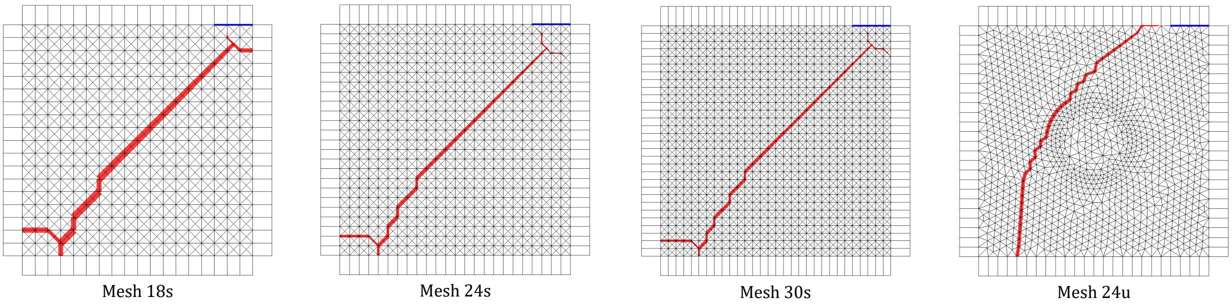

Figure 2.265: Case D – FE meshes considered for sensitivity analysis. The red lines represent the crack geometry at the end of the simulation. The varying thickness of the lines corresponds to the normal crack aperture (r_n) magnified by $\times 5.5$. The blue segment indicates the position of the gas sink.

The results obtained are presented in Figure 2.266 in terms of the time evolution of the gas injection pressure and the gas mass outflow through the back-pressure filter. The crack geometry at the end of the simulation is shown in Figure 2.265 for the four different FE meshes considered.

The value and time of the injection pressure peaks are very similar with the four different meshes. This peak corresponds to the initiation of the crack propagation into the sample. The effect of the mesh can only be appreciated in the post-peak behaviour.

Consider first the structured meshes 18s, 24s and 30s. Although the final crack geometry in the three cases are very similar (Figure 2.265), it is apparent from the injection pressure curves, that the model response is ‘embrittled’ as the mesh size is reduced, in the sense that the crack reaches more rapidly the back-pressure filter. The coarser the mesh, the more unlikely that the optimal (minimum energy) cracking path can be accurately reproduced by the model, and, consequently, additional mechanical work needs to be invested to propagate the crack.

Compare now the results obtained from meshes 24s and 24u, both featuring a similar element size, with one being structured and the other unstructured. Although the crack geometries obtained with these meshes are quite different, the time evolution curves of the injection pressure and gas outflow are very similar until well past the post-peak zone. The injection pressure curve of mesh 24u shows a similar drop when the crack reaches the back-pressure filter, but it occurs 0.02 Ms before. This difference is explained (at least in part) by the fact that the last part of the crack propagation is developed along the top clay-plate interface, which has 1/10 of the tensile strength of the bulk material.

As for Case C, a cycle of oscillations in the gas injection pressure and outflow is obtained after the break-through event, for all four different meshes. These oscillations are associated to partial closure and re-opening of the crack tip(s).

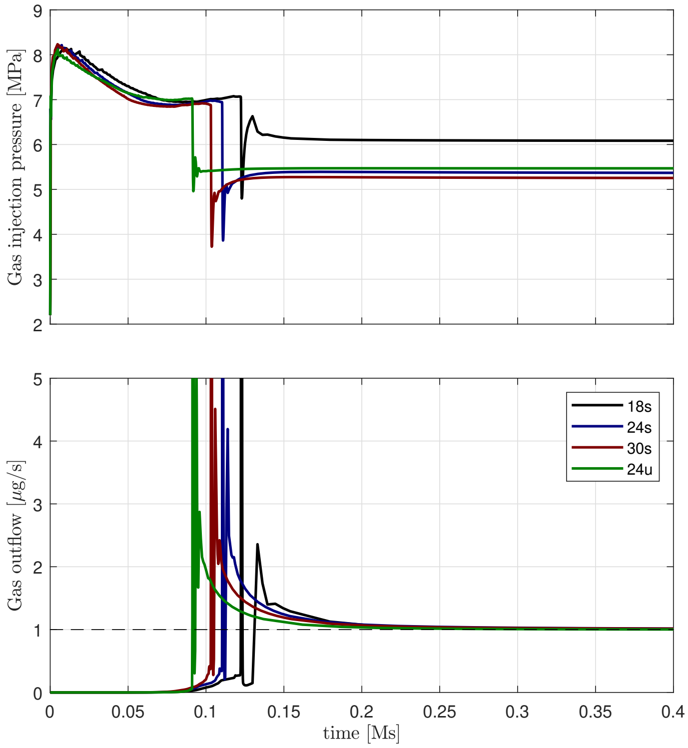

Figure 2.266: Case D – Time evolution of the gas injection pressure and the gas mass outflow obtained with four different FE meshes.

.

ULiège

2.11. Multi-scale hydromechanical model within the FE code LAGAMINE (ULiège)

2.11.1. Introduction

Within the scope of Task 2 of the WP GAS, the primary objective of the work performed at the University of Liège is to contribute to conceptualise the gas transport processes taking place in the post-closure phase of a disposal system both at micro- and macro-scales, in order to improve understanding of the observed gas transport modes and their main controls.

These objectives have stimulated the development of novel and robust numerical models that can realistically simulate the gas transport mechanisms in low permeable clay rocks as well as the accompanied HM processes (Corman, 2024). Two distinct zones of the repository system have been more specifically identified in Figure 2.267, dividing the task into two sub-objectives:

- In the excavation damaged zone (EDZ), the gas migration is supposed to be governed by the hydraulic properties modification induced by the fracturation following the storage drifts excavation (Tsang et al., 2005a; Armand et al., 2014). A first contribution aims thus at extending the second gradient method to two-phase flow hydro-mechanically coupled conditions in order to simultaneously capture the multi-physics interactions related to gas transfers and the development of fractures (Corman et al., 2022). This work is part of Task 3, and has been summarised in Deliverable D6.8 - Part 2.
- In the sound clay rock, the gas migration is supposed to be governed by the rock structure at a micro-level (Harrington et al., 2012c; Gonzalez-Blanco et al., 2016a). A second contribution aims thus at building a multi-scale model which captures the micro-scale effects on the macroscopic gas flow, by embedding the description of the microstructure constituents, like the pore network and the separation planes, on a representative element volume (REV) Corman et al. (2024). This work is summarised in the present Deliverable D6.7.

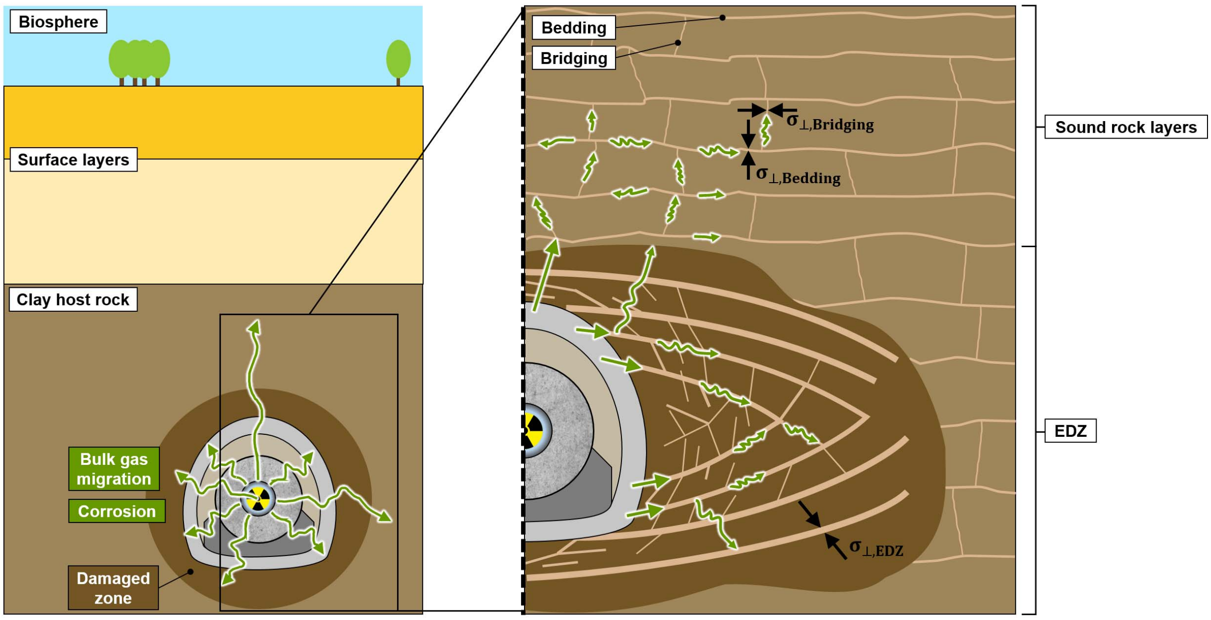

(a) (b)

Figure 2.267: Conceptual scheme of a deep geological repository (a) focusing on the gas generation process with (b) the potential expected gas transport modes in the EDZ and the sound host rock.

2.11.1.1. Conceptual model

Modelling approach

The multi-scale modelling approach adopted in this work lays its foundations on the experimental findings associated to the creation of gas-filled pathways in clay materials. Indeed, it is now accepted that such a gas transport mode exploits the weakest zones inherent to the formation or previously disturbed portions around excavations, which emphasises the fundamental role played by the HM couplings between the deformational response and the gas pressure (Cuss et al., 2014c; Liu et al., 2016; Harrington et al., 2017b), and the ensuing impact on the host rock properties (Harrington et al., 2012c; Gonzalez-Blanco et al., 2016a, 2022). In that sense, microstructural information before and after gas injection tests such as those shown in Figure 2.268a (Gonzalez-Blanco and Romero, 2022) proves to be essential to the development of advanced coupled numerical models for predicting gas flow processes through low-permeability rock formations.

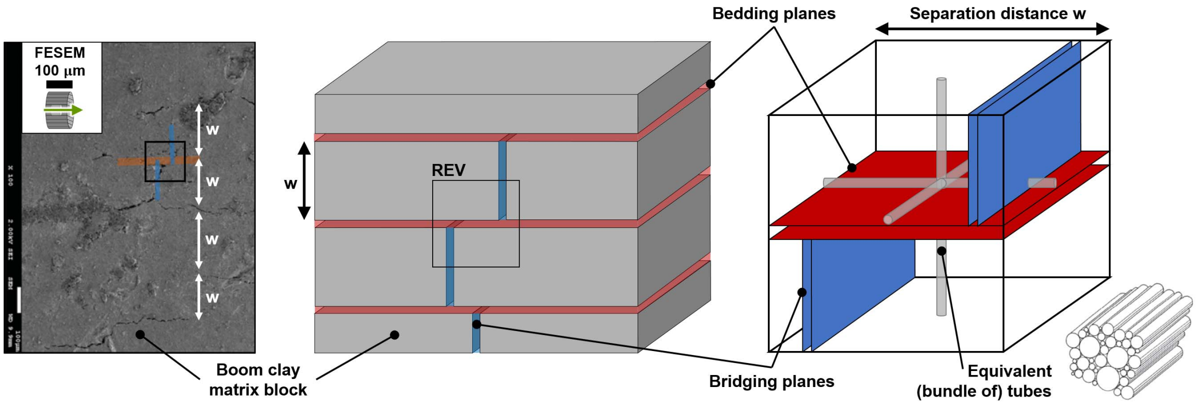

(a) *(b)* *(c)*

Figure 2.268: (a) Internal visualisation of a Boom Clay sample using FESEM, after (Gonzalez-Blanco and Romero, 2022). (b) Physical idealisation of the microstructure. (c) Definition of the REV.

This method is based on the concept of Representative Element Volume (REV) which is somehow introduced to decouple the macro-scale medium from the micro-scale in a computational way (Smit et al., 1998). The material behaviour and properties are therefore not valid for the whole macrostructure, but rather at some macroscopic points where relevant estimations are acquired from direct computations on the REV assigned to those integration points of the discretised macroscopic medium. Although the use of a REV seems questionable for natural materials which are heterogeneous in essence, clay rocks are generally characterised by a horizontal layered structure owing to their process of deposition (Vandenberghe, 1978; Wenk et al., 2008). In the proposed modelling of Boom Clay material, it is possible to extrapolate a physical idealisation of the microstructure from the experimental data, as depicted in Figure 2.268b. This latter includes matrix blocks of Boom Clay separated by dominant horizontal fractures, corresponding to the bedding planes. In the vertical direction, secondary narrow-aperture fissures connecting the bedding planes were also detected experimentally as contributors to the flow normal to the bedding. This simplification allows to identify the main constituents to include in the REV. Considering first the repeated separation distance w between the horizontal fractures, one of these bedding planes (red element) is integrated as the central element of the REV, as depicted in Figure 2.268c. Another fracture element prone to develop in the vertical direction is added to the REV, and is referred to as a bridging plane (blue element). Finally, the matrix block is substituted by an assembly of tubes with specific diameters and tortuosities, so as to match the pore size distribution curve. In the REV, this bundle of tubes is gathered into one equivalent tube (grey elements) in the three guiding directions of the micro-scale problem.

Once the REV has been built, the double-scale procedure relies on a series of sequential steps, illustrated in Figure 2.269. The macroscopic quantities are first converted into specific boundary conditions applied to the REV. Once the analysis on the REV level has been carried out, a homogenisation technique is used to bridge the gap between the micro and macro-levels, in such a way that the global response of the REV serves as a numerical constitutive law for the computation at the macro-scale.

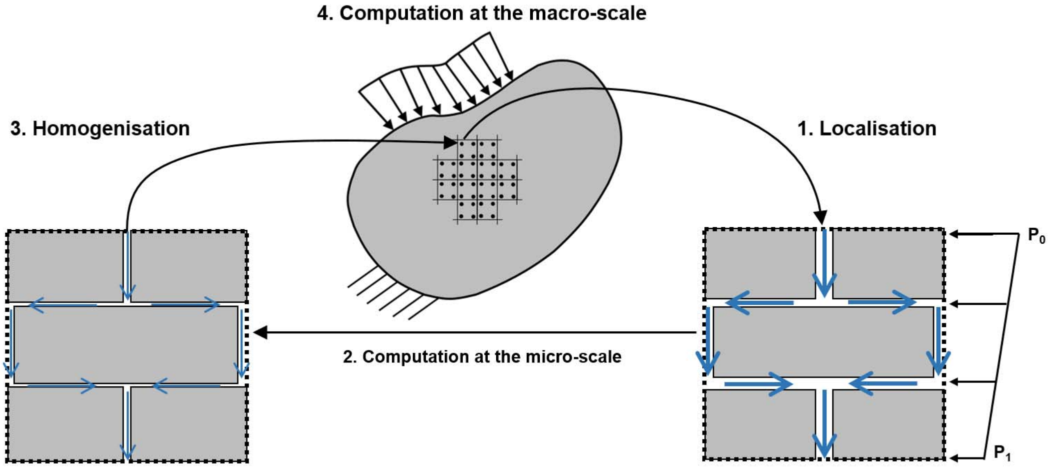

Figure 2.269: Conceptual scheme of the iterative process for the multi-scale modelling approach.

Basic features

In the model, the complex structure of the clay material is treated as a porous medium commonly assimilated as the superposition of several continua, relying on the mixture theory. In order to cope with multiphase flows through such a medium, a binary fluid mixture is considered, which includes a liquid and a gaseous phase. The former phase is a combination of two species, namely liquid water and dissolved gas, while the latter is solely made of dry gas, assuming water vapour is negligible. In the proposed formulation, it is also assumed that the mineral species and the solid phase coincide, and that solid and fluid phases are immiscible.

The proposed numerical tool can be seen as hybrid, in the sense that a complete hydraulic system is explicitly implemented and solved at the micro-scale to determine the fluids flows, while the effects of the mechanical problem are addressed at the macroscopic scale and implicitly integrated at the lower level by means of HM couplings. The evolution of fracture aperture and tube opening at the micro-scale is linked to the variation in fluids pressure at the macro-scale, without any change in the total stress following the concept of effective stress. As a consequence, there is a dependency of the intrinsic permeability on the fracture and tube apertures. In addition, as the gas entry pressure is likely to decrease with the progressive opening of fractures and tubes, the respective aperture or diameter of each of these micro-elements is used to scale the entry value of each specific element. All these HM interactions are expressed later in the document, in Equations (2.105), (2.106)-(2.109) and (2.110)-(2.111).

Regarding anisotropic aspects, the pore network is supposed to be the same in all directions, and the anisotropy comes from the different separation planes, *i.e.* the bedding planes and the bridging planes. As for heterogeneity, it is introduced into the model in a deterministic way, by adjusting the parameters of stiffness and initial aperture of same planes, in order to simulate zones of weakness where the gas-specific pathways are more prone to occur.

Microscale hydraulic model

Since the mechanical problem is exclusively solved at the macroscopic scale, only mass balance equations for water and gas are required at the microscopic scale. The terms representing the variations of fluid contents vanish out under the assumption of steady state at the micro-scale, leading to the following equations:

$$\cancel{\dot{\mathrm{M}}^{\mathrm{m}}_{\mathrm{w}}} + \frac{\partial f^m_{w_i}}{\partial x_i} = 0 \tag{2.88}$$

$$\cancel{\dot{\mathrm{M}}^{\mathrm{m}}_{\mathrm{g}}} + \frac{\partial f^m_{g_i}}{\partial x_i} + \cancel{\dot{\mathrm{M}}^{\mathrm{m}}_{\mathrm{dg}}} + \frac{\partial f^m_{dg_i}}{\partial x_i} = 0 \tag{2.89}$$

where $\dot{\mathrm{M}}^{\mathrm{m}}_{\mathrm{w}}$, $\dot{\mathrm{M}}^{\mathrm{m}}_{\mathrm{g}}$ and $\dot{\mathrm{M}}^{\mathrm{m}}_{\mathrm{dg}}$ represent the variations of the fluid contents, namely water, gas and dissolved gas, that vanish out under the assumption of steady state at the microscale, and $\mathrm{f}^{\mathrm{m}}_{\mathrm{w_i}}$, $\mathrm{f}^{\mathrm{m}}_{\mathrm{g_i}}$ and $\mathrm{f}^{\mathrm{m}}_{\mathrm{dg_i}}$ are the total mass flows of water gas, and dissolved gas respectively, that take into account the advection of each phase using the generalised Darcy's law (Darcy, 1856) and the diffusion of the components within each phase by Fick's law (Fick, 1855), as follows:

$$f^m_{w_i} = \rho_w q_{w_i} \tag{2.90}$$

$$f^m_{g_i} = \rho_g q_{g_i} \tag{2.91}$$

$$f^m_{dg_i} = \rho_{dg} q_{w_i} + i_{dg_i} \tag{2.92}$$

where ρ_{w}, ρ_{g} and ρ_{dg} are the densities of water, gas and dissolved gas respectively, $\mathrm{q_{w_i}}$ and $\mathrm{q_{g_i}}$ are the advective fluxes respectively of the liquid and gaseous phases, $\mathrm{i_{dg_i}}$ is the diffusion flux for dissolved gas in the liquid phase.

Since the hydraulic problem is solved by considering a channel flow model extended to unsaturated conditions to simultaneously consider gas and water flows at the micro-scale, the longitudinal advective components of the multiphase flow along a fracture and a tube embedded in a REV of section $\mathrm{A} = (\mathrm{w} + \mathrm{h_b})^2 \simeq \mathrm{w}^2$ assuming $\mathrm{w} \gg \mathrm{h_b}$, are respectively expressed as:

$$q_{\alpha_i} = -\frac{k_{r_\alpha}}{\mu_\alpha}\frac{1}{A}\kappa_{frac}\frac{\partial p_\alpha}{\partial x_i} = -\frac{k_{r_\alpha}}{\mu_\alpha}\frac{h_b^3}{12w}\frac{\partial p_\alpha}{\partial x_i} \tag{2.93}$$

$$q_{\alpha_i} = -\frac{k_{r_\alpha}}{\mu_\alpha}\frac{1}{A}\kappa_{tube}\frac{\partial p}{\partial x_i} = -\frac{k_{r_\alpha}}{\mu_\alpha}\pi\frac{D^4}{128w^2}\frac{\partial p}{\partial x_i} \tag{2.94}$$

where the subscript $\alpha = \mathrm{w}, \mathrm{g}$ represents the liquid or gaseous phase respectively, p is the applied pressure, either of water or gas, $\mathrm{k_{r_\alpha}}$ is the relative permeability, μ_α is the dynamic viscosity, $\mathrm{h_b}$ is the fracture aperture, D is the tube diameter, w is the size of the REV, and κ_{frac} and κ_{tube} are the hydraulic transmissivity functions for a fracture (simplified by two parallel plates with an hydraulic aperture $\mathrm{h_b}$, Figure 2.270a), and a tube (simplified as a circular pipe of diameter D, Figure 2.270b), whose expressions can be derived using the Navier-Stokes equations for a laminar flow under steady state conditions :

$$\kappa_{frac} = -\frac{h_b^2}{12}h_b \cdot w \tag{2.95}$$

$$\kappa_{tube} = -\pi\frac{D^4}{128} \tag{2.96}$$

In porous media, these relative permeabilities of water $\mathrm{k_{r_w}}$ and gas $\mathrm{k_{r_g}}$ are often expressed as power functions of the saturation, according to (Corey (1954)), which reads for a single fracture:

$$k_{r_w} = \frac{S_r^{*^2}}{2}(3 - S_r^*) \tag{2.97}$$

$$k_{r_g} = (1 - S_r^*)^3 \tag{2.98}$$

and a single capillary:

$$k_{r_w} = S_r^{*^2} \tag{2.99}$$

$$k_{r_g} = (1 - S_r^*)^2 \tag{2.100}$$

where $\mathrm{S_r^*} = \frac{\mathrm{S_{rw}} - \mathrm{S_{rw,res}}}{1 - \mathrm{S_{rw,res}} - \mathrm{S_{rg,res}}}$ is the normalised saturation.

As for the longitudinal diffusive component of the multiphase flow along a fracture or a tube, it is defined by Fick's law (Fick, 1855), which states that the flux in the direction i for a diffusing species is directly proportional to the concentration gradient in that direction. Thence, the diffusion flux of dissolved gas within the liquid phase reads:

$$i_{dg_i} = -\, S_{r_w}\, \bar{\tau}\, D_{dg/w}\, \rho_w A_{el}\, \frac{\partial}{\partial x_i}\left(\frac{\rho_{dg}}{\rho_w}\right) \tag{2.101}$$

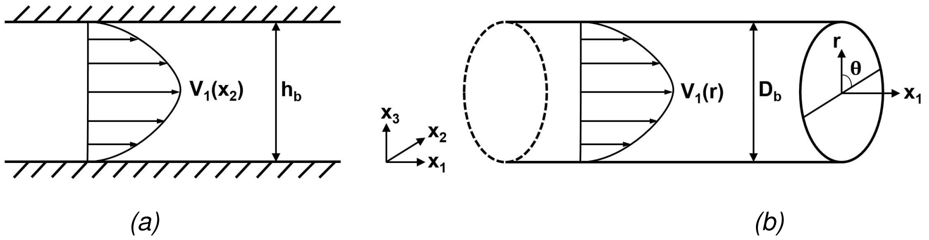

Figure 2.270: Laminar fluid flow profiles (a) between two parallel plates and (b) in a circular pipe.

where $D_{dg/w}$ is the diffusion coefficient for the dissolved gas in liquid water, A_{el} is the section of the micro-element (fracture or tube) and $\bar{\tau}$ is the tortuosity of the REV constituent, which characterises the path followed by the dissolved gas particles across the REV in the direction i. It is supposed that $\bar{\tau} = 1$ for the fractures.

Under isothermal conditions, the isotropic compressibility of water is thus assumed to respect the following relationship, which predicts an increase in water density as a function of the macro-scale water pressure:

$$\rho_w = \rho_{w_0}\left(1 + \frac{p_w^M - p_{w_0}^M}{\chi_w}\right) \tag{2.102}$$

where the superscript M refers to a macroscopic quantity, ρ_{w_0} is the liquid density at the pressure $p_{w_0}^M$ and $\frac{1}{\chi_w}$ is the liquid compressibility.

The density of dry gas phase in a fracture or a tube is expressed according to the classical ideal gas equation of state (Clapeyron, 1834) as a function of the macro-scale gas pressure, which yields:

$$\rho_g = \frac{m_g}{RT} p_g^M \tag{2.103}$$

where m_g is the molar mass of dry gas, R is the universal gas constant and T is the absolute temperature, and p_g^M is the macro-scale gas pressure.

The density of the dissolved gas is obtained with Henry's law (Weast, 1987), which states that the amount of dissolved gas in the liquid phase is always in thermodynamic equilibrium and proportional with the quantity of dry gas, such that:

$$\rho_g^d = H_g \rho_g \tag{2.104}$$

where H_g is the so-called Henry's coefficient.

Specific HM laws are also introduced into the model. First of all, with a view to represent multiphasic materials in the model, the total stress σ_{ij} is defined with the Bishop's postulate (Bishop, 1959) to account for partially saturated conditions, which reads:

$$\sigma_{ij} = \sigma'_{ij} + b_{ij}\left[S_{r_w} p_w^M + (1 - S_{r_w}) p_g^M\right]\delta_{ij} \tag{2.105}$$

where δ_{ij} is the Kronecker symbol, $b_{ij} = \delta_{ij} - \frac{C^e_{ijkl}}{3K_s}$ is Biot's tensor, K_s is the isotropic bulk modulus of the solid grains, C^e_{ijkl} is the elastic stiffness tensor of the material, and σ'_{ij} is the Bishop's effective stress. This latter concept corresponding to the total stress reduced by the fluid pressures weighted by the degree of saturation of each phase represents a first important hydro-mechanical coupling that connects the two levels of the model. Note that in previous Equation (2.105), the stress field is defined under soil mechanics convention in which compressive stress is positive.

Since the effective stress introduced at the macroscale is transferred to the microscopic scale, it is possible to relate the evolution of fracture aperture and tube opening at the microscale to the variation in fluids pressure at the macroscale, without any change in the total stress. Specific HM laws are therefore formulated to express the fracture and tube apertures as a function of the effective stress.

The interface HM law used for the fractures relates the displacement of the facing edges to the stress state via the normal stiffness K_n. A hyperbolic law (Goodman, 1976; Bandis et al., 1983b) is generally used to account for the deforming asperities in the evolution of the normal stiffness with the fracture closure (Gens et al., 1990b), such that the relation between the normal effective stress rate and the fracture aperture reads:

$$\dot{\sigma}' = K_n \dot{h} \qquad \text{with} \qquad K_n = \frac{K_n^0}{\left(1 + \frac{\Delta h}{h_0}\right)^2} \tag{2.106}$$

where K_n^0 is the stiffness corresponding to the initial aperture h_0, defined for a null stress. Thus, when considering some initial stresses and that $\Delta h = h - h_0$, the initial normal closure is given by:

$$\Delta h_0 = \frac{-\sigma_0'\ h_0}{K_n^0\ h_0 + \sigma_0'} \tag{2.107}$$

where σ_0' is the effective stress normal to the fracture wall.

Finally, the relationship between effective stresses and displacements for the fractures governing the bedding and bridging planes is given by:

$$\sigma_0' + \Delta\sigma' = \frac{K_n^0 h_0}{h}(\Delta h_0 + \Delta h) \tag{2.108}$$

The HM law used for the tubes representing the matrix blocks relates the circumference closure to the normal effective stresses via a linear relation derived from the convergence-confinement theory (Panet and Guenot, 1982):

$$\Delta\sigma' = K\ \Delta D_b \qquad K = \frac{2G}{D_0} \tag{2.109}$$

where D_0 is the tube diameter defined for a null stress, and G is the shear modulus of the clay rock.

A second implicit coupling is the dependency of the intrinsic permeability on the fracture and tube apertures, which are stress-dependent as formulated in Equations (2.93) and (2.94). Furthermore, as the gas entry pressure is likely to decrease with the progressive opening of fractures and tubes, the respective aperture or diameter of each of these micro-elements can be used to scale the entry value of each specific element as:

$$p_e = p_{e_0}\left(\frac{h_{b_0}}{h_b}\right)^m \tag{2.110}$$

$$p_e = p_{e_0}\left(\frac{D_{b_0}}{D_b}\right)^m \tag{2.111}$$

where m is a material parameter of the power law, which is assigned a value of 0 for a constant entry pressure, and a value of 3.3 in (Dieudonné (2016)) based on experimental results on bentonite. The parameter p_{e_0} is the initial entry pressure defined for the aperture h_{b_0} of a fracture or the diameter D_{b_0} of a tube, and is directly derived from the Young-Laplace equilibrium, which defines the mechanical balance between the capillary pressure p_c and the surface tensions σ_{GL} in a fracture and a tube respectively as:

$$p_{e_0} = \frac{2\sigma_{GL}cos\theta}{D_b/2} \tag{2.112}$$

$$p_{e_0} = \frac{2\sigma_{GL}cos\theta}{h_b} \tag{2.113}$$

Note that hydraulic apertures h_b and D_b are considered in order to take into account the non-smoothness of the fracture and tube edges, which respectively reads:

$$h_b = h_0 + h \tag{2.114}$$

$$D_b = D_0 + D \tag{2.115}$$

It means that a mechanically closed fracture/tube ($h = D = 0$) still allows a residual flow to circulate between the asperities as long as a non-zero minimal hydraulic opening is defined.

2.11.1.2. Numerical model

The simulations are carried out with the Lagamine Finite Element code, which is a non-linear finite element tool initially elaborated at the University of Liège, which has been constantly evolving with time since the 1980s (Charlier, 1987b; Habraken, 1989), supported by successive doctoral research and developments. The code has been primarily developed in two different fields namely the behaviour of metals and geomechanics. More specifically, the latter explores multiple facets of the geomechanical environment, which requires Chemo-Thermo-Hydro-Mechanical coupled models. Accordingly, the code compiles highly coupled constitutive laws based on elasto-plastic, elasto-visco-plastic frameworks, second gradient models (Collin et al., 2006b) or on a multi-scale approach on the one hand. And on the other hand, it deals with coupled finite elements (Gerard et al., 2008a) (monolithic approach) dedicated to the modelling of multiphase or multiphysical problems (Collin et al., 2002b). This way, the Lagamine software constitutes an advanced numerical tool to tackle civil engineering problems involving soil-structure interactions (Cerfontaine et al., 2015a) or soils and rocks mechanics problems, with specific applications to the modelling of nuclear waste disposal, slope stability and reservoir engineering.

Modelling design

The multi-scale HM model briefly conceptualised in the previous section is now applied to the numerical modelling of air injection tests under oedometer conditions on initially saturated samples of Boom Clay, whose experimental design is reported by (Gonzalez-Blanco et al. (2016a)). This experimental design is translated into a numerical model which requires several ingredients that are listed below.

Regarding first the geometry, the modelling design of the air injection tests consists of a 2D axisymmetric representation of the Boom Clay sample, taking advantage of the radial symmetry of the oedometer geometry. Thence, null vertical displacements at the bottom of the system and null radial displacement on the sample lateral wall are imposed by the oedometer conditions. To properly simulate the stages of the gas injection tests, injection (bottom) and recovery (top) reservoirs surrounding the sample are also included in the model as illustrated in Figure 2.271, which materialise the injection and recovery pistons, lines and coarse porous rings of the experimental setup.

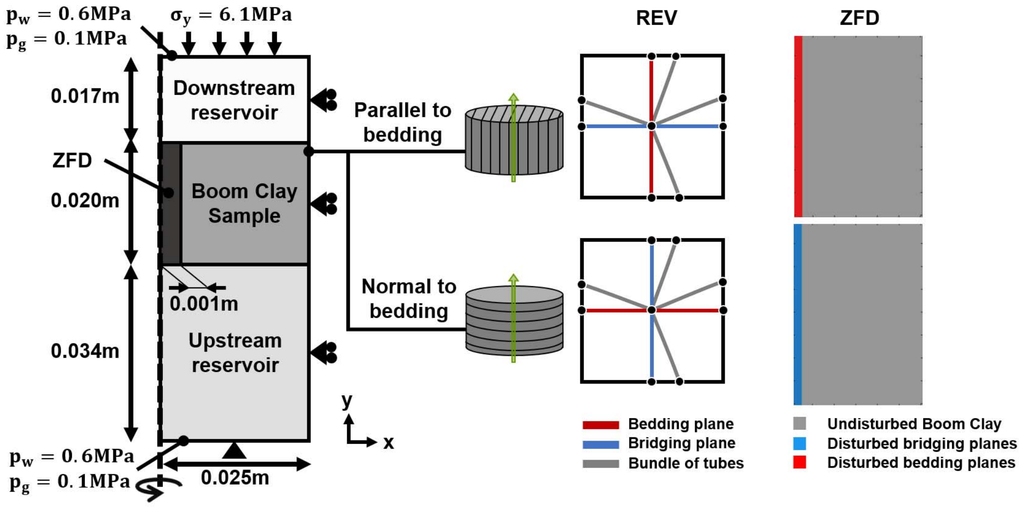

(a) *(b)* *(c)*

Figure 2.271: (a) Geometry and initial boundary conditions, with (b) the REV idealisation showing the two orientations of the studied sample, and (c) the two configurations of the ZFD.

In order to investigate the consequences of the development of gas-filled preferential pathways, the sample is divided into two zones having different hydraulic properties as depicted in Figure 2.271c: the matrix (undisturbed clay, coloured in grey) and a zone of fracture development (ZFD), including either disturbed bedding planes in red or disturbed bridging planes in blue, depending on the orientation of the sample. This latter part located in a single predefined central band with a thickness of 2 mm, represents a zone where cracks will preferentially open and is characterised by weaker properties for the rock corresponding to the ones obtained after the injection test. Such an imposed arrangement allows to reproduce the global effect of the preferential pathways activation on the global sample response but does not account for the local distribution of the fractures.

Whatever the orientation of the sample is, the initial conditions in the Boom Clay sample following the initial pre-conditioning phase are defined by an isotropic stress state and homogeneous water and air pressures as:

$$\sigma_{x,0} = \sigma_{y,0} = 6 \text{ MPa}, \; p_{w,0} = 0.6 \text{ MPa}, \; p_{g,0} = 0.1 \text{ MPa} \tag{2.116}$$

where $\sigma_{\mathrm{x,0}}$ and $\sigma_{\mathrm{y,0}}$ are the horizontal and vertical principal total stress respectively, while $\mathrm{p_{w,0}}$ and $\mathrm{p_{g,0}}$ correspond to the initial pore water and gas pressures respectively.

The sequential evolution of the experiment is translated into a boundary value problem which is conducted by progressively adjusting the boundary conditions at the two sides of the geometry, as highlighted in Figure 2.272. Since the numerical simulations focus solely on the slow gas injection tests carried out parallel and perpendicular to the bedding planes of the sample, it should be first mentioned that the initial pre-conditioning and final unloading stages are neglected. Before the air injection starts, the sample was fully saturated, as well as both reservoirs. First, water is replaced by air in the upstream reservoir with an upstream air pressure increasing up to 0.6 MPa. Then the air injection phase is performed with a pressure ramp applied at the bottom of the injection reservoir, which follows the data recorded experimentally up to a pressure of 4.2 MPa. Once the injection pressure reaches this maximum value, the dissipation phase starts, during which the bottom boundary becomes impermeable forcing the accumulated air in the upstream reservoir to flow upwards. As for the downstream reservoir, the pressure there is kept constant at 0.6 MPa throughout the tests. In practise, this device is capable of maintaining the pressure constant by changing the volume, but if the air continues to flow through the sample when the tank of the controller is full, it is not able to keep the pressure anymore. Accordingly, the pressure boundary condition in the recovery system is increased up to 1.6 MPa and 1.0 MPa in a second part of the dissipation stage for injection parallel and perpendicular to the bedding respectively.

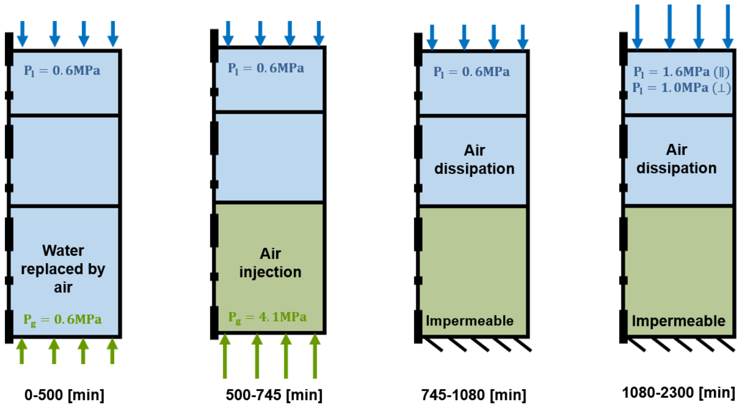

Figure 2.272: Evolution of the boundary conditions in terms of water and gas pressures during the successive steps of the numerical simulation.

Mechanical model

An elasto-plastic internal friction model with cross-anisotropy and horizontal isotropic bedding planes is considered for the mechanical behaviour of the Boom Clay, which can be decomposed into an elastic and a plastic components.

The linear elastic behaviour of the rock is based on the classical Hooke's law, where the elastic compliance tensor is expressed as a function of five independent parameters for cross-anisotropic materials (Amadei, 1983). The Boom Clay formation is indeed characterised by a strong anisotropy of its mechanical properties between the directions parallel and perpendicular to the bedding planes (Chen et al., 2011a), but the behaviour remains isotropic in the parallel bedding planes.

The elasto-plastic behaviour of the Boom Clay is characterised by an internal friction model with a non-associated plasticity and a van Eekelen yield surface (Van Eekelen, 1980) (under soil mechanics convention with positive compressive stress). Furthermore, the model allows isotropic hardening or softening of the cohesion and of the friction angles upon loading. Further details about the elasto-plastic model are available in (Pardoen, 2015).

The elasto-plastic parameters of the Boom Clay, reported in Table 2.81, are taken from (François, 2014) where calibration is realised based on experimental data.

Table 2.81: Set of elasto-plastic parameters of the Boom Clay, from [François (2014)].

Parameter	Symbol	Value	Unit
Parallel Young's modulus	$E_{\|\|}$	400	[MPa]
Perpendicular Young's modulus	$E_{\perp}$	200	[MPa]
Poisson's ratio	$\nu_{\|\|\|\|}$	0.125	[−]
Poisson's ratio	$\nu_{\|\|\perp}$	0.125	[−]
Poisson's ratio	$\nu_{\perp\|\|}$	0.0625	[−]
Shear modulus	$G_{\|\|\perp}$	178	[MPa]
Shear modulus	$G_{\|\|\|\|}$	178	[MPa]
Solid grain density	ρ_s	2650	[kg/m^3]
Initial cohesion	c_i	255 (0°)	[kPa]
		240 (45°)	[kPa]
		330 (90°)	[kPa]
Ratio of cohesion softening	ξ_c	3	[−]
Cohesion softening parameter	B_c	0.01	[−]
Cohesion softening shifting	dec_c	0	[−]
Initial compressive friction angle	$\varphi_{c,0}$	5	[°]
Final compressive friction angle	$\varphi_{c,f}$	18	[°]
Friction angle hardening param.	B_φ	0.01	[−]
Friction angle hardening shifting	dec_φ	0	[−]
Dilatancy angle	ψ_c	0	[°]

Hydraulic model

The hydraulic model used for the Boom Clay is based on the multi-scale HM model presented in the previous section. All the parameters characterising the microstructural components of the REV must be defined, in order to approach as closely as possible the *in situ* behaviour of the studied host rock.

First of all, a physical value of the bedding plane separation is selected so that it is in the range of the averaged data for Boom Clay, obtained experimentally with different techniques by (Gonzalez-Blanco, 2017a) and summarized in Table 2.82. This value constitutes the reference size w of the REV. In the present case, a value of $w = 3 \cdot 10^{-4}$m is chosen.

Then, each individual tube of the bundle representing the micro-scale porous matrix, is assigned a specific value of a calibration parameter. This latter can be assimilated to a tortuosity parameter in the sense that it is used to artificially increase the volume of each individual straight tube. This way, it is possible to fit the experimental pore size distribution curve (Lima, 2011; Gonzalez-Blanco, 2017a) as highlighted in Figure 2.273a, and get the right value of the macro-porosity of Boom Clay, *i.e.* around $n = 0.38$. Of course, increasing the number of tubes included in the REV, especially the smaller ones, allows the value of the

Table 2.82: Initial apertures and separation values obtained from different techniques by [Gonzalez-Blanco and Romero (2022)].

Geometric property	Unit	MIP	FESEM	μCT
Aperture h	μm	>2	$3-10$	$90^{\parallel}-153^{\perp}$
Separation w	μm	–	$150-270$	$410^{\parallel}-558^{\perp}$

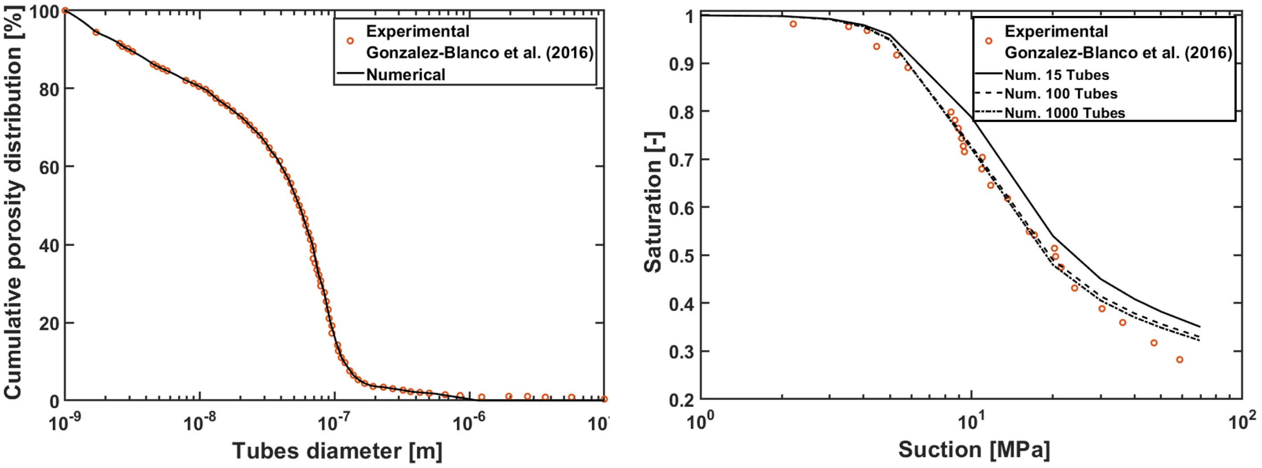

(a) *(b)*

Figure 2.273: (a) Experimental data for the cumulative porosity distribution of the Boom Clay [Gonzalez-Blanco et al. (2016a)], with respective fitted numerical results. (b) Experimental data for the water retention curve of intact Boom Clay (Gonzalez-Blanco et al., 2016a), together with van Genuchten's model fitting.

calibration parameter to gradually converge towards the estimates of the natural equivalent tortuosity of the Boom Clay established around $\bar{\tau} = 0.6$ (Wiseall et al., 2015a). Nevertheless, to keep reasonable computation times during simulations, a limited number of tubes is integrated in the implemented REV.

To characterise the Boom Clay retention behaviour, a retention curve of van Genuchten's type (van Genuchten, 1980) linking the capillary pressure to the degree of water saturation is assigned to each microstructural constituent, *i.e.* tubes and fractures:

$$S_{r_w} = S_{r_{res}} + (S_{max} - S_{r_{res}})\left(1 + \left(\frac{p_c}{P_r}\right)^{\mathcal{N}}\right)^{\frac{1}{\mathcal{N}}-1} \tag{2.117}$$

where P_r is a parameter identified as the gas entry pressure, S_{max} and $S_{r_{res}}$ are the maximum and residual degrees of water saturation, $\mathcal{N}$ is a model parameter controlling the curve shape, and $p_c = s$ is the capillary pressure or suction.

Hence, the global retention response of the material is not computed at the macroscopic scale but results from the integration of the whole individual retention curves of the microstructure elements, which allows to reasonably capture the experimental data (Gonzalez-Blanco, 2017a) as the number of tubes is increased.

In addition, knowing that the permeability in Boom Clay is anisotropic with a ratio of more or less two between the horizontal and vertical directions, the initial aperture of the bedding planes is chosen so that it contributes to half of the permeability in this principal direction:

$$k_{x,0} = \underbrace{\frac{\pi}{8}\left(\frac{D_{b,0}}{2}\right)^4\left(\frac{1}{w^2}\right)}_{\sum k_{tube,0}} + \underbrace{\frac{h_{b,0}^2}{12}\frac{h_{b,0}\cdot w}{w^2}}_{k_{frac,0}} \longrightarrow h_{b,0} = \sqrt[3]{12\,w\,k_{frac,0}} \tag{2.118}$$

where $k_{x,0}$ is the intrinsic permeability in the horizontal direction, $k_{frac,0}$ and $k_{tube,0}$ are the initial permeabilities of the bedding plane and the tubes respectively. In practise, bedding and bridging plane apertures of $h_{b0,\parallel} = 0.060\ \mu m$ and $h_{b0,\perp} = 0.035\ \mu m$ are respectively prescribed for an intact sample of Boom Clay. This corroborates experimental results (Lima, 2011; Gonzalez-Blanco et al., 2016a) that assimilate the dominant entrance pore size of the statistical distribution of apertures as representative of the initial bedding or bridging apertures, with values of the order of $0.1\ \mu m$.

The other fraction of the permeability is obviously provided by the macro-pores which are responsible for the majority of the permeability in the vertical direction, such that:

$$k_{y,0} = \underbrace{\frac{\pi}{8}\left(\frac{D_{b,0}}{2}\right)^4\left(\frac{1}{w^2}\right)}_{\sum k_{tube,0}} \tag{2.119}$$

where $k_{y,0}$ is the intrinsic permeability in the vertical direction.

On top of that, relative permeability coefficients for the liquid and gas phases are expressed as functions of the effective degree of saturation S_r^*, according to the power law Equations (2.97)-(2.98) for the fracture, and (2.99)-(2.100) for the tube respectively. These expressions provide a rather good fitting of the experimental data for bulk Boom Clay reported by (Volckaert et al., 1995b) despite the dispersion, as highlighted in Figure 2.274a.

Given the hydro-mechanical coupling in Equation (2.107) which relates the stress state to the fracture aperture and thus implicitly to its permeability, it is possible to estimate the initial stiffness of the bedding plane K_n^0. Practically, this value is obtained by fitting the experimental compilation of the permeability evolution as a function of the isotropic effective stress given in Figure 2.274b (Coll, 2005; Bésuelle et al., 2014), considering that the rest of the permeability (shaded area) arises from the porosity related to the bundle of tubes.

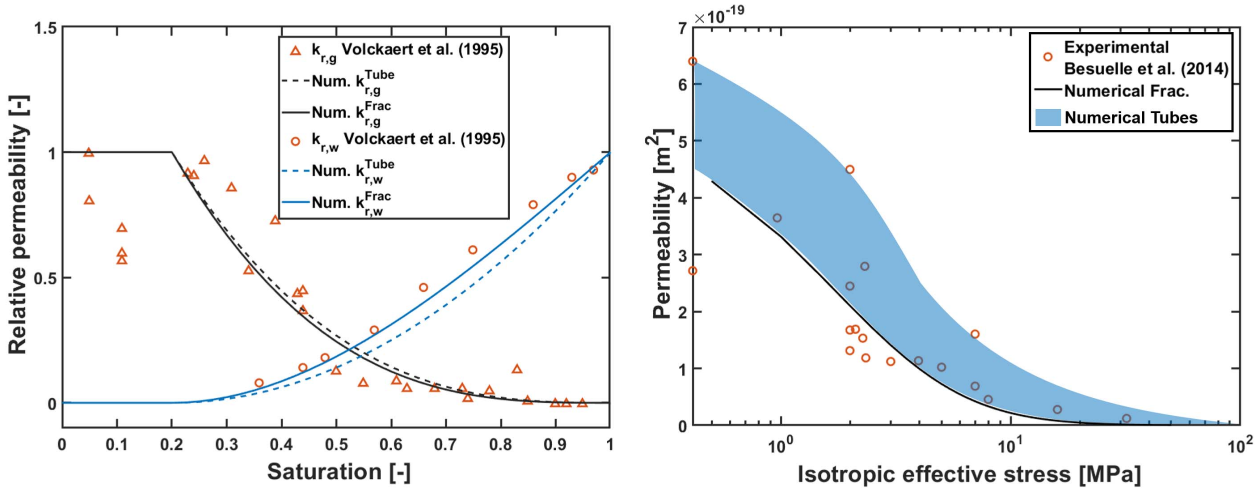

(a) (b)

Figure 2.274: Experimental data for (a) the water and gas relative permeability curves (Volckaert et al., 1995b), with fitted numerical formulation for fractures and tubes, and (b) the water retention curve of intact Boom Clay (Gonzalez-Blanco et al., 2016a), together with van Genuchten's model fitting.

Regarding the zone of fracture development, it is assumed to be characterised by weaker properties corresponding to the ones experimentally obtained at the end of the air injection tests. More specifically, as it is expected that the fissures closed up during the air pressure dissipation where the sample undergoes compression, it is supposed that the measured fissure opening are in between the initial and the maximum aperture of the generated pathways during gas migrations (Gonzalez-Blanco, 2017a). Therefore, in the ZFD, the bedding and bridging plane take initial values of aperture of $b_{0,||} = 0.200\ \mu m$ and $b_{0,\perp} = 0.095\ \mu m$ respectively. Moreover, it is also assumed that the initial stiffness of any fissure belonging to one of these two families of fractures in this zone is reduced due to the damage compared to the intact stiffness deduced from Figure 2.274b. It means that for a given evolution of the stress state, the bedding and bridging planes are prone to open/close in a more important way in this zone of the sample, compared to the intact portions of the material, as depicted in Figures 2.275a and 2.275b.

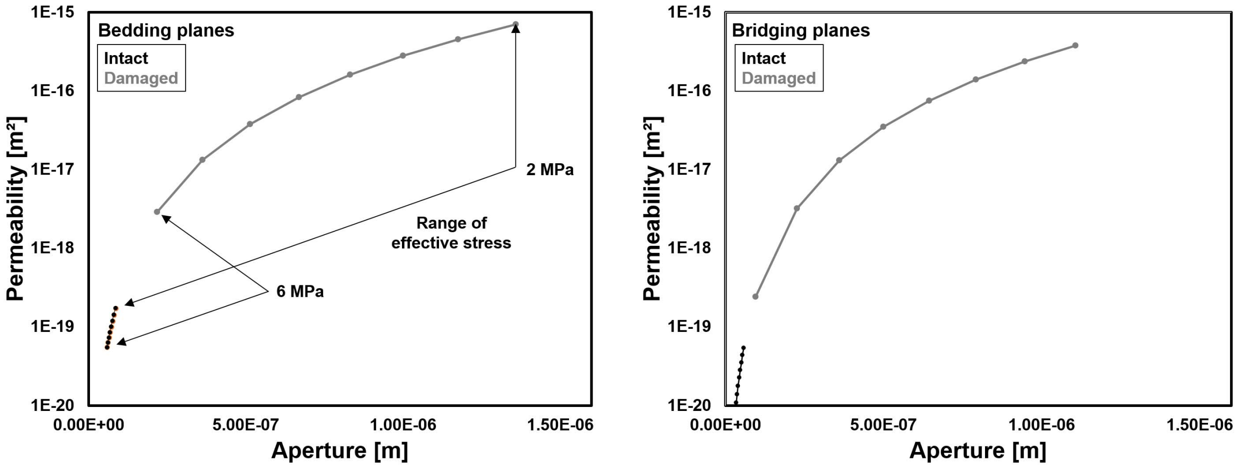

(a)

(b)

Figure 2.275: Experimental data for (a) the water and gas relative permeability curves (Volckaert et al., 1995b), with fitted numerical formulation for fractures and tubes, and (b) the water retention curve of intact Boom Clay (Gonzalez-Blanco et al., 2016a), together with van Genuchten's model fitting.

All the hydraulic parameters of the Boom Clay are summarised in Table 2.83, which also gathers the parameters related to the zone of fracture development in the last part.

Injection and recovery systems

These two reservoirs are idealised as very stiff elements having a linear elastic mechanical law with a very high Young modulus. The total volume of each system corresponds to the dead volumes obtained from calibration tests of the equipment (Gonzalez-Blanco et al., 2016a). Hydraulically, they are characterised by a porosity of 0.5 since the code does not model non-porous materials, with a high conductivity and a flat retention curve including a very low air entry value. All the hydro-mechanical parameters of the injection and recovery systems are retrieved from (Gonzalez-Blanco et al., 2016a), and gathered in Table 2.84.

2.11.2. Results

2.11.2.1. Modelling of the air injection tests

Numerical simulations are performed by implementing the predefined geometry of the Boom Clay sample surrounded by the injection and outflow systems, with the corresponding boundary conditions applied on these two sides. The numerical results are computed for a specimen oriented parallel and perpendicular to the air flow, at a slow injection rate of 2 mL/min.

It is first proposed to observe how the system behaves mechanically under the effect of gas injection and propagation through the Boom Clay material. To that end, the evolution of the average axial strain along the sample height as a function of time is represented in Figures 2.276a and 2.276b for bedding planes oriented parallel and perpendicular to the air flow respectively. Whatever the orientation is, it appears that the sample undergoes expansion under the increasing pressure of injected gas, before being subjected to

Table 2.83: Set of hydraulic parameters of the Boom Clay, from [Gonzalez-Blanco et al. (2016a)].

Parameter	Symbol	Value		Unit
		Bedding (∥)	*Bridging* (⊥)	
Initial porosity	n	0.38	0.36	$[-]$
Initial parallel intrinsic permeability	$k_{w,0}$	4.2×10^{-19}	2.1×10^{-19}	$[m^2]$
Water density	ρ_w	1000		$[kg/m^3]$
Gas density (*Air*)	ρ_g	1.205		$[kg/m^3]$
Water dynamic viscosity	μ_w	0.001		$[Pa.s]$
Gas dynamic viscosity (He)	μ_g	1.86×10^{-5}		$[Pa.s]$
Water compressibility	χ_w^{-1}	5×10^{-10}		$[Pa^{-1}]$
Henry coefficient (He)	H_i	0.0234		$[-]$
Gas entry pressure (1st coeff. of S_{r_w})	P_r	10.0		$[MPa]$
Parameter (2nd coeff. of S_{r_w})	$\mathcal{N}$	2.5		$[-]$
Max. degree of water saturation	$S_{r,max}$	1		$[-]$
Residual degree of water saturation	$S_{r_w,res}$	0.2		$[-]$
Bedding plane separation	w	4×10^{-4}		$[m]$
Initial aperture	h_{b0}	0.060	0.035	$[\mu m]$
Initial fracture stiffness	K_n^0	4×10^{13}	$1 \times 1 \times 10^{14}$	$[Pa/m]$
Zone of fracture development (ZFD)				
Initial aperture	h_{b0}^{ZFD}	0.20	0.095	$[\mu m]$
Initial fracture stiffness	$K_n^{0,ZFD}$	2.15×10^{12}	$1 \times 2.55 \times 10^{12}$	$[Pa/m]$
Gas entry pressure (1st coeff. of S_{r_w})	P_r^{ZFD}	1.0		$[MPa]$

Table 2.84: Set of hydromechanical parameters of the injection and recovery systems, from [Gonzalez-Blanco et al. (2016a)].

Parameter	Symbol	Value	Unit
Young's modulus	E	1×10^5	$[MPa]$
Poisson coefficient	ν	0.3	$[-]$
Porosity	n	0.5	$[-]$
Intrinsic permeability	k	10^{-10}	$[m^2]$
Entry pressure parameter	P_r	0.001	$[MPa]$

contraction during the air dissipation phases. The sample volume change is reasonably well reproduced during gas injection, in the sense that the computed results show the same expansion as the experimental measurements in both cases of Figure 2.276. Over the phase of air dissipation however, the empirical points seem to be underestimated for injection parallel to bedding and overestimated in the other case.

Then, the evolution of the outflow volume over time, computed as the sum of water and air volumes in the downstream reservoir is represented in Figure 2.277a and 2.277b for bedding planes oriented parallel and perpendicular to the air flow respectively. These results show that the time in which the outflow takes place is relatively well captured by the model compared with the measurements, but it tends to increase faster than the experimental data, once the gas breakthrough occurs in both directions.

At this point, it is good to analyse the fractures behaviour under gas pressure variations throughout the simulation. The time evolution of the normalised apertures of the bedding and bridging planes are depicted in Figures 2.278a and 2.278b respectively. An important fracture opening is first noted during the injection phase, which tends to partially close once the maximum pressure has been reached and the gas starts to dissipate through the sample. However, the order of magnitude of variation is much more pronounced in the ZFD compared to the undisturbed clay matrix, given the properties assigned to the fissures of these two zones from experimental observations. Moreover, microstructural observations from the laboratory tests (Gonzalez-Blanco, 2017a) have attested that the different families of fractures remain open after the

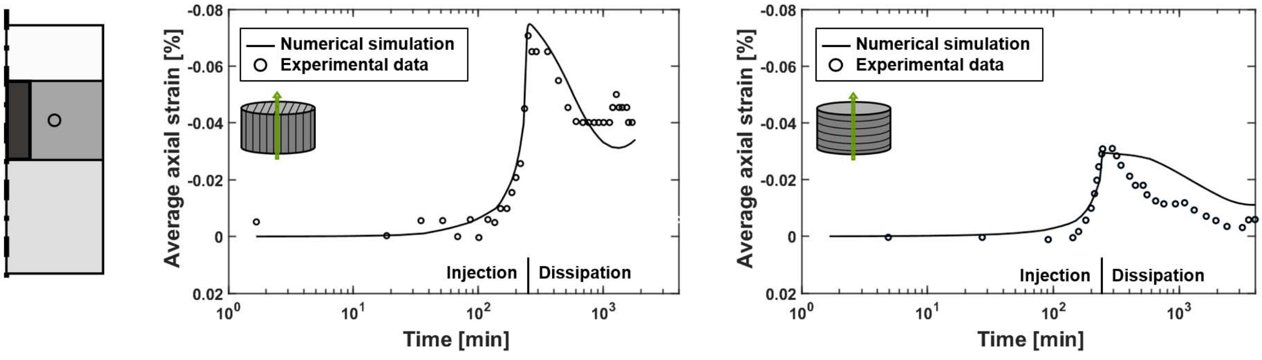

(a) *(b)*

Figure 2.276: Computed versus measured (Gonzalez-Blanco et al., 2016a) average axial strain for slow injection (a) parallel and (b) normal to bedding.

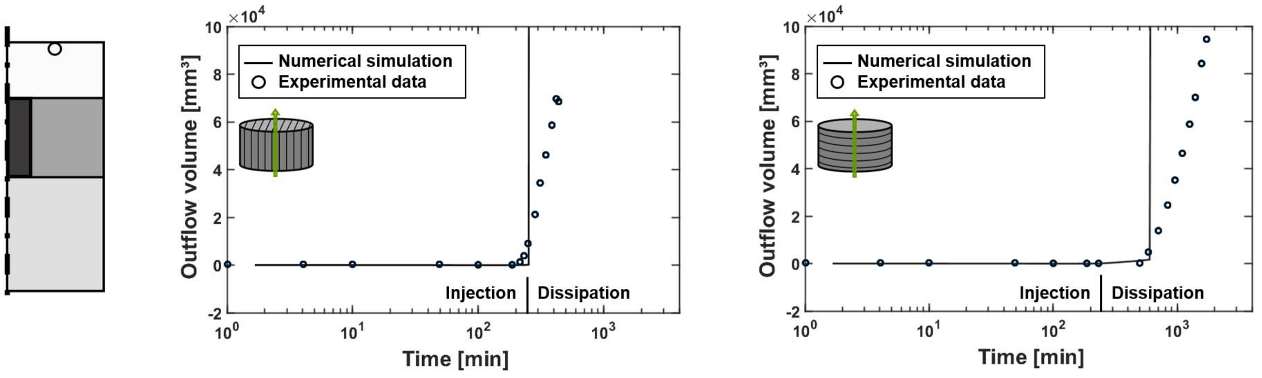

(a) *(b)*

Figure 2.277: Computed versus measured (Gonzalez-Blanco et al., 2016a) outflow volumes for slow injection (a) parallel and (b) normal to bedding.

passage of the gas, as it has been exposed in Figure 2.268a. As bedding and bridging planes attract the majority of the gas in the ZFD during the injection, they could remain partially open during the dissipation phase. Therefore, accounting for a rough hypothesis of constant fracture aperture after shutoff to refine the numerical modelling leads to the dotted grey lines in Figure 2.278.

Finally, Figures 2.279a and 2.279b display the results of the numerically computed injection and outflow pressure response as a function of time for bedding planes oriented parallel and perpendicular to the air flow respectively. These results are expressed as relative pressure, namely it is zero-referenced against atmospheric pressure. It appears that the air pressure decay at the bottom of the sample during the dissipation stages (triangle marker) is rather well fitted. Accounting for a constant fracture opening in the ZFD after the peak of gas pressure allows to slightly improve the pressure drop, as illustrated by the dashed lines in Figure 2.278. Good agreement is also found on the fluid pressures at the top of the system for both orientations of the sample (circle marker), which is computed as the maximum between air and water pressures.

In order to better apprehend the influence of the zone of fractures development in the overall sample response to gas migration, the gas pressure variations at different time steps are displayed in the form of contour plots in Figure 2.280, for gas injection parallel (top) and perpendicular to the bedding planes (bottom).

In both cases, it appears that the prevailing fractures in the ZFD tend to significantly open up only when

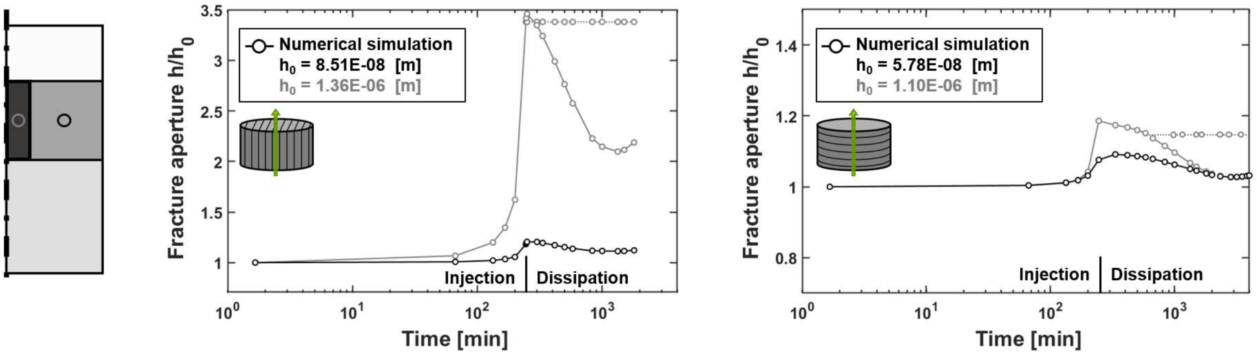

(a) *(b)*

Figure 2.278: Computed versus measured (Gonzalez-Blanco et al., 2016a) outflow volumes for slow injection (a) parallel and (b) normal to bedding.

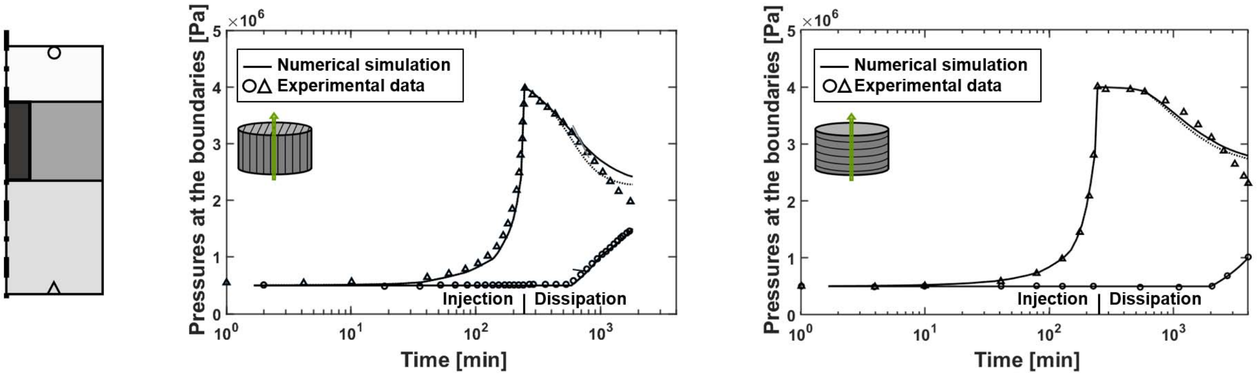

(a) *(b)*

Figure 2.279: Computed versus measured (Gonzalez-Blanco et al., 2016a) injection and recovery pressures for slow injection (a) parallel and (b) normal to bedding.

the air has sufficiently raised in pressure during the air injection phase. Once this pressure threshold has been exceeded, it follows that the fractured zone progressively desaturates, which creates a preferred outlet to allow the air to flow. On the contrary, the matrix of Boom Clay remains in a state close to the full saturation. as evidenced experimentally, the main transport modes that enable gas to enter the sample are therefore the fast-paced initiation of preferential gas-filled pathways through the ZFD on the one hand, and the slow-paced diffusion of dissolved air within the undisturbed clay matrix on the other hand.

Due to the rapid propagation of gas by pathway development, a clear breakthrough event occurs by the end of the injection phase if the sample is oriented parallel to air injection flow, and a couple of minutes later once the air dissipation has already started, if the sample is tested in the other direction. This time delay is directly related to the different fracture behaviours attributed to the bedding and the bridging planes on the basis of the experimental observations as presented in Figure 2.275.

As a result of this gas outflow at the top of the sample, the gas pressure gradually decreases during the dissipation phase. This leads to the progressive closure of the different fractures, as the global effective stress gets back to its initial value, following the hydro-mechanical coupling given in Equations (2.107). In consequence, the diffusion of dissolved gas takes over to transport the air through the sample until the end of the simulation.

The analysis of the gas transport mode involved can be further detailed on the basis of Figure 2.281, which shows the contribution of the diffusive and advective flows in the matrix and in the ZFD for gas injection

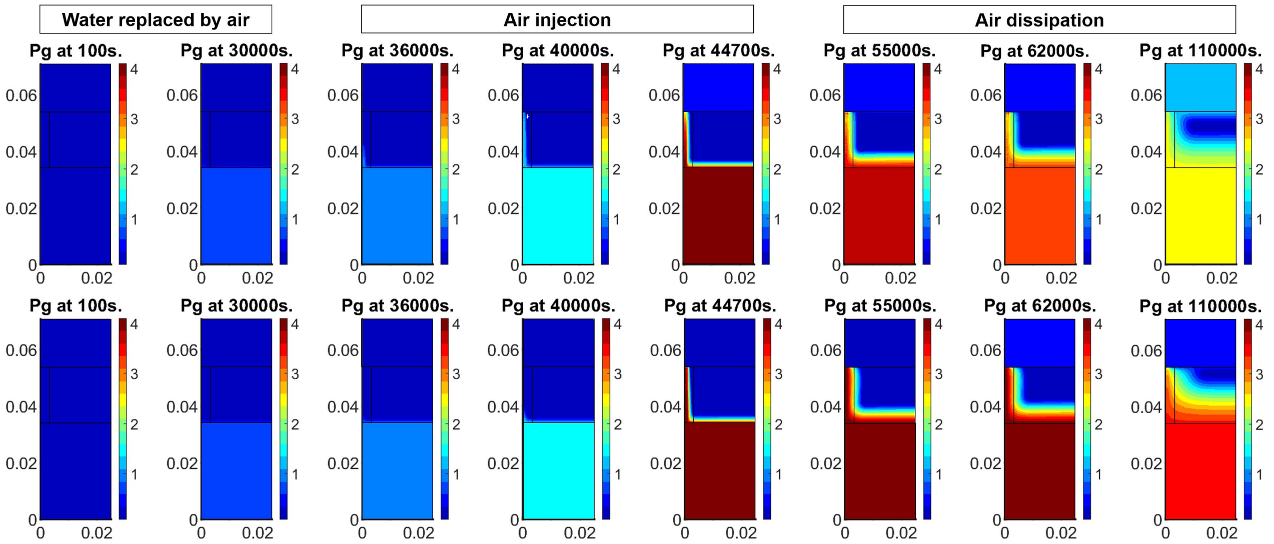

Figure 2.280: Maps of gas pressures throughout the simulation for slow injection parallel (top) and normal (bottom) to the bedding.

parallel (left) and perpendicular (right) to the bedding planes. It appears that the diffusion of dissolved air within the liquid phase prevails in the intact matrix of Boom Clay, even if advective flows progressively develop as the gas front enters the sample. In the ZFD on the contrary, a dominant advective flow is observed and amplifies as the preferential path develops along the height of the sample.

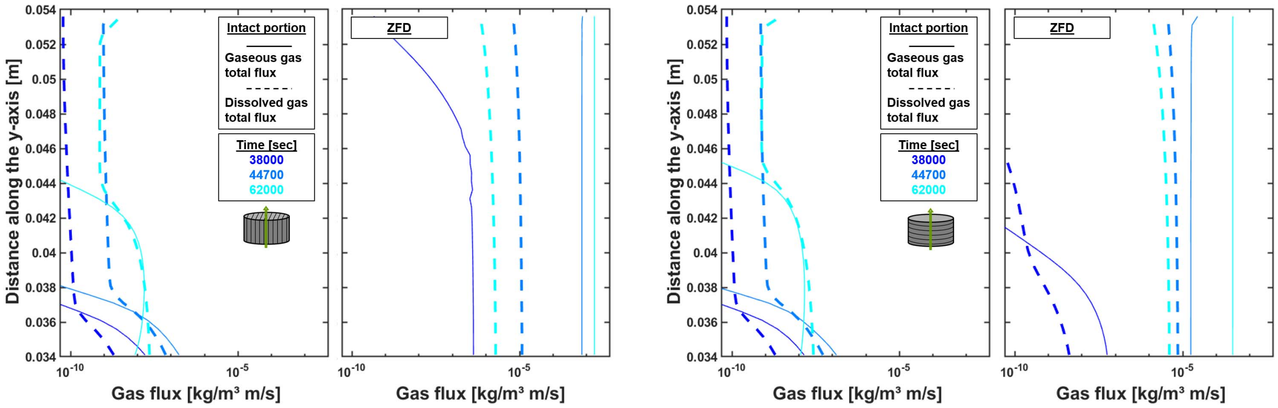

(a) (b)

Figure 2.281: Profiles of the gaseous gas and dissolved gas total fluxes along the sample height in the intact matrix (left) and in the ZFD (right) for slow injection (a) parallel and (b) normal to bedding.

2.11.2.2. Modelling of gas-filled pathways

The HM multiscale model implemented for the analysis of the oedometer tests in the previous section provides a suitable reproduction of the key features of the Boom Clay response under gas pressurisation and migration, including the evolution of the gas pressure fields and the coupling with the material deformation. These encouraging numerical predictions of the main outcomes of the air injection tests attest in some ways of a good implementation of the constituents of the microstructure, *i.e.* the two families of fractures and the bundle of tubes.

And yet, with a straight zone of fracture development representing the easiest path for gas to flow, the heterogeneous aspect of natural materials is avoided in the model. Also, the possibility to extrapolate the phenomena associated with gas-induced damage evolution in clayey materials at a scale closer to the repository size still needs to be demonstrated.

The ensuing objective is therefore twofold:

- Propose a more general configuration for modelling the development of the gas-induced pathways.
- Up-scale the lab-scale to a behaviour closer to the *in situ* scale (about one order of magnitude).

To perform such simulations, the same modelling design and parameters as the ones used for the gas injection tests are adopted, except that the axisymmetric geometry is now converted to plane strain conditions, as shown in Figures 2.282 and 2.284. Orientations of the bedding planes parallel and normal to the gas seepage are both investigated, as illustrated in Figures 2.282b and 2.284b. In addition, a similar three-step procedure is envisaged comprising first the replacement of water by air in the upstream reservoir followed by the injection of air up to an inlet pressure of 4.1 MPa (44700 s) that is kept constant until breakthrough, and completed by a final phase of air dissipation.

More general pathway configuration

The axisymmetric configurations discussed in the previous section can be seen as an oversimplification of the ZFD, which was assumed to be straight and located at the centre of the sample. Nevertheless, the computed responses yielded results that were quite accurate in approximating the experimental behaviour. Therefore, it is not unreasonable to conclude that the ZFD remains continuous over the height of the specimen.

In order to propose a more general configuration for the evolution of the gas-filled pathway, it was decided to introduce some kind of heterogeneity in the numerical model by making some adjustments to the zone of fracture development, while keeping it continuous. For the two orientations of the bedding planes, the idea is to propose a representation of the ZDF closer to the gas flow sequences that have been observed experimentally and conceptualised in Figure 2.282c, according to (Gonzalez-Blanco and Romero, 2022). Therefore, a more tortuous pattern of affected micro-elements is delineated in the central part of the Boom Clay material. This specific ZFD remains continuous at the scale of the sample and includes both damaged bedding planes illustrated by the elements coloured in red, and bridging planes highlighted by the elements coloured in blue, which are more heterogeneously distributed. In the case of flow parallel to the bedding planes (top), a rather simple and direct pathway geometry is assumed, whereas in the other case (bottom) the activation of low-aperture fissures connecting the bedding planes is necessary to allow the gas to jump from one bedding plane to the other, resulting in a more complex pathway geometry.

Figure 2.283 shows the contour plots of gas phase pressure at different characteristic times, for a continuous pattern of damaged elements in the zone of fractures development, considering a sample oriented parallel (top) and perpendicular (bottom) to the gas flow. It is thus possible to examine the influence of the fractures connectivity and the twisted aspect of the ZFD on the gas migration behaviour. As soon as the air rises in pressure, there is a quick and tangible opening of the bedding and bridging planes in the disturbed elements initiating the creation of a clear preferential pathway as main gas transport mechanism. Provided that the air pressure keeps increasing, there is a rapid activation of all disturbed elements by domino effect, leading to the development of a fully air-filled pathway through the whole Boom Clay sample. During this phase, the advection of air via the predefined families of damaged planes governs the gas flow. The propagation rate of the air through the material remains in the same proportions as in the previous reference cases, so that the breakthrough event occurs shortly after the air pressure has reached its maximum of 4.1 MPa, at around 47000 s for injection parallel to the bedding and at 51600 s for injection perpendicular to the bedding. This delay is mainly due to the tortuosity of the implemented pathway pattern. The most winding the geometry, the longer the gas takes to flow through the material. This is well corroborated by experimental observations that gas has to jump from one bedding plane to another via the bridging planes when gas is injected normally to the bedding planes. During the subsequent dissipation phase, the air

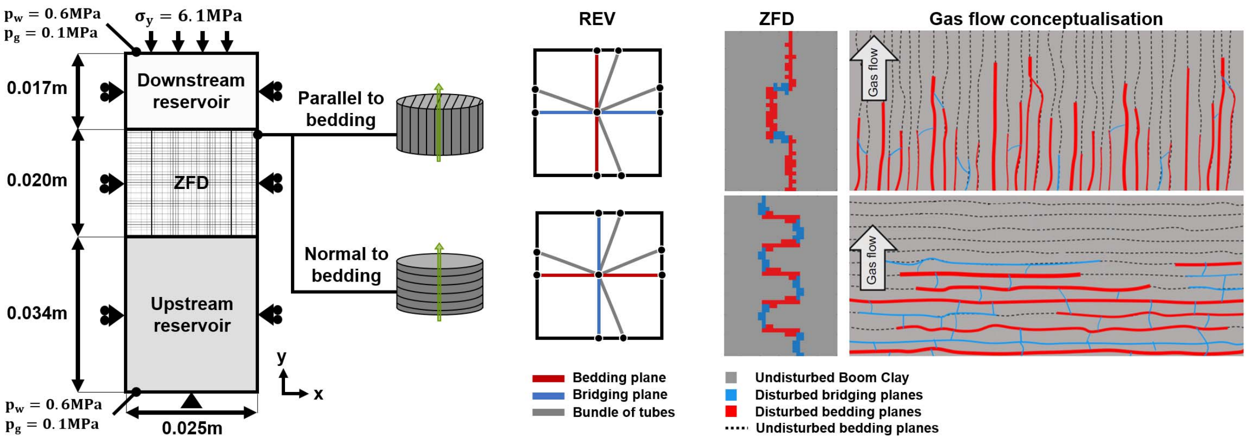

(a) *(b)* *(c)*

Figure 2.282: (a) Geometry and initial boundary conditions, with (b) the REV idealisation for the two orientations of the sample, and (c) the two configurations of the ZFD regarding the schematic representation of expected gas flow, conceptualised by (Gonzalez-Blanco and Romero, 2022).

transport by the mechanism of diffusion takes hold as slow background process throughout the sample, and gradually supplants the prevailing advective flows in the ZFD. Despite this, the preferential direction of air flow towards the downstream reservoir is maintained, which tends to reduce gas pressure in the overall system until the end of the simulation.

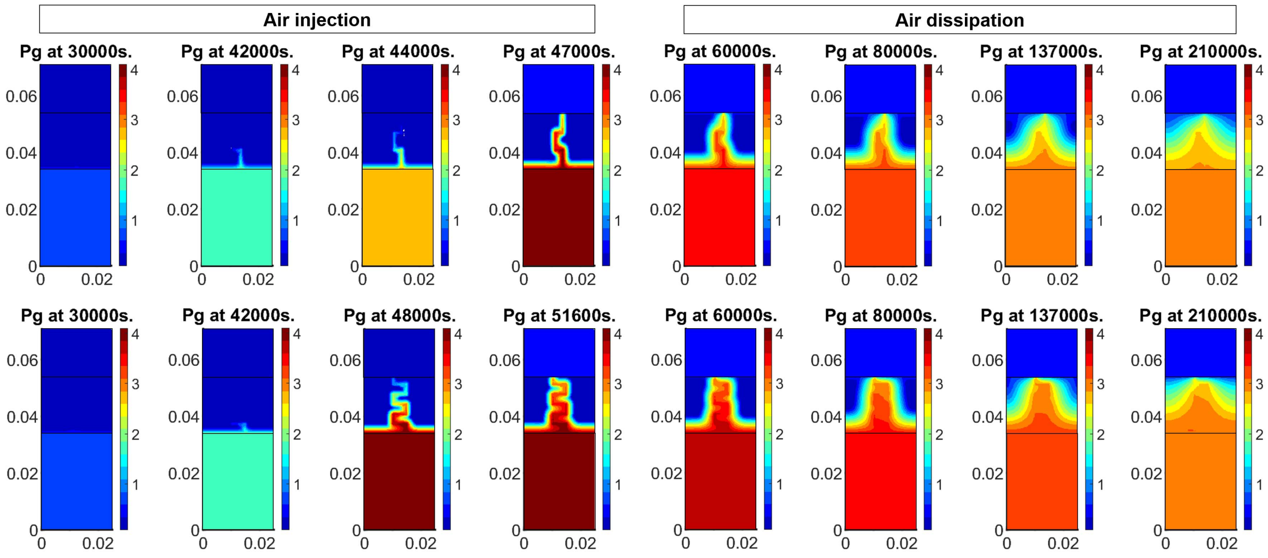

Figure 2.283: Maps of gas pressures throughout the simulation for slow injection (top) parallel and (bottom) perpendicular to the bedding planes.

Up-scaled pathway configuration

Understanding the potential propagation of gas through pathway development on a larger scale is still an open key issue that needs to be addressed to ensure a safe ultimate repository for nuclear waste. However, extrapolating the interpretations of preferential pathway development to the field scale is not an easy task as it is not yet possible to rely on experimental data, as it is the case at the laboratory scale.

While it may seem reasonable to consider a continuous ZFD at the scale of the sample, this hypothesis is more questionable when it comes to zooming out on the problem. For this reason, a four times larger mesh has been implemented for injection parallel to bedding in Figure 2.284a, integrating different ZFDs ranging from continuous patterns to increasingly disconnected and heterogeneous patterns, as shown in Figure 2.284c. These ZFDs remain tortuous regardless of sample orientation and include both damaged bedding planes captured by red elements and bridging planes highlighted by blue elements, while the intact portions of the Boom Clay are represented in grey.

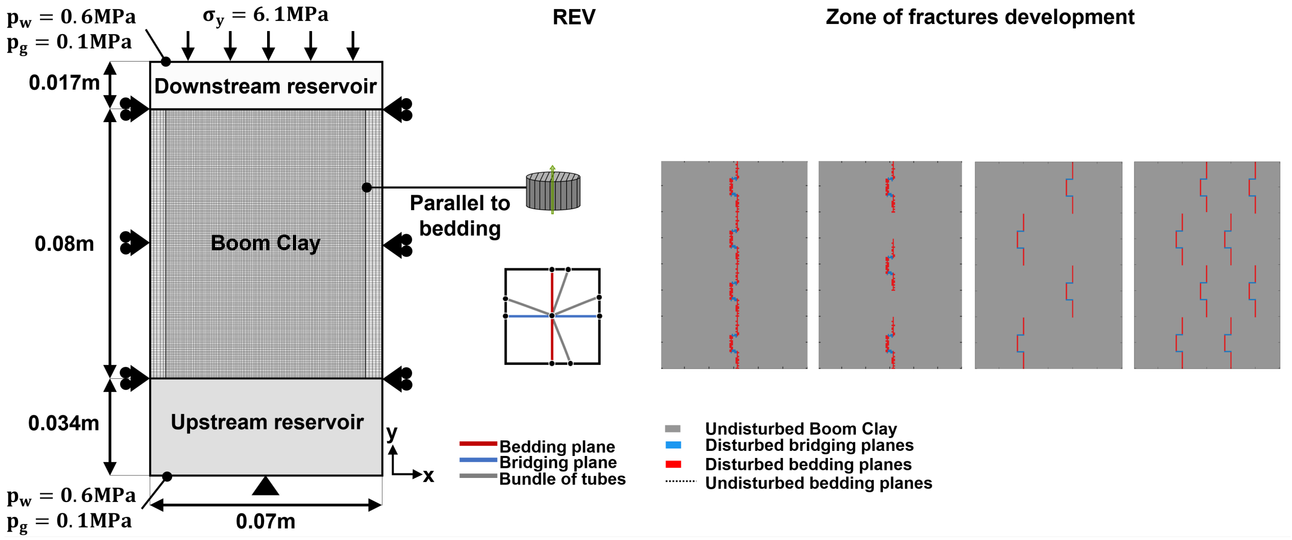

(a) (b) (c)

Figure 2.284: (a) Geometry and initial boundary conditions, with (b) the REV idealisation for the two orientations of the sample, and (c) the two configurations of the ZFD regarding the schematic representation of expected gas flow, conceptualised by [Gonzalez-Blanco and Romero (2022)].

The results for the different configurations of ZFD are proposed in Figure 2.285. It appears from these maps of gas pressure evolution, that the connectivity of the weakest zones of the material is a key driving factor for the gas. As long as the continuity of these zones is ensured as depicted in Figure 2.285 (top row), the propagation of the gas through the material remains very fast by advection of gas through the creation of a preferential pathway, giving rise to a breakthrough after 100.000 s. Nevertheless, while the continuity between the weakest zones of the material could be assumed at the scale of the laboratory, it seems however less probable at the *in situ* or the repository scale given the heterogeneity of the clay rock. As soon as the ZFD is not continuous, one can observe in Figure 2.285 (three bottom rows) that the propagation of gas is significantly slowed down. In this case, the migration of gas is mainly governed by the density of weaker parts in the material. In fact, the gas flows rapidly through the first ZFD by advection but then has to reach the next one to keep propagating very fast, which let the time for gas to slowly diffuse and invade the rest of the material. The mechanism of transfer by pathway development tends to be supplanted by the slow background process of gas diffusion. Therefore, despite some local acceleration of the gas propagation in the heterogeneously distributed ZFD, it appears that the gas tends to migrate through the material in the form of a gaseous front, which is a much slower mode of gas propagation.

2.11.3. Summary

The work presented by the University of Liège with respect to Task 2 is devoted to the numerical analysis of the gas migrations in the mechanically undisturbed parts of the host rock, and its interaction with the material microstructure leading to the emergence of gas-specific pathways. To that end, a multi-scale modelling approach has been adopted to take into account the role played by the rock structure at a micro-level in the initiation and propagation of such a macro-scale gas transport mechanism. Based on experimental data, a suitable REV has been defined to idealise the material microstructure with different families of discontinuities, and an assembly of tubes substituting the flow behaviour of the porous matrix blocks. This complete hydraulic constitutive model is solved at the scale of the microstructural constituents, and it is directly affected by the mechanical effects addressed at the macroscopic scale, which makes the whole model hydro-mechanically coupled in an implicit way. The transition between the two scales is achieved by means of homogenisation and localisation techniques. With these developments, the proposed model configures a robust tool to explore and assess the impact of the weakest zones, whether inherent to the heterogeneous nature of the rock or induced by previously disturbed portions, on the propagation of localised gas flows in clay-rich materials.

After a brief description of the equations of the microscale model implemented in the `LAGAMINE` finite element code, the multi-scale model has been applied to a lab-scale case study, dealing with air injection tests conducted parallel and normal to the bedding orientation in the Boom Clay. A full characterisation of the microstructure components has been performed to reproduce the macro-scale behaviour of this low-permeable host rock. Hydraulically, a model of advection-diffusion of a multiphase flow along the fractures and tubes embedded in the REV is used to simulate the flow response, with specific retention behaviour and relative permeability curves assigned to each micro-element. To stimulate the development of a preferential pathway, the sample is modelled with two zones having different hydraulic properties, namely an intact matrix block and a zone of fractures development characterised by the properties of the fissures experimentally detected after the gas injection. For both orientations of the specimen, the comparison between the experimental results and the model predictions provides encouraging agreement, especially in terms of gas pressure evolution, volume change and outflow volume computation.

The application of the multi-scale HM model has also been extended to a more general and random configuration, which has been up-scaled in order to evaluate the possibility to extrapolate the lab observations of gas-induced damage processes on a larger scale.

2.11.4. Key learning points

2.11.4.1. New knowledge acquired

Developing a multi-scale model offers the possibility of reproducing the mechanisms inherent to gas propagation in a low-permeable sound clay rock, and especially the development of gas-filled pathways, by simply idealising the rock microstructure as an assembly of fractures and tubes. The performed simulations highlight two essential aspects in the development of preferential pathways. One the one hand, the more continuous the connectivity between the disturbed planes, the faster the gas flow through this discrete zone. On the other hand, these links between the planes of weakness need to be repeated regularly to ensure a rapid gas propagation at a larger scale. Otherwise, the fast mechanism of gas transport by advective fluxes through the developed pathways is supplanted by the diffusion of dissolved gas in the liquid phase, which is a slower and less damaging mode of gas transfer.

2.11.4.2. Impact of the acquired knowledge

The performed numerical analysis corroborates the current state of knowledge of gas impact at repository scale.

As long as gas releases from the repository system and the adjacent EDZ remain low, the transport of gas in solution is expected to be the governing mechanism leading to a slow gas penetration in the water-saturated clay barrier, as presented in Figure 2.286a (bottom). The multi-scale model has shown capabilities of reproducing the diffusion mechanism of dissolved gas provided that low pressure build-up is applied, as presented in Figure 2.286a (top).

Once the saturated low-strength clay rock is exposed to pressurised gas, the transport of gas phase is expected to appear once gas pressure has built up sufficiently to get close or exceed the strength of the material. As this pressure threshold is reached, the weakest zones in the rock are step by step activated leading to micro-fracture creation and the coalescence of larger pores concentrating the gas flow in some discrete gas-filled pathways, as shown in Figure 2.286b (bottom). The developed multi-scale model has also shown capabilities of replicating the main markers associated to the development of gas-filled pathways by suitably relying on fracture heterogeneities present within the microstructure of the material, as presented in Figure 2.286b (top). It is worth noted that the partial closure of the preferential paths occurring as soon as gas transport by pathway development is faster than any continued gas generation can also be captured.

Moreover, depending on the connectivity between the heterogeneous zones of the material at a larger scale, the model is also able to reproduce the concentrated and intermittent development of preferential pathways that is supplanted by a dominant background process of diffusion, resulting in the global propagation of a gas front rather than local discrete penetration of gas through the material.

Overall, the conditions for the activation and transition from one gas transport process to another are defectively managed by the model, which is a key requirement for evaluating the influence of each of these gas transfer modes on the global performance of the system.

2.11.4.3. Remaining knowledge gaps

Numerical models play an important role in the assessment of long-term repository safety, as they allow for instance for parameter identification based on experiments, for fundamental process understanding and for prediction of repository evolution in the future. Although the advanced HM models proposed in this work have shown the ability to qualitatively reproduce the experimental response, they however still fail being predictive, as some model parameters are tuned in order to mimic the data, which is another shortcoming to tackle.

Another challenge lies in up-scaling the promising laboratory-scale results to the *in situ*-scale behaviour. Since the mineralogical variability, the microstructural heterogeneity of the clay properties, such as stiffness and strength, and the connectivity of the macro-pores and micro-fractures are all driven factors for gas-specific pathway initiation that cannot be easily anticipated at large scale, further experimental work is still required. In parallel, the computational costs associated to up-scaled meshes and geometries represent another resulting challenge in terms of modelling. Therefore, such a modelling task would be mainly restricted to a process-level investigation.

Since the problems relating to gas migrations in rocks are characterised by a multi-directional propagation, extending the modelling developments to 3D framework is another perspective of the present work.

2.11.4.4. Recommendations for the future

The proposed multi-scale HM model has shown capabilities to reproduce the first mode of gas transport by diffusion of dissolved gas within the liquid phase, and the two primary modes for gas transport as a separate phase, namely two-phase flow, in which gas displaces pore water to flow through the pre-existing porosity, and the propagation of gas-specific pathways, in which the gas production rate is balanced steadily by the newly created pore volume at the pathway tips. However, this model is not able to reproduce the last mode of gas transport by sudden fracture propagation, *i.e.* gas fracturing, which relates to fracture mechanics. While the formation of gas-specific pathways is associated to local damage of the material of a clay barrier, which does not imply the structural failure of the component, gas fracturing is associated to the sudden and energetic relief of accumulated pressure, which could induce cascading effects through the multi-barrier system. Furthermore, the self-sealing capacity of the rock after gas transport is another mechanism that could be integrated into the conceptual model to capture the closure and sealing of the pathways once the gas pressure is released. Implementing these two additional mechanisms in the model is part of the future work that can be performed to improve the model.

It must also be kept in mind that the numerical modelling of physical processes in the earth science field also involves inherent uncertainties, arising from the variable nature of geological properties and the simplification of the conceptual models. Rather than using a strictly deterministic model where the output relies on a single set of parameters values and initial conditions, introducing ranges of values in the form of probability distributions for each parameter of the material and applying a stochastic approach would be appropriate to upgrade the multi-scale model.

To go further and gain a unified and comprehensive vision of gas transport processes in the clay host rock surrounding a storage cell, integrating the multi-scale model developed for gas transport processes in sound host rocks, with another model developed for gas migrations in the EDZ Corman et al. (2022), in one single simulation of gas release from the system would be beneficial. Nonetheless, such a modelling task would be restricted to a process-level investigation in the close vicinity of the storage drift because of the high computational costs of both approaches. Building an efficient and exhaustive model that describe the complex physical processes involved in the gas transport modes at the scale of the repository is indeed still missing at present.

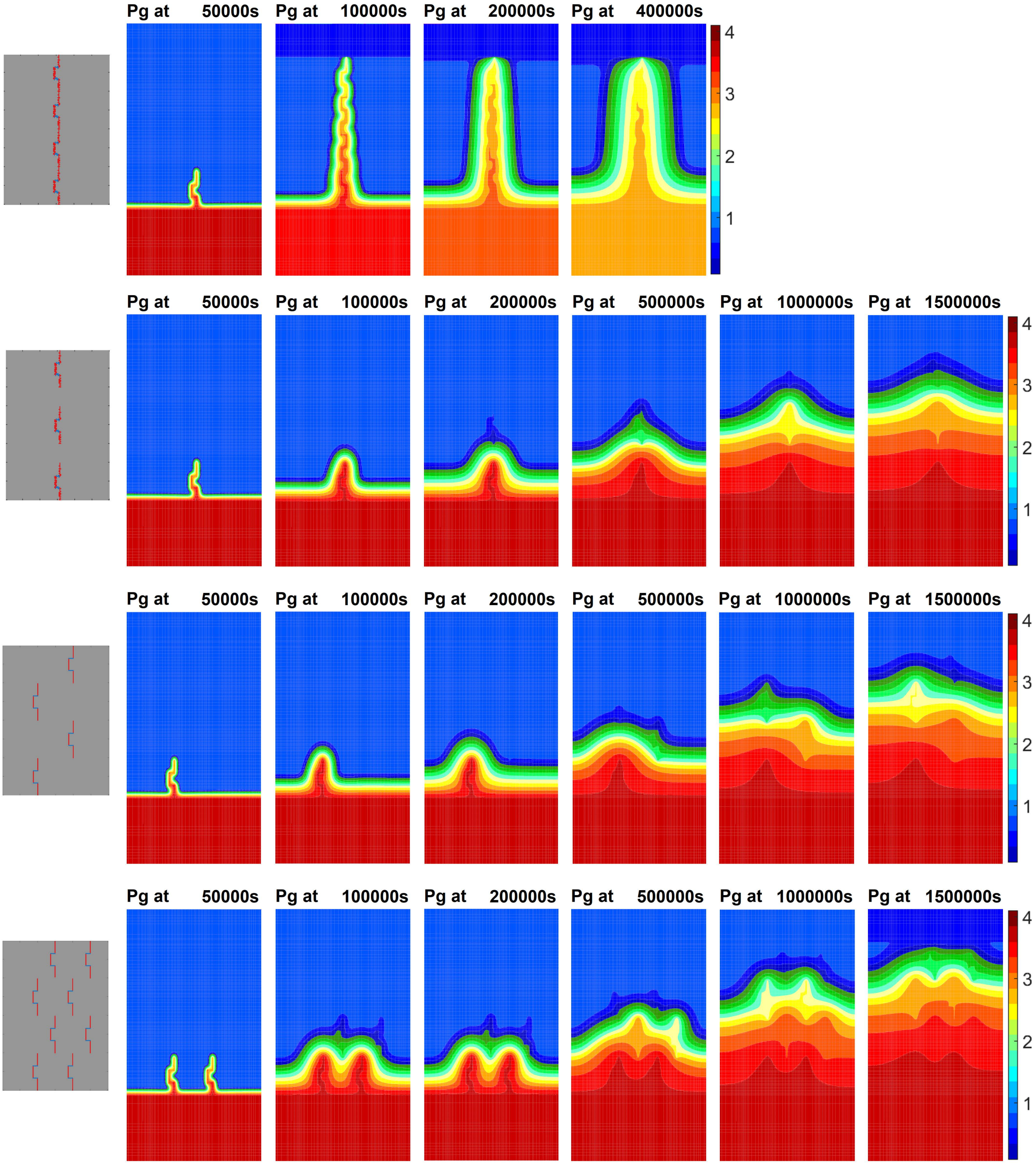

Figure 2.285: Maps of gas pressure showing the evolution of the gas propagation for the different configurations of ZFD displayed on the left.

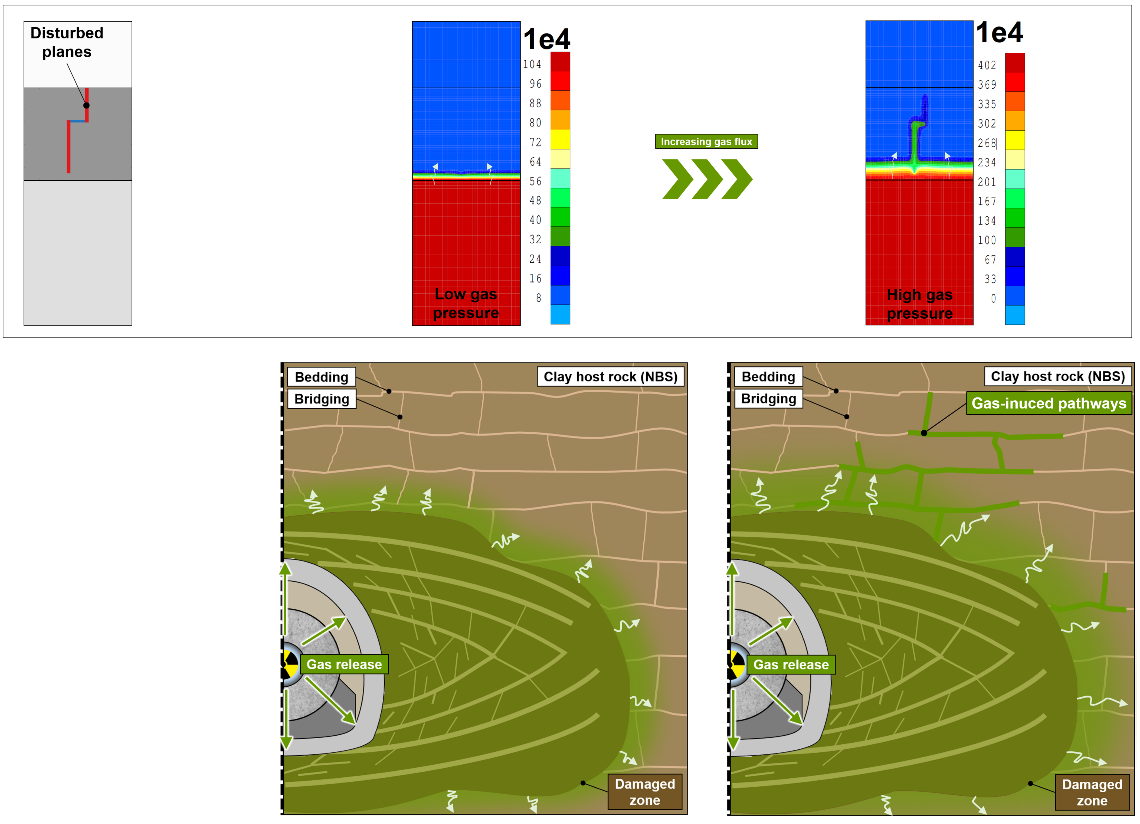

(a) (b)

Figure 2.286: Schematic representation of expected gas flow regimes in an undisturbed clayey host rock (not at scale, at the bottom): (a) diffusion of dissolved gas, (b) creation of gas-specific pathways. Inspired from [Levasseur et al. (2024)]. Corresponding modelling at the scale of the sample (at the top).

.

OpenGeoSys Team
(UFZ, BGE, BGR)

2.12. Process model for TH^{2}M coupling within OpenGeoSys (UFZ, BGE, BGR)

2.12.1. Model introduction

2.12.1.1. Process model development

In the scope of EURAD-GAS, a process model for TH2M coupling process has been further developed and has reached a mature state. The governing equations of this process model have been already presented in the previous progress report and are briefly recalled here.

We provide an overview of the governing equations for OGS-TH^{2}M problems Grunwald et al. (2022). The equation system given below shows an example formulation for non-isothermal two-phase flow in porous media. All of the partial differential equations are developed from basic balance equations of mass, linear momentum and energy. For the hydraulic part, gas pressure p_{GR} and capillary pressure p_{cap} have been chosen to be primary variables. Temperature T and displacement u_S serve as primary variables for the thermodynamic and mechanical parts.

Mass balance governing equations are given by

$$\begin{aligned}&\underbrace{s_G\left(\phi\beta_{p,GR}+\frac{\alpha_B-\phi}{K_{SR}}\right)\frac{d_S p_{GR}}{dt}}_{\text{storage term (gas pressure)}}-\underbrace{s_G\left(\phi\beta_{T,GR}+\left(\alpha_B-\phi\right)\beta_{T,SR}\right)\frac{d_S T}{dt}}_{\text{thermal expansion}}+\underbrace{s_G\alpha_B\operatorname{div}\frac{d_S u_S}{dt}}_{\text{deformation}}\\&-\underbrace{\left(s_G\left(\alpha_B-\phi\right)\beta_{p,SR}\left[s_L+p_{cap}\frac{\partial s_L}{\partial p_{cap}}\right]+\phi\frac{\partial s_L}{\partial p_{cap}}\right)\frac{d_S p_{cap}}{dt}}_{\text{storage term (capillary effects)}}+\underbrace{\operatorname{div}\left(\tilde{w}_{GS}\right)}_{\text{gas flow}}=0\end{aligned}\tag{2.120}$$

for the gas phase and

$$\begin{aligned}&\underbrace{s_L\left(\phi\beta_{p,LR}+\frac{\alpha_B-\phi}{K_{SR}}\right)\frac{d_S p_{GR}}{dt}}_{\text{storage term (gas pressure)}}-\underbrace{s_L\left(\phi\beta_{T,LR}+\left(\alpha_B-\phi\right)\beta_{T,SR}\right)\frac{d_S T}{dt}}_{\text{thermal expansion}}+\underbrace{s_L\alpha_B\operatorname{div}\frac{d_S u_S}{dt}}_{\text{deformation}}\\&-\underbrace{\left(s_L\left(\alpha_B-\phi\right)\beta_{p,SR}\left[s_L+p_{cap}\frac{\partial s_L}{\partial p_{cap}}\right]+\phi\left[s_L\beta_{p,LR}-\frac{\partial s_L}{\partial p_{cap}}\right]\right)\frac{d_S p_{cap}}{dt}}_{\text{storage term (capillary effects)}}+\underbrace{\operatorname{div}\left(\tilde{w}_{LS}\right)}_{\text{liquid flow}}=0\end{aligned}\tag{2.121}$$

for the liquid phase. Phase saturation s_α is the ratio of phase volume fraction ϕ_α (for $\alpha = L, G$) to porosity ϕ, with $s_G = 1 - s_L$ and where s_L is usually a function of capillary pressure. The volume fraction ϕ_α is the ratio of the volume occupied by phase α over the total volume ($d\Omega_\alpha\left(d\Omega^{-1}\right)$). The *Darcy*-velocities $\tilde{w}_{\alpha S}$ given by

$$\phi_\alpha\boldsymbol{w}_{\alpha S}=\tilde{\boldsymbol{w}}_{\alpha S}=-\frac{k_\alpha^{Rel}\boldsymbol{k}_S}{\mu_{\alpha R}}\left(\operatorname{grad}p_{\alpha R}+\rho_{\alpha R}\boldsymbol{a}_\alpha-\rho_{\alpha R}\boldsymbol{b}_\alpha\right)\tag{2.122}$$

are velocities of the fluid phases relative to the deforming solid phase. The remaining symbols are defined in table 2.85. The Energy equation for the overall multiphase aggregate can be written as

$$\begin{aligned}&\underbrace{\left(\rho c_p\right)_{eff}\frac{d_S T}{dt}}_{\text{thermal energy storage}}-\underbrace{\left(\phi_L\beta_{T,LR}+\phi_G\beta_{T,GR}+\phi_S\beta_{T,SR}\right)T\frac{d_S p_{GR}}{dt}}_{\text{pressure work storage (gas phase)}}+\underbrace{\beta_{T,LR}T\tilde{w}_{LS}\cdot\operatorname{grad}p_{cap}}_{\text{advection}}\\&+\underbrace{\left(\phi_L\beta_{T,LR}T+\phi_S\beta_{T,SR}T\left(s_L+p_{cap}\frac{\partial s_L}{\partial p_{cap}}\right)+\phi p_{cap}\frac{\partial s_L}{\partial p_{cap}}\right)\frac{d_S p_{cap}}{dt}}_{\text{pressure work storage (gas and liquid phase)}}+\underbrace{\operatorname{div}q}_{\text{heat conduction}}\\&-\underbrace{\left(\beta_{T,LR}\tilde{w}_{LS}+\beta_{T,GR}\tilde{w}_{GS}\right)T\cdot\operatorname{grad}p_{GR}+\left(\rho_{LR}c_{pL}\tilde{w}_{LS}+\rho_{GR}c_{pG}\tilde{w}_{GS}\right)\cdot\operatorname{grad}T}_{\text{advection}}=0\end{aligned}$$

where the assumption of local thermal equilibrium was made. This assumption follows the idea that heat transfer among the phases occurs very fast such that all phases share the same temperature at a certain point. The effective heat capacity of the overall aggregate $\left(\rho c_{p}\right)_{\text{eff}}$ is defined as $\left(\rho c_{p}\right)_{\text{eff}} = \sum_{\alpha} \phi_{\alpha}\rho_{\alpha R} c_{p,\alpha}$ for $\alpha = G, L, S$ with intrinsic phase mass densities $\rho_{\alpha R}$. Similarly, the combined heat conductive flux $q = q_{GLS}$ is defined as $q = \sum_{\alpha} q_{\alpha}$.

The mechanical part of the equation system is governed by the displacement equation given by

$$0 = \rho \boldsymbol{b} + \operatorname{div}\left(\boldsymbol{\sigma}_{S}^{E} - \alpha_{B} p_{FR} \mathbf{I}\right) \tag{2.123}$$

where ρ is the bulk density of the overall multiphase aggregate defined as $\rho = \sum_{\alpha} \phi_{\alpha}\rho_{\alpha R}$ for $\alpha = G, L, S$ and b are body force accelerations acting equally on all phases. The total stress $\boldsymbol{\sigma}$ is given by the effective stress $\boldsymbol{\sigma}_{S}^{E}$, which is governed by constitutive laws, attenuated by the pore fluid pressure p_{FR}, which is given by $p_{FR} = \sum_{\alpha} s_{\alpha} p_{\alpha R}$. To close the above equation system, constitutive laws or material property relations are required.

Symbol	Description
$\beta_{p,GR}$	gas phase compressibility
$\beta_{p,LR}$	liquid phase compressibility
$\beta_{T,GR}$	gas phase thermal expansivity
$\beta_{T,LR}$	liquid phase thermal expansivity
$\beta_{T,SR}$	solid phase thermal expansivity
K_{SR}	compression modulus of solid phase
$\frac{d_S(\bullet)}{dt}$	material time derivative of • w.r.t. solid phase

Table 2.85: Symbols.

2.12.1.2. Gas permeability models

Numerous laboratory and in-situ studies were conducted in FORGE (Shaw, 2013) on gas transport within clay systems, as cited by researchers such as Birgersson and Karnland (2013) and Zhang et al. (2013). A shared conclusion from these studies is that free gas transport in low-permeable water-saturated or near-saturated porous media happens via the formation of specific gas pathways. This leads to either sample dilatancy or the emergence/reactivation of discontinuities in the tested material. Laboratory experiments, like those of Harrington et al. (2013), have distinctly observed this dilation. Yet, according to Nosek et (2013), no experiment could evidence the two-phase flow transport in FORGE on low-permeability clay media nearing water saturation.

Traditional models based on a continuum two-phase flow approach couldn't accurately mimic these preferential pathways formed during gas transport in clay. To better represent the influence of pathway dilation on gas transport on a relevant scale, FORGE introduced several strategies. Some involve pressure-dependent porosity and permeability to better simulate a swift gas flow increase post a certain injection pressure threshold. Others, like suggestions from Arnedo et al. (2013) and Yamamoto et al. (2013), proposed a more explicit coupling of two-phase flow transport models with poro-mechanics models. This was to more adequately consider the evolving stress field and its potential impact on pathway dilation during gas transport.

In many instances, the FORGE models reasonably mirrored experimental results. Nonetheless, their predictive accuracy remains unconfirmed. Under WP GAS, we revisited and applied some of these models to experiments from EURAD to evaluate their predictive reliability.

In Task 2.2 of WP GAS, BGE in collaboration with UFZ and BGR implemented different gas permeability models aiming at modelling the dilatancy controlled gas flow in clay materials.

Gas pressure dependent permeability model

The first model put forward by Xu et al. (2013b,a) provides a functional relationship between the permeability of the material and the local gas pressure. The model assumes based on in situ observations that permeability changes increase significantly when a specific gas pressure threshold is exceeded. When the critical gas pressure threshold is exceeded, micro-cracks are formed which significantly increase permeability through the development of a percolation network.

$$k(p) = \begin{cases} (1 + \mathrm{a}_1\mathrm{p})\mathrm{k}_0, & \text{if } p < p_{th}. \\ [1 + \mathrm{a}_1\mathrm{p}_{\mathrm{th}} + (\mathrm{p} - \mathrm{p}_{\mathrm{th}})\mathrm{a}_2]\mathrm{k}_0, & \text{otherwise.} \end{cases} \tag{2.124}$$

a_1 and a_2 are empirical parameters.

Strain dependent permeability model

In the second model, the change of permeability is expressed as function of changes in deformation . The deformation considers the volumetric strain ($\varepsilon_{\mathrm{vol}}$) and the equivalent plastic strain (ε_{p}) Xu et al. (2013b,a). It describes an increase of permeability as soon as a plastic failure occurs. It is expressed byions of these three models.

Strain dependent permeability model presents the gas permeability as a function of total volumetric elastic strain ε and an equivalent plastic strain ε^{p} and can be expressed by

$$k(\varepsilon) = \begin{cases} (10^{\mathrm{b}_2\Delta\varepsilon}\mathrm{e}^{\mathrm{b}_1\varepsilon^{\mathrm{p}}}\mathrm{k}_0, & \text{compression.} \\ (10^{\mathrm{b}_3\Delta\varepsilon}\mathrm{e}^{\mathrm{b}_1\varepsilon^{\mathrm{p}}}\mathrm{k}_0, & \text{tension.} \end{cases} \tag{2.125}$$

where b_1, b_2 and b_3 are empirical parameters.

Failure index permeability model

The third model has been developed in the scope of the DECOVALEX project and implemented in OpenGeoSys. It is based on the Mohr-Coulomb Failure Index Wang et al. (2021). The failure index dependent permeability model according to Wang et al. (2020a) is defined as

$$k = k_0 + H(f - 1)\, k_r\, e^{bf}\, I \tag{2.126}$$

where k_0 is the intrinsic permeability of the undamaged material, H is the Heaviside step function, f is the failure index, k_r is a reference permeability, b is a fitting parameter. k_r and b can be calibrated by experimental data.

The failure index f is calculated from the Mohr-Coulomb failure criterion comparing an acting shear stress. With the conventional mechanics notations, which mean that tensile stress is positive, the Mohr-Coulomb failure criterion Labuz and Zang (2012) takes the form

$$\tau_{\mathrm{f}}(\sigma) = c - \sigma \tan\phi \tag{2.127}$$

with τ the shear strength, c the cohesion, σ the normal stress, and ϕ the internal friction angle. We further introduce the maximum shear stress $\tau_{\mathrm{m}} = (\sigma_3 - \sigma_1)/2$ and the mean stress $\sigma_{\mathrm{m}} = (\sigma_1 + \sigma_3)/2$, where σ_1 and σ_3 are the minimum and maximum principal stress, respectively. The criterion varies depending on whether it is below or above a specific threshold value, denoted as $\sigma_{\mathrm{m}}^{\mathrm{max}} \in (0, \mathrm{c}/\tan\phi)$, which falls within the range $(0, \mathrm{c}/\tan\phi)$. This threshold is related to, but not equivalent to, the material's tensile strength.

Then, the failure index is determined by

$$f = \begin{cases} \dfrac{|\tau_\mathrm{m}|}{\cos(\phi)\tau_\mathrm{f}(\sigma_\mathrm{m})} & \text{if } \sigma_\mathrm{m} \leq \sigma_\mathrm{m}^\mathrm{max} \\ \max\left\{\dfrac{|\tau_\mathrm{m}|}{\cos(\phi)\tau_\mathrm{f}(\sigma_\mathrm{m})}, \dfrac{\sigma_\mathrm{m}}{\sigma_\mathrm{m}^\mathrm{max}}\right\} & \text{if } \sigma_\mathrm{m} > \sigma_\mathrm{m}^\mathrm{max} \end{cases} \tag{2.128}$$

The computed permeability components are restricted with an upper bound, i.e. $\mathrm{k} := \mathrm{k}_\mathrm{ij} < \mathrm{k}_\mathrm{max}$.

Embedded fracture permeability model

A fourth model originally put forward by (Alonso et al., 2006) and applied to model gas transport in clay barriers by (Olivella and Alonso, 2008c) has been recently further developed and introduced in OpenGeoSys by (Zill et al., 2021). The proposed approach is based on a homogenizing sets of parallel fractures on the micro-scale, as illustrated in Figure 2.287. The geometry of these fractures can be characterized by several parameters. The mean fracture distance a represents the average distance between adjacent fractures, while the fracture aperture b represents the opening of each fracture. The fracture normal vector n describes the orientation of the fractures. Additionally, the height of the volume element in the fracture normal direction s is required for the derivation of the permeability equation. These parameters are crucial in determining the flow behavior of fluids through fractured porous media, making them essential for developing accurate models and predictions Zill et al. (2021). Assuming the tensor notation $\mathrm{M} = \mathrm{n} \cdot \mathrm{n}$ the equation for the permeability tensor can be written as

$$k = k_\perp M + k_{||}\,(I - M) \tag{2.129}$$

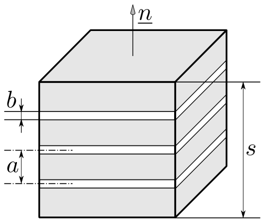

Figure 2.287: Volume element with embedded fractures.

Here, we have the permeability perpendicular to the fracture plane denoted by $\mathrm{k}_\perp$, which is typically assumed to be equal to the matrix permeability k_m. On the other hand, the permeability parallel to the fracture plane $\mathrm{k}_{||}$ is a combination of k_m and the fracture permeability k_f. The contribution of k_m and k_f to $\mathrm{k}_{||}$ is weighted based on the combined height of the fractures in the volume element. This height is determined by the product of the number of fractures per element n and the mean fracture aperture b Zill et al. (2021).

$$\mathrm{k} = \mathrm{k}_\mathrm{m}\mathrm{M} + \left(\frac{\mathrm{s}-\mathrm{nb}}{\mathrm{s}}\mathrm{k}_\mathrm{m} + \frac{\mathrm{nb}}{\mathrm{s}}\mathrm{k}_\mathrm{f}\right)(\mathbf{I} - \mathrm{M}) \tag{2.130}$$

$$\mathrm{k} = \mathrm{k}_\mathrm{m}\mathbf{I} + \frac{\mathrm{nb}}{\mathrm{s}}\,(\mathrm{k}_\mathrm{f} - \mathrm{k}_\mathrm{m})\,(\mathbf{I} - \mathrm{M}) \tag{2.131}$$

By using the parallel plate approximation (Witherspoon et al., 1980), the fracture permeability can be derived as $\mathrm{k}_\mathrm{f} = \frac{\mathrm{b}^2}{12}$. By also considering the geometry of the fracture network, we can express the number of fractures per volume element as $\mathrm{n} = \frac{\mathrm{s}}{\mathrm{a}}$. Substituting these expressions into the equation allows us to eliminate the dependence on n and s, resulting in a simplified equation Zill et al. (2021).

$$\mathrm{k} = \mathrm{k}_\mathrm{m}\mathbf{I} + \frac{\mathrm{b}}{\mathrm{a}}\left(\frac{\mathrm{b}^2}{12} - \mathrm{k}_\mathrm{m}\right)(\mathbf{I} - \mathrm{M}) \tag{2.132}$$

The models outlined above have been employed to simulate laboratory experiments in WP GAS Task 3. These experiments aimed to explore and enhance the impact of gas on the integrity of clay barriers. For a detailed analysis, please refer to the MS29+230 report.

2.12.2. Model verification

OGS is participating in several benchmarking initiatives. BenVaSim (section 2.12.2.2) is dedicated to verify TH2M models. DECOVALEX is a long-term international benchmarking initiative for validation of THMC models against experiments (section 2.12.2.3).

2.12.2.1. TH^{2}M benchmark gallery

An extensive suite of test examples was created for the development of the OGS-TH2M model Grunwald et al. (2022). A hierarchical concept was developed and implemented that systematically checks all (reasonable) process couplings based on the individual processes (Figure 2.288). The extensive collection of benchmarks (>100 tested test examples) from OGS is directly available via the portal and offers users an ideal introduction to THM/CB modelling. Some of the OGS benchmarks are already available as Jupyter notebooks (see section 2.12.2.4) and can thus be integrated into other Python applications with the corresponding advantages of user-specific data analysis.

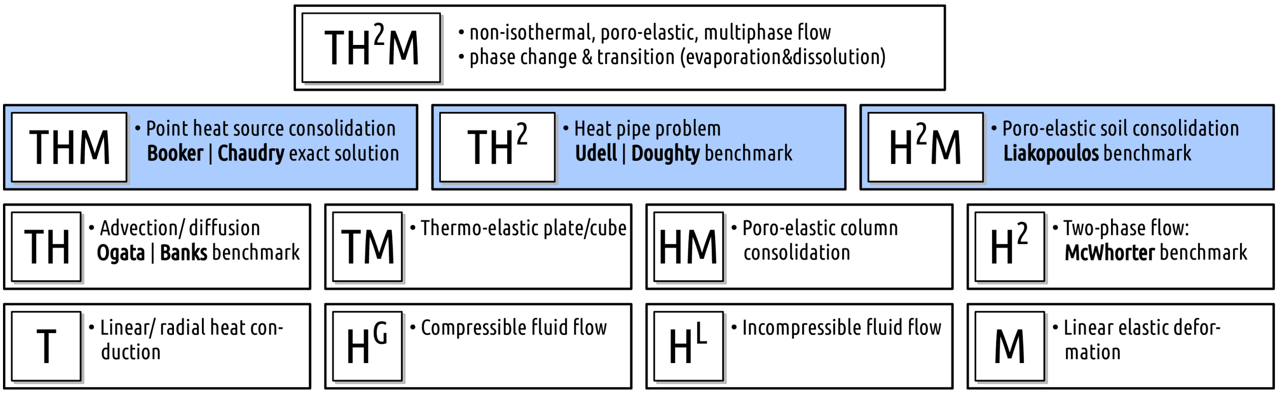

Figure 2.288: Benchmarking hierarchy for TH2M processes Grunwald et al. (2022).

2.12.2.2. TH^{2}M Model Verification

Before the application of the non-isothermal two-phase flow implementation in deformable porous media (TH^{2}M model), an extensive verification of the implementation was conducted. While the TH^{2}M reference paper Grunwald et al. (2022) features a set of benchmarks already, some further testing and documenting took place in the scope of the EURAD WP GAS modelling activities. The suite of benchmarks used for this purpose originates from the international BenVaSim benchmarking initiative Lux and Rutenberg (2018); Lux et al. (2021). The focus of these benchmarks are two-phase flow phenomena coupled to mechanical medium deformation as well as temperature-driven processes as introduced in section 2.12.1.1. The layout of each modelling test is motivated with TH^{2}M processes in deep geological nuclear waste repositories in mind Pitz et al. (2023a). A variety of well established codes and teams from international institutions participated in the BenVaSim project Lux et al. (2021), modelling and comparing in detail the results for different benchmark cases. The verification of the numerical implementation and results is achieved via the comparison with analytical results and –where analytical results are not available due to the high complexity of a benchmark – the systematic comparison of results obtained by the different codes. In Pitz et al. (2023a), all test cases were revisited using the new TH^{2}M implementation in OGS-6, and a comparison of the newly obtained results with other codes (like COMSOL, CodeBright, ToughFlac) and/or analytical solutions is conducted and documented. Thus, the verification/validation basis for the application of OGS-6 for the experimental modelling of the EURAD WP Gas experiment is provided.

2.12.2.3. DECOVALEX benchmarking project

The DECOVALEX project is an international research and model comparison collaboration, initiated in 1992, for advancing the understanding and modeling of coupled thermo-hydro-mechanical-chemical (THMC) processes in geological systems [3]. Regarding the model validation process, the DECOVALEX project plays an extraordinary role since three decades. In the current phase D2023, Tasks A, B and G are also related to fluid transport and barrier integrity aspects due to gas migration processes in clay rocks. Another focus in D2023 are thermally induced THM processes (Tasks C, D, E) which are not in the focus of this report. In Task A gas migration processes due to container corrosion, microbial degradation and radiolysis of water are in the focus of model analyses based on experimental data from the Meuse/Haute-Marne Underground Research Laboratory (MHM URL) located in Callovo-Oxfordian claystone (COx), e.g. gas injection tests with low and high rates in the PGZ experiment. Task B, based on the Lasgit experiment in Äspö HRL, is investigating possible development of dilatant pathways, permeability changes associated to this pathway development, and the coupling between permeability and stress in bentonite buffer systems. Task G is a more fundamental exercise on fracture evolution resulting from pressure and thermally induced effects and comparing various conceptual and numerical approaches of fracture mechanics for HM and TM coupled processes. The experimental basis stems from laboratory experiments. EURAD GAS also benefits from DECOVALEX progress in model verification and in turn already provides ideas for the next DECOVALEX phase D2027.

---

[3] https://decovalex.org/

2.12.2.4. Benchmarking workflows

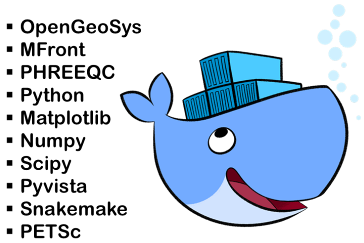

Figure 2.289: Illustration of the OGS-Container concept (Docker) for Jupyter applications (figures source: Docker).

Benchmarks and Jupyter notebooks A new technical development in OGS is the provision of container applications for Jupyter Notebooks Kolditz et al. (2023)[4]. In addition to the OGS core and external modules / libraries (e.g. MFront, PHREEQC, PETSc), these containers also contain the Jupyter Notebook server application and a number of Python packages which can be added as needed (Figure 2.289). After starting the container, the Jupyter Notebook can be accessed as a browser application as usual and OGS can be executed using notebooks. Jupyter Notebooks also forming a new basis for OGS benchmark presentation and integration. New test cases are formulated and explained in Python-based Jupyter notebooks which can intermix script logic with explanatory text and images. Moreover, the large variety of existing Python tools can be used for pre- and postprocessing of OGS simulation results. Figure 2.291 shows the OGS benchmark gallery page[5] which is organized the according to the THMC process coupling hierarchy (Figure 2.290).

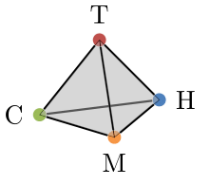

Figure 2.290: THMC processes.

Benchmark gallery The OpenGeoSys benchmark gallery (Fig. 2.291) is organized according to the THM/RTP process hierarchy, thermo-hydro-mechanical and reactive transport processes. A specific process class is represented by a tile showing a simulation result of the related process class. After clicking a tile, the available benchmarks of a process class become visible and can be further selected. Typically, an OGS benchmark starts with a short description of the problem description and showing most important results for the benchmark test. All benchmarks are linked with the OGS project file (prj-file), therefore, the benchmark settings are directly available through the gallery. All benchmarks are part of the OGS quality assurance workflow which is continuously running all tests (benchmarks and so-called unit-tests for basic functionalities) after any code changes, automatically. For new benchmarks Jupyter notebooks are available for user convenience and user-specific pre- and postprocessing operations. New process classes and/or those with new benchmarks are highlighted as featured processes on top of the benchmark gallery.

---

[4] https://www.opengeosys.org/docs/userguide/basics/jupyter-notebooks/

[5] https://www.opengeosys.org/docs/benchmarks/

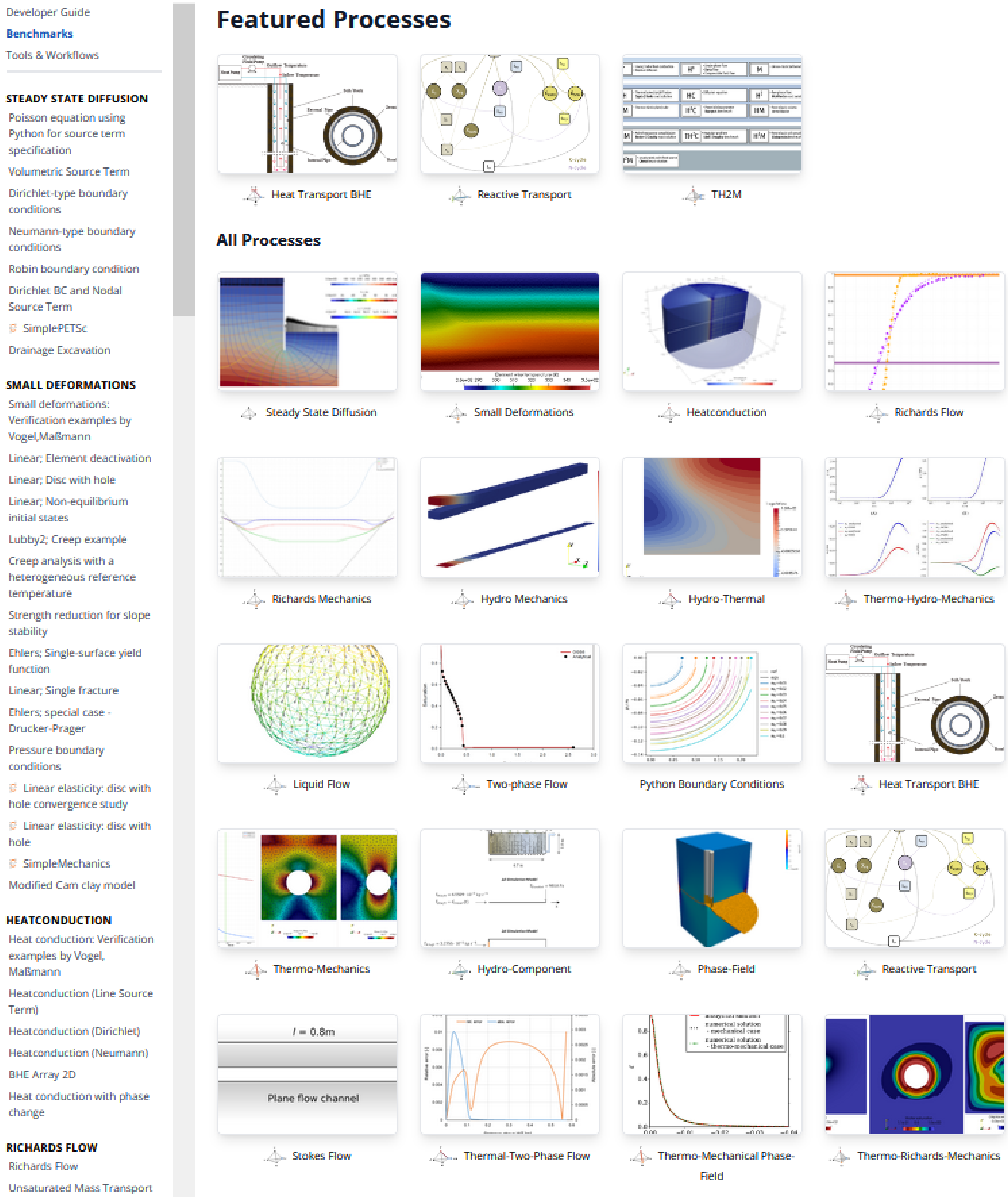

Developer Guide
Benchmarks
Tools & Workflows

STEADY STATE DIFFUSION
Poisson equation using Python for source term specification
Volumetric Source Term
Dirichlet-type boundary conditions
Neumann-type boundary conditions
Robin boundary condition
Dirichlet BC and Nodal Source Term
SimplePETSc
Drainage Excavation

SMALL DEFORMATIONS
Small deformations: Verification examples by Vogel,Maßmann
Linear; Element deactivation
Linear; Disc with hole
Linear; Non-equilibrium initial states
Lubby2; Creep example
Creep analysis with a heterogeneous reference temperature
Strength reduction for slope stability
Ehlers; Single-surface yield function
Linear; Single fracture
Ehlers; special case - Drucker-Prager
Pressure boundary conditions
Linear elasticity: disc with hole convergence study
Linear elasticity: disc with hole
SimpleMechanics
Modified Cam clay model

HEATCONDUCTION
Heat conduction: Verification examples by Vogel, Maßmann
Heatconduction (Line Source Term)
Heatconduction (Dirichlet)
Heatconduction (Neumann)
BHE Array 2D
Heat conduction with phase change

RICHARDS FLOW
Richards Flow
Unsaturated Mass Transport

Featured Processes

Heat Transport BHE
Reactive Transport
TH2M

All Processes

Steady State Diffusion
Small Deformations
Heatconduction
Richards Flow
Richards Mechanics
Hydro Mechanics
Hydro-Thermal
Thermo-Hydro-Mechanics
Liquid Flow
Two-phase Flow
Python Boundary Conditions
Heat Transport BHE
Thermo-Mechanics
Hydro-Component
Phase-Field
Reactive Transport
Stokes Flow
Thermal-Two-Phase Flow
Thermo-Mechanical Phase-Field
Thermo-Richards-Mechanics

Figure 2.291: OGS Benchmark Gallery organized by process classes. Benchmarks of a specific process class are behind the tiles.

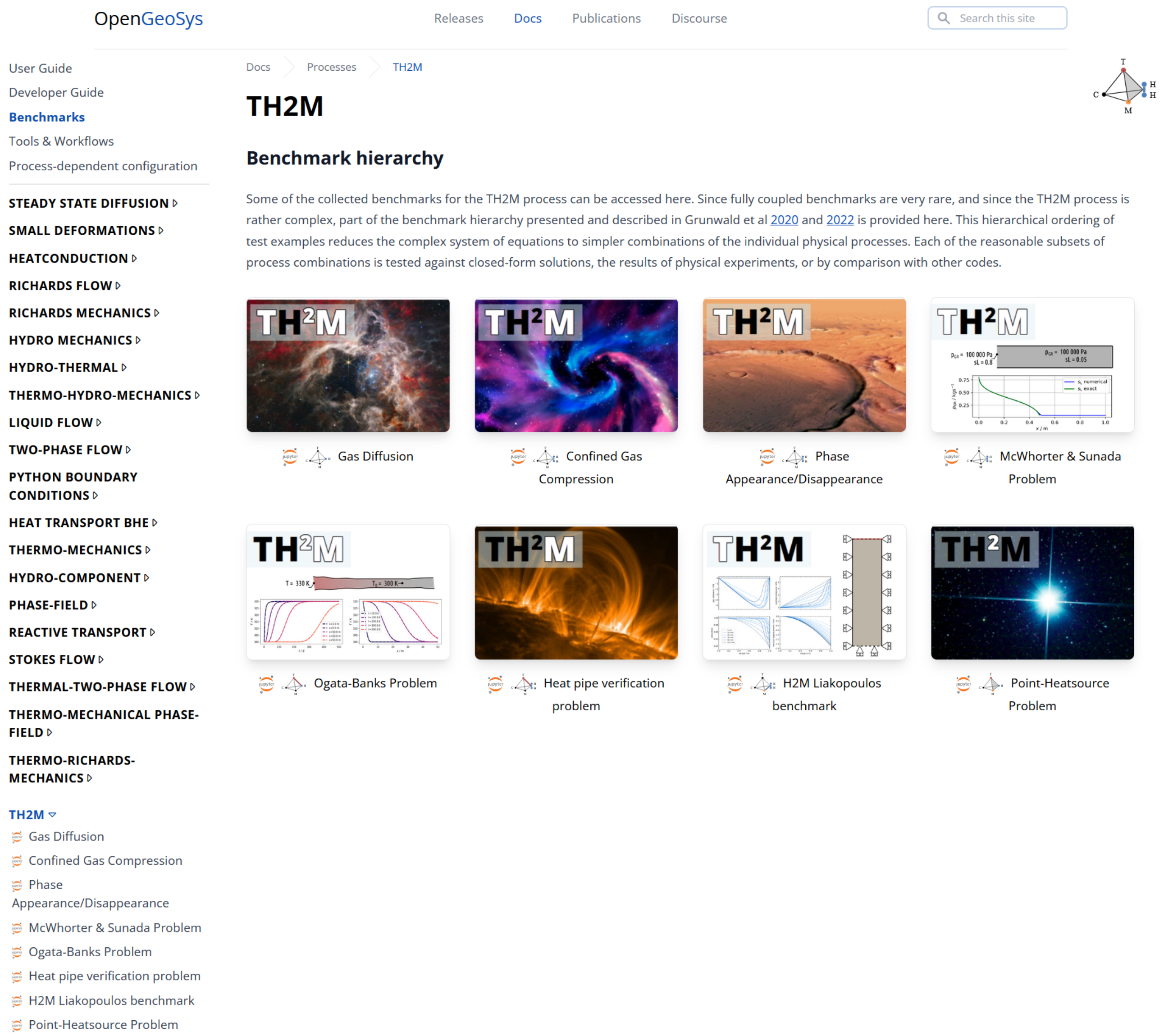

OpenGeoSys

Releases Docs Publications Discourse

Search this site

User Guide
Developer Guide
Benchmarks
Tools & Workflows
Process-dependent configuration

STEADY STATE DIFFUSION
SMALL DEFORMATIONS
HEATCONDUCTION
RICHARDS FLOW
RICHARDS MECHANICS
HYDRO MECHANICS
HYDRO-THERMAL
THERMO-HYDRO-MECHANICS
LIQUID FLOW
TWO-PHASE FLOW
PYTHON BOUNDARY CONDITIONS
HEAT TRANSPORT BHE
THERMO-MECHANICS
HYDRO-COMPONENT
PHASE-FIELD
REACTIVE TRANSPORT
STOKES FLOW
THERMAL-TWO-PHASE FLOW
THERMO-MECHANICAL PHASE-FIELD
THERMO-RICHARDS-MECHANICS

TH2M
- Gas Diffusion
- Confined Gas Compression
- Phase Appearance/Disappearance
- McWhorter & Sunada Problem
- Ogata-Banks Problem
- Heat pipe verification problem
- H2M Liakopoulos benchmark
- Point-Heatsource Problem

Docs > Processes > TH2M

TH2M

Benchmark hierarchy

Some of the collected benchmarks for the TH2M process can be accessed here. Since fully coupled benchmarks are very rare, and since the TH2M process is rather complex, part of the benchmark hierarchy presented and described in Grunwald et al 2020 and 2022 is provided here. This hierarchical ordering of test examples reduces the complex system of equations to simpler combinations of the individual physical processes. Each of the reasonable subsets of process combinations is tested against closed-form solutions, the results of physical experiments, or by comparison with other codes.

Gas Diffusion | Confined Gas Compression | Phase Appearance/Disappearance | McWhorter & Sunada Problem

Ogata-Banks Problem | Heat pipe verification problem | H2M Liakopoulos benchmark | Point-Heatsource Problem

Figure 2.292: Benchmark collection of the OGS-TH2M model class with increasing complexity.

2.12.3. Numerical simulations uncover phase transitions in gas transport in clay rock

A comprehensive, numerical study has been conducted to explore the behaviour of gas flows in clay rock, specifically targeting the transition from single-phase to two-phase flow conditions (Grunwald et al. (2023)). These two conditions are among the most common gas transport regimes in low-permeability porous media, cf. Figure 2.293.

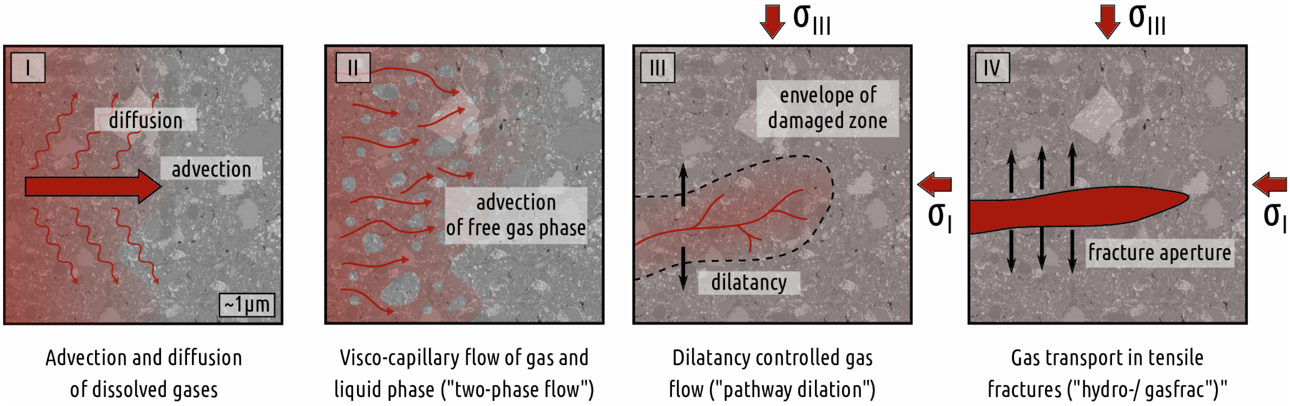

Advection and diffusion of dissolved gases

Visco-capillary flow of gas and liquid phase ("two-phase flow")

Dilatancy controlled gas flow ("pathway dilation")

Gas transport in tensile fractures ("hydro-/ gasfrac")"

Figure 2.293: Modified version of an overview of gas transport regimes in low-permeable clay rock after Marschall et al. (2005a), Figure 2. and Cuss et al. (2014c), Figure 1.

In fully saturated clay materials, dissolved gases migrate through the matrix via diffusion driven by concentration gradients and transport of dissolved gases within an advective fluid phase. A transition from a single phase regime to a multiphase system occurs when gas pressures increase or gas production rates rise, leading to the emergence of a separate gas phase.

Our study is based on a well-known scenario in radioactive waste disposal, originally proposed by the *French National Radioactive Waste Management Agency* (ANDRA) as part of the MoMaS project. This test involves injecting hydrogen gas into a fully saturated, two-dimensional representation of a claystone host rock, with dimensions H = 20 m in height and L = 200 m in length. The model, with impermeable upper and lower boundaries, effectively renders the test into a one-dimensional problem, as illustrated in Figure 2.294.

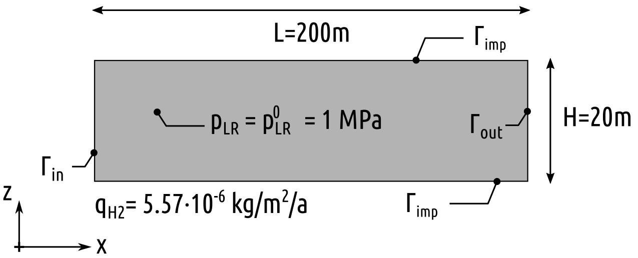

Figure 2.294: Domain and model concept of the 1d test.

The injection rate, maintained constant over a 500,000-year period, is calibrated such that the gas initially dissolves entirely in the water phase. At the right model boundary Γ_{out}, both water and gas pressures are held constant, facilitating the exit of water and hydrogen from the domain. This test has been extensively explored in prior studies (see Bourgeat et al. (2010, 2013); Amaziane et al. (2014); Gharbia and Jaffré (2014); Marchand and Knabner (2014); Huang et al. (2015b)) for tool validation and result verification. Our results were benchmarked against these studies to validate our model (OGS6, TH2M process) and to deepen our understanding of the phase transition phenomena. Bourgeat et al. (2013) provided valuable insights by comparing six different modeling approaches. Our OGS model results, particularly the phase pressures and gas saturation, aligned well with most findings presented in Bourgeat et al. (2013), as depicted in Figure 2.295.

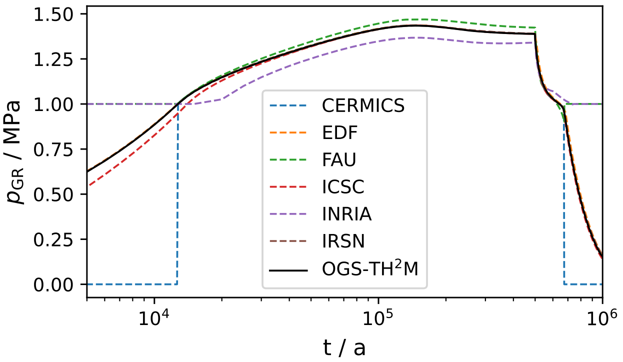

(a) Gas phase pressure

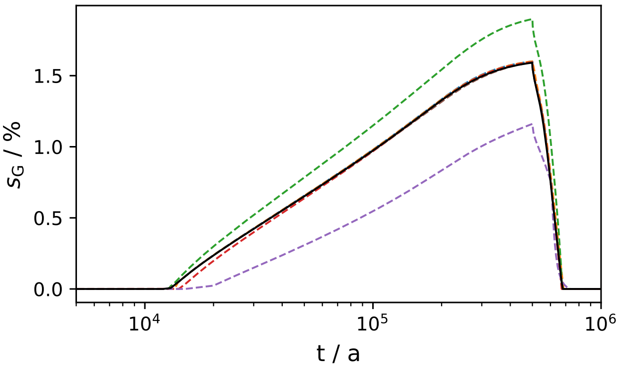

(b) Gas saturation

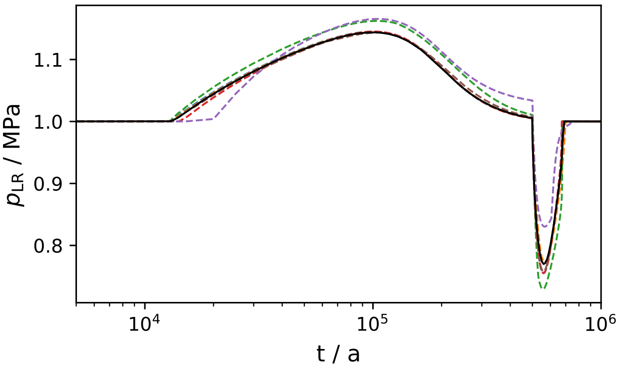

(c) Liquid phase pressure

Figure 2.295: Comparative plot of different codes' results (Bourgeat et al., 2013) of gas pressure (a), liquid phase pressure (b), and gas saturation (c) at the injection point Γ_{in} : x = 0 m.

Initially, for about t = 12,700 years, only the gas pressure increased slowly while the liquid phase pressure and gas saturation remained stable. With no gas phase present, the gas pressure is merely a virtual measure, indicative of the concentration of dissolved hydrogen as per Henry's law.

Subsequently, the gas pressure surpassed the liquid pressure, resulting in the formation of a separate gas phase, and an increase in both gas saturation and liquid phase pressure. The pressures of the gas and liquid phases reached their peaks around t = 150,000 yr and t = 100,000 yr, respectively. After this, the gas pressure slightly declined until the end of the injection period, while the liquid pressure returned almost to its initial level. The maximum gas saturation value of $s_G = 0.0162$ was reached at t = 500,000 yr, coinciding with the abrupt cessation of hydrogen injection.

Post-injection, a decline in both pressures and gas saturation was observed. The liquid pressure initially fell below its original level, then gradually recovered, whereas the gas pressure steadily decreased, eventually leading to full liquid saturation at approximately t = 680,000 years. During the initial period up to $t \leq$ 12,700 yr, the system maintained single-phase conditions with negative capillary pressure, precluding the presence of a gas phase.

With no physical gas pressure in the initial stage and hydrogen only in a dissolved state, the water phase pressure showed a negligible increase, as illustrated in Figure 2.295c. Hydrogen transport was primarily through diffusion J_L^H and, to a much lesser extent, advection A_L^H. At t = 12,700 yr, with the onset of positive capillary pressure, a gas phase formed. This led to a substantial decrease in the diffusive hydrogen mass flux in the liquid phase, as the hydrogen transport increasingly shifted to advective transport in the gas phase A_G^H, as shown in Figure 2.296.

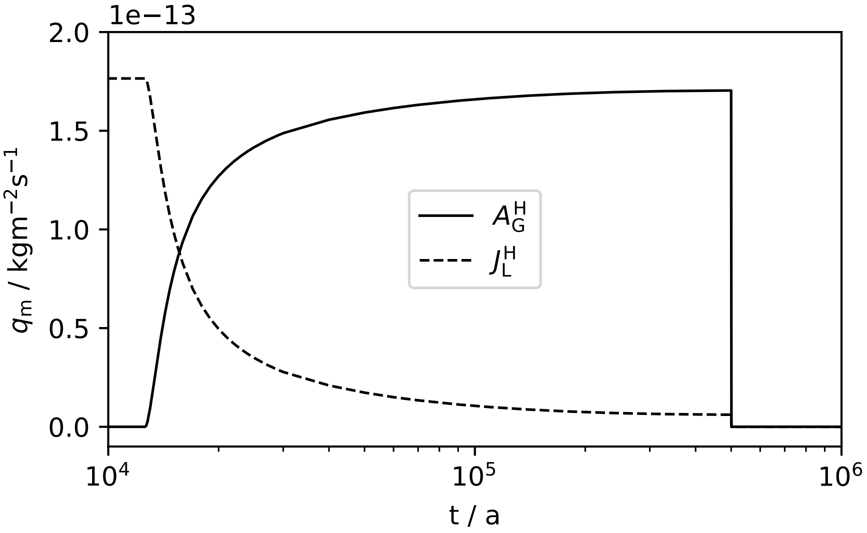

Figure 2.296: Hydrogen mass fluxes A_G^H *(solid) and* J_L^H *(dashed) at the injection point in the period between* t = 10,000 *years and* t = 1,000,000 *years. With the appearance of the gas phase at* t_1 = 12,700 years*, the hydrogen is transported advectively in the gas phase to an increasing extent.*

During the subsequent phase up to the end of the injection period at t = 500,000 yr, gas phase saturation steadily increased. Figure 2.297 illustrates the expansion of the gas phase across the domain over time. The diagram highlights the absence of a gas phase at the simulation's start, its rapid spread following emergence, and its eventual disappearance post-injection at t = 680,000 yr.

The primary objective of this research is to improve the understanding and confidence in models used for large-scale repository simulations. The study successfully captures the transition from single-phase to two-phase gas transport, providing valuable insights into the behavior of gas in clay rock.

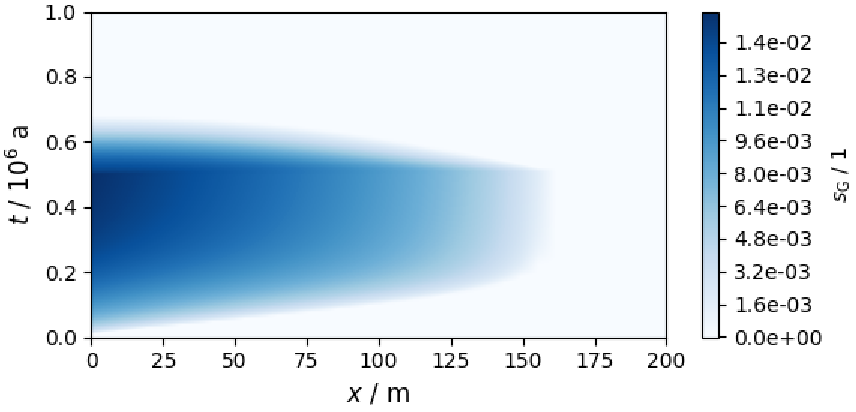

Figure 2.297: Temporal evolution of gas saturation (SG) in a 1D domain. The x-axis denotes domain length (in meters) and the y-axis represents time scaled by 1 million years. Darker shades signify higher gas saturation, while white indicates the absence of a gas phase.

.

IRSN and CNRS-GeoRessources

2.13. Direct Numerical Simulation (DNS): pore-scale models (IRSN and CNRS-GeoRessources)

2.13.1. Introduction

2.13.1.1. Conceptual model

IRSN and CNRS-Georessources conduct numerical simulations of multiphase fluid transport through deformable nanoporous geomaterials using Direct Numerical Simulation (DNS) modeling approaches. A focus was put on the inclusion of processes specific to the nanoporous nature of the host clayrocks in regard to the advective transport of gas. The studied processes include the hydromechanical coupling for dilatant flow, Kelvin effect and electrokinetic coupling. A DNS approach implies description of the physical phenomena at the pore scale as well as explicit description of the pore space (for instance based of model geometries such channels, channel network or pore doublets or structure obtained from imaging (*e.g.* CT-scans or FIB-SEM)). DNS approaches are classically used in a Digital Rock Physics framework aiming at numerically upscaling effective properties (*e.g.* curve, relative permeability curve) or correlations (*e.g.* deformation dependent properties).

IRSN has extended its Smooth Particle Hydrodynamics (SPH) code capable of simulating dilatancy flow by adding an appropriate damage model and an original drying algorithm adapted for SPH method. Simulations on simplified poral structures have been made to validate these models. Numerical simulation on realistic porous structures (obtained by other teams from CT-scans and FIB-SEM imaging) have been initiated and will be conducted in the aim to upscale effective properties (deformation-dependent saturation curve, relative permeability). To better understand gas entry and transport in COx, a numerical study at the pore scale is proposed using Smoothed Particle Hydrodynamics (SPH) formulation, considering the strongly coupled thermodynamic (water evaporation and vapor diffusion) and hydromechanical (HM) phenomena. A joint PhD thesis between GeoRessources and IRSN (and in collaboration with A. Obliger, from the University of Bordeaux) was conducted to address these questions (Amrofel et al. (2024)).

Similarly to the SPH method, the Lattice Boltzmann Method is a commonly used DNS (Direct Numerical Simulation) approach based on a mesoscale representation of flow and transport phenomena. The advantage of the method includes a straightforward representation of the fluid – solid interfaces as well as good parallelization capacity, hence attenuating the drawback of heavy computational cost associated with DNS. The Lattice Boltzmann is based on the modeling of collision and propagation of distribution functions (which represent the likeliness of fluid ‘particles’ moving with a discrete speed in a discrete direction at each lattice node and at each time increment). The Lattice Boltzmann Method has been initially developed for modeling single phase flow under laminar conditions (Stokes flow). Since then, it has been extended to tackle various phenomena, including multi-phase flow, reactive transport as well as hydro-mechanical coupling. In preliminary work to the EURAD program, the GeoRessources and IRSN teams have developed and used a Lattice Boltzmann Method to model the Klinkerberg effect for gas flow in a nanoporous medium, based on a FIB-SEM set of images Pazdniakou and Dymitrowska (2018a). The GeoRessources team had also developed and used both a flow and transport LBM to assess the efficiency of reconstructed 3D nanoporous medium Tinet et al. (2020). In parallel, numerical multiscale methods have been developed for solving multiphase flow in the presence of heterogeneities Wang et al. (2020b). Based on this expertise, the objective of the present work is to use an improved LBM to model behavior specific to gas flow in clayrock. More specifically, two behaviors are the focus of this work using the LBM approach: gas flow considering dilatant pathways within a partially saturated clay-rock and electrokinetic coupling.

Models with the SPH approach Considering the high amount of generated gas from anaerobic corrosion, the gas phase invasion into the host rock is expected to cause a dilation of the porosity, leading to localized gas flow and displacement of water along these paths. This phenomenon may be a precursor of damage to the clay matrix and lead to irreversible rock fracturing, *Figure 2.298*. Given the nanometer scale of the pores, considerable capillary pressures must be overcome by the gas phase to allow water displacement and gas entry. Evaporation of the pore water can thus enhance drying of smallest pores. The thermodynamic equilibrium between liquid and gas at nanoscale depend on the curvature of the liquid-gas interface and is governed by Kelvin equation.

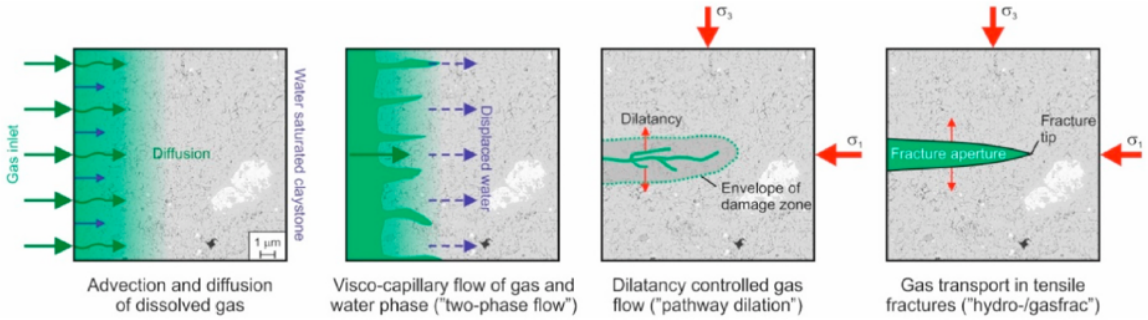

Figure 2.298: Different gas transport mechanisms within the Callovo-Oxfordian claystone (Cuss et al., 2014)

This is a mesoscopic approach where pore space, fluid phases etc are explicitly present and evolving following their individual laws: Navier-Stokes for fluids, elastic with damage for solids. The mechanical coupling between phases is also explicit. However, for the moment the mechanical (and damage) models as kept as simple as possible (homogeneous and isotropic). This is justified by the explicit complexity of the obtained model that should be already used and understood before adding extra features. And the possibility to treat explicitly different poral structures and to follow flows of two phases, deformation of pores and fracture propagation will help to get rid of a priori hypothesis often found in homogenised models. Especially any description of permeability can be obtained from an upscaling approach (for example numerical one). Heterogeneity in terms of solid phase can be taken into account by adding rigid inclusions into elastic matrix.

Fluid flow Description of the motion of fluids as continuous phases is useful to establish force equilibrium at the liquid/gas interface. At the considered scale, the Navier-Stokes equations in their simplified forms expressed in Lagrangian formulation are used to model weakly compressible two-phase flow at low Reynolds number. The mass conservation for fluid phases is then stated as:

$$\frac{D\rho_{w,g}}{Dt} = -\rho_{w,g}\nabla.\mathbf{v}_{w,g} \tag{2.133}$$

with ρ the density and v the velocity of the fluid. Indices w or g indicate the phase (w liquid, g gas). For Newtonian fluids, the momentum equations can be expressed as:

$$\rho_{\mathrm{w,g}}\frac{\mathrm{D}\mathbf{v}_{\mathrm{w,g}}}{\mathrm{Dt}} = -\nabla \mathrm{p}_{\mathrm{w,g}} + \mu_{\mathrm{w,g}}\Delta\mathbf{v}_{\mathrm{w,g}} + \rho_{\mathrm{w,g}}\mathbf{g} \tag{2.134}$$

with μ the dynamic viscosity of the fluid and **g** the acceleration of gravity.

When two fluid phases are described by means of the Navier-Stokes equations, it is necessary to ensure the continuity of the viscous stress tensor at the fluid-fluid interface. Thermodynamic effects being neglected, the pressure p is linked to the density ρ using the ideal gas equation:

$$\mathrm{p}_{\mathrm{w,g}} = \mathrm{c}^2_{\mathrm{w,g}}(\rho_{\mathrm{w,g}} - \rho^0_{\mathrm{w,g}}) \tag{2.135}$$

with c speed of sound, often used as a numerical parameter, and ρ^0 is the initial fluid density.

Mass transfer The vapor mass transfer at interfaces between the fluid phases will promote disappearance of the liquid phase in favor of the gas phase. Since the pressure of migrating gas phase is expected to be relatively high (of several MPa), the vapor can be considered as tracer component and solve its transport by a simple diffusion equation (and eventually the convective transport within the gas phase). The most important physical parameter is then the saturated vapor pressure P_{vs} which will be the maximal vapor pressure possible in the system. It can be calculated by the Rankine formula which is enough precise in the studied range of temperature:

$$\ln\left(\mathrm{P_{vs}}\right) = 13,7 - \frac{5120}{\mathrm{T}} \tag{2.136}$$

with P_{vs} only depending on temperature T. The ideal gas approximation will be used to define vapor density:

$$\rho_{vs} = \frac{P_{vs}M}{RT} \tag{2.137}$$

with M the molecular weight of the vapor, R the universal gas constant, T the temperature.

To model diffusion of vapor in gas phase, Fick equation is used Bird (2002a) :

$$\frac{\mathrm{DC}}{\mathrm{Dt}} = \nabla.(\mathrm{D}\nabla\mathrm{C}) \tag{2.138}$$

with C the concentration of vapor in the gas phase and D its diffusion coefficient. Water vapor is therefore considered as a tracer, i.e., the mass of water vapor is negligible compared to the mass of the gas that contains it, density variation being less than 0,1%. We restrain our modelling cases to those with very small Peclet number, which allows us to neglect natural convection. At the pore scale it is the Kelvin equation which locally defines the vapor density near the water-gas interface:

$$\frac{\mathrm{C_{veq.}}}{\mathrm{C_{vs}}} = \exp\left(-\frac{\mathrm{P_c M}}{\rho_{\mathrm{w}}\mathrm{RT}}\right) \tag{2.139}$$

where $\mathrm{C_{veq.}}$ is the equilibrium vapor density at a flat liquid-gas interface, $\mathrm{C_{vs}}$ is the saturation vapor density, $\mathrm{P_c}$ the capillary pressure, M is the molecular weight of the vapor, ρ_{w} the density of liquid water, R the universal gas constant, T the temperature. We consider liquid water phase saturated with the other gases of the gas phase so that gas dissolution and diffusion in water are neglected.

Solid elastic behavior The strain ε of an elastic, homogeneous, isotropic, and continuous medium is defined as a tensor associated with it:

$$\varepsilon = \frac{1}{2}\left(\nabla\mathbf{u} + (\nabla\mathbf{u})^{\mathrm{T}}\right) \tag{2.140}$$

where $\mathbf{u}$ is the local displacement. Hooke's law $\sigma = \mathbf{C} : \varepsilon$ with $\mathbf{C}$ being the stiffness tensor - relates the strain tensor ε to the stress tensor σ. For an isotropic material, we can write:

$$\sigma{=}2\mu_{\mathrm{s}}\varepsilon + \lambda_{\mathrm{s}}(\nabla.\mathbf{u})\mathbf{I} = \mu_{\mathrm{s}}\left(\nabla\mathbf{u} + (\nabla\mathbf{u})^{\mathrm{T}}\right) + \lambda_{\mathrm{s}}(\nabla.\mathbf{u})\mathbf{I} \tag{2.141}$$

with λ_{s} and μ_{s} being the Lamé coefficients and **I** the identity tensor.

The dynamic behavior of continuous elastic media is described by the following equation:

$$\rho\frac{\partial^2\mathbf{u}}{\partial t^2} = -\nabla.\sigma \tag{2.142}$$

Thus, deformation of elastic material can be deduced form stresses (internal and applied) in the material.

Thermodynamics-based damage models If a mechanical stress applied to a clay rock is high enough, its mechanical properties can be damaged, causing the material to lose rigidity. In the simplest models, degradation processes are quantified by introducing a scalar variable D that varies from 0 for an intact material to 1 for a completely damaged one. The Young's modulus of the elastic material will then evolve as a function of the damage, for example as follows:

$$E = (1 - D)^2 E_0 \tag{2.143}$$

where E_0 is the Young's modulus for the intact material, and D is damage variable. In the context of generalized standard materials and based on the first two laws of thermodynamics, it is possible to express the damage criterion of an elastic material as:

$$f(Y) = Y - Y_c(D) \ \leq 0 \tag{2.144}$$

where Y is the rate of energy release due to damage and Y_c is its critical value. Y is calculated as follows:

$$Y = \ -\rho \frac{\partial w}{\partial D} = -\frac{1}{2}\varepsilon : \mathbf{C}'(D) : \varepsilon \tag{2.145}$$

where $w(\varepsilon, D)$ is the Helmholtz specific free energy of the material, and ε is the strain tensor. The damage evolution law is therefore expressed as:

$$\dot{D} = \begin{cases} 0 & \text{Si } f(Y) < 0 \ || \ f(Y) = 0 \text{ et } \dot{f}(Y) < 0 \\ \frac{-C'(D):\varepsilon:\dot{\varepsilon}}{\frac{1}{2}\varepsilon:C''(D):\varepsilon + Y_c'(D)} & \text{Si } f(Y) = 0 \text{ et } \dot{f}(Y) = 0 \end{cases} \tag{2.146}$$

A completely damaged material will lose all rigidity and will have no cohesion to resist to imposed stress, for example induced by a pressurized fluid. This fluid, thanks to the local displacement caused at the fracture walls, will thus be able to propagate the fracture.

Boundary conditions The difference in intermolecular interactions and/or density between two immiscible fluids causes surface tension effects at the interface between them. The resulting macroscopic force acting on the particles near this interface tends to minimize its surface area and generates a pressure jump p_c between the two fluids. In the presence of a solid phase forming a capillary tube, the law describing the capillary pressure is classically written as (Finn (1986)):

$$p_c = p_g - p_w = \sigma \nabla \times \widehat{\mathbf{n}} \tag{2.147}$$

where σ is the surface tension coefficient considered constant along interface, R_1 and R_2 are the principal radii of curvature and $\widehat{\mathbf{n}}$ the unit normal to the interface. A good accuracy of capillary pressure modelling is essential for a good equilibrium vapor density assessment, as it is clearly demonstrated equation 2.147. Description of the interface between two immiscible fluids is a critical point of multiphasic flow modeling by continuous methods.

In this work we use the continuum surface force (CSF) model initially developed by Brackbill et al. (1992b). It consists of assigning a color constant value to each material point in the same phase. We introduce the color field defined as:

$$\mathrm{c}\left(\mathbf{x}\right)=\frac{\rho_{\mathrm{w}}(\mathbf{x})-\rho_{\mathrm{g}}(\mathbf{x})}{\rho_{\mathrm{w}}(\mathbf{x})+\rho_{\mathrm{g}}(\mathbf{x})} \tag{2.148}$$

Where the letters l and g, respectively, refer to liquid and gas. Then it is possible to calculate $\widehat{\mathbf{n}}$ the unit vector normal to the interface:

$$\widehat{\mathbf{n}}=\frac{\nabla \mathrm{c}(\mathbf{x})}{\|\nabla \mathrm{c}(\mathbf{x})\|} \tag{2.149}$$

The local curvature of the interface κ can be calculated as:

$$\kappa=-\nabla\times\widehat{\mathbf{n}} \tag{2.150}$$

A volumetric surface tension force $\mathbf{F}_{\mathrm{ts}}\left(\mathbf{r}\right)$ is calculated, the magnitude of which is proportional to the local curvature of the interface κ:

$$\mathbf{F}_{\mathrm{ts}}\left(\mathbf{x}\right)=\frac{1}{2}\sigma\kappa\mathbf{n} \tag{2.151}$$

The constant value of the color assigned to the solid phase is:

$$\mathrm{c}_{\mathrm{s}}(\mathbf{x})=\cos(\vartheta) \tag{2.152}$$

with ϑ the contact angle between liquid and solid phases. In this study we will mostly consider immobile and non-deformable solid phase forming pore walls. Finally, a non-slip condition is imposed at the fluid/solid medium interface:

$$\mathbf{v}_{\mathrm{w,g}}\left(\mathbf{r}_{\mathrm{i}}\right)=\mathbf{v}_{\mathrm{s}}\left(\mathbf{r}_{\mathrm{i}}\right) \tag{2.153}$$

where $\mathbf{v}_{\mathrm{f}}$ denotes the velocity of the fluid and $\mathbf{v}_{\mathrm{s}}$ denotes the velocity of the solid at the border. No vapor mass transfer is supposed between gas phase and solid wall:

$$\frac{\mathrm{dC}}{\mathrm{d}\mathbf{n}_{\mathrm{s}}}=0 \tag{2.154}$$

For vapor diffusion, Dirichlet condition will be applied at the surface of porous media:

$$\mathrm{C}=\alpha \tag{2.155}$$

Equation 2.136 is applied at the liquid - gas interface as Dirichlet condition to saturate gas phase with water vapor.

When needed, HM coupling, between solid elastic phase and fluid phases, is ensured by the condition of continuity of normal stresses, such that:

$$\sigma_{\mathrm{e}}.\mathbf{n}_{\mathrm{e}}=-\sigma_{\mathrm{w,g}}.\mathbf{n}_{\mathrm{w,g}} \tag{2.156}$$

Here, σ_{s} and $\sigma_{\mathrm{w,g}}$ are the stress tensors in the solid and fluid phases, respectively, $\mathbf{n}_{\mathrm{w,g}}$ is the unit vector normal to the fluid-solid interface, and $\mathbf{n}_{\mathrm{e}}=-\mathbf{n}_{\mathrm{w,g}}$

Models using the LBM approach The LBM model is used to study two nano-scale specific behaviours:

- Simplified hydro-mechanical coupling for gas flow using dilatant pathways in an elastic porous media. The challenges and context are like the study using the SPH approach described above.

- Electrokinetic coupling

In the context of radioactive waste storage, due to the introduction of ionic radionuclides into the geological layer, which adds to the naturally dissolved ions in the pore water, and the mostly mesoscopic pore size distribution of the COx, electrokinetic phenomena are particularly important. These phenomena are related to the presence of an electrical double layer at the surface of the rock, which can generate non-negligible osmotic flows.

Usually, rock walls are negatively charged. This leads to the formation of an accumulation of positive charges in their immediate vicinity, which tends to ensure local electroneutrality. These adsorbed ions are immobile and form the Stern layer, which is a few Å thick. The quantity of positive ions decreases as one moves away from these walls. Conversely, the quantity of negative ions increases until they are in equal proportions and satisfy electroneutrality. The zone of transition between the Stern layer and the electrically neutral zone is called the diffuse layer or the Gouy-Chapmann layer.

The thickness of the diffuse layer is characterized by the Debye length:

$$d^{-1} = \sqrt{\frac{\sum_i z_i^2 c_i^0}{4\pi\epsilon k_B T}} \tag{2.157}$$

With c_i^0 representing the concentration of ions i far from the interface, z_i their valences (number and sign of charges carried by ions), k_B the Boltzmann constant, ϵ the dielectric permittivity of the solvent, and T the temperature. Electro-osmosis is the generation of displacement of an electrolyte, ions and solvent, by applying an electric field. When the Debye length is of the order of the pore diameter, electrokinetic coupling significantly impact flows.

Fluid Flow Similarly to the SPH model, the fluid flow is modelled based on the quasi-incompressible Navier-Stokes equation at low Reynolds (Stokes conditions). When modelling multiphase flow, a Navier-Stokes equation is used for each fluid phase. The fluid-fluid interface is then generated by implementing a fluid separation force and fluid-solid adhesion forces (so-called pseudopotential LBM model).

Solid elastic behavior In the present work, the mechanical model is applied through the displacement of the fluid-solid interfaces following a linear dependence (i.e. elastic deformation) of the displacement with the local pore pressure (i.e. pressure is the fluid node neighboring the interface). Consequently, the fluid-solid boundary may cease to be located on the lattice nodes and therefore a numerical approach to deal with non-conform boundaries is required.

Electrokinetic coupling The model consists of the Poisson equation for the electrostatic potential, two Nernst-Planck equations for the concentration of positive and negative ions, and Navier-Stokes equations for the flow of the electrolytic solution.

2.13.1.2. Numerical model

Models using the SPH approach (in-house code at IRSN) In this section, each equation of the evaporation-condensation model that have been presented above will be introduced in SPH discretized form. Flow equations and curvature model has been presented in detail and validated in Pazdniakou and Dymitrowska (2018a).

SPH method Among the methods making it possible to simulate the mechanical behaviors in continuous medium, the SPH is characterized by its absence of grid, its Lagrangian nature and its adaptation to a massive parallelization. Indeed, the medium is discretized there in a cloud of material points of constant mass, which, in fluids, are often called particles. The convolution of any function $f(\mathbf{x})$ by the Dirac delta function d constitutes the starting point of the SPH method:

$$f(\mathbf{x}) = \int_\Omega f\left(\mathbf{x}'\right) \delta\left(\mathbf{x} - \mathbf{x}'\right) d\mathbf{x}' \tag{2.158}$$

where $\mathbf{x}$ and $\mathbf{x}'$ denote positions. To create a numerically useful approximation of $f(\mathbf{x})$ denoted $\langle \_ \rangle$, the singular form of δ is replaced by a smoothing kernel function $W\left(\mathbf{x} - \mathbf{x}', h\right)$ such that:

$$\langle f(\mathbf{x}) \rangle = \int_\Omega f\left(\mathbf{x}'\right) W\left(\mathbf{x} - \mathbf{x}', h\right) d\mathbf{x}' + O\left(h^2\right) \tag{2.159}$$

with h the smoothing length such that:

$$W\left(\mathbf{x} - \mathbf{x}', h\right) = 0 \tag{2.160}$$

for $(\mathbf{x} - \mathbf{x}') \geq h$.

To ensure the consistency of the method, the kernel function $W\left(\mathbf{x} - \mathbf{x}', h\right)$ must also follow the following conditions:

$$\begin{cases} \lim_{h \to 0} W\left(\mathbf{x} - \mathbf{x}', h\right) = \delta\left(\mathbf{x} - \mathbf{x}'\right) \\ \int_\Omega W\left(\mathbf{x} - \mathbf{x}', h\right) d\mathbf{x}' = 1 \end{cases} \tag{2.161}$$

Finally, discrete approximation $\ll \_ \gg$ of equations *(18)* is constructed by replacing the continuous form by a sum over a set of materials points such that:

$$\ll f(\mathbf{x}_i) \gg = \sum_{j=1}^{N} \frac{m_j}{\rho_j} f\left(\mathbf{x}_j\right) W\left(\mathbf{x}_i - \mathbf{x}_j, h\right) \tag{2.162}$$

$$\ll \nabla f(\mathbf{x}_i) \gg = \sum_{j=1}^{N} \frac{m_j}{\rho_j} f\left(\mathbf{x}_j\right) \nabla W\left(\mathbf{x}_i - \mathbf{x}_j, h\right) \tag{2.163}$$

$$\ll \nabla . f(\mathbf{x}_i) \gg = -\sum_{j=1}^{N} \frac{m_j}{\rho_j} f\left(\mathbf{x}_j\right) . \nabla W\left(\mathbf{x}_i - \mathbf{x}_j, h\right) \tag{2.164}$$

with $V_j = \frac{m_j}{\rho_j}$, V_j is volume associated with the material point j, m_j its mass and ρ_j its density.

The cubic B-spline function proposed by (Monaghan and Lattanzio, 1985) has been used as kernel W:

$$W\left(\mathbf{x}_i - \mathbf{x}_j, h\right) = \alpha \begin{cases} \frac{2}{3} - r^2 + \frac{1}{2} r^3 & 0 \leq r < 1 \\ \frac{(2-r)^3}{6} & \left(1 \leq r < 2\right) \\ 0 & r \geq 2 \end{cases} \tag{2.165}$$

where r is the normalized spacing between particles given by $\frac{\left\|\mathbf{x}_i - \mathbf{x}_j\right\|}{h}$ and α is a parameter depending on whether the domain is defined in one, two, or three dimensions ($1/h$, $15/(7\pi h^2)$, and $3/(2\pi h^3)$).

Flow equations The SPH version of the continuity equation can be written as:

$$\frac{D\rho_a}{Dt} = \rho_a \sum_b \frac{m_b}{\rho_b} \left(\mathbf{v}_a - \mathbf{v}_b\right).\nabla W \left(\mathbf{x}_a - \mathbf{x}_b, h\right) \tag{2.166}$$

Nevertheless, it is common to replace it by a simpler formulation, which guarantees an exact conservation of the mass:

$$\rho_a = \sum_b m_b W \left(\mathbf{x}_a - \mathbf{x}_b, h\right) \tag{2.167}$$

Momentum conservation equation can be written as follows:

$$\begin{aligned} \frac{D\mathbf{v}_a}{Dt} &= -\sum_b \left(\frac{p_b}{\rho_b^2} + \frac{p_a}{\rho_a^2}\right) m_b \nabla W \left(\mathbf{x}_a - \mathbf{x}_b, h\right) \\ &+ \sum_b \frac{4\mu_a\mu_b}{\mu_a+\mu_b} \frac{m_b}{\rho_b\rho_a} \frac{\mathbf{v}_a-\mathbf{v}_b}{\left\|\mathbf{x}_a-\mathbf{x}_b\right\|} \frac{\partial W(r_{ab},h)}{\partial r_{ab}} + \mathbf{g} + \frac{\mathbf{F}_s}{\rho_a} \end{aligned} \tag{2.168}$$

Combined with a method to determine forces at the interfaces (presented hereafter), the Navier-Stokes equation allows the establishment of curvature at the fluid-fluid interfaces.

Curvature First, it is necessary to assign to liquid and gas SPH particles a value serving as color parameter $c_l = -1$ and $c_g = 1$, respectively. It is the most straightforward approach to do it. The color field is then smoothed using SPH method as following:

$$c\left(\mathbf{x}_i\right) = \sum_{j=1}^{N} \frac{m_j}{\rho_j} c_j W\left(\mathbf{x}_i - \mathbf{x}_j, h\right) \tag{2.169}$$

The color function gradient vector is obtained by discretizing equation 2.139 with SPH method as:

$$\mathbf{n}\left(\mathbf{x}_i\right) = \sum_{j=1}^{N} \frac{m_j}{\rho_j} \left(c\left(\mathbf{x}_j\right) - c\left(\mathbf{x}_i\right)\right) \nabla W\left(\mathbf{x}_i - \mathbf{x}_j, h\right) \tag{2.170}$$

This last allow us to calculate the interface local curvature given by 2.140 as:

$$\kappa\left(\mathbf{x}_i\right) = \frac{1}{\left\|\mathbf{n}(\mathbf{x}_i)\right\|^2} \sum_{j=1}^{N} \frac{m_j}{\rho_j} \left(\mathbf{n}\left(\mathbf{x}_j\right)\left\|\mathbf{n}\left(\mathbf{x}_i\right)\right\| - \mathbf{n}\left(\mathbf{x}_i\right)\left\|\mathbf{n}\left(\mathbf{x}_j\right)\right\|\right).\nabla W\left(\mathbf{x}_i - \mathbf{x}_j, h\right) \tag{2.171}$$

Following the calculation of local curvature, local resultant force $\mathbf{F}_{ts}\left(\mathbf{r}\right)$ is calculated using equation 2.140. Spatial distribution of particles near interfaces is then rules by CSF model, considering through equation 2.141 the contact angle between the wetting phase and the solid phase.

Evaporation-condensation model In this section, we present the general idea of our evaporation algorithm is in which liquid phase conversion into gas takes place. Figure 2.299 illustrates the explanations that follows. First of all, we take from equation of diffusion 2.138 the second derivative that can be discretize as:

$$\frac{dC}{dt}\left(\mathbf{x}_i\right) = \sum_{j=1}^{N} \frac{m_j}{\rho_j} \left(D_a + D_b\right) \frac{\left(C_a - C_b\right)}{\left\|\mathbf{x}_i - \mathbf{x}_j\right\|} \frac{\partial W\left(\mathbf{r}_{ij}, h\right)}{\partial \mathbf{r}_{ij}} \tag{2.172}$$

Where $\mathbf{r}_{ij} = \mathbf{x}_i - \mathbf{x}_j$. Formulation 2.172 does not guarantee that the diffusive flux will be continuous across material interfaces, either a jump on the value of the diffusion coefficient. Cleary and Monaghan have shown that this problem can be solved by replacing $(D_a + D_b)$ by

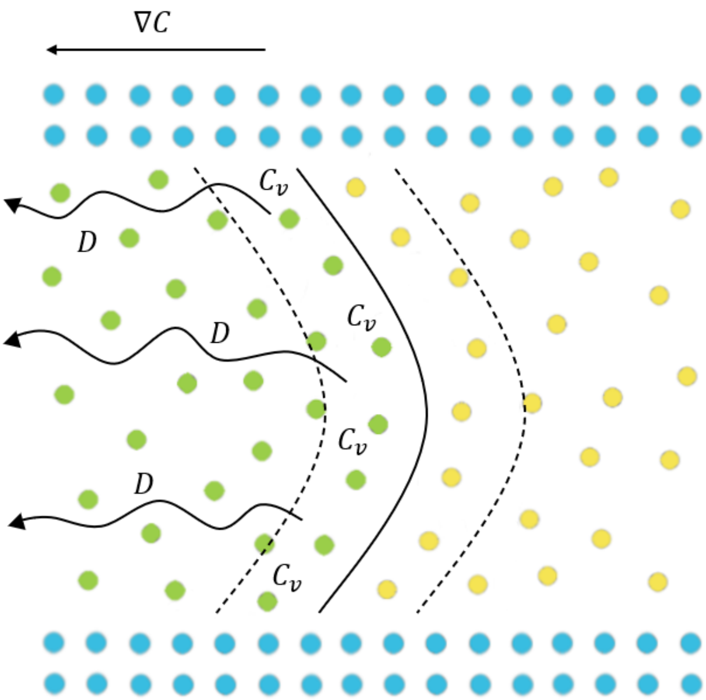

Figure 2.299: Illustration of the SPH evaporation model

$$\frac{4D_aD_b}{(D_a+D_b)} \tag{2.173}$$

The variation in concentration is then calculated such that:

$$\frac{dC}{dt}(\mathbf{x}_i) = \sum_{j=1}^{N} \frac{m_j}{\rho_j}\frac{4D_aD_b}{(D_a+D_b)}\frac{(C_a-C_b)}{\left\|\mathbf{x}_i-\mathbf{x}_j\right\|}\frac{\partial W(\mathbf{r}_{ij},h)}{\partial \mathbf{r}_{ij}} \tag{2.174}$$

This formulation ensures continuity of mass flux across discontinuities in density and diffusion coefficient even when material properties exhibit significant spatial variations.

Gas particles located in transition band near liquid interface are saturated with vapor at each time step. The vapor mass injected at the gas particle at x $_i$, is calculated as $m_{inj} = (C_{vs}(x_i) = -C\ (x_i)) * V_g$ is then deduced uniformly from the counters of mass balance of fluid particles present within the compact support of (x_i). This local mass loss or gain counters allow for proper triggering of particles phase conversion. The ability of gaseous particles to accommodate vapor is renewed by the diffusion of the latter through the gas.

When the mass counter of a fluid particle reaches a mass loss equivalent to the mass of a fluid particle, a conversion into a gaseous particle is made and evaporation occurs. When the counter of a fluid particle reaches a mass gain equivalent to the mass of a fluid particle, the nearest gaseous particle on its compact support is converted into a fluid particle and condensation occurs. Obviously, the mass of a water particle is then subtracted from an appropriate counter.

Challenge concerning the consideration of the Kelvin effect and the calculations of the pressure at the scale of an interface will be developed in following sections.

Elasticity model To compute the force components via SPH, the second derivatives of local displacement using the following approximation for second derivatives:

$$\left(\frac{\partial^2 \mathbf{u}}{\partial x_\alpha \partial x_\beta}\right) = \sum_{j=1}^{N} \frac{m_j}{\rho_j} \left(5\frac{(\mathbf{x}_{\alpha,i} - \mathbf{x}_{\alpha,j})(\mathbf{x}_{\beta,i} - \mathbf{x}_{\beta,j})}{\left\|\mathbf{x}_i - \mathbf{x}_j\right\|} - \delta_{\alpha\beta}\right) \bullet \left(\mathbf{u}_i - \mathbf{u}_j\right) \frac{1}{\left\|\mathbf{x}_i - \mathbf{x}_j\right\|} \frac{\partial W(\mathbf{r}_{ij},h)}{\partial \mathbf{r}_{ij}} \tag{2.175}$$

Here, the Greek indices α and β refer to the spatial dimensions, and $\delta_{\alpha\beta}$ represents the Kronecker delta function.

Models using the LBM approach (in-house code at GeoRessources-CNRS) In general, the LBM model is based on a regular cubic lattice in n-dimensions space, based on the input geometry (either a segmented image or a model geometry), with q discrete velocity directions, the model is then labelled DnQq. The state of a given fluid phase s at a lattice point **x** and at a time t is defined by its distribution function $f_s(\mathbf{x},t)$. Each distribution function is undergoing collision and propagation processes:

$$f(\mathbf{x} + \mathbf{e}dt, t + dt) = f(\mathbf{x}, t) - M^{-1} \cdot S \cdot M \left(f(\mathbf{x}, t) - f^{eq}(\mathbf{x}, t)\right) + M^{-1} \cdot \left(I - \frac{1}{2}S\right) \cdot M \cdot \mathbf{F}$$

Where M represent the transformation matrix (dependent on the DnQq type LBM), **e** is the velocity direction, dt the time step S is the collision operator, f^{eq} is the equilibrium function (dependent on the process studied) and **F** represent the forcing discretization. The forcing scheme used is the GZS approach, preserving Galilean invariance. The collision scheme is either the BGK or TRT collision. In both cases, S is only dependent on one parameter, the relaxation time t, the TRT method offering improved precision and numerical stability.

For the hydro-mechanical coupling, we use a D3Q19 TRT-LBM.

Flow model The LBM is developed for both single and two-phase flow. For two-phase flow, a single-phase model is applied to each fluid phase with additional forces including to consider fluid separation ($\mathbf{F_f}$) and adhesion ($\mathbf{F_a}$).

$$\mathbf{F_f} = -\rho_\sigma(x, t) \sum_{i=1}^{q} w_i G \rho_{\overline{\sigma}} (\mathbf{x} + \mathbf{e_i} dt, t) .\mathbf{e_i}$$

$$\mathbf{F_a} = -\rho_\sigma(x, t) \sum_{i=1}^{q} w_i A_\sigma s (\mathbf{x} + \mathbf{e_i} dt, t) .\mathbf{e_i}$$

Where $\rho_\sigma(x, t)$ represent the phase density, w_i is a weight (dependent on the DnQq model), σ ($\overline{\sigma}$) represent the studied (other) phase. G and A_σ are parameters related to the phase separation and interfacial tension for G and contact angle for A_σ. Usually, the value G is strongly constrained by keeping little diffusion at the interface whilst ensuring numerical stability.

Macroscopic parameters including kinematic viscosity, phase density, bulk velocity and pore pressure are computed based on the distribution and model parameters.

It should be noted that all properties are provided in lattice units (lu). Conversion from lattice units to physical units are performed through dimensionless quantities (e.g., Reynolds number for single phase flow, or Capillary number for two phase flow). The properties are such that the Reynolds number is low (Stokes flow) and the Capillary number is low (capillary dominated flow).

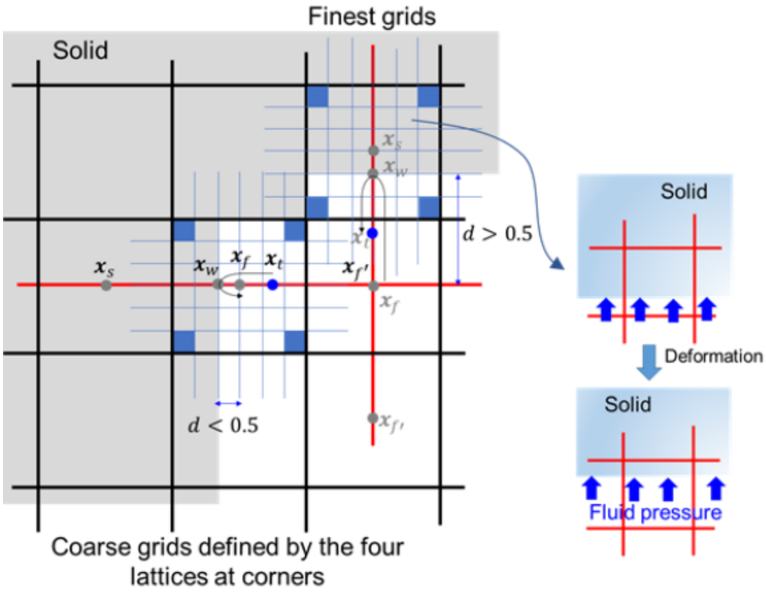

Figure 2.300: Schematic of treatment of wall deformation using IBB

Deformation model As described above, the displacement of the fluid-solid interfaces is commuted locally based on the local pore pressure at interfaces nodes. The challenge is then to accurately describe flow behavior considering evolutive non-conform boundaries.

To this end, an interpolated bounce-back scheme (IBB) is applied (2.300). This formulation provides a non-conforming grid scheme, respecting the no-slip boundary condition at the walls, with the interface being captured by the interpolation function and does not need to be assigned along the edge of lattices.

In this work, we use a linear IBB (following Lallemand and Luo (2003b); Pan et al. (2006b)). The distributions in the directions opposing the wall are computed as follow, considering d as the distance between the fluid node and the actual position of the wall:

$$f_{\bar{i}}(x_f, t+\delta t) = \begin{Bmatrix} \frac{1}{2d} f_i'(x_f, t) + \frac{2d-1}{2d} f_{\bar{i}}(x_{f'}, t+\delta t) & \text{if } d \geq 0.5 \\ 2d f_i'(x_f, t) + (1-2d) f_i'(x_{f'}, t) & \text{if } d < 0.5 \end{Bmatrix} \tag{2.176}$$

It should be noted that if d is negative, the node is transformed into a solid node and if d > 1, the node is no more impacted by the wall.

Physically, the IBB is basically an upwind scheme with respect to the velocity if $d < 0.5$ and downwind if $d > 0.5$. Especially, it will be reduced to the standard bounce-back if $d = 0.5$.

Model workflow, geometry and boundary conditions for the hydro-mechanical coupling A weak coupling between flow and mechanical processed is performed. Flowchart of iteration process in fluid-solid interaction is given in Figure 2.301 (p represents here the difference between pore pressure at a given time and the reference pore pressure, L is a characteristic length and E is the elastic modulus).

We are considering flow in a pore represented as a rough channel. Interaction between pores is not considered. Inlet and outlet boundary conditions are a pressure condition. The inlet pressure is increased stepwise to induce the mechanical deformation.

Model description, workflow, and boundary conditions for the electrokinetic coupling The prospects regarding the electrokinetic coupling are presented in Figure 2.302, where ϕ is the potential field, e_0 vac-

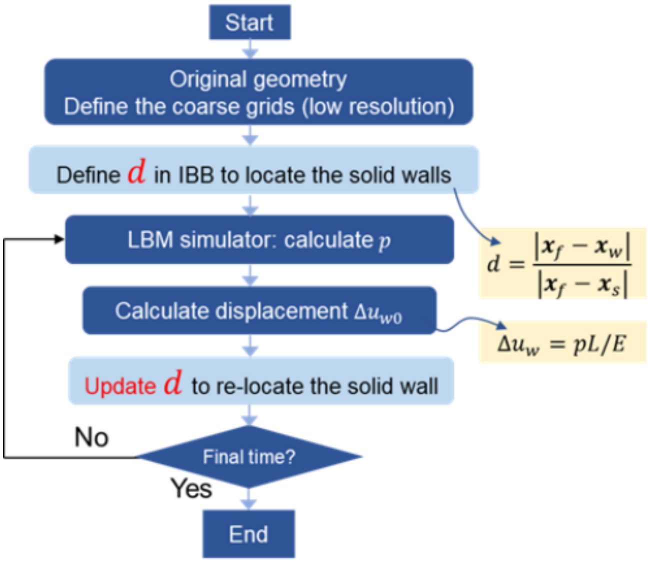

Figure 2.301: Flowchart of iteration process in fluid-solid interaction

uum permittivity, e_r dimensionless dielectric constant, e the elementary charge, ρ_+ and ρ_- the charge density. For Navier-Stokes equations, u is fluid velocity, ρ fluid density, μ fluid dynamic viscosity and p the pressure. D present in Nernst-Planck equation is ions diffusion coefficient. f^i is related to distribution functions where eq relate equilibrium, G_i is sources terms, ω_i are weight coefficient, $c_s=\Delta x/\Delta t$ and t relaxation-time coefficient. Λ is equal to 1/3.

The electrokinetic coupling will be considered using the Lattice Boltzmann method (LBM), for single-phase flow conditions, with the so-called "integral" method (Yoshida et al. (2014a)).

The model also proposes Dirichlet and Neumann-type boundary condition at the solid/liquid interface that is correctly imposed. It can be extended to two-phase flow where gas is generated from radioactive waste storage. One should keep in mind that this model describes the coupled dynamics of ions and solvent in mesoscopic pores (d > 2 nm), where hydrodynamic equations hold and molecular aspects of ions such as solvation or excluded volume effects can be neglected.

2.13.2. Results

2.13.2.1. Benchmark comparison for upscaling multiphase flow properties

The purpose of this study is to evaluate the consistency and limitations of different numerical approaches for the estimation of the multiphase transport properties of low permeability sedimentary formations. Specifically two approaches for numerically upscaling the water retention curve were studied, one using the classical drainage simulations (with LBM) and the other using co-current flow simulations alongside the upscaling of the relative permeability (with LBM and SPH). Both computations were performed on a set of FIB-SEM images and compared to the experimentally measured water retention curve.

Drainage simulation Two reservoirs of 10 voxels thickness are set at the inlet and outlet of the porous medium with closed boundaries set laterally. Initially the porous medium is fully saturated with the wetting fluid (e.g. water) as well as the outlet reservoir and the inlet reservoir is filled with the non-wetting fluid (e.g. air). Following Vogel et al. (2005), we imposed a pressure boundary at the inlet with step by step increasing value, whilst pressure was maintained constant at the outlet. At each step, simulation was performed until reaching static condition. The pressure step duration was imposed, but static conditions were checked. At the end of each step, water saturation is computed, based on the fluid distribution obtained. Averaged pressure is then computed on each phase. For the LBM, since the interface is diffusive, pressure is

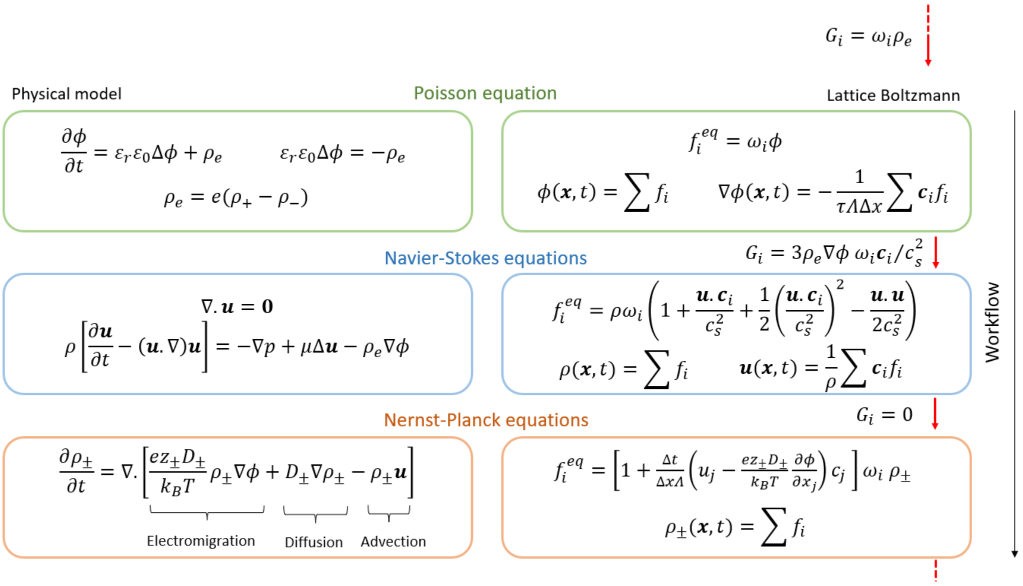

Figure 2.302: Physical model for Electrokinetic coupling and its LBM formulation order in workflow

computed from voxels which are pure enough.

Co-current flow simulations A co-current flow is imposed from the inlet towards the outlet using a body force. Initially, the medium is filled with both fluid so as to reach a prescribed saturation. The simulation is then performed until reaching equilibrium. Then, fluxes can be averaged on each phase and, using Darcy's law, the relative permeability is derived. Similarly to the capillary pressure, for the LBM, fluxes are computed disregarding the fluid-fluid interface voxels. The choice of the initial fluid distribution is varying depending on the authors. For example, Li et al. (2005) chose a uniform distribution,Wang et al. (2020b) imposed the distribution based on the pore size and Li et al. (2019) based theirs on a preliminary co-current flow simulation. In the following, both a random cluster distribution (LBM) and a pore-size based distribution (SPH and LBM) are used. Capillary pressures are computed from such simulations and therefore water retention curves can be also determined. This procedure has significantly lower numerical cost required compared to drainage simulations.

Image data image data used in this study corresponds to an illite sample from Le Puy en Velay basin (Gaboreau et al. (2016)). The powdered illite sample was purified and compacted to the dry density of 1.7 g/cm3 before being processed which corresponds to a porosity e = 0.39. Details on the sample, image acquisition and image segmentation may be found in Gaboreau et al. (2016). In the present work, we use their image segmented by the watersheding-based method. This method has demonstrated the best fit considering the total porosity and pore size distribution. The influence of the segmentation technique on the numerically calculated single phase permeability was considered in Pazdniakou and Dymitrowska (2018a). There are 180 images of 1096 × 1095 pixels in total, with pixel size 5 × 5 nm. Since the distance between the consecutive images is also 5 nm, the voxel is a cube with 5 nm side. The total porosity of the image sample is e = 0.2928. Since the whole image was too large even for the single phase flow simulation (Pazdniakou and Dymitrowska (2018a)), the simulations are performed on a sub-sample extracted from the original image. The sub-sample size is 101 × 101 × 102 voxels (Figure 2.303). Following removal of the isolated pores, the porosity of the sub-sample is e = 0.2926. The sub-sample is chosen so as to preserve the pore size distribution.

Gravimetric water vapour adsorption-desorption isotherms (Poirier et al. (1987)) were performed at 303K using a reconstructed illite sample with the same characteristics as the imaged sample and allows the

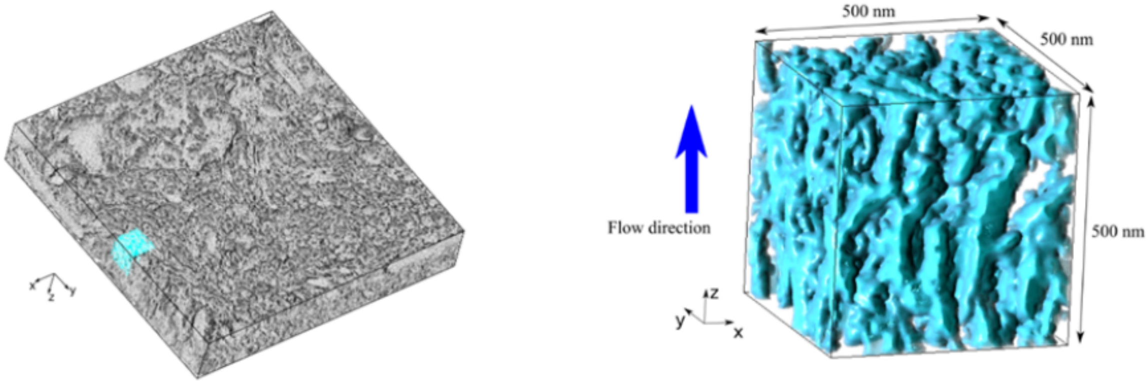

Figure 2.303: The pore space of the total illite sample (Left) and the selected subsample (in blue) (Right)

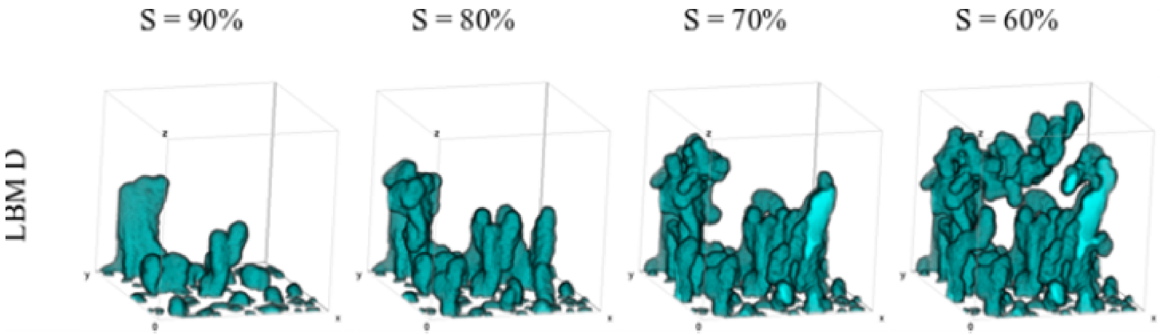

Figure 2.304: Results of the drainage simulation for different saturation levels. In cyan is shown the non-wetting phase invading the medium from the inlet (bottom) reservoirs. Inlet reservoir is cropped

recovery of the drainage and imbibition retention curves.

Water retention curve *Drainage simulation:*

Results of the drainage simulation are shown in Figure 2.304 and Figure 2.305. Breakthrough was reached around 60%. As shown in the simulation phase distribution (Figure 2.304) a clear cut-length appears leading to sample size dependency of the results. In order to limit this effect in the analysis of the results and similarly to the approach used, for instance, in reactive transport, the upscaling is performed on a volume cropped at the cut-length distance ("LBMd – cropped"). It should be noted that the upscaled water retention curve obtained considering or not the cut-length are both agreeing well with experimental data. Considering the cut-length leads, however, to results encompassed between the experimental drainage and imbibition curves whilst without considering the cut-length the results overshoots the drainage curve.

Drainage simulation were however computationally expensive.

Co-current flow simulations:

Co-current flow were much less computationally expensive (over one order of magnitude faster, using similar hardware). Comparison of simulations for SPH and LBM simulations are shown in Figure 2.306 and Figure 2.307. Water phase remains percolating until a saturation of 50% whilst gas phase becomes percolating from a saturation of 60%, with consistent results between all methods and conditions. When phases are not percolating, they are distributed among multiple clusters (2.306), and even when phases are percolating it can be through multiple non-interconnected channels. As a consequence, defining a single capillary pressure might be disputable, as local capillary pressure between a given cluster and the surrounding fluid is variable, mostly constrained by the size of the cluster. Therefore, in the following, the

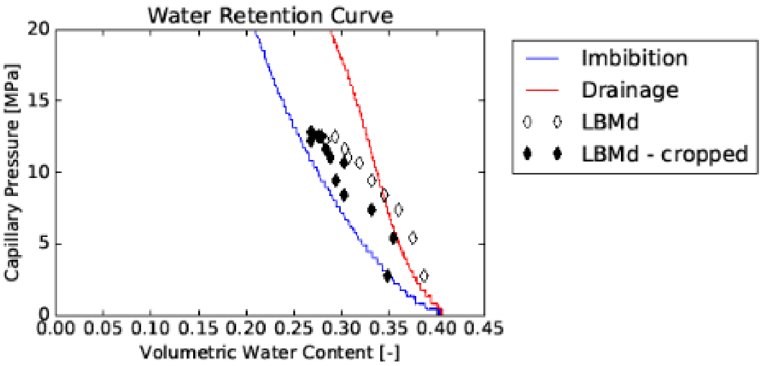

Figure 2.305: Water retention curve. Experimental data for drainage and imbibition are shown by thick blue and red lines, data from LBM drainage simulation with black diamonds. Filled markers are used for saturations computed considering cut-off length

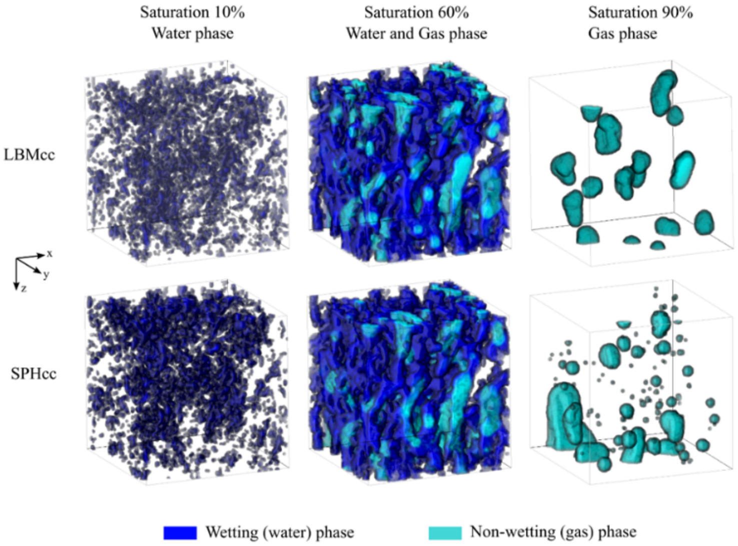

Figure 2.306: Results of the co-current flow simulations using LBM and SPH methods. LBM simulations shown are for a random cluster and initial distribution and SPH using an initial uniform distribution of 8 particles per voxel and a smoothing length of 1 voxel.

range of capillary pressure for a given image is provided, rather than a single value.

Distribution of capillary pressures for the different fluid clusters tend to overlap experimental and drainage simulation values, for large water saturation though tend to underestimate the capillary pressure at the lowest saturation. It should also be noted that the capillary pressure ranges tend to increase when saturation decreases. Besides median values of capillary pressures do not seem to provide satisfying value in regards to experimental data or drainage simulations despite providing the accurate order of magnitude. An explanation could be the lack of consideration of historicity. As a consequence, pore are mobilized by the non-wetting phase prior being connected, and therefore at a lower capillary pressure than under a drainage configuration.

Averaged capillary pressures calculated by the LBM and SPH are very close to each other (Figure 2.307). The observed differences in phase distributions and the very small bubbles obtained in the SPH simulation (Figure 2.306) do not influence the averaged capillary values, which confirm the robustness of the approach.

A discrepancy between the LBM and SPH simulations is appearing for low water saturation (below 30%)

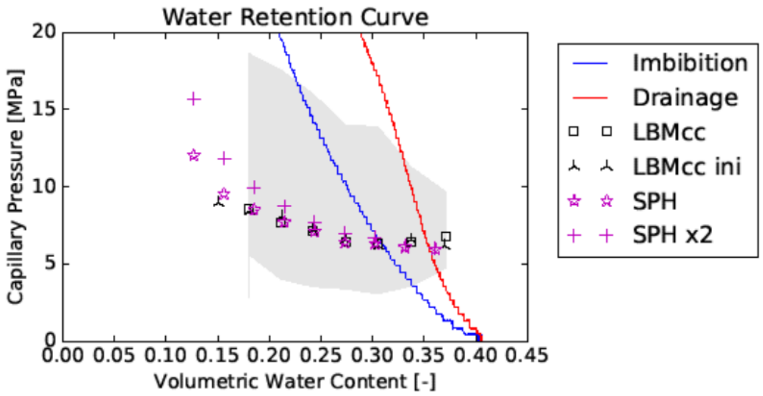

Figure 2.307: Water retention curve. Experimental data for drainage and imbibition are shown by thick lines, data from LBM co-current simulations in black, SPH in magenta. 'ini' indicates that the initial distribution used was based on pore size (same as SPH) and x2 represents the simulation with increased number of material points.

when resolution is increased with the SPH solution (Figure 2.307). Under such conditions, the water phase is concentrated in smallest pores or water films which makes the calculation of capillary pressures a challenging task due to difficulties to capture correctly the interface curvature, and due to a low number of the water points located sufficiently far from the water-gas interface. The LBM seems to be more affected than the SPH due to the water-gas interface which spans over several lattice nodes. Therefore, the capillary pressure value corresponding to the initial saturation of 10% was not calculated by the LBM exactly due to the absence of the water points located sufficiently far from the interface. Improved resolution has therefore a significant role to assess the impact of small pores as well as water film.

The limited descriptions of water films is also likely a reason as to why capillary pressure range is underestimated at lower saturation.

Finally, the initial distributions also do not impact the capillary pressure curves. It should be noted, however, that the random cluster distribution will tend to favour distribution in the largest pores (higher probability since the volume is larger) and therefore the two compared initial distribution have similarities.

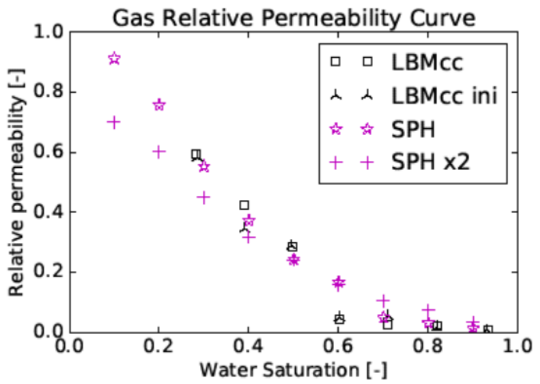

Figure 2.308: Gas relative permeability curves

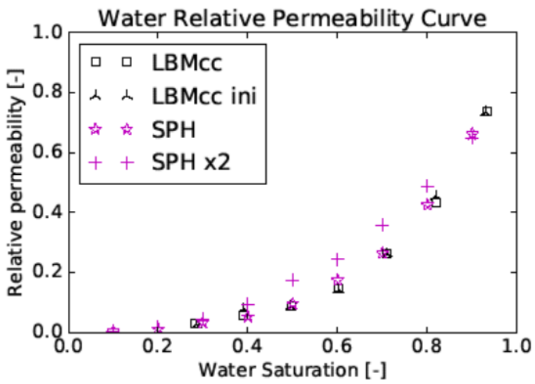

Figure 2.309: Water relative permeability curves

Relative permeability The water K_w and gas K_g relative permeabilities are displayed in Figure 2.308 and Figure 2.309. As expected, it can be observed that the water phase permeability grows gradually with saturation, while the gas phase permeability evolves differently in two regions. The water phase appears to stop percolating at a saturation of 20%. The water relative permeabilities are similar for the different approaches, demonstrating little effects of initial distribution or model (SPH or LBM). However, the relative permeability for the high resolution SPH positively deviates from the other cases, especially at intermediate saturation. The higher relative permeabilities could be explained by a better consideration of the water phase connectivity, especially through smaller pores or water films. In regards to gas relative permeabilities, results show good agreement between methods at higher saturation (> 30%). At lower saturation, the high resolution SPH), deviates negatively from the other cases. This, once again, may be due to a better representation of the water films, as they will limit the gas flow.

2.13.2.2. Competition between evaporation and capillary redistribution including Kelvin effect

The following study aims at studying the competition between phase change (evaporation and/or condensation) induced by variations in relative humidity and phase displacement induced by capillary forces. The computational domain geometry will rely on 2D idealized structures of connected pores with narrows pores of few nanometers. We will take advantage of this simplification to conduct a sensitivity analysis of physical parameters governing evaporation and condensation processes using dimensionless quantities. For all simulations, models are periodic laterally and closed (for fluid flow) at the top and bottom boundaries. Drying is induced by imposing a constant relative humidity at the top boundary.

Evaporation patterns and regime diagram In order to observe the impact of capillary and Kelvin effects on drying patterns, we focused first on so-called 3x2 2D pore network. The distribution of channel diameters, between 5 and 10 nm is presented in Figure 2.310. It is discretized by 145000 particles including 92000 fluid particles. The Kelvin equation should govern the establishment of capillary pressure in pores up to 10 nm diameter. Working with this type of distribution allows us to study drying of a network not accessible to gas breakthrough by drainage without fracturing the medium, typically for diameters less than 20nm (Boulin (2008)), and for which Kelvin effect is significant.

A series of simulations is carried out for which the influence of capillary forces, diffusion rate, and evaporation rate are investigated through different values attributed to the dimensionless numbers such as Peclet ($\mathrm{Pe} = \frac{v_{int} L}{D}$) and Capillary ($\mathrm{Ca} = \frac{\mu_w v_{int}}{\sigma}$) numbers and the vapor concentration ratio

$$\Delta C' = \frac{C_{veq} - C_{in}}{C_{vs}}$$

with C_{in} the vapor concentration fixed at the inlet (v_{int} is the interface velocity, L a characteristic length, D the diffusion, μ_w the liquid water dynamic viscosity, σ the surface tension). The different cases with the corresponding dimensionless parameter values used in the simulations are gathered in Table 2.86. For some of them, the Kelvin effect was cancelled and the classical Laplace equation was used instead (cases *b.*, *e.*, *k.* and *m.*) Different patterns are observed and the most representative ones are illustrated in Figure 2.312.

As depicted in Figure 2.312, two representative regimes are exhibited: the capillary-dominated regime (e.g. case *c.*) and the evaporation-dominated regime (e.g. case *n.*). To further interpret and identify these patterns, a dimensionless evaporation-capillary number e is proposed. It is calculated as the ratio between the characteristic times of evaporation and capillary forces. Inspired from Benner and Petsev (2018); Engeland et al. (2020), our formulation was modified to take into account the pore-scale features and the Kelvin effect. It can be written as follows:

$$\varepsilon = 12 \, \frac{\mathrm{Ca}}{\mathrm{Pe}} \, \Delta C' \, C'_s \qquad (2.177)$$

with $C'_s = \frac{C_s}{\rho_w}$

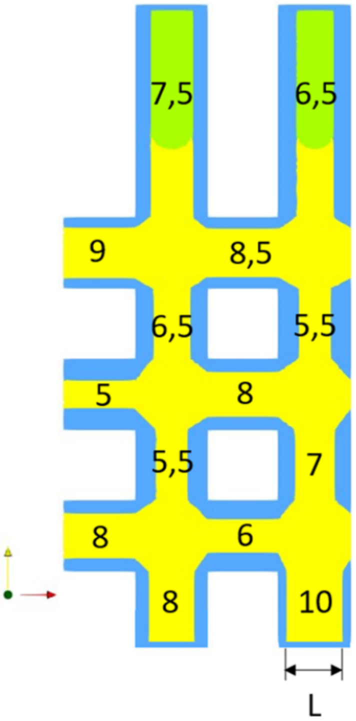

Figure 2.310: Pore size distributions on the initialized network, the aperture is expressed as a function of the compact support length h. Yellow represents water phase and green represent gas phase. Those both phases are surrounded by solid rigid phase, in blue. Pores are connected laterally through periodic conditions.

Table 2.86: Dimensionless parametrization for studied case sorted by ascending e. For the sake of comparison, the expected in situ conditions for COx are also given.

	ε	**Ca**	**Pe**	$\Delta C'$	**RH**	**Kelvin effect**
in-situ	1.5E-04	5.5E-10	3.3E-09	4.0E-01	0.6 - 0.98	Yes
a.	1.4E-03	1.1E-05	1.7E-04	8.8E-01	0.00	Yes
b.	1.6E-03	1.1E-05	1.7E-04	8.8E-01	0.00	No
c.	1.9E-03	2.5E-05	4.1E-04	1.2E-01	0.76	Yes
d.	1.4E-02	1.1E-04	1.7E-03	8.8E-01	0.00	Yes
e.	1.6E-02	1.1E-04	1.7E-03	8.8E-01	0.00	No
f.	1.9E-02	2.5E-04	4.1E-03	1.2E-01	0.76	Yes
g.	4.5E-02	4.2E-04	6.8E-03	2.8E-01	0.70	Yes
h.	6.2E-02	8.2E-04	4.1E-03	1.2E-01	0.76	Yes
i.	1.2E-01	1.6E-03	8.2E-03	1.2E-01	0.76	Yes
j.	1.4E-01	1.1E-03	1.7E-02	8.8E-01	0.00	Yes
k.	1.6E-01	1.1E-03	1.7E-02	8.8E-01	0.00	No
l.	4.4E-01	3.4E-03	1.7E-02	8.8E-01	0.00	Yes
m.	5.0E-01	3.4E-03	1.7E-02	8.8E-01	0.00	No
n.	1.6E+00	1.1E-02	1.7E-03	1.0E+00	0.00	Yes

A regime diagram $\mathsf{Ca} - \varepsilon$ is illustrated in Figure 2.311 and supports the role of ε as driving parameter of drying patterns. For the sake of comparison, the ε value for the representative in situ conditions in COx

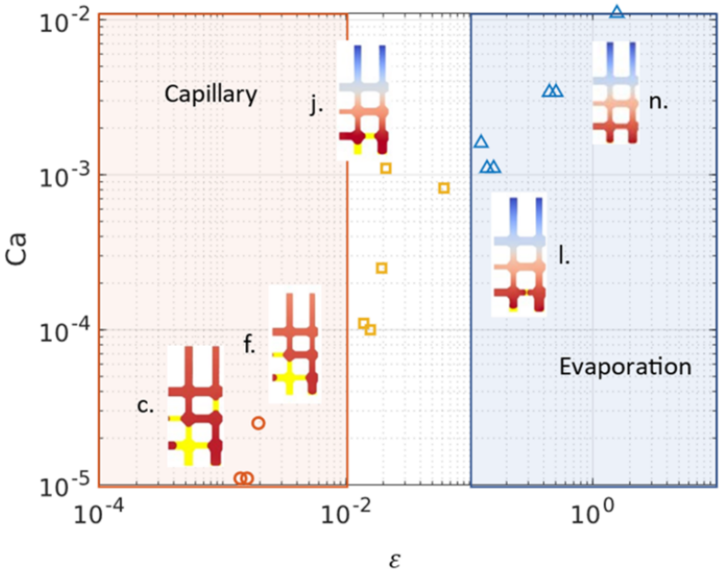

Figure 2.311: Regimes diagram function of capillary-evaporation number for evaporation simulations with capillary effect and/or Kelvin effect.

formation (based on data from ANDRA (2005b); Boulin (2008) are also indicated in Table 2.86. Given the computational constraints, the range of epsilon values explored in our study is as close as possible to the one for in situ conditions.

The capillary-dominated drying regime corresponds to conditions of very low ε ($\varepsilon < 1 \cdot 10^{-2}$). Capillary forces are high enough to prevent evaporation in the smallest pores which remain saturated. The equilibrium vapor concentration at the liquid-gas meniscus in such pores is lower than the vapor concentration in the surrounding gas and cannot be diffused away. This results into the formation of preferential evaporation pathways (Figure 2.311). This phenomenon is accentuated by the Kelvin effect. Similar result holds when increasing the inlet vapor concentration, and hence, reducing the evaporation rate. The higher the ambient humidity conditions, the less pores will have the ability to empty and the more heterogeneous the drying pattern will be (Figure 2.312*c.*). At the macro-scale, the time to breakthrough is shorter and the residual water saturation higher. It may also facilitate the formation of disconnected water clusters if the pore size distribution is large enough.

In contrast, for high values of ε ($\varepsilon > 1 \cdot 10^{-1}$), evaporation rate and viscous forces have taken advantage over capillary forces. All the pores in contact with the gas front evaporate in the same time. A uniform drying pattern is observed with practically no residual water saturation (Figure 2.312 *n.*). This is the evaporation-dominated regime. The impact of the Kelvin effect is negligible at low ambient humidity.

Between these two values ($1 \cdot 10^{-2} > \varepsilon > 1 \cdot 10^{-1}$), the gas invasion pattern becomes transient between capillary-dominated and evaporation-dominated. In this intermediate regime, both capillary forces and evaporation rate are competing. Small instabilities may appear but they don't propagate too much (Figure 2.311).

This discrepancy between these two contrasted drying regimes is also visible into the drying dynamics. As illustrated in Figure 2.313, the evolution of gas saturation S_g with dimensionless time changes drastically from the evaporation to capillary-driven regime. For the first one, the saturations increase quasi linearly with time and slows down by the end. In contrast, in the capillary-driven regime, the saturation to breakthrough is significantly lower (75% against 100%) due to the formation of preferential pathways for drying and the presence of residual water clusters. The heterogeneity of pore size distribution in the medium combined with the low value of Capillary number and the Kelvin effect results also into the strong

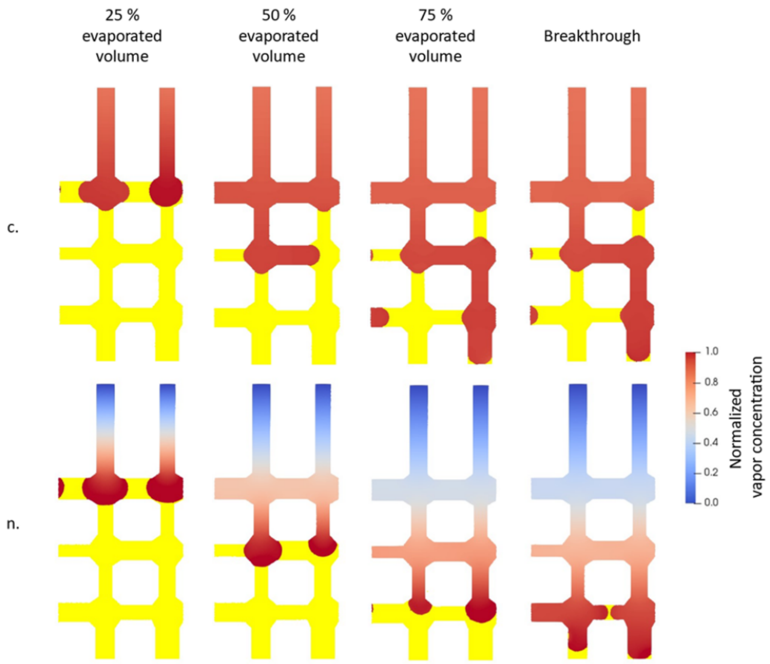

Figure 2.312: Study of the parameters defining the drying regime and the creation of preferential pathways for gas invasion into the clay matrix at the nanoscale. The comparison is made at equivalent evaporated volume and on a normalized vapor concentration scale. Water phase is represented in yellow.

variability of equilibrium vapor concentration at the different gas-water menisci along the drying front. It thus induces fluctuations of drying rate with time as shown in Figure 2.313.

Kelvin effect on gas invasion pattern In order to investigate further the impact of Kelvin effect and determine to which extent it may affect the gas invasion, we performed supplementary simulations with or without Kelvin effect on a 5x5 network, under the same conditions that were presented for the case j. and k. in Table 2.86, except for the inlet relative humidity, set at 0.75. Such conditions leads to an evaporation-capillary number equal to about $\varepsilon \approx 10^{-2}$ for the simulations. We therefore expect a capillary-dominated regime more pronounced in the presence of Kelvin effect.

Figure 2.314 compares, at equivalent gas saturation, the fluids distribution within the pore space in the presence (right) or not (left) of the Kelvin effect. As expected, instabilities appear, more important when the Kelvin effect occurs but they remain bounded by the limited size of the domain. It also generates competition between channels with variable drying front velocity from one pore to another leading to complex fluid redistribution. As on the smaller networks, Kelvin effect with high ambient humidity significantly accentuates heterogeneities so that breakthrough occur at 78.6% of gas saturation against 97.8% without Kelvin effect. The presence of accentuated capillary effects and smaller concentration gradients induced by high ambient humidity conditions increase heterogeneities and the appearance of disconnected clusters of the liquid phase during the drying of the network.

As expected, these difference in evaporation patterns also affect the dynamics of drying. Evolution of gas saturation with dimensionless time (using the time to breakthrough without Kelvin effect as reference time), in *Figure 2.315*, shows similar trend for both curves but with a lower gas saturation to breakthrough in the presence of Kelvin effect. Impact of mass transfer limitations are more pronounced than for 3x2 networks due to larger pore network size but no fluctuation of front velocity occurs probably because the heterogeneity of pore size distribution was not high enough. The drying rate is also reduced because of equilibrium vapor densities smaller than saturation vapor concentration and in spite of preferential pathways. This is consistent with the experimental results of Thiery et al. (2017). Note that PNM simulations of Maalal

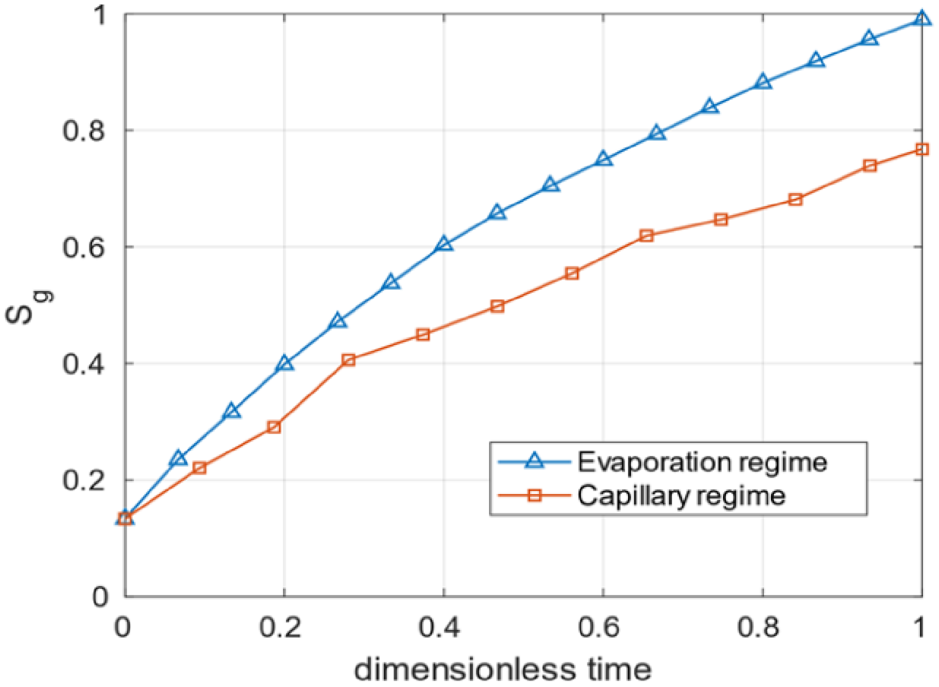

Figure 2.313: Evolution of gas saturation with dimensionless time for capillary-dominated (case c.) and evaporation dominated (case n.) regimes

et al. (2021) predict an opposite result of Kelvin effect on time to breakthrough, probably because the impact of pattern instabilities prevail. This competition driven by the Kelvin effect between reduction of local equilibrium vapor concentration and development of preferential pathways will require further investigation.

Impact of condensation Another interesting finding, not highlighted previously, is the impact of condensation, made possible by the Kelvin effect, on the gas invasion pattern. In the example shown in *Figure 2.316*, we can observe that condensation occurs, especially at the bottom interface. We have represented at different times the mass transported by liquid particles close to the interface in the transition band (a negative value implies vapor loss and so, water condensation) and the relative humidity within the gas phase (color scale ranges between the relative humidity at equilibrium and the highest value in the gas phase). In the presence of Kelvin effect, capillary forces induced by the throat size of 5.5 nmn reduce the equilibrium relative humidity to 0.79. In addition, the vicinity of the drying front in the lower part favors high ambient vapor concentration in the gas phase (*Figure 2.316*, time t_1). This results in a displacement of vapor from higher (gas phase) to lower (gas-liquid interface) concentration and hence, condensation occurs (*Figure 2.316*, time t_2). Liquid cluster expands but in the upward direction because of capillary forces which force water to move through the narrowest pore (*Figure 2.316*, time t_3). This mechanism can be quite fast with local condensation rate much higher than the average drying rate. It could contribute to reduce the vapor concentration at the front head and hence increase the vapor gradient and speed up the evaporation front breakthrough.

2.13.2.3. Modelling of hydro-mechanical coupling (hydrofracturing) by SPH

Linear elastic behaviour with HM coupling (SPH model) To verify the linear elastic behavior within HM coupling, the geometry presented in *Figure 2.317* is used. It is a liquid-filled slot of length $2l_0$ and width w, with imposed varying in time liquid pressure. The elastic domain is a square of side length L, with $L \gg w$, assuming that the displacement and stress fields vanish at ininity. Dimensions used are: $2l_0 = 20.10^{-2}$m, $w = 2.10^{-2}$m and $L = 100.10^{-2}$m. Young modulus is $E_0 = 3$GPa, the Poisson ratio is $\nu = 0.2$. The smoothed length is fixed at $h = 2.10^{-2}$m and 3 particles per h are used.

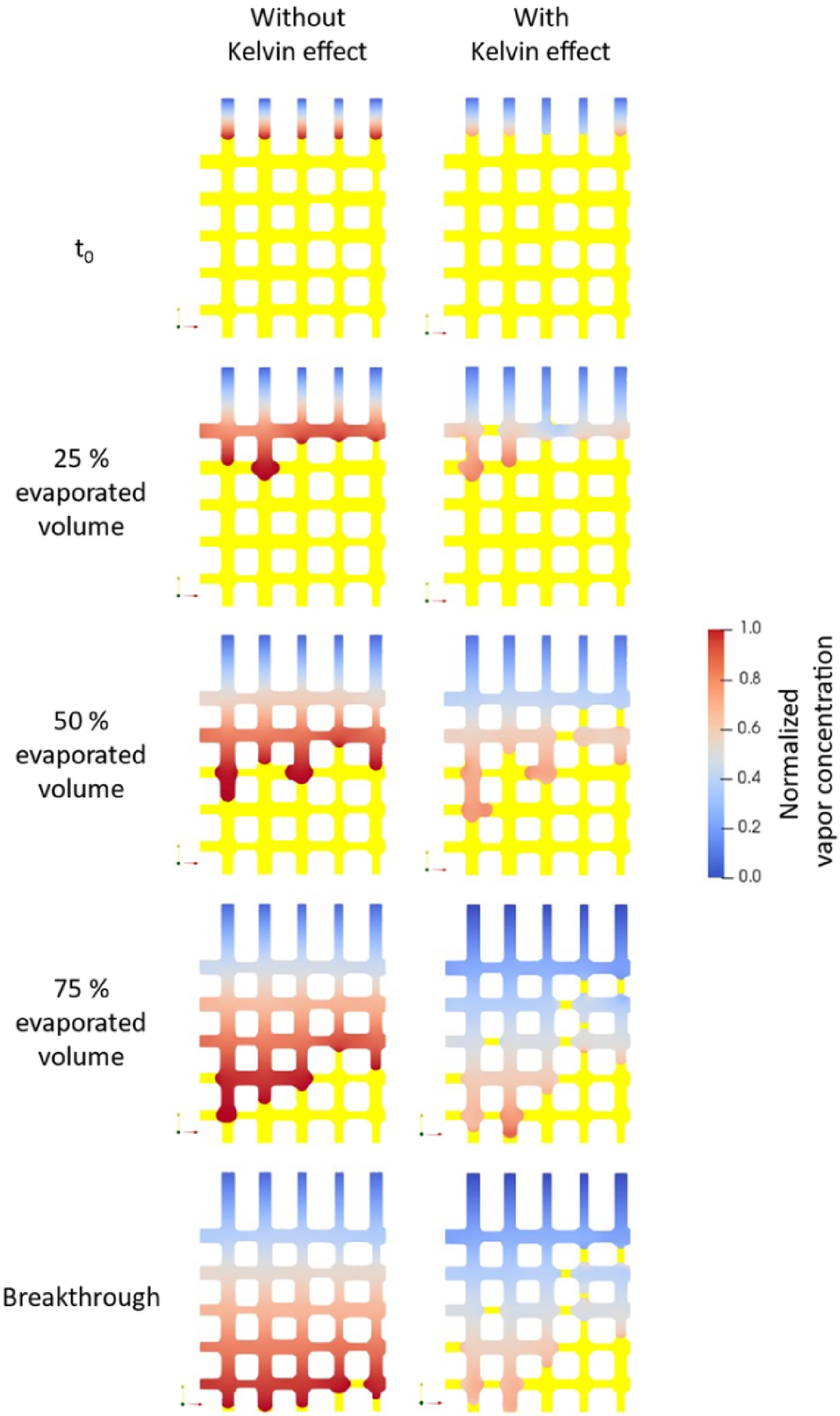

Figure 2.314: Large network comparison without (left) and with Kelvin effect (right) for two different equivalent evaporated volume and on a normalized vapor concentration scale. Water phase is represented in yellow. Periodic conditions are applied to lateral domain boundaries. Gas invasion is made from the top, RH=0.75. Bottom is closed

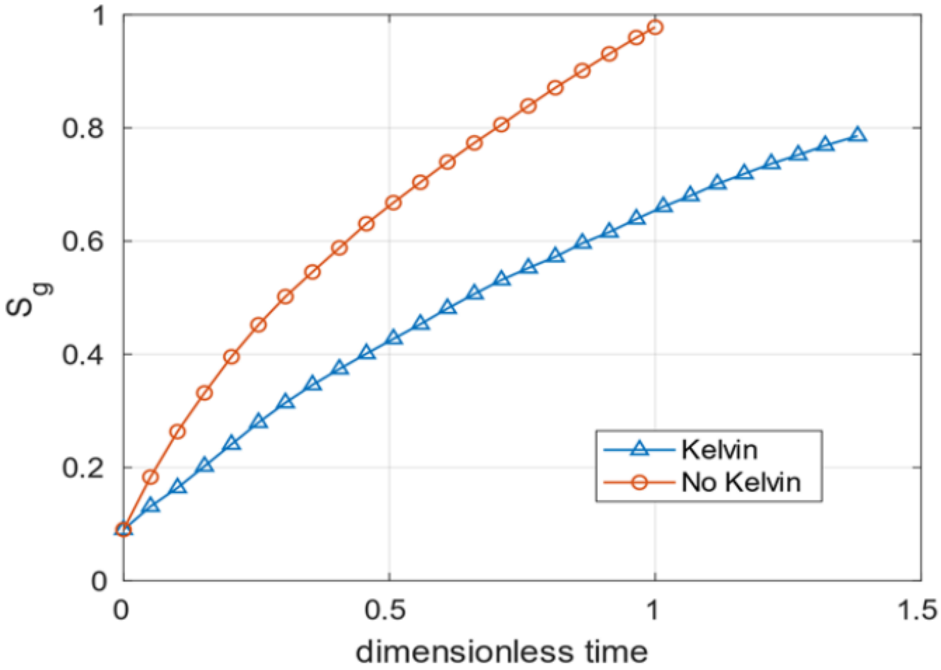

Figure 2.315: Evolution of gas saturation with dimensionless time with and without Kelvin effect.

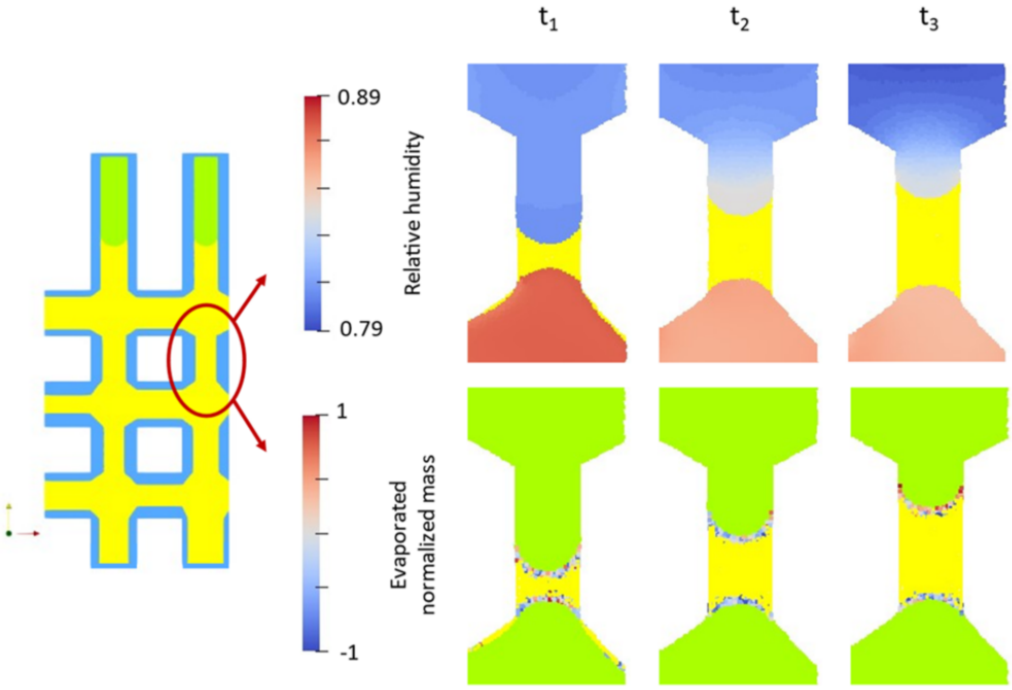

Figure 2.316: Evidence of the filling of the smallest pores by condensation. The water phase is in yellow. The color field shows the local mass balance per particle before conversion. A positive balance leads to evaporation. A negative balance leads to condensation.

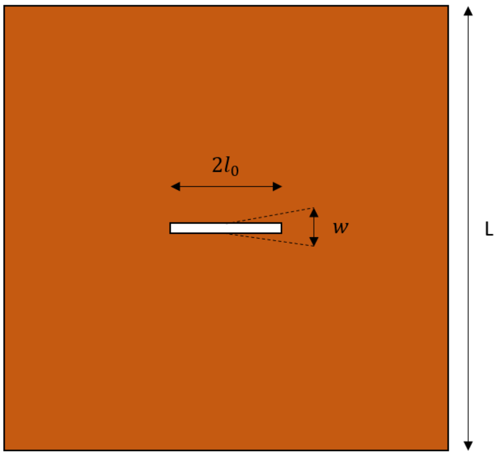

Figure 2.317: Domain for elastic and HM verification.

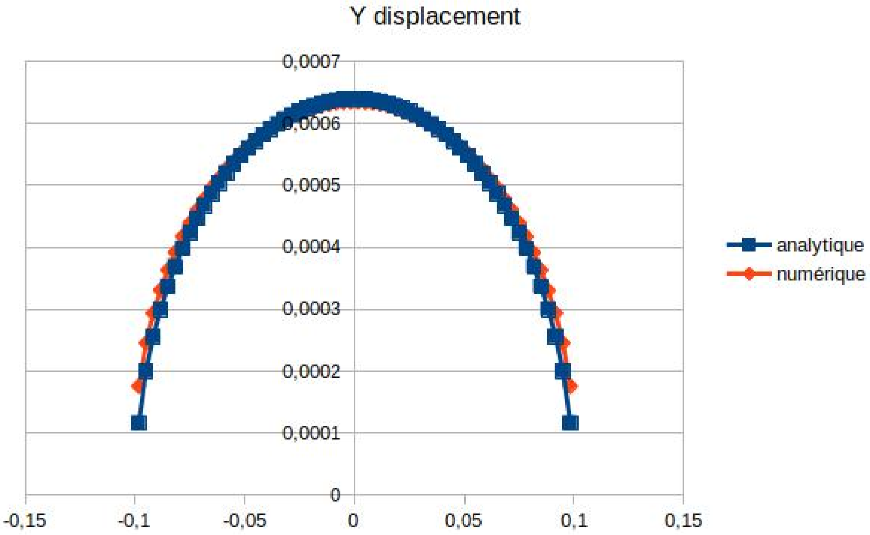

Figure 2.318: Comparison between SPH results and analytical expectations for slit border displacement.

For the boundary displacement of the slit surface subject to a constant pressure force p, setting $E' = E_0/(1 - \nu^2)$ and for $-l_0 \leq x \leq l_0$, the exact formula is:

$$u^+(x,0) = \frac{2pl_0}{E'}\left(1 - \frac{x^2}{l_0^2}\right)^{\frac{1}{2}} \tag{2.178}$$

Of course, $u^-(x,0) = -u^+(x,0)$. Comparison between SPH results and this analytical solution presented *Figure 2.318* shows very good agreement. *Figure 2.319* shows that the relative error on the calculation of elastic deformation is less than 1% along vertical symmetry axis. However, this error increases as it approaches the edges of the slot, reaching a value of 50%. Despite this increase, the error remains within an acceptable range and consistent with expectations, remaining in the right order of magnitude.

Hydrofracking preliminary results (SPH model) Two preliminary tests were set up regarding the propagation of a hydrofractures. The first, shown in *Figure 2.320*, is a proof of concept of the ability of the SPH code to propagate a fracture through fluid flow within it. The second, shown in *Figure 2.321*, replicates the conditions used for verifying the static elastic case in *Figure 2.317*, corresponding to COx properties, but

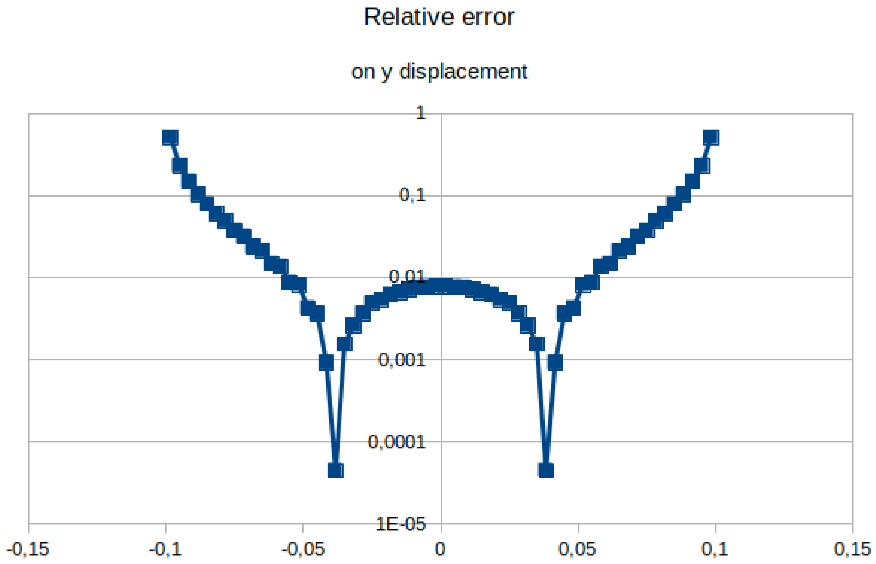

Figure 2.319: Relative error along the slit.

including now a damage model. In this second case, the fluid does not flow within the fracture and does not propagate the boundary condition. However, we generate damage localization and propagation.

The properties assigned to the fluid are those of water: $\rho = 1000\ \mathrm{kg.m^{-3}}$ and $\mu = 10^{-3}\mathrm{Pa.s}$. A confinement stress $\sigma_0 = 3.7\mathrm{MPa}$ is applied on either side of the sample to ensure that the fluid propagation front and the fracture front are coincident. The horizontal displacements of the injection surface are blocked. All these conditions are schematized in *Figure 2.320* (a). To control the injection flow rate, a piston was created with dimensions adapted to a flow characterized by Reynolds number Re<1. By respecting all boundary conditions previously described and with elastic phase parameters facilitating fracture propagation, it was possible to demonstrate the ability of the SPH model to reproduce hydro-fracture propagation *Figure 2.320* (b). Even though this simulation was done in a finite domain, we have observed that the critical fluid pressure at which fracture propagation initiated was of the same order of magnitude as expected from Bourdin et al (2012) – it was 20% to high.

For the second case in *Figure 2.321*, linear elastic behavior is used. For damage model our critical damage energy release Yc(D) may be dependent on D. There exist two well-known versions of Yc(D) based in the Ambrosio-Tortorelli (AT) model, one of which depends on D and the other does not, respectively called AT2 and AT1 and they can be written as follows:

$$\begin{aligned} \mathrm{Y_c(D)} &= \mathrm{Y_c^0} \\ \mathrm{Y_c(D)} &= \mathrm{2DY_c^0} \end{aligned} \tag{2.179}$$

The critical value of rate of energy release used here is $\mathrm{Y_c^0} = 4,5.10^1\mathrm{MPa}$. The first model corresponds to an elastic regime occurring before damage initiation. This type of response is typically observed in the mechanical behavior of various geomaterials. In contrast, the second case does not exhibit any elastic range, and the degradation process begins as soon as deformation is nonzero. Therefore, we can observe in *Figure 2.321* a more localized fracture with AT1 model and damage propagating around the crack with AT2 model. Indeed, since the fluid does not flow into the crack, it is the edges of the slit that deforms to accommodate pressure increase of the fluid contained therein.

Model of dilatant multiphase-flow coupled to damage in COx (SPH) The application of the SPH code was made to the case of water-gas drainage of a poral space obtained from FIB/SEM imaging of COx,

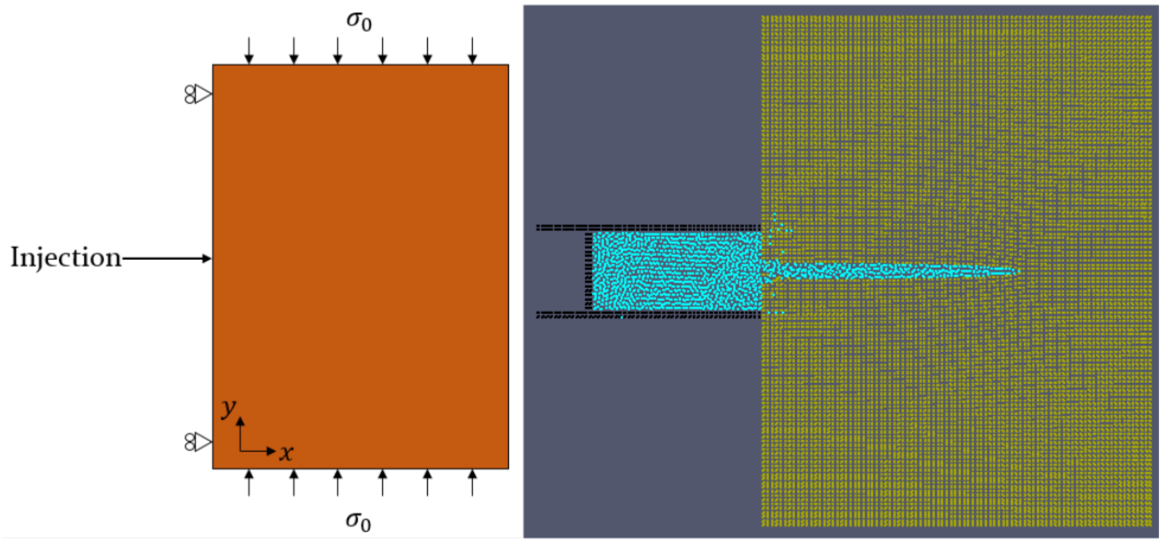

(a) (b)

Figure 2.320: Geometry and boundary conditions (a), corresponding fracture propagation example (b).

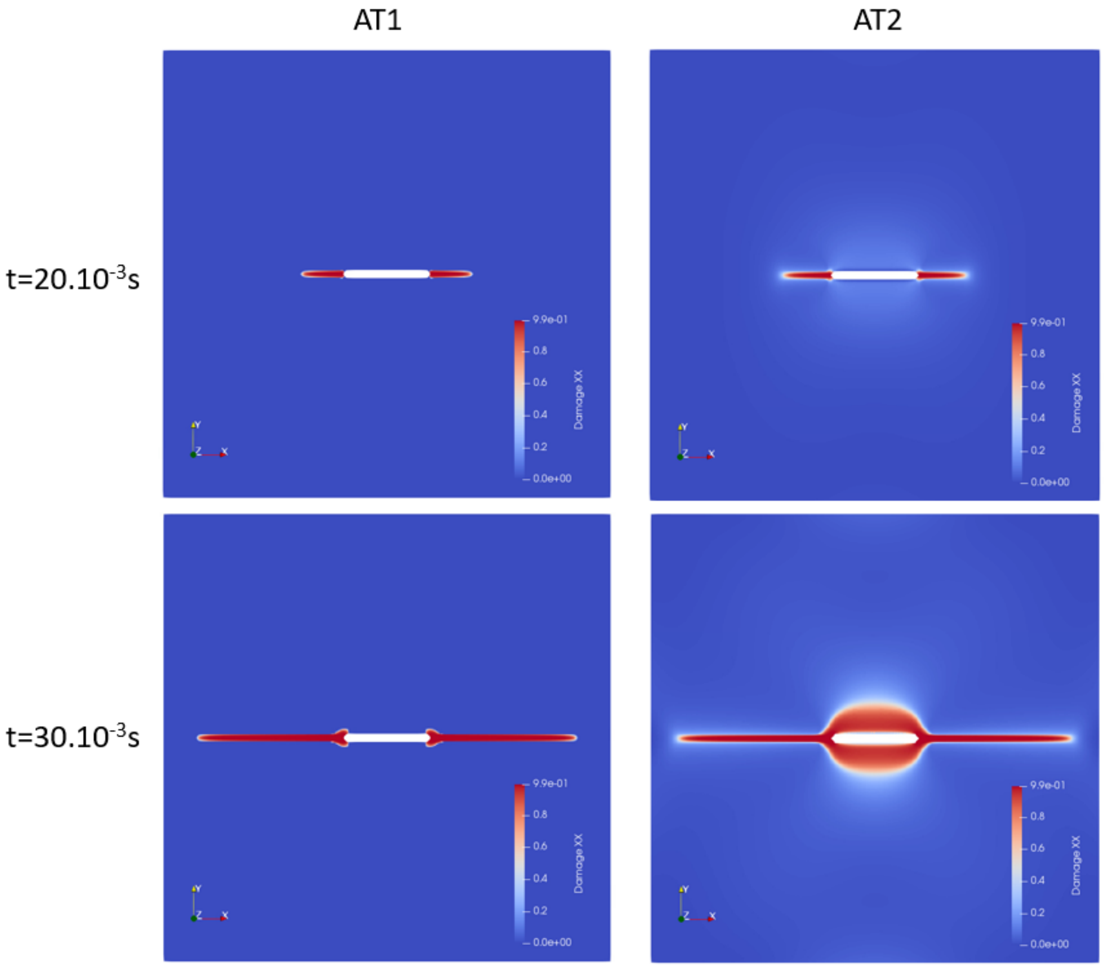

Figure 2.321: Fracturing (damage propagation) with increasing water pressure in the slit.

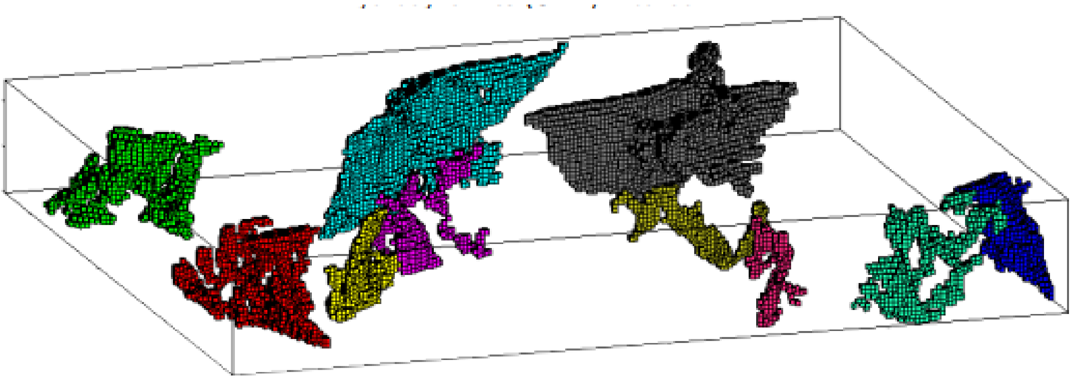

Figure 2.322: A total set of percolating pores in a Callovo-Oxfordian clay sample after Pazdniakou and Dymitrowska (2018a)

by Song et al. (2016). This sample measures 5.64 × 7.96 × 1.03 µm^3 with a porosity of 0.0307 ± 0.0039. For this material the most significant part of poral space possesses a few nanometer sizes, which is not large enough to be observed by FIB imaging with a resolution of about 10 nm. Therefore, at this scale, only a part of the total porosity is visible with many connections missing, which leads to the observation of mainly disconnected pores. The reconstruction of the percolating poral network from Pazdniakou and Dymitrowska (2018a) shows several disjoint pores that connect opposite sides of the sample . This set of percolating pores is converted in a numerical sample resulting in a 3D sample of 771 × 739 × 103 voxels. This configuration presents more than 58 million of voxels and is much too big for the actual memory limitations. Thus, to reduce the size and the simulation time, a coarsening of the original sample is adopted reducing the sample to 1/8 of the original volume (i.e. 385 × 369 × 51 voxels) covering the volume with only one connected pore (dark blue in the lower right corner). Besides, the phase identification is set to segment only two different phases: solids and pores. It means that, in this approach, the clay matrix and the rigid inclusions are considered parts of one REV. The principal simulation parameters are given in PhD thesis of Deptulski (2021).

In previous results from Pazdniakou and Dymitrowska (2018a) where the simple Mohr-Coulomb damage criteria was used, it was not possible to obtain localised damage and thus fracture propagation. With the thermodynamic damage model the localisation is much better, however still unsatisfactory due to limited sample size and damage interaction with sample borders. What is more we observe that the fracture propagation depends on the confining pressure. Indeed, we make simulation of gas percolation into fully water saturated samples at three different confining pressures: 6-8-10 MPa. When the confining pressure is lowered from 8 MPa to 6 MPa, we obtain a clear fracture propagation with new pore space connecting isolated pores and with fluid flow, see *Figure 2.323* In additional simulation, not shown here, for reduced confining stress of 6MPa, it was possible to connect initially completely isolated pores and to generate new percolating pathways in a non-percolating numerical sample.

2.13.3. Summary

Two pore-scale models (SPH – Figure 2.324 and LBM – Figure 2.325) were improved and used to assess different processes regarding gas flow, including evaporation (considering Kelvin effect), visco-capillary flow, dilatant flow and fracturing.

The pore-scale models (either SPH or LBM or both) were used to:

- Perform a benchmark comparison of visco-capillary flow on FIB-SEM images of a reconstructed clay sample (illite) with upscaling of macroscopic multiphase flow properties (relative permeabilities and suction curve).
- Improve the understanding of the relative impact of phase changes (evaporation and condensation)

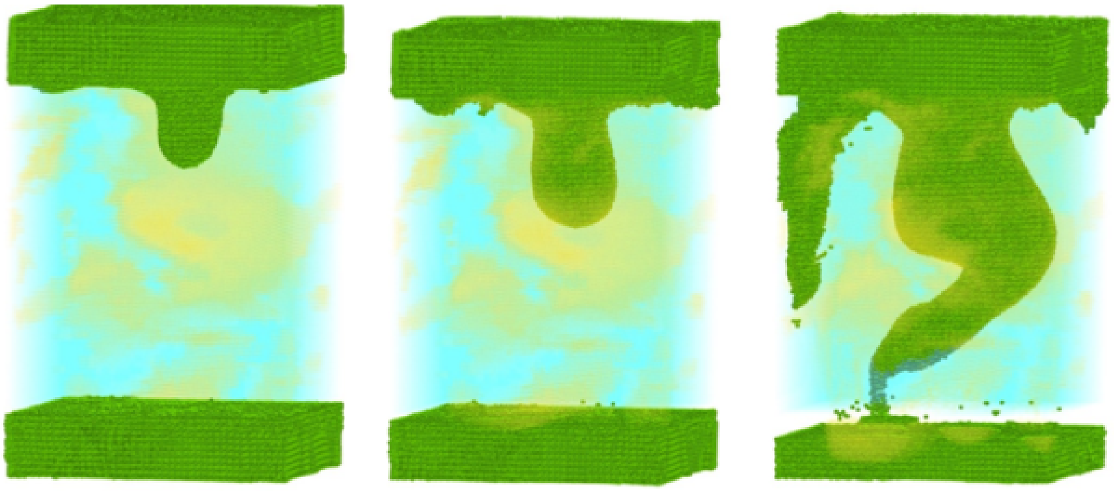

(a) 3D sample at t=2s (b) 3D sample at t=8s (c) 3D sample at t=18s

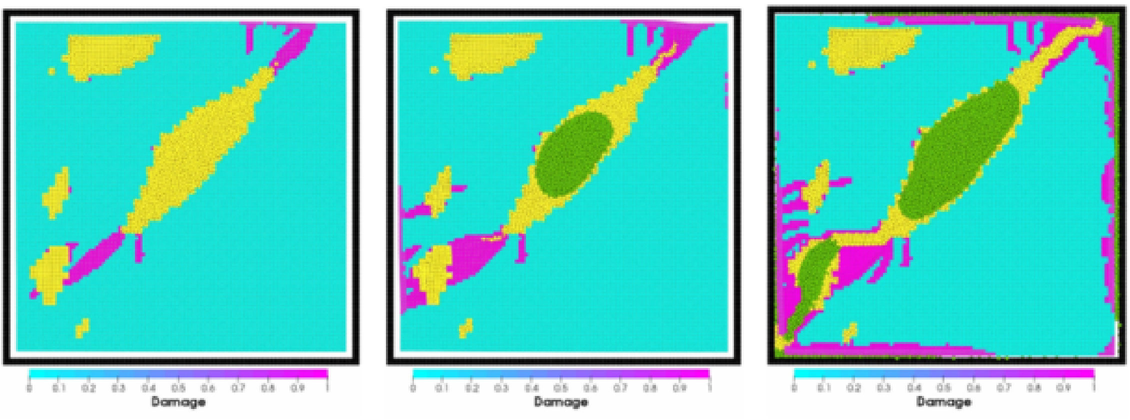

(d) Damage field at t=2s (e) Damage field at t=8s (f) Damage field at t=18s

Figure 2.323: Drainage with confining lateral stress of 6MPa. 3D view of solid (blue) and fluid phases (water in yellow, gas in green) at three different times (a,b and c) as well as damage field within the solid phase (d, e and f) on xy cross-section at z=45h (Deptulski (2021)).

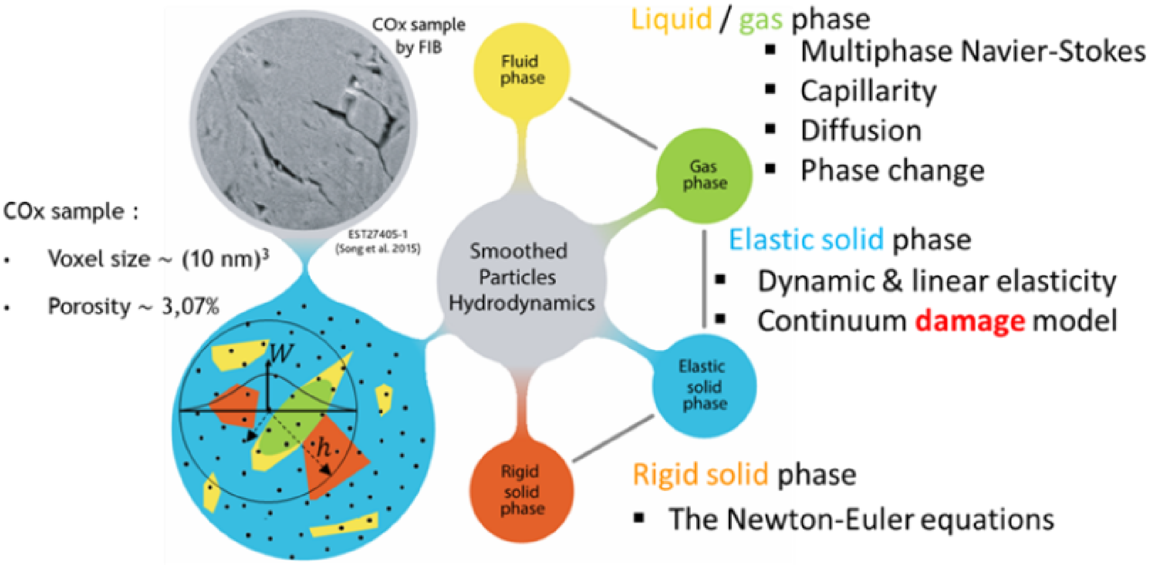

Figure 2.324: Schematic of the SPH model content

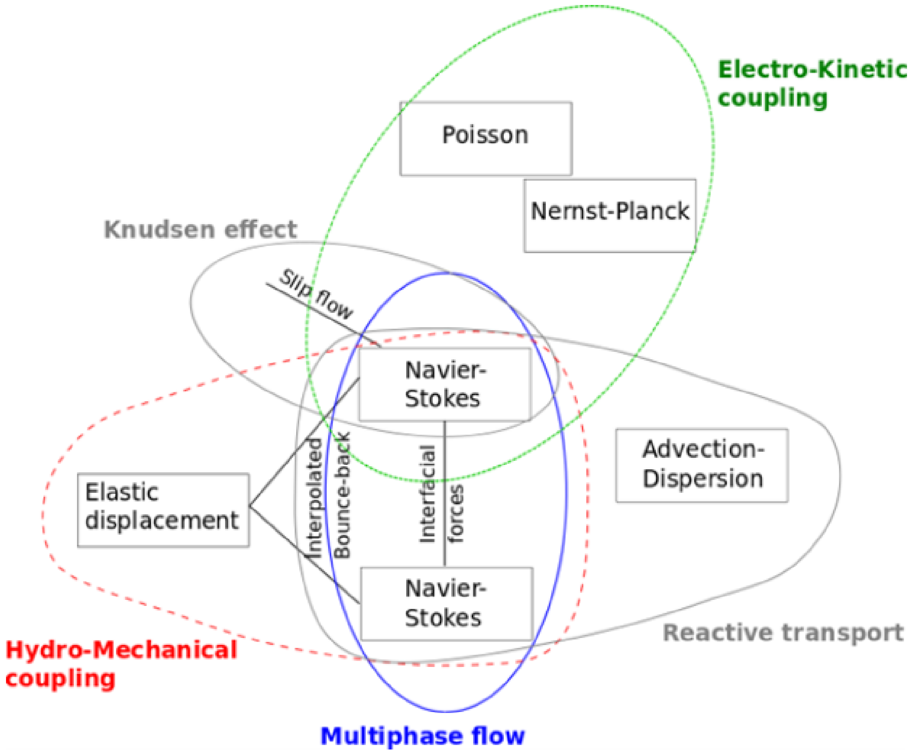

Figure 2.325: Schematic of the LBM model content. Dashed line (red) indicates that the validation of HM coupling in multiphase flow failed (succeeded in single phase flow). Dashed line (green) indicates that validation is under process.

and capillary redistribution and the competition between these processes in nanopores network drying.

- Test the ability of SPH model to deal with HM coupling related to hydrofracturing an then to use this approach to model dilatant flow of gas in a realistic poral network of COx.

2.13.4. Key learning points

2.13.4.1. New knowledge acquired

In general, DNS simulations on pore-scale have proved to be feasible in terms of numerical stability for adequate physical parameters. Several multiphysical couplings were studied and in particular it was observed that:

- FIB-SEM images can be used with DNS to compute upscaled properties, including multiphase properties at high water saturation
  - However, there are still limitations in computational capacity leading to choosing either domain sizes smaller than the REV, or to insufficient resolution in particular to tackle multiscale heterogeneities or sub-resolution processes such as water films at lower saturation.
- In nano-scale poral networks Kelvin effect is a significant phenomenon impacting invasion patterns, breakthrough time and breakthrough saturation.
  - Relative importance of Kelvin effect with drying, drainage and dilatant flow remains to be evaluated, but the developed SPH software enables this study.

- Drying patterns can be categorized using evaporation – capillary number. Possible impact of condensation on breakthrough time and multiphasic behavior is highlighted.

- SPH method is able to solve explicit interaction of pressurized fluid and deformable elastic media with a satisfactory precision.
- In planer stress conditions, SPH with an appropriate damage model can simulate hydrofracturing with a reasonable approximation of critical fracturing pressure.
- This upgraded damage model allows for simulating of gas percolation inside COx poral network with damage driven fracturation (mimicking dilatant flows) and confining stress dependence of breakthrough behavior.

2.13.4.2. Impact of acquired knowledge

Numerical upscaling of multiphasic properties and a better understanding of significant phenomena at the pore scale allows the improvement of core scale parametrisation and hypotheses respectively.

Since small scale experimental results were (or still will be) produced later than initially foreseen in the project, we have concentrated in our work on model development and validation. However, the existence of pore-level HMgas codes will bring new possibilities in the future for interpreting laboratory data and shall be an interesting starting point for upscaling approaches.

2.13.4.3. Remaining knowledge gaps

Various phenomena (capillary flow with drainage, capillary flow and drying with Kelvin effect, dilatant flow and fracturing) are modelled, but relative importance and coupling of which phenomena is still to study, as well as introducing other coupling (e.g. reactivity) thus requiring development and improvement of THMC coupling including at the pore scale.

Upscaling towards macroscopic properties remains challenging considering:

- Availability of 3D images with pertinent resolution (lower than 10nm)
- Computational performance and limitations of DNS, including limitations for using actual in situ parametrisation (e.g. very low capillary number)
- Dependence of some properties on environmental characteristics (such as temperature) and their implementation in DNS
- Determination of effective properties for coupled processes.

2.13.4.4. Recommendations for the future

DNS modelling should be continued since it allows to bring valuable insights on low scale processes. In order to overcome the difficulties related with computational performance it would be interesting to couple DNS with novel simulation tools (surrogate models, IA, etc.) for which DNS can provide training inputs or constitute lowest size stage for multi-scale embedded applications.

.

UPC

2.14. Two-phase flow model coupled with mechanical deformations within the FE code CODE_BRIGHT (UPC)

Executive Summary

The safest long-term management solution for high-activity radioactive waste is known as geological disposal. Many countries (e.g. Canada, Finland, France, Switzerland, Sweden, UK and USA) have chosen to dispose of all or part of their spent nuclear fuel in facilities constructed at an appropriate depth in stable geological formations. Bentonite based materials have been proposed as engineered barrier system around the canister because of their high retention capacity, high swelling ability and low permeability (Toprak et al., 2020) (Toprak et al., 2020).

In the repository gas will be generated by several mechanisms, such as the anaerobic corrosion of metals, the microbial degradation of organic wastes and the radiolysis of water, which generate hydrogen, oxygen, methane and carbon dioxide. In the case of the engineer barriers, gas transport could take place mainly through preferential pathways, like the joints between compacted bentonite blocks, interfaces between different components or along the interface between host rock and buffer material. After the complete saturation of the barrier, gas generated will increase up to a locally defined threshold or breakthrough pressure, from which gas flow will take place through temporary pathways. Once breakthrough pressure is reached, preferential pathways will be created. The size of these pathways would depend on gas local pressure and structural clay restrictions. These pathways would close once gas pressure decrease below a certain value, known as residual pressure. Meanwhile, gas pressure will increase again at the interface up to a new threshold pressure. Therefore, the gas generated will be transported outwards in a cyclic manner, regulated by the opening and closure of pathways, which will depend on the pressure reached (Gutiérrez Rodrigo, 2019).

In order to investigate gas migration from bentonite barrier (FEBEX bentonite) and gas pathway development along the barrier; hydro-mechanical simulations of breakthrough tests on FEBEX material (Gutiérrez Rodrigo, 2019) have been performed.

2.14.1. Model introduction

Gas diffusion, two-phase flow and two-phase flow coupled with mechanical effects are some of mechanisms for gas transport that may lead to generation of apertures (small fractures) in the porous medium. Due to low permeability of EBS components, the air entry pressure is higher. Therefore, a higher capillary pressure is needed for the desaturation of clay based material during gas injection.

Under a certain rate of gas generation, the gas pressure may increase and once reaching values of BT, gas fracture processes will begin. Alternatively, through gas generation, gas may flow through existing discontinuities (Olivella et al., 1994). In order to take into account fracture opening and/or fracture formation because of gas generation a proper mechanical model is required.

In this work, a standard two-phase flow model has been used to simulate gas breakthrough tests on FEBEX material. The flow model is coupled to mechanical deformation. During gas injection, gas flow pathways develops (Figure 2.326). It is a continuous model where apertures have cubic law for permeability (Olivella and Alonso, 2008a).Generated gas is transported in a cyclic manner, regulated by the opening and closure of pathways.

Permeability increases during gas injection because of aperture of the fractures and reduces during closure of these apertures. Basic features of the model such as permeability coupled to mechanical behaviour evolution of intrinsic permeability according to deformation rate (Olivella and Alonso, 2008a) and its impact on pathway development are shown in Figure 2.326. Hydro-mechanical models' equations and parameters are summarized from Table 2.87 to Table 2.90. Equations for the advective and dissolved non-advective gas flow can be found in details in (Olivella and Alonso, 2008a) and Olivella et al., 1994 (Olivella et al., 1994).

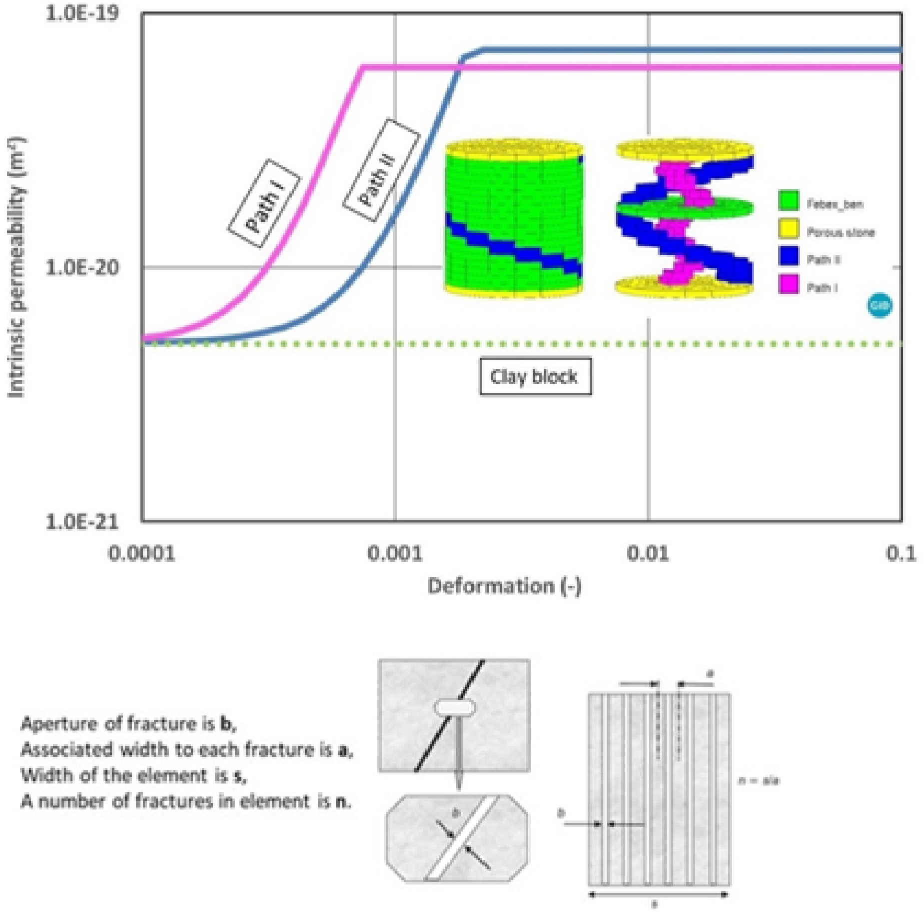

Aperture of fracture is **b**,
Associated width to each fracture is **a**,
Width of the element is **s**,
A number of fractures in element is **n**.

$$k_{\text{int}} = k_{\text{matrix}} + k_{\text{fractures}}$$

$$k_{\text{fractures}} = \frac{b^3}{12a}, \qquad b = b_0 + \langle \varepsilon - \varepsilon_0 \rangle a \leq b_{\max}$$

Figure 2.326: Relationship between intrinsic permeability and deformation in the Model. Cubic law for permeability used for preferential paths.

Laws	Parameter	Units	Symbol	Equations
Van Genuchten retention curve	Capillary pressure parameter (in $P(\phi)$)	(MPa)	P_0	$S_l = \left(1 + \left(\frac{p_g - p_l}{P}\right)^{\frac{1}{1-\lambda}}\right)^{-\lambda}$
	Shape parameter in $\lambda(\phi)$	(–)	λ_0	
	Maximum saturation	(–)	S_{ls}	
Advective Darcy flux	Reference intrinsic permeability	(m^2)	k_0	$\mathbf{q}_l = -\frac{\mathbf{k}k_{rl}}{\mu_l}(\nabla p_l + \rho_l g \nabla z)$
	Reference porosity	(–)	ϕ_0	$\mathbf{k} = \mathbf{k}_0 \frac{\psi^3}{(1-\psi)^2} \frac{(1-\psi_0)^2}{\psi_0^3}$
	Initial porosity	(–)	ψ	
Gas relative permeability	Gas relative permeability – constant	(–)	A	$k_{rl} = AS_{eg}^{\lambda}$
	Gas relative permeability – power	(–)	λ	$S_{eg} = \frac{S_g - S_{rg}}{S_{gs} - S_{rg}}$
	Maximum gas saturation – power	(–)	S_{gs}	
Cubic law for permeability	Initial aperture to calculate a variable aperture	(m)	b_0	$b = b_0 + \Delta b$
	Spacing of the fractures:	(m)	a	$k = k_{max} + \frac{b^3}{12a}$
	Reference strain to calculate aperture variations	(–)	ε_0	$\Delta b = a\Delta\varepsilon = a(\varepsilon - \varepsilon_0)$
	Maximum aperture. Upper bound of aperture.	(m)	b_{max}	for $\varepsilon > \varepsilon_0$

Table 2.87: Constitutive equations for hydraulic laws used in the model

Equation	Parameter	Units	Symbol	FEBEX	Path I	Path II
Van Genuchten retention curve	Capillary pressure parameter (in $P(\phi)$)	(MPa)	P_0	20	20	20
	Shape parameter in $\lambda(\phi)$	(–)	λ_0	0.18	0.18	0.18
	Maximum saturation	(–)	Sls	1	1	1
Advective Darcy flux	Reference intrinsic permeability	(m^2)	k_0	5×10^{-21}	5×10^{-21}	5×10^{-21}
	Reference porosity	(–)	ϕ_0	0.33	0.33	0.33
	Initial porosity	(–)	ψ	0.33	0.33	0.33
Gas relative permeability	Gas relative permeability – constant	(–)	A	100	100	100
	Gas relative permeability – power	(–)	λ	3	3	3
	Maximum gas saturation – power	(–)	Sgs	1	1	1
Cubic law for permeability	Initial aperture to calculate a variable aperture	(m)	b_0	–	1×10^{-9}	1×10^{-9}
	Spacing of the fractures:	(m)	a	–	1×10^{-5}	4×10^{-5}
	Reference strain to calculate aperture variations	(–)	ε_0	–	1×10^{-6}	1×10^{-6}
	Maximum aperture. Upper bound of aperture.	(m)	b_{max}	–	2×10^{-8}	3×10^{-8}
Diffusive Fick flux	Tortuosity coefficient	(–)	τ	0.8	0.8	0.8

Table 2.88: Hydraulic parameters of materials.

Most of the mechanical model (BBM) parameters have been derived from Alonso et al. (1990) and Gens et al. (2009). Back analyses of a swelling pressure test on FEBEX material has been performed in order to calibrate some of BBM parameters listed in Table 2.90. More details about FEBEX material can be found in (Enresa,2000) (Enresa, 2000) and (Enresa,2006) (Enresa, 2006).

Calibration of gas permeability is shown in Figure 2.327 . Water retention curve, LC curve and *s*-p_{eff}-*q* path for the clay are shown in Figure 2.328. Sensitivity analyses have been performed on these parameters in Chapter 3.

2.14.2. Initial Calculations

GID as a CAD system and Code_Bright as a Finite Element Method (FEM) program have been used in order to simulate gas breakthrough test (Gutiérrez Rodrigo, 2019) (laboratory scale – Figure 2.329) on FEBEX bentonite material.

Model A and Model B correspond to arbitrary realization of heterogeneity assuming some preferential paths (A and B) and some random heterogeneous zones (B). In the future, more realizations should be

Parameters	Units	Symbol	Equations
Parameters for elastic volumetric compressibility against mean net stress change	(–)	κ_{i0}	$d\varepsilon_v^e = \frac{\kappa_i(s)}{1+e}\frac{dp'}{p'} + \frac{\kappa_s(p',s)}{1+e}\frac{ds}{s+0.1}$
Parameters for elastic volumetric compressibility against suction change	(–)	κ_{s0}	
Minimum bulk modulus Poisson ratio	(MPa) (–)	K_{min} ν	$K = \frac{1+e}{\kappa}p', G = \frac{3K(1-2\nu)}{2(1+\nu)}$
Slope of void ratio – mean net stress curve at zero suction	(–)	$\lambda(0)$	$p_0 = p^c \left(\frac{p_0^*(T)}{p^c}\right)^{\frac{\lambda(0)-\kappa_{i0}}{\lambda(s)-\kappa_{i0}}}$
Parameters for the slope void ratio mean net stress at variable suction	(–) (MPa^{-1})	r β	$\lambda(s) = \lambda(0)\left[(1-r)\exp(-\beta s) + r\right]$
Parameter for increase of tensile strength due to suction	(–)	k	$p_s = p_{s0} + ks\ \exp(-\rho\Delta T)$
Tensile strength in saturated conditions Reference pressure for the p_0 function Critical state line Non-associativity parameter	(MPa) (MPa) (–) (–)	p_{s0} p_c M α	$G = q^2 - \alpha M^2\left(p' + p_s\right)\left(p_0 - p'\right)$
Initial void ratio Pre-consolidation mean stress for saturated soil	(–) (MPa)	ε_0 $p*_0$	$dp_0^* = \frac{1+e}{\lambda(0)-\kappa_{i0}}p_0^* d\varepsilon_v^p$

Table 2.89: Constitutive equations for mechanical law used in the model.

Parameters	Units	Symbol	FEBEX
Parameters for elastic volumetric compressibility against mean net stress change	(–)	κ_{i0}	0.04
Parameters for elastic volumetric compressibility against suction change	(–)	κ_{s0}	0.03
Minimum bulk modulus	(MPa)	K_{min}	10
Poisson ratio	(–)	ν	0.4
Slope of void ratio – mean net stress curve at zero suction	(–)	$\lambda(0)$	0.15
Parameters for the slope void ratio mean net stress at variable suction	(–)	r	0.925
	(MPa^{-1})	β	0.1
Parameter for decrease of tensile strength due to temperature	(°C^{-1})	ρ	0.2
Parameter for increase of tensile strength due to suction	(–)	k	0.1
Tensile strength in saturated conditions	(MPa)	p_{s0}	0.1
Reference pressure for the p_0 function	(MPa)	p_c	0.5
Critical state line	(–)	M	1
Non-associativity parameter	(–)	α	0.53
Initial void ratio	(–)	ε_0	0.66
Pre-consolidation mean stress for saturated soil	(MPa)	$p*_0$	12

Table 2.90: Mechanical parameters for materials.

done to analyse the response depending on the distribution of properties.

The sample (FEBEX bentonite) diameter is 38 mm and initial height of the sample is 20 mm. Initial saturation degree of the material is 81% which corresponds to initial water content of 15.3%. The test has been performed under constant volume.

The model has a 3D full geometry where porous stones have been simulate as separate materials. The geometry has structured mesh and the number of hexahedra elements is 960. There are 1197 nodes.

The injector system have been introduced to the model as a boundary condition. Prescribed gas pressure has been applied from one end of the sample in the model. Boundary conditions have been shown in Figure 2.330). The model calibration has been performed by means of comparison of back pressures.

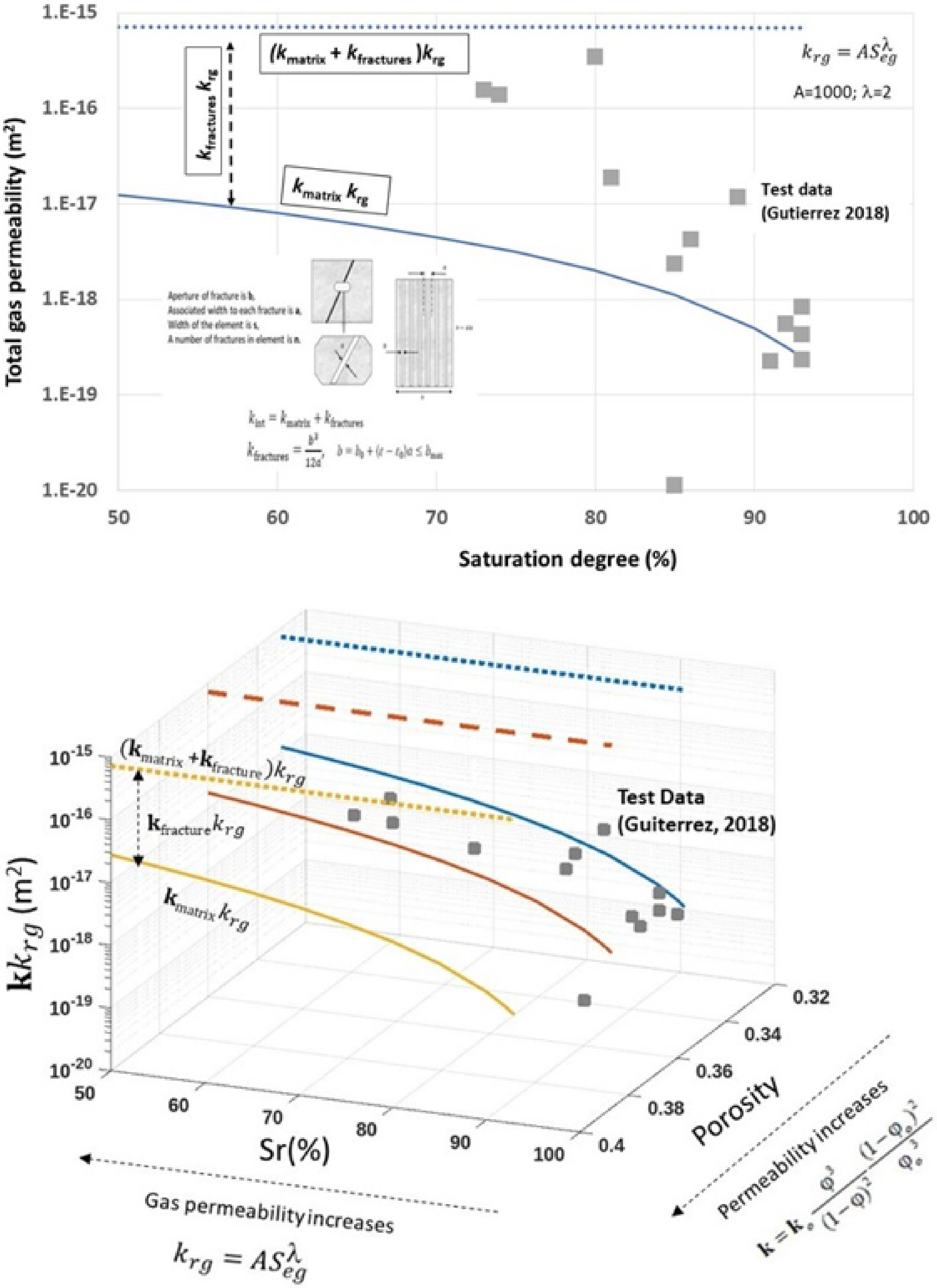

Figure 2.327: Calibration of total gas permeability parameters.

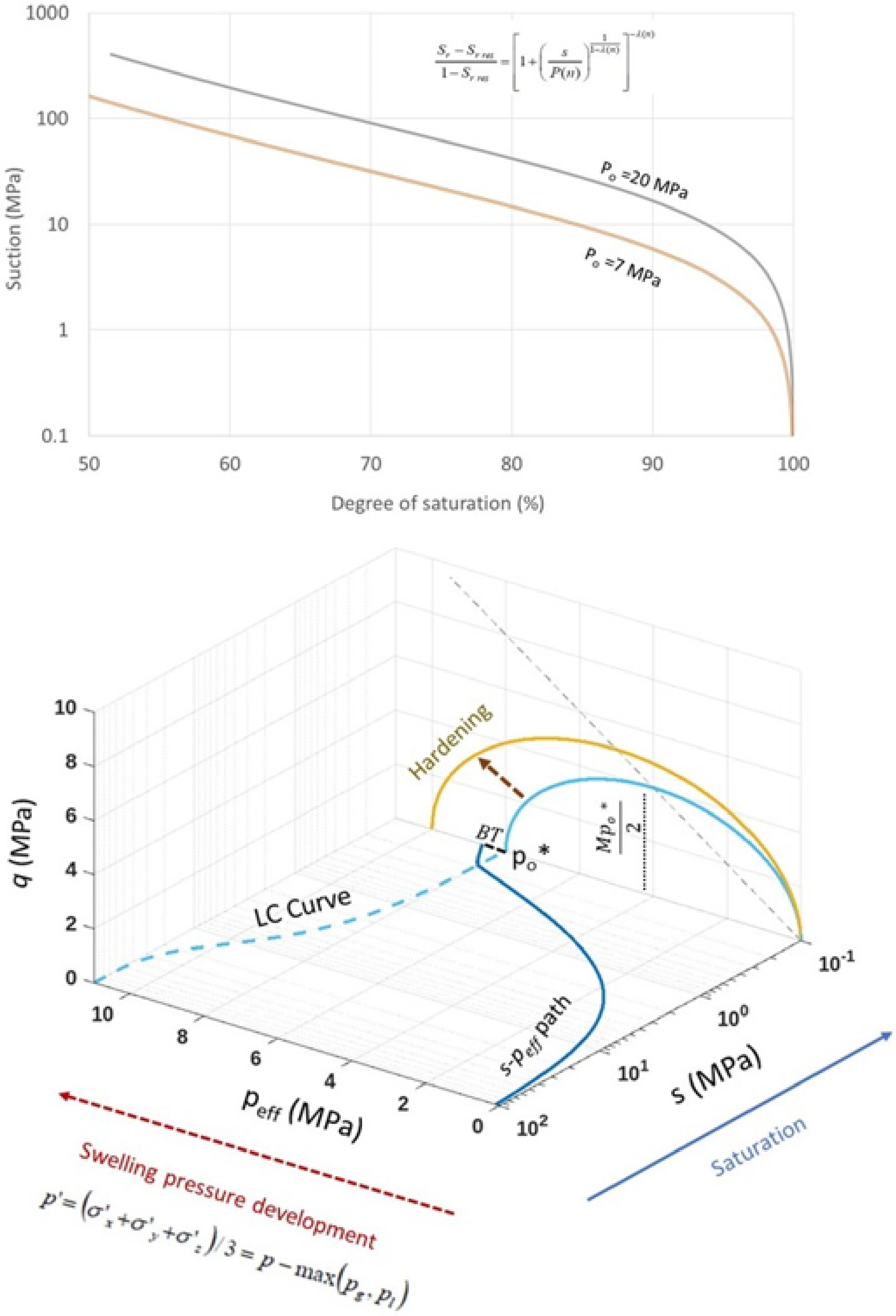

Figure 2.328: Water retention curve (above) and calibration of mechanical parameters (BBM) of the clay. LC curve and p_{eff}-q-s path (below).

Hydraulic boundary conditions, together with time stepping and prescribed gas pressure on the upper and lower boundaries are depicted in Figure 2.330. The sample has been saturated during 60 days. After reaching the full saturation, gas injection takes place till breakthrough pressure. When the second breakthrough happens, the gas pressure source is closed. There is no water supply from lower or upper

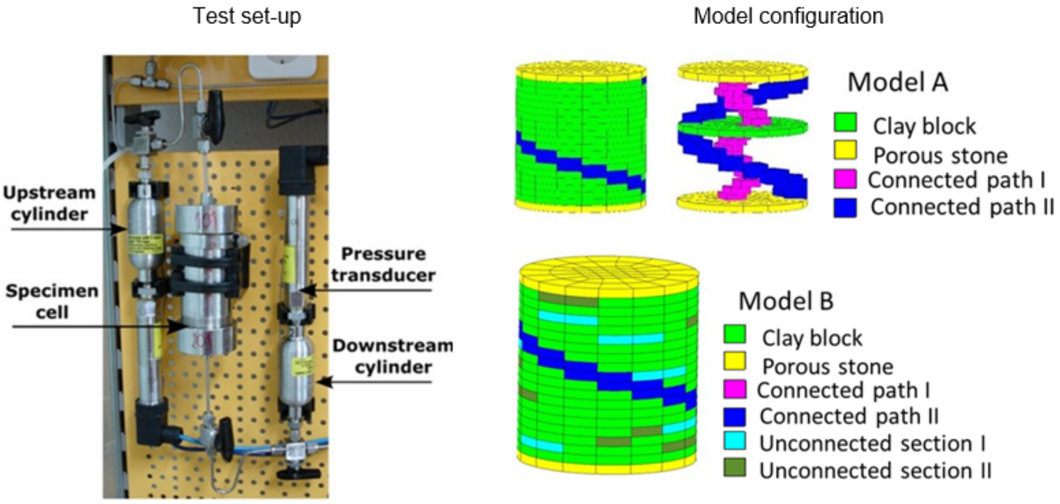

Figure 2.329: Test set-up and models (A and B) presentation (Gutiérrez Rodrigo, 2019). Model A and Model B correspond to arbitrary realization of heterogeneity assuming some preferential paths (A and B) and some random heterogeneous zones (B). In the future, more realizations should be done to analyse the response depending on the distribution of properties.

part of the sample during gas injection steps. There is no water or gas injection from lower part during gas injection steps. Lower part remains under initial conditions following to saturation (no gas or water injection).

Total inflow from upper boundary where the gas injection takes place and corresponding accumulated gas volume in the model are shown in Figure 2.331. At the end of first breakthrough, both in the test and in the model; total injected volume of gas is around 0.29 cm^3.

Hydro-mechanical parameters used for materials are listed in Table 2.91 and Table 2.92. Cubic law (Olivella and Alonso, 2008) has been used to simulate preferential paths as a permeability model (Figure 2.326 and Figure 2.327). The global intrinsic permeability is defined as sum of material matrix and internal fracture permeabilities. Cubic law parameters are calibrated by means of back-analyses. Barcelona Basic Model (BBM) (Alonso et al., 1990) has been used as the mechanical model for FEBEX. Porous stones are simulated as separate materials and have elastic parameters.

2.14.3. Model A

Figure 2.332 shows distribution of preferential paths in Model A. Two connected pathways have been incorporated to the geometry in a random manner. Model A corresponds to arbitrary realization of heterogeneity assuming some preferential paths. In the future, more realizations should be done to analyse the response depending on the distribution of properties.

Comparison of back pressure data and Model A results during Phase 2 and Phase 4 is summarised in Table 2.91. In Phase 4, a bigger back pressure has been succeeded. Figure 2.333 shows gas pressure development in the test (Phase 2 and Phase 4) and in the model. The response of back pressure in the Model A is similar to Phase 4. In the numerical model, back pressure develops in a more gradual way compare to the test.

Figure 2.334 shows gas pressure distributions in 30, 58 (first BT), 90 (second BT) and 137 days later the gas injection initiation. Gas pressure evolution on the upper and lower part of the sample is also shown in Figure 2.334. First BT has occurred on 8.6 MPa and 4.4 MPa of back pressure has been achieved. Second BT has occurred in 7.6 MPa and 3.3 MPa of back pressure has been succeeded.

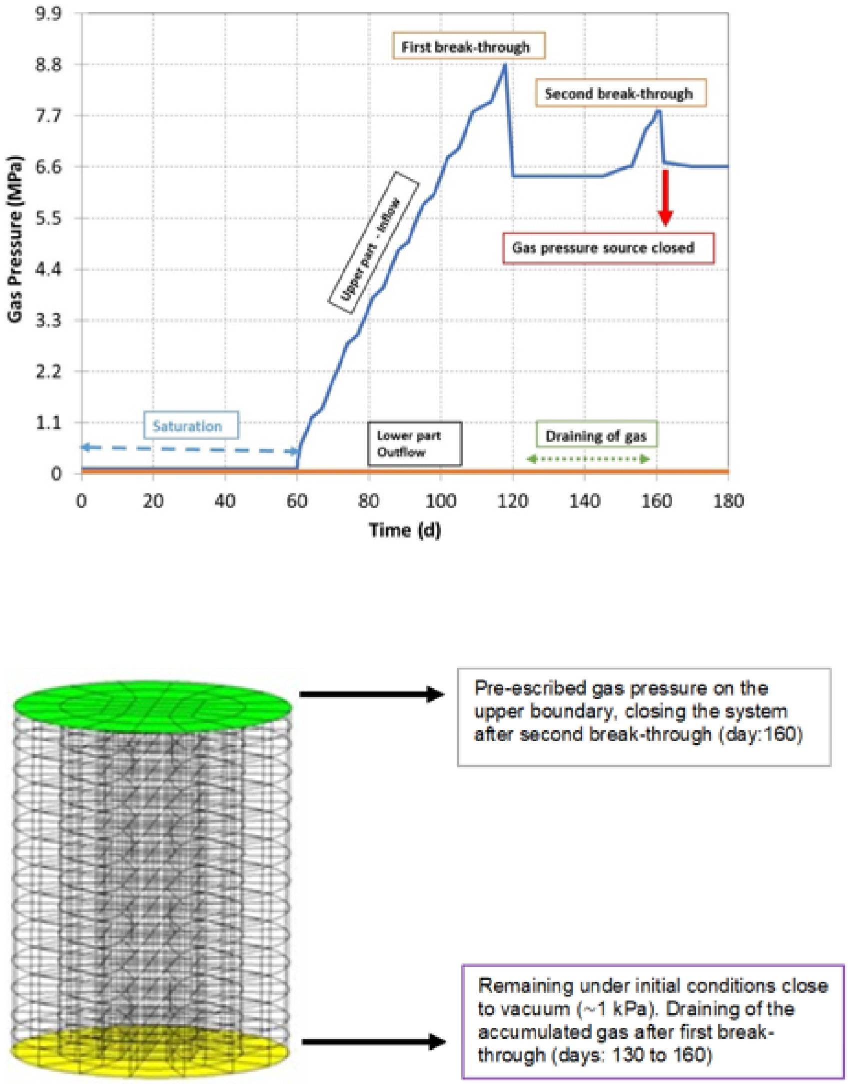

Pre-escribed gas pressure on the upper boundary, closing the system after second break-through (day:160)

Remaining under initial conditions close to vacuum (~1 kPa). Draining of the accumulated gas after first break-through (days: 130 to 160)

Figure 2.330: Gas pressure on the boundaries during gas injection steps.

Figure 2.335 shows distribution of gas diffusion and gas advective flux in 30, 58 (first BT), 90 (second BT) and 137 days later the gas injection initiation. Gas advective fluxes through preferential pathways can be clearly seen during second BT (90 days).

Figure 2.336 shows mean total stresses distributions in 30, 58 (first BT), 90 (second BT) and 137 days later the gas injection initiation. In the Figure 2.336, mean total stress evolution in upper part of the sample is also shown. FEBEX bentonite was initially unsaturated. During the saturation period, swelling pressures have been developed. The total pressure reaches 8.9 MPa at the end of saturation process. After the saturation, water has been drained from the filters and gas injection test has re-started. Mean total stresses has reached to 8.6 MPa at the end of first BT. After first BT, residual gas has been drained from lower part of the sample and finally second BT test has started. The model is capable to simulate swelling pressure development during hydration; gas pressure development during gas injection test including draining process of water and gas under the same 3D configuration.

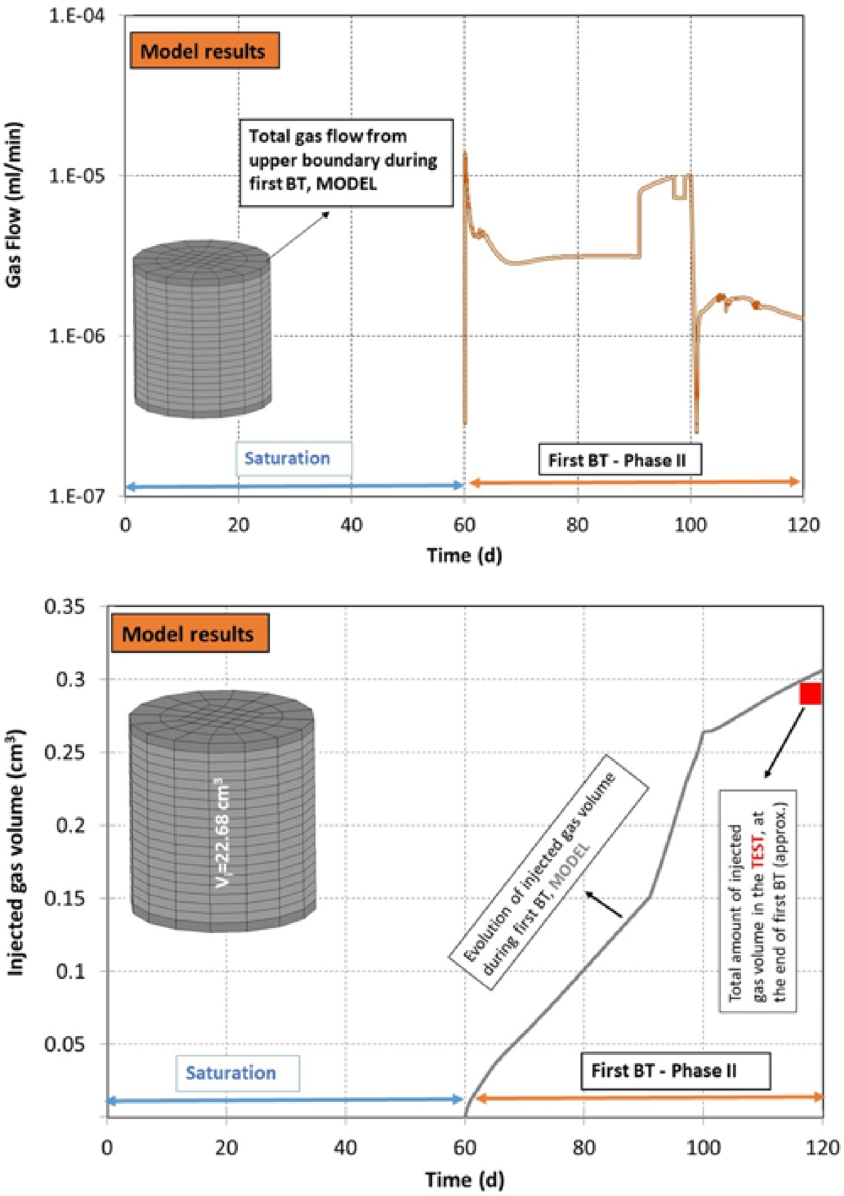

Figure 2.331: Total gas flow from upper boundary and corresponding accumulated injected gas volume in the Model A and in the Test.

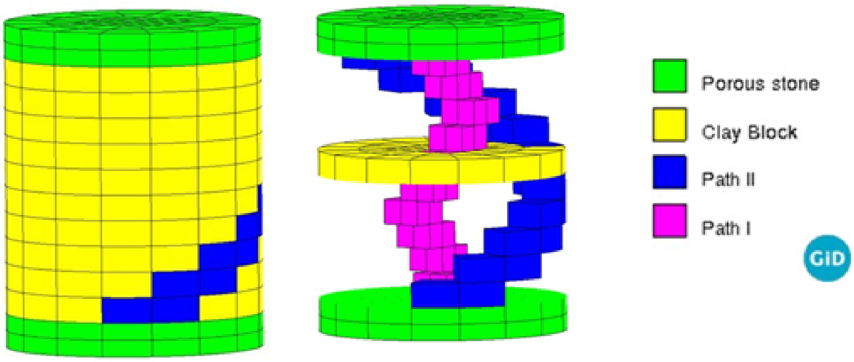

Figure 2.332: Materials considered in the model (A).

Table 2.91: Comparison of back pressure data and model results (Model A).

Breakthrough sequence	Back pressure (MPa) Phase II	Phase IV	Model A

Table 2.91: Comparison of back pressure data and model results (Model A).

Breakthrough sequence	Back pressure (MPa) Phase II	Phase IV	Model A
First BT	2.2	3.5	4.4
Second BT	1.7	3.4	3.3

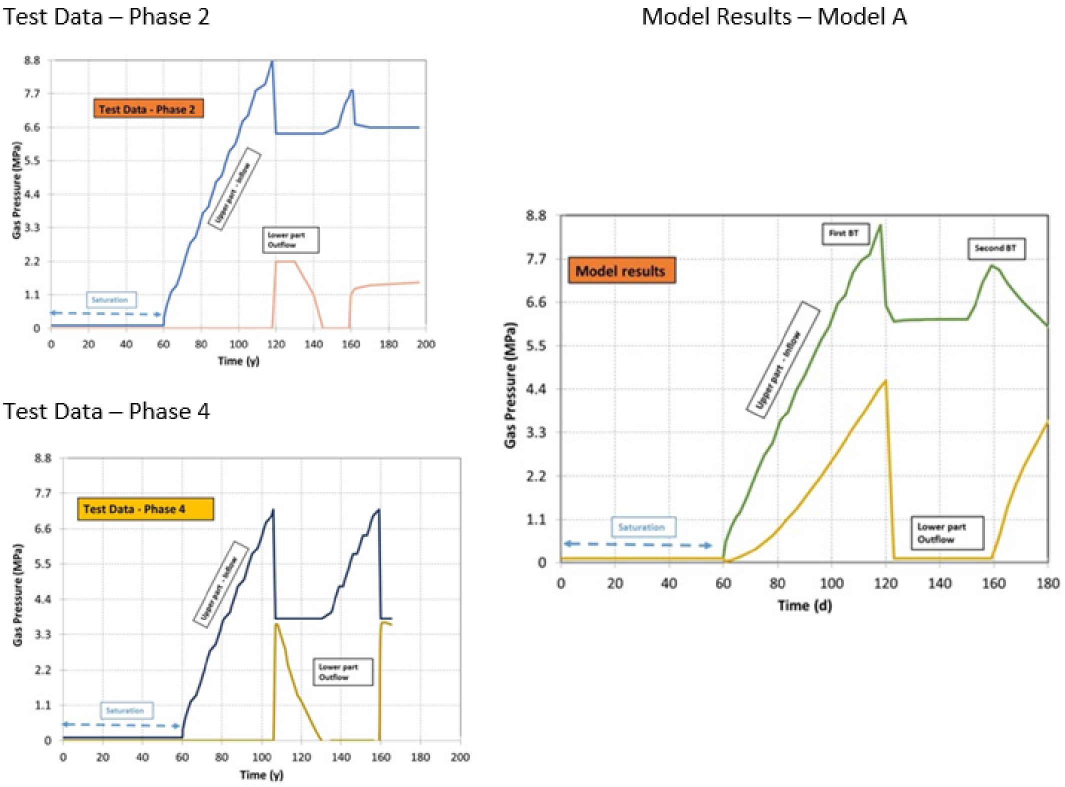

Figure 2.333: Gas pressure development in the tests and in the numerical simulation. (Model A)

2.14.4. Model B

Model B has been generated by means of incorporation of two unconnected sections into Model A geometry. Unconnected section I and unconnected section II has the same parameter set as Path I and Path II, respectively. As there are two unconnected sections in Model B, it is more heterogenous than Model A. Figure 2.337 shows distribution of connected paths and unconnected sections in Model B.

Model A and Model B correspond to arbitrary realizations of heterogeneity assuming some preferential paths (A and B) and some random heterogeneous zones (B). In the future, more realizations should be done to analyse the response depending on the distribution of properties.

Figure 2.338 shows gas pressure development in the test (Phase 2 and Phase 4) and in the Model B. Response of back pressure in the Model B is similar to Phase 4. In the numerical model, back pressure develops in a more gradual way compare to the test.

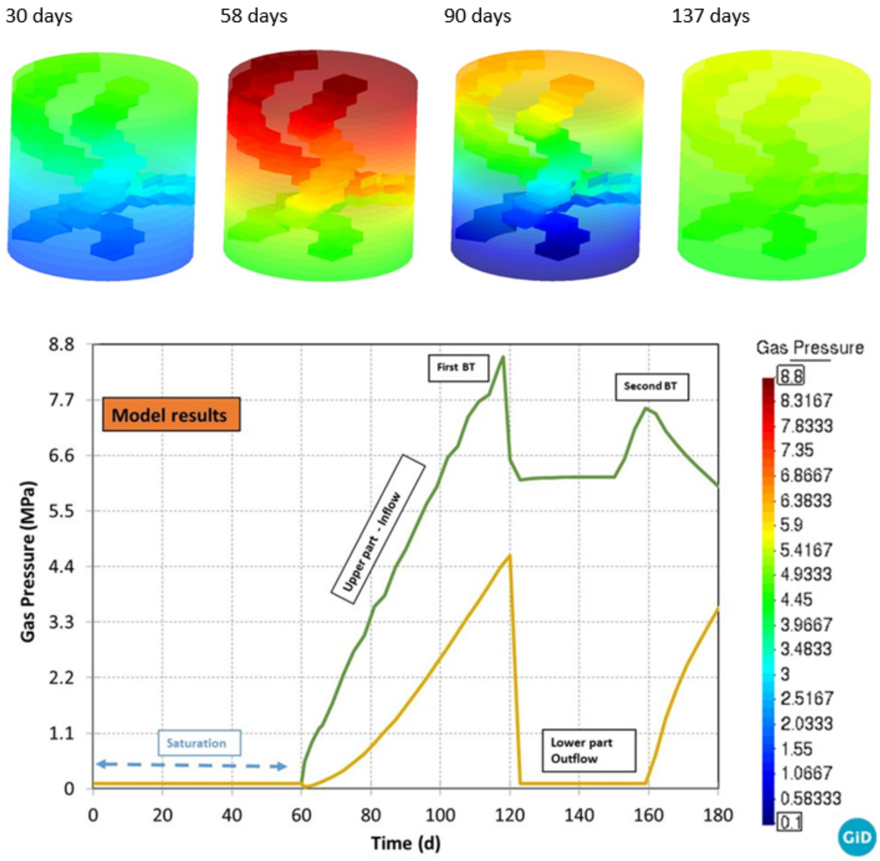

Figure 2.334: Gas pressure distributions in 30, 58 (first BT), 90 (second BT) and 137 days later the gas injection initiation. Gas pressure evolution on the upper and lower part of the sample. (Model A)

Figure 2.339 shows permeability evolution on the upper parts of the sections and distribution (during second BT) in Model B. As the pathways and unconnected sections have cubic law, intrinsic permeability increases during the aperture of these pathways. After the first breakthrough, intrinsic permeability of pathways stabilizes. Once the gas injection re-starts (second BT), pathways are activated and intrinsic permeability starts increasing again. After second BT, gas injection stops and intrinsic permeability of pathways decreases because of closure of fractures.

Figure 2.340 shows distribution of gas advective fluxes in 15, 30, 45 and 60 days in Model B. Gas advective fluxes have been concentrated on preferential pathways. Figure 2.341 shows comparison of gas diffusion (plus gas dispersion), gas advection and gas pressure at 60 days later injection. Diffusion is active in all model domain because it is non advective flux and there is no need of apertures and/or desaturation for gas diffusion. Additionally, gas diffusion is more dominant where gas advection is less relevant. Gas advection shows the preferential path formation.

2.14.5. Extended Models A and B

Model A_Extended and Model B_Extended correspond to time prolonged models that simulate all phases of the test. A summary of the phases and comparison of time stepping of the models are given in Table 2.92. After Phase II, the sample was dismantled and re-saturated. Following to re-saturation, gas injection was performed till first BT in Phase IV. The first BT pressure in Phase IV was 7.1 MPa resulting 3.5 MPa of back pressure. The second BT pressure in Phase IV was 6.6 MPa resulting 3.4 MPa of back pressure. compared to Phase II, gas BT pressures are lower but back pressures are higher. Mean value of gas BT pressure for the whole processes is 7.6 MPa and back pressure is around 3 MPa. There are differences between Phase II and Phase IV in terms of gas BT and back pressures because of changes in porosity-

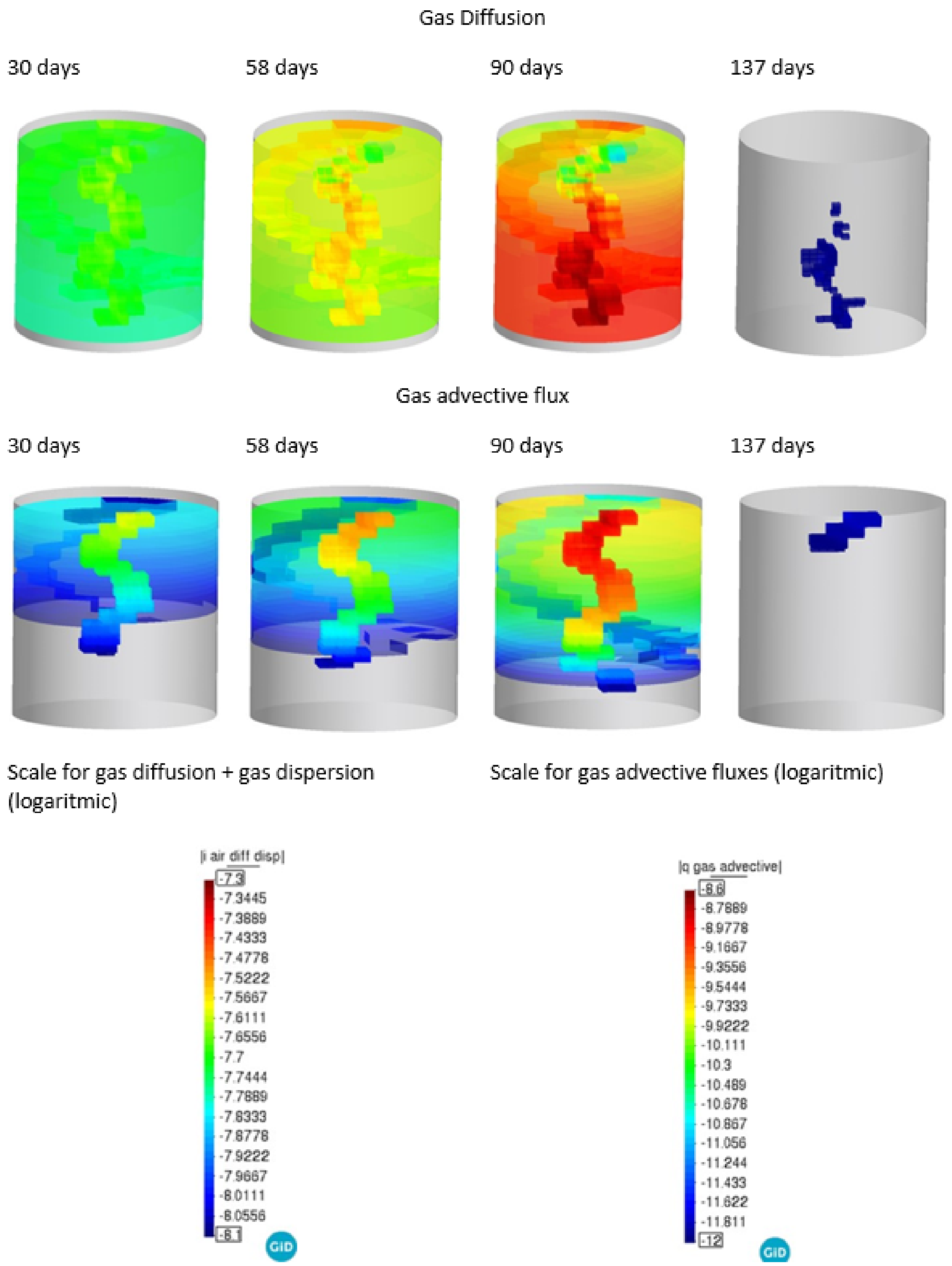

Figure 2.335: Distribution of gas diffusion and gas advective flux in 30, 58 (first BT), 90 (second BT) and 137 days later the gas injection initiation. (Model A)

permeability and material structure during the whole process.

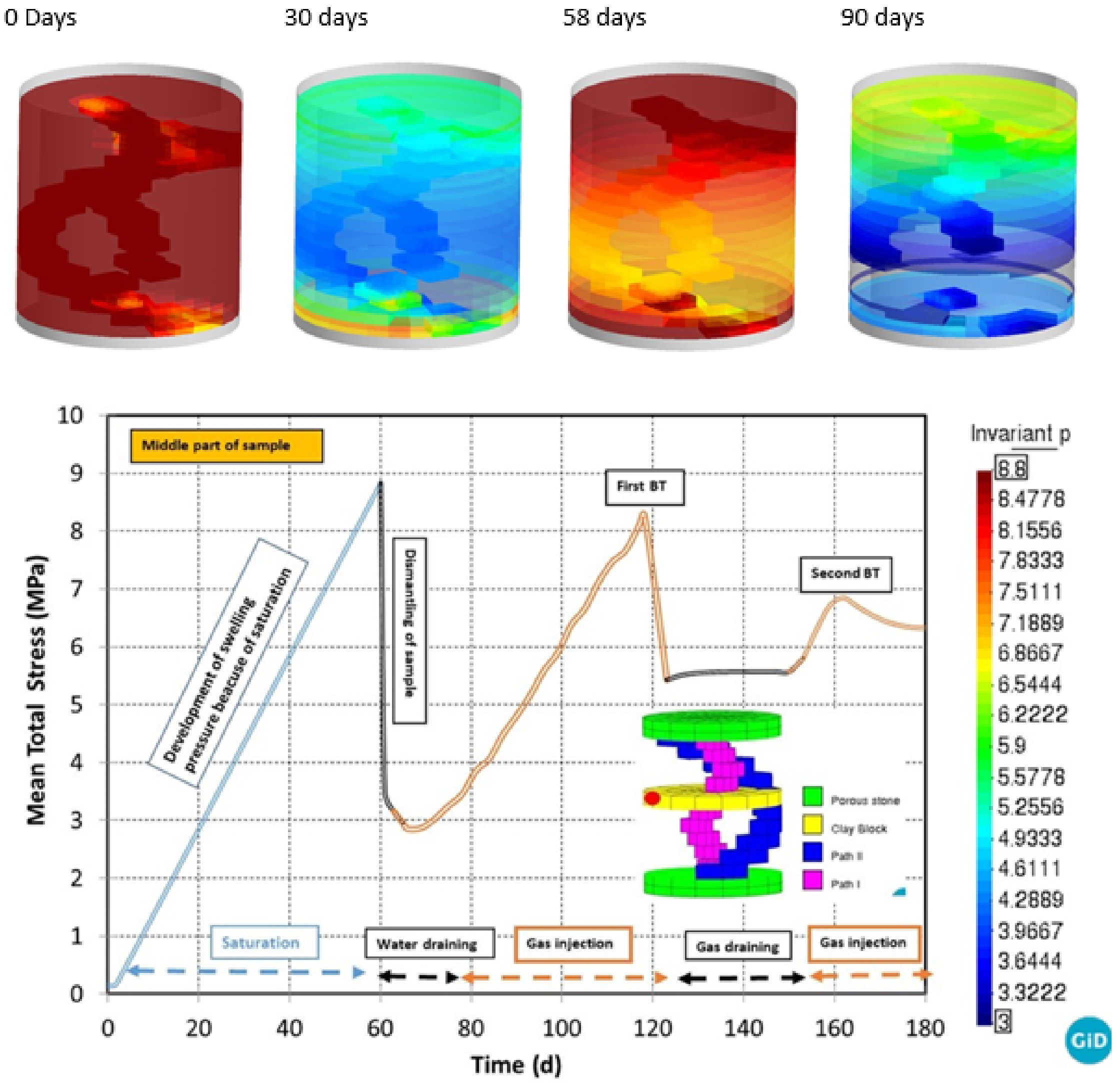

Figure 2.336: Mean total stresses distributions in 30,58 (first BT), 90 (second BT) and 137 days later the gas injection initiation. Mean total stress evolution on the middle part of the sample. (Model A)

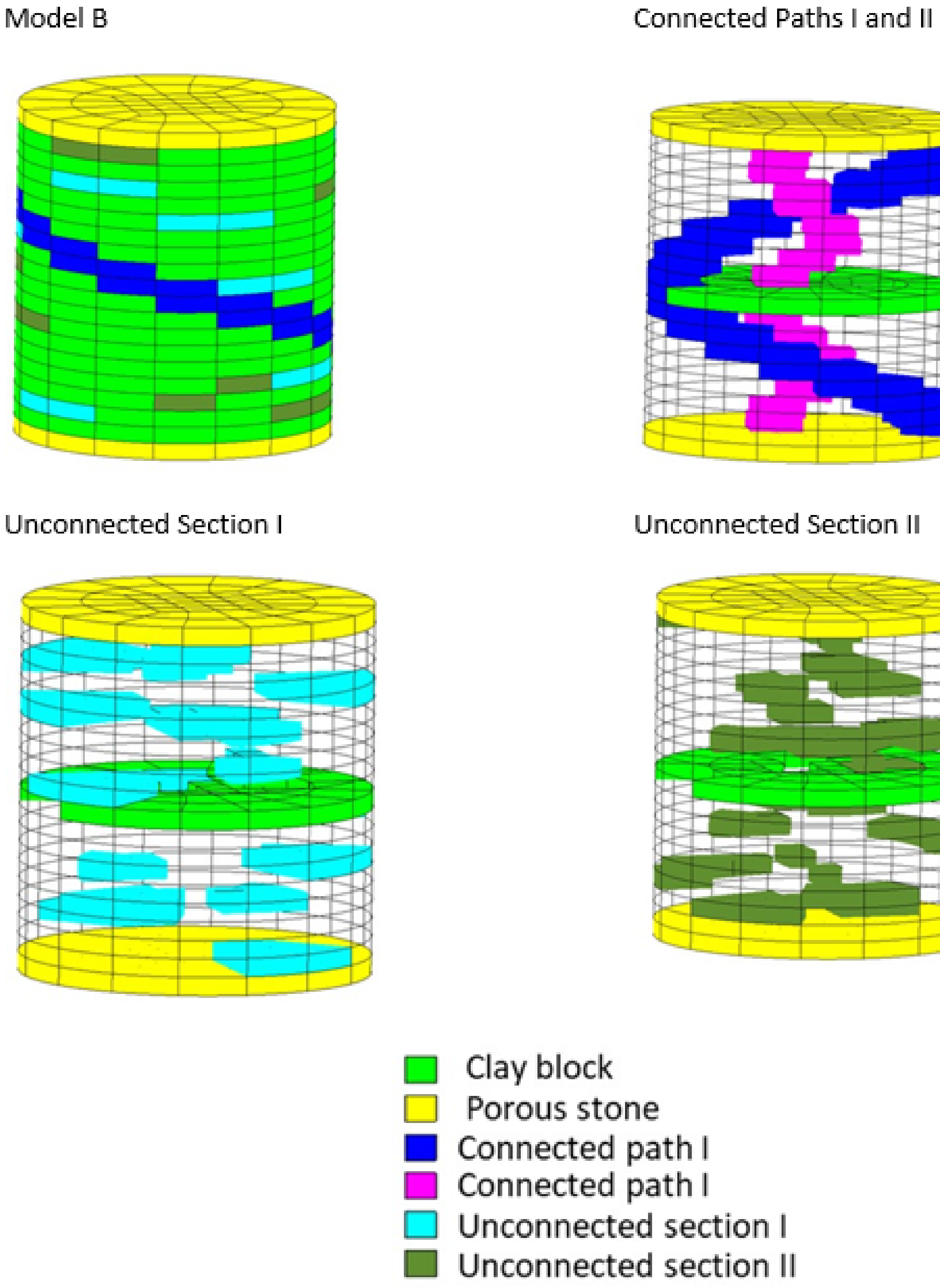

Figure 2.337: Distribution of materials in Model A.

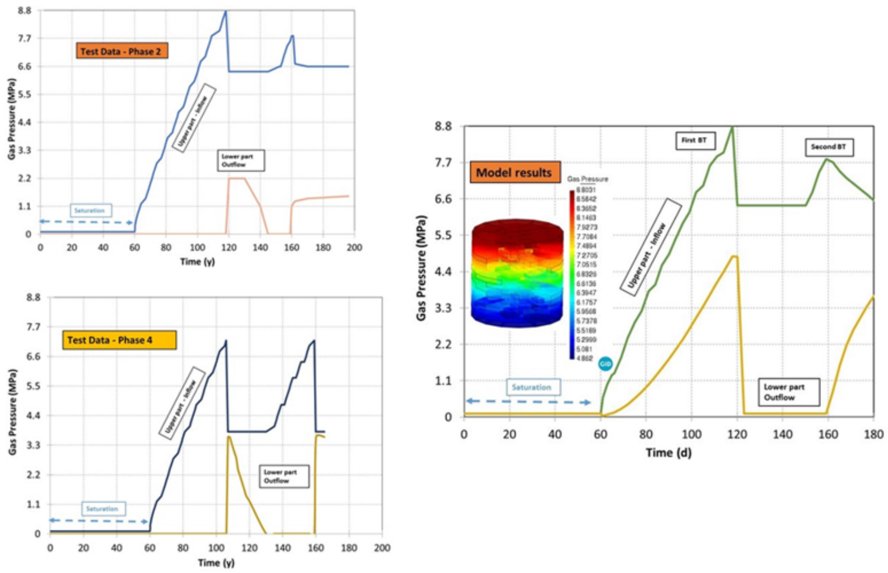

Figure 2.338: Gas pressure development in the tests and in the numerical simulation. (Model B)

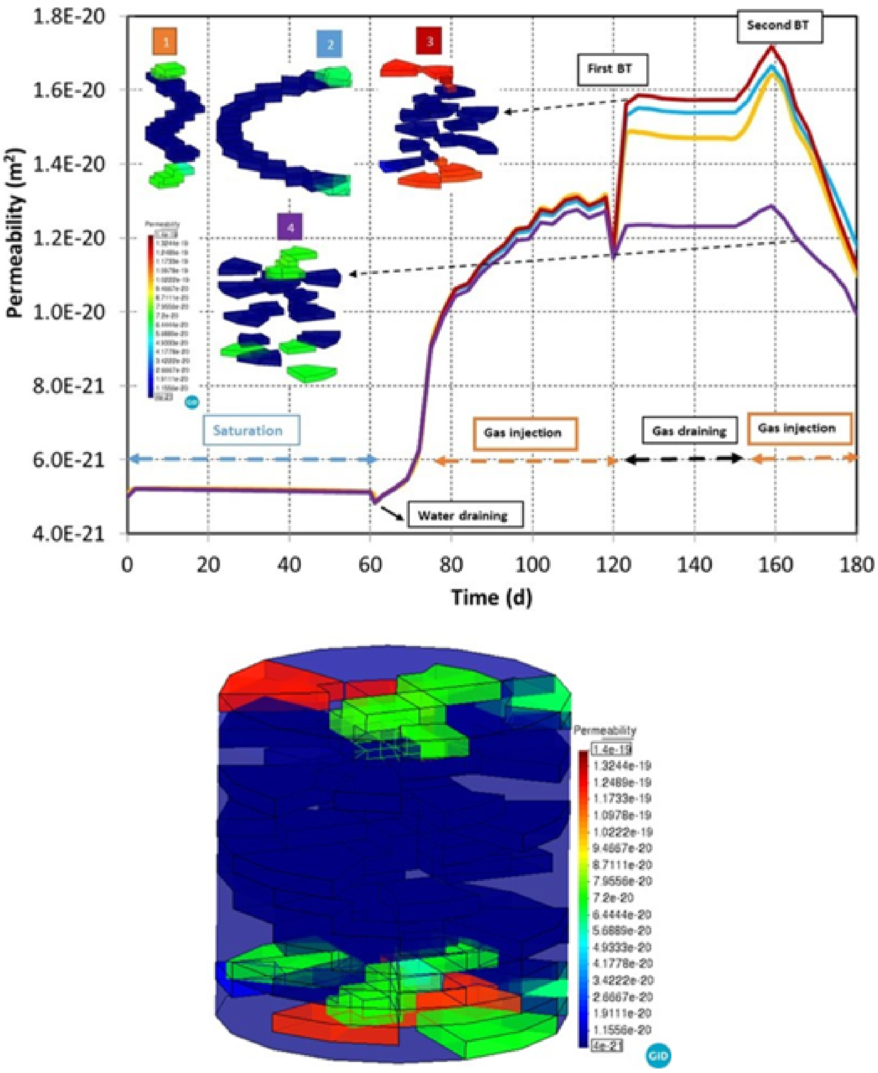

Figure 2.339: Permeability evolution on upper part of the sections and distribution (during second BT) for Model B.

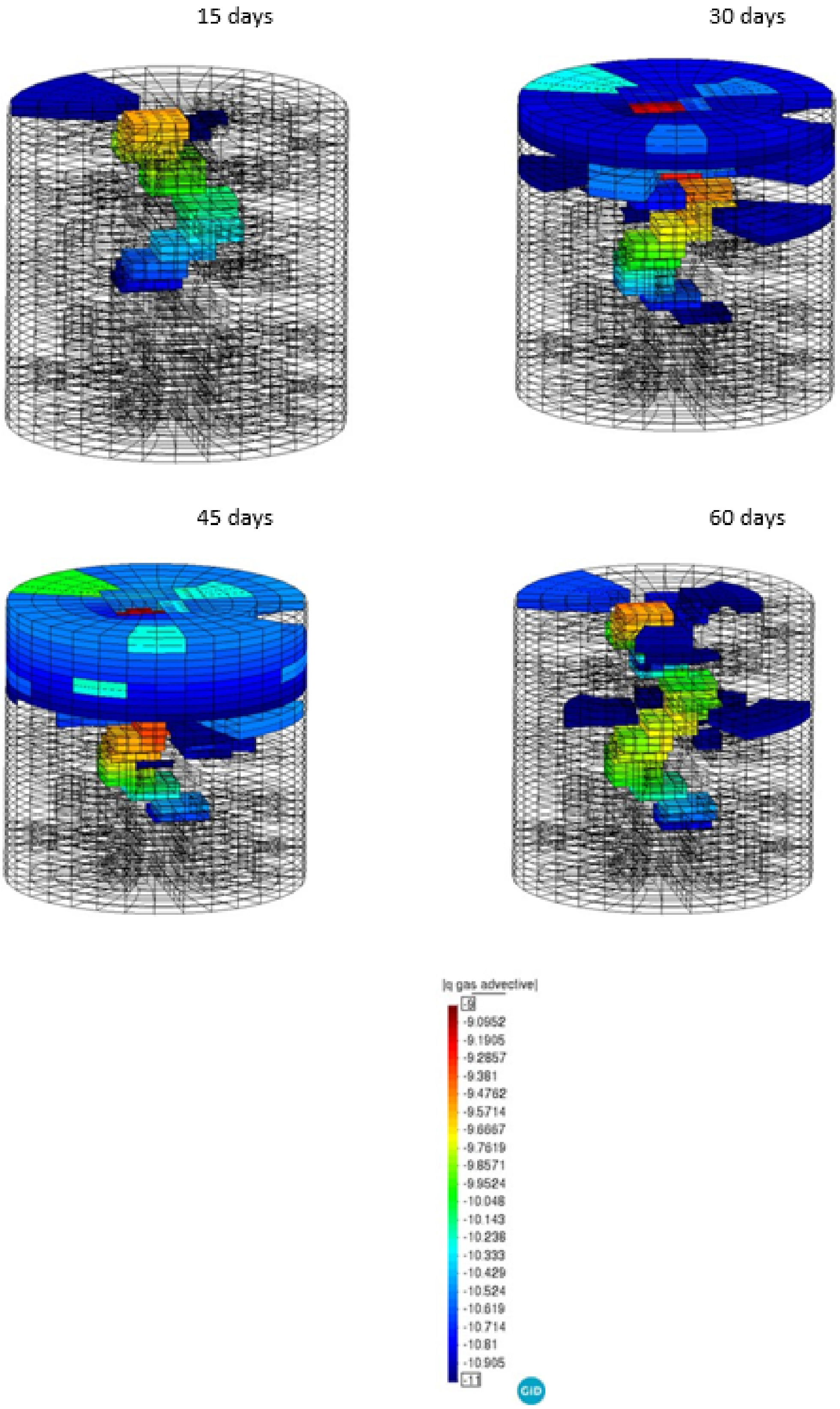

Figure 2.340: Distribution of gas advective fluxes (logarithmic scale) at 15, 30, 45 and 60 days for Model B.

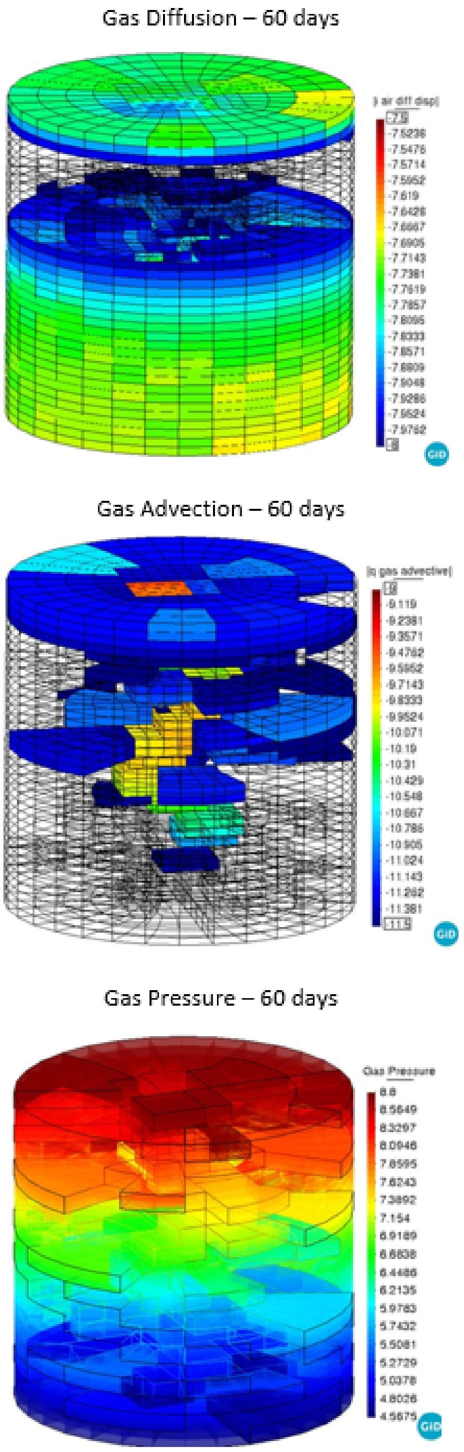

Gas Diffusion – 60 days

Gas Advection – 60 days

Gas Pressure – 60 days

Figure 2.341: Distribution of gas diffusion (plus dispersion), gas advection and gas pressure at 60 days (Model B).

Table 2.92: Comparison of Model A, Model B and Model A_Extended.

Steps of breakthrough tests	Description	Duration (d)	Model A Model B	Model A_Extended Model B_Extended
Phase I	Saturation of the sample	60	+	+
Phase II	Gas injection - first breakthrough pressure	60	+	+
	Gas injection - second breakthrough pressure	80	+	+
Phase III	Dismantling of the sample and re-saturation	60	-	+
Phase IV	Gas injection - first breakthrough pressure	50	-	+
	Gas injection - second breakthrough pressure	50	-	+

Comparison of back pressures in the test and in the models are summarized in **Table 2.93**. Models prediction of back pressures at Phase IV is better than Phase II.

Table 2.93: Comparison of back pressure data and model results (Model A_Extended and Model B_Extended).

Breakthrough sequence	Back pressure (MPa) Test		Model A_Extended		Model B_Extended	
	Phase II	Phase IV	Phase II	Phase IV	Phase II	Phase IV
First BT	2.2	3.5	4.5	3.5	4.5	3.6
Second BT	1.7	3.4	4.5	3	4.6	3

Figure 2.342 shows gas pressure distributions in 120 (Phase II - first BT), 160 (Phase II - second BT), 310 (Phase IV - first BT) and 365 days (Phase IV - second BT). Gas pressure evolution on the upper and lower part of the model domain is also shown in Figure 2.342. In Model A_Extended and in Model B_Extended, back pressure value in Phase IV (first BT) is around 3.5 MPa which is consistent with the test data. Model A_Extended slightly overestimates back pressure in Phase II.

Figure 2.343 and Figure 2.344 shows evolution of total mass fluxes. There are three gas fluxes in the system which are gas advective fluxes (acting on preferential pathways and causing de-saturation because of water replaced by gas), dissolved advective fluxes (flux of dissolved gas into liquid phase) and non-advective fluxes (gas diffusion + dispersion). The sum of these three fluxes gives the total mass fluxes. As shown in Figure 2.343 and Figure 2.344, on the upper part where gas injection takes place; the dominant flux is gas advective flux. However, in central area of the model domain gas diffusion (dissolved non-advective flux) is more significant.

2.14.6. Sensitivity Analyses

In this Chapter, sensitivity analyses are described. The aim of the sensitivity analyses is to improve model capabilities and deal with the data uncertainties. Sensitivity analyses represent alternative material models, geomechanic model parameters and/or initial and boundary conditions. Sensitivity analyses shall remain within the scope set for the reference model in order to maintain modelling consistency. In this study, Model A has been selected as a reference model in order to develop further sensitivity analyses. Beside Model A_Extended, two more models have been prepared in order to check impact of time step

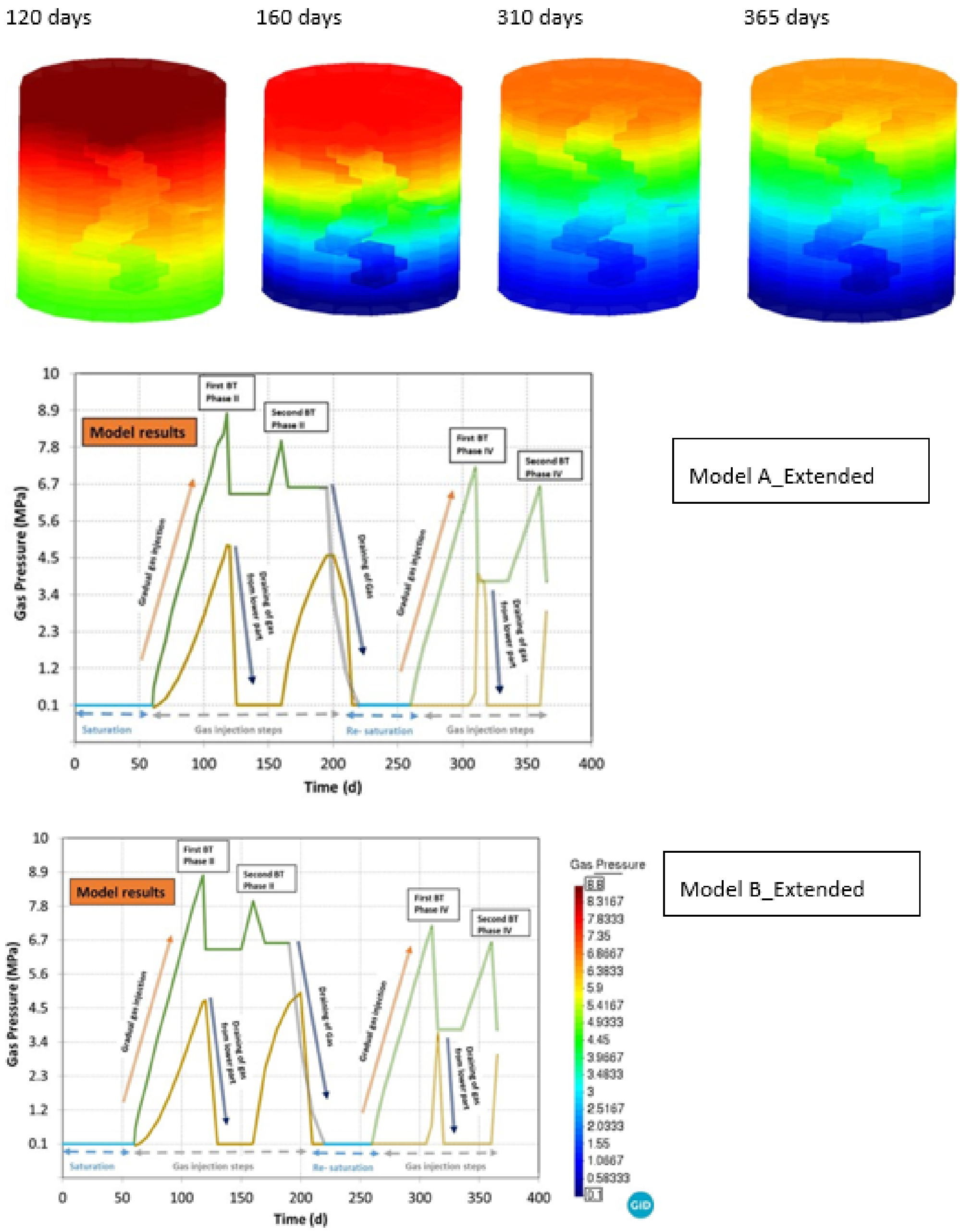

Figure 2.342: Gas pressure distributions in 120 (Phase II - first BT), 160 (Phase II - second BT) and 310 (Phase IV - first BT), 365 (Phase IV - second BT). Gas pressure evolution upper and lower part of the sample (Model A_Extended and Model B_Extended).

(adding more phases of the test), number of nodes-elements and hydro-mechanical model parameters (gas relative permeability parameters, water retention curve parameters, pressure of pre-consolidation and heterogeneous porosity distribution) on the model response. These models are summarized in Table 2.94.

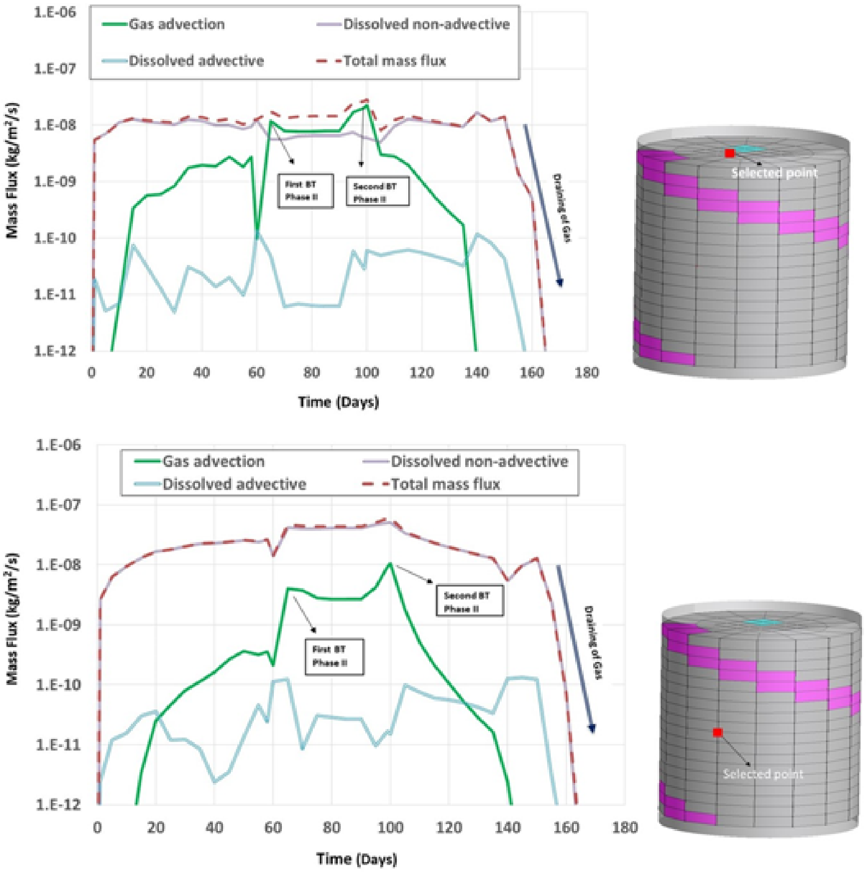

Figure 2.343: Evolution of mass fluxes till Phase III at selected points for Model A_Extended.

Table 2.94: Sensitivity analyses plan

Concept	Observation	Model
Time step	Phase III (re-saturation) and Phase IV (secondary gas injection steps) have been incorporated to Model A.	Model A_Extended (described in Chapter 2)
Hydro-mechanic	Initial heterogenous distribution of porosity has been incorporated to Model A.	Model A_Extended_1
Hydraulic	Gas relative permeability parameters have been modified. Total gas permeability has been increased. Gas entry pressure has been decreased. P_0 (WRC) has been decreased to 7 MPa from 20 MPa. (Figure 2.328, Chapter 1).	Model A_Extended_2
Mechanic	Pressure of pre-consolidation of the clay has been decreased to 8 MPa from 12 MPa (Figure 2.328, Chapter 1). Plasticity has been targeted as the Gas BT pressure was 8.8 MPa.	Model A_Extended_2

Table 2.94: Sensitivity analyses plan

Concept	Observation	Model
Computational	Number of nodes and elements have been increased in order to simulate better heterogeneity of the system.	Model A_Extended_1

Model A_Extended is a prolongation of Model A under the same geometrical configuration (connected paths). Phase III (dismantling of the sample and re-saturation) followed by Phase IV (gas injection steps) have been incorporated to Model A_Extended as discussed in Chapter 2. Figure 2.345 shows initial porosity distribution and describes main differences between the models.

Distribution of gas advective fluxes during the first BT (58 days later gas injection) are shown in Figure 2.346. Gas advective fluxes are mainly concentrated on preferential pathways. Permeability increases on these paths during gas injection because of apertures (cubic law for permeability). In Model A_Extended_2, gas permeability is the highest. Therefore, gas advection flux is the biggest in this model.

Distribution of gas diffusion (plus dispersion) during the first BT (58 days later gas injection) are shown in Figure 2.347. Gas diffusion is less relevant where the gas advection is more significant. While gas advection fluxes are mainly intensified on preferential pathways, gas diffusion is active in whole domain. For the gas diffusion there is no need of neither desaturation nor gas flow pathways development. Gas diffusion is mainly controlled by the porosity.

In Model A_Extended_1, initial distribution of porosity is heterogeneous. Consequently, distribution of gas advection fluxes and gas diffusion is relatively more heterogeneous in Model A_Extended_1 compare to other two models.

Figure 2.348 and Figure 2.349 shows evolution of total mass fluxes. There are three fluxes in the system which are gas advective fluxes, dissolved advective fluxes (dissolved gas into liquid phase) and non-advective fluxes (diffusion + dispersion). The sum of these three fluxes gives total mass fluxes as discussed in Chapter 2.

A node close to gas injection source has been selected in order to compare total fluxes in these three models. Gas advection is dominant in this selected point. Gas advection is more active in Model A_Extended_2 compare to other models because of higher gas permeability. As shown in Figure 2.349, total mass fluxes are bigger in Model A_Extended_2. There is no significant differences between Model A_Extended and Model A_Extended_1 during the first and second BT in terms of total mass fluxes. In the model, prescribed gas pressure has been applied from the upper part of the model domain. In three models, the prescribed pressures are same. However, there have been more total gas fluxes in Model A_Extended_2 because of higher permeability (both liquid and gas) and lower gas entry pressure.

Distribution of permeability during the first BT (58 days later gas injection) for three models are shown in Figure 2.350. In the preferential pathways, the permeability is higher compare to other sections in all three models. Model A_Extended_2 is more permeable than the other two models.

Distribution of liquid saturation degree during the first BT (58 days later gas injection) for three models are shown in Figure 2.351. Evolution of permeability and degree of saturation are shown in Figure 2.352. The sample was initially unsaturated. During the hydration period, it reaches the full saturation. Once the gas injection started, liquid replaced by the gas because of gas advective fluxes. Therefore, de-saturated zones correspond to gas advective fluxes and show the preferential gas flow pathways. Similarly, permeability increases where the gas advective fluxes are significant. Hence both distribution of de-saturated zones and increased permeabilities indicate possible gas flow pathways.

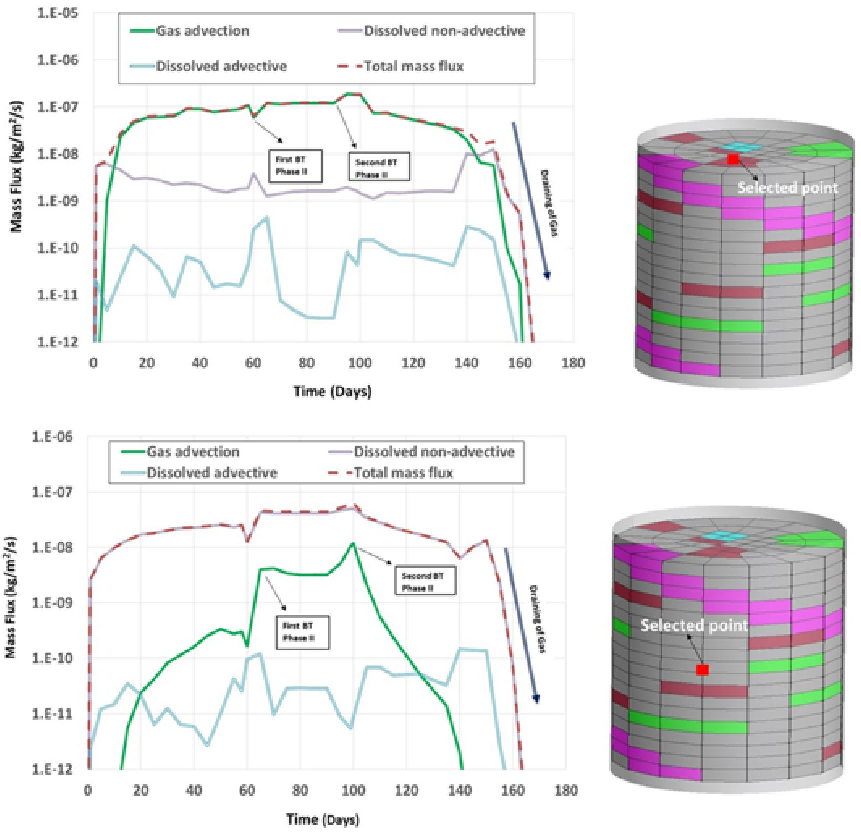

Figure 2.344: Evolution of mass fluxes till Phase III for Model B_Extended.

Initial permeability (Figure 2.352) in Model A_Extended and Model A_Extended_1 is not same because of heterogenous distribution of porosity in Model A_Extended_1. In Model A_Extended_2, initial liquid permeability is one order bigger than the other two models. Permeability increases during gas injection and decreases during draining of gas in all three models.

Although Model A_Extended_2 is more permeable, it has a lower P_0 (water retention curve) value. Therefore, during gas breakthrough the de-saturation has been more significant (Figure 2.352) in Model A_Extended_2. However, re-saturation because of gas draining is faster in Model A_Extended_2 as it is more permeable.

Distribution of gas pressure during the first BT (58 days later gas injection) for three models are shown in Figure 2.353. Back pressures are around 4.6 MPa in Model A_Extended and Model A_Extended_1. Gas pressure distribution is relatively heterogeneous in Model A_Extended_1 because of initial heterogeneous distribution of porosity. In Model A_Extended_2, the highest back pressure has been succeeded as the total gas permeability was bigger in this model. The back pressure reaches to 8.4 MPa at the end of 58 days later gas injection initiation in Model A_Extended_2, which is significantly bigger than the test data.

Distribution of mean total stresses during the first BT (58 days later gas injection) for three models are shown in Figure 2.354. In Model A_Extended_2, the mean total stresses are bigger than the other two models at the end of 58 days of gas injection (first BT).

Evolution of gas pressure on the top (close to gas injection source) and the bottom (back pressure) together with evolution of mean total stresses on central area are shown in Figure 2.355. In Phase II, back pressures were around 2.3 MPa and in Phase IV it was 3.5 MPa in the test. Model A_Extended and Model A_Extended_1 can predict adequately back pressures in Phase IV and slightly overestimate back pressures in Phase II. However, Model A_Extended_2 overestimates significantly back pressures in Phase II as it has a bigger permeability and lower gas entry pressure compare to other two models.

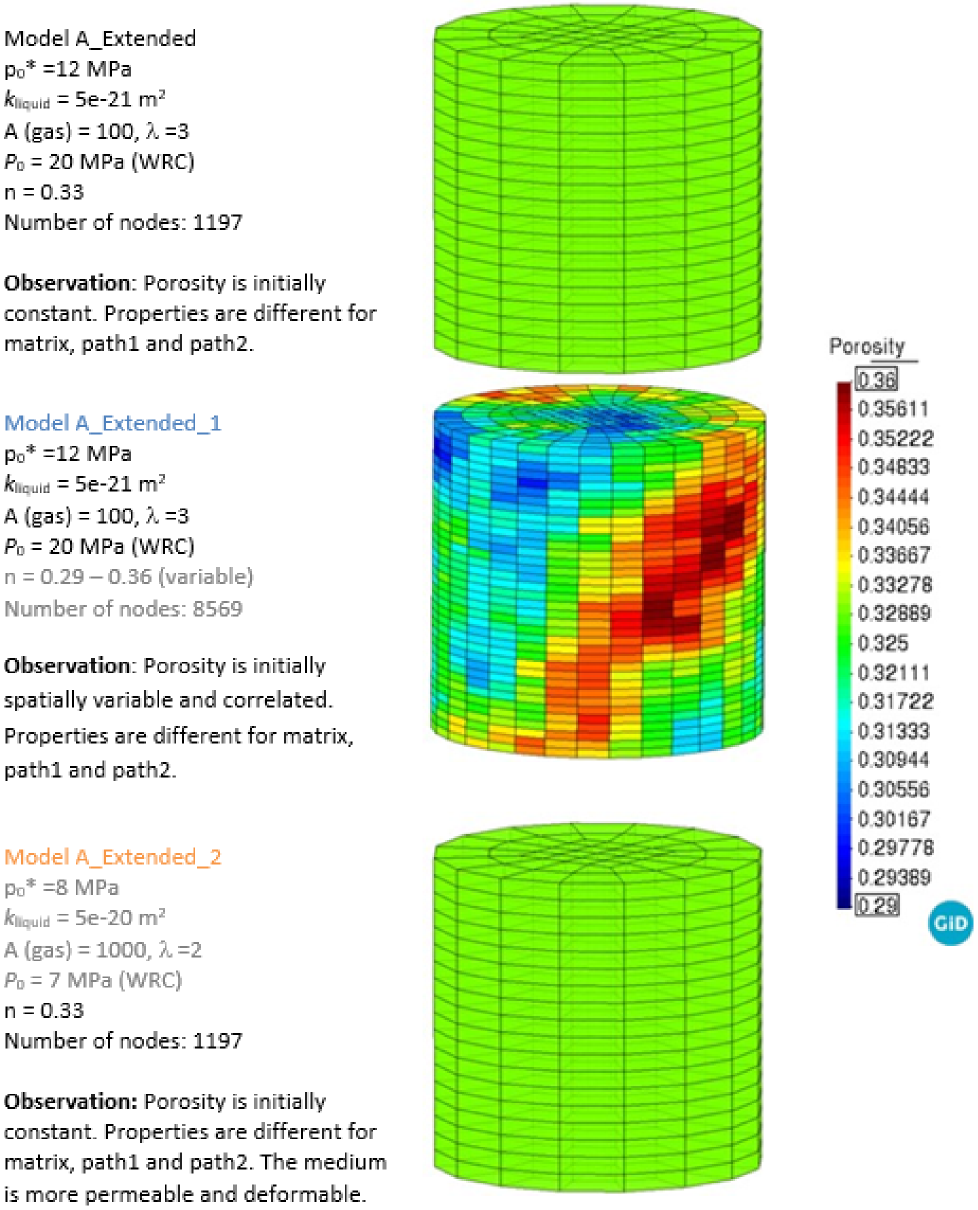

Model A_Extended
p_0^* =12 MPa
k_{liquid} = 5e-21 m^2
A (gas) = 100, λ =3
P_0 = 20 MPa (WRC)
n = 0.33
Number of nodes: 1197

Observation: Porosity is initially constant. Properties are different for matrix, path1 and path2.

Model A_Extended_1
p_0^* =12 MPa
k_{liquid} = 5e-21 m^2
A (gas) = 100, λ =3
P_0 = 20 MPa (WRC)
n = 0.29 – 0.36 (variable)
Number of nodes: 8569

Observation: Porosity is initially spatially variable and correlated. Properties are different for matrix, path1 and path2.

Model A_Extended_2
p_0^* =8 MPa
k_{liquid} = 5e-20 m^2
A (gas) = 1000, λ =2
P_0 = 7 MPa (WRC)
n = 0.33
Number of nodes: 1197

Observation: Porosity is initially constant. Properties are different for matrix, path1 and path2. The medium is more permeable and deformable.

Figure 2.345: Distribution of initial porosity in three models.

As shown Figure 2.355, developed mean total stresses during hydration (swelling pressure plus liquid pressure) in Model A_Extended_2 are lower compare to other two models. As preconsolidation pressure is lower in Model A_Extended_2, there has been less swelling pressure development during saturation phase. However, mean total stresses in Model A_Extended_2 are higher compare to other models during gas injection. As Model A_Extended_2 is more permeable, there is more gas pressure development on the selected point (central area) leading to higher mean total stresses. During the gas withdrawal from the lower part (draining of gas), the pressure dissipation is more significant in Model A_Extended_2 compare to other two models as it is more permeable.

Distribution of preconsolidation pressures during the first BT (58 days later gas injection) for three models are shown in Figure 2.356. In Model A_Extended_2, preconsolidation pressure has been considered as 8 MPa which is lower than the maximum gas BT pressure (8.8 MPa). Therefore, plasticity has been observed in this model. In Model A_Extended and Model A_Extended_1 preconsolidation pressure has been set as 12 MPa. Therefore, these two models are in elastic regime.

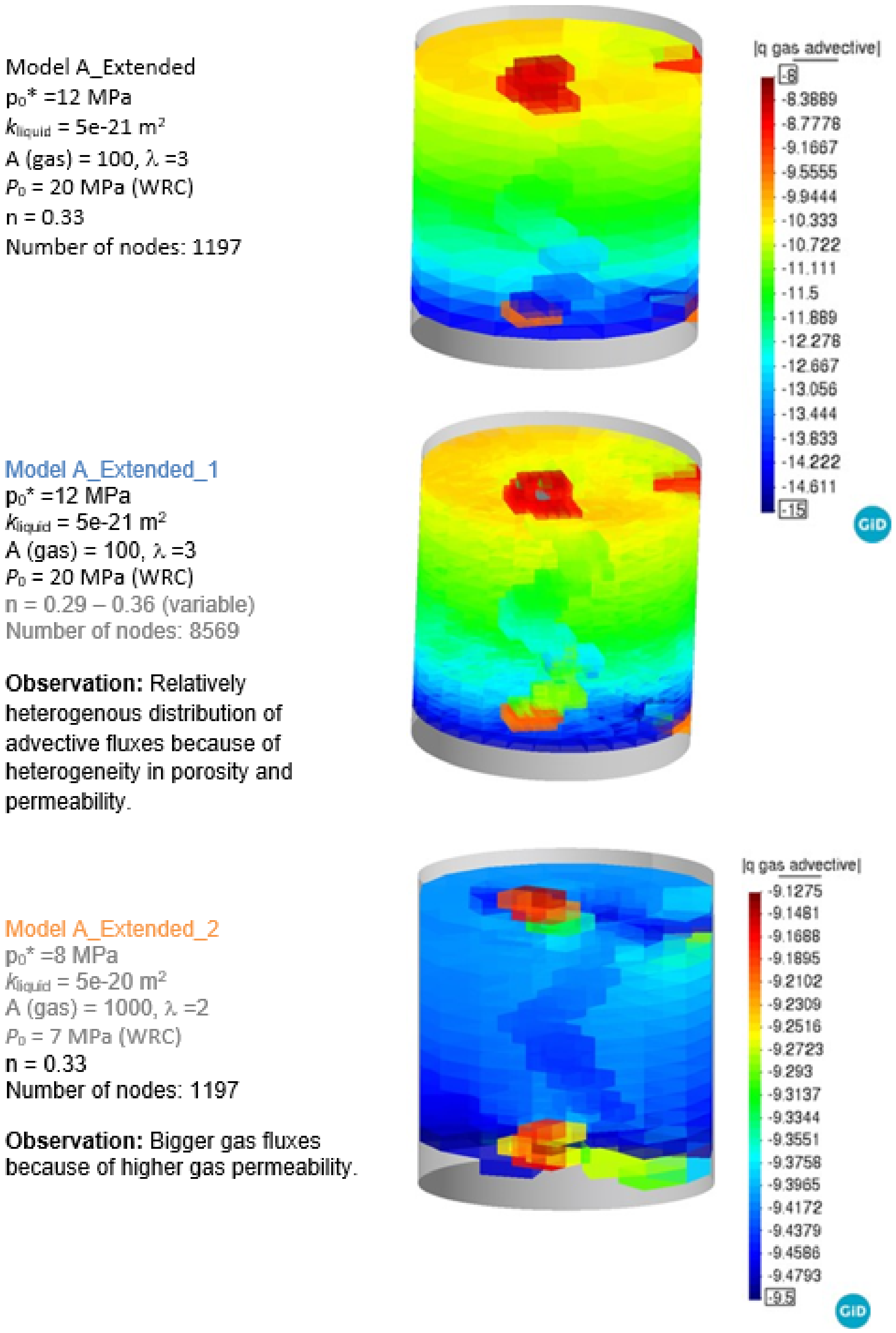

Model A_Extended
p_0^* =12 MPa
k_{liquid} = 5e-21 m^2
A (gas) = 100, λ =3
P_0 = 20 MPa (WRC)
n = 0.33
Number of nodes: 1197

Model A_Extended_1
p_0^* =12 MPa
k_{liquid} = 5e-21 m^2
A (gas) = 100, λ =3
P_0 = 20 MPa (WRC)
n = 0.29 – 0.36 (variable)
Number of nodes: 8569

Observation: Relatively heterogenous distribution of advective fluxes because of heterogeneity in porosity and permeability.

Model A_Extended_2
p_0^* =8 MPa
k_{liquid} = 5e-20 m^2
A (gas) = 1000, λ =2
P_0 = 7 MPa (WRC)
n = 0.33
Number of nodes: 1197

Observation: Bigger gas fluxes because of higher gas permeability.

Figure 2.346: Distribution of gas advective fluxes (logarithmic scale) in three models during first breakthrough (58 days later gas injection).

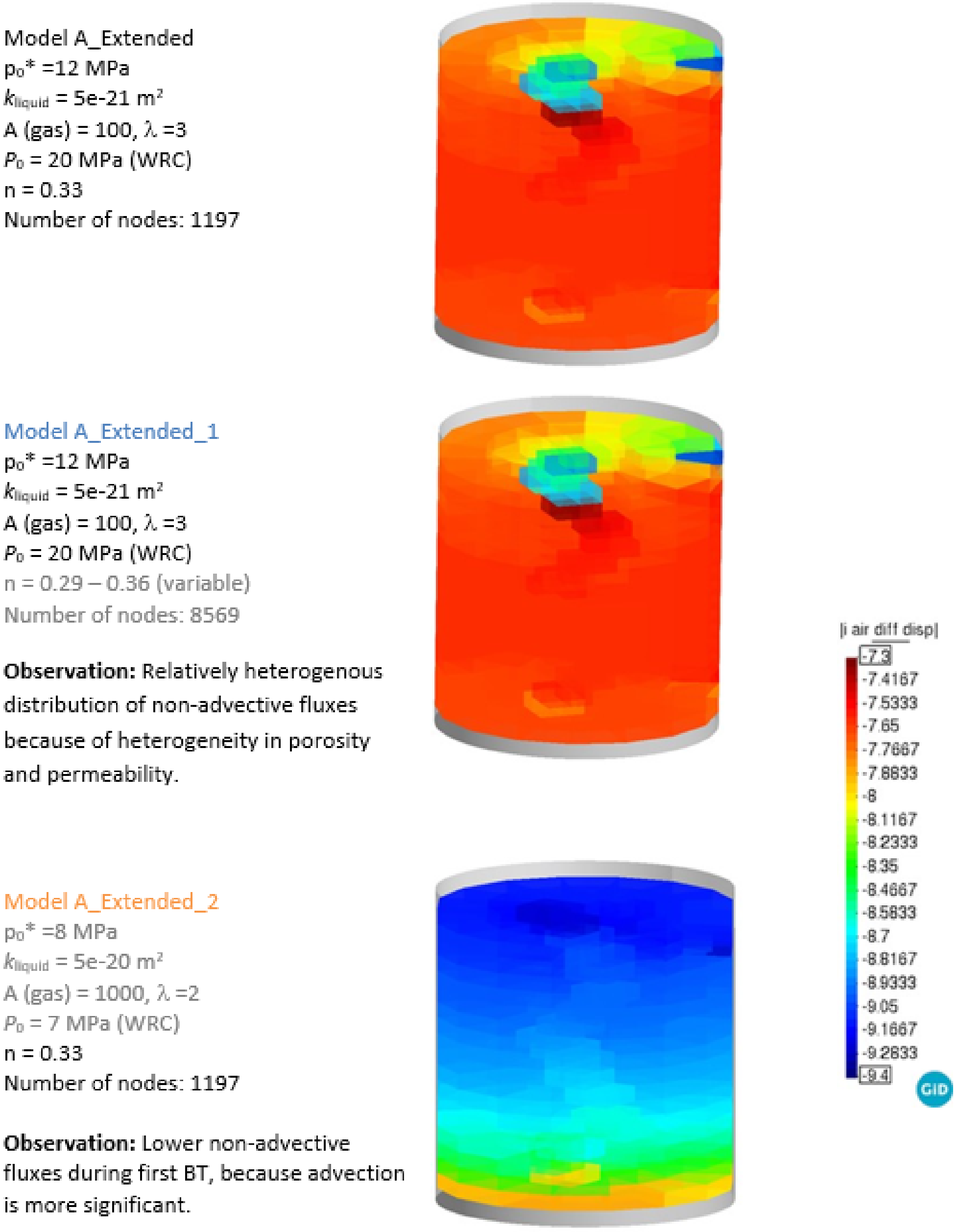

Model A_Extended
p_0^* =12 MPa
k_{liquid} = 5e-21 m^2
A (gas) = 100, λ =3
P_0 = 20 MPa (WRC)
n = 0.33
Number of nodes: 1197

Model A_Extended_1
p_0^* =12 MPa
k_{liquid} = 5e-21 m^2
A (gas) = 100, λ =3
P_0 = 20 MPa (WRC)
n = 0.29 – 0.36 (variable)
Number of nodes: 8569

Observation: Relatively heterogenous distribution of non-advective fluxes because of heterogeneity in porosity and permeability.

Model A_Extended_2
p_0^* =8 MPa
k_{liquid} = 5e-20 m^2
A (gas) = 1000, λ =2
P_0 = 7 MPa (WRC)
n = 0.33
Number of nodes: 1197

Observation: Lower non-advective fluxes during first BT, because advection is more significant.

Figure 2.347: Distribution of gas diffusion plus dispersion (logarithmic scale) in three models during first breakthrough (58 days later gas injection).

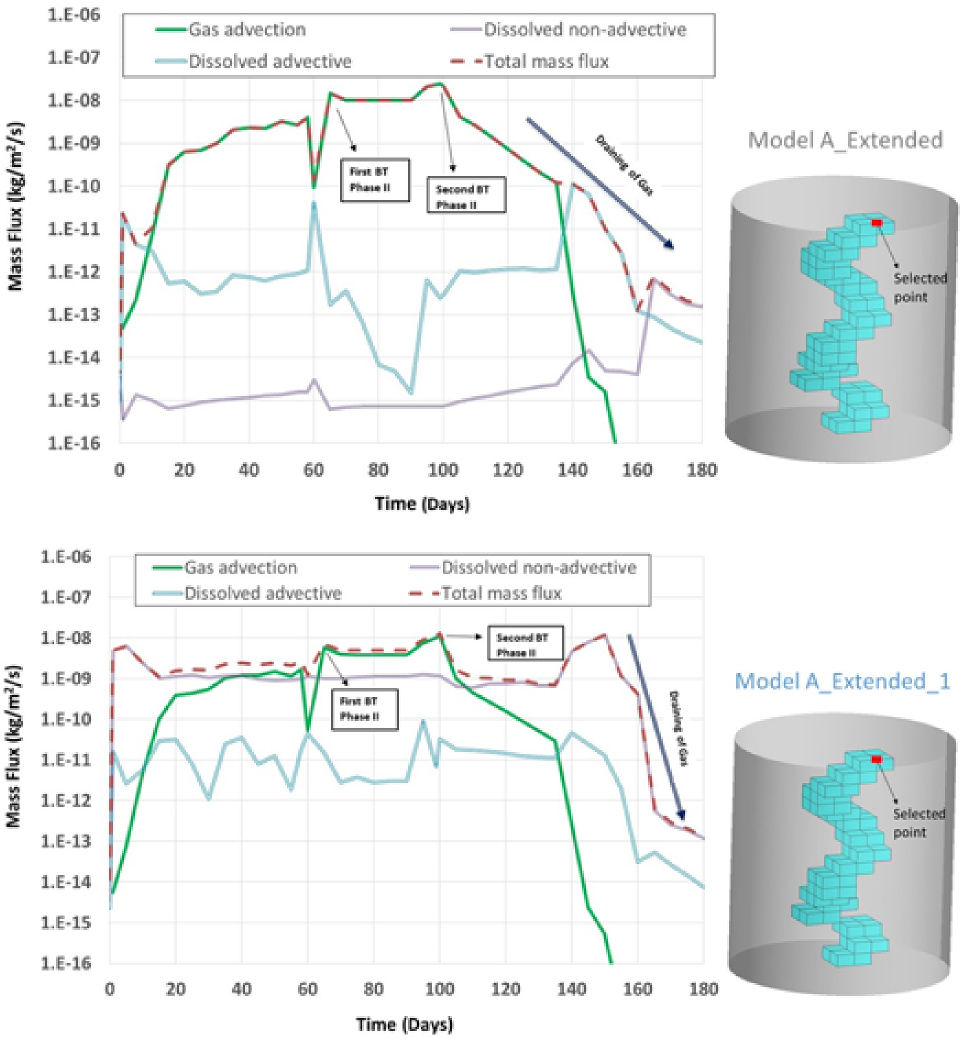

Figure 2.348: Mass fluxes at selected points in Model A_Extended (above) and Model A_Extended_1 (below).

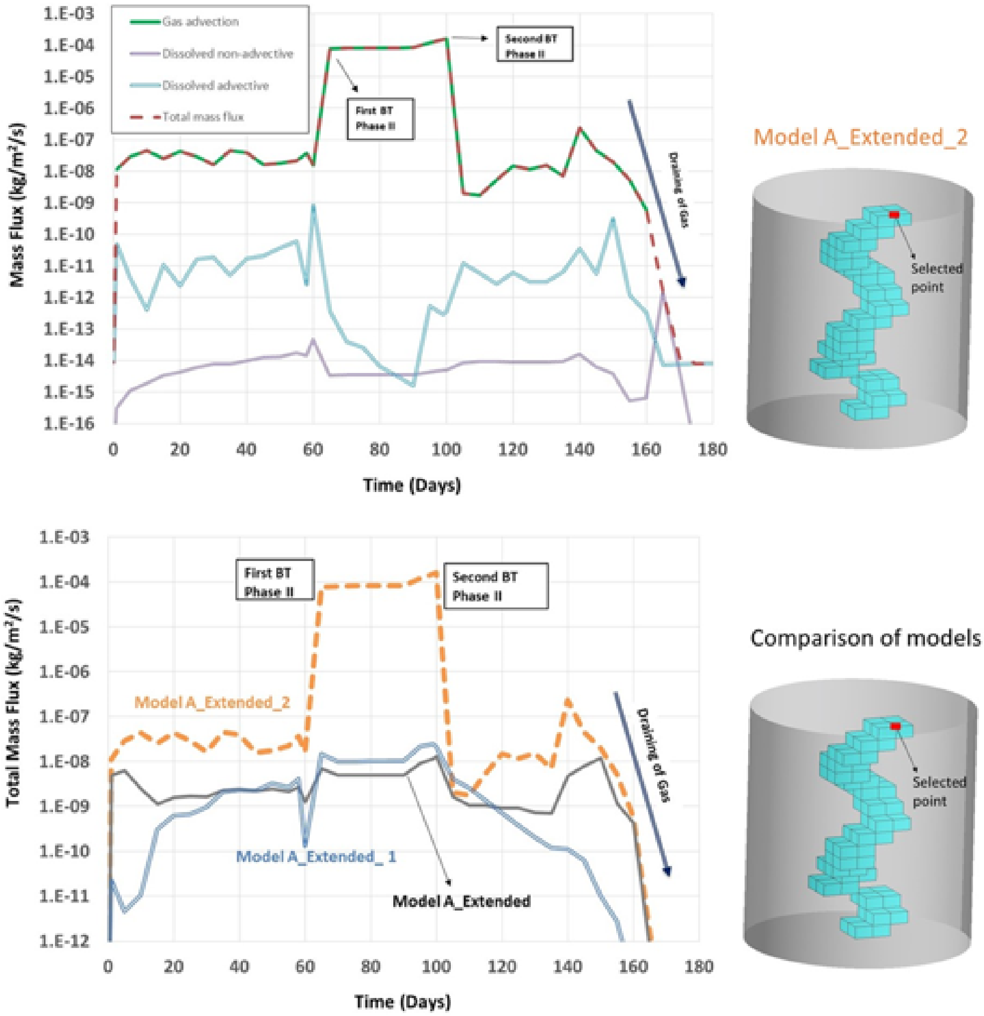

Figure 2.349: Mass fluxes in Model A_Extended_2 (above) and comparison of total mass fluxes for the different models (below).

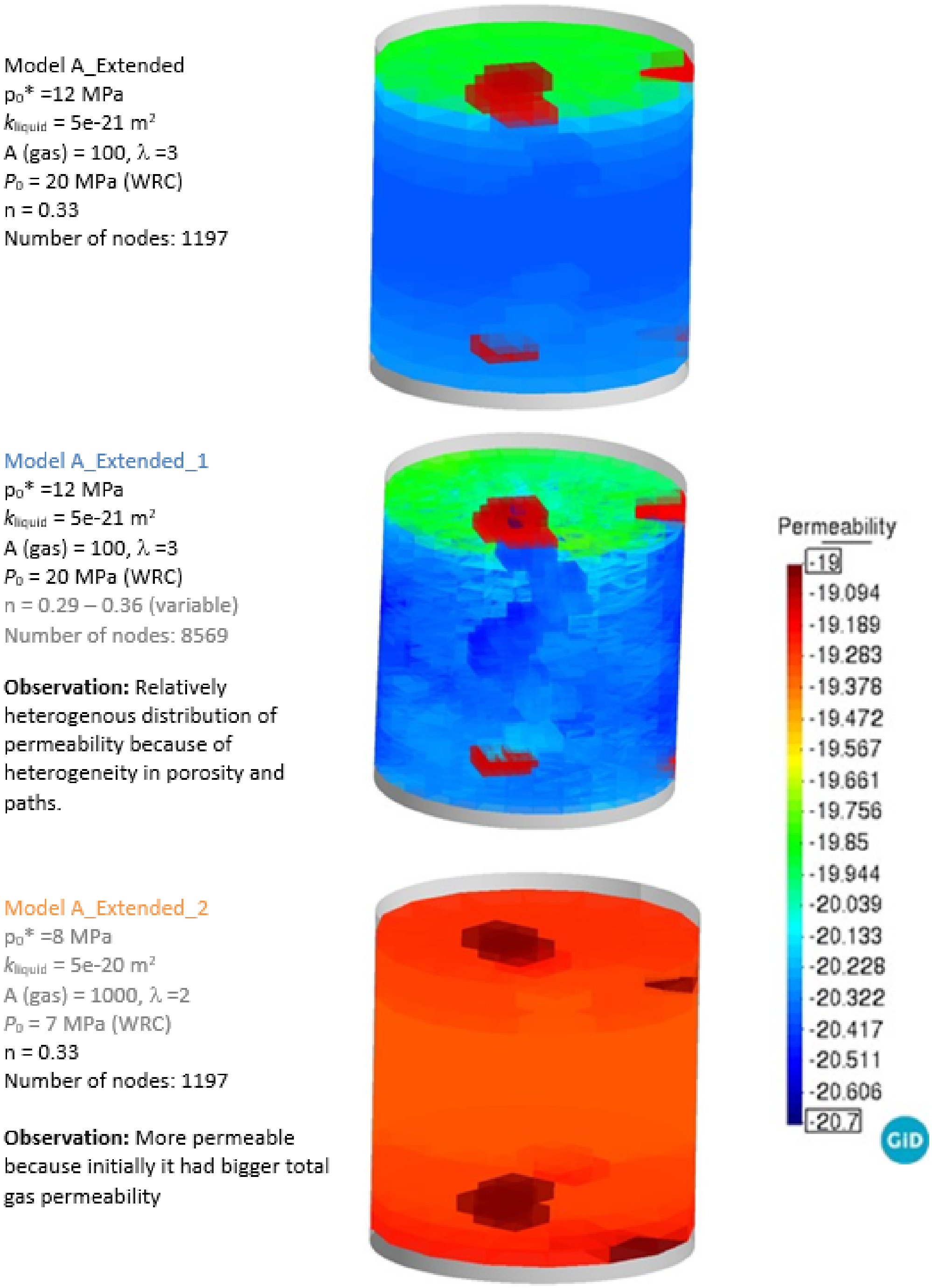

Model A_Extended
p_0^* =12 MPa
k_{liquid} = 5e-21 m^2
A (gas) = 100, λ =3
P_0 = 20 MPa (WRC)
n = 0.33
Number of nodes: 1197

Model A_Extended_1
p_0^* =12 MPa
k_{liquid} = 5e-21 m^2
A (gas) = 100, λ =3
P_0 = 20 MPa (WRC)
n = 0.29 – 0.36 (variable)
Number of nodes: 8569

Observation: Relatively heterogenous distribution of permeability because of heterogeneity in porosity and paths.

Model A_Extended_2
p_0^* =8 MPa
k_{liquid} = 5e-20 m^2
A (gas) = 1000, λ =2
P_0 = 7 MPa (WRC)
n = 0.33
Number of nodes: 1197

Observation: More permeable because initially it had bigger total gas permeability

Figure 2.350: Distribution of permeability (logarithmic scale) in three models during first breakthrough (58 days later gas injection).

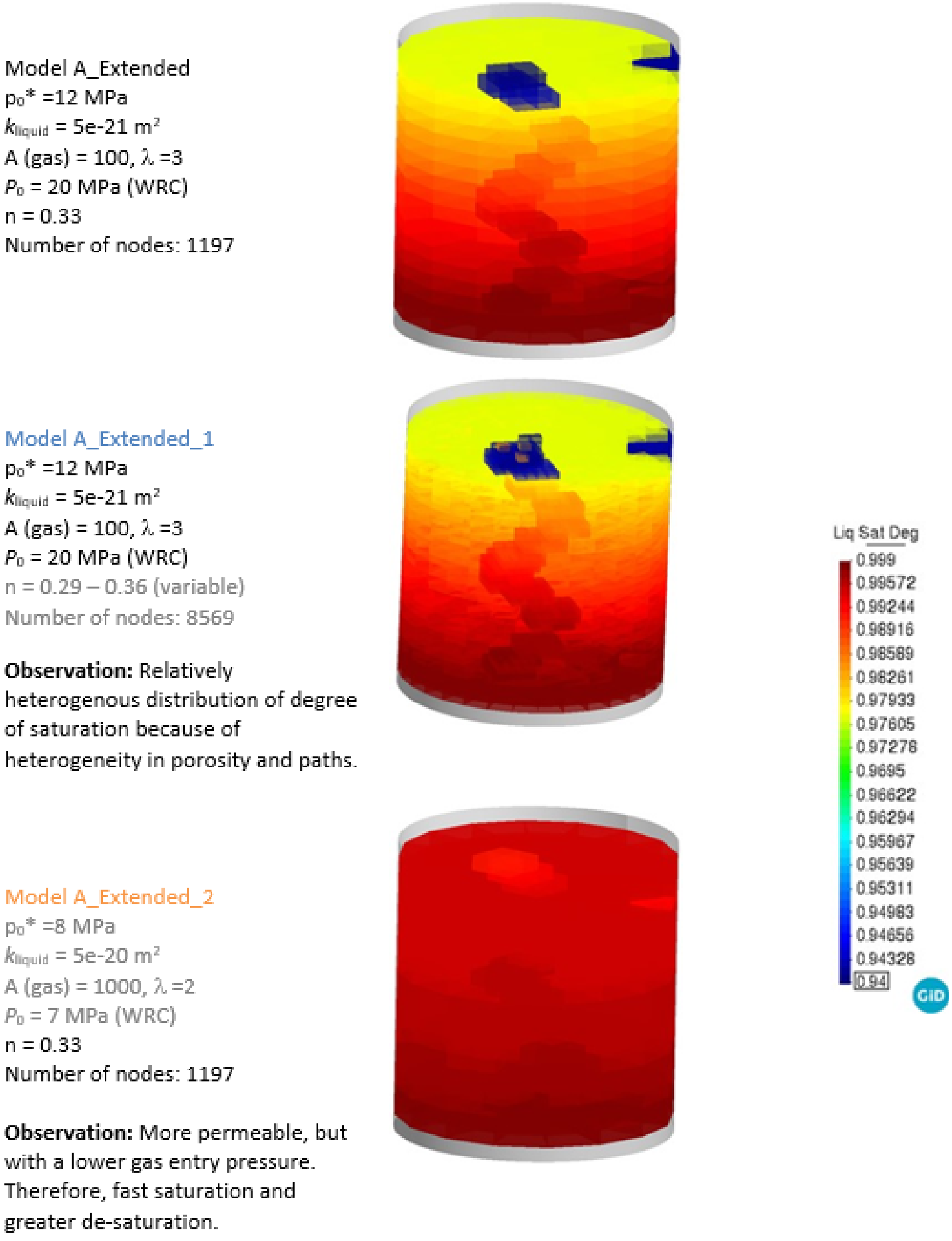

Model A_Extended
p_0^* =12 MPa
k_{liquid} = 5e-21 m²
A (gas) = 100, λ =3
P_0 = 20 MPa (WRC)
n = 0.33
Number of nodes: 1197

Model A_Extended_1
p_0^* =12 MPa
k_{liquid} = 5e-21 m²
A (gas) = 100, λ =3
P_0 = 20 MPa (WRC)
n = 0.29 – 0.36 (variable)
Number of nodes: 8569

Observation: Relatively heterogenous distribution of degree of saturation because of heterogeneity in porosity and paths.

Model A_Extended_2
p_0^* =8 MPa
k_{liquid} = 5e-20 m²
A (gas) = 1000, λ =2
P_0 = 7 MPa (WRC)
n = 0.33
Number of nodes: 1197

Observation: More permeable, but with a lower gas entry pressure. Therefore, fast saturation and greater de-saturation.

Figure 2.351: Distribution of liquid saturation degree in three models during first breakthrough (58 days later gas injection).

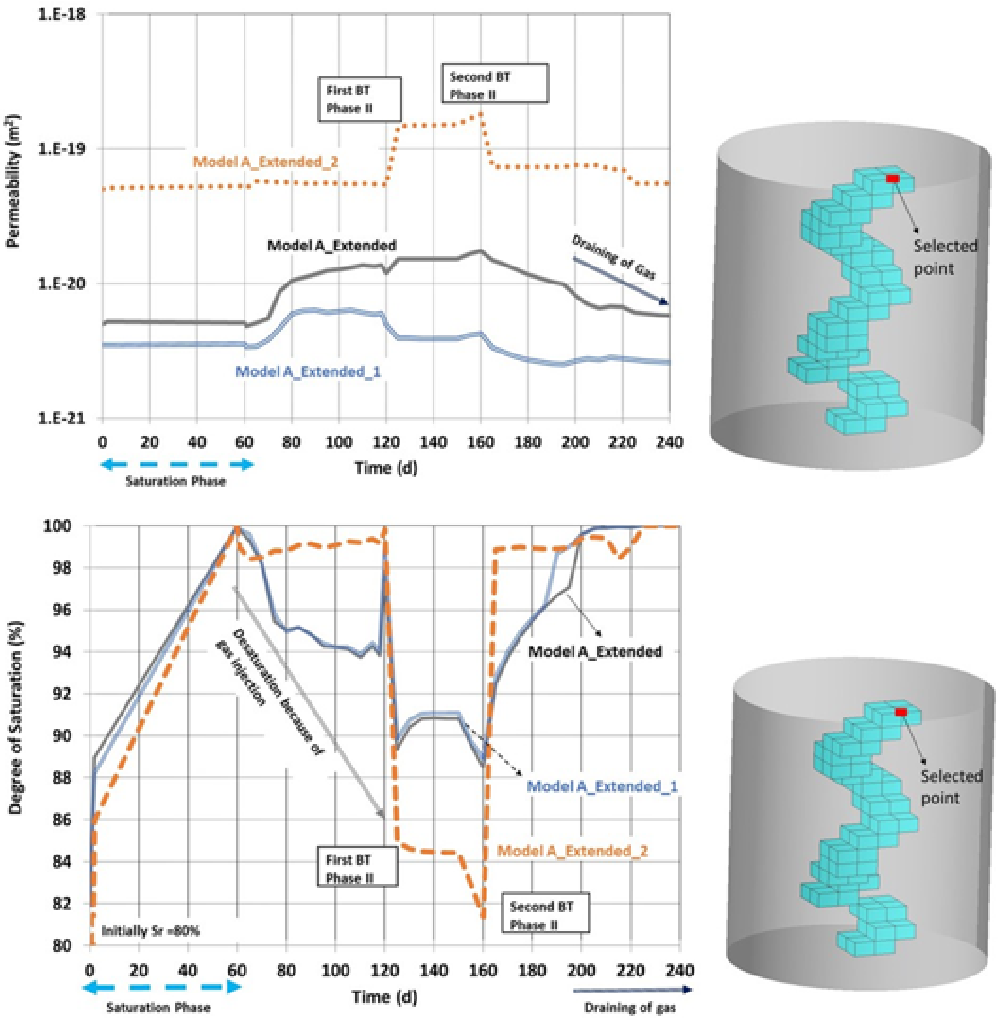

Figure 2.352: Comparison of permeability and degree of saturation evolutions in the models.

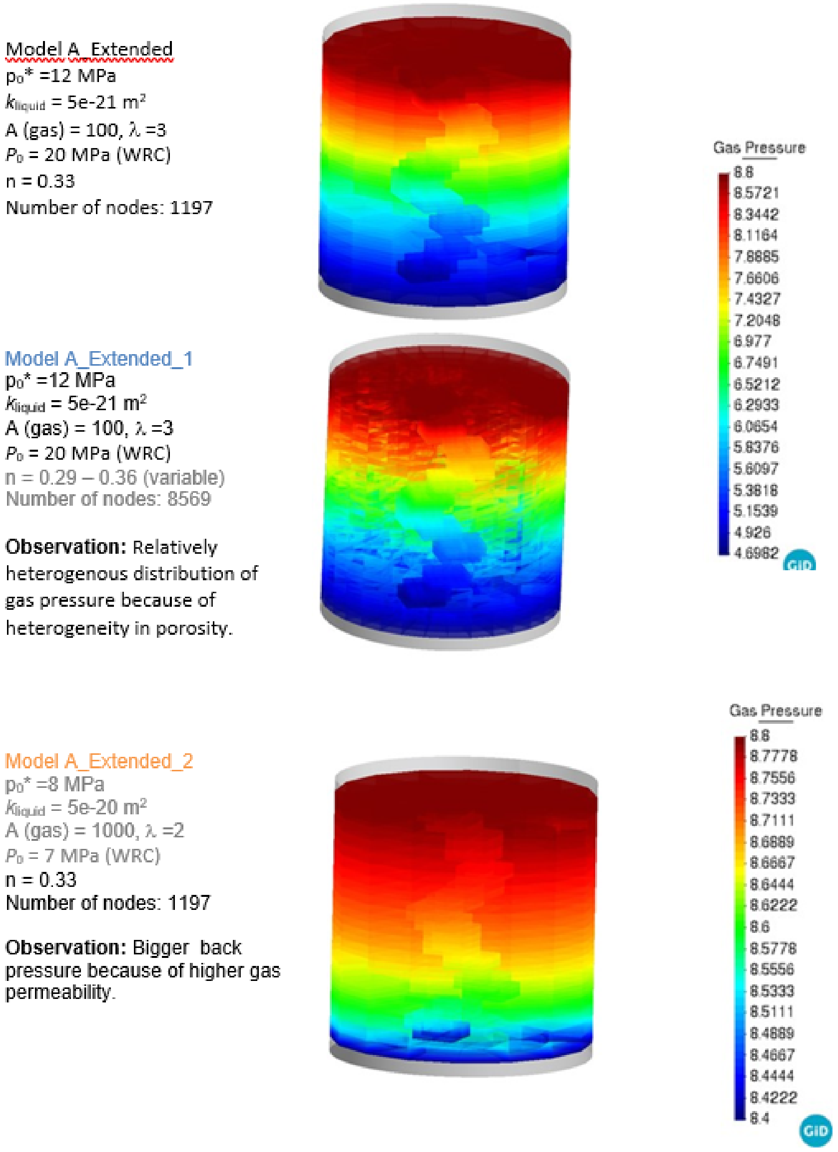

Model A_Extended
p_0^* =12 MPa
k_{liquid} = 5e-21 m^2
A (gas) = 100, λ =3
P_0 = 20 MPa (WRC)
n = 0.33
Number of nodes: 1197

Model A_Extended_1
p_0^* =12 MPa
k_{liquid} = 5e-21 m^2
A (gas) = 100, λ =3
P_0 = 20 MPa (WRC)
n = 0.29 – 0.36 (variable)
Number of nodes: 8569

Observation: Relatively heterogenous distribution of gas pressure because of heterogeneity in porosity.

Model A_Extended_2
p_0^* =8 MPa
k_{liquid} = 5e-20 m^2
A (gas) = 1000, λ =2
P_0 = 7 MPa (WRC)
n = 0.33
Number of nodes: 1197

Observation: Bigger back pressure because of higher gas permeability.

Figure 2.353: Distribution of gas pressure in three models during first breakthrough (58 days later gas injection).

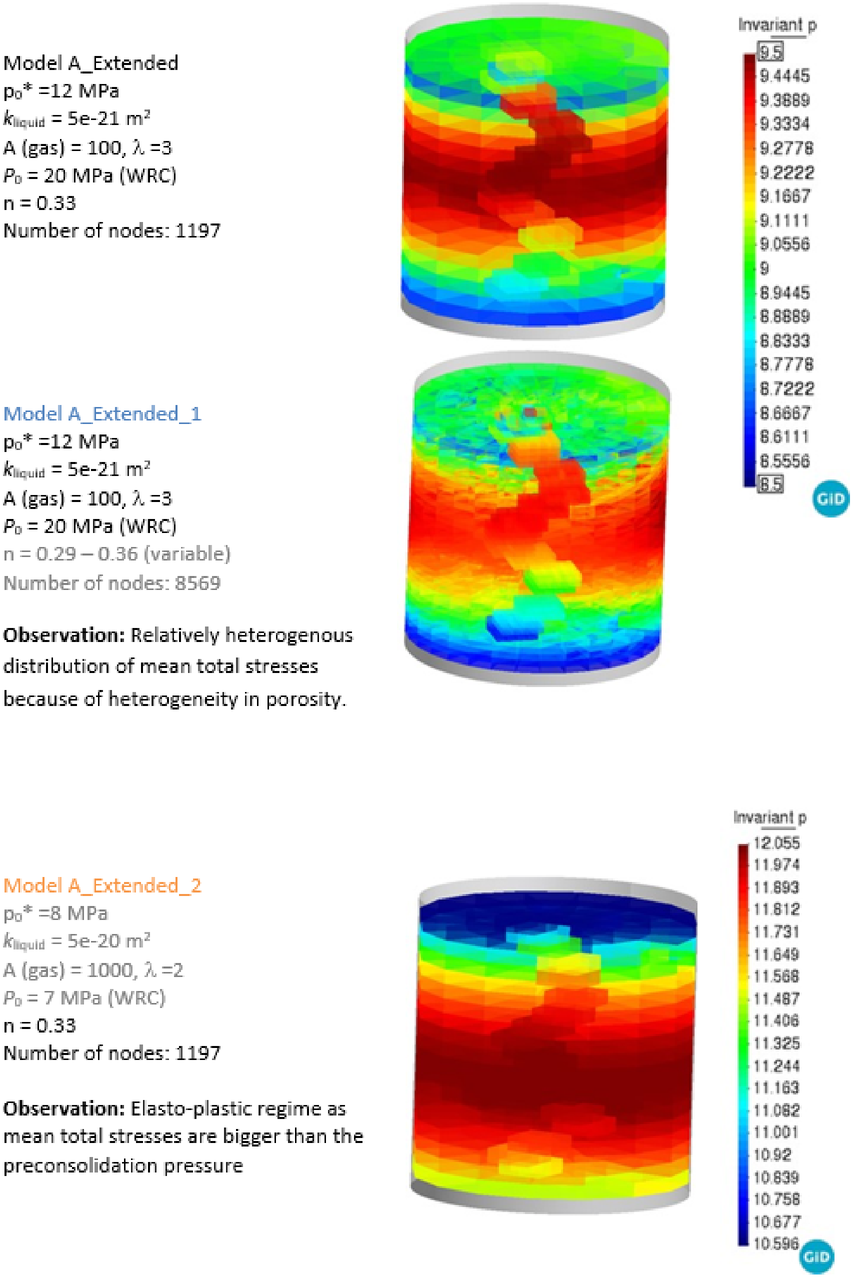

Model A_Extended
p_0^* =12 MPa
k_{liquid} = 5e-21 m²
A (gas) = 100, λ =3
P_0 = 20 MPa (WRC)
n = 0.33
Number of nodes: 1197

Model A_Extended_1
p_0^* =12 MPa
k_{liquid} = 5e-21 m²
A (gas) = 100, λ =3
P_0 = 20 MPa (WRC)
n = 0.29 – 0.36 (variable)
Number of nodes: 8569

Observation: Relatively heterogenous distribution of mean total stresses because of heterogeneity in porosity.

Model A_Extended_2
p_0^* =8 MPa
k_{liquid} = 5e-20 m²
A (gas) = 1000, λ =2
P_0 = 7 MPa (WRC)
n = 0.33
Number of nodes: 1197

Observation: Elasto-plastic regime as mean total stresses are bigger than the preconsolidation pressure

Figure 2.354: Distribution of mean total stresses in three models during first breakthrough (58 days later gas injection).

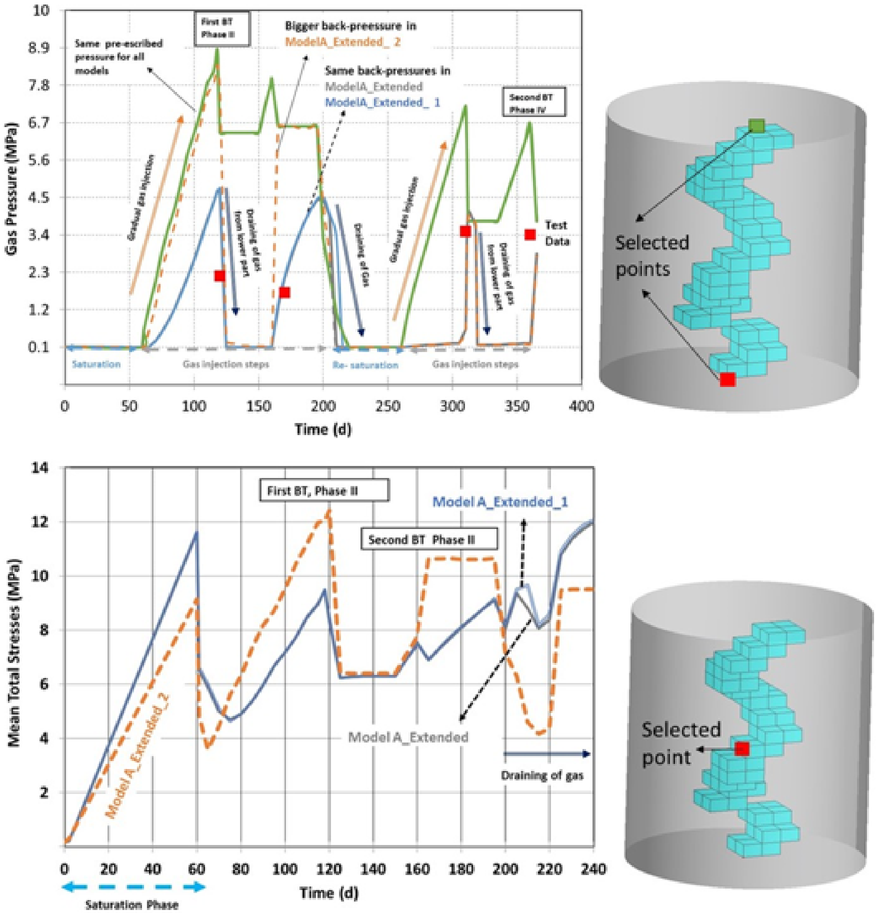

Figure 2.355: Comparison of gas pressure (above) and mean total stresses (below) in the models.

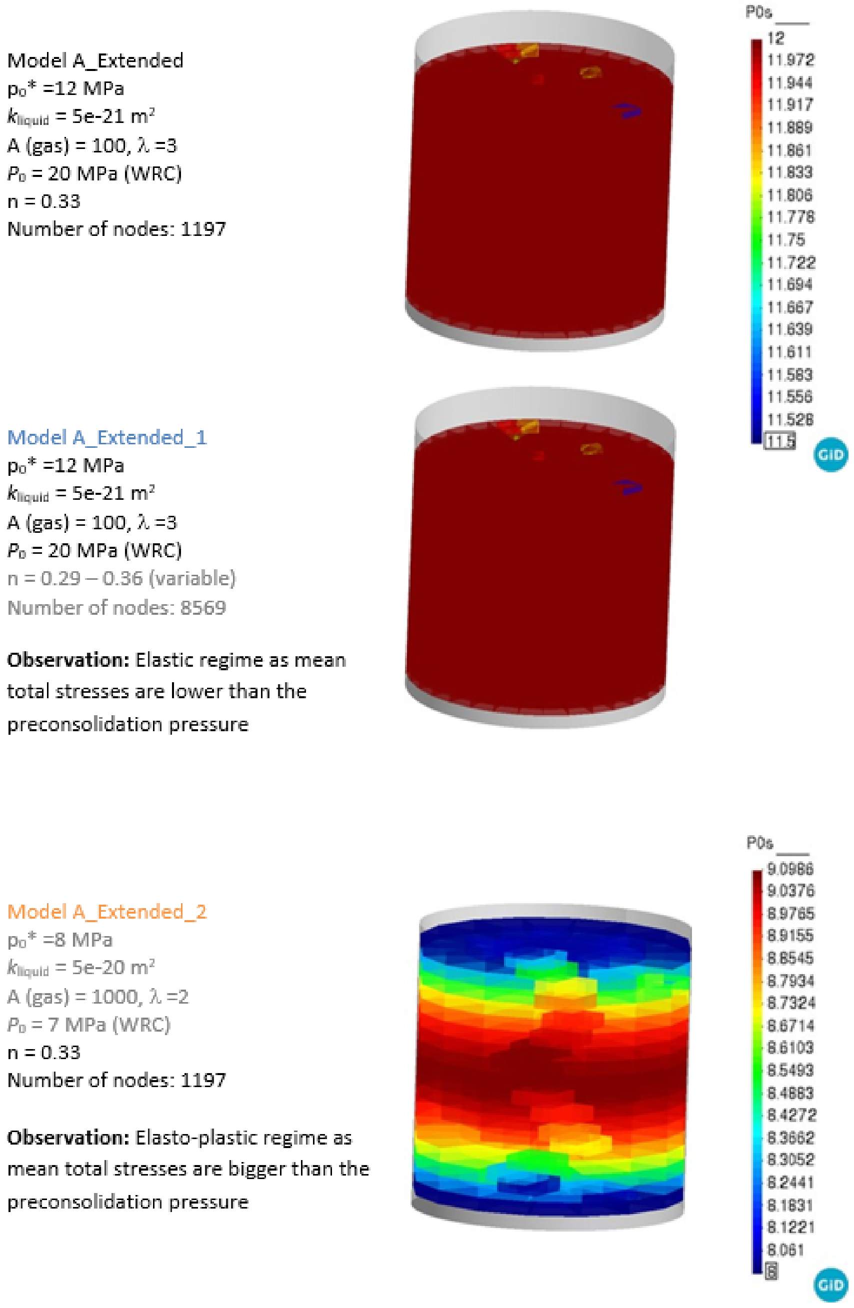

Model A_Extended
p_0^* =12 MPa
k_{liquid} = 5e-21 m^2
A (gas) = 100, λ =3
P_0 = 20 MPa (WRC)
n = 0.33
Number of nodes: 1197

Model A_Extended_1
p_0^* =12 MPa
k_{liquid} = 5e-21 m^2
A (gas) = 100, λ =3
P_0 = 20 MPa (WRC)
n = 0.29 – 0.36 (variable)
Number of nodes: 8569

Observation: Elastic regime as mean total stresses are lower than the preconsolidation pressure

Model A_Extended_2
p_0^* =8 MPa
k_{liquid} = 5e-20 m^2
A (gas) = 1000, λ =2
P_0 = 7 MPa (WRC)
n = 0.33
Number of nodes: 1197

Observation: Elasto-plastic regime as mean total stresses are bigger than the preconsolidation pressure

Figure 2.356: Distribution of pressure of pre-consolidation in three models during first breakthrough (58 days later gas injection).

2.14.7. Summary

In order to investigate gas transport process in bentonite barrier (FEBEX bentonite) and gas pathway development along the barrier; hydro-mechanical simulation of a breakthrough test (Gutierrez, 2018) has been performed. The objective of the modelling work was to simulate all phases of the test under proper boundary conditions, material model options and geometrical configuration.

BBM has been selected as a geo-mechanical model for the clay (FEBEX). In order to simulate increase in permeability during gas injection, cubic law for permeability has been used as a hydro-mechanical model for the gas flow pathways.

A full 3D geometry with different heterogeneity configurations (connected and unconnected paths), including porous stones, has been developed for the purpose of simulation of the test. One of the aims of the test was to simulate all processes (saturation, draining, gas injection, dismantling, etc.) taking place in the test.

A sensitivity analyses plan has been followed in order to improve model response and deal with test robustness and uncertainties. Table 2.95 summarizes objective, challenges, solutions and achievements of the modelling work.

Table 2.95: Summary, challenges and progress of the modelling work

Objective	• To investigate gas transport mechanism in FEBEX (initially unsaturated) material.
Challenges Limitations	• Mechanical Model : Using BBM in a 3D model with complex boundary conditions. • Boundary Conditions: Water/gas exchange procedure. Saturation and gas injection steps under the same 3D model. • Hydraulic Model: Verification and validation of heterogenous zones, preferential pathways and cubic law parameters.
Solutions Suggestions	• Preparation of a continues and layered geometry with structured mesh • Gradual gas injection and draining on the boundaries. • Follow a sensitivity analysis plan.
Sensitivity analyses	• Geometrical : Connected (Model A) and unconnected paths (Model B). • Time stepping : Prolongation of the test, including dismantling of the sample and re-saturation followed by new gas injection steps (Model A_Extended, Model B_Extended). • Hydro-mechanical model parameters: Variation of gas permeability, gas entry pressure; initial variable porosity and preconsolidation pressure (Model A_Extended_1 and Model A_Extended_2) • Computational: Refine of meshing, increasing number of elements (Model A_Extended_1)
Achievements Progress	• HM Model**:** 3D modelling of a gas BT test on FEBEX with BBM and cubic law for permeability. • Full process: Saturation, draining, water/gas exchange, gas injection and gas/water exchange processes under the same 3D model. • Improvement of model response especially for Phase IV.

2.14.8. Key learning points

New knowledge acquired

It has been shown the possibility of modelling of gas breakthrough test with all experimental steps (saturation, gas injection, draining of gas, re-saturation and second gas injection) under a 3D full geometry by using complex hydro-mechanical models (cubic law for permeability and BBM as a mechanical model). The methodology can be applied to model other experiments and using other realizations of the heterogeneity field (based on imaging techniques for observation of real heterogeneity).

Impact of acquired knowledge

The model with heterogeneous zones (connected paths and/or unconnected paths) has been generated for a laboratory scale test. The model can be considered as a reference case and can be served to model in-situ and full scale gas injection tests under 3D geometries with complex hydro-mechanical models. The methodology used to generate heterogeneous zones and pathways can be used for upscaling.

Remaining knowledge gaps

The model is capable to predict test results. However, it considers arbitrarily random distribution of permeability zones (corresponding to realizations). By providing a better instrumentation and sensor data, imaging techniques, transparent walls, etc; permeability and porosity zones can be defined better.

Regarding material properties, it can also be interesting to incorporate double structure models (BExM) and geochemistry. In this way macro-porosity can play a key role on gas migration, and chemistry can have an influence on swelling capacity of the clay components.

Recommendations for the future

In this work, it was not possible to localize heterogeneous permeability fields as the sample was small and the instrumentation was limited. For this kind of tests, a better instrumentation is recommended. Also it is very important to collect realistic distributions of density or porosity for real samples before and after testing them.

There are two levels of heterogeneity observed during gas injection test. The first level of heterogeneity is associated with the variation of dry density (porosity) during the hydration. Gas BT pressures are associated with the final dry density (swelling pressure varies according to dry density) prior to gas injection rather than the initial dry density. Therefore, hydration step shall be integrated in the modelling in order to improve the model predictions. The second level of heterogeneity is related to gas effective permeability. In intact clay (no advection of free gas), gas permeability and WRC is porosity dependent. In contrast, gas permeability and WRC is strain dependent in dilatant pathways. The magnitude of the apertures in dilatant pathways is variable. Therefore, at least two different gas flow pathways with different aperture characteristics shall be integrated into model. An elasto-plastic model such as BBM is required not only to reproduce development of swelling pressures during hydration part but also to simulate possible irreversible strains induced by gas injection under the heterogenous model configuration.

References

Alonso EE, Gens A and Josa A (1990) A constitutive model for partially saturated soils. Géotechnique 40(3): 405-430. 1990. pp. 405-430.

Enresa (2000) FEBEX Project. Full-scale engineered barriers experiment for a deep geological repository for high level radioactive waste in crystalline host rock. Enresa, Madrid, Spain. Final report, 1/2000.

Enresa (2006) Full-scale engineered barriers experiment. Enresa. Madrid. Spain. Updated final report 1994-2004. Technical publication 05-0/2006.

Gens A, Sánchez M and Guimaraes LN et al. (2009) A full-scale in situ heating test for high-level nuclear waste disposal: observations, analysis and interpretation. s.l.: Géotechnique, 59(4): 377-399, 2009. pp.

377-399.

Olivella S, Carrera J, Gens A & Alonso EE (1994) Nonisothermal multiphase flow of brine and gas through saline media. Barcelona, Spain. Transport in Porous Media, 1994. 271–293.

Olivella S. And E.E. Alonso, Gas flow through clay barriers, 2008, Geotechnique 58, No. 3, 157–176 [doi: 10.1680/geot.2008.58.3.157]

Gutiérrez Vanesa Transporte de gas en materiales de barrera, PhD dissertation, 2018.

Toprak E, Olivella S and Pintado X, (2020) Modelling engineered barriers for spent nuclear fuel repository using a double-structure model for pellets. Environmental Geotechnics, [doi: 10.1680/jenge.17.00086.

General conclusions

During the EURAD-GAS project, many experiments and modelling activities have been performed in the framework of the Task 2 and substantial progress has been made on the characterisation of gas transport processes. This general conclusion aims at coupling the initial objectives of task 2 “Gas transport mechanisms” to the results obtained by all partners.

Subtask 2.1 “Gas diffusion and retardation processes at high level of water saturation”

As described in the general introduction, the specific objectives of Subtask 2.1 “Gas diffusion and retardation processes at high level of water saturation” were:

- In order to compare the rates of gas generation and gas evacuation by dissolution and diffusion, knowledge of the diffusion parameters of dissolved gas through the host rock and engineered materials is essential. Up to now, diffusion parameters were only available in water saturated systems. As partial desaturation might occur at some point during the repository evolution, this WP extended the available experimental data for gas diffusion to partially desaturated conditions.
- In line with the general objective to improve mechanistic understanding, interpretation of the experimental results were supported by pore network modelling. The experimental and modelling work programme aimed in particular to investigate how petrophysical parameters (e.g. mineralogy and density) and the stress state influenced the diffusion parameters.
- While diffusing through the pore water, dissolved gas might also interact with the barrier materials. Up to now, interactions (mainly gas sorption) have only been studied under dry conditions. In particular, hydrogen uptake due to sorption processes has only been studied under dry conditions. One objective of this subtask was to determine if gas sorption could be a relevant retardation mechanism for diffusive transport under repository conditions, in clays that are partially, or, fully saturated with pore water. Again, the impacts of the pore network morphologies and the nature of the mineral assemblages on the gas sorption mechanisms was investigated.

How is gas diffusivity changing in partially saturated clay?

Depending on the host rock and disposal concept, unsaturated conditions may prevail. Therefore, the impact of desaturation on gas diffusivity was measured on synthetic samples, containing different amounts of clay, silt and sand, at saturation degrees between 73 and 100%. Results showed that diffusivity increased only slightly, about 20% when desaturating the sample towards 73%. As this dataset is too small to draw further conclusions, further research is recommended.

When desaturated samples are used, it was uncertain whether small scale samples can be considered homogeneous in relation to the degree of desaturation, an assumption which is often made for evaluation of unsaturated transport properties. A study by IRSN, using X-ray Synchrotron imaging and lab-based CT to study the host rock candidates (Toarcian, Boom Clay/Eigenbilzen sand) at a submicron scale revealed that porosity profile observations indicate that desaturation takes place in the largest pores first, and may be homogeneous within sub-centimeter size samples, even when close to the full water saturation.

How do petrophysical parameters (e.g. mineralogy and density) and the stress state influence the diffusion parameters, from both experimental and modelling point of view?

Diffusion of gas in different clayey materials has been studied by BGS. Results presented in this report show that, when studying anisotropy in Boom Clay samples, helium was shown to diffuse preferentially along bedding planes with approximately 60% of the diffusional capacity of Boom Clay moving parallel to bedding. Of greater importance was the observed coupling between diffusion and intrinsic permeability which was clear in the data set of synthetic samples. Examining the data as a whole suggests that a fundamental relationship exists between permeability and diffusivity, and when plotted in logarithmic scale the Boom Clay and Eigenbilzen sand fall on a common projection. If correct, such relationships could be used to predict diffusivity across a range of material and permeability scales. However, as this dataset is too small to draw further conclusions, further research is recommended.

Up to now, diffusion of gases was measured only on samples of a few centimeter in diameter, no data are available at larger scale. The NEMESIS experiment (Neon diffusion in MEgaS In Situ), which measures diffusion of neon on a meter scale in Boom Clay will allow the upscaling of diffusion of dissolved gas in a 3D diffusion experiment. After a long preparation phase, the in situ experiment was started in September 2023, and will run for at least 5 years. So far, only preliminary data on a preparative in-diffusion test are available, more data will follow in the coming years.

Major progress was made in modelling gas diffusion in saturated and unsaturated conditions using molecular dynamic simulations. Findings revealed that the diffusion of gases is significantly influenced by three key factors: the mineralogy (specifically, the type of clay), the size of the clay nanopore, and the hydrodynamic radius of the gas molecule (which indicates the gas type). In unsaturated clay, gas diffusion is influenced by multiple factors, including the thickness of the water films, the mean free path of the gas molecules, and the average available pore width.

Could gas sorption could be a relevant retardation mechanism for diffusive transport under repository conditions?

Sorption of gas on clay was, in previous publications, considered to be a potentially relevant process in a geological disposal facility. However, complementary work which is described in this report has shown that these results could in fact be attributed to experimental artifacts. Recent results show generation of gases such as CO_2, H_2 and CH_4 upon heating of Boom Clay and Callovo-Oxfordian Clay (Cox). With respect to gas sorption, the assessed hydrogen uptake by dry COx at 25℃ and 100 bar is 0.02 wt% which would translate to the adsorption of 480 tons of H_2 per 1 x 10^6 m^3 of COx. Gas sorption experiments on Boom Clay have been performed too, but results are not reported in this report.

Assessment of sub-task 2.1 with regards to the key objectives

- To determine gas diffusion parameters on different clayey materials at different degrees of water saturation and support experimental data interpretation by pore network modelling.
  - These objectives have been met: the data set has been extended with diffusion coefficients on different materials (both natural and synthetic), using different orientations with respect to bedding plane and testing different saturation states. With respect to the more fundamental understanding on the key parameters which influence diffusion under different conditions, progress has been made but more experiments are required to support hypothesis and draw firm conclusions.
  - Major progress has been made on the pore network modelling as different models used different scales, and several variables were investigated.
- To understand gas physisorption mechanisms in microporous systems.
  - Results for Callovo-Oxfordian clay, state that hydrogen uptake by dry COx at 25℃ and 100 bar is 0.02 wt.%. Adsorption of hydrogen by the COx decreases drastically with the water saturation. Under repository conditions, COx will be mainly fully saturated (a few meters away from the tunnels) or close to full saturation in the vicinity of the tunnels and H_2 adsorption should be neglected.

Specific objectives of Subtask 2.2 “Advection (displacement vs. dilation)”

As described in the general introduction, the specific objectives of Subtask 2.2 “Advection (displacement vs. dilation)” were:

1. Provide reference data for various natural and engineered clay materials under a sufficiently broad range of conditions, which will make it possible to investigate in a more systematic way *how petrophysical parameters, like mineralogy or density, and conditions such as the stress state influence free gas transport*.
2. *Improve understanding* of the observed gas transport modes and *identify their main controls*, through interpretation of the experimental results *by models in which the representation of crack propagation and pathway dilatancy is implemented at a process level*.
3. *Conceptualisations of the transport mechanisms limited to the macro-scale* (continuum representation and discrete conducting features) such as those developed, for instance, in the EC FORGE project were compared to conceptualisations in which the micro-scale is also represented to better improve understanding of how micro-level heterogeneities and deformations affect macro scale properties.

The experimental and modelling programmes of the subtask 2.2 aimed at characterising and understanding advective gas transport in fully saturated (or close to saturation) clayey materials.

How do petrophysical parameters, like mineralogy or density, and conditions such as the stress state influence free gas transport?

Experiments by BGS on Boom Clay and Callovo-Oxfordian Clay showed that (1) visco-capillary flow was not observed during the gas flow but dilatancy controlled flow was the only mechanism observed; (2) the control of the gas entry pressure was the minimum principal stress and (3) the dilatant pathways are not fracture related. No firm conclusions can be drawn yet regarding the role of stress as a control of the physics of gas flow and whether there is a transition from visco-capillary flow to dilatant pathway formation, further research is recommended.

Gas injection experiment in synthetic samples leads to the following key learning points: (1) swelling pressure is correlated with clay content in engineered clays and anti-correlated with sand + silt fraction in synthetic mixtures; (2) at fully saturated conditions, pathway dilatancy can occur at lower clay contents than previously thought; and (3) clay content appears to play a significant role regarding the stress field behaviour and to directly relate to gas entry pressure. Gas entry and flow through Czech Ca-Mg BCV bentonite at different dry densities by CTU showed (1) the formation of dilatant pathways via gas-exerted pressure occurs following the exceeding of the measured axial total stress, which is related to the swelling pressure of the material; and (2) the source of gas injection exerts no influence on the breakthrough pressure value. Gas injection experiments in BCV, MX-80 and Kunipia bentonite at two different densities by UJV showed no difference with respect to the tested gas (air vs. H_2) and the potential of BCV to reseal and all bentonite materials behaved in a similar way regarding gas flow processes.

Do we understand the observed gas transport modes, and which are the main controls? Can experimental results be described by models in which the representation of crack propagation and pathway dilatancy is implemented at a process level?

Experiments in a fracture visualization rig of BGS showed that multiple pathways form at the same time, with variable size, with variable velocity and the distribution of pathways is stochastic. The walls of a dilatant pathway elastically compress to accommodate the pathway and self-sealing is observed.

With respect to upscaling, all observations from Lasgit (a full-scale demonstration experiment operated by The Swedish Nuclear Fuel and Waste Management Company (SKB) at the Äspö Hard Rock Laboratory) support the idea that gas is mainly transported through dilatant pathways, which is consistent with observations made within the laboratory.

Experiments on FEBEX bentonite (CIEMAT) show that below a value referred to as gas entry pressure, the predominant transport mechanism is the diffusion in pore-water. Once this gas entry pressure is exceeded, gas flows through existing porosity or via self-created and stress-induced pathways. Gas flow is localised and little water is displaced, and considered to occur by the formation and propagation of dilatant pathways.

All these experiments evidence that standard hydraulic models should be enhanced with mechanisms to account for discrete pathways in order to better reflect some experimentally-observed phenomena. Following this direction, different models implemented within different software have been developed. Major progress has been made since several models have proved successful in describing key experimental features such as (1) the initiation and propagation of gas cracks inside deformable materials, (2) the sharp drop of the gas injection pressure when the gas crack reaches the back-pressure filter, and (3) the closure of the gas cracks when the gas injection ceases. However, further developments are still required to allow them to be predictive, as some model parameters are tuned in order to mimic the benchmark data. Work in the framework of EURAD-GAS has also highlighted that the introduction of variable material properties might play a significant role when describing localised pathways. However, their definition is still in a very preliminary phase and, in the absence of real density/porosity heterogeneous distributions, arbitrarily random distributions are currently assumed.

How does conceptualisation of transport mechanisms on macro-scale (with discrete conducting fractures) compare to micro-scale (with heterogeneities and deformations)?

The TU Delft team developed a new finite element model that is able to reproduce (within a unified framework), the diffusion and advection of dissolved gas and the displacement of the liquid phase filling the clay pores by the invading gas, together with the localised gas flow along macroscopic cracks induced and propagated by the gas pressure. This approach has been validated against synthetic benchmark examples and further developments are still necessary to allow a quantitative validation of the model, such as the implementation of the pathway dilation mechanism, the introduction of variability/heterogeneity of the material properties, and extension to a three-dimensional setting.

The University of Liège concluded that (1) the more continuous the connectivity between the disturbed planes is, the faster the gas flow through this discrete zone; and (2) these links between the planes of weakness need to be repeated regularly to ensure a rapid gas propagation at a larger scale. However, further developments are needed especially to up-scale the laboratory-scale results to the in situ-scale behaviour, since the microstructural heterogeneity of some clay properties (stiffness and strength) and the connectivity of the macro-pores and micro-fractures cannot be easily defined at a large scale.

The BGE in collaboration with the UFZ and the BGR developed an approach based on the macroscopic gas flow behaviour that includes micro-cracks being formed through the development of a percolation network. This approach has been validated via a benchmark test, originally proposed by the French National Radioactive Waste Management Agency (ANDRA) and successfully captures the transition from a single-phase to a two-phase gas transport.

IRNS and CNRS-Georessources noted that their Direct Numerical Simulations approach could be combined with FIB-SEM (Focused Ion Beam Scanning Electron Microscope) images to compute upscaled properties. However, there are still limitations in computational capacity to describe (1) domain sizes smaller than the REV or (2) multiscale scanning techniques are currently seen as potential techniques to overcome this limitation. However, associated computational costs need to be overcome before describing up-scaled heterogeneities.

UPC found that their approach could model gas breakthrough tests considering arbitrarily random distributions of permeability zones. However, the localisation of heterogenous permeability fields has not been possible and thus, the collection of realistic distributions of density or porosity for real samples is highly recommended.

In the frame of EURAD-GAS, different multi-scale modelling approaches have been developed, where the rock structure at a micro-scale level is included into the description of the macro-scale gas transport mechanisms. Special emphasis is placed on the transition between the two scales, which is currently achieved by means of homogenisation and localisation techniques. Performed simulations have highlighted that further work is still needed to better understand the definition of upscaled properties. Indeed, the microstructural heterogeneity of some clay properties (stiffness and strength) and the connectivity of the macro-pores and micro-fractures cannot be easily defined at a large scale. Scanning techniques are currently seen as potential techniques to overcome this limitation. However, associated computational costs need to be overcome before describing upscaled heterogeneities and geometries.

Assessment of sub-task 2.2 with regards to the key objectives

- How do petrophysical parameters, like mineralogy or density, and conditions such as the stress state influence free gas transport?
  - In all experiments which cover a broad range of materials such as natural clay (Boom Clay and Callovo-Oxfordian clay), synthetic clay samples, and also backfilling and sealing materials such as bentonite (MX-80, BCV, Kunipia) dilatancy flow was observed. Gas entry occurred around the minimum principal stress, which was influenced by e.g. the dry density of the material and the material composition. After gas breakthrough, sealing of dilatant pathways was observed.
  - It remains unclear which parameters influence free gas transport the most. Experiments with synthetic samples can provide more insight, but the amount of data is currently too limited and further research is recommended.
- Do we understand the observed gas transport modes, and which are the main controls? Can experimental results be described by models in which the representation of crack propagation and pathway dilatancy is implemented at a process level?
  - In all reported experiments, only dilatancy flow was observed. Pathways are unstable over time and highly variable. Gas flow is very local, with little water displacement and followed by sealing. We understand the observed transport modes, with refinement of modelling approaches needed to describe behaviour better.
  - It is still unclear what the main controls are. There are some first indications, but further research is required.
  - It is therefore important for a deterministic numerical analysis to understand and distinguish between the key experimental features reproducible across all experiments and those that only occur in specific experiments. Therefore, being able to analyse and model similar high-quality experimental datasets is required to help give confidence in the process of understanding.
- How does conceptualisation of transport mechanisms on macro-scale (with discrete conducting fractures) compare to micro-scale (with heterogeneities and deformations)?
  - All developed multi-scale modelling approaches have highlighted that further work is still needed to better understand the definition of upscaled properties, since the microstructural heterogeneity of some clay properties and the connectivity of the macro-pores and micro-fractures cannot be easily defined at a large scale.
  - Scanning techniques can be used to define up-scaled heterogeneities. However, there are still limitations in computational capacity.

Bibliography

(c2023). Deep geological repository.

Abell, A. B., Willis, K. L., and Lange, D. A. (1999). Mercury intrusion porosimetry and image analysis of cement-based materials. *Journal of Colloid and Interface Science*, 211:39–44.

Aertsens, M. (2011a). Migration in clay: experiments and models. sck-cen er-165. Report.

Aertsens, M. (2011b). Migration in clay: experiments and models. sck-cen er-165. Report.

Aertsens, M., Weetjens, E., Govaerts, J., Maes, N., and Brassinnes, S. (2023). Cp1 and tribicarb-3d: unique long-term and large-scale in situ migration tests in boom clay at the hades underground research laboratory. *Geological Society, London, Special Publications*, 536(1):SP536–2022–41.

Afagwu, C., Alafnan, S., Mahmoud, M. A., and Patil, S. (2021). Permeability model for shale and ultra-tight gas formations: Critical insights into the impact of dynamic adsorption. *Energy Reports*, 7:3302–3316.

Agrawal, A. and Prabhu, S. (2008). Deduction of slip coefficient in slip and transition regimes from existing cylindrical couette flow data. *Experimental Thermal and Fluid Science*, 32(4):991–996.

Akai, T., Blunt, M. J., and Bijeljic, B. (2020). Pore-scale numerical simulation of low salinity water flooding using the lattice boltzmann method. *Journal of colloid and interface science*, 566:444–453.

Ali, I. and Malik, N. A. (2018). A realistic transport model with pressure-dependent parameters for gas flow in tight porous media with application to determining shale rock properties. *Transport in Porous Media*, 124(3):723–742.

Aljama, H. and Wilcox, J. (2017). Microscopic diffusion of co2 in clay nanopores. *Chemical Physics Letters*, 677:162–166.

Alkan, H. and Müller, W. (2006). GASTON - Evaluation of modelling approaches of gas transport in clay formations (Auswertung von Modellierungsansätzen zum Gastransport in Tonformationen). Technical report, Institut für Sicherheitstechnologie (ISTec) GmbH, 85740 Garching, Germany. in English.

Alonso, E., Gens, A., and Josa, A. (1990). A constitutive model for partially saturated soils. *Geotechnique*, 40(3):405 – 430. Cited by: 2248; All Open Access, Green Open Access.

Alonso, E. E. and Alcoverro, J. (1999a). Catsius clay project: Calculation and testing of behaviour of unsaturated clay as barrier in radioactive waste repositories. Stage 1: Validation exercises. (Publication Technica Num. 10/99 ENRESA).

Alonso, E. E. and Alcoverro, J. (1999b). Catsius clay project: Calculation and testing of behaviour of unsaturated clay as barrier in radioactive waste repositories. Stage 2: Validation exercises at laboratory scale. Technical Report Publication Technica Num. 11/99 ENRESA, ENRESA, Madrid, Spain.

Alonso, E. E., Olivella, S., and Arnedo, D. (2006). Mechanisms of gas transport in clay barriers. *J. Iber. Geol.*, 32(2):175–196.

Altinier, M., Savoye, S., Michelot, J., Beaucaire, C., Massault, M., Tessier, D., and Waber, H. (2007). The isotopic composition of pore-water from tournemire argillite (france): An inter-comparison study. *Physics and Chemistry of the Earth, Parts A/B/C*, 32(1-7):209–218.

Altmann, S., Tournassat, C., Goutelard, F., Parneix, J.-C., Gimmi, T., and Maes, N. (2012). Diffusion-driven transport in clayrock formations. *Applied Geochemistry*, 27(2):463–478.

Amadei, B. (1983). *Rock anisotropy and the theory of stress measurements*. Springer-Verlag. Lecture Notes in Engineering Series., New-York, The United States.

Amaziane, B., Jurak, M., and Žgaljić Keko, A. (2014). Modeling compositional compressible two-phase flow in porous media by the concept of the global pressure. *Computational geosciences*, 18:297–309.

Amrofel, N., Dymitrowska, M., Obliger, A., Tinet, A.-J., and Golfier, F. (2024). Drying in nanoporous media with Kelvin effect: Capillary imbibition against evaporation by smoothed particle hydrodynamics method. *Physics of Fluids*, 36(2):022028.

ANDRA (2005a). Dossier 2005: Synthesis-evaluation of the feasibility of a geological re- pository in an argillaceous formation. https://international.andra.fr/documents-and-visual-ressources.

ANDRA (2005b). Evalution phénoménologique du stockage géologique, agence nationale pour la gestion des déchets radioactifs.

Andra (2016a). Analyse de l'interaction (thermo-)hydro-mécanique des alvéoles MAVL - Approche milieu continu. Technical report, Agence natioanle pour la gestion des déchets radioactifs, Châtenay-Malabry, France.

Andra (2016b). Dossier d'options de sûreté – partie après fermeture (dos-af.

Apostolopoulou, M., Santos, M. S., Hamza, M., Bui, T., Economou, I. G., Stamatakis, M., and Striolo, A. (2019). Quantifying pore width effects on diffusivity via a novel 3d stochastic approach with input from atomistic molecular dynamics simulations. *Journal of chemical theory and computation*, 15(12):6907–6922.

Appelo, C., Van Loon, L., and Wersin, P. (2010). Multicomponent diffusion of a suite of tracers (hto, cl, br, i, na, sr, cs) in a single sample of opalinus clay. *Geochimica et Cosmochimica Acta*, 74(4):1201–1219.

Appelo, C. A. J. and Wersin, P. (2007). Multicomponent diffusion modeling in clay systems with application to the diffusion of tritium, iodide, and sodium in opalinus clay. *Environmental science & technology*, 41(14):5002–5007.

Argilaga, A., Collin, F., Lacarrière, L., Charlier, R., Armand, G., and Cerfontaine, B. (2019). Modelling of Short-Term Interactions Between Concrete Support and the Excavated Damage Zone Around Galleries Drilled in Callovo–Oxfordian Claystone. *International Journal of Civil Engineering*, 17(1).

Arkai, P., Balogh, K., Demény, A., Fórizs, I., Nagy, G., and Máthé, Z. (2000). Composition, diagenetic and post-diagenetic alterations of a possible radioactive waste repository site: the boda albitic claystone formation, southern hungary. *Acta Geologica Hungarica*, 43(4):351–378.

Armand, G., Conil, N., Talandier, J., and Seyedi, D. M. (2017). Fundamental aspects of the hydromechanical behaviour of callovo-oxfordian claystone: from experimental studies to model calibration and validation. *Computers and Geotechnics*, 85:277–286.

Armand, G., Djizanne, H., Zghondi, J., de La Vaissière, R., Talandier, J., and Conil, N. (2016). Inputs from in situ experiments to the understanding of the unsaturated behaviour of callovo-oxfordian claystone. In *E3S Web of Conferences*, volume 9, page 03004. EDP Sciences.

Armand, G., Leveau, F., Nussbaum, C., de La Vaissiere, R., Noiret, A., Jaeggi, D., Landrein, P., and Righini, C. (2014). Geometry and properties of the excavation-induced fractures at the Meuse/Haute-Marne URL drifts. *Rock Mechanics and Rock Engineering*, 47(1):21–41.

Armand, G., Leveau, F., Nussbaum, C., de La Vaissière, R., Noiret, A., Jaeggi, D., Landrein, P., and Righini-Waz, C. (2013). Geometry and properties of the excavation-induced fractures at the meuse/haute-marne url drifts. *Rock Mechanics and Rock Engineering*, 47.

Arnold, D. N. (1990). Mixed finite element methods for elliptic problems. *Computer methods in applied mechanics and engineering*, 82(1-3):281–300.

Arnold, P., Vardon, P., Hicks, M., Fokkens, J., and Fokker, P. A. (2015). A numerical and reliability-based investigation into the technical feasibility of a Dutch radioactive waste repository in Boom Clay. Technical report, Delft University of Technology.

Avisar, D., Primor, O., Gozlan, I., and Mamane, H. (2010). Sorption of sulfonamides and tetracyclines to montmorillonite clay. *Water, Air, & Soil Pollution*, 209:439–450.

Aylmore, L. (1974). Gas sorption in clay mineral systems. *Clays and Clay Minerals*, 22:175–183.

B., B., Ch., C., and K, Y. (2012). A variational approach to the numerical simulation of hydraulic fracturing. In *SPE Annual Technical Conference and Exhibition*, San Antonio, Texas, USA.

Bandis, S., Lumsden, A., and Barton, N. (1983a). Fundamentals of rock joint deformation. In *International Journal of Rock Mechanics and Mining Sciences & Geomechanics Abstracts*, volume 20, pages 249–268. Elsevier.

Bandis, S. C., Lumsden, A. C., and Barton, N. R. (1983b). Fundamentals of rock joint deformation. *International Journal of Rock Mechanics and Mining Sciences & Geomechanics Abstracts*, 20(6):249–268.

Barber, R. W. and Emerson, D. R. (2006). Challenges in modeling gas-phase flow in microchannels: from slip to transition. *Heat Transfer Engineering*, 27(4):3–12.

Bardelli, F., Mondelli, C., Didier, M., Vitillo, J. G., Cavicchia, D. R., Robinet, J.-C., Leone, L., and Charlet, L. (2014). Hydrogen uptake and diffusion in callovo-oxfordian clay rock for nuclear waste disposal technology. *Applied Geochemistry*, 49:168–177.

Bardestani, R., Patience, G. S., and Kaliaguine, S. (2019). Experimental methods in chemical engineering: specific surface area and pore size distribution measurements—bet, bjh, and dft. *The Canadian Journal of Chemical Engineering*, 97:2781–2791.

Barnichon, J.-D. and Volckaert, G. (2003). Observations and predictions of hydromechanical coupling effects in the boom clay, mol underground research laboratory, belgium. *Hydrogeology Journal*, 11(1):193 – 202.

Barrett, E. P., Joyner, L. G., and Halenda, P. P. (1951). The determination of pore volume and area distributions in porous substances. i. computations from nitrogen isotherms. *Journal of the American Chemical Society*, 73:373–380.

Bart, M., Shao, J., Lydzba, D., and Haji-Sotoudeh, M. (2004). Coupled hydromechanical modeling of rock fractures under normal stress. *Canadian geotechnical journal*, 41(4):686–697.

Bastiaens, W., Bernier, F., and Li, X. L. (2007). Selfrac: Experiments and conclusions on fracturing, self-healing and self-sealing processes in clays. *Physics and Chemistry of the Earth, Parts A/B/C*, 32(8-14):600–615.

Baumgarten, N. and Wieners, C. (2020). The parallel finite element system M++ with integrated multilevel preconditioning and multilevel Monte Carlo methods. *Computers and Mathematics with Applications*. cited By 0.

Bear, J. and Bachmat, Y. (2012). *Introduction to modeling of transport phenomena in porous media*, volume 4. Springer Science & Business Media.

Bekker, H., Berendsen, H., Dijkstra, E., Achterop, S., Vondrumen, R., Vanderspoel, D., Sijbers, A., Keegstra, H., and Renardus, M. (1993). Gromacs-a parallel computer for molecular-dynamics simulations. In *4th international conference on computational physics (PC 92)*, pages 252–256. World Scientific Publishing.

Belgacem, F. B., Hild, P., and Laborde, P. (1998). The mortar finite element method for contact problems. *Mathematical and Computer Modelling*, 28(4):263–271.

Benazzouz, B. K., Ho, K. H., Nguyen, P. T., Hoang, H., and Galliero, G. (2022a). Diffusive transport of gases in saturated nanopores: Caprock leakage from a molecular simulation perspective. *Journal of Natural Gas Science and Engineering*, 98:104383.

Benazzouz, B. K., Ho, K. H., Nguyen, P. T., Hoang, H., and Galliero, G. (2022b). Diffusive transport of gases in saturated nanopores: Caprock leakage from a molecular simulation perspective. *Journal of Natural Gas Science and Engineering*, 98:104383.

Benner, E. and Petsev, D. (2018). Evaporation effect on two-dimensional wicking in porous media. *Journal of Colloid and Interface Science*, 514:21–29.

Bensenouci, F., Michelot, J., Matray, J., Savoye, S., Lavielle, B., Thomas, B., and Dick, P. (2011). A profile of helium-4 concentration in pore-water for assessing the transport phenomena through an argillaceous formation (tournemire, france). *Physics and Chemistry of the Earth, Parts A/B/C*, 36(17-18):1521–1530.

Bensenouci, F., Michelot, J., Matray, J., Savoye, S., Massault, M., and Vinsot, A. (2014). Coupled study of water-stable isotopes and anions in porewater for characterizing aqueous transport through the mesozoic sedimentary series in the eastern paris basin. *Marine and Petroleum Geology*, 53:88–101.

Benson, C. H. and Trast, J. M. (1995). Hydraulic conductivity of thirteen compacted clays. *Clays and clay minerals*, 43:669–681.

Berendsen, H., Grigera, J., and Straatsma, T. (1987). The missing term in effective pair potentials. *Journal of Physical Chemistry*, 91(24):6269–6271.

Bernaud, D. and Rousset, G. (1992). La « nouvelle méthode implicite » pour l'étude du dimensionnement des tunnels. *Revue Française de Géotechnique*, 60:5–26.

Bernier, F., Li, X., Bastiaens, W., Ortiz, L., Van Geet, M., and Wouters, L. (2007a). Selfrac: fractures and self-healing within the excavation disturbed zone in clays. final report. *EURIDICE Rep.*

Bernier, F., Li, X.-L., and Bastiaens, W. (2007b). Twenty-five years' geotechnical observation and testing in the Tertiary Boom Clay format. *Géotechnique*, 57(2):229–237.

Berre, I., Doster, F., and Keilegavlen, E. (2019). Flow in Fractured Porous Media: A Review of Conceptual Models and Discretization Approaches. *Transport in Porous Media*, 130(1):215–236. cited By 15.

Bestel, M., Glaus, M. A., Frick, S., Gimmi, T., Juranyi, F., Van Loon, L. R., and Diamond, L. W. (2018). Combined tracer through-diffusion of hto and 22na through na-montmorillonite with different bulk dry densities. *Applied geochemistry*, 93:158–166.

Bésuelle, P., Viggiani, G., Desrues, J., Coll, C., and Charrier, P. (2014). A laboratory experimental study of the hydromechanical behavior of boom clay. *Rock Mechanics and Rock Engineering*, 47(1):143–155.

Bhatnagar, P. L., Gross, E. P., and Krook, M. (1954). A model for collision processes in gases. i. small amplitude processes in charged and neutral one-component systems. *Physical review*, 94(3):511.

Bhatt, A., Valentic, T., Reimer, A., Lamarche, L., Reyes, P., and Cosgrove, R. (2020). Reproducible Software Environment: A tool enabling computational reproducibility in geospace sciences and facilitating collaboration. *Journal of Space Weather and Space Climate*, 10. cited By 0.

Bigler, T., Beat, I., Lehmann, B. E., Niklaus Waber, H., Vinsot, A., Latoui, K., Tolstikhin, I., and Gautschi, A. (2005). Helium production and transport in the low permeability callovo-oxfordian at the bure site, france.

Bilke, L., Flemisch, B., Kalbacher, T., Kolditz, O., Helmig, R., and Nagel, T. (2019). Development of Open-Source Porous Media Simulators: Principles and Experiences. *Transport in Porous Media*, 130(1):337–361. cited By 5.

Biot, M. A. (1941a). General theory for three-dimensional consolidation. *Journal of Applied Physics*, 12(2):155–164.

Biot, M. A. (1941b). General theory of three-dimensional consolidation. *Journal of Applied Physics*, 12(2):155 – 164.

Bird, R. (2002a). Transport phenomena. *Appl. Mech. Rev.*, 55(1):R1–R4.

Bird, R. B. (2002b). Transport phenomena. *Applied Mechanics Reviews*, 55(1):R1. Cited by: 333.

Birkholzer, J., Bond, A., Hudson, J., Jing, L., Tsang, C.-F., Shao, H., and Kolditz, O. (2018). DECOVALEX-2015: an international collaboration for advancing the understanding and modeling of coupled thermo-hydro-mechanical-chemical (THMC) processes in geological systems. *Environmental Earth Sciences*, 77(14). cited By 4.

Birkholzer, J., Tsang, C.-F., Bond, A., Hudson, J., Jing, L., and Stephansson, O. (2019). 25 years of DECOVALEX - Scientific advances and lessons learned from an international research collaboration in coupled subsurface processes. *International Journal of Rock Mechanics and Mining Sciences*, 122. cited By 0.

Bishop, A. W. (1959). The principle of effective stress. *Teknisk Ukeblad*, 39:859–863.

Blecha, C., Raith, F., Scheuermann, G., Nagel, T., Kolditz, O., and Maßmann, J. (2019). Analysis of coupled thermo-hydro-mechanical simulations of a generic nuclear waste repository in clay rock using fiber surfaces. *IEEE Pacific Visualization Symposium*, 2019-April:189–201. cited By 0.

Bock, H., Dehandschutter, B., Martin, C. D., Mazurek, M., de Haller, A., Skoczylas, F., and Davy, C. (2010). Self-sealing of fractures in argillaceous formations in the context of geological disposal of radioactive waste. *NEA*. https://www.oecd-nea.org/jcms/pl_14208.

Boek, E. S. and Venturoli, M. (2010). Lattice-boltzmann studies of fluid flow in porous media with realistic rock geometries. *Computers & Mathematics with Applications*, 59(7):2305–2314.

Boisson, Y., Bertrand, L., and Heitz, J. (2001). In situ and laboratory investigations of fluid flow through an argillaceous formation at different scales of space and time, tournemire tunnel, southern france. *Hydrogeology journal*, 9(1):108–123.

Borden, D. and Giese, R. (2001). Baseline studies of the clay minerals society source clays: cation exchange capacity measurements by the ammonia-electrode method. *Clays and Clay Minerals*, 49(5):444–445.

Bose, T., Sochanski, J. S., and Cole, R. (1972). Dielectric and pressure virial coefficients of imperfect gases. v. octopole moments of ch4 and cf4. *The Journal of Chemical Physics*, 57(9):3592–3595.

Bossart, P., Jaeggi, D., and Nussbaum, C. (2017). Experiments on thermo-hydro-mechanical behaviour of Opalinus Clay at Mont Terri rock laboratory, Switzerland. *Journal of Rock Mechanics and Geotechnical Engineering*, 9(3):502–510. cited By 12.

Botan, A., Marry, V., Rotenberg, B., Turq, P., and Noetinger, B. (2013). How electrostatics influences hydrodynamic boundary conditions: Poiseuille and electro-osmostic flows in clay nanopores. *The Journal of Physical Chemistry C*, 117(2):978–985.

Botan, A., Rotenberg, B., Marry, V., Turq, P., and Noetinger, B. (2010). Carbon dioxide in montmorillonite clay hydrates: thermodynamics, structure, and transport from molecular simulation. *The Journal of Physical Chemistry C*, 114(35):14962–14969.

Botan, A., Rotenberg, B., Marry, V., Turq, P., and Noetinger, B. (2011). Hydrodynamics in clay nanopores. *The Journal of Physical Chemistry C*, 115(32):16109–16115.

Boudreau, B. P. (1997). *Diagenetic models and their implementation*, volume 505. Springer Berlin.

Boulin, P. (2008). *Expérimentation et Modélisation du transfert d'hydrogène à travers des argiles de centre de stockage de déchets radioactifs*. Phd thesis, Grenoble INPG.

Bourg, I. C., Bourg, A. C., and Sposito, G. (2003). Modeling diffusion and adsorption in compacted bentonite: a critical review. *Journal of Contaminant Hydrology*, 61(1-4):293–302.

Bourg, I. C., Richter, F. M., Christensen, J. N., and Sposito, G. (2010). Isotopic mass dependence of metal cation diffusion coefficients in liquid water. *Geochimica et Cosmochimica Acta*, 74(8):2249–2256.

Bourg, I. C. and Sposito, G. (2008). Isotopic fractionation of noble gases by diffusion in liquid water: Molecular dynamics simulations and hydrologic applications. *Geochimica et Cosmochimica Acta*, 72(9):2237–2247.

Bourg, I. C. and Sposito, G. (2010). Connecting the molecular scale to the continuum scale for diffusion processes in smectite-rich porous media. *Environmental science & technology*, 44(6):2085–2091.

Bourg, I. C. and Tournassat, C. (2015a). *Chapter 6 - Self-Diffusion of Water and Ions in Clay Barriers*, volume Volume 6, pages 189–226. Elsevier.

Bourg, I. C. and Tournassat, C. (2015b). *Chapter 6 - Self-Diffusion of Water and Ions in Clay Barriers*, volume Volume 6, pages 189–226. Elsevier.

Bourgeat, A., Jurak, M., and Smai, F. (2010). Modelling and numerical simulation of gas migration in a nuclear waste repository. *arXiv preprint arXiv:1006.2914*.

Bourgeat, A., Smaï, F., and Granet, S. (2013). Compositional Two-Phase Flow in Saturated-Unsaturated Porous Media: Benchmarks for Phase Appearance/Disappearance. In *Simulation of Flow in Porous Media*, pages 81–106. De Gruyter.

Brackbill, J., Kothe, D., and Zemach, C. (1992a). A continuum method for modeling surface tension. *Journal of Computational Physics*, 100(2):335 – 354. Cited by: 7579.

Brackbill, J., Kothe, D., and Zemach, C. (1992b). A continuum method for modeling surface tension. *Journal of Computational Physics*, 100(2):335–354.

Bradshaw, J., Bachu, S., Bonijoly, D., Burruss, R., Holloway, S., Christensen, N. P., and Mathiassen, O. M. (2007). Co2 storage capacity estimation: issues and development of standards. *International journal of greenhouse gas control*, 1(1):62–68.

Brennwald, M. S., Tomonaga, Y., and Kipfer, R. (2020). Deconvolution and compensation of mass spectrometric overlap interferences with the miniruedi portable mass spectrometer. *MethodsX*, 7:101038.

Brezzi, F. and Bathe, K.-J. (1990). A discourse on the stability conditions for mixed finite element formulations. *Computer methods in applied mechanics and engineering*, 82(1-3):27–57.

Broadbent, R. and Neilson, G. (1994). The interatomic structure of argon in water. *The Journal of chemical physics*, 100(10):7543–7547.

Brusseau, M. L., Popovicova, J., and Silva, J. A. (1997). Characterizing gas- water interfacial and bulk-water partitioning for gas-phase transport of organic contaminants in unsaturated porous media. *Environmental science & technology*, 31(6):1645–1649.

Burland, J. B. (1990). On the compressibility and shear strength of natural clays. *Geotechnique*, 40(3):329–378.

Bussi, G., Donadio, D., and Parrinello, M. (2007). Canonical sampling through velocity rescaling. *The Journal of chemical physics*, 126(1):014101.

Bésuelle, P., Viggiani, G., Desrues, J., Coll, C., and Charrier, P. (2014). A laboratory experimental study of the hydromechanical behavior of boom clay. *Rock Mechanics and Rock Engineering*, 47(1):143 – 155.

Cabrera, J. (2001). Characterization of discontinuities in an argillaceous medium (tournemire site): key questions related to safety assessment of radioactive waste disposal.

Campos, M. D., Akkutlu, I. Y., and Sigal, R. F. (2009). A molecular dynamics study on natural gas solubility enhancement in water confined to small pores. In *SPE annual technical conference and exhibition*. OnePetro.

Carbonell, B. and Gutiérrez, C. (2017). Ensayo de permeabilidad al gas en equipo de alta presión de carga fija. Report, CIEMAT.

Carbonell, B., Villar, M. V., Martín, P., and Gutiérrez-Álvarez, C. (2019). Gas transport in compacted bentonite after 18 years under barrier conditions. *Geomechanics for Energy and the Environment*, 17:66–74.

Cariou, S., Dormieux, L., and Skoczylas, F. (2013). An original constitutive law for Callovo-Oxfordian argillite, a two-scale double-porosity material. *Applied Clay Science*, 80:18–30.

Carol, I., López, C. M., and Roa, O. (2001). Micromechanical analysis of quasi-brittle materials using fracture-based interface elements. *International Journal for Numerical Methods in Engineering*, 52(1-2):193–215.

Carrier, B. and Granet, S. (2012). Numerical modeling of hydraulic fracture problem in permeable medium using cohesive zone model. *Engineering Fracture Mechanics*, 79:312–328.

Catalano, E., Chareyre, B., and Barthélemy, E. (2014). Pore-scale modeling of fluid-particles interaction and emerging poromechanical effects. *International Journal for Numerical and Analytical Methods in Geomechanics*, 38(1):51–71.

Cencek, W., Przybytek, M., Komasa, J., Mehl, J. B., Jeziorski, B., and Szalewicz, K. (2012). Effects of adiabatic, relativistic, and quantum electrodynamics interactions on the pair potential and thermophysical properties of helium. *The Journal of Chemical Physics*, 136(22):224303.

Cerfontaine, B., Dieudonné, A. C., Radu, J. P., Collin, F., and Charlier, R. (2015a). 3D zero-thickness coupled interface finite element: Formulation and application. *Computers and Geotechnics*, 69:124–140.

Cerfontaine, B., Dieudonné, A., Radu, J., Collin, F., and Charlier, R. (2015b). 3D zero-thickness coupled interface finite element: Formulation and application. *Computers and Geotechnics*, 69:124–140. cited By 29 [6].

Chambon, R., Caillerie, D., and El Hassan, N. (1998). One-dimensional localisation studied with a second grade model. *European Journal of Mechanics, A/Solids*, 17(4):637–656.

Chan, S. and Elsheikh, A. (2020). Data-driven acceleration of multiscale methods for uncertainty quantification: application in transient multiphase flow in porous media. *GEM - International Journal on Geomathematics*, 11(1). cited By 0.

Chapman, S. and Cowling, T. G. (1990). *The mathematical theory of non-uniform gases: an account of the kinetic theory of viscosity, thermal conduction and diffusion in gases*. Cambridge university press.

Charlier, R. (1987a). *Approche unifiée de quelques problèmes non linéaires de mécanique des milieux continus par la méthode des éléments finis: (grandes déformations des métaux et des sols, contact unilatéral de solides, conduction thermique et écoulements en milieu poreux)*. Collection des publications de la Faculté des Sciences Appliquées.

Charlier, R. (1987b). *Approche unifiée de quelques problèmes non linéaires de mécanique des milieux continus par la méthode des éléments finis (grandes déformations des métaux et des sols, contact unilatéral de solides, conduction thermique et écoulements en milieux poreux)*. PhD thesis, Faculty of Applied Sciences, University of Liège, Belgium.

Charlier, R. and Cescotto, S. (1988). Modélisation du phénomène de contact unilatéral avec frottement dans un contexte de grandes déformations. *Journal de Mécanique Théorique et Appliquée*, 7(Suppl. 1).

Charlier, R., Collin, F., Pardoen, B., Talandier, J., Radu, J.-P., and Gerard, P. (2013). An unsaturated hydro-mechanical modelling of two in-situ experiments in callovo-oxfordian argillite. *Engineering geology*, 165:46–63.

Chen, C., Hu, D., Westacott, D., and Loveless, D. (2013). Nanometer-scale characterization of microscopic pores in shale kerogen by image analysis and pore-scale modeling. *Geochemistry, Geophysics, Geosystems*, 14(10):4066–4075.

Chen, G. J., Sillen, X., Verstricht, J., and Li, X. L. (2011a). ATLAS III in situ heating test in boom clay: Field data, observation and interpretation. *Computers and Geotechnics*, 38(5):683–696.

Chen, L., Groß, T., Krienke, H., and Lüdemann, H.-D. (2001). T, p-dependence of the self-diffusion and spin–lattice relaxation in fluid hydrogen and deuterium. *Physical Chemistry Chemical Physics*, 3(11):2025–2030.

Chen, L. L.-y., Katz, D. L., and Tek, M. R. (1977). Binary gas diffusion of methane-nitrogen through porous solids. *AIChE Journal*, 23(3):336–341.

Chen, Q. and Zhou, J. (2023). Investigating the validity of the bosanquet equation for predicting the self-diffusivities of fluids inside nanotubes using equilibrium molecular dynamics simulations. *AIP Advances*, 13(2):025338.

Chen, S., Tölke, J., and Krafczyk, M. (2009). Simulation of buoyancy-driven flows in a vertical cylinder using a simple lattice boltzmann model. *Physical Review E*, 79(1):016704.

Chen, X.-P., Zhong, C.-W., and Yuan, X.-L. (2011b). Lattice boltzmann simulation of cavitating bubble growth with large density ratio. *Computers & Mathematics with Applications*, 61(12):3577–3584.

Chenzhong, C. and Zhiliang, L. (1998). Molecular polarizability. 1. relationship to water solubility of alkanes and alcohols. *Journal of chemical information and computer sciences*, 38(1):1–7.

Choi, J.-H., Seol, Y., Boswell, R., and Juanes, R. (2011). X-ray computed-tomography imaging of gas migration in water-saturated sediments: From capillary invasion to conduit opening. *Geophysical Research Letters*, 38(17).

Choi, J.-W. and Oscarson, D. (1996). Diffusive transport through compacted na-and ca-bentonite. *Journal of Contaminant Hydrology*, 22(3-4):189–202.

Chukwudozie, C., Bourdin, B., and Yoshioka, K. (2019). A variational phase-field model for hydraulic fracturing in porous media. *Computer Methods in Applied Mechanics and Engineering*, 347:957–982. cited By 27.

Churakov, S. and Gottschalk, M. (2003). Perturbation theory based equation of state for polar molecular fluids: I. pure fluids. *Geochimica et Cosmochimica Acta*, 67(13):2397–2414.

Churakov, S. V. (2013a). Mobility of na and cs on montmorillonite surface under partially saturated conditions. *Environmental science & technology*, 47(17):9816–9823.

Churakov, S. V. (2013b). Mobility of na and cs on montmorillonite surface under partially saturated conditions. *Environmental science & technology*, 47(17):9816–9823.

Churakov, S. V. and D ahn, R. (2012). Zinc adsorption on clays inferred from atomistic simulations and exafs spectroscopy. *Environmental science & technology*, 46(11):5713–5719.

Churakov, S. V. and Gimmi, T. (2011a). Up-scaling of molecular diffusion coefficients in clays: A two-step approach. *The Journal of Physical Chemistry C*, 115(14):6703–6714.

Churakov, S. V. and Gimmi, T. (2011b). Up-scaling of molecular diffusion coefficients in clays: A two-step approach. *The Journal of Physical Chemistry C*, 115(14):6703–6714.

Churakov, S. V. and Kosakowski, G. (2010). An ab initio molecular dynamics study of hydronium complexation in na-montmorillonite. *Philosophical magazine*, 90(17-18):2459–2474.

Clapeyron, E. (1834). Mémoire sur la Puissance Motrice de la Chaleur. *Journal de l'École polytechnique*, 23:153–191.

Coll, C. (2005). *Endommagement des Roches Argileuses et PErméabilité Induite au Voisinage d'Ouvrages Souterrains*. PhD thesis, Université Joseph Fourier, Grenoble, France.

Collin, F. (2003a). *Couplages thermo-hydro-mécaniques dans les sols et les roches tendres partiellement saturés*. Phd thesis, Faculty of Applied Sciences, University of Liège, Belgium.

Collin, F. (2003b). Couplages thermo-hydro-mécaniques dans les sols et les roches tendres partiellement saturés.

Collin, F., Chambon, R., and Charlier, R. (2006a). A finite element method for poro mechanical modelling of geotechnical problems using local second gradient models. *International Journal for Numerical Methods in Engineering*, 65(11):1749–1772. cited By 72 [3].

Collin, F., Chambon, R., and Charlier, R. (2006b). A finite element method for poro mechanical modelling of geotechnical problems using local second gradient models. *International Journal for Numerical Methods in Engineering*, 65(11):1749–1772.

Collin, F., Cui, Y. J., Schroeder, C., and Charlier, R. (2003). Mechanical behaviour of chalk reservoir: numerical modelling of water sensitivity and time dependence effects. In *ISRM Congress*, pages ISRM–10CONGRESS. ISRM.

Collin, F., Li, X., Radu, J., and Charlier, R. (2002a). Thermo-hydro-mechanical coupling in clay barriers. *Engineering Geology*, 64(2-3):179–193. cited By 94 [5].

Collin, F., Li, X. L., Radu, J. P., and Charlier, R. (2002b). Thermo-hydro-mechanical coupling in clay barriers. *Engineering Geology*, 64:179–193.

Colombani, J., Bert, J., and Dupuy-Philon, J. (1999). Thermal diffusion in (licl, rh 2 o). *The Journal of chemical physics*, 110(17):8622–8627.

Colombo, D. (2015). Consolidation d'une colonne de sol poro-élastique saturée et fracturée: utilisation de la méthode xfem. *Documentation Code_Aster [V7.31.144]*.

Conil, N., Talandier, J., Djizanne, H., de La Vaissière, R., Righini-Waz, C., Auvray, C., Morlot, C., and Armand, G. (2018). How rock samples can be representative of in situ condition: A case study of callovo-oxfordian claystones. *Journal of Rock Mechanics and Geotechnical Engineering*, 10(4):613–623.

Cooper, D., Turinsky, A., Sensen, C., and Hallgrimsson, B. (2007). Effect of voxel size on 3d micro-ct analysis of cortical bone porosity. *Calcified Tissue International*, 80:211–219.

coopérative nationale pour l'entreposage de déchets radioactifs (Suisse), S. and Johnson, L. (2002). *Project Opalinus Clay: safety report: demonstration of disposal feasibility for spent fuel, vitrified high-level waste and long-lived intermediate-level waste (Entsorgungsnachweis)*. Nagra.

Cordero, J. A. R., Sanchez, E. C. M., and Roehl, D. (2019a). Hydromechanical modeling of unrestricted crack propagation in fractured formations using intrinsic cohesive zone model. *Engineering Fracture Mechanics*, 221:106655.

Cordero, J. A. R., Sanchez, E. C. M., Roehl, D., and Pereira, L. C. (2019b). Hydro-mechanical modeling of hydraulic fracture propagation and its interactions with frictional natural fractures. *Computers and Geotechnics*, 111:290–300.

Corey, A. T. (1954). The Interrelation Between Gas and Oil Relative Permeabilites. *Producers Monthly*, 19(1):38–41.

Corman, G. (2024). *Hydro-mechanical modelling of gas transport processes in clay host rocks in the context of a nuclear waste repository*. Phd thesis, Faculty of Applied Sciences, University of Liège, Belgium.

Corman, G., Gonzalez-Blanco, L., Levasseur, S., and Collin, F. (2024). Hydro-mechanical modelling of gas transport processes in clay materials using a multi-scale approach. *Computers and Geotechnics*, Under review.

Corman, G., Vu, M. N., and Collin, F. (2022). Numerical investigation of the couplings between strain localisation processes and gas migrations in clay materials. *International Journal of Solids and Structures*, 256(June):111974.

Corominas, J., Martínez-Bofill, J., and Soler, A. (2015). A textural classification of argillaceous rocks and their durability. *Landslides*, 12:669–687.

Coussy, O. and Ulm, F. (1995). *Mechanics of Porous Continua*. John Wiley & Sons, Ltd, New-York, The United States.

Crunelle, B., Surdyk, D., Pauwels, J. F., and Sochet, L. R. (1997). Experimental study of low-pressure premixed methane and ethane flames by molecular beam sampling and mass spectrometry analysis. *Journal de Chimie Physique*, 94:433–459.

Cuss, R., Harrington, J., Giot, R., and Auvray, C. (2014a). Experimental observations of mechanical dilation at the onset of gas flow in callovo-oxfordian claystone. *Geological Society, London, Special Publications*, 400(1):507–519.

Cuss, R., Harrington, J., Graham, C., and Noy, D. (2014b). Observations of pore pressure in clay-rich materials; implications for the concept of effective stress applied to unconventional hydrocarbons. volume 59, page 59 – 66. Cited by: 7; All Open Access, Bronze Open Access, Green Open Access.

Cuss, R. J., Harrington, J. F., Noy, D. J., Graham, C. C., and Sellin, P. (2014c). Evidence of localised gas propagation pathways in a field-scale bentonite engineered barrier system; results from three gas injection tests in the large scale gas injection test (Lasgit). *Applied Clay Science*, 102:81–92.

Cuvilliez, S., Djouadi, I., and Raude, S. (2017a). An elastoviscoplastic constitutive model for geomaterials: Application to hydromechanical modelling of claystone response to drift excavation. *Computers and Geotechnics*, 85:321–340.

Cuvilliez, S., Djouadi, I., Raude, S., and Fernandes, R. (2017b). An elastoviscoplastic constitutive model for geomaterials: application to hydromechanical of claystone response to drift. *Comput Geotech*, 85:321–340.

Cygan, R. T., Greathouse, J. A., Heinz, H., and Kalinichev, A. G. (2009). Molecular models and simulations of layered materials. *Journal of Materials Chemistry*, 19(17):2470–2481.

Cygan, R. T., Guggenheim, S., and Koster van Groos, A. F. (2004a). Molecular models for the intercalation of methane hydrate complexes in montmorillonite clay. *The Journal of Physical Chemistry B*, 108(39):15141–15149.

Cygan, R. T., Liang, J.-J., and Kalinichev, A. G. (2004b). Molecular models of hydroxide, oxyhydroxide, and clay phases and the development of a general force field. *The Journal of Physical Chemistry B*, 108(4):1255–1266.

Dalton, J. (1802). Essay IV. On the expansion of elastic fluids by heat. *Memoirs of the Literary and Philosophical Society of Manchester*, 5(2):595–602.

Damians, I., Olivella, S., and Gens, A. (2020). Modelling gas flow in clay materials incorporating material heterogeneity and embedded fractures. *International Journal of Rock Mechanics and Mining Sciences*, 136. cited By 1.

Daniels, K. and Harrington, J. (2017). The response of compact bentonite during a 1-D gas flow test. Technical report, British Geological Survey.

Darcy, H. (1856). *Les fontaines publiques de la ville de Dijon*. Librairie des Corps Impériaux des Ponts et Chaussées et des Mines, Paris, France.

Darden, T., York, D., and Pedersen, L. (1993). Particle mesh ewald: An nlog(n) method for ewald sums in large systems. *The Journal of chemical physics*, 98(12):10089–10092.

Davy, C. A., Skoczylas, F., Barnichon, J.-D., and Lebon, P. (2007). Permeability of macro-cracked argillite under confinement: gas and water testing. *Physics and Chemistry of the Earth, Parts A/B/C*, 32(8-14):667–680.

Day, R. and Potts, D. (1994). Zero thickness interface elements—numerical stability and application. *International Journal for numerical and analytical methods in geomechanics*, 18(10):689–708.

De Borst, R. and Mühlhaus, H.-B. (1992). Gradient-Dependent Plasticity: Formulation and Algorithmic Aspects. *International Journal for Numerical Methods in Engineering*, 35(3):521–539.

De Craen, M., Wang, L., Van Geet, M., and Moors, H. (2004a). Geochemistry of boom clay pore water at the mol site. sck-cen blg-990. Report SCK-CEN BLG-990, Belgian Nuclear Research Centre - SCK CEN.

De Craen, M., Wang, L., Van Geet, M., and Moors, H. (2004b). Geochemistry of boom clay pore water at the mol site. sck-cen blg-990. Report SCK-CEN BLG-990.

De Craen, M., Wang, L., Van Geet, M., and Moors, H. (2004c). Geochemistry of boom clay pore water at the mol site. sck-cen blg-990. Report SCK-CEN BLG-990, Belgian Nuclear Research Centre - SCK CEN.

De Jong, P., Wilson, J., Neilson, G., and Buckingham, A. (1997). Hydrophobic hydration of methane. *Molecular physics*, 91(1):99–104.

de La Vaissière, R., Armand, G., and Talandier, J. (2015). Gas and water flow in an excavation-induced fracture network around an underground drift: a case study for a radioactive waste repository in clay rock. *Journal of Hydrology*, 521:141–156.

De La Vaissière, R., Gerard, P., Radu, J.-P., Charlier, R., Collin, F., Granet, S., Talandier, J., Piedevache, M., and Helmlinger, B. (2014). Gas injection test in the Callovo-Oxfordian claystone: Data analysis and numerical modelling. *Geological Society Special Publication*, 400(1):427–441. cited By 3.

DEFRA (2008). Managing Radioactive Waste Safely – A Framework For Implementing Geological Disposal: White Paper, Cm 7386. *Department for Environment, Food and Rural Affairs, BERR and the Devolved Administrations for Wales and Northern Ireland, 2008*, page 94pp.

Dehbi, A. (2011). Prediction of extrathoracic aerosol deposition using rans-random walk and les approaches. *Aerosol Science and Technology*, 45(5):555–569.

Delage, P., Cui, Y.-J., and Tang, A. M. (2010). Clays in radioactive waste disposal. *Journal of Rock Mechanics and Geotechnical Engineering*, 2(2):111–123.

Delage, P., Howat, M. D., and Cui, Y. J. (1998). The relationship between suction and swelling properties in a heavily compacted unsaturated clay. *Engineering Geology*, 50:31–48.

Delay, J., Vinsot, A., Krieguer, J.-M., Rebours, H., and Armand, G. (2007). Making of the underground scientific experimental programme at the meuse/haute-marne underground research laboratory, north eastern france. *Physics and Chemistry of the Earth, Parts A/B/C*, 32(1):2–18.

Dellano-Paz, F., Calvo-Silvosa, A., Iglesias Antelo, S., and Soares, I. (2015). The European low-carbon mix for 2030: The role of renewable energy sources in an environmentally and socially efficient approach. *Renewable and Sustainable Energy Reviews*, 48:49–61.

Deng, Y. F., Tang, A. M., Cui, Y. J., Nguyen, X. P., Li, X. L., and Wouters, L. (2011). Laboratory hydro-mechanical characterisation of Boom Clay at Essen and Mol. *Physics and Chemistry of the Earth, Parts A/B/C*, 36:1878–1890.

Deptulski, R. C. (2021). *Modélisation des écoulements diphasiques à l'échelle de pores dans des milieux déformables à l'aide de méthodes particulaires (SPH)*. PhD thesis, Sorbonne Université. Thèse de doctorat dirigée par Kondo, Djimédo et Dymitrowska, Magdalena Mécanique des fluides Sorbonne université 2021.

Derjaguin, B., Churaev, N., and Muller, V. (1987). *Surface Forces*.

Desbois, G., Urai, J., and Craen, M. (2010). In-situ and direct characterization of porosity in boom clay (mol site, belgium) by using novel combination of ion beam cross-sectioning, sem and cryogenic methods. motivations, first results and perspectives. *External Report of the Belgian Nuclear Research Centre*.

Di Donna, A., Charrier, P., Dijkstra, J., Andò, E., and Bésuelle, P. (2022). The contribution of swelling to self-sealing of claystone studied through x-ray tomography. *Physics and Chemistry of the Earth, Parts A/B/C*, 127:103191.

Di Donna, A., Charrier, P., Salager, S., and Bésuelle, P. (2019). Self-sealing capacity of argillite samples. In *7th International Symposium on Deformation Characteristics of Geomaterials*.

Dieudonné, A.-C. (2016). *Hydromechanical behaviour of compacted bentonite : from micro-scale analysis to macro-scale modelling*. PhD thesis, University of Liège.

Dieudonné, A.-C., Cerfontaine, B., Collin, F., and Charlier, R. (2015). Hydromechanical modelling of shaft sealing for CO2 storage. *Engineering geology*, 193:97–105.

Diomidis, N., Cloet, V., Leupin, O., Marschall, P., Poller, A., and Stein, M. (2016). Production, consumption and transport of gases in deep geological repositories according to the swiss disposal concept. Technical report, National Cooperative for the Disposal of Radioactive Waste (NAGRA).

Djouadi, I., Giot, R., Raude, S., Cuvilliez, S., Laigle, F., and Fernandes, R. (2020). Integration of Transverse Isotropy in the Instantaneous Behaviour of Geomaterials with Application to Numerical Modelling of Underground Structures. *Geotechnical and Geological Engineering*, 38:4917–4938.

Dobrev, D., Gondolli, J., Mendoza, M. A. N., Steinova, J., and Zun, a. M. (2017). Corrosion test in natural granitic environment. participation in the material corrosion test (macote) project, part 2 of the contract implementation and evaluation of the macote experiment at the grimsel test site. – technical report 194/2017. Report Technical Report 194/2017, .

Donev, A., Fai, T. G., and Vanden-Eijnden, E. (2014). A reversible mesoscopic model of diffusion in liquids: from giant fluctuations to fick's law. *Journal of Statistical Mechanics: Theory and Experiment*, 2014(4):P04004.

Dongari, N., Sambasivam, R., and Durst, F. (2009). Extended navier-stokes equations and treatments of micro-channel gas flows. *Journal of Fluid Science and Technology*, 4(2):454–467.

Draper, D., Pereira, A., Prado, P., Saltelli, A., Cheal, R., Eguilior, S., Mendes, B., and Tarantola, S. (1999). Scenario and parametric uncertainty in GESAMAC: A methodological study in nuclear waste disposal risk assessment. *Computer Physics Communications*, 117(1):142–155.

EC (2004). Geological Disposal of Radioactive Wastes Produced by Nuclear Power. From Concept to Implementation. *Report of the European Commission, EUR 21224. European Commission, Luxembourg*, page 43pp.

(Eds), G. A. (2018). Description of the constitutive models available at the start of the project. Conceptual bases, mathematical description and capabilities and shortcomings. Technical report, BEACON Project. Technical Report DELIVERABLE (D3.1).

Ehlers, W. and Volk, W. (1998). On theoretical and numerical methods in the theory of porous media based on polar and non-polar elasto-plastic solid materials. *Int J Solids Struct*, 35(34-35):4597–4617.

Eiermann, M., Ernst, O. G., and Ullmann, E. (2007). Computational aspects of the stochastic finite element method. In *Computing and Visualization in Science*.

Ellis, C. and Holsen, J. (1969). Diffusion coefficients for he-n2 and n2-co2 at elevated temperatures. *Industrial & Engineering Chemistry Fundamentals*, 8(4):787–791.

Engeland, C., Haut, B., Spreutels, L., and Sobac, B. (2020). Evaporation versus imbibition in a porous medium. *Journal of Colloid and Interface Science*, 576:280–290.

Enresa (2000). FEBEX Project. Full-scale engineered barriers experiment for a deep geological repository for high level radioactive waste in crystalline host rock, Final report, 1/2000. Technical report, Enresa, Madrid, Spain.

ENRESA (2006). *FEBEX: Full-scale Engineered Barriers Experiment, Updated Final Report 1994-2004*. Publicación Técnica ENRESA 05-0/2006. ENRESA, Madrid.

Enresa (2006). Full-scale engineered barriers experiment. Enresa. Madrid. Spain. Updated final report 1994-2004. Technical publication 05-0/2006. Technical report, Enresa, Madrid, Spain.

ENSI (2008). Sectoral plan for deep geological repositories. https://www.ensi.ch/en/waste-disposal/deep-geological-repository/sectoral-plan-for-deep-geological-repositories-sgt/ [Accessed: 2023-04-08].

ENSI (2009). Guideline for Swiss Nuclear Installations. Specific design principles for deep geological repositories and requirements for the safety case. *ENSI Report ENSI-G03/e, Swiss Federal Nuclear Safety Inspectorate (ENSI), Brugg, Switzerland*.

Errington, J. R. and Panagiotopoulos, A. Z. (1998). A fixed point charge model for water optimized to the vapor- liquid coexistence properties. *The Journal of Physical Chemistry B*, 102(38):7470–7475.

EURAD (2020). Deliverable 6.1: Initial state-of-the-art on gas transport in clayey materials. HORIZON 2020 project EURAD. EC Grant agreement no: 847593.

Ezzatneshan, E. (2017). Study of surface wettability effect on cavitation inception by implementation of the lattice boltzmann method. *Physics of Fluids*, 29(11):113304.

Faivre, M., Paul, B., Golfier, F., Giot, R., Massin, P., and Colombo, D. (2016). 2D coupled HM-XFEM modeling with cohesive zone model and applications to fluid-driven fracture network. *Engineering Fracture Mechanics*, 159:115–143.

Fedoseev, A., Demin, N., Salnikov, M., and Sukhinin, G. (2018). Numerical modelling of heat and moisture transfer in a clay-like porous material. In *Journal of Physics: Conference Series*, volume 1105, page 012048. IOP Publishing.

Fernandes, R. (2014). Consolidation d'une colonne de sol poro-élastique sarurée (terzaghi). *Documentation Code_Aster [V7.30.100]*.

Fernandez-Prini, R., Crovetto, R., Japas, M. L., and Laria, D. (1985). Thermodynamics of dissolution of simple gases in water. *Accounts of Chemical Research*, 18(7):207–212.

Ferrage, E., Sakharov, B. A., Michot, L. J., Delville, A., Bauer, A., Lanson, B., Grangeon, S., Frapper, G., Jiménez-Ruiz, M., and Cuello, G. J. (2011). Hydration properties and interlayer organization of water and ions in synthetic na-smectite with tetrahedral layer charge. part 2. toward a precise coupling between molecular simulations and diffraction data. *The Journal of Physical Chemistry C*, 115(5):1867–1881.

Fick, A. (1855). Über Diffusion [Translated: On liquid diffusion]. *Poggendorff's Annalen der Physik und Chemie*, 170(1):59–86.

Finn, R. (1986). The capillary contact angle. *Equilibrium Capillary Surfaces. Grundlehren der mathematischen Wissenschaften*, 284(Springer).

Finn, R. and Shinbrot, M. (1987). The capillary contact angle i. the horizontal plane and stick-slip motion. *Journal of Mathematical Analysis and Applications*, 123(1):1 – 17. Cited by: 14; All Open Access, Bronze Open Access.

Finn, R. and Shinbrot, M. (1988). The capillary contact angle, ii: The inclined plane. *Mathematical Methods in the Applied Sciences*, 10(2):165 – 196. Cited by: 8.

Fischer, K. A. and Wriggers, P. (2006). Mortar based frictional contact formulation for higher order interpolations using the moving friction cone. *Computer methods in applied mechanics and engineering*, 195(37-40):5020–5036.

Forsyth, P., Gillespie, D. R., McGilvray, M., and Galoul, V. (2016). Validation and assessment of the continuous random walk model for particle deposition in gas turbine engines. In *Turbo Expo: Power for Land, Sea, and Air*, volume 49682, page V001T01A026. American Society of Mechanical Engineers.

Foster, M. D. (1951). The importance of exchangeable magnesium and cation-exchange capacity in the study of montmorillonitic clays. *American Mineralogist: Journal of Earth and Planetary Materials*, 36(9-10):717–730.

François, B. (2014). Hollow Cylinder Tests on Boom Clay : Modelling of Strain Localization in the Anisotropic Excavation Damaged Zone. *Rock Mech Rock Eng*, 47:71–86.

Frederickx, L., Honty, M., Craen, M. D., and Elsen, J. (2021). Evaluating the quantification of the clay mineralogy of the rupelian boom clay in belgium by a detailed study of size fractions. *Applied Clay Science*, 201:105954.

Frentrup, H., Avendaño, C., Horsch, M., Salih, A., and Müller, E. A. (2012). Transport diffusivities of fluids in nanopores by non-equilibrium molecular dynamics simulation. *Molecular Simulation*, 38(7):540–553.

Froning, D., Brinkmann, J., Reimer, U., Schmidt, V., Lehnert, W., and Stolten, D. (2013). 3d analysis, modeling and simulation of transport processes in compressed fibrous microstructures, using the lattice boltzmann method. *Electrochimica Acta*, 110:325–334.

G., G. and M., F. (2018). Modelling of dilatancy-controlled gas flow in saturated bentonite with double porosity and double effective stress concepts. *Engineering Geology*, 243:253–271.

Gaboreau, S., Robinet, J.-C., and Pret, D. (2016). Optimization of pore-network characterization of a compacted clay material by tem and fib/sem imaging. *Microporous and Mesoporous Materials*, 224:116–128.

Gadikota, G., Dazas, B., Rother, G., Cheshire, M. C., and Bourg, I. C. (2017a). Hydrophobic solvation of gases (co2, ch4, h2, noble gases) in clay interlayer nanopores. *The Journal of Physical Chemistry C*, 121(47):26539–26550.

Gadikota, G., Dazas, B., Rother, G., Cheshire, M. C., and Bourg, I. C. (2017b). Hydrophobic solvation of gases (co2, ch4, h2, noble gases) in clay interlayer nanopores. *The Journal of Physical Chemistry C*, 121(47):26539–26550.

Gao, J., Xing, H., Tian, Z., and Muhlhaus, H. (2014). Lattice boltzmann modeling and evaluation of fluid flow in heterogeneous porous media involving multiple matrix constituents. *Computers & Geosciences*, 62:198–207.

Gao, J., Xing, H., Tian, Z., Pearce, J. K., Sedek, M., Golding, S. D., and Rudolph, V. (2017). Reactive transport in porous media for co2 sequestration: Pore scale modeling using the lattice boltzmann method. *Computers & Geosciences*, 98:9–20.

Garde, S., Garcıa, A. E., Pratt, L. R., and Hummer, G. (1999). Temperature dependence of the solubility of non-polar gases in water. *Biophysical chemistry*, 78(1-2):21–32.

Garello, C. M. L. (1999). *Análisis microestructural de la fractura del hormigón utilizando elementos finitos tipo junta. Aplicación a diferentes hormigones*. PhD thesis, Universitat Politècnica de Catalunya (UPC).

Gens, A., Carol, I., and Alonso, E. (1990a). A constitutive model for rock joints formulation and numerical implementation. *Computers and Geotechnics*, 9(1-2):3–20.

Gens, A., Carol, I., and Alonso, E. E. (1990b). A constitutive model for rock joints formulation and numerical implementation. *Computers and Geotechnics*, 9(1-2):3–20.

Gens, A., Sánchez, M., Guimarães, L., Alonso, E., Lloret, A., Olivella, S., Villar, M., and Huertas, F. (2009). A full-scale in situ heating test for high-level nuclear waste disposal: Observations, analysis and interpretation. *Geotechnique*, 59(4):377–399. cited By 180.

Gentier, S., Petitjean, C., Riss, J., and Archambault, G. (1996). Hydromechanical behavior of a natural joint under shearing. In *ARMA North America Rock Mechanics Symposium*, pages ARMA–96. ARMA.

Genty, A., Gueddani, S., and Dymitrowska, M. (2017a). Computation of saturation dependence of effective diffusion coefficient in unsaturated argillite micro-fracture by lattice boltzmann method. *Transport in Porous Media*, 117(1):149–168.

Genty, A., Gueddani, S., and Dymitrowska, M. (2017b). Computation of saturation dependence of effective diffusion coefficient in unsaturated argillite micro-fracture by lattice boltzmann method. *Transport in Porous Media*, 117(1):149–168.

Genty, A. and Pot, V. (2013). Numerical simulation of 3d liquid–gas distribution in porous media by a two-phase trt lattice boltzmann method. *Transport in porous media*, 96:271–294.

Gerard, P., Charlier, R., Chambon, R., and Collin, F. (2008a). Influence of evaporation and seepage on the convergence of a ventilated cavity. *Water Resources Research*, 44(7). cited By 27 [4].

Gerard, P., Charlier, R., Su, K., Duveau, G., Giot, R., Chavant, C., and Collin, F. (2008b). Numerical modelling of coupled mechanics and gas tansfer around radioactive waste in long-term storage. *Journal of Theoretical and Applied Mechanics*, 38:25–44.

Ghanbarian, B., Daigle, H., Hunt, A. G., Ewing, R. P., and Sahimi, M. (2015). Gas and solute diffusion in partially saturated porous media: Percolation theory and effective medium approximation compared with lattice boltzmann simulations. *Journal of Geophysical Research: Solid Earth*, 120(1):182–190.

Ghanem, R. G. and Spanos, P. D. (1991). *Stochastic Finite Elements: A Spectral Approach*.

Gharbia, I. B. and Jaffré, J. (2014). Gas phase appearance and disappearance as a problem with complementarity constraints. *Mathematics and Computers in Simulation*, 99:28–36.

Gimmi, T. and Churakov, S. V. (2019a). Water retention and diffusion in unsaturated clays: Connecting atomistic and pore scale simulations. *Applied Clay Science*, 175:169–183.

Gimmi, T. and Churakov, S. V. (2019b). Water retention and diffusion in unsaturated clays: Connecting atomistic and pore scale simulations. *Applied Clay Science*, 175:169–183.

Gimmi, T., Schneebeli, M., Flühler, H., Wydler, H., and Baer, T. (1997). Field-scale water transport in unsaturated crystalline rock. *Water Resources Research*, 33(4):589–598.

Gimmi, T., Waber, H., Gautschi, A., and Rübel, A. (2007). Stable water isotopes in pore water of jurassic argillaceous rocks as tracers for solute transport over large spatial and temporal scales. *Water Resources Research*, 43(4).

Giot, R., Auvray, C., and Talandier, J. (2019). Self-sealing of claystone under x-ray nanotomography. *Geological Society, London, Special Publications*, 482(1):213–223.

Glaus, M. A., Frick, S., Rossé, R., and Van Loon, L. R. (2010). Comparative study of tracer diffusion of hto, 22na+ and 36cl- in compacted kaolinite, illite and montmorillonite. *Geochimica et Cosmochimica Acta*, 74(7):1999–2010.

Gomez-Hernandez, J. (2000). Fm-c experiment: Part a) effective diffusivity and accessible porosity derived from in-situ he-4 tests. part b) prediction of he-3 concentration in a cross-hole experiment.

Gonzalez Blanco, L. (2017). *Gas Migration in Deep Argillaceous Formations: Boom Clay and Indurated Clays*. Thesis, Universitat Politècnica de Catalunya.

Gonzalez-Blanco, L. (2017). Gas migration in deep argillaceous formations: Boom clay and indurated clays.

Gonzalez-Blanco, L., Romero, E., Jommi, C., Li, X., and Sillen, X. (2016a). Gas migration in a Cenozoic clay: Experimental results and numerical modelling. *Geomechanics for Energy and the Environment*, 6:81–100.

Gonzalez-Blanco, L., Romero, E., Jommi, C., Li, X., and Sillen, X. (2016b). Gas migration in a cenozoic clay: Experimental results and numerical modelling. *Geomechanics for Energy and the Environment*, 6:81–100.

Gonzalez-Blanco, L., Romero, E., Marschall, P., and Levasseur, S. (2021). He waste disposal. *Rock Mechanics and Rock Engineering*.

Gonzalez-Blanco, L., Romero, E., Marschall, P., and Levasseur, S. (2022). Hydro - mechanical Response to Gas Transfer of Deep Argillaceous Host Rocks for Radioactive Waste Disposal. *Rock Mechanics and Rock Engineering*, 55(3):1159–1177.

Gonzalez-Blanco, L. (2017a). *Gas migration in deep argillaceous formations : Boom Clay and indurated clays*. PhD thesis, Universitat Politècnica de Catalunya (UPC).

Gonzalez-Blanco, L. (2017b). *Gas migration in deep argillaceous formations: Boom Clay and indurated clays*. Doctoral dissertation.

Gonzalez-Blanco, L. and Romero, E. (2022). A multi-scale insight into gas transport in a deep Cenozoic clay A multi-scale insight into gas transport in a deep Cenozoic clay. *Géotechnique*. Published Online.

Goodman, R. (1976). *Methods of geological engineering in Discontinuous Rocks*. West Publishing Co.

Goodman, R. E., Taylor, R. L., and Brekke, T. L. (1968). A model for the mechanics of jointed rock. *Journal of the soil mechanics and foundations division*, 94(3):637–659.

Graham, C. C., Harrington, J. F., and Sellin, P. (2016). Gas migration in pre-compacted bentonite under elevated pore-water pressure conditions. *Applied Clay Science*, 132:353–365.

Grambow, B. (2016). Geological disposal of radioactive waste in clay. *Elements*, 12(4):239–245.

Greenwell, H. C., Jones, W., Coveney, P. V., and Stackhouse, S. (2006). On the application of computer simulation techniques to anionic and cationic clays: A materials chemistry perspective. *Journal of Materials Chemistry*, 16(8):708–723.

Groß, T., Buchhauser, J., and Lüdemann, H.-D. (1998). Self-diffusion in fluid carbon dioxide at high pressures. *The Journal of chemical physics*, 109(11):4518–4522.

Grunwald, N., Lehmann, C., Maßmann, J., Naumov, D., Kolditz, O., and Nagel, T. (2022). Non-isothermal two-phase flow in deformable porous media: systematic open-source implementation and verification procedure. *Geomechanics and Geophysics for Geo-Energy and Geo-Resources*, 8(3). cited By 2.

Grunwald, N., Nagel, T., Pitz, M., and Kolditz, O. (2023). Extended analysis of benchmarks for gas phase appearance in low-permeable rocks. *Geomechanics and Geophysics for Geo-Energy and Geo-Resources*, 9(1):170.

Guerra, A., Aimedieu, P., Bornert, M., Cui, Y., Tang, A., Sun, Z., Mokni, N., Delage, P., and Bernier, F. (2018). Analysis of the structural changes of a pellet/powder bentonite mixture upon wetting by x-ray computed microtomography. *Applied Clay Science*, 165:164–169.

Guiducci, C., Collin, F., Radu, J.-P., Pellegrino, A., and Charlier, R. (2003). Numerical modeling of hydro-mechanical fracture behavior. In *ISRM Congress*, pages ISRM–10CONGRESS. ISRM.

Guiducci, C., Pellegrino, A., Radu, J., Collin, F., and Charlier, R. (2002). *Numerical modeling of hydro-mechanical fracture behavior*, pages 293–299.

Guillot, B. (2002). A reappraisal of what we have learnt during three decades of computer simulations on water. *Journal of molecular liquids*, 101(1-3):219–260.

Guo, C., Wei, M., and Liu, H. (2015). Modeling of gas production from shale reservoirs considering multiple transport mechanisms. *PloS one*, 10(12):e0143649.

Guo, Y., He, X., Huang, W., and Wang, M. (2019). Microstructure effects on effective gas diffusion coefficient of nanoporous materials. *Transport in Porous Media*, 126:431–453.

Gutiérrez-Rodrigo, V., Martín, P. L., and Villar, M. V. (2021). Effect of interfaces on gas breaktrough pressure in compacted bentonite used as engineered barrier for radioactive waste disposal. *Process Safety and Environmental Protection*, 149:244–257.

Gutiérrez, V. (2017). Ensayo para determinar la presión de paso de gas ("breakthrough") en materiales expansivos. Report, CIEMAT.

Gutiérrez Rodrigo, V. (2019). *Transporte de gas en materiales de barrera*. PhD thesis, Universidad Complutense de Madrid, Facultad de Ciencias Geológicas, Departamento de Geodinámica.

Gutiérrez-Rodrigo, V., Martín, P. L., and Villar, M. V. (2021). Effect of interfaces on gas breaktrough pressure in compacted bentonite used as engineered barrier for radioactive waste disposal. *Process Safety and Environmental Protection*, 149:244–257.

Görke, U.-J., Taron, J., Singh, A., Wang, W., and Kolditz, O. (2011). Towards the generic conceptual and numerical framework for the simulation of CO <inf>2</inf> sequestration in different types of georeservoirs. pages 160–171. cited By 1.

Habraken, A. (1989). *Contribution à la modélisation du formage des métaux par la méthode des éléments finis*. PhD thesis, University of Liège.

Habraken, A. and Cescotto, S. (1998a). Contact between deformable solids: the fully coupled approach. *Mathematical and Computer modelling*, 28(4-8):153–169.

Habraken, A. M. and Cescotto, S. (1998b). Contact between deformable solids: The fully coupled approach. *Mathematical and Computer Modelling*, 28(4):153–169.

Haldorsen, H. H. and Lake, L. W. (1984). A new approach to shale management in field-scale models. *Society of Petroleum Engineers Journal*, 24(04):447–457.

Han, P. and Bartels, D. M. (1996). Temperature dependence of oxygen diffusion in h2o and d2o. *The Journal of physical chemistry*, 100(13):5597–5602.

Harrington, J., Graham, C., Cuss, R., and Norris, S. (2019). Gas network development in compact bentonite: key controls on the stability of flow pathways. *Geofluids*, 2019:1–19.

Harrington, J., Milodowski, A., Graham, C., Rushton, J., and Cuss, R. (2012a). Evidence for gas-induced pathways in clay using a nanoparticle injection technique. *Mineralogical Magazine*, 76(8):3327–3336.

Harrington, J. F., Cuss, R. J., and Talandier, J. (2017a). Gas transport properties through intact and fractured Callovo-Oxfordian mudstones. In Rutter, E. H., Mecklenburgh, J., and Taylor, K. G., editors, *Geomechanical and Petrophysical Properties of Mudrock*, volume 454, pages 131–154. Geological Society, London, Special Publications.

Harrington, J. F., Cuss, R. J., and Talandier, J. (2017b). Gas transport properties through intact and fractured Callovo-Oxfordian mudstones. In Rutter, E. H., Mecklenburgh, J., and Taylor, K. G., editors, *Geomechanical and Petrophysical Properties of Mudrock*, volume 454, pages 131–154. Geological Society, London, Special Publications.

Harrington, J. F., Graham, C. C., Cuss, R. J., and Norris, S. (2017c). Gas network development in a precompacted bentonite experiment: Evidence of generation and evolution. *Applied Clay Science*, 147:80–89.

Harrington, J. F., Milodowski, A. E., Graham, C. C., Rushton, J. C., and Cuss, R. J. (2012b). Evidence for gas-induced pathways in clay using a nanoparticle injection technique. *Mineralogical Magazine*, 76(8):3327–3336.

Harrington, J. F., Milodowski, A. E., Graham, C. C., Rushton, J. C., and Cuss, R. J. (2012c). Evidence for gas-induced pathways in clay using a nanoparticle injection technique. *Mineralogical Magazine*, 76(8):3327–3336.

Harris, J. G. and Yung, K. H. (1995). Carbon dioxide's liquid-vapor coexistence curve and critical properties as predicted by a simple molecular model. *The Journal of Physical Chemistry*, 99(31):12021–12024.

Haupt, P. (2002). *Continuum mechanics and theory of materials*. Springer, Heidelberg-Berlin.

Hausmannová, L., Hanusová, I., and Dohnálková, M. (2018). Summary of the research of czech bentonites for use in the deep geological repository–up to 2018.

Hausmannová, L. (2017). *The influence of water pressure on the hydraulic conductivity and swelling pressure of Czech bentonites*. dissertation thesis, Czech Technical University in Prague, Faculty of Civil Engineering, Prague.

Haynes, W. (2014). *CRC Handbook of Chemistry and Physics*. CRC Handbook of Chemistry and Physics. CRC Press, 95 edition.

Haynes, W. M. (2004). *CRC handbook of chemistry and physics*, volume 97. CRC press.

He, S., Jiang, Y., Conrad, J. C., and Qin, G. (2015). Molecular simulation of natural gas transport and storage in shale rocks with heterogeneous nano-pore structures. *Journal of Petroleum Science and Engineering*, 133:401–409.

He, X. and Luo, L.-S. (1997). Lattice boltzmann model for the incompressible navier–stokes equation. *Journal of statistical Physics*, 88:927–944.

He, X., Zou, Q., Luo, L.-S., and Dembo, M. (1997). Analytic solutions of simple flows and analysis of nonslip boundary conditions for the lattice boltzmann bgk model. *Journal of Statistical Physics*, 87:115–136.

Hedan, S., Cosenza, P., and Valle, V. (2012). Investigation of the damage induced by desiccation and heating of tournemire argillite using digital image correlation. *International Journal of Rock Mechanics and Mining Sciences*, 51:64–75.

Hedan, S., L, F. A., and Valle, V. (2014). One-year monitoring of desiccation cracks in tournemire argillite using digital image correlation. *International Journal of Rock Mechanics and Mining Sciences*, 68:22–35.

Hegde, J. and Rokseth, B. (2020). Applications of machine learning methods for engineering risk assessment – A review. *Safety Science*, 122. cited By 4.

Helfer, T., Bleyer, J., Frondelius, T., Yashchuk, I., Nagel, T., and Naumov, D. (2020). The `MFrontGenericInterfaceSupport` project. *Journal of Open Source Software*, 5(48):1–8.

Helton, J. C. (1993). Uncertainty and sensitivity analysis techniques for use in performance assessment for radioactive waste disposal. *Reliability Engineering and System Safety*, 42(2-3):327–367.

Heyes, D. M. (1994). Pressure tensor of partial-charge and point-dipole lattices with bulk and surface geometries. *Physical Review B*, 49(2):755.

Hildebrand, J. H. (1916). Solubility. *Journal of the American Chemical Society*, 38(8):1452–1473.

Hirschfelder, J. O., Curtiss, C. F., and Bird, R. B. (1964). Molecular theory of gases and liquids. *Molecular theory of gases and liquids*.

Ho, L. N., Schuurman, Y., Farrusseng, D., and Coasne, B. (2015). Solubility of gases in water confined in nanoporous materials: Zsm-5, mcm-41, and mil-100. *The Journal of Physical Chemistry C*, 119(37):21547–21554.

Hoang, H., Ho, K. H., Battani, A., Pujol, M., and Galliero, G. (2021). On elemental and isotopic fractionation of noble gases in geological fluids by molecular diffusion. *Geochimica et Cosmochimica Acta*, 315:172–184.

Holloway, S. (2005). Underground sequestration of carbon dioxide—a viable greenhouse gas mitigation option. *Energy*, 30(11-12):2318–2333.

Holmboe, M. and Bourg, I. C. (2014). Molecular dynamics simulations of water and sodium diffusion in smectite interlayer nanopores as a function of pore size and temperature. *The Journal of Physical Chemistry C*, 118(2):1001–1013.

Horseman, S. and Harrington, J. (1994). Migration of repository gases in an overconsolidated clay. Technical report, British Geological Survey, British Geological Survey. Technical report WE/94/7.

Horseman, S., Harrington, J., and Sellin, P. (1999a). Gas migration in clay barriers. *Engineering geology*, 54(1-2):139–149.

Horseman, S., Harrington, J., and Sellin, P. (1999b). Gas migration in clay barriers. *Engineering Geology*, 54(1-2):139–149.

Horseman, S., Harrington, J., and Sellin, P. (1999c). Gas migration in clay barriers. *Engineering Geology*, 54(1-2):139–149.

Hoteit, H. and Firoozabadi, A. (2009). Numerical modeling of diffusion in fractured media for gas-injection and-recycling schemes. *Spe Journal*, 14(02):323–337.

Hu, H., Xing, Y., Wang, B., Lv, Y., Zhang, Q., and Li, X. (2021). Ch4 diffusion in intra-pore of montmorillonite: From self-diffusion to fick-diffusion. *Journal of Petroleum Science and Engineering*, 197:107977.

Hu, Q. and Wang, J. S. (2003). Aqueous-phase diffusion in unsaturated geologic media: A review. *Critical Reviews in Environmental Science and Technology*, 33:275–297.

Huang, H., Sukop, M., and Lu, X. (2015a). Multiphase lattice boltzmann methods: Theory and application.

Huang, Y., Kolditz, O., and Shao, H. (2015b). Extending the persistent primary variable algorithm to simulate non-isothermal two-phase two-component flow with phase change phenomena. *Geothermal Energy*, 3:1–23.

Huang, Y., Shao, H., Wieland, E., Kolditz, O., and Kosakowski, G. (2018). A new approach to coupled two-phase reactive transport simulation for long-term degradation of concrete. *Construction and Building Materials*, 190:805–829. cited By 6.

Hummel, W. and Schneider, J. W. (2005). Safety of nuclear waste repositories. *Chimia*, 59(12):909–909.

Hura, G., Russo, D., Glaeser, R. M., Head-Gordon, T., Krack, M., and Parrinello, M. (2003). Water structure as a function of temperature from x-ray scattering experiments and ab initio molecular dynamics. *Physical Chemistry Chemical Physics*, 5(10):1981–1991.

IAEA (2009). Classification of Radioactive Waste. *IAEA Safety Standards Series. No. GSG-1.IAEA, Vienna, Austria*.

IAEA (2011). Geological disposal facilities for radioactive waste. *IAEA Safety Standards Series. No. SSG-14. IAEA, Vienna, Austria*.

Idiart, A. E., López, C. M., and Carol, I. (2011a). Chemo-mechanical analysis of concrete cracking and degradation due to external sulfate attack: A meso-scale model. *Cement and Concrete Composites*, 33(3):411–423.

Idiart, A. E., López, C. M., and Carol, I. (2011b). Modeling of drying shrinkage of concrete specimens at the meso-level. *Materials and structures*, 44:415–435.

Jacops, E., Aertsens, M., Maes, N., Bruggeman, C., Krooss, B., Amann-Hildenbrand, A., Swennen, R., and Littke, R. (2017a). Interplay of molecular size and pore network geometry on the diffusion of dissolved gases and hto in boom clay. *Applied Geochemistry*, 76:182–195.

Jacops, E., Aertsens, M., Maes, N., Bruggeman, C., Krooss, B. M., Amann-Hildenbrand, A., Swennen, R., and Littke, R. (2017b). Interplay of molecular size and pore network geometry on the diffusion of dissolved gases and hto in boom clay. *Applied Geochemistry*, 76:182–195.

Jacops, E., Aertsens, M., Maes, N., Bruggeman, C., Swennen, R., Krooss, B., Amann-Hildenbrand, A., and Littke, R. (2017c). The dependency of diffusion coefficients and geometric factor on the size of the diffusing molecule: observations for different clay-based materials. *Geofluids*, 2017.

Jacops, E., Aertsens, M., Maes, N., Bruggeman, C., Swennen, R., Krooss, B., Amann-Hildenbrand, A., and Littke, R. (2017d). The dependency of diffusion coefficients and geometric factor on the size of the diffusing molecule: Observations for different clay-based materials. *Geofluids*, 2017.

Jacops, E., Chen, G., Yu, L., Vanleeuw, A., Nackaerts, D., and Aertens, M. (2023a). Nemesis progress report 2023; sck cen r-9349; mol, belgium. Report.

Jacops, E., Chen, G., Yu, L., Vanleeuw, A., Nackaerts, D., and Aertens, M. (2023b). Nemesis progress report 2023; sck cen r-9349; mol, belgium. Report.

Jacops, E., Maes, T., Vanleeuw, A., and De Soete, H. (2022a). *Long term gas injection in Boom Clay*. Preparation and construction phase. SCK CEN.

Jacops, E., Maes, T., Vanleeuw, A., and De Soete, H. (2022b). *Long term gas injection in Boom Clay*. Preparation and construction phase. SCK CEN.

Jacops, E., Rogiers, B., Frederick, L., Swennen, R., Littke, R., Krooss, B., Amann-Hildenbrand, A., and Bruggeman, C. (2020a). The relation between petrophysical and transport properties of the boom clay and eigenbilzen sands. *Applied Geochemistry*, 114.

Jacops, E., Rogiers, B., Frederickx, L., Swennen, R., Littke, R., Krooss, B., Amann-Hildenbrand, A., and Bruggeman, C. (2020b). The relation between petrophysical and transport properties of the boom clay and eigenbilzen sands. *Applied Geochemistry*, 114. Cited by: 3.

Jacops, E., Volckaert, G., Maes, N., Weetjens, E., and Govaerts, J. (2013a). Determination of gas diffusion coefficients in saturated porous media: He and ch4 diffusion in boom clay. *Applied Clay Science*, 83-84:217–223.

Jacops, E., Volckaert, G., Maes, N., Weetjens, E., and Govaerts, J. (2013b). Determination of gas diffusion coefficients in saturated porous media: He and CH4 diffusion in Boom Clay. *Applied Clay Science*, 83:217–223.

Jacops, E., Volckaert, G., Maes, N., Weetjens, E., and Govaerts, J. (2013c). Determination of gas diffusion coefficients in saturated porous media: He and ch4 diffusion in boom clay. *Applied Clay Science*, 83-84:217–223.

Jacops, E., Wouters, K., Volckaert, G., Moors, H., Maes, N., Bruggeman, C., Swennen, R., and Littke, R. (2015). Measuring the effective diffusion coefficient of dissolved hydrogen in saturated Boom Clay. *Applied Geochemistry*, 61:175–184.

Jacops, E., Yu, L., and Maes, N. (2020c). A new in situ gas diffusion experiment: objectives, design and experimental protocol. Report, SCK CEN.

Jacops, E., Yu, L., and Vanleeuw, A. (2020d). *Long-term slow gas injection experiment under isostatic conditions in the Boom Clay: design of the setup and experimental protocol Status 2020 SCK CEN R-7363*. Belgian Nuclear Research Center.

Jacops, E., Yu, L., and Vanleeuw, A. (2020e). *Long-term slow gas injection experiment under isostatic conditions in the Boom Clay: design of the setup and experimental protocol Status 2020 SCK CEN R-7363*. Belgian Nuclear Research Center.

Jähne, B., Heinz, G., and Dietrich, W. (1987a). Measurement of the diffusion coefficients of sparingly soluble gases in water. *Journal of Geophysical Research: Oceans*, 92(C10):10767–10776.

Jähne, B., Heinz, G., and Dietrich, W. (1987b). Measurement of the diffusion coefficients of sparingly soluble gases in water. *Journal of Geophysical Research: Oceans*, 92(C10):10767–10776.

Jaynes, D. and Rogowski, A. (1983). Applicability of fick's law to gas diffusion. *Soil Science Society of America Journal*, 47(3):425–430.

Jha, B. and Juanes, R. (2014). Coupled multiphase flow and poromechanics: A computational model of pore pressure effects on fault slip and earthquake triggering. *Water Resources Research*, 50(5):3776–3808.

Jia, Y., Bian, H. B., Duveau, G., Su, K., and Shao, J. F. (2008). Hydromechanical modelling of shaft excavation in Meuse/Haute-Marne laboratory. *Physics and Chemistry of the Earth*, 33(SUPPL. 1):422–435.

Jiang, W. and Lin, M. (2018a). Molecular dynamics investigation of conversion methods for excess adsorption amount of shale gas. *Journal of Natural Gas Science and Engineering*, 49:241–249.

Jiang, W. and Lin, M. (2018b). Molecular dynamics investigation of conversion methods for excess adsorption amount of shale gas. *Journal of Natural Gas Science and Engineering*, 49:241–249.

Johnson, L., Marschall, P., Zuidema, P., and Gribi, P. (2004). Effects of post-disposal gas generation in a repository for spent fuel, high-level waste and long-lived intermediate level waste sited in Opalinus clay. Technical report, National Cooperative for the Disposal of Radioactive Waste (Nagra), Hardstrasse 73, CH-5430 Wettingen, Switzerland. Technical Report 04-06.

Kadoura, A., Narayanan Nair, A. K., and Sun, S. (2016). Molecular dynamics simulations of carbon dioxide, methane, and their mixture in montmorillonite clay hydrates. *The Journal of Physical Chemistry C*, 120(23):12517–12529.

Kamberaj, H., Low, R., and Neal, M. (2005). Time reversible and symplectic integrators for molecular dynamics simulations of rigid molecules. *The Journal of chemical physics*, 122(22):224114.

Kamrava, S., Tahmasebi, P., and Sahimi, M. (2020). Linking Morphology of Porous Media to Their Macroscopic Permeability by Deep Learning. *Transport in Porous Media*, 131(2):427–448. cited By 4.

Kang, J., Prasianakis, N. I., and Mantzaras, J. (2013). Lattice boltzmann model for thermal binary-mixture gas flows. *Physical Review E*, 87(5):053304.

Kang, Q., Lichtner, P. C., and Zhang, D. (2006). Lattice boltzmann pore-scale model for multicomponent reactive transport in porous media. *Journal of Geophysical Research: Solid Earth*, 111(B5).

Karnland, O., Nilsson, U., Weber, H., and Wersin, P. (2008). Sealing ability of wyoming bentonite pellets foreseen as buffer material–laboratory results. *Physics and Chemistry of the Earth, Parts A/B/C*, 33:S472–S475.

Karnland, O., Olsson, S., and Nilsson, U. (2006). Mineralogy and sealing properties of various bentonites and smectite-rich clay materials. technical report tr-06-30. Report Technical Report TR-06-30, .

Kato, H., Muroi, M., Yamada, N., Ishida, H., and Sato, H. (1994). Estimation of effective diffusivity in compacted ben tonite. *MRS Online Proceedings Library (OPL)*, 353:277.

Kaufhold, S. and Dohrmann, R. (2016). Distinguishing between more and less suitable bentonites for storage of high-level radioactive waste. *Clay Minerals*, 51(2):289–302.

Kestin, J., Imaishi, N., Nott, S., Nieuwoudt, J., and Sengers, J. (1985). Viscosity of light and heavy water and their mixtures. *Physica A: Statistical Mechanics and its Applications*, 134(1):38–58.

KIELICH, S. (1965). Octopole moment of the methane molecule. *Acta Physica Polonica*, 27:457.

Kim, C., Jang, H., and Lee, J. (2015). Experimental investigation on the characteristics of gas diffusion in shale gas reservoir using porosity and permeability of nanopore scale. *Journal of Petroleum Science and Engineering*, 133:226–237.

Kim, H., Annable, M. D., and Rao, P. S. C. (2001). Gaseous transport of volatile organic chemicals in unsaturated porous media: Effect of water-partitioning and air- water interfacial adsorption. *Environmental science & technology*, 35(22):4457–4462.

King, F. (2012). Gaseous hydrogen issues in nuclear waste disposal. *Gaseous Hydrogen Embrittlement of Materials in Energy Technologies: The Problem, its Characterisation and Effects on Particular Alloy Classes*, pages 126–148.

Kneuker, T., Dohrmann, R., Ufer, K., and Jaeggi, D. (2023). Compositional-structural characterization of the opalinus clay and passwang formation: New insights from rietveld refinement (mont terri url, switzerland). *Applied Clay Science*, 242:107017.

Koch, T., Gläser, D., Weishaupt, K., Ackermann, S., Beck, M., Becker, B., Burbulla, S., Class, H., Coltman, E., Emmert, S., Fetzer, T., Grüninger, C., Heck, K., Hommel, J., Kurz, T., Lipp, M., Mohammadi, F., Scherrer, S., Schneider, M., Seitz, G., Stadler, L., Utz, M., Weinhardt, F., and Flemisch, B. (2020). DuMux 3 – an open-source simulator for solving flow and transport problems in porous media with a focus on model coupling. *Computers and Mathematics with Applications*. cited By 0.

Koh, C. A., Wisbey, R. P., Wu, X., Westacott, R. E., and Soper, A. K. (2000). Water ordering around methane during hydrate formation. *The Journal of Chemical Physics*, 113(15):6390–6397.

Kolditz, O. and Bauer, S. (2004). A process-oriented approach to computing multi-field problems in porous media. *Journal of Hydroinformatics*, 6(3):225–244. cited By 69.

Kolditz, O., Bauer, S., Bilke, L., Böttcher, N., Delfs, J., Fischer, T., Görke, U., Kalbacher, T., Kosakowski, G., McDermott, C., Park, C., Radu, F., Rink, K., Shao, H., Shao, H., Sun, F., Sun, Y., Singh, A., Taron, J., Walther, M., Wang, W., Watanabe, N., Wu, Y., Xie, M., Xu, W., and Zehner, B. (2012). OpenGeoSys: An open-source initiative for numerical simulation of thermo-hydro-mechanical/chemical (THM/C) processes in porous media. *Environmental Earth Sciences*, 67(2):589–599. cited By 297.

Kolditz, O., Gorke, U.-J., Shao, H., Shao, H., and Nagel, T. (2019). Workflows in environmental geotechnics: Status-quo and perspectives. *Environmental Science and Engineering*, pages 119–127. cited By 0.

Kolditz, O., Görke, U.-J., Konietzky, H., Maßmann, J., Nest, M., Steeb, H., Wuttke, F., and Nagel, T. (2021). GeomInt – Mechnanical Integrity of Host Rocks. In *Terrestrial Environmental Sciences*, page 277. Springer, Heidelberg.

Kolditz, O., Görke, U.-J., Konietzky, H., Maßmann, J., Nest, M., Steeb, H., and Wuttke, F. Nagel, T. (2020). GeomInt - Geomechanical integrity of host and barrier rocks - experiment, modeling and analysis of discontinuities. In *Terrestrial Environmental Sciences*, volume 4, page 250. Springer, Heidelberg. forthcoming.

Kolditz, O., Nagel, T., Shao, H., Wang, W., and Bauer, S. (2016). Thermo-Hydro-Mechanical-Chemical Processes in Fractured Porous Media: Modelling and Benchmarking - Benchmarking Initiatives. In *Terrestrial Environmental Sciences*, volume 3, page 260. Springer, Heidelberg.

Kolditz, O., Yoshioka, K., Cajuhi, T., Günther, R.-M., Steeb, H., Wuttke, F., and Nagel, T. (2023). GeomInt - Discontinuities in Geosystems From Lab to Field Scale. In *SpringerBriefs in Earth System Sciences*, page 120. Springer, Heidelberg.

Kosakowski, G., Churakov, S. V., and Thoenen, T. (2008a). Diffusion of na and cs in montmorillonite. *Clays and Clay Minerals*, 56(2):190–206.

Kosakowski, G., Churakov, S. V., and Thoenen, T. (2008b). Diffusion of na and cs in montmorillonite. *Clays and Clay Minerals*, 56(2):190–206.

Kouznetsova, V., Brekelmans, W. A., and Baaijens, F. P. (2001). Approach to micro-macro modeling of heterogeneous materials. *Computational Mechanics*, 27(1):37–48.

Kozaki, T., Saito, N., Fujishima, A., Sato, S., and Ohashi, H. (1998). Activation energy for diffusion of chloride ions in compacted sodium montmorillonite. *Journal of Contaminant Hydrology*, 35(1-3):67–75.

Kozaki, T., Sato, H., Fujishima, A., Sato, S., and Ohashi, H. (1996). Activation energy for diffusion of cesium in compacted sodium montmorillonite. *Journal of Nuclear Science and Technology*, 33(6):522–524.

Kozaki, T., Sato, H., Sato, S., and Ohashi, H. (1999). Diffusion mechanism of cesium ions in compacted montmorillonite. *Engineering Geology*, 54(1-2):223–230.

Krishna, R. and van Baten, J. M. (2012). Investigating the validity of the bosanquet formula for estimation of diffusivities in mesopores. *Chemical engineering science*, 69(1):684–688.

Kristensen, A. H., Thorbjørn, A., Jensen, M. P., Pedersen, M., and Moldrup, P. (2010). Gas-phase diffusivity and tortuosity of structured soils. *Journal of contaminant hydrology*, 115(1-4):26–33.

Krooss, B. and Leythaeuser, D. (1988). Experimental measurements of the diffusion parameters of light hydrocarbons in water-saturated sedimentary rocks—ii. results and geochemical significance. *Organic Geochemistry*, 12(2):91–108.

Krooss, B. and Schaefer, R. (1987). Experimental measurements of the diffusion parameters of light hydrocarbons in water-saturated sedimentary rocks—i. a new experimental procedure. *Organic Geochemistry*, 11(3):193–199.

Krynicki, K., Green, C. D., and Sawyer, D. W. (1978). Pressure and temperature dependence of self-diffusion in water. *Faraday Discussions of the Chemical Society*, 66:199–208.

Kutay, M. E., Aydilek, A. H., and Masad, E. (2006). Laboratory validation of lattice boltzmann method for modeling pore-scale flow in granular materials. *Computers and Geotechnics*, 33(8):381–395.

Labani, M. M., Rezaee, R., Saeedi, A., and Hinai, A. A. (2013). Evaluation of pore size spectrum of gas shale reservoirs using low pressure nitrogen adsorption, gas expansion and mercury porosimetry: A case study from the perth and canning basins, western australia. *Journal of Petroleum Science and Engineering*, 112:7–16.

LaBolle, E. M., Fogg, G. E., and Tompson, A. F. (1996). Random-walk simulation of transport in heterogeneous porous media: Local mass-conservation problem and implementation methods. *Water Resources Research*, 32(3):583–593.

LaBolle, E. M., Quastel, J., and Fogg, G. E. (1998). Diffusion theory for transport in porous media: Transition-probability densities of diffusion processes corresponding to advection-dispersion equations. *Water Resources Research*, 34(7):1685–1693.

LaBolle, E. M., Quastel, J., Fogg, G. E., and Gravner, J. (2000). Diffusion processes in composite porous media and their numerical integration by random walks: Generalized stochastic differential equations with discontinuous coefficients. *Water Resources Research*, 36(3):651–662.

Labuz, J. and Zang, A. (2012). Mohr–Coulomb failure criterion. *Rock Mechanics and Rock Engineering*, 45(6):975–979.

Laesecke, A. and Muzny, C. D. (2017a). Ab initio calculated results require new formulations for properties in the limit of zero density: The viscosity of methane (ch _ 4 ch 4). *International Journal of Thermophysics*, 38:1–12.

Laesecke, A. and Muzny, C. D. (2017b). Reference correlation for the viscosity of carbon dioxide. *Journal of physical and chemical reference data*, 46(1):013107.

Lallemand, P. and Luo, L.-S. (2003a). Lattice boltzmann method for moving boundaries. *Journal of Computational Physics*, 184(2):406 – 421. Cited by: 473.

Lallemand, P. and Luo, L.-S. (2003b). Lattice boltzmann method for moving boundaries. *Journal of Computational Physics*, 184(2):406–412.

Laloui, L., Ferrari, A., and Bosch Llufriu, J. A. (2020). Bentonite clay barriers in nuclear waste repositories. In *E3S Web of Conferences*, volume 205. EDP SCIENCES.

Lamb, W., Hoffman, G., and Jonas, J. (1981). Self-diffusion in compressed supercritical water. *The Journal of Chemical Physics*, 74(12):6875–6880.

Laufek, F., Hanusová, I., Svoboda, J., Vašíček, R., Najser, J., Koubová, M., Čurda, M., Pticem, F., Vaculíková, L., Sun, H., and Mašín, D. (2021). Mineralogická, geochemická a geotechnická studie bcv 2017 bentonit – výchozí stav a stav po tepelném zpracování při 200 °c. Article Minerály 11(8), 871, .

Le, T. T., Delage, P., Cui, Y. J., Tang, A. M., Lima, A., Romero, E., Gens, A., and Li, X. L. (2008). Water retention properties of boom clay: A comparison between different experimental techniques. *Unsaturated Soils: Advances in Geo-Engineering - Proceedings of the 1st European Conference on Unsaturated Soils, E-UNSAT 2008*, pages 229–234.

Le Crom, S., Tournassat, C., Robinet, J.-C., and Marry, V. (2021). Influence of water saturation level on electrical double layer properties in a clay mineral mesopore: A molecular dynamics study. *The Journal of Physical Chemistry C*, 126(1):647–654.

Lee, S. and Tank, R. (1985). Role of clays in the disposal of nuclear waste: a review. *Applied clay science*, 1(1-2):145–162.

Lehmann, C., Bilke, L., Buchwald, J., Graebling, N., Grunwald, N., Heinze, J., Meisel, T., Lu, R., Naumov, D., Rink, K., Özgür Sen, O., Selzer, P., Shao, H., Wang, W., Zill, F., Nagel, T., and Kolditz, O. (2024). Openworkflow—development of an open-source synthesis-platform for safety investigations in the site selection process. *Grundwasser*, 29(1):31–47.

Lenoir, N., Bornert, M., Desrues, J., Besuelle, P., and Viggiani, G. (2007). Volumetric digital image correlation applied to x-ray microtomography images from triaxial compression tests on argillaceous rock. *Strain*, 43(3):193–205.

Lepillier, B., Yoshioka, K., Parisio, F., Bakker, R., and Bruhn, D. (2020). Variational Phase-Field Modeling of Hydraulic Fracture Interaction With Natural Fractures and Application to Enhanced Geothermal Systems. *Journal of Geophysical Research: Solid Earth*, 125(7). cited By 2.

Lequesne, C. (2009). Modeling of fracture in heavy steel welded beam-to-column connection submitted to cyclic loading by finite elements.

Leupin, O., Marschall, P., Johnson, L., Cloet, V., Schneider, J., Smith, P., Savage, D., and Senger, R. (2016a). High-level waste repository-induced effects. NAGRA Technical Report NTB–14-13, National Cooperative for the Disposal of Radioactive Waste (NAGRA).

Leupin, O., Marschall, P., Johnson, L., Cloet, V., Schneider, J., Smith, P., Savage, D., and Senger, R. (2016b). Low- and intermediate-level waste repository-induced effects. NAGRA Technical Report NTB–14-14, National Cooperative for the Disposal of Radioactive Waste (NAGRA).

Levasseur, S., Collin, F., Daniels, K., Dymitrowska, M., Harrington, J., Jacops, E., Kolditz, O., Marschall, P., Norris, S., Sillen, X., et al. (2021a). Initial state of the art on gas transport in clayey materials. *Deliverable D6*, 1.

Levasseur, S., Collin, F., Daniels, K., Dymitrowska, M., Harrington, J., Jacops, E., Kolditz, O., Marschall, P., Norris, S., Sillen, X., Talandier, J., Truche, L., and Wendling, J. (2020). Initial state-of-the-art on gas transport in clayey materials.

Levasseur, S., Collin, F., Daniels, K., Dymitrowska, M., Harrington, J., Jacops, E., Kolditz, O., Marschall, P., Norris, S., Sillen, X., Talandier, J., Truche, L., and Wendling, J. (2021b). Initial state of the art on gas transport in clayey materials. Report.

Levasseur, S., Collin, F., Daniels, K., Dymitrowska, M., Harrington, J., Jacops, E., Kolditz, O., Marschall, P., Norris, S., Sillen, X., Talandier, J., Truche, L., and Wendling, J. (2021c). Initial State of the Art on Gas Transport in Clayey Materials. Deliverable D6.1 of HORIZON 2020 project EURAD, Work Package Gas. EC Grant agreement no: 847593. Technical Report 847593, European commission.

Levasseur, S., Collin, F., Daniels, K., Dymitrowska, M., Harrington, J., Jacops, E., Kolditz, O., Marschall, P., Norris, S., Sillen, X., Talandier, J., Truche, L., and Wendling, J. (2024). State of the Art on Gas Transport in Clayey Materials II. Deliverable D6.2 of HORIZON 2020 project EURAD, Work Package Gas. EC Grant agreement no: 847593. Technical report, European commission.

Lewis, D. F. (1989). The calculation of molar polarizabilities by the cndo/2 method: Correlation with the hydrophobic parameter, log p. *Journal of computational chemistry*, 10(2):145–151.

Lewis, R. and Schrefler, B. (1998). The Finite Element Method in the Static and Dynamic Deformation and Consolidation of Porous Media. Second Edition. *Communications in Numerical Methods in Engineering*, 34.

Li, H., Pan, C., and Miller, C. (2005). Pore-scale investigation of viscous coupling effects for two-phase flow in porous media. *Physical Review E*, 72(2).

Li, Q., Luo, K., Kang, Q., and Chen, Q. (2014). Contact angles in the pseudopotential lattice boltzmann modeling of wetting. *Physical Review E*, 90(5):053301.

Li, Z., Dong, M., Li, S., and Huang, S. (2006). Co2 sequestration in depleted oil and gas reservoirs—caprock characterization and storage capacity. *Energy Conversion and Management*, 47(11-12):1372–1382.

Li, Z., Galindo-Torres, S., Yan, G., Scheuermann, A., and Li, L. (2019). simulations of simultaneous steady-state two-phase flow dynamics using a lattice boltzmann model: Interfacial area, capillary pressure and relative permeability. Transport in Porous Media 129,295-320.

Liaudat, J., Carol, I., and López, C. M. (2020). Model for alkali-silica reaction expansions in concrete using zero-thickness chemo-mechanical interface elements. *International Journal of Solids and Structures*, 207:145–177.

Liaudat, J., Dieudonné, A.-c., and Vardon, P. J. (2023). Modelling gas fracturing in saturated clay samples using triple-node zero-thickness interface elements. *Computers and Geotechnics*, 154:105128.

Lima, A. (2011). *Thermo-Hydro-Mechanical Behaviour of two deep Belgian formations: Boom and Ypresian Clays*. PhD thesis, Universitat Politècnica de Catalunya (UPC).

Lippmann-Pipke, J., Gerasch, R., Schikora, J., and Kulenkampff, J. (2017). Benchmarking pet for geoscientific applications: 3d quantitative diffusion coefficient determination in clay rock. *Computers & Geosciences*, 101:21–27.

Liu, H.-H. (2014). Non-darcian flow in low-permeability media: key issues related to geological disposal of high-level nuclear waste in shale formations. *Hydrogeology Journal*, 22(7):1525.

Liu, J., Davy, C., Talandier, J., and Skoczylas, F. (2014). Effect of gas pressure on the sealing efficiency of compacted bentonite–sand plugs. *Journal of Contaminant Hydrology*, 170:10–27.

Liu, K., Boardman, R., Mavrogordato, M., Loveridge, F., and Powrie, W. (2020). The importance of the heel effect in x-ray computed tomography imaging of soils. *Environmental Geotechnics*, 40:1–16.

Liu, P., Harder, E., and Berne, B. (2004). On the calculation of diffusion coefficients in confined fluids and interfaces with an application to the liquid- vapor interface of water. *The Journal of Physical Chemistry B*, 108(21):6595–6602.

Liu, X., Lu, X., Wang, R., and Zhou, H. (2008a). Effects of layer-charge distribution on the thermodynamic and microscopic properties of cs-smectite. *Geochimica et Cosmochimica Acta*, 72(7):1837–1847.

Liu, X., Lu, X., Wang, R., and Zhou, H. (2008b). Effects of layer-charge distribution on the thermodynamic and microscopic properties of cs-smectite. *Geochimica et Cosmochimica Acta*, 72(7):1837–1847.

Liu, Z. B., Shao, J. F., Liu, T. G., Xie, S. Y., and Conil, N. (2016). Gas permeability evolution mechanism during creep of a low permeable claystone. *Applied Clay Science*, 129:47–53.

Lloret, A. and Villar, M. (2007). Advances on the knowledge of the thermo-hydro-mechanical behaviour of heavily compacted "febex" bentonite. *Physics and Chemistry of the Earth*, 32(8-14):701–715.

Lloret, A., Villar, M., Sánchez, M., Gens, A., Pintado, X., and Alonso, E. (2003). Mechanical behaviour of heavily compacted bentonite under high suction changes. *Géotechnique*, 53(1):27–40.

Lo, I. M., Mak, R. K., and Lee, S. C. (1997). Modified clays for waste containment and pollutant attenuation. *Journal of Environmental Engineering*, 123(1):25–32.

Longsworth, L. (1954). Temperature dependence of diffusion in aqueous solutions. *The Journal of Physical Chemistry*, 58(9):770–773.

Loomer, D. B., Scott, L., Al, T. A., Mayer, K. U., and Bea, S. (2013). Diffusion–reaction studies in low permeability shale using x-ray radiography with cesium. *Applied geochemistry*, 39:49–58.

Loon, L. R. V., Soler, J. M., Jakob, A., and Bradbury, M. H. (2003). Effect of confining pressure on the diffusion of hto, 36cl- and 125i- in a layered argillaceous rock (opalinus clay): diffusion perpendicular to the fabric. *Applied Geochemistry*, 18:1653–1662.

Lorenz, P., Meier, L., and Kahr, G. (1999). Determination of the cation exchange capacity (cec) of clay minerals using the complexes of copper (ii) ion with triethylenetetramine and tetraethylenepentamine. *Clays and clay minerals*, 47(3):386–388.

Lu, R., Nagel, T., Shao, H., Kolditz, O., and Shao, H. (2018). Modeling of Dissolution-Induced Permeability Evolution of a Granite Fracture Under Crustal Conditions. *Journal of Geophysical Research: Solid Earth*, 123(7):5609–5627. cited By 3.

Luboń, K. and Tarkowski, R. (2021). Influence of capillary threshold pressure and injection well location on the dynamic co2 and h2 storage capacity for the deep geological structure. *International Journal of Hydrogen Energy*, 46(58):30048–30060.

Luo, L.-S. (1998). Unified theory of lattice boltzmann models for nonideal gases. *Physical review letters*, 81(8):1618.

Lux, K.-H. and Rutenberg, M. (2018). Vorprojekt - Internationales Benchmarking zur Verifizierung und Validierung von TH2M-Simulatoren insbesondere im Hinblick auf fluiddynamische Prozesse in Endlagersystemen (BenVaSim) : Abschlussbericht zum BMWi-Forschungsvorhaben : Zeitraum: 01.07.2016-30.04.2017. Technical report, Lehrstuhl für Deponietechnik und Geomechanik, Technische Universität Clausthal, Clausthal-Zellerfeld. in German.

Lux, K.-H., Rutenberg, M., Feierabend, J., Czaikowski, O., Friedenberg, L., Maßmann, J., Pitz, M., Sentís, M. L., Graupner, B. J., Hansmann, J., Hotzel, S., Kock, I., Rutqvist, J., Hu, M., and Rinaldi, A. P. (2021). Synthesis report. BenVaSim – International Benchmarking for Verification and Validation of TH2M Simulators with Special Consideration of Fluid Dynamical Processes in Radioactive Waste Repository Systems. Technical report, Technische Universität Clausthal.

López, C. M., Carol, I., and Aguado, A. (2008). Meso-structural study of concrete fracture using interface elements. I: numerical model and tensile behavior. *Materials and structures*, 41:583–599.

M, M. J., S, S., and J, C. (2007). Desaturation and structure relationships around drifts excavated in the well-compacted tournemire's argillite (aveyron, france). *Engineering Geology*, 90(1-2):1–16.

Maalal, O., Prat, M., and D. (2021). Pore network model of drying with kelvin effect. *Physics of Fluids*, 33:027103.

Mahjoub, M. (2017). *Modeling of damage-permeability coupling in anisotropic geomaterials. Application to Bure underground works.* PhD thesis, Université Paris sciences et lettres.

Mahjoub, M., Rouabhi, A., Tijani, M., Granet, S., M'Jahad, S., and Talandier, J. (2018). Numerical Study of Callovo-Oxfordian Argillite Expansion due to Gas Injection. . *International Journal of Geomechanics*, 18.

Maier, M.-L., Patel, R. A., Prasianakis, N. I., Churakov, S. V., Nirschl, H., and Krause, M. J. (2021). Coupling of multiscale lattice boltzmann discrete-element method for reactive particle fluid flows. *Physical Review E*, 103(3):033306.

Marchand, E. and Knabner, P. (2014). Results of the momas benchmark for gas phase appearance and disappearance using generalized mhfe. *Advances in water resources*, 73:74–96.

Marry, V., Dubois, E., Malikova, N., Durand-Vidal, S., Longeville, S., and Breu, J. (2011). Water dynamics in hectorite clays: Infuence of temperature studied by coupling neutron spin echo and molecular dynamics. *Environmental Science & Technology*, 45(7):2850–2855.

Marry, V., Dufrêche, J.-F., Jardat, M., and Turq, P. (2003). Equilibrium and electrokinetic phenomena in charged porous media from microscopic and mesoscopic models: electro-osmosis in montmorillonite. *Molecular Physics*, 101(20):3111–3119.

Marry, V. and Turq, P. (2003). Microscopic simulations of interlayer structure and dynamics in bihydrated heteroionic montmorillonites. *The Journal of Physical Chemistry B*, 107(8):1832–1839.

Marschall, P., Giger, S., De La Vassière, R., Shao, H., Leung, H., Nussbaum, C., Trick, T., Lanyon, B., Senger, R., Lisjak, A., and Alcolea, A. (2017). Hydro-mechanical evolution of the EDZ as transport path for radionuclides and gas: insights from the Mont Terri rock laboratory (Switzerland). *Swiss Journal of Geosciences*, 110(1):173–194. cited By 15.

Marschall, P. and Holzer, L. (2009). Laboratory and field experiments on gas transport in the Opalinus Clay of Northern Switzerland. cited By 0.

Marschall, P., Horseman, S., and Gimmi, T. (2005a). Characterisation of gas transport properties of the opalinus clay, a potential host rock formation for radioactive waste disposal. *Oil & gas science and technology*, 60(1):121–139.

Marschall, P., Horseman, S., and Gimmi, T. (2005b). Characterisation of gas transport properties of the Opalinus Clay, a potential host rock formation for radioactive waste disposal. *Oil and Gas Science and Technology*, 60(1):121–139. cited By 173.

Martin, M. G. and Siepmann, J. I. (1997). Predicting multicomponent phase equilibria and free energies of transfer for alkanes by molecular simulation. *Journal of the American Chemical Society*, 119(38):8921–8924.

Marty, B., Dewonck, S., and France-Lanord, C. (2003). Geochemical evidence for efficient aquifer isolation over geological timeframes. *Nature*, 425(6953):55–58.

Matsushima, T., Chambon, R., and Caillerie, D. (2002). Large strain finite element analysis of a local second gradient model: application to localisation. *International Journal for Numerical Methods in Engineering*, 54(4):499–521.

May, E. F., Berg, R. F., and Moldover, M. R. (2007). Reference viscosities of h2, ch4, ar, and xe at low densities. *International Journal of Thermophysics*, 28(4):1085–1110.

Mayor, J.-C., García-Siñeriz, J., Alonso, E., Alheid, H.-J., and Blümbling, P. (2007). Engineered barrier emplacement experiment in opalinus clay for the disposal of radioactive waste in underground repositories. *Rep. Swiss Geol. Surv.*, 1:115–180.

Mazurek, M., Alt-Epping, P., Bath, A., Gimmi, T., Waber, H. N., Buschaert, S., De Cannière, P., De Craen, M., Gautschi, A., Savoye, S., et al. (2011). Natural tracer profiles across argillaceous formations. *Applied Geochemistry*, 26(7):1035–1064.

McGregor, F., Heath, A., Shea, A., and Lawrence, M. (2014). The moisture buffering capacity of unfired clay masonry. *Building and Environment*, 82:599–607.

Medina, J., Prosmiti, R., Villarreal, P., Delgado-Barrio, G., Winter, G., González, B., Alemán, J., and Collado, C. (2011). Molecular dynamics simulations of rigid and flexible water models: Temperature dependence of viscosity. *Chemical Physics*, 388(1-3):9–18.

Melchionna, S., Ciccotti, G., and Lee Holian, B. (1993). Hoover npt dynamics for systems varying in shape and size. *Molecular Physics*, 78(3):533–544.

Mendoza, A. (2019). Hydrogen transport experiment in bentonite – final report. technical report 383/2019/eng. Report Technical Report 383/2019/ENG, .

Mertens, J., Bastiaens, W., and Dehandschutter, B. (2004). Characterisation of induced discontinuities in the Boom Clay around the underground excavations (URF, Mol, Belgium). *Applied clay science*, 26(1-4):413–428.

Meunier, A., Velde, B., and Griffault, L. (1998). The reactivity of bentonites: a review. an application to clay barrier stability for nuclear waste storage. *Clay Minerals*, 33(2):187–196.

Mi, Y., Crisfield, M. A., Davies, G., and Hellweg, H.-B. (1998). Progressive delamination using interface elements. *Journal of Composite Materials*, 32:1246–1272.

Mialdun, A. and Shevtsova, V. (2008). Development of optical digital interferometry technique for measurement of thermodiffusion coefficients. *International Journal of Heat and Mass Transfer*, 51(11-12):3164–3178.

Miao, X.-Y., Kolditz, O., and Nagel, T. (2019). Modelling thermal performance degradation of high and low-temperature solid thermal energy storage due to cracking processes using a phase-field approach. *Energy Conversion and Management*, 180:977–989. cited By 3.

Michalis, V. K., Kalarakis, A. N., Skouras, E. D., and Burganos, V. N. (2010). Rarefaction effects on gas viscosity in the knudsen transition regime. *Microfluidics and nanofluidics*, 9:847–853.

Michels, L., Méheust, Y., Altoe, M. A., Dos Santos, É. C., Hemmen, H., Droppa Jr, R., Fossum, J. O., and da Silva, G. J. (2019). Water vapor diffusive transport in a smectite clay: Cationic control of normal versus anomalous diffusion. *Physical Review E*, 99(1):013102.

Minardi, A. (2018). Hydro-mechanical characterization of gas shales and Opalinus Clay shale in partially saturated conditions. Technical report, IIC, Lausanne.

Mindlin, R. D. (1965). Second gradient of strain and surface-tension in linear elasticity. *International Journal of Solids and Structures*, 1(4):417–438.

Mofakham, A. A. and Ahmadi, G. (2020). On random walk models for simulation of particle-laden turbulent flows. *International Journal of Multiphase Flow*, 122:103157.

Mohammed, S. and Gadikota, G. (2018). The effect of hydration on the structure and transport properties of confined carbon dioxide and methane in calcite nanopores. *Frontiers in Energy Research*, 6:86.

Monaghan, J. and Lattanzio, J. (1985). A refined particle method for astrophysical problems. *Astronomy and Astrophysics*, 149(1):135–143.

Monaghan, J. J. and Lattanzio, J. C. (1991). A simulation of the collapse and fragmentation of cooling molecular clouds. *Astrophysical Journal*, 375(1):177 – 189. Cited by: 74.

Mondal, S., Ghosh, S., and Chattaraj, P. (2013). A molecular dynamics study on si hydrogen hydrate. *Journal of molecular modeling*, 19(7):2785–2790.

Morgenroth, J., Khan, U., and Perras, M. (2019). An overview of opportunities for machine learning methods in underground rock engineering design. *Geosciences (Switzerland)*, 9(12). cited By 0.

Moultos, O. A., Tsimpanogiannis, I. N., Panagiotopoulos, A. Z., and Economou, I. G. (2014). Atomistic molecular dynamics simulations of co2 diffusivity in h2o for a wide range of temperatures and pressures. *The Journal of Physical Chemistry B*, 118(20):5532–5541.

Mualem, J. (1976). A new model for predicting the hydraulic conductivity of unsaturated porous media. *Water Resources Research*, 12(3):513–522.

Myshakin, E. M., Saidi, W. A., Romanov, V. N., Cygan, R. T., and Jordan, K. D. (2013). Molecular dynamics simulations of carbon dioxide intercalation in hydrated na-montmorillonite. *The Journal of Physical Chemistry C*, 117(21):11028–11039.

N., A., M., D., A., O., A-J., T., and F., G. (2023). Numerical modeling of evaporation-condensation in nanoporous media by sph method.

Nagel, T., Beckert, S., Lehmann, C., Gläser, R., and Kolditz, O. (2016). Multi-physical continuum models of thermochemical heat storage and transformation in porous media and powder beds—A review. *Applied Energy*, 178:323–345. cited By 27.

Nagra (2002). Projekt opalinuston synthese der geowissenschaftlichen untersuchungsergebnisse. *Nagra Technischer Bericht 02-03 (in German)*.

Nakashima, Y. (2003). Diffusivity measurement of heavy ions in wyoming montmorillonite gels by x-ray computed tomography. *Journal of contaminant hydrology*, 61(1-4):147–156.

NEA (2007). Regulating the Long-term Safety of Geological Disposal: Towards a Common Understanding of the Main Objectives and Bases of Safety Criteria. *OECD Nuclear Energy Agency, Publication 6182, Paris (2007)*.

NEA (2014). The safety case for deep geological disposal of radioactive waste: 2013 state of the art. *Symposium Proceedings 7–9 Octiber 2013, Paris, France. Radioactive Waste Management Report NEA/RWM/R(2013)9, OECD/NEA, Paris, France*.

Nelson, N. T., Brusseau, M. L., Carlson, T., Costanza, M., Young, M., Johnson, G., and Wierenga, P. (1999). A gas-phase partitioning tracer method for the in situ measurement of soil-water content. *Water Resources Research*, 35(12):3699–3707.

Ng, E.-P. and Mintova, S. (2008). Nanoporous materials with enhanced hydrophilicity and high water sorption capacity. *Microporous and Mesoporous Materials*, 114(1-3):1–26.

Ngouana W, B. F. and Kalinichev, A. G. (2014a). Structural arrangements of isomorphic substitutions in smectites: Molecular simulation of the swelling properties, interlayer structure, and dynamics of hydrated cs–montmorillonite revisited with new clay models. *The Journal of Physical Chemistry C*, 118(24):12758–12773.

Ngouana W, B. F. and Kalinichev, A. G. (2014b). Structural arrangements of isomorphic substitutions in smectites: Molecular simulation of the swelling properties, interlayer structure, and dynamics of hydrated cs–montmorillonite revisited with new clay models. *The Journal of Physical Chemistry C*, 118(24):12758–12773.

Nguyen, V. P. (2014). An open source program to generate zero-thickness cohesive interface elements. *Advances in Engineering Software*, 74:27–39.

Nguyen, V. P., Lian, H., Rabczuk, T., and Bordas, S. (2017). Modelling hydraulic fractures in porous media using flow cohesive interface elements. *Engineering Geology*, 225:68–82.

Ning, F. L., Glavatskiy, K., Ji, Z., Kjelstrup, S., and H. Vlugt, T. J. (2015). Compressibility, thermal expansion coefficient and heat capacity of ch4 and co2 hydrate mixtures using molecular dynamics simulations. *Phys. Chem. Chem. Phys.*, 17:2869–2883.

Noorishad, J. and Tsang, C.-F. (1996). ROCMAS simulator; A thermohydromechanical computer code. *Developments in Geotechnical Engineering*, 79(C):551–558. cited By 19.

Nordstrom, B. H. (1984). The effect of polarity on solubility. *Journal of Chemical Education*, 61(11):1009.

Norris, S. (2013). Synthesis report: Updated treatment of gas generation and migration in the safety case.

Norris, S. (2017). Radioactive waste confinement: clays in natural and engineered barriers–introduction.

Norris, S. (2019). Multiple roles of clays in radioactive waste confinement–introduction.

Nosé, S. (1984a). A molecular dynamics method for simulations in the canonical ensemble. *Molecular physics*, 52(2):255–268.

Nosé, S. (1984b). A unified formulation of the constant temperature molecular dynamics methods. *The Journal of chemical physics*, 81(1):511–519.

NRC (1957). The Disposal of Radioactive Waste on Land. National Research Council. *National Academy Press, Washington, DC, USA*.

Nuth, M. and Laloui, L. (2008). Effective stress concept in unsaturated soils: Clarification and validation of a unified framework. *International journal for numerical and analytical methods in Geomechanics*, 32(7):771–801.

O'Brien, G., Bean, C., and McDermott, F. (2002). A comparison of published experimental data with a coupled lattice boltzmann-analytic advection–diffusion method for reactive transport in porous media. *Journal of Hydrology*, 268(1-4):143–157.

Olivella, S. and Alonso, E. (2008a). Gas flow through clay barriers. *Geotechnique*, 58(3):157–176. cited By 106.

Olivella, S. and Alonso, E. (2008b). Gas flow through clay barriers . *Géotechnique*, 58(3):157–176.

Olivella, S. and Alonso, E. E. (2008c). Gas flow through clay barriers. *Géotechnique*, 58(3):157–176.

Olivella, S., Carrera, J., Gens, A., and Alonso, E. (1994). Nonisothermal multiphase flow of brine and gas through saline media. *Transport in Porous Media*, 15(3):271–293. cited By 312.

Olivella, S., Gens, A., Carrera, J., and Alonso, E. (1996). Numerical formulation for a simulator (CODE_BRIGHT) for the coupled analysis of saline media. *Engineering Computations (Swansea, Wales)*, 13(7):87–112. cited By 427.

Olsson, R. and Barton, N. (2001). An improved model for hydromechanical coupling during shearing of rock joints. *International journal of rock mechanics and mining sciences*, 38(3):317–329.

Oron, A. P. and Berkowitz, B. (1998). Flow in rock fractures: The local cubic law assumption reexamined. *Water Resources Research*, 34(11):2811–2825.

Ortiz, L., Volckaert, G., De Cannière, P., Put, M., Sen, M., Horseman, S.T., Harrington, J., Impey, M., and Einchcomb, S. (1997). MEGAS: modelling and experiments on GAS migration in repository host rocks. Final report phase 2. Technical report, Eur. Comm., [Rep.] EUR 17453 EN.

Ortiz, L., Volckaert, G., and Mallants, D. (2002a). Gas generation and migration in boom clay, a potential host rock formation for nuclear waste storage. *Engineering geology*, 64(2-3):287–296.

Ortiz, L., Volckaert, G., and Mallants, D. (2002b). Gas generation and migration in boom clay, a potential host rock formation for nuclear waste storage. *Engineering Geology*, 64:287–296.

Ou, X., Li, J., and Lin, Z. (2014). Dynamic behavior of interfacial water on mg (oh) 2 (001) surface: a molecular dynamics simulation work. *The Journal of Physical Chemistry C*, 118(51):29887–29895.

Owusu, J. P. (2023). *Numerical simulations of gas transport in argillaceous rocks: A molecular dynamics and pore-scale simulation study*. PhD thesis, University of Bern.

Owusu, J. P., Karalis, K., Prasianakis, N. I., and Churakov, S. V. (2022a). Mobility of dissolved gases in smectites under saturated conditions: Effects of pore size, gas types, temperature, and surface interaction. *The Journal of Physical Chemistry C*, 126(40):17441–17455.

Owusu, J. P., Karalis, K., Prasianakis, N. I., and Churakov, S. V. (2022b). Mobility of dissolved gases in smectites under saturated conditions: Effects of pore size, gas types, temperature, and surface interaction. *The Journal of Physical Chemistry C*, 126(40):17441–17455.

Owusu, J. P., Karalis, K., Prasianakis, N. I., and Churakov, S. V. (2023). Diffusion and gas flow dynamics in partially saturated smectites. *The Journal of Physical Chemistry C*, 127(29):14425–14438.

Pagonabarraga, I., Rotenberg, B., and Frenkel, D. (2010). Recent advances in the modelling and simulation of electrokinetic effects: bridging the gap between atomistic and macroscopic descriptions. *Physical Chemistry Chemical Physics*, 12(33):9566–9580.

Pan, C., Luo, L.-S., and Miller, C. T. (2006a). An evaluation of lattice boltzmann schemes for porous medium flow simulation. *Computers and Fluids*, 35(8-9):898 – 909. Cited by: 641.

Pan, C., Luo, L.-S., and Miller, C. T. (2006b). An evaluation of lattice boltzmann schemes for porous medium flow simulation. *Computers & Fluids*, 35(8):898–909.

Pandolfi, A. and Ortiz, M. (1998). Solid modeling aspects of three-dimensional fragmentation. *Engineering with Computers*, 14(4):287–308.

Panet, M. and Guenot, A. (1982). Analysis of convergence behind the face of a tunnel. *proceedings of the 3rd international symposium: Tunnelling 82*.

Pardoen, B. (2015). *Hydro-mechanical analysis of the fracturing induced by the excavation of nuclear waste repository galleries using shear banding*. PhD thesis, University of Liège.

Pardoen, B. and Collin, F. (2017). Modelling the influence of strain localisation and viscosity on the behaviour of underground drifts drilled in claystone. *Computers and Geotechnics*, 85:351–367.

Pardoen, B., Talandier, J., and Collin, F. (2016). Permeability evolution and water transfer in the excavation damaged zone of a ventilated gallery. *International Journal of Rock Mechanics and Mining Sciences*, 85:192–208.

Parisio, F., Naumov, D., Kolditz, O., and Nagel, T. (2018). Material forces: An insight into configurational mechanics. *Mechanics Research Communications*, 93:114–118. cited By 3.

Parisio, F., Tarokh, A., Makhnenko, R., Naumov, D., Miao, X.-Y., Kolditz, O., and Nagel, T. (2019a). Experimental characterization and numerical modelling of fracture processes in granite. *International Journal of Solids and Structures*, 163:102–116. cited By 4.

Parisio, F., Vilarrasa, V., Wang, W., Kolditz, O., and Nagel, T. (2019b). The risks of long-term re-injection in supercritical geothermal systems. *Nature Communications*, 10(1). cited By 1.

Parisio, F., Vinciguerra, S., Kolditz, O., and Nagel, T. (2019c). The brittle-ductile transition in active volcanoes. *Scientific Reports*, 9(1). cited By 4.

Park, S.-H. and Sposito, G. (2003). Do montmorillonite surfaces promote methane hydrate formation? monte carlo and molecular dynamics simulations. *The Journal of Physical Chemistry B*, 107(10):2281–2290.

Pastusek, P., Payette, G., Shor, R., Cayeux, E., Aarsnes, U., Hedengren, J., Menand, S., Macpherson, J., Gandikota, R., Behounek, M., Harmer, R., Detournay, E., Illerhaus, R., and Liu, Y. (2019). Creating open source models, test cases, and data for oilfield drilling challenges. volume 2019-March. cited By 2.

Patriarche, D., Ledoux, E., Michelot, J.-L., Simon-Coinçon, R., and Savoye, S. (2004). Diffusion as the main process for mass transport in very low water content argillites: 2. fluid flow and mass transport modeling. *Water Resources Research*, 40(1).

Paul, B. (2016). *Modélisation de la propagation de fractures hydrauliques par la méthode des éléments finis étendue*. PhD thesis, Université de Lorraine.

Paul, B., Faivre, M., Massin, P., Giot, R., Colombo, D., Golfier, F., and Martin, M. (2018). 3D coupled HM–XFEM modeling with cohesive zone model and applications to non-planar hydraulic fracture propagation and multiple hydraulic fractures interference. *Computer Methods in Applied Mechanics and Engineering*, 342:321–353.

Pazdniakou, A. and Dymitrowska, M. (2018a). Migration of gas in water saturated clays by coupled hydraulic-mechanical model. *Geofluids*, 2018. Cited by: 11; All Open Access, Gold Open Access, Green Open Access.

Pazdniakou, A. and Dymitrowska, M. (2018b). Migration of gas in water saturated clays by coupled hydraulic-mechanical model. *Geofluids*.

Pazdniakou, A., Tinet, A.-J., Golfier, F., Kalo, K., Gaboreau, S., and Gaire, P. (2018). Numerical efficiency assessment of the lattice boltzmann model for digital nano-porous rock applications. *Advances in Water Resources*, 121:44 – 56. Cited by: 4; All Open Access, Green Open Access.

Pellenard, P. and Deconinck, J. F. (2006). Mineralogical variability of callovo-oxfordian clays from the paris basin and the subalpine basin. *Comptes Rendus Geoscience*, 338:854–866.

Peng, Y., Zhou, J., and Burrows, R. (2011). Modelling solute transport in shallow water with the lattice boltzmann method. *Computers & fluids*, 50(1):181–188.

Philip, J. R. and de Vries, D. A. (1957). Moisture movement in porous materials under temperature gradients. *Eos, Trans Amer Geophys Union*, 38(2):222–232.

Pietruszczak, S. and Mróz, Z. (1981). Finite element analysis of deformation of strain-softening materials. *International Journal for Numerical Methods in Engineering*, 17(3):327–334.

Pitz, M., Grunwald, N., Graupner, B., Radeisen, E., Maßmann, J., Ziefle, G., Thiedau, J., and Nagel, T. (2023a). Benchmarking a new TH2M implementation in OGS-6 with regard to processes relevant for nuclear waste disposal. *Environmental Earth Sciences*. under review.

Pitz, M., Jacops, E., Grunwald, N., Ziefle, G., and Nagel, T. (2023b). On Multicomponent Gas Migration in Single Phase Systems. *Rock Mechanics and Rock Engineering*. submitted.

Pitz et al., M. (2023). On Conceptual Uncertainties in Gas Transport Phenomena in Argillaceous Rocks. in preparation.

Plesha, M. E. (1995). Rock joints: theory, constitutive equations. In *Studies in applied mechanics*, volume 42, pages 375–393. Elsevier.

Plimpton, S. (1995). Fast parallel algorithms for short-range molecular dynamics. *Journal of computational physics*, 117(1):1–19.

Plonsky, L. and Ghanbar, H. (2018). Multiple regression in l2 research: A methodological synthesis and guide to interpreting r2 values. *The Modern Language Journal*, 102:713–731.

Poirier, J., François, M., Cases, J., and Rouquerol (1987). J. In Liapis, A., editor, *Proceedings of the Second Engineering Foundation Conference on Fundamentals of Adsorption*, page 473, New York.

Pollard, W. and Present, R. D. (1948). On gaseous self-diffusion in long capillary tubes. *Physical Review*, 73(7):762.

Poller, A., Mayer, G., Darcis, M., and Smith, P. (2016). Modelling of gas generation in deep geological repositories after closure. Technical report, National Cooperative for the Disposal of Radioactive Waste (NAGRA).

Pollock, D. (1986). Simulation of fluid flow and energy transport processes associated with high-level radioactive waste disposal in unsaturated alluvium. *Water Resources Research*, 22(5):765–775.

Popp, T., Wiedemann, M., Böhnel, H., Minkley, W., and Manthei, G. (2007a). Untersuchungen zur Barriereintegrität im Hinblick auf das Ein-Endlager-Konzept. *Insitut fur Gebirgsmechanik GmbH, Leipzig, Germany*.

Popp, T., Wiedemann, M., Böhnel, H., and Minkley, W. (2007b). Untersuchungen zur Barriereintegrität im Hinblick auf das Ein-Endlager-Konzept. Technical report, Institut für Gebirgsmechanik GmbH, Leipzig.

Praetorius, A., Tufenkji, N., Goss, K.-U., Scheringer, M., Von der Kammer, F., and Elimelech, M. (2014). The road to nowhere: equilibrium partition coefficients for nanoparticles. *Environmental Science: Nano*, 1(4):317–323.

Prasianakis, N., Curti, E., Kosakowski, G., Poonoosamy, J., and Churakov, S. (2017). Deciphering pore-level precipitation mechanisms. *Scientific reports*, 7(1):13765.

Prasianakis, N., Karlin, I., Mantzaras, J., and Boulouchos, K. (2009). Lattice boltzmann method with restored galilean invariance. *Physical Review E*, 79(6):066702.

Prat, M. (2002). Recent advances in pore-scale models for drying of porous media. *Chemical engineering journal*, 86(1-2):153–164.

Prime, N., Levasseur, S., Miny, L., Charlier, R., Léonard, A., and Collin, F. (2016). Drying-induced shrinkage of boom clay: An experimental investigation. *Canadian Geotechnical Journal*, 53(3):396–409.

Pusch, R. (2006). Clays and nuclear waste management. *Developments in Clay Science*, 1:703–716.

Pusch, R. and Yong, R. N. (2006). *Microstructure of smectite clays and engineering performance*. CRC Press.

Qian, Y.-H., d'Humières, D., and Lallemand, P. (1992). Lattice bgk models for navier-stokes equation. *Europhysics letters*, 17(6):479.

Qin, F., Del Carro, L., Moqaddam, A. M., Kang, Q., Brunschwiler, T., Derome, D., and Carmeliet, J. (2019). Study of non-isothermal liquid evaporation in synthetic micro-pore structures with hybrid lattice boltzmann model. *Journal of Fluid Mechanics*, 866:33–60.

Raevsky, O. A., Perlovich, G. L., Kazachenko, V. P., Strakhova, N. N., and Schaper, K.-J. (2009). Octanol/water partition coefficients of sulfonamides: experimental determination and calculation using physicochemical descriptors. *Journal of Chemical & Engineering Data*, 54(11):3121–3124.

Raude, S., Laigle, F., Giot, R., and Fernandes, R. (2016). A unified thermoplastic/viscoplastic constitutive model for geomaterials. *Acta Geotechnica*, 11(4):849–869.

Rebour, V., Billiotte, J., Deveughele, M., Jambon, A., and Le Guen, C. (1997). Molecular diffusion in water-saturated rocks: A new experimental method. *Journal of contaminant hydrology*, 28(1-2):71–93.

Reitenbach, V., Ganzer, L., Albrecht, D., and Hagemann, B. (2015). Influence of added hydrogen on underground gas storage: a review of key issues. *Environmental Earth Sciences*, 73(11):6927–6937.

Relyea, J. F., Trott, D. P., McIntyre, C., and Rieger, C. G. (1986). Diffusion of tritiated water and chloride in basalt-bentonite mixtures. *Nuclear Technology*, 74(3):317–323.

Rink, K., Bilke, L., Raith, F., Zänker, S., Jaeggi, D., Kunz, H., Maßmann, J., Naumov, D., Schefer, S., Scheuermann, G., Shao, H., Wang, W., Ziefle, G., Bossart, P., Nussbaum, C., Nagel, T., and Kolditz (2020). A Virtual Exploration of the Underground Rock Laboratory Mont Terri. *EUROVIS 2020, Eurographics Proceedings, Norrköping, Sweden*, pages 1–3.

Robb, W. and Drickamer, H. (1951). Diffusion in co2 up to 150-atmospheres pressure. *The Journal of Chemical Physics*, 19(12):1504–1508.

Robinet, J. (2008). *Minéralogie, porosité et diffusion des solutés dans l'argilite du Callovo-Oxfordien de Bure (Meuse, Haute-Marne, France) de l'échelle centimétrique à micrométrique (Doctoral dissertation, Poitiers)*. Doctoral dissertation, University of Poitiers, France.

Rodwell, W., Harris, A., Horseman, S., Lalieux, P., Müller, W., Ortiz Amaya, L., and Pruess, K. (1999). Gas migration and two-phase flow through engineered and geological barriers for a deep repository for radioactive waste. *EUR(Luxembourg)*.

Rosanne, R., Paszkuta, M., Tevissen, E., and Adler, P. (2003). Thermodiffusion in compact clays. *Journal of Colloid and Interface Science*, 267(1):194–203.

Roscoe, K. and Burland, J. B. (1968). On the generalized stress-strain behaviour of wet clay.

Rosén, T., Eller, J., Kang, J., Prasianakis, N. I., Mantzaras, J., and Büchi, F. N. (2012). Saturation dependent effective transport properties of pefc gas diffusion layers. *Journal of The Electrochemical Society*, 159(9):F536.

Rowe, R. K. (2005). Long-term performance of contaminant barrier systems. *Geotechnique*, 55(9):631–678.

Rübel, A. P., Sonntag, C., Lippmann, J., Pearson, F., and Gautschi, A. (2002). Solute transport in formations of very low permeability: Profiles of stable isotope and dissolved noble gas contents of pore water in the opalinus clay, mont terri, switzerland. *Geochimica et Cosmochimica Acta*, 66(8):1311–1321.

Ruthven, D. M., Kärger, J., and Theodorou, D. N. (2012). *Diffusion in nanoporous materials*. John Wiley & Sons.

Ryckaert, J.-P., Ciccotti, G., and Berendsen, H. J. (1977). Numerical integration of the cartesian equations of motion of a system with constraints: molecular dynamics of n-alkanes. *Journal of computational physics*, 23(3):327–341.

Saba, S. (2013). *Hydro-mechanical behaviour of bentonite-sand mixture used as sealing materials in radioactive waste disposal galleries*. Doctoral dissertation, Université Paris-Est.

Sabo, D., Rempe, S., Greathouse, J., and Martin, M. (2006). Molecular studies of the structural properties of hydrogen gas in bulk water. *Molecular Simulation*, 32(3-4):269–278.

Salehnia, F., Sillen, X., Li, X., and Charlier, R. (2017). Numerical simulation of a discontinuous gallery lining's behavior, and its interaction with rock. *International Journal for Numerical and Analytical Methods in Geomechanics*, 41(15):1569–1589.

Saltelli, A., Annoni, P., Azzini, I., Campolongo, F., Ratto, M., and Tarantola, S. (2010). Variance based sensitivity analysis of model output. Design and estimator for the total sensitivity index. *Computer Physics Communications*, 181(2):259–270.

Saltelli, A. and Tarantola, S. (2002). On the relative importance of input factors in mathematical models: Safety assessment for nuclear waste disposal. *Journal of the American Statistical Association*, 97(459):702–709.

Sammartino, S., Bouchet, A., Prêt, D., Parneix, J. C., and Tevissen, E. (2003). Spatial distribution of porosity and minerals in clay rocks from the callovo-oxfordian formation (meuse/haute-marne, eastern france)—implications on ionic species diffusion and rock sorption capability. *Applied Clay Science*, 23:157–166.

Samsatli, S. and Samsatli, N. J. (2019). The role of renewable hydrogen and inter-seasonal storage in decarbonising heat–comprehensive optimisation of future renewable energy value chains. *Applied Energy*, 233:854–893.

Sánchez, F. G., Gimmi, T., Jurányi, F., Loon, L. V., and Diamond, L. W. (2009). Linking the diffusion of water in compacted clays at two different time scales: Tracer through-diffusion and quasielastic neutron scattering. *Environmental science & technology*, 43(10):3487–3493.

Sander, R. (2015). Compilation of Henry's law constants (version 4.0) for water as solvent. *Atmospheric Chemistry and Physics*, 15(8):4399–4981.

Santos, J., Xu, D., Jo, H., Landry, C., Prodanović, M., and Pyrcz, M. (2020). PoreFlow-Net: A 3D convolutional neural network to predict fluid flow through porous media. *Advances in Water Resources*, 138. cited By 1.

Sarkisov, L. and Monson, P. (2001). Modeling of adsorption and desorption in pores of simple geometry using molecular dynamics. *Langmuir*, 17(24):7600–7604.

Sato, H. (2000). The effect of pore structural factors on diffusion in compacted sodium bentonite. *MRS Online Proceedings Library (OPL)*, 663.

Savoye, S., Beaucaire, C., Fayette, A., Herbette, M., and Coelho, D. (2012). Mobility of cesium through the callovo-oxfordian claystones under partially saturated conditions. *Environmental Science and Technology*, 46:2633–2641.

Savoye, S., L, M. J., and Bensenouci, F. (2008). Transfers through argillaceous rocks over large space and time scales: insights given by water stable isotopes. *Physics and Chemistry of the Earth, Parts A/B/C*, 33:67– 74.

Savoye, S., Page, J., Puente, C., Imbert, C., and Coelho, D. (2010a). New experimental approach for studying diffusion through an intact and unsaturated medium: a case study with callovo-oxfordian argillite. *Environmental science & technology*, 44(10):3698–3704.

Savoye, S., Page, J., Puente, C., Imbert, C., and Coelho, D. (2010b). New experimental approach for studying diffusion through an intact and unsaturated medium: a case study with callovo-oxfordian argillite. *Environmental science & technology*, 44(10):3698–3704.

Savoye, S., Rajyaguru, A., Macé, N., Lefèvre, S., Spir, G., and Robinet, J. C. (2018). How mobile is tritiated water through unsaturated cement-based materials? new insights from two complementary approaches. *Applied Radiation and Isotopes*, 139:98–106.

Schaefer, C., Arands, R., Van der Sloot, H., and Kosson, D. (1997). Modeling of the gaseous diffusion coefficient through unsaturated soil systems. *Journal of contaminant hydrology*, 29(1):1–21.

Scheibe, T. D., Perkins, W. A., Richmond, M. C., McKinley, M. I., Romero-Gomez, P. D., Oostrom, M., Wietsma, T. W., Serkowski, J. A., and Zachara, J. M. (2015). Pore-scale and multiscale numerical simulation of flow and transport in a laboratory-scale column. *Water Resources Research*, 51(2):1023–1035.

Scheidegger, A. (1974). *The physics of flow through porous media*. University of Toronto Press, Toronto, 3rd edition.

Segura, J. and Carol, I. (2004). On zero-thickness interface elements for diffusion problems. *International journal for numerical and analytical methods in geomechanics*, 28(9):947–962.

Segura, J. M. and Carol, I. (2008a). Coupled HM analysis using zero-thickness interface elements with double nodes. Part I: Theoretical model. *International Journal for Numerical and Analytical Methods in Geomechanics*, 32(18):2083–2101.

Segura, J. M. and Carol, I. (2008b). Coupled HM analysis using zero-thickness interface elements with double nodes—Part II: Verification and application. *International Journal for Numerical and Analytical Methods in Geomechanics*, 32(18):2103–2123.

Sengers, J. and Watson, J. T. R. (1986). Improved international formulations for the viscosity and thermal conductivity of water substance. *Journal of physical and chemical reference data*, 15(4):1291–1314.

Seyedi, D., Armand, G., and Noiret, A. (2017). "Transverse Action" – A model benchmark exercise for numerical analysis of the Callovo-Oxfordian claystone hydromechanical response to excavation operations. *Computers and Geotechnics*, 85:287–305. cited By 12.

Shao, H., Hesser, J., Kolditz, O., and Wang, W. (2019). Hydraulic characterisation of clay rock under consideration of coupled THM properties. *Environmental Science and Engineering*, pages 33–40. cited By 0.

Shao, J. F., Zhu, Q. Z., and Su, K. (2003). Modeling of creep in rock materials in terms of material degradation. *Computers and Geotechnics*, 30(7):549–555.

Shaw, R. E. (2013). Gas Generation and Migration, International Symposium and Workshop. In *Conference Book*. cited By 0.

Shimmo, M., Saarnio, K., Aalto, P., Hartonen, K., Hyötyläinen, T., Kulmala, M., and Riekkola, M.-L. (2004). Particle size distribution and gas-particle partition of polycyclic aromatic hydrocarbons in helsinki urban area. *Journal of Atmospheric Chemistry*, 47(3):223.

Sim, J. and Reid, N. (1999). Statistical inference by confidence intervals: Issues of interpretation and utilization. *Physical Therapy*, 79:186–195.

Simonnin, P., Noetinger, B., Nieto-Draghi, C., Marry, V., and Rotenberg, B. (2017). Diffusion under confinement: Hydrodynamic finite-size effects in simulation. *Journal of Chemical Theory and Computation*, 13(6):2881–2889.

Sing, K. (2001). The use of nitrogen adsorption for the characterisation of porous materials. *Colloids and Surfaces A: Physicochemical and Engineering Aspects*, 187-188:3–9.

Skoulidas, A. I., Ackerman, D. M., Johnson, J. K., and Sholl, D. S. (2002). Rapid transport of gases in carbon nanotubes. *Physical review letters*, 89(18):185901.

Slattery, J. C. and Bird, R. B. (1958). Calculation of the diffusion coefficient of dilute gases and of the self-diffusion coefficient of dense gases. *AIChE Journal*, 4(2):137–142.

Small, J. S., Nykyri, M., Vikman, M., Itävaara, M., and Heikinheimo, L. (2017). The biogeochemistry of gas generation from low-level nuclear waste: Modelling after 18 years study under in situ conditions. *Applied Geochemistry*, 84:360–372.

Smedes, F., Geertsma, R. W., Zande, T. v. d., and Booij, K. (2009). Polymer- water partition coefficients of hydrophobic compounds for passive sampling: Application of cosolvent models for validation. *Environmental science & technology*, 43(18):7047–7054.

Smirnov, G. S. and Stegailov, V. V. (2013). Toward determination of the new hydrogen hydrate clathrate structures. *The Journal of Physical Chemistry Letters*, 4(21):3560–3564.

Smit, R. J., Brekelmans, W. A., and Meijer, H. E. (1998). Prediction of the mechanical behavior of nonlinear heterogeneous systems by multi-level finite element modeling. *Computer Methods in Applied Mechanics and Engineering*, 155(1-2):181–192.

Smith, D. E. and Dang, L. X. (1994). Computer simulations of nacl association in polarizable water. *The Journal of Chemical Physics*, 100(5):3757–3766.

Sobol, I. M. (2001). Global sensitivity indices for nonlinear mathematical models and their Monte Carlo estimates. *Mathematics and Computers in Simulation*, 55(1-3):271–280.

Song, H., Corman, G., and Collin, F. (2023). Thermal Impact on the Excavation Damage Zone Around a Supported Drift Using the 2nd Gradient Model. *Rock Mechanics and Rock Engineering*, (0123456789).

Song, J. and Zhang, D. (2013). Comprehensive review of caprock-sealing mechanisms for geologic carbon sequestration. *Environmental science & technology*, 47(1):9–22.

Song, Y., Davy, C., and Troadec, D. (2016). Gas breakthrough pressure (gbp), through claystones: Correlation with fib/sem imaging of the pore volume. *Oil Gas Sci. Technol. - Rev. IFP Energies nouvelles*, 71:51.

Spaid, M. A. and Phelan Jr, F. R. (1997). Lattice boltzmann methods for modeling microscale flow in fibrous porous media. *Physics of fluids*, 9(9):2468–2474.

Sposito, G. et al. (1984). *The surface chemistry of soils*. Oxford university press.

Sposito, G., Skipper, N. T., Sutton, R., Park, S.-h., Soper, A. K., and Greathouse, J. A. (1999). Surface geochemistry of the clay minerals. *Proceedings of the National Academy of Sciences*, 96(7):3358–3364.

Squires, T. M. and Quake, S. R. (2005). Microfluidics: Fluid physics at the nanoliter scale. *Reviews of modern physics*, 77(3):977.

Srinivasan, S., Karra, S., Hyman, J., Viswanathan, H., and Srinivasan, G. (2019). Model reduction for fractured porous media: a machine learning approach for identifying main flow pathways. *Computational Geosciences*, 23(3):617–629. cited By 2.

Staikova, M., Wania, F., and Donaldson, D. (2004). Molecular polarizability as a single-parameter predictor of vapour pressures and octanol–air partitioning coefficients of non-polar compounds: a priori approach and results. *Atmospheric Environment*, 38(2):213–225.

Stavropoulou, E., Andò, E., Roubin, E., Lenoir, N., Tengattini, A., Briffaut, M., and Bésuelle, P. (2020). Dynamics of water absorption in callovo-oxfordian claystone revealed with multimodal x-ray and neutron tomography. *Frontiers in Earth Science*, 8:6.

Steefel, C., Appelo, C., Arora, B., Jacques, D., Kalbacher, T., Kolditz, O., Lagneau, V., Lichtner, P., Mayer, K., Meeussen, J., Molins, S., Moulton, D., Shao, H., Šimůnek, J., Spycher, N., Yabusaki, S., and Yeh, G. (2015). Reactive transport codes for subsurface environmental simulation. *Computational Geosciences*, 19(3):445–478. cited By 232.

Stefanou, G. (2009). The stochastic finite element method: Past, present and future. *Computer Methods in Applied Mechanics and Engineering*, 198(9-12):1031–1051.

Stiel, L. I. and Thodos, G. (1965). The self-diffusivity of dilute and dense gases. *The Canadian Journal of Chemical Engineering*, 43(4):186–190.

Strangfeld, C. (2021). Quantification of the knudsen effect on the effective gas diffusion coefficient in partially saturated pore distributions. *Advanced Engineering Materials*, 23(10):2100106.

Succi, S. (2001). *The lattice Boltzmann equation: for fluid dynamics and beyond*. Oxford university press.

Sui, H., Yao, J., and Zhang, L. (2015). Molecular simulation of shale gas adsorption and diffusion in clay nanopores. *Computation*, 3(4):687–700.

Sukop, M. (2006). Dt thorne, jr. lattice boltzmann modeling lattice boltzmann modeling.

Sukop, M. C. and Or, D. (2004). Lattice boltzmann method for modeling liquid-vapor interface configurations in porous media. *Water Resources Research*, 40(1).

Sun, L., Ling, C. Y., Lavikainen, L. P., Hirvi, J. T., Kasa, S., and Pakkanen, T. A. (2016). Influence of layer charge and charge location on the swelling pressure of dioctahedral smectites. *Chemical Physics*, 473:40–45.

Surblys, D., Matsubara, H., Kikugawa, G., and Ohara, T. (2019). Application of atomic stress to compute heat flux via molecular dynamics for systems with many-body interactions. *Physical Review E*, 99(5):051301.

Surblys, D., Matsubara, H., Kikugawa, G., and Ohara, T. (2021). Methodology and meaning of computing heat flux via atomic stress in systems with constraint dynamics. *Journal of Applied Physics*, 130(21):215104.

Suter, J. L., Anderson, R. L., Greenwell, H. C., and Coveney, P. V. (2009). Recent advances in large-scale atomistic and coarse-grained molecular dynamics simulation of clay minerals. *Journal of Materials Chemistry*, 19(17):2482–2493.

Suter, J. L., Coveney, P. V., Greenwell, H. C., and Thyveetil, M.-A. (2007). Large-scale molecular dynamics study of montmorillonite clay: emergence of undulatory fluctuations and determination of material properties. *The Journal of Physical Chemistry C*, 111(23):8248–8259.

Sutton, R. and Sposito, G. (2001). Molecular simulation of interlayer structure and dynamics in 12.4 å cs-smectite hydrates. *Journal of Colloid and Interface Science*, 237(2):174–184.

Suzuki, S., Sato, H., Ishidera, T., and Fujii, N. (2004). Study on anisotropy of effective diffusion coefficient and activation energy for deuterated water in compacted sodium bentonite. *Journal of Contaminant Hydrology*, 68(1-2):23–37.

SYSTAT-SOFTWARE, I. (2002). Table curve 2d - automated curve fitting and equation discovery.

Szczerba, M., Kalinichev, A. G., and Kowalik, M. (2020). Intrinsic hydrophobicity of smectite basal surfaces quantitatively probed by molecular dynamics simulations. *Applied Clay Science*, 188:105497.

Talandier, J. (2005). La production et le transfert de gaz dans un stockage et dans la couche du Callovo-Oxfordien - Lien avec le transitoire hydraulique - Site de Meuse / Haute-Marne. Rapport Andra n° C.NT.ASCM.03.0042. Technical report, Andra.

Tamayo-Mas, E., Harrington, J., and Graham, C. (2018). On modelling of consolidation processes in geological materials. *International Journal of Engineering Science*, 131:61 – 79.

Tang, C.-S., Pei, X.-J., Wang, D.-Y., Shi, B., and Li, J. (2015). Tensile strength of compacted clayey soil. *Journal of Geotechnical and Geoenvironmental Engineering*, 141(4):04014122.

Tarkowski, R. (2019). Underground hydrogen storage: Characteristics and prospects. *Renewable and Sustainable Energy Reviews*, 105:86–94.

Taron, J., Hickman, S., Ingebritsen, S., and Williams, C. (2014). Using a fully coupled, open-source THM simulator to examine the role of thermal stresses in shear stimulation of enhanced geothermal systems. volume 1, pages 525–533. cited By 5.

Tartakovsky, A. M. and Meakin, P. (2006). Pore scale modeling of immiscible and miscible fluid flows using smoothed particle hydrodynamics. *Advances in Water Resources*, 29(10):1464–1478.

Thiery, J., Rodts, D., Weitz, D., and Coussot, P. (2017). Drying regimes in homogeneous porous media from macro- to nanoscale. *Phys. Rev. Fluids*, 2:074201.

Thiyam, P., Parashar, P., Shajesh, K., Persson, C., Schaden, M., Brevik, I., Parsons, D. F., Milton, K. A., Malyi, O. I., and Boström, M. (2015a). Anisotropic contribution to the van der waals and the casimir-polder energies for co 2 and ch 4 molecules near surfaces and thin films. *Physical Review A*, 92(5):052704.

Thiyam, P., Persson, C., Parsons, D., Huang, D., Buhmann, S., and Boström, M. (2015b). Trends of co2 adsorption on cellulose due to van der waals forces. *Colloids and Surfaces A: Physicochemical and Engineering Aspects*, 470:316–321.

Thiyam, P., Persson, C., Sernelius, B. E., Parsons, D. F., Malthe-Sørenssen, A., and Boström, M. (2014). Intermolecular casimir-polder forces in water and near surfaces. *Physical Review E*, 90(3):032122.

Thompson, A. P., Plimpton, S. J., and Mattson, W. (2009). General formulation of pressure and stress tensor for arbitrary many-body interaction potentials under periodic boundary conditions. *The Journal of chemical physics*, 131(15):154107.

Thomson, P.-R., Aituar-Zhakupova, A., and Hier-Majumder, S. (2018). Image segmentation and analysis of pore network geometry in two natural sandstones. *Frontiers in Earth Science*, 6. Cited by: 35; All Open Access, Gold Open Access.

Thorstenson, D. and Pollock, D. (1989). Gas transport in unsaturated porous media: The adequacy of fick's law. *Reviews of Geophysics*, 27(1):61–78.

Timm, K., Kusumaatmaja, H., Kuzmin, A., Shardt, O., Silva, G., and Viggen, E. (2016). The lattice boltzmann method: principles and practice. *Cham, Switzerland: Springer International Publishing AG*.

Tinet, A.-J., Corlay, Q., Collon, P., Golfier, F., and Kalo, K. (2020). Comparison of various 3d pore space reconstruction methods and implications on transport properties of nanoporous rocks. *Advances in Water Resources*, 141. Cited by: 6; All Open Access, Bronze Open Access, Green Open Access.

Tomadakis, M. M. and Sotirchos, S. V. (1993). Ordinary and transition regime diffusion in random fiber structures. *AIChE Journal*, 39(3):397–412.

Tonon, F., Bernardini, A., and Mammino, A. (2000). Reliability analysis of rock mass response by means of Random Set Theory. *Reliability Engineering and System Safety*, 70(3):263–282.

Toprak, E., Olivella, S., and Pintado, X. (2020). Modelling engineered barriers for spent nuclear fuel repository using a double-structure model for pellets. *Environmental Geotechnics*, 7(1):72–94. cited By 10.

Torgersen, T., Kennedy, B., and van Soest, M. (2004). Diffusive separation of noble gases and noble gas abundance patterns in sedimentary rocks. *Earth and Planetary Science Letters*, 226(3-4):477–489.

Tournassat, C., Bourg, I. C., Holmboe, M., Sposito, G., and Steefel, C. I. (2016). Molecular dynamics simulations of anion exclusion in clay interlayer nanopores. *Clays and Clay Minerals*, 64(4):374–388.

Trabelsi, H., Romero, E., and Jamei, M. (2018). Tensile strength during drying of remoulded and compacted clay: The role of fabric and water retention. *Applied Clay Science*, 162:57–68.

Tsang, C., Bernier, F., and Davies, C. (2005a). Geohydromechanical processes in the Excavation Damaged Zone in crystalline rock, rock salt, and indurated and plastic clays - In the context of radioactive waste disposal. *International Journal of Rock Mechanics and Mining Sciences*, 42(1):109–125.

Tsang, C.-F., Bernier, F., and Davies, C. (2005b). Geohydromechanical processes in the excavation damaged zone in crystalline rock, rock salt, and indurated and plastic clays—in the context of radioactive waste disposal. *International Journal of Rock Mechanics and Mining Sciences*, 42(1):109–125.

Tsang, C. F., Neretnieks, I., and Tsang, Y. (2015). Hydrologic issues associated with nuclear waste repositories. *Water Resources Research*, 51:6923–6972.

Tsang, Y. W. and Witherspoon, P. (1981). Hydromechanical behavior of a deformable rock fracture subject to normal stress. *Journal of Geophysical Research: Solid Earth*, 86(B10):9287–9298.

Tse, J. S., Klein, M. L., and McDonald, I. R. (1984). Computer simulation studies of the structure i clathrate hydrates of methane, tetrafluoromethane, cyclopropane, and ethylene oxide. *The Journal of chemical physics*, 81(12):6146–6153.

Tsimpanogiannis, I. N., Moultos, O. A., Franco, L. F., Spera, M. B. d. M., Erdős, M., and Economou, I. G. (2019). Self-diffusion coefficient of bulk and confined water: a critical review of classical molecular simulation studies. *Molecular Simulation*, 45(4-5):425–453.

Underwood, T. R. and Bourg, I. C. (2020). Large-scale molecular dynamics simulation of the dehydration of a suspension of smectite clay nanoparticles. *The Journal of Physical Chemistry C*, 124(6):3702–3714.

Valle, V., Bokam, P., Germaneau, A., and Hedan, S. (2019). New development of digital volume correlation for the study of fractured materials. *Experimental Mechanics*, 59(1):1 – 15.

Van Eekelen, H. A. M. (1980). Isotropic yield surfaces in three dimensions for use in soil mechanics. *International Journal for Numerical and Analytical Methods in Geomechanics*, 4(1):89–101.

Van Geet, M., Bastiaens, W., and Ortiz, L. (2008). Self-sealing capacity of argillaceous rocks: Review of laboratory results obtained from the selfrac project. *Physics and Chemistry of the Earth, Parts A/B/C*, 33:S396–S406. Clays in Natural & Engineered Barriers for Radioactive Waste Confinement.

Van Geet, M., Bastiaens, W., and Ortiz, L. (2008). Self-sealing capacity of argillaceous rocks: review of laboratory results obtained from the selfrac project. *Physics and Chemistry of the Earth, Parts A/B/C*, 33:S396–S406.

van Genuchten, M. (1980). Predicting the hydraulic conductivity of unsaturated soils. *Soil. Sci. Soc. Am. J*, 44(5):892–898.

Van Genuchten, M. T. (1980). A closed-form equation for predicting the hydraulic conductivity of unsaturated soils. *Soil science society of America journal*, 44(5):892–898.

Van Loon, L., Mueller, W., Gimmi, T., and Iijima, K. (2002). Activation energy of the self-diffusion of water in compacted clay systems: a case study with opalinus clay.

Van Loon, L., Müller, W., and Iijima, K. (2005). Activation energies of the self-diffusion of hto, 22na+ and 36cl- in a highly compacted argillaceous rock (opalinus clay). *Applied Geochemistry*, 20(5):961–972.

Van Milligen, B. P., Bons, P., Carreras, B. A., and Sanchez, R. (2005). On the applicability of fick's law to diffusion in inhomogeneous systems. *European journal of physics*, 26(5):913.

Vandenberghe, N. (1978). Sedimentology of the Boom Clay (Rupelian) in Belgium. *Verhandeling Koninklijke Academie voor Wetenschappen, Letteren en Schone Kunsten van België, Klasse Wetenschappen, XL/147*, page 147.

Vandenberghe, N., Craen, M. D., and Wouters, L. (2014). The boom clay geology from sedimentation to present-day occurrence - a review. *Memoirs of the Geological Survey of Belgium*, 60:76.

Vargaftik, N., Volkov, B., and Voljak, L. (1983). International tables of the surface tension of water. *Journal of Physical and Chemical Reference Data*, 12(3):817–820.

Vasconcelos, I. F., Bunker, B. A., and Cygan, R. T. (2007). Molecular dynamics modeling of ion adsorption to the basal surfaces of kaolinite. *The Journal of Physical Chemistry C*, 111(18):6753–6762.

Vasilyeva, M., Leung, W., Chung, E., Efendiev, Y., and Wheeler, M. (2020). Learning macroscopic parameters in nonlinear multiscale simulations using nonlocal multicontinua upscaling techniques. *Journal of Computational Physics*, 412. cited By 0.

Villar, M., García-Siñeriz, J., Bárcena, I., and Lloret, A. (2005). State of the bentonite barrier after five years operation of an in situ test simulating a high level radioactive waste repository. *Engineering Geology*, 80(3-4):175–198.

Villar, M. V. and Gómez-Espina, R. (2009). Report on thermo-hydro-mechanical laboratory tests performed by ciemat on febex bentonite 2004-2008. Report, CIEMAT.

Villard, P., Chevalier, B., Le Hello, B., and Combe, G. (2009). Coupling between finite and discrete element methods for the modelling of earth structures reinforced by geosynthetic. *Computers and Geotechnics*, 36(5):709–717.

Vinsot, A., Appelo, C. A. J., Lundy, M., Wechner, S., Cailteau-Fischbach, C., de Donato, P., Pironon, J., Lettry, Y., Lerouge, C., and De Canniere, P. (2018). Natural gas extraction and artificial gas injection experiments in opalinus clay, mont terri rock laboratory (switzerland). In *Mont Terri Rock Laboratory, 20 Years*, pages 377–392. Springer.

Vogel, E. (2010). Reference viscosity of argon at low density in the temperature range from 290 k to 680 k. *International Journal of Thermophysics*, 31:447–461.

Vogel, H.-J., Tolke, J., Schulz, V., Krafczyk, M., and Roth, K. (2005). Comparison of a lattice-boltzmann model, a full-morphology model, and a pore network model for determining capillary pressure-saturation relationships. *Vadose Zone Journal*, 4(2):380–388.

Volckaert, G., Bernier, F., Sillen, X., Van Geet, M., Mayor, J. C., Göbel, I., Blümling, P., Frieg, B., and Su, K. (2004). Similarities and Differences in the Behaviour of Plastic and Indurated Clays. In *6th European Commission Conference on the Management and Disposal of Radioactive Waste (Euradwaste'04), Community Policy and Research & Training Activities*, pages 281–291.

Volckaert, G., Ortiz, L., Canniere, P. D., Put, M., Horseman, S. T., Harrington, J. F., Fioravante, V., and Impey, M. (1995a). MEGAS: modelling and experiments on GAS migration in repository host rocks. Final report phase 1. Technical report, SCK-CEN.

Volckaert, G., Ortiz, L., Canniere, P. D., Put, M., Horseman, S. T., Harrington, J. F., Fioravante, V., and Impey, M. (1995b). MEGAS: modelling and experiments on GAS migration in repository host rocks. Final report phase 1. Technical report, Eur. Comm., [Rep.] EUR 16235 EN.

Volckaert, G., Ortiz, L., De Cannière, P., Put, M., Horseman, S., Harrington, J., Fioravante, V., and M, I. (1995c). Megas modelling and experiments on gas migration in repository host rocks. final report phase 1. eur-16235. Report EUR16235.

Vomvoris, S., Claudel, A., Blechschmidt, I., and Muller, H. (2013). The swiss radioactive waste management program-brief history, status, and outlook. *Journal of Nuclear Fuel Cycle and Waste Technology*, 1(1):9–27.

Vulava, V. M., Perry, E. B., Romanek, C. S., and Seaman, J. C. (2002). Dissolved gases as partitioning tracers for determination of hydrogeological parameters. *Environmental science & technology*, 36(2):254–262.

Walsh, S. D. and Saar, M. O. (2010). Macroscale lattice-boltzmann methods for low peclet number solute and heat transport in heterogeneous porous media. *Water Resources Research*, 46(7).

Wang, C., Talandier, J., and Skoczylas, F. (2022a). Swelling and fluid transport of re-sealed callovo–oxfordian claystone. *Rock Mechanics and Rock Engineering*, pages 1–16.

Wang, H., Cui, Y.-J., Vu, M. N., Talandier, J., and Conil, N. (2022b). Fracture effect on the hydro-mechanical behaviour of callovo-oxfordian claystone. *Engineering Geology*, 303:106674.

Wang, H., de La Vaissière, R., Vu, M.-N., La Borderie, C., and Gallipoli, D. (2022c). Numerical modelling and in-situ experiment for self-sealing of the induced fracture network of drift into the callovo-oxfordian claystone during a hydration process. *Computers and Geotechnics*, 141:104487.

Wang, J., Chen, L., Kang, Q., and Rahman, S. S. (2016a). The lattice boltzmann method for isothermal micro-gaseous flow and its application in shale gas flow: A review. *International Journal of Heat and Mass Transfer*, 95:94–108.

Wang, J., Kalinichev, A. G., and Kirkpatrick, R. J. (2006). Effects of substrate structure and composition on the structure, dynamics, and energetics of water at mineral surfaces: A molecular dynamics modeling study. *Geochimica et cosmochimica acta*, 70(3):562–582.

Wang, J.-J., Zhu, J.-G., Chiu, C., and Zhang, H. (2007). Experimental study on fracture toughness and tensile strength of a clay. *Engineering Geology*, 94(1-2):65–75.

Wang, L., Golfier, F., Tinet, A.-J., Chen, W., and Vuik, C. (2022d). An efficient adaptative implicit scheme with equivalent continuum approach for two-phase flow in fractured vuggy porous media. *Advances in Water Resources*, 163:104186.

Wang, S., Feng, Q., Zha, M., Javadpour, F., and Hu, Q. (2018). Supercritical methane diffusion in shale nanopores: effects of pressure, mineral types, and moisture content. *Energy & fuels*, 32(1):169–180.

Wang, S., Javadpour, F., and Feng, Q. (2016b). Fast mass transport of oil and supercritical carbon dioxide through organic nanopores in shale. *Fuel*, 181:741–758.

Wang, S., Javadpour, F., and Feng, Q. (2016c). Molecular dynamics simulations of oil transport through inorganic nanopores in shale. *Fuel*, 171:74–86.

Wang, S., Javadpour, F., and Feng, Q. (2016d). Molecular dynamics simulations of oil transport through inorganic nanopores in shale. *Fuel*, 171:74–86.

Wang, W. and Kolditz, O. (2007). Object-oriented finite element analysis of thermo-hydro-mechanical (THM) problems in porous media. *International Journal for Numerical Methods in Engineering*, 69(1):162–201. cited By 86.

Wang, W., Shao, H., Nagel, T., and Kolditz, O. (2020a). Analysis of coupled thermal-hydro-mechanical processes during small scale in-situ heater experiment in Callovo-Oxfordian clay rock introducing a failure-index permeability model. *International Journal of Rock Mechanics and Mining Sciences*, revised manuscript under review.

Wang, W., Shao, H., Nagel, T., and Kolditz, O. (2021). Analysis of coupled thermal-hydro-mechanical processes during small scale in situ heater experiment in Callovo-Oxfordian clay rock introducing a failure-index permeability model. *International Journal of Rock Mechanics and Mining Sciences*.

Wang, X., Shao, H., Hesser, J., Zhang, C., Wang, W., and Kolditz, O. (2014). Numerical analysis of thermal impact on hydro-mechanical properties of clay. *Journal of Rock Mechanics and Geotechnical Engineering*, 6(5):405–416. cited By 12.

Wang, Y., Chung, T., Armstrong, R., McClure, J., Ramstad, T., and Mostaghimi, P. (2020b). Accelerated computation of relative permeability by coupled morphological and direct multiphase flow simulation. *Journal of Computational Physics*, 401:108966.

Wanner, P. and Hunkeler, D. (2019). Molecular dynamic simulations of carbon and chlorine isotopologue fractionation of chlorohydrocarbons during diffusion in liquid water. *Environmental Science & Technology Letters*, 6(11):681–685.

Wasserman, E., Wood, B., and Brodhol, J. (1995). The static dielectric constant of water at pressures up to 20 kbar and temperatures to 1273 k: experiment, simulations, and empirical equations. *Geochimica et cosmochimica acta*, 59(1):1–6.

Watanabe, H. and Iizuka, K. (1985). The influence of dissolved gases on the density of water. *Metrologia*, 21(1):19.

Weast, R. (1987). *Handbook of Chemistry and Physics*, volume 51. CRC Press, Cleveland, The United States.

Webb, S. W. and Pruess, K. (2003). The use of fick's law for modeling trace gas diffusion in porous media. *Transport in porous media*, 51(3):327–341.

Wei, X., Wang, G., Massarotto, P., Golding, S., and Rudolph, V. (2007). Numerical simulation of multicomponent gas diffusion and flow in coals for co2 enhanced coalbed methane recovery. *Chemical engineering science*, 62(16):4193–4203.

Wemaere, I., Marivoet, J., and Labat, S. (2008). Hydraulic conductivity variability of the boom clay in north-east belgium based on four core drilled boreholes. *Physics and Chemistry of the Earth, Parts A/B/C*, 33:S24–S36.

Wenk, H. R., Voltolini, M., Mazurek, M., Van Loon, L. R., and Vinsot, A. (2008). Preferred orientations and anisotropy in shales: Callovo-oxfordian shale (France) and opalinus clay (Switzerland). *Clays and Clay Minerals*, 56(3):285–306.

Wersin, P., Van Loon, L., Soler, J., Yllera, A., Eikenberg, J., Gimmi, T., Hernán, P., and Boisson, J.-Y. (2004). Long-term diffusion experiment at mont terri: first results from field and laboratory data. *Applied Clay Science*, 26(1-4):123–135.

Wesenauer, F., Jordan, C., Azam, M., Harasek, M., and Winter, F. (2021). Considerations on temperature dependent effective diffusion and permeability of natural clays. *Materials*, 14(17):4942.

Wick, C. D., Siepmann, J. I., and Schure, M. R. (2003). Temperature dependence of transfer properties: Importance of heat capacity effects. *The Journal of Physical Chemistry B*, 107(38):10623–10627.

Wileveau, Y., Cornet, F. H., Desroches, J., and Blumling, P. (2007). Complete in situ stress determination in an argillite sedimentary formation. *Physics and Chemistry of the Earth*, 32(8-14):866–878.

Wilhelm, E., Battino, R., and Wilcock, R. J. (1977). Low-pressure solubility of gases in liquid water. *Chemical reviews*, 77(2):219–262.

Wise, D. L. and Houghton, G. (1966a). The diffusion coefficients of ten slightly soluble gases in water at 10–60 c. *Chemical Engineering Science*, 21(11):999–1010.

Wise, D. L. and Houghton, G. (1966b). The diffusion coefficients of ten slightly soluble gases in water at 10–60 c. *Chemical Engineering Science*, 21(11):999–1010.

Wiseall, A., Graham, C., Zihms, S., Harrington, J., Cuss, R., Gregory, S., and Shaw, R. (2015a). Properties and Behaviour of the Boom Clay Formation within a Dutch Repository Concept. OPERA-PU-BGS615. Technical report, British Geological Survey.

Wiseall, A. C., Cuss, R., and Hough, E. (2019). Visualising hydraulic fractures in bedded and fractured shales: A series of analogue experiments. *5th International Conference on Fault and Top Seals 2019*, (September 2019):1–5.

Wiseall, A. C., Cuss, R. J., Graham, C. C., and Harrington, J. F. (2015b). The visualization of flow paths in experimental studies of clay-rich materials. *Mineralogical Magazine*, 79(6):1335–1342.

Witherspoon, P. A., Wang, J. S. Y., Iwai, K., and Gale, J. E. (1980). Validity of cubic law for fluid flow in a deformable rock fracture. *Water Resour. Res.*, 16(6):1016–1024.

Woessner, D., Snowden Jr, B., George, R., and Melrose, J. (1969). Dense gas diffusion coefficients for the methane-propane system. *Industrial & Engineering Chemistry Fundamentals*, 8(4):779–786.

Wolf-Gladrow, D. A. (2004). *Lattice-gas cellular automata and lattice Boltzmann models: an introduction*. Springer.

Wollenweber, J., Alles, S., Busch, A., Krooss, B. M., Stanjek, H., and Littke, R. (2010). Experimental investigation of the co2 sealing efficiency of caprocks. *International Journal of Greenhouse Gas Control*, 4(2):231–241.

Xu, T., Senger, R., and Finsterle, S. (2008). Corrosion-induced gas generation in a nuclear waste repository: Reactive geochemistry and multiphase flow effects. *Applied Geochemistry*, 23(12):3423–3433.

Xu, W., Shao, H., Hesser, J., Wang, W., Kolditz, O., and Popp, T. (2011). Simulation of dilatancy-controlled gas migration process in saturated argillaceous rock. *Computational Geomechanics, COMGEO II - Proceedings of the 2nd International Symposium on Computational Geomechanics*, pages 693–703. cited By 5.

Xu, W., Shao, H., Hesser, J., Wang, W., Schuster, K., and Kolditz, O. (2013a). Coupled multiphase flow and elasto-plastic modelling of in-situ gas injection experiments in saturated claystone (Mont Terri Rock Laboratory). *Engineering Geology*, 157:55–68. cited By 21.

Xu, W., Shao, H., Marschall, P., Hesser, J., and Kolditz, O. (2013b). Analysis of flow path around the sealing section HG-A experiment in the Mont Terri Rock Laboratory. *Environmental Earth Sciences*, 70(7):3363–3380. cited By 14.

Yang, Y. and Aplin, A. C. (2010). A permeability-porosity relationship for mudstones. *Marine and Petroleum Geology*, 27(8):1692–1697.

Yang, Y., Wang, K., Zhang, L., Sun, H., Zhang, K., and Ma, J. (2019). Pore-scale simulation of shale oil flow based on pore network model. *Fuel*, 251:683–692.

Yang, Y. and Wang, M. (2018). Pore-scale study of thermal effects on ion diffusion in clay with inhomogeneous surface charge. *Journal of colloid and interface science*, 514:443–451.

Yao, X., Liu, Y., Cao, Q., Li, J., Huang, R., Woodcock, R., Paget, M., Wang, J., and Li, G. (2019). China Data Cube (CDC) for Big Earth Observation Data: Lessons Learned from the Design and Implementation. cited By 2.

Yeh, I.-C. and Hummer, G. (2004). System-size dependence of diffusion coefficients and viscosities from molecular dynamics simulations with periodic boundary conditions. *The Journal of Physical Chemistry B*, 108(40):15873–15879.

Yi, M., Wang, L., Cheng, Y., Wang, C., and Hu, B. (2022). Calculation of gas concentration-dependent diffusion coefficient in coal particles: Influencing mechanism of gas pressure and desorption time on diffusion behavior. *Fuel*, 320:123973.

Yin, H., Felicelli, S., and Wang, L. (2011). Simulation of a dendritic microstructure with the lattice boltzmann and cellular automaton methods. *Acta Materialia*, 59(8):3124–3136.

Yin, Y., Qu, Z., and Zhang, J. (2019a). Multiple diffusion mechanisms of shale gas in nanoporous organic matter predicted by the local diffusivity lattice boltzmann model. *International Journal of Heat and Mass Transfer*, 143:118571.

Yin, Y., Qu, Z., and Zhang, J. (2019b). Multiple diffusion mechanisms of shale gas in nanoporous organic matter predicted by the local diffusivity lattice boltzmann model. *International Journal of Heat and Mass Transfer*, 143:118571.

Yong, R. N., Warkentin, B. P., Phadungchewit, Y., and Galvez, R. (1990). Buffer capacity and lead retention in some clay materials. *Water, Air, and Soil Pollution*, 53:53–67.

Yoshida, H., Kinjo, T., and Washizu, H. (2014a). Coupled lattice boltzmann method for simulating electrokinetic flows: A localized scheme for the nernst–plank model. *Communications in Nonlinear Science and Numerical Simulation*, 19(10):3570–3590.

Yoshida, H., Kinjo, T., and Washizu, H. (2014b). Coupled lattice boltzmann method for simulating electrokinetic flows: A localized scheme for the nernst-plank model. *Communications in Nonlinear Science and Numerical Simulation*, 19(10):3570 – 3590. Cited by: 43.

Yoshioka, K., Naumov, D., and Kolditz, O. (2020). On crack opening computation in variational phase-field models for fracture. *Computer Methods in Applied Mechanics and Engineering*, 369. cited By 0.

Yoshioka, K., Parisio, F., Naumov, D., Lu, R., Kolditz, O., and Nagel, T. (2019). Comparative verification of discrete and smeared numerical approaches for the simulation of hydraulic fracturing. *GEM - International Journal on Geomathematics*, 10(1). cited By 12.

Yu, L., Rogiers, B., Gedeon, M., Marivoet, J., De Craen, M., and Mallants, D. (2013). A critical review of laboratory and in-situ hydraulic conductivity measurements for the boom clay in belgium. *Applied Clay Science*, 75:1–12.

Yu, L. and Weetjens, E. (2009). Summary of gas generation and migration. *Current State-of-the-Art. SCK-CEN ER-106. SCK† CEN, Mol, Belgium*.

Yu, Q.-Y., Bagas, L., Yang, P.-H., and Zhang, D. (2019). GeoPyTool: A cross-platform software solution for common geological calculations and plots. *Geoscience Frontiers*, 10(4):1437–1447. cited By 1.

Yuan, S., Liu, X., and Buzzi, O. (2020). Technical aspects of mercury intrusion porosimetry for clays. *https://doi.org/10.1680/jenge.16.00039*, 8:255–263.

Yuan, W., Pan, Z., Li, X., Yang, Y., Zhao, C., Connell, L. D., Li, S., and He, J. (2014). Experimental study and modelling of methane adsorption and diffusion in shale. *Fuel*, 117:509–519.

Yven, B., Sammartino, S., Geraud, Y., Homand, F., and Villieras, F. (2007). Mineralogy, texture and porosity of callovo-oxfordian argillites of the meuse/haute-marne region (eastern paris basin). *Mémoires de la Société géologique de France*, 178(1):73–90.

Zervos, A., Papanastasiou, P., and Vardoulakis, I. (2001). A finite element displacement formulation for gradient elastoplasticity. *International Journal for Numerical Methods in Engineering*, 50(6):1369–1388.

Zhang, C.-L. (2013). Sealing of fractures in claystone. *Journal of Rock Mechanics and Geotechnical Engineering*, 5(3):214–220.

Zhang, C.-L. (2018a). Thermo-hydro-mechanical behavior of clay rock for deep geological disposal of high-level radioactive waste. *Journal of Rock Mechanics and Geotechnical Engineering*, 10(5):992–1008. cited By 6.

Zhang, C.-L. (2018b). Thermo-hydro-mechanical behavior of clay rock for deep geological disposal of high-level radioactive waste. *Journal of Rock Mechanics and Geotechnical Engineering*, 10(5):992–1008.

Zhang, C.-L. and Talandier, J. (2023). Self-sealing of fractures in indurated claystones measured by water and gas flow. *Journal of Rock Mechanics and Geotechnical Engineering*, 15(1):227–238.

Zhang, F., Cui, Y.-J., Conil, N., and Talandier, J. (2020). Assessment of swelling pressure determination methods with intact callovo-oxfordian claystone. *Rock Mechanics and Rock Engineering*, 53:1879–1888.

Zhang, J. (2011). Lattice boltzmann method for microfluidics: models and applications. *Microfluidics and Nanofluidics*, 10:1–28.

Zhang, M., Chakraborty, N., Karpyn, Z. T., Emami-Meybodi, H., and Ayala, L. F. (2021). Experimental and numerical study of gas diffusion and sorption kinetics in ultratight rocks. *Fuel*, 286:119300.

Zhang, N. and Nagel, T. (2020). Error-controlled implicit time integration of elasto-visco-plastic constitutive models for rock salt. *International Journal for Numerical and Analytical Methods in Geomechanics*, 44(8):1109–1127. cited By 0.

Zhang, X., Xiao, L., Shan, X., and Guo, L. (2014). Lattice boltzmann simulation of shale gas transport in organic nano-pores. *Scientific reports*, 4(1):4843.

Zhao, Y., Luo, M., Liu, L., Wu, J., Chen, M., and Zhang, L. (2022). Molecular dynamics simulations of shale gas transport in rough nanopores. *Journal of Petroleum Science and Engineering*, 217:110884.

Zhou, H., Jia, Y., and Shao, J. F. (2008). A unified elastic–plastic and viscoplastic damage model for quasi-brittle rocks. *International Journal of Rock Mechanics and Mining Sciences*, 45(8):1237–1251.

Zhou, J., Lu, X., and Boek, E. S. (2016). Confined water in tunnel nanopores of sepiolite: Insights from molecular simulations. *American Mineralogist*, 101(3):713–718.

Zhou, W. and Arthur, R. (2017). Near-field processes, evolution, and performance assessment in geological repository systems. In *Geological Repository Systems for Safe Disposal of Spent Nuclear Fuels and Radioactive Waste*, pages 297–318. Elsevier.

Zhou, Y., Zhang, R., Staroselsky, I., and Chen, H. (2004). Numerical simulation of laminar and turbulent buoyancy-driven flows using a lattice boltzmann based algorithm. *International journal of heat and mass transfer*, 47(22):4869–4879.

Zhu, H.-L., Wang, S.-F., Yin, G.-J., Chen, Q., Xu, F.-L., Peng, W., Tan, Y.-H., and Zhang, K. (2018a). Study of the numerical simulation of tight sandstone gas molecular diffusion based on digital core technology. *Petroleum Science*, 15(1):68–76.

Zhu, H.-L., Wang, S.-F., Yin, G.-J., Chen, Q., Xu, F.-L., Peng, W., Tan, Y.-H., and Zhang, K. (2018b). Study of the numerical simulation of tight sandstone gas molecular diffusion based on digital core technology. *Petroleum Science*, 15(1):68–76.

Zhu, Y. and Fox, P. J. (2002). Simulation of pore-scale dispersion in periodic porous media using smoothed particle hydrodynamics. *Journal of Computational Physics*, 182(2):622–645.

Zill, F., Lüdeling, C., Kolditz, O., and Nagel, T. (2021). Hydro-mechanical continuum modelling of fluid percolation through rock salt. *International Journal of Rock Mechanics and Mining Sciences*, 147:104879.

Zio, E. and Apostolakis, G. E. (1996). Two methods for the structured assessment of model uncertainty by experts in performance assessments of radioactive waste repositories. *Reliability Engineering and System Safety*, 54(2-3):225–241.

Červinka, R., Vašíček, R., Večerník, P., and Kašpar, V. (2019). Complete characterization of bentonite bcv technical report 419/2019. Report Technical Report 419/2019, .